Seismic Load Path Effects in Reinforced Concrete Bridge Columns and Wall Piers

Volume 1: Strain Limit States for RC Bridge Columns

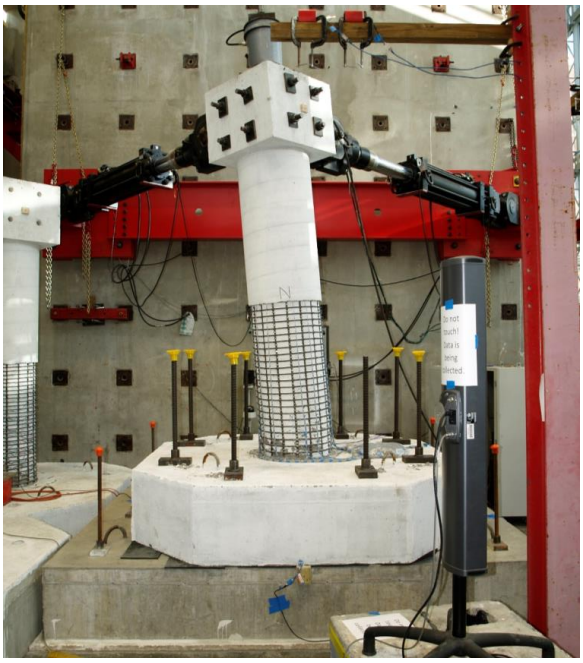

Photo of Test 11 taken by Jason Chad Goodnight, June 2017

Prepared By:
Jason Chad Goodnight, Postdoc
Mervyn J. Kowalsky, Professor
James M. Nau, Professor

Prepared For:
Alaska Department of Transportation & Public Facilities
Research, Development, and Technology Transfer
P.O. Box 112500
3132 Channel Drive
Juneau, Alaska 99811-2500

and

Federal Highway Administration
P.O. Box 21648
709 West 9th Street
Juneau, Alaska 99802-1648

REPORT DOCUMENTATION PAGE

Form approved OMB No.

Public reporting for this collection of information is estimated to average 1 hour per response, including the time for reviewing instructions, searching existing data sources, gathering and maintaining the data needed, and completing and reviewing the collection of information. Send comments regarding this burden estimate or any other aspect of this collection of information, including suggestion for reducing this burden to Washington Headquarters Services, Directorate for Information Operations and Reports, 1215 Jefferson Davis Highway, Suite 1204, Arlington, VA 22202-4302, and to the Office of Management and Budget, Paperwork Reduction Project (0704-1833), Washington, DC 20503

1. AGENCY USE ONLY (LEAVE BLANK)	2. REPORT DATE	3. REPORT TYPE AND DATES COVERED
4000(134)	June 2017	FINAL, February 2015 through June 2017

4. TITLE AND SUBTITLE
Seismic Load Path Effects in Reinforced Concrete Bridge Columns and Wall Piers
Volume 1: Strain Limit States for RC Bridge Columns

5. FUNDING NUMBERS
Federal # 4000(134)
IRIS# Z642030000

6. AUTHOR(S)
Jason Chad Goodnight
Mervyn J. Kowalsky
James M. Nau

7. PERFORMING ORGANIZATION NAME(S) AND ADDRESS(ES)
North Carolina State University

8. PERFORMING ORGANIZATION REPORT NUMBER
4000(134)

9. SPONSORING/MONITORING AGENCY NAME(S) AND ADDRESS(ES)
Alaska Department of Transportation and Public Facilities
Research, Development &Technology Transfer
3132 Channel Drive
Juneau, Alaska 99811-2500

10. SPONSORING/MONITORING AGENCY REPORT NUMBER
4000(134)

11. SUPPLEMENTARY NOTES

12a. DISTRIBUTION / AVAILABILITY STATEMENT
Copies available online at http://www.dot.alaska.gov/stwddes/research/search_lib.shtml

12b. DISTRIBUTION CODE

13. ABSTRACT (Maximum 200 words)
This report discusses the impact of bidirectional seismic load path on limit state strains and the spread of plasticity in twelve reinforced concrete bridge column tests. The main variables included longitudinal steel content, transverse steel detailing, and the bidirectional seismic load path. The tests employed an advanced instrumentation system which provided detailed strain and curvature data. This data was used to generate predictive expressions for concrete and steel strains preceding important limit states, which included: cover concrete crushing, initial yielding of confinement steel, and longitudinal bar buckling. This data was used to create a new plastic hinge method which converts curvatures at limit state strains to lateral displacements, which are needed in design. The new plastic hinge method collapses down to the accepted design approach for compression strain-displacement, while still matching the measured extent of plasticity and tensile strain-displacement relationship necessary for accurate bar buckling predictions. An effort was made to provide mean value predictions for the displacement at each limit state. These recommendations serve as input into a displacement-based design procedure to achieve a particular level of performance under a defined seismic hazard.

14. KEYWORDS :
Out-of-plane buckling stability, pier walls, structural walls, maximum tensile strain, maximum thickness, boundary elements

15. NUMBER OF PAGES
755

16. PRICE CODE
N/A

17. SECURITY CLASSIFICATION OF REPORT	18. SECURITY CLASSIFICATION OF THIS PAGE	19. SECURITY CLASSIFICATION OF ABSTRACT	20. LIMITATION OF ABSTRACT
Unclassified	Unclassified	Unclassified	None

Notice

This document is disseminated under the sponsorship of the U.S. Department of Transportation in the interest of information exchange. The U.S. Government assumes no liability for the use of the information contained in this document.

The U.S. Government does not endorse products or manufacturers. Trademarks or manufacturers' names appear in this report only because they are considered essential to the objective of the document.

Quality Assurance Statement

The Federal Highway Administration (FHWA) provides high-quality information to serve Government, industry, and the public in a manner that promotes public understanding. Standards and policies are used to ensure and maximize the quality, objectivity, utility, and integrity of its information. FHWA periodically reviews quality issues and adjusts its programs and processes to ensure continuous quality improvement.

Author's Disclaimer

Opinions and conclusions expressed or implied in the report are those of the author. They are not necessarily those of the Alaska DOT&PF or funding agencies.

SI* (MODERN METRIC) CONVERSION FACTORS

APPROXIMATE CONVERSIONS TO SI UNITS

Symbol	When You Know	Multiply By	To Find	Symbol
		LENGTH		
in	inches	25.4	millimeters	mm
ft	feet	0.305	meters	m
yd	yards	0.914	meters	m
mi	miles	1.61	kilometers	km
		AREA		
in^2	square inches	645.2	square millimeters	mm^2
ft^2	square feet	0.093	square meters	m^2
yd^2	square yard	0.836	square meters	m^2
ac	acres	0.405	hectares	ha
mi^2	square miles	2.59	square kilometers	km^2
		VOLUME		
fl oz	fluid ounces	29.57	milliliters	mL
gal	gallons	3.785	liters	L
ft^3	cubic feet	0.028	cubic meters	m^3
yd^3	cubic yards	0.765	cubic meters	m^3
	NOTE: volumes greater than 1000 L shall be shown in m^3			
		MASS		
oz	ounces	28.35	grams	g
lb	pounds	0.454	kilograms	kg
T	short tons (2000 lb)	0.907	megagrams (or "metric ton")	Mg (or "t")
		TEMPERATURE (exact degrees)		
^oF	Fahrenheit	5 (F-32)/9 or (F-32)/1.8	Celsius	^oC
		ILLUMINATION		
fc	foot-candles	10.76	lux	lx
fl	foot-Lamberts	3.426	$candela/m^2$	cd/m^2
		FORCE and PRESSURE or STRESS		
lbf	poundforce	4.45	newtons	N
lbf/in^2	poundforce per square inch	6.89	kilopascals	kPa

APPROXIMATE CONVERSIONS FROM SI UNITS

Symbol	When You Know	Multiply By	To Find	Symbol
		LENGTH		
mm	millimeters	0.039	inches	in
m	meters	3.28	feet	ft
m	meters	1.09	yards	yd
km	kilometers	0.621	miles	mi
		AREA		
mm^2	square millimeters	0.0016	square inches	in^2 m^2
square meters	10.764	square feet	ft^2 m^2	square
meters	1.195	square yards	yd^2	
ha	hectares	2.47	acres	ac
km^2	square kilometers	0.386	square miles	mi^2
		VOLUME		
mL	milliliters	0.034	fluid ounces	fl oz
L	liters	0.264	gallons	gal
m^3	cubic meters	35.314	cubic feet	ft^3 m^3
	cubic meters	1.307	cubic yards	yd^3
		MASS		
g	grams	0.035	ounces	oz
kg	kilograms	2.202	pounds	lb
Mg (or "t")	megagrams (or "metric ton")	1.103	short tons (2000 lb)	T
		TEMPERATURE (exact degrees)		
^oC	Celsius	1.8C+32	Fahrenheit	^oF
		ILLUMINATION		
lx	lux	0.0929	foot-candles	fc
cd/m^2	$candela/m^2$	0.2919	foot-Lamberts	fl
		FORCE and PRESSURE or STRESS		
N	newtons	0.225	poundforce	lbf
kPa	kilopascals	0.145	poundforce per square inch	lbf/in^2

*SI is the symbol for the International System of Units. Appropriate rounding should be made to comply with Section 4 of ASTM E380.
(Revised March 2003)

Table of Contents

List of Figures vi
List of Tables xlvii
Acknowledgements xlix
Abstract l
Summary of Findings, refer to Chapter 16 l
Chapter 1 - Introduction 1
Background on the Definition of Damage States 1
Background on Equivalent Curvature Distributions 4
Summary of (Goodnight, Kowalsky and Nau 2015) Experimental Program 6
Modified Lpr Plastic Hinge Method from (Goodnight, Kowalsky and Nau 2015a) 10
Performance Strain Limit Recommendations from (Goodnight, Kowalsky and Nau 2015b) 13
Literature Review on the Effects of Bidirectional Loading 16
(Wong, Paulay and Priestley 1993) “Response of Circular Reinforced Concrete Columns to Multi-Directional Seismic Attack” 16
(Osorio, Bairán and Marí 2012) “Effects of Biaxial Shear Loading on the Seismic Response of RC Columns” 17
(Tsuno and Park 2004) “Experimental Study of Reinforced Concrete Bridge Piers Subjected to Bi-Directional Quasi-Static Loading” 18
(Bousias, et al. 1995) “Load Path Effects in Column Biaxial Bending with Axial Force” 20
(Mazzoni and Moehle 2001) “Seismic Response of Beam-Column Joints in Double-Deck Reinforced Concrete Bridge Frames” 21
(Terzic and Stojadinovic 2015) “Evaluation of Post-Earthquake Axial Load Capacity of Circular Bridge Columns” 25
Chapter 2 - Research Approach 27
Project Scope 27
Test Matrix 27
Test Setup 31
Instrumentation 37
Specimen Design 39
Capacity Design for the Footing Considering the Hinge Relocation Repair Technique 43
Specimen and Transfer Footing Reinforcement 47
Fixture Design 54
Specimen Construction 59

Actuator Control 78
Verification of Column Displacements using String and Linear Potentiometers 80
Method of Axial Load Application 86
Chapter 3 - Material Properties and Response Prediction 87
Reinforcing Steel Properties for Tests 1-6 87
Reinforcing Steel Properties for Tests 7-12 92
Fiber Modeling In OpenSees 95
Reinforcing Steel Material in OpenSees 97
Bond SP01 Material in OpenSees 99
Concrete02 Material in OpenSees Adapted to (Mander, Priestley and Park 1988) 100
Chapter 4 - Test 1 Summary Report 103
Test 1 - Experimental Observations 113
Test 1 - Strain Data Analysis 129
North Bar Strains 129
South Bar Strains 130
East Bar Strains 137
West Bar Strains 137
Test 1 - Curvature and Strain Penetration Data 144
Test 1 - Response Predictions with Moment-Curvature and Fiber Modeling 153
Moment-Curvature Analysis and Pre-Yield Column Flexibility 153
Fiber-Based Modeling in OpenSees 159
Chapter 5 - Test 2 Summary Report 164
Test 2 - Method of Correction for Lateral Displacements 175
Test 2 - Experimental Observations 175
Test 2 - Strain Data Analysis 190
North and South Bar Strains 190
East and West Bar Strains 197
Test 2 - Curvature and Strain Penetration Data 205
Response Comparison for Nominally Identical Tests 1 and 2 215
Chapter 6 - Test 3 Summary Report 216
Test 3 - Experimental Observations 225
Test 3 - Strain Data Analysis 240
North and South Bar Strains 240

East and West Bar Strains 247
Test 3 - Curvature and Strain Penetration Data 254
Response Comparison for Nominally Identical Tests 1, 2, and 3 264
Chapter 7 - Test 4 Summary Report 266
Test 4 - Experimental Observations 277
Test 4 - Strain Data Analysis 295
North and South Bar Strains 295
East and West Bar Strains 303
Test 4 - Curvature and Strain Penetration Data 311
Response Comparison for Test 1 (0.7%) and Test 4 (1% Transverse Volumetric Steel) 321
Chapter 8 - Test 5 Summary Report 323
Test 5 - Experimental Observations 332
Test 5 - Strain Data Analysis 351
North and South Bar Strains 351
East and West Bar Strains 359
Test 5 - Curvature and Strain Penetration Data 366
Response Comparison for Tests 4 (Two-Cycle-Set) and 5 (Three-Cycle-Set) 376
Chapter 9 - Test 6 Summary Report 377
Test 6 - Experimental Observations 386
Test 6 - Strain Data Analysis 404
North and South Bar Strains 404
East and West Bar Strains 414
Test 6 - Curvature and Strain Penetration Data 423
Response Comparison to Previous Experiments 431
Comparison of Tests 4 (Symmetric) and 6 (Asymmetric Two-Cycle-Set) 431
Comparison of Tests 3 $\rho s = 0.7\%$ and 6 $\rho s = 1\%$ both with Asymmetric Two-Cycle-Set 432
Chapter 10 – Test 7 Summary Report 435
Test 7 - Experimental Observations 443
Test 7 - Strain Data Analysis 449
North and South Bar Strains 449
East and West Bar Strains 456
Test 7 - Curvature and Strain Penetration Data 466
Chapter 11 – Test 8 Summary Report 475

Test 8 - Experimental Observations 483
Test 8 - Strain Data Analysis 489
North and South Bar Strains 489
East and West Bar Strains 496
Test 8 - Curvature and Strain Penetration Data 505
Response Comparison for Test 7 (1.3%) and Test 8 (1% Transverse Volumetric Steel) 514
Chapter 12 – Test 9 Summary Report 515
Test 9 - Experimental Observations 523
Test 9 - Strain Data Analysis 530
North and South Bar Strains 530
East and West Bar Strains 539
Test 9 - Curvature and Strain Penetration Data 547
Response Comparison to Previous Experiments 556
Comparison of Tests 7 (1.3%) and 9 (0.7% Transverse Volumetric Steel) 556
Comparison of Tests 8 (1%) and 9 (0.7% Transverse Volumetric Steel) 557
Chapter 13 – Test 10 Summary Report 558
Test 10 - Experimental Observations 566
Test 10 - Strain Data Analysis 574
North and South Bar Strains 574
East and West Bar Strains 582
Test 10 - Curvature and Strain Penetration Data 590
Response Comparison to Previous Experiments 599
Comparison of Tests 10 (1.3%) and 4 (1% Transverse Volumetric Steel) 599
Comparison of Tests 10 (2.1%) and 7 (1.6% Longitudinal Steel) 600
Chapter 14 – Test 11 Summary Report 601
Subduction Megathrust Load Path Selected for Tests 11 and 12 601
Test 11 - Experimental Observations 610
Test 11 - Strain Data Analysis 628
North and South Bar Strains 628
East and West Bar Strains 636
Test 11 - Curvature and Strain Penetration Data 644
Response Comparison of Tests 8 (Sym. 2-Cycle-Set) and 11 (Scaled Megathrust) 653
Chapter 15 – Test 12 Summary Report 654

Test 12 - Experimental Observations 662
Test 12 - Strain Data Analysis 672
North and South Bar Strains 672
East and West Bar Strains 679
Test 12 - Curvature and Strain Penetration Data 687
Response Comparison to Previous Experiments 696
Comparison of Megathrust Tests 11 (1%) and 12 (0.7% Transverse Volumetric Steel) 696
Comparison of Megathrust Load History Test 12 and Symmetric Two-Cycle-Set Test 9 697
Chapter 16 – Design Recommendations 698
Summary of Measured Strain and Curvature Data 698
Test Matrix, Material Properties, and Damage Summaries for Column Datasets 710
Plastic Hinge Method Design Recommendations 714
Equivalent Strain Penetration Length and Tension/Compression Plastic Hinge Lengths 716
Equations Needed to Compute Disp. using the Triangular Plastic Curvature Geometry 717
Equations Needed to Compute Disp. using the Rectangular Plastic Curvature Geometry 718
Predictive comparison of Plastic Hinge Models 719
Design Recommendations for Performance Strain Limits 734
Serviceability Limit States 734
Intermediate Compressive Limit State Prompting a Change in Repair Strategy 735
Damage Control Limit States 737
References 753

List of Figures

Figure 1-1. Displacement History, Hysteretic Response, and Limit States for Test 2 in (Goodnight, Kowalsky and Nau 2015) 2
Figure 1-2. (Feng, Kowalsky and Nau 2015) Method Applied to Test 9 from (Goodnight, Kowalsky and Nau 2015) 4
Figure 1-3 Equivalent curvature Distributions 6
Figure 1-4. Test Setup, Instrumentation, and Measurement Comparison from (Goodnight, Kowalsky and Nau 2015) 8
Figure 1-5. Strain Hysteresis for (Left) Longitudinal Bar and (Right) Overlaying Spiral Reinforcement 8
Figure 1-6. (Left) Curvature Profiles and (Right) Fixed-End Rotations 8
Figure 1-7. Equivalent Curvature Distributions for the Modified Lpr Plastic Hinge Method 11
Figure 1-8. Cumulative Probability Distribution for (Left) Analytical First Yield Force and (Right) Tensile Bar Buckling Strain 13
Figure 1-9. Cumulative Probability Distribution for (Left) Initial Cover Crushing and (Right) Initial Spiral Yielding 13
Figure 1-10. Cumulative Probability Distribution for (Left) Compressive Strain and (Right) Disp. at Initial Yielding of Confinement Steel 14
Figure 1-11. Cumulative Probability Distribution for (Left) Tensile Strain and (Right) Disp. at Bar Buckling 15
Figure 1-12. (Wong, Paulay and Priestley 1993) Lateral Displacement Histories 17
Figure 1-13. (Osorio, Bairán and Marí 2012) (Left) Biaxial Disp. History and (Right) Measured Hoop Strains for Uniaxial and Biaxial Displacement Patterns 18
Figure 1-14. (Tsuno and Park 2004) Bi-Directional Load History for Specimen S3 19
Figure 1-15. (Tsuno and Park 2004) Bi-Directional Load History for Specimen S4 19
Figure 1-16. (Tsuno and Park 2004) Calculated Plastic Hinge Lengths from Measured Curvature Profiles 20
Figure 1-17. (Bousias, et al. 1995) (Left) Load Histories and (Right) Test S7 Demonstrates Lag of Force Resultant behind the Disp. Resultant 21
Figure 1-18. Test Setup and Specimen from (Mazzoni and Moehle 2001) 22
Figure 1-19. Column and Beam Cross-Sections of Specimen 1 from (Mazzoni and Moehle 2001) 22
Figure 1-20. Joint Reinforcement for Specimen 2 from (Mazzoni and Moehle 2001) 23
Figure 1-21. Bidirectional Loading Sequence from (Mazzoni and Moehle 2001) 23
Figure 1-22. Hysteretic Response for Orthogonal Loading Cycles from (Mazzoni and Moehle 2001) 24
Figure 1-23. Load Path Effects on Flexural Reinforcement from (Mazzoni and Moehle 2001) 24
Figure 1-24. (Left) Column Long. And Tran. Response, (Mid) Normalized Response, and (Right) Bidirectional Displacement Pattern from (Terzic and Stojadinovic 2015) 25
Figure 1-25. Hysteretic Response for Base45 Specimen from (Terzic and Stojadinovic 2015) 26
Figure 1-26. Axial Load Capacity Degradation Envelope from (Terzic and Stojadinovic 2015) 26
Figure 2-1. Definition of the Type-B Load Histories 30
Figure 2-2. (Bazaez and Dusicka 2016) Megathrust Load History Compared to the Type-B Sym. 2-Cycle-Set 31
Figure 2-3. Top View of Test Setup 33
Figure 2-4. Front View of Test Specimen (Actuators Omitted for Clarity) 34
Figure 2-5. Side View of Test Specimen (Actuators Omitted for Clarity) 35

Figure 2-6. General Dimensions for the Specimen and Transfer Footing 36
Figure 2-7. Comparison of Measurement Techniques for Tensile Rebar Test from (Goodnight, Kowalsky and Nau 2015) 37
Figure 2-8. Optotrak Instrumentation for Test 27 from (Goodnight, Kowalsky and Nau 2015) 38
Figure 2-9. Force-Displacement with Expected Material Properties 40
Figure 2-10. Tensile Strain-Displacement with Expected Material Properties 41
Figure 2-11. Compressive Strain-Displacement with Expected Material Properties 41
Figure 2-12. Force-Displacement with Overstrength Material Properties 42
Figure 2-13. Force-Displacement and (Kowalsky and Priestley 2000) Modified UCSD Shear Model 42
Figure 2-14. Plastic Hinge Relocation Technique from (Rutledge, et al. 2013) 43
Figure 2-15. Force Transfer Mechanism using External Vertical Joint Reinforcement from (Priestley, Seible and Calvi 1996) 45
Figure 2-16. Method to Find Equivalent Area of Column Steel for the Repaired Overstrength Base Section Moment 46
Figure 2-17. Column Cross-Section Geometry and Reinforcement 47
Figure 2-18. Specimen Reinforcing Details 48
Figure 2-19. Specimen Footing Reinforcing Details 49
Figure 2-20. Transfer Footing Reinforcing Details 50
Figure 2-21. Longitudinal and Transverse Side Views of the Transfer Footing 51
Figure 2-22. Fabricated Steel Pockets for 1-3/8” Dywidag Tie Down Bars 52
Figure 2-23. Fabricated Steel Pocket for 1-3/4” Dywidag Axial Load Bar 53
Figure 2-24. Dimensions from Actuator Knuckle Pin to CG of the 45° Stiffener Weld Group 54
Figure 2-25. Fabrication Details for the 45° Loading Fixtures 55
Figure 2-26. Fabrication Details for the 45° Loading Fixtures 56
Figure 2-27. Fabricated Steel Loading Fixture 57
Figure 2-28. Existing Side Coped Link Beam for Actuator Lateral Forces 57
Figure 2-29. Stand Alone Cap Constructed to Test Actuator Control Prior to the First Test 58
Figure 2-30. Column Cage Template and Tying Stand 63
Figure 2-31. Orientation of Column 90o Bends in the Footing Joint 64
Figure 2-32. Procedure for Tying in Joint Shear Steal 65
Figure 2-33. Specimen Footing Steel-Ply Formwork 66
Figure 2-34. Bottom Mat of Steel and Procedure for Holding up the Top Mat of Steel 67
Figure 2-35. Specimens on Casting Slab Prior to Footing Casting 67
Figure 2-36. Footing and Joint Reinforcement 68
Figure 2-37. Footings on the Day of Casting 69
Figure 2-38. Removal of Footing Forms and Application of Foam Cover Concrete Blockouts 69
Figure 2-39. Inside Layer of ½” Foam Blockouts Placed between Spiral Layers 70
Figure 2-40. Column Stabilization and Cap Formwork 71
Figure 2-41. Column Stabilization and Cap Formwork 72
Figure 2-42. Cap Reinforcement 72
Figure 2-43. Column Concrete Placed and Consolidated in Multiple Lifts 73
Figure 2-44. Completed Specimens 74
Figure 2-45. Lifting the Specimens with Four Hydraulic Jacks and HSS Spreader Beams 74
Figure 2-46. Secondary Footing Steel-Ply Formwork 75

Figure 2-47. Secondary Footing Details and Additional Steel for Center Axial Hole 76
Figure 2-48. Casting and Curing of the Secondary Footing 77
Figure 2-49. Top and Side Views of the Lateral Actuators 79
Figure 2-50. Test 1: Actuator and Wall Side Actuator Pivot Points 79
Figure 2-51. Deformed Geometry of the Four Cap String Potentiometers and Footing Interface Linear Potentiometers 81
Figure 2-52. Initial Actuator Configuration and Coordinate System 82
Figure 2-53. Deformed Geometry of the Actuator Setup 83
Figure 2-54. Actuator Global Force Components 84
Figure 2-55. Geometry of Retracted Actuators Tied Back to the Strong Wall While Not in Use 85
Figure 2-56. Self-Regulating Axial Load System 86
Figure 3-1. Tensile Test for #7 Longitudinal Bar (Sample 6) from Tests 1-6, High Strain Measurement Comparison 88
Figure 3-2. Tensile Test for #7 Longitudinal Bar (Sample 6) from Tests 1-6, Low Strain Measurement Comparison 89
Figure 3-3. Tensile Test for #7 Longitudinal Bar (Sample 3) from Tests 1-6, Comparison Including Necking 89
Figure 3-4. Tensile Test for #3 Spiral (Sample 4) from Tests 1-6, Comparison Including Necking 90
Figure 3-5. Tensile Test for #3 Spiral (Sample 4) from Tests 1-6, Low Strain Comparison 90
Figure 3-6. Tensile Test for #3 Spiral (Sample 3) from Tests 1-6, 0.2% Offset Method 91
Figure 3-7. Tensile Test for #3 Spiral (Sample 4) from Tests 1-6, 0.2% Offset Method 91
Figure 3-8. Tensile Test for #7 Longitudinal Bar from Columns 7-12 93
Figure 3-9. Tensile Test for #6 Longitudinal Bar from Columns 7-12 93
Figure 3-10. Tensile Test for #3 Spiral from Tests 7-12 94
Figure 3-11. Tensile Tests for #3 Spirals from Tests 7-12 94
Figure 3-12. Column Analysis Model in OpenSees 96
Figure 3-13. Fiber Discretization in Column Section, 2 Unconfined and 8 Confined Concrete Rings with 24 Wedges 97
Figure 3-14. Comparison of Models in OpenSees and Cumbia to Rebar Tensile Test 1 98
Figure 3-15. Reinforcing Steel Material in OpenSees without Buckling 98
Figure 3-16. Reinforcing Steel Material in OpenSees with (Dhakal and Maekawa 2002) Buckling 99
Figure 3-17. Bond SP01 Stress-Slip Model from (Zhao and Sritharan 2007) 100
Figure 3-18. Confined and Unconfined Concrete Stress-Strain Curves for Columns 1-3 with 2” Spiral Spacing 101
Figure 3-19. Confined and Unconfined Concrete Stress-Strain Curves for Columns 4-6 with 2.75” Spiral Spacing 101
Figure 3-20. Example of Cyclic Response of the Concrete02 Model in OpenSees for Columns 1-3 with 2” Spiral Spacing 102
Figure 4-1. Test 1: Load History and Labeling System for Reinforcement and Cracks 103
Figure 4-2. Test 1: Experimental Setup 105
Figure 4-3. Test 1: Axial and Lateral Load Setup 106
Figure 4-4. Test 1: String Potentiometer Setup (Highlighted with Blue Lines) 106
Figure 4-5. Test 1: Plastic Hinge Region with Optotrak Target Marker Instrumentation 107
Figure 4-6. Test 1: Close Up of the Instrumented Region on the South Side of the Specimen 107

Figure 4-7. Test 1: Y-Displacement History 108
Figure 4-8. Test 1: X-Displacement History, Note Accidental Repeat of $\mu\Delta 1 + 1X$ 108
Figure 4-9. Test 1: Y-Force History 109
Figure 4-10. Test 1: X-Force History, Note Accidental Repeat of $\mu\Delta 1 + 1X$ 109
Figure 4-11. Test 1: Type-B Symmetric Two-Cycle-Set Displacement History 110
Figure 4-12. Test 1: Load Path 110
Figure 4-13. Test 1: Y-Direction Hysteretic Response 111
Figure 4-14. Test 1: X-Direction Hysteretic Response 111
Figure 4-15. Test 1: Y-Direction Axial Force History, Unloading after Day 1 of Testing 112
Figure 4-16. Test 1: X-Direction Axial Force History, Unloading after Day 1 of Testing 112
Figure 4-17. Test 1: First Cracking on the South and North Sides of the Specimen during $\Delta y = 0.38"$ and $\Delta y = -0.39"$ 115
Figure 4-18. Test 1: First Cracking on the West and East Sides of the Specimen during $\Delta x = 0.30"$ and $\Delta x = -0.37"$ 115
Figure 4-19. Test 1: Cracking on the South and North Sides during $\Delta y' = 1.10"$ and $\Delta y' = -1.11"$ in Y-Direction 116
Figure 4-20. Test 1: Cracking on the West and East Sides during $\Delta y' = 1.12"$ and $\Delta y' = -1.13"$ in X-Direction 116
Figure 4-21. Test1: Cracking on the (Left) South Side at $\mu\Delta 1 + 2y = 1.51"$ and (Right) North Side at $\mu\Delta 1 - 2y = -1.49"$ 117
Figure 4-22. Test 1: Cracking on the (Left) West Side at $\mu\Delta 1 + 2x = 1.55"$ and (Right) East Side at $\mu\Delta 1 - 2x = -1.41"$ 117
Figure 4-23. Test 1: Concrete Flacking on the (Left) South at $\mu\Delta 1.5 - 1y = -2.25"$ and (Right) East at $\mu\Delta 1.5 + 1x = 2.28"$ 118
Figure 4-24. Test 1: (Left) South and (Right) North Sides of the Specimen at the End of $\mu\Delta 1.5$ 118
Figure 4-25. Test 1: (Left) West Side at $\mu\Delta 1.5 + 2x = 2.25"$ and (Right) East Side at $\mu\Delta 1.5 - 2x = -2.28"$ 119
Figure 4-26. Test 1: First Crushing on the (Left) North Side at $\mu\Delta 2 + 1y = 3.01"$ and (Right) South Side at $\mu\Delta 2 - 1y = -3.03"$ 119
Figure 4-27. Test 1: First Crushing on the (Left) East Side at $\mu\Delta 2 + 1x = 3.02"$ and (Right) West Side at $\mu\Delta 2 - 1x = -3.03"$ 120
Figure 4-28. Test 1: (Left) South and (Right) North Sides of the Specimen at the End of $\mu\Delta 2$ 120
Figure 4-29. Test 1: (Left) West Side at $\mu\Delta 2 + 2x = 3.02"$ and (Right) East Side at $\mu\Delta 2 - 2x = -3.02"$ 121
Figure 4-30. Test 1: (Left) South and (Right) North Sides of the Specimen at the End of $\mu\Delta 3$ 121
Figure 4-31. Test 1: (Left) West Side at $\mu\Delta 3 + 2x = 4.52"$ and (Right) East Side at $\mu\Delta 3 - 2x = -4.54"$ 122
Figure 4-32. Test 1: Crushing on the (Left) North Side at $\mu\Delta 4 + 1y = 6.05"$ and (Right) South Side at $\mu\Delta 4 - 1y = -6.04"$ 122
Figure 4-33. Test 1: Crushing on the (Left) East Side at $\mu\Delta 4 + 1x = 6.05"$ and (Right) West Side at $\mu\Delta 4 - 1x = -6.05"$ 123
Figure 4-34. Test 1: (Left) South and (Right) North Sides of the Specimen at the End of $\mu\Delta 4$ 123
Figure 4-35. Test 1: (Left) West Side at $\mu\Delta 4 + 2x = 6.03"$ and (Right) East Side at $\mu\Delta 4 - 2x = -6.04"$ 124

Figure 4-36. Test 1: Buckling of (Left) North Bar during $\mu\Delta 5 + 1y = 7.51$" and (Right) South Bar during $\mu\Delta 5 - 1y = -7.55$" 124
Figure 4-37. Test 1: Buckling of (Left) East Bar during $\mu\Delta 5 + 1x = 7.48$" and (Right) West Bar during $\mu\Delta 5 - 1x = -7.56$" 125
Figure 4-38. Test 1: Buckling of Bars (Left) NNE & NNW during $\mu\Delta 5 + 2y = 7.42$" and (Right) SSE & SSW during $\mu\Delta 5 - 2y = -7.55$" 125
Figure 4-39. Test 1: Specimen Deformation at $\mu\Delta 5 + 1y = 7.51$" 126
Figure 4-40. Test 1: Buckling of (Left) All East Bars during $\mu\Delta 5 + 2x = 7.44$" and (Right) All West Bars during $\mu\Delta 5 - 2x = 7.56$" 127
Figure 4-41. Test 1: (Left) Additional Deformation in North Buckled Reinforcement during $\mu\Delta 5 + 3x = 7.33$" and (Right) Fracture of North Bar at $\Delta y = -2.90$" $during\ \mu\Delta 5 - 3Y$ 127
Figure 4-42.Test 1: (Left) North and (Right) West Sides after Instrumentation Removal 128
Figure 4-43. Test 1: (Left) South and (Right) East Sides after Instrumentation Removal 128
Figure 4-44. Test 1: Vertical Strain Profiles for Loading in the +Y-direction 131
Figure 4-45. Test 1: Vertical Strain Profiles for Loading in the -Y-direction 131
Figure 4-46. Test 1: Optotrak Strains in Six Spiral Layers over the North Extreme Fiber Bar 132
Figure 4-47. Test 1: Optotrak Strains in Six Spiral Layers over the South Extreme Fiber Bar 132
Figure 4-48. Test 1: Tension Strain-Disp. for Bar S (Gauge Length 4 Centered 10.58” above the Footing) 133
Figure 4-49. Test 1: Compression Strain-Disp. for Bar N (Gauge Length 2 Centered 6.41” above the Footing) 133
Figure 4-50. Test 1: Tension Strain-Disp. for Bar N (Gauge Length 2 Centered 6.41” above the Footing) 134
Figure 4-51. Test 1: Compression Strain-Disp. for Bar S (Gauge Length 2 Centered 5.19” above the Footing) 134
Figure 4-52. Test 1: Strain Hysteresis over the North Buckled Bar (Gauge Length 1 Centered 3.55” above the Footing) 135
Figure 4-53. Test 1: Spiral Strains in the Second North Layer (3.81” above the Footing) 135
Figure 4-54. Test 1: Strain Hysteresis over the South Buckled Bar (Gauge Length 1 Centered 2.43” above the Footing) 136
Figure 4-55. Test 1: Spiral Strains in the First South Layer (2.74” above the Footing) 136
Figure 4-56. Test 1: Vertical Strain Profiles for Loading in the +X-direction 138
Figure 4-57. Test 1: Vertical Strain Profiles for Loading in the -X-direction 139
Figure 4-58. Test 1: Optotrak Strains in Six Spiral Layers over the East Extreme Fiber Bar 139
Figure 4-59. Test 1: Data from Strain Gauges for Four Spiral Layers over the West Extreme Fiber Bar 140
Figure 4-60. Test 1: Tension Strain-Disp. for Bar W (Gauge Length 2 Centered 5.10” above the Footing) 140
Figure 4-61. Test 1: Compression Strain-Disp. for Bar E (Gauge Length 1 Centered 2.15” above the Footing) 141
Figure 4-62. Test 1: Tension Strain-Disp. for Bar E (Gauge Length 2 Centered 4.90” above the Footing) 141
Figure 4-63. Test 1: Compression Strain-Disp. for Bar W (Gauge Length 2 Centered 5.10” above the Footing) 142

Figure 4-64. Test 1: Strain Hysteresis over the East Buckled Bar (Gauge Length 2 Centered 4.90” above the Footing) 142
Figure 4-65. Test 1: Spiral Strains in the Second East Layer (5.00” above the Footing) 143
Figure 4-66. Test 1: Strain Hysteresis over the West Buckled Bar (Gauge Length 1 Centered 2.38” above the Footing) 143
Figure 4-67. Test 1: Spiral Strains in the First West Layer (2.64” above the Footing) 144
Figure 4-68. Test 1: Elastic Curvature Profiles for the First Instrumented Section above the Footing 146
Figure 4-69. Test 1: Curvature Profiles for the First Instrumented Section above the Footing 147
Figure 4-70. Test 1: Elastic Vertical Curvature Profiles 147
Figure 4-71. Test 1: Vertical Curvature Profiles for Loading in the +Y-direction 148
Figure 4-72. Test 1: Vertical Curvature Profiles for Loading in the –Y-direction 148
Figure 4-73. Test 1: Vertical Curvature Profiles for Loading in the +X-direction 149
Figure 4-74. Test 1: Vertical Curvature Profiles for Loading in the –X-direction 149
Figure 4-75. Test 1: Extreme Fiber Bar Strain Penetration Bond Slip Hysteresis 150
Figure 4-76. Test 1: Fixed End Rotations due to Strain Penetration during the Elastic Cycles 150
Figure 4-77. Test 1: Fixed-End Rotations due to Strain Penetration 151
Figure 4-78. Test 1: Optotrak Integrated Flexural Disp. Compared to Measured String Pot. Disp. 151
Figure 4-79. Test 1: Optotrak Integrated Flexural Disp. Compared to Measured String Pot. Disp. 152
Figure 4-80. Test 1: Measured Extent of Plasticity Compared to Design Recommendations 152
Figure 4-81. Test 1: Computed Equivalent Strain Penetration Lengths Compared to Design Recommendations 153
Figure 4-82. Test 1: Extreme Fiber Tensile Bar Strains at the Analytical First Yield Force 154
Figure 4-83. Test 1: Y-Direction Curvature History for the Second Layer above the Footing 154
Figure 4-84. Test 1: X-Direction Curvature History for the Second Layer above the Footing 155
Figure 4-85. Test 1: Y-Direction Moment-Curvature Compared to Monotonic Prediction 155
Figure 4-86. Test 1: X-Direction Moment-Curvature Compared to Monotonic Prediction 156
Figure 4-87. Test 1: Y-Direction Hysteretic Response Compared to Monotonic Predictions 156
Figure 4-88. Test 1: X-Direction Hysteretic Response Compared to Monotonic Predictions 157
Figure 4-89. Test 1: Y-Direction Cycles up to the Analytical First Yield Force 157
Figure 4-90. Test 1: X-Direction Cycles up to the Analytical First Yield Force 158
Figure 4-91. Test 1: Measured Curvatures Compared to Superimposed Moment-Curvature Response at Equivalent Moments 158
Figure 4-92. Test 1: Difference in the Measured and Analytical Base Section Curvature at Equivalent Moments 159
Figure 4-93. Test 1: Measured Response Compared to the OpenSees Fiber Model Prediction in the Y-direction 160
Figure 4-94. Test 1: Measured Response Compared to the OpenSees Fiber Model Prediction in the X-direction 160
Figure 4-95. Test 1: Measured Load Path Compared to OpenSees Fiber Model Result 161
Figure 4-96. Test 1: Method of Calibration of SP01 Stress-Slip Material for Strain Penetration in OpenSees 161
Figure 4-97. Test 1: OpenSees Model Prediction for North Bar Strains 162
Figure 4-98. Test 1: OpenSees Model Prediction for South Bar Strains 162

Figure 4-99. Test 1: OpenSees Model Prediction for East Bar Strains 163
Figure 4-100. Test 1: OpenSees Model Prediction for West Bar Strains 163
Figure 5-1. Test 2: Load History and Labeling System for Reinforcement and Cracks 164
Figure 5-2. Test 2: Specimen Deformation at $\mu\Delta 5 + 1y = 8.09"$ 166
Figure 5-3. Test 3: Measured Linear Potentiometer Relative Footing Displacement with Monotonic SP01 Model Fit 167
Figure 5-4. Test 3: Cyclic Performance of SP01 Model Fit Used to Correct Test 2 for Relative Footing Displacement 167
Figure 5-5. Test 2: Relative Footing Displacement Obtained from Truss with SP01 Fit from Test 3 . 168
Figure 5-6. Test 2: Relative Footing Displacement Obtained from Truss with SP01 Fit from Test 3 . 168
Figure 5-7. Test 2: Y-Displacement History 169
Figure 5-8. Test 2: X-Displacement History 169
Figure 5-9. Test 2: Y-Force History 170
Figure 5-10. Test 2: X-Force History 170
Figure 5-11. Test 2: Type-B Symmetric Three-Cycle-Set Displacement History 171
Figure 5-12. Test 2: Load Path 171
Figure 5-13. Test 2: Y-Direction Hysteretic Response 172
Figure 5-14. Test 2: X-Direction Hysteretic Response 172
Figure 5-15. Test 2: Y-Direction Axial Force History, Noted Cycles with Lower Axial Force 173
Figure 5-16. Test 2: X-Direction Axial Force History, Noted Cycles with Lower Axial Force 173
Figure 5-17. Test 2: Target Marker Instrumentation of Longitudinal and Transverse Steel 174
Figure 5-18. Test 2: Optotrak 3D Rendering from Target Markers Applied to Reinforcement 174
Figure 5-19. Test 2: First Cracking on the South and North Sides of the Specimen during $\Delta y = 0.41"$ and $\Delta y = -0.43"$ 177
Figure 5-20. Test 2: First Cracking on the West and East Sides of the Specimen during $\Delta x = 0.41"$ and $\Delta x = -0.38"$ 178
Figure 5-21. Test 2: Cracking on the South and North Sides during $\Delta y' = 1.12"$ and $\Delta y' = -1.18"$ in Y-Direction 178
Figure 5-22. Test 2: Cracking on the West and East Sides during $\Delta y' = 1.16"$ and $\Delta y' = -1.15"$ in X-Direction 179
Figure 5-23. Test 2: Cracking on the (Left) South Side at $\mu\Delta 1 + 3y = 1.57"$ and (Right) North Side at $\mu\Delta 1 - 3y = -1.57"$ 179
Figure 5-24. Test 2: Cracking on the (Left) West Side at $\mu\Delta 1 + 3x = 1.57"$ and (Right) East Side at $\mu\Delta 1 - 3x = -1.56"$ 180
Figure 5-25. Test 2: Concrete Crushing on the (Left) West at $\mu\Delta 1.5 - 1x = -2.39"$ and (Right) East at $\mu\Delta 1.5 + 2x = 2.38"$ 180
Figure 5-26. Test 2: Concrete Crushing on the (Left) North at $\mu\Delta 1.5 + 3y = 2.38"$ and (Right) South at $\mu\Delta 1.5 - 3y = -2.38"$ 181
Figure 5-27. Test 2: (Left) North and (Right) South Sides of the Specimen at the End of $\mu\Delta 1.5$ 181
Figure 5-28. Test 2: (Left) West Side at $\mu\Delta 1.5 + 3x = 2.43"$ and (Right) East Side at $\mu\Delta 1.5 - 3x = -2.41"$ 182
Figure 5-29. Test 2: (Left) North and (Right) South Sides of the Specimen at the End of $\mu\Delta 2$ 182
Figure 5-30. Test 2: (Left) West Side at $\mu\Delta 2 + 3x = 3.19"$ and (Right) East Side at $\mu\Delta 2 - 3x = -3.21"$ 183

Figure 5-31. Test 2: Crushing on the (Left) North Side at $\mu\Delta 3 + 1y = 4.85$" and (Right) South Side at $\mu\Delta 3 - 1y = -4.85$" 183
Figure 5-32. Test 2: Crushing on the (Left) East Side at $\mu\Delta 3 + 1x = 4.85$" and (Right) West Side at $\mu\Delta 3 - 1x = -4.84$" 184
Figure 5-33. Test 2: (Left) North and (Right) South Sides of the Specimen at the End of $\mu\Delta 3$ 184
Figure 5-34. Test 2: (Left) West Side at $\mu\Delta 3 + 3x = 4.83$" and (Right) East Side at $\mu\Delta 3 - 3x = -4.81$" 185
Figure 5-35. Test 2: Reinforcement Remained Straight, (Left) North at $\mu\Delta 4 + 1y = 6.48$" and (Right) South at $\mu\Delta 4 - 1y = -6.48$" 185
Figure 5-36. Test 2: Reinforcement Remained Straight, (Left) East at $\mu\Delta 4 + 1x = 6.48$" and (Right) West at $\mu\Delta 4 - 1x = -6.46$" 186
Figure 5-37. Test 2: Buckling of Bars (Left) N and NNE during $\mu\Delta 4 + 2y = 6.44$" and (Right) S and SSE during $\mu\Delta 4 - 2y = -6.51$" 186
Figure 5-38. Test 2: Buckling of (Left) Bar W during $\mu\Delta 4 - 2x = -6.48$" and (Right) Bar NNW during $\mu\Delta 4 + 3y = 6.45$" 187
Figure 5-39. Test 2: (Left) Bar SSW Buckled during $\mu\Delta 4 - 3y = -6.48$" and (Right) Deformed North Spirals at $\mu\Delta 4 - 3y = -6.48$" 187
Figure 5-40. Test 2: Buckling of Bars (Left) E and ESE during $\mu\Delta 4 + 3x = 6.43$" and (Right) WSW and WNW at $\mu\Delta 4 - 3x = -6.48$" 188
Figure 5-41. Test 2: (Left) Buckling of NE and NW during $\mu\Delta 5 + 1y = 8.09$" and (Right) Fracture of Bar N at -0.39" during $\mu\Delta 5 - 1Y$ 188
Figure 5-42. Test 2: (Left) North and (Right) South Sides of the Specimen after Instrumentation Removal 189
Figure 5-43. Test 2: (Left) West and (Right) East Sides of the Specimen after Instrumentation Removal 189
Figure 5-44. Test 2: Vertical Strain Profiles for Loading in the +Y-direction 190
Figure 5-45. Test 2: Vertical Strain Profiles for Loading in the -Y-direction 191
Figure 5-46. Test 2: Spiral Strains Measured Over the North Extreme Fiber Bar during +Y Cycles 191
Figure 5-47. Test 2: Spiral Strains Measured Over the South Extreme Fiber Bar during -Y Cycles 192
Figure 5-48. Test 2: Tension Strain-Disp. for Bar S (Gauge Length 3 Centered 7.60” above the Footing) 192
Figure 5-49. Test 2: Compression Strain-Disp. for Bar N (Gauge Length 2 Centered 5.23” above the Footing) 193
Figure 5-50. Test 2: Tension Strain-Disp. for Bar N (Gauge Length 3 Centered 7.95” above the Footing) 193
Figure 5-51. Test 2: Compression Strain-Disp. for Bar S (Gauge Length 1 Centered 2.28” above the Footing) 194
Figure 5-52. Test 2: Strain Hysteresis over the North Buckled Bar (Gauge Length 2 Centered 5.23” above the Footing) 194
Figure 5-53. Test 2: North Spiral Strain Gauge Hysteresis for the First Layer above the Footing 195
Figure 5-54. Test 2: North Spiral Strain Gauge Hysteresis for the Second Layer above the Footing 195
Figure 5-55. Test 2: Strain Hysteresis over the South Buckled Bar (Gauge Length 1 Centered 2.28” above the Footing) 196
Figure 5-56. Test 2: South Spiral Strain Gauge Hysteresis for the First Layer above the Footing 196

Figure 5-57. Test 2: South Spiral Strain Gauge Hysteresis for the Second Layer above the Footing . 197
Figure 5-58. Test 2: Vertical Strain Profiles for Loading in the +X-direction 198
Figure 5-59. Test 2: Vertical Strain Profiles for Loading in the -X-direction 198
Figure 5-60. Test 2: Spiral Strains Measured Over the East Extreme Fiber Bar during +X Cycles 199
Figure 5-61. Test 2: Spiral Strains Measured Over the West Extreme Fiber Bar during -X Cycles 199
Figure 5-62. Test 2: Tension Strain-Disp. for Bar W (Gauge Length 2 Centered 4.90" above the Footing) 200
Figure 5-63. Test 2: Compression Strain-Disp. for Bar E (Gauge Length 1 Centered 3.38" above the Footing) 200
Figure 5-64. Test 2: Tension Strain-Disp. for Bar E (Gauge Length 2 Centered 6.15" above the Footing) 201
Figure 5-65. Test 2: Compression Strain-Disp. for Bar W (Gauge Length 2 Centered 4.90" above the Footing) 201
Figure 5-66. Test 2: Strain Hysteresis over the East Buckled Bar (Gauge Length 2 Centered 6.15" above the Footing) 202
Figure 5-67. Test 2: East Spiral Strain Gauge Hysteresis for the Second Layer above the Footing 202
Figure 5-68. Test 2: East Spiral Strain Gauge Hysteresis for the Third Layer above the Footing 203
Figure 5-69. Test 2: Strain Hysteresis over the West Buckled Bar (Gauge Length 2 Centered 4.90" above the Footing) 203
Figure 5-70. Test 2: West Spiral Strain Gauge Hysteresis for the First Layer above the Footing 204
Figure 5-71. Test 2: West Spiral Strain Gauge Hysteresis for the Second Layer above the Footing .. 204
Figure 5-72. Test 2: Elastic Curvature Profiles for the First Instrumented Section above the Footing 205
Figure 5-73. Test 2: Curvature Profiles for the Second Instrumented Section above the Footing 206
Figure 5-74. Test 2: Elastic Vertical Curvature Profiles 206
Figure 5-75. Test 2: Vertical Curvature Profiles for Loading in the +Y-direction 207
Figure 5-76. Test 2: Vertical Curvature Profiles for Loading in the -Y-direction 207
Figure 5-77. Test 2: Vertical Curvature Profiles for Loading in the +X-direction 208
Figure 5-78. Test 2: Vertical Curvature Profiles for Loading in the -X-direction 208
Figure 5-79. Test 2: Extreme Fiber Bar Strain Penetration Bond Slip Hysteresis 209
Figure 5-80. Test 2: Fixed End Rotations due to Strain Penetration during the Elastic Cycles 209
Figure 5-81. Test 2: Fixed-End Rotations due to Strain Penetration 210
Figure 5-82. Test 2: Optotrak Integrated Flexural Disp. Compared to Measured String Pot. Disp. 210
Figure 5-83. Test 2: Optotrak Integrated Flexural Disp. Compared to Measured String Pot. Disp. 211
Figure 5-84. Test 2: Measured Extent of Plasticity Compared to Tensile Hinge Lengths 211
Figure 5-85. Test 2: Measured Equivalent Strain Penetration Lengths Compared to Design Expressions 212
Figure 5-86. Test 2: Y-Direction Hysteretic Response Compared to PCK (2007) Hinge Length Monotonic Prediction 212
Figure 5-87. Test 2: X-Direction Hysteretic Response Compared to PCK (2007) Hinge Length Monotonic Prediction 213
Figure 5-88. Test 2: Y-Direction Sectional Response Compared to Monotonic Moment Curvature Analysis 213

Figure 5-89. Test 2: X-Direction Sectional Response Compared to Monotonic Moment Curvature Analysis 214
Figure 5-90. Test 1 Symmetric Two-Cycle-Set and Test 2 Symmetric Three-Cycle-Set 215
Figure 5-91. Test 1 Symmetric Two-Cycle-Set and Test 2 Symmetric Three-Cycle-Set 215
Figure 6-1. Test 3: Load History and Labeling System for Reinforcement and Cracks 216
Figure 6-2. Test 3: Optotrak Target Marker Instrumentation and 3D Rendering of Measured Data 218
Figure 6-3. Linear Potentiometers Installed to Monitor Relative Footing Displacement at the 3/8" Neoprene Interface 219
Figure 6-4. Test 3: Measured Linear Potentiometer Relative Footing Displacement with Monotonic SP01 Model Fit 219
Figure 6-5. Test 3: Y-Displacement History 220
Figure 6-6. Test 3: X-Displacement History 220
Figure 6-7. Test 3: Y-Force History 221
Figure 6-8. Test 3: X-Force History 221
Figure 6-9. Test 3: Type-B Asymmetric Two-Cycle-Set Displacement History 222
Figure 6-10. Test 3: Load Path 222
Figure 6-11. Test 3: Y-Direction Hysteretic Response 223
Figure 6-12. Test 3: X-Direction Hysteretic Response 223
Figure 6-13. Test 3: Y-Direction Axial Force History 224
Figure 6-14. Test 3: X-Direction Axial Force History 224
Figure 6-15. First Cracking on the South and North Sides of the Specimen during $\Delta y = 0.35"$ and $\Delta y = -0.43"$ 227
Figure 6-16. Test 3: First Cracking on the West and East Sides of the Specimen during $\Delta x = 0.36"$ and $\Delta x = -0.38"$ 228
Figure 6-17. Test 3: Cracking on the South and North Sides during $\Delta y' = 1.07"$ and $\Delta y' = -1.13"$ in Y-Direction 228
Figure 6-18. Test3: Cracking on the West and East Sides during $\Delta y' = 1.08"$ and $\Delta y' = -1.10"$ in X-Direction 229
Figure 6-19. Test 3: Cracking on the (Left) South Side at $\mu\Delta 1 + 2y = 1.54"$ and (Right) North Side at $\mu\Delta 1 - 2y = -1.51"$ 229
Figure 6-20. Test 3: Cracking on the (Left) West Side at $\mu\Delta 1 + 2x = 1.55"$ and (Right) East Side at $\mu\Delta 1 - 2x = -1.51"$ 230
Figure 6-21. Test 3: (Left) North Concrete Crushing at $\mu\Delta 1.5 + 2y = 2.26"$ and (Right) South Concrete Crushing at $\mu\Delta 1.5 - 1y = -2.26"$ 230
Figure 6-22. Test 3: Cracking on the (Left) South Side at $\mu\Delta 1.5 + 2y = 2.26"$ and (Right) North Side at $\mu\Delta 1.5 - 2y = -2.26"$ 231
Figure 6-23. Test 3: Cracking on the (Left) East and (Right) West Sides after $\mu\Delta 1.5 \pm 2y$ and $\mu\Delta 1 \pm 4x$ 231
Figure 6-24. Test 3: Cracking on the (Left) South Side at $\mu\Delta 2 + 2y = 3.02"$ and (Right) North Side at $\mu\Delta 2 - 2y = -3.01"$ 232
Figure 6-25. Test 3: Cracking on the (Left) West Side at $\mu\Delta 1 + 6x = 1.53"$ and (Right) East Side at $\mu\Delta 1 - 6x = -1.50"$ 232
Figure 6-26. Test 3: Initial Spiral Yield on the (Left) North during $\mu\Delta 3 + 1y = 4.51"$ and (Right) South during $\mu\Delta 3 - 1y = -4.51"$ 233

Figure 6-27. Test 3: Cracking on the (Left) South Side at $\mu\Delta 3 + 2y = 4.51$" and (Right) North Side at $\mu\Delta 3 - 2y = -4.51$" 233
Figure 6-28. Test 3: Cracking on the (Left) East and (Right) West Sides after $\mu\Delta 3 \pm 2y$ and $\mu\Delta 1.5 \pm 2x$ 234
Figure 6-29. Test 3: Unbuckled Reinforcement on the (Left) North at $\mu\Delta 4 + 1y = 6.01$" and (Right) South at $\mu\Delta 4 - 1y = -6.01$" 234
Figure 6-30. Test 3: (Left) East Flaking at $\mu\Delta 2 + 1x = 3.02$" and (Right) Buckling of Bars N and NNE during $\mu\Delta 4 + 2y = 6.04$" 235
Figure 6-31. Test 3: (Left) South Bar Buckling during $\mu\Delta 4 - 2y = -6.03$" and (Right) East Concrete Crushing at $\mu\Delta 2 + 2x = 3.01$" 235
Figure 6-32. Test 3: Crushing on the (Left) East Side at $\mu\Delta 3 + 1x = 4.52$" and (Right) West Side at $\mu\Delta 3 - 1x = -4.51$" 236
Figure 6-33. Test 3: Initial Spiral Yielding on the (Left) East during $\mu\Delta 4 + 1x = 6.02$" and (Right) West during $\mu\Delta 4 - 1x = -6.02$" 236
Figure 6-34. Test 3: Reinforcement Remained Straight on (Left) East at $\mu\Delta 4 + 2x = 6.00$" and (Right) West at $\mu\Delta 4 - 2x = -5.99$" 237
Figure 6-35. Test 3: Buckling of (Left) Bar NNW during $\mu\Delta 5 + 1y = 7.52$" and (Right) Bars SSW and SSE during $\mu\Delta 5 - 1y = -7.52$" 237
Figure 6-36. Test 3: Buckling of Bars (Left) E, ENE, & ESE at $\mu\Delta 5 + 1x = 7.53$" and (Right) W, WNW, & WSW at $\mu\Delta 5 - 1x = -7.52$" 238
Figure 6-37. Test 3: (Left) Buckling of Bars NE & NW at $\mu\Delta 5 + 2y = 7.50$" and (Right) Fracture of Bar N at -3.71" during $\mu\Delta 5 - 2y$ 238
Figure 6-38. Test 3: (Left North and (Right) South Sides of the Specimen after Removal of Instrumentation 239
Figure 6-39. Test 3: (Left) East and (Right) West Sides of the Specimen after Removal of Instrumentation 239
Figure 6-40. Test 3: Vertical Strain Profiles for Loading in the +Y-direction 240
Figure 6-41. Test 3: Vertical Strain Profiles for Loading in the -Y-direction 241
Figure 6-42. Test 3: Spiral Strains Measured Over the North Extreme Fiber Bar during +Y Cycles 241
Figure 6-43. Test 3: Spiral Strains Measured Over the South Extreme Fiber Bar during –Y Cycles 242
Figure 6-44. Test 3: Tension Strain-Disp. for Bar S (Gauge Length 3 Centered 7.62” above the Footing) 242
Figure 6-45. Test 3: Compression Strain-Disp. for Bar N (Gauge Length 1 Centered 1.86” above the Footing) 243
Figure 6-46. Test 3: Tension Strain-Disp. for Bar N (Gauge Length 4 Centered 9.96” above the Footing) 243
Figure 6-47. Test 3: Compression Strain-Disp. for Bar S (Gauge Length 1 Centered 2.15” above the Footing) 244
Figure 6-48. Test 3: Strain Hysteresis over the North Buckled Bar (Gauge Length 2 Centered 4.43” above the Footing) 244
Figure 6-49. Test 3: North Spiral Strain Gauge Hysteresis for the First Layer above the Footing 245
Figure 6-50. Test 3: North Spiral Strain Gauge Hysteresis for the Second Layer above the Footing 245
Figure 6-51. Test 3: Strain Hysteresis over the South Buckled Bar (Gauge Length 1 Centered 2.15” above the Footing) 246

Figure 6-52. Test 3: South Spiral Strain Gauge Hysteresis for the First Layer above the Footing..... 246
Figure 6-53. Test 3: South Spiral Strain Gauge Hysteresis for the Second Layer above the Footing . 247
Figure 6-54. Test 3: Vertical Strain Profiles for Loading in the +X-direction 248
Figure 6-55. Test 3: Vertical Strain Profiles for Loading in the -X-direction 248
Figure 6-56. Test 3: Spiral Strains Measured Over the East Extreme Fiber Bar during +X Cycles..... 249
Figure 6-57. Test 3: Spiral Strains Measured Over the West Extreme Fiber Bar during -X Cycles..... 249
Figure 6-58. Test 3: Tension Strain-Disp. for Bar W (Gauge Length 2 Centered 5.58” above the Footing) 250
Figure 6-59. Test 3: Compression Strain-Disp. for Bar E (Gauge Length 2 Centered 4.65” above the Footing) 250
Figure 6-60. Test 3: Tension Strain-Disp. for Bar E (Gauge Length 2 Centered 4.65” above the Footing) 251
Figure 6-61. Test 3: Compression Strain-Disp. for Bar W (Gauge Length 2 Centered 5.58” above the Footing) 251
Figure 6-62. Test 3: Strain Hysteresis over the East Buckled Bar (Gauge Length 1 Centered 2.11” above the Footing) 252
Figure 6-63. Test 3: East Spiral Strain Gauge Hysteresis for the First Layer above the Footing 252
Figure 6-64. Test 3: East Spiral Strain Gauge Hysteresis for the Second Layer above the Footing.... 253
Figure 6-65. Test 3: Strain Hysteresis over the West Buckled Bar (Gauge Length 2 Centered 5.58” above the Footing) 253
Figure 6-66. Test 3: West Spiral Strain Gauge Hysteresis for the First Layer above the Footing..... 254
Figure 6-67. Test 3: Elastic Curvature Profiles for the Second Instrumented Section above the Footing 255
Figure 6-68. Test 3: Curvature Profiles for the Second Instrumented Section above the Footing 255
Figure 6-69. Test 3: Elastic Vertical Curvature Profiles 256
Figure 6-70. Test 3: Vertical Curvature Profiles for Loading in the +Y-direction..... 256
Figure 6-71. Test 3: Vertical Curvature Profiles for Loading in the -Y-direction 257
Figure 6-72. Test 3: Vertical Curvature Profiles for Loading in the +X-direction..... 257
Figure 6-73. Test 3: Vertical Curvature Profiles for Loading in the -X-direction 258
Figure 6-74. Test 3: Extreme Fiber Bar Strain Penetration Bond Slip Hysteresis 258
Figure 6-75. Test 3: Fixed End Rotations due to Strain Penetration during the Elastic Cycles 259
Figure 6-76. Test 3: Fixed-End Rotations due to Strain Penetration..... 259
Figure 6-77. Test 3: Optotrak Integrated Flexural Disp. Compared to Measured String Pot. Disp.... 260
Figure 6-78. Test 3: Optotrak Integrated Flexural Disp. Compared to Measured String Pot. Disp.... 260
Figure 6-79. Test 3: Measured Extent of Plasticity Compared to Tensile Hinge Lengths..... 261
Figure 6-80. Test 3: Measured Equivalent Strain Penetration Lengths Compared to Design Expressions 261
Figure 6-81. Test 3: Y-Direction Hysteretic Response Compared to PCK (2007) Hinge Length Monotonic Prediction 262
Figure 6-82. Test 3: X-Direction Hysteretic Response Compared to PCK (2007) Hinge Length Monotonic Prediction 262
Figure 6-83. Test 3: Y-Direction Sectional Response Compared to Monotonic Moment Curvature Analysis..... 263

Figure 6-84. Test 3: X-Direction Sectional Response Compared to Monotonic Moment Curvature Analysis 263
Figure 6-85. Test 1 "Symmetric" and Test 3 "Asymmetric" Two-Cycle-Set Hysteretic Comparison .. 264
Figure 6-86. Test 1 "Symmetric" and Test 3 "Asymmetric" Two-Cycle-Set Hysteretic Comparison .. 264
Figure 6-87. Test 2 Symmetric Three-Cycle-Set and Test 3 Asymmetric Two-Cycle-Set 265
Figure 6-88. Test 2 Symmetric Three-Cycle-Set and Test 3 Asymmetric Two-Cycle-Set 265
Figure 7-1. Test 4: Load History and Labeling System for Reinforcement and Cracks 266
Figure 7-2. Comparison of Tests 1 and 4 (Mander, Priestley and Park 1988) Concrete Curves 267
Figure 7-3. Monotonic Prediction Comparison for Tests 1 and 4 267
Figure 7-4. Test 4: 3D Rendering of Initial Optotrak Data, (Left) Cross Section and (Right) Profile ... 269
Figure 7-5. Test 4: Vertical and Horizontal Linear Potentiometers at Footing Interface 269
Figure 7-6. Test 4: Specimen Deformation at $\mu\Delta 6 + 1x = 8.20$" 270
Figure 7-7. Test 4: Y-Displacement History 271
Figure 7-8. Test 4: X-Displacement History 271
Figure 7-9. Test 4: Y-Force History 272
Figure 7-10. Test 4: X-Force History 272
Figure 7-11. Test 4: Type-B Symmetric Two-Cycle-Set Displacement History 273
Figure 7-12. Test 4: Load Path 273
Figure 7-13. Test 4: Y-Direction Hysteretic Response 274
Figure 7-14. Test 4: X-Direction Hysteretic Response 274
Figure 7-15. Test 4: Y-Direction Axial Load History 275
Figure 7-16. Test 4: X-Direction Axial Load History 275
Figure 7-17. Test 4: X-Direction Horizontal Relative Footing Interface Displacement, see Figure 7-5 276
Figure 7-18. Test 4: X-Displacement due to Global Footing Rotation, see Figure 7-5 276
Figure 7-19. Test 4: First Cracking on the South and North Sides of the Specimen during $\Delta y = 0.30$" and $\Delta y = -0.34$" 279
Figure 7-20. Test 4: First Cracking on the West and East Sides of the Specimen during $\Delta x = 0.34$" and $\Delta x = -0.35$" 279
Figure 7-21. Test 4: Cracking on the South and North Sides during $\Delta y' = 0.97$" and $\Delta y' = -0.99$" in Y-Direction 280
Figure 7-22. Test 4: Cracking on the West and East Sides during $\Delta y' = 1.02$" and $\Delta y' = -1.04$" in X-Direction 280
Figure 7-23. Test 4: Cracking on the (Left) South Side at $\mu\Delta 1 + 2y = 1.38$" and (Right) North Side at $\mu\Delta 1 - 2y = -1.39$" 281
Figure 7-24. Test 4: Cracking on the (Left) West Side at $\mu\Delta 1 + 2x = 1.37$" and (Right) East Side at $\mu\Delta 1 - 2x = -1.37$" 281
Figure 7-25. Test 4: Initial Concrete Flaking on (Left) North Side at $\mu\Delta 1.5 + 1y = 2.06$" and (Right) South Side at $\mu\Delta 1.5 - 1y = -2.09$" 282
Figure 7-26. Test 4: Initial Concrete Flaking on (Left) East Side at $\mu\Delta 1.5 + 1x = 2.05$" and (Right) West Side at $\mu\Delta 1.5 - 1x = -2.05$" 282
Figure 7-27. Test 4: (Left) North and (Right) South Sides of the Specimen at the End of $\mu\Delta 1.5$ 283
Figure 7-28. Test 4: Cracking on the (Left) West Side at $\mu\Delta 1.5 + 2x = 2.06$" and (Right) East Side at $\mu\Delta 1.5 - 2x = -2.05$" 283

Figure 7-29. Test 4: Concrete Crushing on the (Left) North Side at $\mu\Delta 2 + 1y = 2.73$" and (Right) South Side at $\mu\Delta 2 - 1y = -2.73$" 284
Figure 7-30. Test 4: Concrete Crushing on the (Left) East Side at $\mu\Delta 2 + 1x = 2.73$" and (Right) West Side at $\mu\Delta 2 - 1x = -2.74$" 284
Figure 7-31. Test 4: (Left) North and (Right) South Sides of the Specimen at the End of $\mu\Delta 2$ 285
Figure 7-32. Test 4: Cracking on the (Left) West Side at $\mu\Delta 2 + 2x = 2.74$" and (Right) East Side at $\mu\Delta 2 - 2x = -2.76$" 285
Figure 7-33. Test 4: Crushing on the (Left) North Side at $\mu\Delta 3 + 1y = 4.11$" and (Right) South Side at $\mu\Delta 3 - 1y = -4.09$" 286
Figure 7-34. Test 4: Crushing on the (Left) East Side at $\mu\Delta 3 + 1x = 4.11$" and (Right) West Side at $\mu\Delta 3 - 1x = -4.14$" 286
Figure 7-35. Test 4: (Left) North and (Right) South Sides of the Specimen at the End of $\mu\Delta 3$ 287
Figure 7-36. Test 4: Cracking on the (Left) West Side at $\mu\Delta 3 + 2x = 4.09$" and (Right) East Side at $\mu\Delta 3 - 2x = -4.09$" 287
Figure 7-37. Test 4: Crushing on the (Left) North Side at $\mu\Delta 4 + 1y = 5.47$" and (Right) South Side at $\mu\Delta 4 - 1y = -5.51$" 288
Figure 7-38. Test 4: Crushing on the (Left) East Side at $\mu\Delta 4 + 1x = 5.47$" and (Right) West Side at $\mu\Delta 4 - 1x = -5.48$" 288
Figure 7-39. Test 4: (Left) North and (Right) South Sides of the Specimen at the End of $\mu\Delta 4$ 289
Figure 7-40. Test 4: Cracking on the (Left) West Side at $\mu\Delta 4 + 2x = 5.48$" and (Right) East Side at $\mu\Delta 4 - 2x = -5.46$" 289
Figure 7-41. Test 4: Unbuckled Reinforcement on the (Left) North at $\mu\Delta 5 + 1y = 6.84$" and (Right) South at $\mu\Delta 5 - 1y = -6.84$" 290
Figure 7-42. Test 4: Unbuckled Reinforcement on the (Left) East at $\mu\Delta 5 + 1x = 6.85$" and (Left) West at $\mu\Delta 5 - 1x = -6.85$" 290
Figure 7-43. Test 4: (Left) Buckling of Bar N at $\mu\Delta 5 + 2y = 6.84$" and (Right) South Bars Remained Straight at $\mu\Delta 5 - 2y = -6.83$" 291
Figure 7-44. Test 4: (Left) Buckling of Bar E at $\mu\Delta 5 + 2x = 6.85$" and (Right) West Bars Remained Straight at $\mu\Delta 5 - 2x = -6.85$" 291
Figure 7-45. Test 4: Buckling of (Left) Bar NNE at $\mu\Delta 6 + 1y = 8.22$" and (Right) Bars S, SSE, and SSW at $\mu\Delta 6 - 1y = -8.23$" 292
Figure 7-46. Test 4: Buckling of (Left) Bars ENE &ESE at $\mu\Delta 6 + 1x = 8.20$" and (Right) Bars W, WNW, & WSW at $\mu\Delta 6 - 1x = -8.21$" 292
Figure 7-47. Test 4: (Left) Buckling of Bars NNW & NE at $\mu\Delta 6 + 2y = 8.21$" and (Right) Fracture of Bar N at -4.75" during $\mu\Delta 6 - 2y$ 293
Figure 7-48. Test 4: (Left) North and (Right) South Sides of the Specimen after Instrumentation Removal 293
Figure 7-49. Test 4: (Left) East and (Right) West Sides of the Specimen after Instrumentation Removal 294
Figure 7-50. Test 4: Close Up of Damage on the North Side of the Specimen 294
Figure 7-51. Test 4: Vertical Strain Profiles for Loading in the +Y-direction 296
Figure 7-52. Test 4: Vertical Strain Profiles for Loading in the -Y-direction 296
Figure 7-53. Test 4: Spiral Strains Measured Over the North Extreme Fiber Bar during +Y Cycles 297
Figure 7-54. Test 4: Spiral Strains Measured Over the South Extreme Fiber Bar during –Y Cycles 297

Figure 7-55. Test 4: Tension Strain-Disp. for Bar S (Gauge Length 4 Centered 6.99” above the Footing) 298
Figure 7-56. Test 4: Compression Strain-Disp. for Bar N (Gauge Length 3 Centered 5.40” above the Footing) 298
Figure 7-57. Test 4: Tension Strain-Disp. for Bar N (Gauge Length 4 Centered 7.37” above the Footing) 299
Figure 7-58. Test 4: Compression Strain-Disp. for Bar S (Gauge Length 1 Centered 1.32” above the Footing) 299
Figure 7-59. Test 4: Compression Strain-Disp. for Bar S (Gauge Length 3 Centered 5.02” above the Footing) 300
Figure 7-60. Test 4: Strain Hysteresis over the North Buckled Bar (Gauge Length 2 Centered 3.46” above the Footing) 300
Figure 7-61. Test 4: North Spiral Strain Gauge Hysteresis for the First Layer above the Footing 301
Figure 7-62. Test 4: North Spiral Strain Gauge Hysteresis for the Second Layer above the Footing 301
Figure 7-63. Test 4: Strain Hysteresis over the South Buckled Bar (Gauge Length 2 Centered 3.05” above the Footing) 302
Figure 7-64. Test 4: South Spiral Strain Gauge Hysteresis for the First Layer above the Footing 302
Figure 7-65. Test 4: South Spiral Strain Gauge Hysteresis for the Second Layer above the Footing 303
Figure 7-66. Test 4: Vertical Strain Profiles for Loading in the +X-direction 304
Figure 7-67. Test 4: Vertical Strain Profiles for Loading in the -X-direction 304
Figure 7-68. Test 4: Spiral Strains Measured Over the East Extreme Fiber Bar during +X Cycles 305
Figure 7-69. Test 4: Spiral Strains Measured Over the West Extreme Fiber Bar during -X Cycles 305
Figure 7-70. Test 4: Tension Strain-Disp. for Bar W (Gauge Length 4 Centered 7.57” above the Footing) 306
Figure 7-71. Test 4: Compression Strain-Disp. for Bar E (Gauge Length 2 Centered 3.62” above the Footing) 306
Figure 7-72. Test 4: Compression Strain-Disp. for Bar E (Gauge Length 3 Centered 5.61” above the Footing) 307
Figure 7-73. Test 4: Tension Strain-Disp. for Bar E (Gauge Length 4 Centered 7.63” above the Footing) 307
Figure 7-74. Test 4: Compression Strain-Disp. for Bar W (Gauge Length 3 Centered 5.62” above the Footing) 308
Figure 7-75. Test 4: Strain Hysteresis over the East Buckled Bar (Gauge Length 2 Centered 3.62” above the Footing) 308
Figure 7-76. Test 4: East Spiral Strain Gauge Hysteresis for the First Layer above the Footing 309
Figure 7-77. Test 4: East Spiral Strain Gauge Hysteresis for the Second Layer above the Footing 309
Figure 7-78. Test 4: Strain Hysteresis over the West Buckled Bar (Gauge Length 3 Centered 5.62” above the Footing) 310
Figure 7-79. Test 4: West Spiral Strain Gauge Hysteresis for the First Layer above the Footing 310
Figure 7-80. Test 4: West Spiral Strain Gauge Hysteresis for the Second Layer above the Footing 311
Figure 7-81. Test 4: Elastic Curvature Profiles for the First Instrumented Section above the Footing 312
Figure 7-82. Test 4: Curvature Profiles for the Second Instrumented Section above the Footing 312
Figure 7-83. Test 4: Elastic Vertical Curvature Profiles 313

Figure 7-84. Test 4: Vertical Curvature Profiles for Loading in the +Y-direction 313
Figure 7-85. Test 4: Vertical Curvature Profiles for Loading in the -Y-direction 314
Figure 7-86. Test 4: Vertical Curvature Profiles for Loading in the +X-direction 314
Figure 7-87. Test 4: Vertical Curvature Profiles for Loading in the -X-direction 315
Figure 7-88. Test 4: Extreme Fiber Bar Strain Penetration Bond Slip Hysteresis 315
Figure 7-89. Test 4: Fixed End Rotations due to Strain Penetration during the Elastic Cycles 316
Figure 7-90. Test 4: Fixed End Rotations due to Strain Penetration 316
Figure 7-91. Test 4: Optotrak Integrated Flexural Disp. Compared to Measured String Pot. Disp. 317
Figure 7-92. Test 4: Optotrak Integrated Flexural Disp. Compared to Measured String Pot. Disp. 317
Figure 7-93. Test 4: Measured Extent of Plasticity Compared to Tensile Hinge Lengths 318
Figure 7-94. Test 4: Measured Equivalent Strain Penetration Lengths Compared to Design Expressions 318
Figure 7-95. Test 4: Y-Direction Hysteretic Response Compared to PCK (2007) Hinge Length Monotonic Prediction 319
Figure 7-96. Test 4: X-Direction Hysteretic Response Compared to PCK (2007) Hinge Length Monotonic Prediction 319
Figure 7-97. Test 4: Y-Direction Sectional Response Compared to Monotonic Moment Curvature Analysis 320
Figure 7-98. Test 4: X-Direction Sectional Response Compared to Monotonic Moment Curvature Analysis 320
Figure 7-99. Tests 1 (0.7%) and 4 (1% Transverse Steel) Hysteretic Response Comparison in the Y-Direction 321
Figure 7-100. Tests 1 (0.7%) and 4 (1% Transverse Steel) Hysteretic Response Comparison in the X-Direction 321
Figure 7-101. Tests 1 and 4 Symmetric Two-Cycle-Set Bidirectional Load History 322
Figure 7-102. Tests 1 and 4 Load Path Comparison 322
Figure 8-1. Test 5: Load History and Labeling System for Reinforcement and Cracks 323
Figure 8-2. Test 5: Optotrak Target Marker and Strain Gauge Instrumentation on the East Side of the Specimen 325
Figure 8-3. Test 5: Y-Displacement History 326
Figure 8-4. Test 5: X-Displacement History 326
Figure 8-5. Test 5: Y-Force History 327
Figure 8-6. Test 5: X-Force History 327
Figure 8-7. Test 5: Type-B Symmetric Three-Cycle-Set Displacement History 328
Figure 8-8. Test 5: Load Path 328
Figure 8-9. Test 5: Y-Direction Hysteretic Response 329
Figure 8-10. Test 5: X-Direction Hysteretic Response 329
Figure 8-11. Test 5: Y-Direction Axial Force History 330
Figure 8-12. Test 5: X-Direction Axial Force History 330
Figure 8-13. Test 5: X-Direction Horizontal Relative Footing Interface Displacement 331
Figure 8-14. Test 5: X-Displacement due to Global Footing Rotation 331
Figure 8-15. Test 5: First Cracking on the South and North Sides of the Specimen during $\Delta y = 0.34$" and $\Delta y = -0.31$" 334

Figure 8-16. Test 5: First Cracking on the West and East Sides of the Specimen during $\Delta x = 0.34$" and $\Delta x = -0.35$" 335
Figure 8-17. Test 5: Cracking on the South and North Sides during $\Delta y' = 1.00$" and $\Delta y' = -0.96$" in Y-Direction 335
Figure 8-18. Test 5: Cracking on the West and East Sides during $\Delta y' = 1.00$" and $\Delta y' = -1.05$" in X-Direction 336
Figure 8-19. Test 5: Cracking on the (Left) South Side at $\mu\Delta 1 + 3y = 1.38$" and (Right) North Side at $\mu\Delta 1 - 3y = -1.38$" 336
Figure 8-20. Test 5: Cracking on the (Left) West Side at $\mu\Delta 1 + 3x = 1.38$" and (Right) East Side at $\mu\Delta 1 - 3x = -1.36$" 337
Figure 8-21. Test 5: Initial Concrete Flaking on (Left) North Side at $\mu\Delta 1.5 + 1y = 2.07$" and (Right) South Side at $\mu\Delta 1.5 - 1y = -2.05$" 337
Figure 8-22. Test 5: (Left) East Concrete Crushing at $\mu\Delta 1.5 + 2x = 2.05$" and (Right) North Concrete Crushing at $\mu\Delta 1.5 + 2y = 2.05$" 338
Figure 8-23. Test 5: (Left) North and (Right) South Sides of the Specimen at the End of $\mu\Delta 1.5$ 338
Figure 8-24. Test 5: Cracking on the (Left) West Side at $\mu\Delta 1.5 + 3x = 2.07$" and (Right) East Side at $\mu\Delta 1.5 - 3x = -2.09$" 339
Figure 8-25. Test 5: Concrete Crushing on the (Left) North Side at $\mu\Delta 2 + 1y = 2.73$" and (Right) South Side at $\mu\Delta 2 - 1y = -2.73$" 339
Figure 8-26. Test 5: Concrete Crushing on the (Left) East Side at $\mu\Delta 2 + 1x = 2.73$" and (Right) West Side at $\mu\Delta 2 - 1x = -2.72$" 340
Figure 8-27. Test 5: (Left) North and (Right) South Sides of the Specimen at the End of $\mu\Delta 2$ 340
Figure 8-28. Test 5: Cracking on the (Left) West Side at $\mu\Delta 2 + 3x = 2.73$" and (Right) East Side at $\mu\Delta 2 - 3x = -2.73$" 341
Figure 8-29. Test 5: (Left) North and (Right) South Sides of the Specimen at the End of $\mu\Delta 3$ 341
Figure 8-30. Test 5: Cracking on the (Left) West Side at $\mu\Delta 3 + 3x = 4.09$" and (Right) East Side at $\mu\Delta 3 - 3x = -4.08$" 342
Figure 8-31. Test 5: Initial Spiral Yield on the (Left) North Side at $\mu\Delta 4 + 1y = 5.48$" and (Right) South Side at $\mu\Delta 4 - 2y = -5.46$" 342
Figure 8-32. Test 5: Initial Spiral Yield on the (Left) East Side at $\mu\Delta 4 + 1x = 5.47$" and (Right) West Side at $\mu\Delta 4 - 2x = -5.46$" 343
Figure 8-33. Test 5: (Left) North and (Right) South Sides of the Specimen at the End of $\mu\Delta 4$ 343
Figure 8-34. Test 5: Cracking on the (Left) West Side at $\mu\Delta 4 + 3x = 5.45$" and (Right) East Side at $\mu\Delta 4 - 3x = -5.45$" 344
Figure 8-35. Test 5: Bars Remained Visibly Straight on (Left) North at $\mu\Delta 5 + 2y = 6.84$" and (Right) South at $\mu\Delta 5 - 2y = -6.85$" 344
Figure 8-36. Test 5: (Left) East Bar Buckling at $\mu\Delta 5 + 2x = 6.84$" and (Right) West Bars Visibly Straight at $\mu\Delta 5 - 2x = -6.81$" 345
Figure 8-37. Test 5: (Left) Bar N and NNE Buckling at $\mu\Delta 5 + 3y = 6.81$" and (Right) South Bars Straight at $\mu\Delta 5 - 3y = -6.82$" 345
Figure 8-38. Test 5: (Left) Buckling of Bars ENE and ESE at $\mu\Delta 5 + 3x = 6.83$" and (Right) Buckling of Bar W at $\mu\Delta 5 - 3x = -6.83$" 346
Figure 8-39. Test 5: (Left) North Side at $\mu\Delta 6 + 1y = 8.20$" and (Right) Buckling of Bars S and SSE at $\mu\Delta 6 - 1y = -8.20$" 346

Figure 8-40. Test 5: (Left) Buckling of Bars NE and SE at $\mu\Delta 6 + 1x = 8.19$" and (Right) Deformation in the East Buckled Bar 347
Figure 8-41. Test 5: Buckling of Bars (Left) WNW and WSW at $\mu\Delta 6 - 1x = -8.19$" and (Right) NNW and NW at $\mu\Delta 6 + 2y = 8.23$" 347
Figure 8-42. Test 5: Buckling of Bars SSW and SW at $\mu\Delta 6 - 2y = -8.19$" 348
Figure 8-43. Test 5: Sideways Buckling of Bars on the SE side of the Specimen at $\mu\Delta 6 - 2y = -8.19$" 348
Figure 8-44. Test 5: Spiral Fracture at 7.13" during $\mu\Delta 6 + 2x$ Led to a Counterclockwise Twist of the Column about the Base 349
Figure 8-45. Test 5: (Left) South and (Right) North Sides of the Specimen after Instrumentation Removal 349
Figure 8-46. Test 5: (Left) West and (Right) East Sides of the Specimen after Instrumentation Removal 350
Figure 8-47. Test 5: Close-Up of SE Region where the Second Spiral Layer Fractured 350
Figure 8-48. Test 5: Vertical Strain Profiles for Loading in the +Y-direction 352
Figure 8-49. Test 5: Vertical Strain Profiles for Loading in the -Y-direction 352
Figure 8-50. Test 5: Spiral Strains Measured Over the North Extreme Fiber Bar during +Y Cycles 353
Figure 8-51. Test 5: Spiral Strains Measured Over the South Extreme Fiber Bar during -Y Cycles 353
Figure 8-52. Test 5: Tension Strain-Disp. for Bar S (Gauge Length 3 Centered 5.23” above the Footing) 354
Figure 8-53. Test 5: Compression Strain-Disp. for Bar N (Gauge Length 2 Centered 3.14” above the Footing) 354
Figure 8-54. Test 5: Tension Strain-Disp. for Bar N (Gauge Length 3 Centered 5.07” above the Footing) 355
Figure 8-55. Test 5: Compression Strain-Disp. for Bar S (Gauge Length 2 Centered 3.27” above the Footing) 355
Figure 8-56. Test 5: Strain Hysteresis over the North Buckled Bar (Gauge Length 2 Centered 3.14” above the Footing) 356
Figure 8-57. Test 5: North Spiral Strain Gauge Hysteresis for the First Layer above the Footing 356
Figure 8-58. Test 5: North Spiral Strain Gauge Hysteresis for the Second Layer above the Footing 357
Figure 8-59. Test 5: Strain Hysteresis over the South Buckled Bar (Gauge Length 2 Centered 3.27” above the Footing) 357
Figure 8-60. Test 5: South Spiral Strain Gauge Hysteresis for the Second Layer above the Footing 358
Figure 8-61. Test 5: South Spiral Strain Gauge Hysteresis for the Third Layer above the Footing 358
Figure 8-62. Test 5: Vertical Strain Profiles for Loading in the +X-direction 359
Figure 8-63. Test 5: Vertical Strain Profiles for Loading in the -X-direction 360
Figure 8-64. Test 5: Spiral Strains Measured Over the East Extreme Fiber Bar during +X Cycles 360
Figure 8-65. Test 5: Spiral Strains Measured Over the West Extreme Fiber Bar during -X Cycles 361
Figure 8-66. Test 5: Tension Strain-Disp. for Bar W (Gauge Length 3 Centered 5.39” above the Footing) 361
Figure 8-67. Test 5: Compression Strain-Disp. for Bar E (Gauge Length 3 Centered 5.39” above the Footing) 362
Figure 8-68. Test 5: Tension Strain-Disp. for Bar E (Gauge Length 4 Centered 7.46” above the Footing) 362

Figure 8-69. Test 5: Tension Strain-Disp. for Bar W (Gauge Length 2 Centered 3.42" above the Footing) 363
Figure 8-70. Test 5: Strain Hysteresis over the East Buckled Bar (Gauge Length 2 Centered 3.46" above the Footing) 363
Figure 8-71. Test 5: East Spiral Strain Gauge Hysteresis for the First Layer above the Footing 364
Figure 8-72. Test 5: East Spiral Strain Gauge Hysteresis for the Second Layer above the Footing..... 364
Figure 8-73. Test 5: Strain Hysteresis over the West Buckled Bar (Gauge Length 2 Centered 3.42" above the Footing) 365
Figure 8-74. Test 5: West Spiral Strain Gauge Hysteresis for the First Layer above the Footing..... 365
Figure 8-75. Test 5: West Spiral Strain Gauge Hysteresis for the Second Layer above the Footing .. 366
Figure 8-76. Test 5: Elastic Curvature Profiles for the First Instrumented Section above the Footing 367
Figure 8-77. Test 5: Curvature Profiles for the Third Instrumented Section above the Footing 367
Figure 8-78. Test 5: Elastic Vertical Curvature Profiles 368
Figure 8-79. Test 5: Vertical Curvature Profiles for Loading in the +Y-direction..... 368
Figure 8-80. Test 5: Vertical Curvature Profiles for Loading in the -Y-direction 369
Figure 8-81. Test 5: Vertical Curvature Profiles for Loading in the +X-direction..... 369
Figure 8-82. Test 5: Vertical Curvature Profiles for Loading in the -X-direction 370
Figure 8-83. Test 5: Extreme Fiber Bar Strain Penetration Bond Slip Hysteresis 370
Figure 8-84. Test 5: Fixed End Rotations due to Strain Penetration during the Elastic Cycles 371
Figure 8-85. Test 5: Fixed End Rotations due to Strain Penetration 371
Figure 8-86. Test 5: Optotrak Integrated Flexural Disp. Compared to Measured String Pot. Disp.... 372
Figure 8-87. Test 5: Optotrak Integrated Flexural Disp. Compared to Measured String Pot. Disp.... 372
Figure 8-88. Test 5: Measured Extent of Plasticity Compared to Tensile Hinge Lengths..... 373
Figure 8-89. Test 5: Measured Equivalent Strain Penetration Lengths Compared to Design Expressions 373
Figure 8-90. Test 5: Y-Direction Hysteretic Response Compared to PCK (2007) Hinge Length Monotonic Prediction 374
Figure 8-91. Test 5: X-Direction Hysteretic Response Compared to PCK (2007) Hinge Length Monotonic Prediction 374
Figure 8-92. Test 5: Y-Direction Sectional Response Compared to Monotonic Moment Curvature Analysis..... 375
Figure 8-93. Test 5: X-Direction Sectional Response Compared to Monotonic Moment Curvature Analysis..... 375
Figure 8-94. Y-Direction Hysteretic Comparison for Tests 4 (Two-Cycle-Set) and 5 (Three-Cycle-Set) 376
Figure 8-95. X-Direction Hysteretic Comparison for Tests 4 (Two-Cycle-Set) and 5 (Three-Cycle-Set) 376
Figure 9-1. Test 6: Load History and Labeling System for Reinforcement and Cracks..... 377
Figure 9-2. Test 6: Optotrak Target Marker and Strain Gauge Instrumentation on the East Side of the Specimen 379
Figure 9-3. Test 6: Specimen Deformation at $\mu\Delta 6 + 1y = 8.22$" 380
Figure 9-4. Test 6: Y-Displacement History 381
Figure 9-5. Test 6: X-Displacement History 381

Figure 9-6. Test 6: Y-Force History 382
Figure 9-7. Test 6: X-Force History 382
Figure 9-8. Test 6: Type-B Asymmetric Two-Cycle-Set Displacement History 383
Figure 9-9. Test 6: Load Path 383
Figure 9-10. Test 6: Y-Direction Hysteretic Response 384
Figure 9-11. Test 6: X-Direction Hysteretic Response 384
Figure 9-12. Test 6: Y-Direction Axial Force History 385
Figure 9-13. Test 6: X-Direction Axial Force History 385
Figure 9-14. Test 6: Linear Potentiometers at the Transfer Footing Interface, (Left) North and (Right) West Sides 386
Figure 9-15. Test 6: First Cracking on the South and North Sides of the Specimen during $\Delta y = 0.35$" and $\Delta y = -0.36$" 389
Figure 9-16. Test 6: First Cracking on the West and East Sides of the Specimen during $\Delta x = 0.38$" and $\Delta x = -0.32$" 389
Figure 9-17. Test 6: Cracking on the South and North Sides during $\Delta y' = 1.05$" and $\Delta y' = -1.05$" in Y-Direction 390
Figure 9-18. Test 6: Cracking on the West and East Sides during $\Delta y' = 1.06$" and $\Delta y' = -0.96$" in X-Direction 390
Figure 9-19. Test 6: Cracking on the (Left) South Side at $\mu\Delta 1 + 2y = 1.40$" and (Right) North Side at $\mu\Delta 1 - 2y = -1.36$" 391
Figure 9-20. Test 6: Cracking on the (Left) West Side at $\mu\Delta 1 + 2x = 1.39$" and (Right) East Side at $\mu\Delta 1 - 2x = -1.36$" 391
Figure 9-21. Test 6: Cracking on the (Left) South Side at $\mu\Delta 1.5 + 2y = 2.07$" and (Right) North Side at $\mu\Delta 1.5 - 2y = -2.05$" 392
Figure 9-22. Test 6: Cracking on the (Left) West and (Right) East Sides after $\mu\Delta 1.5 \pm 2y$ and $\mu\Delta 1 \pm 4x$ 392
Figure 9-23. Test 6: (Left) North Concrete Crushing at $\mu\Delta 2 + 1y = 2.73$" and (Right) South Concrete Crushing at $\mu\Delta 2 - 1y = -2.75$" 393
Figure 9-24. Test 6: Cracking on the (Left) South Side at $\mu\Delta 2 + 2y = 2.77$" and (Right) North Side at $\mu\Delta 2 - 2y = -2.73$" 393
Figure 9-25. Test 6: Cracking on the (Left) West and (Right) East Sides after $\mu\Delta 2 \pm 2y$ and $\mu\Delta 1 \pm 6x$ 394
Figure 9-26. Test 6: (Left) Initial North Spiral Yielding during $\mu\Delta 3 + 1y = 4.12$" and (Right) South Crushing at $\mu\Delta 3 - 1y = -4.09$" 394
Figure 9-27. Test 6: Cracking on the (Left) South Side at $\mu\Delta 3 + 2y = 4.13$" and (Right) North Side at $\mu\Delta 3 - 2y = -4.10$" 395
Figure 9-28. Test 6: Cracking on the (Left) West and (Right) East Sides after $\mu\Delta 3 \pm 2y$ and $\mu\Delta 1.5 \pm 2x$ 395
Figure 9-29. Test 6: (Left) North Crushing at $\mu\Delta 4 + 1y = 5.48$" and (Right) Initial South Spiral Yielding during $\mu\Delta 4 - 1y = -5.51$" 396
Figure 9-30. Test 6: (Left) West Concrete Crushing at $\mu\Delta 2 - 1x = -2.76$" and (Right) East Concrete Crushing at $\mu\Delta 2 + 2x = 2.74$" 396
Figure 9-31. Test 6: Cracking on the (Left) South Side at $\mu\Delta 4 + 2y = 5.48$" and (Right) North Side at $\mu\Delta 4 - 2y = -5.49$" 397

Figure 9-32. Test 6: Cracking on the (Left) West and (Right) East Sides after $\mu\Delta 4 \pm 2y$ and $\mu\Delta 2 \pm 2x$ 397
Figure 9-33. Test 6: Reinforcement Remained Straight on (Left) North at $\mu\Delta 5 + 1y = 6.82$" and (Right) South at $\mu\Delta 5 - 1y = -6.85$" 398
Figure 9-34. Test 6: Buckling of (Left) Bars N and NNE at $\mu\Delta 5 + 2y = 6.87$" and (Right) Bar S at $\mu\Delta 5 - 2y = -6.84$" 398
Figure 9-35. Test 6: Initial Spiral Yielding on the (Left) East Side at $\mu\Delta 4 + 2x = 5.48$" and (Right) West Side at $\mu\Delta 4 - 2x = -5.46$" 399
Figure 9-36. Test 6: Crushing on the (Left) East Side at $\mu\Delta 5 + 2x = 6.84$" and (Right) West Side at $\mu\Delta 5 - 2x = -6.84$" 399
Figure 9-37. Test 6: Reinforcement Remained Straight on (Left) East at $\mu\Delta 5 + 2x = 6.84$" and (Right) West at $\mu\Delta 5 - 2x = -6.84$" 400
Figure 9-38. Test 6: Buckling of (Left) Bar NNW at $\mu\Delta 6 + 1y = 8.22$" and (Right) Bars SSW and SSE at $\mu\Delta 6 - 1y = -8.21$" 400
Figure 9-39. Test 6: Buckling of Bars (Left) E, ESE, & ENE at $\mu\Delta 6 + 1x = 8.21$" and (Right) W, WSW, & WNW at $\mu\Delta 6 - 1x = -8.21$" 401
Figure 9-40. Test 6: Buckling of Bar NE during $\mu\Delta 6 + 2y = 8.21$" 401
Figure 9-41. Test 6: Specimen Deformation at $\mu\Delta 6 + 1x = 8.21$" 402
Figure 9-42. Test 6: (Left) North and (Right) South Sides of the Specimen after Instrumentation Removal 403
Figure 9-43. Test 6: (Left) North and (Right) South Sides of the Specimen after Instrumentation Removal 403
Figure 9-44. Test 6: (Left) West and (Right) East Sides of the Specimen after Instrumentation Removal 404
Figure 9-45. Test 6: Vertical Strain Profiles for Loading in the +Y-direction 405
Figure 9-46. Test 6: Vertical Strain Profiles for Loading in the -Y-direction 406
Figure 9-47. Test 6: Spiral Strains Measured Over the North Extreme Fiber Bar during +Y Cycles 406
Figure 9-48. Test 6: Spiral Strains Measured Over the South Extreme Fiber Bar during -Y Cycles 407
Figure 9-49. Test 6: Tension Strain-Disp. for Bar S (Gauge Length 4 Centered 7.46” above the Footing) 407
Figure 9-50. Test 6: Compression Strain-Disp. for Bar N (Gauge Length 3 Centered 5.28” above the Footing) 408
Figure 9-51. Test 6: Tension Strain-Disp. for Bar N (Gauge Length 5 Centered 9.20” above the Footing) 408
Figure 9-52. Test 6: Compression Strain-Disp. for Bar S (Gauge Length 1 Centered 1.59” above the Footing) 409
Figure 9-53. Test 6: Compression Strain-Disp. for Bar S (Gauge Length 3 Centered 5.52” above the Footing) 409
Figure 9-54. Test 6: Strain Hysteresis over the North Buckled Bar (Gauge Length 2 Centered 3.26” above the Footing) 410
Figure 9-55. Test 6: Strain Hysteresis over the North Buckled Bar (Gauge Length 3 Centered 5.28” above the Footing) 410
Figure 9-56. Test 6: North Spiral Strain Gauge Hysteresis for the Second Layer above the Footing 411
Figure 9-57. Test 6: North Spiral Strain Gauge Hysteresis for the Third Layer above the Footing 411

Figure 9-58. Test 6: Strain Hysteresis over the South Buckled Bar (Gauge Length 2 Centered 3.53" above the Footing) 412
Figure 9-59. Test 6: Strain Hysteresis over the South Buckled Bar (Gauge Length 3 Centered 5.52" above the Footing) 412
Figure 9-60. Test 6: South Spiral Strain Gauge Hysteresis for the First Layer above the Footing..... 413
Figure 9-61. Test 6: South Spiral Strain Gauge Hysteresis for the Second Layer above the Footing . 413
Figure 9-62. Test 6: Vertical Strain Profiles for Loading in the +X-direction 415
Figure 9-63. Test 6: Vertical Strain Profiles for Loading in the -X-direction 415
Figure 9-64. Test 6: Spiral Strains Measured Over the East Extreme Fiber Bar during +X Cycles..... 416
Figure 9-65. Test 6: Spiral Strains Measured Over the West Extreme Fiber Bar during -X Cycles..... 416
Figure 9-66. Test 6: Tension Strain-Disp. for Bar W (Gauge Length 1 Centered 1.88" above the Footing) 417
Figure 9-67. Test 6: Tension Strain-Disp. for Bar W (Gauge Length 2 Centered 3.92" above the Footing) 417
Figure 9-68. Test 6: Compression Strain-Disp. for Bar E (Gauge Length 2 Centered 3.54" above the Footing) 418
Figure 9-69. Test 6: Tension Strain-Disp. for Bar E (Gauge Length 2 Centered 3.54" above the Footing) 418
Figure 9-70. Test 6: Compression Strain-Disp. for Bar W (Gauge Length 2 Centered 3.92" above the Footing) 419
Figure 9-71. Test 6: Strain Hysteresis over the East Buckled Bar (Gauge Length 2 Centered 3.54" above the Footing) 419
Figure 9-72. Test 6: East Spiral Strain Gauge (Black) and Optotrak (Blue) Hysteresis for the First Layer above the Footing..... 420
Figure 9-73. Test 6: East Spiral Optotrak Strain Hysteresis for the Second Layer above the Footing420
Figure 9-74. Test 6: Strain Hysteresis over the West Buckled Bar (Gauge Length 2 Centered 3.92" above the Footing) 421
Figure 9-75. Test 6: Strain Hysteresis over the West Buckled Bar (Gauge Length 3 Centered 5.99" above the Footing) 421
Figure 9-76. Test 6: West Spiral Strain Gauge Hysteresis for the First Layer above the Footing..... 422
Figure 9-77. Test 6: West Spiral Strain Gauge Hysteresis for the Second Layer above the Footing .. 422
Figure 9-78. Test 6: Elastic Curvature Profiles for the First Instrumented Section above the Footing 423
Figure 9-79. Test 6: Curvature Profiles for the Third Instrumented Section above the Footing 424
Figure 9-80. Test 6: Elastic Vertical Curvature Profiles 424
Figure 9-81. Test 6: Vertical Curvature Profiles for Loading in the +Y-direction..... 425
Figure 9-82. Test 6: Vertical Curvature Profiles for Loading in the -Y-direction 425
Figure 9-83. Test 6: Vertical Curvature Profiles for Loading in the +X-direction..... 426
Figure 9-84. Test 6: Vertical Curvature Profiles for Loading in the -X-direction 426
Figure 9-85. Test 6: Extreme Fiber Bar Strain Penetration Bond Slip Hysteresis 427
Figure 9-86. Test 6: Fixed End Rotations due to Strain Penetration during the Elastic Cycles 427
Figure 9-87. Test 6: Fixed End Rotations due to Strain Penetration 428
Figure 9-88. Test 6: Optotrak Integrated Flexural Disp. Compared to Measured String Pot. Disp.... 428
Figure 9-89. Test 6: Optotrak Integrated Flexural Disp. Compared to Measured String Pot. Disp.... 429

Figure 9-90. Test 6: Measured Extent of Plasticity Compared to Tensile Hinge Lengths 429
Figure 9-91. Test 6: Measured Equivalent Strain Penetration Lengths Compared to Design Expressions 430
Figure 9-92. Test 6: Y-Direction Hysteretic Response Compared to PCK (2007) Hinge Length Monotonic Prediction 430
Figure 9-93. Test 6: X-Direction Hysteretic Response Compared to PCK (2007) Hinge Length Monotonic Prediction 431
Figure 9-94. Y-Direction Hysteretic Comparison for Tests 4 (Symmetric) and 6 (Asymmetric) Two-Cycle-Set 432
Figure 9-95. X-Direction Hysteretic Comparison for Tests 4 (Symmetric) and 6 (Asymmetric) Two-Cycle-Set 433
Figure 9-96. Y-Direction Hysteretic Comparison for Tests 3 (Asymmetric) and 6 (Asymmetric) Two-Cycle-Set 433
Figure 9-97. X-Direction Hysteretic Comparison for Tests 3 (Asymmetric) and 6 (Asymmetric) Two-Cycle-Set 434
Figure 9-98. Y-Direction Asymmetric Two-Cycle-Set Displacement History Comparison for Tests 3 and 6 434
Figure 9-99. X-Direction Asymmetric Two-Cycle-Set Displacement History Comparison for Tests 3 and 6 434
Figure 10-1. Test 7: Load History Orientation and Labeling System for Reinforcement and Cracks 435
Figure 10-2. Test 7: Deformed Specimen at $\mu\Delta 7 + 1y = 8.67$" 437
Figure 10-3. Test 7: Y-Displacement History 438
Figure 10-4. Test 7: X-Displacement History 438
Figure 10-5. Test 7: Y-Force History 439
Figure 10-6. Test 7: X-Force History 439
Figure 10-7. Test 7: Type-B Symmetric Two-Cycle-Set Displacement History 440
Figure 10-8. Test 7: Load Path 440
Figure 10-9. Test 7: Y-Direction Hysteretic Response 441
Figure 10-10. Test 7: X-Direction Hysteretic Response 441
Figure 10-11. Test 7: Y-Direction Axial Force History 442
Figure 10-12. Test 7: X-Direction Axial Force History 442
Figure 10-13. Test 7: Cracking on the (Left) South Side at $\mu\Delta 1 + 2y = 1.25$" and (Right) North Side at $\mu\Delta 1 - 2y = -1.23$" 444
Figure 10-14. Test 7: Cracking on the (Left) West Side at $\mu\Delta 1 + 2x = 1.23$" and (Right) East Side at $\mu\Delta 1 - 2x = -1.28$" 444
Figure 10-15. Test 7: Concrete Crushing on the (Left) South Side at $\mu\Delta 1.5 - 1y = -1.91$" and (Right) East Side at $\mu\Delta 1.5 + 1x = 1.89$" 445
Figure 10-16. Test 7: Concrete Crushing on the (Left) West Side at $\mu\Delta 2 - 1x = -2.48$" and (Right) North Side at $\mu\Delta 2 + 2y = 2.49$" 445
Figure 10-17. Test 7: Spiral Yielding on the (Left) East Side at $\mu\Delta 4 + 1x = 4.96$" and (Right) West Side at $\mu\Delta 5 - 1x = -6.16$" 446
Figure 10-18. Test 7: Spiral Yielding on the (Left) North Side at $\mu\Delta 6 + 1y = 7.40$" and (Right) South Side at $\mu\Delta 6 - 1y = -7.40$" 446

Figure 10-19. Test 7: Bar Buckling on the (Left) East Side at $\mu\Delta 6 + 1x = 7.40$" and (Right) West Side at $\mu\Delta 6 - 2x = -7.39$"..... 447
Figure 10-20. Test 7: (Left) North Bar Buckling at $\mu\Delta 7 + 1y = 8.67$" and (Right) North Bar Fracture at -8.19" during $\mu\Delta 7 - 2y$..... 447
Figure 10-21. Test 7: (Left) North and (Right) South Sides of the Specimen after the Test..... 448
Figure 10-22. Test 7: (Left) East and (Right) West Sides of the Specimen after the Test 448
Figure 10-23. Test 7: Vertical Strain Profiles for Loading in the +Y-direction 449
Figure 10-24. Test 7: Vertical Strain Profiles for Loading in the -Y-direction 450
Figure 10-25. Test 7: Spiral Strains Measured Over the North Extreme Fiber Bar during +Y Cycles . 450
Figure 10-26. Test 7: Spiral Strains Measured Over the South Extreme Fiber Bar during -Y Cycles .. 451
Figure 10-27. Test 7: Tension Strain-Disp. for Bar S (Gauge Length 5 Centered 7.59” above the Footing) 451
Figure 10-28. Test 7: Compression Strain-Disp. for Bar N (Gauge Length 4 Centered 6.03” above the Footing) 452
Figure 10-29. Test 7: Tension Strain-Disp. for Bar N (Gauge Length 1 Centered 1.35” above the Footing) 452
Figure 10-30. Test 7: Tension Strain-Disp. for Bar N (Gauge Length 2 Centered 2.93” above the Footing) 453
Figure 10-31. Test 7: Compression Strain-Disp. for Bar S (Gauge Length 2 Centered 3.03” above the Footing) 453
Figure 10-32. Test 7: Strain Hysteresis over the North Buckled Bar (Gauge Length 2 Centered 2.93” above the Footing) 454
Figure 10-33. Test 7: Spiral Strain Hysteresis for the 3rd North Layer above the Footing..... 454
Figure 10-34. Test 7: Strain Hysteresis over the South Bar (Gauge Length 2 Centered 3.03” above the Footing) 455
Figure 10-35. Test 7: Strain Hysteresis over the South Bar (Gauge Length 3 Centered 4.55” above the Footing) 455
Figure 10-36. Test 7: Spiral Strain Hysteresis for the 2nd South Layer above the Footing 456
Figure 10-37. Test 7: Vertical Strain Profiles for Loading in the +X-direction 457
Figure 10-38. Test 7: Vertical Strain Profiles for Loading in the -X-direction..... 457
Figure 10-39. Test 7: Spiral Strains Measured Over the East Extreme Fiber Bar during +X Cycles.... 458
Figure 10-40. Test 7: Spiral Strains Measured Over the West Extreme Fiber Bar during -X Cycles... 458
Figure 10-41. Test 7: Tension Strain-Disp. for Bar W (Gauge Length 2 Centered 3.30” above the Footing) 459
Figure 10-42. Test 7: Tension Strain-Disp. for Bar W (Gauge Length 3 Centered 4.83” above the Footing) 459
Figure 10-43. Test 7: Compression Strain-Disp. for Bar E (Gauge Length 3 Centered 4.46” above the Footing) 460
Figure 10-44. Test 7: Tension Strain-Disp. for Bar E (Gauge Length 1 Centered 1.43” above the Footing) 460
Figure 10-45. Test 7: Tension Strain-Disp. for Bar E (Gauge Length 2 Centered 2.97” above the Footing) 461
Figure 10-46. Test 7: Compression Strain-Disp. for Bar W (Gauge Length 3 Centered 4.83” above the Footing) 461

Figure 10-47. Test 7: Strain Hysteresis over the East Buckled Bar (Gauge Length 2 Centered 2.97" above the Footing) 462
Figure 10-48. Test 7: Strain Hysteresis over the East Buckled Bar (Gauge Length 3 Centered 4.46" above the Footing) 462
Figure 10-49. Test 7: Spiral Strain Hysteresis for the 2nd East Layer above the Footing 463
Figure 10-50. Test 7: Spiral Strain Hysteresis for the 3rd East Layer above the Footing 463
Figure 10-51. Test 7: Strain Hysteresis over the West Buckled Bar (Gauge Length 2 Centered 3.30" above the Footing) 464
Figure 10-52. Test 7: Strain Hysteresis over the West Buckled Bar (Gauge Length 3 Centered 4.83" above the Footing) 464
Figure 10-53. Test 7: Spiral Strain Hysteresis for the 1st West Layer above the Footing 465
Figure 10-54. Test 7: Spiral Strain Hysteresis for the 2nd West Layer above the Footing 465
Figure 10-55. Test 7: Elastic Curvature Profiles for the First Instrumented Section above the Footing 466
Figure 10-56. Test 7: Curvature Profiles for the Second Instrumented Section above the Footing .. 467
Figure 10-57. Test 7: Elastic Vertical Curvature Profiles 467
Figure 10-58. Test 7: Vertical Curvature Profiles for Loading in the +Y-direction 468
Figure 10-59. Test 7: Vertical Curvature Profiles for Loading in the -Y-direction 468
Figure 10-60. Test 7: Vertical Curvature Profiles for Loading in the +X-direction 469
Figure 10-61. Test 7: Vertical Curvature Profiles for Loading in the -X-direction 469
Figure 10-62. Test 7: Extreme Fiber Bar Strain Penetration Bond Slip Hysteresis 470
Figure 10-63. Test 7: Fixed End Rotations due to Strain Penetration during the Elastic Cycles 470
Figure 10-64. Test 7: Fixed End Rotations due to Strain Penetration 471
Figure 10-65. Test 7: Optotrak Integrated Flexural Disp. Compared to Measured String Pot. Disp. . 471
Figure 10-66. Test 7: Optotrak Integrated Flexural Disp. Compared to Measured String Pot. Disp. . 472
Figure 10-67. Test 7: Measured Extent of Plasticity Compared to Tensile Hinge Lengths 472
Figure 10-68. Test 7: Measured Equivalent Strain Penetration Lengths Compared to Design Expressions 473
Figure 10-69. Test 7: Y-Direction Hysteretic Response Compared to PCK (2007) Hinge Length Monotonic Prediction 473
Figure 10-70. Test 7: X-Direction Hysteretic Response Compared to PCK (2007) Hinge Length Monotonic Prediction 474
Figure 11-1. Test 8: Load History Orientation and Labeling System for Reinforcement and Cracks . 475
Figure 11-2. Test 8: Deformed Specimen at $\mu\Delta 7 + 1x = 8.53$" 477
Figure 11-3. Test 8: Y-Displacement History 478
Figure 11-4. Test 8: X-Displacement History 478
Figure 11-5. Test 8: Y-Force History 479
Figure 11-6. Test 8: X-Force History 479
Figure 11-7. Test 8: Type-B Symmetric Two-Cycle-Set Displacement History 480
Figure 11-8. Test 8: Load Path 480
Figure 11-9. Test 8: Y-Direction Hysteretic Response 481
Figure 11-10. Test 8: X-Direction Hysteretic Response 481
Figure 11-11. Test 8: Y-Direction Axial Force History 482
Figure 11-12. Test 8: X-Direction Axial Force History 482

Figure 11-13. Test 8: Crack Profiles on the (Left) South Side at $\mu\Delta 1 + 2y = 1.24$" and (Right) North Side at $\mu\Delta 1 - 2y = -1.23$" 484
Figure 11-14. Test 8: Crack Profiles on the (Left) West Side at $\mu\Delta 1 + 2x = 1.22$" and (Right) East Side at $\mu\Delta 1 - 2x = -1.21$" 484
Figure 11-15. Test 8: Concrete Crushing on the (Left) North Side at $\mu\Delta 1.5 + 1y = 1.87$" and (Right) South Side at $\mu\Delta 1.5 - 1y = -1.88$" 485
Figure 11-16. Test 8: Concrete Crushing on the (Left) East Side at $\mu\Delta 2 + 1x = 2.46$" and (Right) West Side at $\mu\Delta 2 - 1x = -2.46$" 485
Figure 11-17. Test 8: Spiral Yielding on the (Left) East Side at $\mu\Delta 4 + 1x = 4.88$" and (Right) North Side at $\mu\Delta 5 + 1y = 6.11$" 486
Figure 11-18. Test 8: Spiral Yielding on the (Left) South Side at $\mu\Delta 5 - 1y = -6.11$" and (Right) West Side at $\mu\Delta 5 - 1x = -6.10$" 486
Figure 11-19. Test 8: Bar Buckling on the (Left) East Side at $\mu\Delta 6 + 1x = 7.32$" and (Right) West Side at $\mu\Delta 6 - 1x = -7.36$" 487
Figure 11-20. Test 8: Bar Buckling on the (Left) North Side at $\mu\Delta 6 + 2y = 7.31$" and (Right) South Side at $\mu\Delta 6 - 2y = -7.34$" 487
Figure 11-21. Test 8: (Left) East Side Buckled Deformation at $\mu\Delta 7 + 1x = 8.53$" and (Right) East Bar Fracture during $\mu\Delta 7 - 1X$ 488
Figure 11-22. Test 8: (Left) South and (Right) North Sides of the Column after the Test 488
Figure 11-23. Test 8: (Left) East and (Right) West Sides of the Column after the Test 489
Figure 11-24. Test 8: Vertical Strain Profiles for Loading in the +Y-direction 490
Figure 11-25. Test 8: Vertical Strain Profiles for Loading in the -Y-direction 490
Figure 11-26. Test 8: Spiral Strains Measured Over the North Extreme Fiber Bar during +Y Cycles . 491
Figure 11-27. Test 8: Spiral Strains Measured Over the South Extreme Fiber Bar during -Y Cycles .. 491
Figure 11-28. Test 8: Tension Strain-Disp. for Bar S (Gauge Length 2 Centered 4.11” above the Footing) 492
Figure 11-29. Test 8: Compression Strain-Disp. for Bar N (Gauge Length 2 Centered 4.15” above the Footing) 492
Figure 11-30. Test 8: Tension Strain-Disp. for Bar N (Gauge Length 3 Centered 6.23” above the Footing) 493
Figure 11-31. Test 8: Compression Strain-Disp. for Bar S (Gauge Length 1 Centered 2.06” above the Footing) 493
Figure 11-32. Test 8: Strain Hysteresis over the North Buckled Bar (Gauge Length 1 Centered 2.08” above the Footing) 494
Figure 11-33. Test 8: Spiral Strain Hysteresis for the 2nd North Layer above the Footing 494
Figure 11-34. Test 8: Strain Hysteresis over the South Buckled Bar (Gauge Length 2 Centered 4.11” above the Footing) 495
Figure 11-35. Test 8: Spiral Strain Hysteresis for the 2nd South Layer above the Footing 495
Figure 11-36. Test 8: Vertical Strain Profiles for Loading in the +X-direction 497
Figure 11-37. Test 8: Vertical Strain Profiles for Loading in the -X-direction 497
Figure 11-38. Test 8: Spiral Strains Measured Over the East Extreme Fiber Bar during +X Cycles 498
Figure 11-39. Test 8: Spiral Strains Measured Over the West Extreme Fiber Bar during -X Cycles ... 498
Figure 11-40. Test 8: Tension Strain-Disp. for Bar W (Gauge Length 1 Centered 2.10” above the Footing) 499

Figure 11-41. Test 8: Tension Strain-Disp. for Bar W (Gauge Length 4 Centered 8.08" above the Footing) 499
Figure 11-42. Test 8: Compression Strain-Disp. for Bar E (Gauge Length 1 Centered 1.76" above the Footing) 500
Figure 11-43. Test 8: Compression Strain-Disp. for Bar E (Gauge Length 3 Centered 5.57" above the Footing) 500
Figure 11-44. Test 8: Tension Strain-Disp. for Bar E (Gauge Length 4 Centered 8.08" above the Footing) 501
Figure 11-45. Test 8: Compression Strain-Disp. for Bar W (Gauge Length 3 Centered 6.07" above the Footing) 501
Figure 11-46. Test 8: Strain Hysteresis over the East Buckled Bar (Gauge Length 2 Centered 3.58" above the Footing) 502
Figure 11-47. Test 8: Strain Hysteresis over the East Buckled Bar (Gauge Length 3 Centered 5.57" above the Footing) 502
Figure 11-48. Test 8: Spiral Strain Hysteresis for the 2nd East Layer above the Footing 503
Figure 11-49. Test 8: Spiral Strain Hysteresis for the 3rd East Layer above the Footing 503
Figure 11-50. Test 8: Strain Hysteresis over the West Buckled Bar (Gauge Length 3 Centered 6.07" above the Footing) 504
Figure 11-51. Test 8: Spiral Strain Hysteresis for the 1st West Layer above the Footing 504
Figure 11-52. Test 8: Spiral Strain Hysteresis for the 2nd West Layer above the Footing 505
Figure 11-53. Test 8: Elastic Curvature Profiles for the First Instrumented Section above the Footing 506
Figure 11-54. Test 8: Curvature Profiles for the First Instrumented Section above the Footing 506
Figure 11-55. Test 8: Elastic Vertical Curvature Profiles 507
Figure 11-56. Test 8: Vertical Curvature Profiles for Loading in the +Y-direction 507
Figure 11-57. Test 8: Vertical Curvature Profiles for Loading in the -Y-direction 508
Figure 11-58. Test 8: Vertical Curvature Profiles for Loading in the +X-direction 508
Figure 11-59. Test 8: Vertical Curvature Profiles for Loading in the -X-direction 509
Figure 11-60. Test 8: Extreme Fiber Bar Strain Penetration Bond Slip Hysteresis 509
Figure 11-61. Test 8: Fixed End Rotations due to Strain Penetration during the Elastic Cycles 510
Figure 11-62. Test 8: Fixed End Rotations due to Strain Penetration 510
Figure 11-63. Test 8: Optotrak Integrated Flexural Disp. Compared to Measured String Pot. Disp. . 511
Figure 11-64. Test 8: Optotrak Integrated Flexural Disp. Compared to Measured String Pot. Disp. . 511
Figure 11-65. Test 8: Measured Extent of Plasticity Compared to Tensile Hinge Lengths 512
Figure 11-66. Test 8: Measured Equivalent Strain Penetration Lengths Compared to Design Expressions 512
Figure 11-67. Test 8: Y-Direction Hysteretic Response Compared to PCK (2007) Hinge Length Monotonic Prediction 513
Figure 11-68. Test 8: X-Direction Hysteretic Response Compared to PCK (2007) Hinge Length Monotonic Prediction 513
Figure 11-69. Tests 7 (1.3%) and 8 (1% Transverse Steel) Hysteretic Response Comparison in the Y-Direction 514
Figure 11-70. Tests 7 (1.3%) and 8 (1% Transverse Steel) Hysteretic Response Comparison in the X-Direction 514

Figure 12-1. Test 9: Load History Orientation and Labeling System for Reinforcement and Cracks . 515
Figure 12-2. Test 9: Deformed Specimen at $\mu\Delta 6 + 1x = 7.68$" 517
Figure 12-3. Test 9: Y-Displacement History 518
Figure 12-4. Test 9: X-Displacement History 518
Figure 12-5. Test 9: Y-Force History 519
Figure 12-6. Test 9: X-Force History 519
Figure 12-7. Test 9: Type-B Symmetric Two-Cycle-Set Displacement History 520
Figure 12-8. Test 9: Load Path 520
Figure 12-9. Test 9: Y-Direction Hysteretic Response 521
Figure 12-10. Test 9: X-Direction Hysteretic Response 521
Figure 12-11. Test 9: Y-Direction Axial Force History 522
Figure 12-12. Test 9: X-Direction Axial Force History 522
Figure 12-13. Test 9: Cracking on the (Left) South Side at $\mu\Delta 1 + 2y = 1.28$" and (Right) North Side at $\mu\Delta 1 - 2y = -1.28$" 524
Figure 12-14. Test 9: Cracking on the (Left) West Side at $\mu\Delta 1 + 2x = 1.27$" and (Right) East Side at $\mu\Delta 1 - 2x = -1.28$" 524
Figure 12-15. Test 9: Concrete Crushing on the (Left) South Side at $\mu\Delta 1.5 - 1y = -1.90$" and (Right) North Side at $\mu\Delta 2 + 1y = 2.57$" 525
Figure 12-16. Test 9: Concrete Crushing on the (Left) East Side at $\mu\Delta 2 + 1x = 2.57$" and (Right) West Side at $\mu\Delta 2 - 1x = -2.58$" 525
Figure 12-17. Test 9: Spiral Yielding on the (Left) North Side at $\mu\Delta 4 + 1y = 5.10$" and (Right) South Side at $\mu\Delta 4 - 1y = -5.14$" 526
Figure 12-18. Test 9: Spiral Yielding on the (Left) East Side at $\mu\Delta 4 + 1x = 5.10$" and (Right) West Side at $\mu\Delta 4 - 2x = -5.11$" 526
Figure 12-19. Test 9: Buckling of (Left) Adjacent Bar NNE at $\mu\Delta 5 + 2y = 6.41$" and (Right) Bars S and SSW at $\mu\Delta 5 - 2y = -6.40$" 527
Figure 12-20. Test 9: (Left) Buckling of the East Bar at $\mu\Delta 5 + 2x = 6.41$" and (Right) Buckling of the West Bar at $\mu\Delta 5 - 2x = -6.40$" 527
Figure 12-21. Test 9: Buckling of (Left) North Bar at $\mu\Delta 6 + 1y = 7.66$" and (Right) Adjacent Bars ENE and ESE at $\mu\Delta 6 + 1x = 7.68$" 528
Figure 12-22. Test 9: (Left) Specimen at $\mu\Delta 6 + 1x = 7.68$" and (Right) East Bar Fracture at -6.16" during $\mu\Delta 6 - 1X$ 528
Figure 12-23. Test 9: (Left) North and (Right) West Sides of the Specimen after the Test 529
Figure 12-24. Test 9: (Left) South and (Right) East Sides of the Specimen after the Test 529
Figure 12-25. Test 9: Vertical Strain Profiles for Loading in the +Y-direction 531
Figure 12-26. Test 9: Vertical Strain Profiles for Loading in the -Y-direction 531
Figure 12-27. Test 9: Spiral Strains Measured Over the North Extreme Fiber Bar during +Y Cycles . 532
Figure 12-28. Test 9: Spiral Strains Measured Over the North Extreme Fiber Bar during -Y Cycles .. 532
Figure 12-29. Test 9: Tension Strain-Disp. for Bar S (Gauge Length 2 Centered 5.26” above the Footing) 533
Figure 12-30. Test 9: Compression Strain-Disp. for Bar N (Gauge Length 1 Centered 2.57” above the Footing) 533
Figure 12-31. Test 9: Compression Strain-Disp. for Bar N (Gauge Length 3 Centered 8.17” above the Footing) 534

Figure 12-32. Test 9: Tension Strain-Disp. for Bar N (Gauge Length 5 Centered 13.78" above the Footing) 534
Figure 12-33. Test 9: Compression Strain-Disp. for Bar S (Gauge Length 1 Centered 2.47" above the Footing) 535
Figure 12-34. Test 9: Compression Strain-Disp. for Bar S (Gauge Length 2 Centered 5.26" above the Footing) 535
Figure 12-35. Test 9: Strain Hysteresis over the North Buckled Bar (Gauge Length 2 Centered 5.38" above the Footing) 536
Figure 12-36. Test 9: Spiral Strain Hysteresis for the 1st North Layer above the Footing 536
Figure 12-37. Test 9: Spiral Strain Hysteresis for the 2nd North Layer above the Footing 537
Figure 12-38. Test 9: Strain Hysteresis over the South Buckled Bar (Gauge Length 1 Centered 2.47" above the Footing) 537
Figure 12-39. Test 9: Spiral Strain Hysteresis for the 1st South Layer above the Footing 538
Figure 12-40. Test 9: Spiral Strain Hysteresis for the 2nd South Layer above the Footing 538
Figure 12-41. Test 9: Vertical Strain Profiles for Loading in the +X-direction 540
Figure 12-42. Test 9: Vertical Strain Profiles for Loading in the -X-direction 540
Figure 12-43. Test 9: Spiral Strains Measured Over the East Extreme Fiber Bar during +X Cycles 541
Figure 12-44. Test 9: Spiral Strains Measured Over the East Extreme Fiber Bar during -X Cycles 541
Figure 12-45. Test 9: Tension Strain-Disp. for Bar W (Gauge Length 2 Centered 4.30" above the Footing) 542
Figure 12-46. Test 9: Tension Strain-Disp. for Bar W (Gauge Length 3 Centered 7.02" above the Footing) 542
Figure 12-47. Test 9: Compression Strain-Disp. for Bar E (Gauge Length 1 Centered 2.50" above the Footing) 543
Figure 12-48. Test 9: Compression Strain-Disp. for Bar E (Gauge Length 2 Centered 5.28" above the Footing) 543
Figure 12-49. Test 9: Tension Strain-Disp. for Bar E (Gauge Length 3 Centered 8.07" above the Footing) 544
Figure 12-50. Test 9: Compression Strain-Disp. for Bar W (Gauge Length 2 Centered 4.30" above the Footing) 544
Figure 12-51. Test 9: Strain Hysteresis over the East Buckled Bar (Gauge Length 1 Centered 2.50" above the Footing) 545
Figure 12-52. Test 9: Spiral Strain Hysteresis for the 1st East Layer above the Footing 545
Figure 12-53. Test 9: Spiral Strain Hysteresis for the 2nd East Layer above the Footing 546
Figure 12-54. Test 9: Strain Hysteresis over the West Buckled Bar (Gauge Length 1 Centered 1.92" above the Footing) 546
Figure 12-55. Test 9: Spiral Strain Hysteresis for the 2nd West Layer above the Footing 547
Figure 12-56. Test 9: Elastic Curvature Profiles for the Second Instrumented Section above the Footing 548
Figure 12-57. Test 9: Curvature Profiles for the Second Instrumented Section above the Footing 548
Figure 12-58. Test 9: Elastic Vertical Curvature Profiles 549
Figure 12-59. Test 9: Vertical Curvature Profiles for Loading in the +Y-direction 549
Figure 12-60. Test 9: Vertical Curvature Profiles for Loading in the -Y-direction 550
Figure 12-61. Test 9: Vertical Curvature Profiles for Loading in the +X-direction 550

Figure 12-62. Test 9: Vertical Curvature Profiles for Loading in the -X-direction 551
Figure 12-63. Test 9: Extreme Fiber Bar Strain Penetration Bond Slip Hysteresis 551
Figure 12-64. Test 9: Fixed End Rotations due to Strain Penetration during the Elastic Cycles 552
Figure 12-65. Test 9: Fixed End Rotations due to Strain Penetration 552
Figure 12-66. Test 9: Optotrak Integrated Flexural Disp. Compared to Measured String Pot. Disp.. 553
Figure 12-67. Test 9: Optotrak Integrated Flexural Disp. Compared to Measured String Pot. Disp.. 553
Figure 12-68. Test 9: Measured Extent of Plasticity Compared to Tensile Hinge Lengths..... 554
Figure 12-69. Test 9: Measured Equivalent Strain Penetration Lengths Compared to Design Expressions 554
Figure 12-70. Test 9: Y-Direction Hysteretic Response Compared to PCK (2007) Hinge Length Monotonic Prediction..... 555
Figure 12-71. Test 9: X-Direction Hysteretic Response Compared to PCK (2007) Hinge Length Monotonic Prediction..... 555
Figure 12-72. Tests 7 (1.3%) and 9 (0.7% Transverse Steel) Hysteretic Response Comparison in the Y-Direction 556
Figure 12-73. Tests 7 (1.3%) and 9 (0.7% Transverse Steel) Hysteretic Response Comparison in the X-Direction 556
Figure 12-74. Tests 8 (1%) and 9 (0.7% Transverse Steel) Hysteretic Response Comparison in the Y-Direction 557
Figure 12-75. Tests 8 (1%) and 9 (0.7% Transverse Steel) Hysteretic Response Comparison in the X-Direction 557
Figure 13-1. Test 10: Load History Orientation and Labeling System for Reinforcement and Cracks558
Figure 13-2. Test 10: Specimen Deformation at $\mu\Delta 6 - 1x = -8.13$" 560
Figure 13-3. Test 10: Y-Displacement History 561
Figure 13-4. Test 10: X-Displacement History 561
Figure 13-5. Test 10: Y-Force History 562
Figure 13-6. Test 10: X-Force History 562
Figure 13-7. Test 10: Type-B Symmetric Two-Cycle-Set Displacement History 563
Figure 13-8. Test 10: Load Path 563
Figure 13-9. Test 10: Y-Direction Hysteretic Response 564
Figure 13-10. Test 10: X-Direction Hysteretic Response 564
Figure 13-11. Test 10: Y-Direction Axial Force History 565
Figure 13-12. Test 10: X-Direction Axial Force History 565
Figure 13-13. Test 10: Cracking on the (Left) South Side at $\mu\Delta 1 + 2y = 1.35$" and (Right) North Side at $\mu\Delta 1 - 2y = -1.34$" 567
Figure 13-14. Test 10: Cracking on the (Left) West Side at $\mu\Delta 1 + 2x = 1.36$" and (Right) East Side at $\mu\Delta 1 - 2x = -1.35$"..... 567
Figure 13-15. Test 10: Concrete Crushing on the (Left) North Side at $\mu\Delta 1.5 + 1y = 2.03$" and (Right) South Side at $\mu\Delta 1.5 - 2y = -2.05$" 568
Figure 13-16. Test 10: Concrete Crushing on the (Left) East Side at $\mu\Delta 2 + 1x = 2.72$" and (Right) West Side at $\mu\Delta 2 - 1x = -2.74$"..... 568
Figure 13-17. Test 10: Spiral Yielding on the (Left) North Side at $\mu\Delta 4 + 1y = 5.41$" and (Right) East Side at $\mu\Delta 4 + 1x = 5.44$"..... 569

Figure 13-18. Test 10: Spiral Yielding on the (Left) West Side at $\mu\Delta 5 - 1x = -6.77$" and (Right) South Side at $\mu\Delta 6 - 1y = -8.11$" 569
Figure 13-19. Test 10: Crack Profiles at the end of $\mu\Delta 5$ on the (Left) North Side and (Right) South Side of the Column 570
Figure 13-20. Test 10: Crack Profiles at the end of $\mu\Delta 5$ on the (Left) East Side and (Right) West Side of the Column 570
Figure 13-21. Test 10: Bar Buckling on the (Left) North Side at $\mu\Delta 6 + 1y = 8.15$" and (Right) East Side at $\mu\Delta 6 + 1x = 8.13$" 571
Figure 13-22. Test 10: (Left) Buckling of Bar NNW at $\mu\Delta 6 + 2y = 8.17$" and (Right) More Deformation in Bar E at $\mu\Delta 6 + 2x = 8.15$" 571
Figure 13-23. Test 10: Buckling of (Left) Bar NNE at $\mu\Delta 6.5 + 1y = 8.82$" (Right) Bars SSE, S, and SSW at $\mu\Delta 6.5 - 1y = -8.81$" 572
Figure 13-24. Test 10: North Bar Fracture at -8.00" during $\mu\Delta 6.5 - 1y$ 572
Figure 13-25. Test 10: (Left) South and (Right) West Sides of the Specimen after the Test 573
Figure 13-26. Test 10: (Left) North and (Right) East Sides of the Specimen after the Test 573
Figure 13-27. Test 10: Vertical Strain Profiles for Loading in the +Y-direction 575
Figure 13-28. Test 10: Vertical Strain Profiles for Loading in the -Y-direction 575
Figure 13-29. Test 10: Spiral Strains Measured Over the North Extreme Fiber Bar during +Y Cycles 576
Figure 13-30. Test 10: Spiral Strains Measured Over the South Extreme Fiber Bar during -Y Cycles 576
Figure 13-31. Test 10: Tension Strain-Disp. for Bar S (Gauge Length 2 Centered 4.33” above the Footing) 577
Figure 13-32. Test 10: Compression Strain-Disp. for Bar N (Gauge Length 1 Centered 1.46” above the Footing) 577
Figure 13-33. Test 10: Compression Strain-Disp. for Bar N (Gauge Length 3 Centered 4.53” above the Footing) 578
Figure 13-34. Test 10: Tension Strain-Disp. for Bar N (Gauge Length 5 Centered 7.56” above the Footing) 578
Figure 13-35. Test 10: Compression Strain-Disp. for Bar S (Gauge Length 1 Centered 2.80” above the Footing) 579
Figure 13-36. Test 10: Strain Hysteresis over the North Buckled Bar (Gauge Length 2 Centered 2.98” above the Footing) 579
Figure 13-37. Test 10: Strain Hysteresis over the North Buckled Bar (Gauge Length 3 Centered 4.53” above the Footing) 580
Figure 13-38. Test 10: Spiral Strain Hysteresis for the 1st North Layer above the Footing 580
Figure 13-39. Test 10: Spiral Strain Hysteresis for the 2nd North Layer above the Footing 581
Figure 13-40. Test 10: Strain Hysteresis over the South Buckled Bar (Gauge Length 1 Centered 2.80” above the Footing) 581
Figure 13-41. Test 10: Spiral Strain Hysteresis for the 2nd South Layer above the Footing 582
Figure 13-42. Test 10: Vertical Strain Profiles for Loading in the +X-direction 583
Figure 13-43. Test 10: Vertical Strain Profiles for Loading in the -X-direction 583
Figure 13-44. Test 10: Spiral Strains Measured Over the East Extreme Fiber Bar during +X Cycles .. 584
Figure 13-45. Test 10: Spiral Strains Measured Over the West Extreme Fiber Bar during -X Cycles . 584
Figure 13-46. Test 10: Tension Strain-Disp. for Bar W (Gauge Length 4 Centered 5.95” above the Footing) 585

Figure 13-47. Test 10: Compression Strain-Disp. for Bar E (Gauge Length 3 Centered 1.93" above the Footing) 585
Figure 13-48. Test 10: Compression Strain-Disp. for Bar E (Gauge Length 3 Centered 5.04" above the Footing) 586
Figure 13-49. Test 10: Tension Strain-Disp. for Bar E (Gauge Length 5 Centered 8.14" above the Footing) 586
Figure 13-50. Test 10: Compression Strain-Disp. for Bar W (Gauge Length 3 Centered 4.38" above the Footing) 587
Figure 13-51. Test 10: Strain Hysteresis over the East Buckled Bar (Gauge Length 2 Centered 3.51" above the Footing) 587
Figure 13-52. Test 10: Spiral Strain Hysteresis for the 1st East Layer above the Footing 588
Figure 13-53. Test 10: Spiral Strain Hysteresis for the 2nd East Layer above the Footing 588
Figure 13-54. Test 10: Strain Hysteresis over the West Buckled Bar (Gauge Length 2 Centered 2.84" above the Footing) 589
Figure 13-55. Test 10: Strain Hysteresis over the West Buckled Bar (Gauge Length 2 Centered 4.38" above the Footing) 589
Figure 13-56. Test 10: Spiral Strain Hysteresis for the 2nd West Layer above the Footing 590
Figure 13-57. Test 10: Elastic Curvature Profiles for the First Instrumented Section above the Footing 591
Figure 13-58. Test 10: Curvature Profiles for the Third Instrumented Section above the Footing ... 591
Figure 13-59. Test 10: Elastic Vertical Curvature Profiles 592
Figure 13-60. Test 10: Vertical Curvature Profiles for Loading in the +Y-direction 592
Figure 13-61. Test 10: Vertical Curvature Profiles for Loading in the -Y-direction 593
Figure 13-62. Test 10: Vertical Curvature Profiles for Loading in the +X-direction 593
Figure 13-63. Test 10: Vertical Curvature Profiles for Loading in the -X-direction 594
Figure 13-64. Test 10: Extreme Fiber Bar Strain Penetration Bond Slip Hysteresis 594
Figure 13-65. Test 10: Fixed End Rotations due to Strain Penetration during the Elastic Cycles 595
Figure 13-66. Test 10: Fixed End Rotations due to Strain Penetration 595
Figure 13-67. Test 10: Optotrak Integrated Flexural Disp. Compared to Measured String Pot. Disp. 596
Figure 13-68. Test 10: Optotrak Integrated Flexural Disp. Compared to Measured String Pot. Disp. 596
Figure 13-69. Test 10: Measured Extent of Plasticity Compared to Tensile Hinge Lengths 597
Figure 13-70. Test 10: Measured Equivalent Strain Penetration Lengths Compared to Design Expressions 597
Figure 13-71. Test 10: Y-Direction Hysteretic Response Compared to PCK (2007) Hinge Length Monotonic Prediction 598
Figure 13-72. Test 10: Y-Direction Hysteretic Response Compared to PCK (2007) Hinge Length Monotonic Prediction 598
Figure 13-73. Tests 10 (1.3%) and 4 (1% Transverse Steel) Hysteretic Response Comparison in the Y-Direction 599
Figure 13-74. Tests 10 (1.3%) and 4 (1% Transverse Steel) Hysteretic Response Comparison in the X-Direction 599

Figure 13-75. Tests 10 (2.1%) and 7 (1.6% Longitudinal Steel) Hysteretic Response Comparison in the Y-Direction 600
Figure 13-76. Tests 10 (2.1%) and 7 (1.6% Longitudinal Steel) Hysteretic Response Comparison in the X-Direction 600
Figure 14-1. Test 11: Bidirectional Load History Orientation and Bar Naming System 602
Figure 14-2. Original Megathrust LH Compared to Scaled LH in Test 11 (Y-Direction Displacements) 603
Figure 14-3. Original Megathrust LH Compared to Scaled LH in Test 11 (X-Direction Displacements) 603
Figure 14-4. Test 8: Y-Displacement History (Bidirectional Symmetric 2-Cycle-Set) 1% Transverse Steel 604
Figure 14-5. Test 8: X-Displacement History (Bidirectional Symmetric 2-Cycle-Set) 1% Transverse Steel 604
Figure 14-6. Test 8: Y-Direction Hysteretic Response (Bidirectional Symmetric 2-Cycle-Set) 1% Transverse Steel 605
Figure 14-7. Test 8: X-Direction Hysteretic Response (Bidirectional Symmetric 2-Cycle-Set) 1% Transverse Steel 605
Figure 14-8. Scaled Megathrust Y-Direction Load Path Compared to Symmetric 2-Cycle-Set 606
Figure 14-9. Scaled Megathrust X-Direction Load Path Compared to Symmetric 2-Cycle-Set 606
Figure 14-10. Scaled Megathrust Y-Direction Load Path Compared to Symmetric 3-Cycle-Set 607
Figure 14-11. Scaled Megathrust X-Direction Load Path Compared to Symmetric 3-Cycle-Set 607
Figure 14-12. Test 9: Y-Displacement History (Bidirectional Symmetric 2-Cycle-Set) 0.7% Transverse Steel 608
Figure 14-13. Test 9: X-Displacement History (Bidirectional Symmetric 2-Cycle-Set) 0.7% Transverse Steel 608
Figure 14-14. Test 9: Y-Direction Hysteretic Response (Bidirectional Symmetric 2-Cycle-Set) 0.7% Transverse Steel 609
Figure 14-15. Test 9: X-Direction Hysteretic Response (Bidirectional Symmetric 2-Cycle-Set) 0.7% Transverse Steel 609
Figure 14-16. Test 11: Deformed Specimen at $\mu\Delta 7 + 1x = 8.49"$ 612
Figure 14-17. Test 11: Y-Displacement History 613
Figure 14-18. Test 11: X-Displacement History 613
Figure 14-19. Test 11: Y-Force History 614
Figure 14-20. Test 11: X-Force History 614
Figure 14-21. Test 11: Scaled Megathrust Loading Protocol from (Bazaez and Dusicka 2016) 615
Figure 14-22. Test 11: Load Path 615
Figure 14-23. Test 11: Y-Direction Hysteretic Response 616
Figure 14-24. Test 11: X-Direction Hysteretic Response 616
Figure 14-25. Test 11: Y-Direction Axial Force History 617
Figure 14-26. Test 11: X-Direction Axial Force History 617
Figure 14-27. Test 11: Concrete Crushing on the South Side of the Specimen during $\mu\Delta 2.2 - 1y = -2.69"$ 619
Figure 14-28. Test 11: Concrete Crushing on the East Side of the Specimen during $\mu\Delta 2.2 + 1x = 2.67"$ 620

Figure 14-29. Test 11: Concrete Crushing on the West Side of the Specimen during $\mu\Delta 2.2 - 1x = -2.73"$ 620
Figure 14-30. Test 11: Concrete Crushing on the North Side of the Specimen during $\mu\Delta 2.4 + 1y = 2.96"$ 621
Figure 14-31. Test 11: (Left) North and (Right) South Sides of the Specimen during Compressive Cycles of $\mu\Delta 4$ 621
Figure 14-32. Test 11: (Left) East and (Right) West Sides of the Specimen during Compressive Cycles of $\mu\Delta 4$ 622
Figure 14-33. Test 11: Spiral Yielding on the (Left) North Side at $\mu\Delta 5 + 1y = 6.09"$ and (Right) West Side at $\mu\Delta 5 - 1x = -6.07"$ 622
Figure 14-34. Test 11: Spiral Yielding on the (Left) South Side at $\mu\Delta 6 - 1y = -7.32"$ and (Right) East Side at $\mu\Delta 6 + 1x = 7.35"$ 623
Figure 14-35. Test 11: (Left) North Bar Buckling at $\mu\Delta 7 + 1y = 8.55"$ and (Right) South Remained Straight at $\mu\Delta 7 - 1y = -8.57"$ 623
Figure 14-36. Test 11: Buckling of East bars NE, NNE, E and ENE during $\mu\Delta 7 + 1x = 8.49"$ 624
Figure 14-37. Test 11: Buckling of West bars NW, WNW, and W during $\mu\Delta 7 - 1x = -8.51"$ 624
Figure 14-38. Test: Buckling of Bars (Left) NNW during $\mu\Delta 4.5p + 1y = 5.50"$ (Right) SE and SSE during $\mu\Delta 4.5p - 1y = -5.51"$ 625
Figure 14-39. Test 11: Buckled Deformation on the East Side at $\mu\Delta 4.5p + 1x = 5.48"$ 625
Figure 14-40. Test 11: Buckling of Adjacent West Bars WSW and SW during $\mu\Delta 4.5p - 1x = -5.48"$ 626
Figure 14-41. Test 11: Fracture of the East Extreme Fiber Bar at $\Delta x = -4.56"$ during $\mu\Delta 4.5p - 1x = -5.48"$ 626
Figure 14-42. Test 11: (Left) North and (Right) East Sides of the Specimen after the Test 627
Figure 14-43. Test 11: (Left) South and (Right) West Sides of the Specimen after the Test 627
Figure 14-44. Test 11: Vertical Strain Profiles for Loading in the +Y-direction 629
Figure 14-45. Test 11: Vertical Strain Profiles for Loading in the -Y-direction 629
Figure 14-46. Test 11: Spiral Strains Measured Over the North Extreme Fiber Bar during +Y Cycles 630
Figure 14-47. Test 11: Spiral Strains Measured Over the South Extreme Fiber Bar during -Y Cycles 630
Figure 14-48. Test 11: Tension Strain-Disp. for Bar S (Gauge Length 3 Centered 5.89” above the Footing) 631
Figure 14-49. Test 11: Tension Strain-Disp. for Bar S (Gauge Length 4 Centered 7.88” above the Footing) 631
Figure 14-50. Test 11: Compression Strain-Disp. for Bar N (Gauge Length 1 Centered 2.06” above the Footing) 632
Figure 14-51. Test 11: Tension Strain-Disp. for Bar N (Gauge Length 2 Centered 4.07” above the Footing) 632
Figure 14-52. Test 11: Compression Strain-Disp. for Bar S (Gauge Length 1 Centered 2.05” above the Footing) 633
Figure 14-53. Test 11: Strain Hysteresis over the North Buckled Bar (Gauge Length 2 Centered 4.07” above the Footing) 633
Figure 14-54. Test 11: Spiral Strain Hysteresis for the 2nd North Layer above the Footing 634
Figure 14-55. Test 11: Strain Hysteresis for the South Bar (Gauge Length 1 Centered 2.05” above the Footing) 634

Figure 14-56. Test 11: Strain Hysteresis for the South Bar (Gauge Length 2 Centered 3.92" above the Footing) 635
Figure 14-57. Test 11: Spiral Strain Hysteresis for the 3rd South Layer above the Footing 635
Figure 14-58. Test 11: Vertical Strain Profiles for Loading in the +X-direction 636
Figure 14-59. Test 11: Vertical Strain Profiles for Loading in the -X-direction 637
Figure 14-60. Test 11: Spiral Strains Measured Over the East Extreme Fiber Bar during +X Cycles .. 637
Figure 14-61. Test 11: Spiral Strains Measured Over the East Extreme Fiber Bar during -X Cycles ... 638
Figure 14-62. Test 11: Tension Strain-Disp. for Bar W (Gauge Length 2 Centered 4.13" above the Footing) 638
Figure 14-63. Test 11: Tension Strain-Disp. for Bar W (Gauge Length 3 Centered 6.18" above the Footing) 639
Figure 14-64. Test 11: Compression Strain-Disp. for Bar E (Gauge Length 1 Centered 2.51" above the Footing) 639
Figure 14-65. Test 11: Compression Strain-Disp. for Bar E (Gauge Length 3 Centered 6.74" above the Footing) 640
Figure 14-66. Test 11: Tension Strain-Disp. for Bar E (Gauge Length 1 Centered 2.51" above the Footing) 640
Figure 14-67. Test 11: Compression Strain-Disp. for Bar W (Gauge Length 2 Centered 4.13" above the Footing) 641
Figure 14-68. Test 11: Strain Hysteresis over the East Buckled Bar (Gauge Length 1 Centered 2.51" above the Footing) 641
Figure 14-69. Test 11: Spiral Strain Hysteresis for the 1st East Layer above the Footing 642
Figure 14-70. Test 11: Spiral Strain Hysteresis for the 2nd East Layer above the Footing 642
Figure 14-71. Test 11: Strain Hysteresis over the West Buckled Bar (Gauge Length 1 Centered 2.02" above the Footing) 643
Figure 14-72. Test 11: Strain Hysteresis over the West Buckled Bar (Gauge Length 2 Centered 4.13" above the Footing) 643
Figure 14-73. Test 11: Spiral Strain Hysteresis for the 1st West Layer above the Footing 644
Figure 14-74. Test 11: Elastic Curvature Profiles for the First Instrumented Section above the Footing 645
Figure 14-75. Test 11: Curvature Profiles for the Second Instrumented Section above the Footing 645
Figure 14-76. Test 11: Elastic Vertical Curvature Profiles 646
Figure 14-77. Test 11: Vertical Curvature Profiles for Loading in the +Y-direction 646
Figure 14-78. Test 11: Vertical Curvature Profiles for Loading in the -Y-direction 647
Figure 14-79. Test 11: Vertical Curvature Profiles for Loading in the +X-direction 647
Figure 14-80. Test 11: Vertical Curvature Profiles for Loading in the -X-direction 648
Figure 14-81. Test 11: Extreme Fiber Bar Strain Penetration Bond Slip Hysteresis 648
Figure 14-82. Test 11: Fixed End Rotations due to Strain Penetration during the Elastic Cycles 649
Figure 14-83. Test 11: Fixed End Rotations due to Strain Penetration 649
Figure 14-84. Test 11: Optotrak Integrated Flexural Disp. Compared to Measured String Pot. Disp. 650
Figure 14-85. Test 11: Optotrak Integrated Flexural Disp. Compared to Measured String Pot. Disp. 650
Figure 14-86. Test 11: Measured Extent of Plasticity Compared to Tensile Hinge Lengths 651

Figure 14-87. Test 11: Measured Equivalent Strain Penetration Lengths Compared to Design Expressions 651
Figure 14-88. Test 11: Y-Direction Hysteretic Response Compared to PCK (2007) Hinge Length Monotonic Prediction 652
Figure 14-89. Test 11: X-Direction Hysteretic Response Compared to PCK (2007) Hinge Length Monotonic Prediction 652
Figure 14-90. Y-Direction Hysteretic Comparison for Tests 8 (2-Cycle-Set) and 11 (Megathrust) 653
Figure 14-91. X-Direction Hysteretic Comparison for Tests 8 (2-Cycle-Set) and 11 (Megathrust) 653
Figure 15-1. Test 12: Bidirectional Load History Orientation and Bar Naming System 654
Figure 15-2.Test 12: Experimental Setup 656
Figure 15-3. Test 12: Y-Displacement History 657
Figure 15-4. Test 12: X-Displacement History 657
Figure 15-5. Test 12: Y-Force History 658
Figure 15-6. Test 12: X-Force History 658
Figure 15-7. Test 12: Scaled Megathrust Loading Protocol from (Bazaez and Dusicka 2016) 659
Figure 15-8. Test 12: Load Path 659
Figure 15-9. Test 12: Y-Direction Hysteretic Response 660
Figure 15-10. Test 12: X-Direction Hysteretic Response 660
Figure 15-11. Test 12: Y-Direction Axial Force History 661
Figure 15-12. Test 12: X-Direction Axial Force History 661
Figure 15-13. Test 12: Concrete Crushing on the West Side of the Specimen during $\mu\Delta 1.7 - 1x = -2.11"$ 663
Figure 15-14. Test 12: Concrete Crushing on the East Side of the Specimen during $\mu\Delta 1.8 + 1x = 2.19"$ 663
Figure 15-15. Test 12: (Left) North and (Right) South Sides of the Specimen at the End of $\mu\Delta 2$ 664
Figure 15-16. Test 12: (Left) West Side at $\mu\Delta 2 + 1x = 2.43"$ and (Right) East Side at $\mu\Delta 2 - 1x = -2.46"$ 664
Figure 15-17. Test 12: Concrete Crushing on the South Side of the Specimen during $\mu\Delta 2.2 - 1y = -2.68"$ 665
Figure 15-18. Test 12: Concrete Crushing on the North Side of the Specimen during $\mu\Delta 2.4 + 1y = 2.93"$ 665
Figure 15-19. Test 12: (Left) North and (Right) South Sides of the Specimen at the End of $\mu\Delta 3$ 666
Figure 15-20. Test 12: (Left) West Side at $\mu\Delta 3 + 1x = 3.66"$ and (Right) East Side at $\mu\Delta 3 - 1x = -3.65"$ 666
Figure 15-21. Test 12: (Left) North and (Right) South Sides of the Specimen at the End of $\mu\Delta 4$ 667
Figure 15-22. Test 12: (Left) West Side at $\mu\Delta 4 + 1x = 4.88"$ and (Right) East Side at $\mu\Delta 4 - 1x = -4.85"$ 667
Figure 15-23. Test 12: Spiral Yielding on the (Left) South Side at $\mu\Delta 4 - 1y = -4.87"$ and (Right) North Side at $\mu\Delta 4.5 + 1y = 5.52"$ 668
Figure 15-24. Test 12: Spiral Yielding on the (Left) East Side at $\mu\Delta 4.5 + 1x = 5.47"$ and (Right) West Side at $\mu\Delta 4.5 - 1x = -5.46"$ 668
Figure 15-25. Test 12: Buckling of (Left) Bars S and SSE at $\mu\Delta 5 - 1y = -6.08"$ and (Right) Bar W at $\mu\Delta 5 - 1x = -6.06"$ 669

Figure 15-26. Test 12: Buckling of (Left) Bar N at $\mu\Delta 6 + 1y = 7.30$" and (Right) Adjacent South Bar SSW at $\mu\Delta 6 - 1y = -7.31$" 669
Figure 15-27. Test 12: Buckling of Bars (Left) E, ENE, & ESE at $\mu\Delta 6 - 1x = -7.28$" & (Right) WNW & WSW during Reversal to 0" 670
Figure 15-28. Test 12: Buckling of Bars (Left) NE, NNE, & NNW at $\mu\Delta 4.5p + 1y = 5.47$" and (Right) SE & SW at $\mu\Delta 4.5p - 1y = -5.50$" 670
Figure 15-29. Test 12: Additional Deformation in (Left) East and (Right) West Bars during $\mu\Delta 4.5p \pm 1x$ 671
Figure 15-30. Test 12: Fracture of the Previously Buckled South Bar at 3.30" during $\mu\Delta 4.5p + 2y$ 671
Figure 15-31. Test 12: Vertical Strain Profiles for Loading in the +Y-direction 672
Figure 15-32. Test 12: Vertical Strain Profiles for Loading in the -Y-direction 673
Figure 15-33. Test 12: Spiral Strains Measured Over the North Extreme Fiber Bar during +Y Cycles 673
Figure 15-34. Test 12: Spiral Strains Measured Over the South Extreme Fiber Bar during -Y Cycles 674
Figure 15-35. Test 12: Tension Strain-Disp. for Bar S (Gauge Length 3 Centered 7.72" above the Footing) 674
Figure 15-36. Test 12: Compression Strain-Disp. for Bar N (Gauge Length 1 Centered 2.60" above the Footing) 675
Figure 15-37. Test 12: Compression Strain-Disp. for Bar N (Gauge Length 2 Centered 5.41" above the Footing) 675
Figure 15-38. Test 12: Tension Strain-Disp. for Bar N (Gauge Length 3 Centered 8.19" above the Footing) 676
Figure 15-39. Test 12: Compression Strain-Disp. for Bar S (Gauge Length 2 Centered 4.97" above the Footing) 676
Figure 15-40. Test 12: Strain Hysteresis over the North Buckled Bar (Gauge Length 1 Centered 2.60" above the Footing) 677
Figure 15-41. Test 12: Strain Hysteresis over the North Buckled Bar (Gauge Length 2 Centered 5.41" above the Footing) 677
Figure 15-42. Test 12: Spiral Strain Hysteresis for the 1st North Layer above the Footing 678
Figure 15-43. Test 12: Strain Hysteresis over the South Buckled Bar (Gauge Length 2 Centered 4.97" above the Footing) 678
Figure 15-44. Test 12: Spiral Strain Hysteresis for the 2nd South Layer above the Footing 679
Figure 15-45. Test 12: Vertical Strain Profiles for Loading in the +X-direction 680
Figure 15-46. Test 12: Vertical Strain Profiles for Loading in the -X-direction 680
Figure 15-47. Test 12: Spiral Strains Measured Over the East Extreme Fiber Bar during +X Cycles .. 681
Figure 15-48. Test 12: Spiral Strains Measured Over the West Extreme Fiber Bar during -X Cycles . 681
Figure 15-49. Test 12: Tension Strain-Disp. for Bar W (Gauge Length 1 Centered 2.64" above the Footing) 682
Figure 15-50. Test 12: Compression Strain-Disp. for Bar E (Gauge Length 2 Centered 5.88" above the Footing) 682
Figure 15-51. Test 12: Tension Strain-Disp. for Bar E (Gauge Length 2 Centered 5.88" above the Footing) 683
Figure 15-52. Test 12: Compression Strain-Disp. for Bar W (Gauge Length 1 Centered 2.64" above the Footing) 683

Figure 15-53. Test 12: Strain Hysteresis over the East Buckled Bar (Gauge Length 1 Centered 3.00" above the Footing) 684
Figure 15-54. Test 12: Strain Hysteresis over the East Buckled Bar (Gauge Length 2 Centered 5.88" above the Footing) 684
Figure 15-55. Test 12: Spiral Strain Hysteresis for the 1st East Layer above the Footing 685
Figure 15-56. Test 12: Strain Hysteresis over the West Buckled Bar (Gauge Length 2 Centered 5.45" above the Footing) 685
Figure 15-57. Test 12: Strain Hysteresis over the West Buckled Bar (Gauge Length 3 Centered 8.26" above the Footing) 686
Figure 15-58. Test 12: Spiral Strain Hysteresis for the 1st West Layer above the Footing 686
Figure 15-59. Test 12: Spiral Strain Hysteresis for the 2nd West Layer above the Footing 687
Figure 15-60. Test 12: Elastic Curvature Profiles for the First Instrumented Section above the Footing 688
Figure 15-61. Test 12: Curvature Profiles for the First Instrumented Section above the Footing 688
Figure 15-62. Test 12: Elastic Vertical Curvature Profiles 689
Figure 15-63. Test 12: Vertical Curvature Profiles for Loading in the +Y-direction 689
Figure 15-64. Test 12: Vertical Curvature Profiles for Loading in the -Y-direction 690
Figure 15-65. Test 12: Vertical Curvature Profiles for Loading in the +X-direction 690
Figure 15-66. Test 12: Vertical Curvature Profiles for Loading in the -X-direction 691
Figure 15-67. Test 12: Extreme Fiber Bar Strain Penetration Bond Slip Hysteresis 691
Figure 15-68. Test 12: Fixed End Rotations due to Strain Penetration during the Elastic Cycles 692
Figure 15-69. Test 12: Fixed End Rotations due to Strain Penetration 692
Figure 15-70. Test 11: Optotrak Integrated Flexural Disp. Compared to Measured String Pot. Disp. 693
Figure 15-71. Test 11: Optotrak Integrated Flexural Disp. Compared to Measured String Pot. Disp. 693
Figure 15-72. Test 12: Measured Extent of Plasticity Compared to Tensile Hinge Lengths 694
Figure 15-73. Test 12: Measured Equivalent Strain Penetration Lengths Compared to Design Expressions 694
Figure 15-74. Test 12: Y-Direction Hysteretic Response Compared to PCK (2007) Hinge Length Monotonic Prediction 695
Figure 15-75. Test 12: X-Direction Hysteretic Response Compared to PCK (2007) Hinge Length Monotonic Prediction 695
Figure 15-76. Y-Direction Hysteretic Comparison for Megathrust Tests 11 and 12 (% Transverse Steel) 696
Figure 15-77. X-Direction Hysteretic Comparison for Megathrust Tests 11 and 12 (% Transverse Steel) 696
Figure 15-78. Y-Direction Hysteretic Comparison for Sym. Two-Cycle-Set Test 9 and Scaled Megathrust Test 12 697
Figure 15-79. X-Direction Hysteretic Comparison for Sym. Two-Cycle-Set Test 9 and Scaled Megathrust Test 12 697
Figure 16-1. Test 11: Deformed Specimen at $\mu\Delta 7 + 1x = 8.49"$ 700
Figure 16-2. Test 11: Bidirectional Load History Orientation and Bar Naming System 701
Figure 16-3. Test 11: Y-Displacement History 701

Figure 16-4. Test 11: X-Displacement History 702
Figure 16-5. Test 11: Y-Direction Hysteretic Response 702
Figure 16-6. Test 11: X-Direction Hysteretic Response 703
Figure 16-7. Test 11: North Longitudinal Bar Strain Hysteresis to Bar Buckling 703
Figure 16-8. Test 11: North Spiral Restraint Strain History to Bar Buckling 704
Figure 16-9. Test 11: +Y-Direction Cross Section Curvatures 704
Figure 16-10. Test 11: +Y-Direction Vertical Curvature Profiles 705
Figure 16-11. Test 11: +Y-Direction Vertical Strain Profile 705
Figure 16-12. Test 11: +Y-Direction Fixed-End Rotations due to Strain Penetration 706
Figure 16-13. Test 11: Optotrak Integrated Flexural Disp. Compared to Measured String Pot. Disp. 706
Figure 16-14. Test 11: Measured Extent of Plasticity Compared to Tensile Hinge Lengths 707
Figure 16-15. Test 11: Measured Equivalent Strain Penetration Lengths Compared to Design Expressions 707
Figure 16-16. Test 11: Tension Strain-Disp. for Bar S (Gauge Length 4 Centered 7.88” above the Footing) 708
Figure 16-17. Test 11: Compression Strain-Disp. for Bar N (Gauge Length 1 Centered 2.06” above the Footing) 708
Figure 16-18. Test 11: Tension Strain-Disp. for Bar N (Gauge Length 2 Centered 4.07” above the Footing) 709
Figure 16-19. Test 11: Compression Strain-Disp. for Bar S (Gauge Length 1 Centered 2.05” above the Footing) 709
Figure 16-20. Comparison of the Three Type-B Bidirectional Load Histories of this Study 711
Figure 16-21. Single Bending Equivalent Curvature Profiles, (Left) Triangular and (Right) Rectangular Plastic Hinge Lengths 716
Figure 16-22. Double Bending Equivalent Curvature Profiles, (Left) Triangular and (Right) Rectangular Plastic Hinge Lengths 717
Figure 16-23. Comparison of Average Measured Upperbound Spread of Plasticity to Tensile Hinge Length Expressions 721
Figure 16-24. Comparison of Average Measured Equivalent Strain Penetration Length to Design Recommendations 721
Figure 16-25. Comparison of Average Measured Upperbound Spread of Plasticity to Tensile Hinge Length Expressions 722
Figure 16-26. Comparison of Average Measured Equivalent Strain Penetration Length to Design Recommendations 722
Figure 16-27. Comparison of Measured Lpr and Design Recommendations for Columns with #7 Longitudinal Steel 723
Figure 16-28. Comparison of Measured Lsp and Design Recommendations for Columns with #7 Longitudinal Steel 723
Figure 16-29. Comparison of Measured Lpr and Design Recommendations for Columns with #6 Longitudinal Steel 724
Figure 16-30. Comparison of Measured Lsp and Design Recommendations for Columns with #6 Longitudinal Steel 724

Figure 16-31. Comparison of Measured Lpr and Design Recommendations for Cols. with Asymmetric 2-Cycle-Set Loading 725
Figure 16-32. Comparison of Measured Lsp and Design Recommendations for Cols. with Asymmetric 2-Cycle-Set Loading 725
Figure 16-33. Probability of Exceeding the Measured Upperbound Lpr in the Combined Dataset .. 726
Figure 16-34. Bidirectional Dataset: Cumulative Probability Dist. for Meas/Pred Disp. at Measured Bar Buckling Strain 728
Figure 16-35. Bidirectional Dataset: Cumulative Probability Dist. for Meas/Pred Disp. at the Analytical First Yield Force 728
Figure 16-36. Bidirectional Dataset: Cumulative Probability Dist. for Meas/Pred Disp. at Measured Cover Crushing Strain 729
Figure 16-37. Bidirectional Dataset: Cumulative Probability Dist. for Meas/Pred Disp. at Measured Spiral Yielding Strain 729
Figure 16-38. Unidirectional Dataset: Cumulative Probability Dist. for Meas/Pred Disp. at Measured Bar Buckling Strain 730
Figure 16-39. Unidirectional Dataset: Cumulative Probability Dist. for Meas/Pred Disp. at the Analytical First Yield Force 730
Figure 16-40. Unidirectional Dataset: Cumulative Probability Dist. for Meas/Pred Disp. at Measured Cover Crushing Strain 731
Figure 16-41. Unidirectional Dataset: Cumulative Probability Dist. for Meas/Pred Disp. at Measured Spiral Yielding Strain 731
Figure 16-42. Combined Dataset: Cumulative Probability Dist. for Meas/Pred Disp. at Measured Bar Buckling Strain 732
Figure 16-43. Combined Dataset: Cumulative Probability Dist. for Meas/Pred Disp. at the Analytical First Yield Force 732
Figure 16-44. Combined Dataset: Cumulative Probability Dist. for Meas/Pred Disp. at Measured Cover Crushing Strain 733
Figure 16-45. Combined Dataset: Cumulative Probability Dist. for Meas/Pred Disp. at Measured Spiral Yielding Strain 733
Figure 16-46. Bidirectional Dataset: Predictions for Displacement at Cover Concrete Crushing 741
Figure 16-47. Unidirectional Dataset: Predictions for Displacement at Cover Concrete Crushing 741
Figure 16-48. Bidirectional Dataset: Predictions for Cover Crushing Disp. with Noted Hinge Methods 742
Figure 16-49. Predictions for Cover Crushing Disp. in Noted Datasets with the New Plastic Hinge Method 742
Figure 16-50. Bidirectional Dataset: Predictions for Compression Strain at Initial Confinement Steel Yielding 743
Figure 16-51. Bidirectional Dataset: Predictions for the Displacement at Initial Confinement Steel Yielding 743
Figure 16-52. Unidirectional Dataset: Predictions for Compression Strain at Initial Confinement Steel Yielding 744
Figure 16-53. Unidirectional Dataset: Predictions for the Displacement at Initial Confinement Steel Yielding 744

Figure 16-54. Combined Dataset: Predictions for Compression Strain at Initial Confinement Steel Yielding 745
Figure 16-55. Predictions for Compressive Strain at Initial Spiral Yielding in the Noted Datasets 745
Figure 16-56. Bidirectional Dataset: Predictions for the Displacement at Initial Confinement Steel Yielding 746
Figure 16-57. Unidirectional Dataset: Predictions for the Displacement at Initial Confinement Steel Yielding 746
Figure 16-58. Combined Dataset: Predictions for the Displacement at Initial Confinement Steel Yielding 747
Figure 16-59. Predictions for the Displacement at Initial Confinement Steel Yielding in Noted Datasets 747
Figure 16-60. Bidirectional Dataset: Predictions for the Bar Buckling Peak Tensile Strain..... 748
Figure 16-61. Bidirectional Dataset: Predictions for the Bar Buckling Peak Tensile Displacement ... 748
Figure 16-62. Unidirectional Dataset: Predictions for the Bar Buckling Peak Tensile Strain 749
Figure 16-63. Unidirectional Dataset: Predictions for the Bar Buckling Peak Tensile Displacement. 749
Figure 16-64. Combined Dataset: Predictions for the Bar Buckling Peak Tensile Strain..... 750
Figure 16-65. Predictions for the Bar Buckling Peak Tensile Strain in the Noted Datasets 750
Figure 16-66. Bidirectional Dataset: Predictions for the Bar Buckling Peak Tensile Disp. with the Noted Hinge Methods 751
Figure 16-67. Predictions for the Bar Buckling Peak Tensile Displacement in the Noted Datasets... 751
Figure 16-68. Predictions for the Bar Buckling Peak Tensile Displacement in the Noted Datasets... 752
Figure 16-69. Bar Buckling Displacement Predictions within the (Berry 2006) PEER Column Dataset 752

List of Tables

Table 1-1. Performance Strain Limit State Recommendations from (Kowalsky, Deformation Limit States for Circular Reinforced Concrete Bridge Columns 2000) 2
Table 1-2. Specimen Summary for (Goodnight, Kowalsky and Nau 2015) Dataset 9
Table 1-3. Limit State Strains and Drifts from (Goodnight, Kowalsky and Nau 2015) Dataset 9
Table 1-4. Plastic Hinge Model Comparison, Statistics for Measured/Predicted Dataset 12
Table 2-1. Test Matrix for the Bidirectional Columns of this Study 29
Table 2-2. Uniaxial Experiments from (Goodnight, Kowalsky and Nau 2015) which Serve as Comparison 29
Table 2-3. Longitudinal Steel Design Material Properties 40
Table 2-4. Column Concrete and Transverse Steel Design Material Properties. 40
Table 2-5. Specimens 1-2 Expected Property Modified Lpr Parameters 40
Table 3-1. #7 Column Longitudinal Steel Material Properties for Tests 1-6 88
Table 3-2. #3 Column Transverse Steel Material Properties for Tests 1-6 88
Table 3-3. #7 Column Longitudinal Steel Material Properties for Tests 7-12 92
Table 3-4. #6 Column Longitudinal Steel Material Properties for Tests 7-12 92
Table 3-5. #3 Column Transverse Steel Material Properties for Tests 7-12 92
Table 4-1. Test 1: Values of Interest 104
Table 4-2. Test 1: Damage Observations 104
Table 4-3. Test 1: Damage Predictions 105
Table 5-1. Test 2: Values of Interest 165
Table 5-2. Test 2: Damage Observations 165
Table 5-3. Test 2: Damage Predictions 166
Table 6-1. Test 3: Values of Interest 217
Table 6-2. Test 3: Damage Observations 217
Table 6-3. Test 3: Damage Predictions 218
Table 7-1. Test 4: Values of Interest 268
Table 7-2. Test 4: Damage Observations 268
Table 7-3. Test 4: Damage Predictions 269
Table 8-1. Test 5: Values of Interest 324
Table 8-2. Test 5: Damage Observations 324
Table 8-3. Test 5: Damage Predictions 325
Table 9-1. Test 6: Values of Interest 378
Table 9-2. Test 6: Damage Observations 378
Table 9-3. Test 6: Damage Predictions 379
Table 10-1. Test 7: Values of Interest 436
Table 10-2. Test 7: Damage Observations 436
Table 10-3. Test 7: Damage Predictions 437
Table 11-1. Test 8: Values of Interest 476
Table 11-2. Test 8: Damage Observations 476
Table 11-3. Test 8: Damage Predictions 477
Table 12-1. Test 9: Values of Interest 516
Table 12-2. Test 9: Damage Observations 516
Table 12-3. Test 9: Damage Predictions 517

Table 13-1. Test 10: Values of Interest 559
Table 13-2. Test 10: Damage Observations 559
Table 13-3. Test 10: Damage Predictions 560
Table 14-1. Test 11: Values of Interests 602
Table 14-2. Test 11: Values of Interest 610
Table 14-3. Test 11: Damage Observations 611
Table 14-4. Test 11: Damage Predictions 611
Table 15-1. Test 12: Values of Interest 655
Table 15-2. Test 12: Damage Observations 655
Table 15-3. Test 12: Damage Predictions 656
Table 16-1. Test Matrix for the Bidirectional Load Path Dataset of this Study 710
Table 16-2. Material Properties in the Bidirectional Load Path Dataset of this Study 710
Table 16-3. Limit State Strains and Displacements in the Bidirectional Load Path Dataset of this Study 712
Table 16-4. Specimen Summary for the (Goodnight, Kowalsky and Nau 2015) Unidirectional Dataset 713
Table 16-5. Limit State Strains and Drifts from the (Goodnight, Kowalsky and Nau 2015) Unidirectional Dataset 713
Table 16-6. Comparison of Measured Upperbound Lpr and Design Recommendations in Respective Datasets 726
Table 16-7. Plastic Hinge Model Comparison in Bidirectional Dataset, Statistics for Measured/Predicted Limit State Disp. 726
Table 16-8. Plastic Hinge Model Comparison in Unidirectional Dataset, Statistics for Measured/Predicted Limit State Disp. 727
Table 16-9. Plastic Hinge Model Comparison in Combined Dataset, Statistics for Measured/Predicted Limit State Disp. 727
Table 16-10. Bidirectional Dataset: Cover Concrete Crushing Displacement Predictions with Noted Plastic Hinge Methods 734
Table 16-11. Cover Concrete Crushing Displacement Predictions using the New Plastic Hinge Method 734
Table 16-12. Bidirectional Dataset: Displacement at Initial Spiral Yielding Predictions with Noted Plastic Hinge Methods 736
Table 16-13. Spiral Yielding Strain and Displacement Predictions using the New Plastic Hinge Model 736
Table 16-14. Bidirectional Dataset: Bar Buckling Displacement Predictions with Noted Plastic Hinge Methods 738
Table 16-15. Bar Buckling Strain and Displacement Predictions using the New Plastic Hinge Model 738
Table 16-16. Bar Buckling Strain and Displacement Predictions using the New Plastic Hinge Model 738
Table 16-17. Bar Buckling Displacement Predictions within the (Berry 2006) PEER Column Dataset 739
Table 16-18. (Berry 2006) PEER Column Dataset 740

Acknowledgements

The research reported herein was performed at the Constructed Facilities Laboratory in the Department of Civil, Construction, and Environmental Engineering at North Carolina State University.

Jason Chad Goodnight, Post-Doc

Mervyn J. Kowalsky and James M. Nau, Professors of Civil Engineering at North Carolina State University, were the principal investigators.

The authors wish to acknowledge Alaska DOT&PF who supported this research through a series of grants. Special acknowledgement goes to Elmer Marx of Alaska DOT&PF who was closely involved in this research as the primary technical contact. The assistance of the entire staff of the Constructed Facilities Laboratory is appreciated.

Abstract

This report discusses the impact of bidirectional seismic load path on limit state strains and the spread of plasticity in twelve reinforced concrete bridge column tests. The main variables included longitudinal steel content, transverse steel detailing, and the bidirectional seismic load path. The tests employed an advanced instrumentation system which provided detailed strain and curvature data. This data was used to generate predictive expressions for concrete and steel strains preceding important limit states, which included: cover concrete crushing, initial yielding of confinement steel, and longitudinal bar buckling. This data was used to create a new plastic hinge method which converts curvatures at limit state strains to lateral displacements, which are needed in design. The new plastic hinge method collapses down to the accepted design approach for compression strain-displacement, while still matching the measured extent of plasticity and tensile strain-displacement relationship necessary for accurate bar buckling predictions. An effort was made to provide mean value predictions for the displacement at each limit state. These recommendations serve as input into a displacement-based design procedure to achieve a particular level of performance under a defined seismic hazard.

Summary of Findings, refer to Chapter 16

The results of the experiments and design recommendations are summarized in Chapter 16. In Chapter 16, data from Megathrust load history Test 11 is presented to illustrate the process in which the measured spread in plasticity was quantified. This data will be referenced in the following two sections which focus on summarizing design recommendations for the new plastic hinge method and performance strain limits. Included are tables which provide the text matrix, material properties, and summaries of the strains and displacements at important damage levels. The findings are not repeated here, since they appear in a concise format in Chapter 16 with additional context.

Chapter 1 - Introduction

Background on the Definition of Damage States

Bridge columns are designed as ductile elements which form plastic hinges to dissipate energy in a seismic event. Within the context of performance based design, this results in the need to describe various performance levels using engineering criteria. While several deformation quantities are possible to describe damage, steel and concrete strains are an attractive option as they describe behavior at the material level. Consider the "serviceability" limit state, which is defined as the point, when exceeded, which requires some degree of intervention. Traditionally, this limit state has been connected to cover concrete crushing or residual crack widths sufficiently larger as to require epoxy injection (Priestley, Seible and Calvi 1996). Both of these criteria, while not an issue for safety, are a concern for long term durability, thus necessitating minor repair.

At higher ductility demands produced by larger less frequent earthquakes, longitudinal bar buckling may lead to permanent elongation in the transverse steel, which diminishes its effectiveness in confining the concrete core. Bar buckling and significant damage to the core concrete represent the "damage control" limit states, which when exceeded lead to significant repair costs which may render repair no longer feasible (Priestley, Seible and Calvi 1996). Furthermore, rupture of previously buckled bars during subsequent cycles of loading leads to rapid strength loss. Finally, the "life safety" or "collapse prevention" limit state is characterized by fracture of previously buckled bars or confinement steel. The occurrence of these limit states in a column subjected to unidirectional reversed cyclic loading (Goodnight, Kowalsky and Nau 2015) is shown in Figure 1-1. Initial yielding, cover concrete crushing, longitudinal bar buckling, and bar fracture are marked on the deformation history and hysteretic response.

There have been numerous attempts to connect these qualitative limit states to material strains. For example, a summary of the strain limit state recommendations from (Kowalsky 2000) appears in Table 1-1. However, these recommendations lack adequate experimental basis, particularly at the damage control level, due to the difficulty in measuring material strains at such high levels of response. Traditional instrumentation methods, such as those used in (Hines and Seible 2002), utilized linear potentiometers placed on the ends of threaded rods embedded in the core concrete to calculate changes in displacement outside of the concrete cover. This method provides coarse measurements of average strain over large gauge lengths and may be influenced by rotations of the rods. Material strains at key performance levels have either been calculated based on the strain profile predicted via the curvature rod instrumentation, or inferred by equating the observed displacement to that predicted using moment-curvature analysis and an equivalent curvature distribution. The analytically inferred strains are specific to a given equivalent curvature distribution and may not have any physical meaning so long as the combination of limit state curvature and hinge length produces similar displacements. Utilizing strains from curvature rod instrumentation in bridge column tests of various cross-section geometry, (Hines and Seible 2002) recommended to limit strains according to the following relationship, $(0.035 \leq \varepsilon_c + \varepsilon_s \leq 0.050)$. The range in values for this expression, and the general lower magnitude in comparison to the "damage control" strains from (Kowalsky 2000) highlight the need for further experimental validation.

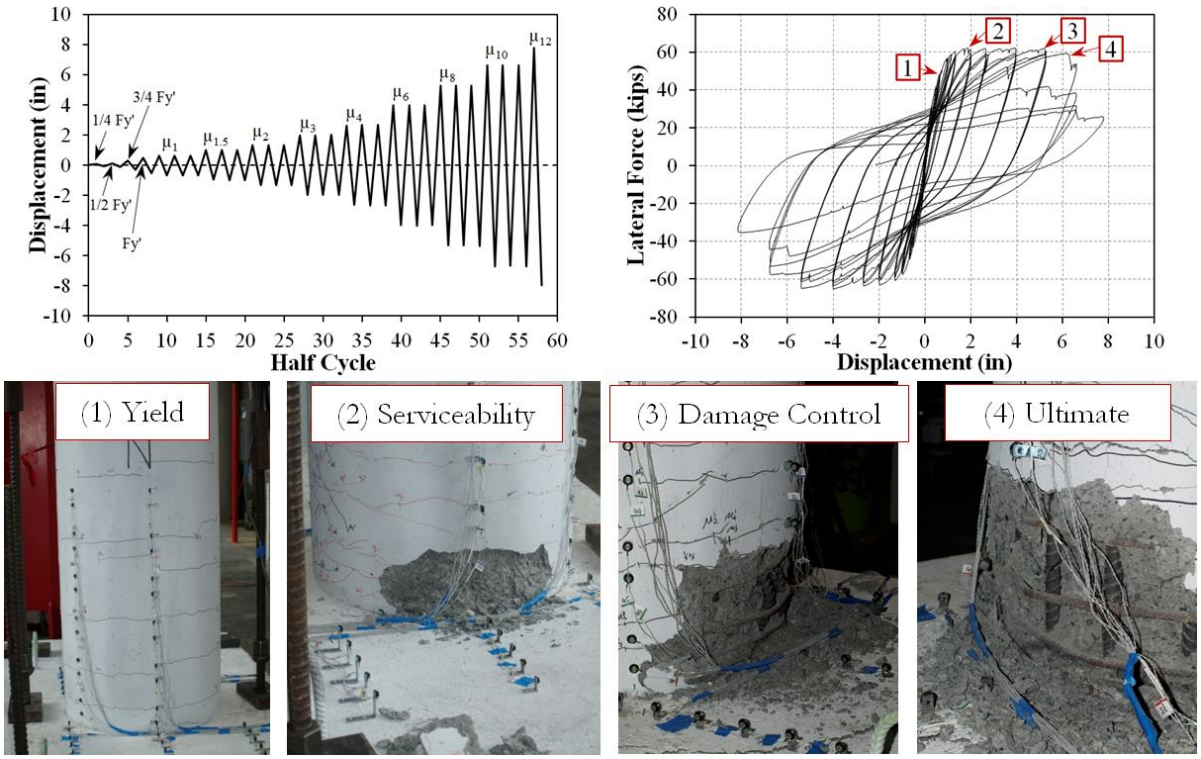

Figure 1-1. Displacement History, Hysteretic Response, and Limit States for Test 2 in (Goodnight, Kowalsky and Nau 2015)

Table 1-1. Performance Strain Limit State Recommendations from (Kowalsky, Deformation Limit States for Circular Reinforced Concrete Bridge Columns 2000)

Limit State	Concrete Compressive Strain Limit	Steel Tensile Strain Limit
Serviceability	0.004 Cover Concrete Crushing	0.015 Residual Crack Widths Exceed 1 mm
Damage Control	(Mander, Priestley and Park 1988) $\varepsilon_{cu} \approx 0.018\ for\ \rho_s \approx 0.01$ Limit of Economical Concrete Repair	0.060 Tension Based Bar Buckling

Due to the lack of reported strain data in the literature, (Berry 2006) developed empirical drift-based expression for the limit states of cover concrete crushing Eqn 1-1, bar buckling Eqn 1-2, and bar fracture Eqn 1-3. Appropriate variables and coefficients for the expressions were determined using a circular bridge column dataset comprised of well-confined bridge column tests reported in the literature. Such a column conformed to the following criteria: $\left(P/A_g f_c' \leq 0.30\right)$, $\left(\rho_{eff} = \rho_s f_{yh}/f_c' \geq 0.05\right)$, $\left(\rho_l = A_{st}/A_g \leq 0.04\right)$, $(s/d_{bl} \leq 6)$, and $(cover/D \leq 0.1)$. Where $P/A_g f_c'$ is the axial load ratio, ρ_{eff} is the effective confinement ratio, $\rho_s = 4A_{sp}/D's$ is the transverse volumetric steel ratio, ρ_l is the longitudinal steel ratio, s/d_{bl} is the transverse steel spacing to longitudinal bar diameter ratio, $cover/D$ is the concrete cover to column diameter ratio, and L is the length from the critical section to the point of contraflexure. Although useful for design, strain limit states are intrinsically related to damage, and can be utilized in a wider variety of column end fixity conditions.

$$\frac{\Delta_{sp}^{calc}}{L}(\%) = 1.6\left(1 - \frac{P}{A_g f_c'}\right)\left(1 + \frac{L}{10D}\right)$$ *(Berry 2006) Drift at Cover Spalling* Eqn 1-1

$$\frac{\Delta_{bb}^{calc}}{L}(\%) = 3.25\left(1 + \frac{150\rho_{eff} d_{bl}}{D}\right)\left(1 - \frac{P}{A_g f_c'}\right)\left(1 + \frac{L}{10D}\right)$$ *(Berry 2006) Drift at Bar Buckling* Eqn 1-2

$$\frac{\Delta_{bf}^{calc}}{L}(\%) = 3.5\left(1 + \frac{150\rho_{eff} d_{bl}}{D}\right)\left(1 - \frac{P}{A_g f_c'}\right)\left(1 + \frac{L}{10D}\right)$$ *(Berry 2006) Drift at Bar Fracture* Eqn 1-3

Recent efforts by (Babazadeh, Burgueño and Silva 2015) and (Feng, Kowalsky and Nau 2015) have focused on quantifying the initiation and spread of damage using experimentally verified numerical models. (Babazadeh, Burgueño and Silva 2015) utilized 3D finite-element modeling to investigate intermediate damage states defined as longitudinal steel yielding, initial crushing of cover concrete over a tenth of the column diameter, and significant concrete crushing that extended over half the section diameter. The analytical results were compared to the measured damage in four column tests, and the method proved effective in predicting the onset and spread of cover concrete crushing. (Babazadeh, Burgueño and Silva 2015) reported that a compressive strain of ($\varepsilon_c = 0.005$) could be used to predict the initial crushing damage state.

(Feng, Kowalsky and Nau 2015) proposed a model to describe bar buckling behavior observed in finite-element analysis. The influence of the following behaviors were included in the analysis: (1) dilation of core concrete under compression, (2) restraint provided by individual spiral layers with representative geometry and material response, and (3) development of the longitudinal bar into the adjoining member. Specific strain histories were applied to the longitudinal bar and core concrete to evaluate the influence of strain history on bar buckling. This behavior, once quantified, was used to create the multi-linear regression Eqn 1-4 through Eqn 1-8 which define a boundary between prior compression and peak tension strain couples which are expected to produce bar buckling upon reversal of load. In the expressions ε_t and ε_c are the tensile and compressive longitudinal bar strains (both taken as positive), d_{bl} and d_h are the longitudinal and transverse steel bar diameters, and s is the centerline spacing of the transverse steel.

An evaluation of the (Feng, Kowalsky and Nau 2015) method applied to Test 9 from (Goodnight, Kowalsky and Nau 2015) appears in Figure 1-2. The bar buckling prediction is defined as the intersection of the multi-linear regression and the tensile-compressive bar strain relationship at each level of curvature in a section analysis. The tension and compression strain couple at the intersection point represents a compression cycle followed by a tension cycle to the same level of displacement, which would induce bar buckling upon reversal of load. The (Priestley, Calvi and Kowalsky 2007) plastic hinge method is used to translate the curvature at the intersection point strains to member deformation. If the displacement amplitudes or the strain history is known, the model can be used to evaluate the influence of previous load history on bar buckling.

$$\varepsilon_t = \frac{-15\left(\varepsilon_c - \frac{0.0205}{\sqrt[3]{\frac{s}{d_{bl}} - 1}}\right)}{\left(\frac{d_{bl}}{d_h} - 1\right)^2}$$ *(Feng, Kowalsky and Nau 2015) Main* *Eqn 1-4*

$$\varepsilon_t \geq -1.7\frac{s}{d_{bl}}\sqrt{\frac{d_h}{d_{bl}}}\varepsilon_c + 0.045\sqrt{\frac{s}{d_{bl}}}$$ *(Feng, Kowalsky and Nau 2015) Lower* *Eqn 1-5*

$$\varepsilon_t \leq 0.09, \quad if\ \frac{s}{d_{bl}} \leq 3$$ *(Feng, Kowalsky and Nau 2015) Upper* *Eqn 1-6*

$$\varepsilon_t \leq 0.06, \quad if\ \frac{s}{d_{bl}} \geq 4$$ *(Feng, Kowalsky and Nau 2015) Upper* *Eqn 1-7*

$$\varepsilon_t \leq 0.09 - 0.03\left(\frac{s}{d_{bl}} - 3\right), \quad if\ 3 < \frac{s}{d_{bl}} < 4$$ *(Feng, Kowalsky and Nau 2015) Upper* *Eqn 1-8*

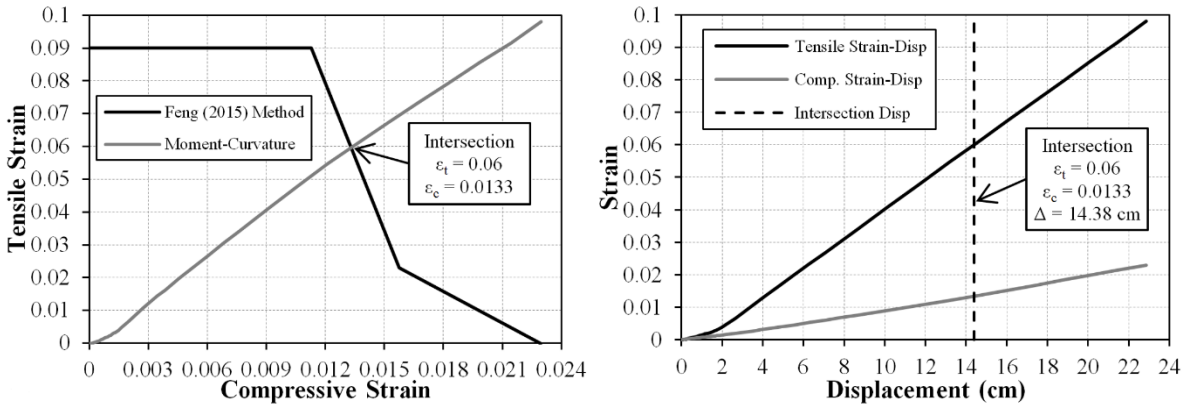

Figure 1-2. (Feng, Kowalsky and Nau 2015) Method Applied to Test 9 from (Goodnight, Kowalsky and Nau 2015)

Background on Equivalent Curvature Distributions

In design, curvatures at limit state strains are translated to top column displacements utilizing an equivalent curvature distribution, such as the plastic hinge method from (Priestley, Calvi and Kowalsky 2007). The member deformation can be obtained by taking the first moment of the curvature profile. An equivalent curvature distribution replaces the actual distribution of curvature with simplified geometry. There are two requirements for an equivalent curvature distribution: (1) the area of individual regions should represent the rotation caused by that deformation component and (2) the placement of the region should be chosen such that the center of rotation matches that of the real curvature profile. Other components of deformation, such as strain penetration of reinforcement into the adjoining member, can be included into the method. Typically, the equivalent curvature profile represents all of the flexural modes of deformation, and a separate shear displacement model is needed to compute the total deflection of the member.

Early approaches to define the member deformation using an equivalent rectangular plastic hinge length are summarized in (Park and Paulay 1975). In these methods, elastic and plastic regions

of the curvature profile are separated, and an equivalent rectangular block is substituted to compute the plastic displacement of the member. The height of this block is termed the plastic hinge length, L_p, while the width is equal to the plastic curvature at the critical section. The plastic hinge length is not a physical parameter, but rather a numerical convenience. Separately, (Baker and Amarakone 1964), (Sawyer 1964), and (Corley 1966) proposed hinge length expressions to predict the ultimate displacement capacity of beams. In a discussion of the published work, (Mattock 1967) offered a simplification of expressions from (Corley 1966). The authors' work had the following variables in common: (1) effective member depth and (2) length from the critical section to the point of contraflexure.

Based on a series of four square column tests, (Park, Priestley and Gill 1982) suggested the hinge length could be approximated by $0.4h$, where h is the overall depth of the column. After conducting experimental tests, (Mander 1983) proposed an expression which included the effects of strain penetration, $32\sqrt{d_{bl}} + 0.06L_c$, where d_{bl} is the longitudinal bar diameter expressed in mm units and L_c is the column length to the point of contraflexure. In a similar format, (Priestley and Park 1987) suggested that the hinge length could be computed as $0.08L_c + 6d_{bl}$. This expression was later revised in (Paulay and Priestley 1992) to the form $0.08L_c + 0.022f_{ye}d_{bl} \geq 0.044f_{ye}d_{bl}$, where f_{ye} is the expected yield stress of the longitudinal reinforcement expressed in MPa units. To account for the influence of the strain hardening ratio of reinforcement on the second slope stiffness of the moment-curvature response, (Priestley, Calvi and Kowalsky 2007) replaced the term 0.08 in the preceding equation with the parameter $k = 0.2\left(f_u/f_y - 1\right) \leq 0.08$. This method is shown in Figure 1-3 for a column in single bending.

Utilizing measured curvature profiles, (Hines, Restrepo and Seible 2004) developed predictive expressions for the spread of plasticity in bridge column tests with varying geometry and reinforcement. The result of these equilibrium-based expressions was a triangular plastic curvature distribution which reflected the measured shape of curvature profiles. This geometry was related back to a rectangular hinge length to compute column displacements. Using an experimental dataset representative of well-confined bridge columns, (Berry, Lehman and Lowes 2008) attempted to relate the plastic hinge length to column performance levels by generating coefficients with an error function that considered the error both in force-deformation envelope and displacement predictions at cover crushing and longitudinal bar buckling. The resulting design expression recommended in (Berry, Lehman and Lowes 2008) takes the form $0.05L_c + 0.1\, f_y d_{bl}/\sqrt{f_c'}$, with stress in MPa units. Similarly, (Alemdar 2010) generated two plastic hinge length expressions based on bridge column tests reported in literature. The first expression attempted to match the measured spread of plasticity reported in experiments, while the second could be used to predict ultimate response based on 20% loss in lateral capacity.

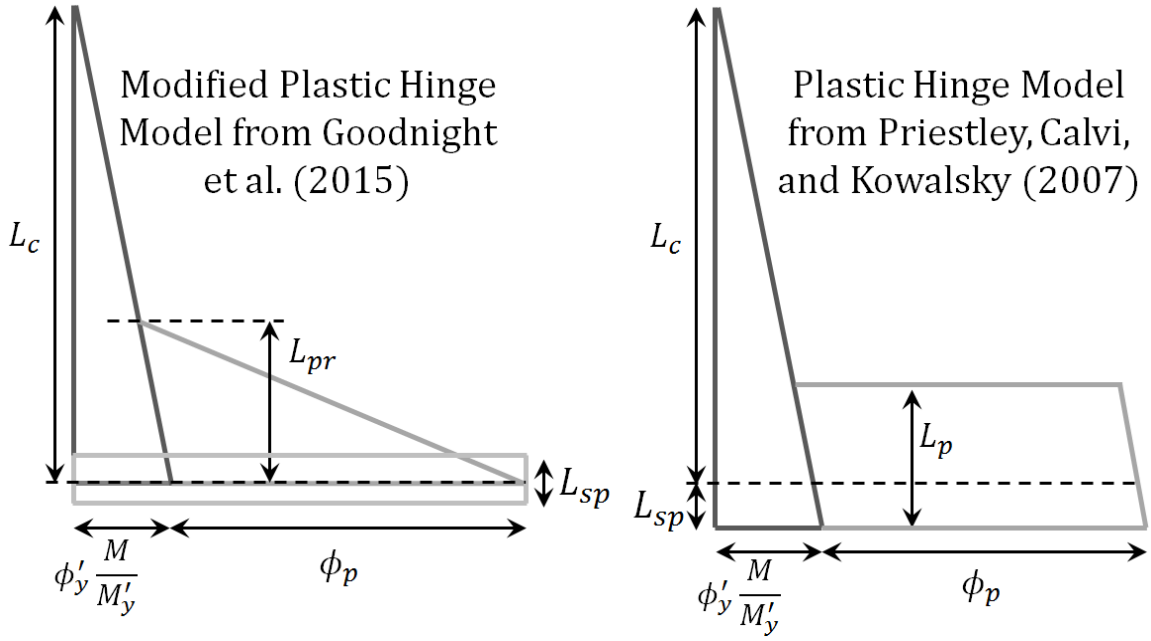

Figure 1-3 Equivalent curvature Distributions

Summary of (Goodnight, Kowalsky and Nau 2015) Experimental Program

The following section describes a recently completed experimental program by the authors which focused on defining damage in columns subjected to unidirectional displacement histories. The experimental program in (Goodnight, Kowalsky and Nau 2015) was devised to assess the performance of thirty circular well-confined bridge columns. A key feature of the experiments was the high fidelity strain data obtained using an optical 3D position monitoring system. The goal of the experimental program was to investigate the impact of unidirectional lateral displacement history and design variables on the relationship between strain and displacement, performance strain limit states, and the spread of plasticity. The main variables for the thirty tests included: (1) lateral displacement history, (2) axial load, (3) longitudinal steel content, (4) aspect ratio, and (5) transverse steel detailing. This summary focuses on deign recommendations formulated using the measured reinforcement strains from Tests 8-30 from (Goodnight, Kowalsky and Nau 2015). These recommendations include the formulation of a new equivalent curvature distribution to improve the accuracy of strain-displacement predictions (Goodnight, Kowalsky and Nau 2015a) and recommendations for strain limit-states for design (Goodnight, Kowalsky and Nau 2015b).

The specimen was designed to represent a single degree of freedom bridge column subjected to lateral and axial load, Figure 1-4. The test specimen consists of a footing, column, and loading cap. The footing is a capacity protected member which secures the specimen to the lab strong floor using post tensioned bars. A 200 kip hydraulic actuator, with a 40” stroke capacity, applied lateral load to the loading cap of the specimen. A spreader beam, two hydraulic jacks, and a load cell were placed above the loading cap to apply a constant axial compressive load. The top column displacement was obtained using a string potentiometer placed at the center of the lateral load. An overview of the

geometric, reinforcing, and material properties for columns in the (Goodnight, Kowalsky and Nau 2015) dataset appears in Table 1-2.

The specimens were subjected to various unidirectional top-column displacement histories including standardized reversed cyclic loading protocols and recreations of the displacement responses obtained from nonlinear time history analysis of multiple earthquakes with distinct characteristics. The symmetric three-cycle-set load history, Figure 1-1, was used to evaluate the performance of the columns prior to the seismic loading tests. The load history begins with unidirectional elastic cycles to the following increments of the analytically predicted first yield force: ¼ F_y', ½ F_y', ¾ F_y', and F_y'. The experimental first yield displacement is then determined by taking the average of the recorded displacements during the first yield push and pull cycles. The equivalent yield displacement, used to determine the displacement ductility levels $\left(\mu_{\Delta n} = n \cdot \Delta_y\right)$, is then calculated as $\left[\Delta_y = \Delta_y'\left(M_n/M_y'\right)\right]$. The symmetric three-cycle-set load history resumes with three balanced cycles at each of the following displacement ductility levels: 1, 1.5, 2, 3, 4, etc. The influence of load history on column performance is summarized in (Goodnight, Kowalsky and Nau 2013) for seismic load history Tests 8, 10, 11, 12 17, and 18 along with companion three-cycle-set Tests 9 and 16.

A key feature of the experiments was the high fidelity strain data obtained through the use of an optical 3D position monitoring system. The experimental program utilized multiple Optotrak Certus HD 3D position sensors developed by Northern Digital Inc. to monitor material strains. The position sensors track the locations of target markers in 3D space, returning X-Y-Z spatial coordinates with an accuracy of 0.1 mm with a resolution of 0.01 mm. A technique of applying target markers to the longitudinal and transverse reinforcement, Figure 1-4, was utilized in the plastic hinge region. Strains were computed by dividing the change in 3D distance between two adjacent target markers by their original unloading gauge length. A comparison of the computed strains and those from traditional measurement techniques is shown in Figure 1-4. An illustration of the measured longitudinal and transverse steel strains obtained via the instrumentation appears in Figure 1-5.

Cross-section curvatures were computed as the slope of a linear regression through the measured strain profile. Curvature profiles were constructed as shown in Figure 1-6, and procedures developed by (Hines and Seible 2002) were followed to extract important information regarding their shape. Linear least squared error lines were fit to the plastic portion of the curvature profiles. The base curvature is calculated as the intersection of the linear plastic curvature profile with the footing-column interface. The extent of plasticity $\left(L_{pr}\right)$ was computed as the intersection of the linear plastic curvature regression and the elastic curvature profile. The spread of plasticity is attributed to the effects of moment gradient and tension shift. Fixed-end rotations attributable to strain penetration were computed based on the slope of a regression through the vertical displacement profile of target markers placed closest to the footing-column interface, Figure 1-6. Development of fully anchored column longitudinal bars into the footing leads to bond slip along the partially anchored region of the bars near the footing-column interface, as described by (Zhao and Sritharan 2007).

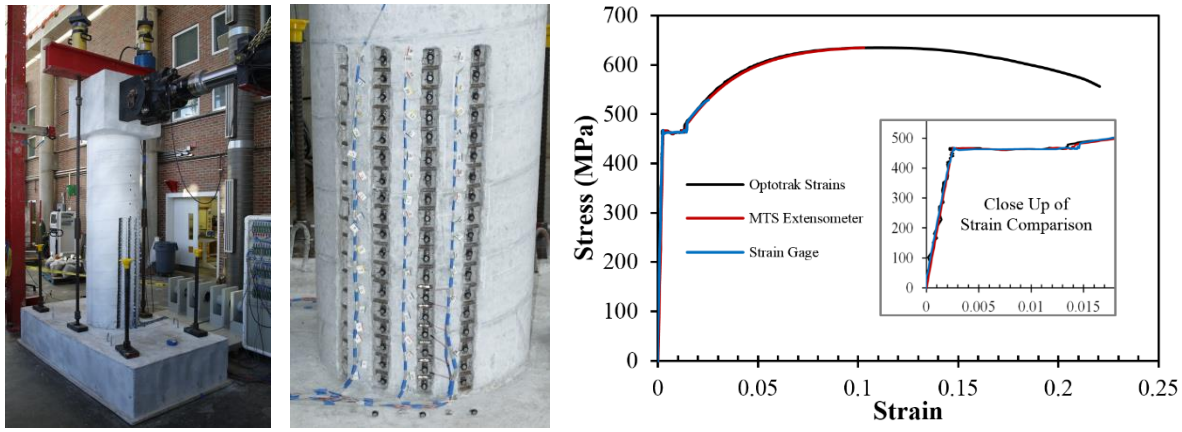

Figure 1-4. Test Setup, Instrumentation, and Measurement Comparison from (Goodnight, Kowalsky and Nau 2015)

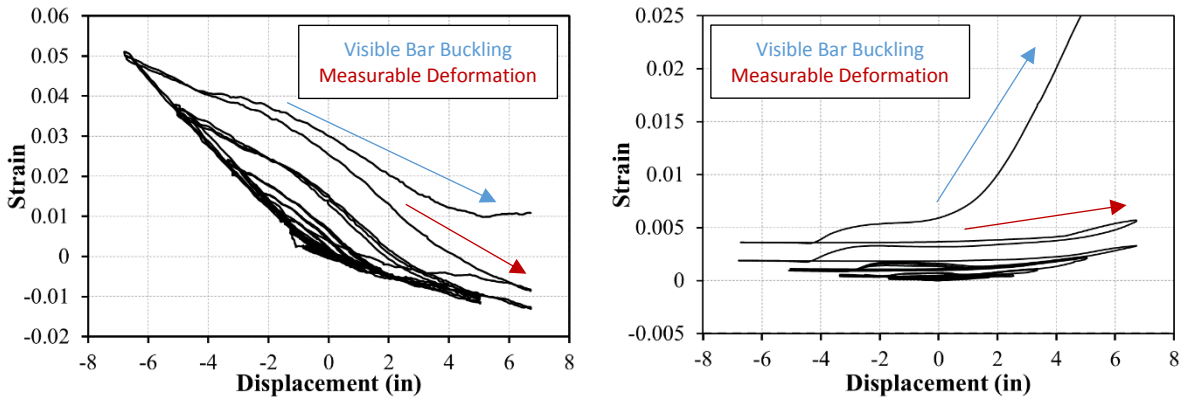

Figure 1-5. Strain Hysteresis for (Left) Longitudinal Bar and (Right) Overlaying Spiral Reinforcement

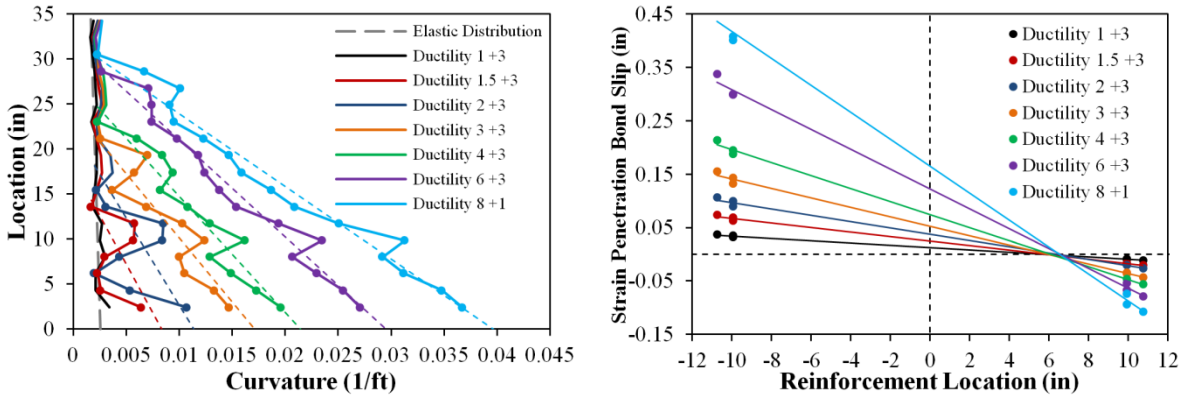

Figure 1-6. (Left) Curvature Profiles and (Right) Fixed-End Rotations

Table 1-2. Specimen Summary for (Goodnight, Kowalsky and Nau 2015) Dataset

Test	Load History	Dia. (in)	Length (ft)	f_{yh} (ksi)	f_y (ksi)	f_u (ksi)	f_c' (ksi)	d_{bl} (in)	$\frac{A_{st}}{A_g}$	$\frac{4A_{sp}}{D's}$	$\frac{P}{f_c'A_g}$
8	EQ LH2	24	8	74.10	68.08	94.79	6.99	0.75	0.016	0.01	0.054
9	Cyclic LH1	24	8	74.10	68.08	94.79	6.81	0.75	0.016	0.01	0.054
10	EQ LH3	24	8	74.10	68.08	94.79	5.26	0.75	0.016	0.01	0.071
11	EQ LH4	24	8	74.10	68.08	94.79	6.18	0.75	0.016	0.01	0.062
12	EQ LH5	24	8	74.10	68.08	94.79	6.10	0.75	0.016	0.01	0.062
13	Cyclic	24	8	69.89	68.08	92.84	6.10	0.75	0.016	0.013	0.062
14	Cyclic	24	8	64.57	68.08	92.84	6.64	0.75	0.016	0.005	0.057
15	Cyclic	24	8	64.57	68.08	92.84	7.23	0.75	0.016	0.007	0.052
16	Cyclic LH6	24	8	64.57	68.08	92.84	6.71	0.75	0.016	0.013	0.056
17	EQ LH7	24	8	64.57	68.08	92.84	7.59	0.75	0.016	0.013	0.05
18	EQ LH8	24	8	64.57	68.08	82.84	7.81	0.75	0.016	0.013	0.048
19	Cyclic	18	8	65.55	68.14	92.43	6.33	0.75	0.017	0.013	0.1
20	Cyclic	18	8	65.55	68.14	92.43	6.47	0.75	0.017	0.013	0.05
21	Cyclic	18	11	65.55	68.14	92.43	6.39	0.75	0.017	0.013	0.05
22	Cyclic	18	11	65.55	68.14	92.43	6.53	0.75	0.017	0.013	0.1
23	Cyclic	18	13	65.55	68.14	92.43	6.61	0.75	0.017	0.013	0.05
24	Cyclic	18	13	65.55	68.14	92.43	6.47	0.75	0.017	0.013	0.1
25	Cyclic	24	8	63.86	69.70	95.54	6.29	0.875	0.021	0.01	0.05
26	Cyclic	24	8	63.86	69.70	95.54	5.89	0.875	0.021	0.01	0.1
27	Cyclic	24	8	63.86	68.74	93.70	6.15	0.75	0.016	0.01	0.1
28	Cyclic	18	8	63.86	68.74	93.70	6.24	0.75	0.017	0.013	0.15
29	Cyclic	18	8	63.86	68.74	93.70	5.91	0.75	0.017	0.013	0.2
30	Cyclic	18	8	63.86	70.47	97.68	6.05	1	0.031	0.013	0.15

Table 1-3. Limit State Strains and Drifts from (Goodnight, Kowalsky and Nau 2015) Dataset

Test	Cover Crushing $\varepsilon_{cc}^{Compressive}$		Cover Crushing Δ_{cc}/L		Spiral Yield $\varepsilon_{sy}^{Compressive}$		Spiral Yield Δ_{sy}/L		Bar Buckling $\varepsilon_{bb}^{Tensile}$		Bar Buckling Δ_{bb}/L	
	North	South	North	South	North	South	North	South	North	South	North	South
8	-	0.006	-	0.0252	-	0.0183	-	0.0623	0.051	0.048	0.0755	0.0693
9	0.0041	0.0032	0.0174	0.0176	0.0139	0.0163	0.0526	0.0699	0.053	0.051	0.0700	0.0698
10	0.0026	0.0039	0.0145	0.0177	0.0092	0.0151	0.0519	0.0466	-	0.038	-	0.0522
11	-	-	-	-	-	0.0163	-	0.0413	0.059	0.033	0.0863	0.0529
12	0.0047	0.0044	0.0193	0.0184	0.0165	0.0176	0.0523	0.0594	0.058	0.044	0.0856	0.0680
13	0.0046	0.0036	0.0168	0.0167	0.0166	0.0162	0.0505	0.0673	0.047	0.047	0.0673	0.0677
14	0.0029	0.0030	0.0124	0.0125	-	0.0152	-	0.0500	0.035	0.035	0.0500	0.0500
15	0.0027	0.0041	0.0130	0.0175	0.0199	0.0125	0.0521	0.0347	0.037	0.038	0.0521	0.0521
16	0.0048	0.0038	0.0172	0.0173	0.0120	0.0152	0.0519	0.0519	0.056	0.052	0.0693	0.0696
17	0.0043	0.0043	0.0167	0.0174	0.0148	0.0168	0.0419	0.0470	0.055	0.039	0.0780	0.0523
18	0.0068	-	0.0230	-	0.0147	0.0136	0.0572	0.0384	-	0.047	-	0.0630
19	0.0068	0.0065	0.0239	0.0239	0.0103	0.0119	0.0356	0.0357	0.037	0.032	0.0596	0.0596
20	0.0065	0.0046	0.0246	0.0246	0.0114	0.0109	0.0492	0.0370	0.046	0.037	0.0740	0.0614
21	0.0046	0.0048	0.0299	0.0301	0.0146	0.0102	0.0599	0.0450	0.051	0.036	0.0898	0.0748
22	0.0063	0.0085	0.0316	0.0316	0.0103	0.0124	0.0475	0.0474	0.041	0.053	0.0792	0.0949
23	0.0052	0.0062	0.0356	0.0355	0.0136	0.0151	0.0713	0.0711	0.051	0.048	0.1067	0.1067
24	0.0085	0.0083	0.0367	0.0367	0.0155	0.0131	0.0550	0.0550	0.037	0.048	0.0916	0.0918
25	0.0036	0.0040	0.0158	0.0159	0.0091	0.0125	0.0319	0.0321	0.042	0.035	0.0640	0.0533
26	0.0045	0.0046	0.0155	0.0156	0.0089	0.0121	0.0311	0.0309	0.032	0.024	0.0519	0.0415
27	0.0036	0.0038	0.0144	0.0144	0.0168	0.0124	0.0288	0.0288	0.036	0.024	0.0479	0.0382
28	0.0051	0.0055	0.0208	0.0208	0.0123	0.0143	0.0417	0.0417	0.036	0.030	0.0696	0.0556
29	0.0055	0.0054	0.0210	0.0209	0.0142	0.0103	0.0420	0.0280	0.055	0.036	0.0840	0.0700
30	0.0052	0.0059	0.0230	0.0230	0.0095	0.0094	0.0307	0.0307	0.036	0.033	0.0770	0.0770

Modified Lpr Plastic Hinge Method from (Goodnight, Kowalsky and Nau 2015a)

The Modified Plastic Hinge Method was developed to improve the accuracy of strain-displacement predictions necessary for successful implementation of strain-based limit states. Equivalent curvature distributions for the Modified Plastic Hinge Method appear in Figure 1-7 for a column in single bending. The key aspects of the proposed Modified Plastic Hinge Model which differentiate it from the method recommended in (Priestley, Calvi and Kowalsky 2007) include: (1) a decoupling of column flexure and strain penetration deformation components, (2) a linear plastic curvature distribution which emulates the measured curvature profiles, and (3) separate plastic hinge lengths for tensile and compressive strain-displacement predictions.

In the experiments, the measured extent of plasticity was found to increase due to the combined effects of moment gradient and tension shift. The proposed tension hinge length, Lpr_t in Eqn 1-11, was calibrated to match the upper bound of the measured spread of plasticity in each test. The proposed compressive hinge length, Lpr_c in Eqn 1-12, only contains a term related to the moment gradient effect. Expressions for the elastic and plastic column flexural displacement for both single and double bending were created. Expressions which describe the additional column deformation due to strain penetration of reinforcement into the adjoining member were developed based on measured fixed-end rotations. This included the formulation of a new equivalent strain penetration length, L_{sp} in Eqn 1-9.

Elastic displacements are computed when the base section curvature is either at or below the first yield curvature, ϕ'_y. The elastic displacement of a column in single bending is calculated using Eqn 1-13 and Eqn 1-17. The elastic displacement of a column in double bending is computed using Eqn 1-19 and Eqn 1-23. The elastic displacement is the addition of elastic column flexural, strain penetration, and shear deformations. Shear displacements were negligible for columns in the (Goodnight, Kowalsky and Nau 2015) dataset, therefore no further guidance is provided.

Inelastic displacements are computed when the base section curvature exceeds the first yield curvature, ϕ'_y. To account for additional elastic flexibility of the column, the first yield displacement is multiplied by the ratio of the current base section moment to the moment at first yield of the longitudinal reinforcement, M/M'_y. The plastic curvature at the base section is obtained by subtracting the elastic curvature from the base section curvature, $\phi_p = \phi_{base} - \phi'_y\left(M/M'_y\right)$. For translation of a tensile strain limit to a lateral displacement, the tensile triangular plastic hinge length should be used, Lpr_t in Eqn 1-11. If instead, a compressive strain limit is translated to a lateral displacement, the compressive triangular plastic hinge length should be employed, Lpr_c in Eqn 1-12. Expressions needed to compute the inelastic displacement of a column in single bending are shown in Eqn 1-14 through Eqn 1-18. Expressions needed to compute the inelastic displacement of a column in double bending appear in Eqn 1-20 through Eqn 1-24. The total displacement is the sum of the elastic column flexural, plastic column flexural, strain penetration, and shear deformation components.

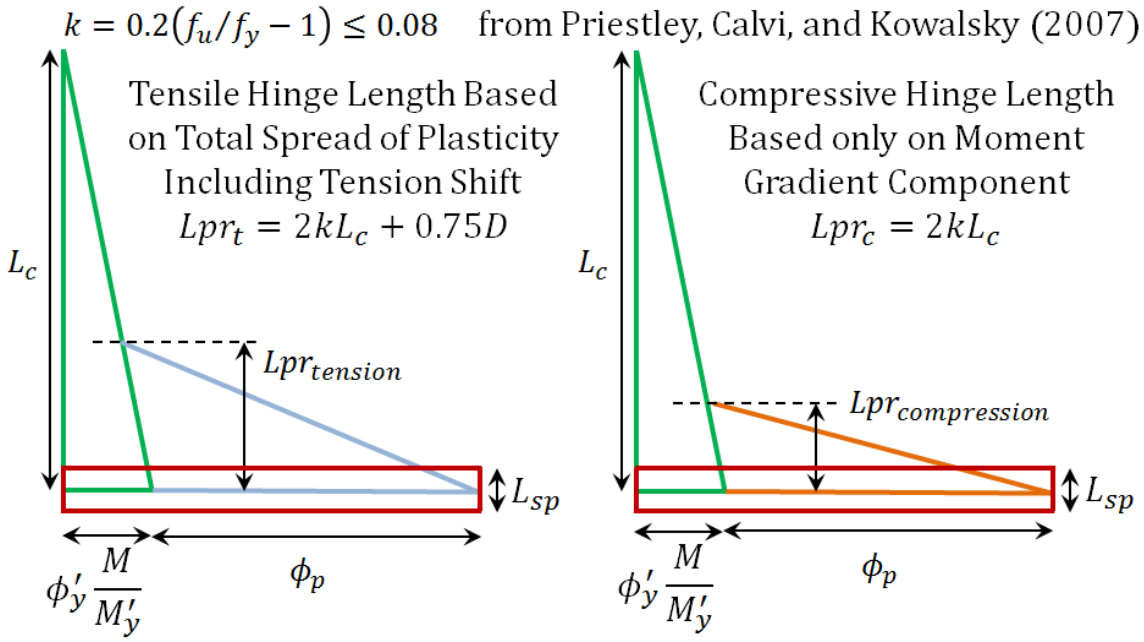

Figure 1-7. Equivalent Curvature Distributions for the Modified Lpr Plastic Hinge Method

Equivalent Strain Penetration Length and Tension/Compression Plastic Hinge Lengths

Where L_c is the length to the point of contraflexure, D is the column diameter, d_{bl} and f_{ye} are the diameter and expected yield stress of the longitudinal reinforcement, and f'_{ce_f} is the expected concrete strength of the adjoining member.

$$L_{sp} = U\left(1 - \frac{P}{f'_{ce}A_g} - \frac{L_c}{16D}\right)\frac{f_{ye}d_{bl}}{\sqrt{f'_{ce_f}}}$$ *Equivalent Strain Penetration Length* — *Eqn 1-9*

$U = 0.4$ *for ksi and* $U = 0.152$ *for MPa units*

$$k = 0.2\left(\frac{f_{ue}}{f_{ye}} - 1\right) \leq 0.08$$ *Same as Priestley, Calvi, and Kowalsky (2007)* — *Eqn 1-10*

$$Lpr_t = 2kL_c + 0.75D$$ *Tension Hinge Length Based on Triangular Distribution* — *Eqn 1-11*

$$Lpr_c = 2kL_c$$ *Compression Hinge Length Based on Triangular Distribution* — *Eqn 1-12*

Displacements for a Column in Single Bending ($L_c = L$)

$$\Delta_e = \phi_{base}L^2/3$$ *(Single) Elastic Flexural Displacement before First Yield* — *Eqn 1-13*

$$\Delta_e = \phi'_y(M/M'_y)L^2/3$$ *(Single) Elastic Flexural Displacement after First Yield* — *Eqn 1-14*

$$\phi_p = \phi_{base} - \phi'_y(M/M'_y)$$ *Plastic Curvature at the Base Section* — *Eqn 1-15*

$$\Delta_p = \phi_p(L_{pr}/2)[L - L_{pr}/3]$$ *(Single) Plastic Flexural Displacement* — *Eqn 1-16*

$$\Delta_{sp} = L_{sp}\phi_{base}L$$ *Displacement due to Strain Penetration* — *Eqn 1-17*

$$\Delta_T = (\Delta_e + \Delta_{sp} + \Delta_p + \Delta_{shear})$$ *Total Top Column Displacement* — *Eqn 1-18*

Displacements for a Column in Double Bending $(L_c = L/2)$

$\Delta_e = \phi_{base} L^2/6$	*(Double) Elastic Flexural Displacement before First Yield*	*Eqn 1-19*
$\Delta_e = \phi'_y (M/M'_y) L^2/6$	*(Double) Elastic Flexural Displacement after First Yield*	*Eqn 1-20*
$\phi_p = \phi_{base} - \phi'_y (M/M'_y)$	*Plastic Curvature at the Base Section*	*Eqn 1-21*
$\Delta_p = \phi_p (L_{pr}/2)[L - 2\,L_{pr}/3]$	*(Double) Plastic Flexural Displacement*	*Eqn 1-22*
$\Delta_{sp} = L_{sp} \phi_{base} L$	*Displacement due to Strain Penetration*	*Eqn 1-23*
$\Delta_T = (\Delta_e + \Delta_{sp} + \Delta_p + \Delta_{shear})$	*Total Top Column Displacement*	*Eqn 1-24*

Predictive comparison of Plastic Hinge Models

Moment-curvature analysis was performed for each experiment in the (Goodnight, Kowalsky and Nau 2015) dataset. The plastic hinge model recommended in (Priestley, Calvi and Kowalsky 2007) was used to translate curvatures to displacements, abbreviated (PCK L_p). The Modified (L_{pr}) Plastic Hinge Model recommended in (Goodnight, Kowalsky and Nau 2015a) was utilized to convert material strain to displacements. Datasets were created for the ratio of Measured/Predicted displacement at each of the following limit states from the physical experiments: (1) analytical column shear force at initial yielding of the longitudinal reinforcement, (2) tensile strain which preceded bar buckling in the following load reversal, (3) initial cover concrete crushing, and (4) initial yielding of confinement steel. Statistics comparing the predictive capacity of each plastic hinge method appear in Table 1-4. Alternatively, cumulative probability distributions can be used to visualize the accuracy of the equivalent curvature distributions. The elastic predictive capacity of both models was found to be similar in accuracy and conservatism, see the left of Figure 1-8. Although tensile strain-displacement predictions at the bar buckling observation were conservative for both models, the Modified L_{pr} Hinge Method shows significant improvement, see the right of Figure 1-8. Compressive strain-displacement predictions for both limit states are conservative, but the Modified L_{pr} Hinge Method shows improvement, refer to Figure 1-9.

Table 1-4. Plastic Hinge Model Comparison, Statistics for Measured/Predicted Dataset

Limit State	Plastic Hinge Method	Mean	COV	RMSE
First Yield Force F'_y	Modified L_{pr}	1.09	0.058	0.404
	PCK (2007) L_p	1.07	0.059	0.332
Bar Buckling $\varepsilon_s^{Tensile}$	Modified L_{pr}	1.12	0.061	0.121
	PCK (2007) L_p	1.27	0.116	0.222
Cover Crushing $\varepsilon_c^{Compressive}$	Modified L_{pr}	0.93	0.105	0.145
	PCK (2007) L_p	0.80	0.152	0.340
Spiral Yielding $\varepsilon_c^{Compressive}$	Modified L_{pr}	0.88	0.192	0.266
	PCK (2007) L_p	0.71	0.221	0.529

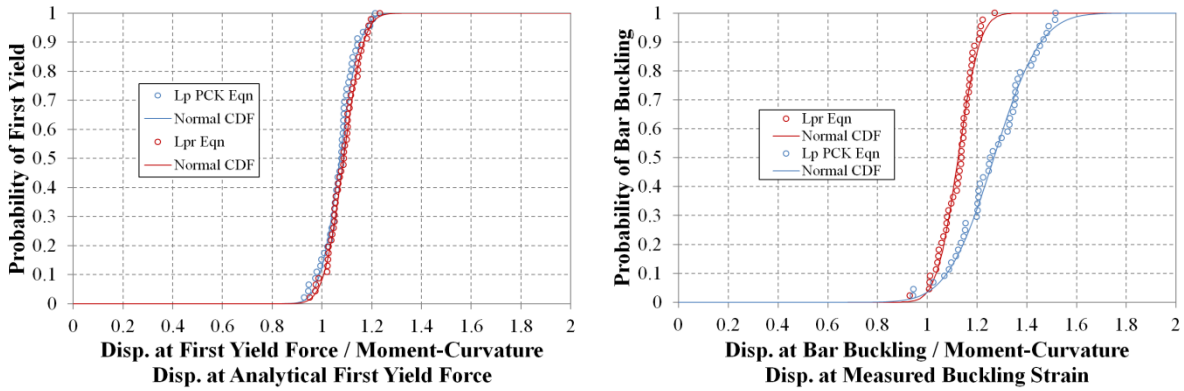

Figure 1-8. Cumulative Probability Distribution for (Left) Analytical First Yield Force and (Right) Tensile Bar Buckling Strain

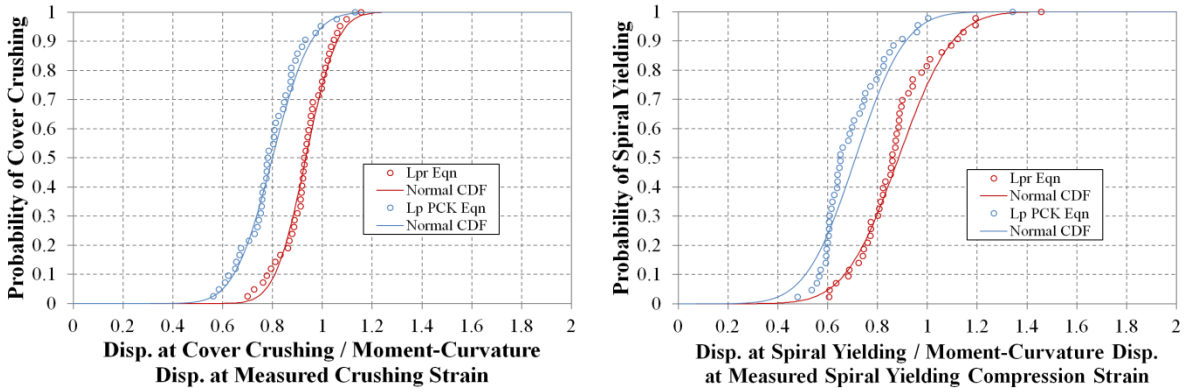

Figure 1-9. Cumulative Probability Distribution for (Left) Initial Cover Crushing and (Right) Initial Spiral Yielding

Performance Strain Limit Recommendations from (Goodnight, Kowalsky and Nau 2015b)

The observed damage and measured strain data for Tests 8-30 in Table 1-3 was used to develop empirical expressions to predict material strains at key performance limit states. Recommendations from (Kowalsky 2000) were evaluated, and when appropriate, new expressions were developed.

Serviceability Limit States

When exceeded, serviceability limit states represent the point at which repair is necessary, interrupting the serviceability of the structure, but not posing a safety concern. The serviceability limit states are characterized by crushing of cover concrete and residual crack widths which exceed 1 mm, which require some degree of intervention to prevent corrosion of internal reinforcing steel. As a result of this study, no changes to the current serviceability strain limits proposed by (Kowalsky 2000) were warranted. The average measured compressive strain at cover concrete crushing was 0.0048, although this observation was made at the end of the cycle with larger measured strains. Cover crushing was observed before residual crack widths reached 1 mm in each experiment, preventing further study of this limit state.

$\varepsilon_c = 0.004$ — *Concrete compression strain related to crushing of the cover concrete. Evaluated at the extreme compression fiber.* — *Eqn 1-25*

$\varepsilon_s = 0.015$ — *Steel tensile strain limit related to residual crack widths which exceed 1 mm. Evaluated at the extreme longitudinal reinforcing bar.* — *Eqn 1-26*

Intermediate Compressive Limit State Prompting a Change in Repair Strategy

Currently there is not an intermediate strain limit between serviceability and damage control which is related to a change in compressive behavior that results due to confinement steel yielding. Experimental results suggest that localization of compressive demand can occur in regions with inelastic transverse steel. This localization can lead to compression strains which exceed predictions utilizing moment-curvature analysis and an equivalent curvature distribution. Furthermore, inelastic transverse steel restraint resulted in measureable outward deformation of longitudinal reinforcement prior to visible bar buckling observations. In the expression below, A_{st}/A_g is the longitudinal reinforcement ratio and f_{yhe}/E_s is the expected yield strain of the transverse steel. The force required to maintain stability of higher levels of longitudinal reinforcement takes away from the remaining strain component utilized for core concrete confinement.

$$\varepsilon_c = 0.009 - 0.3\frac{A_{st}}{A_g} + 3.9\frac{f_{yhe}}{E_s}$$ — *Concrete compression strain at initial yielding of confinement steel. Evaluated at the centerline of the transverse steel, i.e. the concrete core.* — *Eqn 1-27*

$$mean\left(\frac{\varepsilon_c^{Measured}}{\varepsilon_c^{\text{Eqn 1-27}}}\right) = 1.06 \; and \; COV = 0.167$$

$$mean\left(\frac{\Delta_c^{Measured}}{\Delta \; at \; \varepsilon_c^{\text{Eqn 1-27}} \; with \; Modified \; L_{pr} \; Hinge \; Method}\right) = 0.97 \; and \; COV = 0.186$$

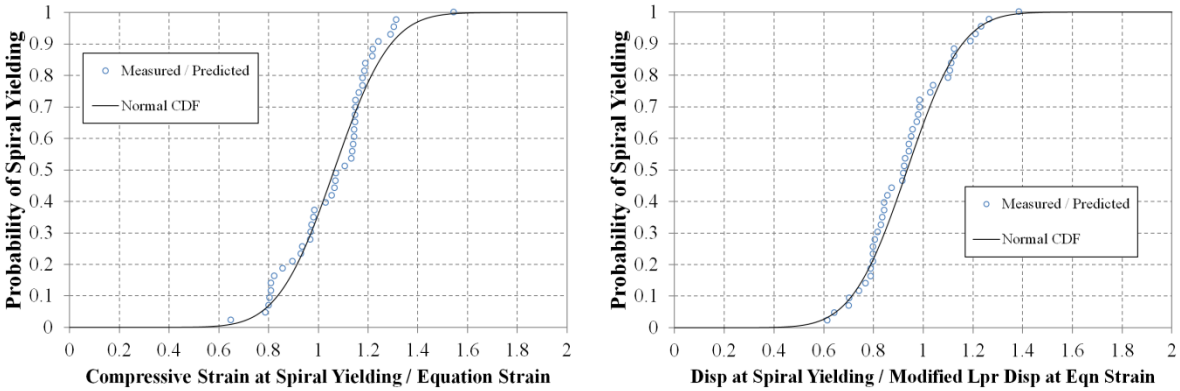

Figure 1-10. Cumulative Probability Distribution for (Left) Compressive Strain and (Right) Disp. at Initial Yielding of Confinement Steel

Damage Control Limit States

The damage control limit state represents the limit of economical repair, and is defined by longitudinal bar buckling or significant damage to the core concrete. Bar buckling was observed to occur after reversal from a peak tensile strain while the bar is under net elongation, but compressive stress. Although prior compression is important to describing the restraint provided by transverse steel, expression developed based on the peak tensile strain before bar buckling upon reversal of load were found to produce the most accurate predictions. Furthermore, higher levels of tensile strain reduce the tangent modulus of the reinforcement during the subsequent stress reversal. An expression for the tensile strain preceding bar buckling, Eqn 1-28, was developed utilizing the measured strain data. The parameters in the expression are known or may be reasonably approximated at the onset of design, and later confirmed after finalizing the transverse steel detailing. As a prediction, expected material properties should be utilized in the expression. Sufficient confinement steel should be provided such that the (Mander, Priestley and Park 1988) Ultimate Concrete Compressive Strain exceeds the core concrete strain at the bar buckling displacement.

$$\varepsilon_s = 0.03 + 700\rho_s \frac{f_{yhe}}{E_s} - 0.1\frac{P}{f'_{ce}A_g}$$

Peak tension strain prior to bar buckling. Evaluated at the location of the extreme longitudinal reinforcing bar. Eqn 1-28

$\rho_s = \frac{4A_{sp}}{D's}$ *Transverse volumetric steel ratio, which influences confinement and bar restraint.*

f_{yhe}/E_s *Inelastic transverse steel is less effective at restraining the longitudinal bars.*

$P/f'_{ce}A_g$ *Axial load ratio expressed as a decimal rather than a percent.*

$$mean\left(\frac{\varepsilon_s^{Measured}}{\varepsilon_s^{\text{Eqn 1-28}}}\right) = 1.05 \; and \; COV = 0.199$$

$$mean\left(\frac{\Delta_s^{Measured}}{\Delta \; at \; \varepsilon_s^{\text{Eqn 1-28}} \; with \; Modified \; L_{pr} \; Hinge \; Method}\right) = 1.17 \; and \; COV = 0.157$$

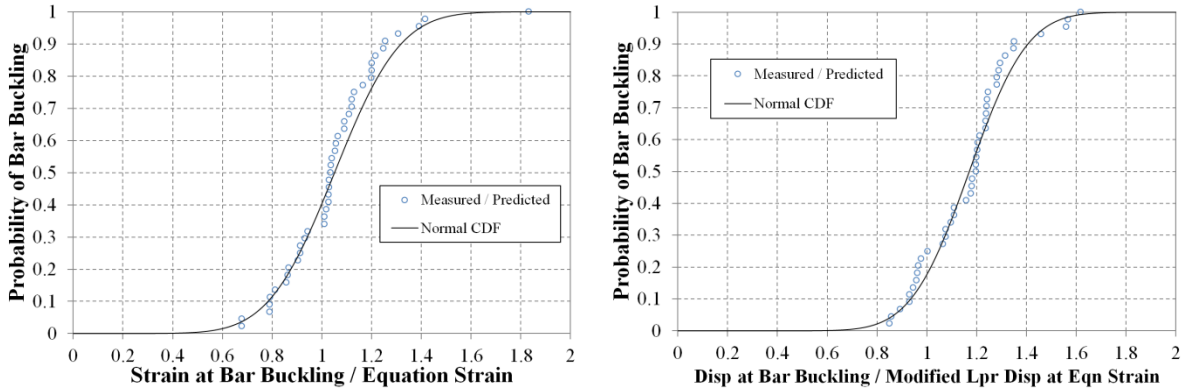

Figure 1-11. Cumulative Probability Distribution for (Left) Tensile Strain and (Right) Disp. at Bar Buckling

Literature Review on the Effects of Bidirectional Loading

In a seismic event, bridge columns undergo demands in the longitudinal and transverse directions simultaneously, which produce a two-dimensional displacement path. Past experimental studies on biaxial bending with either constant or variable axial load provide insight into their effect on member behavior. This section includes a literature review for the effects of bidirectional loading on column performance, which will be updated and expanded through the duration of the project.

(Wong, Paulay and Priestley 1993) "Response of Circular Reinforced Concrete Columns to Multi-Directional Seismic Attack"

Sixteen circular shear-dominated columns were tested with different biaxial displacement histories, volumetric steel ratios, and levels of applied constant axial load. The purpose of the research was to determine the influence of biaxial loading on the "concrete component" of shear resistance. Short circular columns were tested with a 400 mm diameter, an aspect ratio of 2, and a steel content of 3.2%. Axial loads of 0, 19 or 39% were utilized. Transverse volumetric steel ranged between 0.39 and 2.46%. Four displacement patterns were considered, Type u, b, s, and r in Figure 1-12. The uniaxial 'u' pattern had five cycles at a given amplitude before increasing to a larger displacement ductility level. Biaxial 'b' and 's' patterns had two cycles at each amplitude before ramping up the displacement. Due to the bidirectional nature of the loading history, this resulted in four complete reversals at each displacement level. The multi-directional 'r' pattern was used to simulate a displacement path originating from NLTHA of a column under earthquake excitation.

(Wong, Paulay and Priestley 1993) concluded that biaxial response reduced the deformation capacity by one ductility level when compared to a nominally identical column subjected to uniaxial response. Furthermore, (Wong, Paulay and Priestley 1993) conclude that there was not a clear difference in results of the two b- and s-type laboratory biaxial displacement patterns. The following observation is of significance to bar buckling, "For columns reinforced with similar spiral steel content, the commencement of spiral yielding was consistently observed at lower ductilities when more severe displacement orbits were imposed." On the topic of load path effects, (Wong, Paulay and Priestley 1993) note, "The difference in the response of columns with identical properties subjected to simple biaxial b-type displacement patterns or to more sophisticated s-type patterns was small enough to be disregarded in design. Moreover, the performance of the unit tested with the realistic earthquake simulating random biaxial displacement pattern was found to be better than its companion unit under b-type displacement history. These suggest that if biaxial seismic effects are to be studied further, test using biaxial b-type (orthogonal) displacement paths should be sufficient."

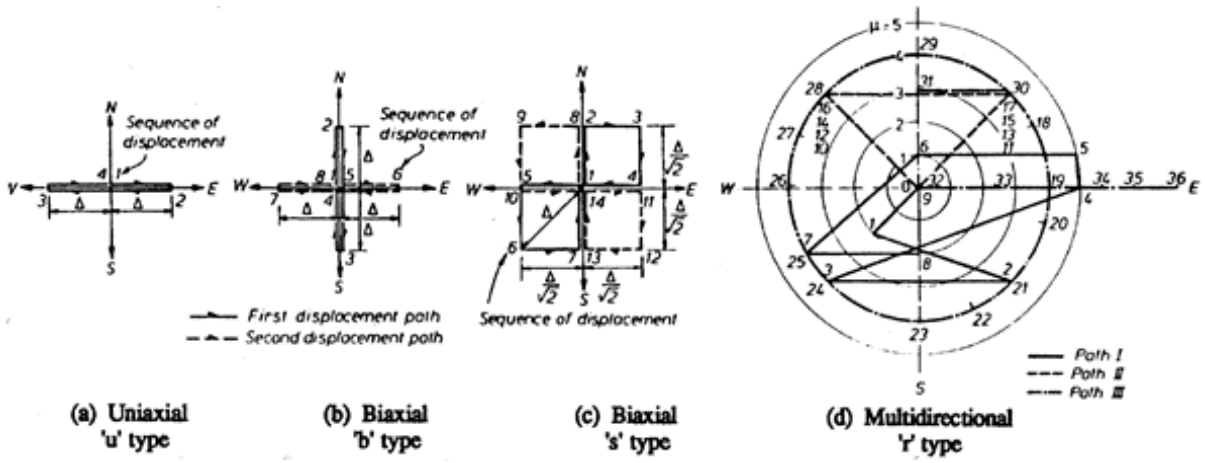

Figure 1-12. (Wong, Paulay and Priestley 1993) Lateral Displacement Histories

(Osorio, Bairán and Marí 2012) "Effects of Biaxial Shear Loading on the Seismic Response of RC Columns"

Two nominally identical circular columns were tested, one subjected to uniaxial and the other to biaxial loading. The specimens were designed for flexural-shear failure. The 350 mm diameter circular specimens had 2.5% longitudinal steel, 0.5% transverse volumetric steel, a constant 20% axial load, and an aspect ratio of 4.3. A clover leaf style lateral displacement history, Figure 1-13, was utilized in the biaxial test. Two complete cycles at a given displacement amplitude were conducted for the bidirectional tests. Strain gauges were applied in each quadrant for the first three spiral layers. The location of these strain gauges directly overlaid the extreme fiber reinforcing bars subjected to the peak excursions. The reported transverse steel strain hysteresis for bidirectional and unidirectional loading appears in Figure 1-13. Although the shape of the measured response is similar, the biaxial loading resulted in an additional accumulation of hoop strain during repeated cycles at a displacement amplitude of 27 mm. The additional hoop strain may reduce the stiffness and thus effectiveness of the hoop as buckling restraint for the longitudinal bars. The reported observations indicate that the spike in measured hoop strains coincided with visible bar buckling. In comparison, bar buckling was reported one displacement amplitude larger in the uniaxial test. (Osorio, Bairán and Marí 2012) note, "Results show that biaxial shear loading affects the shear mechanisms, producing larger transverse strains for the same load intensity and lower crack angles." It is important to note that the displacement amplitudes were small and the level of confinement/restraint was low in the shear dominated columns.

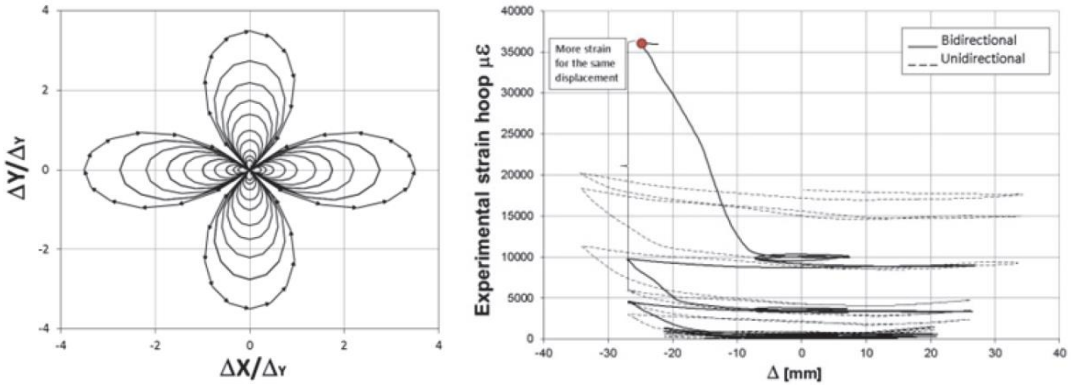

Figure 1-13. (Osorio, Bairán and Marí 2012) (Left) Biaxial Disp. History and (Right) Measured Hoop Strains for Uniaxial and Biaxial Displacement Patterns

(Tsuno and Park 2004) "Experimental Study of Reinforced Concrete Bridge Piers Subjected to Bi-Directional Quasi-Static Loading"

The study considered four rectangular bridge columns subjected to different bidirectional load paths, and one repeat load history for a fifth column with a lower concrete strength. The specimens were 550 mm square with an aspect ratio of 4.1, a steel content of 1.2%, a volumetric steel ratio of 1%, and a constant axial load equivalent to 4.4%. The first specimen, S1, was subjected to a symmetric uniaxial two-cycle-set load history which served as a baseline for comparison for the biaxial tests. Specimen S2 was subjected to the exact opposite of the load history used for S1, with the high amplitude cycles occurring first followed by a gradual decrease in ductility. Specimen S3 utilized a bi-directional orthogonal symmetric two-cycle-set load history, Figure 1-14. Four total cycles were conducted at each ductility level, two in the E-W direction followed by two in the N-S direction. Specimen S4 utilized a bi-directional s-shape load history, Figure 1-15. Two complete orbital paths (1-16) were completed at each ductility level. The fifth column had reduced concrete strength and was subjected to the same uniaxial load history as S1.

(Tsuno and Park 2004) reported that reinforcement buckled at $\mu_{\Delta 8}$ and ruptured at $\mu_{\Delta 12}$ during the uniaxial two-cycle-set load history of S1. Spiral fracture was reported during $\mu_{\Delta 10}$. In specimen S2, bar buckling was reported during the reversal from the first cycle of $\mu_{\Delta 12}$ before the specimen reached zero displacement. Again, this was an inverse of the two-cycle-set load history which began with high ductility reversals. For the bi-directional load history of specimen S3, bar buckling was reported during $\mu_{\Delta 6}$ and bar fracture during $\mu_{\Delta 8}$. For the bi-directional load history of specimen S4, bar buckling was reported during $\mu_{\Delta 6}$ and bar fracture during $\mu_{\Delta 8}$. The fifth specimen, with weaker concrete and a uniaxial two-cycle-set load history had reported bar buckling during $\mu_{\Delta 6}$ and bar fracture during $\mu_{\Delta 10}$.

(Tsuno and Park 2004) utilized an array of linear potentiometers to monitor curvature distributions in the main orthogonal directions of the load histories. Cross section curvature profiles obtained from the potentiometers were used to calculate an equivalent rectangular plastic hinge length L_p. In an equivalent curvature distribution, L_p is the length over which plastic curvatures are assumed to remain constant, and in their formulation it includes the strain penetration component. A sample curvature profile for specimen S1, and the resulting L_p values for all of the experiments is

shown in Figure 1-16. (Tsuno and Park 2004) provide a summary of observations related to the influence of bi-directional loading on curvature profile and computed plastic hinge lengths, which are repeated below.

"1. The plastic hinge zone length L_p tends to be stable at around the theoretical values after some cyclic loadings and is not affected by bi-directional loading. The plastic hinge zone length is shorter than theoretical values until the displacement ductility factor μ_Δ reaches around 4. The concrete strength of a column might affect the plastic hinge zone length L_p. No significant difference in the L_p-μ_Δ relationship was observed between tests S1-S4, which suggests that L_p is not affected by bi-directional loading after some cycles of loading.

2. If an extremely large displacement, such as $\mu_{\Delta 12}$ for the specimens used in this research, is applied to a column at the early stage of cyclic loading, it may lead to the buckling of main-bars and confinement failure with only small energy dissipation. However, as long as the displacement amplitude in the cyclic loading starts at a small level and increases step-by-step, like the standard loading patterns suggested by Park, the energy dissipation capacity of a column until the ultimate state is the same for both uni-directional and bi-directional loading.

3. The maximum displacement of a column when it reaches the ultimate state in a bi-directional cyclic loading, is smaller than that of the same column subjected to the standard uni-directional loading pattern suggested by Park."

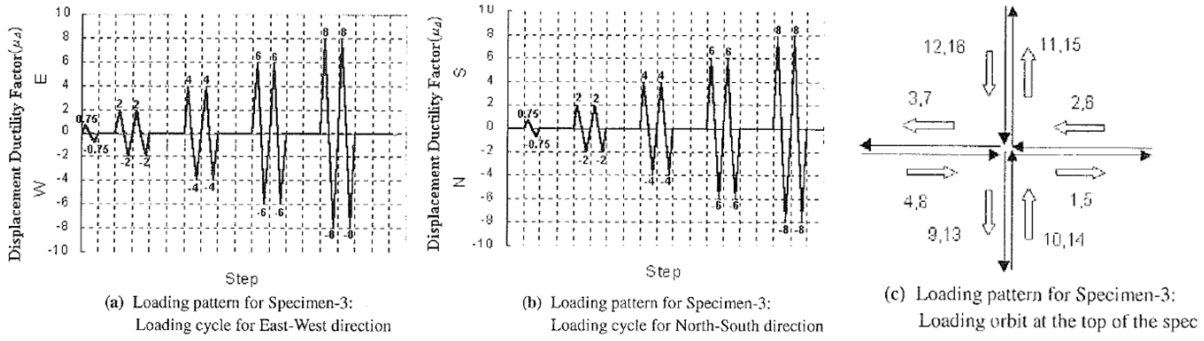

(a) Loading pattern for Specimen-3: Loading cycle for East-West direction

(b) Loading pattern for Specimen-3: Loading cycle for North-South direction

(c) Loading pattern for Specimen-3: Loading orbit at the top of the spec

Figure 1-14. (Tsuno and Park 2004) Bi-Directional Load History for Specimen S3

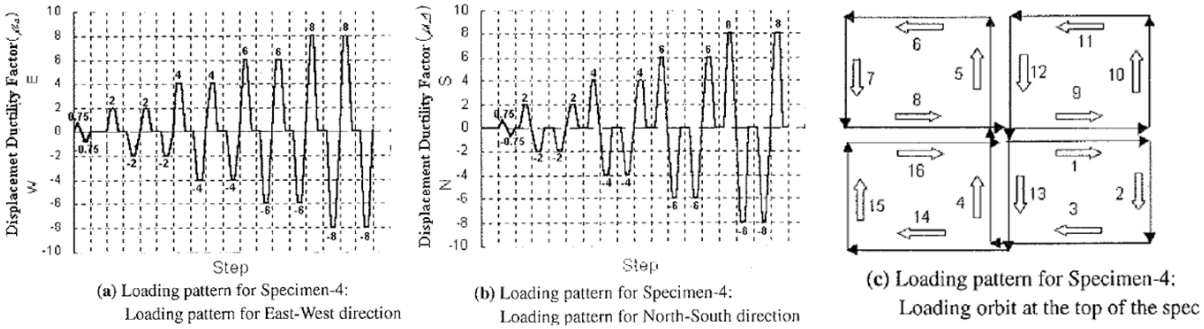

(a) Loading pattern for Specimen-4: Loading pattern for East-West direction

(b) Loading pattern for Specimen-4: Loading pattern for North-South direction

(c) Loading pattern for Specimen-4: Loading orbit at the top of the spec

Figure 1-15. (Tsuno and Park 2004) Bi-Directional Load History for Specimen S4

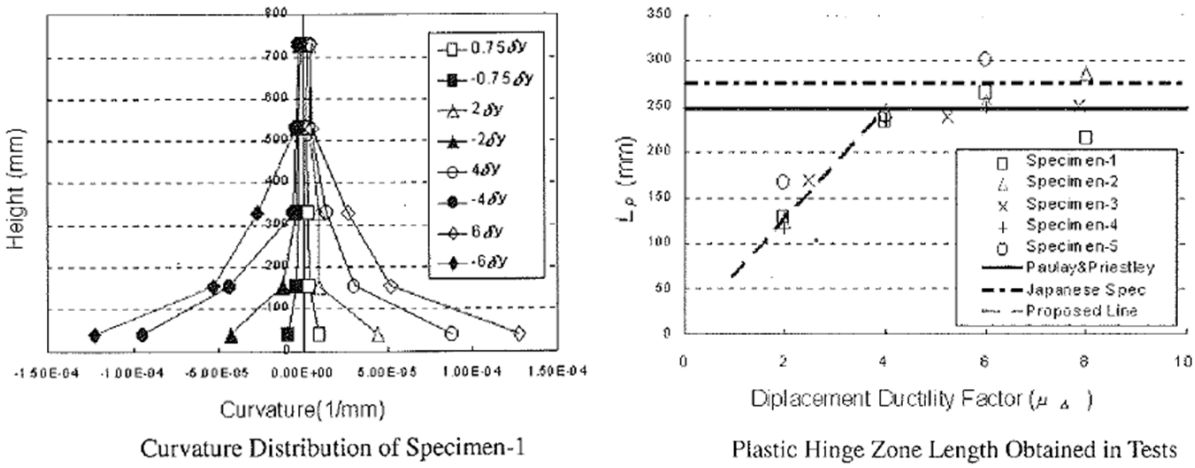

Figure 1-16. (Tsuno and Park 2004) Calculated Plastic Hinge Lengths from Measured Curvature Profiles

(Bousias, et al. 1995) "Load Path Effects in Column Biaxial Bending with Axial Force"

Research by (Bousias, et al. 1995) focused on the effect of three dimensional load path, including a mixture of displacement and force controlled lateral input as well as varying axial load for square columns. The columns were 250 mm square and had an aspect ratio of six. The cross section had 8, 16 mm bars uniformly distributed around the perimeter and a double 8 mm diameter hoop arrangement with 70 mm spacing. The load history utilized in the experiments are shown in Figure 1-17. Load histories S0, S1, S2, S5, S6, S7, and S8 utilized constant axial force and varying imposed lateral displacement history. Specimens S3 and S4 has a mixture of force control and displacement controlled loading histories in the orthogonal directions and a constant axial force. Test units S9, S10, and S11 had varying lateral and axial loading history. The load histories were devised to evaluate specific characteristics unique to bidirectional loading.

(Bousias, et al. 1995) note the following regarding the influence of load path, "The strong coupling between the two transverse directions produced an apparent reduction of strength and stiffness in each of the two transverse directions considered separately, but also increased the hysteretic energy dissipation. This increase is manifested by the larger width of the hysteresis loops in a transverse direction in the presence of a nonzero force or deflection in the orthogonal direction, as compared with the cases of cyclic uniaxial bending. Moreover, biaxial force paths are rotated with respect to the biaxial deflection paths in the sense in which these are traced, so that the vector resultant of transverse displacements always lags behind the vector resultant of transverse forces." This lag in the resultant force vector is apparent in the results from Tests S7 depicted in Figure 1-17.

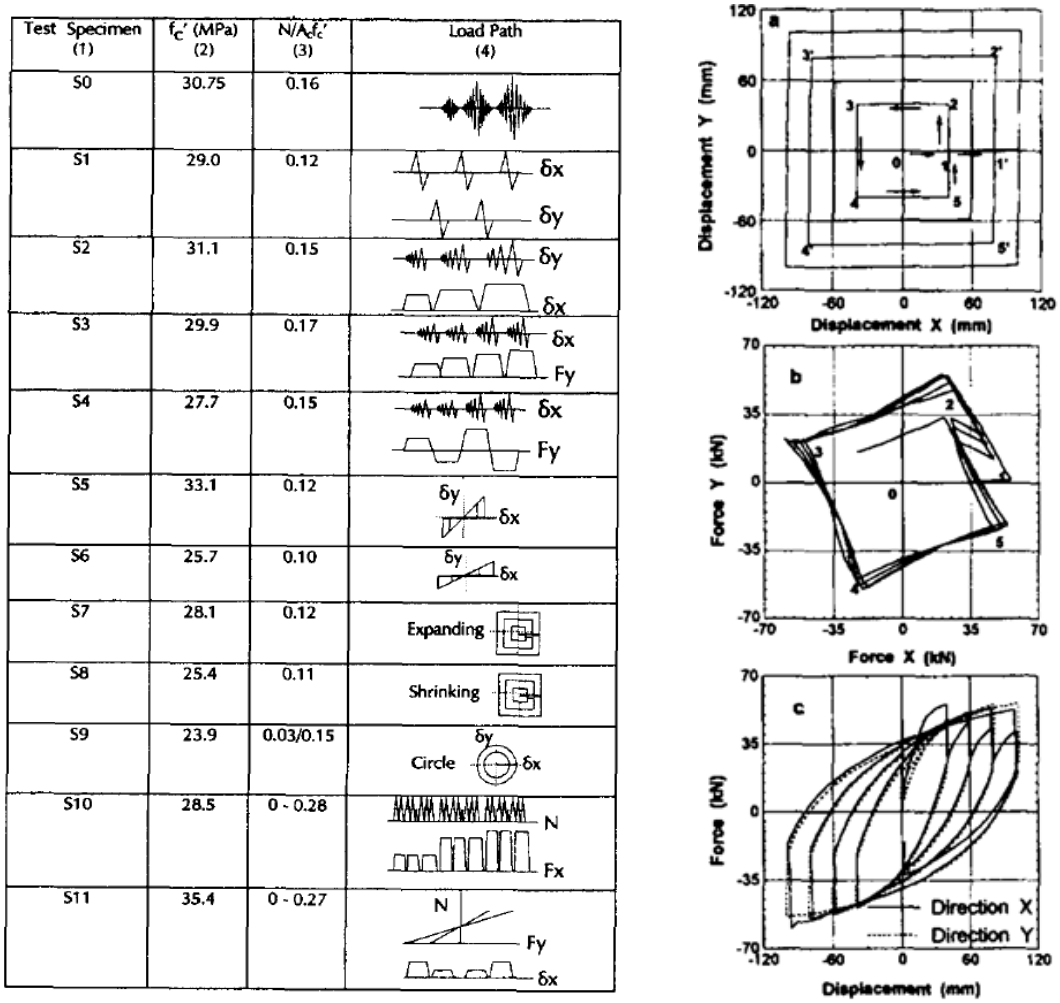

Figure 1-17. (Bousias, et al. 1995) (Left) Load Histories and (Right) Test S7 Demonstrates Lag of Force Resultant behind the Disp. Resultant

(Mazzoni and Moehle 2001) "Seismic Response of Beam-Column Joints in Double-Deck Reinforced Concrete Bridge Frames"

(Mazzoni and Moehle 2001) investigated the seismic performance of beam-column joints in double-deck reinforced concrete bridge frames subjected to bidirectional loading. The specimens consisted of a column above and below the joint, with two longitudinal girder beams and one transverse cap beam framing into the beam-column joint as shown in Figure 1-18. Two one-third scale specimens were tested using simulated gravity and bidirectional lateral load as shown in Figure 1-18. These were nominally identical, except for the column and beam longitudinal bar diameter, which influenced demands on the joint. The column and beam reinforcing details were chosen to achieve two specific levels of nominal joint shear stress, (1) $v_{n1} = 1.25\sqrt{f_c'}\,MPa$ prescribed by the Joint ACI-ASCE Committee 352 recommendations and (2) $v_{n2} = 1.66\sqrt{f_c'}\,MPa$. The column longitudinal reinforcement ratios for Specimen 1 and 2 were 1.3 and 1.8%. Both of the 22" diameter columns contained a #3 spiral at 2.25" pitch, which corresponded to a volumetric ratio of 1%. The ratio of joint depth to column diameter for Specimens 1 and 2 was 42 and 35. The joints contained a #3 spiral at

1.75” pitch, which is equivalent to a volumetric ratio of 1.2%. The beam reinforcement for both specimens was determined using capacity design principles. The column and beam cross-section details for Specimen 1 appear in Figure 1-19. The transverse cap beam longitudinal reinforcement was anchored outside of the joint within a stub as shown in Figure 1-20. The bidirectional loading sequence in Figure 1-21 was repeated at increasing displacement amplitudes until failure. Gravity loads were applied through an unbonded post tensioning rod placed in a duct which ran through the center of the column cross-section.

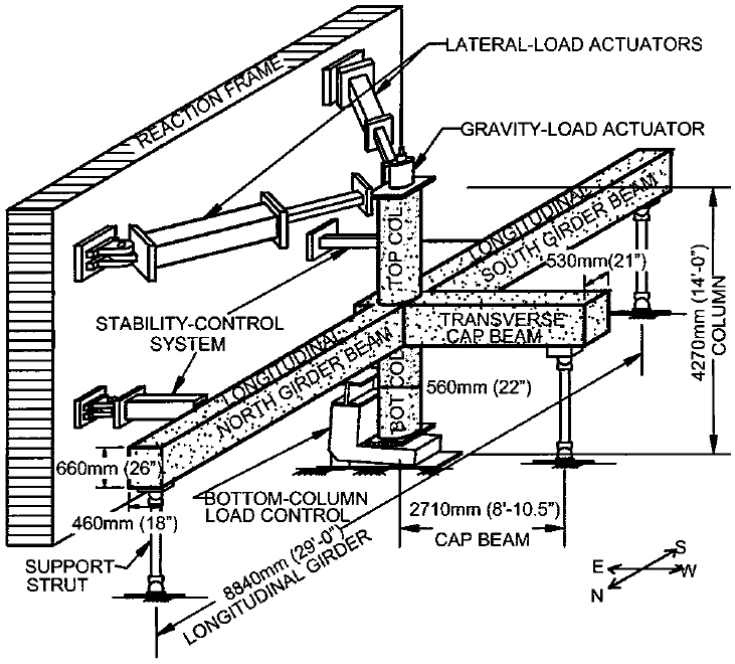

Figure 1-18. Test Setup and Specimen from (Mazzoni and Moehle 2001)

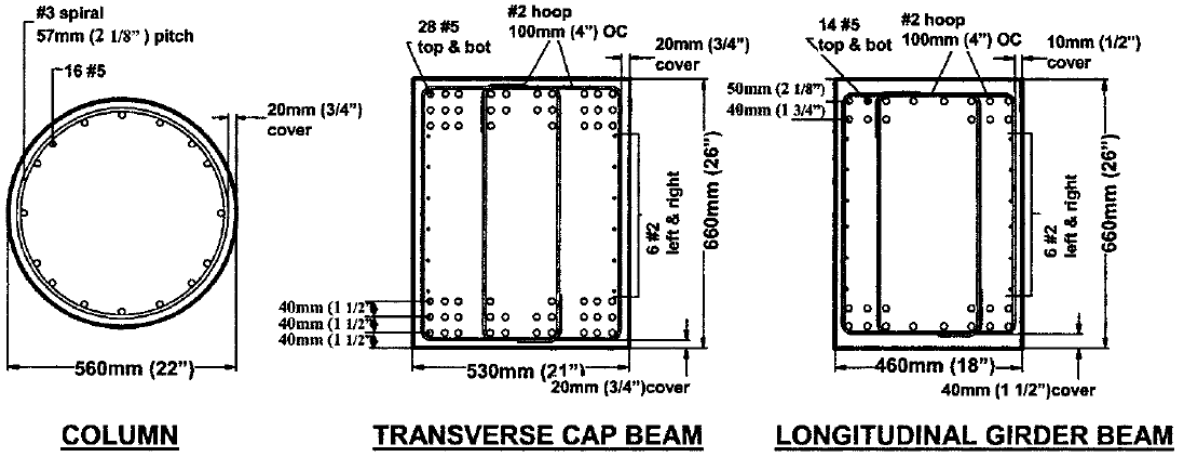

Figure 1-19. Column and Beam Cross-Sections of Specimen 1 from (Mazzoni and Moehle 2001)

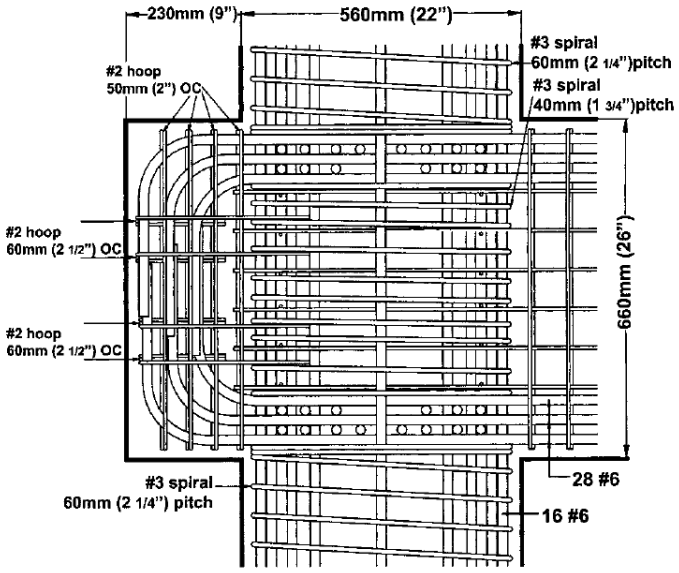

Figure 1-20. Joint Reinforcement for Specimen 2 from (Mazzoni and Moehle 2001)

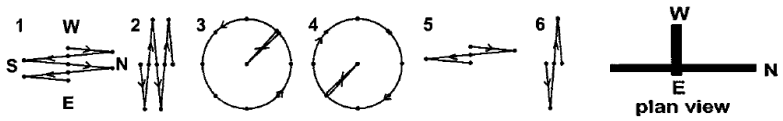

Figure 1-21. Bidirectional Loading Sequence from (Mazzoni and Moehle 2001)

(Mazzoni and Moehle 2001) note that the damage in Specimen 1 progressed from flexural cracking in the columns, crushing of cover concrete, buckling of longitudinal steel, and then fracture of previously buckled reinforcement. They note that although concrete crushing was observed in both the upper and lower columns of Specimen 1, the flexural deformation and damage were greater in the top column. The damage in Specimen 2 was distributed more evenly, however the test was ended after buckling of the bottom column longitudinal reinforcement. Diagonal cracks were observed on the face of the beam stub in Specimen 2, reflecting the increased joint demands for the larger column reinforcement ratio. The hysteretic response for these specimens for the primary orthogonal load cycles appears in Figure 1-22. (Mazzoni and Moehle 2001) note that the lower forces for Specimen #2 in the longitudinal direction were attributed anchorage and yield penetration of the column reinforcement on both sides of the joint.

(Mazzoni and Moehle 2001) developed a graphic which describes the influence of load path on the stress in the flexural reinforcement. Consider Figure 1-23, following loading from the origin to location 1, bar f is placed into tension within the strain hardening region. Following the displacement orbit from location 1 to location 2, the tensile stress in bar f differs from that which would be assumed from a purely monotonic excursion from the origin to location 2. This change in bar stress due to load path is manifested as a reduction in the apparent column flexural strength.

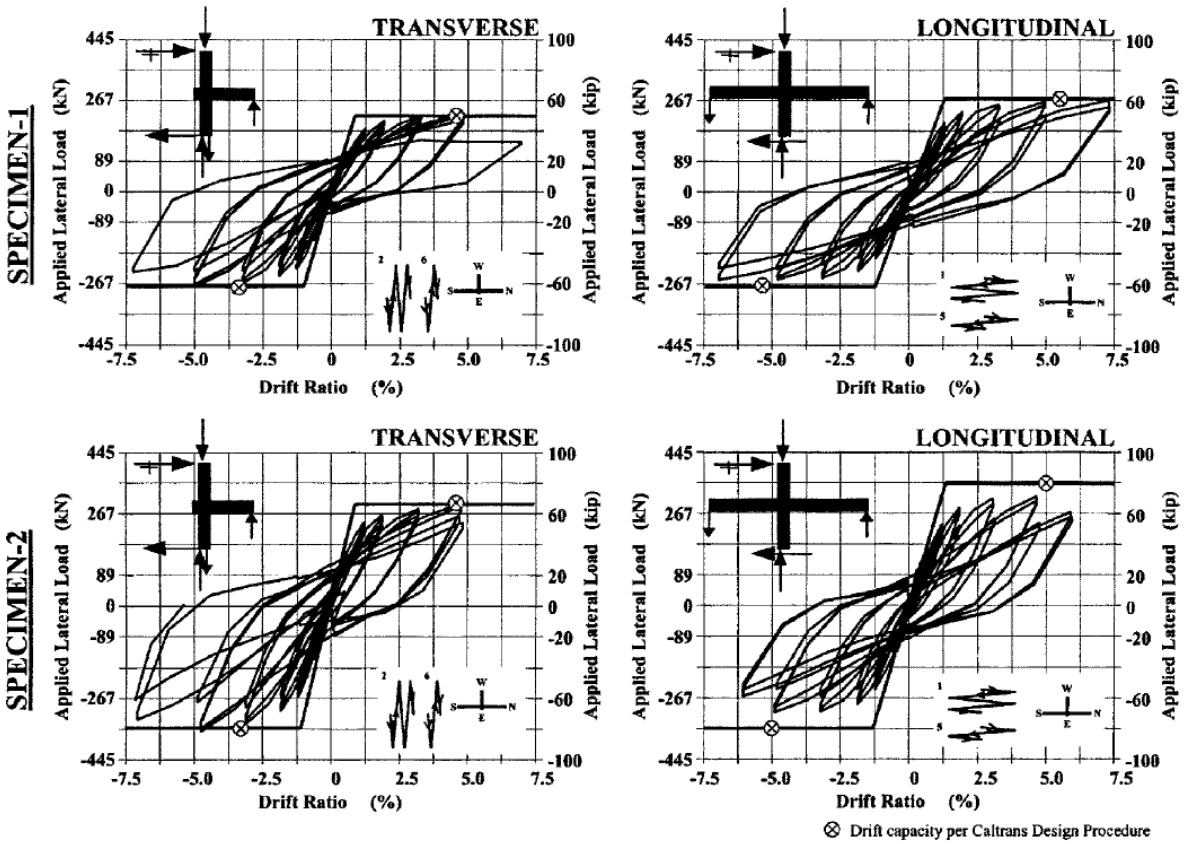

Figure 1-22. Hysteretic Response for Orthogonal Loading Cycles from (Mazzoni and Moehle 2001)

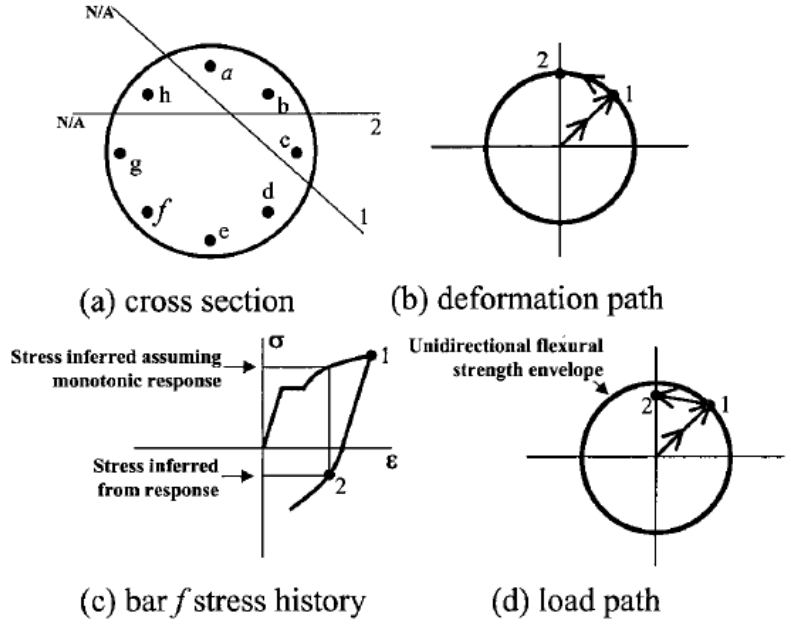

Figure 1-23. Load Path Effects on Flexural Reinforcement from (Mazzoni and Moehle 2001)

(Terzic and Stojadinovic 2015) "Evaluation of Post-Earthquake Axial Load Capacity of Circular Bridge Columns"

(Terzic and Stojadinovic 2015) conducted an experimental study to evaluate the influence of bidirectional loading and induced seismic damage on the remaining axial capacity of four circular bridge columns. The 16" diameter columns contained 1.17% longitudinal steel and had a transverse volumetric ratio of 0.76%. The cantilever columns had an aspect ratio of four and were subjected to a constant axial force equivalent to 10% of the column's nominal axial capacity. The shape of the imposed bidirectional load path was selected based on column response observed in finite element analysis of a prototype bridge subjected to forty three-component ground motion records composed of both near and far-field events. Bridge Type 11 from (Ketchum, Chang and Shantz 2004) was selected. This is a five span single-column bridge designed in accordance to Caltrans SDC. The resulting column displacement response histories were normalized to the yield displacement, which was different in the longitudinal and transverse directions. The circular bidirectional displacement pattern in Figure 1-24 was selected for the experimental tests based on the shape of the normalized ductility response from the prototype bridge analysis. The clockwise and counterclockwise circular displacement orbits are more severe and thus conservative given that the goal of the experiments was to determine the influence of induced damage on the remaining axial capacity. The Base45 specimen was subjected to the bidirectional circular pattern to the following levels of displacement ductility prior to testing of the specimen under axial compression until failure: 0.08, 0.2, 0.4, 1.0, 1.5, 2.0, 3.0, and 4.5. The Base30 and Base15 specimens were subjected to lateral loads until displacement ductility 3.0 and 1.5, respectively. These experiments contained the same number of cycles as Base45, with displacement amplitudes defined as 0.6 and 0.3 multiplied by those used in Base45. The Base0 specimen was subjected to axial compression to failure without prior lateral loading.

The lateral loading in the Base15 specimen resulted in inelastic longitudinal steel and slight cracking. The Base30 specimen had significant yielding of the longitudinal steel into the strain hardening region and crushing of cover concrete in the plastic hinge region. Lateral loading of the Base45 specimen led to extensive yielding of reinforcing steel, additional cover concrete crushing, and a reduction in volume of the concrete core due to crushing. The hysteretic response for Base45 appears in Figure 1-25. Buckling of longitudinal reinforcement was not observed by (Terzic and Stojadinovic 2015).

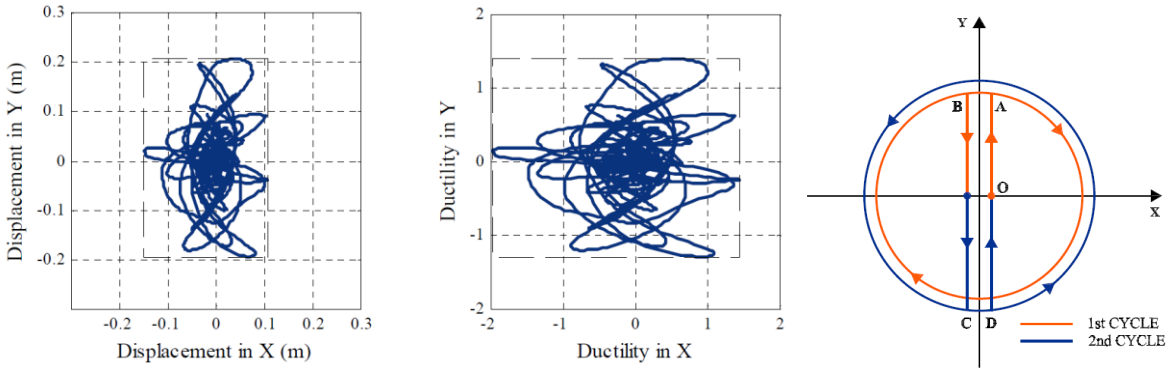

Figure 1-24. (Left) Column Long. And Tran. Response, (Mid) Normalized Response, and (Right) Bidirectional Displacement Pattern from (Terzic and Stojadinovic 2015)

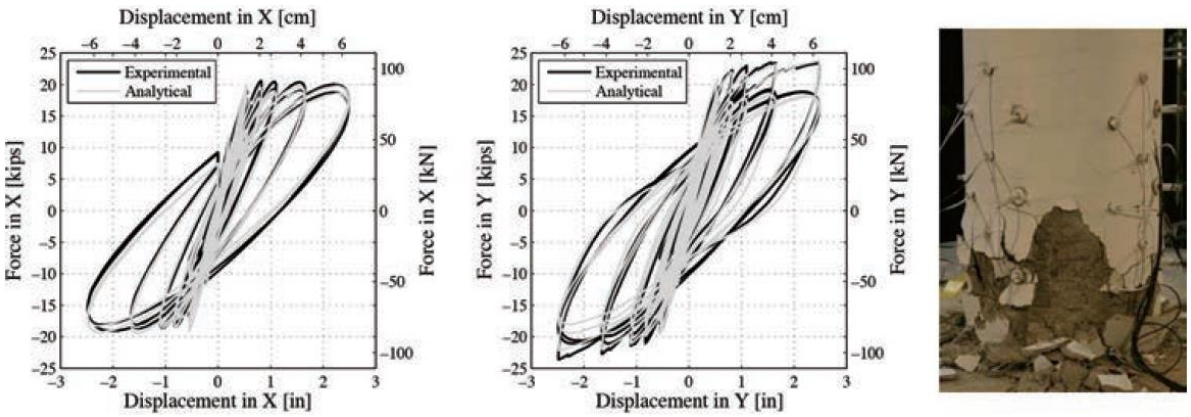

Figure 1-25. Hysteretic Response for Base45 Specimen from (Terzic and Stojadinovic 2015)

These three damaged columns and the undamaged Base0 specimen were then recentered and subjected to axial compression until failure. The Base0 specimen had an axial a tested axial capacity of 1459 $kips$. The ultimate capacity was predicted as 1455 $kips$ by adding the compressive strength of the reinforcing steel at yield and the concrete compressive force evaluated using the effective area of the confined core at a stress of f'_{cc} predicted using the (Mander, Priestley and Park 1988) confined concrete model. The Base15 specimen had an axial capacity 78% of the original, however the specimen was found to have induced moments due to initial unlevel application of the load. The axial capacity of Base30 was 93% of the original and the axial capacity of Base45 was 80% of the original strength. Based on these results (Terzic and Stojadinovic 2015) generated a column axial load capacity degradation envelope as a function of displacement ductility, see Figure 1-26. (Terzic and Stojadinovic 2015) note that no reduction in the axial capacity is expected for displacement ductility demands at or below 1.5.

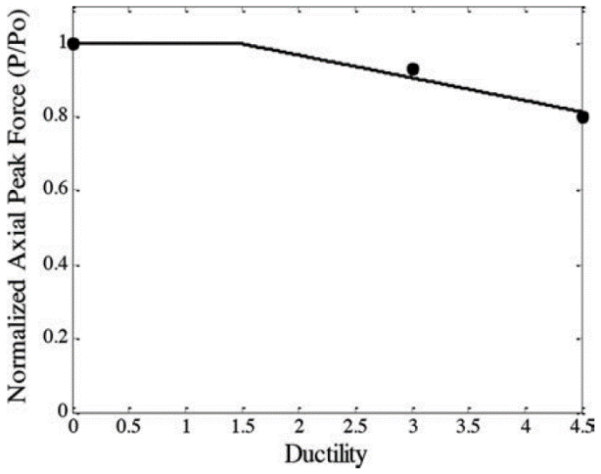

Figure 1-26. Axial Load Capacity Degradation Envelope from (Terzic and Stojadinovic 2015)

Chapter 2 - Research Approach

Project Scope

The objective of the research program is to determine the impact of two-dimensional loading path on the definition of displacement-based performance limit states and the relationship between strain and displacement (i.e., plastic hinges). The specific issues with regard to load path are the impact of multi-directional loading on: (1) Accumulation of strain in reinforcing steel; (2) Unidirectional design (which is the normal practice); and (3) Crack formation and the plastic hinge method for member deformations. The research program contains an analytical and experimental component. The impact of load path is explored analytically using accurate fiber models capable of predicting force deformation response and local strain information. The experimental work involves a series of twelve circular bridge column tests described in the following section.

Test Matrix

The test matrix for the twelve load path columns appears in Table 2-1. Since the uniaxial experiments from (Goodnight, Kowalsky and Nau 2015) serve as a baseline of comparison, an effort has been made to maintain similar cross-section geometry and reinforcement. An overview of geometry and reinforcement for the 24" diameter uniaxial experiments from (Goodnight, Kowalsky and Nau 2015) appears in Table 2-2.

The Type-B and Megathrust, see Figure 2-1 and Figure 2-2, bidirectional loading protocols from (Wong, Paulay and Priestley 1993) and (Bazaez and Dusicka 2016) were adopted in this study. Prior to first yield of the longitudinal reinforcement, the displacement histories are identical, consisting of Type-B cycles (1-8) at ¼ F_y' increments until F_y', where F_y' represents the analytical column shear force at first yield of the longitudinal reinforcement obtained via a moment-curvature analysis. The experimental first yield displacement Δ_y', is obtained as the average of the measured first yield displacements in each of the four directions, points 1-3-5-7 on the Type-B load history. The equivalent yield displacement is then computed as $\left[\Delta_y = \Delta_y'\left(M_n/M_y'\right)\right]$, where M_n is the nominal moment capacity of the section defined by either $(\varepsilon_c = 0.004)$ or $(\varepsilon_s = 0.015)$, whichever occurs first, and M_y' is the moment at first yield of the longitudinal reinforcement. The displacement ductility levels are defined as multiples of the equivalent yield displacement, $\left(\mu_{\Delta n} = n \cdot \Delta_y\right)$. The loading was continued until failure, defined as the first longitudinal bar fracture or spiral rupture. Since the load path columns will be repaired in a separate experimental program, further damage is not warranted, unless necessary to evaluate the effectiveness of the repair technique.

The three variations of the Type-B load path employed in this study are described in Figure 2-1. They evaluate the impact of cycle count and a scenario in which the ductility demands in one direction lag behind those in the primary direction. A bidirectional version of the Megathrust load path recommended in (Bazaez and Dusicka 2016) is compared to Type-B loading in Figure 2-2. Additional details regarding the selection and scaling of the Megathrust load history are presented in Chapter 14 and Chapter 15 for Tests 11 and 12, respectively.

The test matrix appears in Table 2-1. The first six specimens focus on the impact of the three different Type-B load histories. The 24" diameter columns contained 16 #7 Gr60 A706 longitudinal bars $\left(A_{st}/A_g = 2.1\%\right)$ and had a #3 Gr60 A706 spiral at either 2" $\left(4A_{sp}/D's = 1\%\right)$ or 2.75" (0.7%).

The columns had a cantilever length of 109.4375" $(L/D = 4.56)$ and a ½" concrete cover, measured to the outside of the spiral. Note that this defines the placement of the spiral and longitudinal reinforcement, but the cover itself has been blocked out during construction to allow for instrumentation of the longitudinal and transverse steel in the plastic hinge region. While the goal was to have experiments from each spiral spacing subjected to both $\left(P/f_c'A_g = 5\%\ or\ 10\%\right)$, this was not possible given the upper bound load at which the hydraulic jack could be cycled at $(P = 191\ kips)$, resulting in the axial load ratios listed in Table 2-1.

The remaining six tests focuses on the impact of load path, transverse steel detailing, and longitudinal steel content on column performance. Tests 7-9 are nominally identical, with 16 #6 Gr60 A706 longitudinal bars $\left(A_{st}/A_g = 1.6\%\right)$ and a #3 Gr60 A706 spiral at either 1.5", 2", or 2.75" $\left(4A_{sp}/D's = 0.7, 1, or\ 1.3\%\right)$. Test 10 contained 16 #7 Gr60 A706 longitudinal bars $\left(A_{st}/A_g = 2.1\%\right)$ and had a #3 Gr60 A706 spiral at 1.5" $\left(4A_{sp}/D's = 1.3\%\right)$, allowing it to be compared with the first six experiments. Finally, Tests 11 and 12 were nominally identical to Tests 7 and 8, except they utilized a bidirectional adaptation of the Megathrust loading protocol recommended in (Bazaez and Dusicka 2016). The length, geometry, and magnitude of the constant compressive axial load was the same for all twelve columns.

The impact of unidirectional lateral displacement history on column performance is summarized in (Goodnight, Kowalsky and Nau 2013) for the columns in Table 2-2. Bar buckling occurred during cycles at displacement ductility eight in Tests 9 and 16, which were subjected to 3-Cycle-Set load histories. The displacement path for these tests consisted of three cycles (1-4) at each displacement ductility level on the Type-B load path, Figure 2-1, without any displacements imposed in the orthogonal direction. In the earthquake load histories, the acceleration input was scaled until the peak displacement from nonlinear time history analysis (NLTHA) reached displacement ductility nine for Tests 8, 10, 17, and 18, while Tests 11 and 12 were scaled to displacement ductility ten. The four specimens subjected to unidirectional earthquake load histories with a peak amplitude of displacement ductility nine failed to produce bar buckling after reversal from the peak tensile displacement, even though the displacement amplitude exceeded that which induced buckling in the 3-Cycle-Set load history. The two specimens with unidirectional earthquake load histories scaled to displacement ductility ten produced bar buckling, but at two displacement ductility levels beyond that of the nominally identical specimens subjected a 3-Cyle-Set load history. The same four specimens which did not have buckled reinforcement during earthquake load histories were then subjected to 3-Cycle-Set post-earthquake load histories which produced bar buckling during cycles at displacement ductility six, two levels lower than that which produced buckling in nominally identical specimens subjected only to a 3-Cycle-Set load history.

Table 2-1. Test Matrix for the Bidirectional Columns of this Study

Test	Load Path	Bar Size	Ast/Ag	Spacing (in)	ρs	P/f'cAg	f'c (ksi)
1	2-Cyle-Set	16 #7	2.1%	#3@2.75"	0.7%	7.4%	6.21
2	3-Cycle-Set	16 #7	2.1%	#3@2.75"	0.7%	7.5%	6.16
3	Asym 2-Cycle-Set	16 #7	2.1%	#3@2.75"	0.7%	7.4%	6.24
4	2-Cycle-Set	16 #7	2.1%	#3@2"	1%	6%	7.68
5	3-Cycle-Set	16 #7	2.1%	#3@2"	1%	6%	7.60
6	Asym 2-Cycle-Set	16 #7	2.1%	#3@2"	1%	5.9%	7.81
7	2-Cycle-Set	16 #6	1.6%	#3@1.5"	1.3%	7.9%	5.79
8	2-Cycle-Set	16 #6	1.6%	#3@2"	1%	7.4%	6.24
9	2-Cycle-Set	16 #6	1.6%	#3@2.75"	0.7%	7.3%	6.29
10	2-Cycle-Set	16 #7	2.1%	#3@1.5"	1.3%	7.5%	6.13
11	Megathrust	16 #6	1.6%	#3@2"	1%	7.5%	6.11
12	Megathrust	16 #6	1.6%	#3@2.75"	0.7%	7.4%	6.23

Table 2-2. Uniaxial Experiments from (Goodnight, Kowalsky and Nau 2015) which Serve as Comparison

Test	Load Path	Long. Steel	Trans. Steel	Axial
9	3-Cycle-Set	16 #6 (1.6%)	#3@2" (1%)	5.4%
8	Chile (2010)	16 #6 (1.6%)	#3@2" (1%)	5.4%
10	Chichi (1999)	16 #6 (1.6%)	#3@2" (1%)	7.1%
11	Kobe (1995)	16 #6 (1.6%)	#3@2" (1%)	6.2%
12	Japan (2011)	16 #6 (1.6%)	#3@2" (1%)	6.2%
13	3-Cycle-Set	16 #6 (1.6%)	#4@2.75" (1.3%)	6.2%
14	3-Cycle-Set	16 #6 (1.6%)	#3@4" (0.5%)	5.7%
15	3-Cycle-Set	16 #6 (1.6%)	#3@2.75" (0.7%)	5.2%
16	3-Cycle-Set	16 #6 (1.6%)	#3@1.5" (1.3%)	5.6%
17	Chile (1985)	16 #6 (1.6%)	#3@1.5" (1.3%)	5%
18	Darfield (2010)	16 #6 (1.6%)	#3@1.5" (1.3%)	4.8%
25	3-Cycle-Set	16 #7 (2.1%)	#3@2" (1%)	5%
26	3-Cycle-Set	16 #7 (2.1%)	#3@2" (1%)	10%
27	3-Cycle-Set	16 #6 (1.6%)	#3@2" (1%)	10%

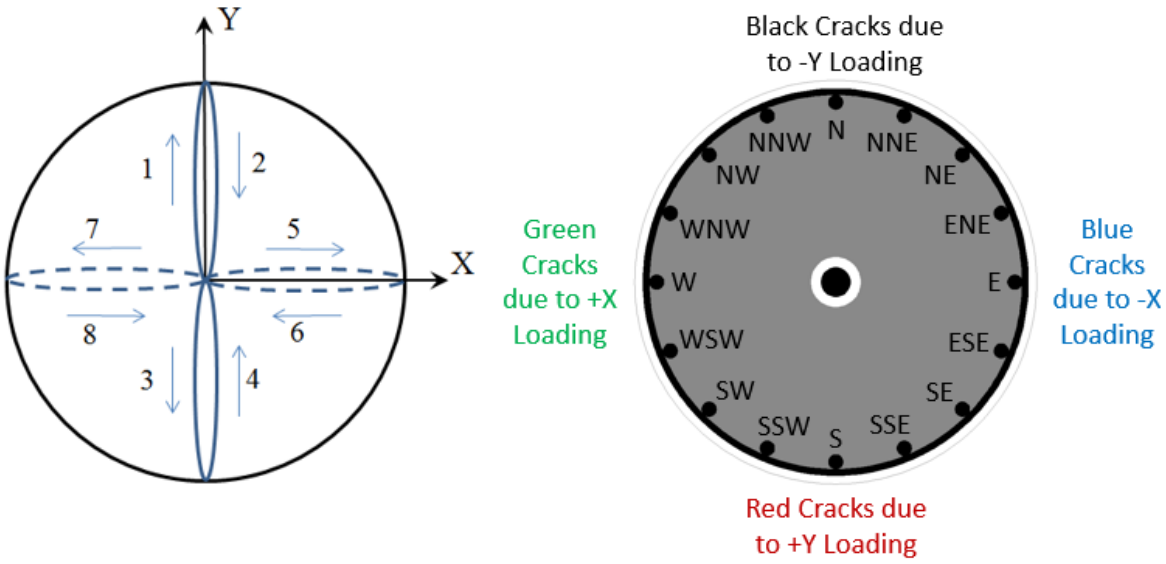

Type-B Symmetric Two-Cycle-Set

- Begins with elastic cycles (1-8) in ¼ yield increments until F_y'
- The equivalent yield displacement is then computed as $\Delta_y = \Delta_y'(M_n/M_y')$
- Two inelastic cycles (1-8) for each displacement ductility level $\mu_{\Delta n} = n \cdot \Delta_y$

Type-B Symmetric Three-Cycle-Set

- Begins with elastic cycles (1-8) in ¼ yield increments until F_y'
- The equivalent yield displacement is then computed as $\Delta_y = \Delta_y'(M_n/M_y')$
- Three inelastic cycles (1-8) for each displacement ductility level $\mu_{\Delta n} = n \cdot \Delta_y$

Type-B Asymmetric Two-Cycle-Set

- Inelastic cycles (1-4) in the Y-direction followed by inelastic cycles (5-8) in the X-direction for each of the following displacement ductility levels $\mu_{\Delta n} = n \cdot \Delta_y$
- $\mu_{\Delta 1}^{\pm Y}$ & $\mu_{\Delta 1}^{\pm X}$, $\mu_{\Delta 1.5}^{\pm Y}$ & $\mu_{\Delta 1}^{\pm X}$, $\mu_{\Delta 2}^{\pm Y}$ & $\mu_{\Delta 1}^{\pm X}$, $\mu_{\Delta 3}^{\pm Y}$ & $\mu_{\Delta 1.5}^{\pm X}$, $\mu_{\Delta 4}^{\pm Y}$ & $\mu_{\Delta 2}^{\pm X}$, etc. where $\mu_{\Delta}^{\pm X}$ lags by two displacement ductility levels until bar buckling is observed, at which time cycling shifts to direct x-direction loading until bar buckling in that direction, followed by symmetric y and x-direction loading until failure

Figure 2-1. Definition of the Type-B Load Histories

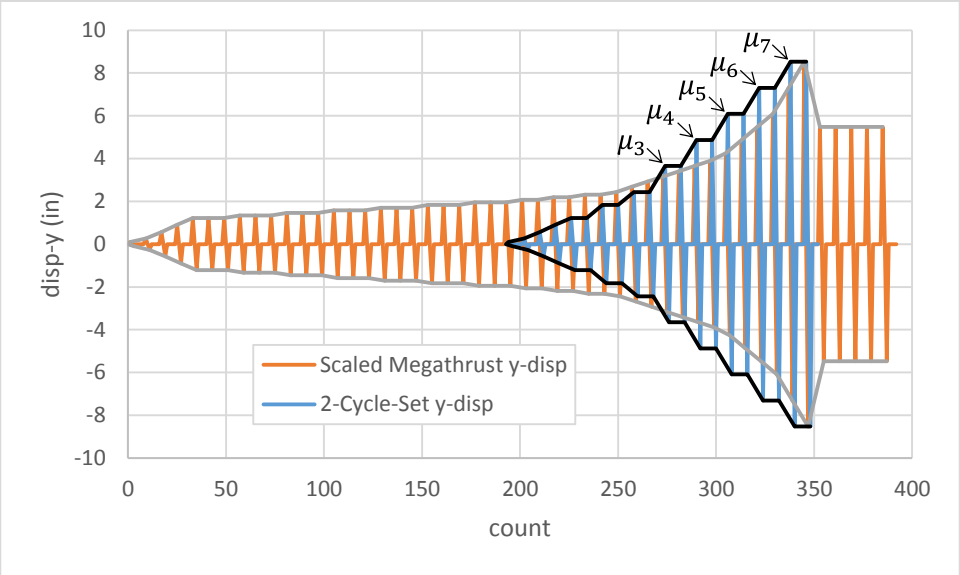

Figure 2-2. (Bazaez and Dusicka 2016) Megathrust Load History Compared to the Type-B Sym. 2-Cycle-Set

Test Setup

Top, front, and side views of the experimental setup appear in Figure 2-3, Figure 2-4, and Figure 2-5, respectively. General dimensions for the specimen and transfer footing appear in Figure 2-6. The lateral load was applied using two hydraulic actuators, which formed a 45-45-90 triangle in the X-Y plane with concentric lines of action passing through the center of the cross section. The lateral actuators had a 200 kip force capacity and a 40" displacement range. Integrated load cells monitored the actuator forces, while the actuator stroke is measured with an integrated temposonic. Control of the actuator displacements and post processing of their loads was defined using deformed geometry between actuator pivot points. Under this geometry, each actuator load was resolved into the X and Y components, providing the global shear forces in the column. The constant compressive axial load of 191 $kips$ was maintained using a single 200 kip hollow core jack placed above the specimen which post tensioned a 1-3/4" (150 ksi) Dywidag bar located within a 3" PVC duct at the center of the column cross-section. In a closed hydraulic system, a second jack was placed in a uniaxial testing machine under force control to regulate the pressure and thus the load of the jack placed above the specimen to maintain a constant axial force.

The specimen consisted of a footing, column, and loading cap. Due to limitations in the capacity and spacing of holes in the lab strong floor, the specimen sits on top of a transfer footing with additional pocketed connections for post tensioning bars. This allowed for a symmetric hole pattern in the specimen footing, which reduced its weight and allowed for symmetric reinforcement in the two orthogonal directions. At the interface of the lab floor and transfer footing, the overturning moment is resisted by four 1-3/8" Dywidag bars running through the main and transfer footings and six bars which passed through only the transfer footing. Eight 1-3/8" Dywidag bars resisted the overturning moment at the interface between the main and transfer footings. Four of these bars pass through to the strong floor, while four are anchored into the transfer footing using pocketed connections. The 1-3/4" axial Dywidag bar which passed through the column was also anchored into

the transfer footing with a specially detailing pocket to allow for a single larger point load. The necessary post tensioning for these bars was computed and applied prior to the experiments to minimize slip and to prevent overturning of the specimen and transfer footing.

The two connections for the lateral actuators were staggered by 2-7/8”, as shown in Figure 2-4, which allowed the threaded rods used for the connection to pass through 2” PVC ducts cast into the loading cap of the specimen. The column length from the footing-column interface to the center of the applied lateral load for Actuator 1 is (110-7/8”) and (108”) for Actuator 2. This stagger in the actuator connections led to a change in the base section moment of 2.66% between the two actuators. The connection between the actuator and strong wall consisted of three separate steel fixtures. Two 45° loading fixtures were fabricated to sit on top of the existing wall plates which the lab had used for previous column tests. The connection between the actuators and the 45° wall plates was also staggered by 2-7/8” so that the actuators remained horizontal. An existing side-coped w-shape was used as a link beam between the two loading fixtures to resist the horizontal load induced by the two lateral actuators. This link beam was part of an existing testing frame used in prior tests at the lab. The geometry of the actuator connection at the wall was selected to maintain the 45-45-90 degree angle between the two actuators, and to maximize the available displacement range of the actuators.

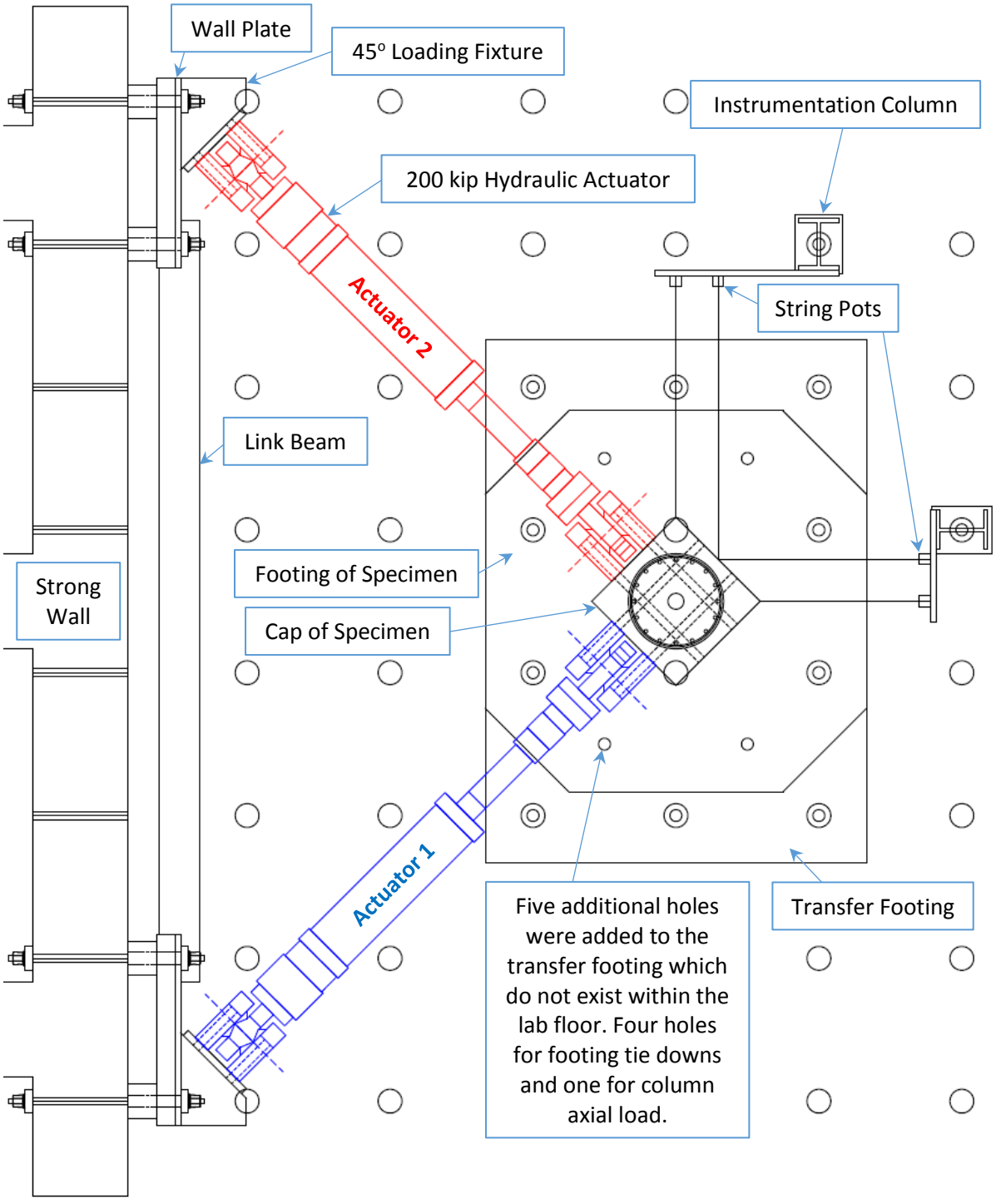

Figure 2-3. Top View of Test Setup

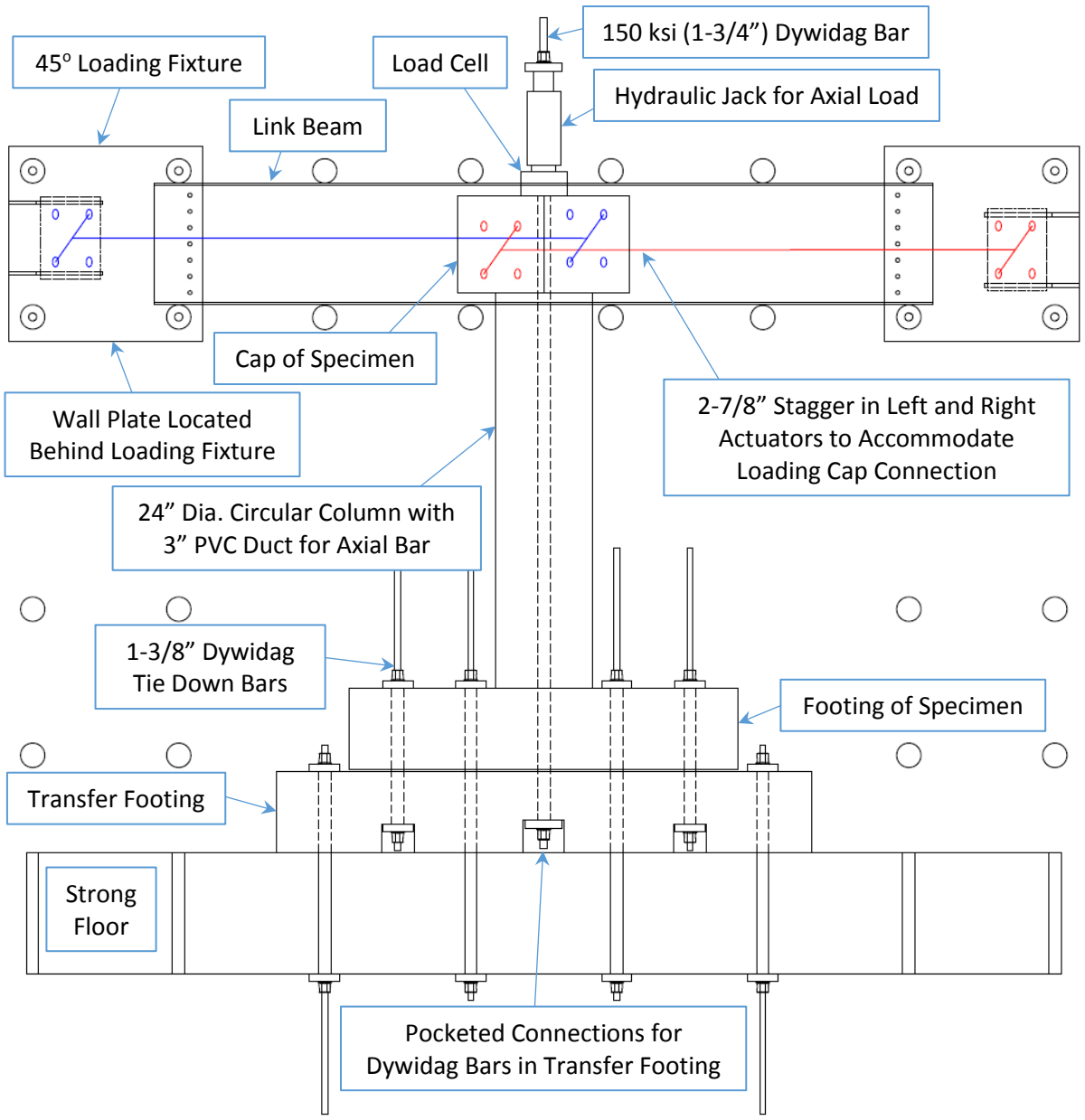

Figure 2-4. Front View of Test Specimen (Actuators Omitted for Clarity)

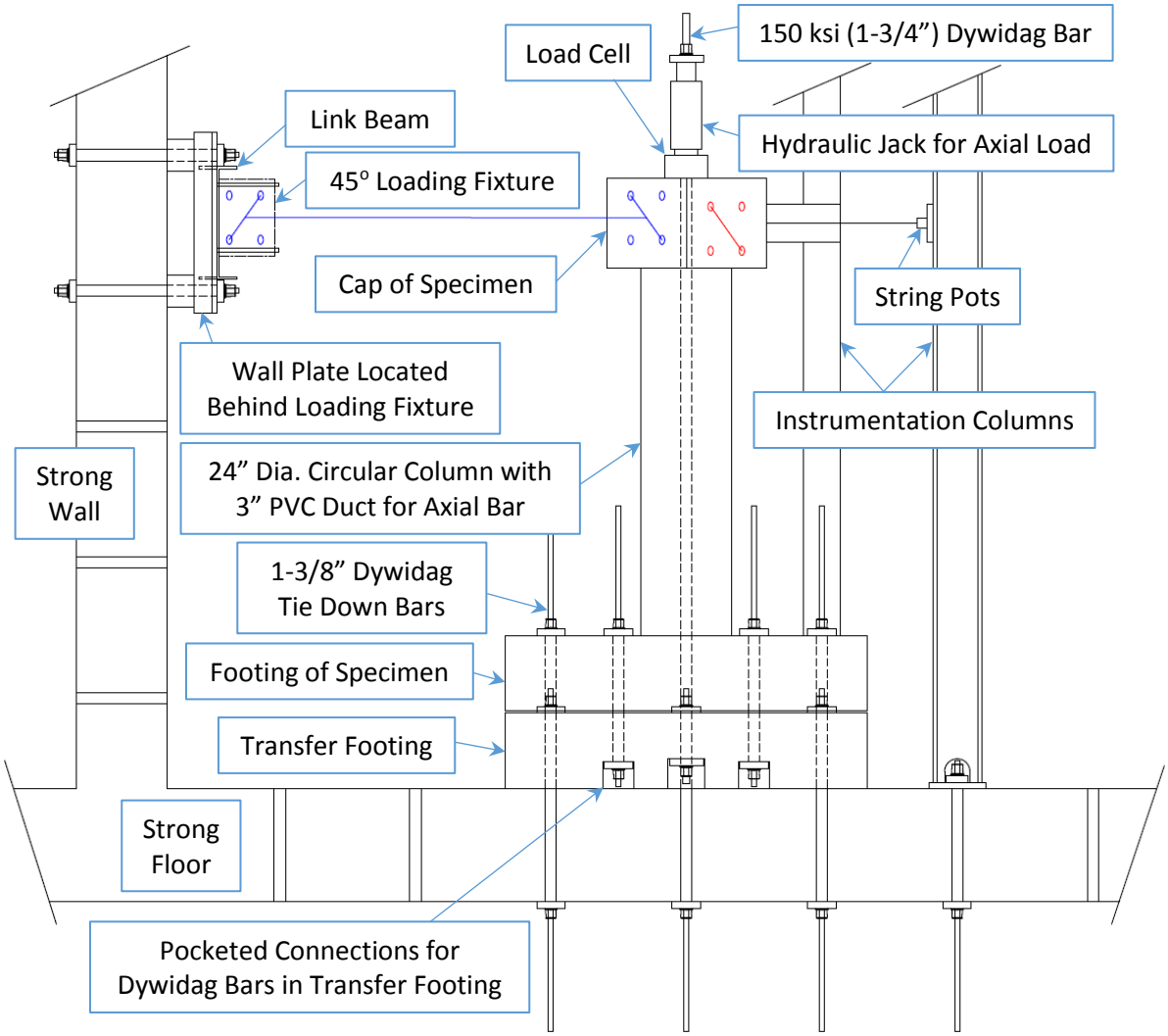

Figure 2-5. Side View of Test Specimen (Actuators Omitted for Clarity)

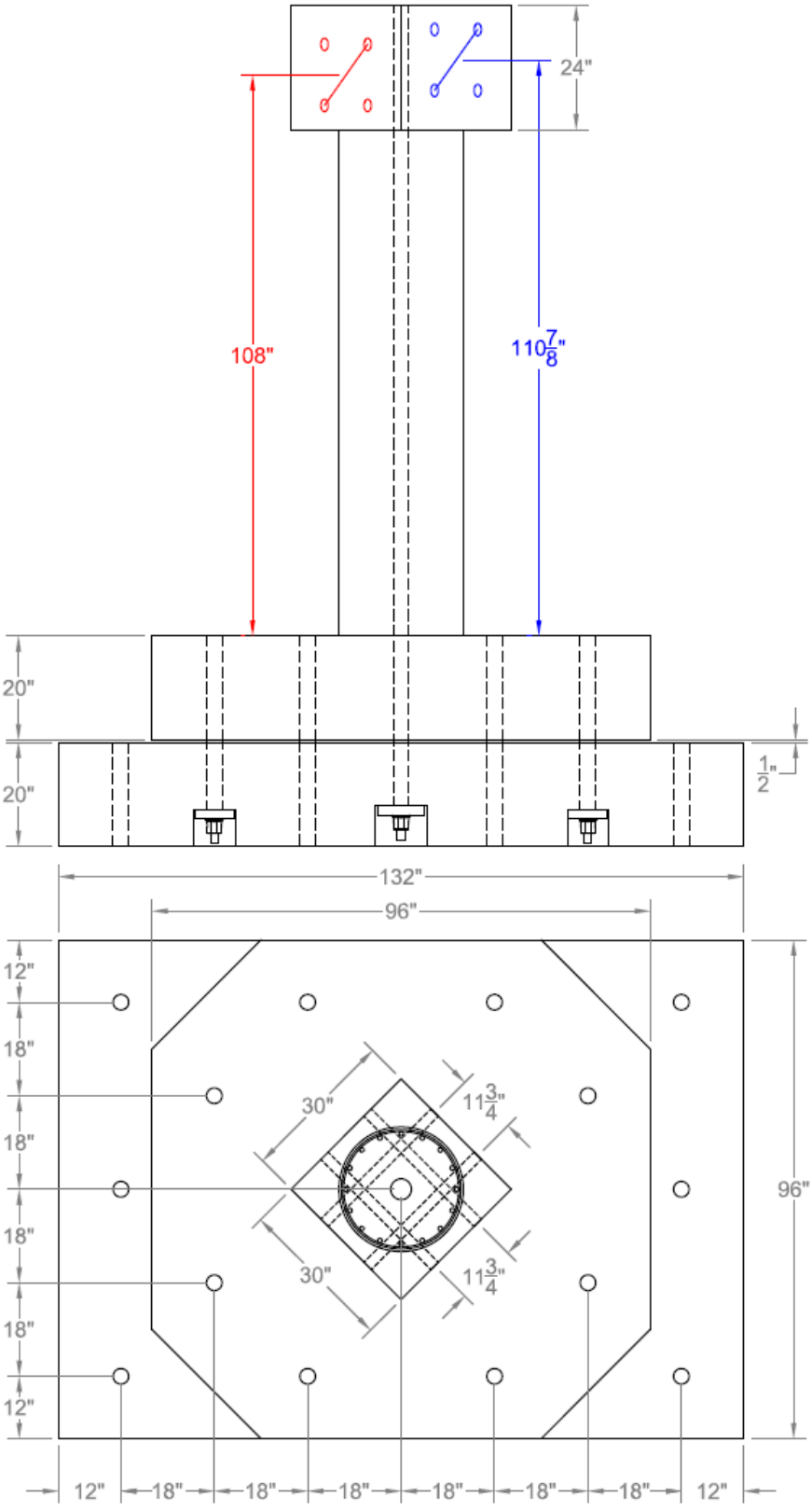

Figure 2-6. General Dimensions for the Specimen and Transfer Footing

Instrumentation

The experimental program utilized an innovative technique of applying a commercially available instrumentation system to measure large strains at the level of the reinforcement with multiple Optotrak Certus HD 3D position sensors produced by Northern Digital Inc. The Optotrak position monitoring system can read the location of target markers placed on the specimen in three dimensional space during a test, Figure 2-8. By calculating the change in three dimensional distance between adjacent target markers, strains can be determined with respect to their original unloaded gauge lengths. The 3D accuracy of the Optotrak Certus HD system reported by Northern Digital Inc. is 0.1 mm with a resolution of 0.01 mm.

The same technique used to monitor longitudinal and transverse steel strains in (Goodnight, Kowalsky and Nau 2015) was applied in this study. The method used three Optotrak position monitors and a complete cover concrete blockout to the depth of the outside surface of the longitudinal reinforcement, Figure 2-8. The spiral was in complete contact with the core, and was tied at every longitudinal bar intersection. Spiral strains were computed based on the change in arc-length between two adjacent target markers. Longitudinal bars were instrumented at different depths within the section to analyze curvatures. Strain gauges were applied to layers of transverse steel overlaying the extreme fiber longitudinal reinforcement in the four primary directions to observe the interaction between compressive demand and the buckling restraint provided by inelastic transverse steel.

An illustration of the accuracy of the Optotrak system compared to traditional instrumentation techniques from (Goodnight, Kowalsky and Nau 2015) appears in Figure 2-7. The tensile test on a reinforcing bar was conducted with a 2" Optotrak gauge length, a 2" extensometer gauge length, and a centrally placed strain gauge. Closer inspection demonstrates that the Optotrak strains oscillate around the measurements predicted by the conventional instrumentation, but the general trend is captured throughout the entire tensile test. Electrical resistance strain gauges fail to remain attached at large inelastic strain levels, which are of interest to this study.

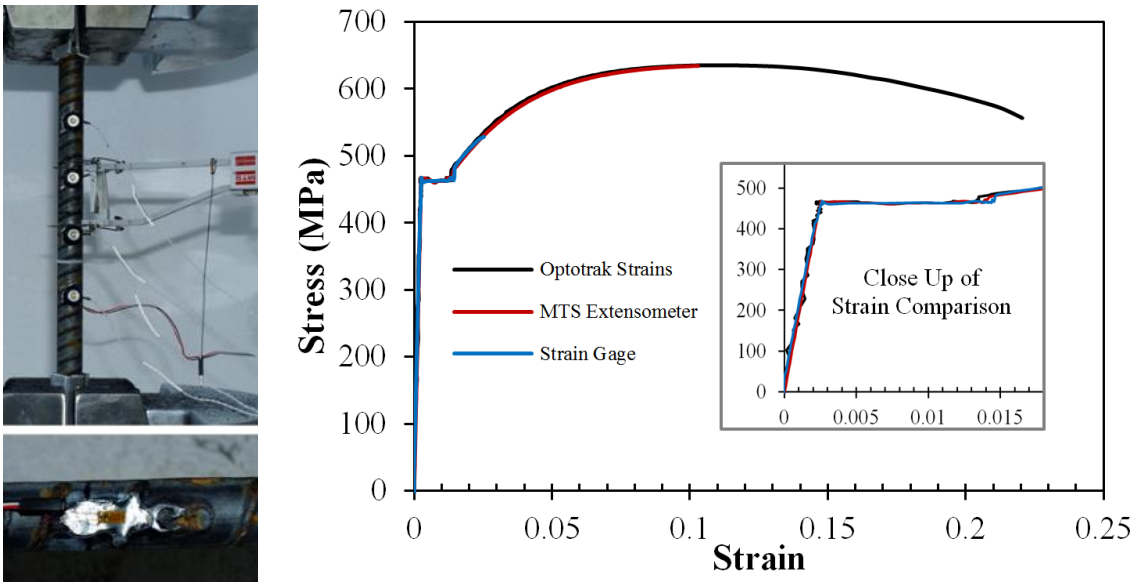

Figure 2-7. Comparison of Measurement Techniques for Tensile Rebar Test from (Goodnight, Kowalsky and Nau 2015)

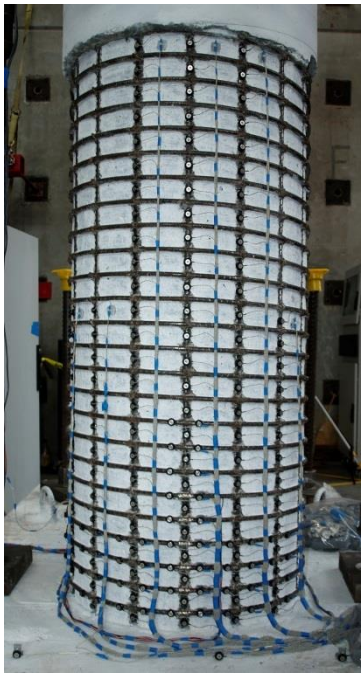

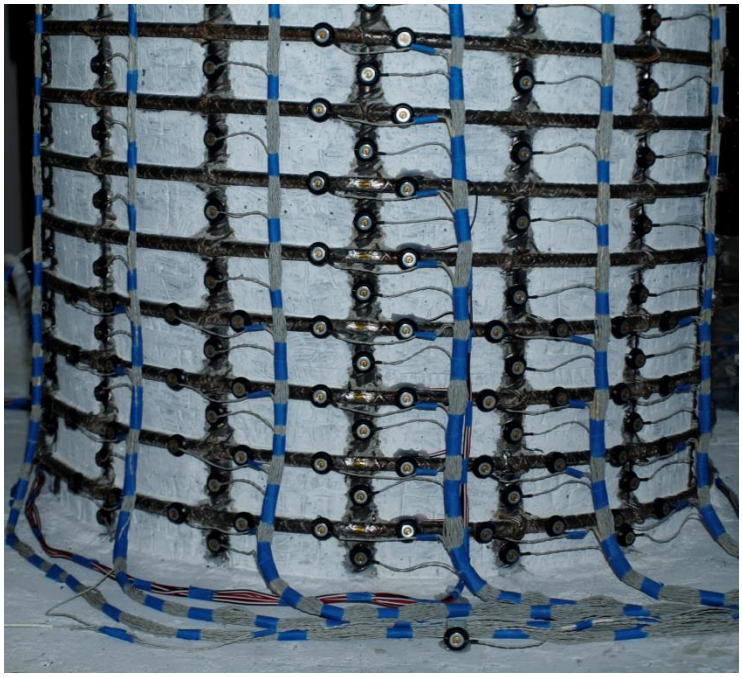

Name	x [mm]	y [mm]	z [mm]
Marker_56	22.605	-768.878	-2823.420
Marker_57	22.023	-723.502	-2823.224
Marker_58	23.611	-675.963	-2823.620
Marker_59	22.914	-627.713	-2823.769
Marker_60	22.309	-578.423	-2823.920
Marker_61	22.457	-530.064	-2824.156
Marker_62	22.898	-481.580	-2824.496
Marker_63	23.570	-429.917	-2824.482
Marker_64	24.335	-381.253	-2824.373
Marker_65	24.346	-332.084	-2824.542
Marker_66	22.813	-283.271	-2824.657
Marker_67	23.262	-234.317	-2824.772
Marker_68	23.264	-183.634	-2825.202
Marker_69	23.365	-134.318	-2825.322
Marker_70	22.845	-86.205	-2825.807
Marker_71	24.211	-35.837	-2825.957
Marker_72	23.834	12.833	-2825.893
Marker_73	24.170	59.599	-2826.011
Marker_74	24.888	108.682	-2825.957
Marker_75	24.585	158.003	-2825.720
Marker_76	24.183	208.389	-2825.508
Marker_77	23.858	256.409	-2825.454
Marker_78	25.731	306.625	-2825.952
Marker_79	26.656	354.616	-2826.074

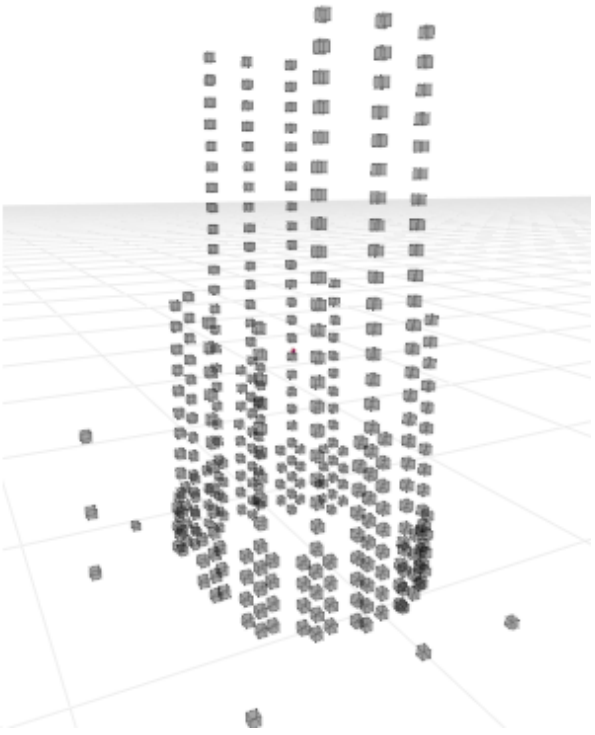

Figure 2-8. Optotrak Instrumentation for Test 27 from (Goodnight, Kowalsky and Nau 2015)

Specimen Design

The specimens were designed in accordance to capacity design recommendations in (Priestley, Seible and Calvi 1996) and (Priestley, Calvi and Kowalsky 2007). The geometry of the twelve specimens was the same, since the only variables were the bidirectional lateral displacement history, transverse steel detailing, and longitudinal steel content. Of the twelve specimens in the test matrix, Table 2-1, it is clear that the first six specimens will produce the largest demands on the footing. These columns had 24" diameter cross sections with 16 #7 Gr60 A706 longitudinal bars $\left(A_{st}/A_g = 2.1\%\right)$ and a #3 Gr60 A706 spiral at 2.75" or 2" $\left(4A_{sp}/D's = 0.7\ or\ 1\%\right)$. They had a cantilever length of 109.4375" $(L/D = 4.56)$ and a concrete cover of ½", measured to the outside of the spiral. Note that this defines the placement of the spiral and longitudinal reinforcement, but the cover itself was blocked out during construction to allow for instrumentation of the longitudinal and transverse steel in the plastic hinge region. A compressive axial load of $(P = 191\ kips)$ was applied to all of the specimens.

Three separate moment-curvature analyses were ran for each column with the following material properties: expected, overstrength, and shear overstrength. These properties are summarized in Table 2-3 and Table 2-4. Expected material properties are used to find the best estimate to the as designed specimen performance. Overstrength material properties are used when designing capacity protected members, such as the footing, for the maximum flexural overstrength of the column plastic hinge. Shear overstrength properties are used for design of the column shear reinforcement, since the concrete compressive strength and transverse steel yield stress are important parameters in the concrete component of shear resistance and the steel truss mechanism. The force-displacement response for the controlling specimen with expected material properties appears in Figure 2-9, while the tensile and compressive strain-displacement response is shown in Figure 2-10 and Figure 2-11. Each figure contains a prediction using the (Priestley, Calvi and Kowalsky 2007) plastic hinge method and the (Goodnight, Kowalsky and Nau 2015a) Modified L_{pr} Hinge Method. Parameters from the Modified L_{pr} Hinge Method used to compute the displacements appear in Table 2-5 with references to their expressions in Chapter 1. The predicted bar buckling strain and its associated displacement using Eqn 1-28 and the Modified L_{pr} Hinge Method are also shown in Table 2-5.

The predicted force-displacement response for the controlling specimen with the highest steel content $\left(A_{st}/A_g = 2.1\%\right)$ and Overstrength material properties appears in Figure 2-12. From this analysis, the maximum flexural overstrength of the column plastic hinge was obtained as $Mo_{col} = 873.46\ kip \cdot ft$. This value was used for the design of capacity projected actions in the footing. The column with $\left(A_{st}/A_g = 2.1\%\right)$ and a #3 Gr60 A706 spiral at 2.75" $\left(4A_{sp}/D's = 0.7\%\right)$ controlled for shear. A comparison of the force-displacement response and Design/Assessment prediction for the shear capacity envelope using the Modified UCSD Shear Model from (Kowalsky and Priestley 2000) is shown in Figure 2-13. This model includes the reduction in strength for the concrete component of shear resistance due to bidirectional loading. The design shear capacity envelope is larger than the force-displacement curve for the entire range of response, indicating that there should not be a shear failure.

Table 2-3. Longitudinal Steel Design Material Properties

Longitudinal Steel $f_y = 60\ ksi$	Yield Stress (ksi)	Ultimate Stress (ksi)	$E_s\ (ksi)$	ε_{sh}	ε_{su}
Expected	$f_{ye} = 1.1f_y = 66$	$f_{ue} = 1.5f_{ye} = 99$	29000	0.013	0.12
Overstrength	$f_{yo} = 1.3f_y = 78$	$f_{uo} = 1.5f_{yo} = 117$	29000	0.013	0.12

Table 2-4. Column Concrete and Transverse Steel Design Material Properties.

Column Concrete	
Expected	$f'_{ce} = 5\ ksi$
Overstrength	$f'_{co} = 1.7 \cdot 5\ ksi = 8.5\ ksi$
Shear Overstrength	$f'_{ce} = 5\ ksi$

Transverse Steel	
Expected	$f_{yhe} = 60\ ksi$
Overstrength	$f_{yho} = 1.3f_{yh} = 78\ ksi$
Shear Overstrength	$f_{yhe} = 60\ ksi$

Table 2-5. Specimens 1-2 Expected Property Modified Lpr Parameters

$L_{sp}^{\text{Eqn 1-9}}$	$k^{\text{Eqn 1-10}}$	$Lpr_t^{\text{Eqn 1-11}}$	$Lpr_c^{\text{Eqn 1-12}}$	$\varepsilon_{bb}^{\text{Eqn 1-28}}$	$\Delta_{bb}^{\text{Eqn 1-28}}$
6.34”	0.08	34.53”	17.28”	0.0354	5.90”

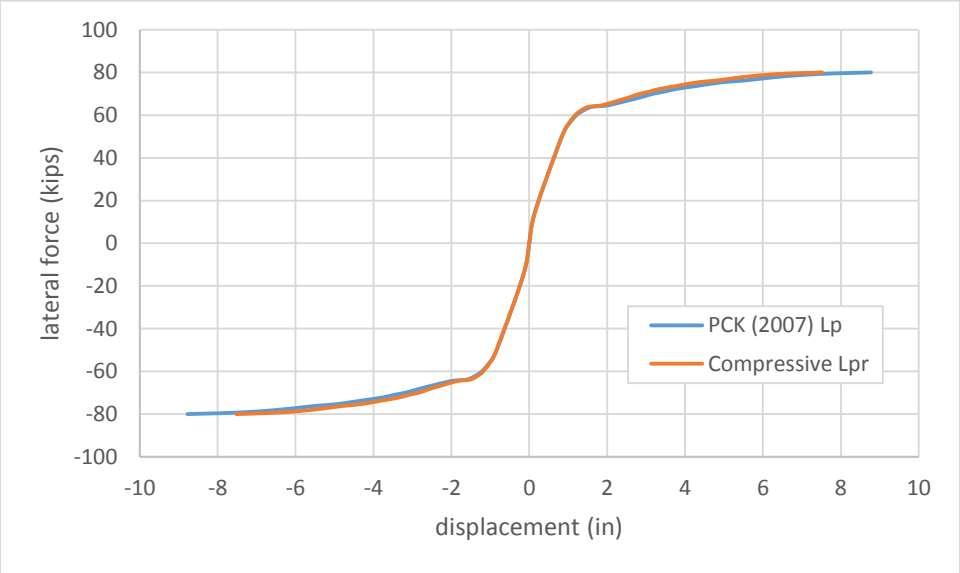

Figure 2-9. Force-Displacement with Expected Material Properties

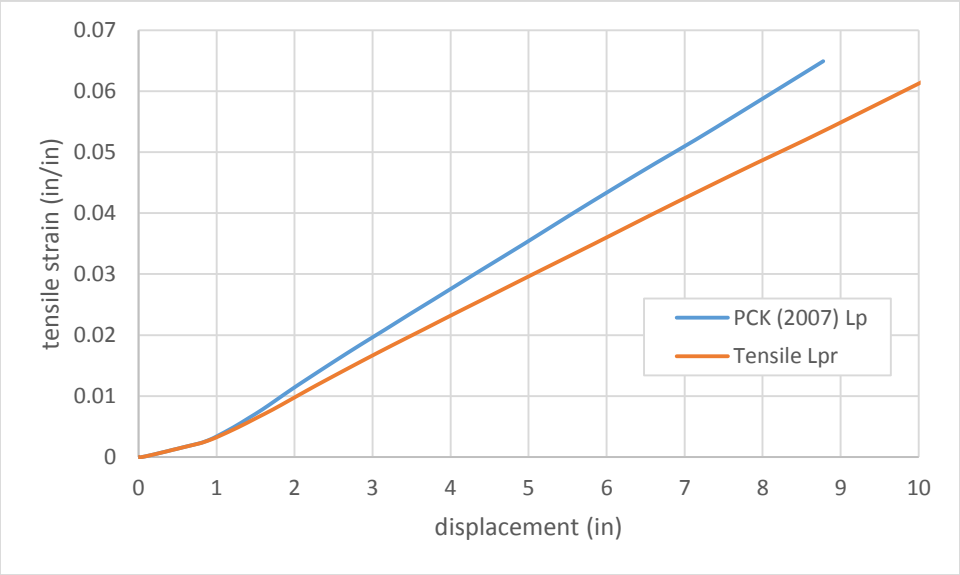

Figure 2-10. Tensile Strain-Displacement with Expected Material Properties

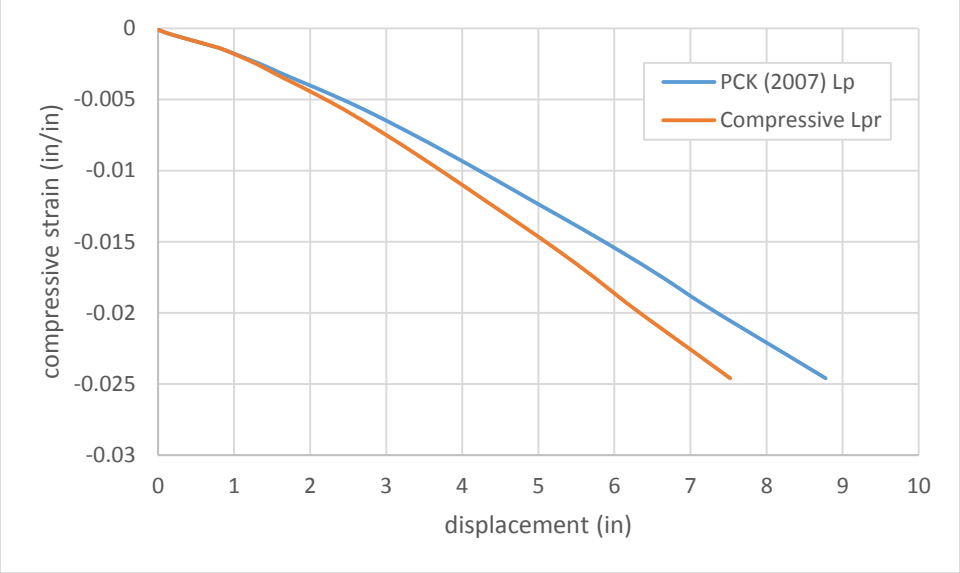

Figure 2-11. Compressive Strain-Displacement with Expected Material Properties

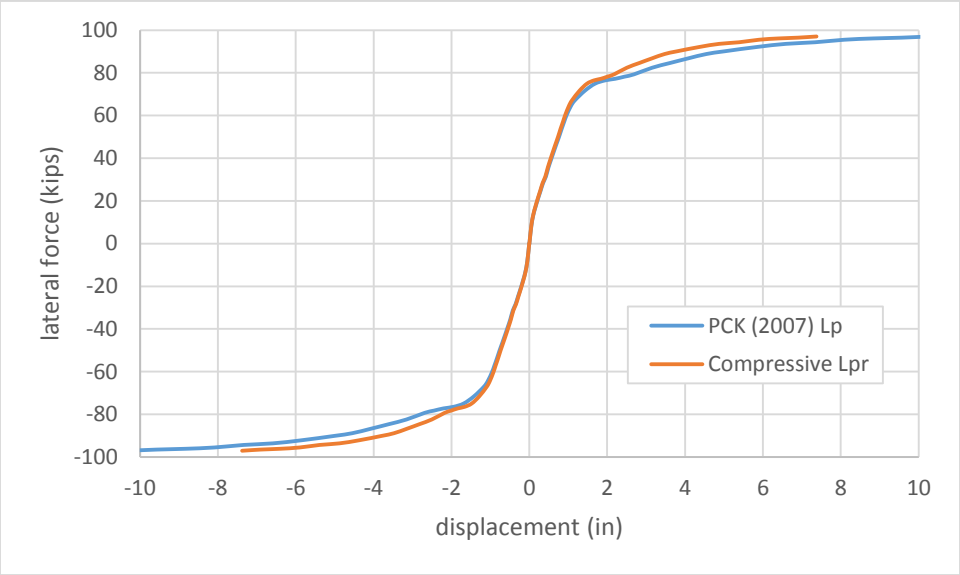

Figure 2-12. Force-Displacement with Overstrength Material Properties

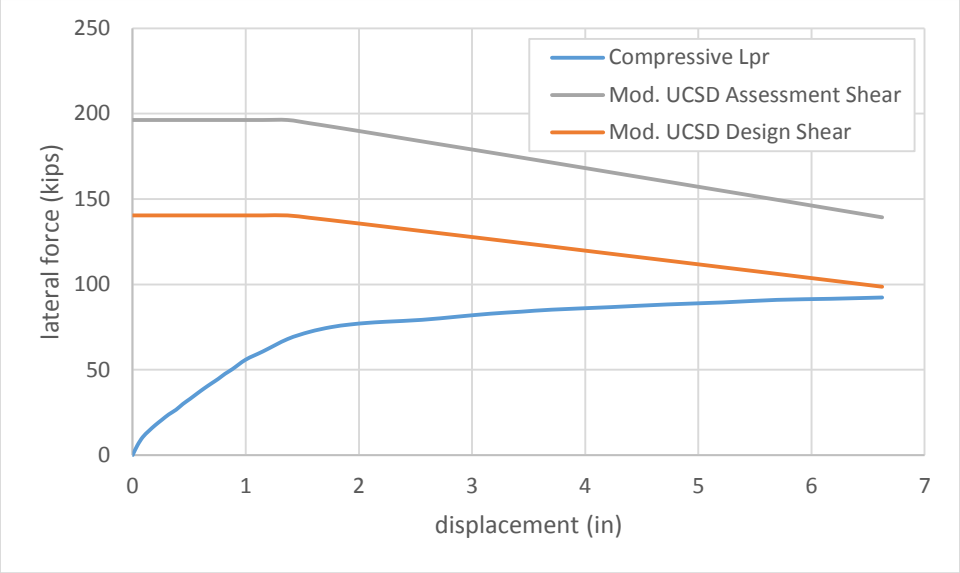

Figure 2-13. Force-Displacement and (Kowalsky and Priestley 2000) Modified UCSD Shear Model

Capacity Design for the Footing Considering the Hinge Relocation Repair Technique

From the moment-curvature analysis of the controlling specimen with the highest steel content $\left(A_{st}/A_g = 2.1\%\right)$ and Overstrength material properties, the maximum flexural overstrength of the column plastic hinge was obtained as $Mo_{col} = 873.46\ kip \cdot ft$. After testing, the specimens will be saved for repair using the plastic hinge relocation technique. In (Rutledge, et al. 2013), the authors' repaired columns from (Goodnight, Kowalsky and Nau 2015) using CFRP wraps and anchors to strengthen the damaged column plastic hinge and relocate the new plastic hinge one diameter above the base of the column in an undamaged region. Following this methodology, the moment at the base of the column in the elastic repaired section at overstrength of the relocated column plastic hinge becomes Mo_{base}^{repair} in Eqn 2-1. In the expression, $(L_c = 9')$ is the cantilever height of the column measured from the footing-column interface, $\left(h_f = 20"\right)$ is the height of the footing, and $(D = 24")$ is the column diameter. Note that the average cantilever length was 109.4375", however the center of the lowest actuator was used for capacity design, since it produces a larger column shear force.

The corresponding moment at the centerline of the footing becomes Mo_{CL}^{repair} in Eqn 2-2. The centerline footing moment, Mo_{CL}^{repair}, was used to compute the required specimen tie down forces to prevent overturning under demands in the two main orthogonal directions, X and Y, and a direction of loading 45° to the axis. The resulting equilibrium expressions appear in Eqn 2-3 and Eqn 2-4. At the onset of design, it was not clear what to lowest value of column axial load would be, therefore the required tie down forces were determined with $(P_{axial} = 0\ kips)$ as $\left(P_{0,90^o} = 51.12\ kips\right)$ and $(P_{45^o} = 48.20\ kips)$. In the experiments, each of the (1-3/8") Dywidag bars will be stressed to 100 $kips$. The footing centerline and face moments were obtained as Eqn 2-5 and Eqn 2-6, which assumes a linear decrease in footing moment from the column centerline to the edge of the footing. This was chosen as a conservative approach.

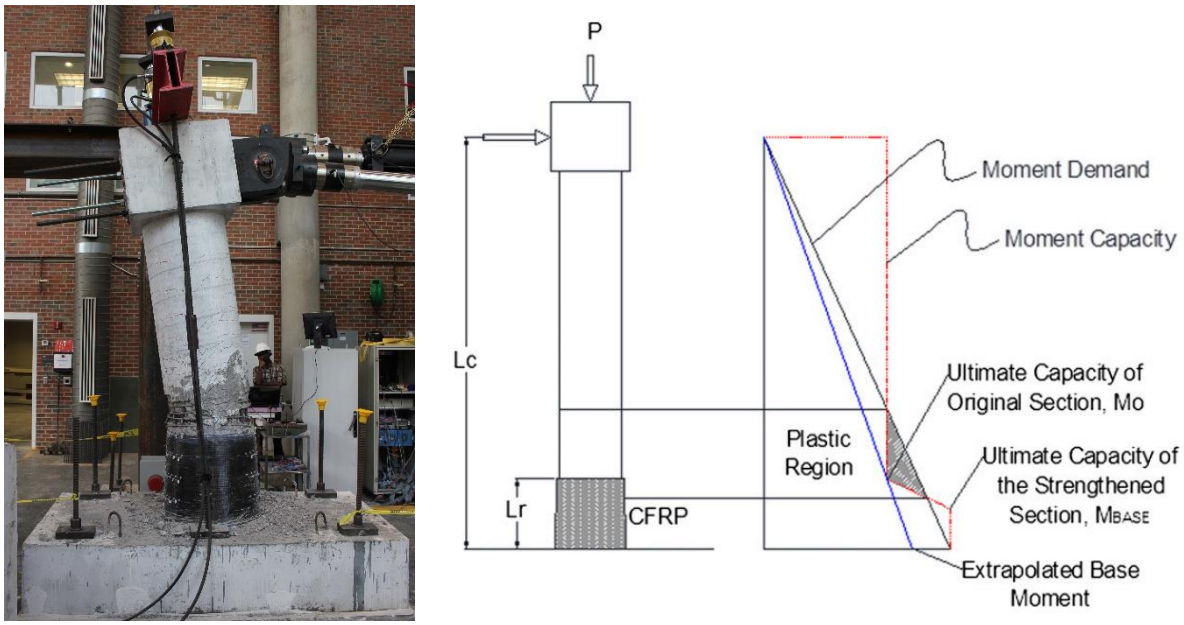

Figure 2-14. Plastic Hinge Relocation Technique from (Rutledge, et al. 2013)

$$Mo_{base}^{repair} = Mo_{col}\left(\frac{L_c}{L_c - D}\right) = 1123.02\ kip \cdot ft$$ *Base Moment of the Repaired Section at Flexural Overstrength* Eqn 2-1

$$Mo_{CL}^{repair} = Mo_{col}\left(\frac{L_c + 0.5h_f}{L_c - D}\right) = 1227.00\ kip \cdot ft$$ *Repaired Footing CL Moment at Flexural Overstrength* Eqn 2-2

$$Mo_{CL}^{repair} = 2P(18") + 2P(54") + 2P(72") + P_{axial}(36")$$ *Equilibrium of Specimen Tie Down Forces about 0-90º* Eqn 2-3

$$Mo_{CL}^{repair} = 2P(25.44") + 2P(50.94") + 2P(76.44") + P_{axial}(38.19")$$ *Equilibrium of Specimen Tie Down Forces about 45º* Eqn 2-4

$$Mf_{CL}^{repair} = 0.5Mo_{CL}^{repair} = 613.50\ kip \cdot ft$$ *Footing Centerline Moment* Eqn 2-5

$$Mf_{face}^{repair} = Mf_{CL}^{repair}\left(\frac{4' - 0.5D}{4'}\right) = 460.13\ kip \cdot ft$$ *Footing Centerline Moment* Eqn 2-6

$$V_{joint}^{repair} = 2Mf_{face}^{repair}/D = 460.13\ kips$$ *Joint Shear Demand* Eqn 2-7

The expected concrete strength and longitudinal bar yield strength for the footing was $(f'_{ce} = 1.3(5\ ksi) = 6.5\ ksi)$ and $\left(f_{ye} = 1.1(60\ ksi) = 66\ ksi\right)$ respectively. With a 1" cover to the outside of the longitudinal bar and two orthogonal rows of #7 longitudinal reinforcement, the depth to the second layer of longitudinal reinforcement becomes $(d = 17.69")$. The effective joint width for accessing joint shear was $\left(bj_{eff} = D\sqrt{2} = 33.94"\right)$, and the effective flexural width for accessing footing moment strength was $\left(b_{eff} = D + 2d = 59.38"\right)$. The average joint shear stress v_{jv} was computed using Eqn 2-8 and compared to the limits of $(0.2f'_{ce} = 1300\ psi)$ and 870 psi. Following recommendations in (Priestley, Seible and Calvi 1996), the appropriate joint shear design technique was determined based on the computed principal stresses, p_c and p_t in Eqn 2-10 and Eqn 2-11. The average stress at the midheight of the footing due to the axial load, assuming a 45º spread from the boundaries of the column, becomes f_v in Eqn 2-9, where $(P_{axial} = 191\ kips)$. Since the footing joint is not post-tensioned, f_h is zero. The joint shear design provisions depend on the value of the principal tension stress, simplified provisions can be applied until $\left(p_t \geq 3.5\sqrt{f'_{ce}} = 282.18\ psi\right)$, full provisions are applied if $\left(p_t \geq 5\sqrt{f'_{ce}} = 403.11\ psi\right)$, with interpolation allowed between the two limits. The computed principal tension stress in Eqn 2-11 necessitated full application of the joint design provisions in (Priestley, Seible and Calvi 1996). The calculated principal compressive stress in Eqn 2-10 is lower than the limiting value of $(0.3f'_{ce} = 1950\ psi)$.

$$v_j = V_{joint}^{repair}/bj_{eff}h_f = 677.83\ psi$$ *Average Joint Shear Stress* Eqn 2-8

$$f_v = \frac{P_{axial}}{\pi\left(0.5D + 0.5h_f \tan 45^o\right)^2} = 125.61\ psi$$ *Average Stress at Midheight of the Footing due to Axial Load* Eqn 2-9

$$p_c = \frac{f_v + f_h}{2} + \sqrt{\left(\frac{f_v - f_h}{2}\right)^2 + {v_j}^2} = 743.83\ psi$$ *Principal Compressive Stress* Eqn 2-10

$$p_t = \frac{f_v + f_h}{2} - \sqrt{\left(\frac{f_v - f_h}{2}\right)^2 + {v_j}^2} = -617.93\ psi$$ *Principal Tensile Stress* Eqn 2-11

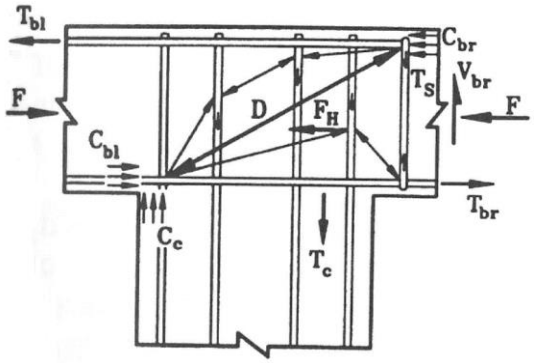

Figure 2-15. Force Transfer Mechanism using External Vertical Joint Reinforcement from (Priestley, Seible and Calvi 1996)

The joint force transfer mechanism utilizing external vertical joint reinforcement from (Priestley, Seible and Calvi 1996) was selected, see Figure 2-15. The required joint shear reinforcement to develop this mechanism depends on the area of reinforcement in the column, A_{sc}. Since the footing-column joint in the specimen must support the overstrength of the repaired section, an equivalent value of A_{sc}^{eq} consistent with the base section moment of the repaired section, $\left(Mo_{base}^{repair} = 1123.02\ kip \cdot ft\right)$, was needed. A moment curvature analysis with overstrength properties and 16 (27 mm) diameter bars, $\left(A_{sc}^{eq} = 14.20\ in^2\right)$ compared to $(A_{sc} = 9.62\ in^2)$, produced a maximum flexural overstrength of $\left(Mo_{base}^{eq} = 1133.54\ kip \cdot ft\right)$. This equates to a 47.6% increase in the required joint shear steel as a result of the repair technique following this conservative design methodology. In the force transfer mechanism, (Priestley, Seible and Calvi 1996) note that the total area of external vertical joint shear reinforcement may be reduced by the percentage of column bars bent inward towards the joint. For the repaired section, additional doweled reinforcement increases the capacity of damaged regions of the column. Even though all of the original column bars have bends towards the joint, a reduction in the area of external vertical joint shear steel was not used due to the fact that the joint is governed by demands of the repaired section. In the footing design, the overstrength stress in the column reinforcement was taken as $\left(f_{yc}^{o} = 1.4f_{ye} = 1.4(66\ ksi) = 92.4\ ksi\right)$ instead of the recommended $\left(f_{yco} = 1.4f_{y}\right)$, which equates to an addition 10% conservatism which was judged to be appropriate given the non-standard design procedure. In the expressions, the transverse steel had a yield strength of $\left(f_{yh} = 60\ ksi\right)$ and the anchorage length in the joint was computed as $(l_a = 15.94")$.

The required hoop reinforcement within the joint was computed using Eqn 2-12, and compared to the minimum value in Eqn 2-13. A #4 Gr60 A706 spiral at (1-3/8”) spacing was selected as shown in Eqn 2-14. The required area of exterior joint shear reinforcement in each quadrant of the specimen was calculated using Eqn 2-15. This equated to 26 Gr60 #3 J-Hooks placed in each quadrant around the specimen, Eqn 2-16, and be able to develop their yield strength within a distance $(0.5d = 8.84")$ from the column face. An additional amount of vertical joint shear reinforcement equal to half of that provided outside the joint should was provided within the joint. This equated to 13 bars, however 16 #3 J-Hooks were provided to individually restrain the inward bar bends of all of the column longitudinal bars, Eqn 2-17. The maximum spacing of J-Hooks within the footing was $(0.5d = 8.84")$. To develop the force transfer mechanism in Figure 2-15, an additional area of top

footing longitudinal reinforcement was provided according to Eqn 2-18. This equated to three additional Gr60 #7 top footing reinforcing bars, Eqn 2-19, which were mirrored in the bottom layer for simplicity of construction. A footing design with two orthogonal layers of #7 Gr60 reinforcement produced a first yield moment of $\left(M'_y = 561.90\ kip \cdot ft\right)$ compared to $\left(Mf_{face}^{repair} = 460.13\ kip \cdot ft\right)$ utilizing 11 Gr60 #7 bars top and bottom over $\left(b_{eff} = 59.38"\right)$. With the three additional footing top longitudinal bars required for the force transfer mechanism, two rows of 14 #7 bars were specified in the two orthogonal directions over the effective flexural width. The footing longitudinal steel is kept in the elastic range under the repaired demands so that additional base rotations due to deformations in the footing will be minimized, since the column behavior is of interest in this study.

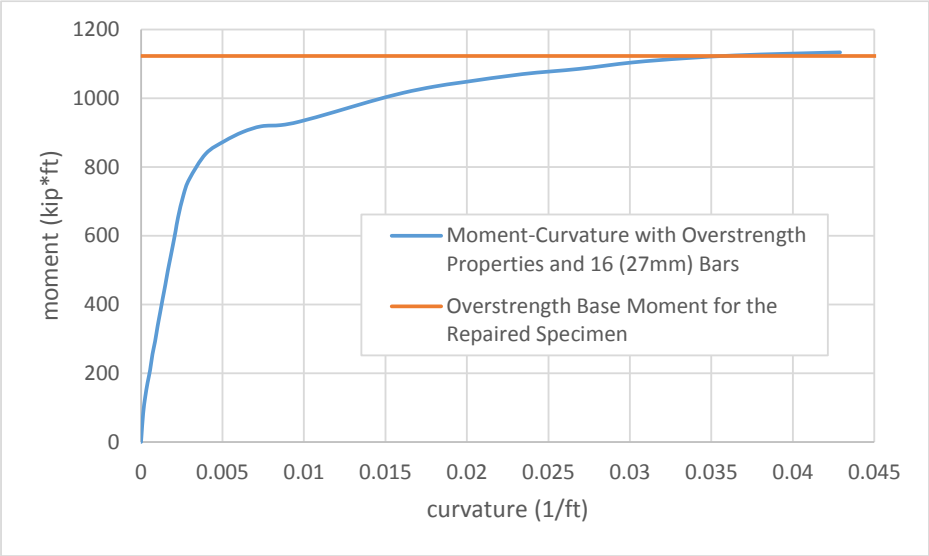

Figure 2-16. Method to Find Equivalent Area of Column Steel for the Repaired Overstrength Base Section Moment

$$\rho_s^{req} = \frac{0.3A_{sc}^{eq} f_{yc}^{o}}{{l_a}^2 f_{yh}} = 2.58\%$$ *Required Hoop Steel within the Joint* *Eqn 2-12*

$$\rho_s^{min} = \frac{3.5\sqrt{f'_{ce}}}{f_{yh}} = 0.47\%$$ *Minimum Hoop Steel within the Joint* *Eqn 2-13*

$$\rho_s^{provided} = \frac{4A_{sp}}{D's} = 2.52\%$$ *With a #4 A706 Spiral at 1-3/8" Spacing* *Eqn 2-14*

$$A_{jv}^{req} = 0.125A_{sc}\, f_{yc}^{o}/f_{yh} = 2.73\ in^3$$ *Required External Vertical Shear Steel* *Eqn 2-15*

$$A_{jv}^{provided} = 26 \cdot A_{bar}^{\#3} = 2.87\ in^2$$ *26 #3 Vertical J-Hooks in Quadrants Around the Col.* *Eqn 2-16*

$$A_{jv}^{interior} = \frac{A_{jv}^{provided}}{2} = 13\ bars\ req$$ *16 #3 Vertical J-Hooks Placed within the Joint* *Eqn 2-17*

$$\Delta A_{sf}^{top} = 0.0625A_{sc}\, f_{yc}^{o}/f_{yf} = 1.37\ in^2$$ *Additional Footing Top Long. Bars* *Eqn 2-18*

$$\Delta A_{sf}^{provided} = 3 \cdot A_{bar}^{\#7} = 1.37\ in^2$$ *Three Additional #7 Footing Top Longitudinal Bars* *Eqn 2-19*

Specimen and Transfer Footing Reinforcement

The reinforcement detailing for the column and footing discussed in the previous section is shown graphically in Figure 2-18 and Figure 2-19. The main footing measured 8'x8'x20", with eliminated corners measuring 21" along the two main orthogonal directions to save weight and material since these regions were not needed for strength, due to the tie down arrangement. The main footing contained two orthogonal layers of symmetrically detailed Gr60 #7 longitudinal reinforcement with a 1" clear cover top and bottom. The tie down holes for the main footing were made using 3" diameter PVC. The resulting joint shear steel needed to develop the force transfer mechanism discussed in the previous section consisted of: (1) Gr60 A706 #4 spiral at (1-3/8") within the joint, (2) 26 Gr60 #3 J-Hooks placed in each quadrant of the specimen just outside of the column perimeter, (3) 16 Gr60 #3 J-Hooks placed within the joint to restraint the inward 90° column longitudinal bar bends, and (4) 3 additional Gr60 #7 top footing longitudinal bars in each direction, which were mirrored to the bottom layer as well to simplify construction. In regions of the footing outside the joint, Gr60 #3 J-Hooks were placed according to the maximum spacing. Four Gr60 #7 lifting hooks with 90° end bends were placed in the corners of the specimen.

The cross-section height and longitudinal reinforcement detailing for the main footing was carried over to the transfer footing, Figure 2-20 and Figure 2-21. The additional pocketed connections were formed using ¼" A36 steel plate fabricated with slotted connections to allow the orthogonal layers of the bottom mat of transfer footing reinforcement to pass through the pockets. The fabricated steel pockets used for the four (1-3/8") Dywidag connections appear in Figure 2-22, while the larger single pocket for the (1-3/4") Dywidag axial bar is shown in Figure 2-23. The size of the box was governed by the plate, nut, and bar extension past the nut for the two bar anchorages. The center pocket and surrounding inclined Gr60 #5 bars and #3 J-Hooks were detailed such that the maximum capacity of the axial load system could be reached, Figure 2-21.

Cross-Section Details
24" Dia. with 109.4375" Cantilever Length
16 Gr60 A706 #6 or #7 Longitudinal Bars
#3 Gr60 A706 Spiral at 1.5", 2" ,or 2.75" Spacing
½" Cover to Outside of Spiral
3" PVC Duct for 1 ¾" (150 ksi) Dywidag Bar

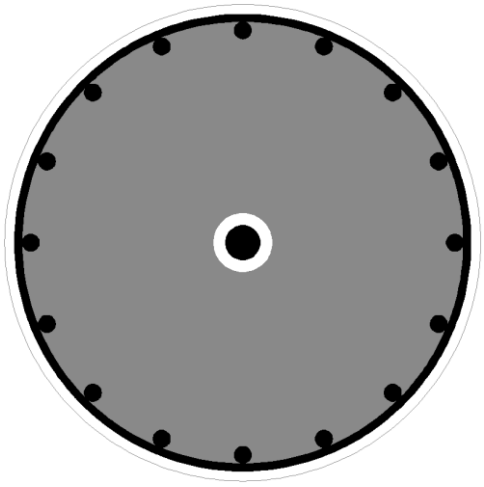

Figure 2-17. Column Cross-Section Geometry and Reinforcement

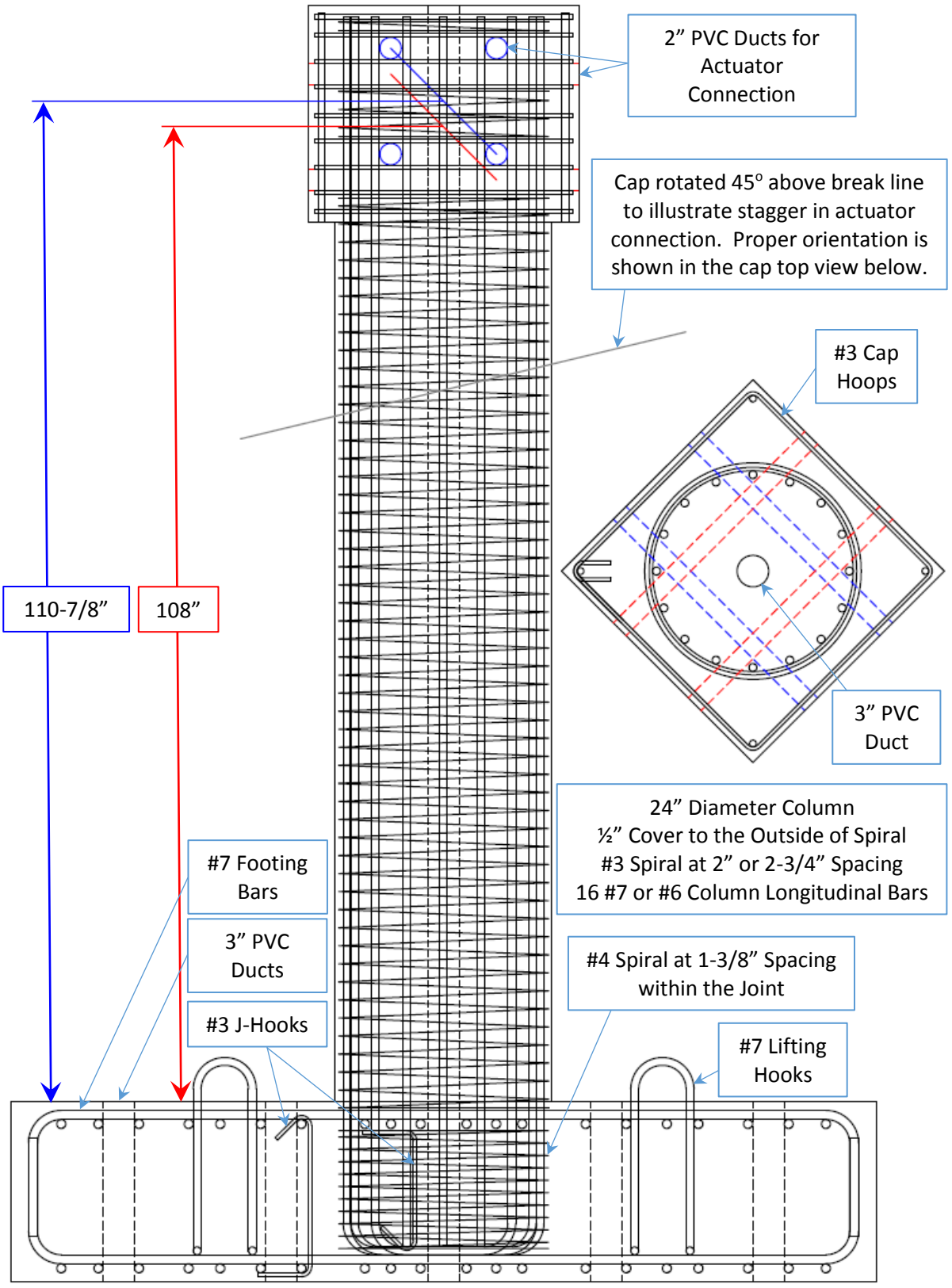

Figure 2-18. Specimen Reinforcing Details

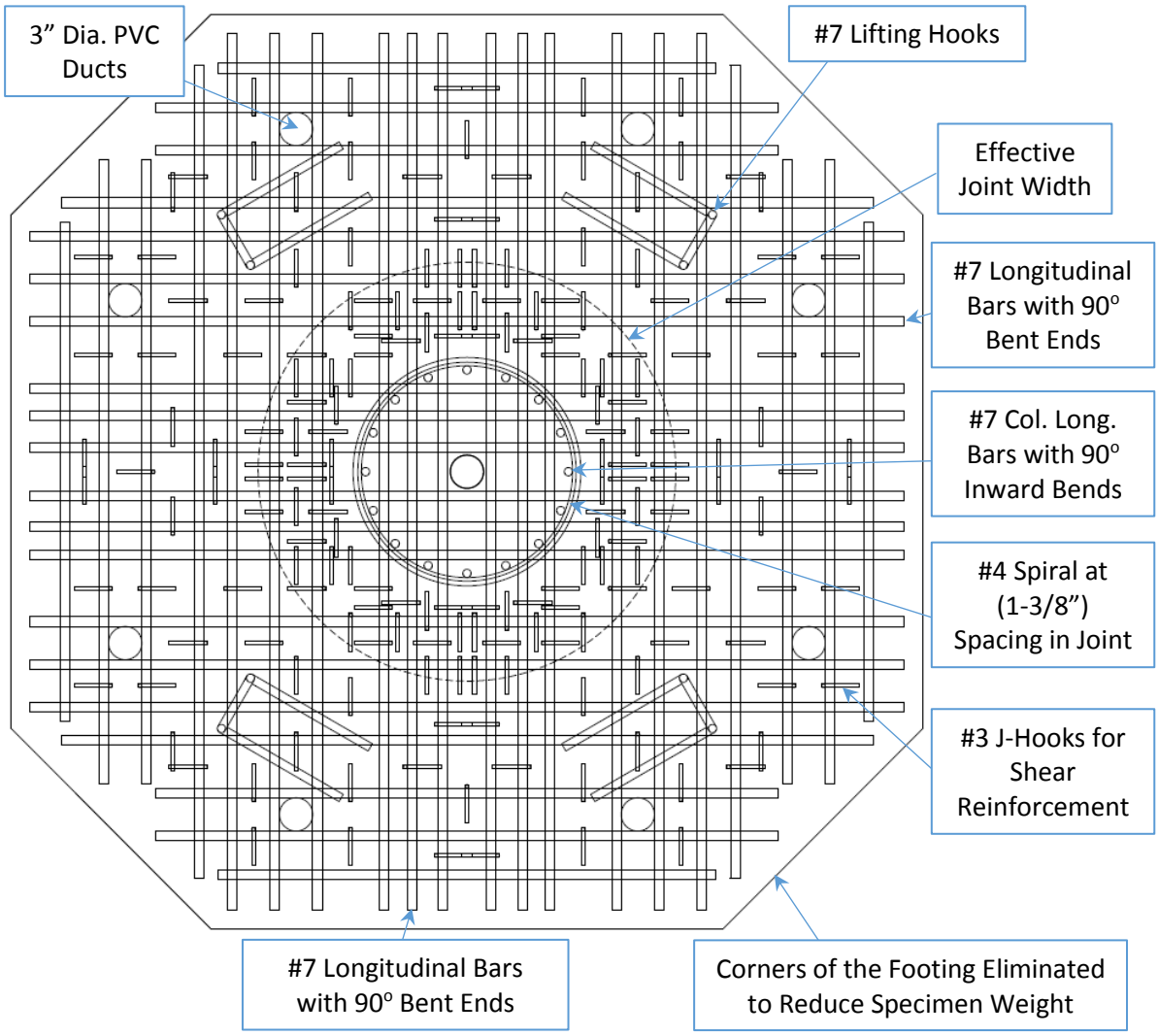

Figure 2-19. Specimen Footing Reinforcing Details

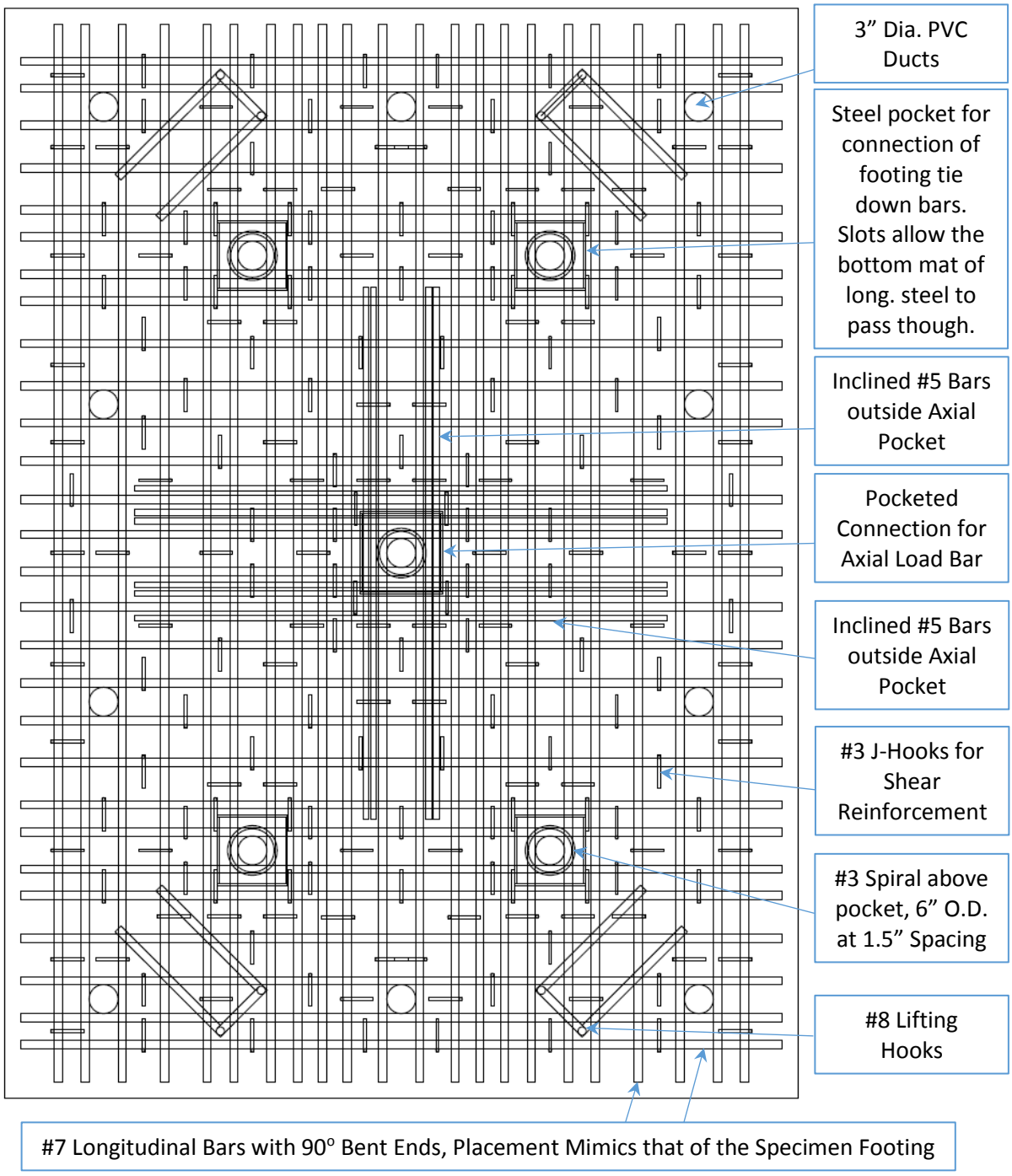

Figure 2-20. Transfer Footing Reinforcing Details

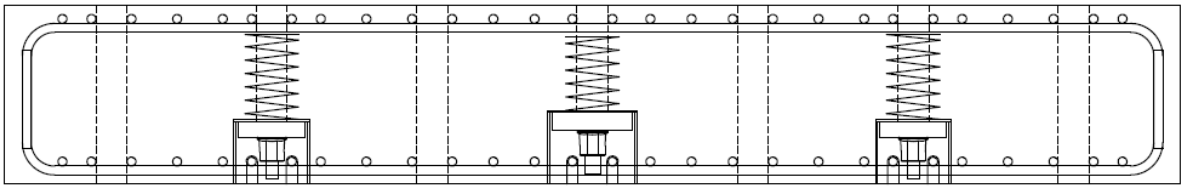

Longitudinal Cross Section of Transfer Footing: Locations for the Dywidag Bar Pockets

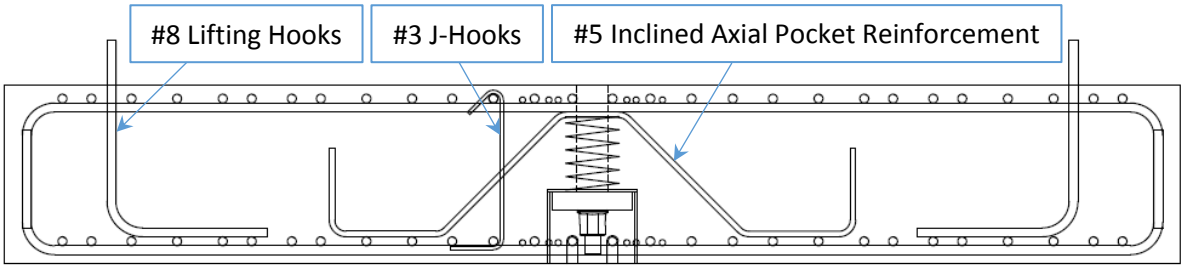

Longitudinal Cross Section of Transfer Footing: Axial Pocket Reinforcement and Lifting Bars

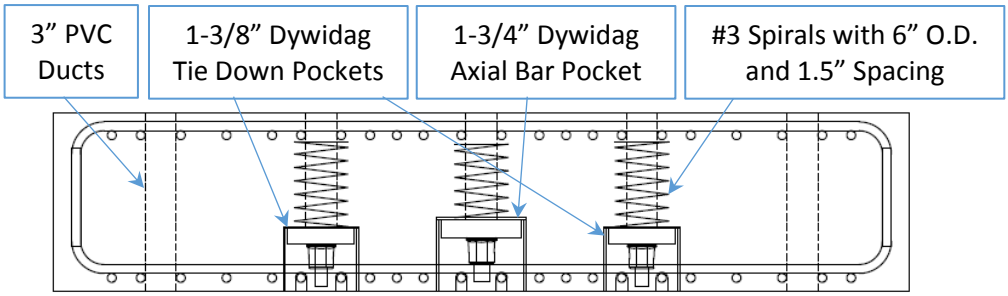

Transverse Cross Section of Transfer Footing: Locations for the Dywidag Bar Pockets

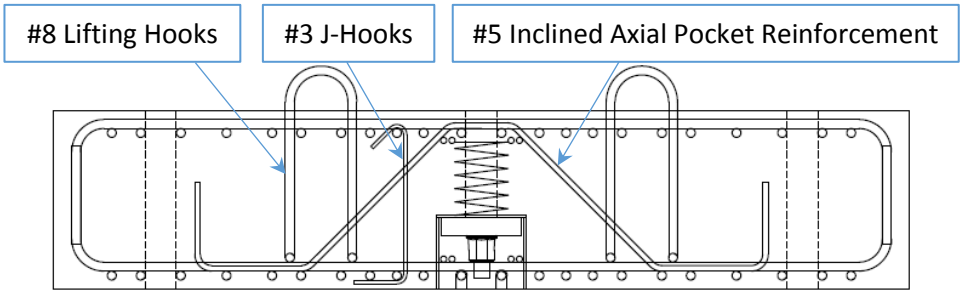

Transverse Cross Section of Transfer Footing: Axial Pocket Reinforcement and Lifting Bars

Figure 2-21. Longitudinal and Transverse Side Views of the Transfer Footing

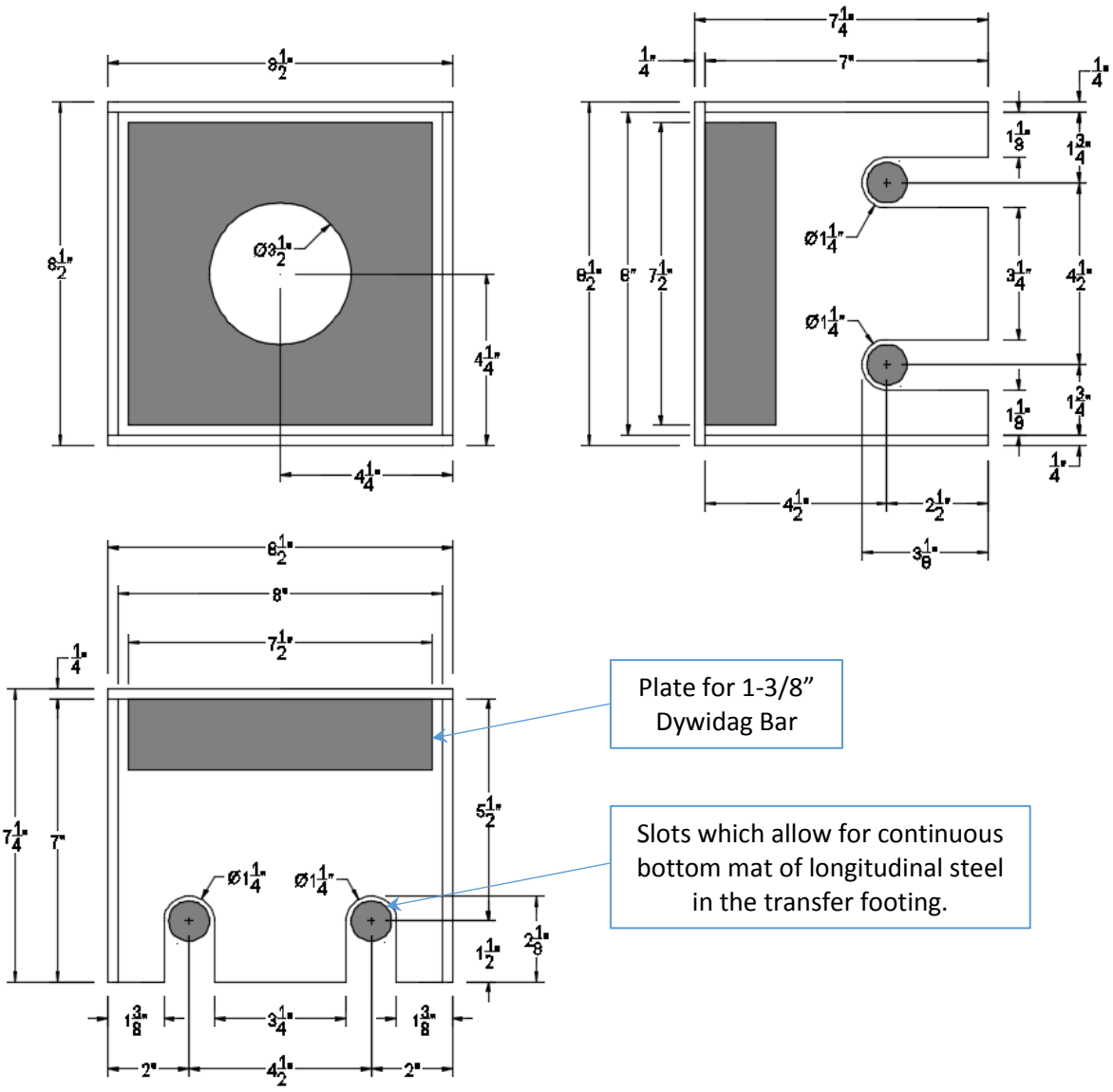

Figure 2-22. Fabricated Steel Pockets for 1-3/8" Dywidag Tie Down Bars

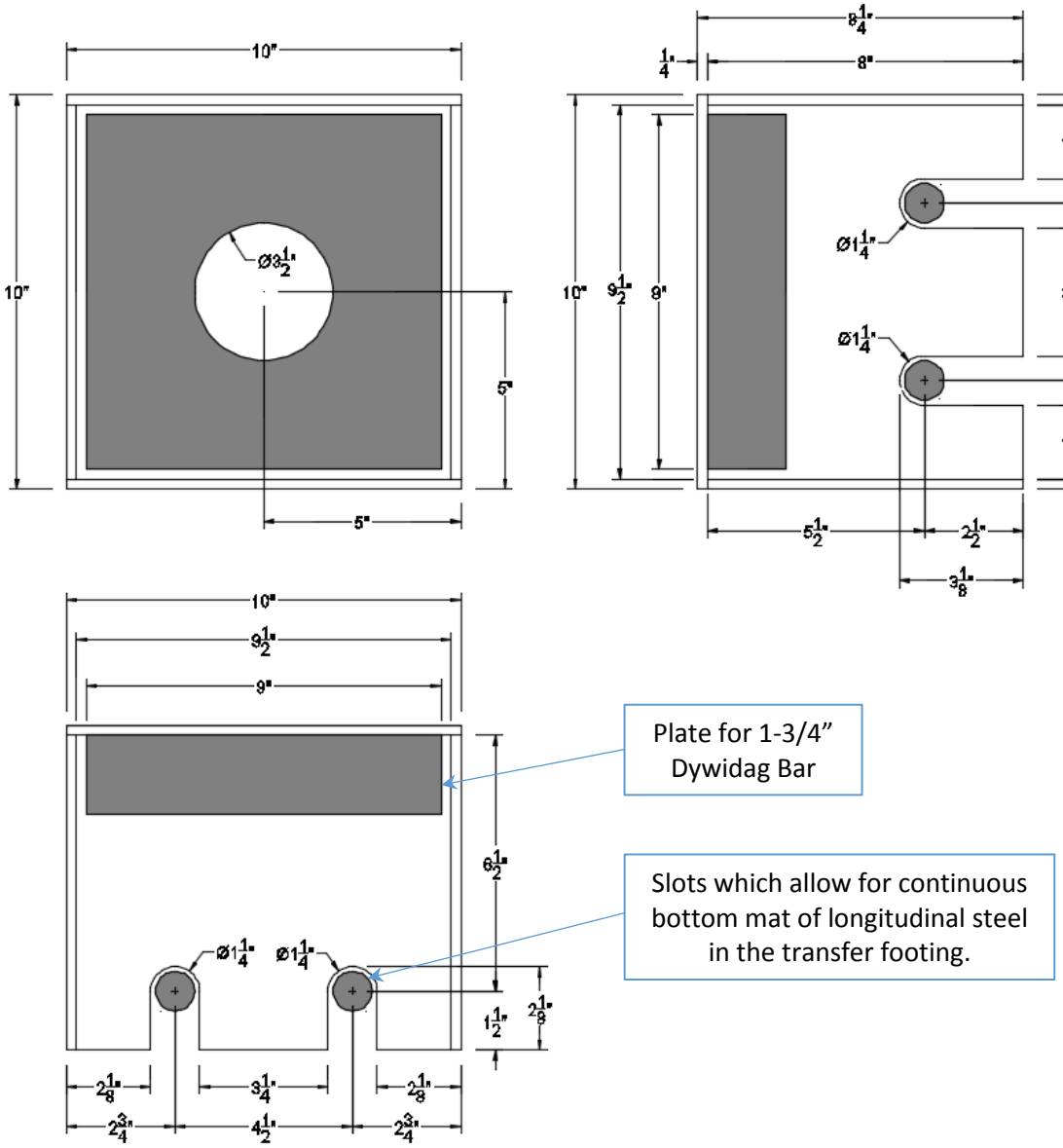

Figure 2-23. Fabricated Steel Pocket for 1-3/4" Dywidag Axial Load Bar

Fixture Design

The 45° steel loading fixture and side coped link beam utilized with the test setup, Figure 2-3, are shown in Figure 2-27 and Figure 2-28. The 45° loading fixture was designed for the maximum tension and compression forces for the actuator, $(P_{tension} = 150\ kips)$ and $\left(P_{comp} = 200\ kips\right)$, and not the column shear forces from flexural overstrength of the repaired section. The final detailing for the fabricated 45° loading fixture appears in Figure 2-25 and Figure 2-26. The fixtures were constructed with A572 Gr50 plate with $f_y = 50\ ksi$ and $f_u = 65\ ksi$. The thickness of the 45° plate was governed by the moment produced by the actuator in compression analyzed as a simply supported beam between stiffener centerlines with line loads over the projected bearing area of the actuator knuckle. The maximum moment in the 45° plate produced a bending stress of 31.57 ksi, which is elastic. The welds at the base of the two 45° stiffeners are under eccentric shear and tension. Dimensions from the centroid of the 45° stiffeners to base plate weld group to the resultant horizontal and vertical actuator forces, located at the pin of the knuckle, are shown in Figure 2-24. For both tension and compression, the resultant critical weld stress was obtained a the vector resultant of the following: (1) weld shear due to horizontal actuator load, (2) weld tension due to vertical actuator load, (3) tension/compression component of weld force resulting from the moment induced by eccentricity. The critical weld resultant for the actuator in compression produced a demand of 3.58 kip/in, while the capacity for a single weld was 6.96 kip/in. The vector resultant of the normal, shear, and bending stress distribution in the weld group was imposed on the base plate as a non-uniform line load to check for the flexural stress. This produced stresses far below the yield stress of the material with the dimensions shown in Figure 2-25. The fixture base plate to side coped W30X116 tension/compression link beam was formed with seven 1" A325-N bolts. The horizontal components of the actuator in tension and compression were 106.07 and 141.42 $kips$ respectively. Five bolts were required to transfer the shear force, however seven were specified to distribute the load over the existing hole pattern on the W-shape depicted in Figure 2-28. The bolt bearing and block shear capacity of the fixture base plate and web of the W-shape significantly exceeded the demands. An extra specimen cap box, Figure 2-29, was constructed so that the control of the horizontal actuators could be tested prior to running the first specimen.

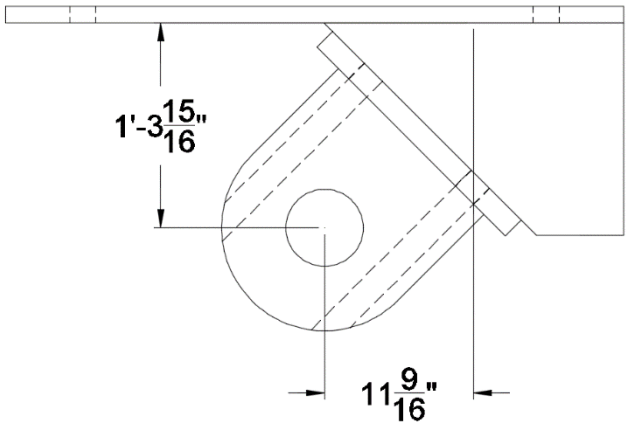

Figure 2-24. Dimensions from Actuator Knuckle Pin to CG of the 45° Stiffener Weld Group

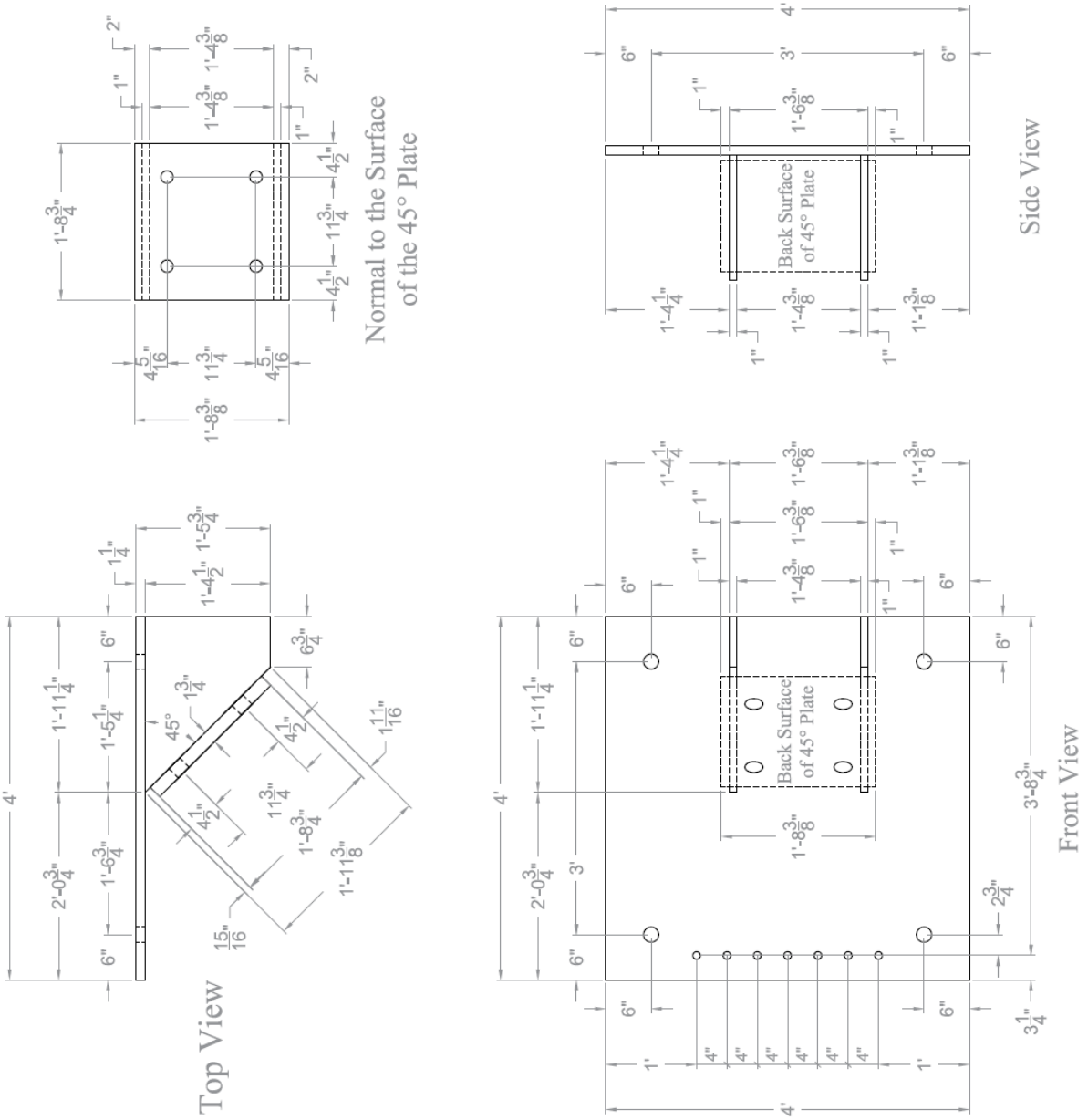

Figure 2-25. Fabrication Details for the 45º Loading Fixtures

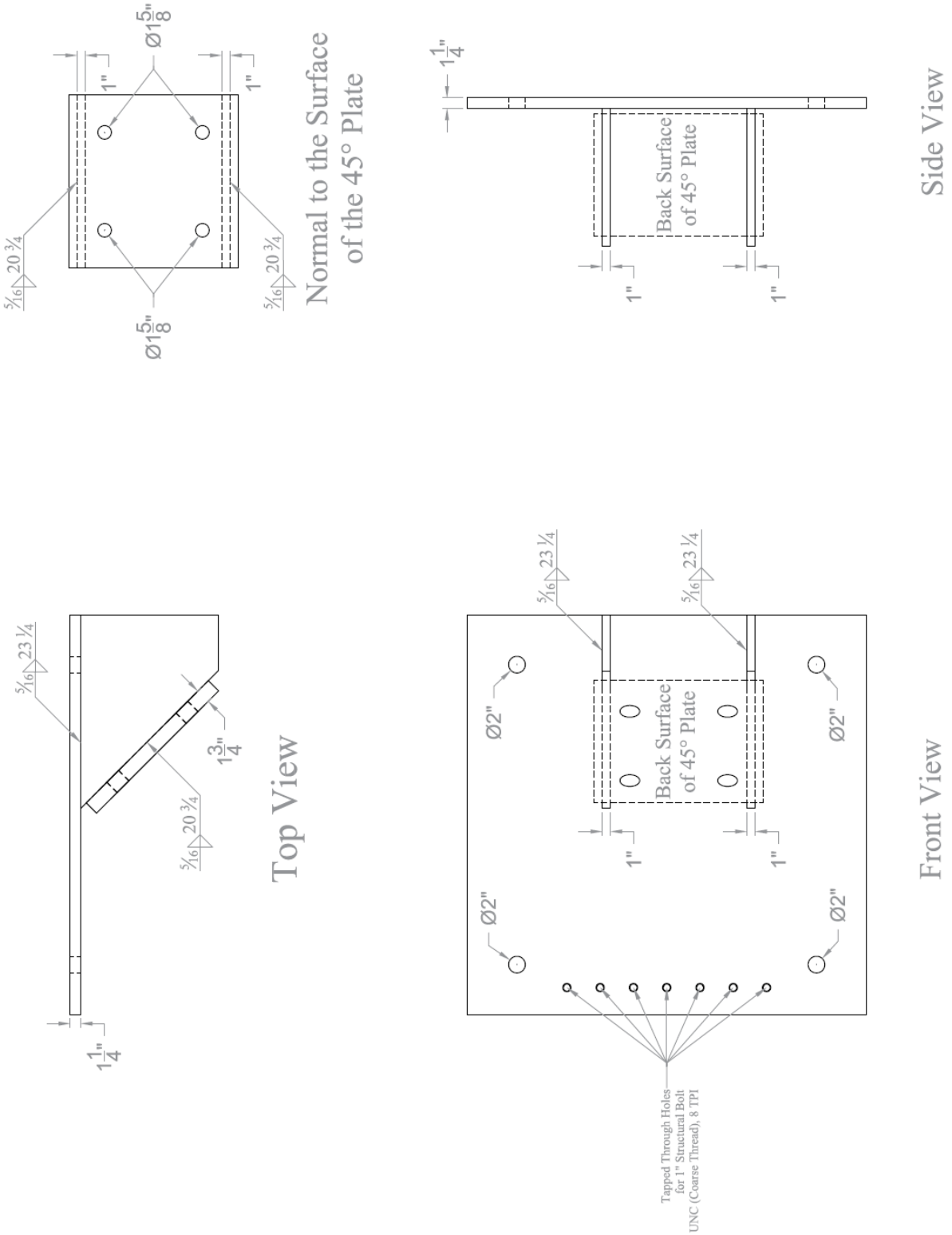

Figure 2-26. Fabrication Details for the 45º Loading Fixtures

Figure 2-27. Fabricated Steel Loading Fixture

Figure 2-28. Existing Side Coped Link Beam for Actuator Lateral Forces

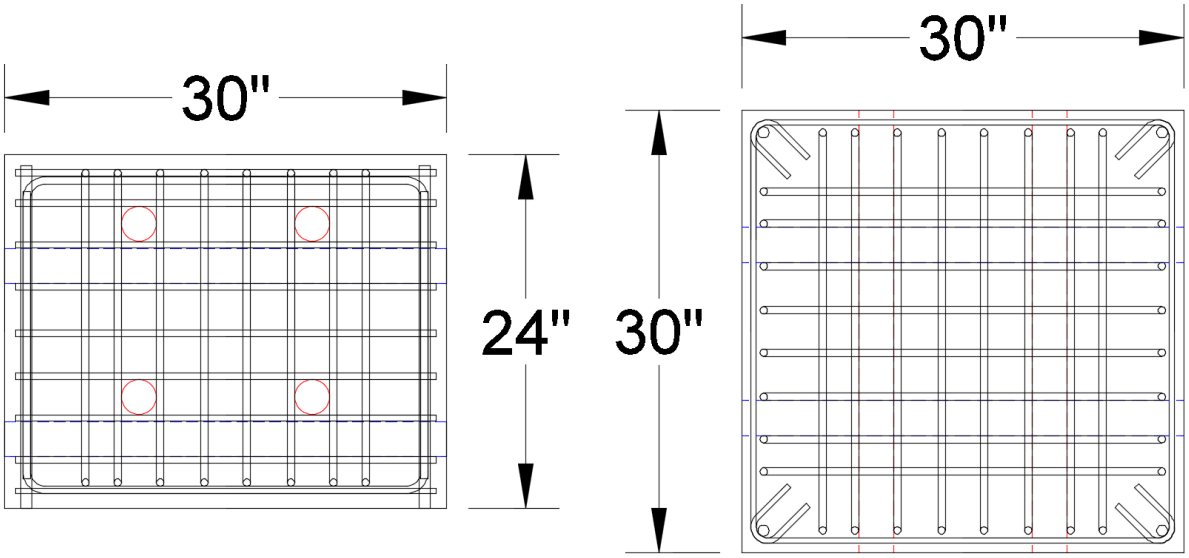

Figure 2-29. Stand Alone Cap Constructed to Test Actuator Control Prior to the First Test

Specimen Construction

Individual specimens weighed 19.9 kips, while the transfer footing weighed 22.0 kips. The specimens were constructed at NCSU by the research team due to the need for accurate detailing beyond the tolerances of typical construction, which was necessary to isolate the impact of specific variables on column performance. The techniques used to construct the specimens and transfer footing are discussed in the following section.

The column longitudinal reinforcement and spiral were tied horizontally in wooden stands, Figure 2-30 and Figure 2-31, which anchored the bars in their proper location within the cross-section. The spiral was held using a crane while individual bars were placed in their respective locations and tied down to the wooden stands using steel tie wire. Between the two supports circular insets were placed within the cross-section with slotted connections for each reinforcement bar to maintain the correct dimensions along the column length. The wooden tying stands and these circular insets were constructed in four pieces such that they could be disassembled and removed after the column cage was completed and used for subsequent specimens. Prior to tying the spiral, the center 3" PVC duct was placed through the center of the column and held in placing using the circular wooden insets discussed previously. The 90° column longitudinal bar end bends were arranged in two layers, Figure 2-31, such that they all pointed towards the interior of the cross section. This detailing technique improves joint performance by anchoring bars in the diagonal compression strut which forms as part of the force transfer mechanism. The first double layer of spiral was placed above the location of the top layer of footing longitudinal reinforcement, but below the footing-column interface as shown in Figure 2-30. The spiral was wound tight and continuously tied from one end to the other along every intersection between the spiral and a longitudinal bar. Care was taken during construction to maintain continuous contact between the spiral and longitudinal bars at every intersection, such that they would provide reliable restraint against longitudinal bar buckling. The spiral was terminated just below the location of the first actuator connection hole in the cap, which would be constructed later in the process. Diagonal #6 bars were placed through the column cage in orthogonal directions to brace the cage prior to removal of the tying stands. This prevented shifting of the cage during subsequent stages of construction.

The column cage was tied horizontally to improve the accuracy of the reinforcement placement; however, this complicated the construction of the joint. The top orthogonal mat of footing longitudinal reinforcement was placed within the joint, Figure 2-32, and used to support the column on a perimeter frame during placement of the joint horizontal reinforcement. Once the column was braced against overturning using ratchet straps, the 16 Gr60 #3 J-Hooks were placed within the joint to restraint the column 90° end bends. The Gr60 A706 #4 spiral was then tied into the joint at (1-3/8") spacing.

The footing formwork consisted of rented Steel-Ply panels, corner angles, and wedge bolts as shown in Figure 2-33. The sides of the footing formwork box consisted of 16"x8' panels and 4"x8' panels. This arrangement was used instead of a single 20" tall panel to allow for installations of ¼" recessed threaded rods which supported the panels and prevented bowing during concrete placement. Seven ¼" threaded rods were placed in each direction at a depth of 4" below the top surface of the footing. This technique was cheaper than purchasing standard panel ties, and simplified the process of leveling out the top surface of the footing concrete.

The bottom mat of Gr60 #7 footing longitudinal reinforcement was supported on 1" slab bolsters and tied into place as shown in Figure 2-34. Wooden disk inserts were drilled into the formwork to hold the ends of the 3" PVC ducts which would form the necessary footing tie down holes. Wooden stud panels were constructed and installed in the corners of the footing to block out those regions during construction, see Figure 2-36. Once the bottom mat of reinforcement was tied, extra column reinforcement was placed orthogonal to the 16" outside panels in one direction to support the bottom layer of the top mat of footing #7 longitudinal reinforcement in the perpendicular direction. Additional 4"x4"x16" posts were used inside the footing to support the extra column bars as shown in Figure 2-34. The bottom layer of the top mat of footing #7 longitudinal steel was initially placed loosely and not tied in. The column cage depicted in Figure 2-32 was lifted over the footing and lowered into place until the center 3" PVC duct for the column axial load aligned with the wooden disk installed into the bottom formwork panel. The additional footing top longitudinal bars were placed, but were not tied until ratchet straps were tightened to insure proper reference dimensions for the outside formwork panels. Once all of the longitudinal bars were tied and the 3" PVC tie down holes were held in the appropriate locations, extra supporting column longitudinal bars were removed along with the 4"x4"x16" posts. Then the footing Gr60 #3 J-Hooks and #7 lifting hooks where installed as shown in Figure 2-36. The final step was to install the fourteen ¼" threaded rods and four 4"x8' panels to finish off the 20" height and restrain the formwork from bowing out while casting.

The specimens with completed footing reinforcement are depicted in Figure 2-35. Three separate concrete trucks were used on the day of casting. Each concrete truck covered two specimen footings. The concrete was placed, vibrated, and leveled off prior to the arrival of the next truck. Cylinders from each truck were collected such that they could be attributed to their respective specimens. A photo of the completed footings appears in Figure 2-37. Curing compound was applied to the top surface of the footing concrete, except for the footing-column interface, where the acrylic layer would interfere with the cold-joint. After seven days, cylinders for the footing concrete were tested and the outside formwork panels were removed. Since the Mi-Jack mobile crane was being repaired at this time, the specimens were lifted with four hydraulic jacks so that the bottom formwork panels could be removed. This process is depicted in Figure 2-45, when it was repeated at a later stage of construction. Two 8"x8"x0.5" HSS spreader beams were supported on the cylinders of 209 kip (931 kN) capacity hollow core jacks. Cloth straps were placed between the HSS and Gr80 A706 #11 bars which spanned between two footing lifting hooks. The hydraulic jacks had a (10-1/8") stroke capacity, which allowed the specimen to be lifted around 7" off of the ground given the stretch of the cloth straps. The bottom formwork panels were removed and debris was cleaned under the footing to insure a level placement on the casting slab.

The next stage in the construction process involved installing the cover concrete blockout in the plastic hinge region. The same technique used for specimens in (Goodnight, Kowalsky and Nau 2015) was carried over to this study. Once again, the purpose of the blockout was to remove the cover concrete and allow for instrumentation of the exposed internal reinforcing steel, shown in Figure 2-8 for a column from (Goodnight, Kowalsky and Nau 2015). The foam blockout was applied in two layers, see Figure 2-38 and Figure 2-39. The first layer consisted of strips of ½" insulation board cut into strips which fit between two adjacent spiral layers. Once the strips were cut, clear packaging tape was applied to the edges to reinforce the foam and prevent the steel tie wire from damaging the strips during installation. The strips were applied starting from the bottom of the column where the gap was

non-uniform and the width of the strip was cut to fill the gap. The foam strips were tied at every intersection with column longitudinal bars. This guaranteed that the strip would block out the cover concrete to a depth tangent to the outside surface of the longitudinal reinforcement, but not interfere with core concrete placed behind the spiral layers. Individual strips were coupled together using clear packaging tape to form one continuous strip from the footing-column interface to a height of 4' up the column, where the blockout was terminated, see Figure 2-39. The outside layer of the foam blockout consisted of ¼" thick fanfold insulation board which was wound tight around the column and secured using clear packaging tape as shown in Figure 2-38.

The dimensions of the blockout were such that the 24" Sonotube had a snug fit over the outside layer of ¼" foam. Form release was applied to the outside layer of foam to reduce friction before lowing the Sonotube over the column. Initially, the Sonotube was lifted over the column and lowered until it contacted the top of the blockout. The foam was carefully wedged underneath the bottom of the bottom of the Sonotube and the tube was lowered a few inches until the friction prevented further movement. A double layer piece of plywood with a center hole cut to allow the column reinforcement to pass through was placed on top of the Sonotube. The first layer formed a pocket which was in contact with the edges of the Sonotube while the top layer had a smaller inside diameter than the 24" Sonotube, but larger than the outside surface of the spiral 23". Four ratchet straps were connected to the footing lifting hooks and the double layer of plywood. Inch by inch the ratchet straps were used to lower the plywood cap and thus the Sonotube over the foam blockout. Once the Sonotube reached the footing-column interface, the plywood cap and ratchet straps were removed. The top surface of the Sonotube was never damaged during this process since the forces needed to overcome the fraction and lower the tube over the foam blockout were low.

Silicone was applied around the base of the Sonotube to create a seal. The column stabilization and cap formwork is shown in Figure 2-40 and Figure 2-41. Two layers of 19/32" plywood with 24.5" holes cut out of the center were placed at the footing-column interface to restrain the Sonotube and support the 4"x4" posts at the corners. The posts were installed and secured to the plywood using toe screws. A perimeter box of 4"x4" lumber was placed above the four posts to support the specimen cap formwork. Two 19/32" plywood sheets formed the bottom surface of the cap box, the first had a 24.5" diameter hole to restraint the Sonotube, while the second had a 24" hole to overlay the Sonotube which had the same inside diameter. Four plumb-bobs were installed at the corners of the top plywood layer. These were stretched down to the top surface of the footing and the entire wooden column frame was adjusted until the proper cap orientation was achieved. These dimensions were locked in by attaching 2"x4" bracing on all sides of the 4"x4" posts which supported the cap box. Two orthogonal wooden stud panels were then installed over the plywood base for the cap formwork. The stud walls included wooden disks which secured the ends of the 2" PVC used to make the actuator holes in the two perpendicular directions of the loading stub. The individual PVC tubes, perimeter rectangular hoops, and interior spiral reinforcement were installed along the cap length before placing the final two wooden stud panels to finish off the cap box, shown in Figure 2-42. The final step of the column cap and stabilization form work included applying plastic over the cap and around the Sonotube to prevent water from entering the column prior to casting.

Two concrete trucks were utilized in the column construction, each filling three of the columns and loading caps. In the initial six specimens, one truck was filled the three specimens with 2.75" transverse steel spacings while the other filled the remaining three specimens which had a 2"

spiral spacing. The concrete was placed in lifts using a 1/3 cubic yard hopper attached to a fork lift as shown in Figure 2-43. Each lift was consolidated using a concrete vibrator. Subsequent lifts were interlocked with the top layer of the prior lift using the concrete vibrator until the entire column and cap was completed. Curing compound was applied over the cap and the specimen were cured for eight days before removal of the cap formwork and Sonotube. The completed specimens are shown in Figure 2-44. One additional loading cap was constructed to test the control of the lateral actuators prior to the first experiment, see Figure 2-29.

The first two specimens were picked up using hydraulic jacks, Figure 2-45, and placed onto rollers to clear room on the casting slab for the transfer footing. In the test setup, Figure 2-4, the transfer footing was used to add additional self-reacting pocketed connections for post tensioning bars running between it and the main specimen footing. This allowed for a smaller specimen footing and a symmetric arrangement of tie downs and reinforcement. Rented Steel-Ply formwork was used for the transfer footing as shown in Figure 2-46. The same technique of recessing ¼" steel rods 4" below the top concrete surface was carried over from the main specimen footing. Since the equipment was readily available, the same HSS spreader beams used to lift the specimen were used to prevent bowing of the formwork in the 11' direction by adding post tensioning bars at the beam ends, see Figure 2-48. After the formwork was assembled, the bottom mat of Gr60 A706 reinforcement was tied over 1" slab bolsters. Wooden disks were screwed into the bottom formwork panel to secure the ten holes which passed through the complete depth of the transfer footing. Plywood half-box inserts with slotted connections for the bottom mat of reinforcement were screwed into the bottom formwork panel at each of the five pocketed connection locations, see Figure 2-20 and Figure 2-21. The fabricated steel boxes for the pocketed connections, Figure 2-22 and Figure 2-23, were fit over the wooden inserts and bottom mat of footing reinforcement with the plates for the post tensioning anchorages placed over the reinforcement, but within the pocket. The pocket creates a void in which the post tensioning bar could be placed through the anchorage plate and a locking nut could be fastened over the extended bar which terminates within the pocket. The additional diagonal reinforcement for the center axial pocket was installed next, Figure 2-47, followed by the top mat of reinforcement. Initially, the top mat of reinforcement was placed loosely over extra column bars which spanned between the 16" side panels in the 8' footing direction. Inside the footing these extra column bars were supported with 4"x4"x16" posts. Ratchet straps were applied to insure the proper dimensions of the side formwork panels so that they could serve as reference dimensions for locating the 3" PVC tie down ducts and top mat of reinforcement. After the reinforcement was tied in place, the ratchet straps, extra column bars, and wooden posts were removed. Next, the Gr60 #3 J-Hooks and #8 lifting hooks were installed, followed by the ¼" recessed threaded rods and HSS exterior formwork supports. The transfer footing concrete was poured and consolidated using a concrete vibrator. Curing compound was applied to the top concrete surface and the transfer footing was covered with plastic, see Figure 2-48. After seven days the side formwork panels were removed and the transfer footing was lifted using hydraulic jacks to remove the bottom formwork.

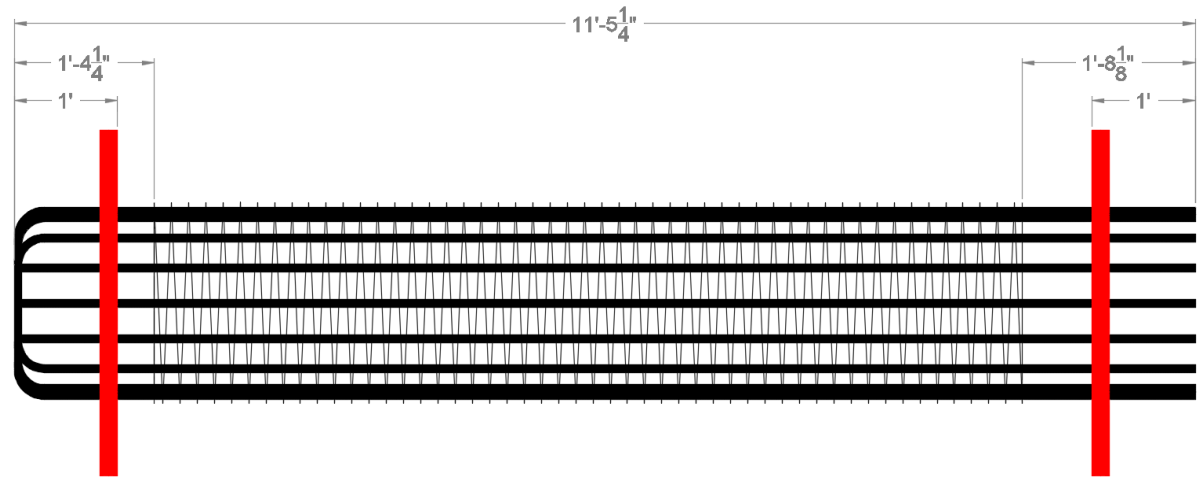

Figure 2-30. Column Cage Template and Tying Stand

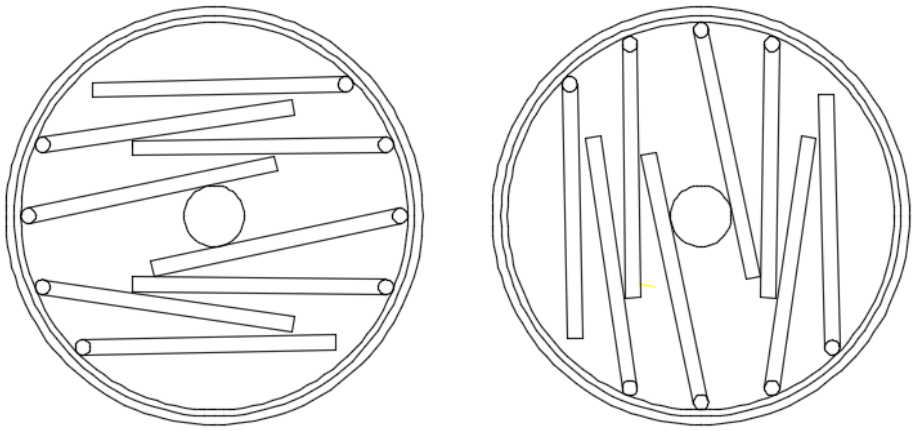

Figure 2-31. Orientation of Column 90o Bends in the Footing Joint

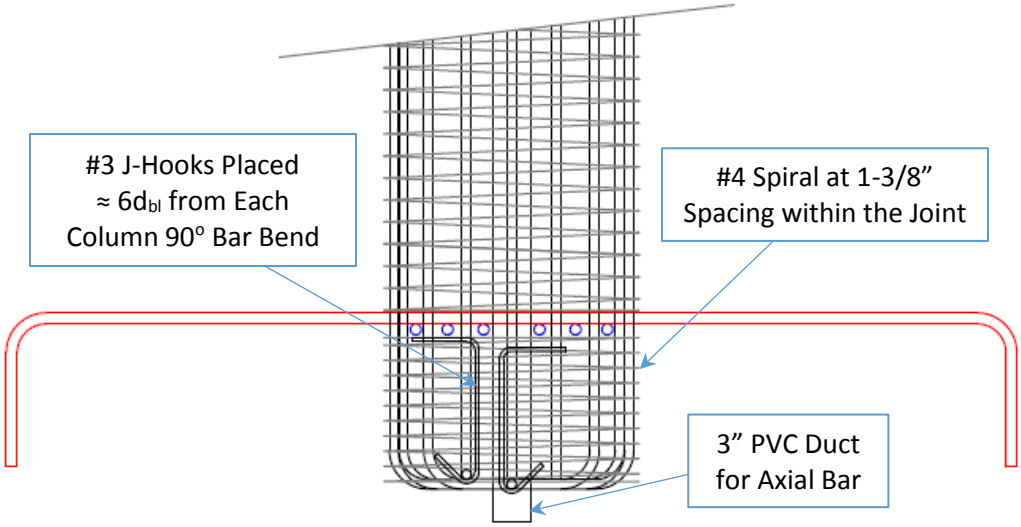

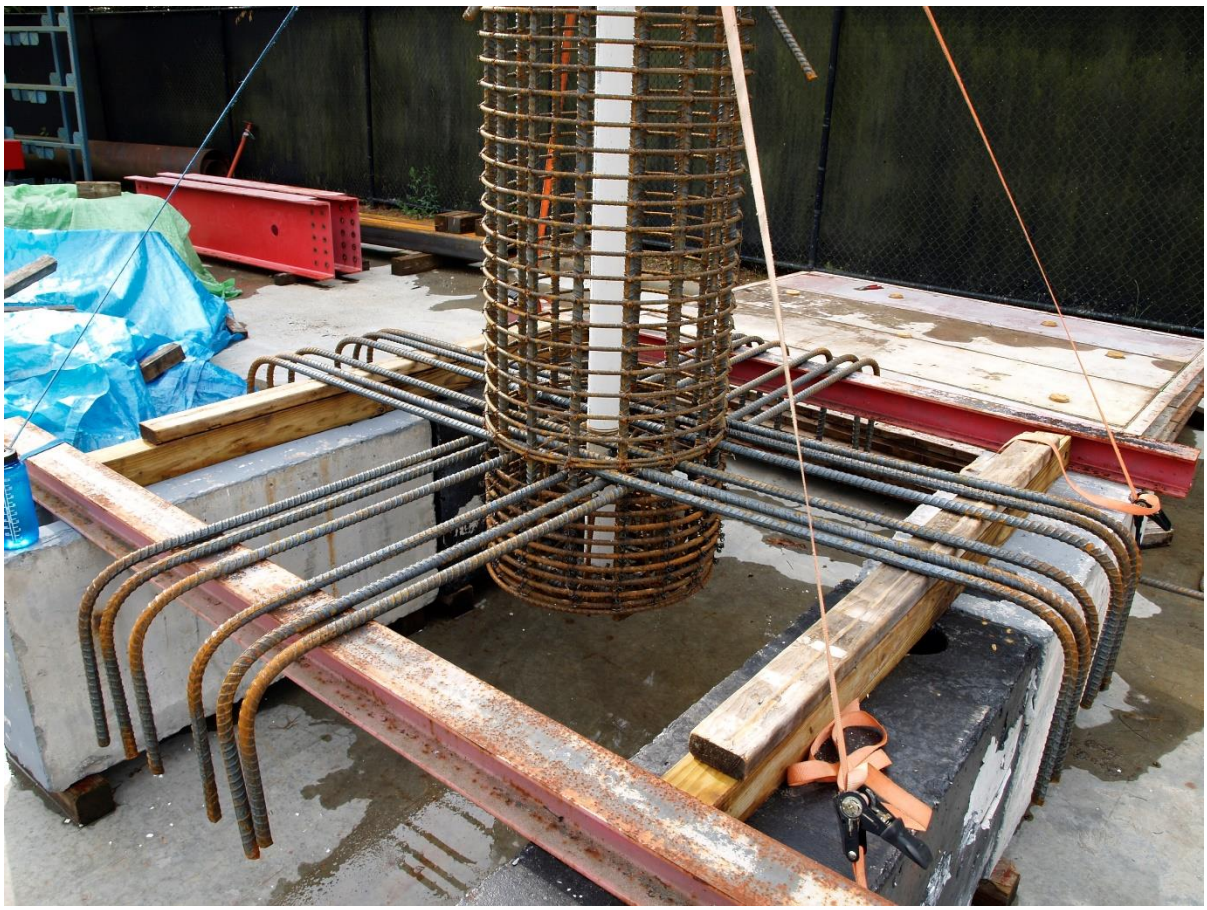

Figure 2-32. Procedure for Tying in Joint Shear Steal

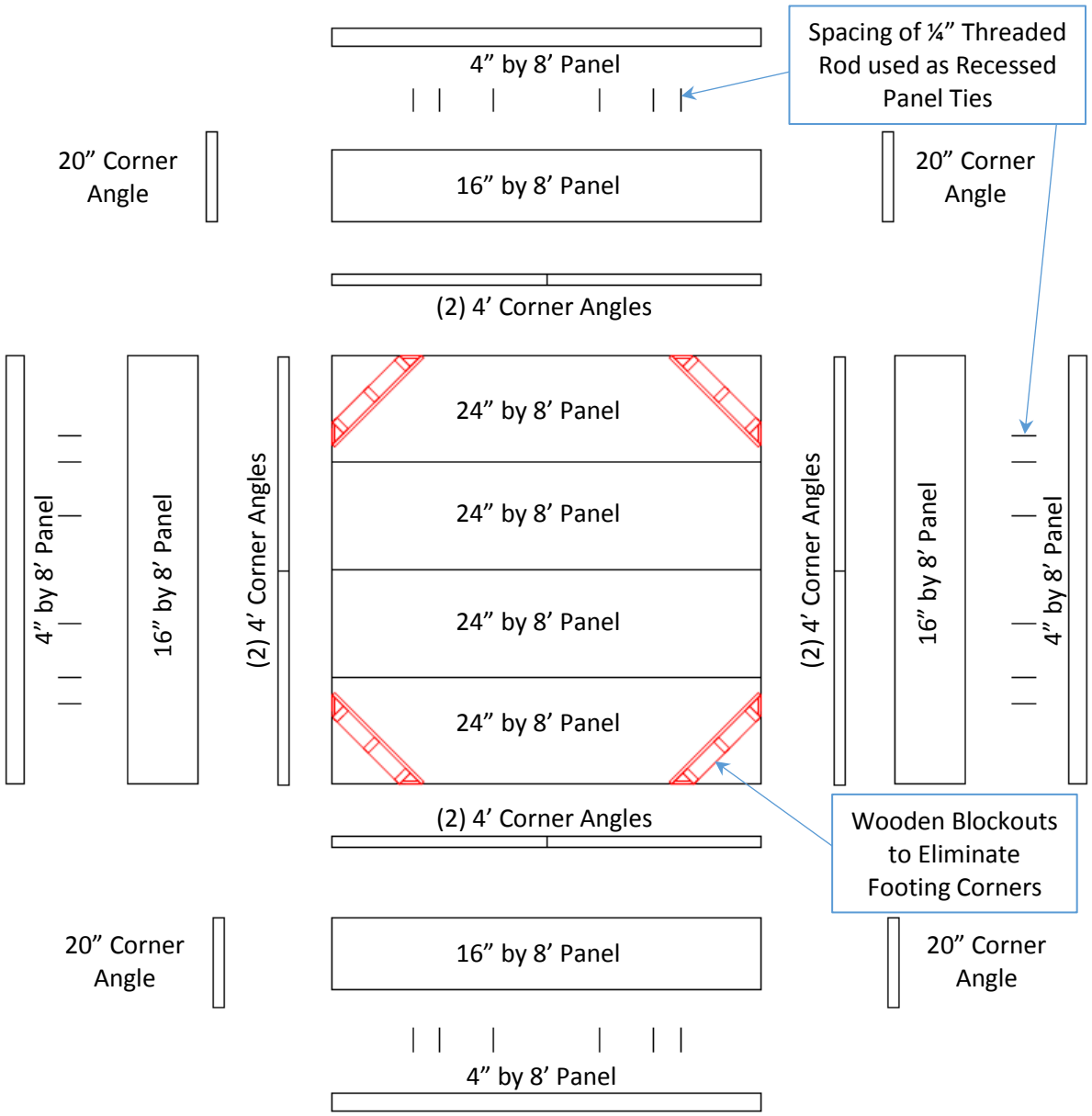

Figure 2-33. Specimen Footing Steel-Ply Formwork

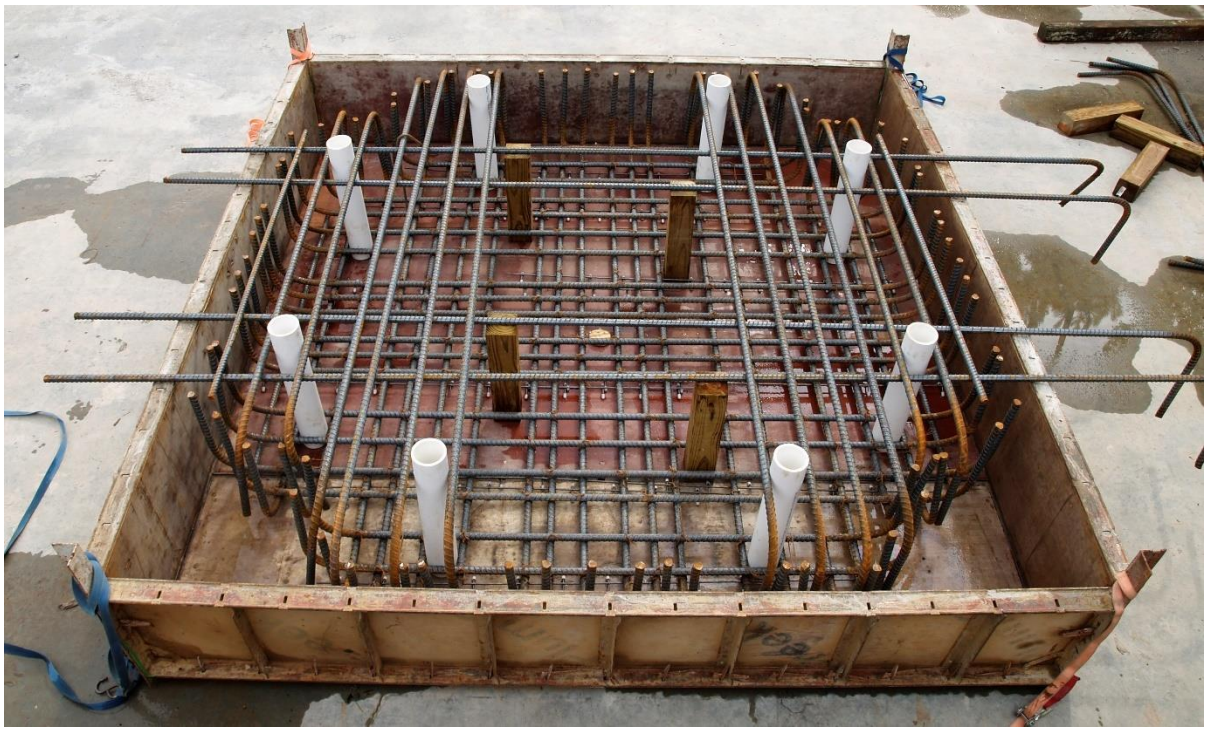

Figure 2-34. Bottom Mat of Steel and Procedure for Holding up the Top Mat of Steel

Figure 2-35. Specimens on Casting Slab Prior to Footing Casting

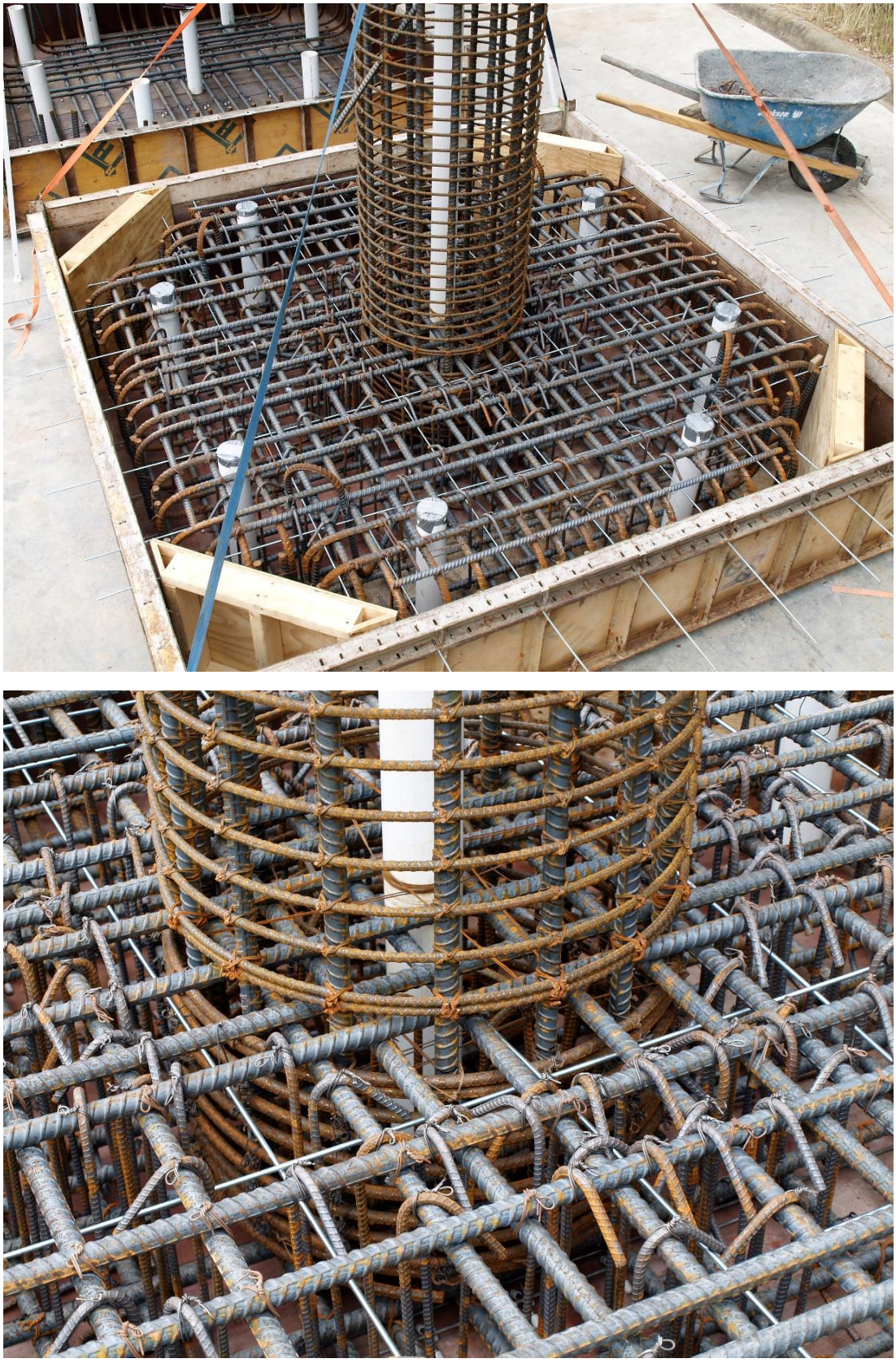

Figure 2-36. Footing and Joint Reinforcement

Figure 2-37. Footings on the Day of Casting

Figure 2-38. Removal of Footing Forms and Application of Foam Cover Concrete Blockouts

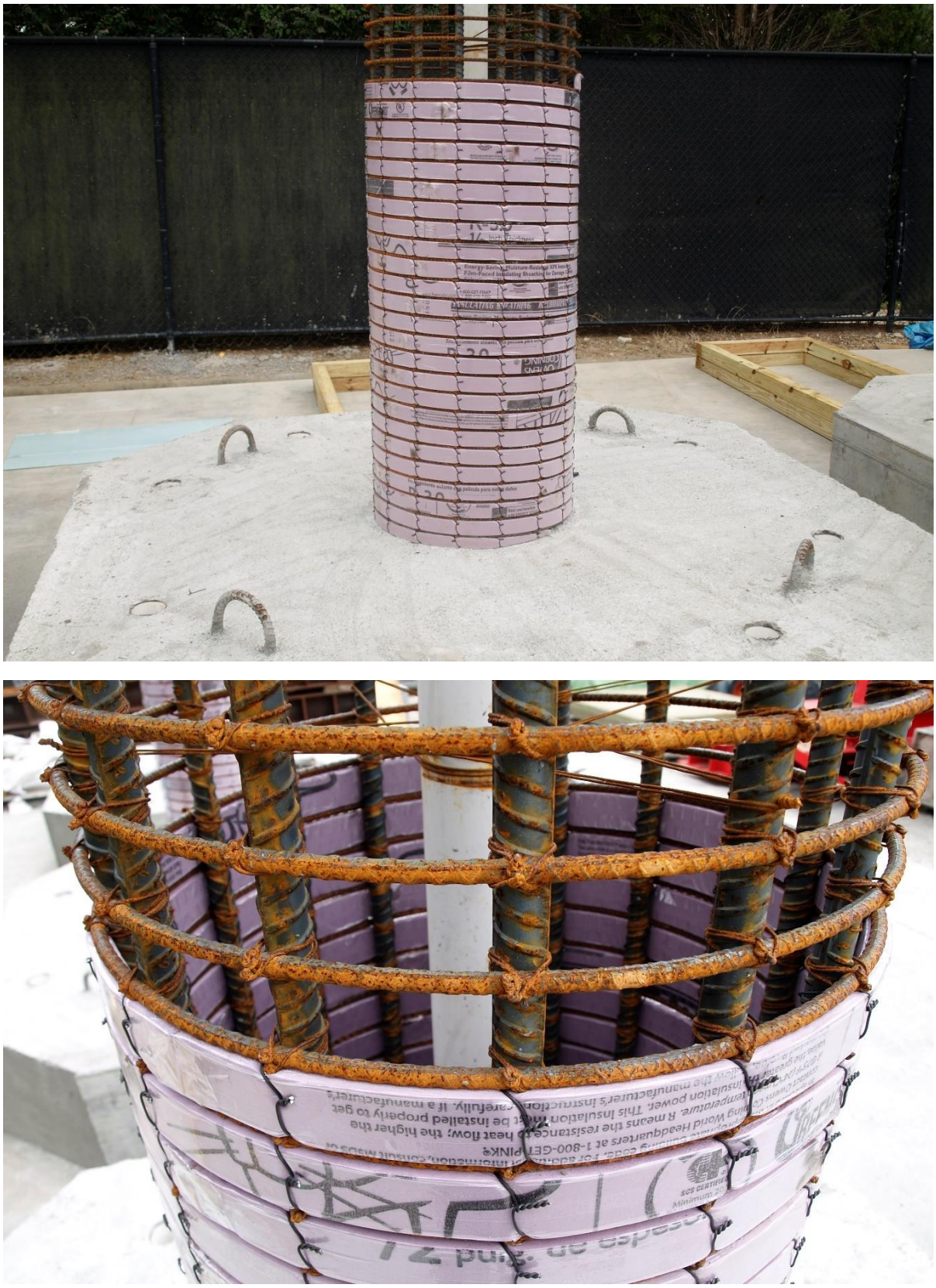

Figure 2-39. Inside Layer of ½" Foam Blockouts Placed between Spiral Layers

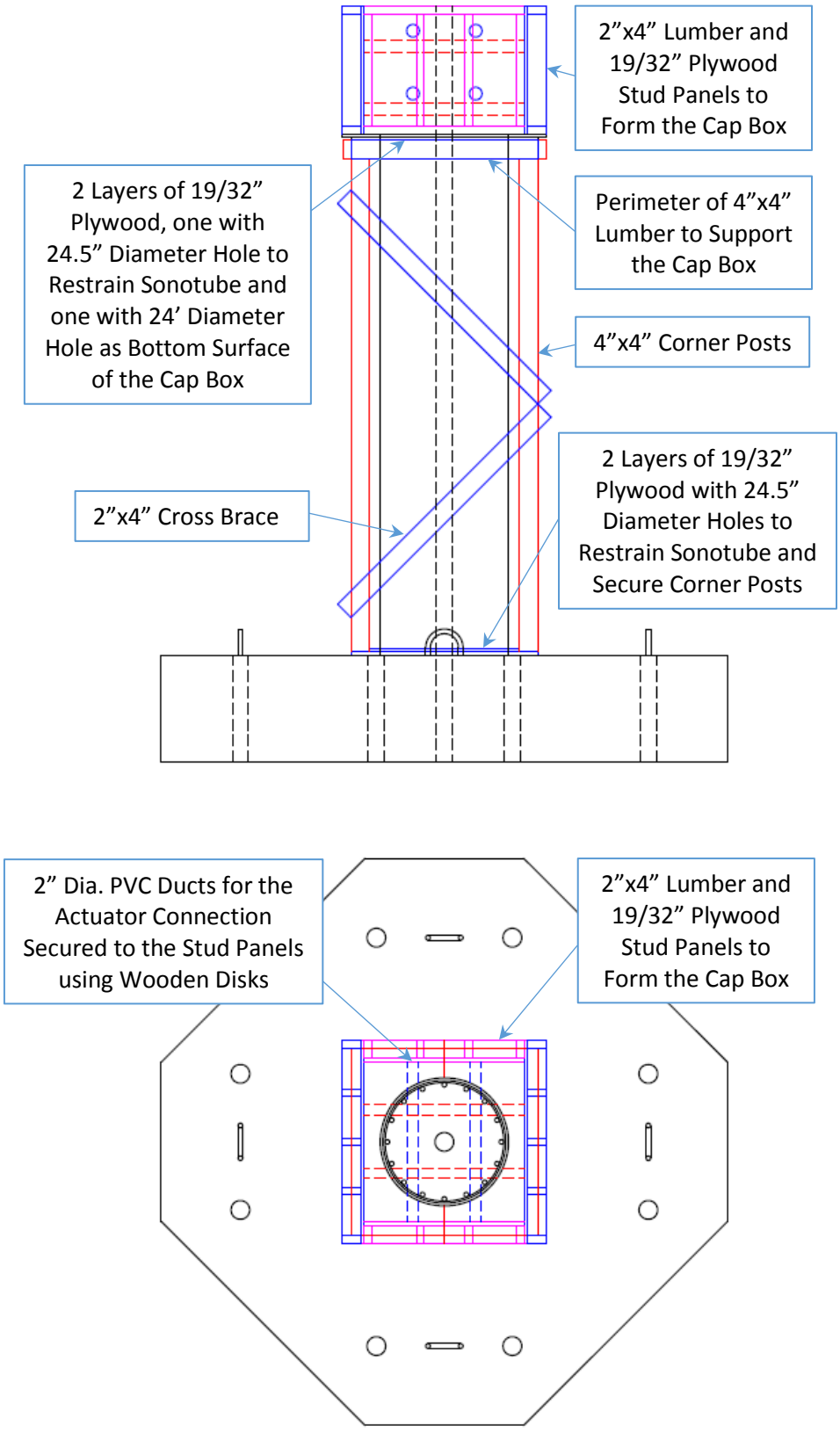

Figure 2-40. Column Stabilization and Cap Formwork

Figure 2-41. Column Stabilization and Cap Formwork

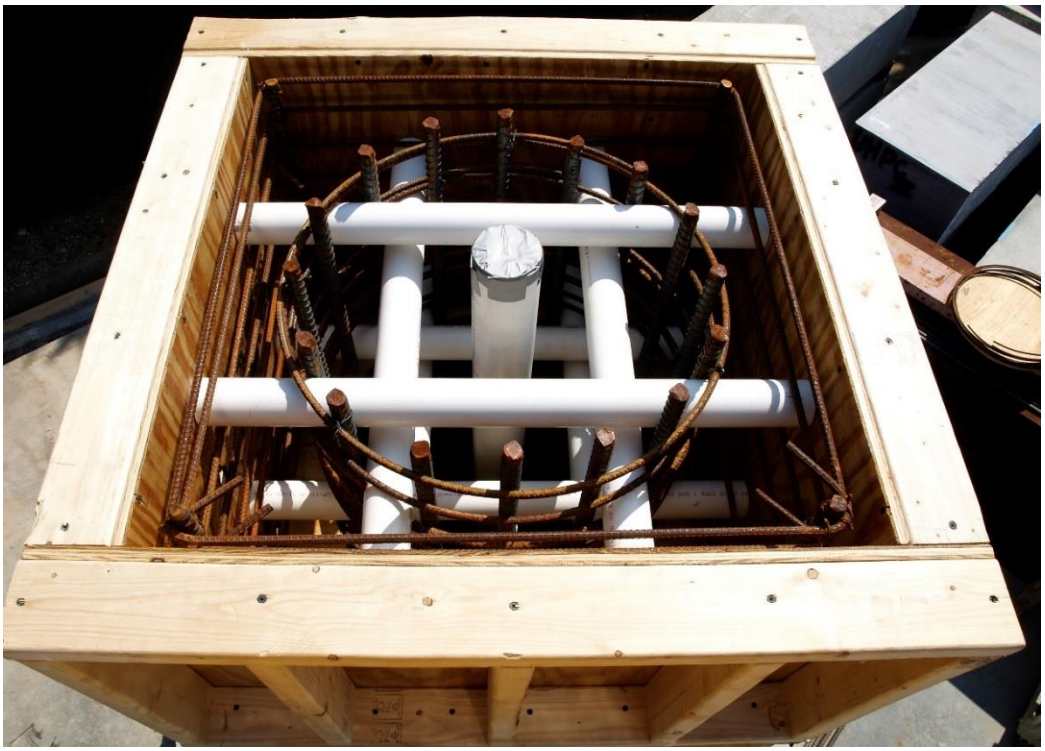

Figure 2-42. Cap Reinforcement

Figure 2-43. Column Concrete Placed and Consolidated in Multiple Lifts

Figure 2-44. Completed Specimens

Figure 2-45. Lifting the Specimens with Four Hydraulic Jacks and HSS Spreader Beams

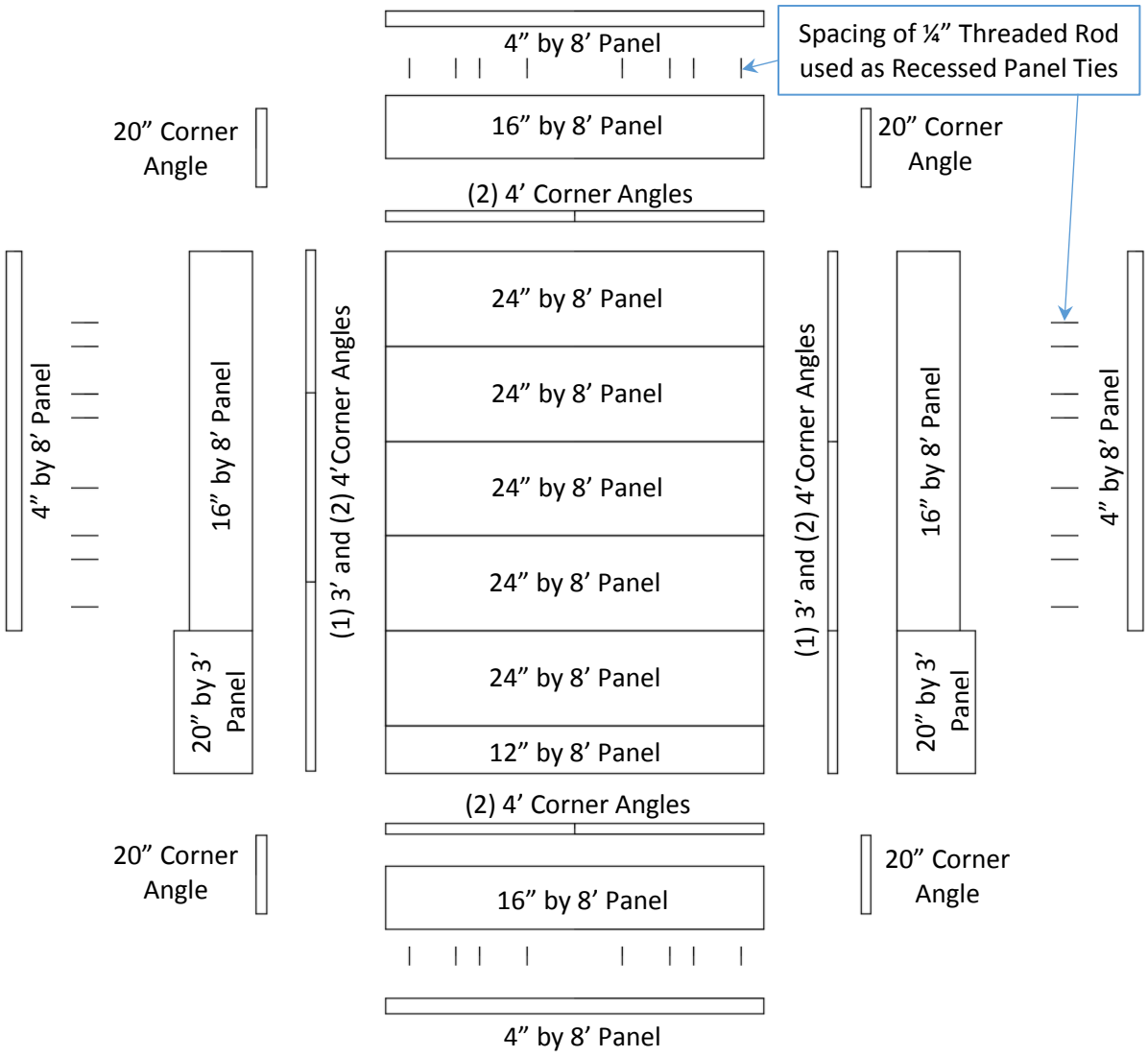

Figure 2-46. Secondary Footing Steel-Ply Formwork

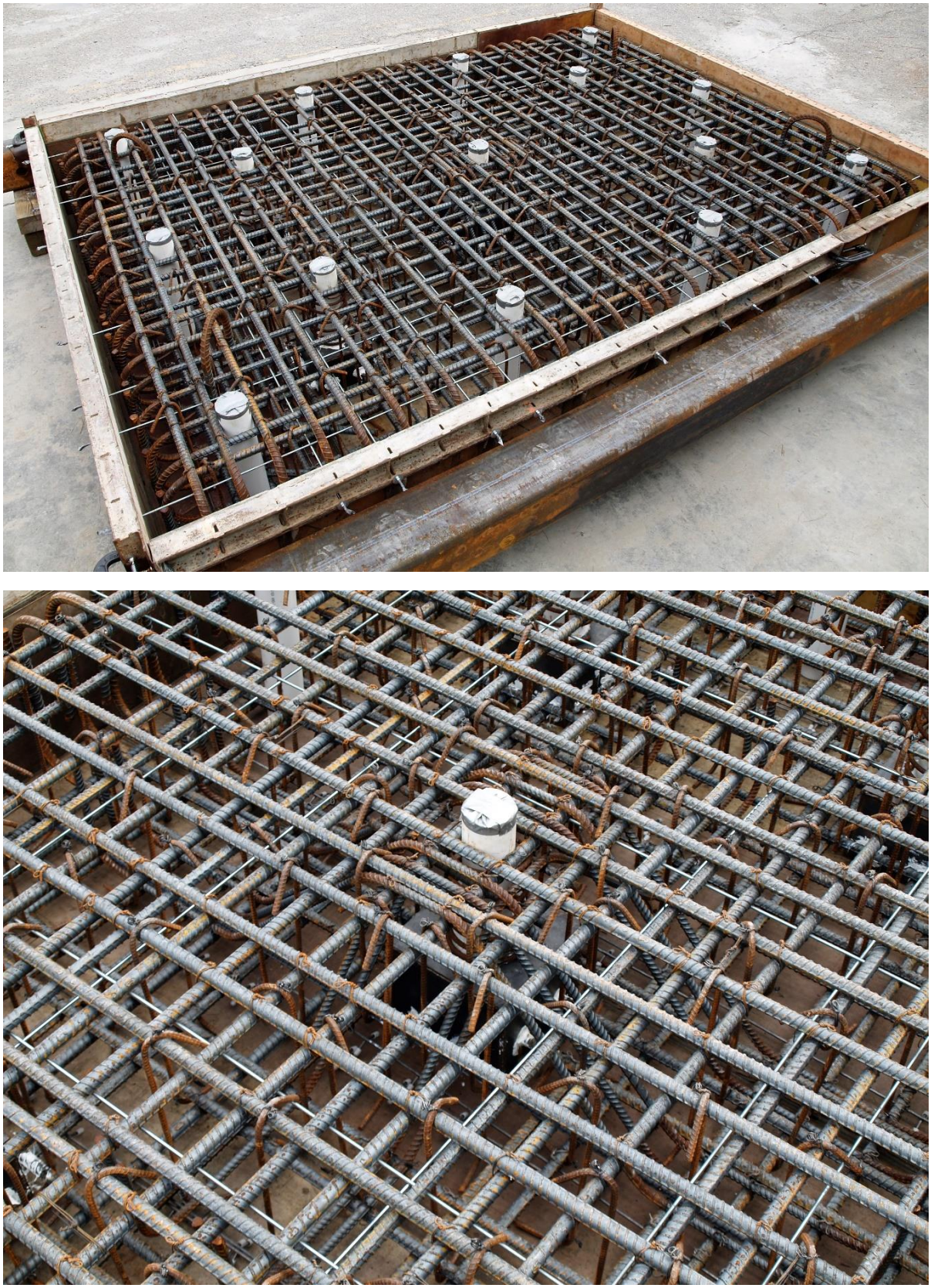

Figure 2-47. Secondary Footing Details and Additional Steel for Center Axial Hole

Figure 2-48. Casting and Curing of the Secondary Footing

Actuator Control

A top view of the test setup depicting the initial actuator configuration and coordinate system are shown in Figure 2-52. An extension or contraction of the actuator leads to a change in length between actuator pivot points. The specimen loading cap, located at the top of the column, and the two actuator knuckles behave as a rigid body, therefore the global displacements X-Y at the center of the loading cap are equal to the displacements at the pivot points of the actuator knuckles. Thus, the deformed geometry of the actuator is in terms of the initial length L_i and the two legs of a 45-45-90 triangle formed in the X-Y directions of the global coordinate system. Each of these legs have an initial length of $\left(a = L_i\sqrt{2}/2\right)$.

A diagram depicting the deformed geometry of the actuator system with the specimen under a generalized displacement (x, y) is shown in Figure 2-53. The body of the horizontal actuators is omitted for clarity, and instead the straight line geometry between actuator pivot points is presented. With the specimen at zero displacement, the initial length between actuator pivot points was $L_i = 129.36"$, which formed two equal legs of length $a = 91.47"$ in the X and Y directions. Under this configuration, the actuators had a 23.14” positive and a 16.86” negative displacement capacity. It was expected that the displacement demands would not exceed 10”. A closer view of the lateral actuators appears in Figure 2-49. The top and side orientations for the actuator knuckles share a central pivot point. The pivot of the actuator knuckle in the top orientation is limited to 8°, allowing for a circular displacement orbit of $[L_i \tan(8^o) = 18.18"]$, which exceeds the negative displacement capacity of the actuators. Based on the fiber analysis presented in the following chapter, the rotations about the horizontal axis for the actuator knuckle connecting to the top of the specimen generated demands exceeding 8° at an upper bound to the expected displacement capacity, requiring the knuckle orientation shown in Figure 2-52. While not in use, the actuators were tied back to the strong wall with the wall plate knuckle rotated inwards by 8°, resulting in the geometry shown in Figure 2-55.

Based on the deformed geometry presented in Figure 2-53, the final length of actuators one and two under a generalized displacement (x, y) can be found using Eqn 2-22 and Eqn 2-23, respectively. The relative change in actuator stroke to go from a current displacement (x_c, y_c) to a final dispalcement $(x_\mathrm{f}, y_\mathrm{f})$ is can be accessed with Eqn 2-24. Since the specimens are ran under quasi-static displacement control, the forces in the actuators are those that arise due to the shear in the column. The individual actuator forces, obtained via the integrated load cells, can be translated into component forces in the global coordinate system using the deformed geometry presented in Figure 2-54. Under a generalized (x, y) displacement, the X and Y component forces for actuator one become Eqn 2-25 and Eqn 2-26, while those for actuator two become Eqn 2-27 and Eqn 2-28. The resultant column shear forces in the X and Y directions thus become Eqn 2-29 and Eqn 2-30.

$$L_{1i} = L_{2i} = 129.36"$$ *Initial Actuator Length between Pivot Points* Eqn 2-20

$$a_1 = a_2 = L_i\sqrt{2}/2 = 91.47"$$ *Legs of the 45-45-90 Triangle in the X-Y Directions* Eqn 2-21

$$L_{1f} = \sqrt{(a_1 - x)^2 + (a_1 + y)^2}$$ *Final Length of Actuator #1* Eqn 2-22

$$L_{2f} = \sqrt{(a_2 + x)^2 + (a_2 + y)^2}$$ *Final Length of Actuator #2* Eqn 2-23

$$\Delta_1 = L_{1f} - L_{1c} \text{ and } \Delta_2 = L_{2f} - L_{2c}$$ *Relative Change in Actuator #1 and #2 Stroke to go from current (x_c, y_c) to final (x_f, y_f)* Eqn 2-24

$$F_{1x} = \frac{F_1(a_1 - x)}{\sqrt{(a_1 - x)^2 + (a_1 + y)^2}}$$ *X-Component of Actuator #1 Force* Eqn 2-25

$$F_{1y} = \frac{F_1(a_1 + y)}{\sqrt{(a_1 - x)^2 + (a_1 + y)^2}}$$ *Y-Component of Actuator #1 Force* Eqn 2-26

$$F_{2x} = \frac{F_2(a_2 + x)}{\sqrt{(a_2 + x)^2 + (a_2 + y)^2}}$$ *X-Component of Actuator #2 Force* Eqn 2-27

$$F_{2y} = \frac{F_2(a_2 + y)}{\sqrt{(a_2 + x)^2 + (a_2 + y)^2}}$$ *Y-Component of Actuator #2 Force* Eqn 2-28

$$F_x = F_{2x} - F_{1x}$$ *X-Component of Column Shear Force* Eqn 2-29

$$F_y = F_{1y} + F_{2y}$$ *Y-Component of Column Shear Force* Eqn 2-30

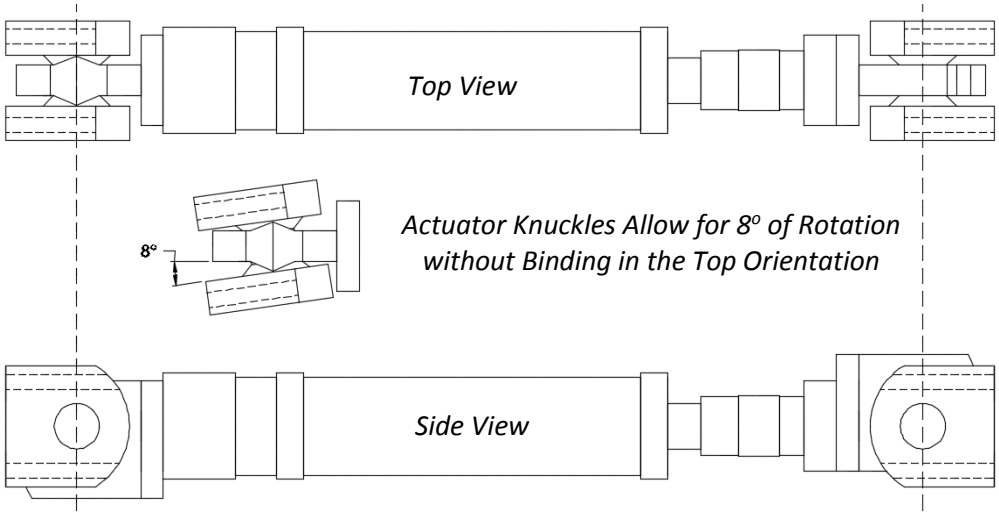

Figure 2-49. Top and Side Views of the Lateral Actuators

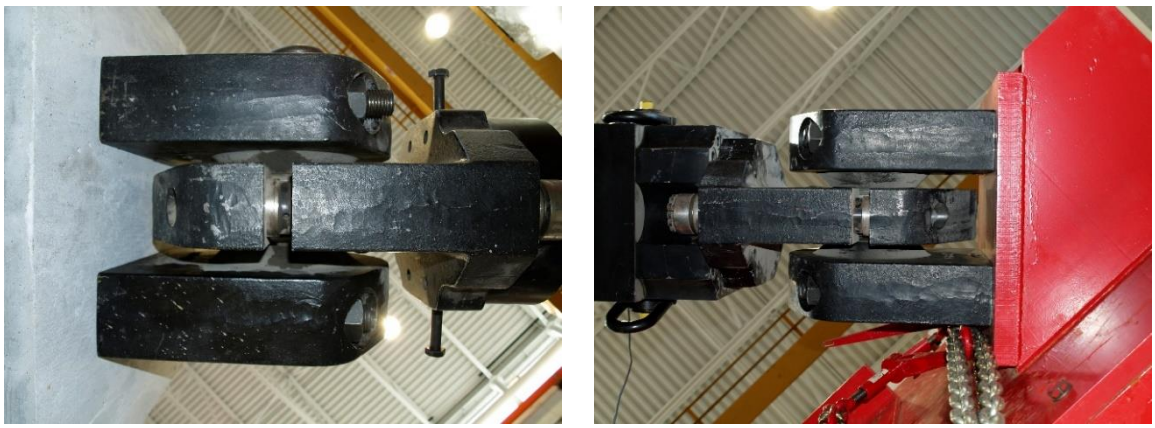

Figure 2-50. Test 1: Actuator and Wall Side Actuator Pivot Points

Verification of Column Displacements using String and Linear Potentiometers

The column displacements obtained via the actuator stroke readings were verified with an array of four string potentiometers placed at the center of loading and an array of linear potentiometers placed at the transfer to main footing interface, see Figure 2-52. SP_1, SP_3, E_h, and W_h were calibrated such that a positive value elongates the string or linear potentiometer, corresponding to a displacement in the X direction. SP_2, SP_4, N_h, and S_h were calibrated such that a positive value shortens the string or linear potentiometer, corresponding to a displacement in the Y direction. The deformed geometry of the four string potentiometers under a generalized (x, y) displacement is depicted in Figure 2-51. This figure also includes the locations of the vertical and horizontal linear potentiometers used to measure horizontal displacements and potential rotations at the transfer and main footing interface.

While testing, the four string potentiometers returned the displacements, Δ_{sp}, measured relative to the origin. Given the initial length of the string potentiometers at the origin, SP_i, the system of equations Eqn 2-31 through Eqn 2-34 can be solved for the displacement (x_{sp}, y_{sp}) which minimizes the error in prediction. The final relative displacement between the footing-column interface and the center of the applied lateral load was computed using Eqn 2-35 and Eqn 2-36. These expressions subtract out the relative horizontal slip at the footing interface and any global footing interface rotations which were extrapolated to the center of the applied load. After inclusion in multiple tests it was found that the column deformation attributed to relative footing interface rotation was negligible, so the vertical footing interface linear potentiometers were left out of future tests. The corrected column displacements (x, y) were processed in real time, which insured that the proper cycle peak displacements were achieved.

$$\sqrt{\left(SP_{1i} + x_{sp}\right)^2 + {y_{sp}}^2} = SP1_i + \Delta_{SP1}$$ *Deformed Geometry of SP1* *Eqn 2-31*

$$\sqrt{\left(SP_{2i} - y_{sp}\right)^2 + {x_{sp}}^2} = SP2_i - \Delta_{SP2}$$ *Deformed Geometry of SP2* *Eqn 2-32*

$$\sqrt{\left(SP_{3i} + x_{sp}\right)^2 + {y_{sp}}^2} = SP3_i + \Delta_{SP3}$$ *Deformed Geometry of SP3* *Eqn 2-33*

$$\sqrt{\left(SP_{4i} - y_{sp}\right)^2 + {x_{sp}}^2} = SP4_i - \Delta_{SP4}$$ *Deformed Geometry of SP4* *Eqn 2-34*

$$y = y_{sp} - (S_h + N_h)/2 - (S_v - N_v)L/h$$ *Final y-direction Displacement* *Eqn 2-35*

$$x = x_{sp} - (W_h + E_h)/2 - (W_v - E_v)L/h$$ *Final x-direction Displacement* *Eqn 2-36*

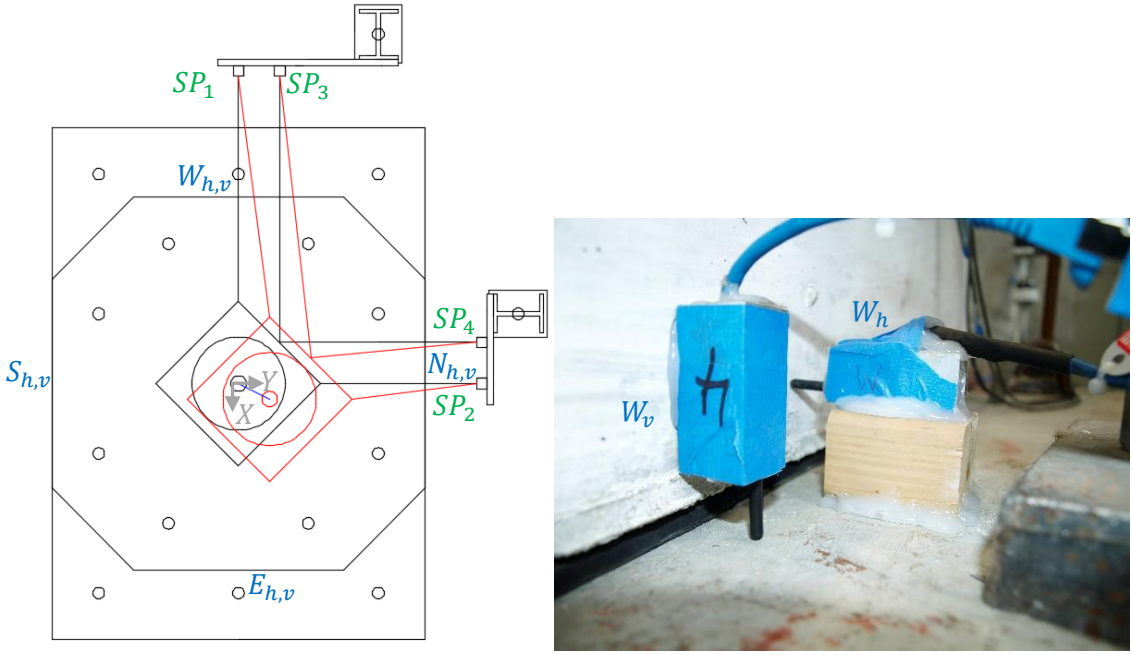

Figure 2-51. Deformed Geometry of the Four Cap String Potentiometers and Footing Interface Linear Potentiometers

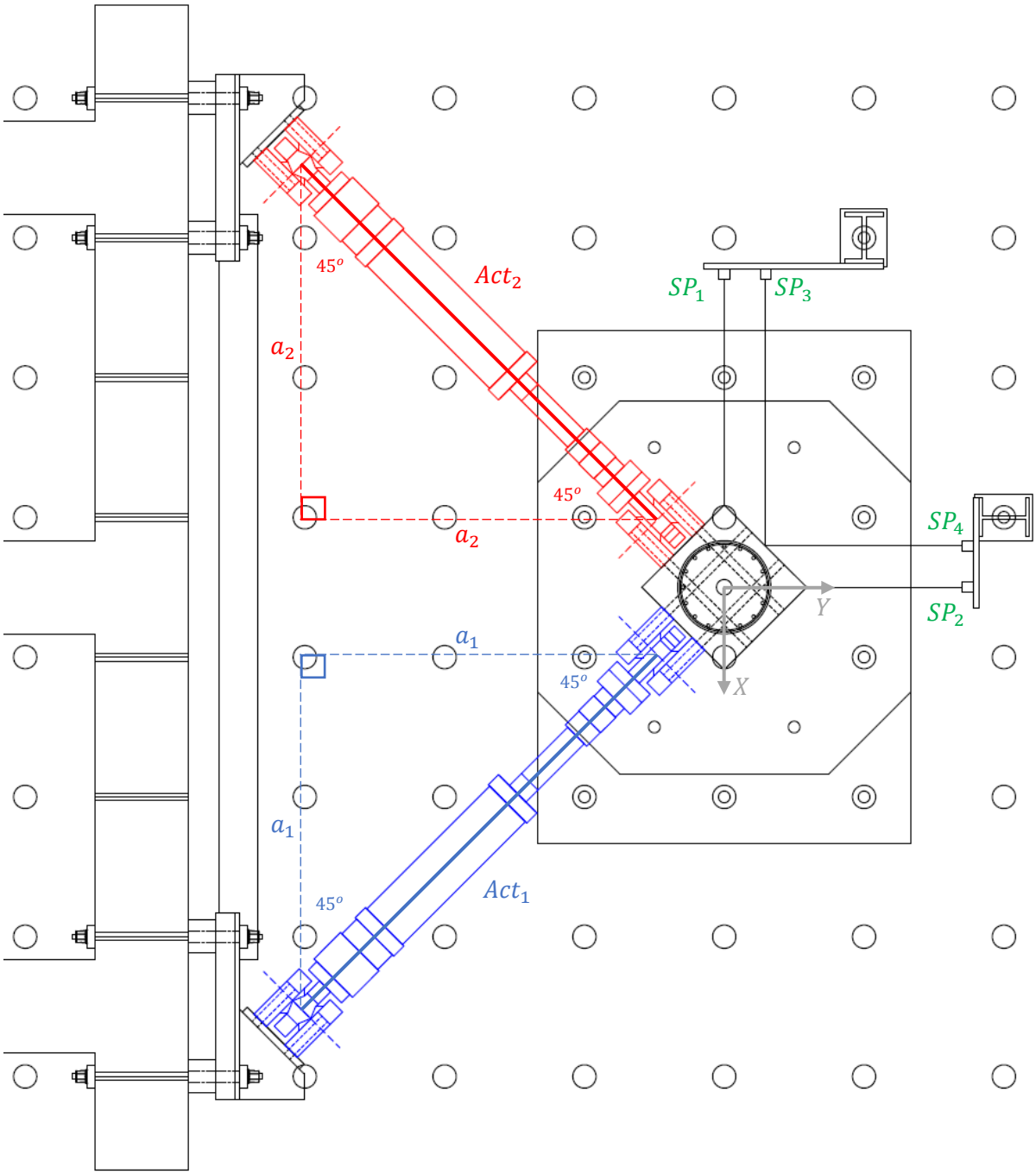

Figure 2-52. Initial Actuator Configuration and Coordinate System

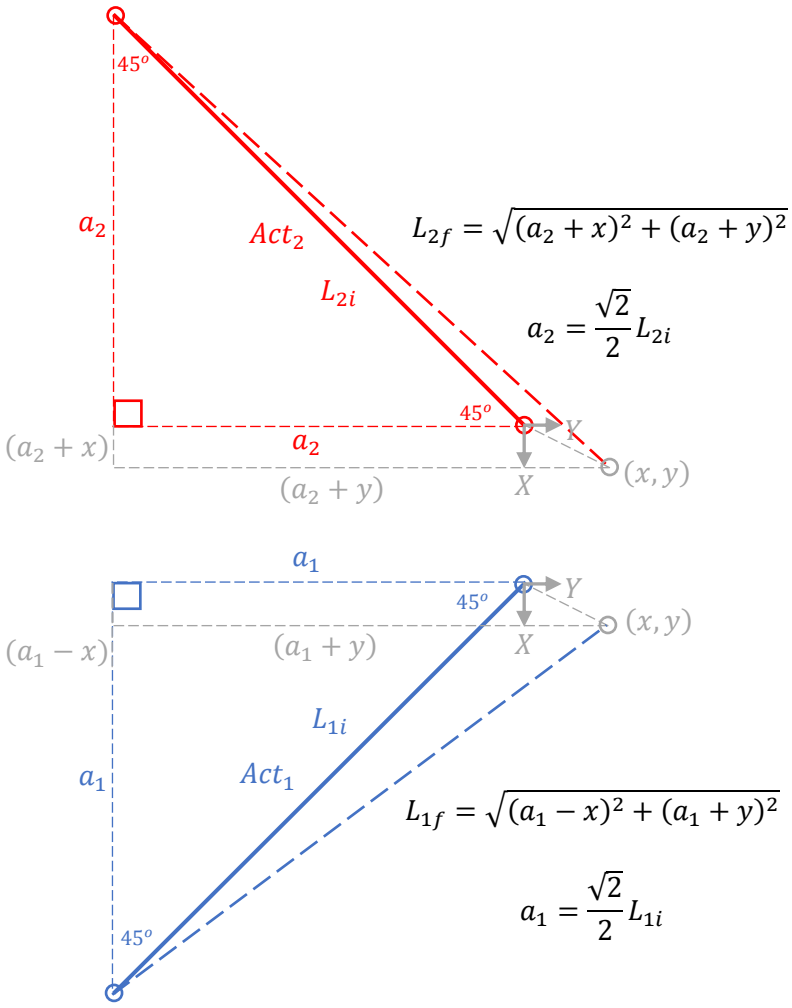

Figure 2-53. Deformed Geometry of the Actuator Setup

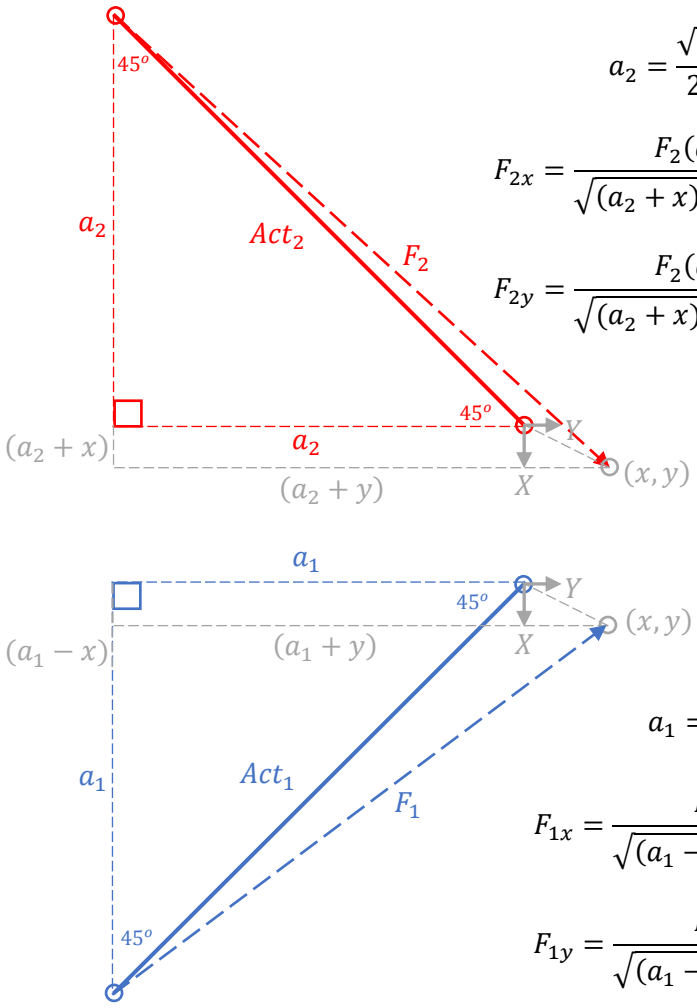

$$a_2 = \frac{\sqrt{2}}{2} L_{2i}$$

$$F_{2x} = \frac{F_2(a_2 + x)}{\sqrt{(a_2 + x)^2 + (a_2 + y)^2}}$$

$$F_{2y} = \frac{F_2(a_2 + y)}{\sqrt{(a_2 + x)^2 + (a_2 + y)^2}}$$

$$a_1 = \frac{\sqrt{2}}{2} L_{1i}$$

$$F_{1x} = \frac{F_1(a_1 - x)}{\sqrt{(a_1 - x)^2 + (a_1 + y)^2}}$$

$$F_{1y} = \frac{F_1(a_1 + y)}{\sqrt{(a_1 - x)^2 + (a_1 + y)^2}}$$

Figure 2-54. Actuator Global Force Components

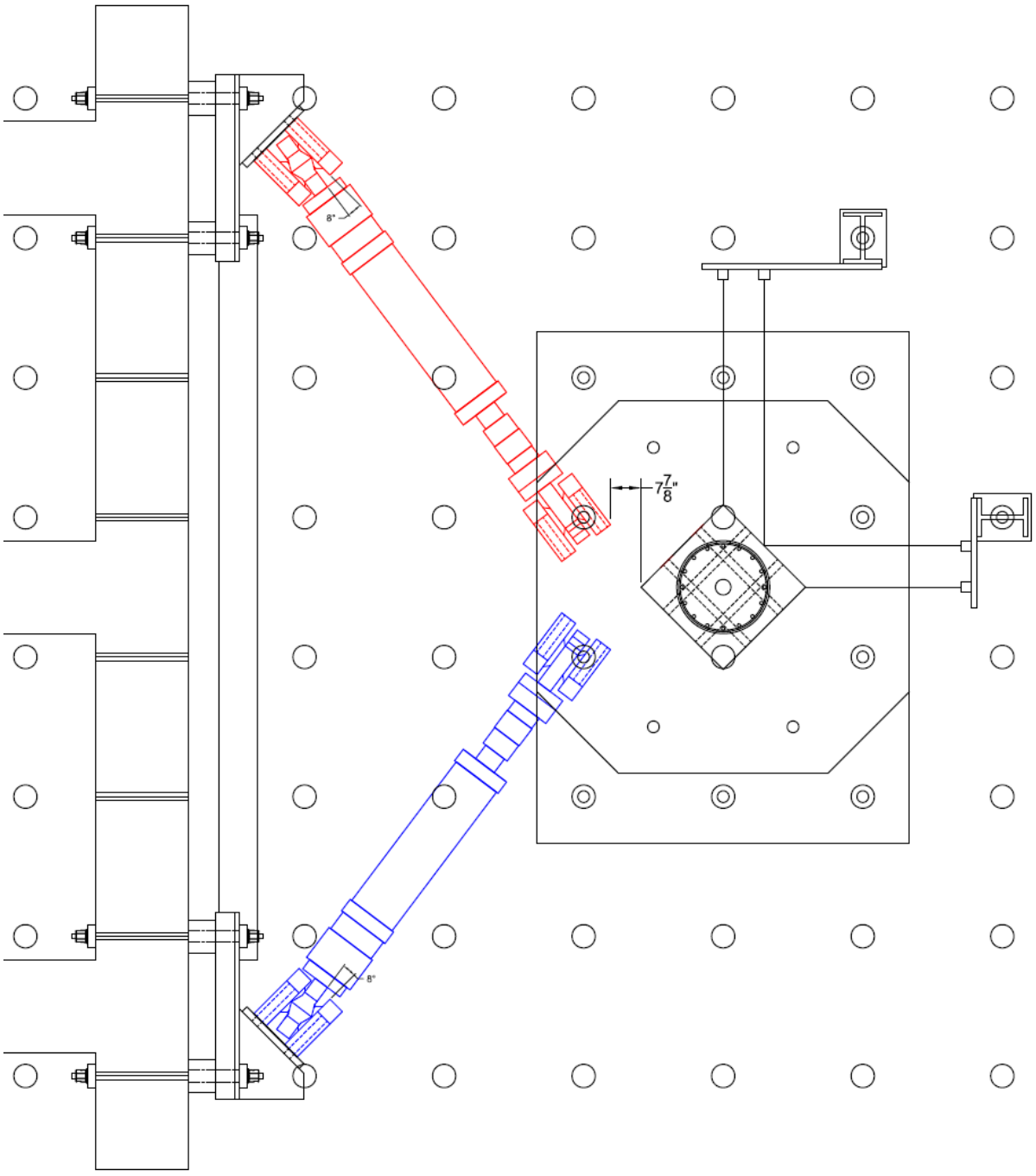

Figure 2-55. Geometry of Retracted Actuators Tied Back to the Strong Wall While Not in Use

Method of Axial Load Application

A self-regulating axial load system was using two hydraulic jacks in a closed system with a force controlled uniaxial testing machine to maintain a constant axial load. First, the uniaxial testing machine was brought in displacement control to center stroke so it could displace 3” in either direction during testing. The top platen of the uniaxial testing machine was lowered to around 4” above the top of the 200 kip hydraulic jack. Similarly, the nut over the unbonded post-tensioning bar was placed around 4” above the top of the jack. A hydraulic line was attached to the pressure sides of the two double acting jacks. The return sides of the double acting jacks were left open with hydraulic reservoirs. A hydraulic pump was used to apply pressure to lines connecting the two jacks until the specified axial load was reached on the uniaxial testing machine and verified using the load cell placed above the column. Once the target axial load was reached, the uniaxial testing machine was switched to force control to maintain this load during the test. Based on the column deformation, the uniaxial testing machine would elongate or contract the hydraulic jack to maintain a constant force, which in turn influenced the pressure in the closed hydraulic system, replicating this change above the specimen. Throughout testing, the axial loads were recorded using the load cell placed above the specimen.

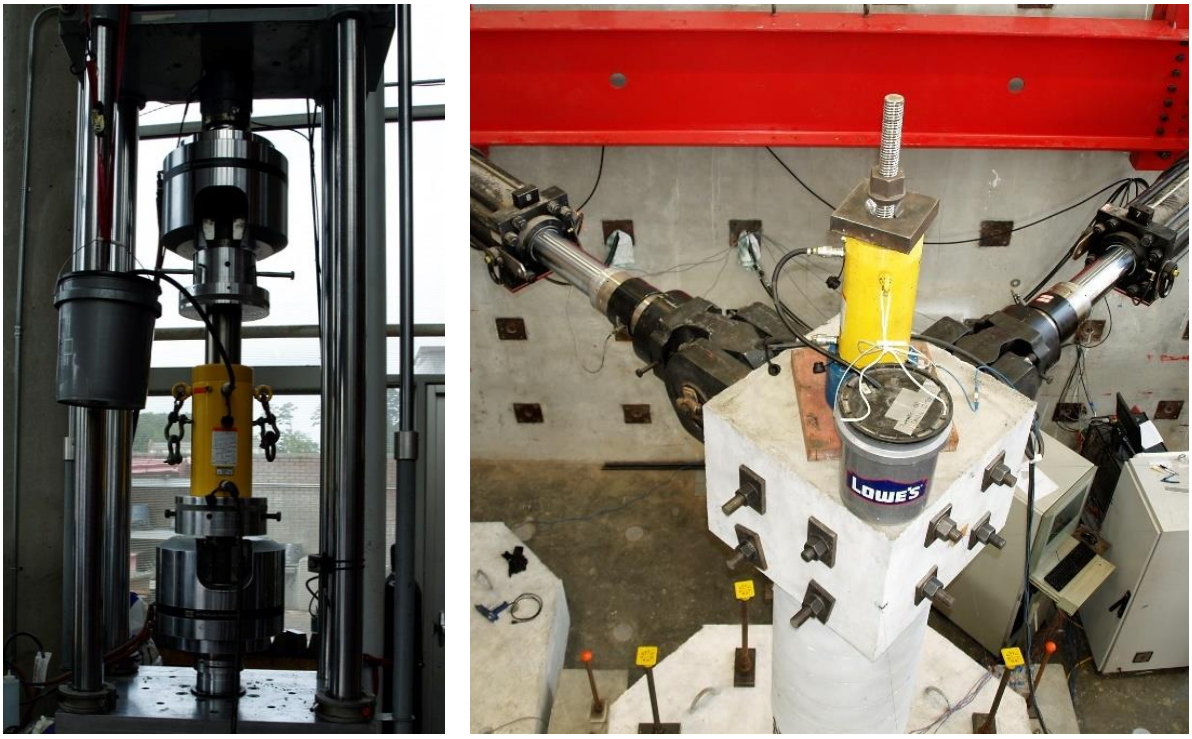

Figure 2-56. Self-Regulating Axial Load System

Chapter 3 - Material Properties and Response Prediction

Both monotonic moment-curvature analysis and fiber modeling in Opensees were used to predict the response of the specimens prior to running the tests. As discussed previously, moment-curvature analysis was used in the initial design process for the specimens. After construction, the material properties for the concrete and reinforcing steel were accessed and more detailed analysis were conducted prior to the tests. The following section provides an overview of the tested material properties and presents a comparison to the models utilized in the respective analysis techniques.

Reinforcing Steel Properties for Tests 1-6

Tensile tests were performed on six column longitudinal bars and four straightened out segments of the spiral reinforcement. Each specimen came from separate bars or spiral coils, such that the consistency of material properties across the heat could be verified. The results for the #7 Gr60 A706 column reinforcement tensile tests are summarized in Table 3-1, while the results for the #3 Gr60 A706 spiral appear in Table 3-2. The length between grips for both bar sizes was $(8" + 4d_{bl})$, resulting in 11.5" for the #7 bars and 9.5" for the #3 bars. The bars were instrumented with three 2" Optotrak gauge lengths and a centrally placed 2" extensometer. The extensometer shared the same location of the middle Optotrak gauge length, see Figure 2-7. A loading rate of 0.075 in/min was used prior to yield, and was later increased to 0.6 in/min after yield.

In the column longitudinal bar property summary, Table 3-1, E_s is the modulus of elasticity and (ε_y, f_y), (ε_h, f_h), and (ε_u, f_u) are the strain and stress at yield, strain hardening, and maximum stress, respectively. These values are evident in the stress-strain response for longitudinal bar Sample 6, shown in Figure 3-1 and Figure 3-2 for high and low strain level comparisons. The results for the three Optotrak gauge lengths and the extensometer are in agreement. After the maximum stress, necking begins, and the results for individual gauge lengths deviate, and only those within the necking region measure the full response, see Figure 3-3.

The column transverse steel samples came from the cut segments of the coiled 23" outside diameter #3 spiral. These segments were initially cold worked to form the required coil diameter, and again cold worked to straighten them out prior to testing. This process eliminated the well-defined yield plateau typical of Gr60 A706 reinforcement, therefore the yield stress was obtained using the 0.2% offset method. In the column transverse steel property summary, Table 3-2, $(\varepsilon_y^{Offset}, f_y)$ are the yield strain and stress obtained via the 0.2% offset method, $(\varepsilon_y = f_y/E_s)$ is the yield strain obtained via a modulus of 29000 ksi, and (ε_u, f_u) are the maximum stress and corresponding strain. The full range of response for the spiral reinforcement appears in Figure 3-4, while the low strain region is highlighted in Figure 3-5. Examples of the 0.2% offset method applied to Samples 3 and 4 appear in Figure 3-6 and Figure 3-7 respectively.

Table 3-1. #7 Column Longitudinal Steel Material Properties for Tests 1-6

Bar Size	Sample	$E_s\ (ksi)$	ε_y	$f_y\ (ksi)$	ε_h	$f_h\ (ksi)$	ε_u	$f_u\ (ksi)$
#7	1	27995	0.00262	71.4	0.01380	71.4	0.10819	97.4
#7	2	28189	0.00258	71.3	0.01400	71.5	0.11247	98.2
#7	3	28269	0.00256	70.8	0.01210	71.2	0.10660	98.9
#7	4	28299	0.00257	71.3	0.01340	71.4	0.12106	98.7
#7	5	28137	0.00253	71.0	0.01385	71.2	0.10491	97.1
#7	6	29290	0.00241	71.3	0.01390	71.3	0.11274	97.3
#7 Average		28363	0.00254	71.2	0.01351	71.3	0.11099	97.9

Table 3-2. #3 Column Transverse Steel Material Properties for Tests 1-6

Bar Size	Sample	ε_y^{Offset}	$\varepsilon_y = f_y/E_s$	$f_y\ (ksi)$	ε_u	$f_u\ (ksi)$
#3	1	0.00430	0.00233	67.7	0.09649	105.7
#3	2	0.00446	0.00233	67.6	0.09820	105.9
#3	3	0.00467	0.00233	67.5	0.10322	105.3
#3	4	0.00450	0.00232	57.4	0.09450	105.5
#3 Average		0.00448	0.00233	67.6	0.09810	105.6

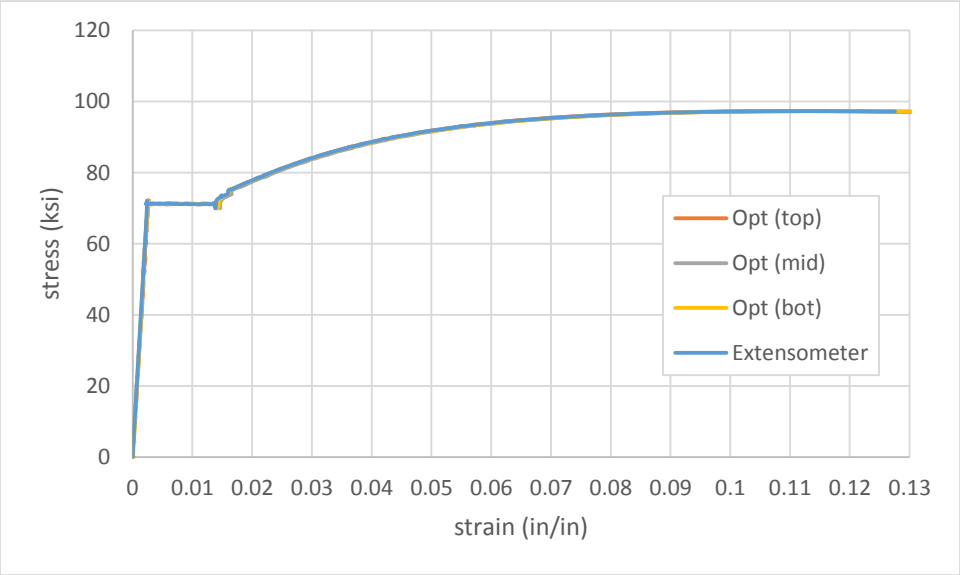

Figure 3-1. Tensile Test for #7 Longitudinal Bar (Sample 6) from Tests 1-6, High Strain Measurement Comparison

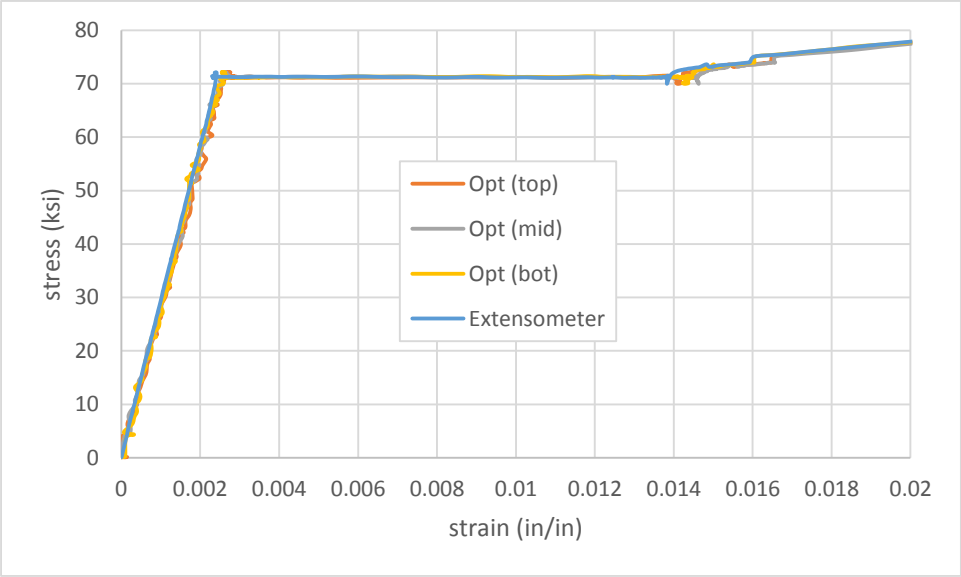

Figure 3-2. Tensile Test for #7 Longitudinal Bar (Sample 6) from Tests 1-6, Low Strain Measurement Comparison

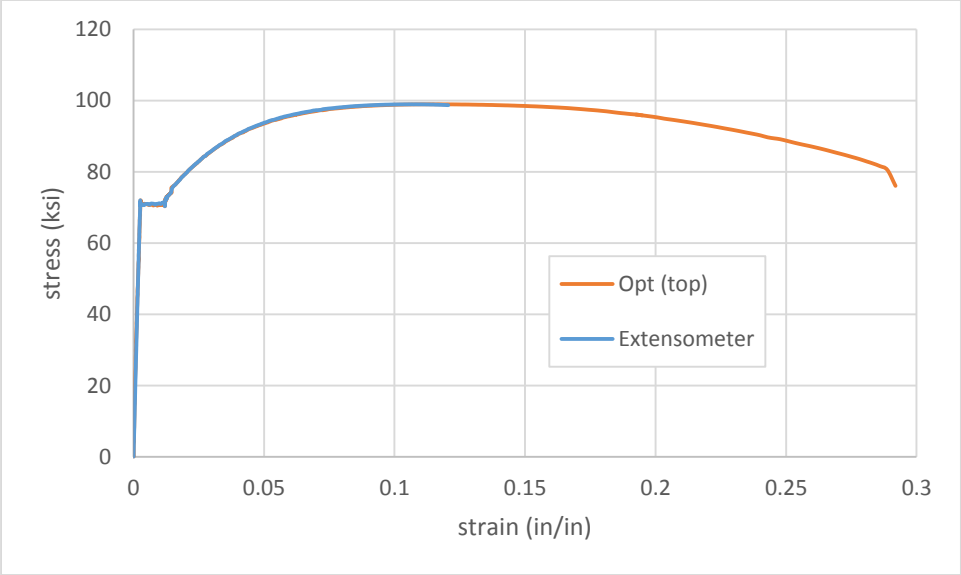

Figure 3-3. Tensile Test for #7 Longitudinal Bar (Sample 3) from Tests 1-6, Comparison Including Necking

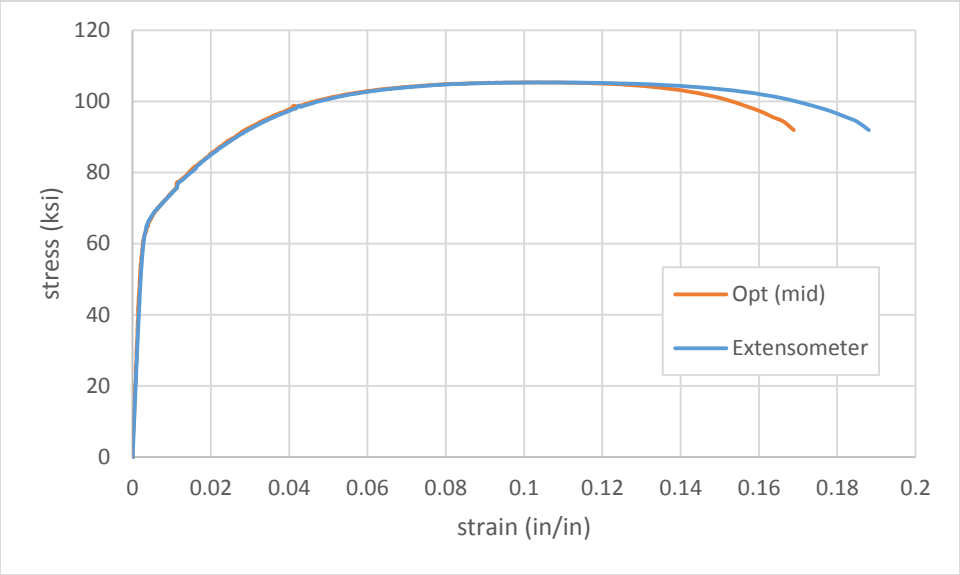

Figure 3-4. Tensile Test for #3 Spiral (Sample 4) from Tests 1-6, Comparison Including Necking

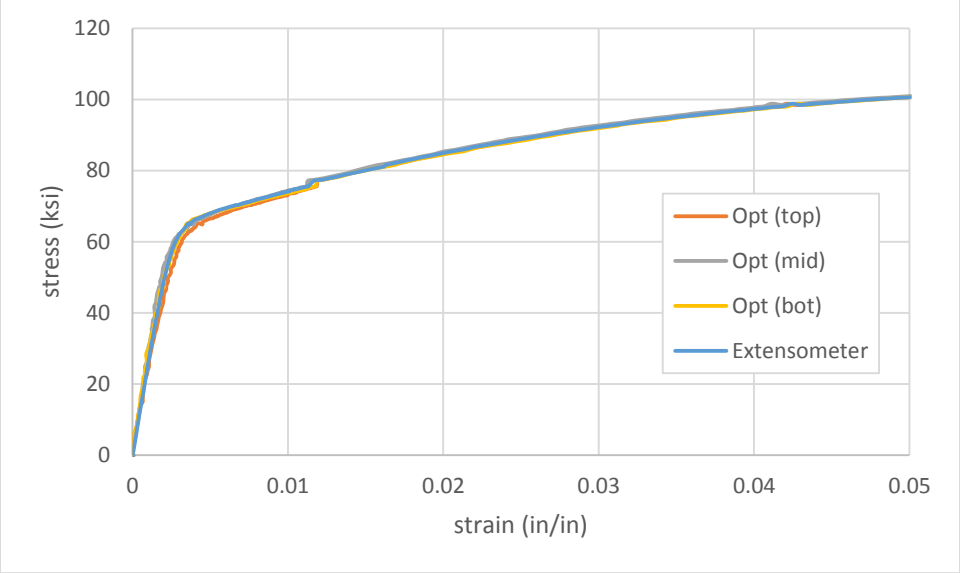

Figure 3-5. Tensile Test for #3 Spiral (Sample 4) from Tests 1-6, Low Strain Comparison

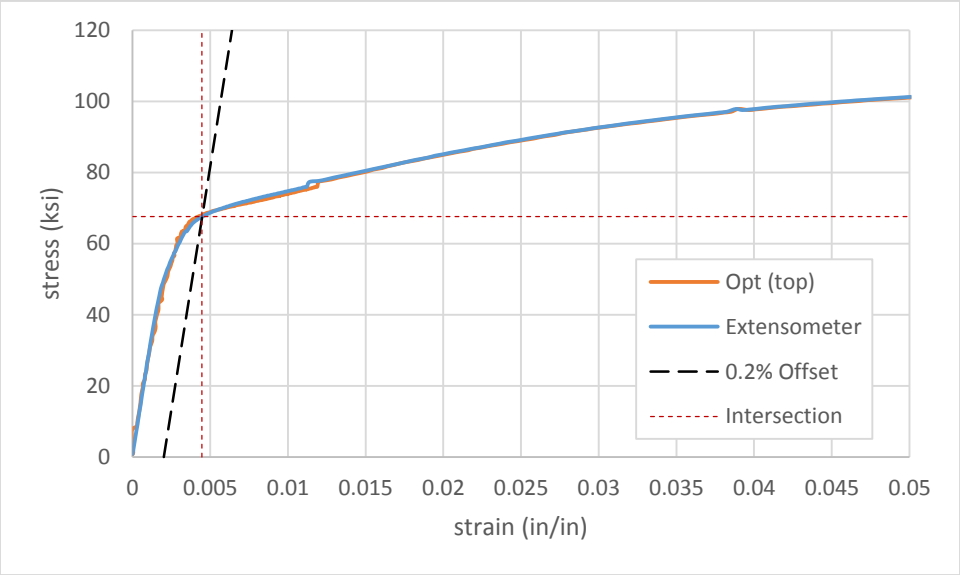

Figure 3-6. Tensile Test for #3 Spiral (Sample 3) from Tests 1-6, 0.2% Offset Method

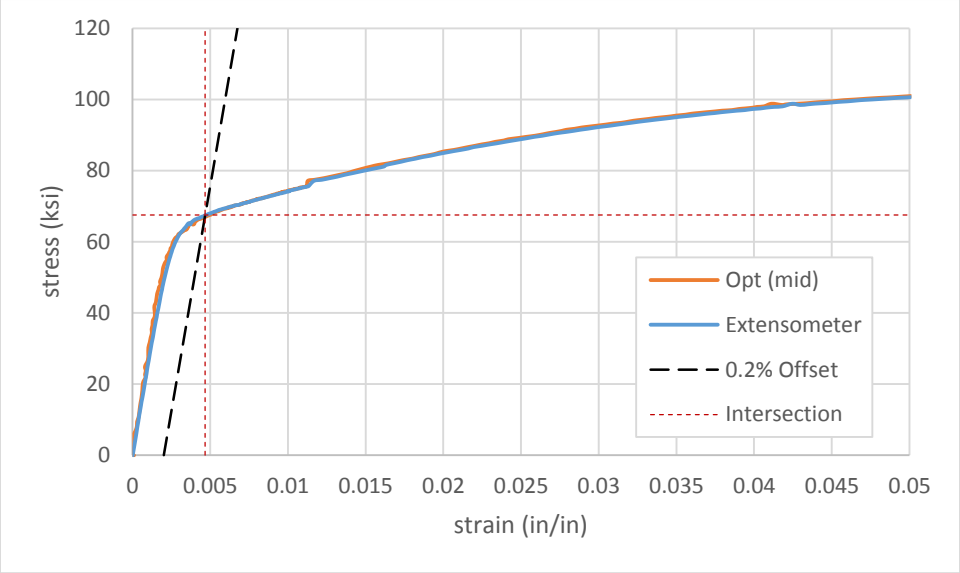

Figure 3-7. Tensile Test for #3 Spiral (Sample 4) from Tests 1-6, 0.2% Offset Method

Reinforcing Steel Properties for Tests 7-12

Following the same techniques described in the previous section, material tests were conducted for the longitudinal and transverse steel of Tests 7-12. The results for the #7 and #6 Gr60 A706 column reinforcement tensile tests are summarized in Table 3-3 and Table 3-4, while the results for the #3 Gr60 A706 spiral appear in Table 3-5. Sample tensile stress-strain curves for the reinforcement are depicted in Figure 3-8 through Figure 3-11.

Table 3-3. #7 Column Longitudinal Steel Material Properties for Tests 7-12

Bar Size	Sample	$E_s\ (ksi)$	ε_y	$f_y\ (ksi)$	ε_h	$f_h\ (ksi)$	ε_u	$f_u\ (ksi)$
7	1	24774	0.00292	69.5	0.01160	69.5	0.11182	95.86
7	2	25804	0.00285	70.0	0.01150	70.0	0.11615	97.21
7	3	27016	0.00265	70.0	0.01000	70.0	0.10675	96.79
7	4	26256	0.00284	70.0	0.01050	70.0	0.10564	96.96
7	5	26395	0.00272	70.1	0.01255	70.1	0.11462	96.98
7	1-cyclic	26955	0.00256	68.9	0.01070	68.9	0.11646	96.15
7	2-cyclic	28256	0.00241	68.9				
#7 Average		26494	0.00271	69.63	0.01114	69.75	0.11191	96.66

Table 3-4. #6 Column Longitudinal Steel Material Properties for Tests 7-12

Bar Size	Sample	$E_s\ (ksi)$	ε_y	$f_y\ (ksi)$	ε_h	$f_h\ (ksi)$	ε_u	$f_u\ (ksi)$
6	1	25047	0.00300	69.2	0.00800	70.0	0.11159	99.45
6	2	24375	0.00300	68.2	0.00800	69.2	0.10944	99.12
6	3	26934	0.00264	72.0	0.01200	72.0	0.10944	98.33
6	4	26501	0.00274	70.8	0.01025	70.8	0.12035	98.77
6	5	26426	0.00287	71.7	0.01200	71.7	0.11139	98.39
6	1-cyclic	25597	0.00280	69.0	0.00850	69.0	0.12349	98.55
6	2-cyclic	26607	0.00278	71.4	0.01130	71.4	0.12906	98.15
#6 Average		25927	0.002832	70.33	0.01001	70.59	0.11639	98.68

Table 3-5. #3 Column Transverse Steel Material Properties for Tests 7-12

Bar Size	Sample	ε_y^{Offset}	$f_y\ (ksi)$	$E_s\ (ksi)$	$\varepsilon_y = f_y/E_s$	ε_u	$f_u\ (ksi)$
3	1	0.00385	64.50	34970	0.002224	0.117306	93.98
3	2	0.00494	62.65	21309	0.002160	0.128041	93.30
3	3	0.00415	64.40	30014	0.002221	0.109760	94.29
3	4	0.00370	65.40	38248	0.002255	0.121811	93.94
3	5	0.00426	62.50	27566	0.002155	0.12837	92.71
#3 Average		0.00418	63.89	30421	0.002203	0.121058	93.64

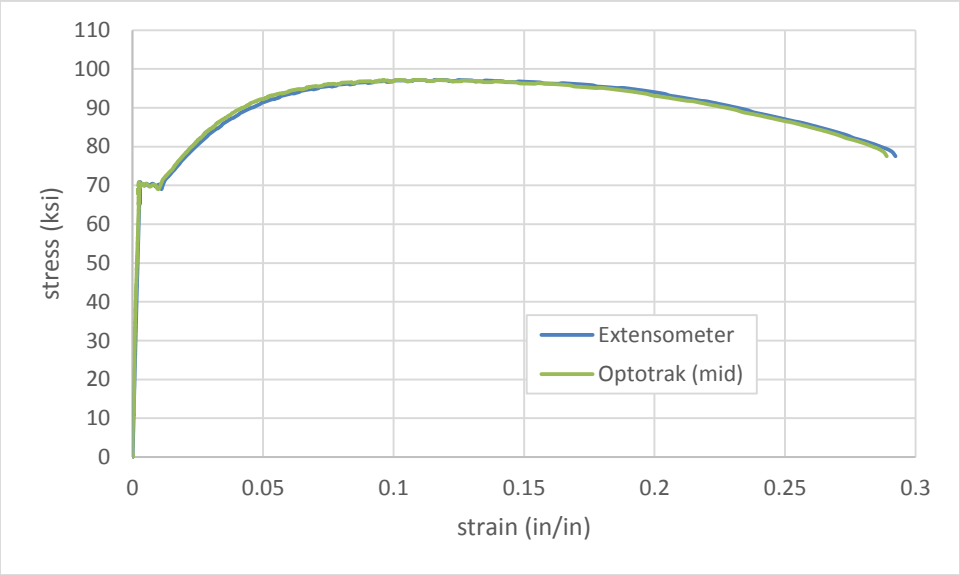

Figure 3-8. Tensile Test for #7 Longitudinal Bar from Columns 7-12

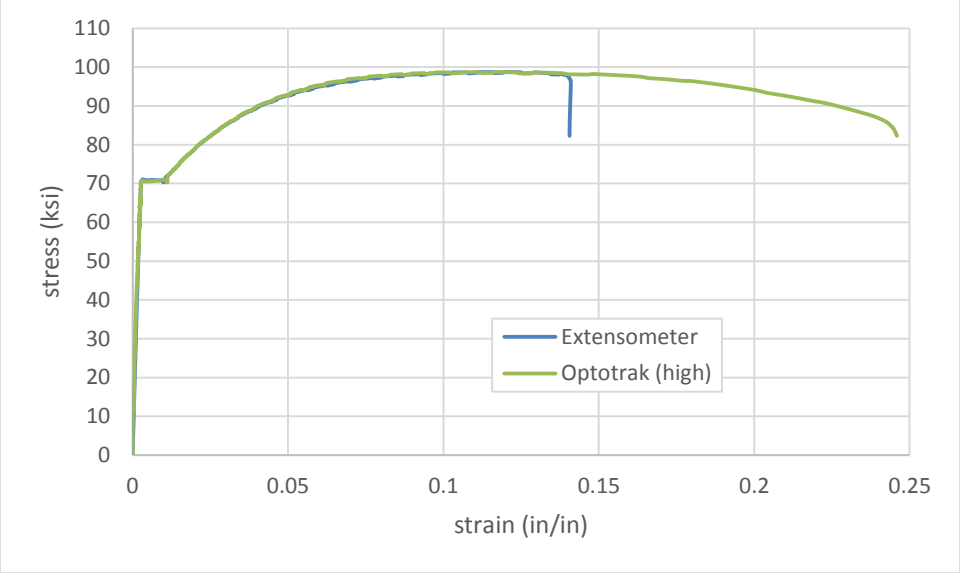

Figure 3-9. Tensile Test for #6 Longitudinal Bar from Columns 7-12

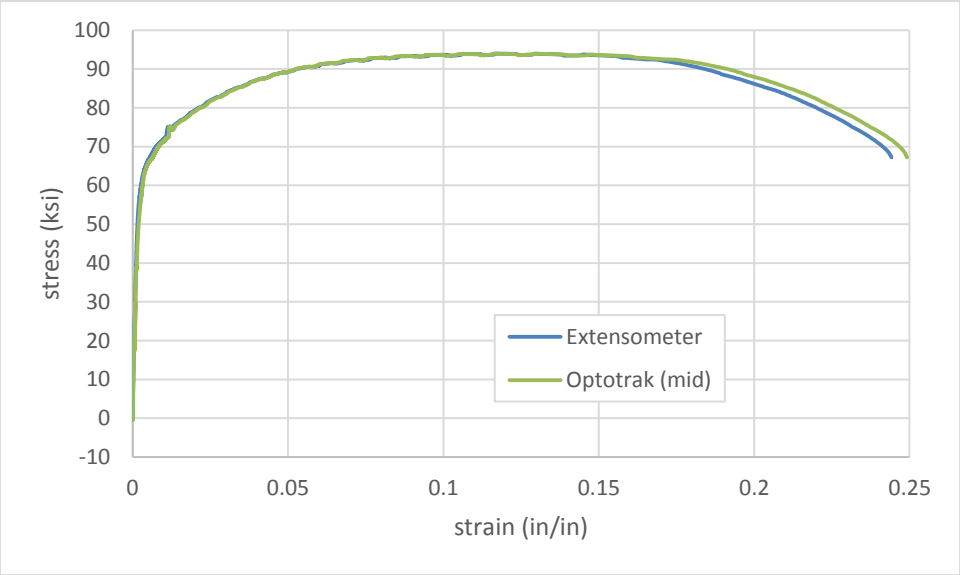

Figure 3-10. Tensile Test for #3 Spiral from Tests 7-12

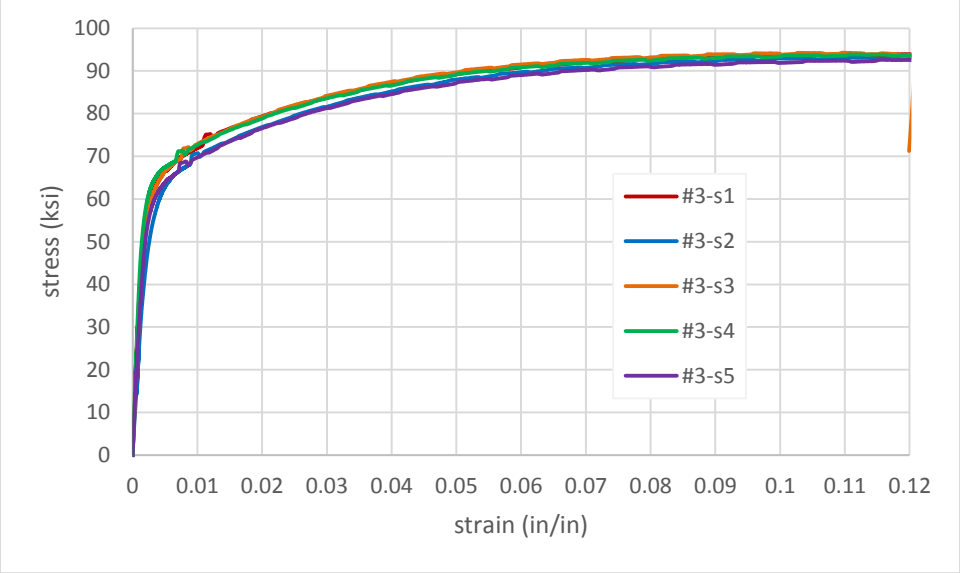

Figure 3-11. Tensile Tests for #3 Spirals from Tests 7-12

Fiber Modeling In OpenSees

Prior to testing, detailed fiber modeling in OpenSees was conducted to predict the response of the test units. This was necessary to gain and understanding of the response and provide predicted actuator forces at each stage of the loading history, which assist in control of the actuators. A diagram depicting the numerical model in OpenSees appears in Figure 3-12. The 3D model consists of three nodes, each with six degrees of freedom. The first and second nodes each lie at the origin, which represents the footing-column interface, while the third node is located at the center of the applied load, representing the cantilever length for the column. Between nodes two and three, a Beam with Hinges Element from (Scott and Fenves 2006) was used to compute the column flexural response. This is a force-based beam-column element with a plastic hinge integration scheme. The "HingeRadau" integration technique was selected, which represents Modified two-point Gauss-Radau integration over each hinge region with an interior linear-elastic region between, as shown in Figure 3-12. The plastic hinge method recommended in (Priestley, Calvi and Kowalsky 2007) was used to describe the length of Lp_i and Lp_j.It is expected that further guidance for the appropriate plastic hinge length to match local response could be determined as a result of the experimental comparison, therefore this value is seen as tentative. Similarly, other formulations of displacement and force-based beam-column elements could be evaluated.

The fiber discretization for the column section at ends i and j is depicted in Figure 3-13. Parameters for the Concrete02 uniaxial material in OpenSees were fit to the (Mander, Priestley and Park 1988) confined and unconfined concrete curves which describe the stress-strain response of cover and core concrete. The Reinforcing Steel Material model by Mohle and Kunnath in OpenSees was used to simulate the cyclic stress-strain response of the column longitudinal steel. A zero-length strain penetration element was placed at node one to model the effects of strain penetration of reinforcement into the footing. In the zero-length section, Bond SP01 uniaxial material from (Zhao and Sritharan 2007) was used for the longitudinal steel. The Bond SP01 material represents the cyclic stress-slip behavior of fully anchored longitudinal reinforcement which is developed into the adjacent member. The same core and cover Concrete02 uniaxial properties from the column section were utilized in the zero-length section, except the strain at maximum response was doubled to elongate the post peak branch of the curve.

A section aggregator was used to apply a large torsional stiffness the zero-length section and the two column sections at ends i and j of the beam with hinges element. Additionally, section aggregators were used to apply a large shear stiffness in the 1 and 2 directions for the zero-length element which is only needed to provide fixed-end rotations attributable to strain penetration. All six degrees of freedom at Node 1 were restrained to represent a fixed support, while Nodes 2 and 3 were unrestrained. A constant compressive axial load was applied to Node 3 prior to application of lateral displacements. The bidirectional displacement controlled loading was modeled using Multi-Support Excitation. Specifically, displacement time-histories with a stretched out time scale were applied in the 1 and 3 directions to recreate the displacement path of the Type-B and Megathrust load histories utilized for the specimens. The time between data points in the displacement time-histories was 100 seconds, while the time step for the analysis was 1 second.

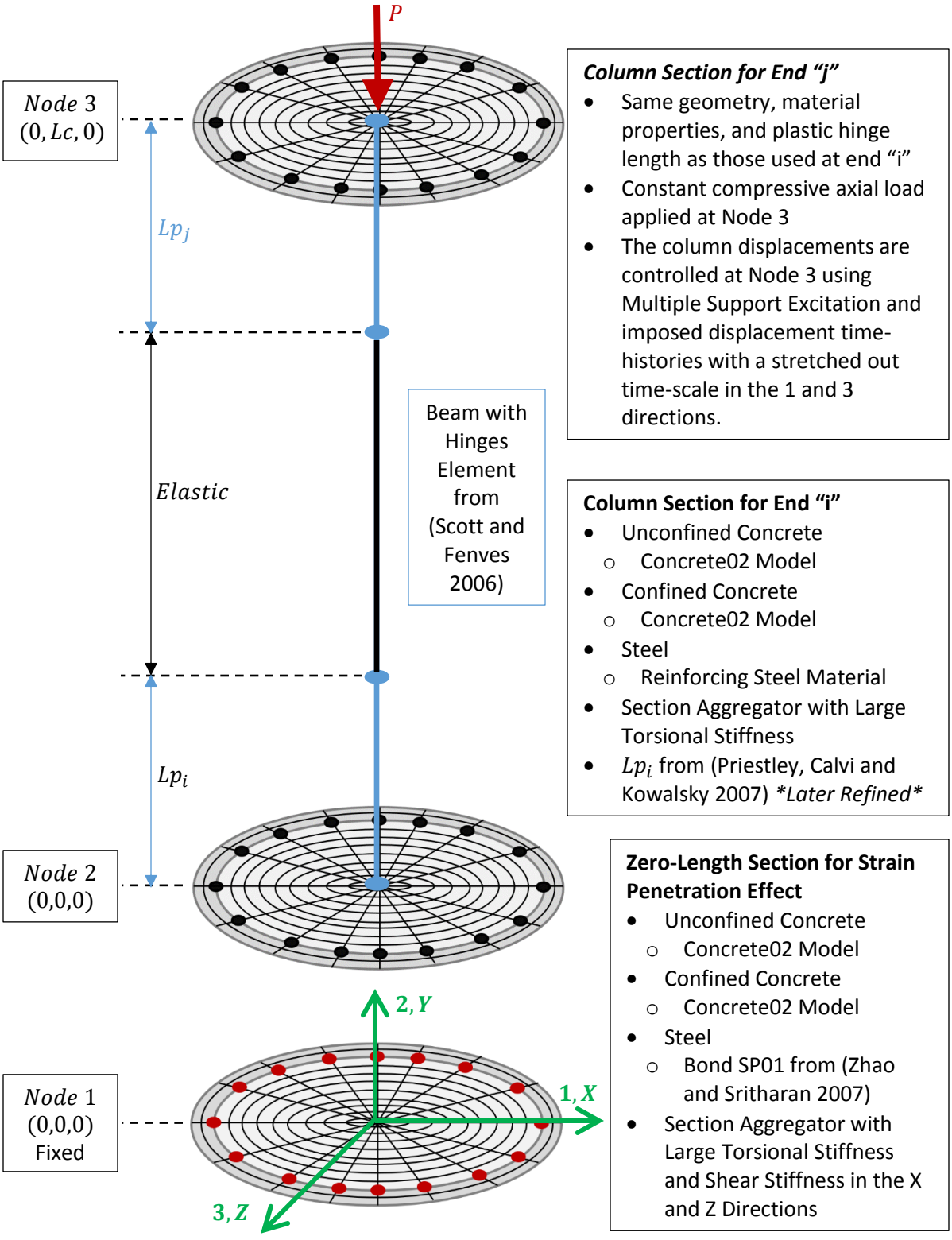

Figure 3-12. Column Analysis Model in OpenSees

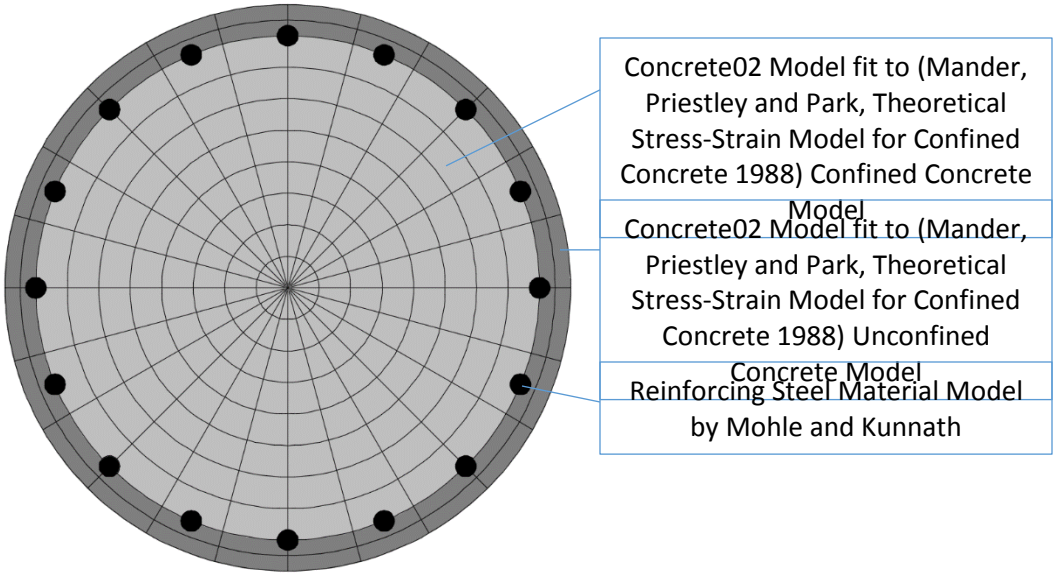

Figure 3-13. Fiber Discretization in Column Section, 2 Unconfined and 8 Confined Concrete Rings with 24 Wedges

Reinforcing Steel Material in OpenSees

In this section, the reinforcing steel material models from the analysis are compared with measured data. The King Steel Model was used for the monotonic moment-curvature analysis in Cumbia, (Montejo and Kowalsky 2007). In OpenSees fiber modeling, the Reinforcing Steel Material Model by Mohle and Kunnath was used. The stress and strain at yielding, strain hardening, and ultimate stress were needed in both models. The average measured values from six material tests on the column longitudinal steel were used as input, see Table 3-1. A comparison of the tensile response of the two models and a sample bar tensile tests appears in Figure 3-14. The two models and test result are in agreement over the entire range of response. The cyclic performance of the Reinforcing Steel Material Model in OpenSees was evaluated against a cyclic bar tests with a distance between grips of $6d_{bl}$, see Figure 3-15. The compressive stresses predicted via the material model exceeded those from the experiment without defining a buckling model in the analysis. Better agreement was obtained when the buckling model from (Dhakal and Maekawa 2002) was used with $(l_{SR} = 6.0\ and\ \alpha = 1.0)$ to represent the $6d_{bl}$ distance between grips. This bar buckling model was not used in the column analysis, since the degree of inelasticity of the critical spiral layers was found to influence bar buckling behavior more than the (s/d_{bl}) ratio in (Goodnight, Kowalsky and Nau 2015).

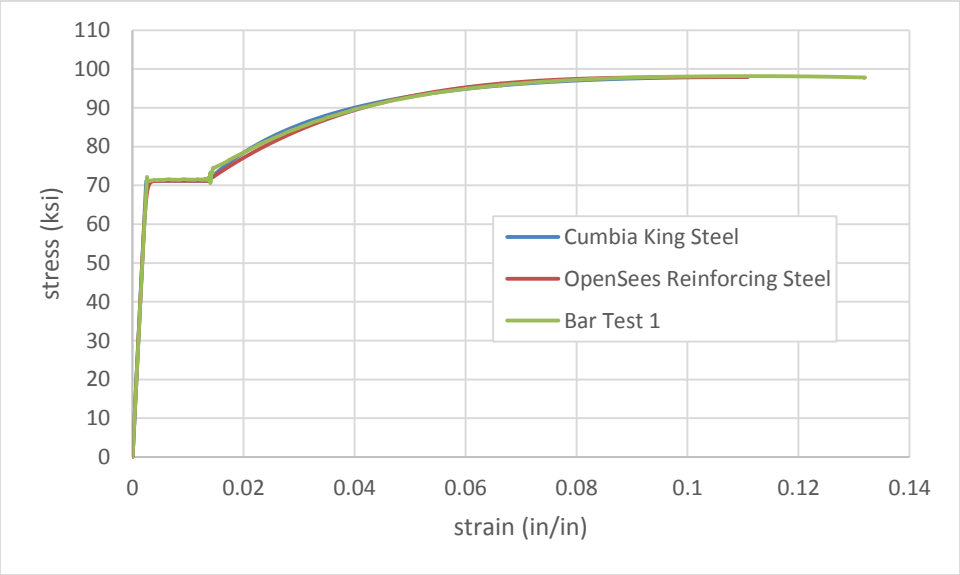

Figure 3-14. Comparison of Models in OpenSees and Cumbia to Rebar Tensile Test 1

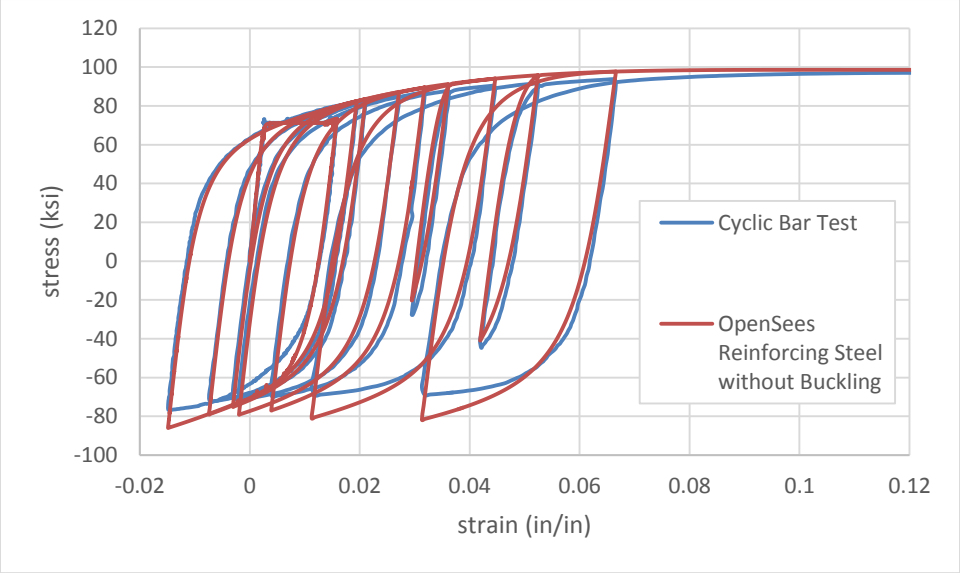

Figure 3-15. Reinforcing Steel Material in OpenSees without Buckling

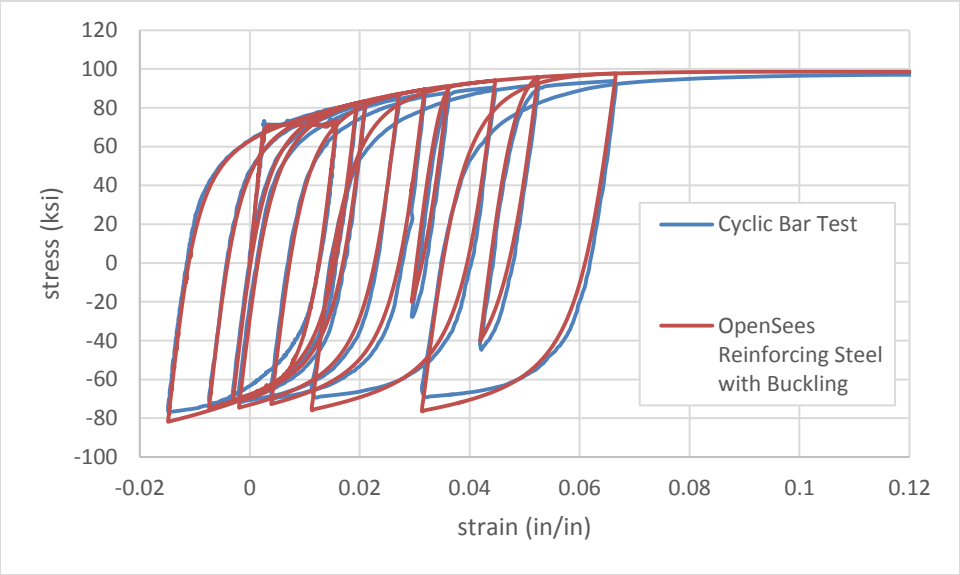

Figure 3-16. Reinforcing Steel Material in OpenSees with (Dhakal and Maekawa 2002) Buckling

Bond SP01 Material in OpenSees

The stress-slip parameters of the Bond SP01 material were computed using recommendations from (Zhao and Sritharan 2007). The slip of the reinforcement at the member interface under the yield stress was computed using Eqn 3-1. In the expression, d_b is the rebar diameter, F_y is the yield strength of the reinforcing steel, f_c' is the concrete compressive strength of the adjoining connection member, and α is a parameter used in the local bond-slip relation, taken as $(\alpha = 0.4)$ in this study as recommended by (FIB Task Group on Bond Models 2000). Following recommendations in (Zhao and Sritharan 2007), the ultimate slip for the reinforcement was approximated as $(S_u = 35S_y)$. The initial monotonic hardening ratio was taken as $(b = 0.15)$ and the cyclic pinching factor taken as $(r = 0.8)$, based on analysis of the measured strain-slip relationship from (Goodnight, Kowalsky and Nau 2015) which was converted to stress-slip response using the Reinforcing Steel Material model. These values serve as an initial assumption which can be refined after test data is collected from the load path columns. An example of the resulting stress-slip response for the Bond SP01 material appears in Figure 3-17.

$$S_y(in) = 0.1\left[\frac{d_b(in)}{4000}\frac{F_y(psi)}{\sqrt{f_c'(psi)}}(2\alpha+1)\right]^{1/\alpha} + 0.013(in)$$

Rebar Slip at Member Interface Under Yield Stress — *Eqn 3-1*

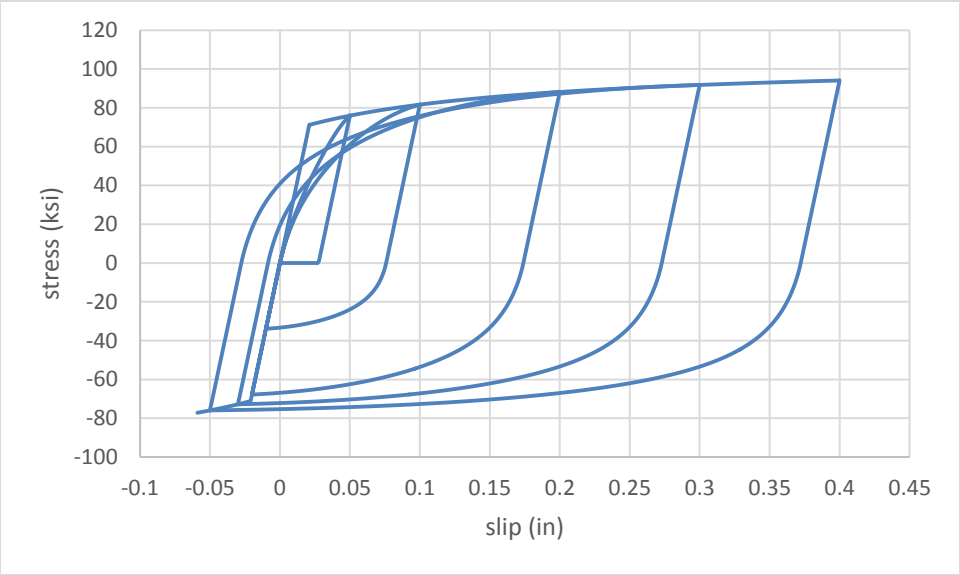

Figure 3-17. Bond SP01 Stress-Slip Model from (Zhao and Sritharan 2007)

Concrete02 Material in OpenSees Adapted to (Mander, Priestley and Park 1988)

Two concrete trucks were utilized in the column construction, each filling three of the columns and loading caps. In the initial six specimens, one truck was filled the three specimens with 2.75" transverse steel spacings while the other filled the remaining three specimens which had a 2" spiral spacing. For the preliminary analysis, the tested 28-day compressive strength for the two batches of concrete was used to compute the unconfined and confined concrete stress-strain curves using the approach from (Mander, Priestley and Park 1988). (Kowalsky 2000) noted that the (Mander, Priestley and Park 1988) ultimate concrete compressive strain (ε_{cu}) was consistently around 50% conservative when compared to the ultimate displacement capacity of bridge column experiments. Following this observation, the monotonic moment-curvature script Cumbia, (Montejo and Kowalsky 2007), utilized a value of $(1.4 \cdot \varepsilon_{cu})$ to elongate the post peak descending branch of the (Mander, Priestley and Park 1988) confined stress-strain curve. This approach was also used when determining parameters for the Concrete02 model in OpenSees.

A comparison of the monotonic confined and unconfined concrete stress-strain response from Cumbia and the Concrete02 model in OpenSees appears in Figure 3-18 for Columns 1-3 with 2" spiral spacing and in Figure 3-19 for Columns 4-6 with 2.75" spiral spacing. The tensile strength of the concrete was neglected in both analysis techniques. For the Concrete02 model in OpenSees, the ratio of the unloading slope at the ultimate concrete compression strain to the initial slope was assumed as $(\lambda = 0.1)$, resulting in the cyclic response depicted in Figure 3-20. For the confined concrete, Figure 3-20, represents compression applied to a value of $(\varepsilon_c = 0.012)$, followed by unloading to zero strain, and then reloading until $(1.4 \cdot \varepsilon_{cu})$. For the unconfined concrete, Figure 3-20, represents compression applied to $(\varepsilon_c = 0.003)$, followed by unloading to zero strain, and then reloading until $(\varepsilon_c = 0.0064)$ where to unconfined concrete is assumed to have zero strength.

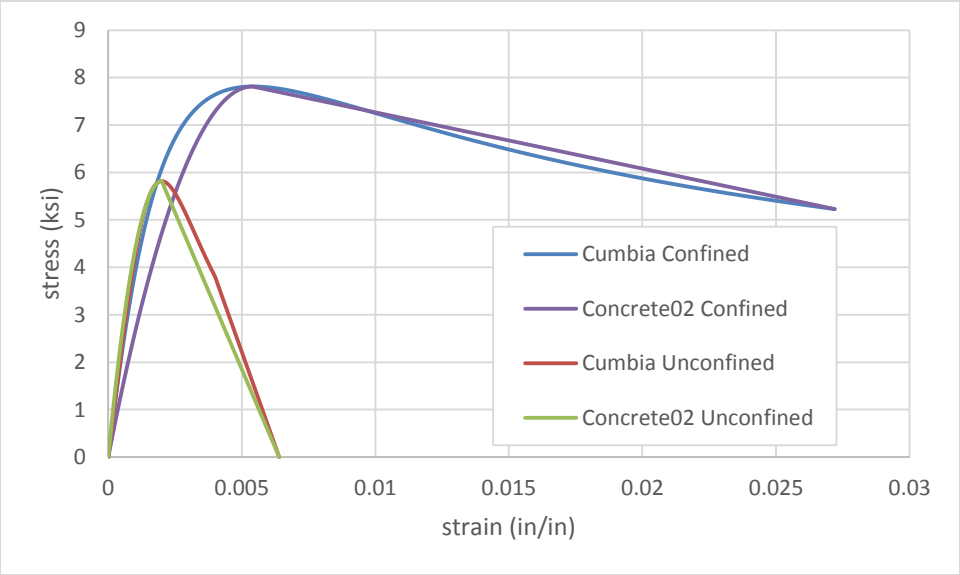

Figure 3-18. Confined and Unconfined Concrete Stress-Strain Curves for Columns 1-3 with 2" Spiral Spacing

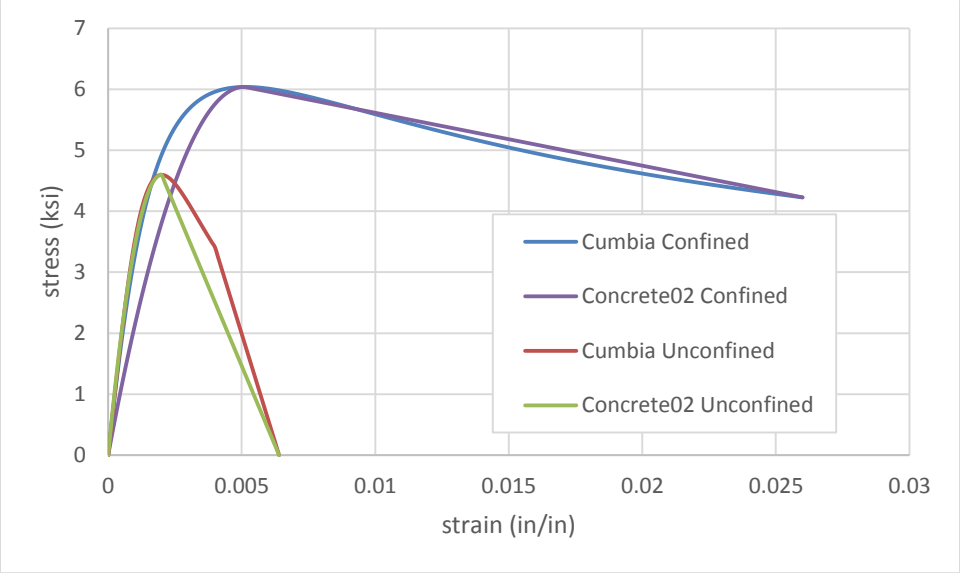

Figure 3-19. Confined and Unconfined Concrete Stress-Strain Curves for Columns 4-6 with 2.75" Spiral Spacing

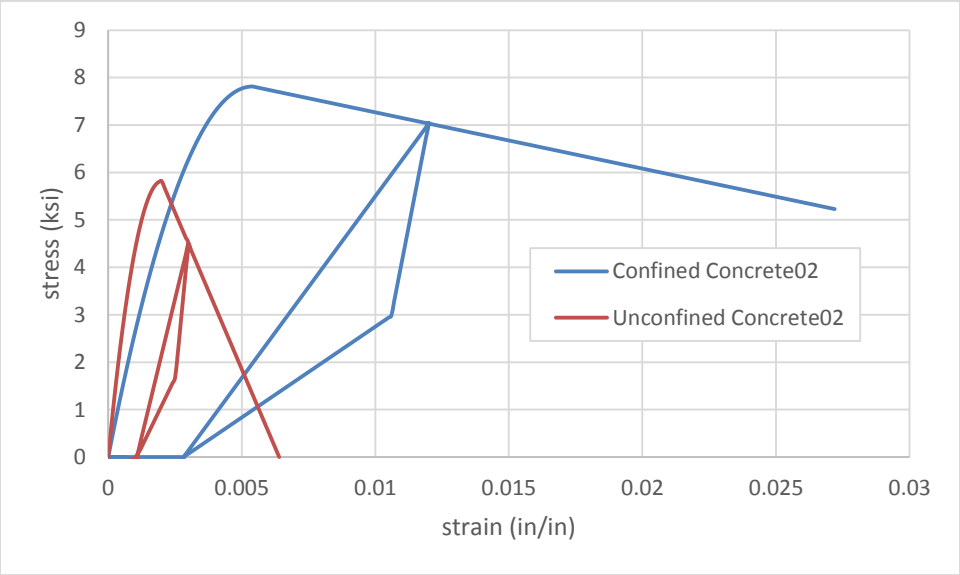

Figure 3-20. Example of Cyclic Response of the Concrete02 Model in OpenSees for Columns 1-3 with 2" Spiral Spacing

Chapter 4 - Test 1 Summary Report

The first specimen had a 24" diameter circular cross-section reinforced with 16 #7 A706 longitudinal bars ($A_{st}/A_g = 2.1\%$) and a #3 spiral at 2.75" on center ($4A_{sp}/D's = 0.7\%$). The column had a 109.4375" cantilever length, measured from the footing-column interface to the center of the applied lateral load. This length was obtained as an average of the staggered actuator connections heights, 108" and 110.875". The string pot array used to triangulate the column deformation was connected at this height. Although eliminated in the instrumented region, the upper portion of the column had a 0.5" cover measured to the outside surface of the spiral. The column had a constant axial load of $191\ kips\ (P/f_c'\ A_g = 7.4\%)$. Details of the test setup, instrumentation, and specimen design appear in Chapter 2. A material properties summary for the longitudinal and transverse steel from the first six experiments appears in Table 3-1 and Table 3-2. The column had a tested concrete strength of $f_c' = 6.21\ ksi$, while the footing had $f_c' = 10.18\ ksi$. The first specimen was subjected to the Type-B Symmetric Two-Cycle-Set Biaxial Load History shown in Figure 4-1. This figure includes a diagram of the column cross-section with the selected bar and crack labeling scheme. Displacements in the +Y-direction placed the South reinforcement in tension. Cracks due to loading in the +Y-direction were labeled as red. The orientation of the X and Y axes are shown in Figure 2-52 with regards to the test setup. The +Y-axis is perpendicular to and points away from the strong wall. Values of interests, damage observations, and a predictions summary for the first test appear in Table 4-1, Table 4-2, and Table 4-3. In the cycle naming scheme, $\mu_{\Delta 5}^{+1X} = 7.48\ in$ represents the first cycle in the +X-direction during displacement ductility five.

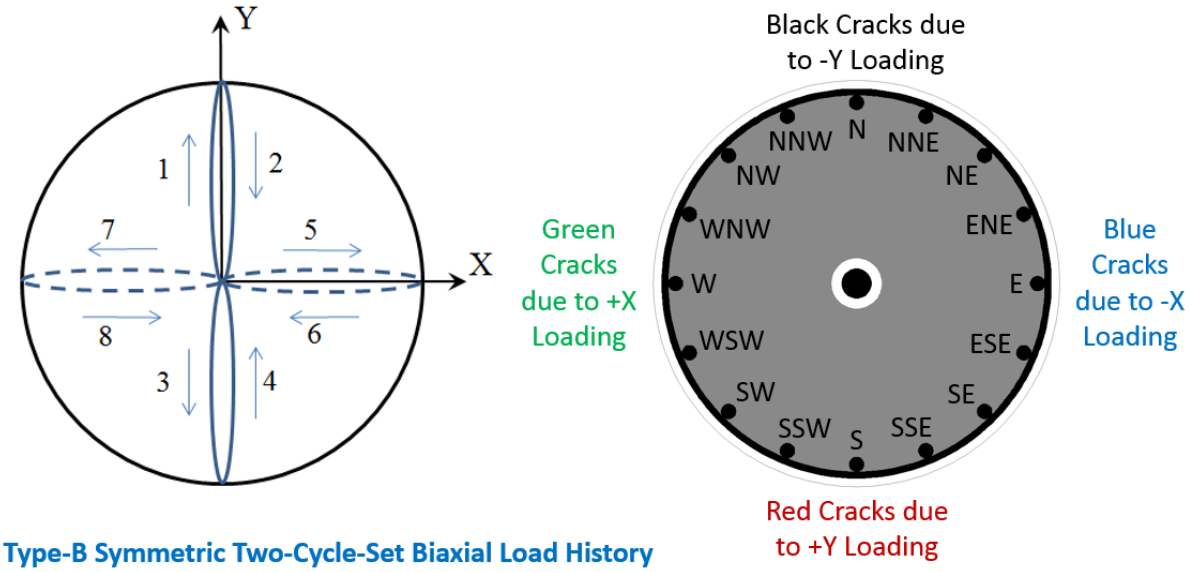

Type-B Symmetric Two-Cycle-Set Biaxial Load History

- Begins with elastic cycles (1-8) in ¼ yield increments until F_y'
- The equivalent yield displacement is then computed as $\Delta_y = \Delta_y'(M_n/M_y')$
- Two inelastic cycles (1-8) for each displacement ductility level $\mu_{\Delta n} = n \cdot \Delta_y$
- Cycle labeling system: $(\mu_{\Delta 5}^{-1Y} = -7.55\ in)$ Represents the first cycle of displacement ductility five in the -Y direction

Figure 4-1. Test 1: Load History and Labeling System for Reinforcement and Cracks

Table 4-1. Test 1: Values of Interest

Load History	Type-B Symmetric Two-Cycle-Set
Length, Diameter, and Aspect Ratio	$L = 109.4375\ in, D = 24\ in,\ (L/D = 4.56)$
Longitudinal Steel Detailing	$16\ \#7\ for\ \rho_l = A_{st}/A_g = 2.1\%$
Longitudinal Steel Properties	$f_y = 71.2\ ksi, f_u = 97.9\ ksi, \varepsilon_y = 0.00254$
Transverse Steel Detailing	$\#3\ @\ 2.75\ in\ for\ \rho_s = 4A_{sp}/D's = 0.7\%$
Transverse Steel Properties	$f_y = 67.6\ ksi, f_u = 105.6\ ksi, \varepsilon_y = 0.00448$
Column Concrete Strength	$f_c' = 6.21\ ksi$
Footing Concrete Strength	$f_c' = 10.18\ ksi$
Axial Load	$P = 191\ kips, \left(P/f_c'\ A_g = 7.4\%\right)$
Analytical First Yield Force	$F_y' = 50.66\ kips$
Experimental First Yield Disp.	$\Delta_y' = 1.12\ in$
Analytical Nominal Moment Capacity	$M_n = 624.58\ kip \cdot ft$
Equivalent Yield Displacement	$\Delta_y = \Delta_y'\left(M_n/M_y'\right) = 1.51\ in$
Maximum Lateral Force	$F_y = 76.98\ kips, F_x = 75.19\ kips$
Failure Mode	Loss in lateral strength due to buckling of all column longitudinal bars, followed by a single fractured bar.

Table 4-2. Test 1: Damage Observations

Damage Observations:		
Cycle Peak at which First Cracking was Observed Visually:		
North	$\Delta_y = 0.5F_y' = -0.39\ in$	$F_y = -25.25\ kips$
South	$\Delta_y = 0.5F_y' = 0.38\ in$	$F_y = 25.50\ kips$
East	$\Delta_x = 0.5F_y' = -0.37\ in$	$F_x = -22.78\ kips$
West	$\Delta_x = 0.5F_y' = 0.30\ in$	$F_x = 20.08\ kips$
Cycle Peak at which Cover Concrete Crushing was Observed Visually:		
North	$\mu_{\Delta 2}^{+1Y} = 3.01\ in$	$\varepsilon_c = -0.00562$
South	$\mu_{\Delta 2}^{-1Y} = -3.03\ in$	$\varepsilon_c = -0.00652$
East	$\mu_{\Delta 2}^{+1X} = 3.02\ in$	$\varepsilon_c = -0.00626$
West	$\mu_{\Delta 2}^{-1X} = -3.03\ in$	$\varepsilon_c = -0.00566$
Exact Displacement and Cycle Label for Initial Spiral Yielding in the Confinement Zone:		
North	$\Delta_y = 4.06\ in\ during\ \mu_{\Delta 3}^{+1Y}$	$\varepsilon_c = -0.00888$
South	$\Delta_y = -4.20\ in\ during\ \mu_{\Delta 3}^{-1Y}$	$\varepsilon_c = -0.00823$
East	$\Delta_x = 4.10\ in\ during\ \mu_{\Delta 4}^{+1X}$	$\varepsilon_c = -0.00722$
West	$\Delta_x = -4.37\ in\ during\ \mu_{\Delta 3}^{-1X}$	$\varepsilon_c = -0.00891$
Peak Tensile Displacement Prior to Visual Bar Buckling During Subsequent Reversal of Load:		
North	$\mu_{\Delta 4}^{-2Y} = -6.01\ in, Observed\ at\ \mu_{\Delta 5}^{+1Y} = 7.51\ in$	$\varepsilon_s = 0.02841$
South	$\mu_{\Delta 5}^{+1Y} = 7.51\ in, Observed\ at\ \mu_{\Delta 5}^{-1Y} = -7.55\ in$	$\varepsilon_s = 0.03887$
East	$\mu_{\Delta 4}^{-2X} = -6.04\ in, Observed\ at\ \mu_{\Delta 5}^{+1X} = 7.48\ in$	$\varepsilon_s = 0.02881$
West	$\mu_{\Delta 5}^{+1X} = 7.48\ in, Observed\ at\ \mu_{\Delta 5}^{-1X} = -7.56\ in$	$\varepsilon_s = 0.03960$
Exact Displacement and Cycle Label for Fracture of Previously Buckled Reinforcement		
North	$\Delta_y = -2.90\ in\ during\ \mu_{\Delta 5}^{-3Y}$	Single North Extreme Bar

Table 4-3. Test 1: Damage Predictions

Damage Predictions with the New Bidirectional Plastic Hinge Model and New Strain Limits:		
Bar Buckling Predictions		
New Method	$\Delta_{bb}^{Lpr} = 6.77\ in$	$\varepsilon_s^{bb} = 0.03452$
Feng et al. (2015)	$\Delta_{bb}^{Lp} = 5.57\ in$	$\varepsilon_s^{bb} = 0.0374$
Cover Crushing Prediction		
New Method	$\Delta_{cc}^{Lpr} = 2.03\ in$	$\varepsilon_c^{cc} = -0.004$
Spiral Yielding Prediction		
New Method	$\Delta_{sy}^{Lpr} = 4.60\ in$	$\varepsilon_c^{sy} = -0.01192 * M, (M = 0.8)$
Original Ultimate Concrete Compression Strain		
Mander et al. (1988)	$\Delta_{cu}^{Lpr} = 6.35\ in$	$\varepsilon_{cu} = -0.0145$

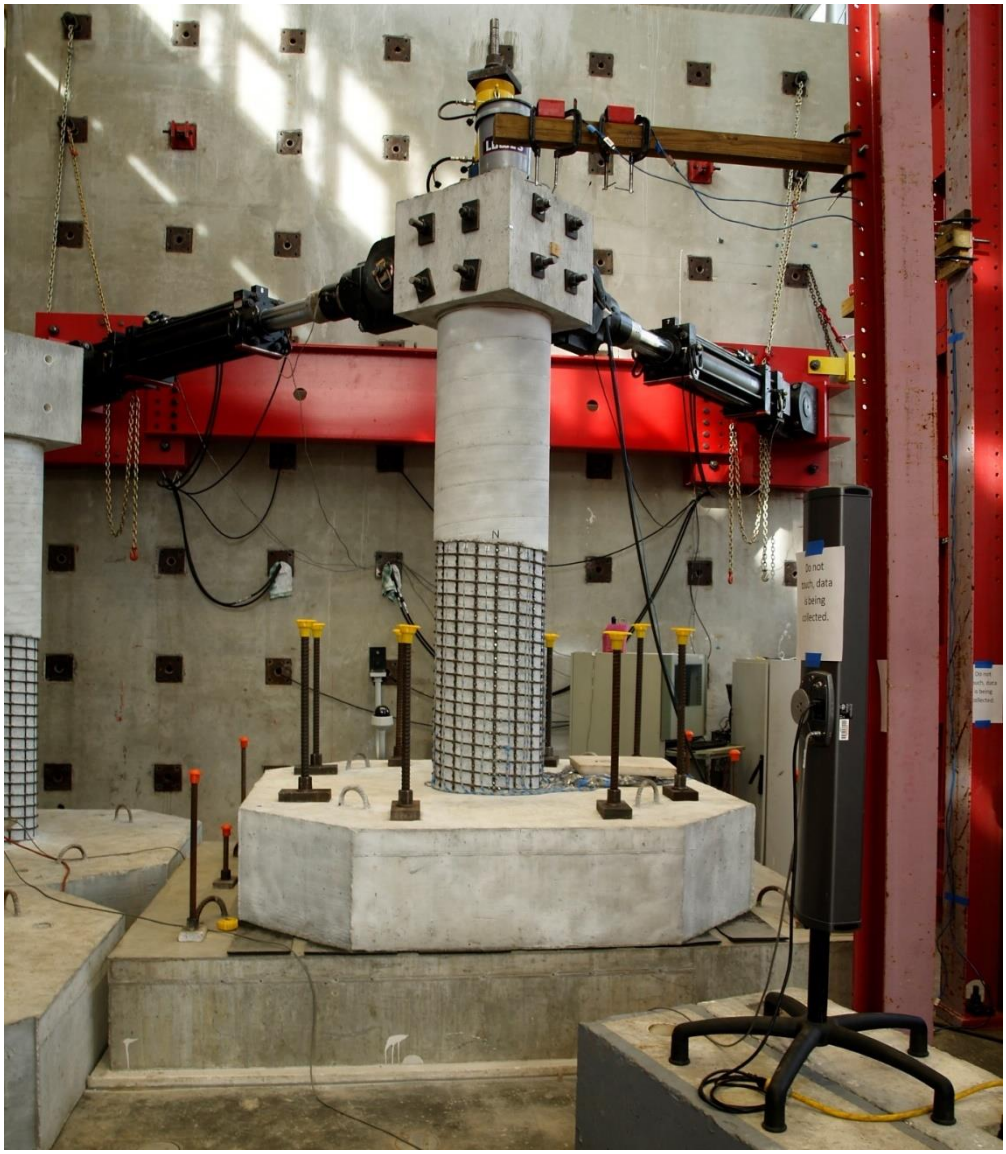

Figure 4-2. Test 1: Experimental Setup

Figure 4-3. Test 1: Axial and Lateral Load Setup

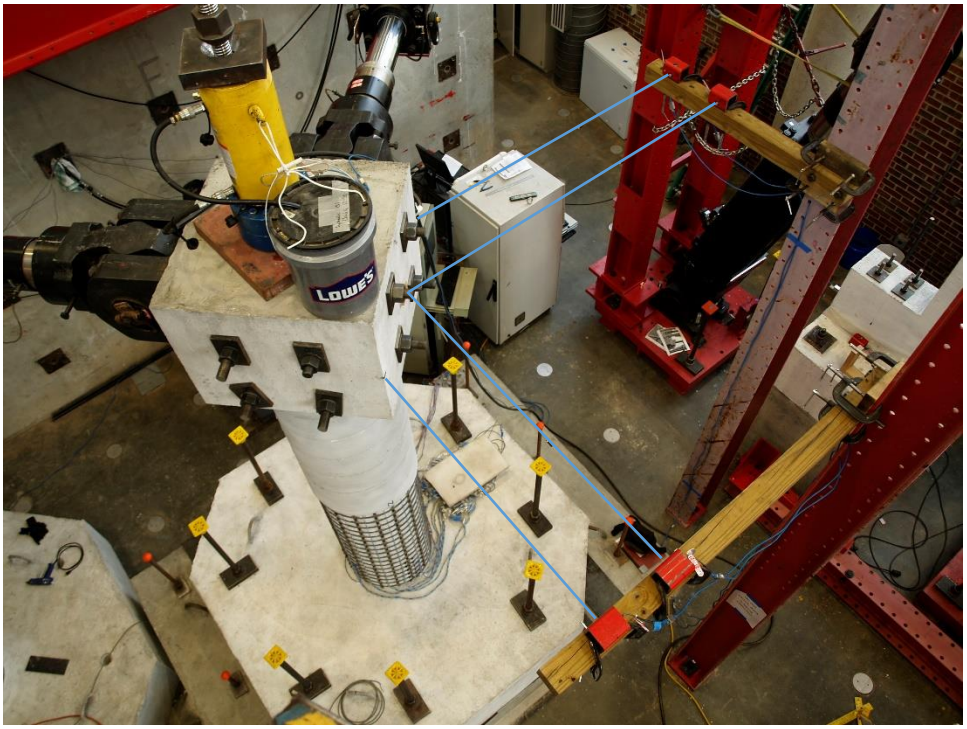

Figure 4-4. Test 1: String Potentiometer Setup (Highlighted with Blue Lines)

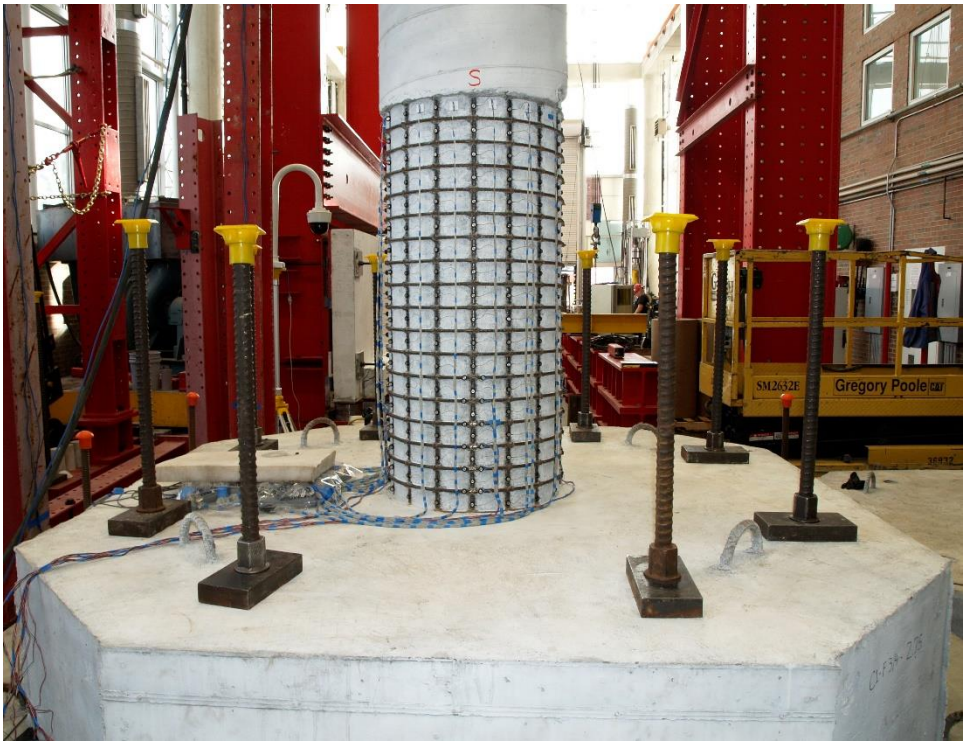

Figure 4-5. Test 1: Plastic Hinge Region with Optotrak Target Marker Instrumentation

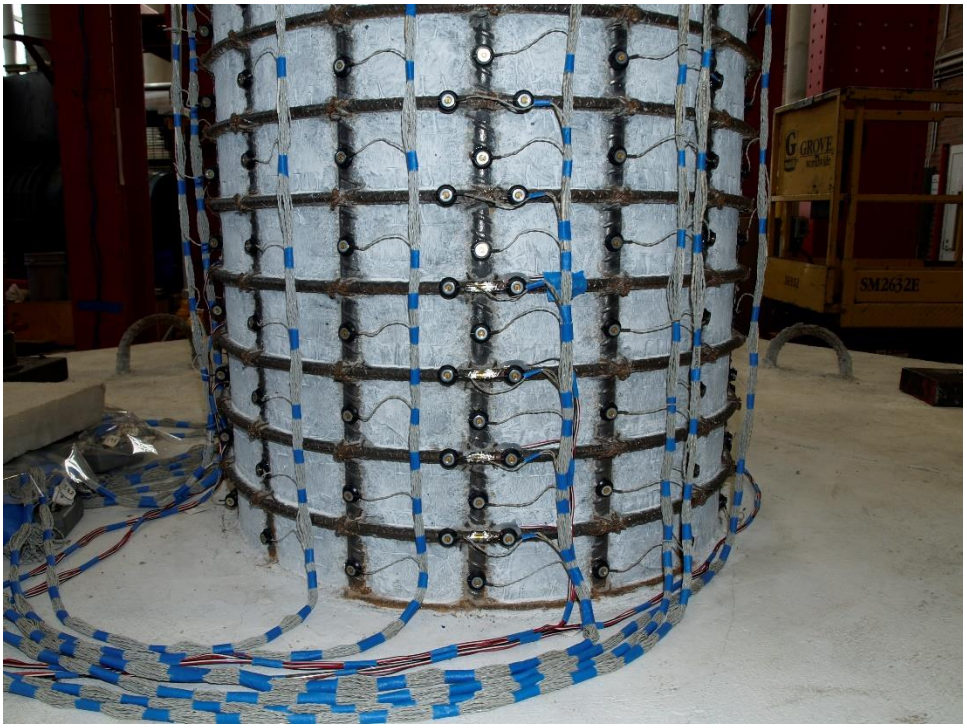

Figure 4-6. Test 1: Close Up of the Instrumented Region on the South Side of the Specimen

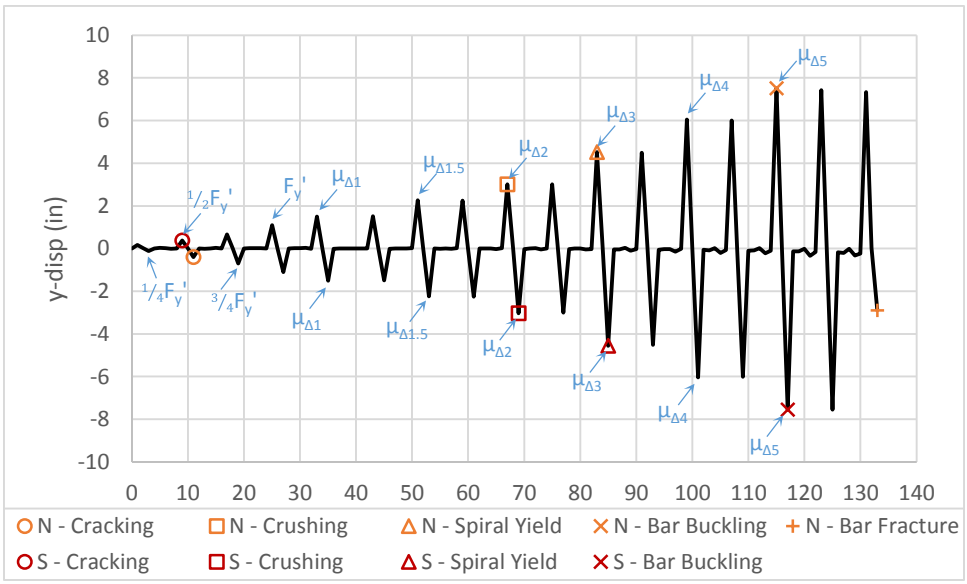

Figure 4-7. Test 1: Y-Displacement History

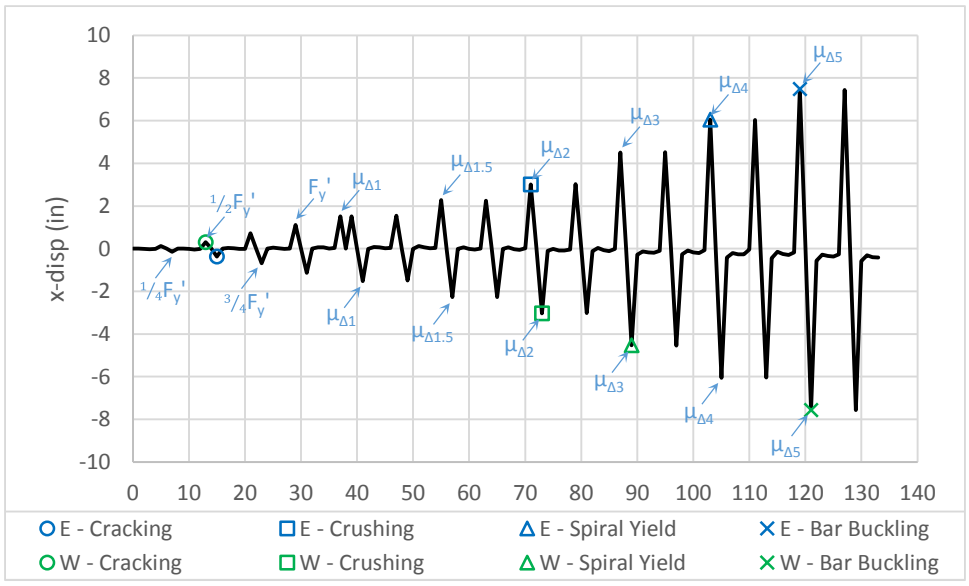

Figure 4-8. Test 1: X-Displacement History, Note Accidental Repeat of $\mu_{\Delta 1}^{+1X}$

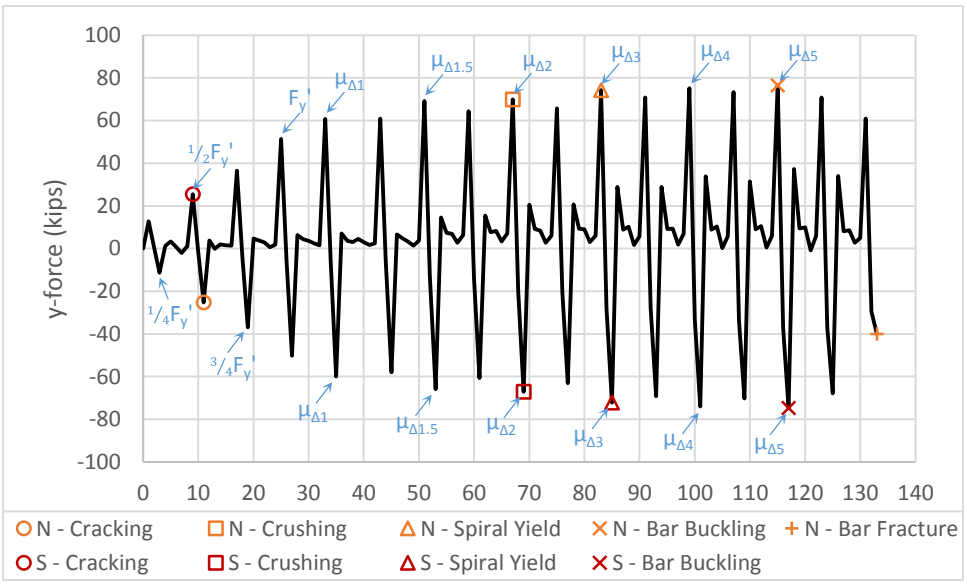

Figure 4-9. Test 1: Y-Force History

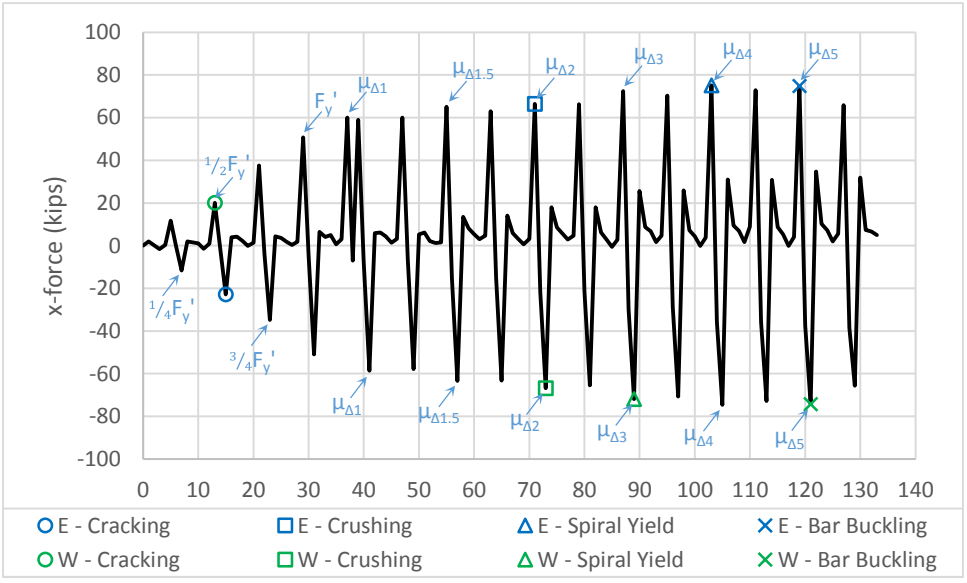

Figure 4-10. Test 1: X-Force History, Note Accidental Repeat of $\mu_{\Delta 1}^{+1X}$

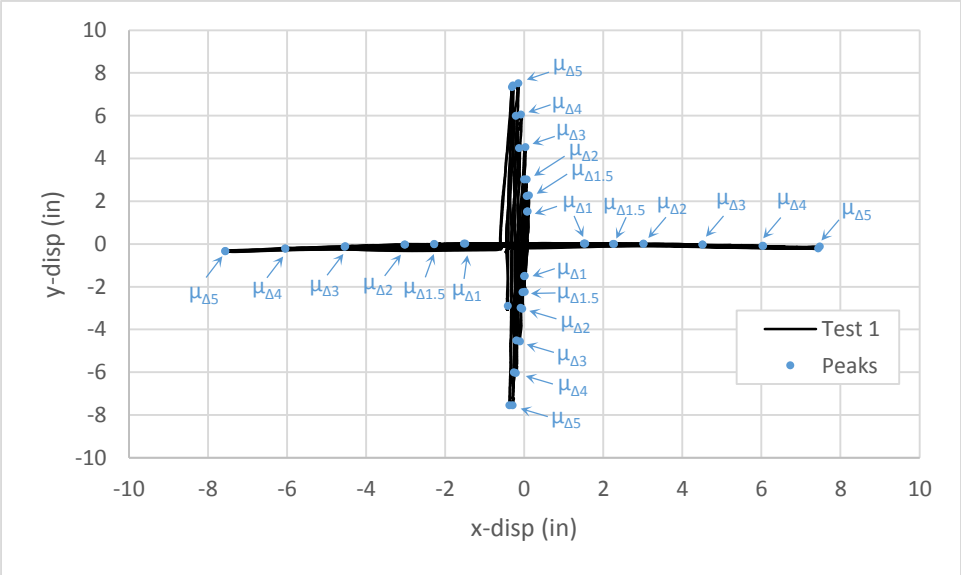

Figure 4-11. Test 1: Type-B Symmetric Two-Cycle-Set Displacement History

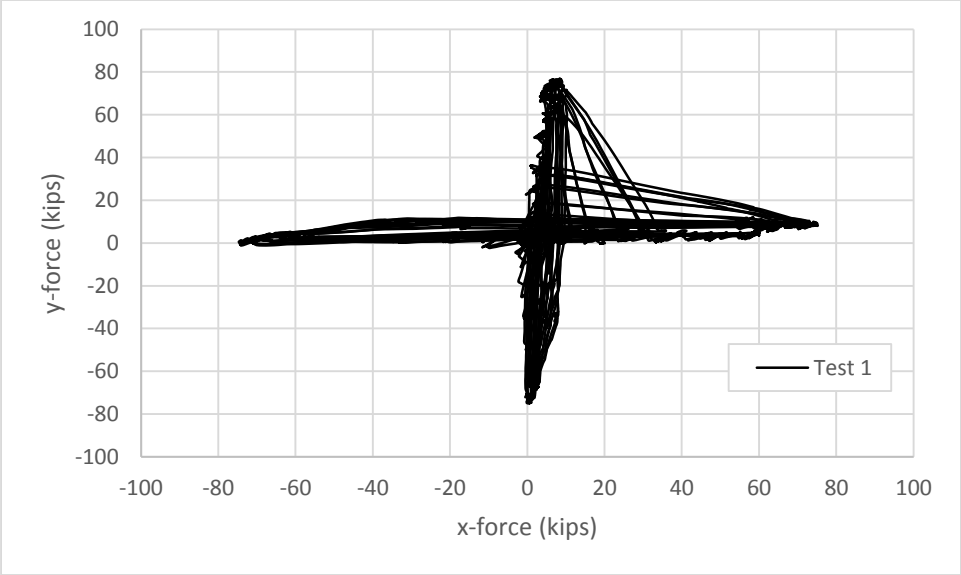

Figure 4-12. Test 1: Load Path

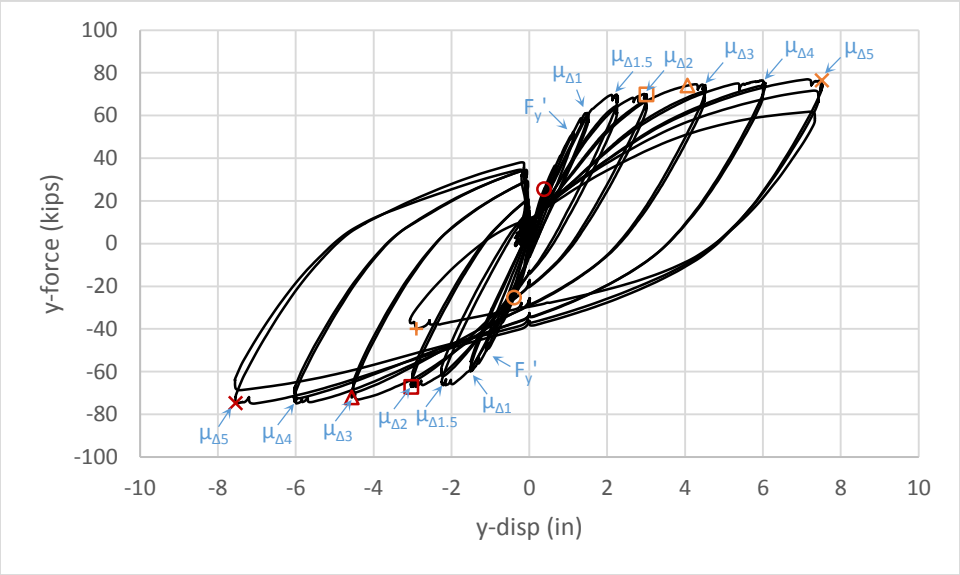

Figure 4-13. Test 1: Y-Direction Hysteretic Response

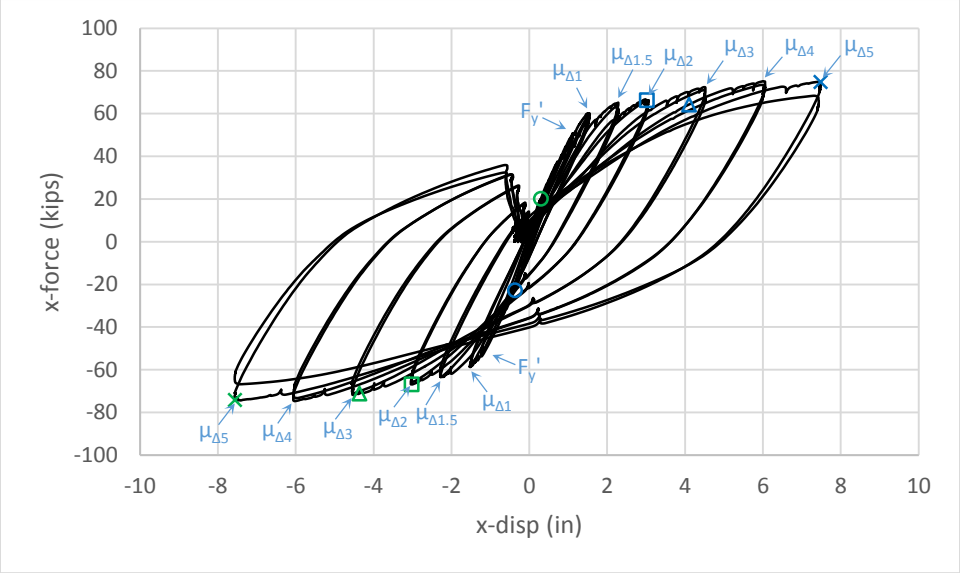

Figure 4-14. Test 1: X-Direction Hysteretic Response

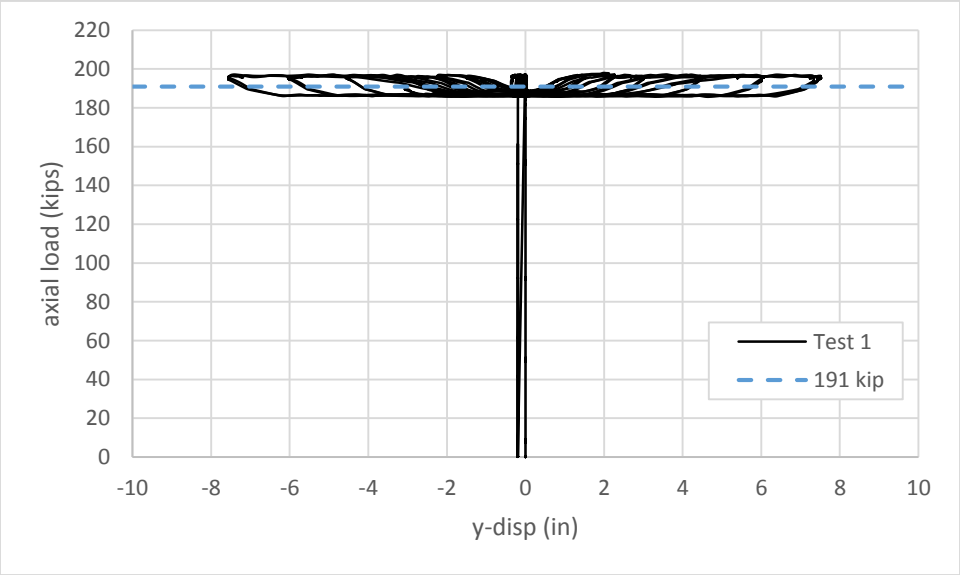

Figure 4-15. Test 1: Y-Direction Axial Force History, Unloading after Day 1 of Testing

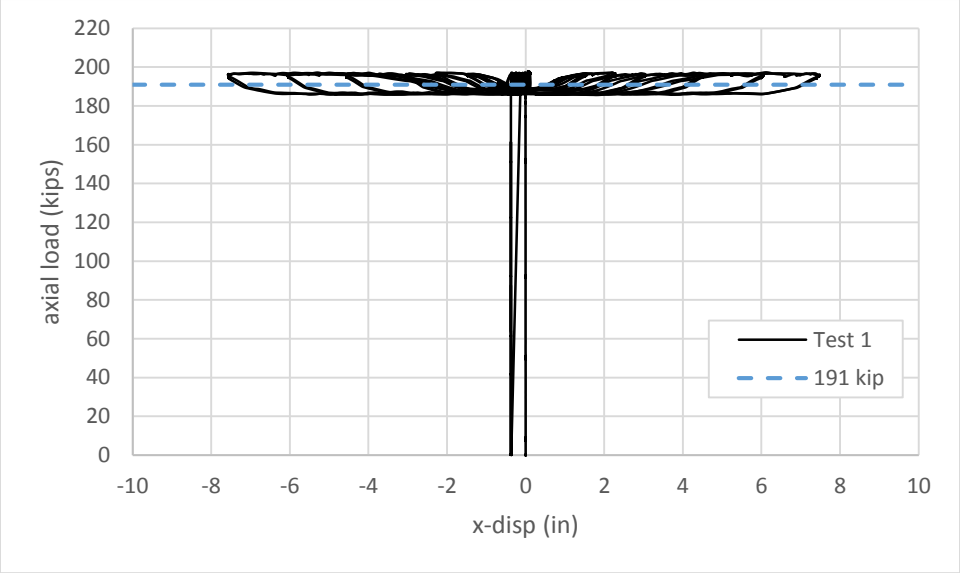

Figure 4-16. Test 1: X-Direction Axial Force History, Unloading after Day 1 of Testing

Test 1 - Experimental Observations

The test began with collection of the initial measurements prior to application of the axial load. A constant axial load of $191\ kips\ \left(P/f_c'\ A_g = 7.4\%\right)$ was then applied using a self-regulating axial load system described in Chapter 2. The imposed displacement histories in the Y and X-directions for the Type-B Symmetric Two-Cycle-Set Biaxial Load History of Figure 4-1 are shown in Figure 4-7 and Figure 4-8. Note that $\mu_{\Delta 1}^{+1X}$ was accidentally repeated twice, but this is of little consequence due to the small displacement amplitude. The resulting column shear force histories in the Y and X-directions appear in Figure 4-9 and Figure 4-10. The full displacement history and resulting load path for Test 1 appear in Figure 4-11 and Figure 4-12. The residual forces due to prior orthogonal loading during each cycle are clearly visible, but this has a smaller impact near the peak of each cycle due to the symmetric application of load. The Y and X-direction column hysteretic response appears in Figure 4-13 and Figure 4-14. The axial load history is shown in Figure 4-15 and Figure 4-16.

The load history began with elastic cycles (1-8) in ¼ F_y' increments until the analytically predicted first yield force ($F_y' = 50.66\ kips$) was reached in each direction of loading. Cracks were first observed on all sides of the specimen during the ½ F_y' cycle, see Figure 4-17 and Figure 4-18. At the analytically predicted first yield force, displacements in the four primary directions were measured at $\Delta_y' = 1.10$" and $\Delta_y' = -1.11$" in Y-direction and $\Delta_y' = 1.12$" and $\Delta_y' = -1.13$" in X-direction, producing an average experimental first yield displacement of $\Delta_y' = 1.12$". This value exceeded the analytical prediction for the first yield displacement of 0.85", however the extreme fiber bar strains at the analytical first yield force closely matched the yield strain of the longitudinal steel, as will be discussed in greater detail later in this summary report. Cracks observed on each side of the specimen at first yield are shown in Figure 4-19 and Figure 4-20. The equivalent yield displacement for the column was then computed as $\Delta_y = \Delta_y'\left(M_n/M_y'\right) = 1.51\ in$, where $M_n = 624.58\ kip \cdot ft$ represents the analytical nominal moment capacity corresponding to an extreme fiber compression strain of $\varepsilon_c = 0.004$ or a steel tensile strain of $\varepsilon_s = 0.015$, whichever occurs first. The remainder of the Symmetric Two-Cycle-Set Load History consists of two cycles (1-8 from Figure 4-1) for each displacement ductility level $\mu_{\Delta n} = n \cdot \Delta_y$, where $n = 1, 1.5, 2, 3, 4, 5, 6\ etc.$

For each displacement ductility level, cracks were marked during the second cycle of loading and those which were visible under two primary directions were still marked with that direction's representative color from Figure 4-1. At displacement ductility one, the cracks remained horizontal, but increased in width and became more numerous as shown in Figure 4-21 and Figure 4-22. During the first cycle of displacement ductility 1.5, the first signs of concrete flaking were observed on the South side at $\mu_{\Delta 1.5}^{-1y} = -2.25$" and the East side at $\mu_{\Delta 1.5}^{+1x} = 2.28$". The slight amount of concrete flaking shown in Figure 4-23 usually precedes crushing, however the damage did not change during the second cycle of loading. In a given direction of loading, cracks on the shear face began to show some inclination in regions above the footing-column interface as shown in Figure 4-24 and Figure 4-25. Those near the footing-column interface remained horizontal. The photo of cracks on the North and South sides of the specimens are shown at the end of the displacement ductility level, so that cracks due to loading in the orthogonal direction appear in the photos.

During the first cycle of displacement ductility two, small amounts of concrete crushing were observed in the four primary directions as shown in Figure 4-26 and Figure 4-27. Photos of the crack profile on each side of the specimen at the conclusion of displacement ductility two appear in Figure

4-28 and Figure 4-29. Compare this to the crack profiles at the end of displacement ductility three shown in Figure 4-30 and Figure 4-31. By this time, there was a distinct crack inclination on the shear faces of the specimen in a given direction of loading. Cracks in one direction were clearly interacting with cracks in the opposing directions, however even in the presence of adjacent horizontal cracks, the diagonal cracks on the shear faces continued to elongate and incline for the remainder of the experiment.

Initial spiral yielding was measured in the confinement regions of the North, South, and West sides of the specimen during the first cycle of displacement ductility three, followed by the East side during the first cycle of displacement ductility four. Photos of the four confinement regions during respective cycles of displacement ductility four appear in Figure 4-32 and Figure 4-33, while crack profiles at the end of the ductility level appear in Figure 4-34 and Figure 4-35. Significant yielding in spiral layers overlaying the extreme fiber reinforcement was measured during displacement ductility four although the reinforcement remained visibly straight.

The North extreme fiber bar (Bar N from Figure 4-1) buckled during $\mu_{\Delta 5}^{+1y} = 7.51"$ without the need for additional tension strain since this was the first cycle in the Y-direction for displacement ductility five, see Figure 4-36. A photo of the deformed column at $\mu_{\Delta 5}^{+1y} = 7.51"$ appears in Figure 4-39. The South extreme fiber bar (Bar S) buckled during $\mu_{\Delta 5}^{-1y} = -7.55"$ as shown in Figure 4-36. The East extreme fiber bar (Bar E) buckled during $\mu_{\Delta 5}^{+1x} = 7.48"$ without the need for additional tension strain since this was the first cycle in the X-direction for displacement ductility five. The buckling on the East side was less severe and more difficult to spot visually as shown in Figure 4-37. The West extreme fiber bar (Bar W) buckled during $\mu_{\Delta 5}^{-1x} = -7.56"$, as shown in Figure 4-37. In summary, all four extreme fiber bars buckled during the first cycle of displacement ductility five, which locally displaced multiple spiral layers away from the core, influencing confinement and bar restraint in those regions during the second cycle when the damage accelerated.

Adjacent North reinforcing bars NNE and NNW buckled during $\mu_{\Delta 5}^{+2y} = 7.42"$, followed by bars SSE and SSW which buckled during $\mu_{\Delta 5}^{-2y} = -7.55"$. At this point, the buckled deformation on the North and South sides of the specimen was so severe that significant crushing of the core had began behind the ineffective spiral layers, see Figure 4-38. All of the remaining East bars buckled during $\mu_{\Delta 5}^{+2x} = 7.44"$, followed by buckled of all remaining West bars during $\mu_{\Delta 5}^{-2x} = 7.56"$. At the conclusion of the second cycle of displacement ductility five, all 16 bars within the cross section had buckled as shown in Figure 4-40. It was decided that rather than proceed to displacement ductility six, an additional cycle at displacement ductility five would be carried out to fracture reinforcement, since the increase in ductility may lead to additional damage beyond the realm of feasibility as a repair candidate. A photo of the additional buckled deformation in the North reinforcement during $\mu_{\Delta 5}^{+3x} = 7.33"$ is shown in Figure 4-41. The North extreme fiber bar (Bar N) fractured at $\Delta_y = -2.90"$ while on the way to $\mu_{\Delta 5}^{-3Y}$, as shown in Figure 4-41. At this time the test was concluded and the specimen was recentered and saved as a repair candidate. Photos of the specimen after removal of the instrumentation and crushed concrete appear in Figure 4-42 and Figure 4-43.

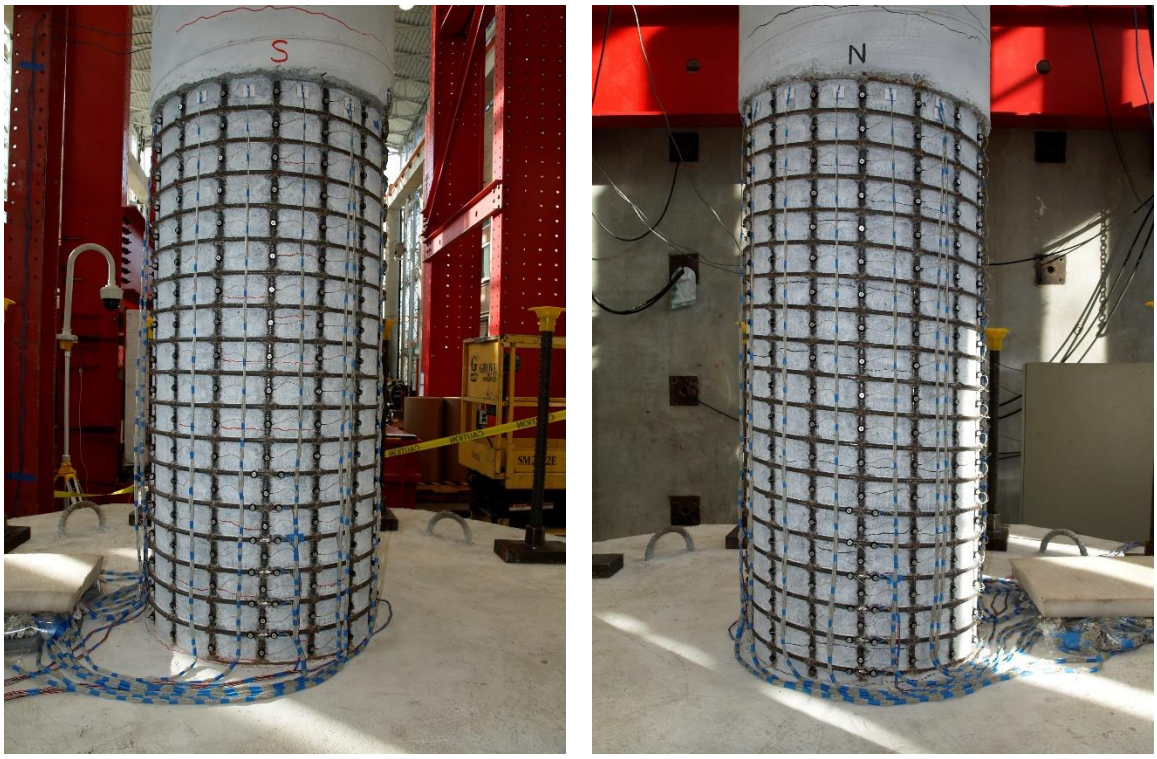

Figure 4-17. Test 1: First Cracking on the South and North Sides of the Specimen during $\Delta_y = 0.38"$ and $\Delta_y = -0.39"$

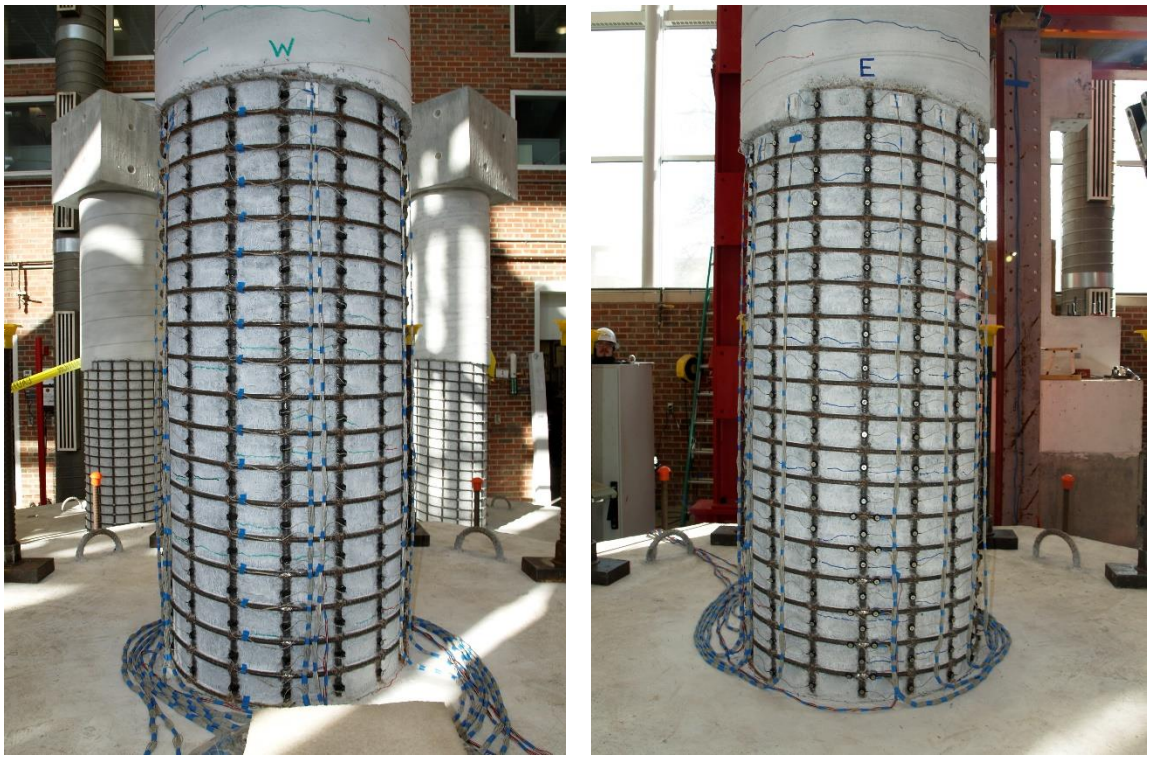

Figure 4-18. Test 1: First Cracking on the West and East Sides of the Specimen during $\Delta_x = 0.30"$ and $\Delta_x = -0.37"$

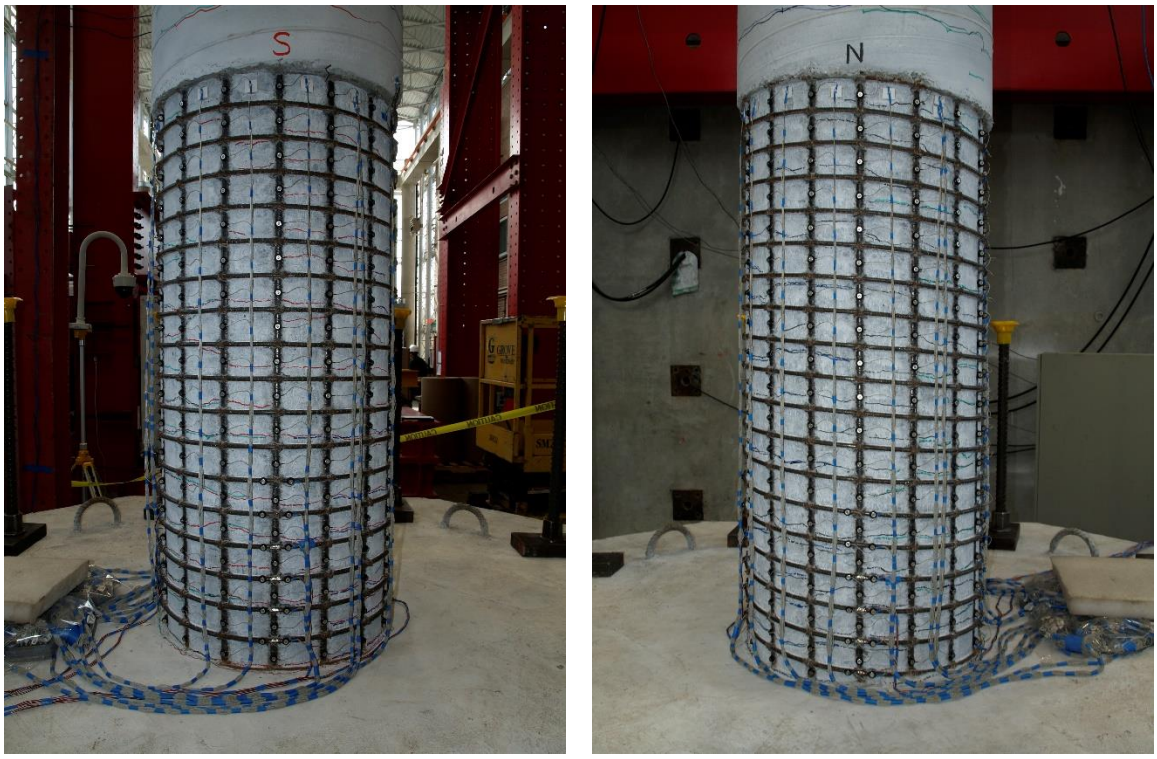

Figure 4-19. Test 1: Cracking on the South and North Sides during $\Delta'_y = 1.10"$ and $\Delta'_y = -1.11"$ in Y-Direction

Figure 4-20. Test 1: Cracking on the West and East Sides during $\Delta'_y = 1.12"$ and $\Delta'_y = -1.13"$ in X-Direction

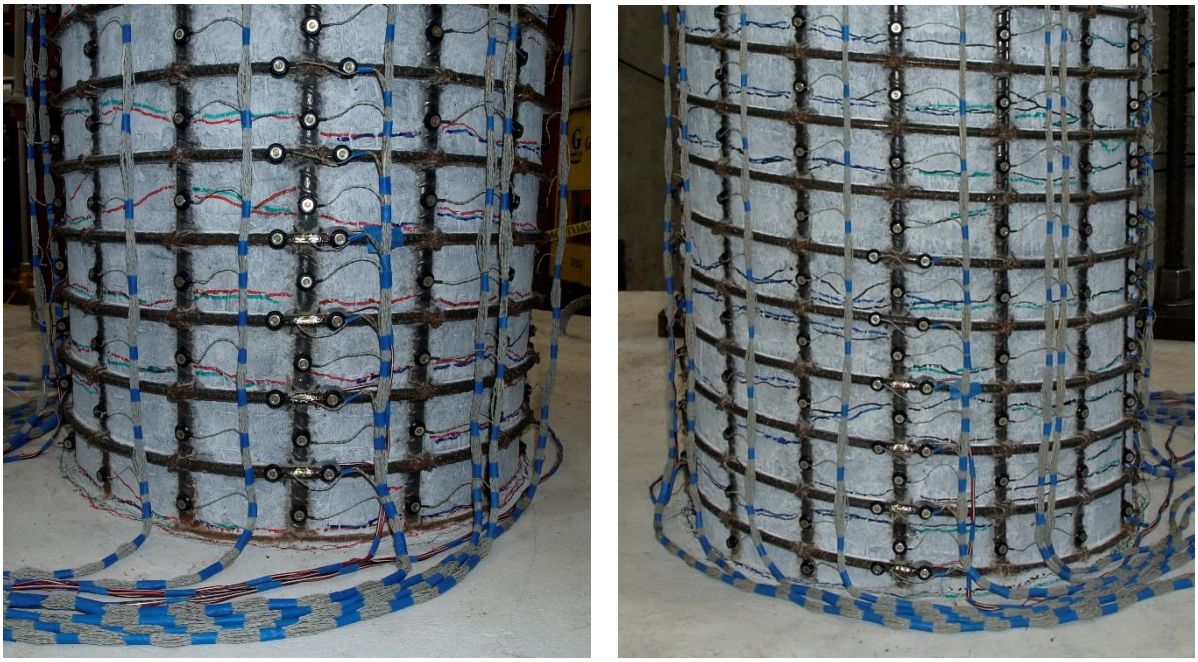

Figure 4-21. Test1: Cracking on the (Left) South Side at $\mu_{\Delta 1}^{+2y} = 1.51"$ and (Right) North Side at $\mu_{\Delta 1}^{-2y} = -1.49"$

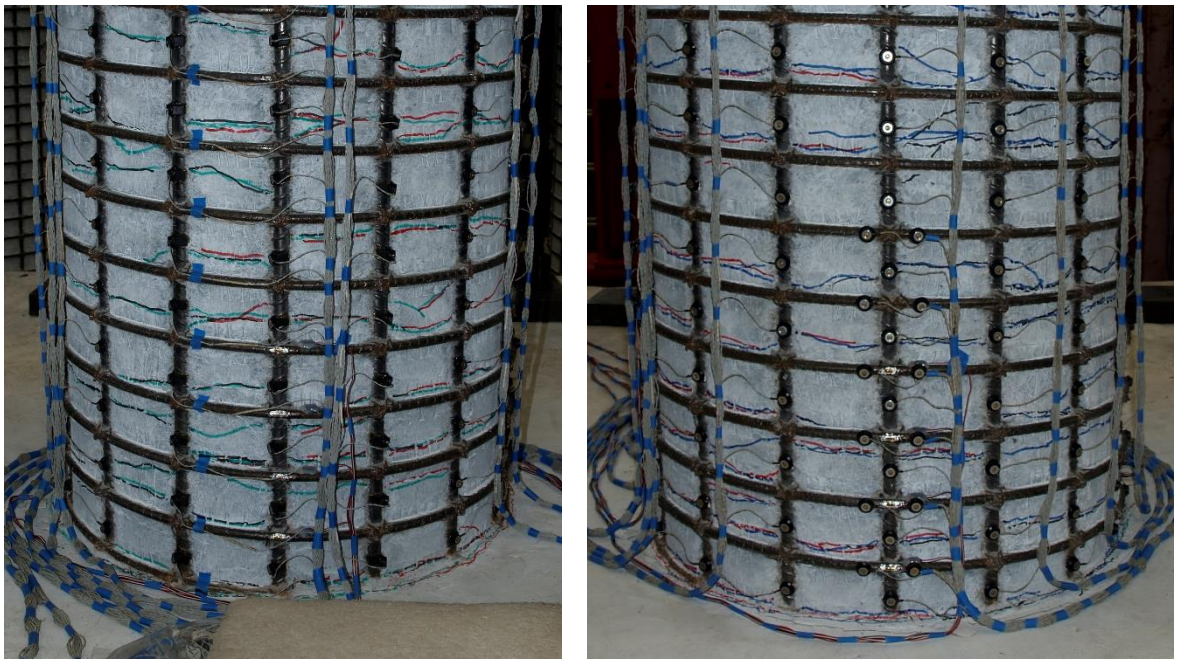

Figure 4-22. Test 1: Cracking on the (Left) West Side at $\mu_{\Delta 1}^{+2x} = 1.55"$ and (Right) East Side at $\mu_{\Delta 1}^{-2x} = -1.41"$

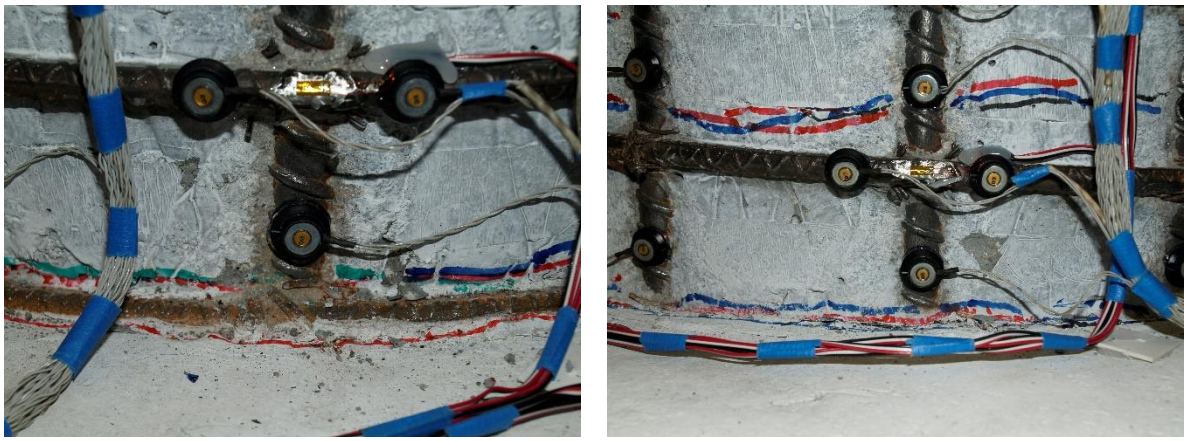

Figure 4-23. Test 1: Concrete Flacking on the (Left) South at $\mu_{\Delta 1.5}^{-1y} = -2.25$" and (Right) East at $\mu_{\Delta 1.5}^{+1x} = 2.28$"

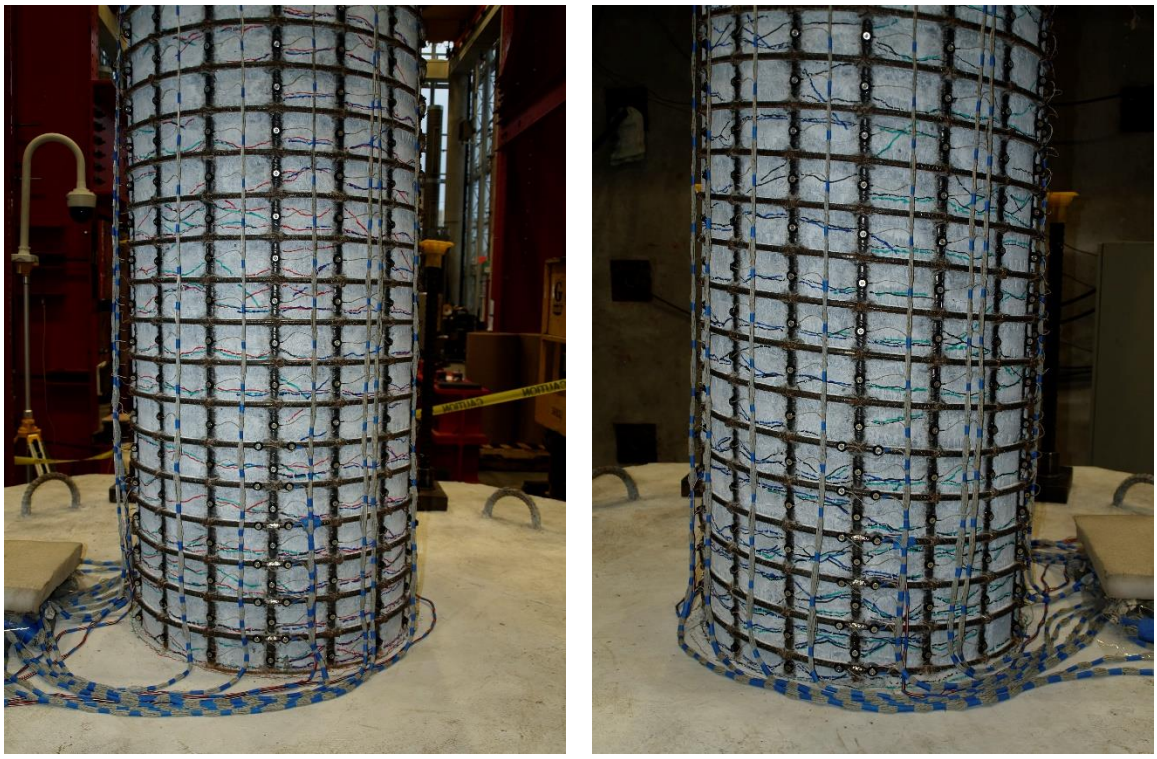

Figure 4-24. Test 1: (Left) South and (Right) North Sides of the Specimen at the End of $\mu_{\Delta 1.5}$

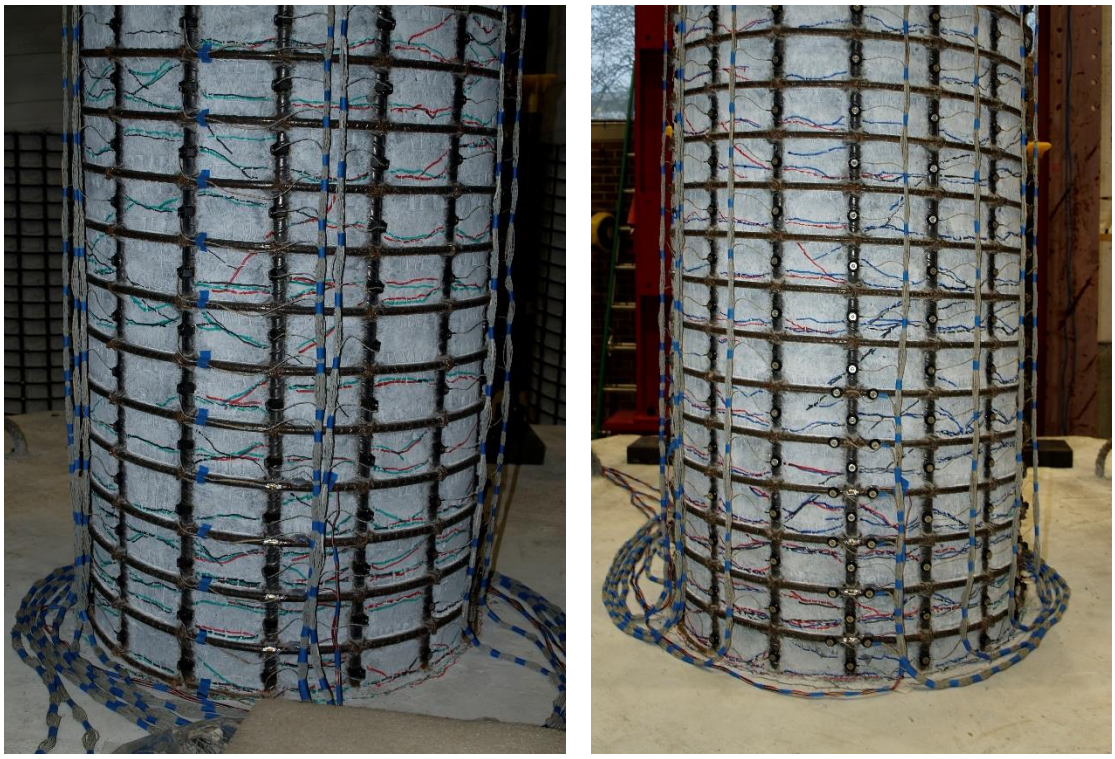

Figure 4-25. Test 1: (Left) West Side at $\mu_{\Delta 1.5}^{+2x} = 2.25"$ and (Right) East Side at $\mu_{\Delta 1.5}^{-2x} = -2.28"$

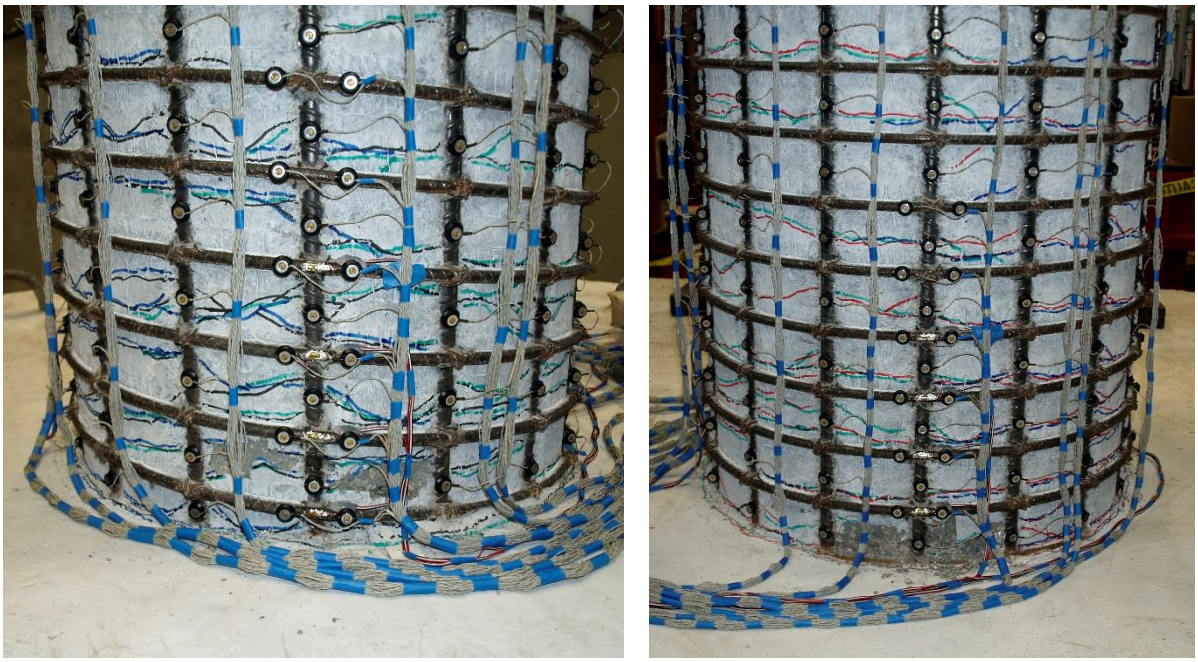

Figure 4-26. Test 1: First Crushing on the (Left) North Side at $\mu_{\Delta 2}^{+1y} = 3.01"$ and (Right) South Side at $\mu_{\Delta 2}^{-1y} = -3.03"$

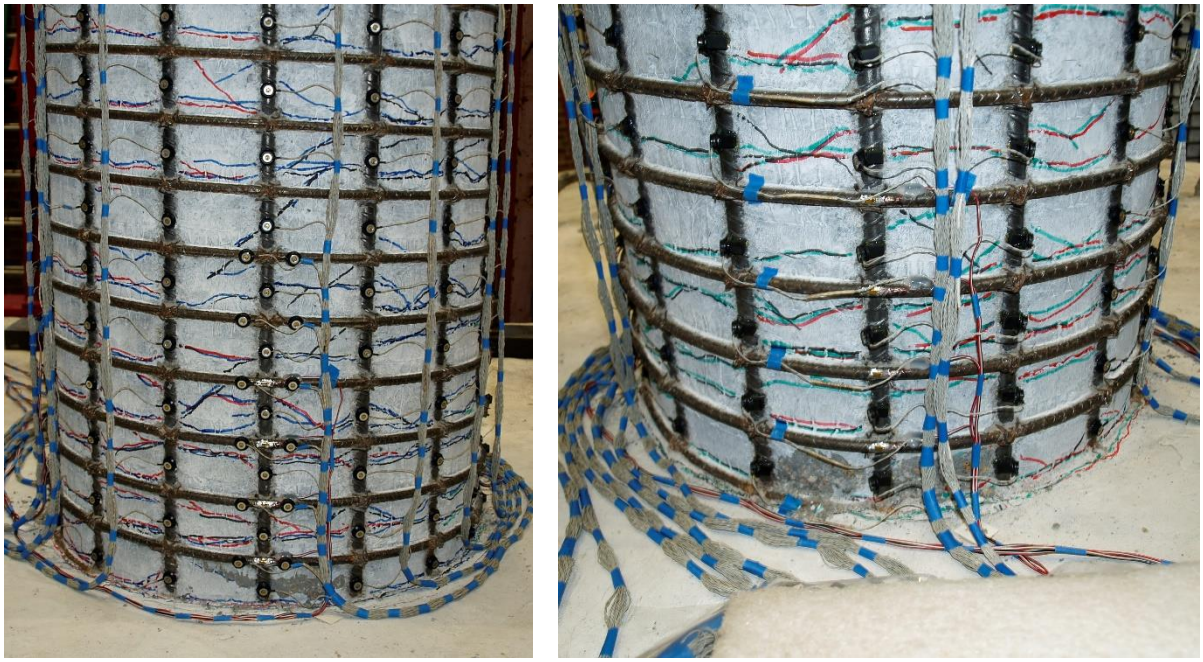

Figure 4-27. Test 1: First Crushing on the (Left) East Side at $\mu_{\Delta 2}^{+1x} = 3.02$" and (Right) West Side at $\mu_{\Delta 2}^{-1x} = -3.03$"

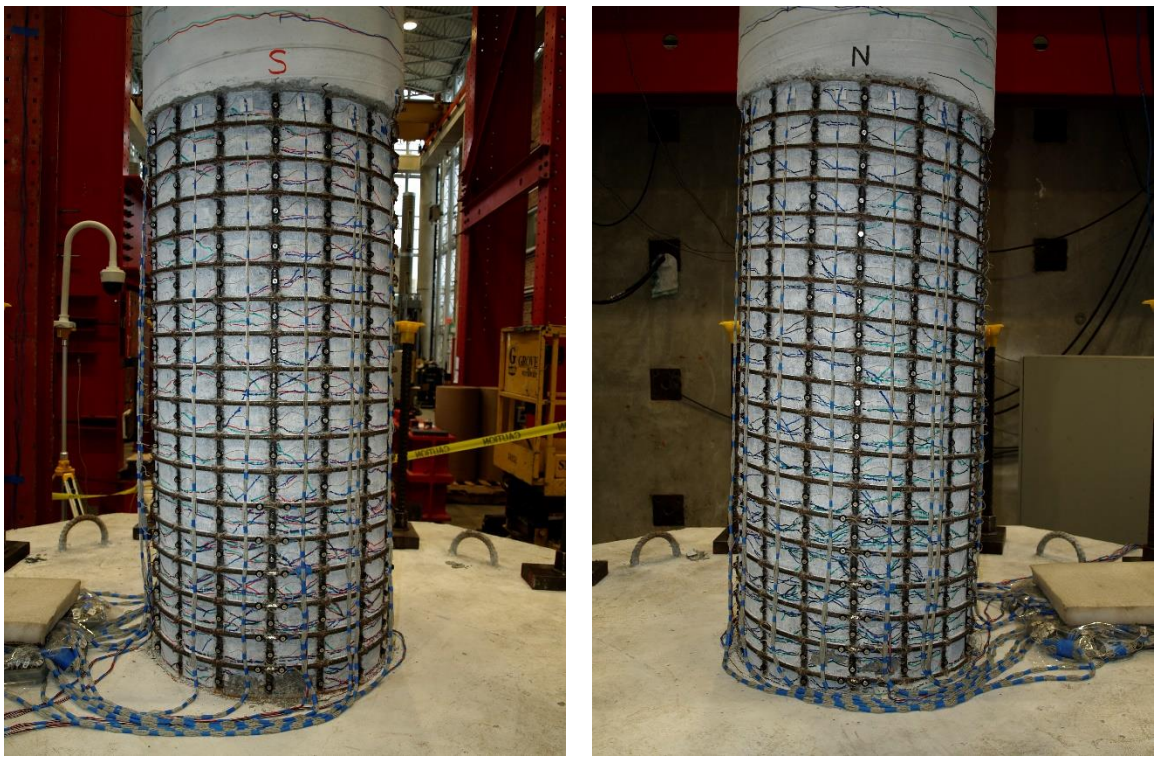

Figure 4-28. Test 1: (Left) South and (Right) North Sides of the Specimen at the End of $\mu_{\Delta 2}$

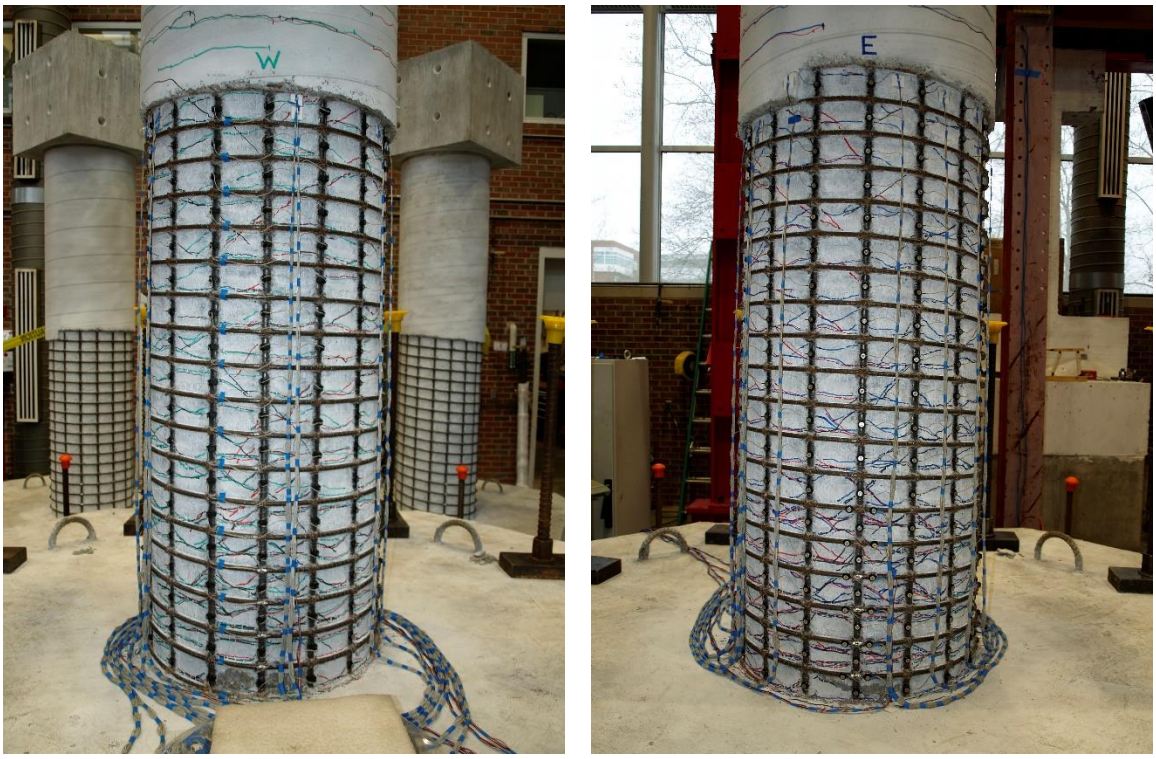

Figure 4-29. Test 1: (Left) West Side at $\mu_{\Delta 2}^{+2x} = 3.02"$ and (Right) East Side at $\mu_{\Delta 2}^{-2x} = -3.02"$

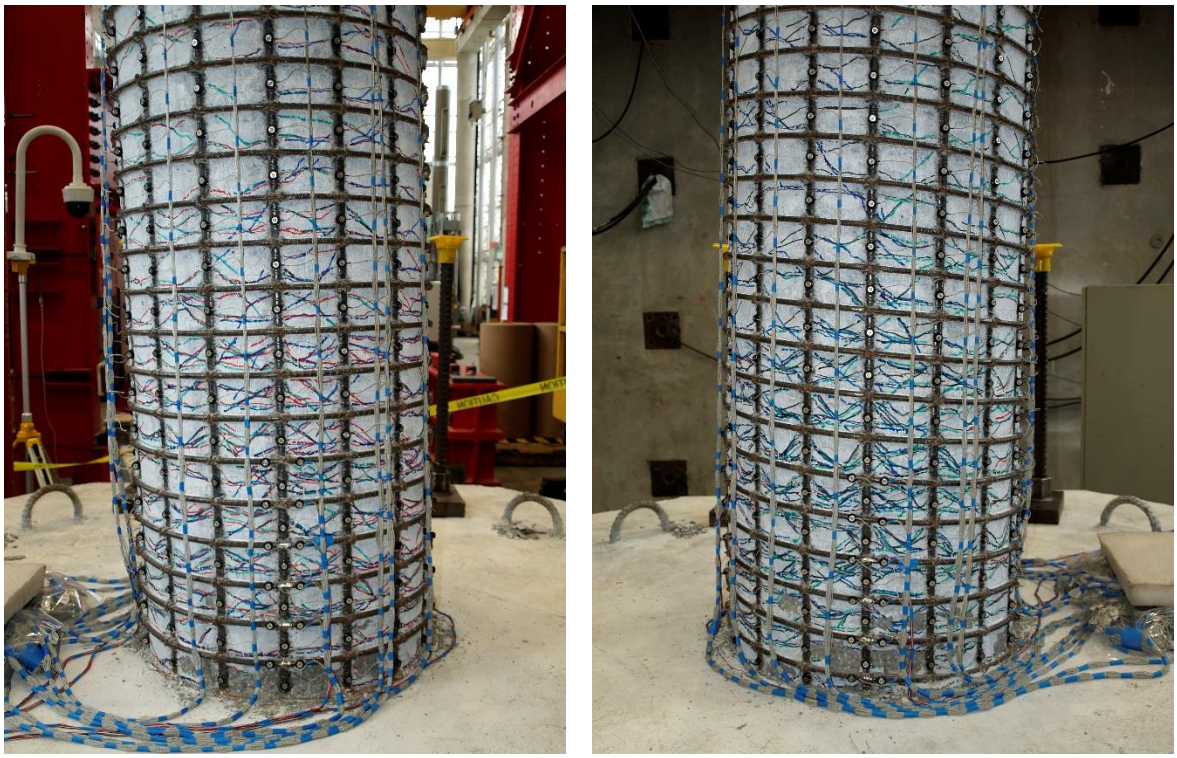

Figure 4-30. Test 1: (Left) South and (Right) North Sides of the Specimen at the End of $\mu_{\Delta 3}$

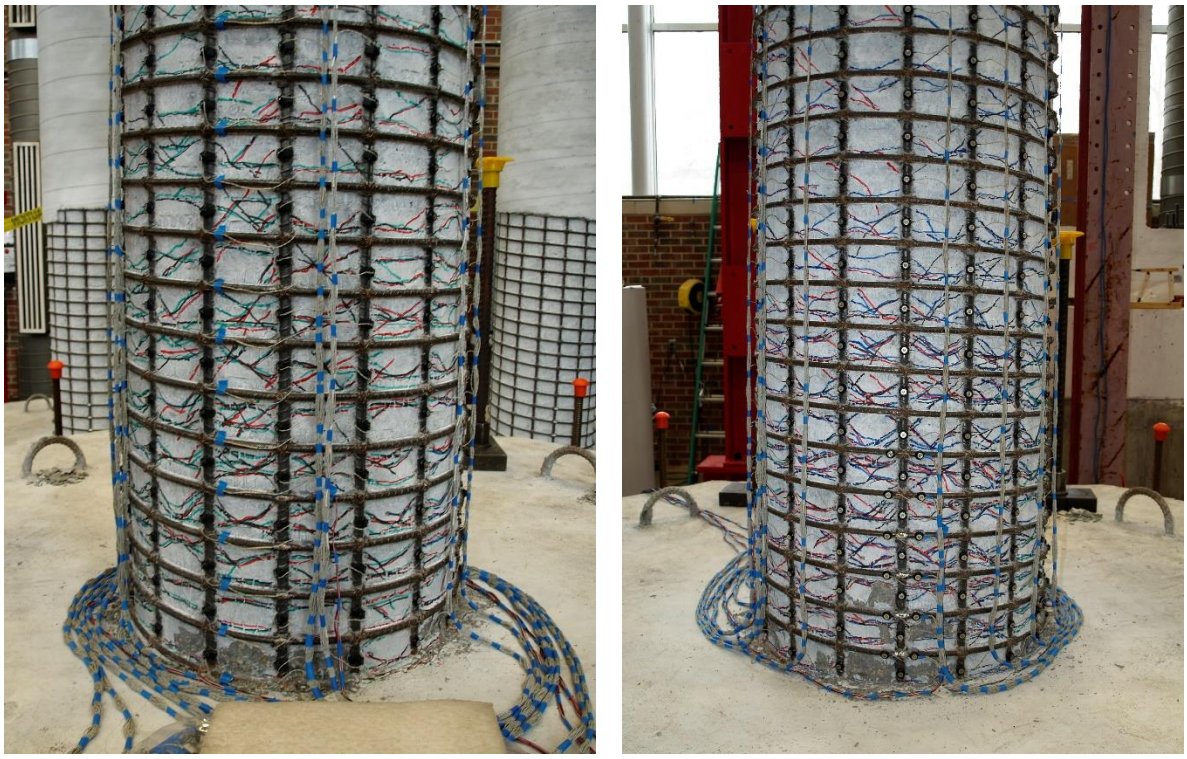

Figure 4-31. Test 1: (Left) West Side at $\mu_{\Delta 3}^{+2x} = 4.52"$ and (Right) East Side at $\mu_{\Delta 3}^{-2x} = -4.54"$

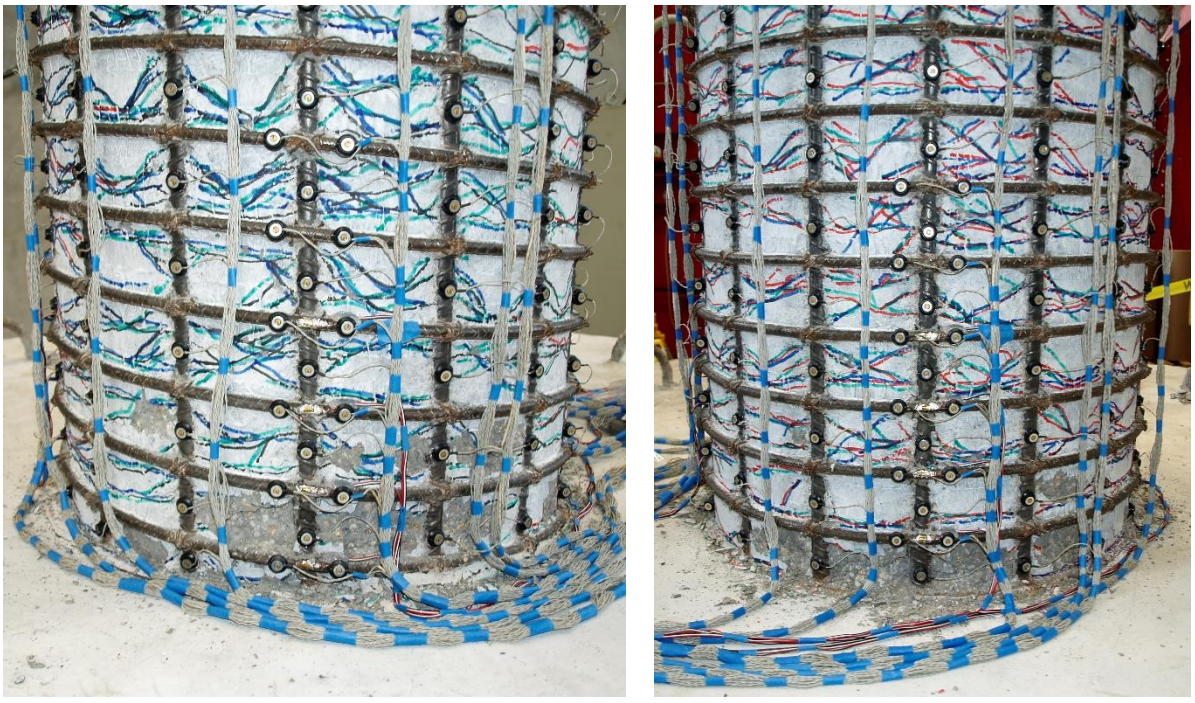

Figure 4-32. Test 1: Crushing on the (Left) North Side at $\mu_{\Delta 4}^{+1y} = 6.05"$ and (Right) South Side at $\mu_{\Delta 4}^{-1y} = -6.04"$

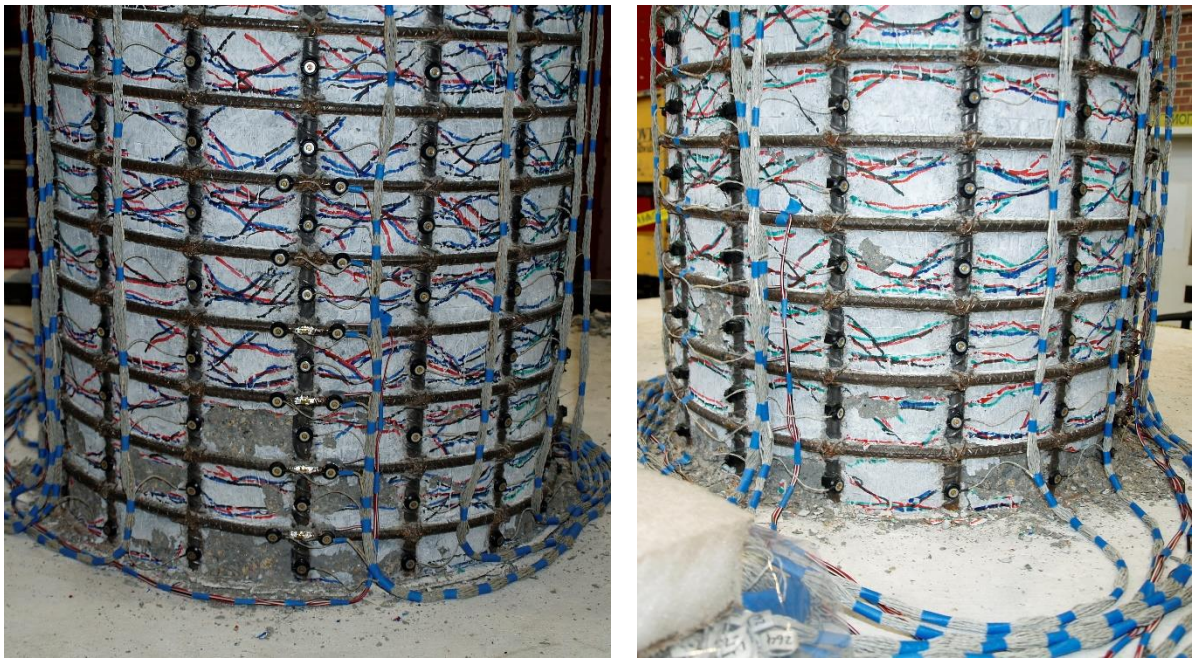

Figure 4-33. Test 1: Crushing on the (Left) East Side at $\mu_{\Delta 4}^{+1x} = 6.05"$ and (Right) West Side at $\mu_{\Delta 4}^{-1x} = -6.05"$

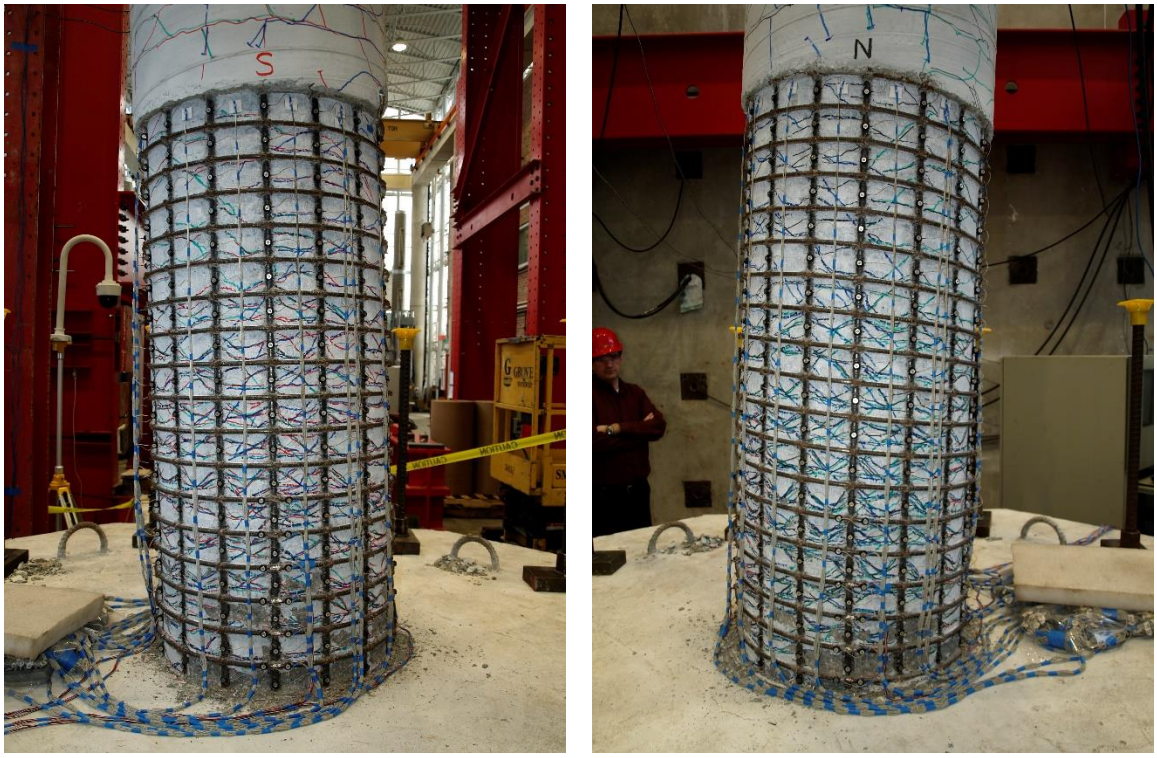

Figure 4-34. Test 1: (Left) South and (Right) North Sides of the Specimen at the End of $\mu_{\Delta 4}$

Figure 4-35. Test 1: (Left) West Side at $\mu_{\Delta 4}^{+2x} = 6.03"$ and (Right) East Side at $\mu_{\Delta 4}^{-2x} = -6.04"$

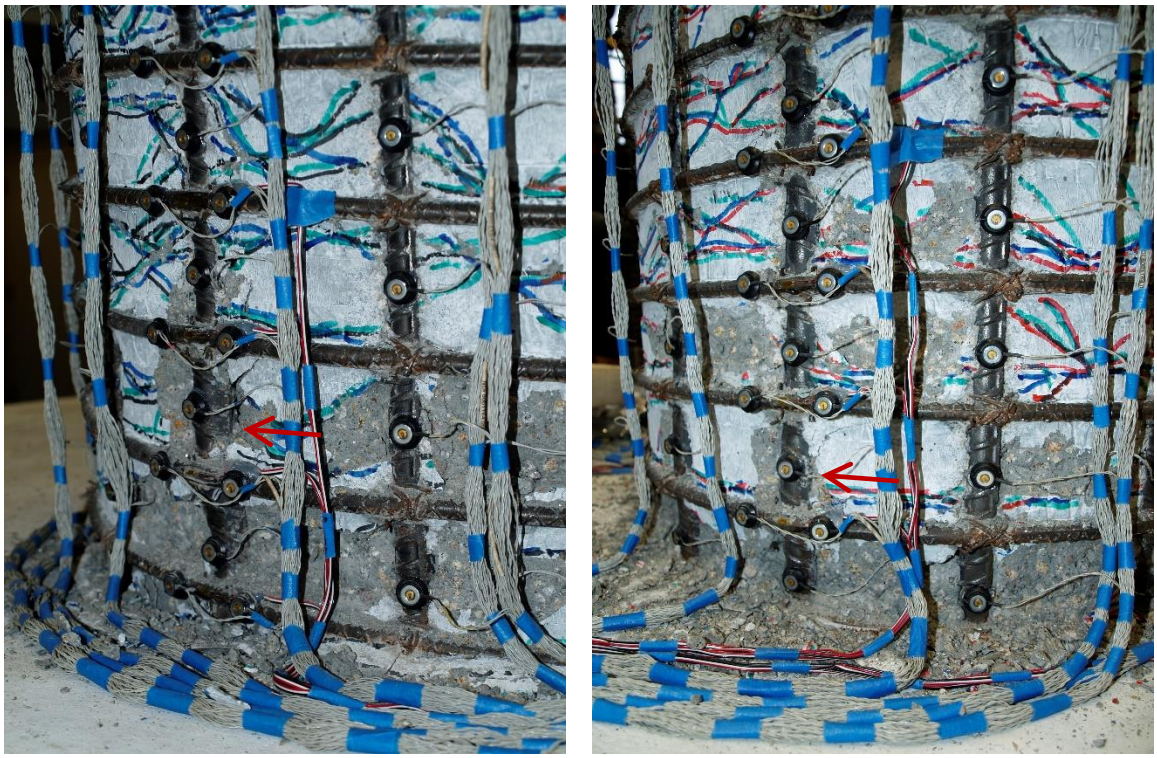

Figure 4-36. Test 1: Buckling of (Left) North Bar during $\mu_{\Delta 5}^{+1y} = 7.51"$ and (Right) South Bar during $\mu_{\Delta 5}^{-1y} = -7.55"$

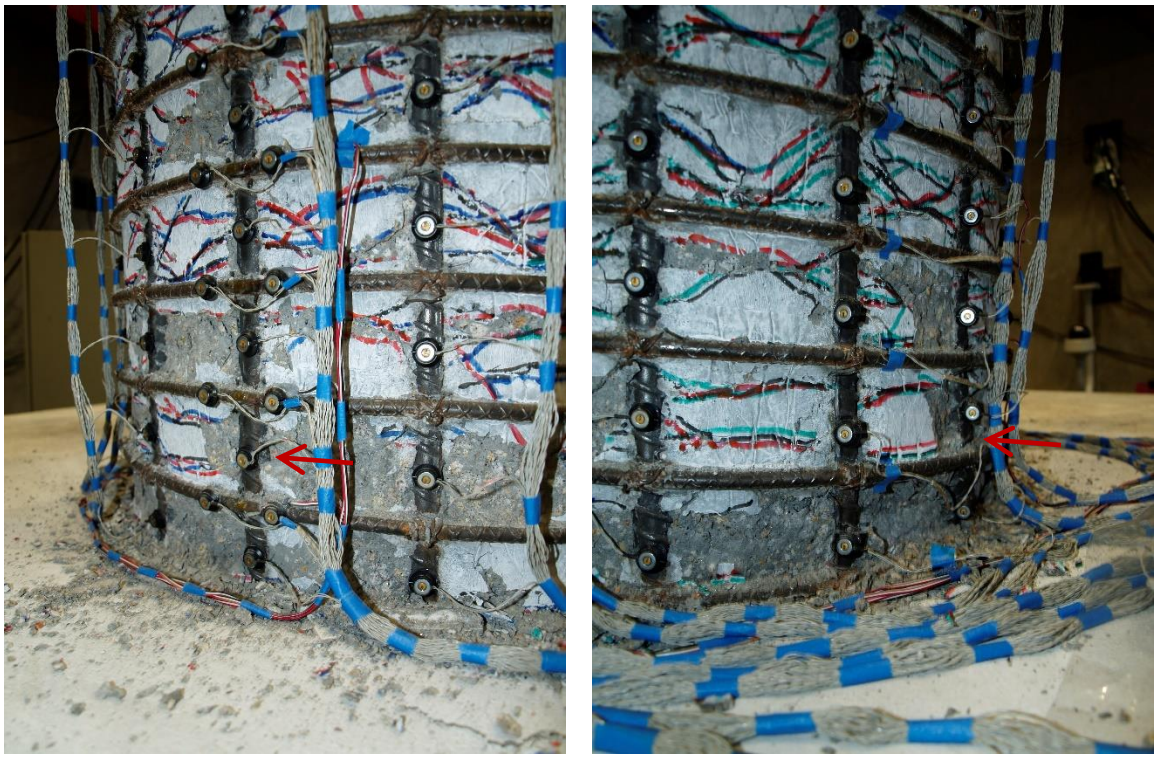

Figure 4-37. Test 1: Buckling of (Left) East Bar during $\mu_{\Delta 5}^{+1x} = 7.48"$ and (Right) West Bar during $\mu_{\Delta 5}^{-1x} = -7.56"$

Figure 4-38. Test 1: Buckling of Bars (Left) NNE & NNW during $\mu_{\Delta 5}^{+2y} = 7.42"$ and (Right) SSE & SSW during $\mu_{\Delta 5}^{-2y} = -7.55"$

Figure 4-39. Test 1: Specimen Deformation at $\mu_{\Delta 5}^{+1y} = 7.51"$

Figure 4-40. Test 1: Buckling of (Left) All East Bars during $\mu_{\Delta 5}^{+2x} = 7.44"$ and (Right) All West Bars during $\mu_{\Delta 5}^{-2x} = 7.56"$

Figure 4-41. Test 1: (Left) Additional Deformation in North Buckled Reinforcement during $\mu_{\Delta 5}^{+3x} = 7.33"$ and (Right) Fracture of North Bar at $\Delta_y = -2.90"$ during $\mu_{\Delta 5}^{-3Y}$

Figure 4-42.Test 1: (Left) North and (Right) West Sides after Instrumentation Removal

Figure 4-43. Test 1: (Left) South and (Right) East Sides after Instrumentation Removal

Test 1 - Strain Data Analysis

North Bar Strains

Vertical strain profiles for the North extreme fiber bar appear in Figure 4-44 and Figure 4-45. Bar N was placed into compression during +Y cycles and tension during -Y cycles. Beyond displacement ductility two, tensile strains recorded in the second to fourth gauge lengths above the footing began to exceed those measured in the lowest gauge length. A peak tensile strain of 0.0284 was observed in Bar N at $\mu_{\Delta 4}^{-2y} = -6.01$" before bar buckling was observed visually during $\mu_{\Delta 5}^{+1y} = 7.51$". The buckled deformation was not severe, and the bar straightened out during $\mu_{\Delta 5}^{-1y} = -7.55$", producing the tensile strains shown in Figure 4-45. The relationship between tensile strain and displacement for the second gauge length above the footing for the North bar appears in Figure 4-50. The strain-displacement comparisons contain monotonic moment curvature predictions for respective plastic hinge methods. PCK (2007) Lp refers to the (Priestley, Calvi and Kowalsky 2007) plastic hinge method, GN15 Tension/Compression Lpr refers to the (Goodnight, Kowalsky and Nau 2015a) unidirectional modified plastic hinge method, TX Adjusted Lpr and Lsp refer to using the measured extent of plasticity and average equivalent strain penetration length from this specific test, and New Equations refers to a new bidirectional plastic hinge method which was created based on this study. Details of the new plastic hinge method appear in a later chapter of this report.

Compression strains in the North bar were localized to the first three gauge lengths above the footing. A compression strain of -0.00562 was measured at $\mu_{\Delta 2}^{+1y} = 3.01$", when concrete crushing was first observed. A compression strain of -0.00888 coincided with initial yielding of confinement steel on the North side of the specimen at $\Delta_y = 4.06$" during $\mu_{\Delta 3}^{+1Y} = 4.52$". A peak compression strain of -0.0160 was measured during $\mu_{\Delta 4}^{+2Y} = 6.00$", prior to visible bar buckling. In comparison, the (Mander, Priestley and Park 1988) original ultimate concrete compression strain was $\varepsilon_{cu} = -0.0145$. Measured spiral strains in six layers overlaying the North extreme fiber bar during compressions cycles appear in Figure 4-46. Larger spiral strains during successive compression cycles of displacement ductility four were observe din the second and third spiral layers above the footing. The measured spiral strains spiked during $\mu_{\Delta 5}^{+1y} = 7.51$", when visible buckling of Bar N was observed.

The sequence of events preceding bar buckling are more easily understood upon inspection of the longitudinal and transverse steel strain histories in the buckled region. The strain hysteresis for the first gauge length above the footing on the North bar is shown in Figure 4-52 along with the strain history for the overlaying spiral layer in Figure 4-53. This region aligns with the location of the bar which outwardly deformed during $\mu_{\Delta 5}^{+1y} = 7.51$" when bar buckling was observed, see Figure 4-36. The spiral strain hysteresis includes both the measurements from the strain gauge and the Optotrak gauge length. The spiral tends to straighten out to the left and right of the more localized inelasticity over the longitudinal bar. Since the strain gauge encompasses a smaller gauge length, it will measure larger strains. The Optotrak strains are computed based on the change in arc length measured between adjacent target markers which were placed approximately 2” apart. Stable hysteretic response was observed in the North longitudinal bar until $\mu_{\Delta 4}^{+2Y} = 6.00$", when compression strains broke away from prior trends indicating some degree of measurable outward deformation in the bar. This observation consider with a cycle-to-cycle increase in the measured tensile strain in the overlaying spiral layer. The non-linear geometry induced by outward deformation in the buckled region leads to measured compression strains that reflect the change in geometry and not the real

magnitude of strain experienced in that region of the column. As the bar visibly buckled during $\mu_{\Delta 5}^{+1y} = 7.51"$, the outward deformation lead to a sharp deviation from the prior compression strain-displacement relationship and a significant increase in the spiral tension strains. The strain hysteresis are plotted one cycle beyond visible bar buckling, when the noted effects of the outward deformation significantly increased.

South Bar Strains

Vertical strain profiles for the South extreme fiber bar appear in Figure 4-44 and Figure 4-45. Bar S was placed into tension during +Y cycles and compression during -Y cycles. A peak tensile strain of 0.0389 was observed in Bar S at $\mu_{\Delta 5}^{+1y} = 7.51"$ before bar buckling was observed visually during $\mu_{\Delta 5}^{-1y} = -7.55"$. The relationship between tensile strain and displacement for the fourth Bar S gauge length above the footing is shown in Figure 4-48. A compression strain of -0.00652 was measured at $\mu_{\Delta 2}^{-1y} = -3.03"$, when concrete crushing was first observed. A compression strain of -0.00823 coincided with initial yielding of confinement steel on the South side of the specimen at $\Delta_y = -4.20"$ during $\mu_{\Delta 3}^{-1Y} = -4.56"$. The influence of compression on spiral strains measured over the South extreme fiber bar is presented in Figure 4-47. Larger spiral strains were observed in the first and second spiral layers during successive cycles of displacement ductility four. A peak compression strain of -0.0192 was measured in the second Bar S gauge length above the footing during $\mu_{\Delta 4}^{-2y} = -6.02"$. In comparison, the (Mander, Priestley and Park 1988) original ultimate concrete compression strain was $\varepsilon_{cu} = -0.0145$. The relationship between compression strain and displacement for the second gauge length above the footing on Bar S appears in Figure 4-51. The influence of bar buckling is clearly visible during $\mu_{\Delta 5}^{-1y} = -7.55"$, which coincided with the visual observation. Spiral strains measured with the Optotrak system in six South spiral layers during compression cycles appear in Figure 4-47.

The strain hysteresis for the first Bar S gauge length above the footing appears in Figure 4-54, while the strain history for the first South spiral layer is shown in Figure 4-55. This location coincided with the outward deformed region of the South bar which buckled during $\mu_{\Delta 5}^{-1y} = -7.55"$, see Figure 4-36. Successive cycles during displacement ductility four led to increased spiral strains and small levels of outward measurable deformation in the longitudinal bar. Since the gauge length is over the outward deformed region, the measurable deformation leads to lower compression strain magnitudes. The opposite effect was observed in the second gauge length, see Figure 4-51. Once measurable deformation occurs, the strain history reflects the non-linear geometry of the bar. Visible buckling of the South extreme fiber bar during $\mu_{\Delta 5}^{-1y} = -7.55"$ led to a significant spike in the measured spiral strains.

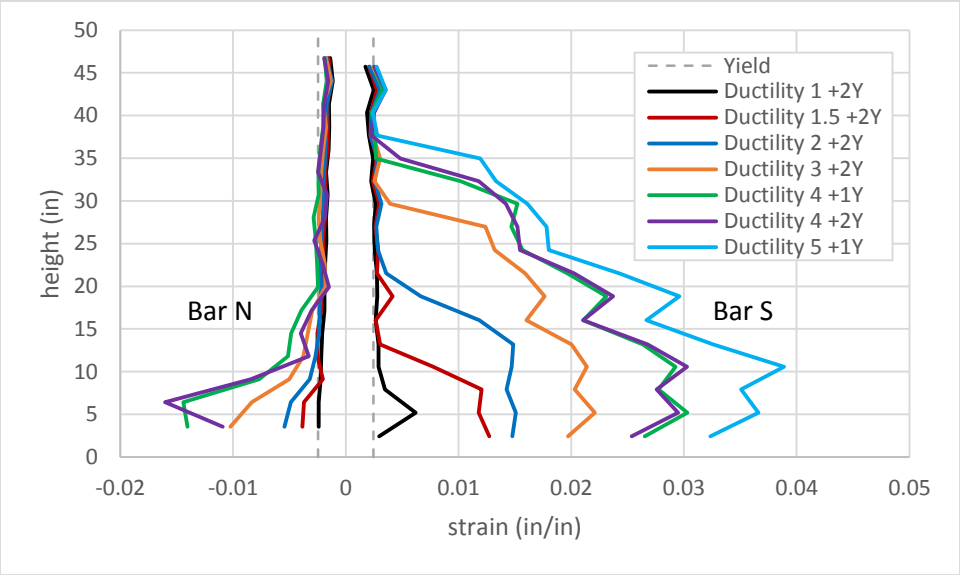

Figure 4-44. Test 1: Vertical Strain Profiles for Loading in the +Y-direction

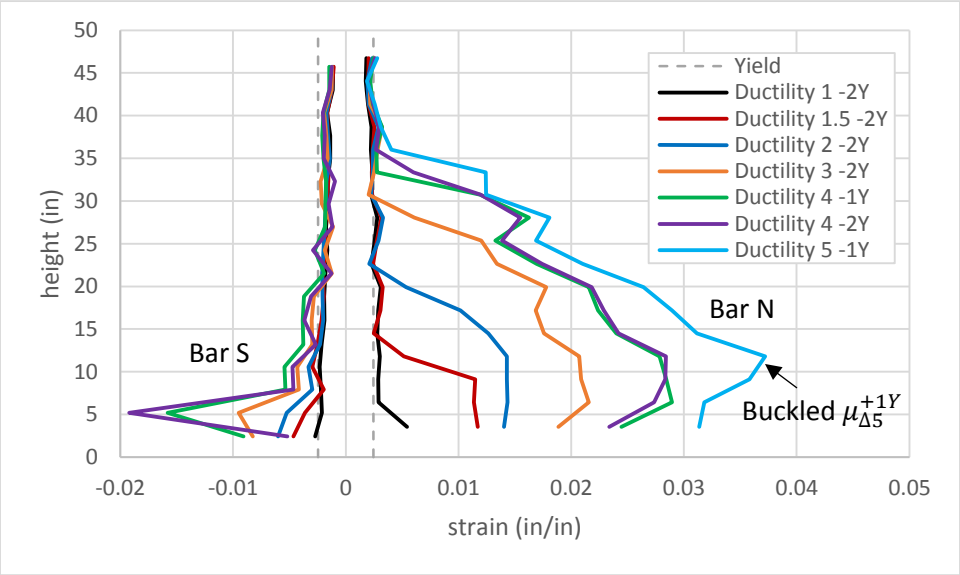

Figure 4-45. Test 1: Vertical Strain Profiles for Loading in the -Y-direction

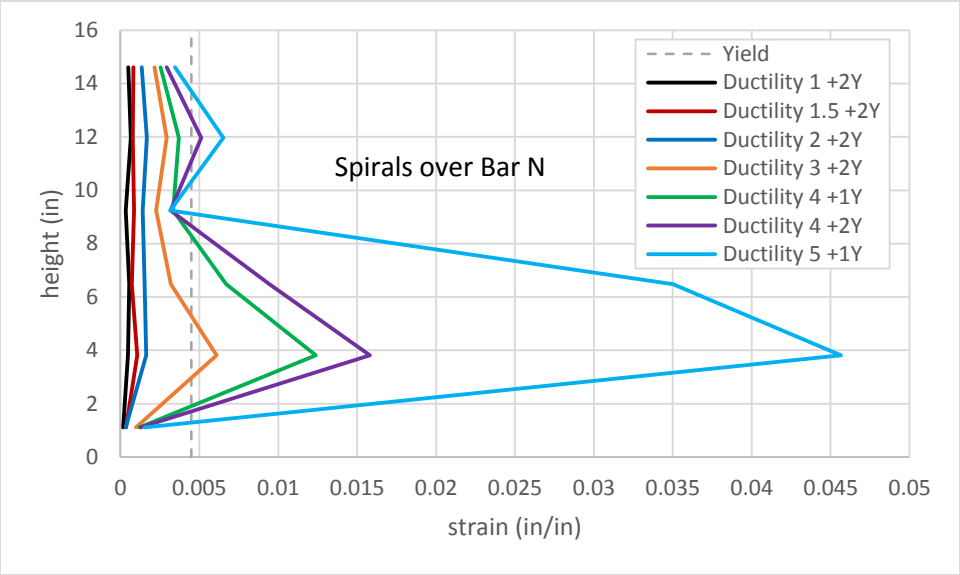

Figure 4-46. Test 1: Optotrak Strains in Six Spiral Layers over the North Extreme Fiber Bar

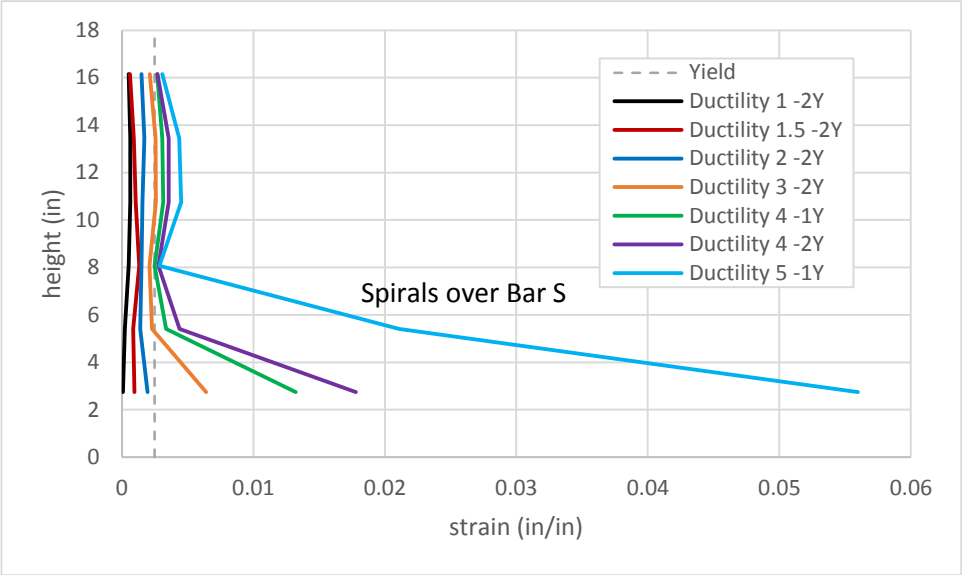

Figure 4-47. Test 1: Optotrak Strains in Six Spiral Layers over the South Extreme Fiber Bar

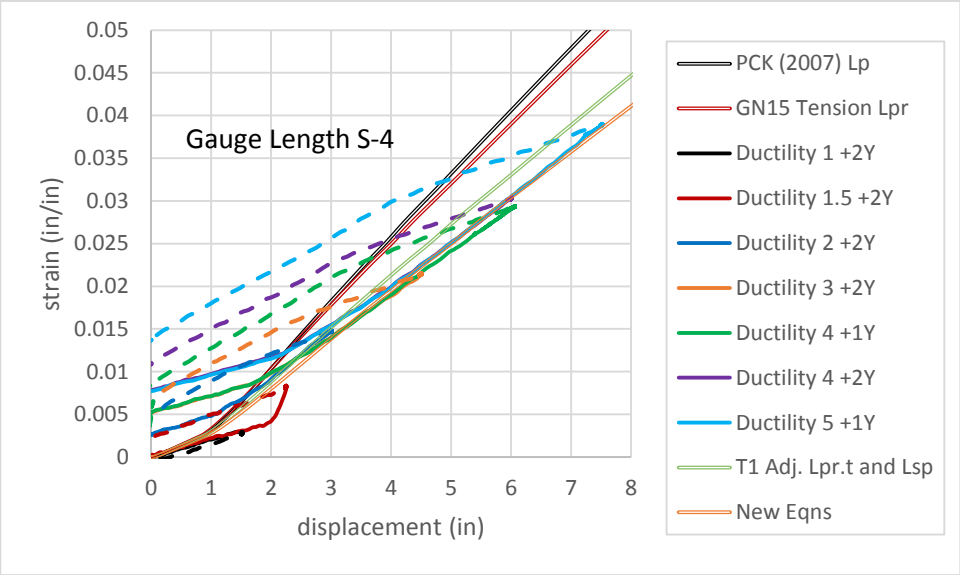

Figure 4-48. Test 1: Tension Strain-Disp. for Bar S (Gauge Length 4 Centered 10.58" above the Footing)

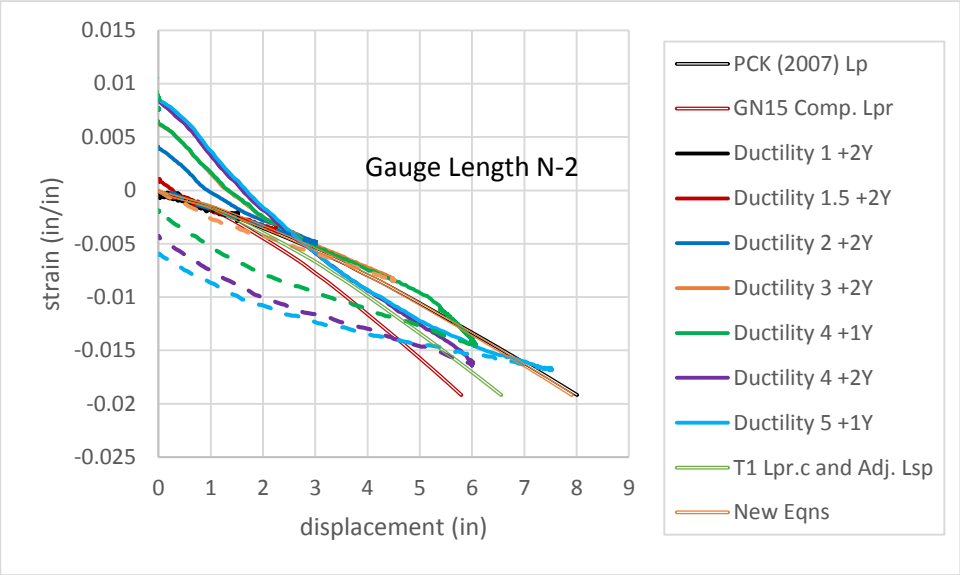

Figure 4-49. Test 1: Compression Strain-Disp. for Bar N (Gauge Length 2 Centered 6.41" above the Footing)

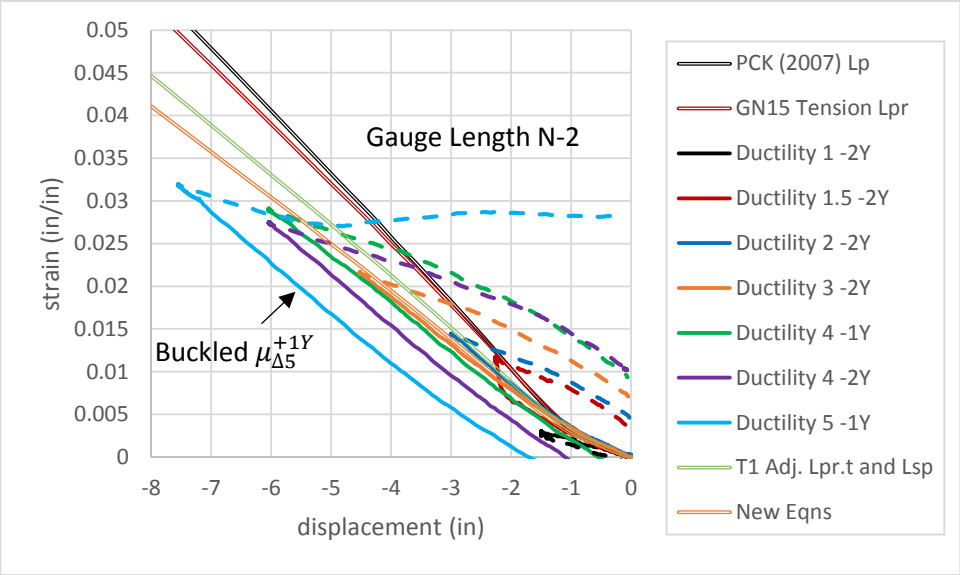

Figure 4-50. Test 1: Tension Strain-Disp. for Bar N (Gauge Length 2 Centered 6.41" above the Footing)

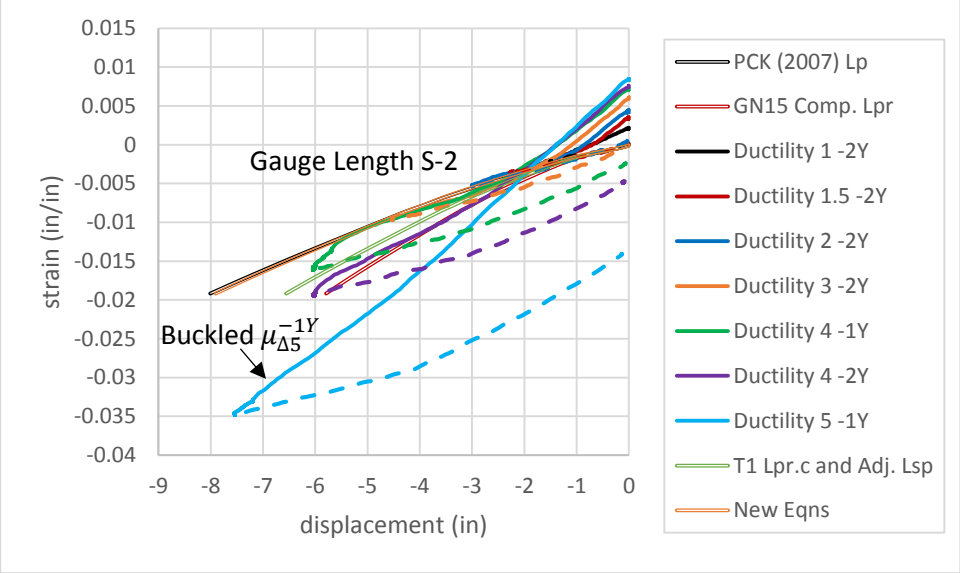

Figure 4-51. Test 1: Compression Strain-Disp. for Bar S (Gauge Length 2 Centered 5.19" above the Footing)

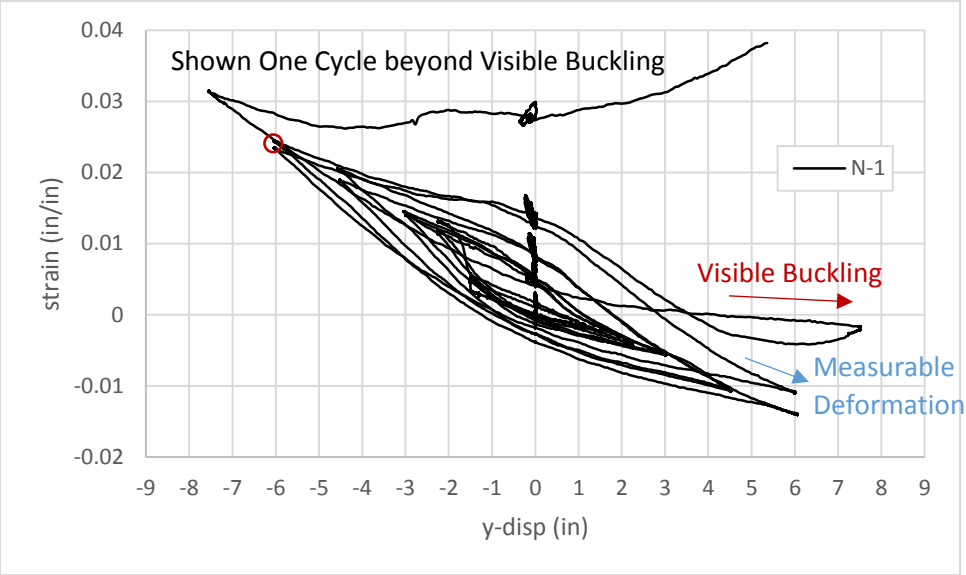

Figure 4-52. Test 1: Strain Hysteresis over the North Buckled Bar (Gauge Length 1 Centered 3.55" above the Footing)

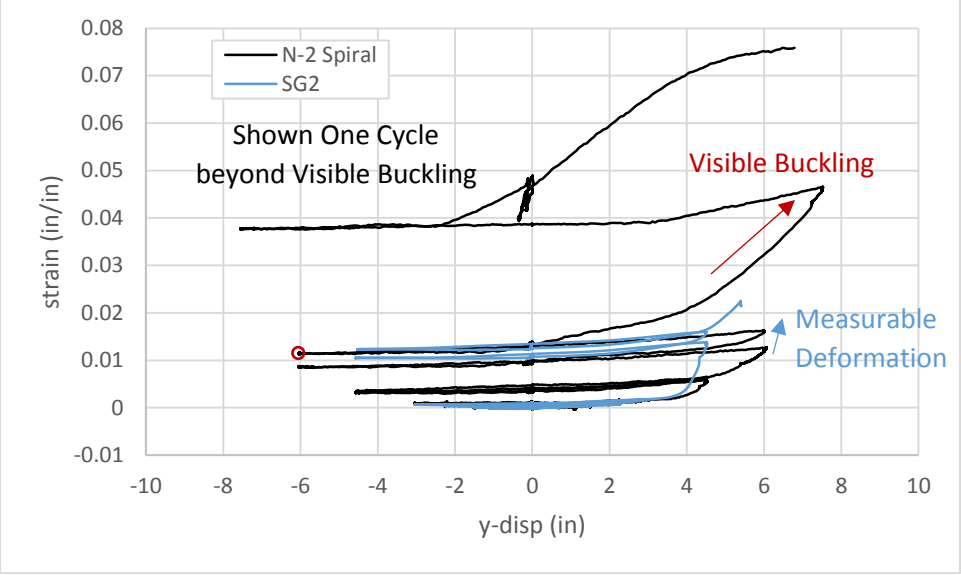

Figure 4-53. Test 1: Spiral Strains in the Second North Layer (3.81" above the Footing)

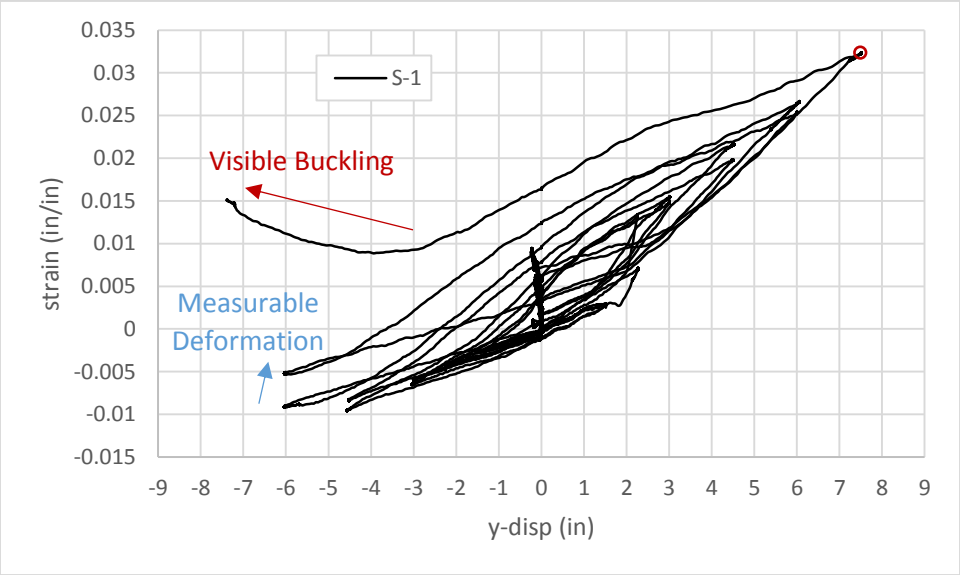

Figure 4-54. Test 1: Strain Hysteresis over the South Buckled Bar (Gauge Length 1 Centered 2.43" above the Footing)

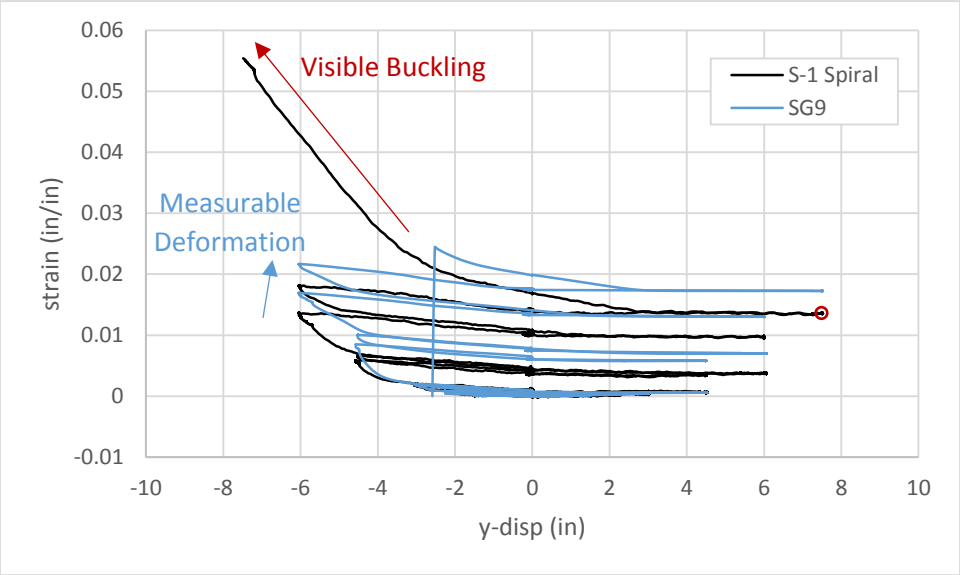

Figure 4-55. Test 1: Spiral Strains in the First South Layer (2.74" above the Footing)

East Bar Strains

Vertical strain profiles for the East extreme fiber bar appear in Figure 4-56 and Figure 4-57. Bar E was placed into tension during –X cycles and compression during +X cycles. A peak tension strain of 0.0288 was measured in Bar E at $\mu_{\Delta 4}^{-2x} = -6.04$", before bar buckling was observed visually during $\mu_{\Delta 5}^{+1x} = 7.48$". The buckled deformation was not severe, and the bar straightened out during $\mu_{\Delta 5}^{-1x} = -7.56$", producing the tensile strains shown in Figure 4-57. The relationship between tensile strain and displacement for the second Bar E gauge length above the footing is shown in Figure 4-62. The strain-displacement comparisons contain monotonic moment curvature predictions for respective plastic hinge methods. PCK (2007) Lp refers to the (Priestley, Calvi and Kowalsky 2007) plastic hinge method, GN15 Tension/Compression Lpr refers to the (Goodnight, Kowalsky and Nau 2015a) unidirectional modified plastic hinge method, TX Adjusted Lpr and Lsp refer to using the measured extent of plasticity and average equivalent strain penetration length from this specific test, and New Equations refers to a new bidirectional plastic hinge method which was created based on this study. Details of the new plastic hinge method appear in a later chapter of this report.

A compression strain of -0.00626 was measured at $\mu_{\Delta 2}^{+1x} = 3.02$", when concrete crushing was first observed. A compression strain of -0.00722 coincided with initial yielding of confinement steel on the East side of the specimen at $\Delta_x = 4.10$" during $\mu_{\Delta 4}^{+1x} = 6.05$". Note that the displacement at initial spiral yielding was lower than those experienced during two prior compression cycles at displacement ductility three. A peak compression strain of -0.0130 was measured in the first Bar E gauge length above the footing during $\mu_{\Delta 4}^{+2x} = 6.03$". In comparison, the (Mander, Priestley and Park 1988) original ultimate concrete compression strain was $\varepsilon_{cu} = -0.0145$. The relationship between compression strain and displacement for the first gauge length above the footing on Bar E appears in Figure 4-61. It is notable that spiral yielding was observed later on Bar E and that localization of compressive demand was not observed to the extent as in the North and South extreme fiber bars. Spiral strains measured with the Optotrak system in six East spiral layers during compression cycles are shown in Figure 4-58.

The strain hysteresis for the second Bar E gauge length above the footing appears in Figure 4-64, while the strain history for the second East spiral layer is shown in Figure 4-65. This location coincided with the outward deformed region of the East bar which buckled during $\mu_{\Delta 5}^{+1x} = 7.48$", see Figure 4-37. Note that the buckled deformation was less severe than at the initial observation of buckling for the other extreme fiber bars. The outward deformation increased significantly during $\mu_{\Delta 5}^{+2x} = 7.44$", which is evident in both the longitudinal and transverse steel hysteresis. The cycle-to-cycle increase in tensile strain in the second spiral layer during compression cycles coincided with only slight measurable deformation in Bar E.

West Bar Strains

Vertical strain profiles for the West extreme fiber bar appear in Figure 4-56 and Figure 4-57. Bar W was placed into tension during +X cycles and compression during -X cycles. A peak tension strain of 0.0396 was measured in Bar W at $\mu_{\Delta 5}^{+1x} = 7.48$", before bar buckling was observed visually during $\mu_{\Delta 5}^{-1x} = -7.56$". The relationship between tensile strain and displacement for the second Bar W gauge length above the footing is shown in Figure 4-60.

A compression strain of -0.00566 was measured at $\mu_{\Delta 2}^{-1x} = -3.03$", when concrete crushing was first observed. A compression strain of -0.00891 coincided with initial yielding of confinement steel on the West side of the specimen at $\Delta_x = -4.37$" during $\mu_{\Delta 3}^{-1x} = -4.52$". A peak compression strain of -0.0133 was measured in the second Bar W gauge length above the footing during $\mu_{\Delta 4}^{-2x} = -6.04$". In comparison, the (Mander, Priestley and Park 1988) original ultimate concrete compression strain was $\varepsilon_{cu} = -0.0145$. The relationship between compression strain and displacement for the second gauge length above the footing on Bar W appears in Figure 4-63. For this gauge length, visible bar buckling during $\mu_{\Delta 5}^{-1x} = -7.56$" led to increased apparent compression strains, however these values reflect the non-linear geometry of the bar rather than the real strain magnitude. Spiral strains measured using four strain gauges placed over the West extreme fiber bar during compression cycles are shown in Figure 4-59. Due to the placement of the three Optotrak position monitors, instrumentation of the spiral reinforcement on the West side of the specimen was not possible.

The strain hysteresis for the first Bar W gauge length above the footing appears in Figure 4-66, while the strain history for the first West spiral layer is shown in Figure 4-67. This location coincided with the outward deformed region of the West bar which buckled during $\mu_{\Delta 5}^{-1x} = -7.56$", see Figure 4-37. Successive compression cycles during displacement ductility four led to increases in the measured spiral strains and measurable outward deformation over the first gauge length. To a much lesser extent, this effect was measured during displacement ductility three after initial spiral yielding.

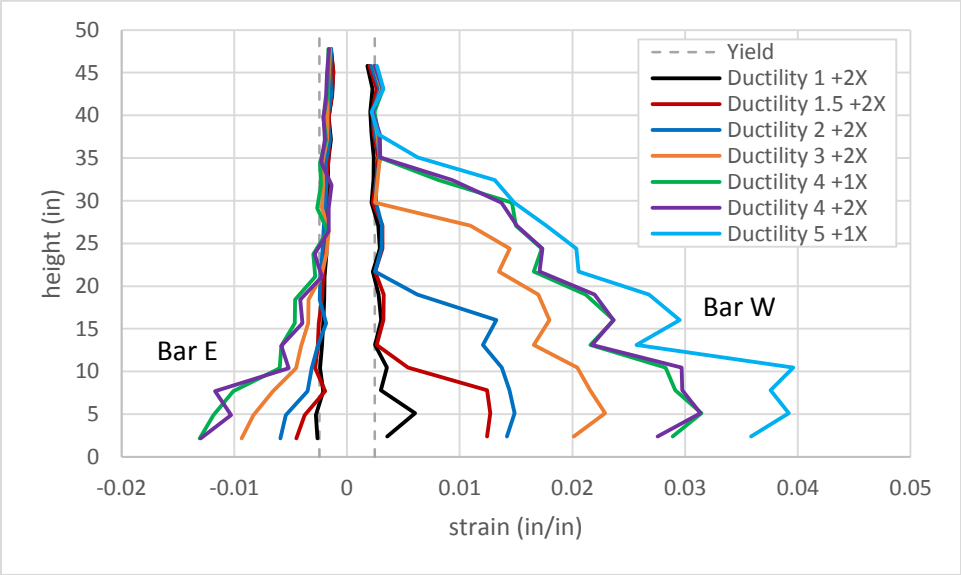

Figure 4-56. Test 1: Vertical Strain Profiles for Loading in the +X-direction

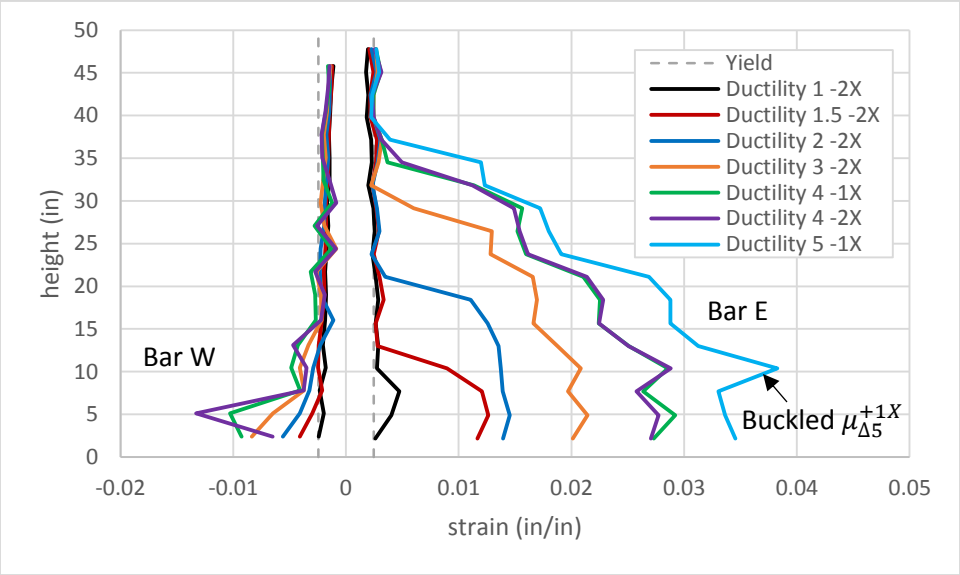

Figure 4-57. Test 1: Vertical Strain Profiles for Loading in the -X-direction

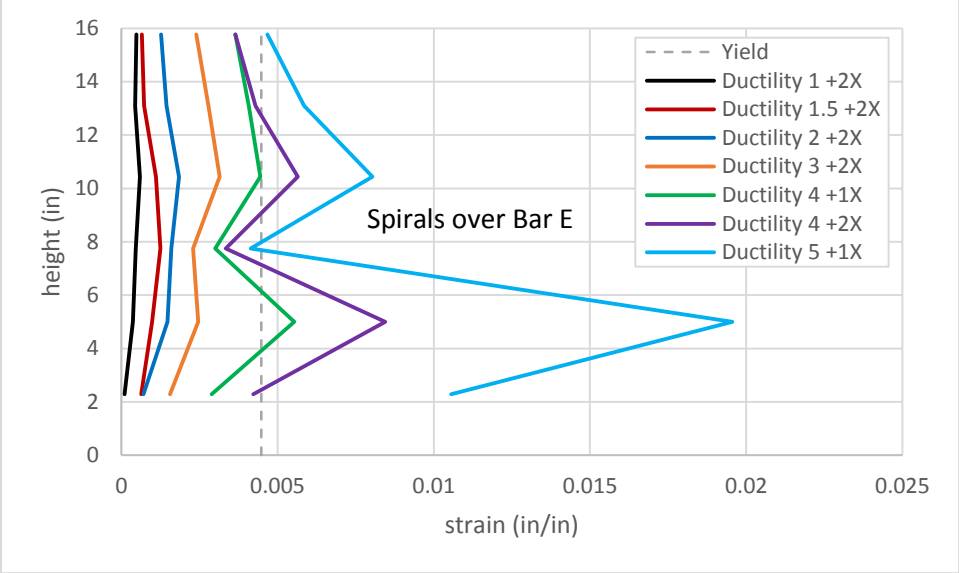

Figure 4-58. Test 1: Optotrak Strains in Six Spiral Layers over the East Extreme Fiber Bar

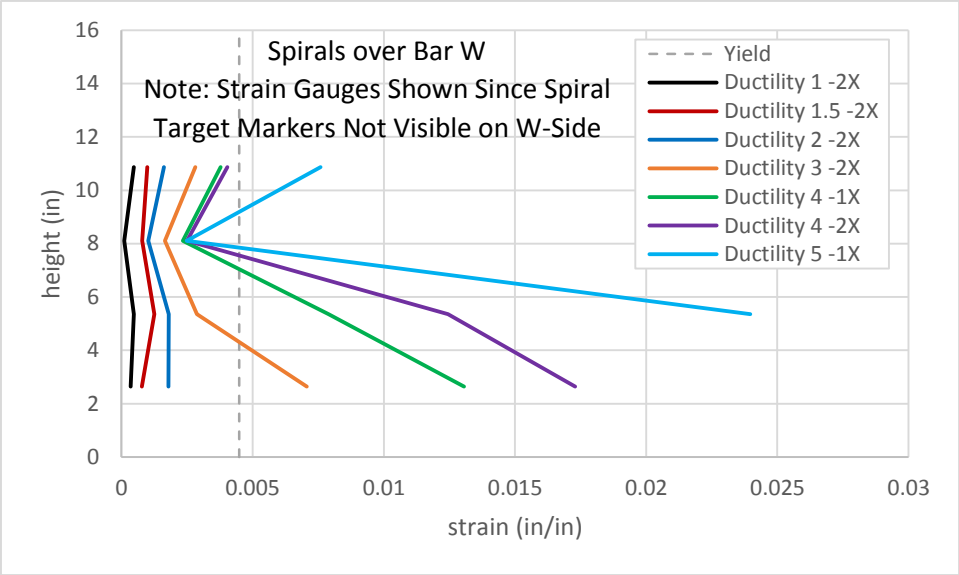

Figure 4-59. Test 1: Data from Strain Gauges for Four Spiral Layers over the West Extreme Fiber Bar

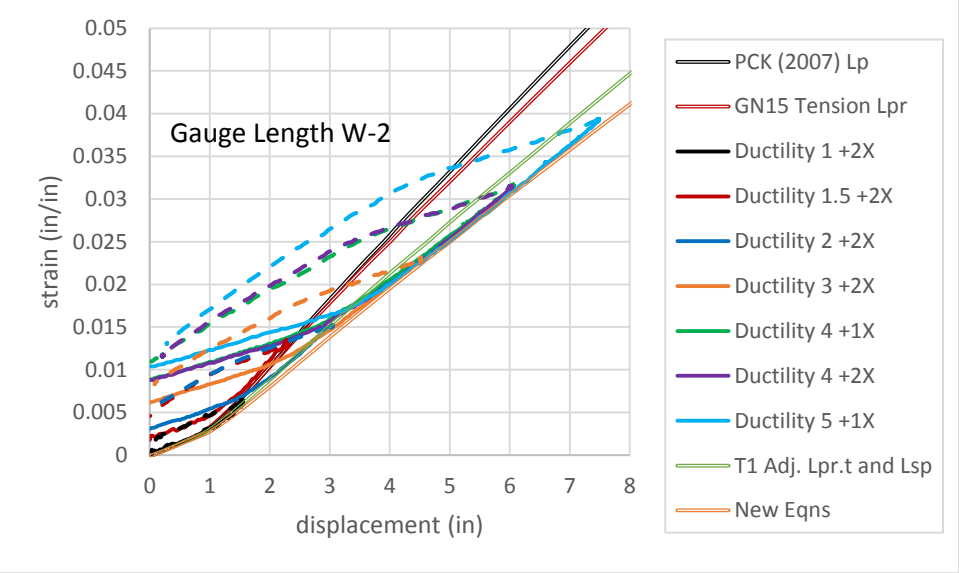

Figure 4-60. Test 1: Tension Strain-Disp. for Bar W (Gauge Length 2 Centered 5.10" above the Footing)

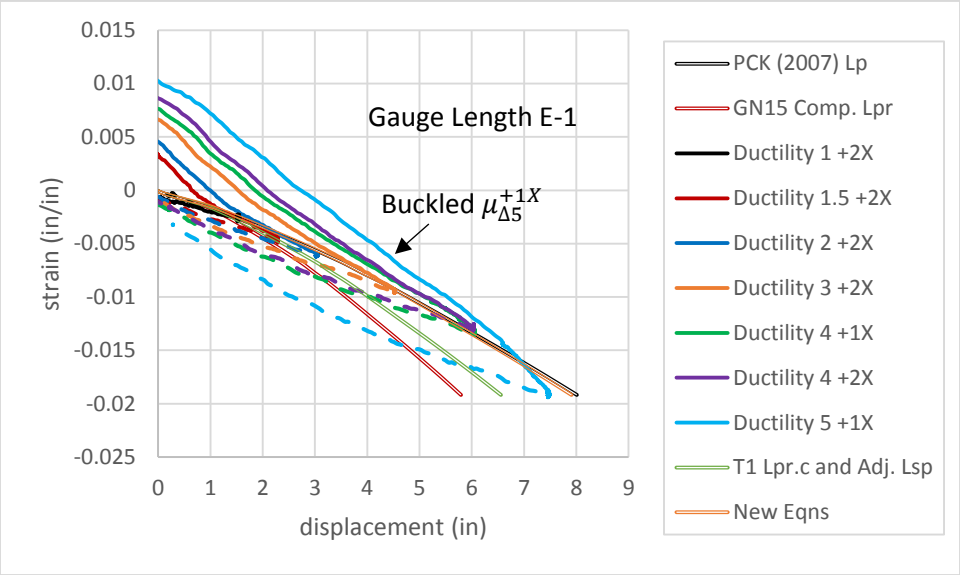

Figure 4-61. Test 1: Compression Strain-Disp. for Bar E (Gauge Length 1 Centered 2.15" above the Footing)

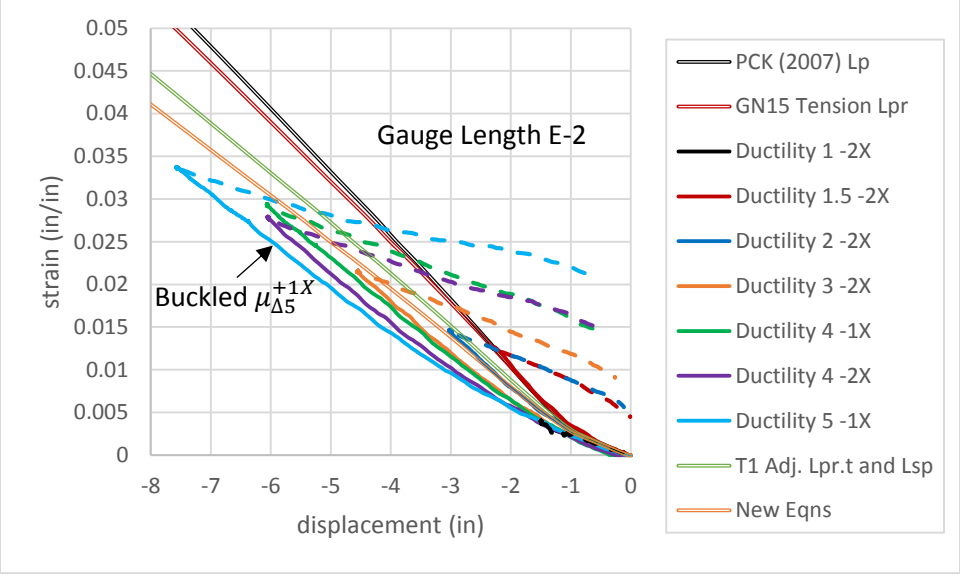

Figure 4-62. Test 1: Tension Strain-Disp. for Bar E (Gauge Length 2 Centered 4.90" above the Footing)

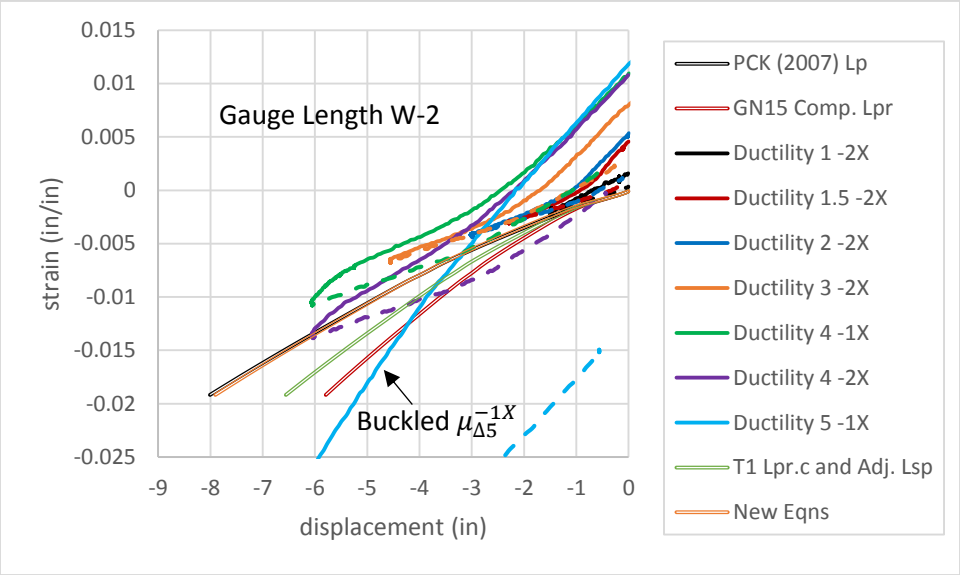

Figure 4-63. Test 1: Compression Strain-Disp. for Bar W (Gauge Length 2 Centered 5.10" above the Footing)

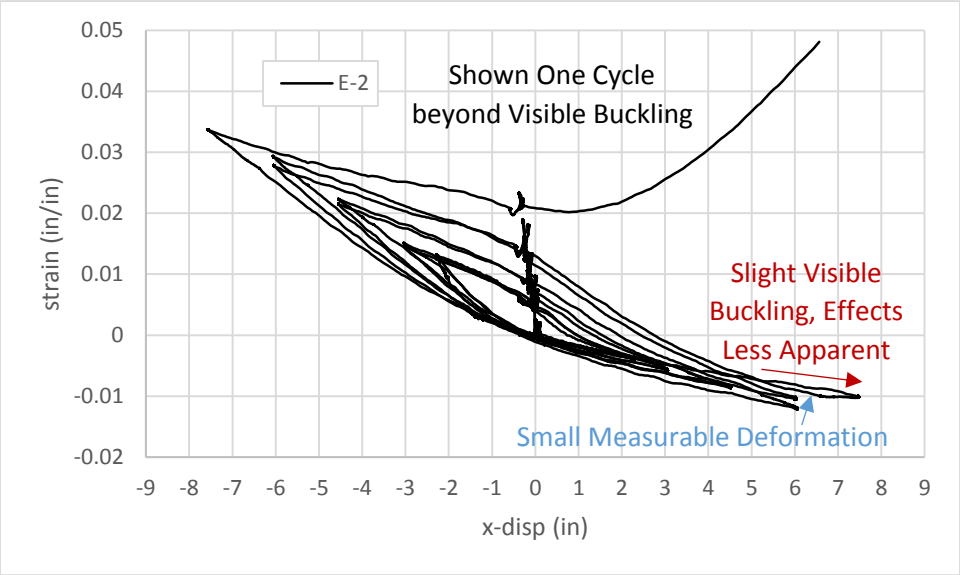

Figure 4-64. Test 1: Strain Hysteresis over the East Buckled Bar (Gauge Length 2 Centered 4.90" above the Footing)

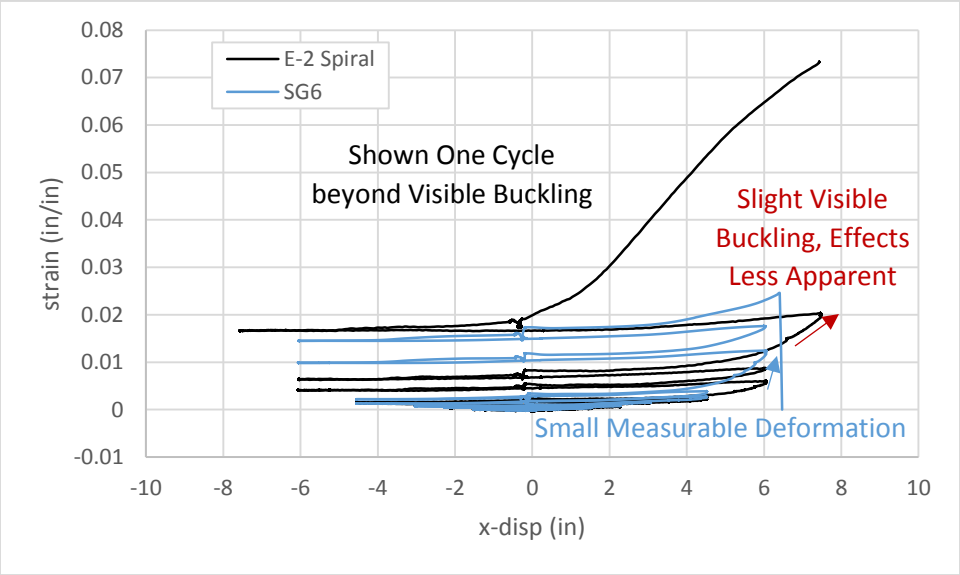

Figure 4-65. Test 1: Spiral Strains in the Second East Layer (5.00" above the Footing)

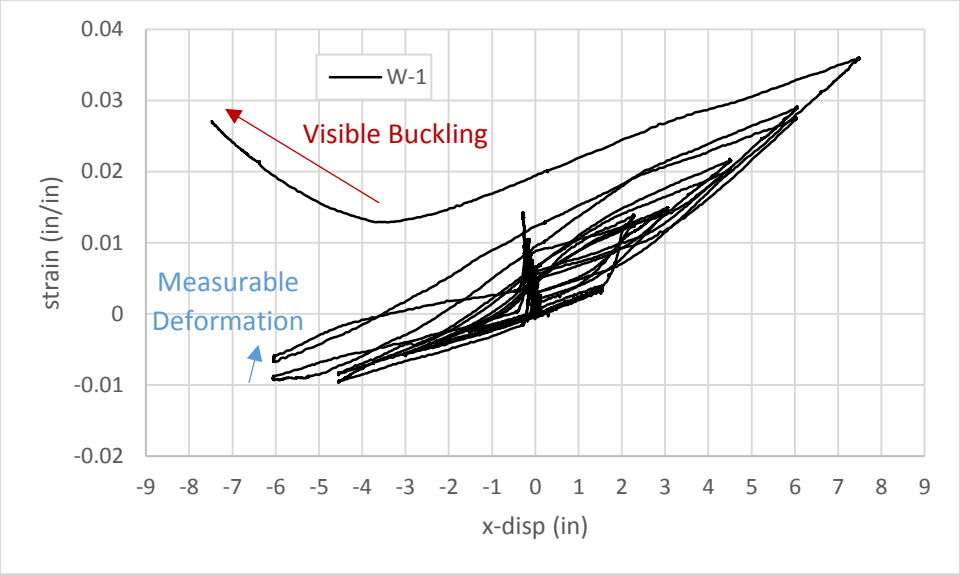

Figure 4-66. Test 1: Strain Hysteresis over the West Buckled Bar (Gauge Length 1 Centered 2.38" above the Footing)

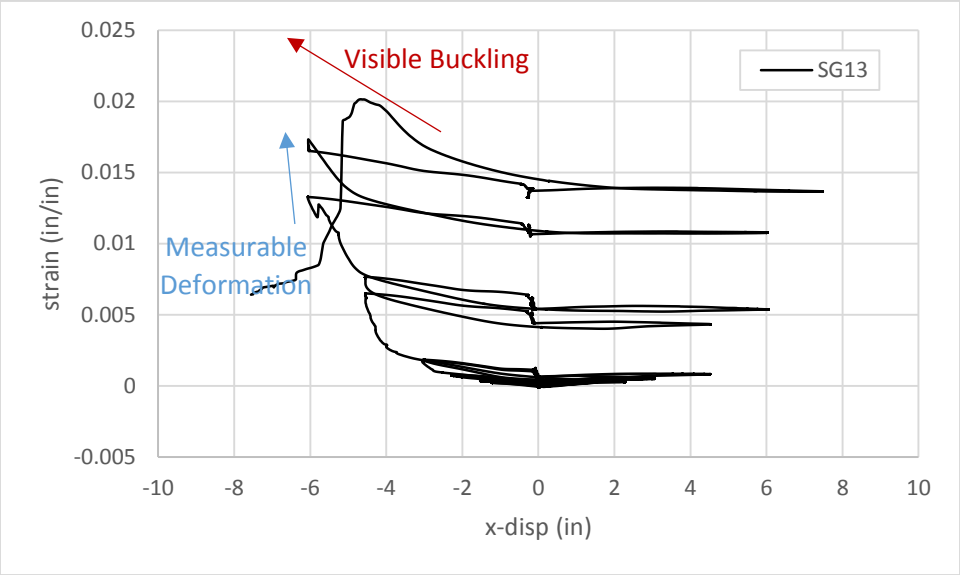

Figure 4-67. Test 1: Spiral Strains in the First West Layer (2.64" above the Footing)

Test 1 - Curvature and Strain Penetration Data

Cross-section curvatures were computed as the slope of a linear regression through the measured strain profile, see Figure 4-68 and Figure 4-69. Curvature profiles were constructed as shown in Figure 4-70, Figure 4-71, Figure 4-72, and Figure 4-73. Procedures developed by (Hines and Seible 2002) were followed to extract important information regarding their shape. Linear least-squared error lines were fit to the plastic portion of the curvature profiles. The base-section curvature is calculated as the intersection of the linear plastic curvature profile with the footing-column interface. The extent of plasticity (L_{pr}) is computed as the intersection of the linear plastic curvature regression and the elastic curvature profile. The elastic profile decreases from the equivalent yield curvature at the footing-column interface to zero at the center of the applied lateral load. The spread of plasticity in the tests is due to the combined effects of moment gradient and tension shift. The moment gradient effect can be described as the influence of larger base-section moments on the distribution of moment and thus curvature along the column length.

Vertical strain profiles in Figure 4-44, Figure 4-45, Figure 4-56, and Figure 4-57 depict strains measured in the extreme fiber reinforcing bars. Compressive strains are concentrated near the footing, while tension strains are fanned out to a greater height following the inclined flexural shear crack distribution. This is due in large part to the effects of tension shift, which leads to tension strains above the base section which exceed those that would develop based on the plane sections hypothesis and the moment at that height alone. Tension shift leads to a fanned compression strut pattern which emanates from the compressive toe region of the column, where the local compressive demand may be increased. Since tension strains are spread further above the base section, the magnitude of the peak tensile strain near the footing may be reduced.

Development of fully anchored column longitudinal bars into the footing leads to bond slip along the partially anchored region of the bars near the footing-column interface, as described by

(Zhao and Sritharan 2007). (Zhao and Sritharan 2007) notes that this bond slip is not a pull-out of the entire bar embedment length resulting from poor bond between the concrete and reinforcing bar. This bond slip is computed as vertical displacement of target markers placed closest to the footing-column interface, see Figure 4-75. Fixed-end rotations attributable to strain penetration of reinforcement into the adjoining member were computed based on the slope of a regression through the measured bond-slips, see Figure 4-76 and Figure 4-77.

In the experiments, the lateral displacement is obtained using an array of linear potentiometers placed at the center of the applied lateral load. The measured curvatures in the instrumented region can be integrated using the moment-area method and added to an assumed elastic profile above the instrumented region which linearly decreases from the highest measured horizontal section curvature to zero at the center of the applied lateral load. This integration represents the column flexural deformation, which can be added to the extrapolation of the fixed-end curvature attributable to strain penetration to find the total flexural displacement. This integrated total flexural displacement is compared to the measured string potentiometer displacement in Figure 4-78 and Figure 4-79. The close agreement implies that the relevant deformation quantities have been included and that shear deformation, which were not calculated directly at this stage of the analysis, are negligible in comparison to the flexural displacements.

As previously discussed, the height at which the linear plastic curvature distribution intersects the elastic curvature profile was termed the extent of plasticity (L_{pr}). This height is plotted as a function of base-section curvature ductility in Figure 4-80 for each direction of loading. The measured spread of plasticity appears to increase linearly, and then level out near maximum response. In (Goodnight, Kowalsky and Nau 2015), the tensile plastic hinge length was calibrated to match the upper bound to the measured spread of plasticity of unidirectional tests. The resulting tensile plastic hinge length, abbreviated as GN15 Tensile Lpr, appears as a grey dashed line. Under bidirectional loading, plasticity was spread further than the expression implies. For a given value of base-section curvature, a larger spread in plasticity would imply lower tensile strains, improving tensile-strain displacement predictions. In Figure 4-80, New Equations refers to a new bidirectional plastic hinge method which was created based on this study. Details of the new plastic hinge method appear in a later chapter of this report.

In the Modified Plastic Hinge Method from (Goodnight, Kowalsky and Nau 2015) an equivalent rectangular curvature block centered at the footing-column interface was used to describe the additional column displacement due to strain penetration of reinforcement into the adjoining member. This width of this block is equal to the base-section curvature while the area of the block represents the fixed-end rotation. The height of this block is termed the equivalent strain penetration length and is equal to the fixed-end rotation divided by the base-section curvature, both of which were measured experimentally. This equivalent strain penetration length is a numerical convenience, which can be used to describe the fixed-end rotation for the equivalent curvature distribution. The measured equivalent strain penetration lengths in each direction of loading appear in Figure 4-81. In (Goodnight, Kowalsky and Nau 2015), an expression was formulated to describe the average equivalent strain penetration length from the unidirectional experiments. This length is a function of the yield stress of the reinforcement, the longitudinal bar diameter, and the square root of the concrete strength in the adjoining member. The result for the expression, abbreviated as GN15 Lsp, under predicts the values obtained from this experiment; however, the observation of the equivalent

strain penetration length remaining constant over the range of curvature ductility remains valid. A higher concrete strength of the adjoining member decreases this length, however the expression was not formulated with footing concrete strengths of $f_c' = 10.18\ ksi$ measured in Test 1. Pending the results of future tests, it will be possible to isolate whether it is the footing concrete strength or the bidirectional loading which led to a more prominent impact of strain penetration. A larger equivalent strain penetration length would mean that for a given lateral displacement, lower tensile strains would result since a larger portion of the column displacement would come from strain penetration, which again would improve the noted issues with the tensile strain-displacement predictions. The equivalent strain penetration length recommended in (Priestley, Calvi and Kowalsky 2007) over predicts the measured behavior.

As a proof of concept, the average upper bound to the measured spread of plasticity was measured as $Lpr_t = 39.05$" and the average equivalent strain penetration length was obtained as $L_{sp} = 6.91$" from Figure 4-80 and Figure 4-81 respectively. These values were substituted into the Modified Plastic Hinge Method equations and new predictions for both the tensile and compressive strain-displacement relationships were made. Keep in mind that the compressive hinge length is $Lpr_c = 2kL_c$ and the original tension hinge length is $Lpr_t = 2kL_c + 0.75D$. The same compressive hinge length was used, since it was found to closely relate to the effects of moment gradient, which is not expected to be a function of bidirectional loading history. The results for this comparison appear in Figure 4-48 through Figure 4-51 and Figure 4-60 through Figure 4-63. Improvements to both tensile and compressive strain-displacement were observed. In the figures, New Equations refers to a new bidirectional plastic hinge method which was created based on this study. Details of the new plastic hinge method appear in a later chapter of this report.

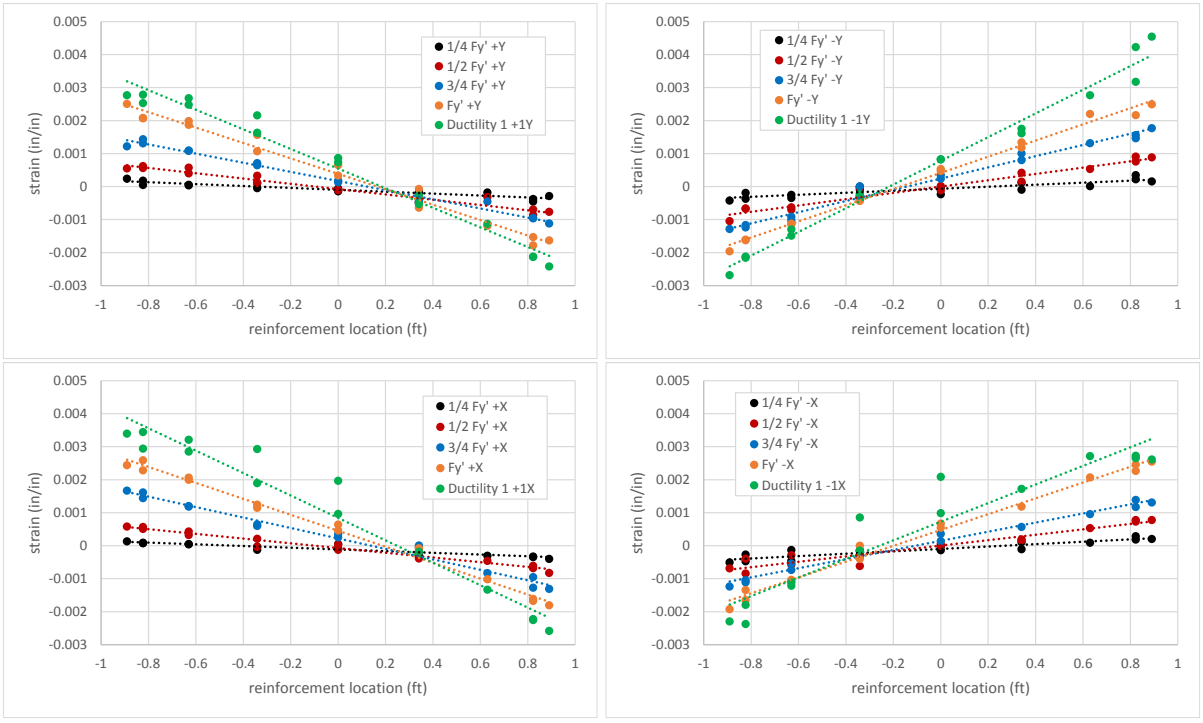

Figure 4-68. Test 1: Elastic Curvature Profiles for the First Instrumented Section above the Footing

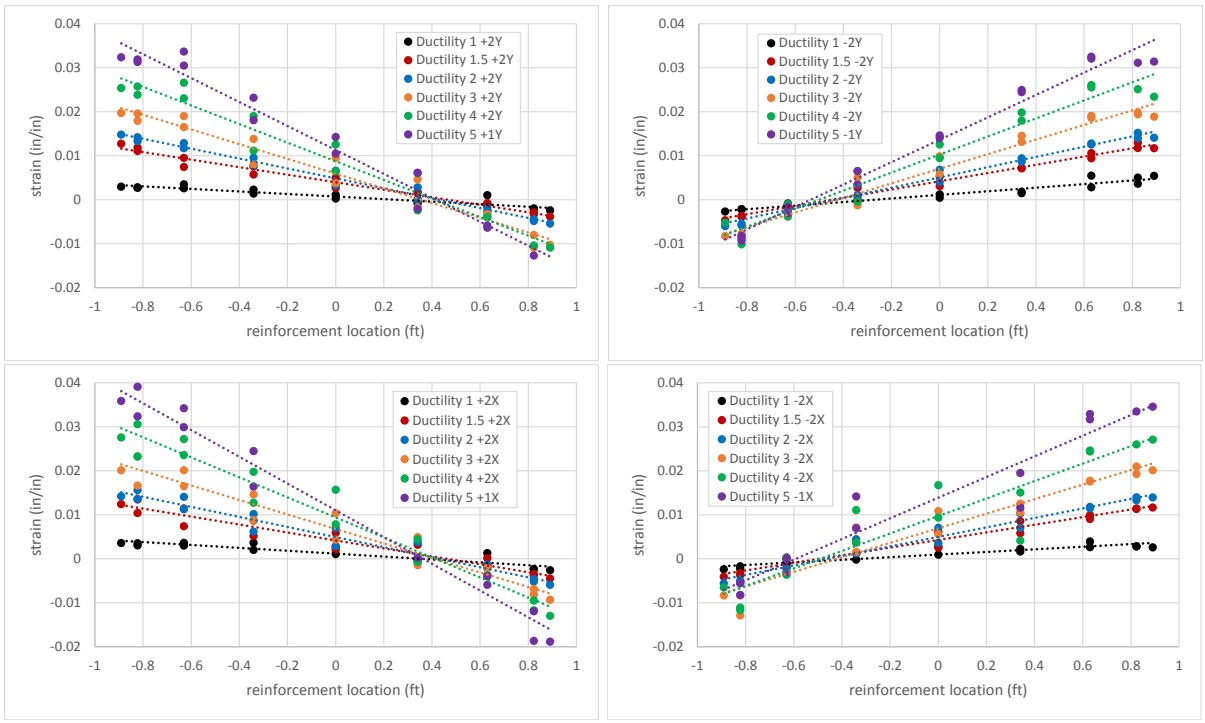

Figure 4-69. Test 1: Curvature Profiles for the First Instrumented Section above the Footing

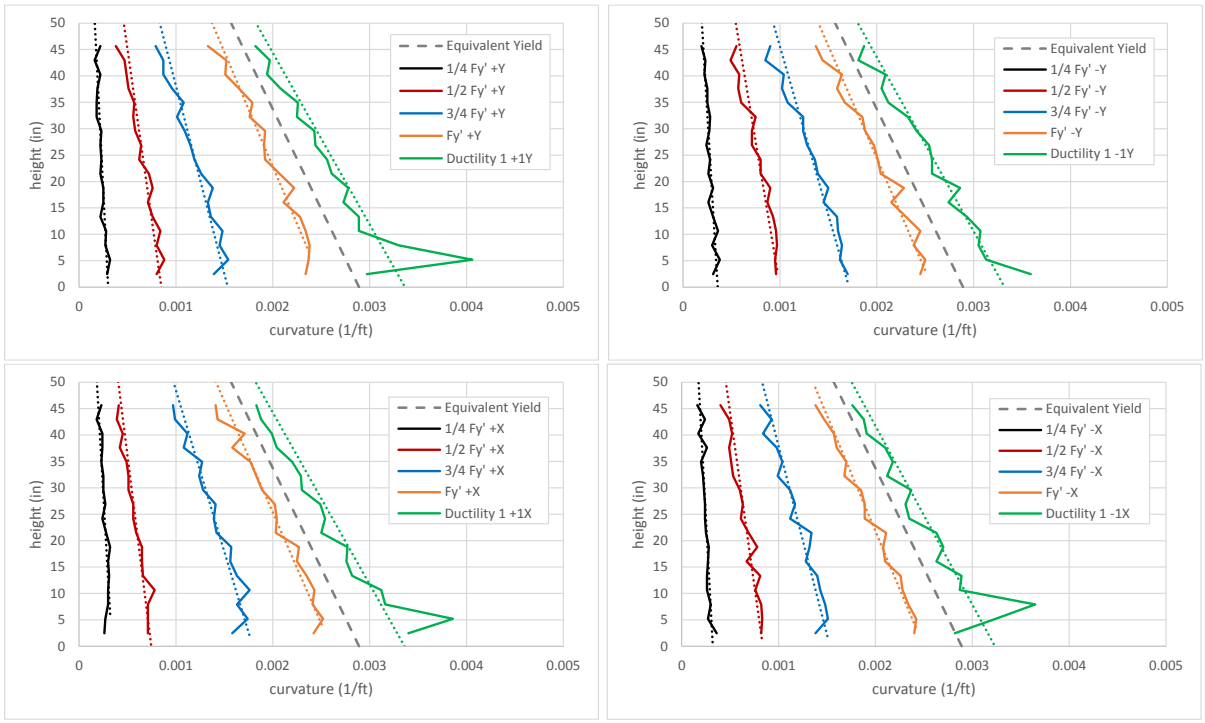

Figure 4-70. Test 1: Elastic Vertical Curvature Profiles

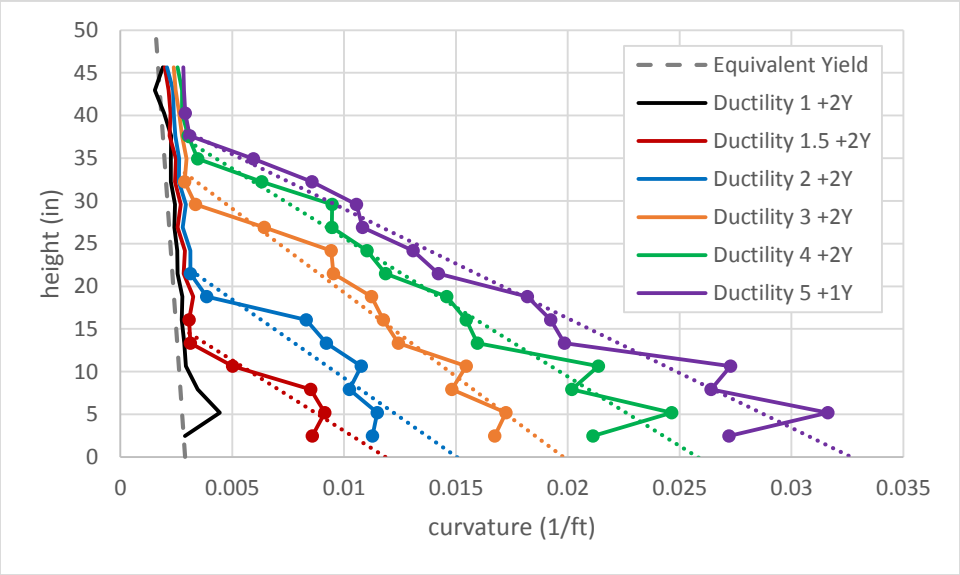

Figure 4-71. Test 1: Vertical Curvature Profiles for Loading in the +Y-direction

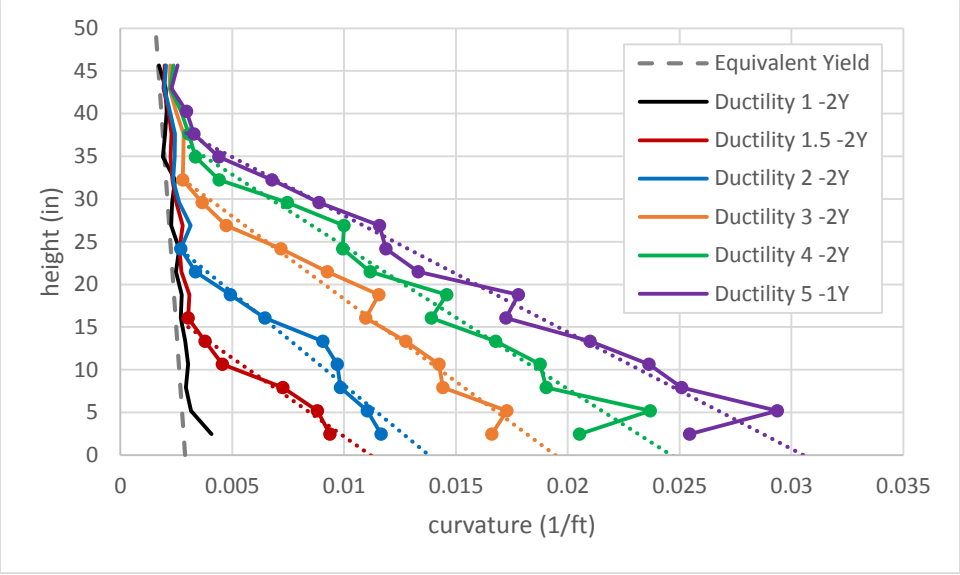

Figure 4-72. Test 1: Vertical Curvature Profiles for Loading in the –Y-direction

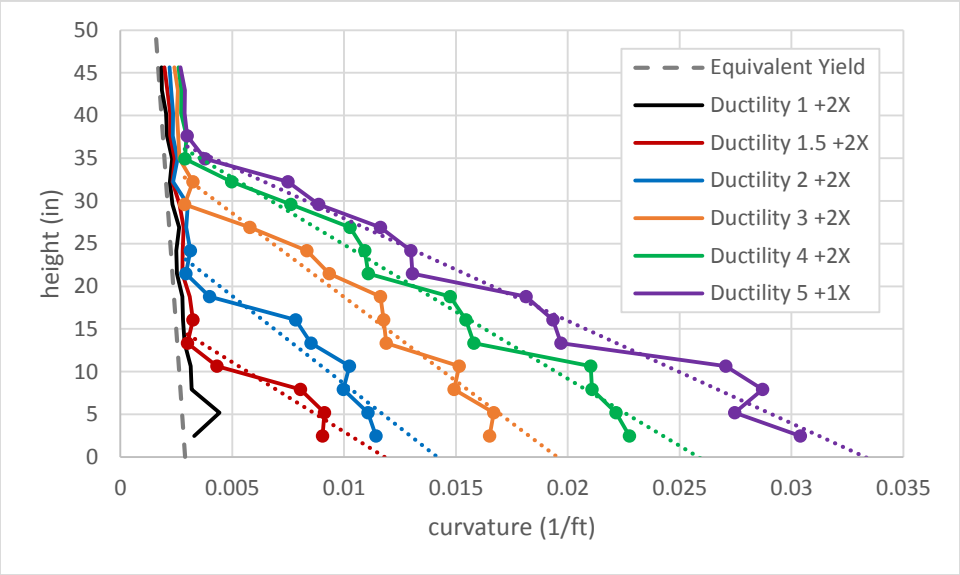

Figure 4-73. Test 1: Vertical Curvature Profiles for Loading in the +X-direction

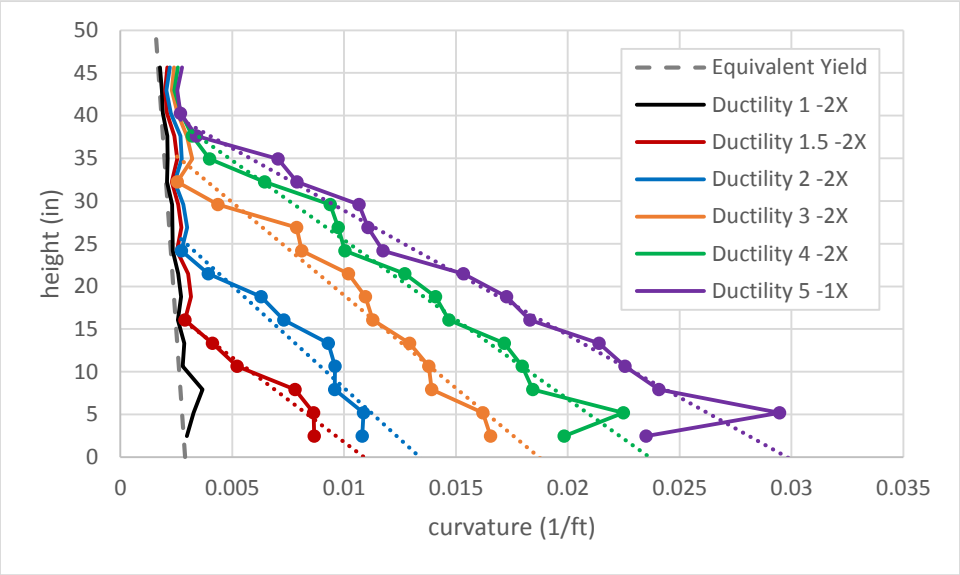

Figure 4-74. Test 1: Vertical Curvature Profiles for Loading in the –X-direction

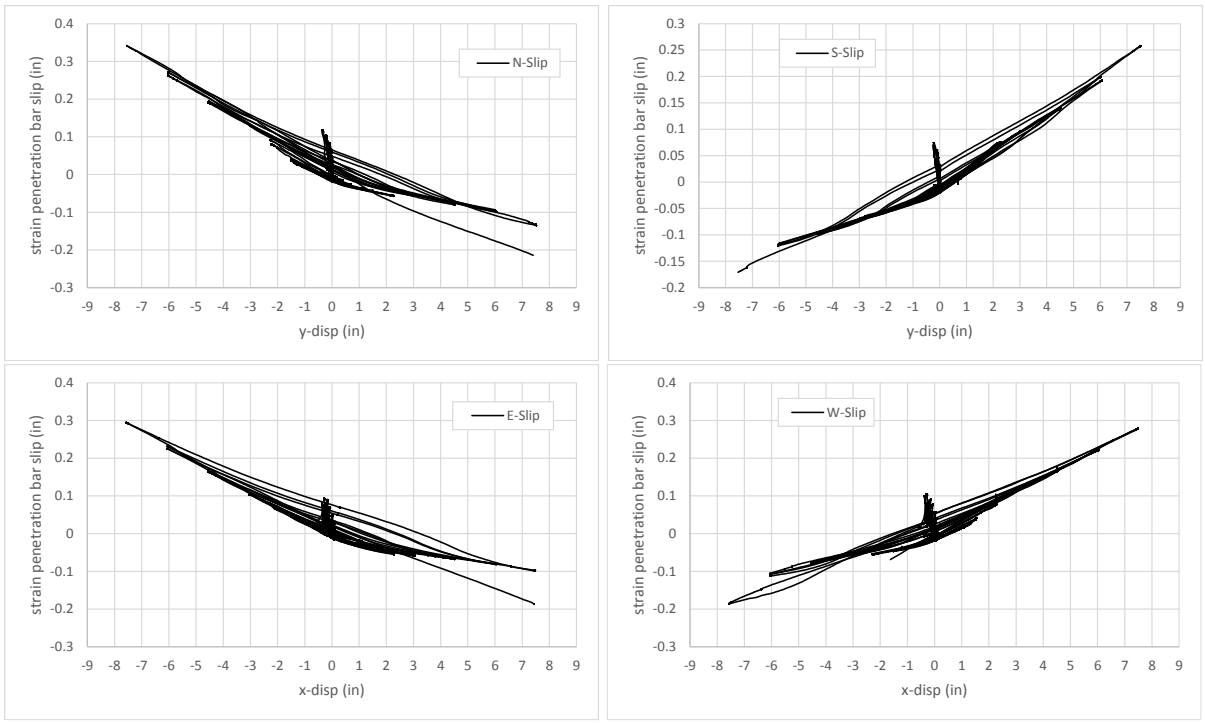

Figure 4-75. Test 1: Extreme Fiber Bar Strain Penetration Bond Slip Hysteresis

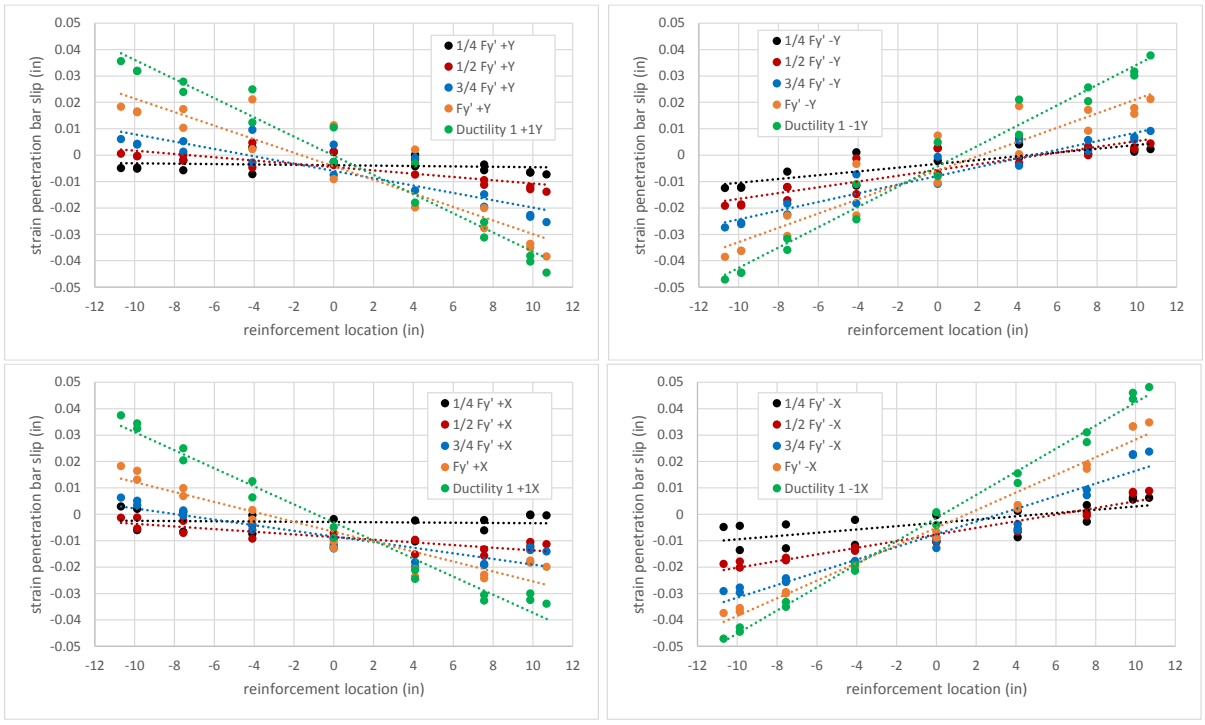

Figure 4-76. Test 1: Fixed End Rotations due to Strain Penetration during the Elastic Cycles

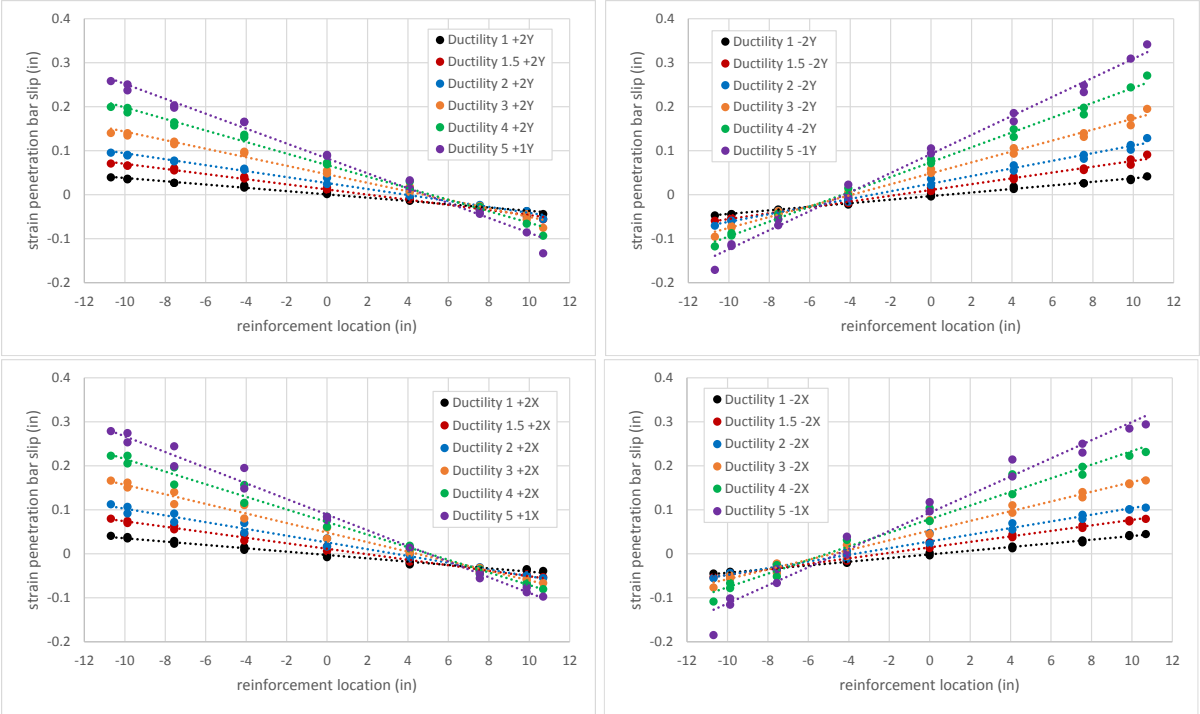

Figure 4-77. Test 1: Fixed-End Rotations due to Strain Penetration

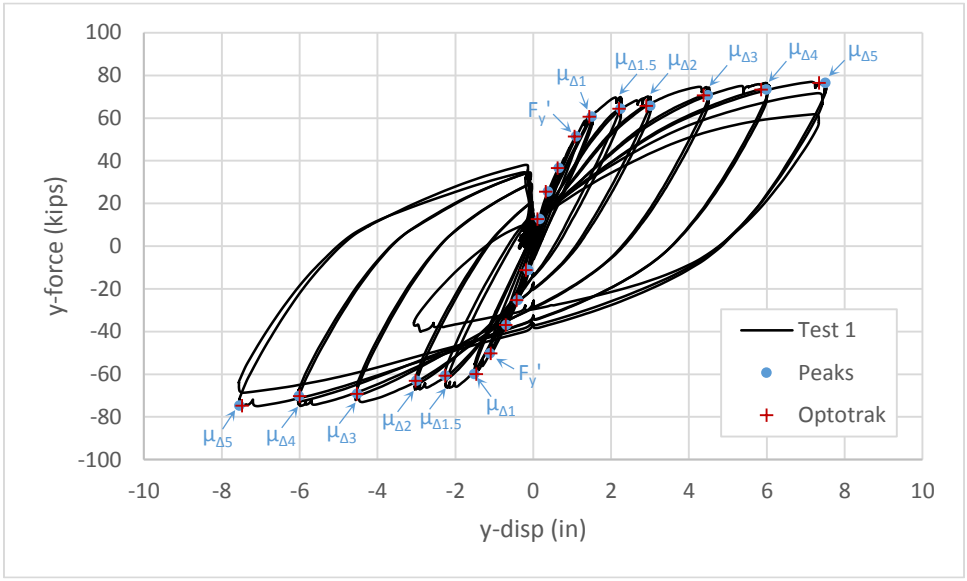

Figure 4-78. Test 1: Optotrak Integrated Flexural Disp. Compared to Measured String Pot. Disp.

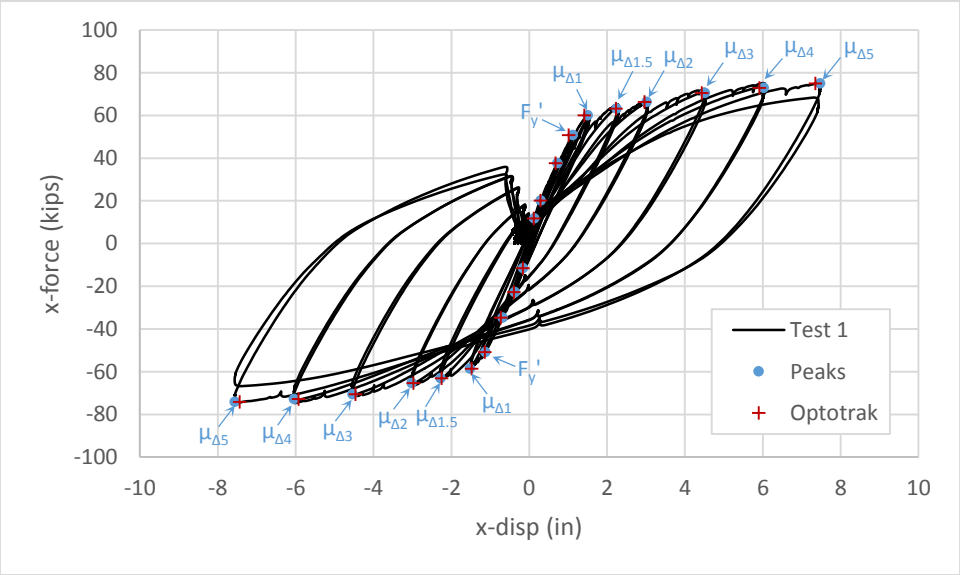

Figure 4-79. Test 1: Optotrak Integrated Flexural Disp. Compared to Measured String Pot. Disp.

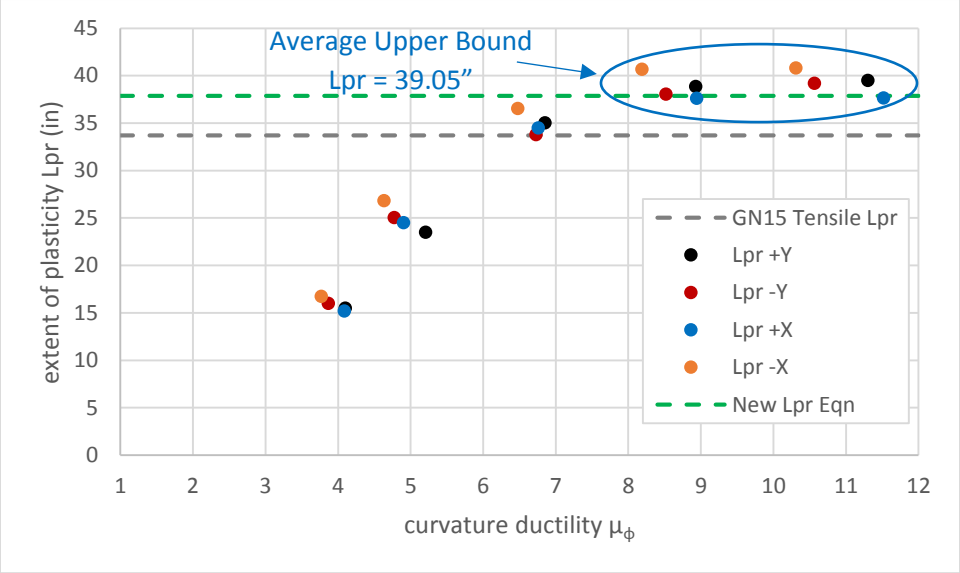

Figure 4-80. Test 1: Measured Extent of Plasticity Compared to Design Recommendations

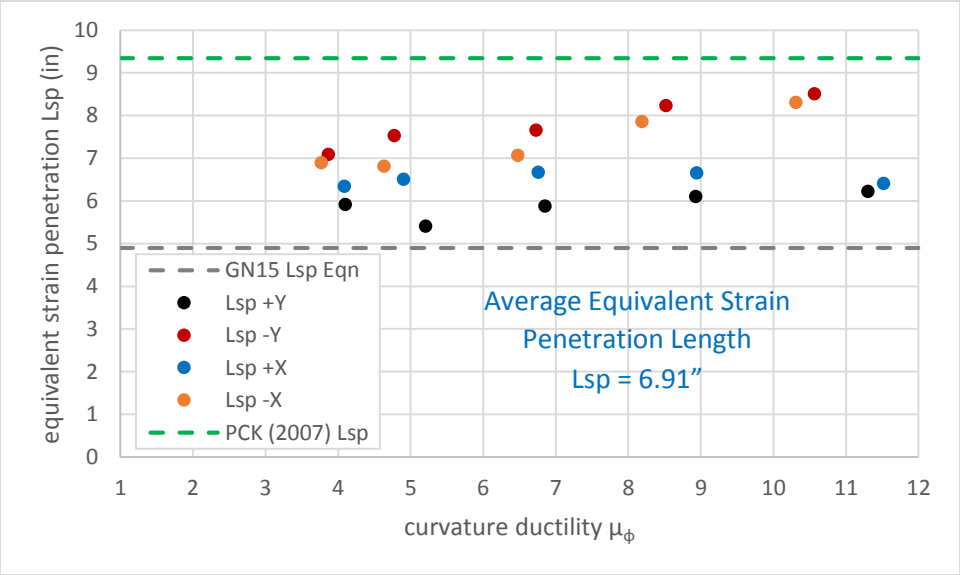

Figure 4-81. Test 1: Computed Equivalent Strain Penetration Lengths Compared to Design Recommendations

Test 1 - Response Predictions with Moment-Curvature and Fiber Modeling

Moment-Curvature Analysis and Pre-Yield Column Flexibility

At the analytically predicted first yield force, displacements in the four primary directions were measured at $\Delta'_y = 1.10"$ and $\Delta'_y = -1.11"$ in Y-direction and $\Delta'_y = 1.12"$ and $\Delta'_y = -1.13"$ in X-direction, producing an average experimental first yield displacement of $\Delta'_y = 1.12"$. This value exceeded the analytical prediction for the first yield displacement of 0.85”, however the extreme fiber bar strains at the analytical first yield force closely matched the yield strain of the longitudinal steel, as shown in Figure 4-82. This prediction was made using monotonic moment-curvature analysis and the plastic hinge method recommended in (Priestley, Calvi and Kowalsky 2007), abbreviated PCK (2007) Lp. There was an apparent increase in the pre-yield flexibility of the column, which will be investigated in greater detail in this section.

First, the sectional stiffness is investigated by comparing the measured moment-curvature response with the analytical monotonic envelope. The curvature history for the Y and X-directions for the second horizontal section above the footing appears in Figure 4-83 and Figure 4-84. As seen in the curvature profiles of Figure 4-71 through Figure 4-74, the largest cross-section curvature was observed in the second layer in three of the four loading directions. The measured moment-curvature response is compared to the analytical monotonic envelope in Figure 4-85 and Figure 4-86. On a section level, the increase in pre-yield flexibility was not observed, since the prediction provided a close match the envelope of the measured cyclic response.

Member level response predictions for the force versus deformation response were made using the plastic hinge method from (Priestley, Calvi and Kowalsky 2007) in Figure 4-87 through Figure 4-90. The method predicts a larger initial stiffness than was observed in the experiment. To investigate this issue, the measured pre-yield curvature distributions were compared to the analytical moment-curvature distributions at an equivalent base-section moment in Figure 4-91. This figure shows

additional measured curvature in the experiment when compared to the analytical curvature distribution at the same value of base-section moment. This helps to explain the additional pre-yield flexibility of the column. In Figure 4-92, the analytical base-section curvature at equivalent moments are compared to the experimental base-section curvature computed using the linear regression lines presented in Figure 4-70. At equivalent moments, larger base-section curvatures were observed in the experiment which also correlated to increased fixed-end rotations due to strain penetration, both of which led to additional column flexibility.

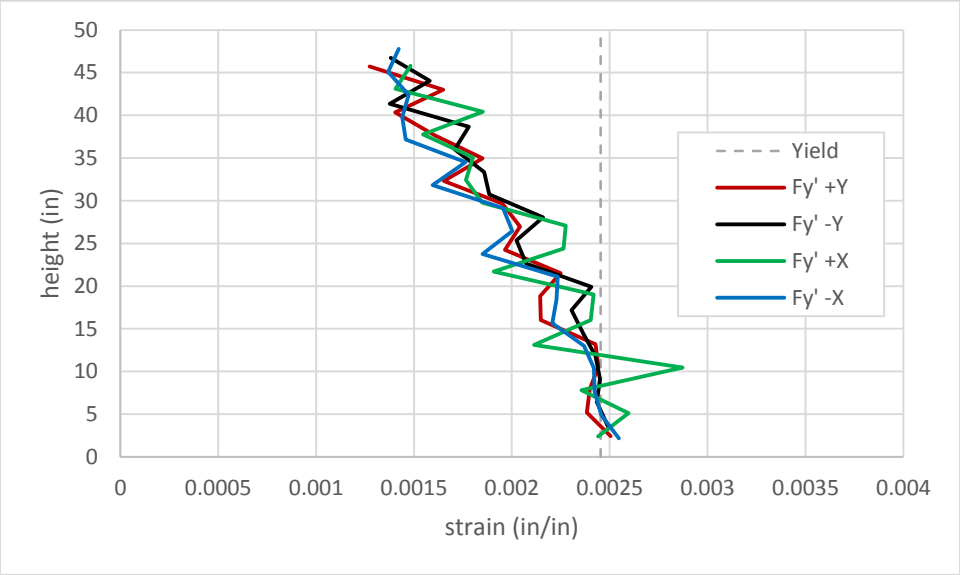

Figure 4-82. Test 1: Extreme Fiber Tensile Bar Strains at the Analytical First Yield Force

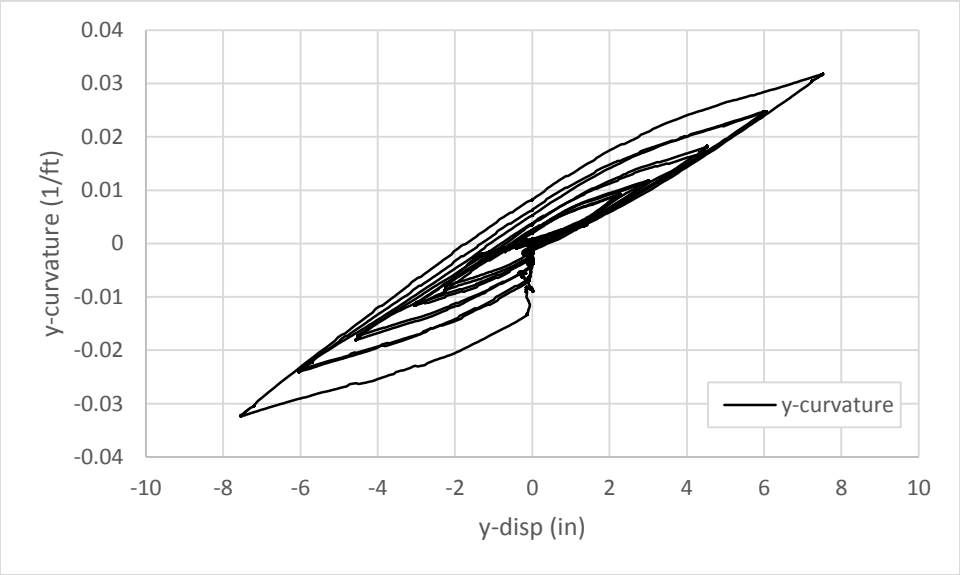

Figure 4-83. Test 1: Y-Direction Curvature History for the Second Layer above the Footing

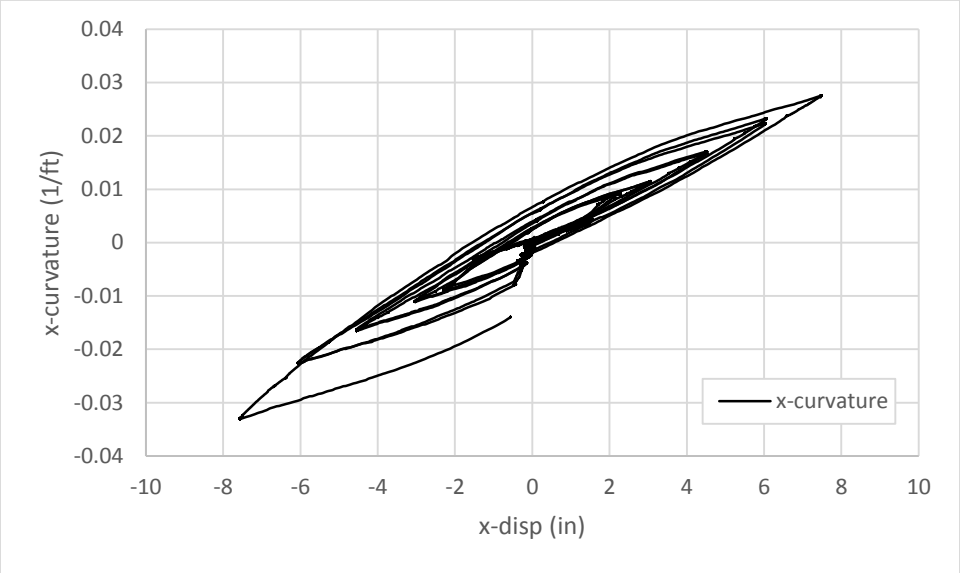

Figure 4-84. Test 1: X-Direction Curvature History for the Second Layer above the Footing

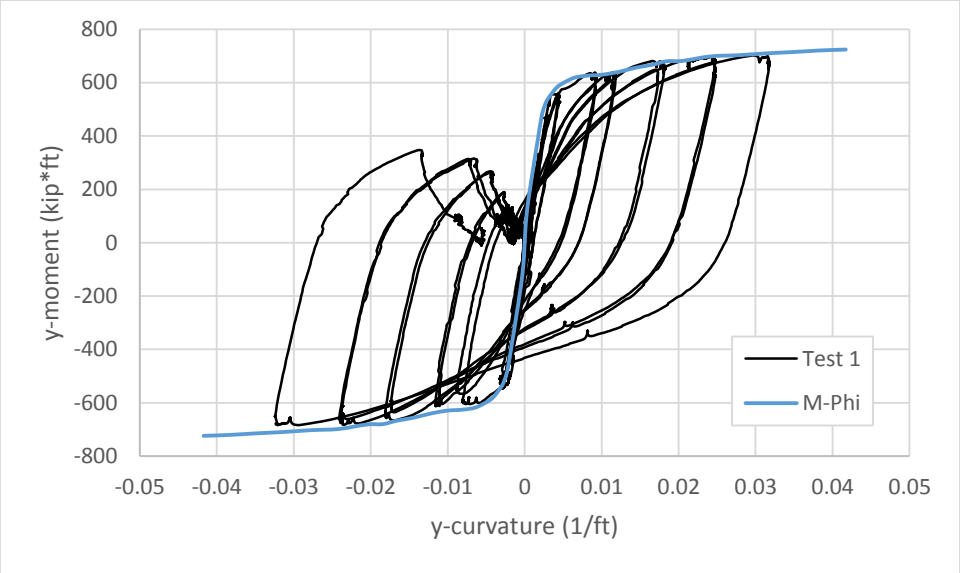

Figure 4-85. Test 1: Y-Direction Moment-Curvature Compared to Monotonic Prediction

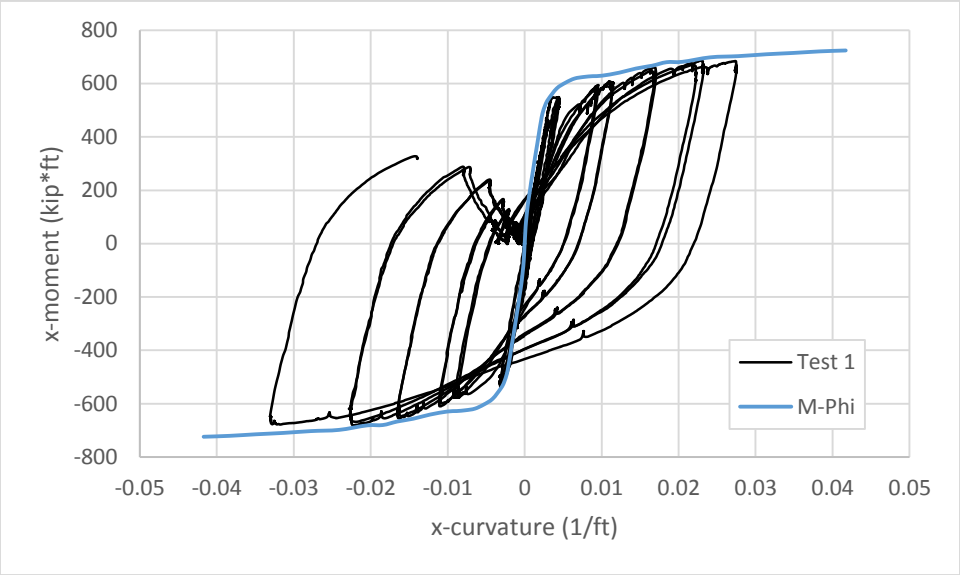

Figure 4-86. Test 1: X-Direction Moment-Curvature Compared to Monotonic Prediction

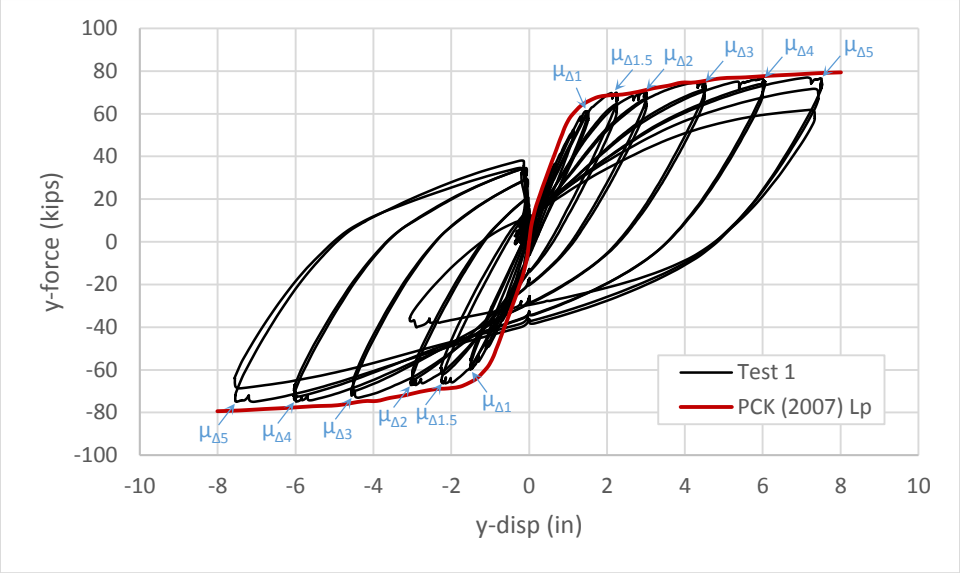

Figure 4-87. Test 1: Y-Direction Hysteretic Response Compared to Monotonic Predictions

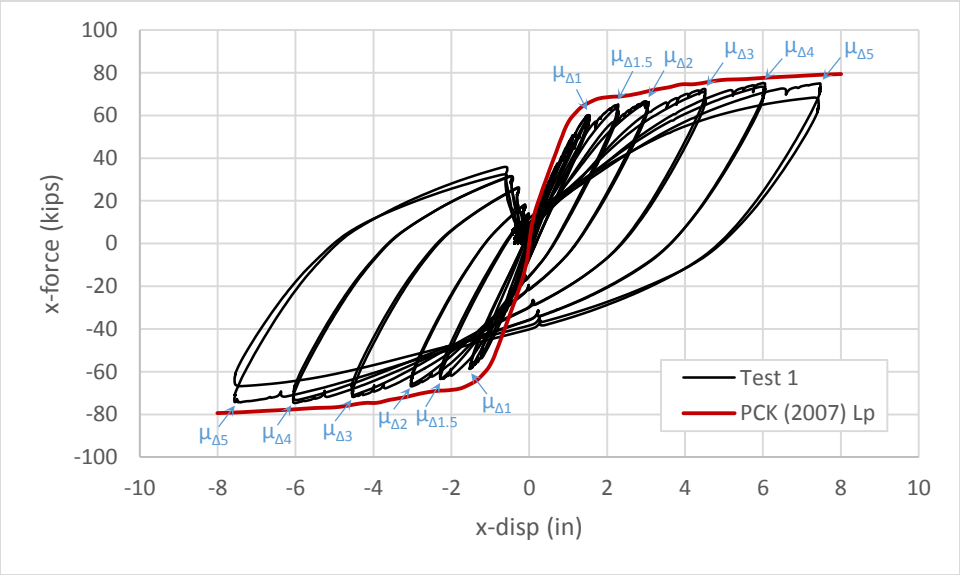

Figure 4-88. Test 1: X-Direction Hysteretic Response Compared to Monotonic Predictions

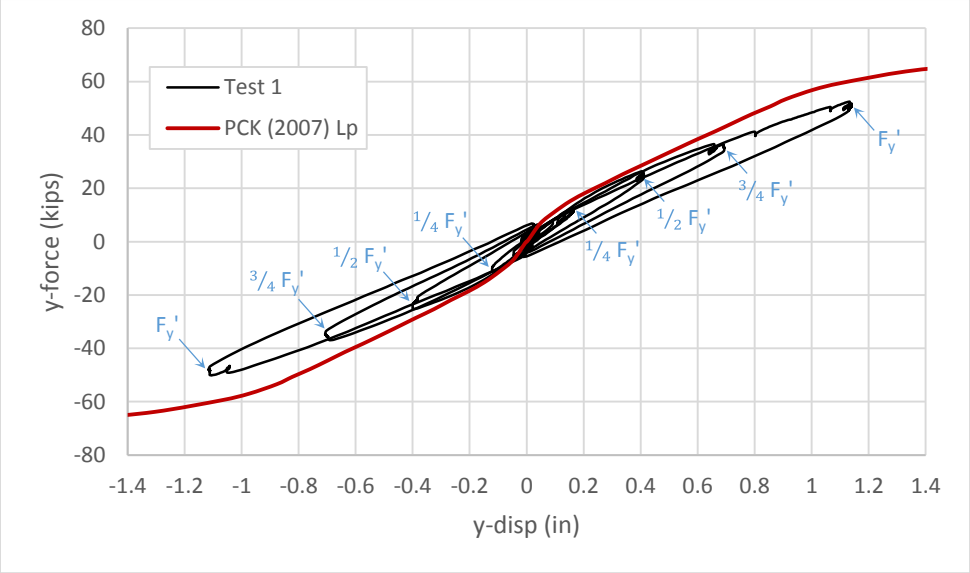

Figure 4-89. Test 1: Y-Direction Cycles up to the Analytical First Yield Force

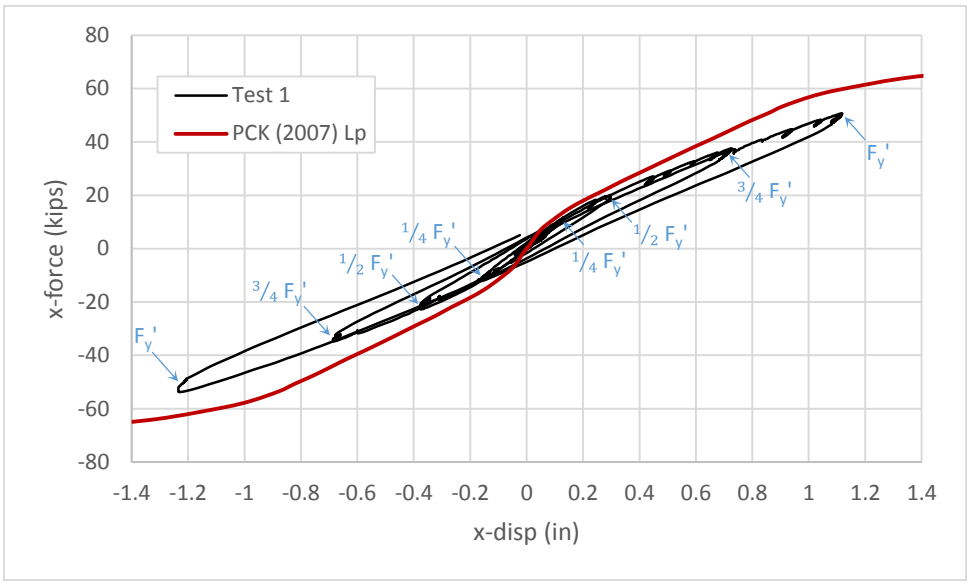

Figure 4-90. Test 1: X-Direction Cycles up to the Analytical First Yield Force

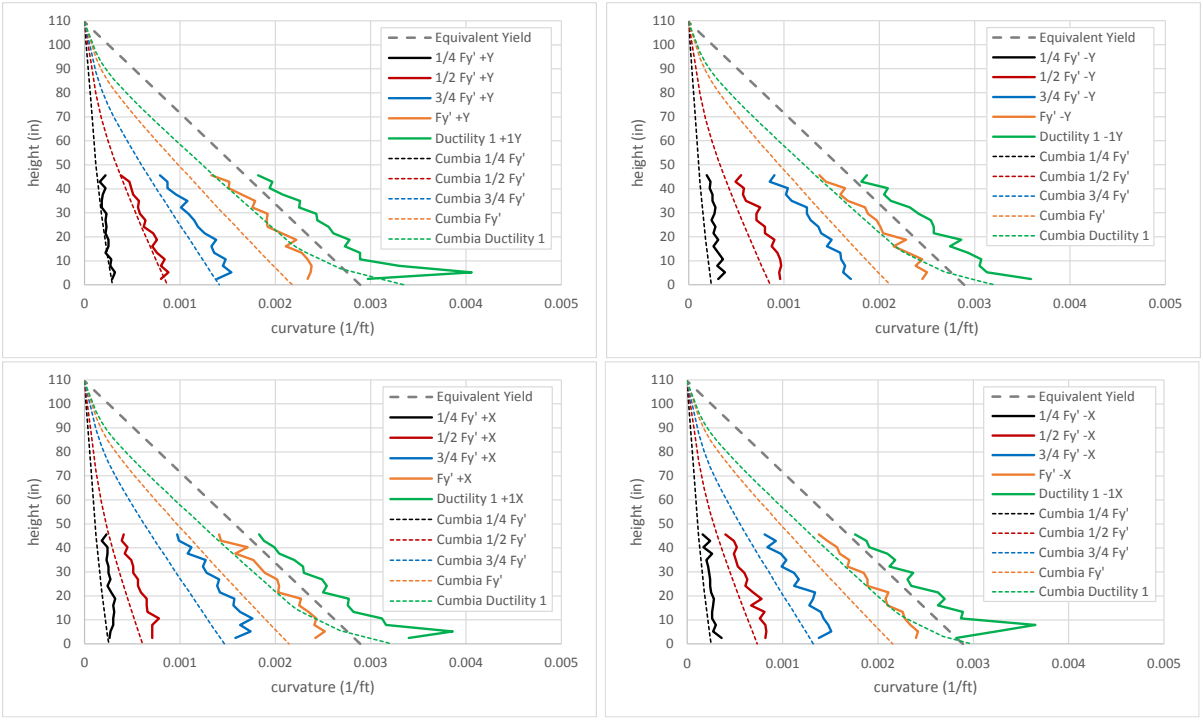

Figure 4-91. Test 1: Measured Curvatures Compared to Superimposed Moment-Curvature Response at Equivalent Moments

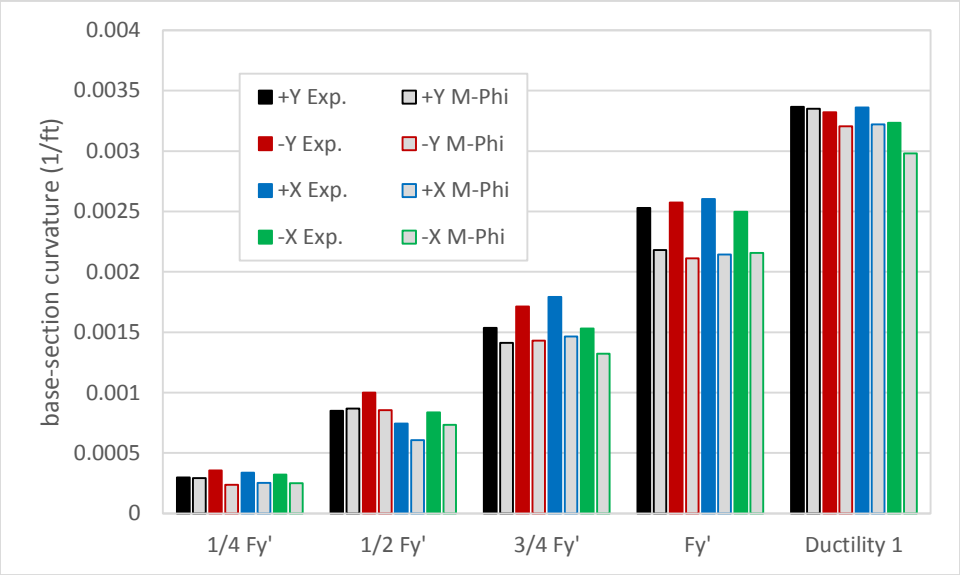

Figure 4-92. Test 1: Difference in the Measured and Analytical Base Section Curvature at Equivalent Moments

Fiber-Based Modeling in OpenSees

Additional details regarding the implementation of fiber-based modeling in OpenSees to predict the response of the bidirectional tests is available in Chapter 3. The cyclic material models for the confined and unconfined concrete were updated to reflect the tested concrete strength of Test 1. The same details for the reinforcing steel material model presented in Chapter 3 were utilized in the analysis. Results from the first test allowed for a more refined calibration of parameters in the zero-length strain penetration element and the plastic hinge length utilized within the force-based beam column element. Specifically, the measured strain history for the first gauge length above the footing on the South side of the footing was converted to bar stresses using the Reinforcing Steel material model in OpenSees, see Figure 4-96. The measured bond-slip of the South bar due to strain penetration was plotted alongside the model inferred bar stresses from the first gauge length. This stress-slip hysteretic response was used to calibrate parameters in the Bond SP01 stress-slip model developed by (Zhao and Sritharan 2007). At this time, this was only done for one reinforcing bar. There is little guidance provided as to which plastic hinge length should be included in the beam with hinges element from (Scott and Fenves 2006), therefore successive analysis runs were completed varying the plastic hinge length until the model predicted strains matched the measured values in the first test. A plastic hinge length of 24” provided an accurate prediction for the force versus deformation response and the material strains as shown in Figure 4-93 through Figure 4-100. Again, the fiber-based modeling predicts a larger initial stiffness than that observed in the experiment, which was investigated in the prior section.

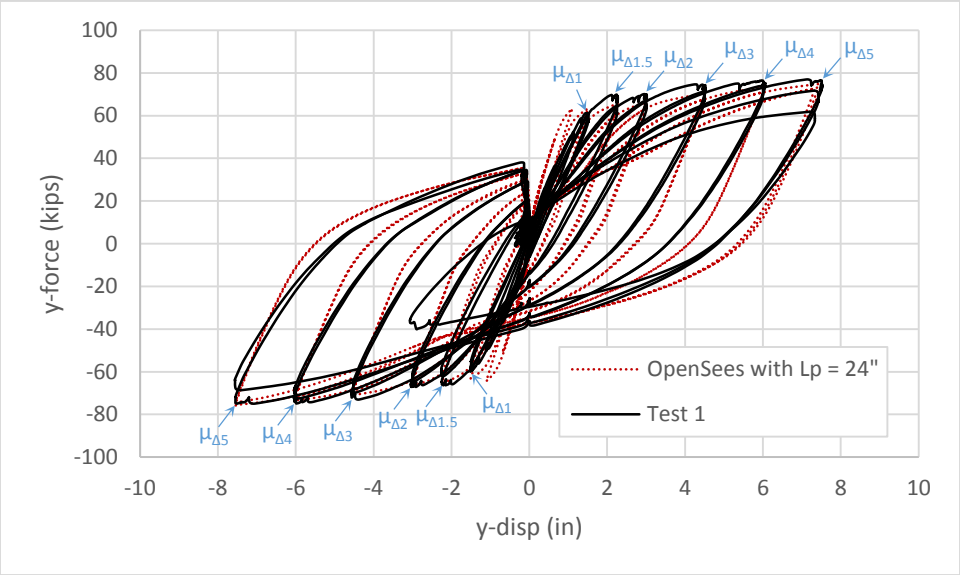

Figure 4-93. Test 1: Measured Response Compared to the OpenSees Fiber Model Prediction in the Y-direction

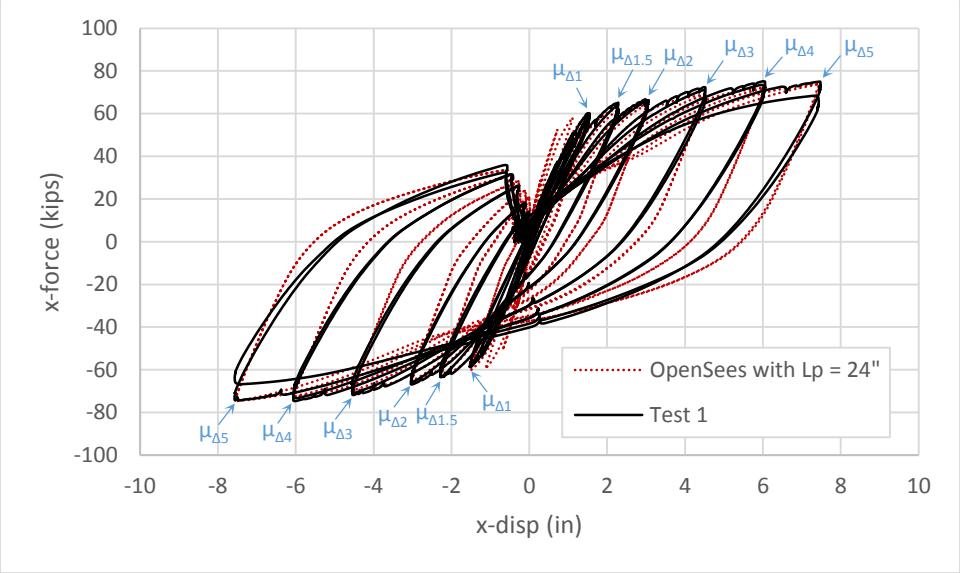

Figure 4-94. Test 1: Measured Response Compared to the OpenSees Fiber Model Prediction in the X-direction

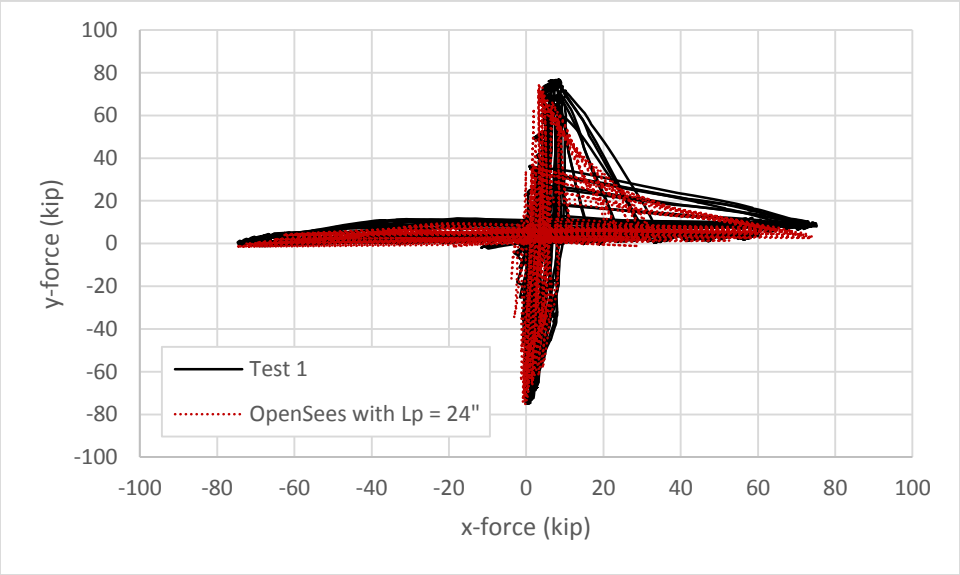

Figure 4-95. Test 1: Measured Load Path Compared to OpenSees Fiber Model Result

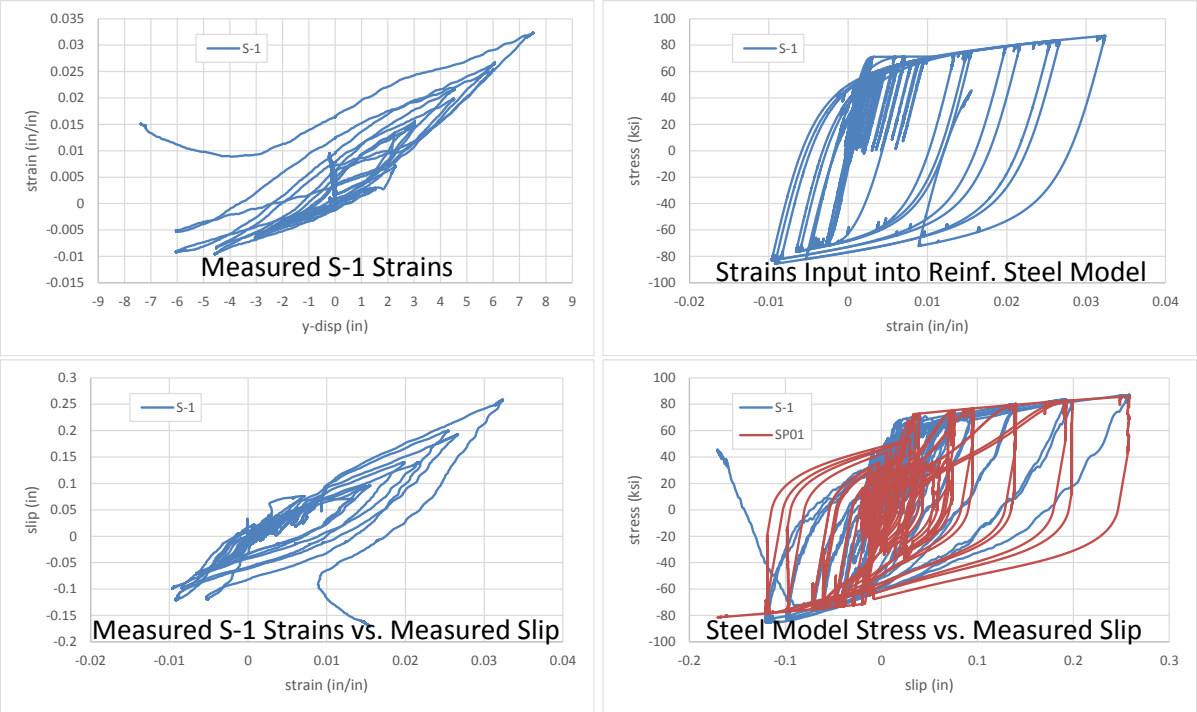

Figure 4-96. Test 1: Method of Calibration of SP01 Stress-Slip Material for Strain Penetration in OpenSees

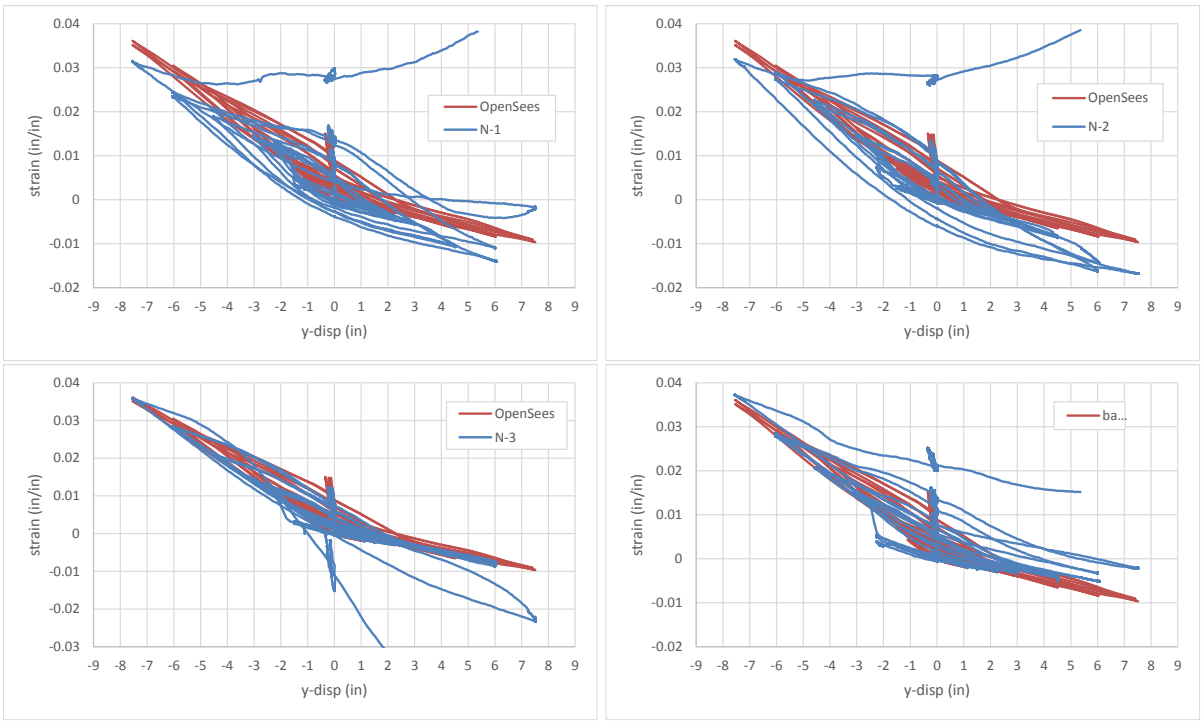

Figure 4-97. Test 1: OpenSees Model Prediction for North Bar Strains

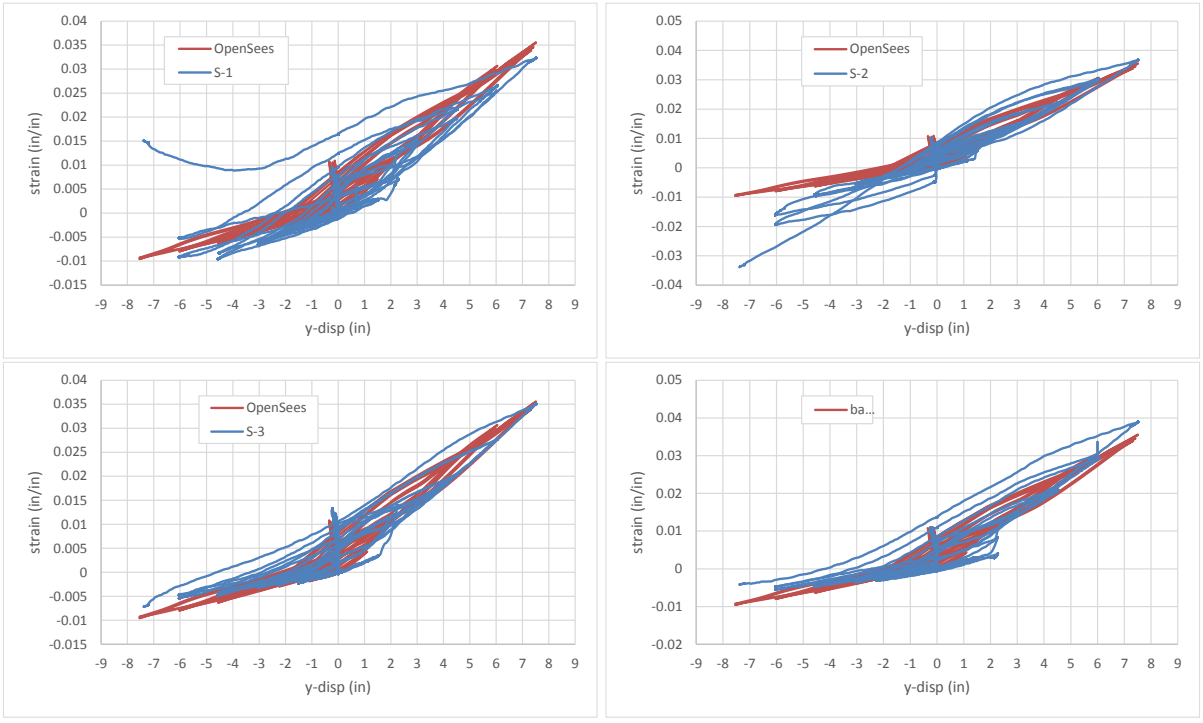

Figure 4-98. Test 1: OpenSees Model Prediction for South Bar Strains

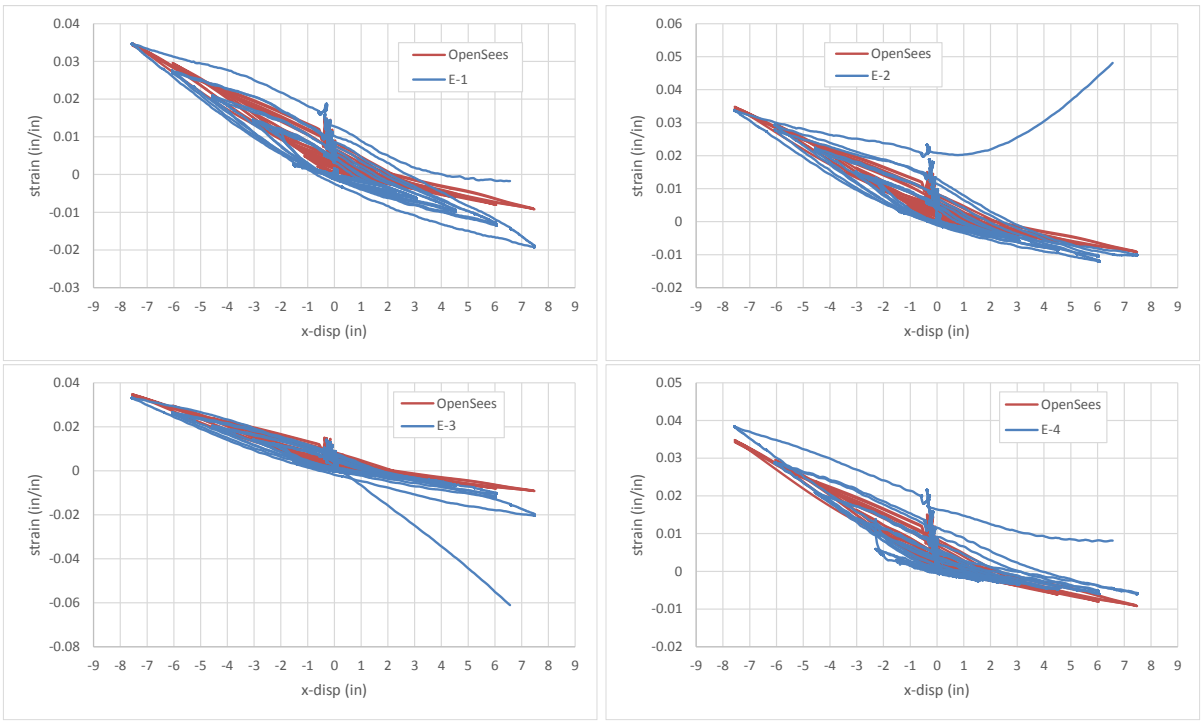

Figure 4-99. Test 1: OpenSees Model Prediction for East Bar Strains

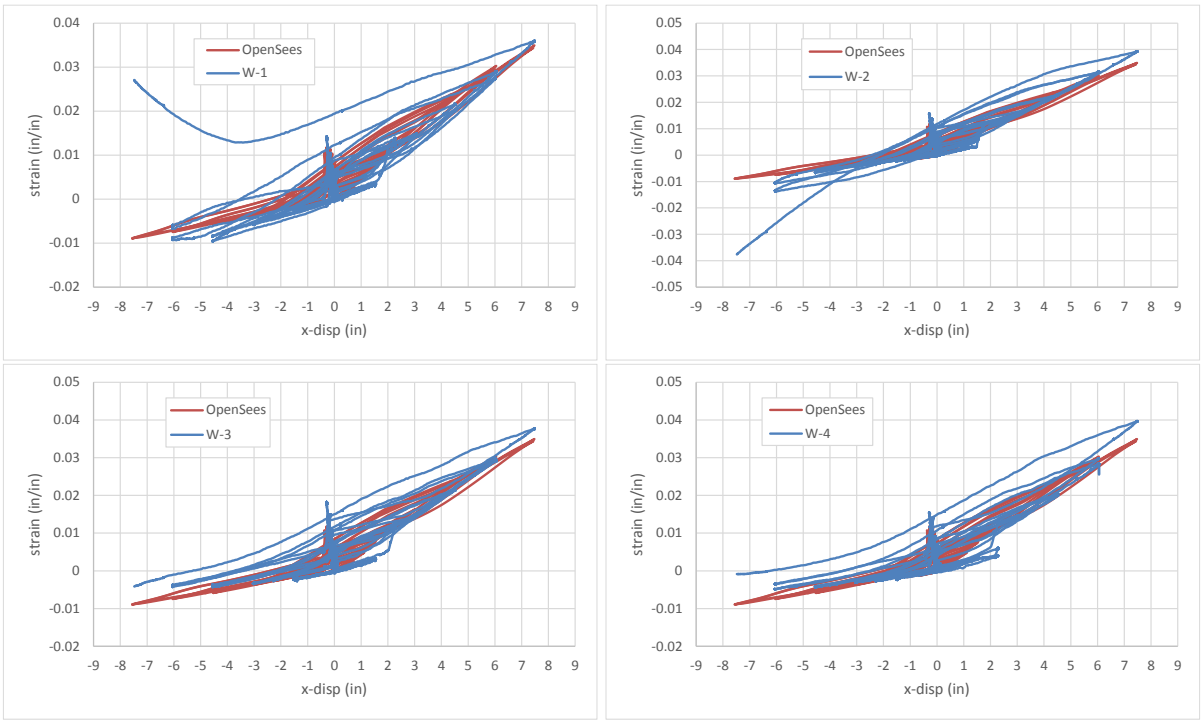

Figure 4-100. Test 1: OpenSees Model Prediction for West Bar Strains

Chapter 5 - Test 2 Summary Report

Test 2 was nominally identical to Test 1, except three cycles were repeated at each displacement ductility level instead of just two. The cycle count was increased to evaluate its influence on localization of compression over inelastic spiral layers and to observe how this influences the initiation of bar buckling. The second specimen had a 24" diameter circular cross-section reinforced with 16 #7 A706 longitudinal bars ($A_{st}/A_g = 2.1\%$) and a #3 spiral at 2.75" on center ($4A_{sp}/D's = 0.7\%$). The column had a 109.4375" cantilever length, measured from the footing-column interface to the center of the applied lateral load. This length was obtained as an average of the staggered actuator connections heights, 108" and 110.875". Although eliminated in the instrumented region, the upper portion of the column had a 0.5" cover measured to the outside surface of the spiral. The column had a constant axial load of $191\ kips$ $\left(P/f_c'\,A_g = 7.4\%\right)$. Details of the test setup, instrumentation, and specimen design appear in Chapter 2. A material properties summary for the longitudinal and transverse steel from the first six experiments appears in Table 3-1 and Table 3-2. The column had a tested concrete strength of $f_c' = 6.16\ ksi$, while the footing had $f_c' = 9.99\ ksi$. The second specimen was subjected to the Type-B Symmetric Three-Cycle-Set Biaxial Load History shown in Figure 5-1. This figure includes a diagram of the column cross-section with the selected bar and crack labeling scheme. Displacements in the +Y-direction placed the South reinforcement in tension. Cracks due to loading in the +Y-direction were labeled as red. The orientation of the X and Y axes are shown in Figure 2-52 with regards to the test setup. The +Y-axis is perpendicular to and points away from the strong wall. Values of interests, damage observations, and moment-curvature predictions for the second test appear in Table 5-1, Table 5-2, and Table 5-3.

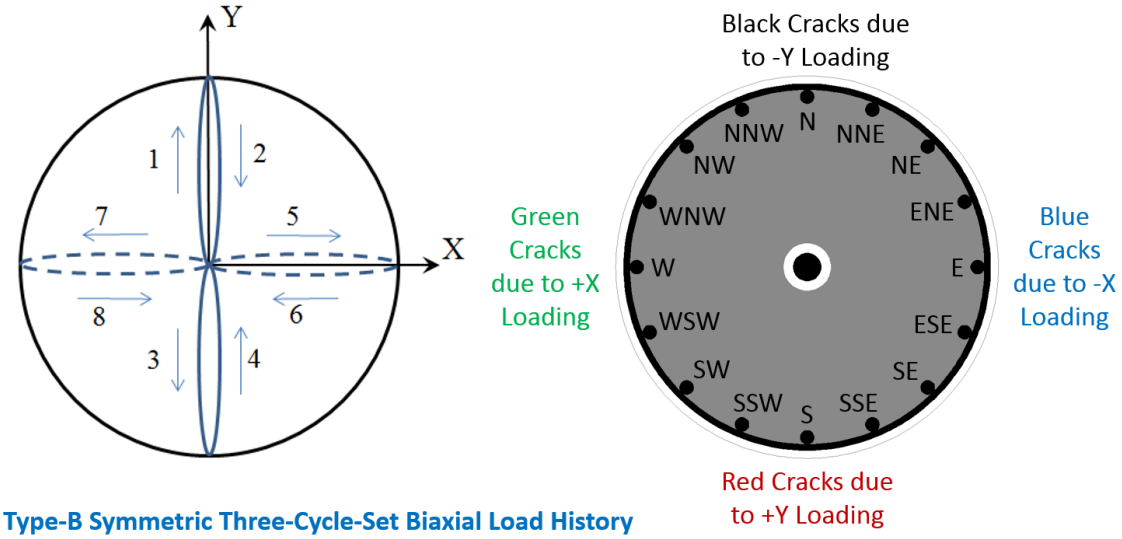

Type-B Symmetric Three-Cycle-Set Biaxial Load History

- Begins with elastic cycles (1-8) in ¼ yield increments until F_y'
- The equivalent yield displacement is then computed as $\Delta_y = \Delta_y'\left(M_n/M_y'\right)$
- Three inelastic cycles (1-8) for each displacement ductility level $\mu_{\Delta n} = n \cdot \Delta_y$
- Cycle labeling system: $\left(\mu_{\Delta 4}^{-2X} = -6.48\ in\right)$ Represents the second cycle of displacement ductility four in the -X direction

Figure 5-1. Test 2: Load History and Labeling System for Reinforcement and Cracks

Table 5-1. Test 2: Values of Interest

Load History	Type-B Symmetric Three-Cycle-Set
Length, Diameter, and Aspect Ratio	$L = 109.4375\ in, D = 24\ in,\ (L/D = 4.56)$
Longitudinal Steel Detailing	$16\ \#7\ for\ \rho_l = A_{st}/A_g = 2.1\%$
Longitudinal Steel Properties	$f_y = 71.2\ ksi, f_u = 97.9\ ksi, \varepsilon_y = 0.00254$
Transverse Steel Detailing	$\#3\ @\ 2.75\ in\ for\ \rho_s = 4A_{sp}/D's = 0.7\%$
Transverse Steel Properties	$f_y = 67.6\ ksi, f_u = 105.6\ ksi, \varepsilon_y = 0.00448$
Column Concrete Strength	$f_c' = 6.16\ ksi$
Footing Concrete Strength	$f_c' = 9.99\ ksi$
Axial Load	$P = 191\ kips, \left(P/f_c'\ A_g = 7.5\%\right)$
Analytical First Yield Force	$F_y' = 50.52\ kips$
Experimental First Yield Disp.	$\Delta_y' = 1.15\ in$
Analytical Nominal Moment Capacity	$M_n = 621.62\ kip \cdot ft$
Equivalent Yield Displacement	$\Delta_y = \Delta_y'\left(M_n/M_y'\right) = 1.55\ in$
Maximum Lateral Force	$F_y = 76.20\ kips, F_x = 75.11\ kips$
Failure Mode	Loss in lateral strength due to buckling of nearly all column longitudinal bars, followed by a single fractured bar.

Table 5-2. Test 2: Damage Observations

Damage Observations:		
Cycle Peak at which First Cracking was Observed Visually:		
North	$\Delta_y = -0.5F_y' = -0.43\ in$	$F_y = -24.41\ kips$
South	$\Delta_y = 0.5F_y' = 0.41\ in$	$F_y = 25.22\ kips$
East	$\Delta_x = -0.5F_y' = -0.38\ in$	$F_x = -24.38\ kips$
West	$\Delta_x = 0.5F_y' = 0.41\ in$	$F_x = 24.44\ kips$
Cycle Peak at which Cover Concrete Crushing was Observed Visually:		
North	$\mu_{\Delta 1.5}^{+3Y} = 2.38\ in$	$\varepsilon_c = -0.0042$
South	$\mu_{\Delta 1.5}^{-3Y} = -2.38\ in$	$\varepsilon_c = -0.00374$
East	$\mu_{\Delta 1.5}^{+2X} = 2.37\ in$	$\varepsilon_c = -0.00438$
West	$\mu_{\Delta 1.5}^{-1X} = -2.39\ in$	$\varepsilon_c = -0.0048$
Exact Displacement and Cycle Label for Initial Spiral Yielding in the Confinement Zone:		
North	$\Delta_y = 4.26\ in\ during\ \mu_{\Delta 3}^{+1Y}$	$\varepsilon_c = -0.01086$
South	$\Delta_y = -4.82\ in\ during\ \mu_{\Delta 3}^{-3Y}$	$\varepsilon_c = -0.00975$
East	$\Delta_x = 4.81\ in\ during\ \mu_{\Delta 3}^{+2X}$	$\varepsilon_c = -0.01079$
West	$\Delta_x = -4.43\ in\ during\ \mu_{\Delta 3}^{-1X}$	$\varepsilon_c = -0.00867$
Peak Tensile Displacement Prior to Visual Bar Buckling During Subsequent Reversal of Load:		
North	$\mu_{\Delta 4}^{-1Y} = -6.48\ in, Observed\ at\ \mu_{\Delta 4}^{+2Y} = 6.44\ in$	$\varepsilon_s = 0.03151$
South	$\mu_{\Delta 4}^{+2Y} = 6.44\ in, Observed\ at\ \mu_{\Delta 4}^{-2Y} = -6.51\ in$	$\varepsilon_s = 0.03337$
East	$\mu_{\Delta 4}^{-2X} = -6.48\ in, Observed\ at\ \mu_{\Delta 4}^{+3X} = 6.43\ in$	$\varepsilon_s = 0.03079$
West	$\mu_{\Delta 4}^{+2X} = 6.47\ in, Observed\ at\ \mu_{\Delta 4}^{-2X} = -6.48\ in$	$\varepsilon_s = 0.03108$
Exact Displacement and Cycle Label for Fracture of Previously Buckled Reinforcement		
North	$\Delta_y = -0.39\ in\ during\ \mu_{\Delta 5}^{-1Y}$	Single North Extreme Bar

Table 5-3. Test 2: Damage Predictions

Damage Predictions with the New Bidirectional Plastic Hinge Model and New Strain Limits:		
Bar Buckling Predictions		
New Method	$\Delta_{bb}^{Lpr} = 6.75\ in$	$\varepsilon_s^{bb} = 0.03438$
Feng et al. (2015)	$\Delta_{bb}^{Lp} = 5.57\ in$	$\varepsilon_s^{bb} = 0.0374$
Cover Crushing Prediction		
New Method	$\Delta_{cc}^{Lpr} = 2.02\ in$	$\varepsilon_c^{cc} = -0.004$
Spiral Yielding Prediction		
New Method	$\Delta_{sy}^{Lpr} = 4.57\ in$	$\varepsilon_c^{sy} = -0.01192 * M, (M = 0.8)$
Original Ultimate Concrete Compression Strain		
Mander et al. (1988)	$\Delta_{cu}^{Lpr} = 6.34\ in$	$\varepsilon_{cu} = -0.0145$

Figure 5-2. Test 2: Specimen Deformation at $\mu_{\Delta 5}^{+1y} = 8.09"$

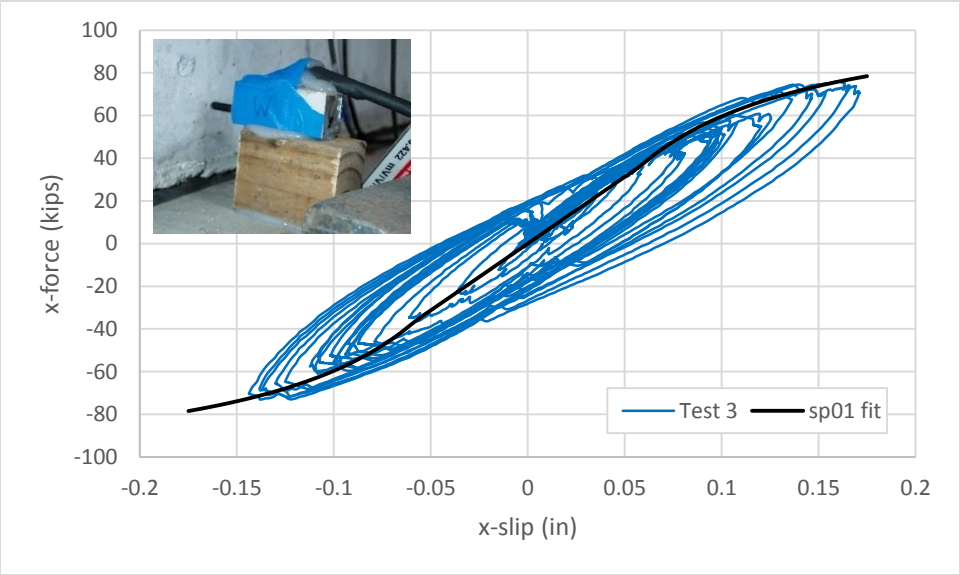

Figure 5-3. Test 3: Measured Linear Potentiometer Relative Footing Displacement with Monotonic SP01 Model Fit

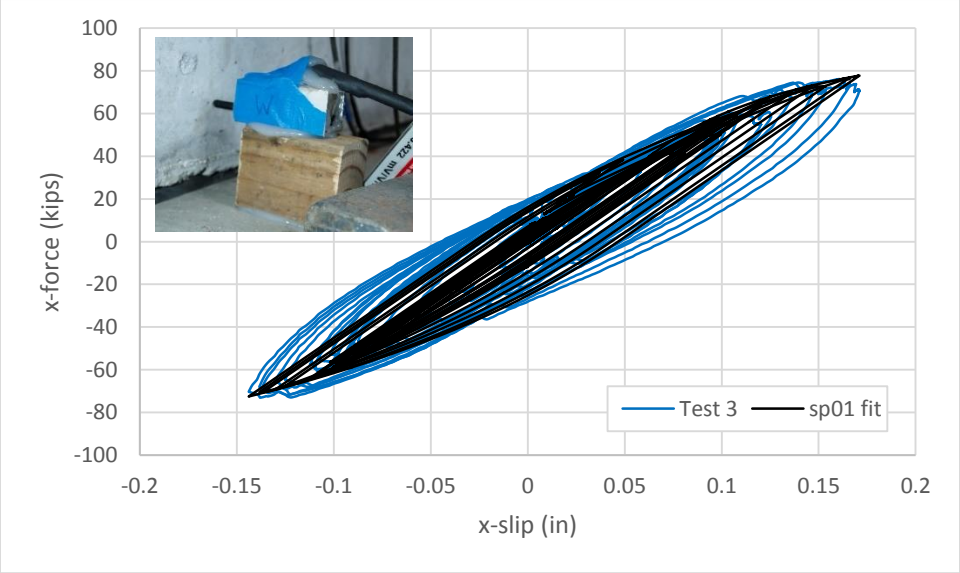

Figure 5-4. Test 3: Cyclic Performance of SP01 Model Fit Used to Correct Test 2 for Relative Footing Displacement

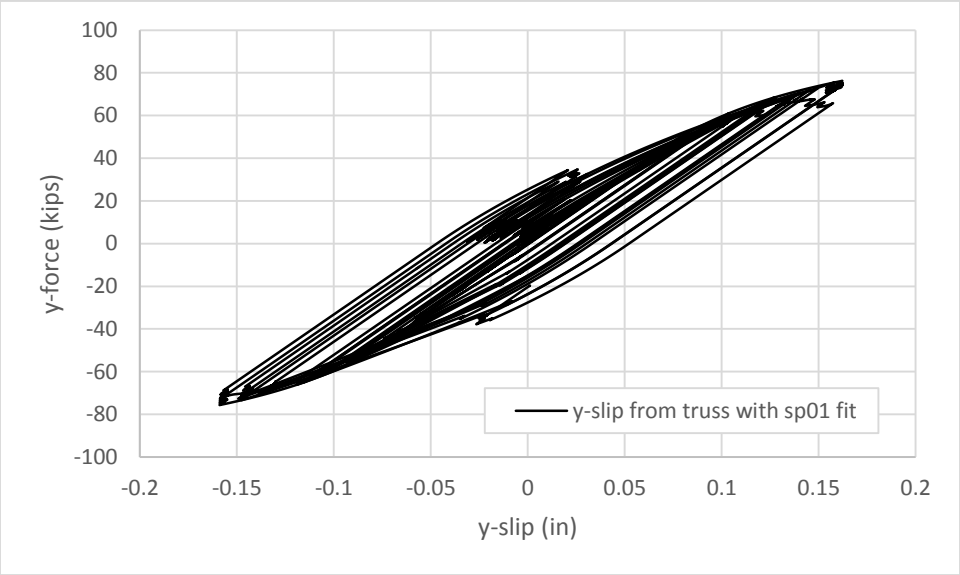

Figure 5-5. Test 2: Relative Footing Displacement Obtained from Truss with SP01 Fit from Test 3

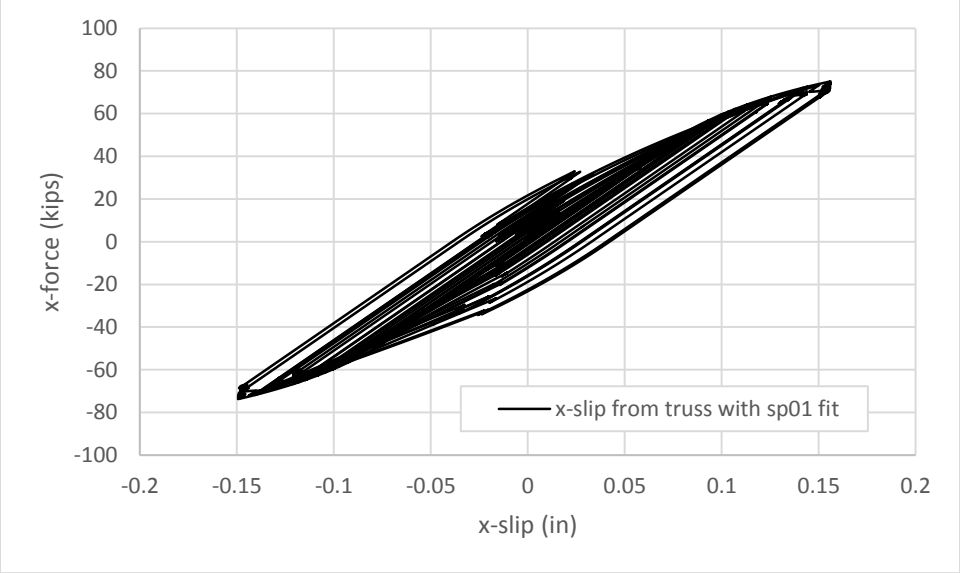

Figure 5-6. Test 2: Relative Footing Displacement Obtained from Truss with SP01 Fit from Test 3

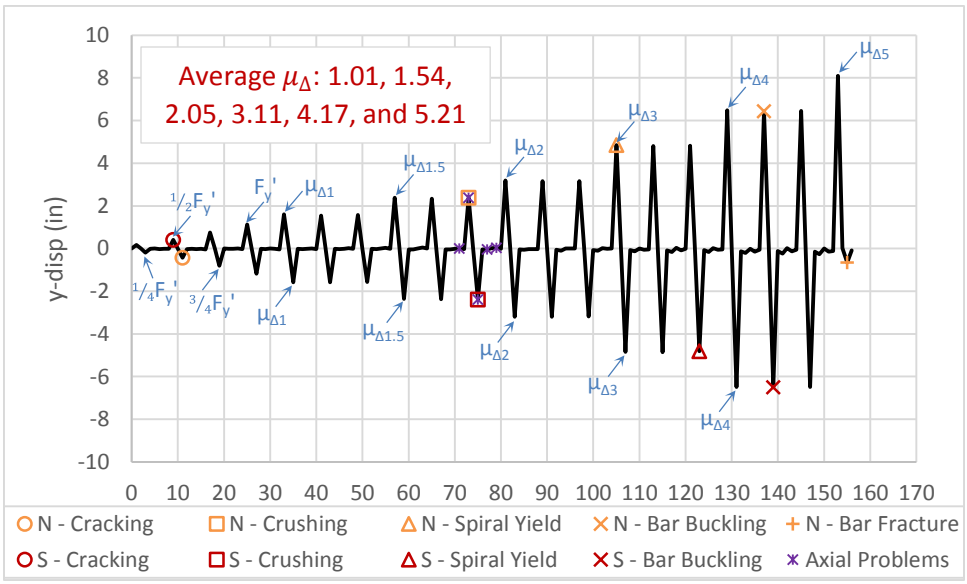

Figure 5-7. Test 2: Y-Displacement History

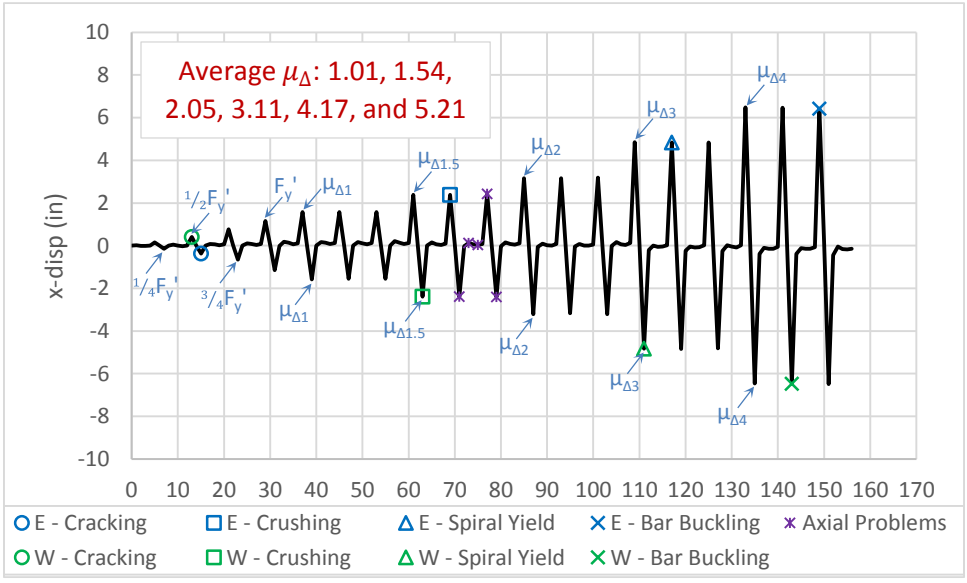

Figure 5-8. Test 2: X-Displacement History

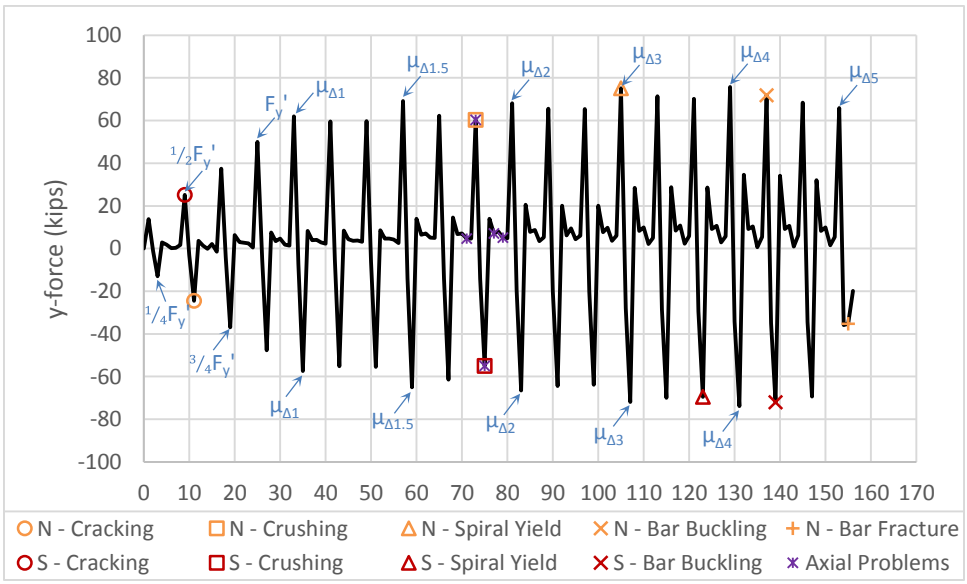

Figure 5-9. Test 2: Y-Force History

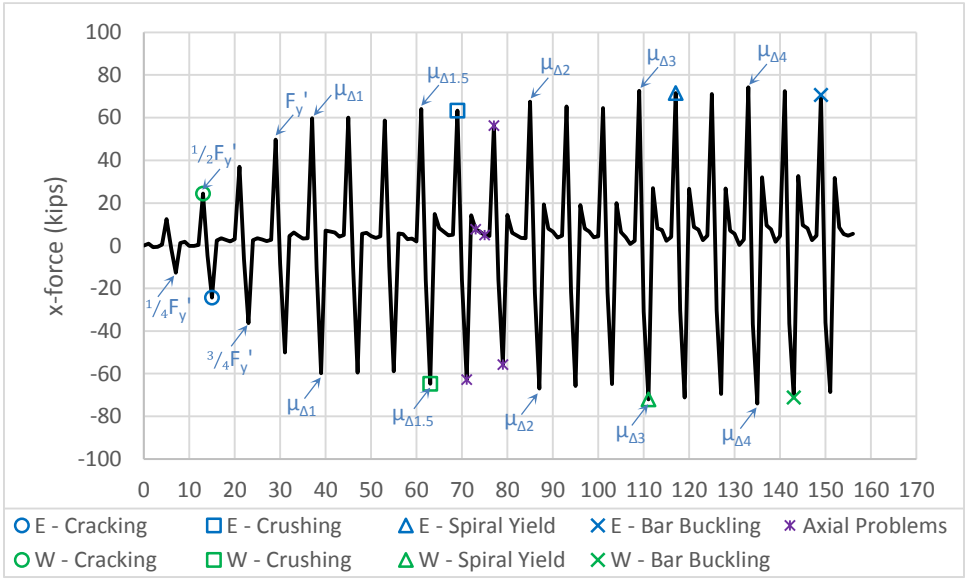

Figure 5-10. Test 2: X-Force History

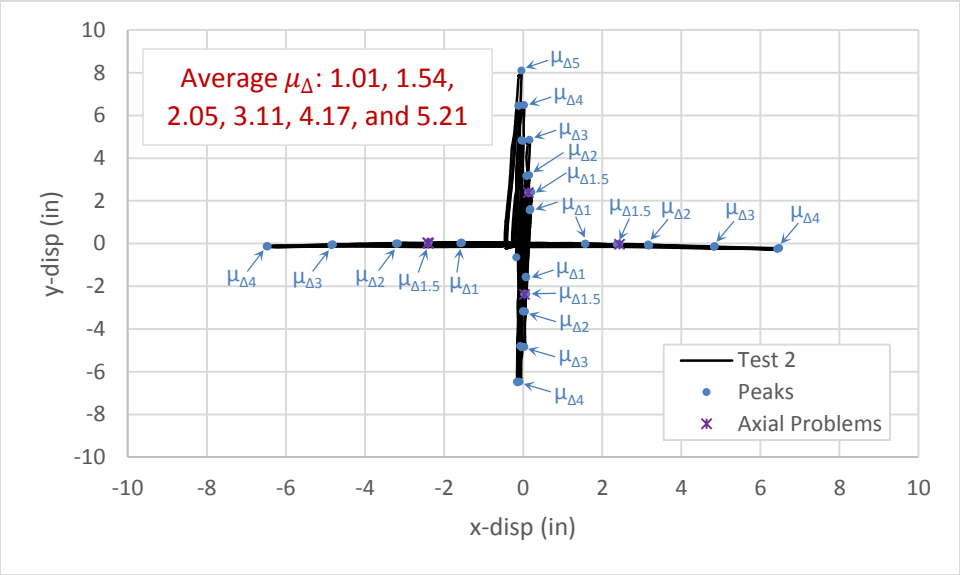

Figure 5-11. Test 2: Type-B Symmetric Three-Cycle-Set Displacement History

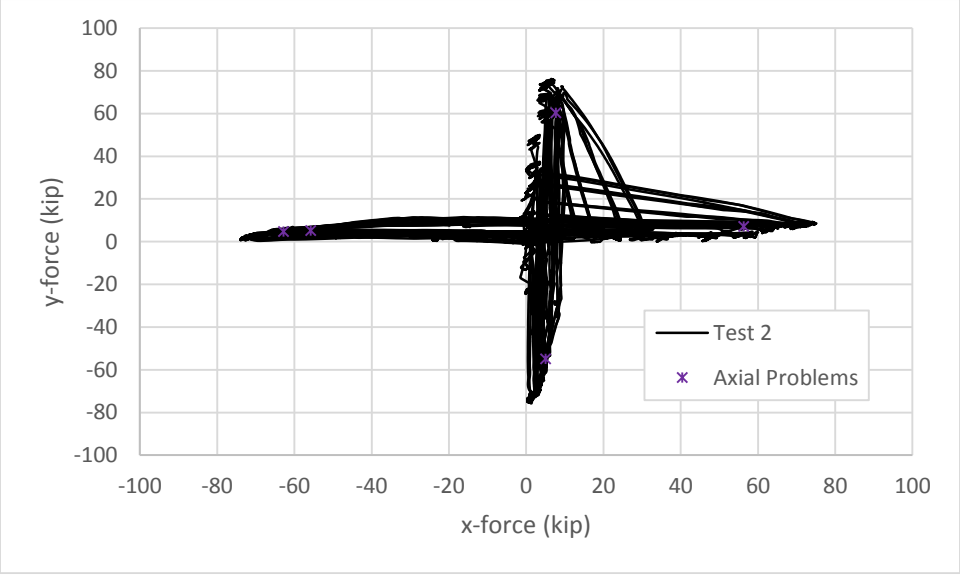

Figure 5-12. Test 2: Load Path

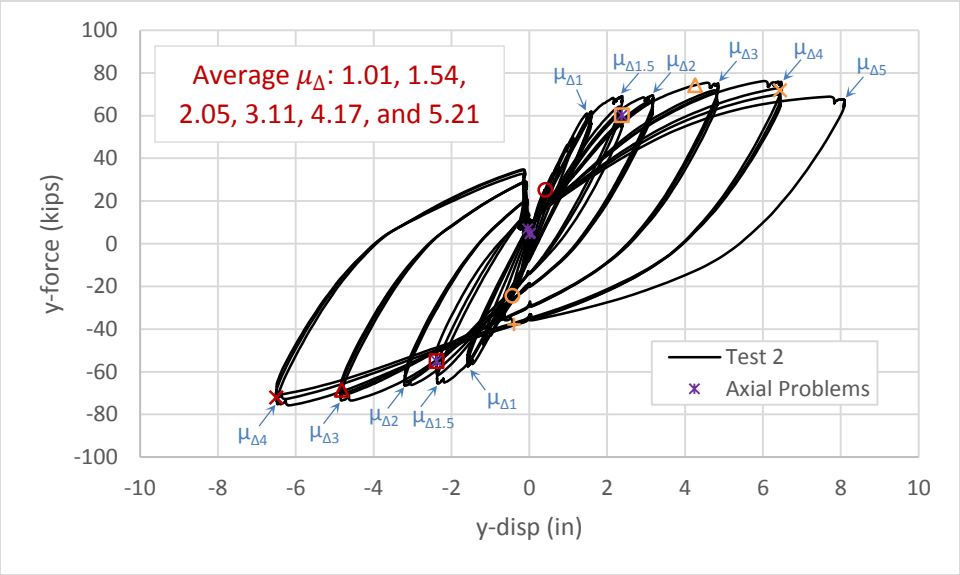

Figure 5-13. Test 2: Y-Direction Hysteretic Response

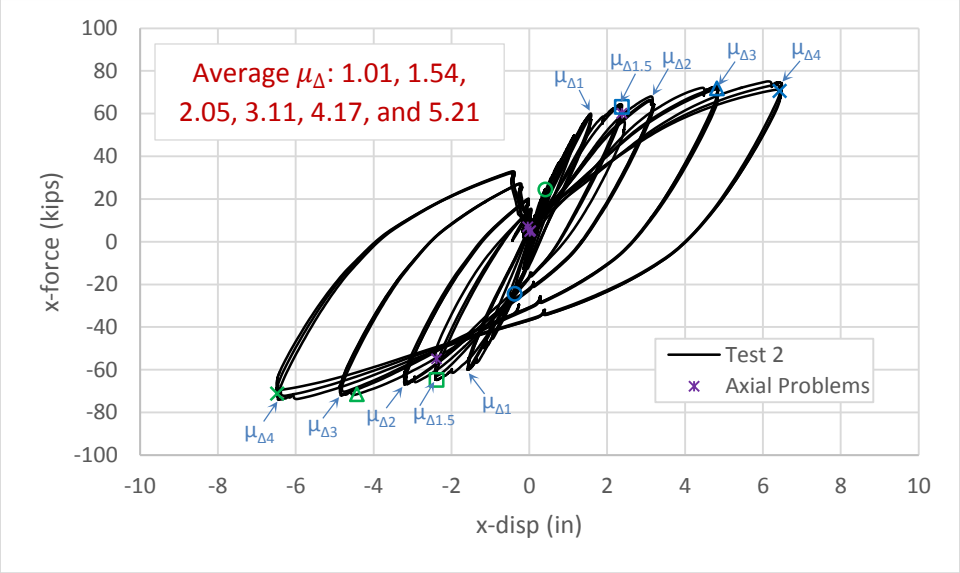

Figure 5-14. Test 2: X-Direction Hysteretic Response

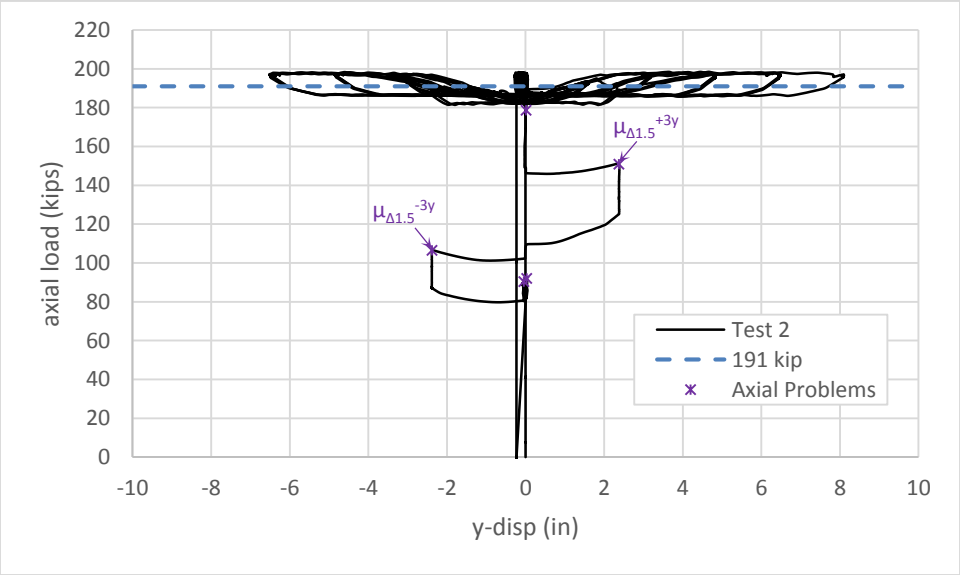

Figure 5-15. Test 2: Y-Direction Axial Force History, Noted Cycles with Lower Axial Force

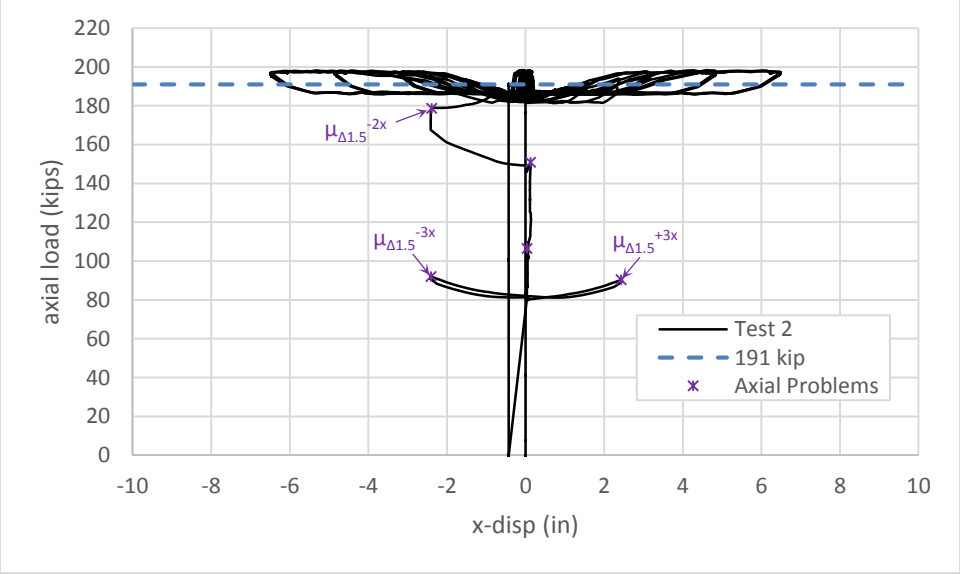

Figure 5-16. Test 2: X-Direction Axial Force History, Noted Cycles with Lower Axial Force

Figure 5-17. Test 2: Target Marker Instrumentation of Longitudinal and Transverse Steel

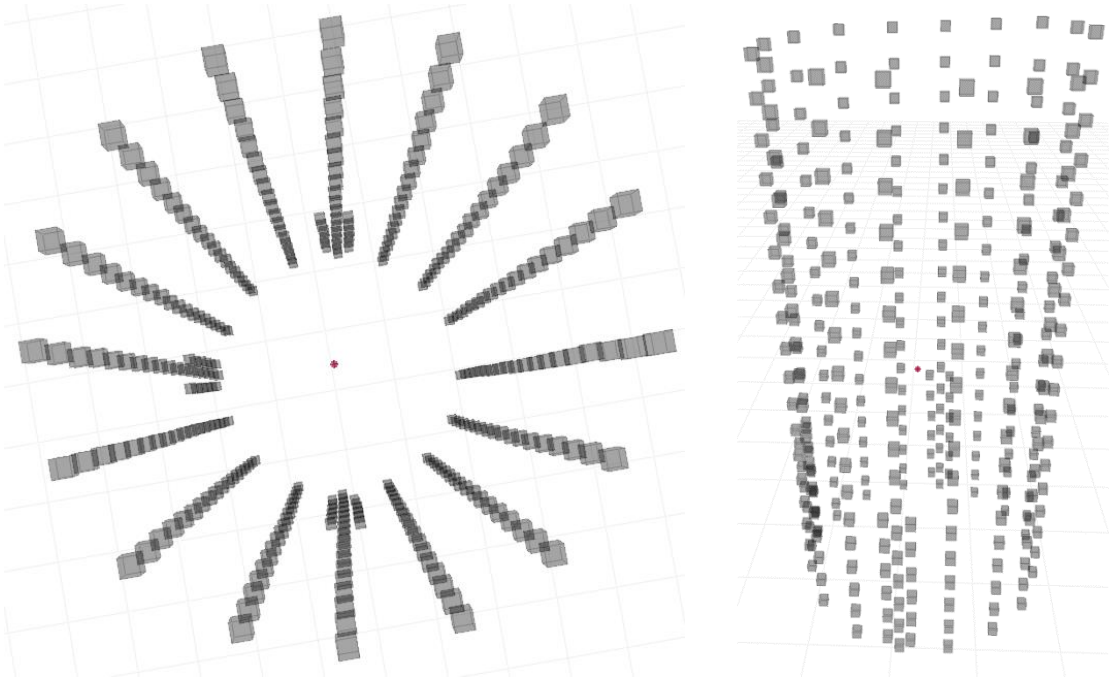

Figure 5-18. Test 2: Optotrak 3D Rendering from Target Markers Applied to Reinforcement

Test 2 - Method of Correction for Lateral Displacements

Near the conclusion of Test 2, small relative displacements were observed at the 3/8" neoprene interface between the transfer footing and specimen footing. This behavior was not visibly observed in Test 1. At the analytically predicted first yield force, $F_y' = 50.52\ kips$, the average experimental first yield displacement measured via the string potentiometer array was $\Delta_y' = 1.23"$. This led to an equivalent yield displacement of $\Delta_y = \Delta_y'(M_n/M_y') = 1.66\ in$, where $M_n = 621.62\ kip \cdot ft$ represents the analytical nominal moment capacity. The Symmetric Three-Cycle-Set Load History proceeded with application of three cycles (1-8 from Figure 5-1) for each displacement ductility level $\mu_{\Delta n} = n \cdot \Delta_y$, where $n = 1, 1.5, 2, 3, 4, 5, etc.$ The displacements at cycle peaks were verified using the string potentiometer array, which measured the total deformation at the center of the applied lateral load. The actual column deformation should have considered the relative displacement between the transfer and specimen footings at the 3/8" neoprene interface. This relative displacement was measured in Test 3 with linear potentiometers in the four primary directions, see Figure 5-3.

In attempt to correct the measured displacements from Test 2, a hysteretic model was fit to the lateral force versus relative footing displacement relationship of Test 3. The Bond SP01 hysteretic model developed by (Zhao and Sritharan 2007) was repurposed for this task. The monotonic performance of the model is depicted in Figure 5-3, while the cyclic performance is shown in Figure 5-4. In OpenSees, a unit area and length truss with a fixed and free end was subjected to the lateral force history F_x and F_y from Test 2. The calibrated Bond SP01 model was used for the uniaxial material of the truss, therefore the displacements at the free end represented the expected relative footing displacements under the imposed lateral force history. The predicted relative footing displacements in the y and x-directions appear in Figure 5-5 and Figure 5-6. These displacements were subtracted from the total values measured using the string potentiometer array to obtain column deformations which were consistent with the force proportional relative footing displacement history of Test 3. This process reduced the first yield displacement from $\Delta_y' = 1.23"$ to $\Delta_y' = 1.15"$, which lowered the equivalent yield displacement from $\Delta_y = 1.66"$ to $\Delta_y = \Delta_y'(M_n/M_y') = 1.55"$. The corrected deformation history in the y and x-directions appears in Figure 5-7 and Figure 5-8. The average displacement ductility levels for each cycle amplitude, referencing the corrected equivalent yield displacement, were 1.01, 1.54, 2.05, 3.11, 4.17, and 5.21. Note that these cycle amplitudes exceed those from the symmetric two-cycle-set load history of Test 1.

Test 2 - Experimental Observations

The test began with collection of the initial measurements prior to application of the axial load. A constant axial load of $191\ kips\ (P/f_c'\ A_g = 7.5\%)$ was then applied using a self-regulating axial load system described in Chapter 2. The imposed displacement histories in the Y and X-directions for the Type-B Symmetric Three-Cycle-Set Biaxial Load History of Figure 5-1 are shown in Figure 5-7 and Figure 5-8. The resulting column shear force histories in the Y and X-directions appear in Figure 5-9 and Figure 5-10. The full displacement history and resulting load path for Test 2 appear in Figure 5-11 and Figure 5-12. The residual forces due to prior orthogonal loading during each cycle are clearly visible, but this has a smaller impact near the peak of each cycle due to the symmetric application of load. The Y and X-direction column hysteretic response appears in Figure 5-13 and Figure 5-14. The axial load history is shown in Figure 5-15 and Figure 5-16. The seals in the hydraulic jack placed above

the column wore out, allowing the pressure and thus axial load to drop during $\mu_{\Delta 1.5}^{-2X}$, $\mu_{\Delta 1.5}^{+3Y}$, $\mu_{\Delta 1.5}^{-3Y}$, $\mu_{\Delta 1.5}^{+3X}$, and $\mu_{\Delta 1.5}^{-3X}$. The loss in axial load during these cycles led to lower measured column shears. The noted cycles during displacement ductility 1.5 where the axial force began to drop are highlighted in figures referenced above.

The load history began with elastic cycles (1-8) in ¼ F_y' increments until the analytically predicted first yield force ($F_y' = 50.52\ kips$) was reached in each direction of loading. Cracks were first observed on all sides of the specimen during the ½ F_y' cycle, see Figure 5-19 and Figure 5-20. At the analytically predicted first yield force, the corrected displacements in the four primary directions were measured at $\Delta_y' = 1.11$" and $\Delta_y' = -1.18$" in Y-direction and $\Delta_y' = 1.16$" and $\Delta_y' = -1.15$" in X-direction, producing an average experimental first yield displacement of $\Delta_y' = 1.15$". Cracks observed on each side of the specimen at first yield are shown in Figure 5-21 and Figure 5-22. The equivalent yield displacement for the column was then computed as $\Delta_y = \Delta_y'(M_n/M_y') = 1.55\ in$, where $M_n = 621.62\ kip \cdot ft$ represents the analytical nominal moment capacity corresponding to an extreme fiber compression strain of $\varepsilon_c = 0.004$ or a steel tensile strain of $\varepsilon_s = 0.015$, whichever occurs first. The remainder of the Symmetric Three-Cycle-Set Load History consists of three cycles (1-8 from Figure 5-1) for each displacement ductility level $\mu_{\Delta n} = n \cdot \Delta_y$, where $n = 1, 1.5, 2, 3, 4, 5, 6\ etc.$ The average displacement ductility levels for each cycle amplitude of Test 2, referencing the corrected equivalent yield displacement, were 1.01, 1.54, 2.05, 3.11, 4.17, and 5.21.

For each displacement ductility level, cracks were marked during the third cycle of loading and those which were visible under two primary directions were still marked with that direction's representative color from Figure 5-1. At displacement ductility one, the cracks remained horizontal, but increased in width and became more numerous as shown in Figure 5-23 and Figure 5-24. Concrete crushing was observed on the West and East sides of the specimen during $\mu_{\Delta 1.5}^{-1x} = -2.39$" and $\mu_{\Delta 1.5}^{+2x} = 2.38$" respectively, as shown in Figure 5-25. Crushing on the North and South sides of the specimen was observed during $\mu_{\Delta 1.5}^{+3y} = 2.38$" and $\mu_{\Delta 1.5}^{-3y} = -2.38$", as depicted in Figure 5-26. In a given direction of loading, cracks on the shear face began to show some inclination in regions above the footing-column interface as shown in Figure 5-27 and Figure 5-28. Those near the footing-column interface remained horizontal. The cracks on the North and South sides of the specimens are shown at the end of the displacement ductility level, so that cracks due to loading in the orthogonal direction appear in the photos.

Photos of the crack profile on each side of the specimen at the conclusion of displacement ductility two appear in Figure 5-29 and Figure 5-30. Compare this to the crack profiles at the end of displacement ductility three shown in Figure 5-33 and Figure 5-34. By this time, there was a distinct crack inclination on the shear faces of the specimen in a given direction of loading. Cracks in one direction were clearly interacting with cracks in the opposing directions, however even in the presence of adjacent horizontal cracks, the diagonal cracks on the shear faces continued to elongate and incline for the remainder of the experiment. Initial spiral yielding under confinement demands was measured on the North, South, and West sides of the specimen during the first cycle of displacement ductility three, followed by spiral yielding on the East side during the second cycle. Photos of crushing on each side of the specimen during the first cycle of displacement ductility three appear in Figure 5-31 and Figure 5-32.

The measured spiral strains on the North and South sides of the specimen spiked during $\mu_{\Delta 4}^{+1y} = 6.48"$ and $\mu_{\Delta 4}^{-1y} = -6.48"$, however the reinforcement remained visibly straight as shown in Figure 5-35. Similarly, the East and West reinforcement remained visibly straight during $\mu_{\Delta 4}^{+1x} = 6.48"$ and $\mu_{\Delta 4}^{-1x} = -6.46"$, as shown in Figure 5-36. During $\mu_{\Delta 4}^{+2y} = 6.44"$, the North extreme fiber bar N and adjacent bar NNE buckled, see Figure 5-37. In the following reversal to $\mu_{\Delta 4}^{-2y} = -6.51"$, the South extreme fiber bar S and adjacent bar SSE buckled, see Figure 5-37. The West extreme fiber bar W buckled during $\mu_{\Delta 4}^{-2x} = -6.48"$ as shown in Figure 5-38. Bar NNW buckled during $\mu_{\Delta 4}^{+3y} = 6.45"$, followed by a bar SSW during $\mu_{\Delta 4}^{-3y} = -6.48"$ as shown in Figure 5-38 and Figure 5-39 respectively.

Permanent deformation in the North spirals which was visible as the North reinforcement straightened out during $\mu_{\Delta 4}^{-3y} = -6.48"$ is shown in Figure 5-39. The East extreme fiber bar E and ESE buckled during $\mu_{\Delta 4}^{+3x} = 6.43"$, see Figure 5-40. Adjacent West bars WSW and WNW buckled during $\mu_{\Delta 4}^{-3x} = -6.48"$, see Figure 5-40. The NW and NE bars buckled during $\mu_{\Delta 5}^{+1y} = 8.09"$ while the buckled deformation in the North bars significantly increased, as shown in Figure 5-41. A photo of the deformed specimen at $\mu_{\Delta 5}^{+1y} = 8.09"$ appears in Figure 5-2. The North extreme fiber bar fractured at $-0.39"$ during $\mu_{\Delta 5}^{-1Y}$, see Figure 5-41. At this time, the test was concluded since an additional cycle of loading was expected to fracture more bars, making it difficult to repurpose this specimen as a repair candidate. It is clear that fracture of the first previously buckled bar represents the beginning of a rapid loss in strength during successive cycles. Photos of the specimen after removal of the instrumentation appear in Figure 5-42 and Figure 5-43.

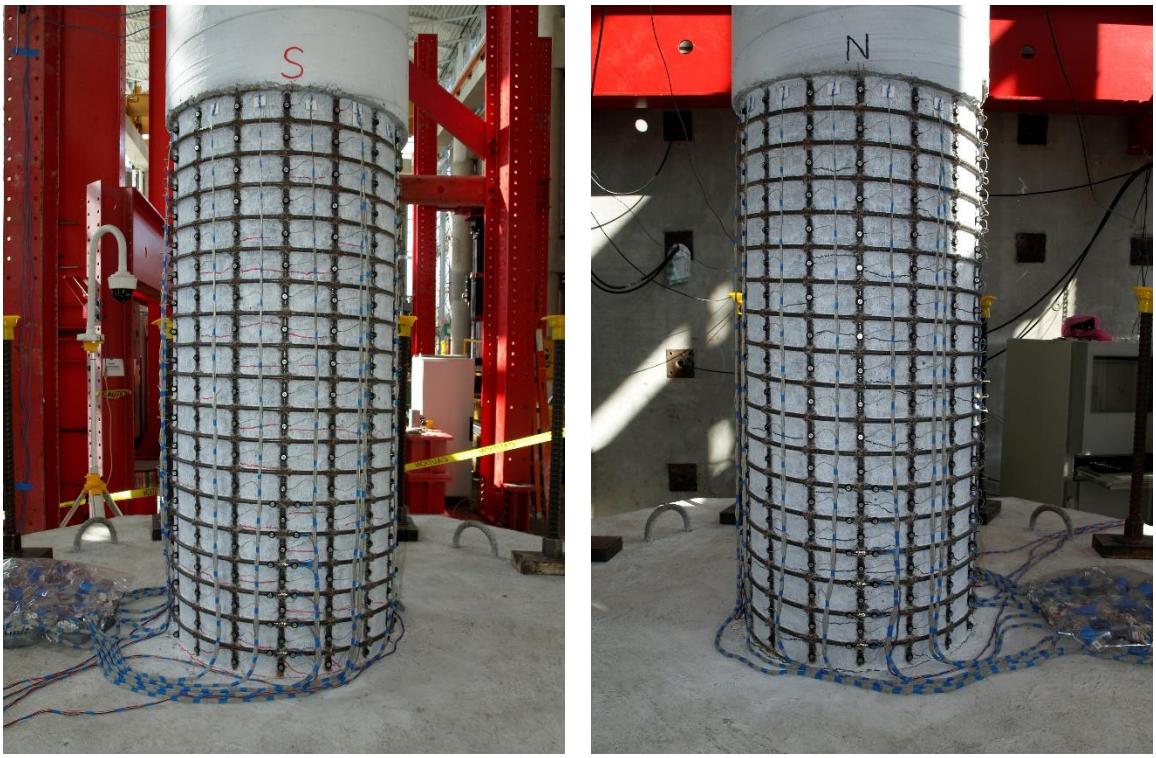

Figure 5-19. Test 2: First Cracking on the South and North Sides of the Specimen during $\Delta_y = 0.41"$ and $\Delta_y = -0.43"$

Figure 5-20. Test 2: First Cracking on the West and East Sides of the Specimen during $\Delta_x = 0.41$" and $\Delta_x = -0.38$"

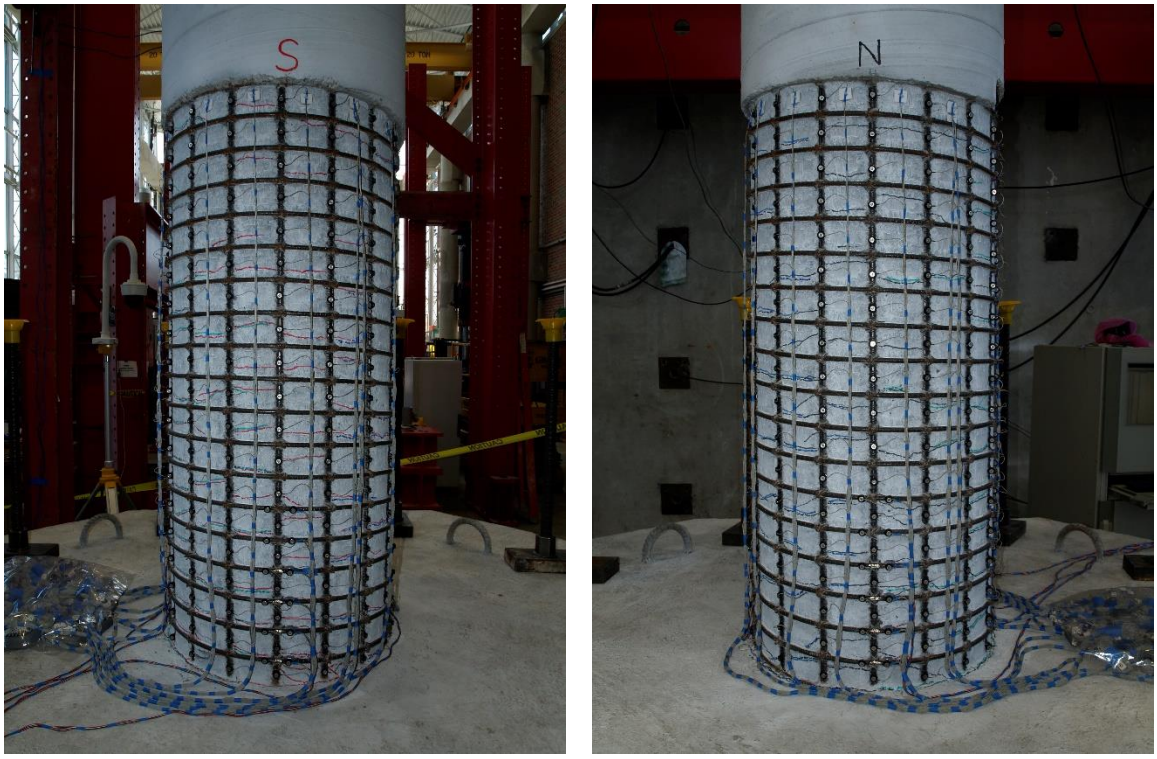

Figure 5-21. Test 2: Cracking on the South and North Sides during $\Delta'_y = 1.12$" and $\Delta'_y = -1.18$" in Y-Direction

Figure 5-22. Test 2: Cracking on the West and East Sides during $\Delta'_y = 1.16"$ and $\Delta'_y = -1.15"$ in X-Direction

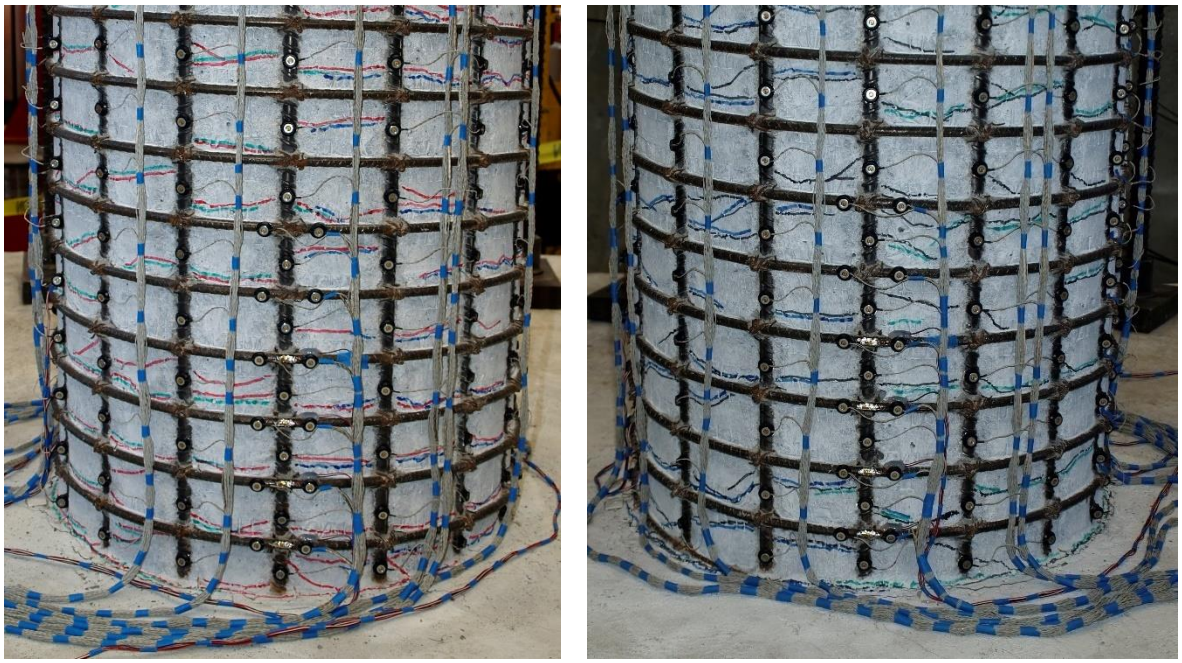

Figure 5-23. Test 2: Cracking on the (Left) South Side at $\mu_{\Delta 1}^{+3y} = 1.57"$ and (Right) North Side at $\mu_{\Delta 1}^{-3y} = -1.57"$

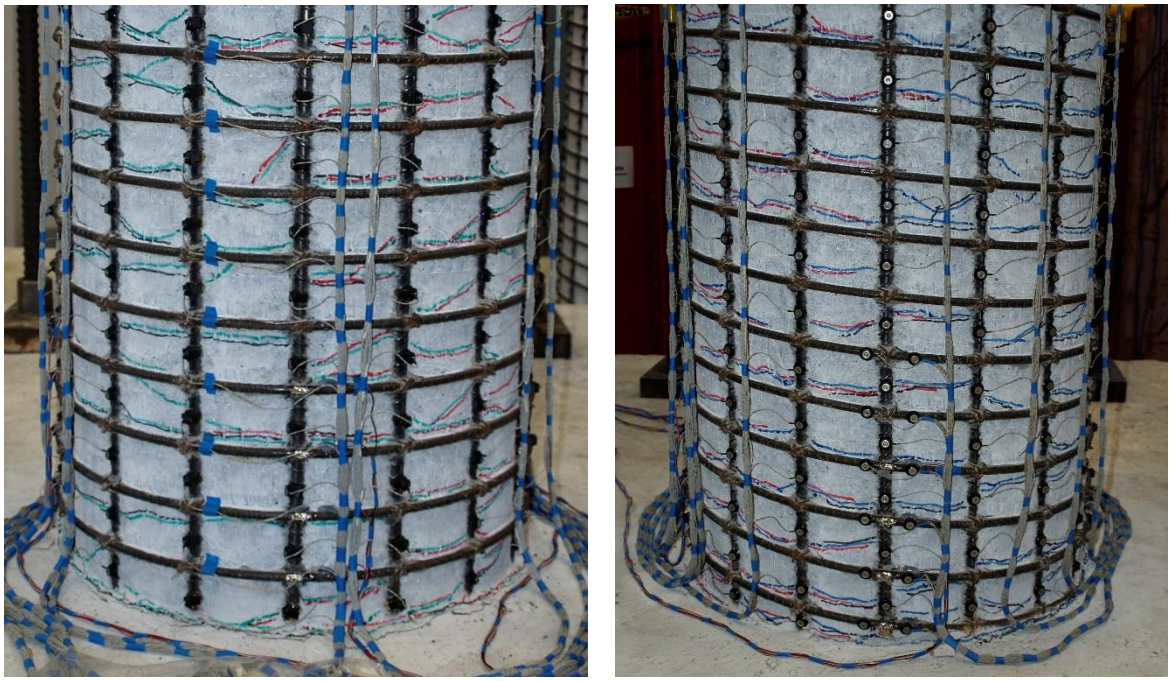

Figure 5-24. Test 2: Cracking on the (Left) West Side at $\mu_{\Delta 1}^{+3x} = 1.57"$ and (Right) East Side at $\mu_{\Delta 1}^{-3x} = -1.56"$

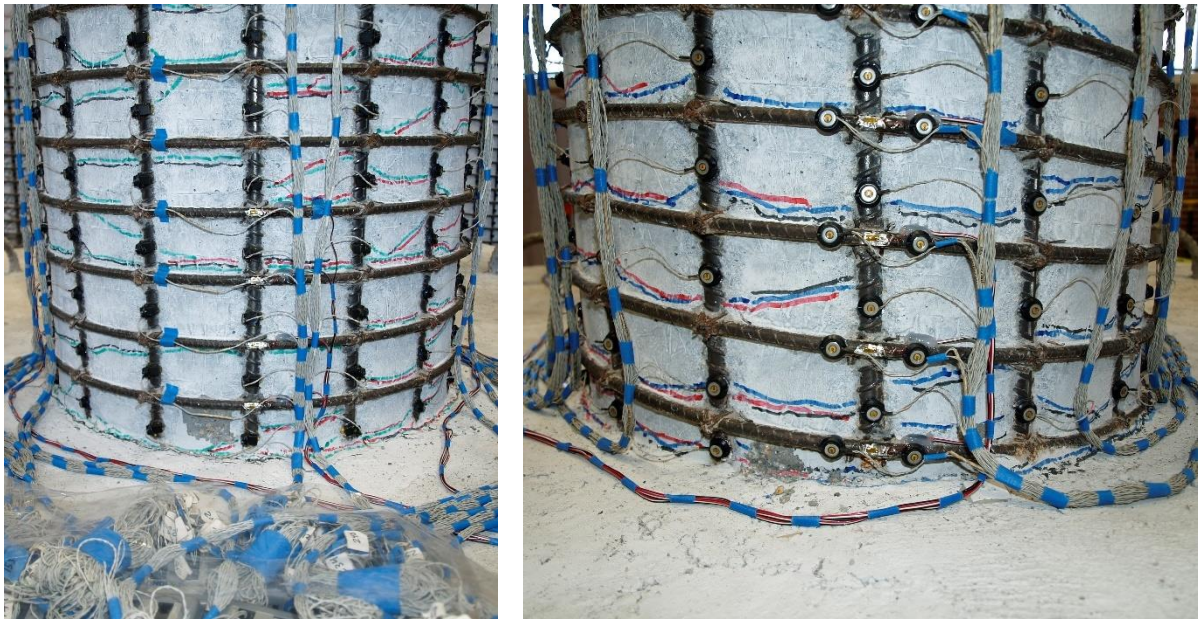

Figure 5-25. Test 2: Concrete Crushing on the (Left) West at $\mu_{\Delta 1.5}^{-1x} = -2.39"$ and (Right) East at $\mu_{\Delta 1.5}^{+2x} = 2.38"$

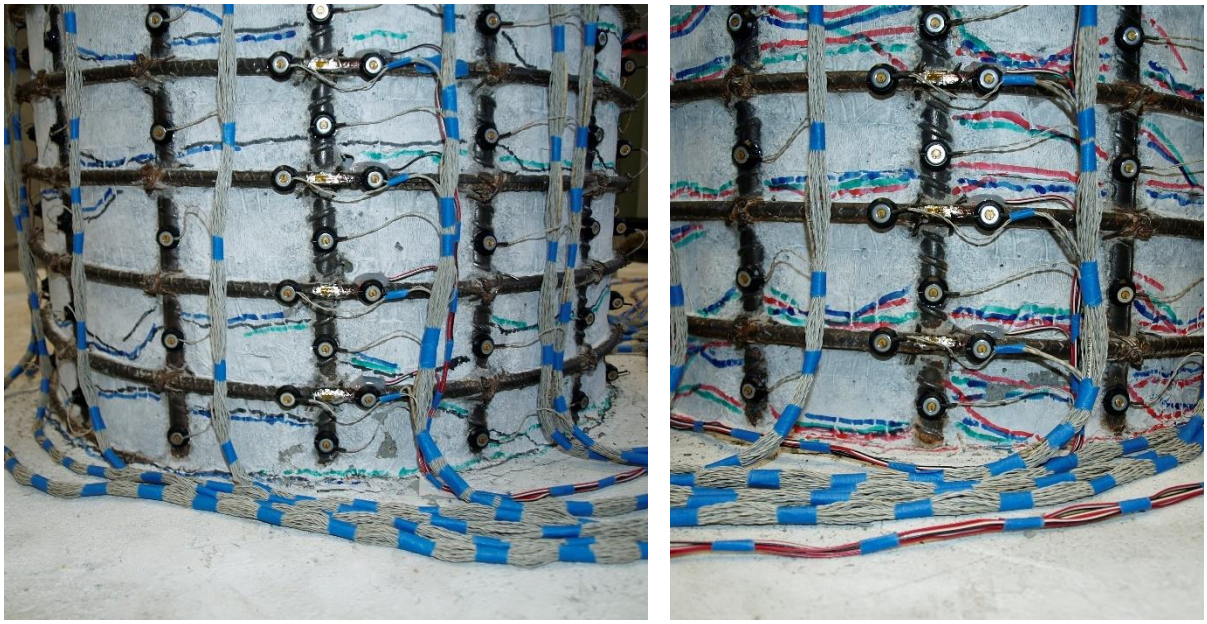

Figure 5-26. Test 2: Concrete Crushing on the (Left) North at $\mu_{\Delta 1.5}^{+3y} = 2.38"$ and (Right) South at $\mu_{\Delta 1.5}^{-3y} = -2.38"$

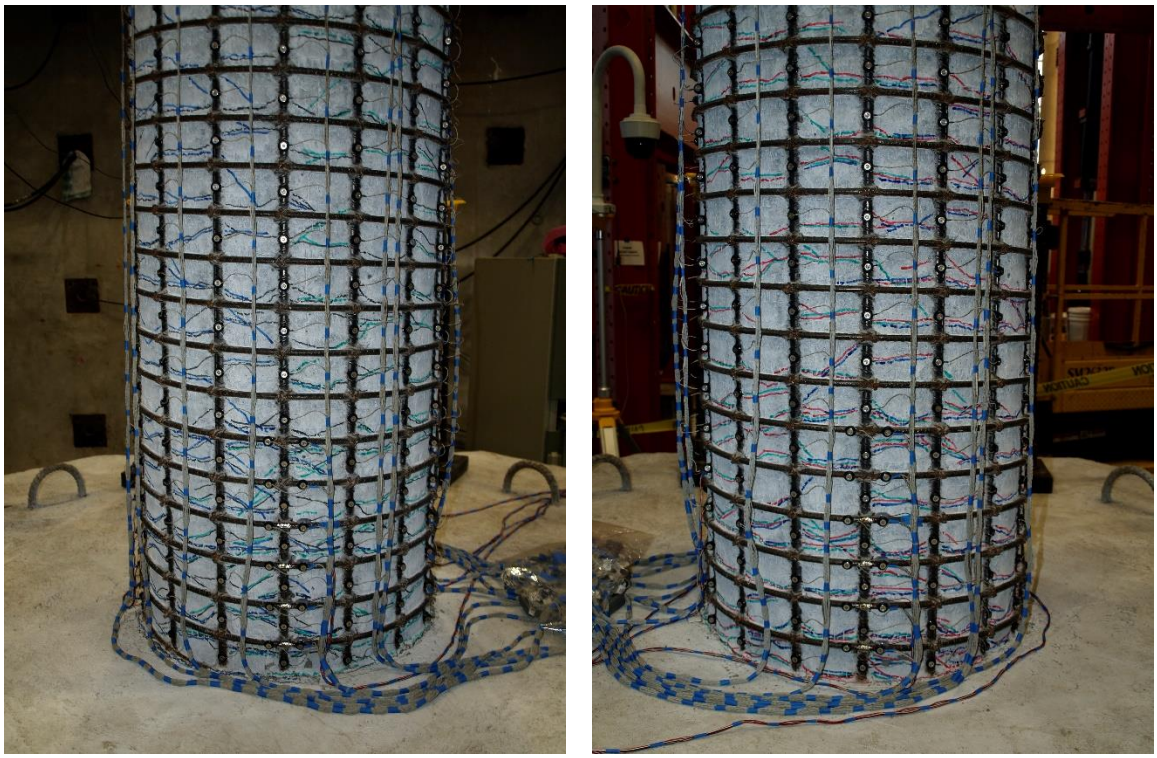

Figure 5-27. Test 2: (Left) North and (Right) South Sides of the Specimen at the End of $\mu_{\Delta 1.5}$

Figure 5-28. Test 2: (Left) West Side at $\mu_{\Delta 1.5}^{+3x} = 2.43"$ and (Right) East Side at $\mu_{\Delta 1.5}^{-3x} = -2.41"$

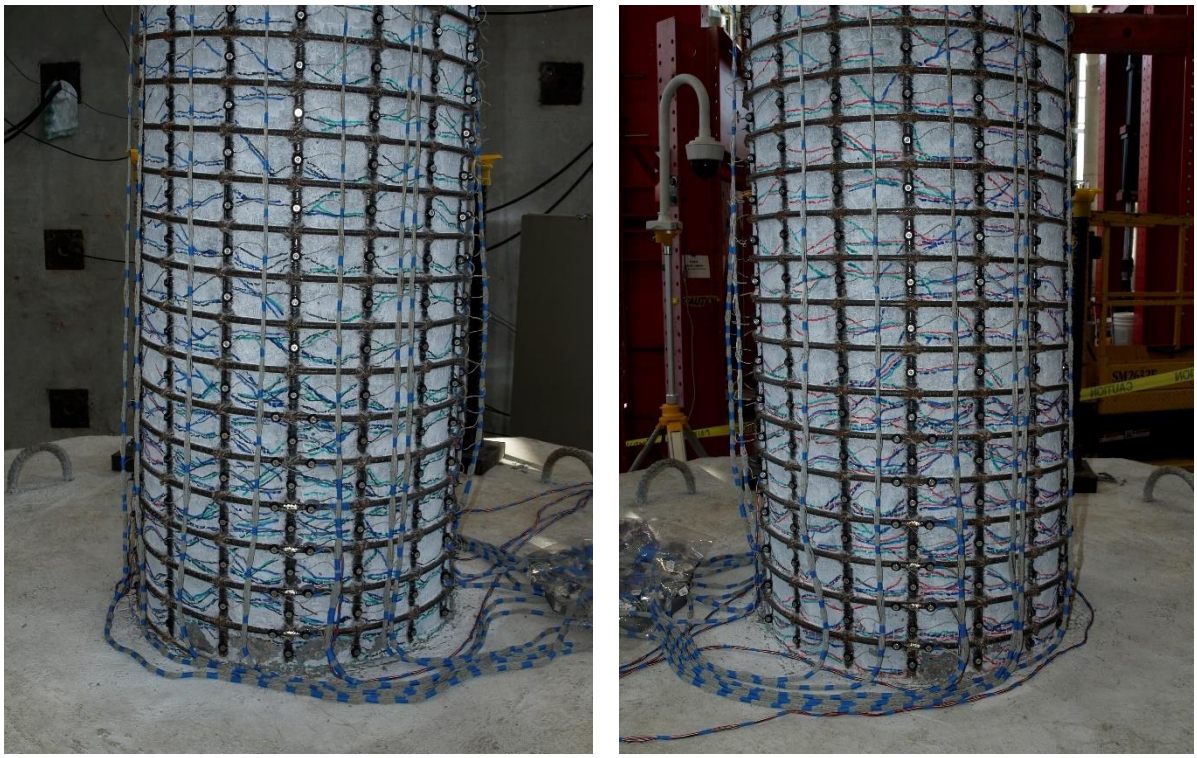

Figure 5-29. Test 2: (Left) North and (Right) South Sides of the Specimen at the End of $\mu_{\Delta 2}$

Figure 5-30. Test 2: (Left) West Side at $\mu_{\Delta 2}^{+3x} = 3.19"$ and (Right) East Side at $\mu_{\Delta 2}^{-3x} = -3.21"$

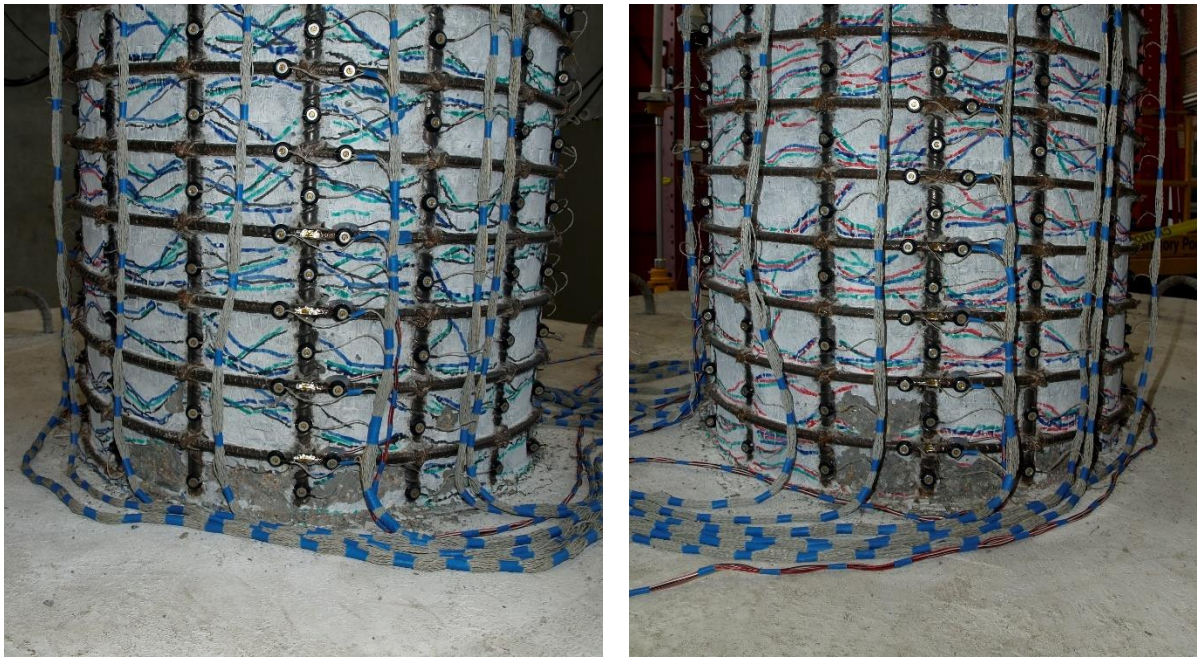

Figure 5-31. Test 2: Crushing on the (Left) North Side at $\mu_{\Delta 3}^{+1y} = 4.85"$ and (Right) South Side at $\mu_{\Delta 3}^{-1y} = -4.85"$

Figure 5-32. Test 2: Crushing on the (Left) East Side at $\mu_{\Delta 3}^{+1x} = 4.85$" and (Right) West Side at $\mu_{\Delta 3}^{-1x} = -4.84$"

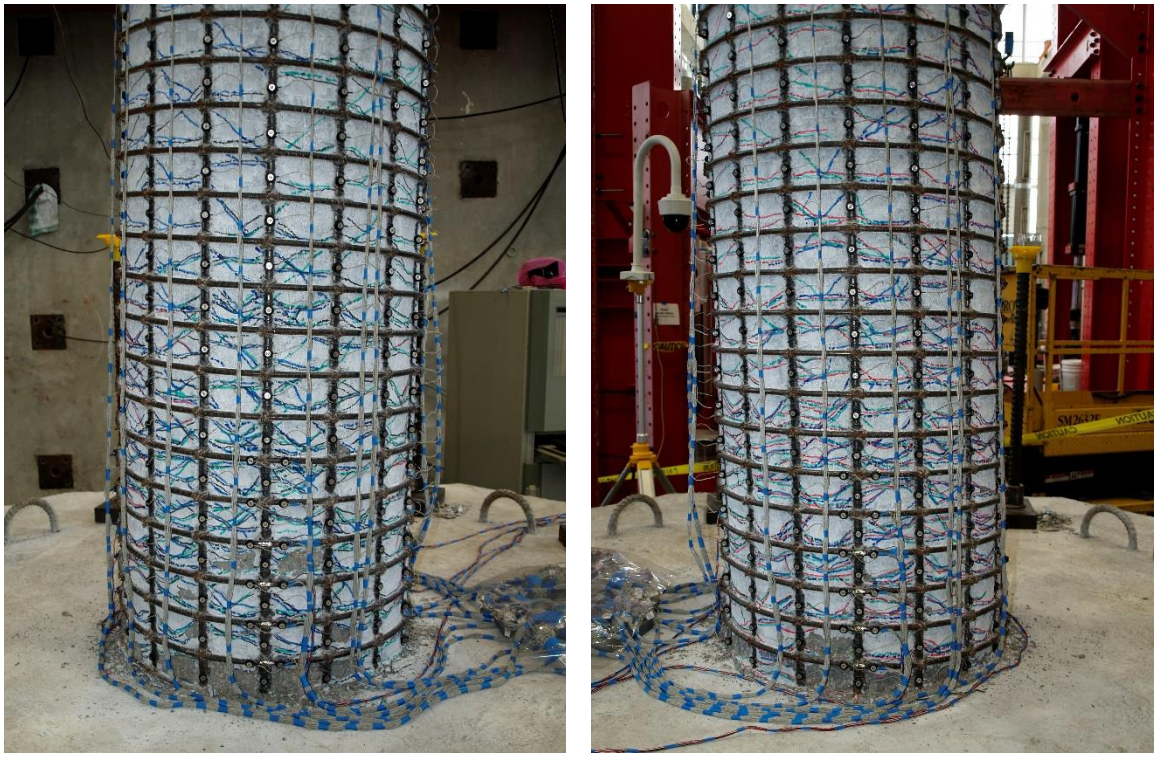

Figure 5-33. Test 2: (Left) North and (Right) South Sides of the Specimen at the End of $\mu_{\Delta 3}$

Figure 5-34. Test 2: (Left) West Side at $\mu_{\Delta 3}^{+3x} = 4.83"$ and (Right) East Side at $\mu_{\Delta 3}^{-3x} = -4.81"$

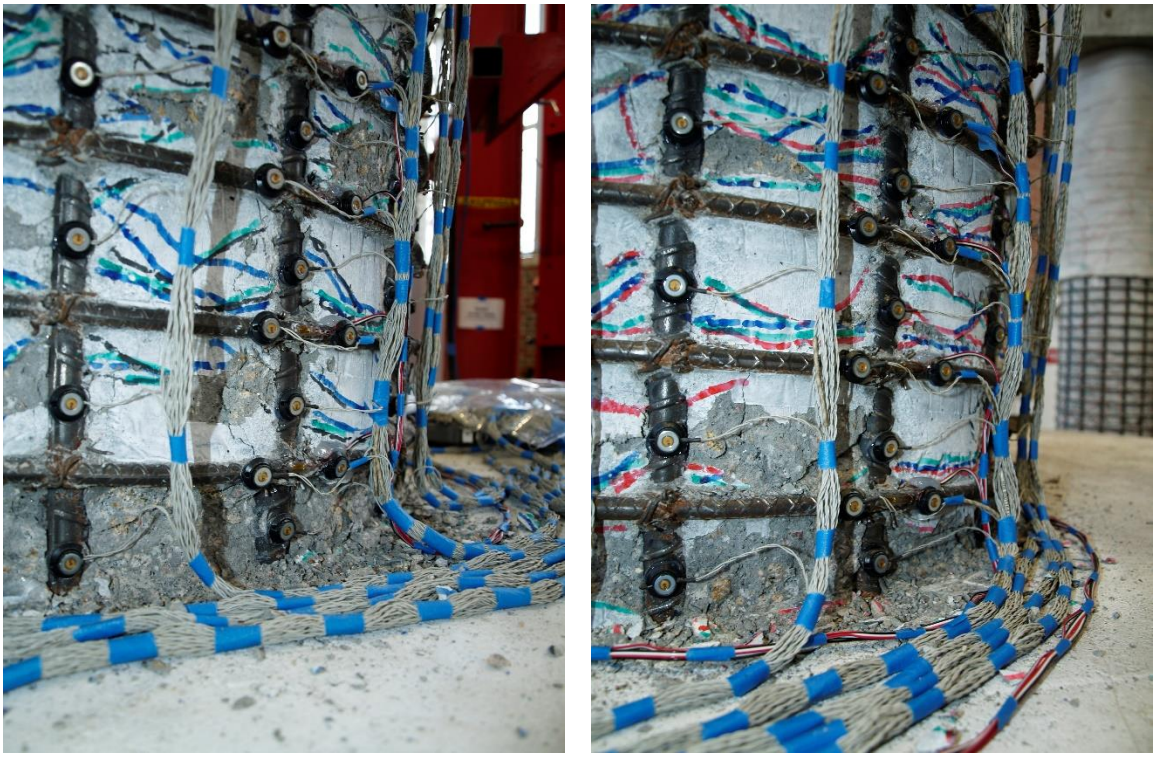

Figure 5-35. Test 2: Reinforcement Remained Straight, (Left) North at $\mu_{\Delta 4}^{+1y} = 6.48"$ and (Right) South at $\mu_{\Delta 4}^{-1y} = -6.48"$

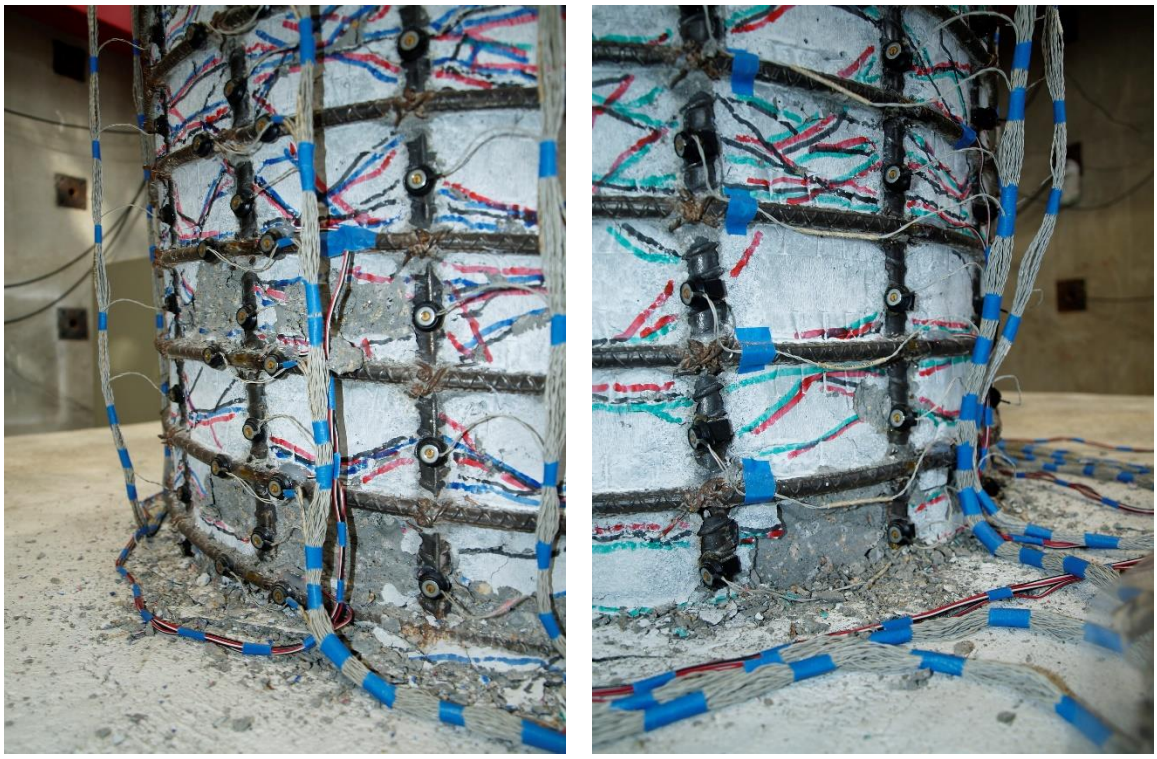

Figure 5-36. Test 2: Reinforcement Remained Straight, (Left) East at $\mu_{\Delta 4}^{+1x} = 6.48$" and (Right) West at $\mu_{\Delta 4}^{-1x} = -6.46$"

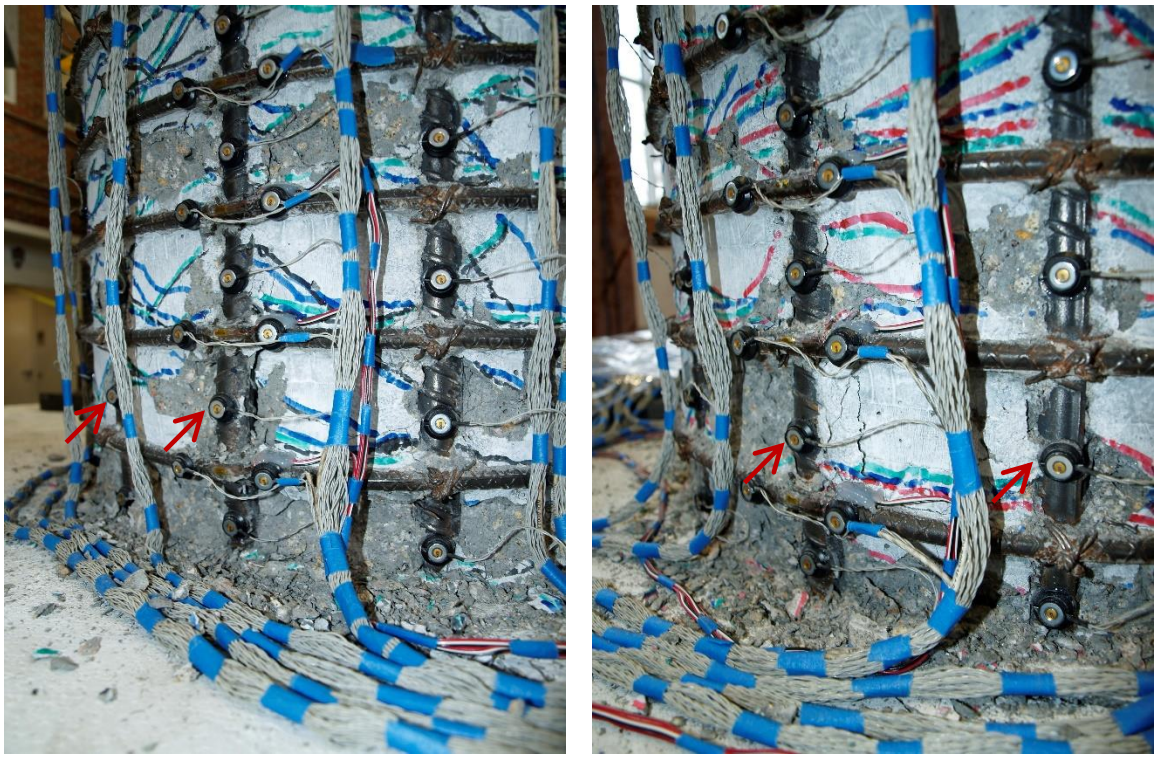

Figure 5-37. Test 2: Buckling of Bars (Left) N and NNE during $\mu_{\Delta 4}^{+2y} = 6.44$" and (Right) S and SSE during $\mu_{\Delta 4}^{-2y} = -6.51$"

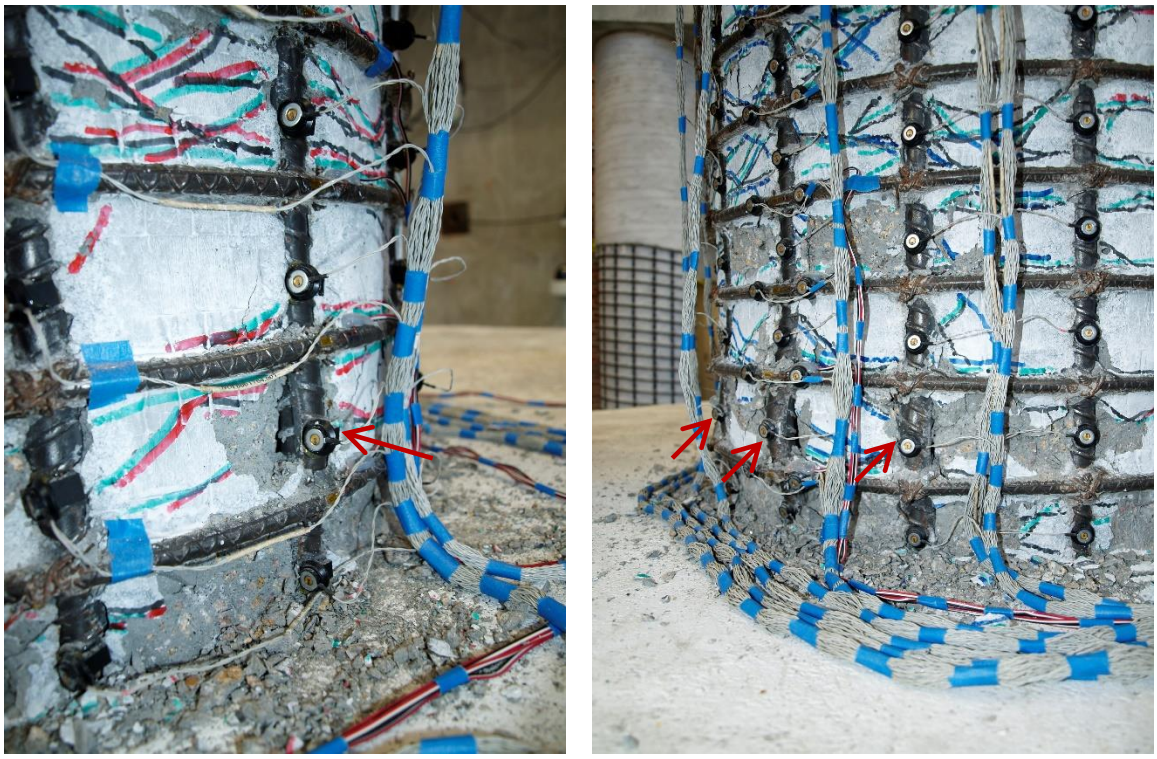

Figure 5-38. Test 2: Buckling of (Left) Bar W during $\mu_{\Delta 4}^{-2x} = -6.48"$ and (Right) Bar NNW during $\mu_{\Delta 4}^{+3y} = 6.45"$

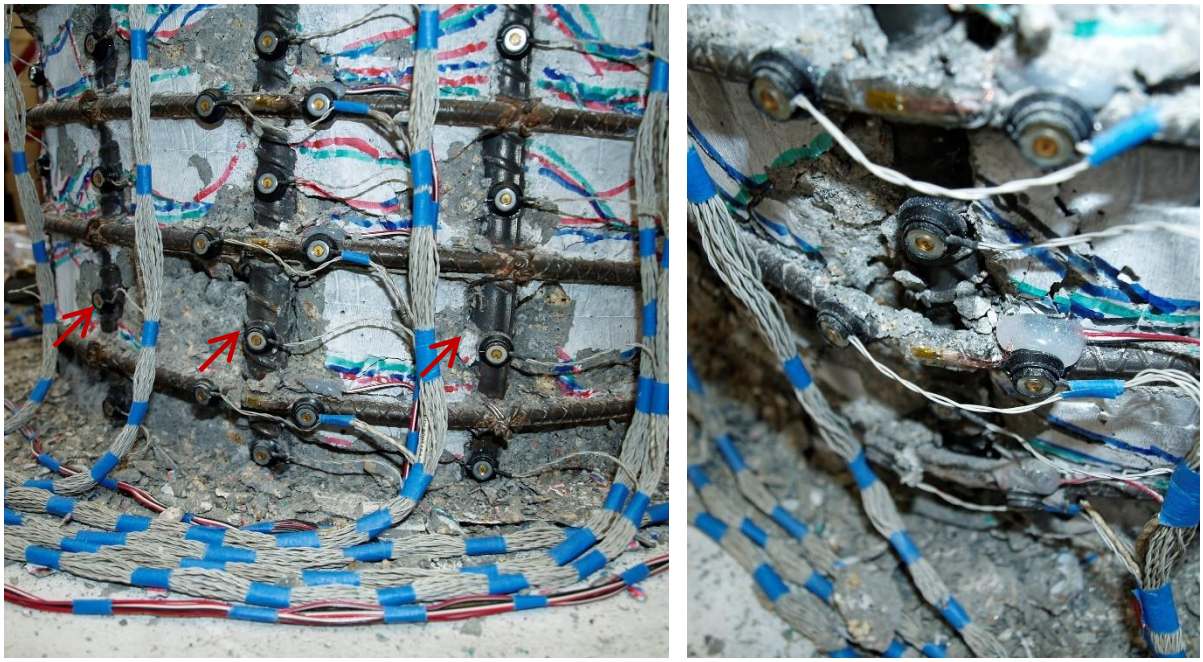

Figure 5-39. Test 2: (Left) Bar SSW Buckled during $\mu_{\Delta 4}^{-3y} = -6.48"$ and (Right) Deformed North Spirals at $\mu_{\Delta 4}^{-3y} = -6.48"$

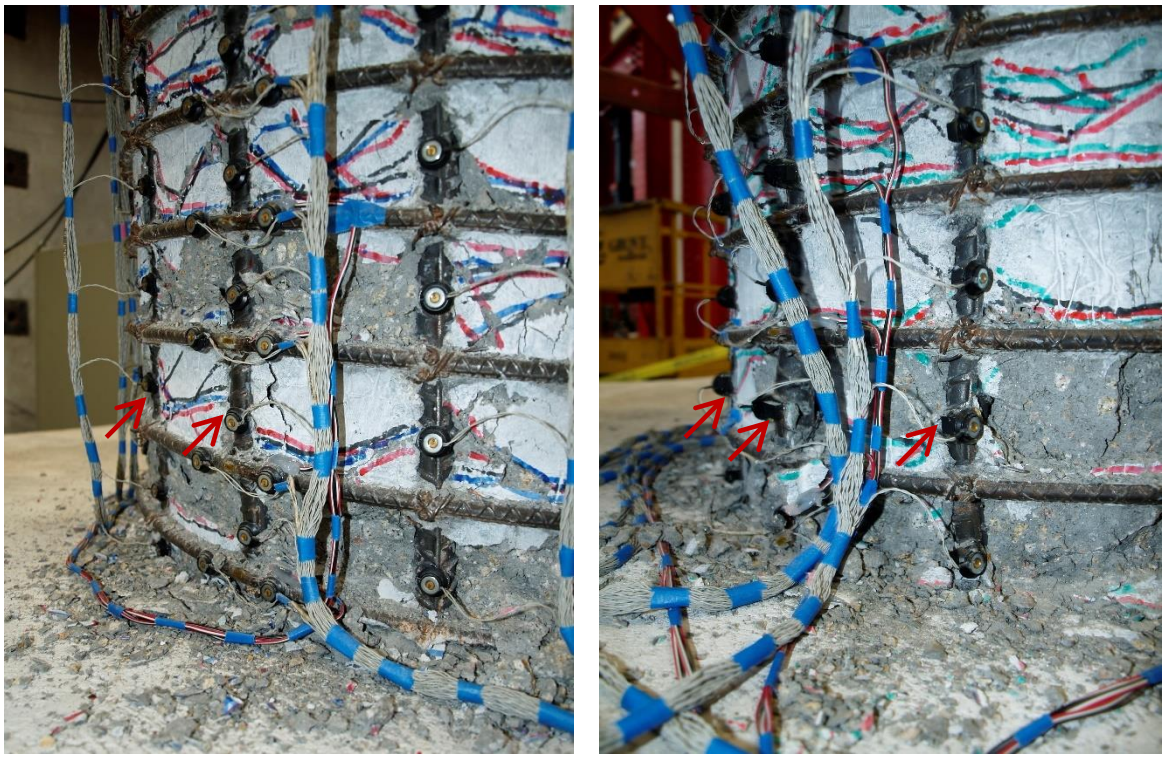

Figure 5-40. Test 2: Buckling of Bars (Left) E and ESE during $\mu_{\Delta 4}^{+3x} = 6.43$" and (Right) WSW and WNW at $\mu_{\Delta 4}^{-3x} = -6.48$"

Figure 5-41. Test 2: (Left) Buckling of NE and NW during $\mu_{\Delta 5}^{+1y} = 8.09$" and (Right) Fracture of Bar N at -0.39" during $\mu_{\Delta 5}^{-1Y}$

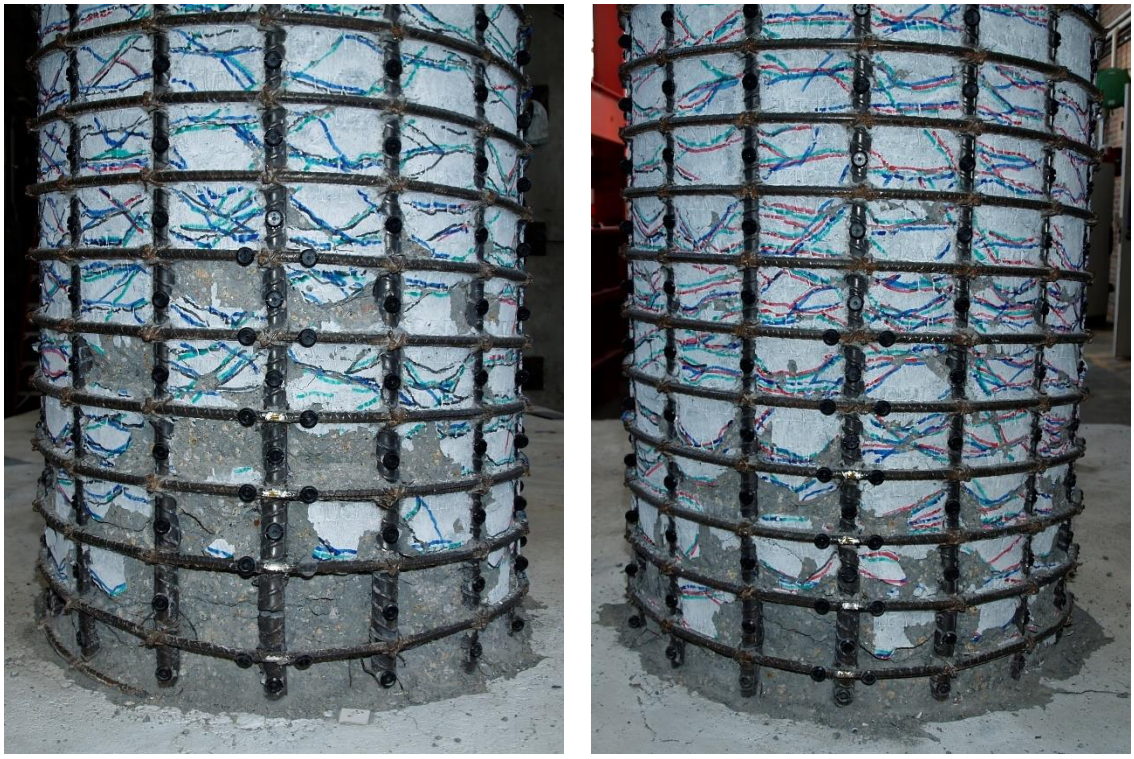

Figure 5-42. Test 2: (Left) North and (Right) South Sides of the Specimen after Instrumentation Removal

Figure 5-43. Test 2: (Left) West and (Right) East Sides of the Specimen after Instrumentation Removal

Test 2 - Strain Data Analysis

North and South Bar Strains

Vertical strain profiles for North and South reinforcement during y-direction cycles are shown in Figure 5-44 and Figure 5-45. Strains in the lowest four spiral layers during compressive y-direction cycles on the North and South sides of the specimen appear in Figure 5-46 and Figure 5-47. The relationship between strain and displacement for either peak tensile or peak compressive gauge lengths appear in Figure 5-48 through Figure 5-51. These figures contain monotonic moment curvature predictions for respective plastic hinge methods. PCK (2007) Lp refers to the (Priestley, Calvi and Kowalsky 2007) plastic hinge method, GN15 Tension/Compression Lpr refers to the (Goodnight, Kowalsky and Nau 2015a) unidirectional modified plastic hinge method, TX Adjusted Lpr and Lsp refer to using the measured extent of plasticity and average equivalent strain penetration length from this specific test, and New Equations refers to a new bidirectional plastic hinge method which was created based on this study. Details of the new plastic hinge method appear in a later chapter of this report.

The spiral strain gauge hysteresis for the first and second layers above the footing on the North side of the specimen are shown in Figure 5-53 and Figure 5-54. The first spiral layer goes off scale during $\mu_{\Delta 4}^{+1y} = 6.48"$, even though bar N remained visibly straight as shown in Figure 5-35. The second North spiral layer above the footing went off scale during $\mu_{\Delta 4}^{+2y} = 6.44"$ as bar N and NNE visibly buckled, see Figure 5-37. The visual observation of bar buckling was confirmed upon inspection of the North longitudinal bar strain hysteresis in Figure 5-52.

The spiral strain gauge hysteresis for the first and second layers above the footing on the South side of the specimen appear in Figure 5-56 and Figure 5-57. Both spiral layers go off scale during $\mu_{\Delta 4}^{-2y} = -6.51"$ as the S and SSE bars buckled, see Figure 5-37. The visual observation of bar buckling was confirmed upon inspection of the South longitudinal bar strain hysteresis in Figure 5-55.

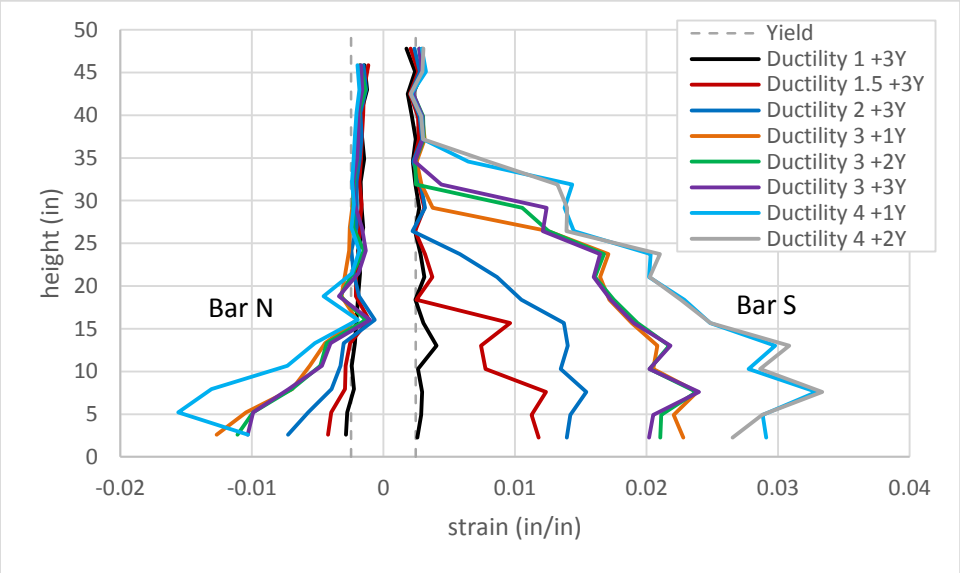

Figure 5-44. Test 2: Vertical Strain Profiles for Loading in the +Y-direction

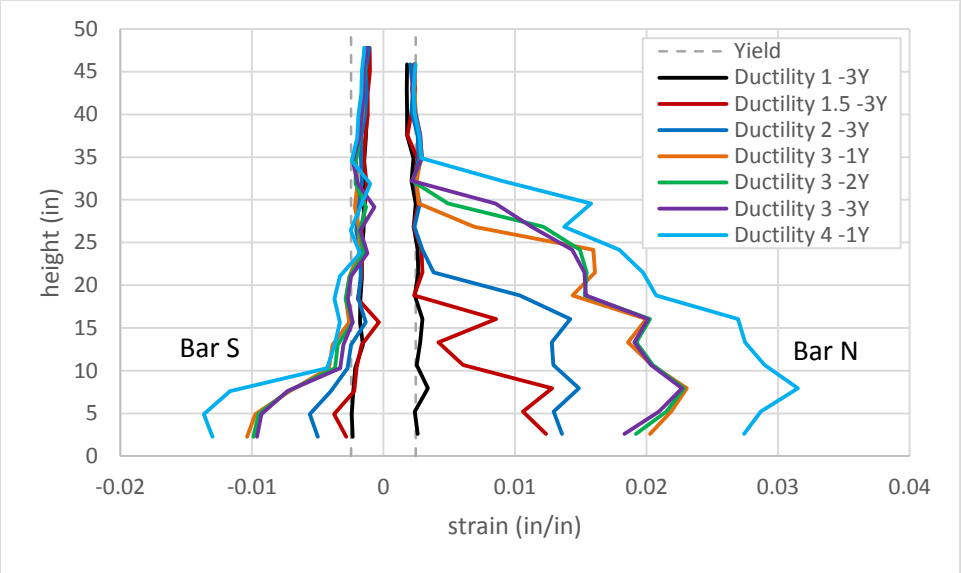

Figure 5-45. Test 2: Vertical Strain Profiles for Loading in the -Y-direction

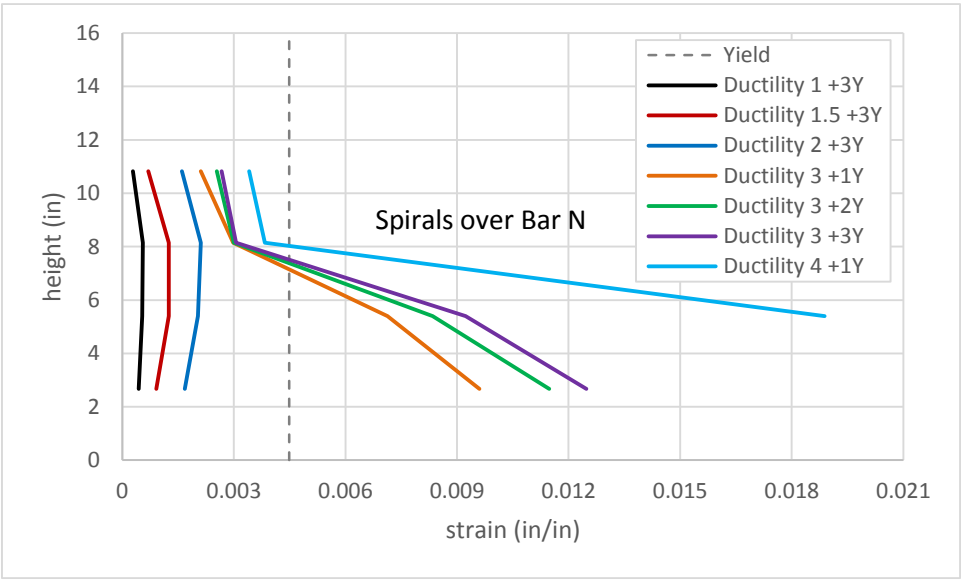

Figure 5-46. Test 2: Spiral Strains Measured Over the North Extreme Fiber Bar during +Y Cycles

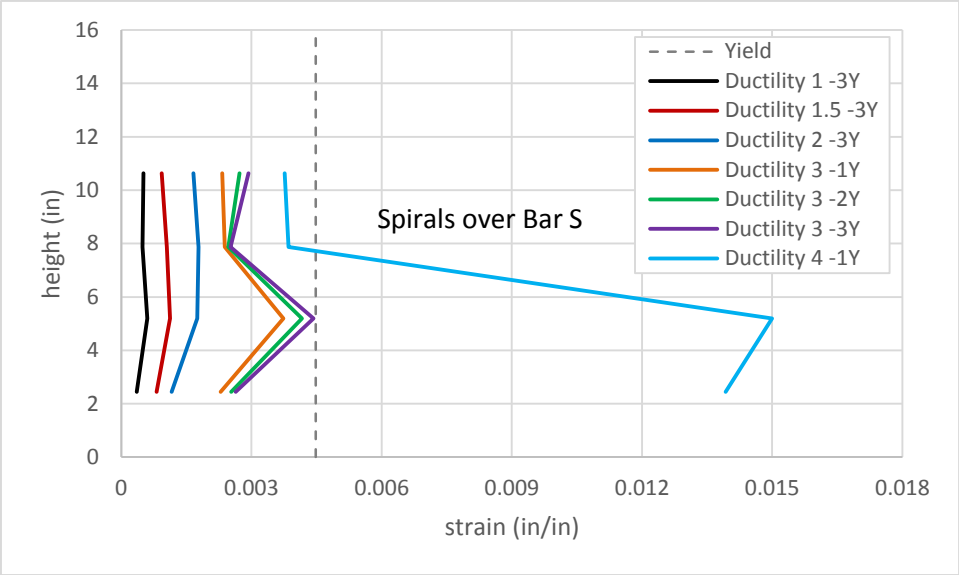

Figure 5-47. Test 2: Spiral Strains Measured Over the South Extreme Fiber Bar during -Y Cycles

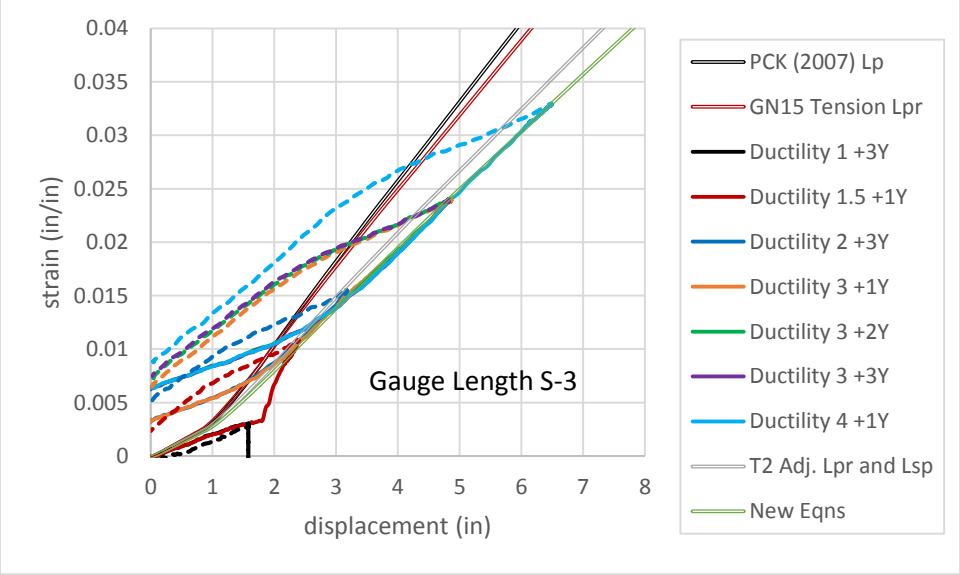

Figure 5-48. Test 2: Tension Strain-Disp. for Bar S (Gauge Length 3 Centered 7.60" above the Footing)

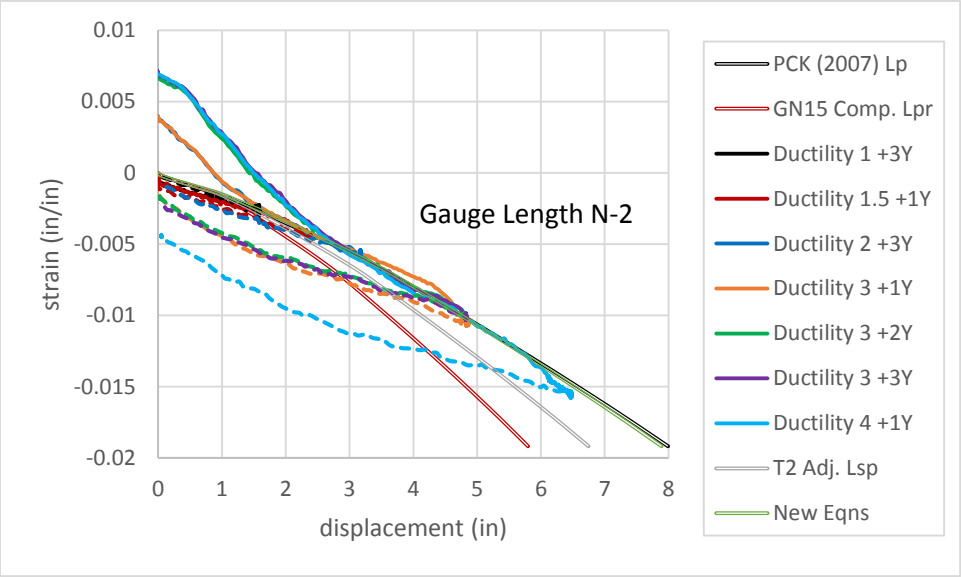

Figure 5-49. Test 2: Compression Strain-Disp. for Bar N (Gauge Length 2 Centered 5.23" above the Footing)

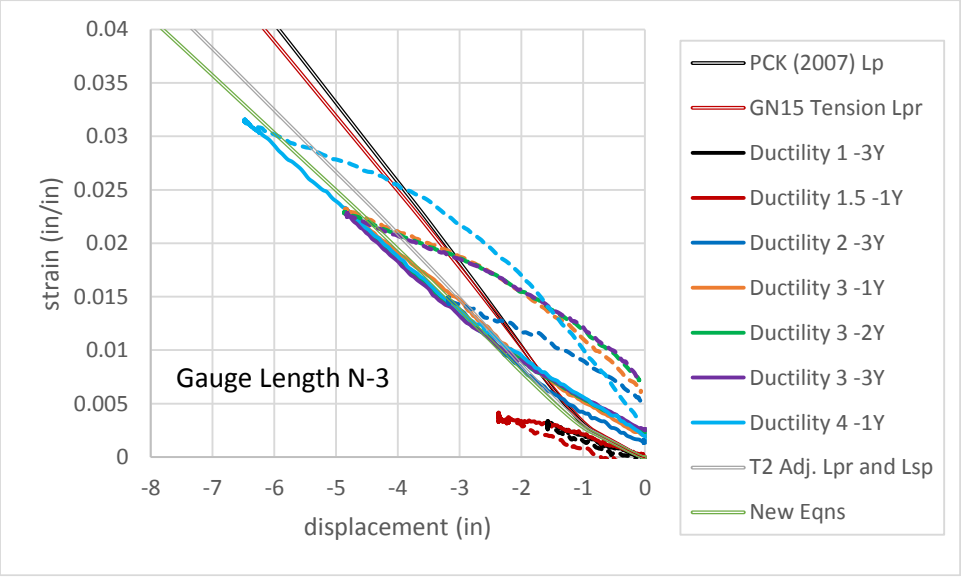

Figure 5-50. Test 2: Tension Strain-Disp. for Bar N (Gauge Length 3 Centered 7.95" above the Footing)

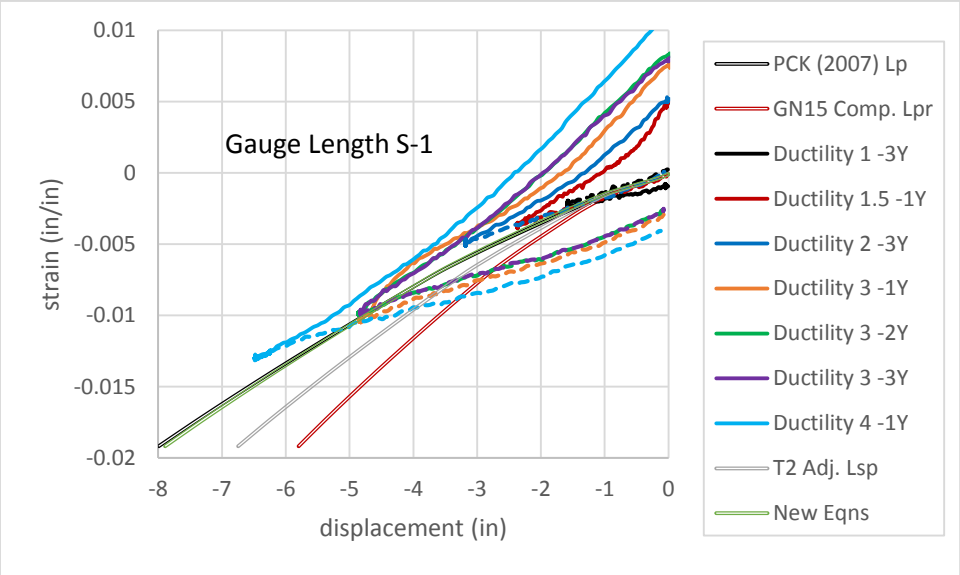

Figure 5-51. Test 2: Compression Strain-Disp. for Bar S (Gauge Length 1 Centered 2.28" above the Footing)

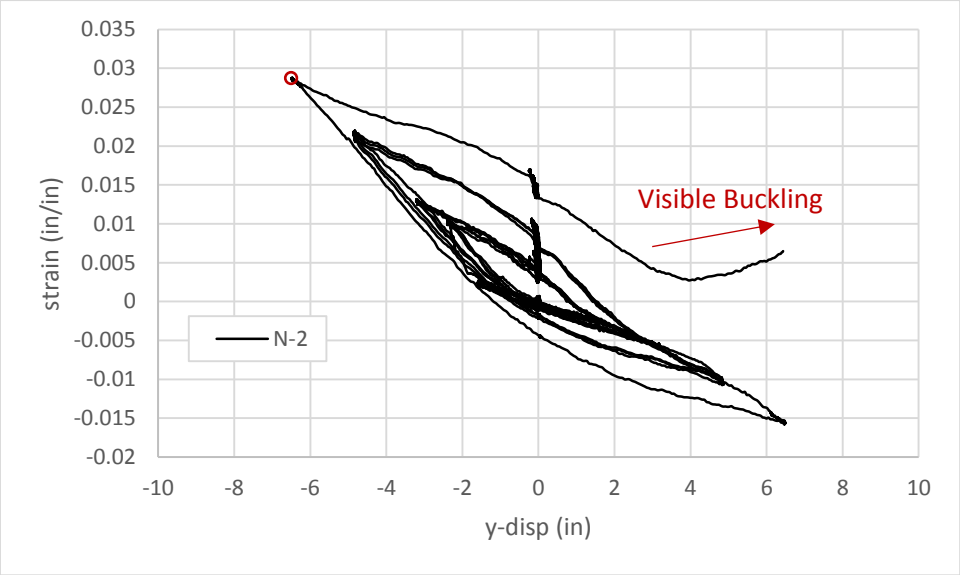

Figure 5-52. Test 2: Strain Hysteresis over the North Buckled Bar (Gauge Length 2 Centered 5.23" above the Footing)

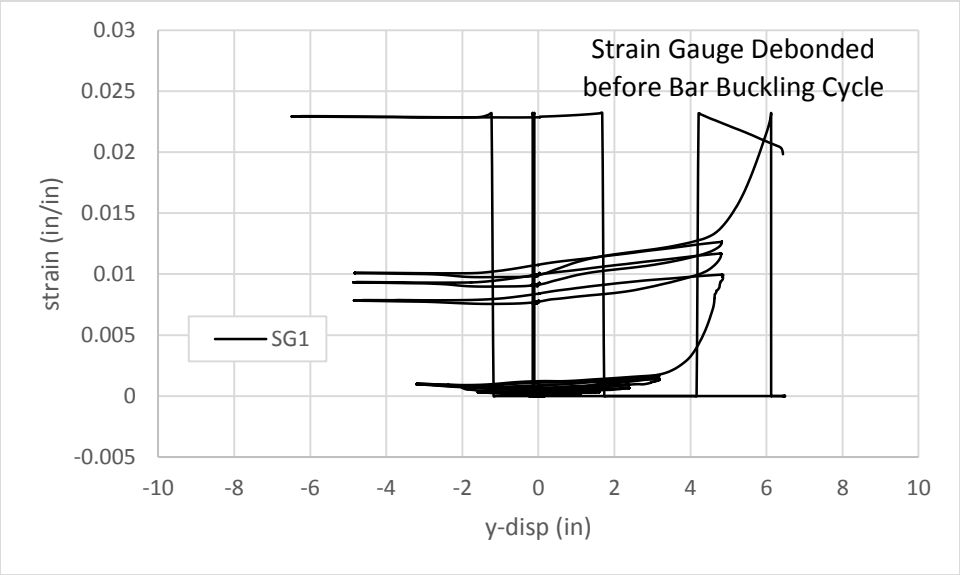

Figure 5-53. Test 2: North Spiral Strain Gauge Hysteresis for the First Layer above the Footing

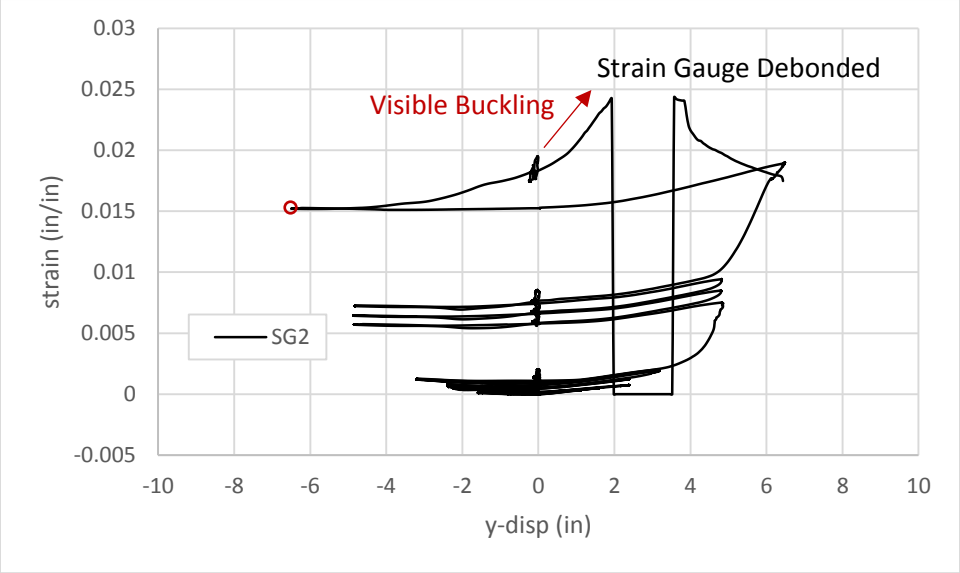

Figure 5-54. Test 2: North Spiral Strain Gauge Hysteresis for the Second Layer above the Footing

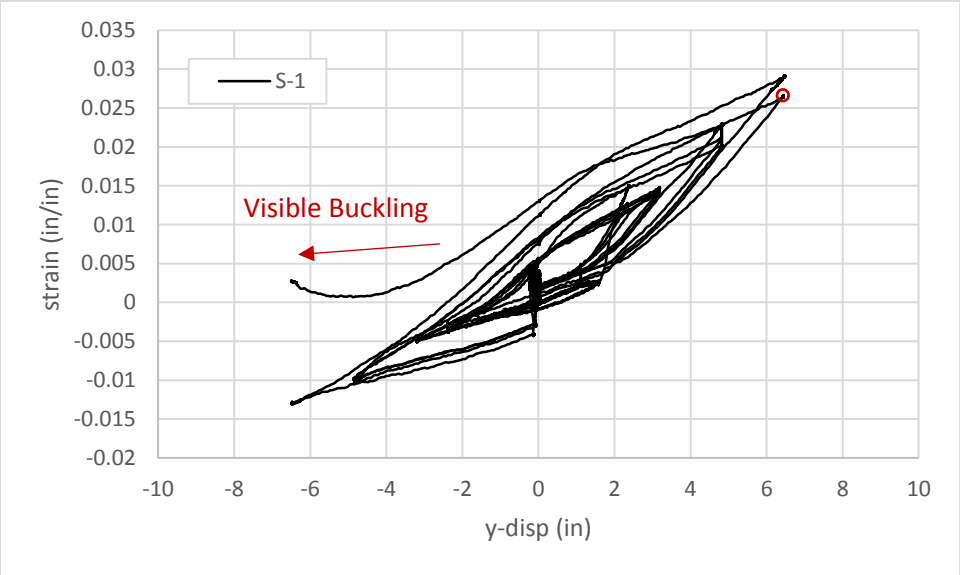

Figure 5-55. Test 2: Strain Hysteresis over the South Buckled Bar (Gauge Length 1 Centered 2.28" above the Footing)

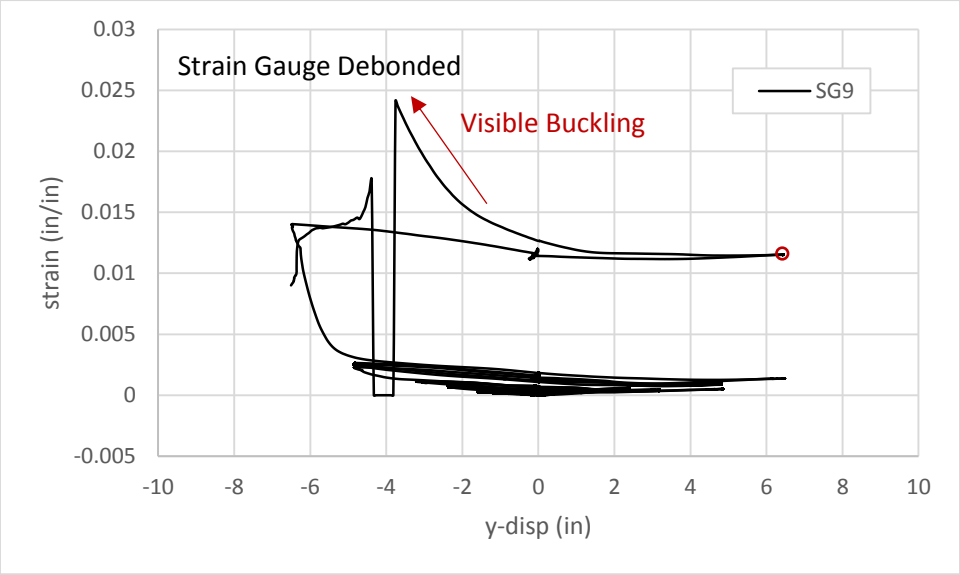

Figure 5-56. Test 2: South Spiral Strain Gauge Hysteresis for the First Layer above the Footing

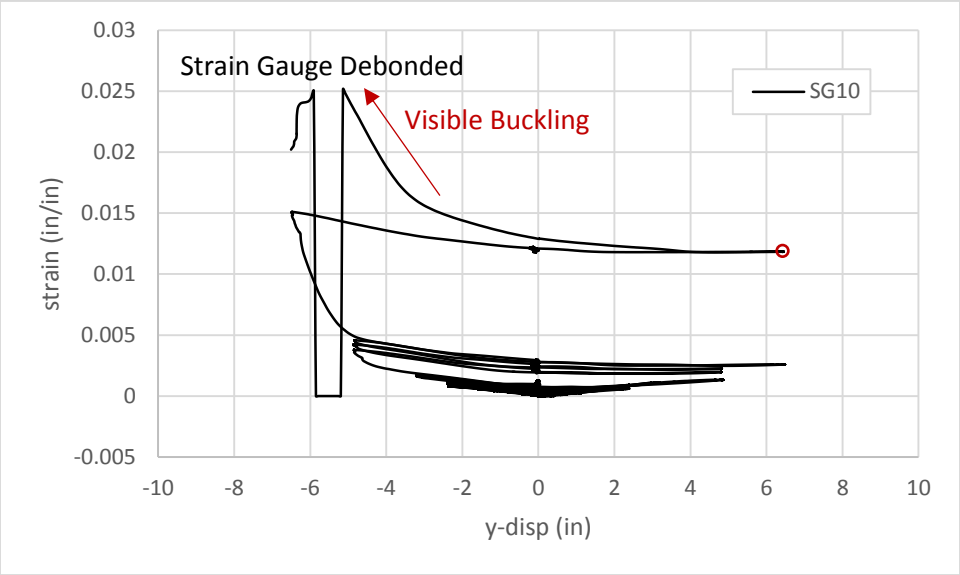

Figure 5-57. Test 2: South Spiral Strain Gauge Hysteresis for the Second Layer above the Footing

East and West Bar Strains

Vertical strain profiles for East and West reinforcement during x-direction cycles are shown in Figure 5-58 and Figure 5-59. Strains in the lowest four spiral layers during compressive x-direction cycles on the East and West sides of the specimen appear in Figure 5-60 and Figure 5-61. The relationship between strain and displacement for either peak tensile or peak compressive gauge lengths appear in Figure 5-62 through Figure 5-65. These figures contain monotonic moment curvature predictions for respective plastic hinge methods. PCK (2007) Lp refers to the (Priestley, Calvi and Kowalsky 2007) plastic hinge method, GN15 Tension/Compression Lpr refers to the (Goodnight, Kowalsky and Nau 2015a) unidirectional modified plastic hinge method, TX Adjusted Lpr and Lsp refer to using the measured extent of plasticity and average equivalent strain penetration length from this specific test, and New Equations refers to a new bidirectional plastic hinge method which was created based on this study. Details of the new plastic hinge method appear in a later chapter of this report.

The spiral strain gauge hysteresis for the first and second layers above the footing on the East side of the specimen appear in Figure 5-67 and Figure 5-68. Both spiral layers go off scale during $\mu_{\Delta 4}^{+3x} = 6.43$" as the E and ESE bars buckled, see Figure 5-40. The visual observation of bar buckling was confirmed upon inspection of the East longitudinal bar strain hysteresis in Figure 5-66.

The spiral strain gauge hysteresis for the first and second layers above the footing on the West side of the specimen appear in Figure 5-70 and Figure 5-71. Both spiral layers go off scale during $\mu_{\Delta 4}^{-2x} = -6.48$" as the West extreme fiber bar W buckled. The visual observation of bar buckling was confirmed upon inspection of the West longitudinal bar strain hysteresis in Figure 5-69.

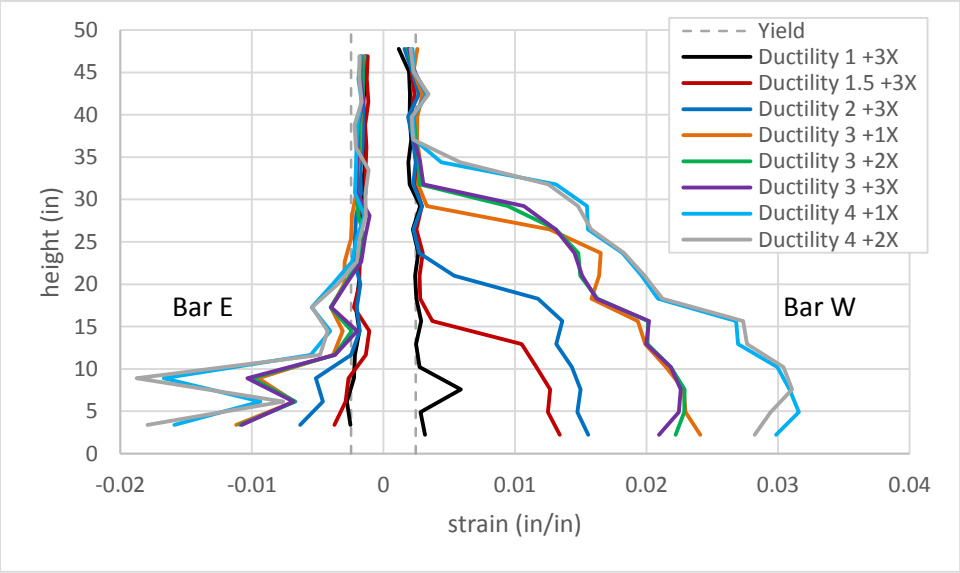

Figure 5-58. Test 2: Vertical Strain Profiles for Loading in the +X-direction

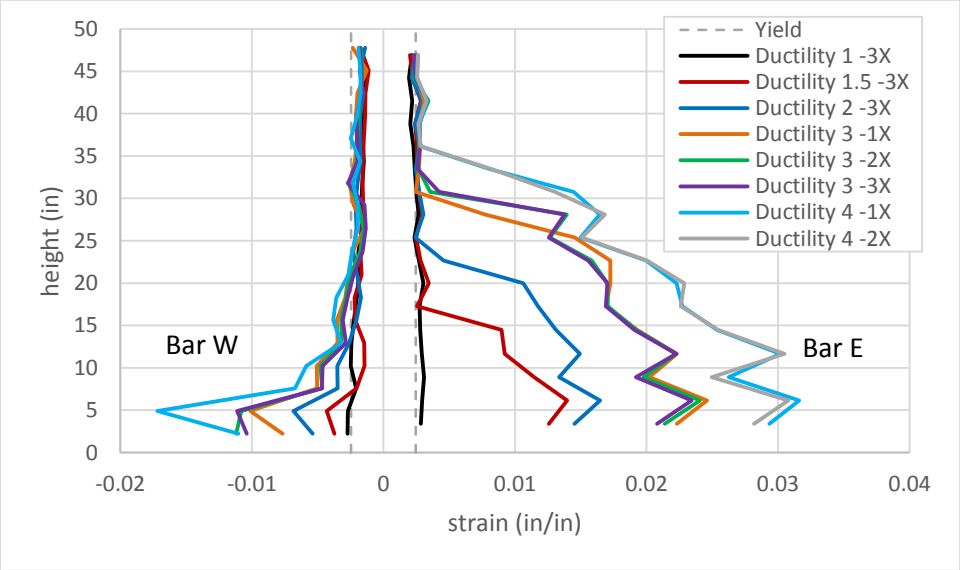

Figure 5-59. Test 2: Vertical Strain Profiles for Loading in the -X-direction

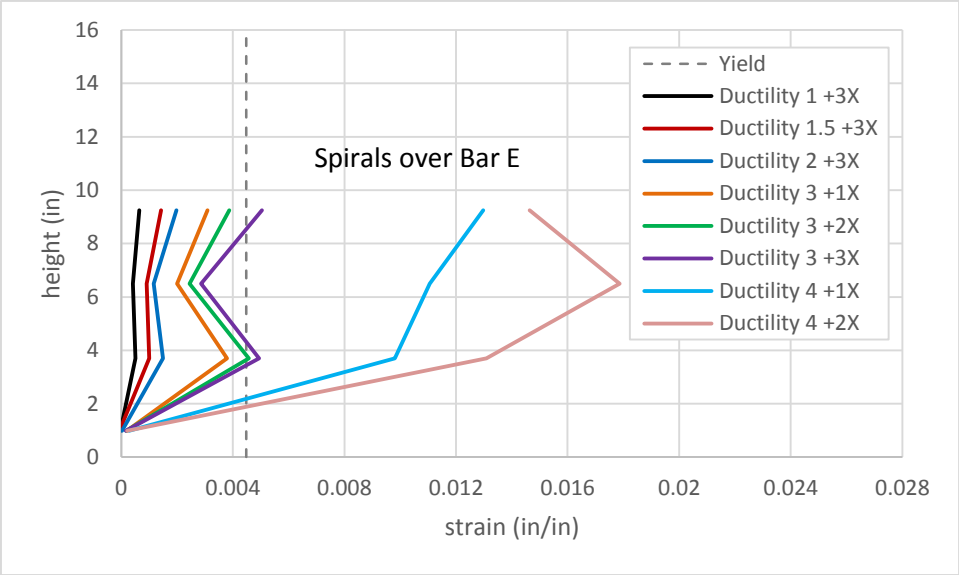

Figure 5-60. Test 2: Spiral Strains Measured Over the East Extreme Fiber Bar during +X Cycles

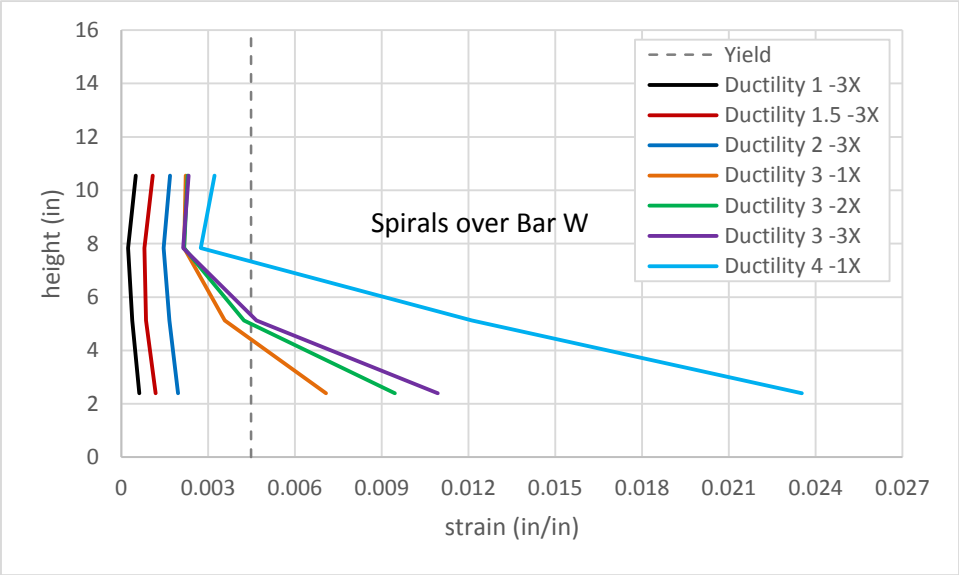

Figure 5-61. Test 2: Spiral Strains Measured Over the West Extreme Fiber Bar during -X Cycles

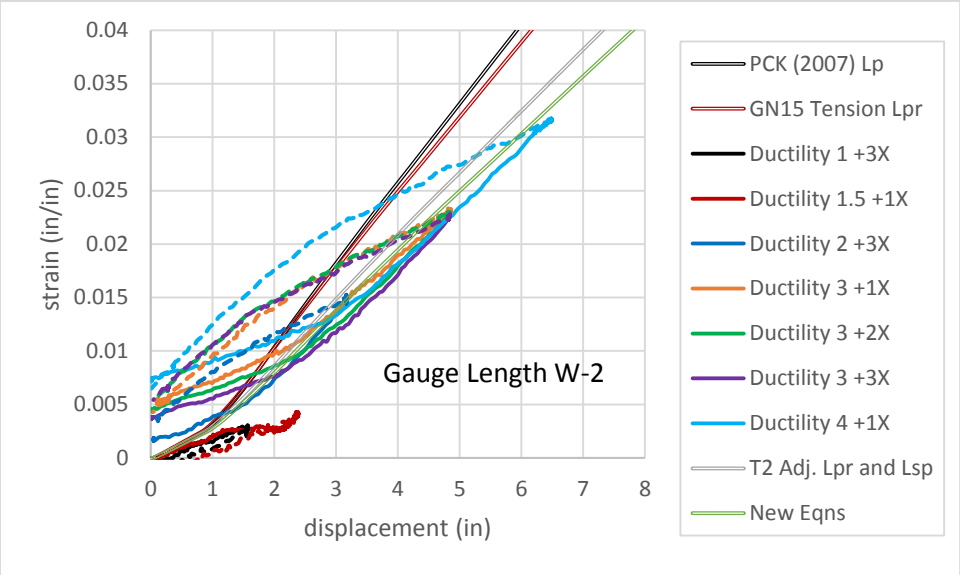

Figure 5-62. Test 2: Tension Strain-Disp. for Bar W (Gauge Length 2 Centered 4.90" above the Footing)

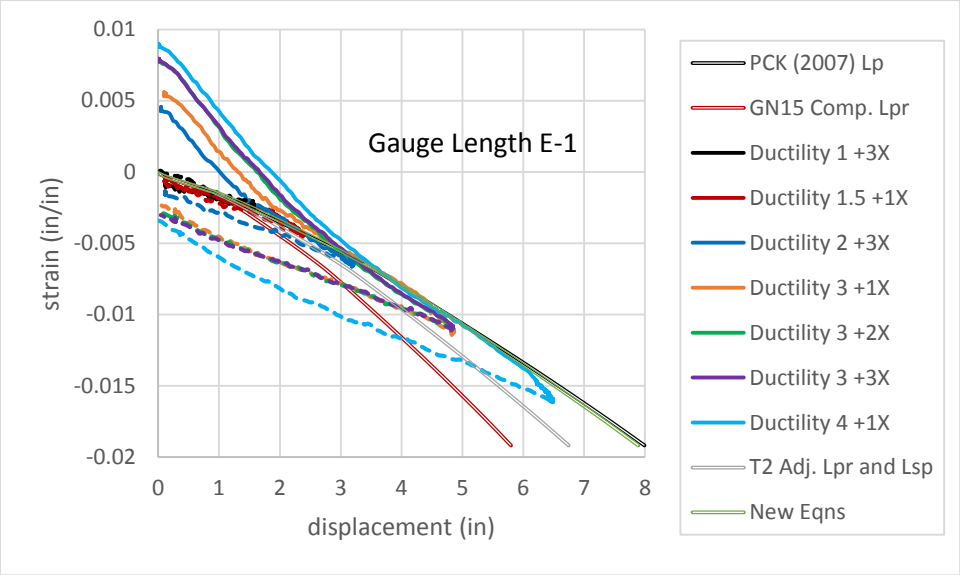

Figure 5-63. Test 2: Compression Strain-Disp. for Bar E (Gauge Length 1 Centered 3.38" above the Footing)

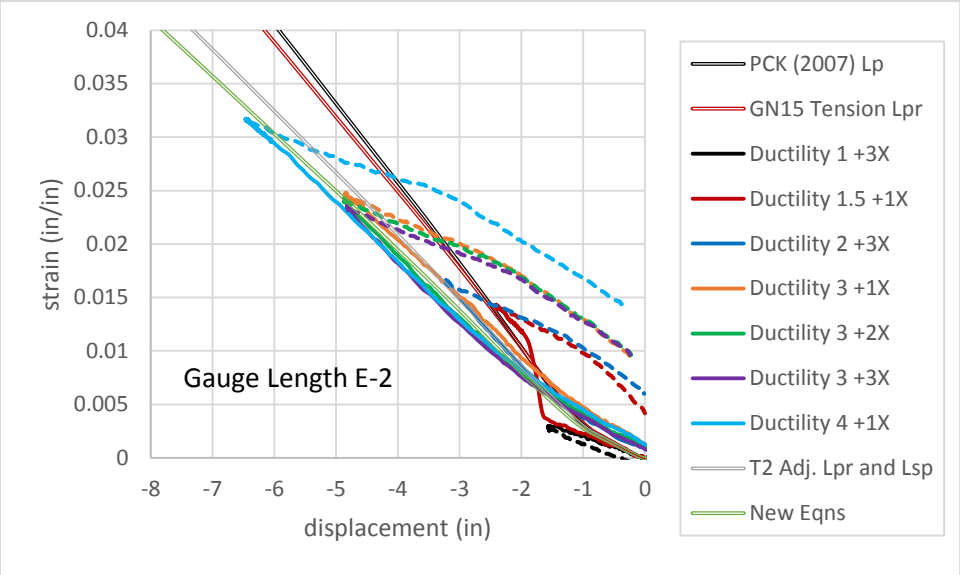

Figure 5-64. Test 2: Tension Strain-Disp. for Bar E (Gauge Length 2 Centered 6.15" above the Footing)

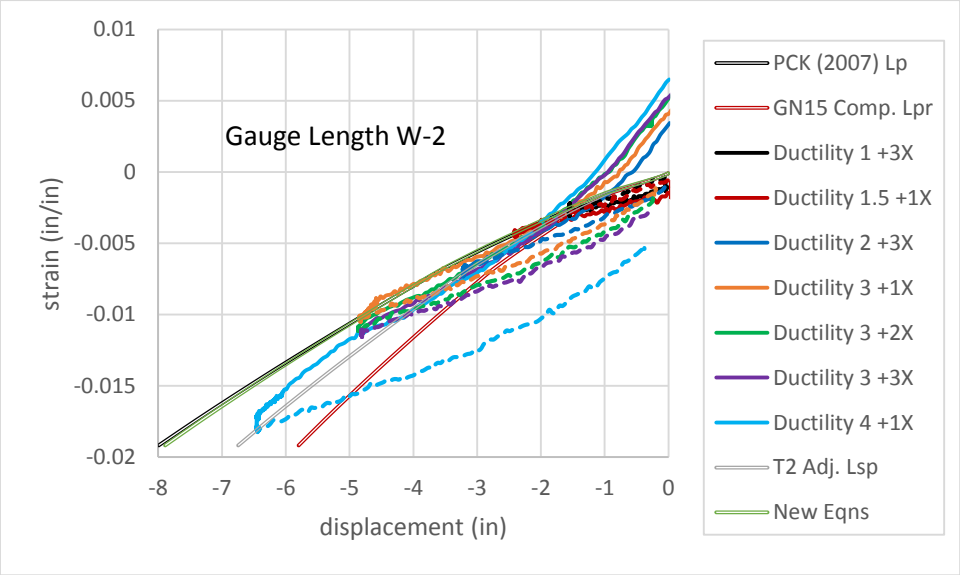

Figure 5-65. Test 2: Compression Strain-Disp. for Bar W (Gauge Length 2 Centered 4.90" above the Footing)

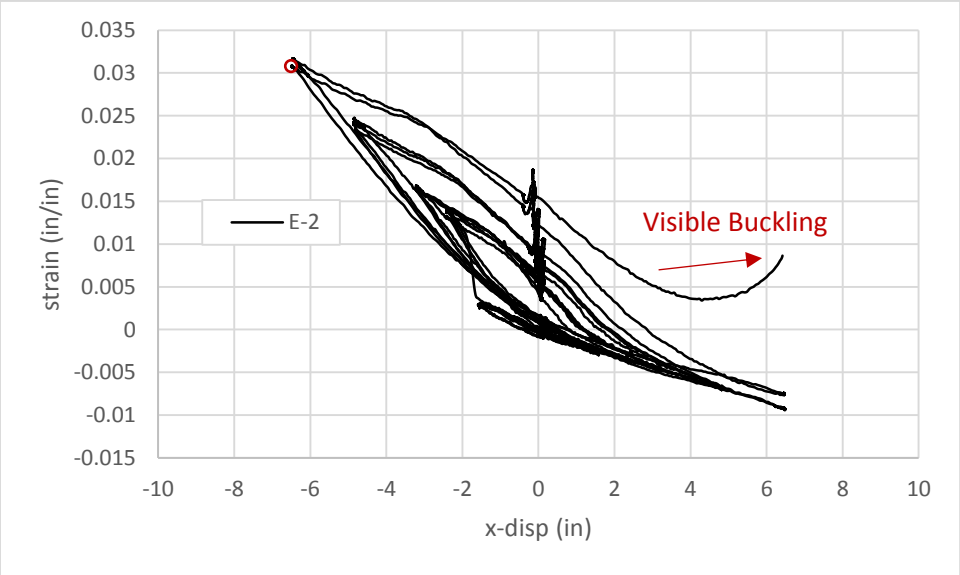

Figure 5-66. Test 2: Strain Hysteresis over the East Buckled Bar (Gauge Length 2 Centered 6.15" above the Footing)

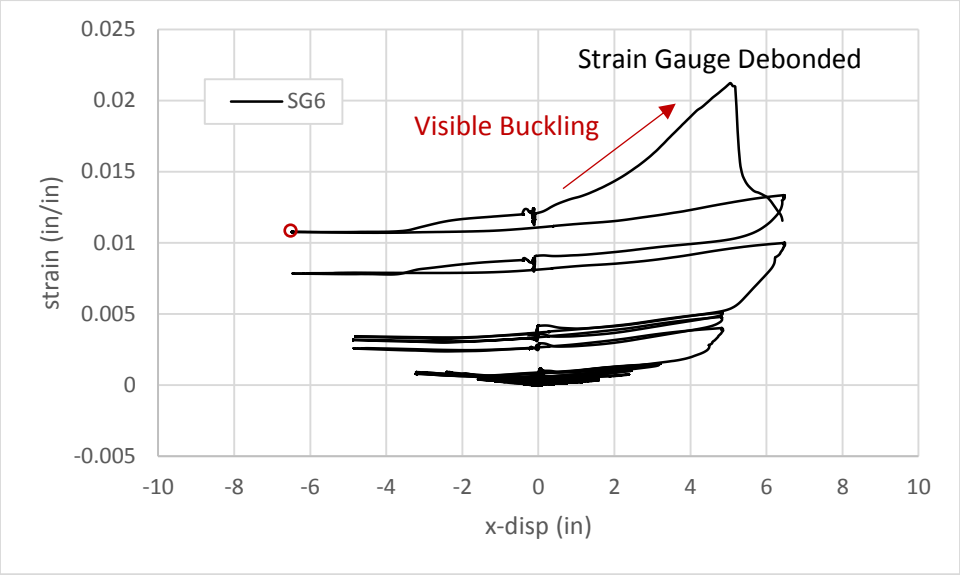

Figure 5-67. Test 2: East Spiral Strain Gauge Hysteresis for the Second Layer above the Footing

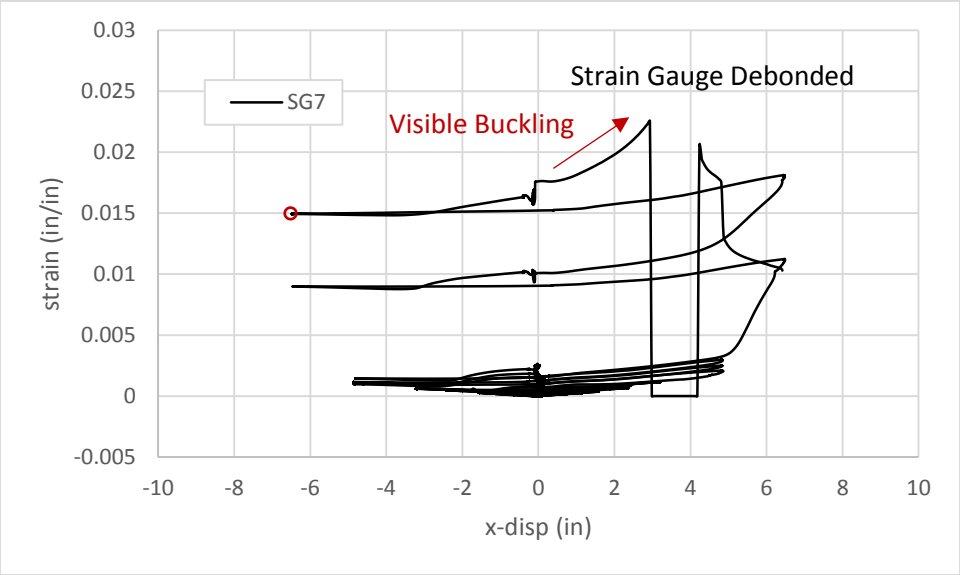

Figure 5-68. Test 2: East Spiral Strain Gauge Hysteresis for the Third Layer above the Footing

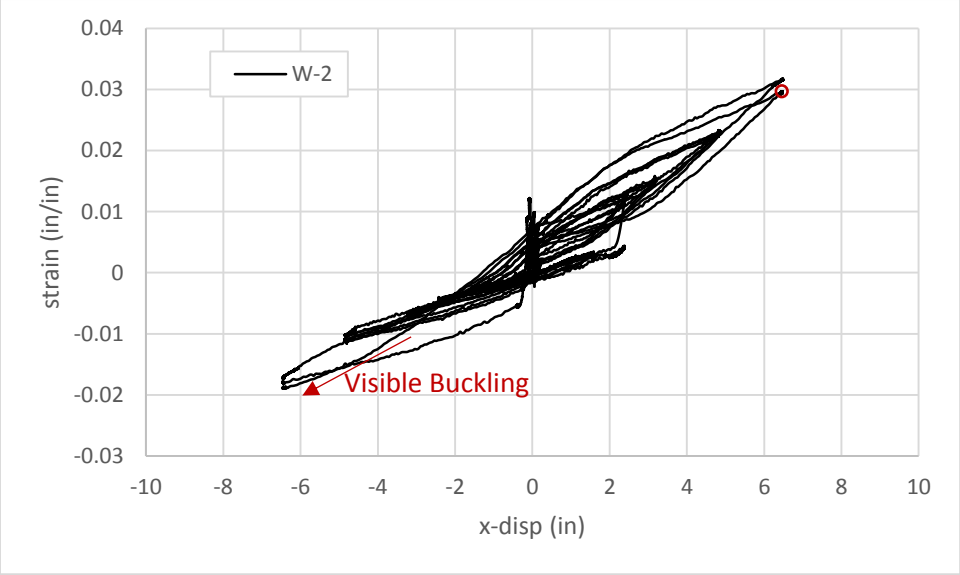

Figure 5-69. Test 2: Strain Hysteresis over the West Buckled Bar (Gauge Length 2 Centered 4.90" above the Footing)

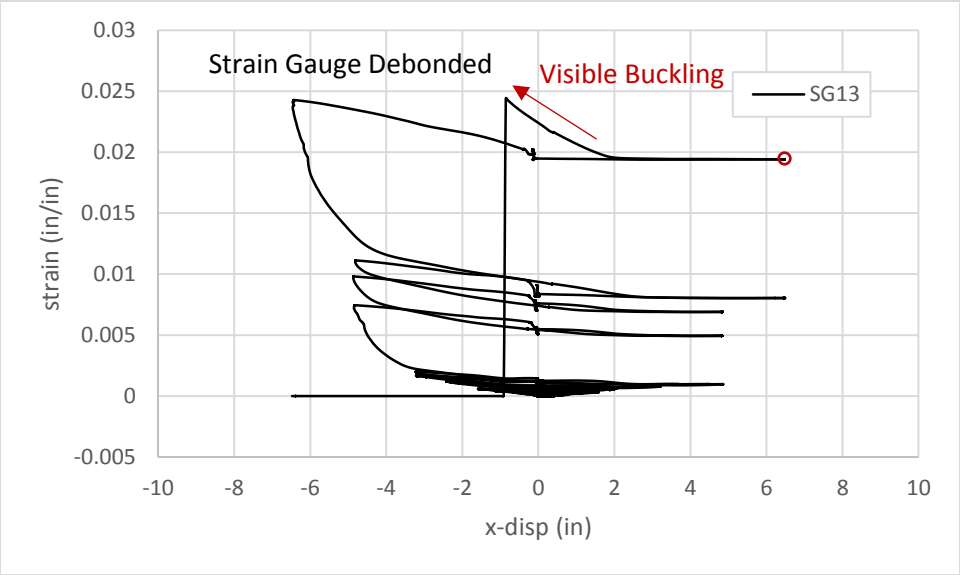

Figure 5-70. Test 2: West Spiral Strain Gauge Hysteresis for the First Layer above the Footing

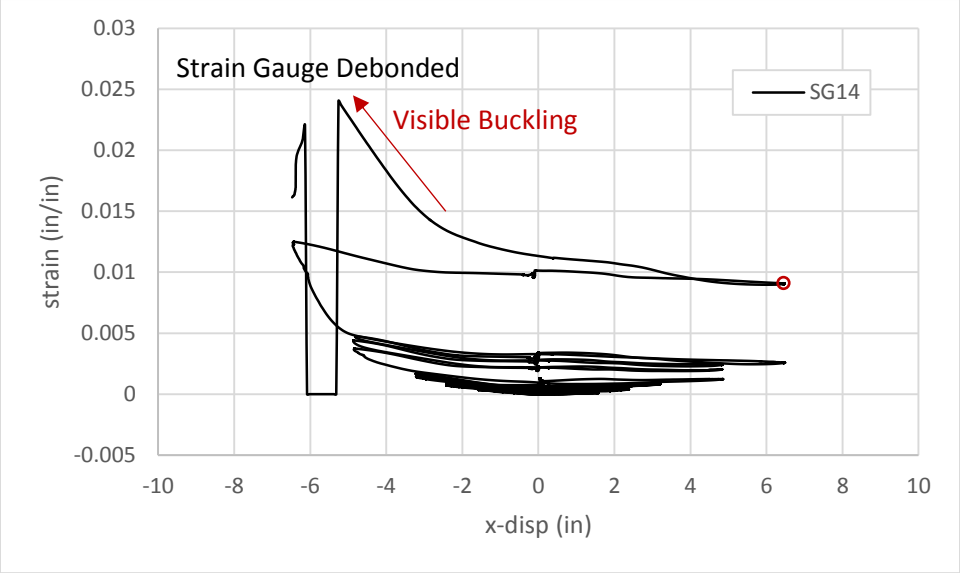

Figure 5-71. Test 2: West Spiral Strain Gauge Hysteresis for the Second Layer above the Footing

Test 2 - Curvature and Strain Penetration Data

Curvature and stain penetration data for Test 2 is presented in the following section. The methods in which this data was generated are outlined in the summary for Test 1. Sample cross section curvature profiles are shown in Figure 5-72 and Figure 5-73. Vertical curvature profiles for respective loading directions appear in Figure 5-74 through Figure 5-78. Fixed-end rotations attributable to strain penetration of longitudinal reinforcement into the footing are shown in Figure 5-79 through Figure 5-81. Comparison of the measured displacements to those obtained via integration of the measured curvature profiles and extrapolation of the fixed-end rotation to the center of the applied lateral load are shown in Figure 5-82 and Figure 5-83.

The measured extent of plasticity is compared to design recommendations for the tensile triangular plastic hinge length in Figure 5-84. GN15 refers to the (Goodnight, Kowalsky and Nau 2015a) unidirectional tensile hinge length while New Equations refers to a new bidirectional plastic hinge method which was created based on this study. Details of the new plastic hinge method appear in a later chapter of this report. The measured equivalent strain penetration lengths are compared to design recommendations in Figure 5-85. GN15 refers to the (Goodnight, Kowalsky and Nau 2015a) unidirectional Lsp while PCK (2007) refers to the (Priestley, Calvi and Kowalsky 2007) definition of Lsp. Finally, the measured hysteretic response is compared to monotonic predictions in Figure 5-86 through Figure 5-89. The larger elastic displacements are not observed when sectional response

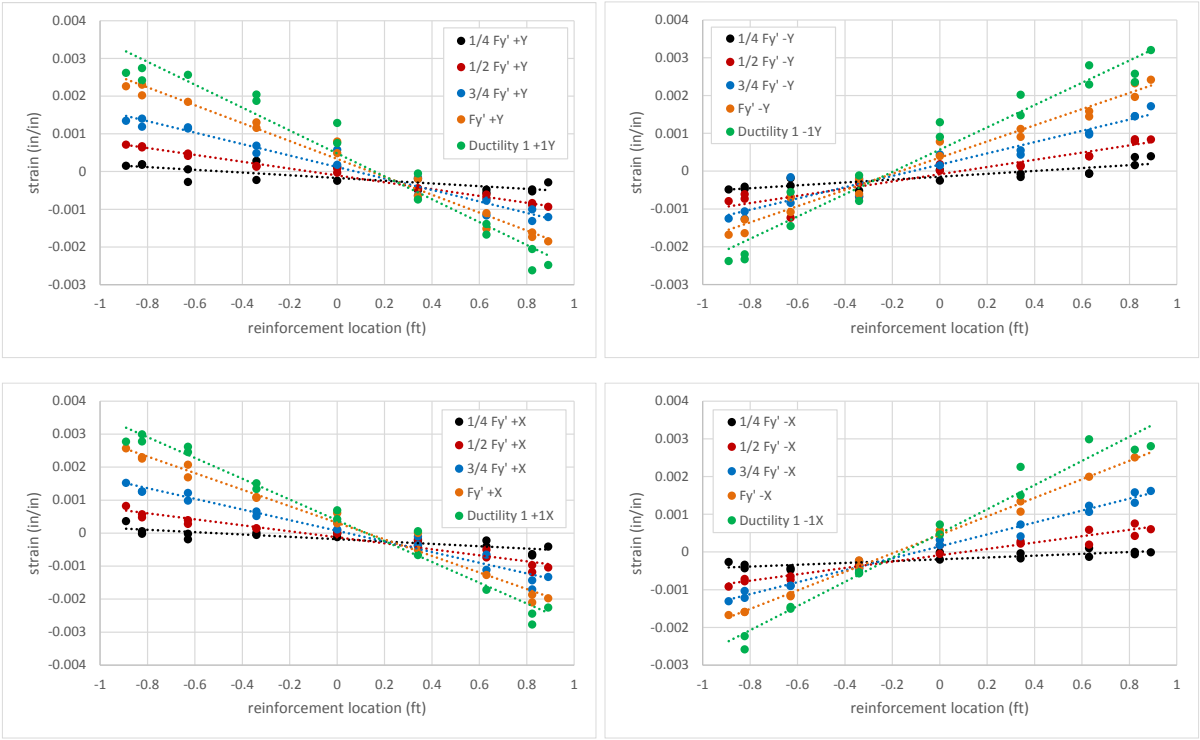

Figure 5-72. Test 2: Elastic Curvature Profiles for the First Instrumented Section above the Footing

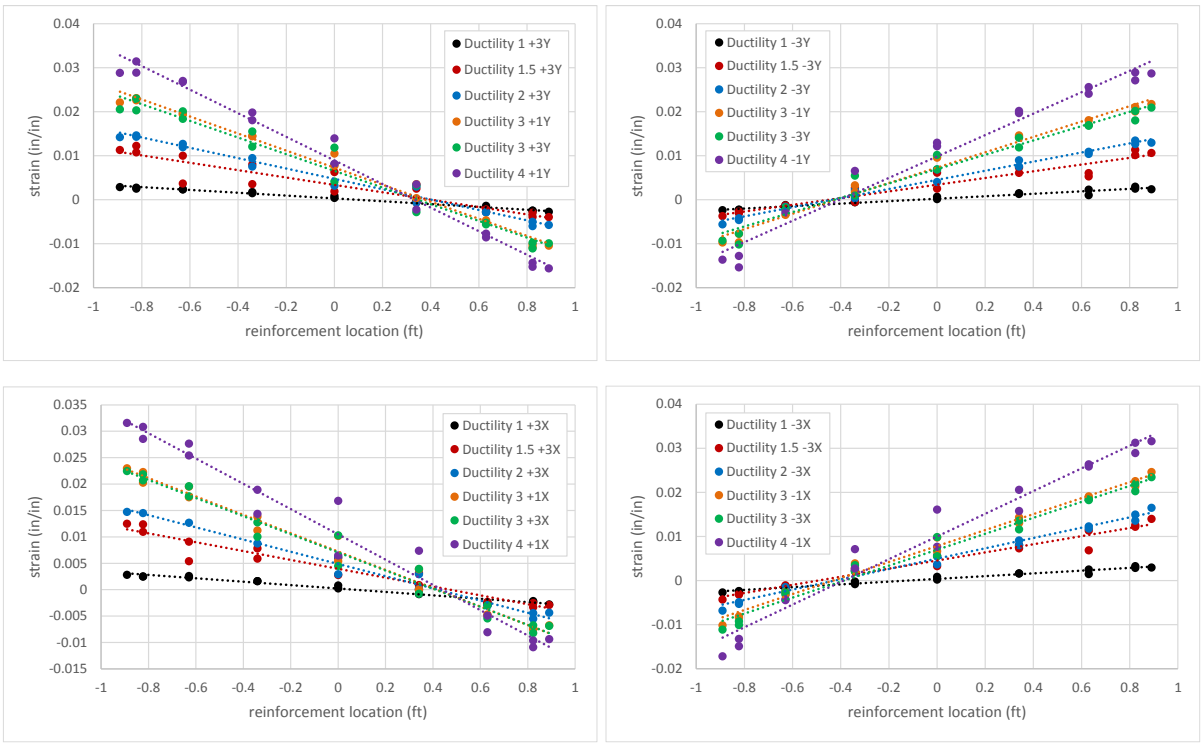

Figure 5-73. Test 2: Curvature Profiles for the Second Instrumented Section above the Footing

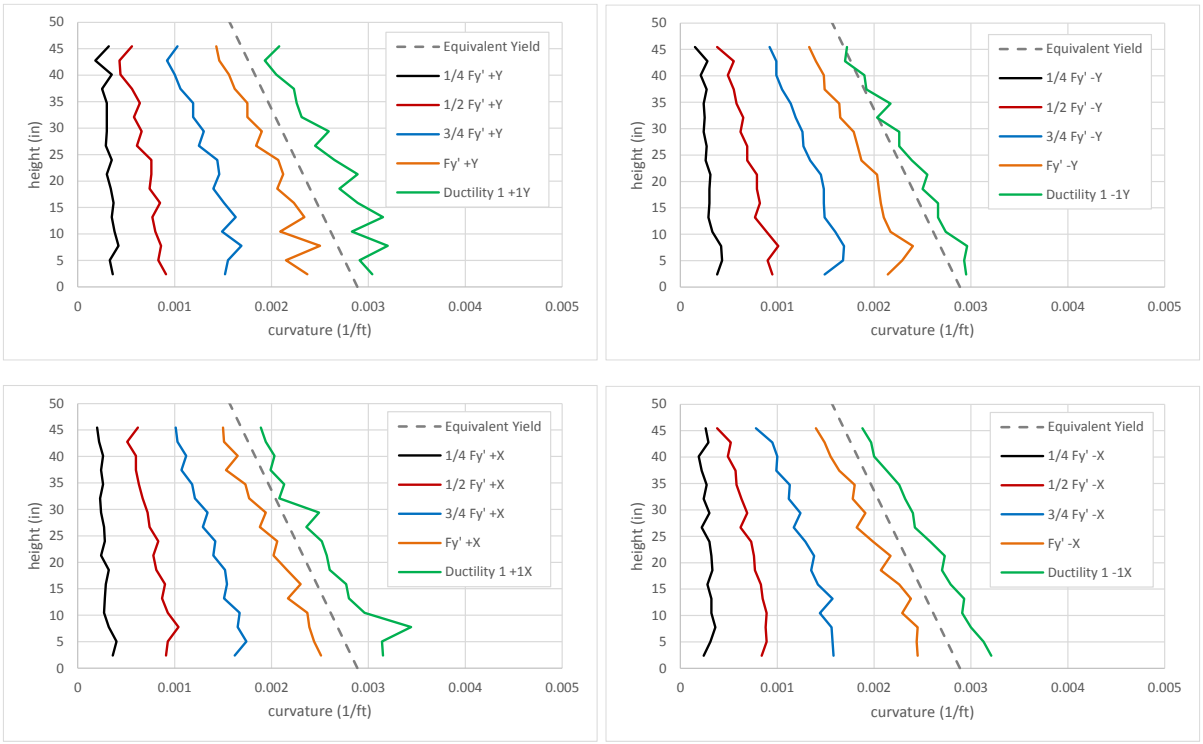

Figure 5-74. Test 2: Elastic Vertical Curvature Profiles

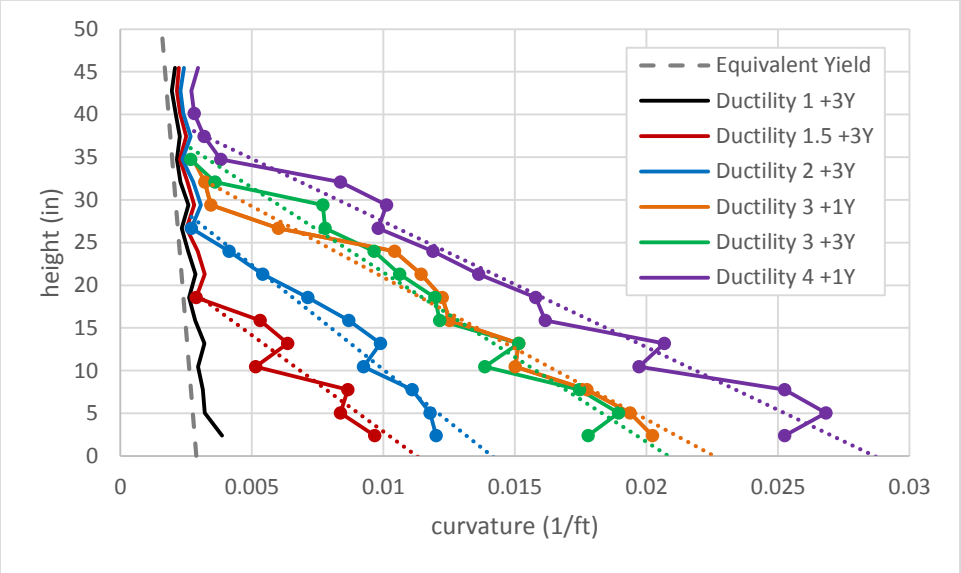

Figure 5-75. Test 2: Vertical Curvature Profiles for Loading in the +Y-direction

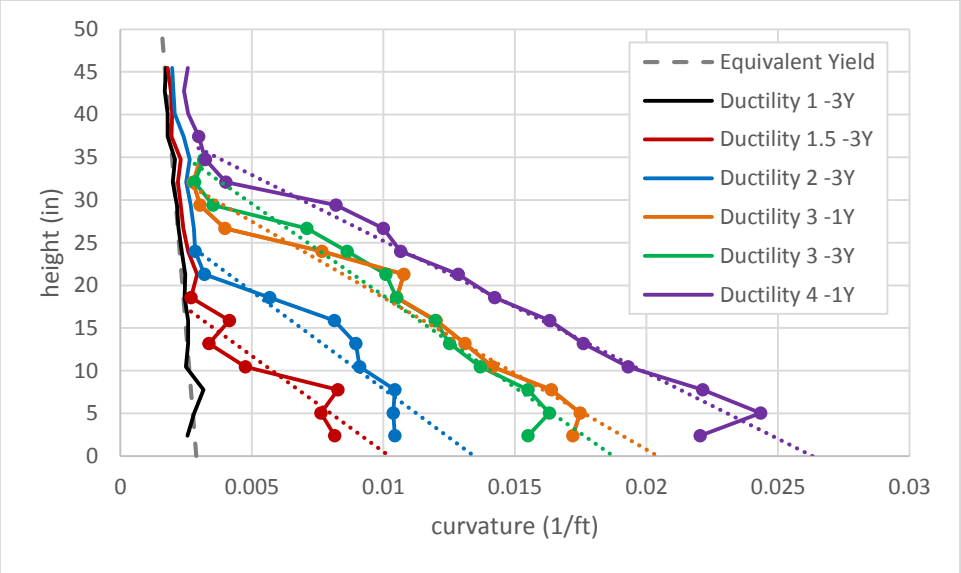

Figure 5-76. Test 2: Vertical Curvature Profiles for Loading in the -Y-direction

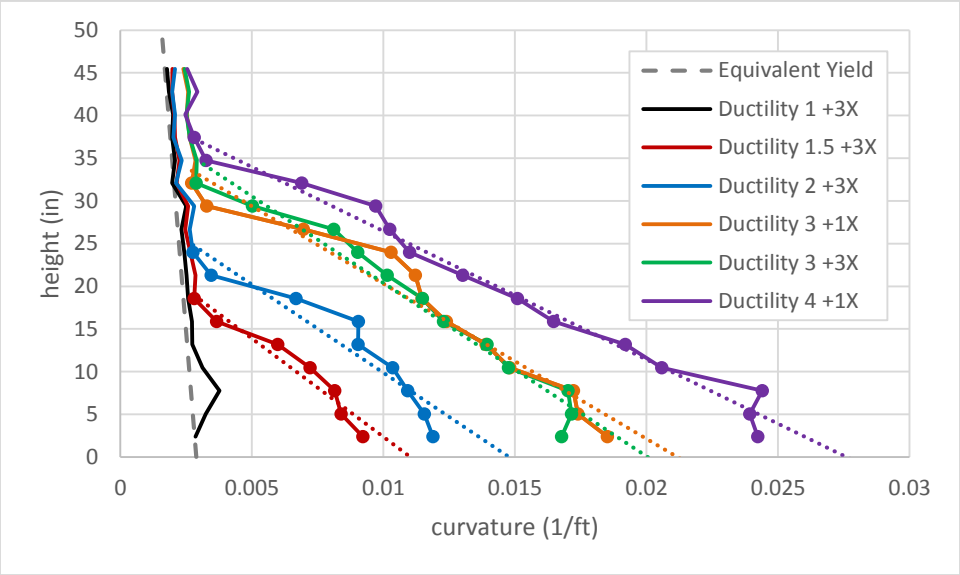

Figure 5-77. Test 2: Vertical Curvature Profiles for Loading in the +X-direction

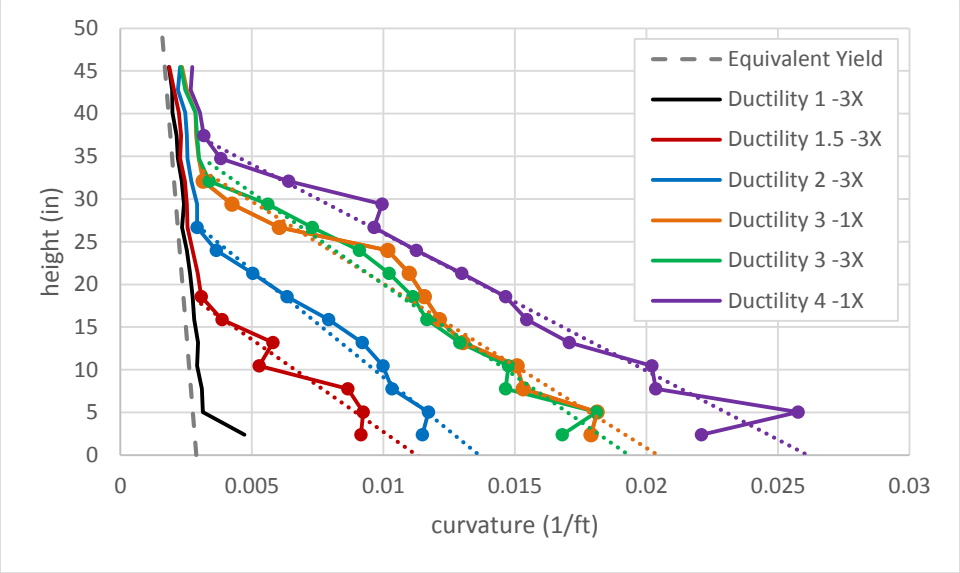

Figure 5-78. Test 2: Vertical Curvature Profiles for Loading in the -X-direction

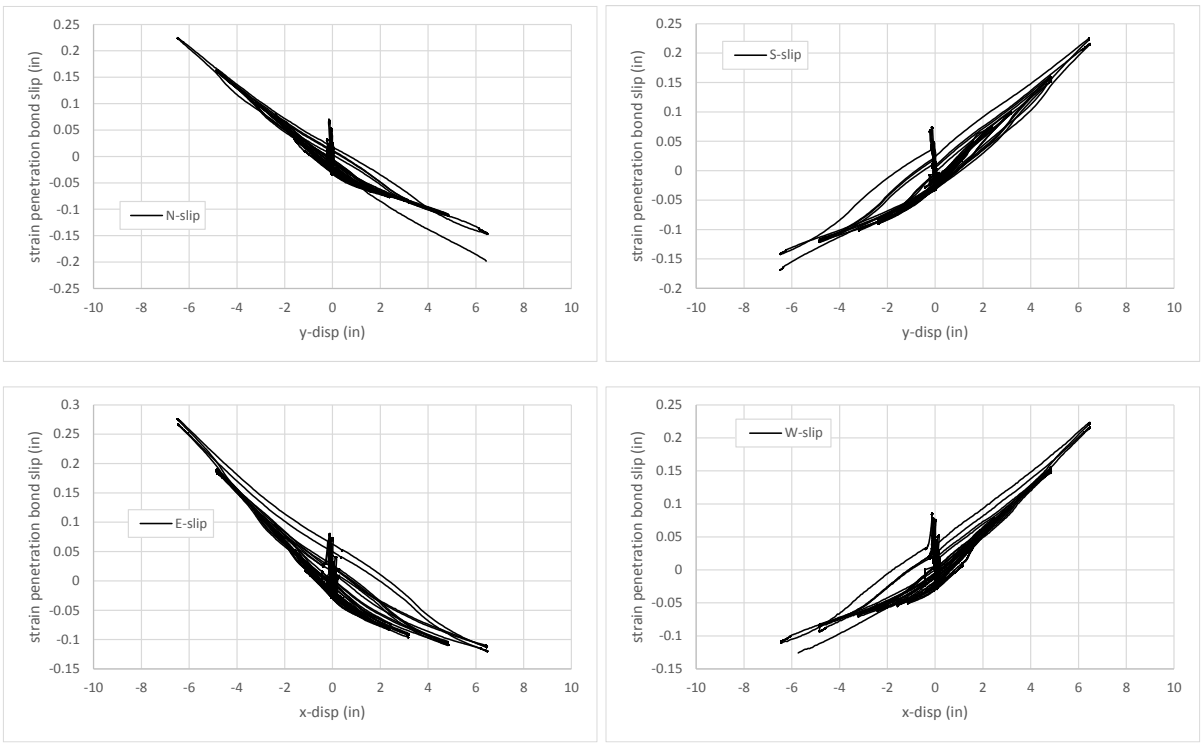

Figure 5-79. Test 2: Extreme Fiber Bar Strain Penetration Bond Slip Hysteresis

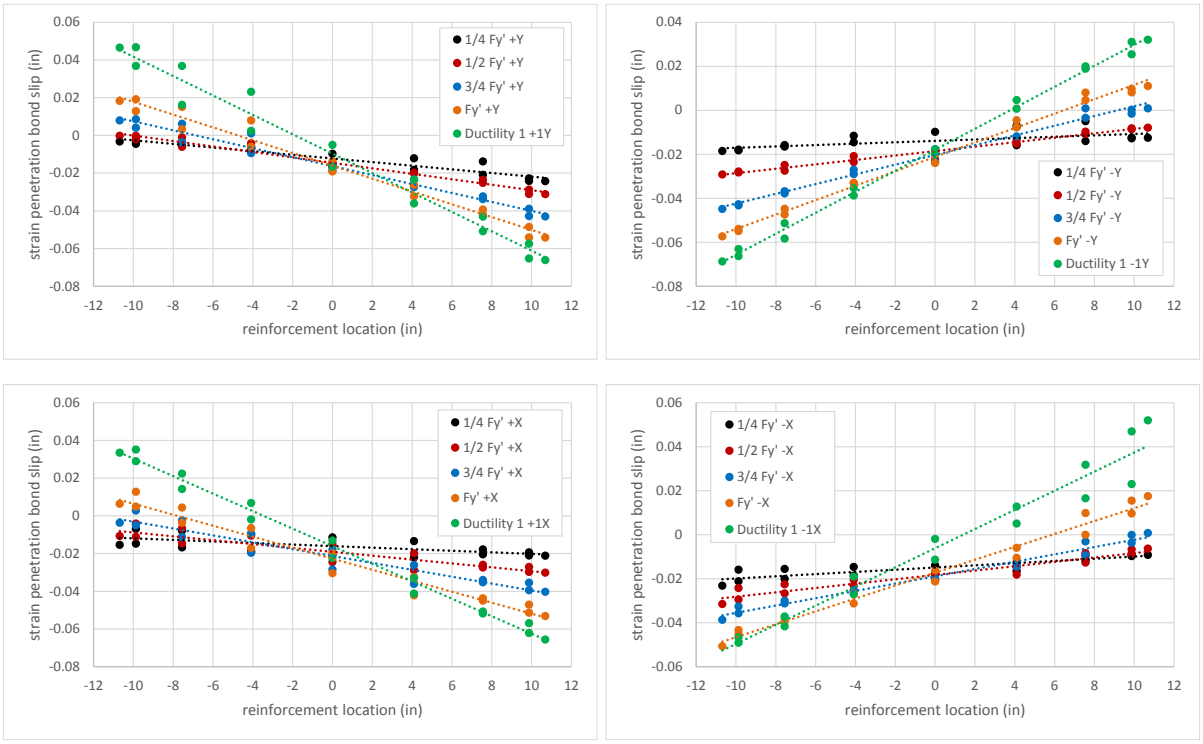

Figure 5-80. Test 2: Fixed End Rotations due to Strain Penetration during the Elastic Cycles

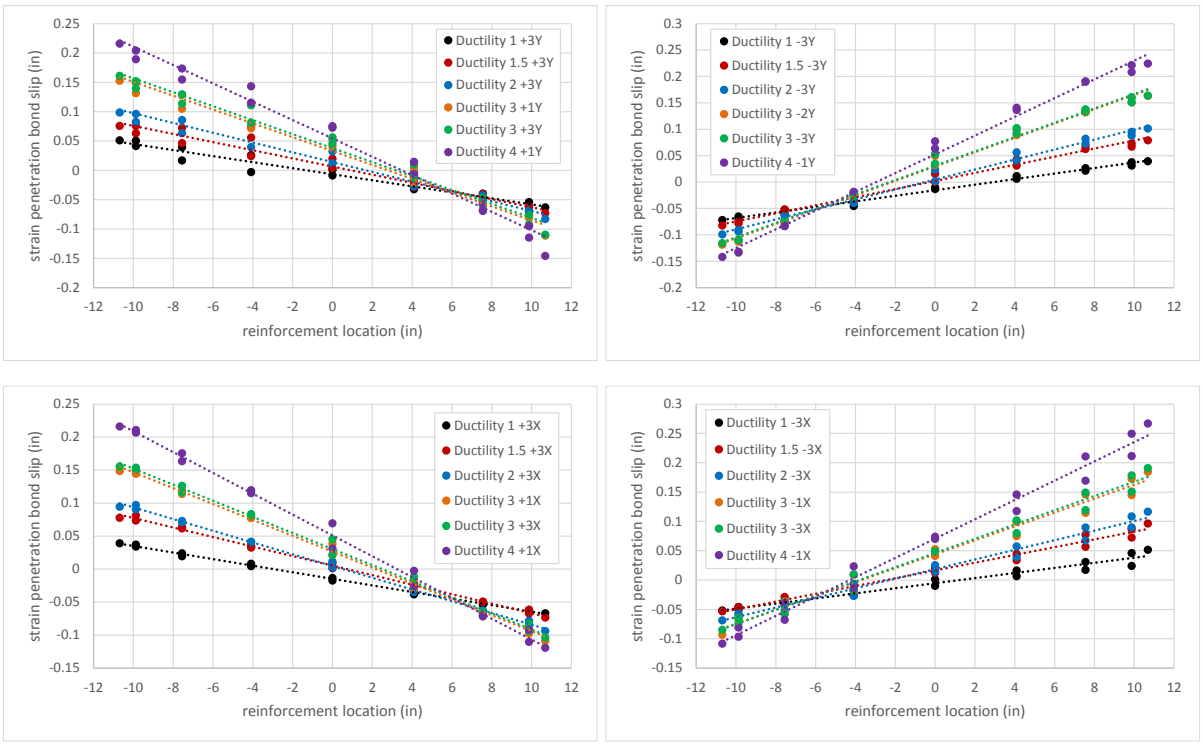

Figure 5-81. Test 2: Fixed-End Rotations due to Strain Penetration

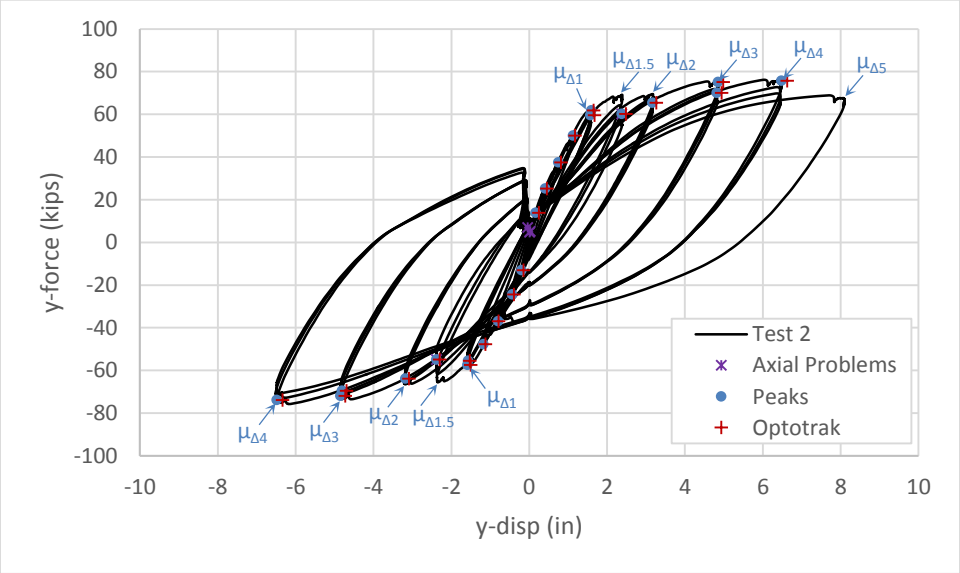

Figure 5-82. Test 2: Optotrak Integrated Flexural Disp. Compared to Measured String Pot. Disp.

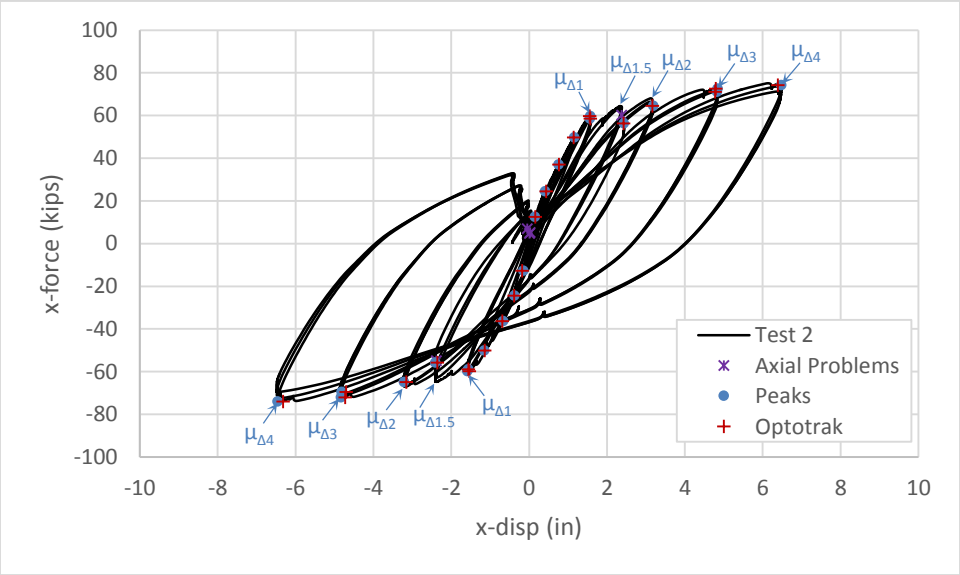

Figure 5-83. Test 2: Optotrak Integrated Flexural Disp. Compared to Measured String Pot. Disp.

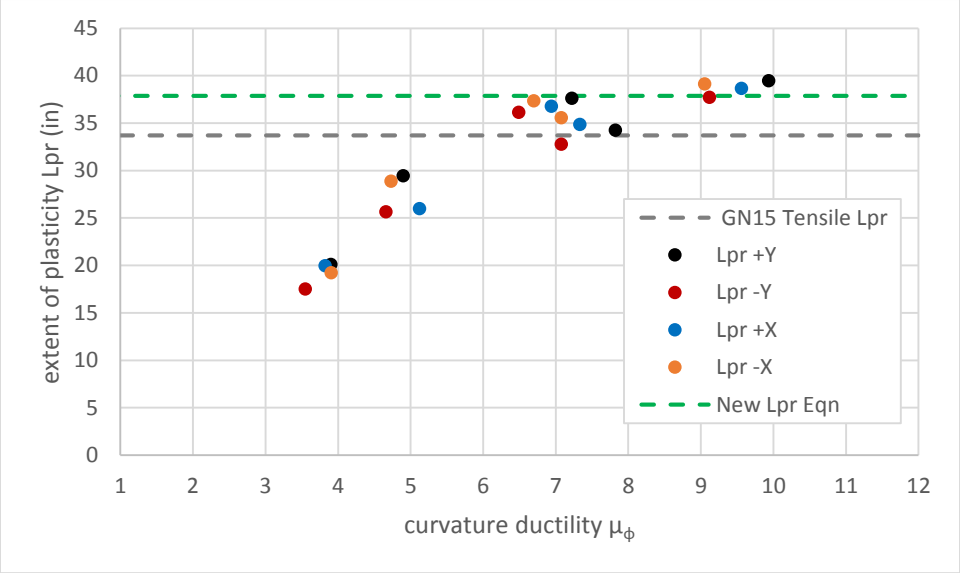

Figure 5-84. Test 2: Measured Extent of Plasticity Compared to Tensile Hinge Lengths

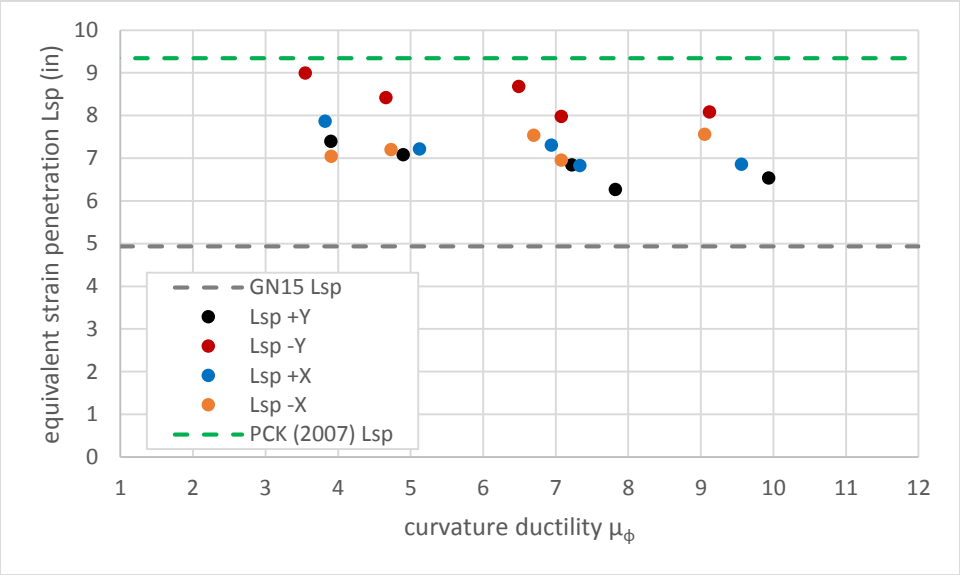

Figure 5-85. Test 2: Measured Equivalent Strain Penetration Lengths Compared to Design Expressions

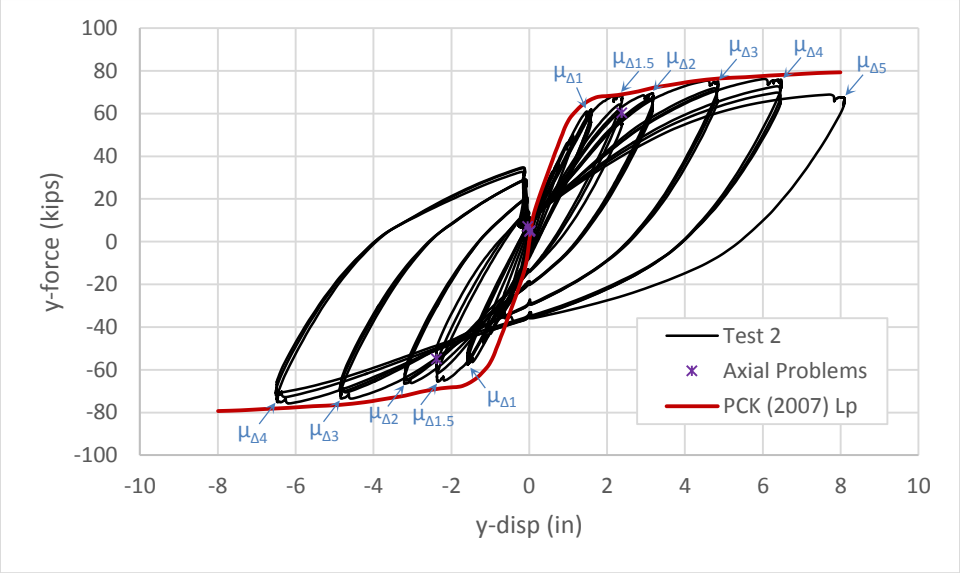

Figure 5-86. Test 2: Y-Direction Hysteretic Response Compared to PCK (2007) Hinge Length Monotonic Prediction

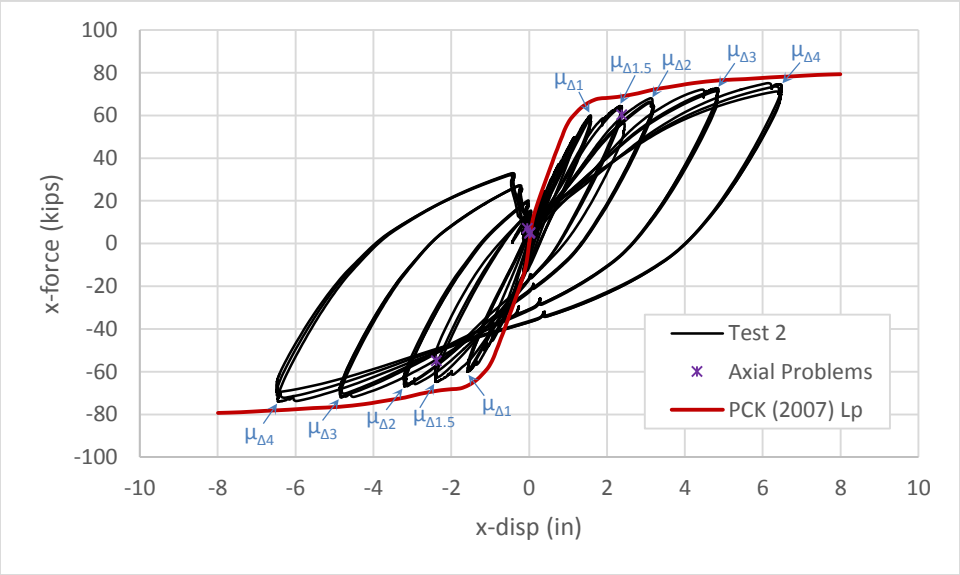

Figure 5-87. Test 2: X-Direction Hysteretic Response Compared to PCK (2007) Hinge Length Monotonic Prediction

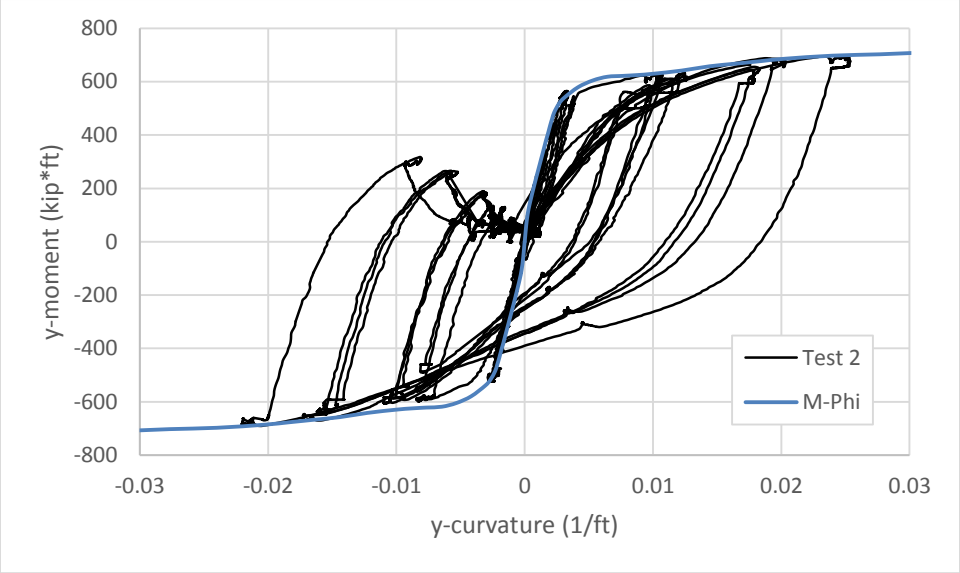

Figure 5-88. Test 2: Y-Direction Sectional Response Compared to Monotonic Moment Curvature Analysis

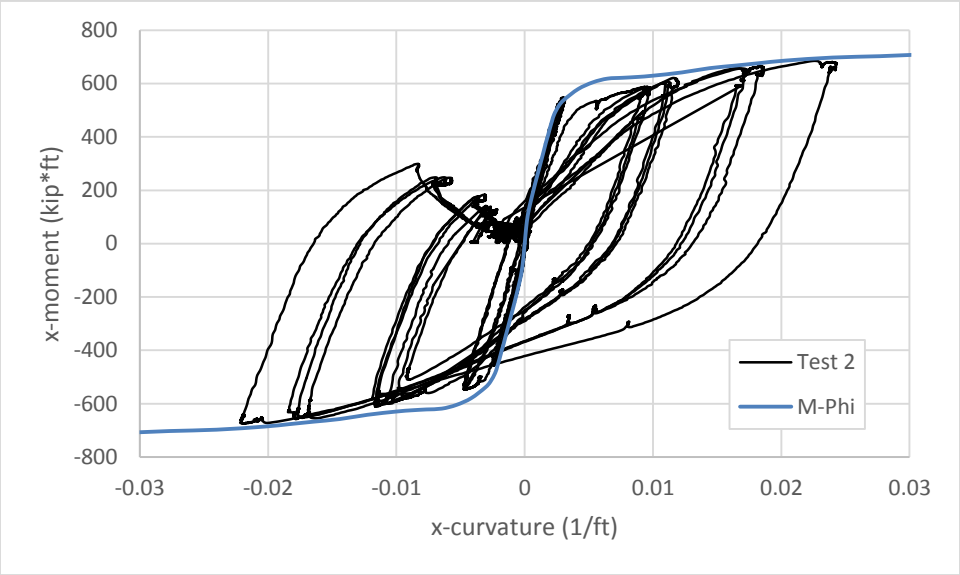

Figure 5-89. Test 2: X-Direction Sectional Response Compared to Monotonic Moment Curvature Analysis

Response Comparison for Nominally Identical Tests 1 and 2

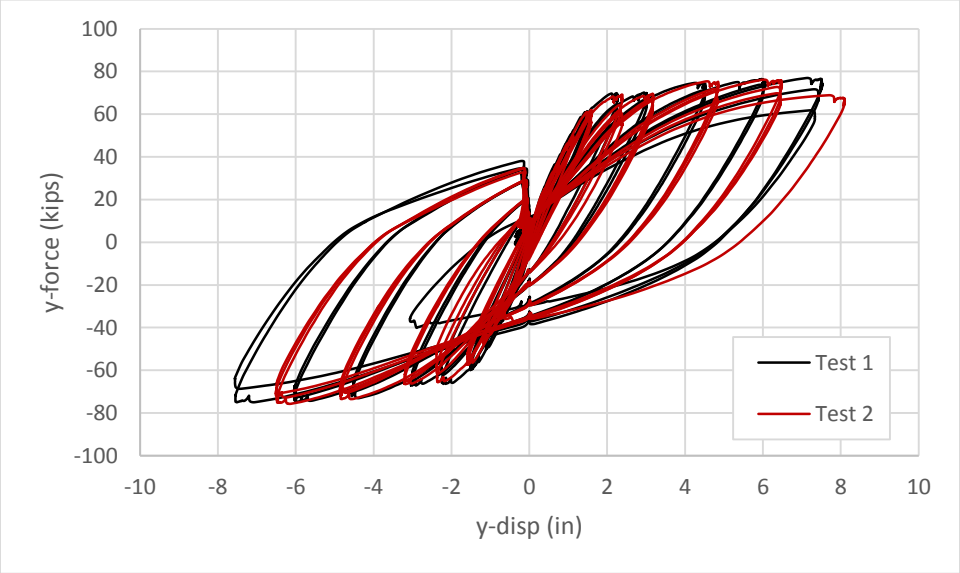

Figure 5-90. Test 1 Symmetric Two-Cycle-Set and Test 2 Symmetric Three-Cycle-Set

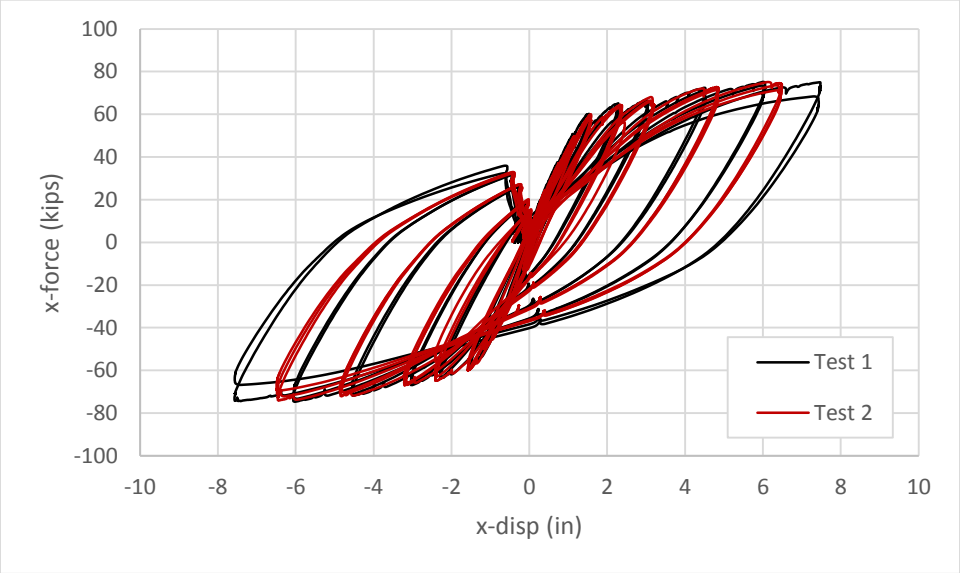

Figure 5-91. Test 1 Symmetric Two-Cycle-Set and Test 2 Symmetric Three-Cycle-Set

Chapter 6 - Test 3 Summary Report

The specimen selected for Test 3 was nominally identical to that of Tests 1 and 2. The third specimen had a 24" diameter circular cross-section reinforced with 16 #7 A706 longitudinal bars $(A_{st}/A_g = 2.1\%)$ and a #3 spiral at 2.75" on center $(4A_{sp}/D's = 0.7\%)$. The column had a 109.4375" cantilever length, measured from the footing-column interface to the center of the applied lateral load. This length was obtained as an average of the staggered actuator connections heights, 108" and 110.875". Although eliminated in the instrumented region, the upper portion of the column had a 0.5" cover measured to the outside surface of the spiral. The column had a constant axial load of $191\ kips\ \left(P/f_c'\,A_g = 7.4\%\right)$. Details of the test setup, instrumentation, and specimen design appear in Chapter 2. A material properties summary for the longitudinal and transverse steel from the first six experiments appears in Table 3-1 and Table 3-2. The column had a tested concrete strength of $f_c' = 6.24\ ksi$, while the footing had $f_c' = 9.06\ ksi$. The third specimen was subjected to an Asymmetric Two-Cycle-Set Biaxial Load History shown in Figure 6-1. This deformation history evaluates the influence of smaller orthogonal deformations on damage states and spread of plasticity. This figure includes a diagram of the column cross-section with the selected bar and crack labeling scheme. Displacements in the +Y-direction placed the South reinforcement in tension. Cracks due to loading in the +Y-direction were labeled as red. The orientation of the X and Y axes are shown in Figure 2-52 with regards to the test setup. The +Y-axis is perpendicular to and points away from the strong wall. Values of interests, damage observations, and moment-curvature predictions for the third test appear in Table 6-1, Table 6-2, and Table 6-3.

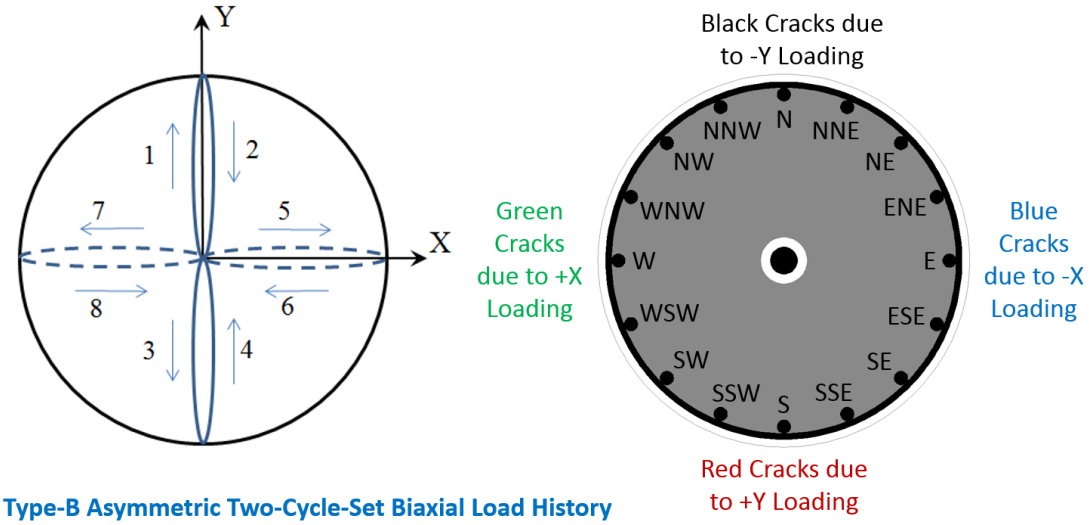

Type-B Asymmetric Two-Cycle-Set Biaxial Load History

- Begins with elastic cycles (1-8) in ¼ yield increments until F_y'
- The equivalent yield displacement is then computed as $\Delta_y = \Delta_y'\left(M_n/M_y'\right)$
- Inelastic cycles (1-4) in the Y-direction followed by inelastic cycles (5-8) in the X-direction for each of the following displacement ductility levels $\mu_{\Delta n} = n \cdot \Delta_y$
  - $\mu_{\Delta 1}^{\pm Y}$ & $\mu_{\Delta 1}^{\pm X}$, $\mu_{\Delta 1.5}^{\pm Y}$ & $\mu_{\Delta 1}^{\pm X}$, $\mu_{\Delta 2}^{\pm Y}$ & $\mu_{\Delta 1}^{\pm X}$, $\mu_{\Delta 3}^{\pm Y}$ & $\mu_{\Delta 1.5}^{\pm X}$, $\mu_{\Delta 4}^{\pm Y}$ & $\mu_{\Delta 2}^{\pm X}$, etc. where $\mu_{\Delta}^{\pm X}$ lags by two displacement ductility levels until bar buckling is observed
- Cycle labeling system: $\left(\mu_{\Delta 4}^{-2Y} = -6.03\ in\right)$ Represents the second cycle of displacement ductility four in the -Y direction

Figure 6-1. Test 3: Load History and Labeling System for Reinforcement and Cracks

Table 6-1. Test 3: Values of Interest

Load History	Type-B Asymmetric Two-Cycle-Set
Length, Diameter, and Aspect Ratio	$L = 109.4375\ in, D = 24\ in,\ (L/D = 4.56)$
Longitudinal Steel Detailing	$16\ \#7\ for\ \rho_l = A_{st}/A_g = 2.1\%$
Longitudinal Steel Properties	$f_y = 71.2\ ksi, f_u = 97.9\ ksi, \varepsilon_y = 0.00254$
Transverse Steel Detailing	$\#3\ @\ 2.75\ in\ for\ \rho_s = 4A_{sp}/D's = 0.7\%$
Transverse Steel Properties	$f_y = 67.6\ ksi, f_u = 105.6\ ksi, \varepsilon_y = 0.00448$
Column Concrete Strength	$f_c' = 6.24\ ksi$
Footing Concrete Strength	$f_c' = 9.06\ ksi$
Axial Load	$P = 191\ kips, \left(P/f_c'\ A_g = 7.4\%\right)$
Analytical First Yield Force	$F_y' = 50.89\ kips$
Experimental First Yield Disp.	$\Delta_y' = 1.10\ in$
Analytical Nominal Moment Capacity	$M_n = 624.47\ kip \cdot ft$
Equivalent Yield Displacement	$\Delta_y = \Delta_y'\left(M_n/M_y'\right) = 1.47\ in$
Maximum Lateral Force	$F_y = 77.61\ kips, F_x = 76.18\ kips$
Failure Mode	Loss in lateral strength due to buckling of nearly all column longitudinal bars, followed by a single fractured bar.

Table 6-2. Test 3: Damage Observations

Damage Observations:		
Cycle Peak at which First Cracking was Observed Visually:		
North	$\Delta_y = -0.5F_y' = -0.43\ in$	$F_y = -25.79\ kips$
South	$\Delta_y = 0.5F_y' = 0.35\ in$	$F_y = 23.45\ kips$
East	$\Delta_x = -0.5F_y' = -0.38\ in$	$F_x = -23.83\ kips$
West	$\Delta_x = 0.5F_y' = 0.36\ in$	$F_x = 24.42\ kips$
Cycle Peak at which Cover Concrete Crushing was Observed Visually:		
North	$\mu_{\Delta 1.5}^{+2Y} = 2.26\ in$	$\varepsilon_c = -0.00525$
South	$\mu_{\Delta 1.5}^{-1Y} = -2.26\ in$	$\varepsilon_c = -0.00544$
East	$\mu_{\Delta 2}^{+2X} = 3.01\ in$	$\varepsilon_c = -0.00422$
West	$\mu_{\Delta 2}^{-2X} = -3.01\ in$	$\varepsilon_c = -0.00448$
Exact Displacement and Cycle Label for Initial Spiral Yielding in the Confinement Zone:		
North	$\Delta_y = 3.86\ in\ during\ \mu_{\Delta 3}^{+1Y}$	$\varepsilon_c = -0.01242$
South	$\Delta_y = -4.46\ in\ during\ \mu_{\Delta 3}^{-1Y}$	$\varepsilon_c = -0.01414$
East	$\Delta_x = 5.64\ in\ during\ \mu_{\Delta 4}^{+1X}$	$\varepsilon_c = -0.01016$
West	$\Delta_x = -5.64\ in\ during\ \mu_{\Delta 4}^{-1X}$	$\varepsilon_c = -0.01005$
Peak Tensile Displacement Prior to Visual Bar Buckling During Subsequent Reversal of Load:		
North	$\mu_{\Delta 4}^{-1Y} = -6.01\ in, Observed\ at\ \mu_{\Delta 4}^{+2Y} = 6.04\ in$	$\varepsilon_s = 0.03196$
South	$\mu_{\Delta 4}^{+2Y} = 6.04\ in, Observed\ at\ \mu_{\Delta 4}^{-2Y} = -6.03\ in$	$\varepsilon_s = 0.03077$
East	$\mu_{\Delta 4}^{-2X} = -5.99\ in, Observed\ at\ \mu_{\Delta 5}^{+1X} = 7.53\ in$	$\varepsilon_s = 0.03013$
West	$\mu_{\Delta 5}^{+1X} = 7.53\ in, Observed\ at\ \mu_{\Delta 5}^{-1X} = -7.52\ in$	$\varepsilon_s = 0.03861$
Exact Displacement and Cycle Label for Fracture of Previously Buckled Reinforcement		
North	$\Delta_y = -3.52\ in\ during\ \mu_{\Delta 5}^{-2Y}$	Single North Extreme Bar

Table 6-3. Test 3: Damage Predictions

Damage Predictions with the New Bidirectional Plastic Hinge Model and New Strain Limits:		
Bar Buckling Predictions		
New Method	$\Delta_{bb}^{Lpr} = 6.76\ in$	$\varepsilon_s^{bb} = 0.03452$
Feng et al. (2015)	$\Delta_{bb}^{Lp} = 5.57\ in$	$\varepsilon_s^{bb} = 0.0374$
Cover Crushing Prediction		
New Method	$\Delta_{cc}^{Lpr} = 2.03\ in$	$\varepsilon_c^{cc} = -0.004$
Spiral Yielding Prediction		
New Method	$\Delta_{sy}^{Lpr} = 4.61\ in$	$\varepsilon_c^{sy} = -0.01192 * M, (M = 0.8)$
Original Ultimate Concrete Compression Strain		
Mander et al. (1988)	$\Delta_{cu}^{Lpr} = 6.32\ in$	$\varepsilon_{cu} = -0.0144$

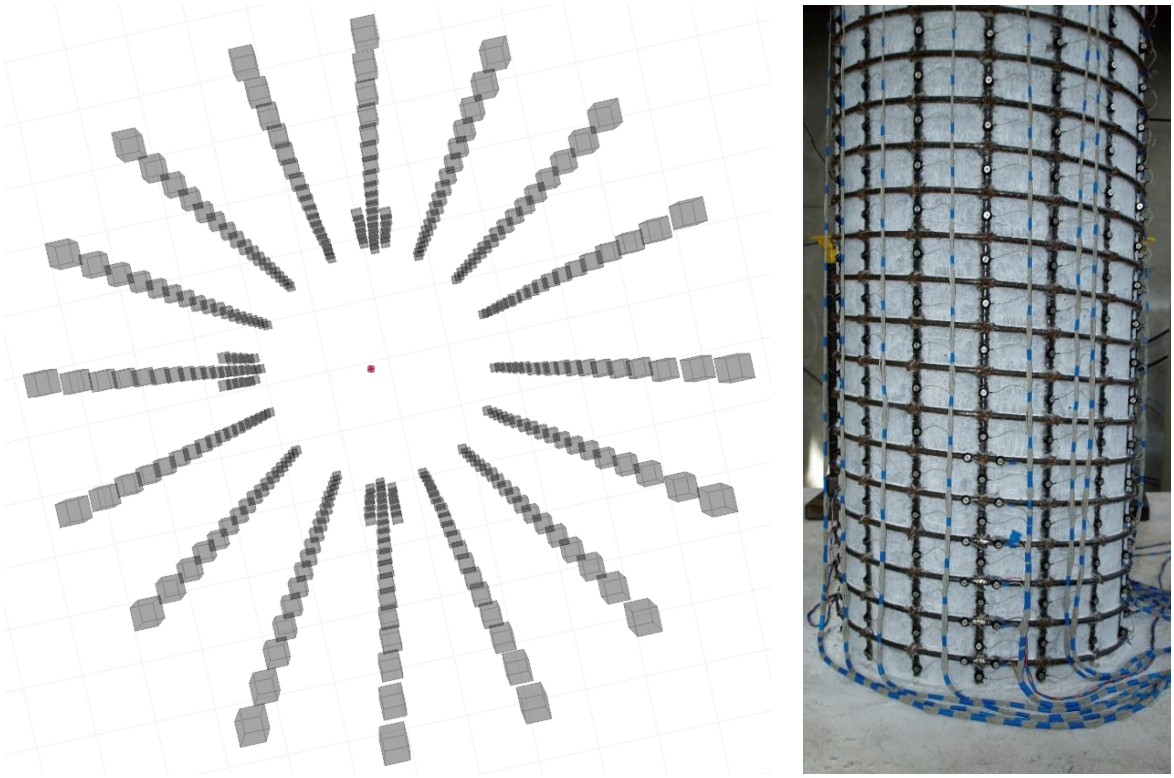

Figure 6-2. Test 3: Optotrak Target Marker Instrumentation and 3D Rendering of Measured Data

Figure 6-3. Linear Potentiometers Installed to Monitor Relative Footing Displacement at the 3/8" Neoprene Interface

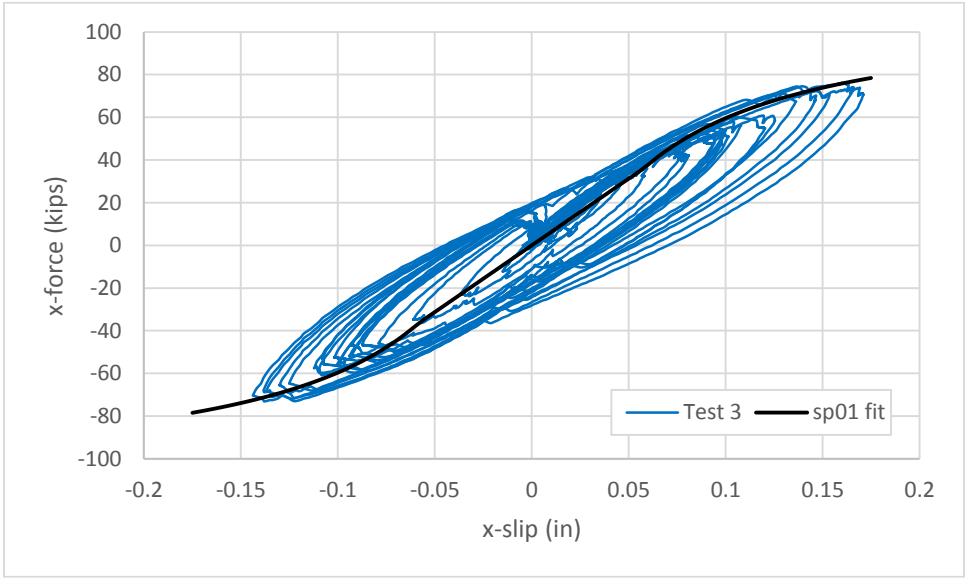

Figure 6-4. Test 3: Measured Linear Potentiometer Relative Footing Displacement with Monotonic SP01 Model Fit

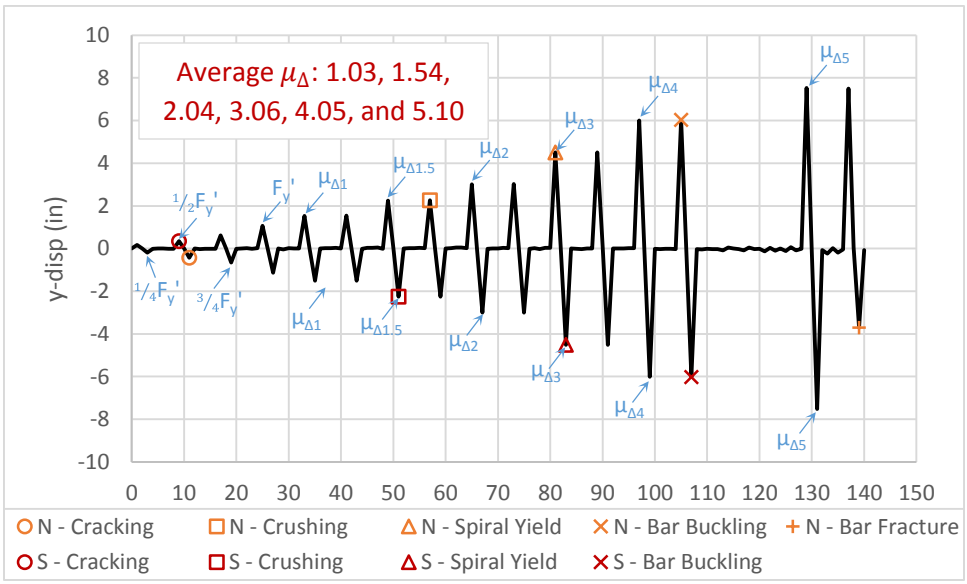

Figure 6-5. Test 3: Y-Displacement History

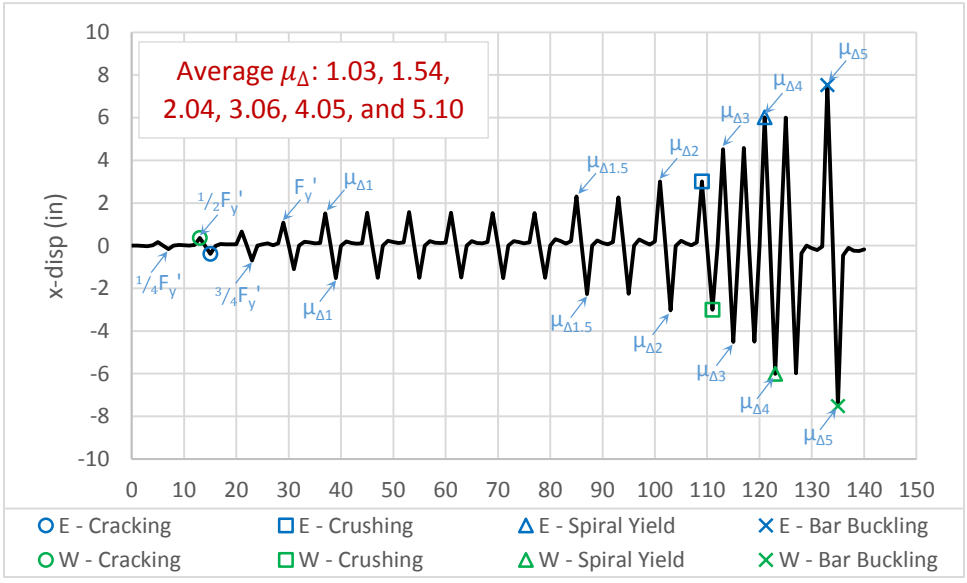

Figure 6-6. Test 3: X-Displacement History

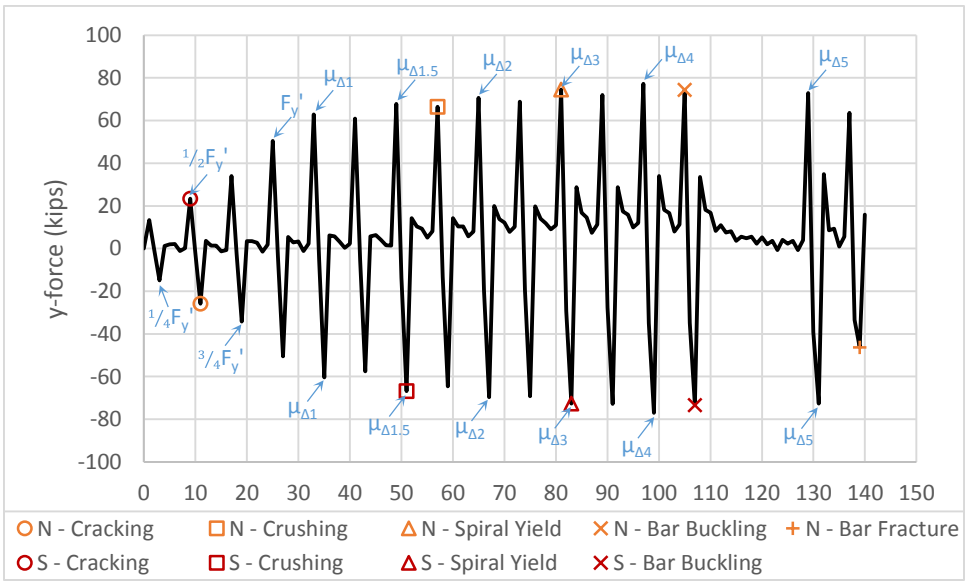

Figure 6-7. Test 3: Y-Force History

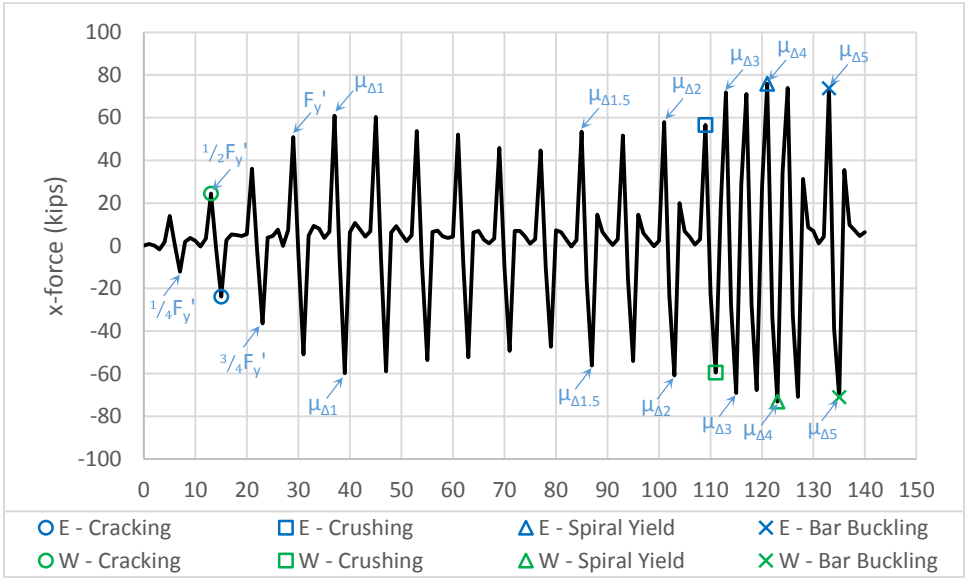

Figure 6-8. Test 3: X-Force History

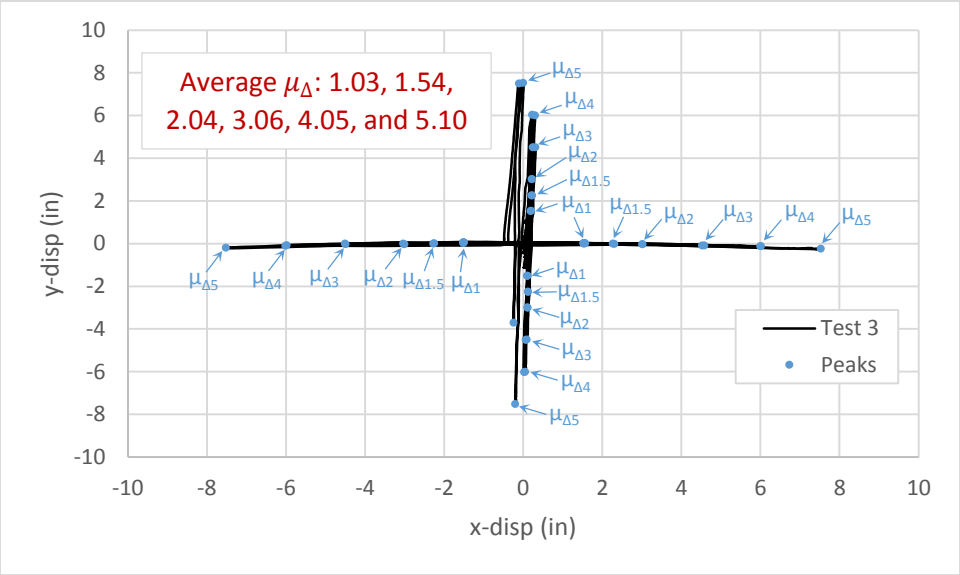

Figure 6-9. Test 3: Type-B Asymmetric Two-Cycle-Set Displacement History

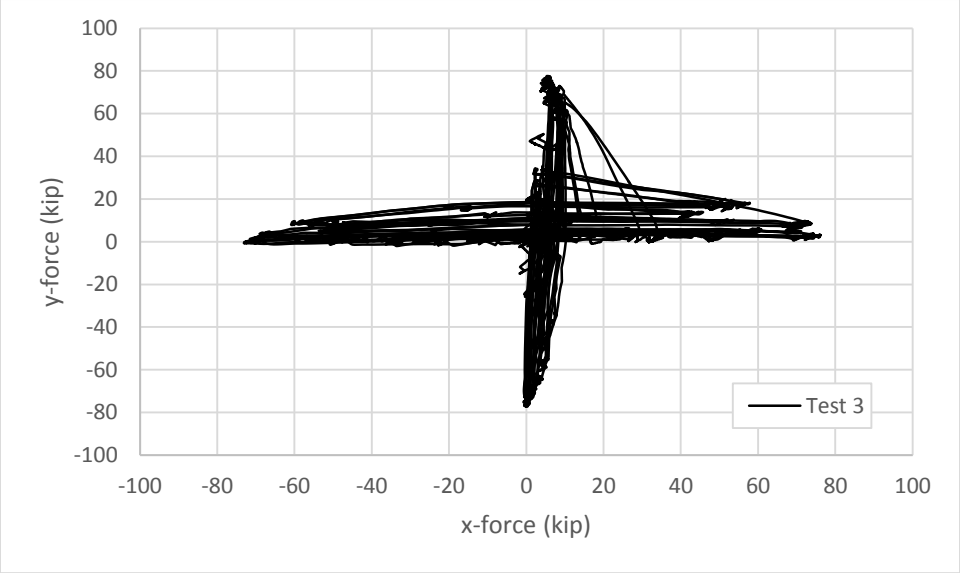

Figure 6-10. Test 3: Load Path

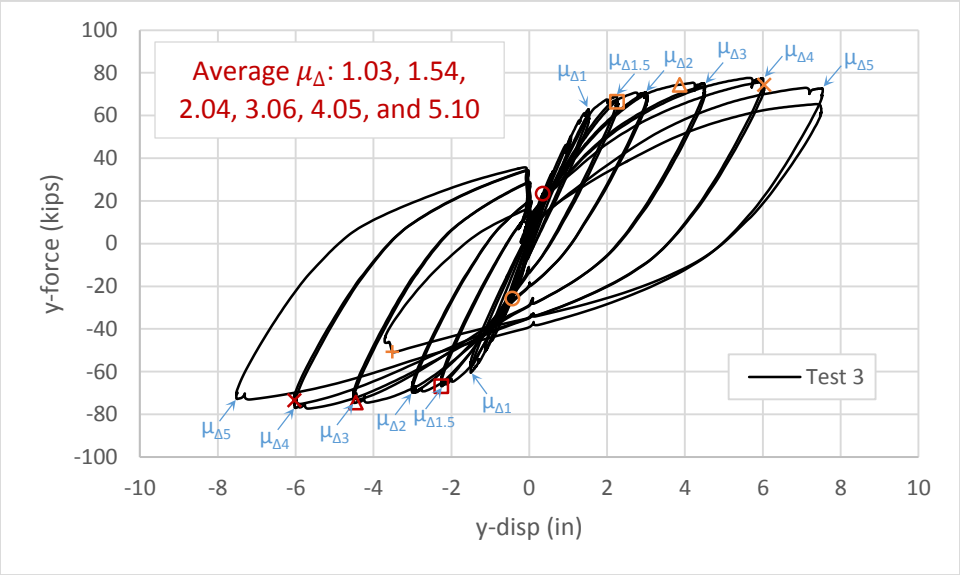

Figure 6-11. Test 3: Y-Direction Hysteretic Response

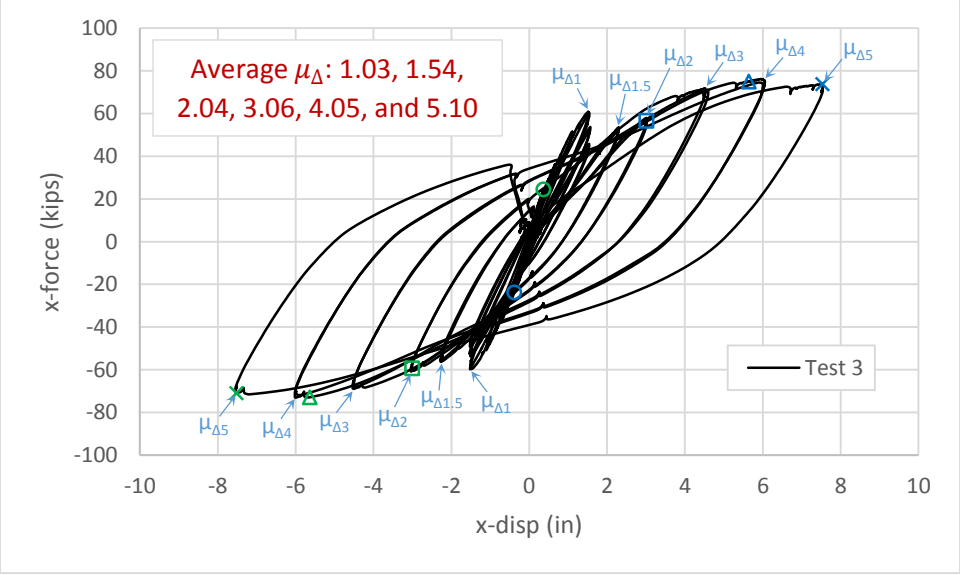

Figure 6-12. Test 3: X-Direction Hysteretic Response

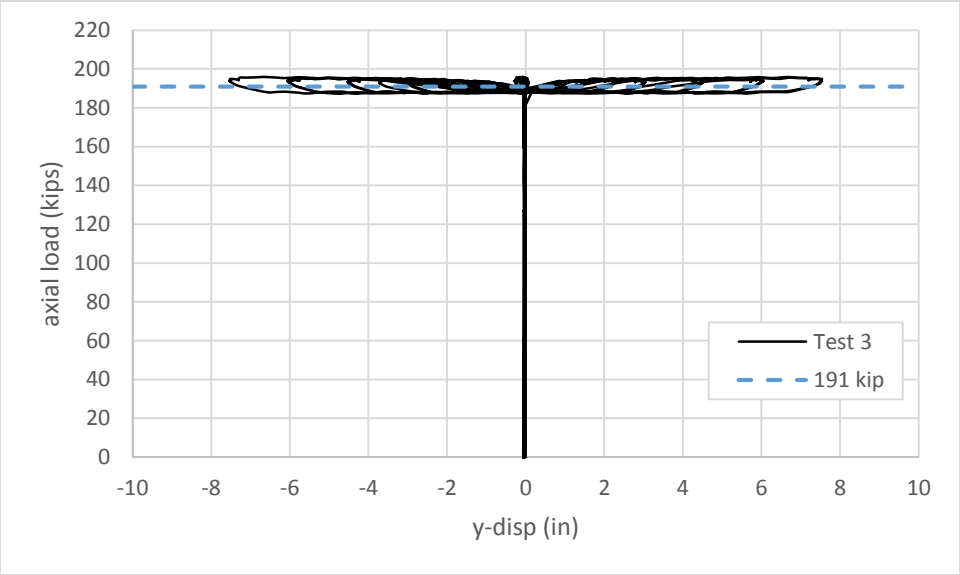

Figure 6-13. Test 3: Y-Direction Axial Force History

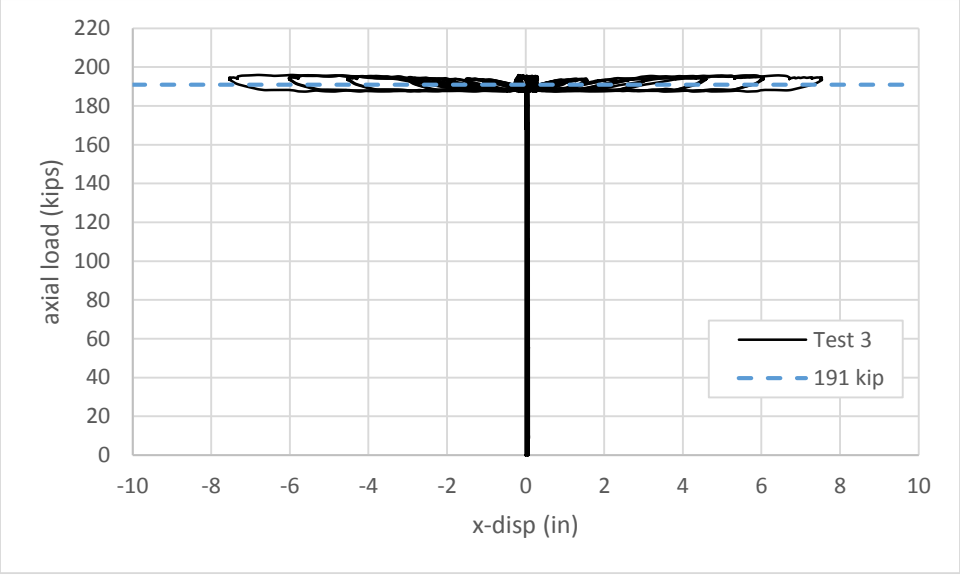

Figure 6-14. Test 3: X-Direction Axial Force History

Test 3 - Experimental Observations

The test began with collection of the initial measurements prior to application of the axial load. A constant axial load of 191 $kips$ $\left(P/f_c' A_g = 7.4\%\right)$ was then applied using a self-regulating axial load system described in Chapter 2. The imposed displacement histories in the Y and X-directions for the Asymmetric Two-Cycle-Set Biaxial Load History of Figure 6-1 are shown in Figure 6-5 and Figure 6-6. The resulting column shear force histories in the Y and X-directions appear in Figure 6-7 and Figure 6-8. The full displacement history and resulting load path for Test 3 appear in Figure 6-9 and Figure 6-10. The Y and X-direction column hysteretic response appears in Figure 6-11 and Figure 6-12. The axial load history is shown in Figure 6-13 and Figure 6-14. In Test 3, the relative displacement between the transfer and secondary footings was measured using linear potentiometers in the four primary directions, see Figure 6-3 and Figure 6-4. A calculation channel was added to the data acquisition to subtract the relative footing displacement from the string potentiometer displacement, providing the total column deformation. The data from this calculation channel was updated in real time, allowing for it to be used as the control for the actuators, which insured that the appropriate displacement amplitudes were reached in each cycle.

The load history began with elastic cycles (1-8) in ¼ F_y' increments until the analytically predicted first yield force ($F_y' = 50.89\ kips$) was reached in each direction of loading. Cracks were first observed on all sides of the specimen during the ½ F_y' cycle, see Figure 6-15 and Figure 6-16. At the analytically predicted first yield force, displacements in the four primary directions were measured at $\Delta_y' = 1.07$" and $\Delta_y' = -1.13$" in Y-direction and $\Delta_y' = 1.08$" and $\Delta_y' = -1.10$" in X-direction, producing an average experimental first yield displacement of $\Delta_y' = 1.10$". Cracks observed on each side of the specimen at first yield are shown in Figure 6-17 and Figure 6-18. The equivalent yield displacement for the column was then computed as $\Delta_y = \Delta_y'\left(M_n/M_y'\right) = 1.47\ in$, where $M_n = 624.47\ kip \cdot ft$ represents the analytical nominal moment capacity corresponding to an extreme fiber compression strain of $\varepsilon_c = 0.004$ or a steel tensile strain of $\varepsilon_s = 0.015$, whichever occurs first. In an effort to make this specimen directly comparable to Test 1 which utilized a Symmetric Two-Cycle-Set bidirectional load history, the equivalent yield displacement of Test 1 ($\Delta_y = 1.51$") was used to define the displacement ductility levels ($\mu_{\Delta n} = n \cdot \Delta_y$) of the asymmetric load history selected for Test 3. The average measured displacement ductility of cycles ran in Test 3 referencing the actual equivalent yield displacement of ($\Delta_y = 1.47$") were as follows: 1.03, 1.54, 2.04, 3.06, 4.05, and 5.10. This was expected to have little influence on the damage observations.

The following set of cycles began the asymmetric portion of the two-cycle-set displacement history where the displacement demands in the x-direction lagged behind those in the y-direction as shown in Figure 6-5 and Figure 6-6. Concrete crushing was first observed on the South and North sides of the specimen during $\mu_{\Delta 1.5}^{-1y} = -2.26$" and $\mu_{\Delta 1.5}^{+2y} = 2.26$" respectively, as shown in Figure 6-21. Cracking on the South and North sides of the specimen at $\mu_{\Delta 1.5}^{+2y} = 2.26$" and $\mu_{\Delta 1.5}^{-2y} = -2.26$" appear in Figure 6-22. Photos of the East and West sides of the specimen at the conclusion of $\mu_{\Delta 1.5}^{\pm 2y}$ and $\mu_{\Delta 1}^{\pm 4x}$ are shown in Figure 6-23. The red and black cracks from $\mu_{\Delta 1.5}^{\pm 2y}$ show a distinct inclination on the shear faces the column. Even though the displacement ductility was not increased during $\mu_{\Delta 1}^{\pm 4x}$, the cracks due to loading in this direction spread following those created during the larger orthogonal loading.

Cracks on South and North sides of the specimen during $\mu_{\Delta 2}^{+2y} = 3.02"$ and $\mu_{\Delta 2}^{-2y} = -3.01"$ are shown in Figure 6-24. The crack profiles on the East and West sides of the specimen after $\mu_{\Delta 2}^{\pm 2y}$ and $\mu_{\Delta 1}^{\pm 6x}$ appear in Figure 6-25. Again, the inclination of cracks due to loading in the y-direction increased, however those due to loading in the x-direction remained horizontal on the shear faces due to the lower displacement demands. Spirals on the North and South sides of the specimen yielded under confinement demands during $\mu_{\Delta 3}^{+1y} = 4.51"$ and $\mu_{\Delta 3}^{-1y} = -4.51"$ as shown in Figure 6-26. The crack profiles on the South and North sides of the specimen during $\mu_{\Delta 3}^{+2y} = 4.51"$ and $\mu_{\Delta 3}^{-2y} = -4.51"$ are depicted in Figure 6-27. Cracks on the East and West sides of the specimen after $\mu_{\Delta 3}^{\pm 2y}$ and $\mu_{\Delta 1.5}^{\pm 2x}$ are shown in Figure 6-28.

The measured strain in spiral layers on the North and South sides of the specimen spiked during $\mu_{\Delta 4}^{+1y} = 6.01"$ and $\mu_{\Delta 4}^{-1y} = -6.01"$, however the extreme fiber reinforcement remained visibly straight as shown in Figure 6-29. Concrete flaking, which precedes more noticeable crushing, was observed on the East side of the specimen during $\mu_{\Delta 2}^{+1x} = 3.02"$, see Figure 6-30. The extreme fiber north bar N and adjacent bar NNE buckled during $\mu_{\Delta 4}^{+2y} = 6.04"$, as shown in Figure 6-30. Note that bar buckling was not observed until $\mu_{\Delta 5}^{+1y} = 7.51"$ in the symmetric two-cycle-set load history of Test 1. Note that buckling on the North side during Test 1 did not require additional tensile strains during displacement ductility five, as it occurred during the first compressive cycle. The South extreme fiber bar S buckled during $\mu_{\Delta 4}^{-2y} = -6.03"$, as shown in Figure 6-31. Concrete crushing on the East side of the specimen was first observed at $\mu_{\Delta 2}^{+2x} = 3.01"$, see Figure 6-31. West concrete crushing was first observed during $\mu_{\Delta 2}^{-2x} = -3.01"$, however a photo is not available.

At this time, two bars had buckled on the North side of the specimen and a single bar had buckled on the South side at the conclusion of $\mu_{\Delta 4}^{\pm 2y}$ and $\mu_{\Delta 2}^{\pm 2x}$. It was clear that if the loading had progressed to displacement ductility five in the y-direction, then previously buckled reinforcement would have fractured, leading to significant strength loss. Instead, loading in the y-direction was paused in favor of direct cycling in the x-direction to evaluate the influence of the prior larger orthogonal loading on the spread of plasticity and damage observations in the x-direction. Note that the deformation history, load history, and hysteretic response in the y and x-directions are shown in Figure 6-5 through Figure 6-12. Crushing on the East and West sides of the specimen during $\mu_{\Delta 3}^{+1x} = 4.52"$ and $\mu_{\Delta 3}^{-1x} = -4.51"$ are depicted in Figure 6-32. This amplitude of loading had originally produced spiral yielding under confinement demands in the y-directions, however the measured spiral strains in the x-direction remained elastic.

Spiral yielding on the East and West sides of the specimen was measured during $\mu_{\Delta 4}^{+1x} = 6.02"$ and $\mu_{\Delta 4}^{-1x} = -6.02"$ respectively, see Figure 6-33. Reinforcement on the North and South sides of the specimen had buckled during displacement ductility four, however the East and West reinforcement remained straight after $\mu_{\Delta 4}^{+2x} = 6.00"$ and $\mu_{\Delta 4}^{-2x} = -5.99"$ as shown in Figure 6-34. The likely explanation for this behavior was that the larger prior displacement demands in the y-direction spread the plasticity further up the column, thus reducing the strains in the later cycles in the x-direction. The increased spread in plasticity would lower the material strains at an equivalent base-section curvature, thus explaining the delayed damage observations in the x-direction since the damage states are closely related to the strains in the reinforcing steel and surrounding concrete.

At this point, the four primary directions had all experienced two complete cycles of loading at displacement ductility four. Loading then resumed in the y-direction, resulting in buckling of an additional North bar NNW during $\mu_{\Delta 5}^{+1y} = 7.52"$, see Figure 6-35. South bars SSW and SSE buckled during $\mu_{\Delta 5}^{-1y} = -7.52"$ as shown in Figure 6-35. Three East bars E, ENE, and ESE buckled during $\mu_{\Delta 5}^{+1x} = 7.53"$, followed by buckling of bars W, WNW, and WSW during $\mu_{\Delta 5}^{-1x} = -7.52"$ as shown in Figure 6-36. By this time, three bars had buckled in each of the four primary directions. Bars NE and NW buckled during $\mu_{\Delta 5}^{+2y} = 7.50"$, see Figure 6-37. The previously buckled north extreme fiber bar N fractured at $-3.71"$ during $\mu_{\Delta 5}^{-2y}$, see Figure 6-37. The test was ended at this time, since fracture of the North bar resulted in significant strength loss as shown in Figure 6-11. Photos of each side of the specimen after instrumentation removal appear in Figure 6-38 and Figure 6-39. As with the previous specimens, the column was recentered and saved as a repair candidate for a separate research program sponsored by the AKDOT.

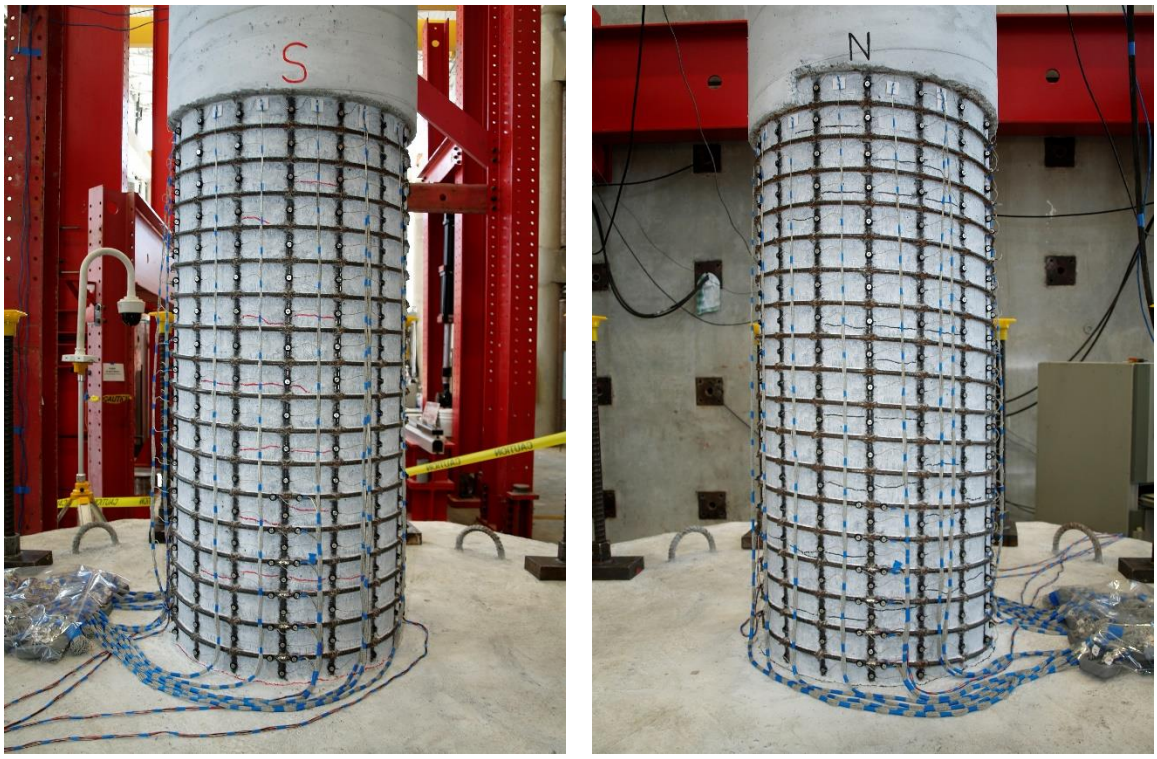

Figure 6-15. First Cracking on the South and North Sides of the Specimen during $\Delta_y = 0.35"$ and $\Delta_y = -0.43"$

Figure 6-16. Test 3: First Cracking on the West and East Sides of the Specimen during $\Delta_x = 0.36$" and $\Delta_x = -0.38$"

Figure 6-17. Test 3: Cracking on the South and North Sides during $\Delta'_y = 1.07$" and $\Delta'_y = -1.13$" in Y-Direction

Figure 6-18. Test3: Cracking on the West and East Sides during $\Delta'_y = 1.08"$ and $\Delta'_y = -1.10"$ in X-Direction

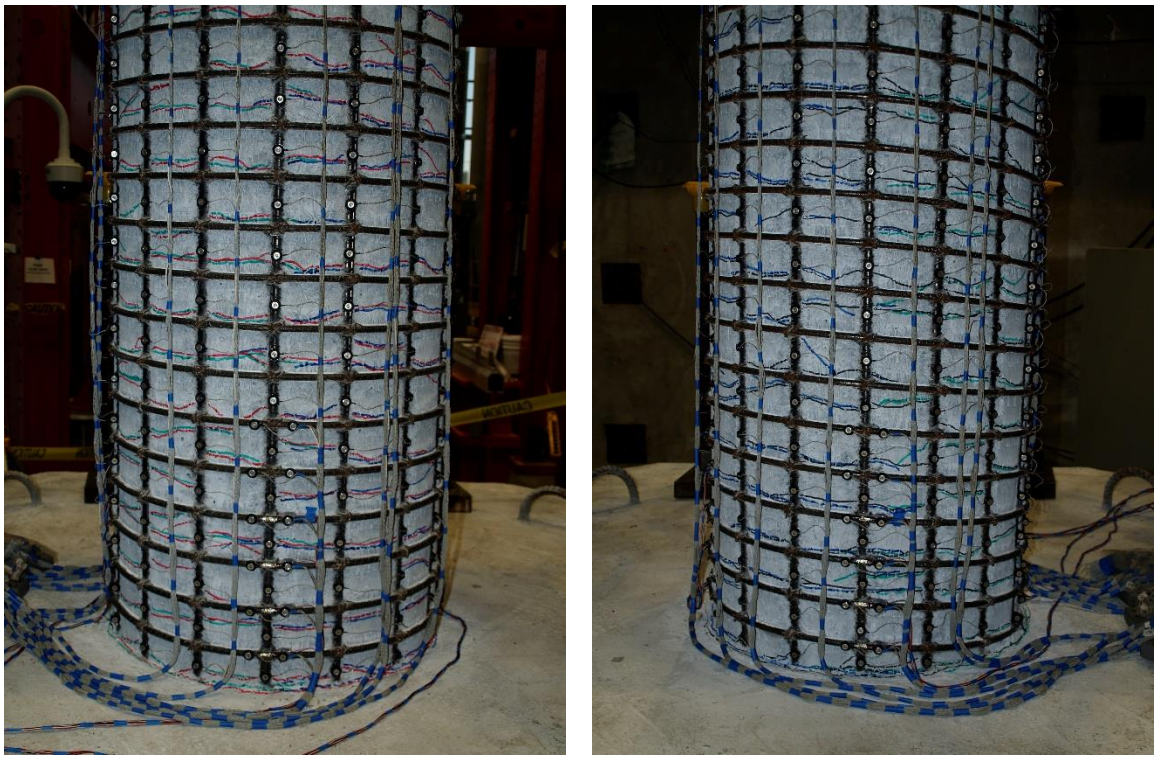

Figure 6-19. Test 3: Cracking on the (Left) South Side at $\mu_{\Delta 1}^{+2y} = 1.54"$ and (Right) North Side at $\mu_{\Delta 1}^{-2y} = -1.51"$

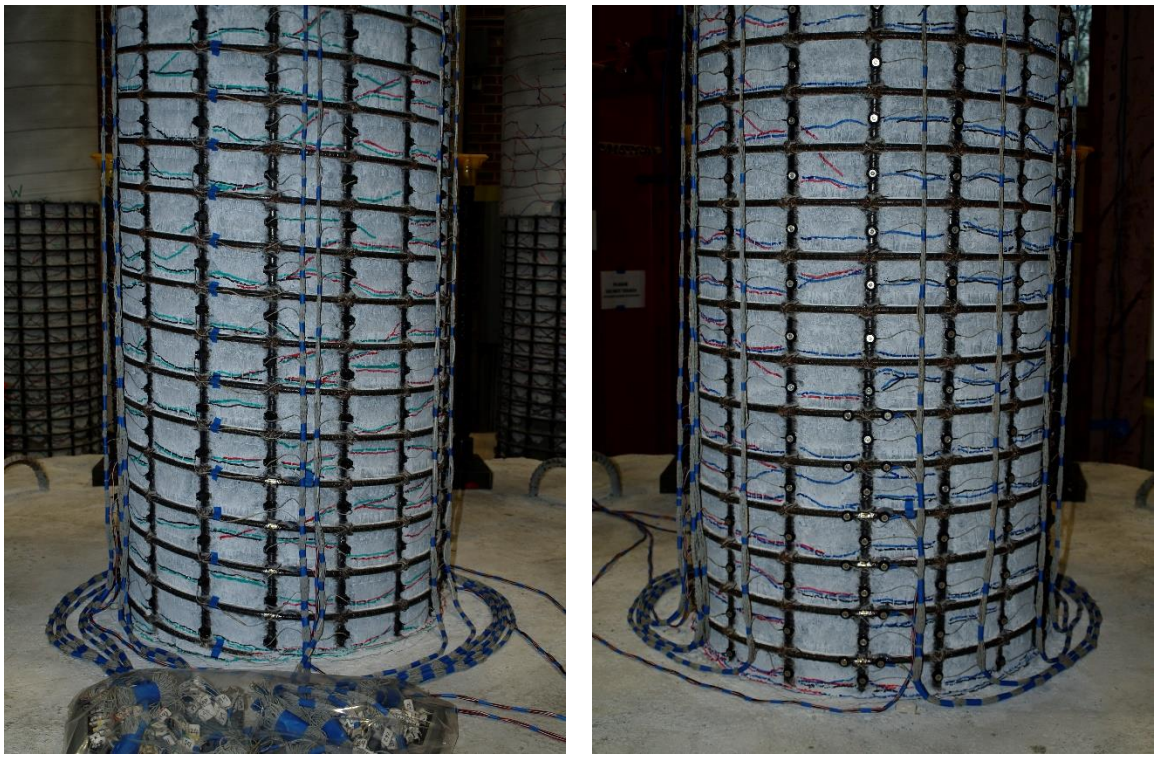

Figure 6-20. Test 3: Cracking on the (Left) West Side at $\mu_{\Delta 1}^{+2x} = 1.55$" and (Right) East Side at $\mu_{\Delta 1}^{-2x} = -1.51$"

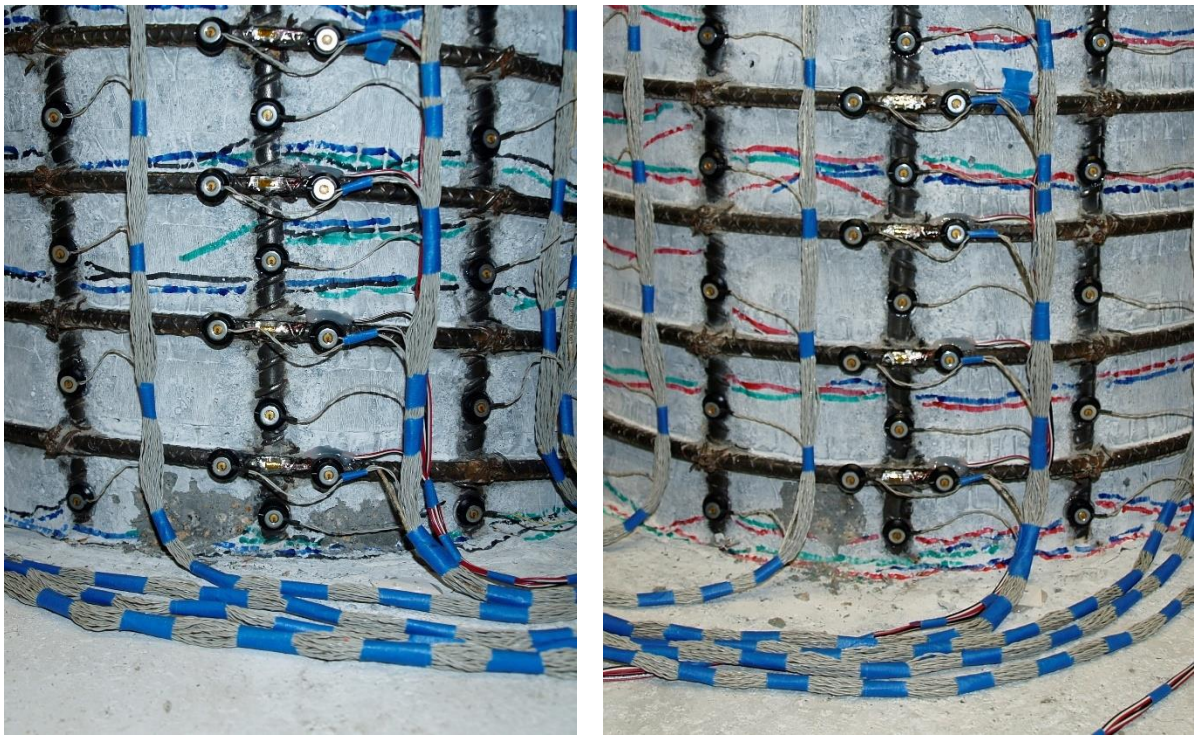

Figure 6-21. Test 3: (Left) North Concrete Crushing at $\mu_{\Delta 1.5}^{+2y} = 2.26$" and (Right) South Concrete Crushing at $\mu_{\Delta 1.5}^{-1y} = -2.26$"

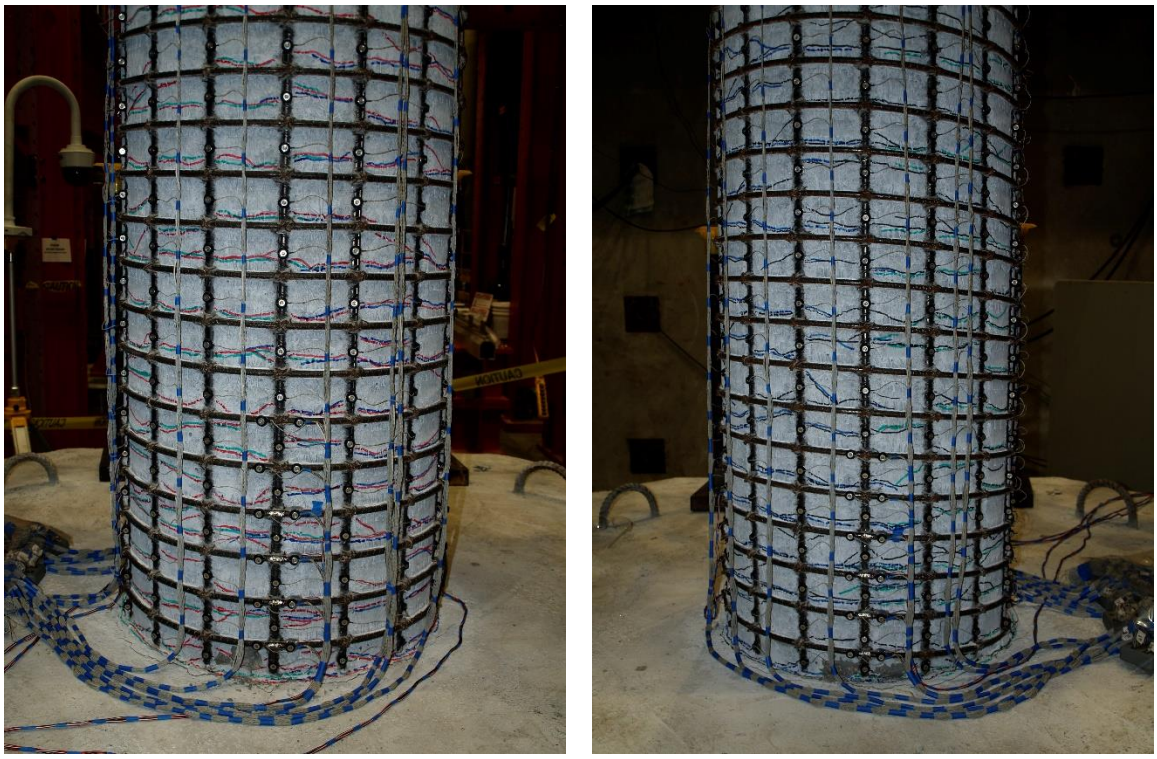

Figure 6-22. Test 3: Cracking on the (Left) South Side at $\mu_{\Delta 1.5}^{+2y} = 2.26$" and (Right) North Side at $\mu_{\Delta 1.5}^{-2y} = -2.26$"

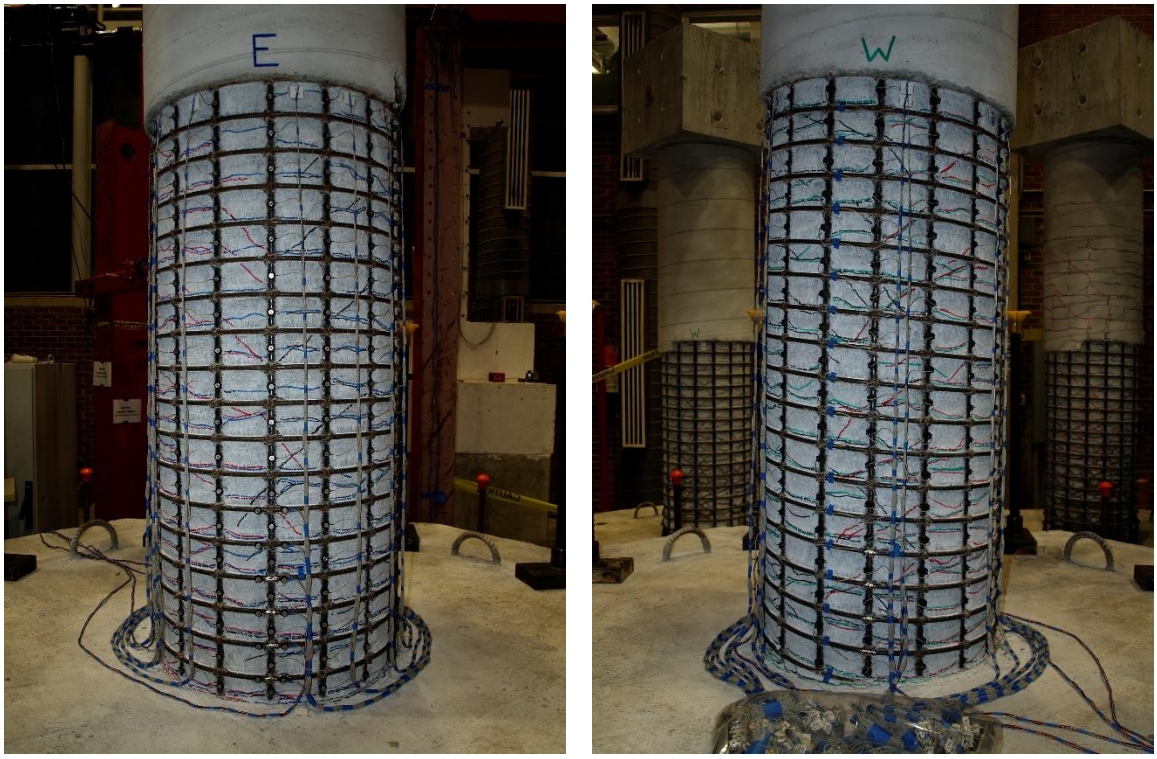

Figure 6-23. Test 3: Cracking on the (Left) East and (Right) West Sides after $\mu_{\Delta 1.5}^{\pm 2y}$ and $\mu_{\Delta 1}^{\pm 4x}$

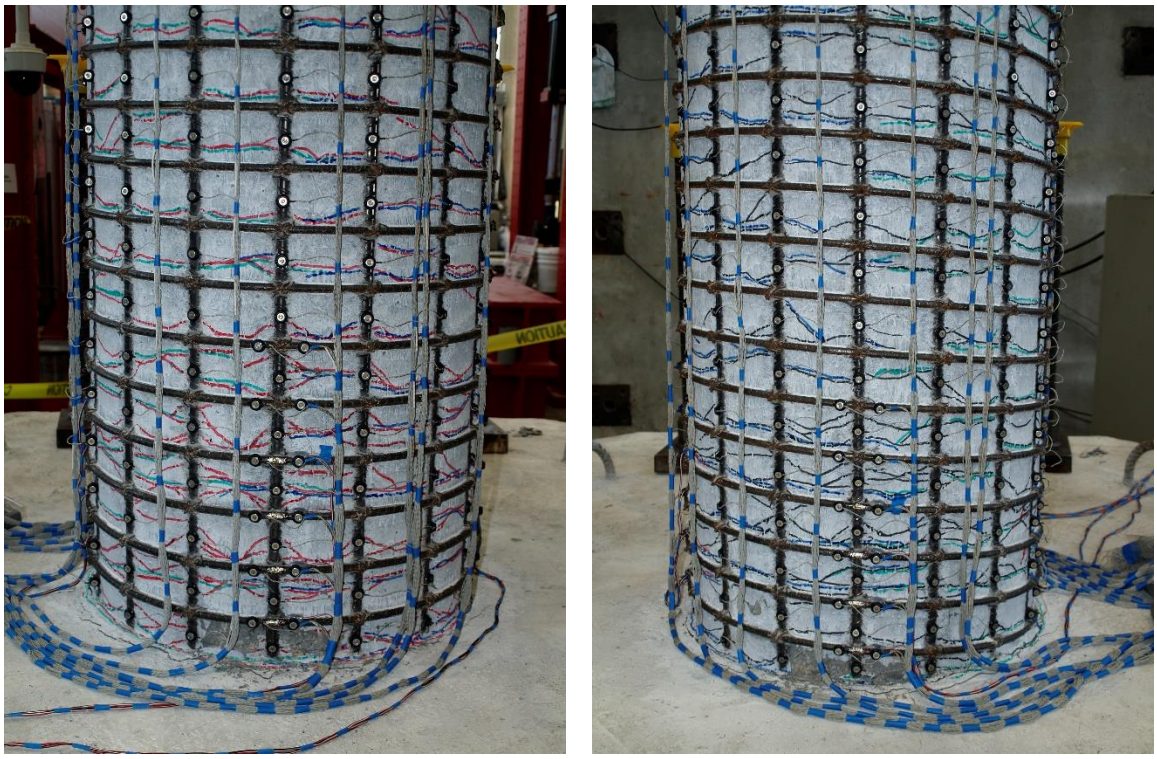

Figure 6-24. Test 3: Cracking on the (Left) South Side at $\mu_{\Delta 2}^{+2y} = 3.02$" and (Right) North Side at $\mu_{\Delta 2}^{-2y} = -3.01$"

Figure 6-25. Test 3: Cracking on the (Left) West Side at $\mu_{\Delta 1}^{+6x} = 1.53$" and (Right) East Side at $\mu_{\Delta 1}^{-6x} = -1.50$"

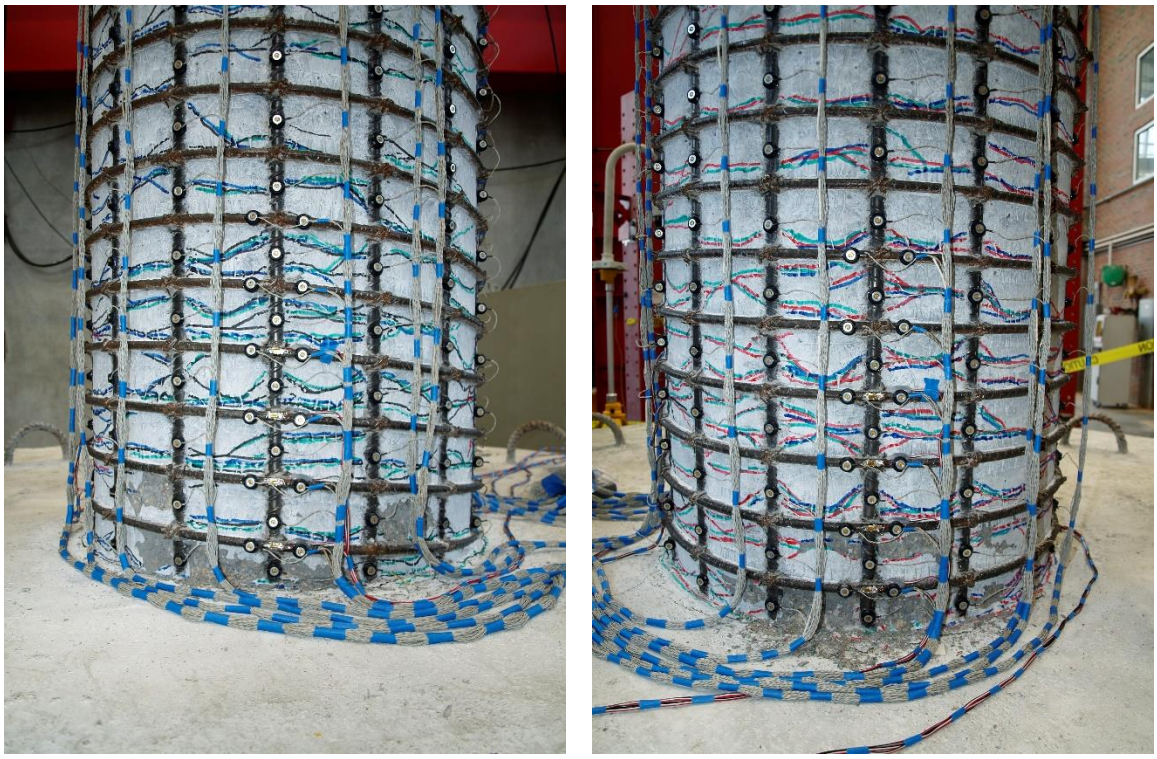

Figure 6-26. Test 3: Initial Spiral Yield on the (Left) North during $\mu_{\Delta 3}^{+1y} = 4.51"$ and (Right) South during $\mu_{\Delta 3}^{-1y} = -4.51"$

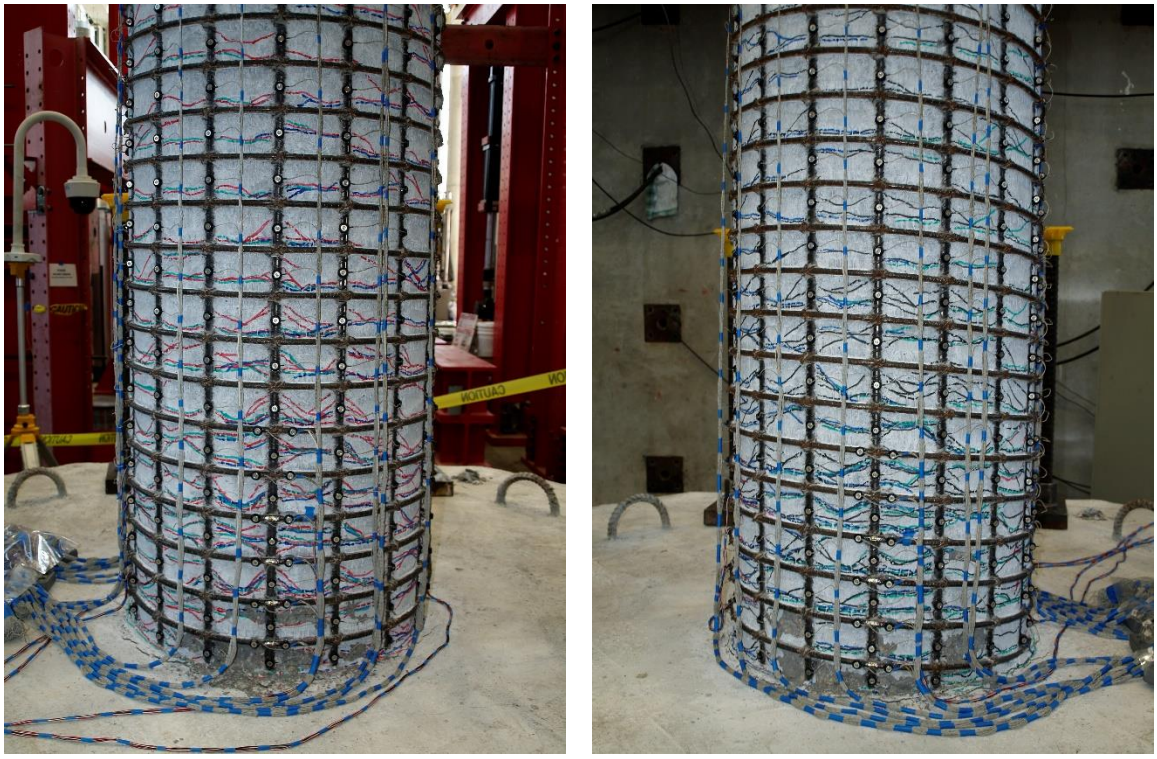

Figure 6-27. Test 3: Cracking on the (Left) South Side at $\mu_{\Delta 3}^{+2y} = 4.51"$ and (Right) North Side at $\mu_{\Delta 3}^{-2y} = -4.51"$

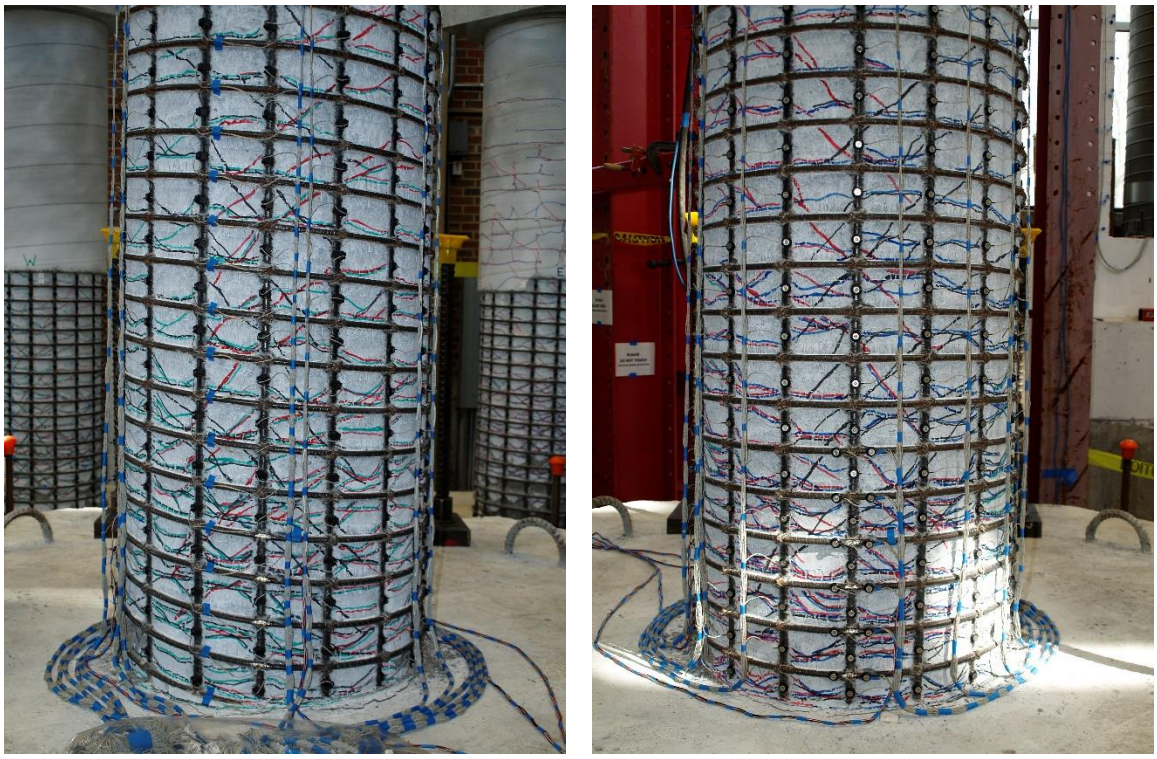

Figure 6-28. Test 3: Cracking on the (Left) East and (Right) West Sides after $\mu_{\Delta 3}^{\pm 2y}$ and $\mu_{\Delta 1.5}^{\pm 2x}$

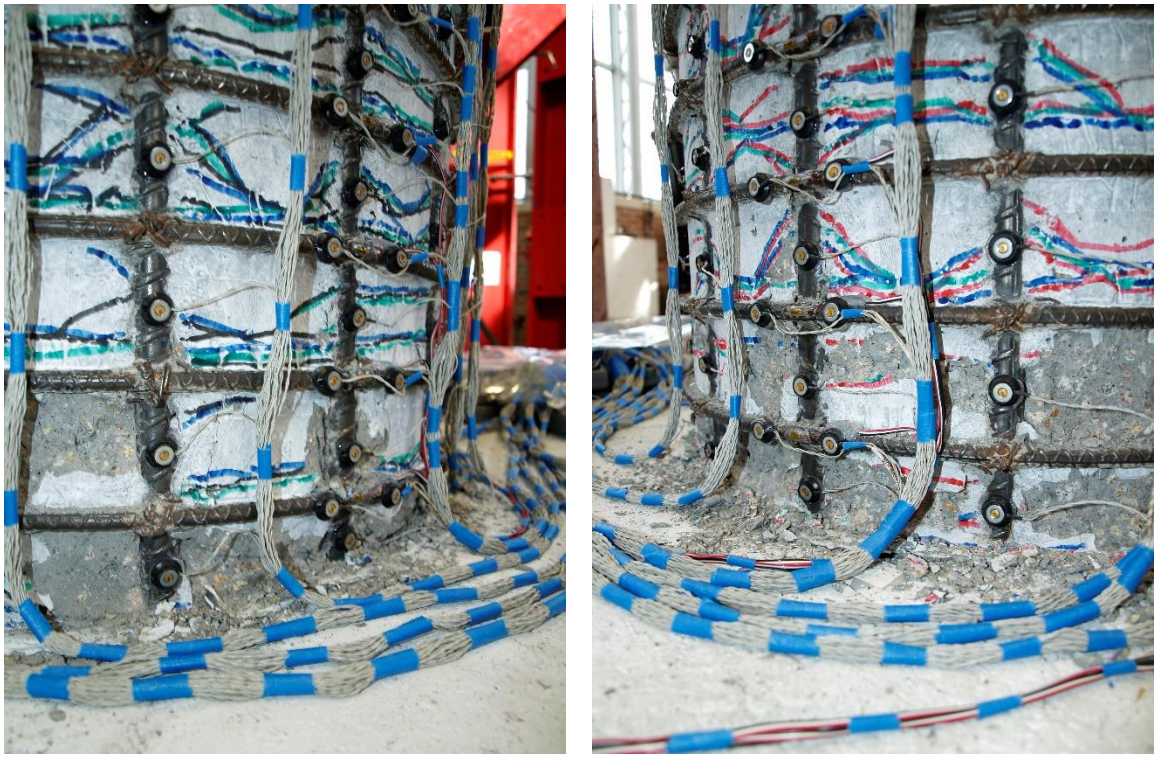

Figure 6-29. Test 3: Unbuckled Reinforcement on the (Left) North at $\mu_{\Delta 4}^{+1y} = 6.01"$ and (Right) South at $\mu_{\Delta 4}^{-1y} = -6.01"$

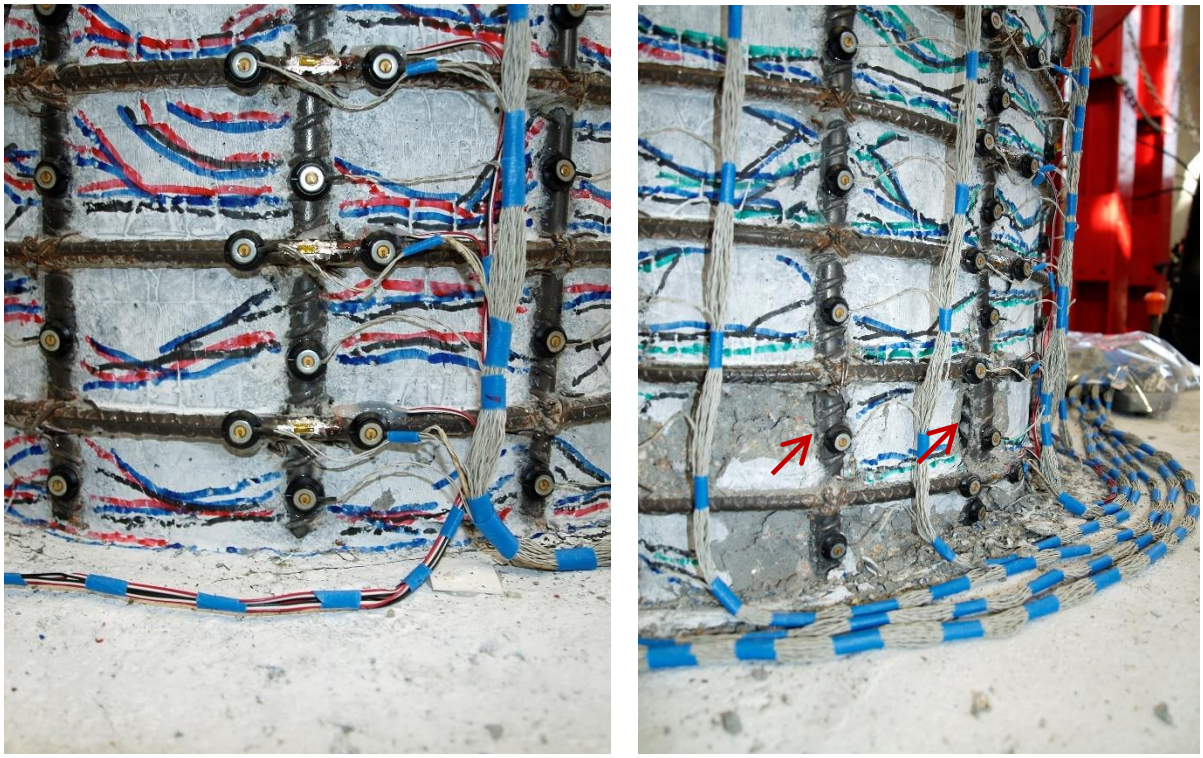

Figure 6-30. Test 3: (Left) East Flaking at $\mu_{\Delta 2}^{+1x} = 3.02$" and (Right) Buckling of Bars N and NNE during $\mu_{\Delta 4}^{+2y} = 6.04$"

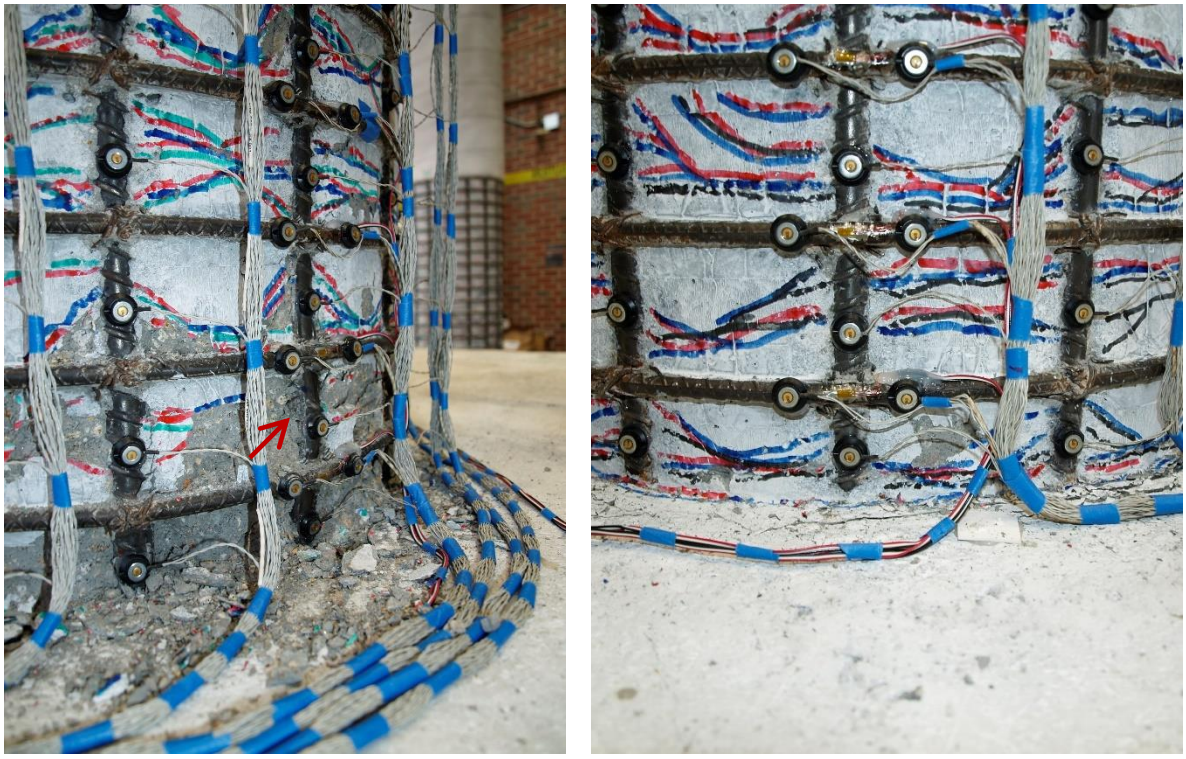

Figure 6-31. Test 3: (Left) South Bar Buckling during $\mu_{\Delta 4}^{-2y} = -6.03$" and (Right) East Concrete Crushing at $\mu_{\Delta 2}^{+2x} = 3.01$"

Figure 6-32. Test 3: Crushing on the (Left) East Side at $\mu_{\Delta 3}^{+1x} = 4.52"$ and (Right) West Side at $\mu_{\Delta 3}^{-1x} = -4.51"$

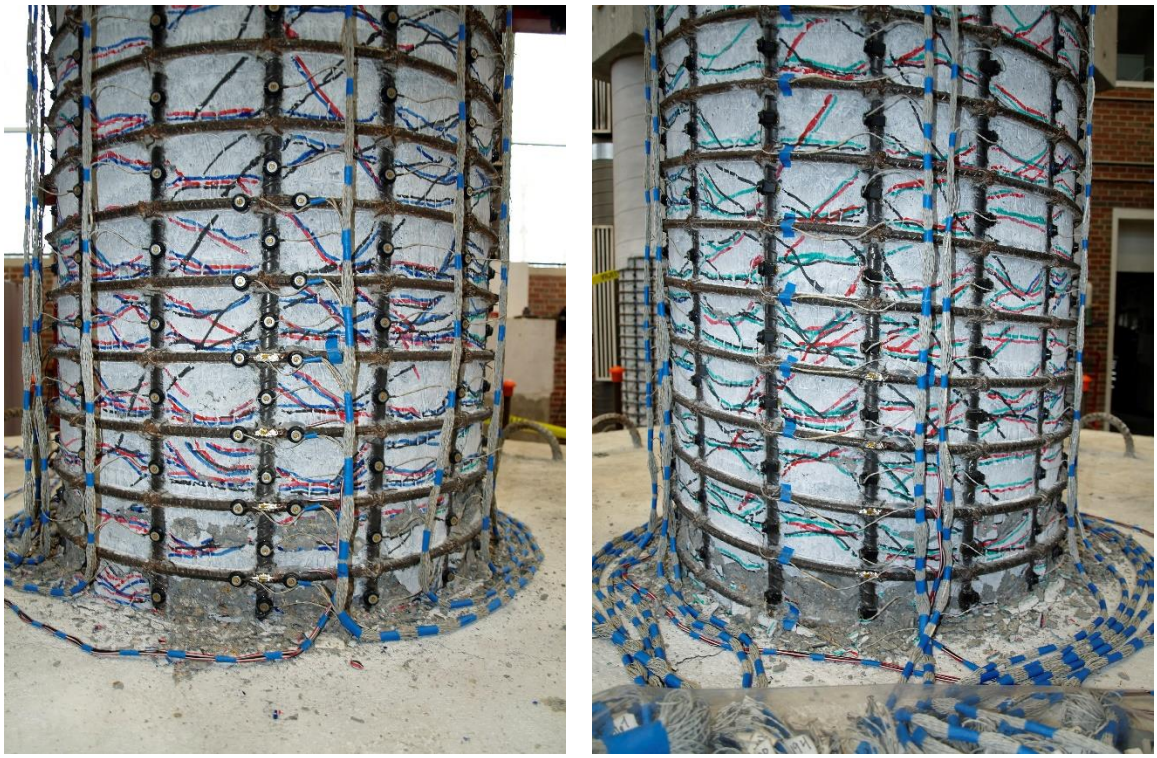

Figure 6-33. Test 3: Initial Spiral Yielding on the (Left) East during $\mu_{\Delta 4}^{+1x} = 6.02"$ and (Right) West during $\mu_{\Delta 4}^{-1x} = -6.02"$

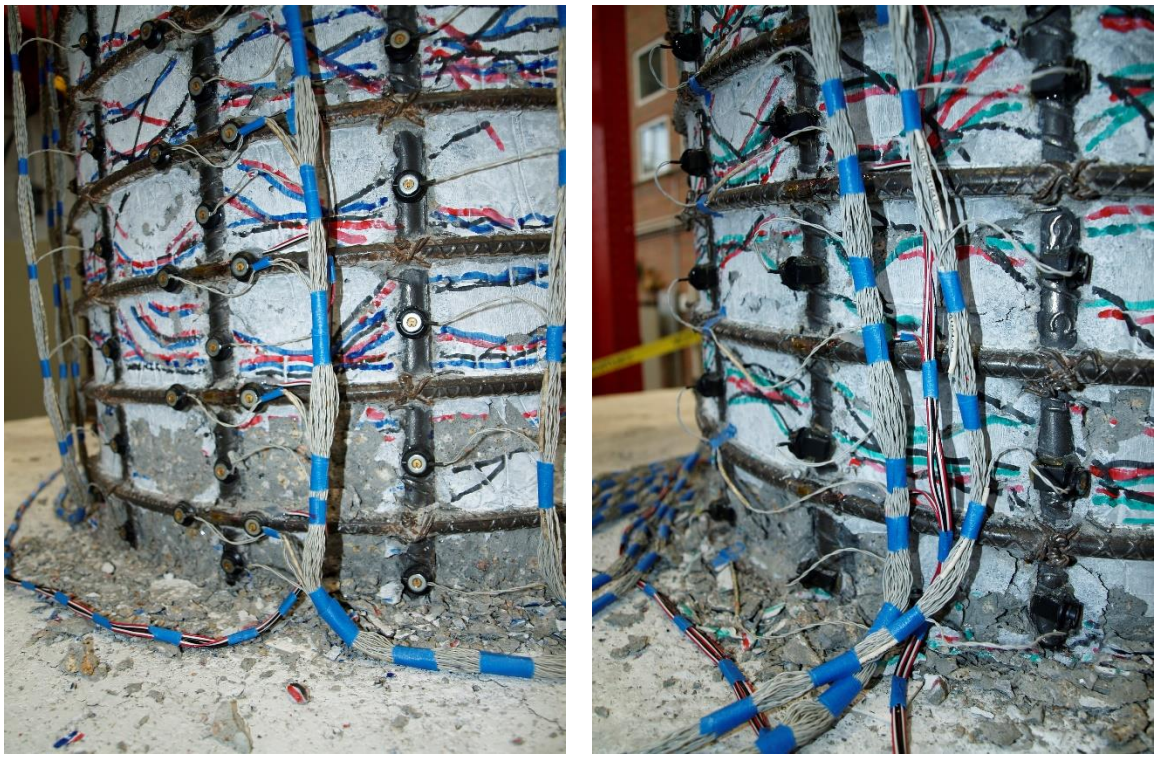

Figure 6-34. Test 3: Reinforcement Remained Straight on (Left) East at $\mu_{\Delta 4}^{+2x} = 6.00$" and (Right) West at $\mu_{\Delta 4}^{-2x} = -5.99$"

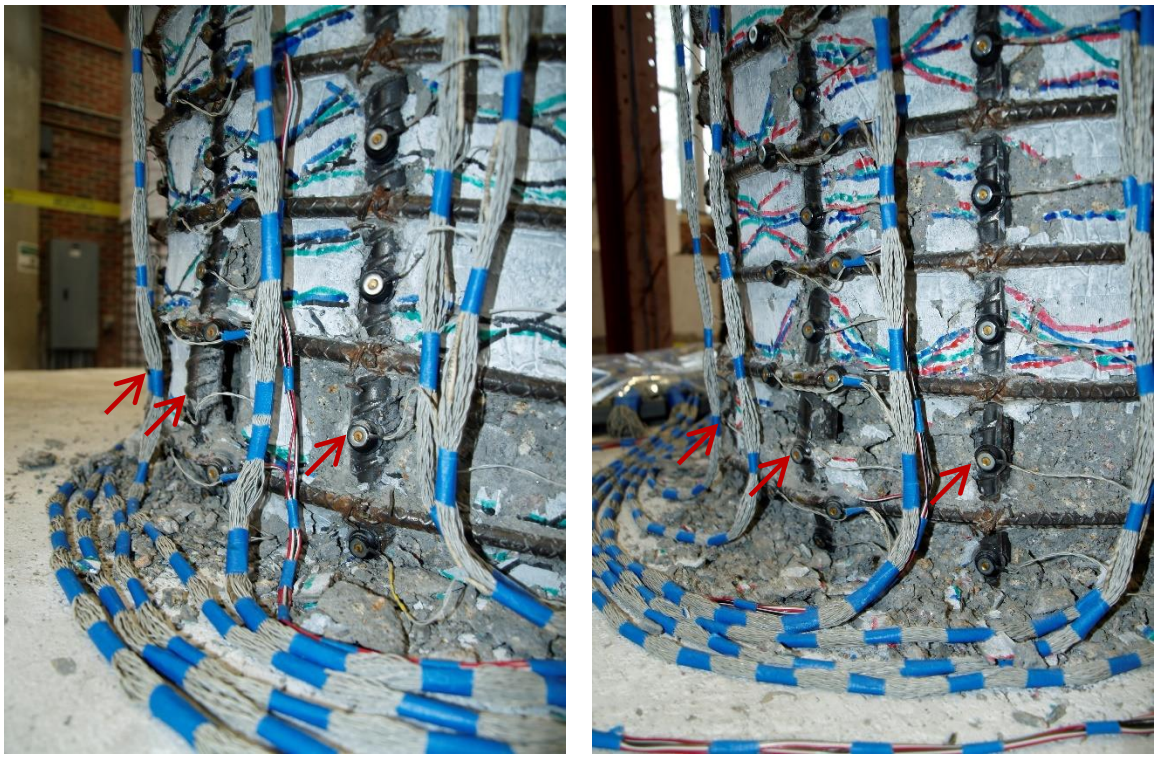

Figure 6-35. Test 3: Buckling of (Left) Bar NNW during $\mu_{\Delta 5}^{+1y} = 7.52$" and (Right) Bars SSW and SSE during $\mu_{\Delta 5}^{-1y} = -7.52$"

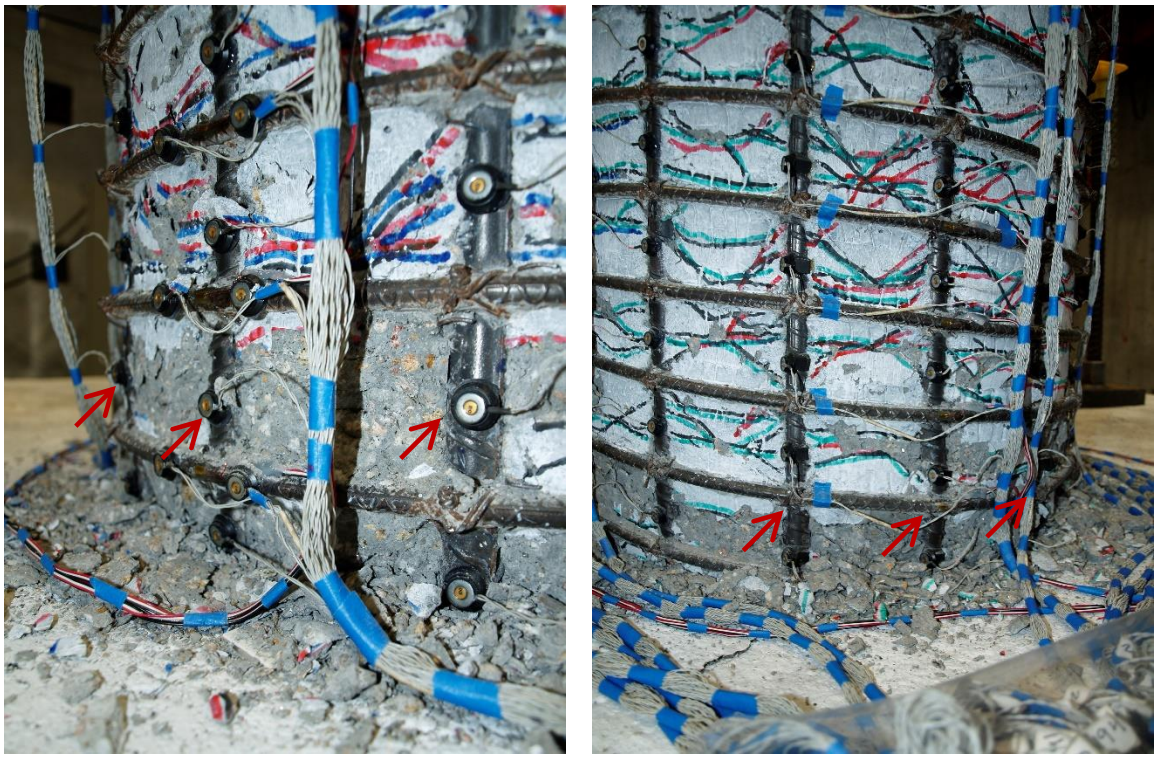

Figure 6-36. Test 3: Buckling of Bars (Left) E, ENE, & ESE at $\mu_{\Delta 5}^{+1x} = 7.53"$ and (Right) W, WNW, & WSW at $\mu_{\Delta 5}^{-1x} = -7.52"$

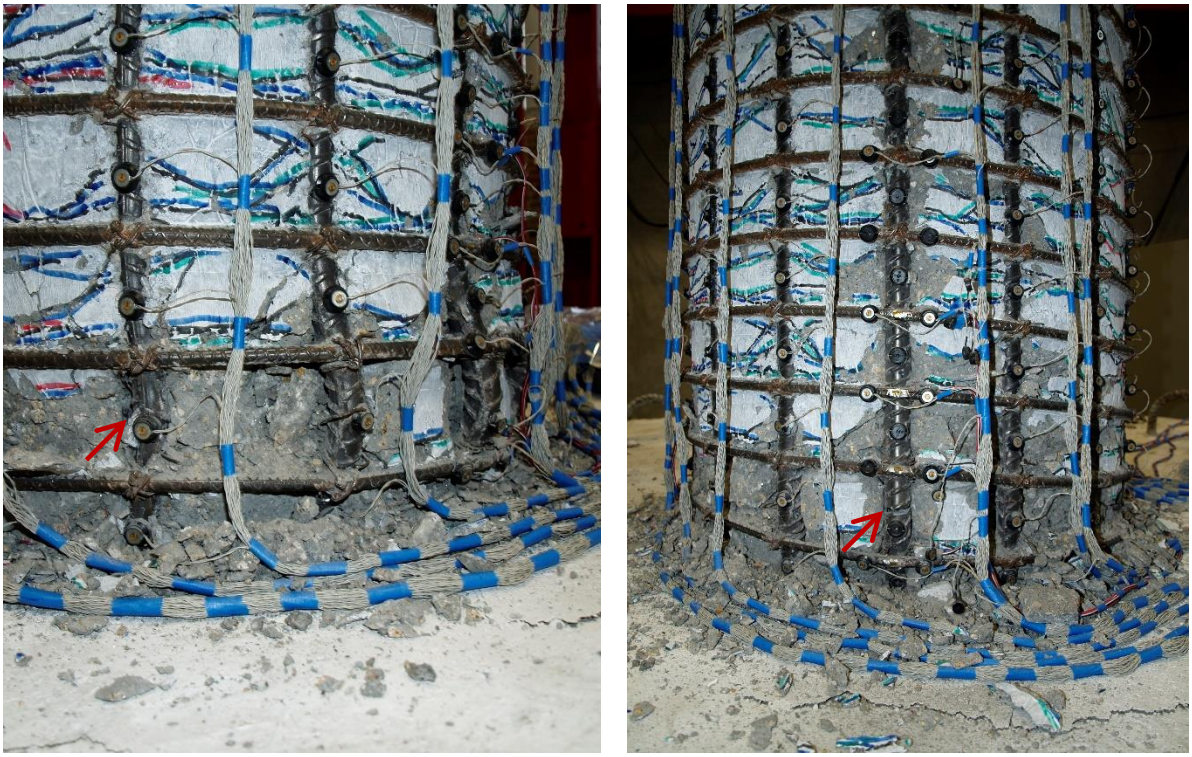

Figure 6-37. Test 3: (Left) Buckling of Bars NE & NW at $\mu_{\Delta 5}^{+2y} = 7.50"$ and (Right) Fracture of Bar N at $-3.71"$ during $\mu_{\Delta 5}^{-2y}$

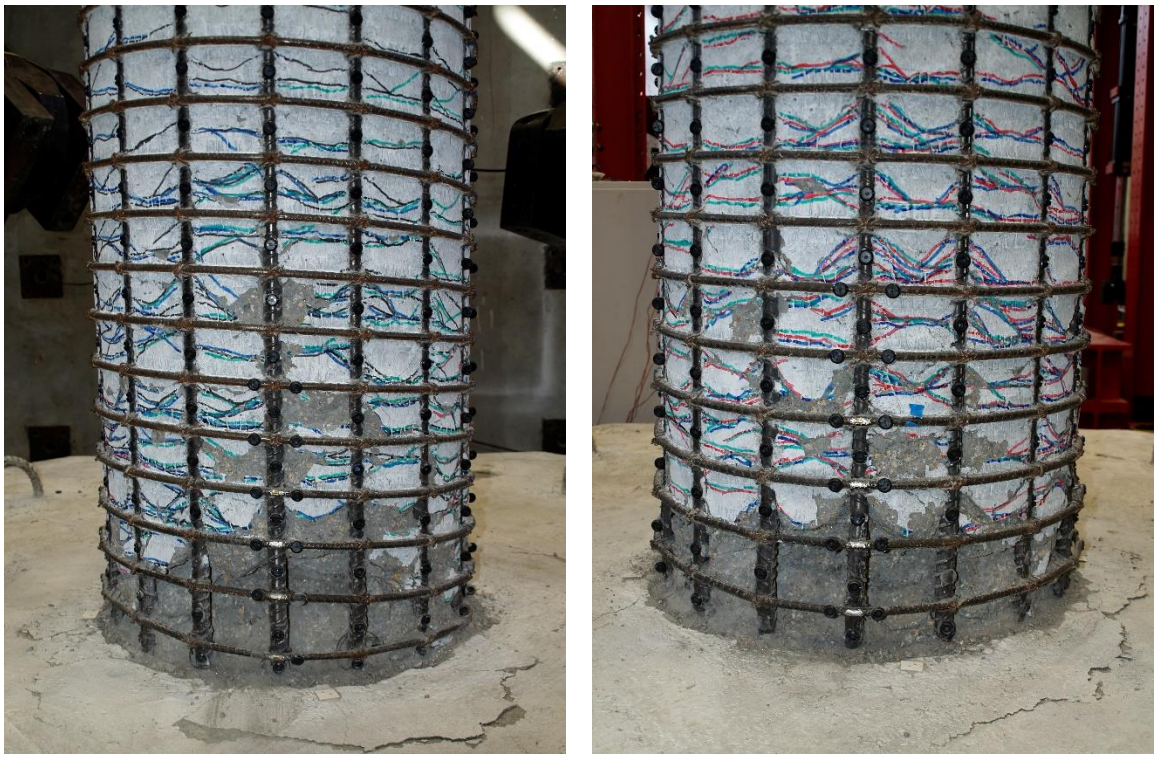

Figure 6-38. Test 3: (Left North and (Right) South Sides of the Specimen after Removal of Instrumentation

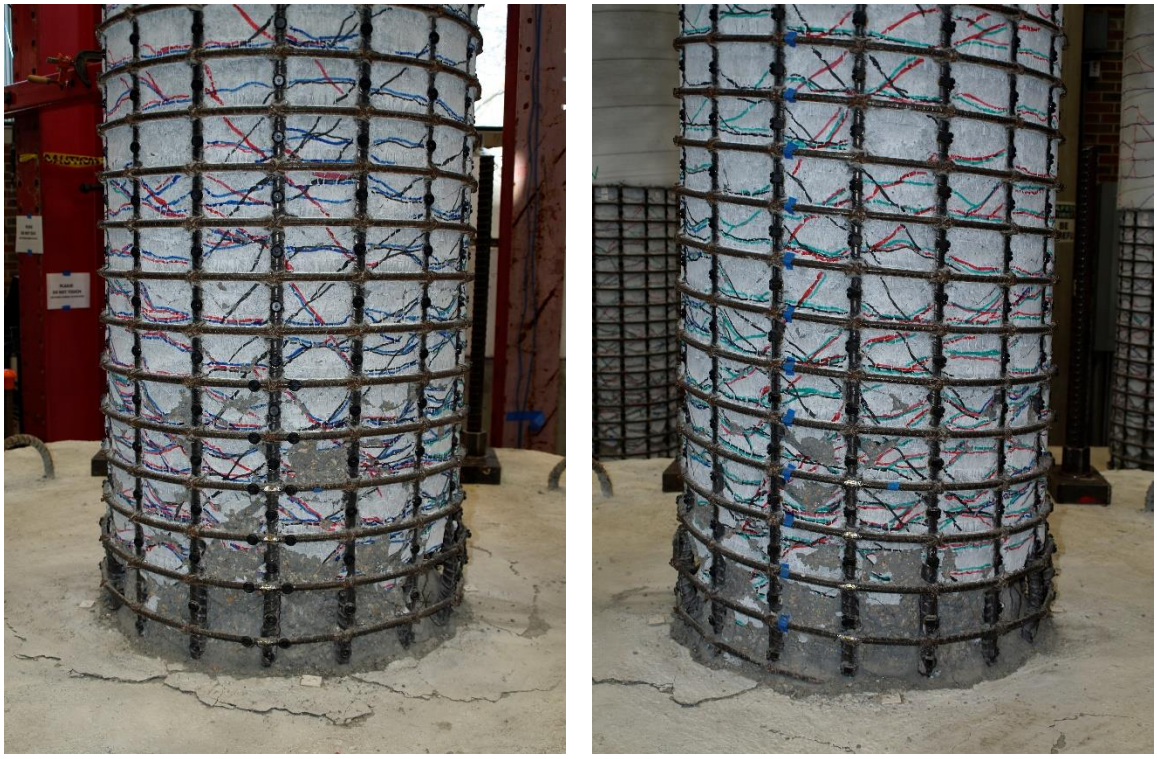

Figure 6-39. Test 3: (Left) East and (Right) West Sides of the Specimen after Removal of Instrumentation

Test 3 - Strain Data Analysis

North and South Bar Strains

Vertical strain profiles for North and South reinforcement during y-direction cycles are shown in Figure 6-40 and Figure 6-41. Strains in the lowest four spiral layers during compressive y-direction cycles on the North and South sides of the specimen appear in Figure 6-42 and Figure 6-43. The relationship between strain and displacement for either peak tensile or peak compressive gauge lengths appear in Figure 6-44 through Figure 6-47. These figures contain monotonic moment curvature predictions for respective plastic hinge methods. PCK (2007) Lp refers to the (Priestley, Calvi and Kowalsky 2007) plastic hinge method, GN15 Tension/Compression Lpr refers to the (Goodnight, Kowalsky and Nau 2015a) unidirectional modified plastic hinge method, TX Adjusted Lpr and Lsp refer to using the measured extent of plasticity and average equivalent strain penetration length from this specific test, and New Equations refers to a new bidirectional plastic hinge method which was created based on this study. Details of the new plastic hinge method appear in a later chapter of this report.

The spiral strain gauge hysteresis for the first and second layers above the footing on the North side of the specimen are shown in Figure 6-49 and Figure 6-50. The first spiral layer goes off scale during $\mu_{\Delta 4}^{+1y} = 6.01$", even though bar N remained visibly straight, as shown in Figure 6-29. The second North spiral layer above the footing went off scale during $\mu_{\Delta 4}^{+2y} = 6.04$" as bar N and NNE visibly buckled, see Figure 6-30. The visual observation bar buckling was confirmed upon inspection of the North longitudinal bar strain hysteresis in Figure 6-48.

The spiral strain gauge hysteresis for the first and second layers above the footing on the South side of the specimen appear in Figure 6-52 and Figure 6-53. Both spiral layers go off scale during $\mu_{\Delta 4}^{-2y} = -6.03$" as the extreme fiber South bar S buckled, see Figure 6-31. The visual observation bar buckling was confirmed upon inspection of the South longitudinal bar strain hysteresis in Figure 6-51.

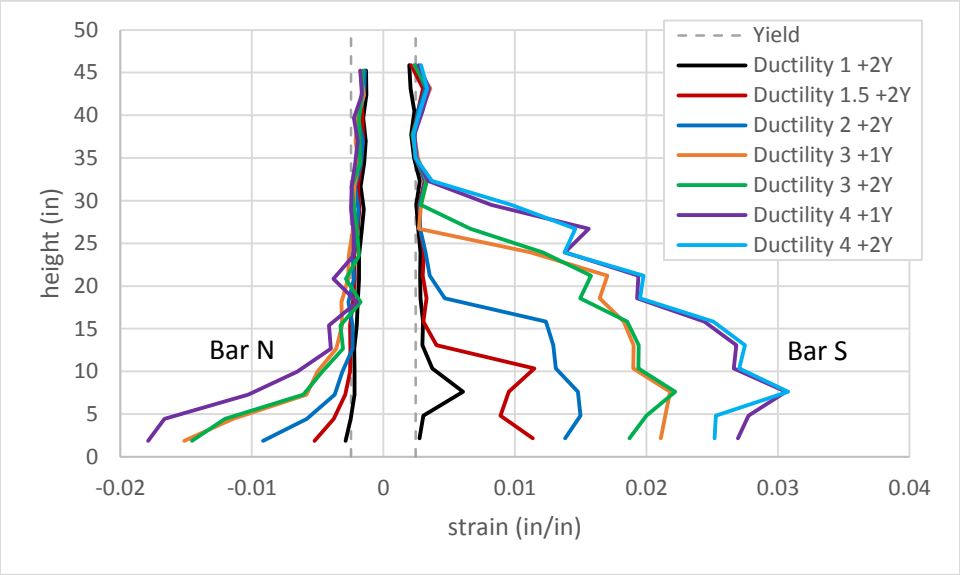

Figure 6-40. Test 3: Vertical Strain Profiles for Loading in the +Y-direction

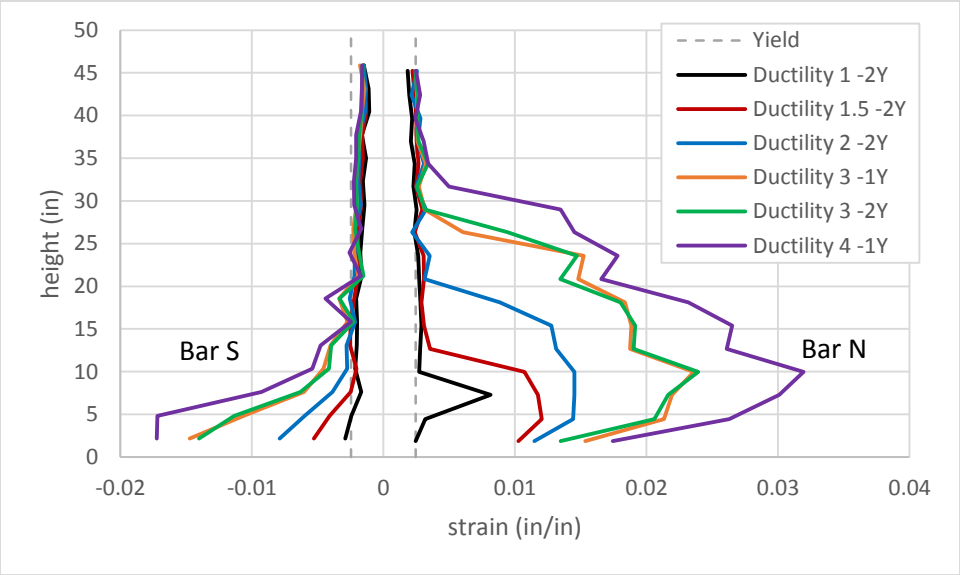

Figure 6-41. Test 3: Vertical Strain Profiles for Loading in the -Y-direction

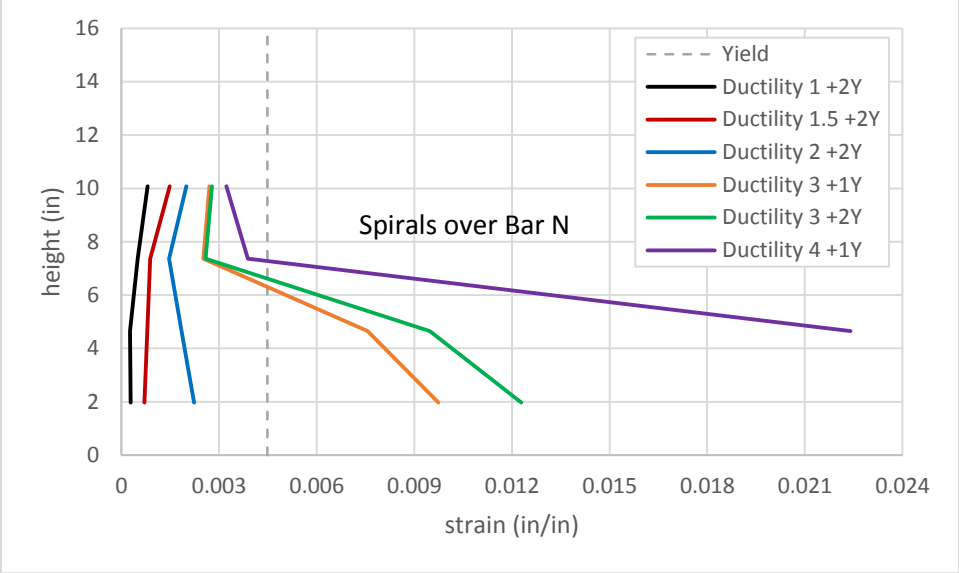

Figure 6-42. Test 3: Spiral Strains Measured Over the North Extreme Fiber Bar during +Y Cycles

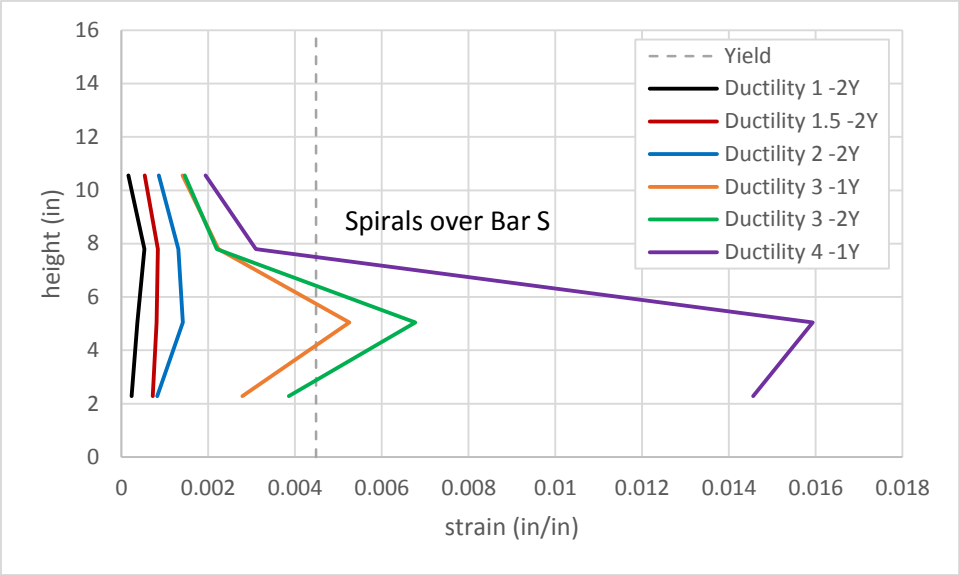

Figure 6-43. Test 3: Spiral Strains Measured Over the South Extreme Fiber Bar during –Y Cycles

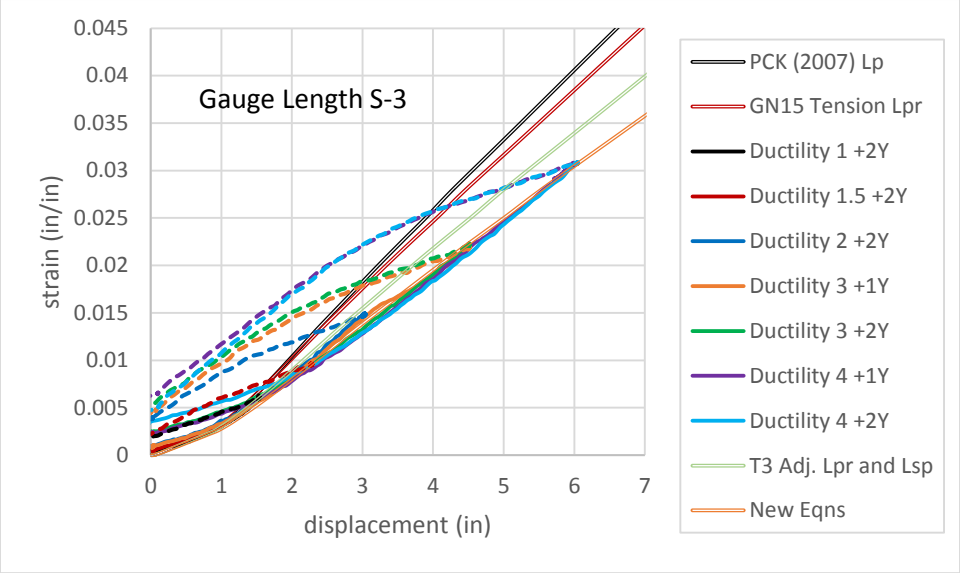

Figure 6-44. Test 3: Tension Strain-Disp. for Bar S (Gauge Length 3 Centered 7.62" above the Footing)

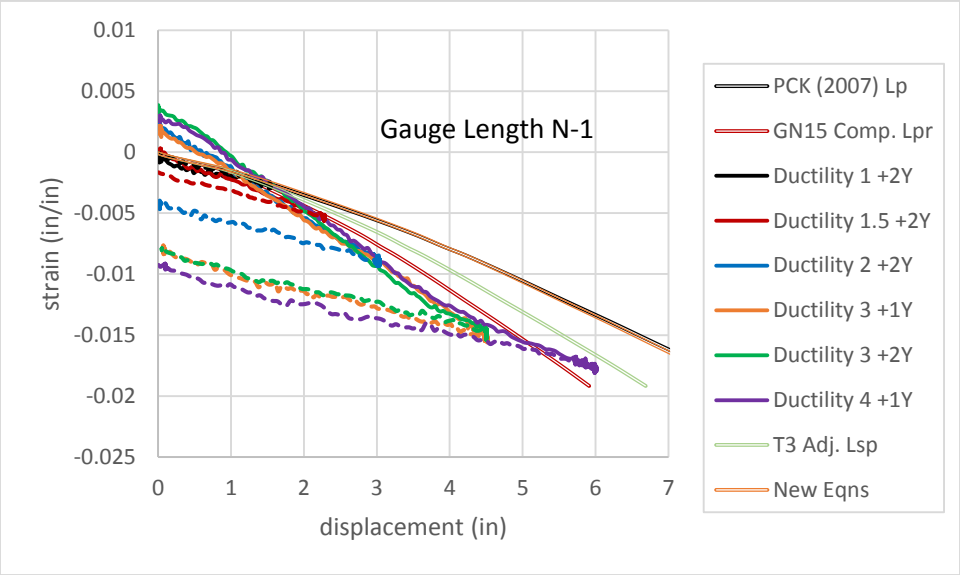

Figure 6-45. Test 3: Compression Strain-Disp. for Bar N (Gauge Length 1 Centered 1.86" above the Footing)

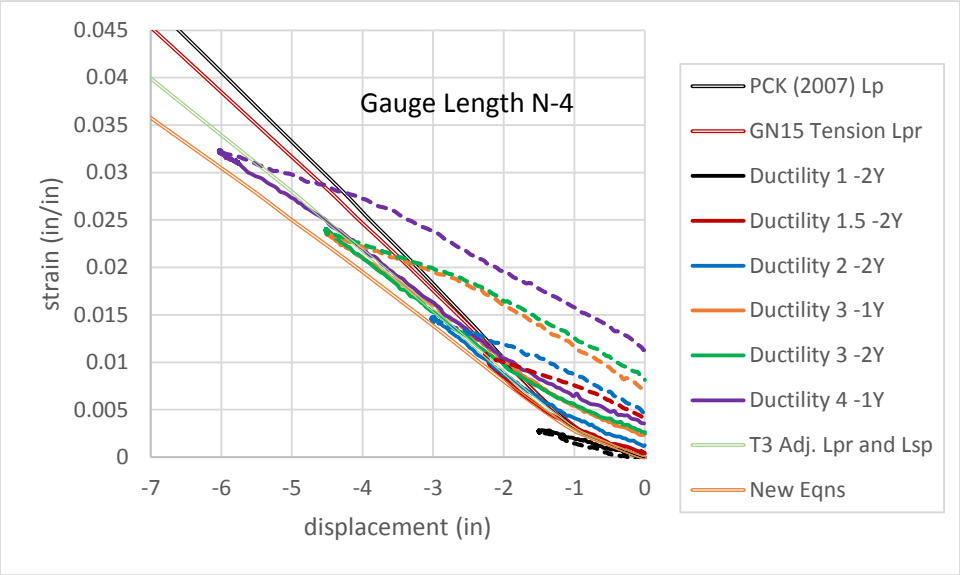

Figure 6-46. Test 3: Tension Strain-Disp. for Bar N (Gauge Length 4 Centered 9.96" above the Footing)

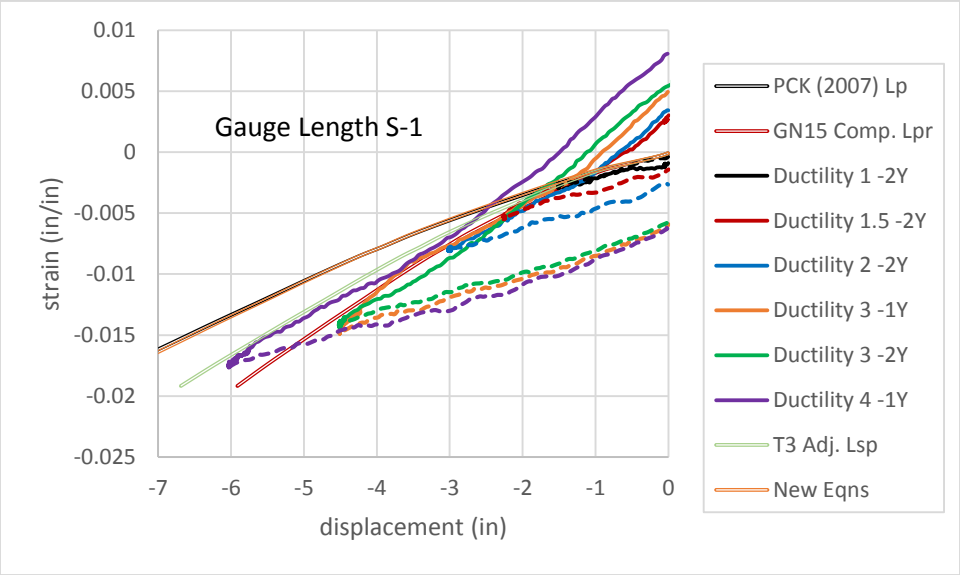

Figure 6-47. Test 3: Compression Strain-Disp. for Bar S (Gauge Length 1 Centered 2.15" above the Footing)

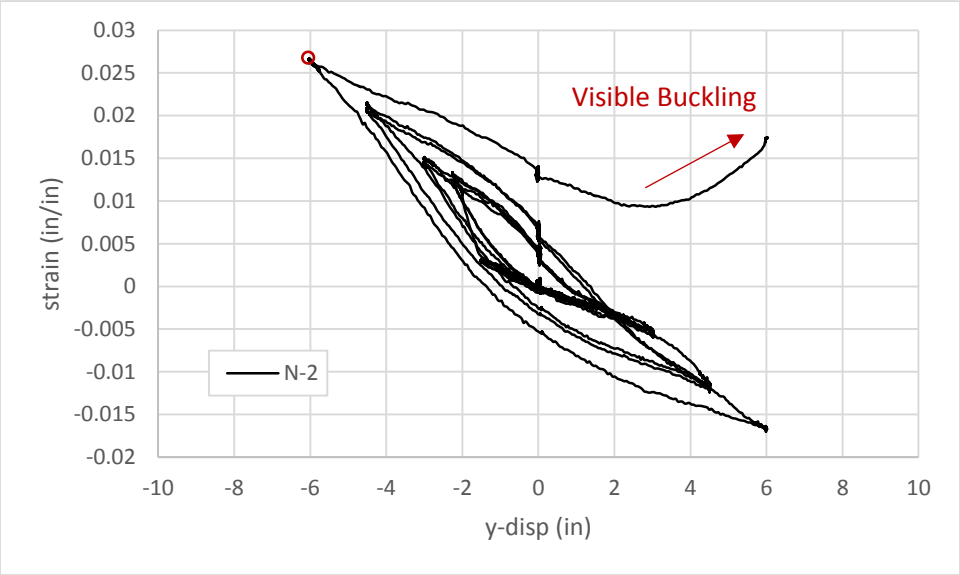

Figure 6-48. Test 3: Strain Hysteresis over the North Buckled Bar (Gauge Length 2 Centered 4.43" above the Footing)

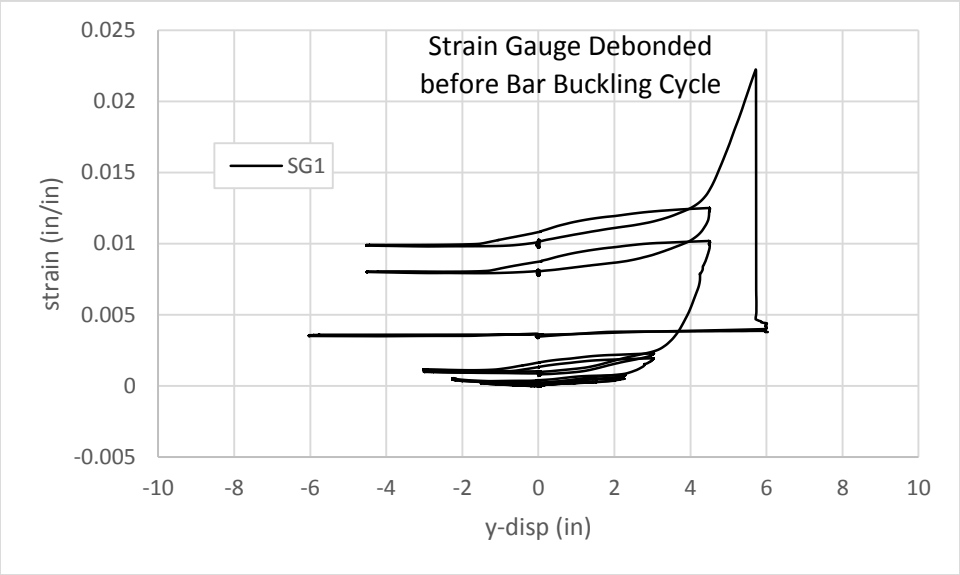

Figure 6-49. Test 3: North Spiral Strain Gauge Hysteresis for the First Layer above the Footing

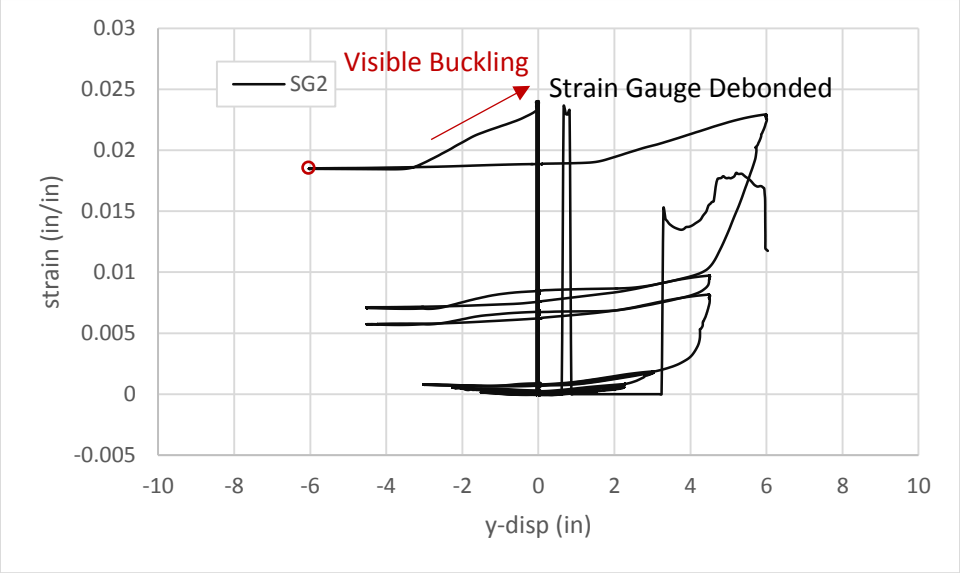

Figure 6-50. Test 3: North Spiral Strain Gauge Hysteresis for the Second Layer above the Footing

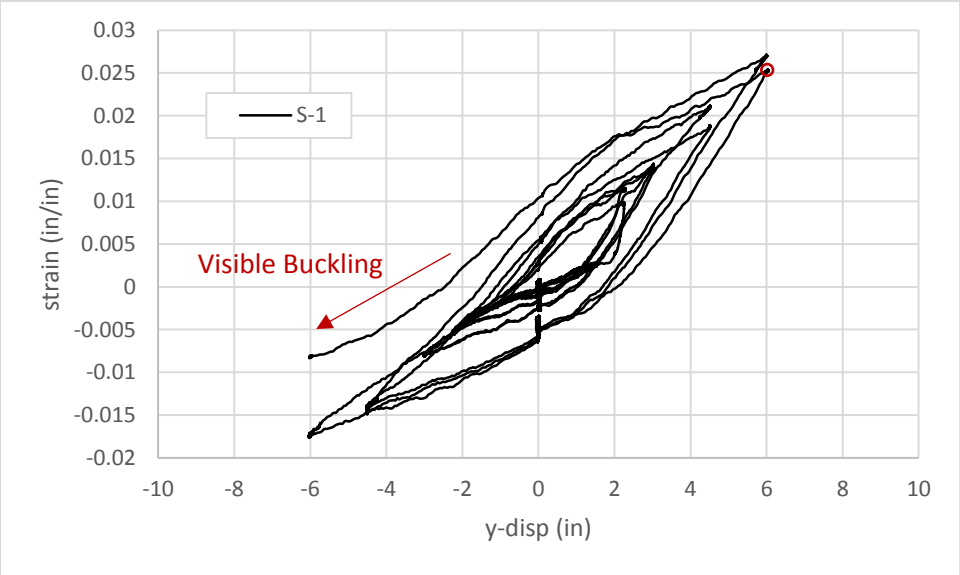

Figure 6-51. Test 3: Strain Hysteresis over the South Buckled Bar (Gauge Length 1 Centered 2.15" above the Footing)

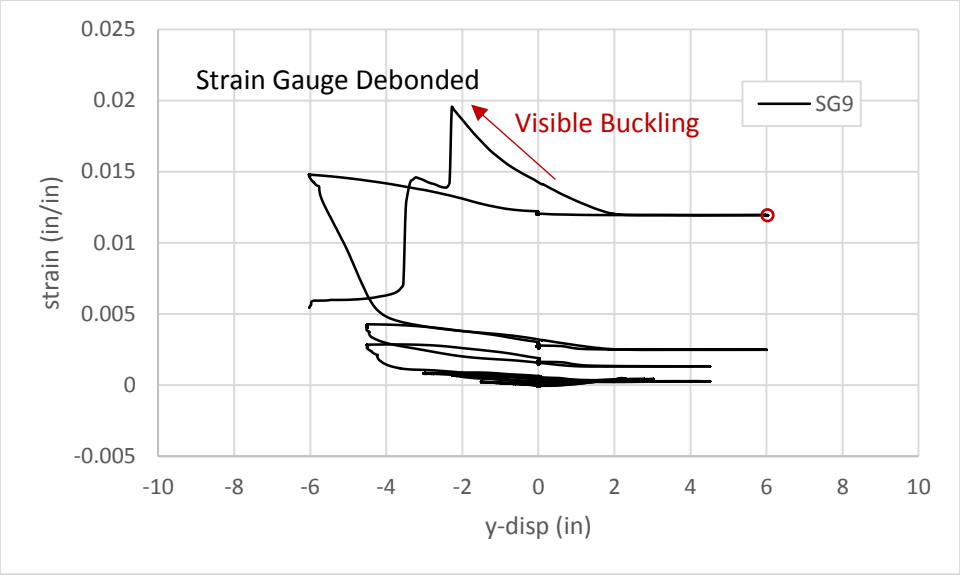

Figure 6-52. Test 3: South Spiral Strain Gauge Hysteresis for the First Layer above the Footing

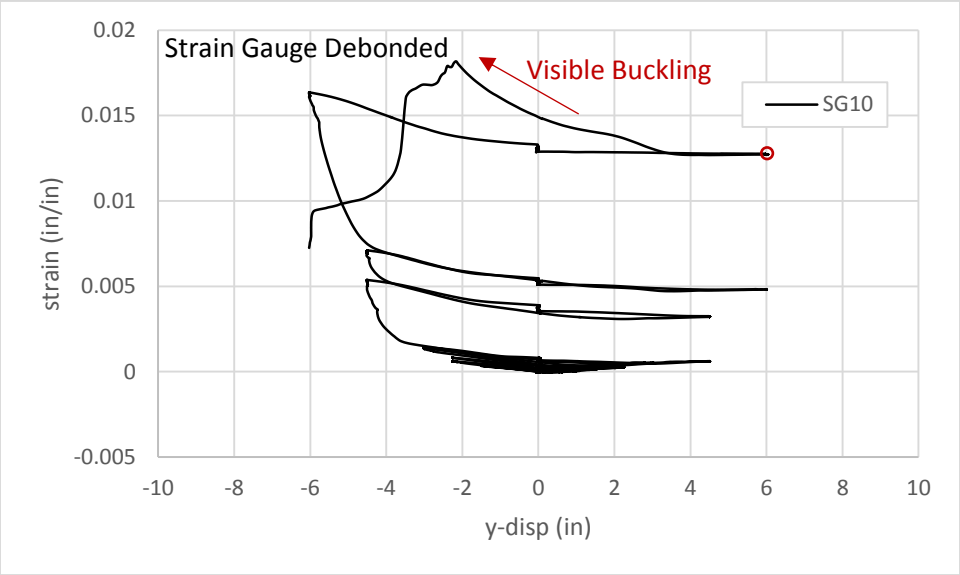

Figure 6-53. Test 3: South Spiral Strain Gauge Hysteresis for the Second Layer above the Footing

East and West Bar Strains

Vertical strain profiles for East and West reinforcement during x-direction cycles are shown in Figure 6-54 and Figure 6-55. Strains in the lowest four spiral layers during compressive x-direction cycles on the East and West sides of the specimen appear in Figure 6-56 and Figure 6-57. The relationship between strain and displacement for either peak tensile or peak compressive gauge lengths appear in Figure 6-58 through Figure 6-61. These figures contain monotonic moment curvature predictions for respective plastic hinge methods. PCK (2007) Lp refers to the (Priestley, Calvi and Kowalsky 2007) plastic hinge method, GN15 Tension/Compression Lpr refers to the (Goodnight, Kowalsky and Nau 2015a) unidirectional modified plastic hinge method, TX Adjusted Lpr and Lsp refer to using the measured extent of plasticity and average equivalent strain penetration length from this specific test, and New Equations refers to a new bidirectional plastic hinge method which was created based on this study. Details of the new plastic hinge method appear in a later chapter of this report.

The spiral strain gauge hysteresis for the first and second layers above the footing on the East side of the specimen appear in Figure 6-63 and Figure 6-64. Both spiral layers go off scale during $\mu_{\Delta 5}^{+1x} = 7.53"$ as the E, ESE, and ENE bars buckled, see Figure 6-36. The visual observation of bar buckling was confirmed upon inspection of the East longitudinal bar strain hysteresis in Figure 6-62. Closer inspection reveals that measurable outward deformation occurred during compressive cycle preceding that which produced visible bar buckling.

The spiral strain gauge hysteresis for the first layers above the footing on the West side of the specimen appears in Figure 6-66. The first spiral layer goes off scale during $\mu_{\Delta 5}^{-1x} = -7.52"$ as bars W, WNW, and WSW buckled, see Figure 6-36. The visual observation of bar buckling was confirmed upon inspection of the West longitudinal bar strain hysteresis in Figure 6-65. Again, measurable deformation occurred during the compressive cycle preceding visible bar buckling.

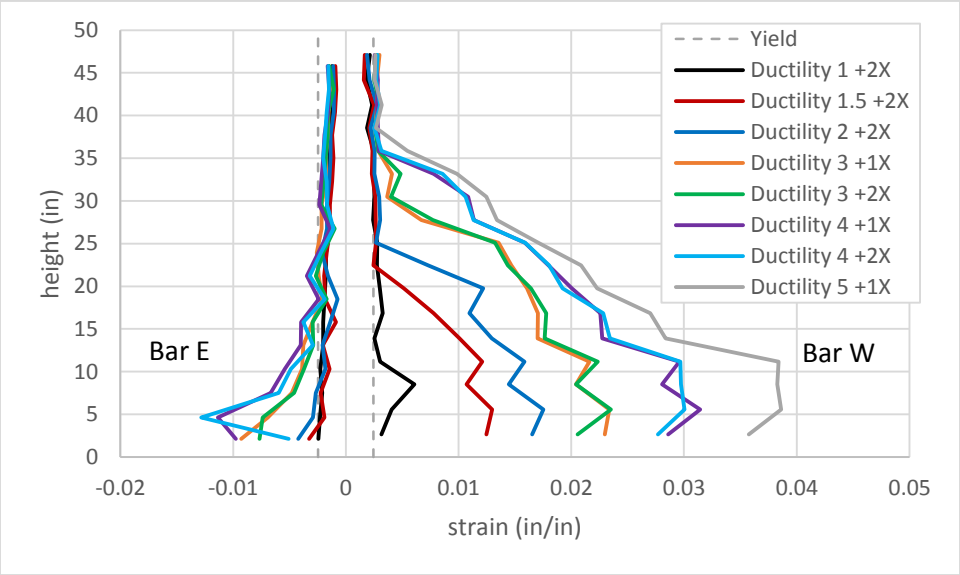

Figure 6-54. Test 3: Vertical Strain Profiles for Loading in the +X-direction

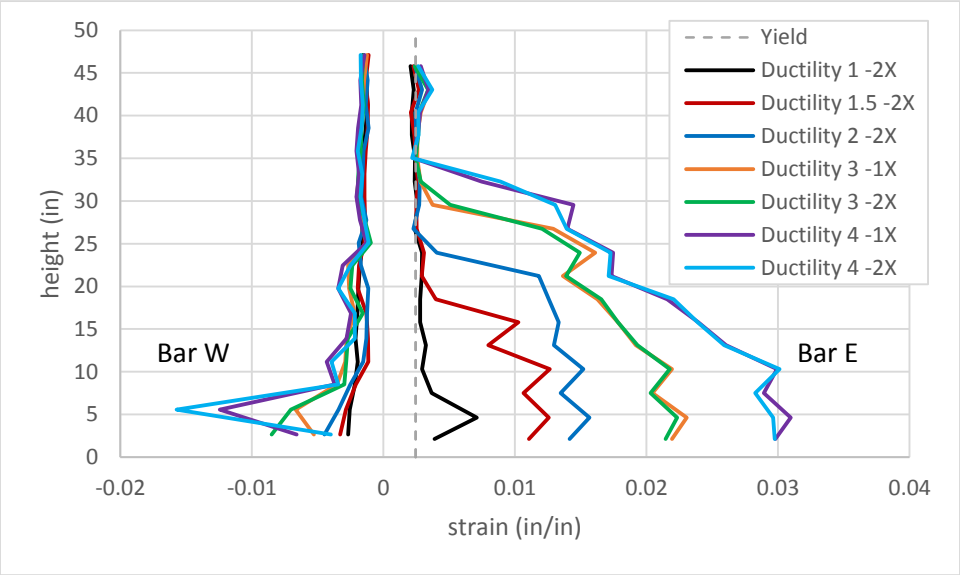

Figure 6-55. Test 3: Vertical Strain Profiles for Loading in the -X-direction

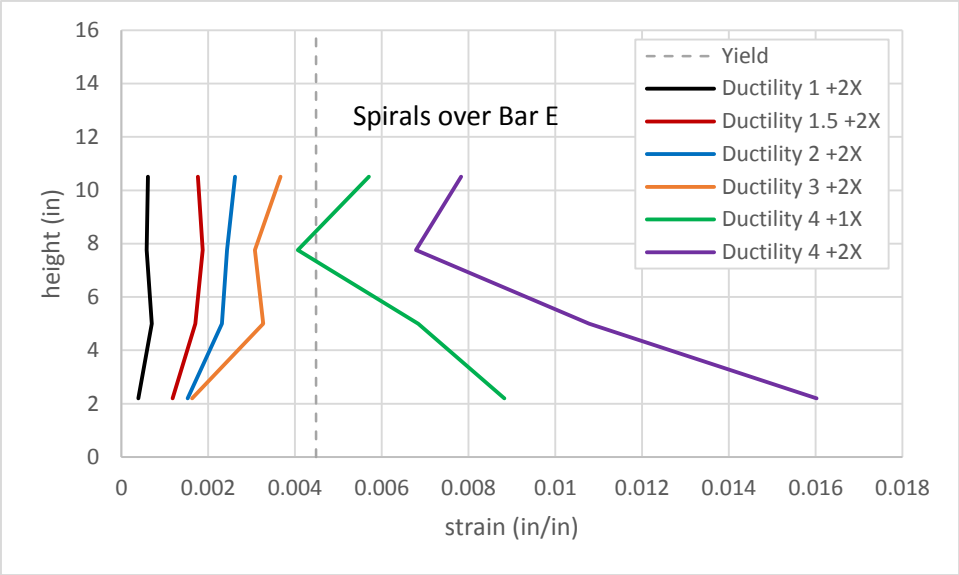

Figure 6-56. Test 3: Spiral Strains Measured Over the East Extreme Fiber Bar during +X Cycles

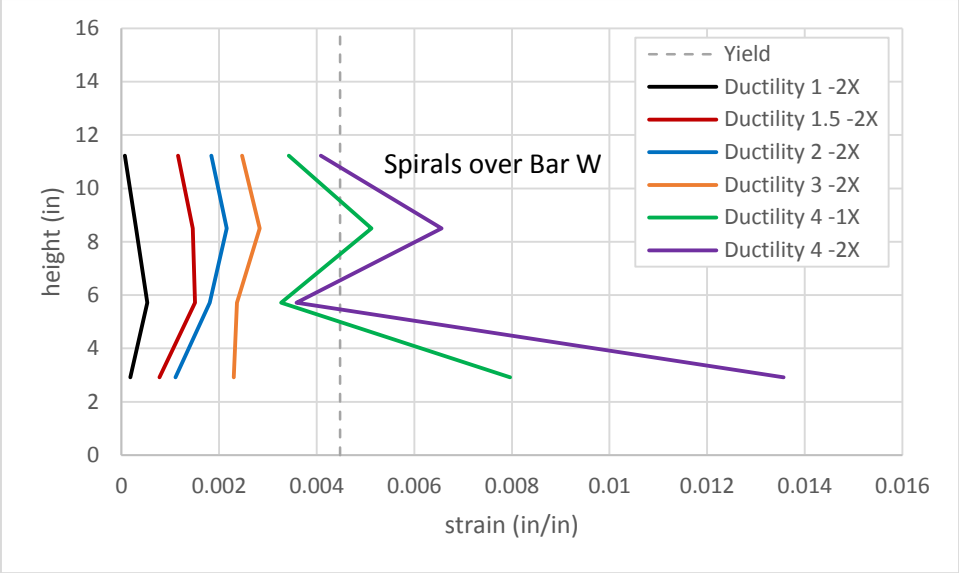

Figure 6-57. Test 3: Spiral Strains Measured Over the West Extreme Fiber Bar during -X Cycles

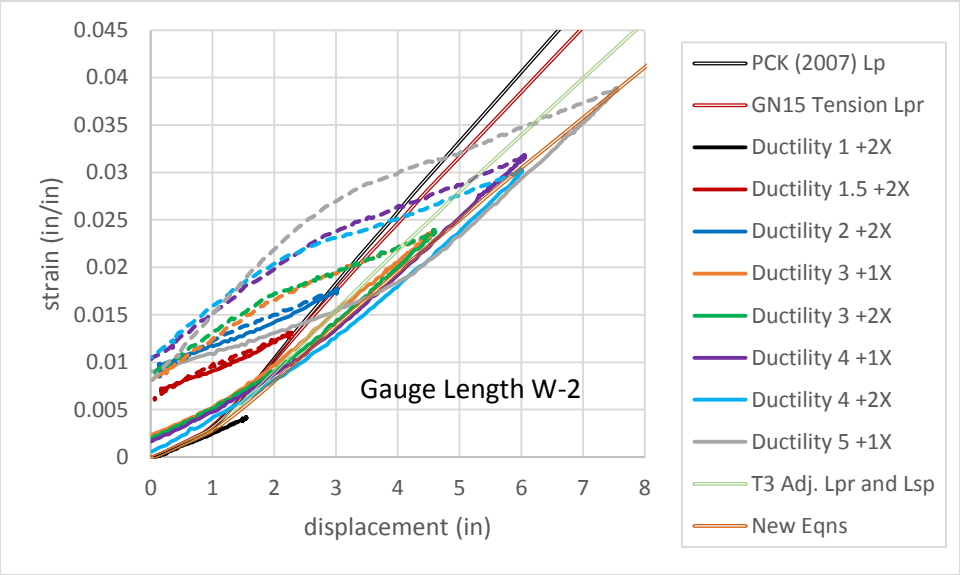

Figure 6-58. Test 3: Tension Strain-Disp. for Bar W (Gauge Length 2 Centered 5.58" above the Footing)

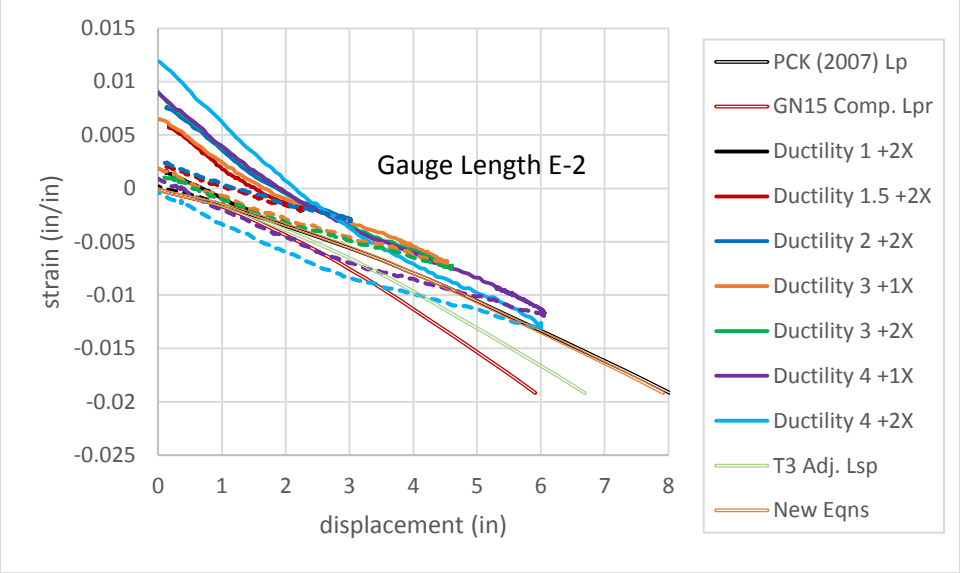

Figure 6-59. Test 3: Compression Strain-Disp. for Bar E (Gauge Length 2 Centered 4.65" above the Footing)

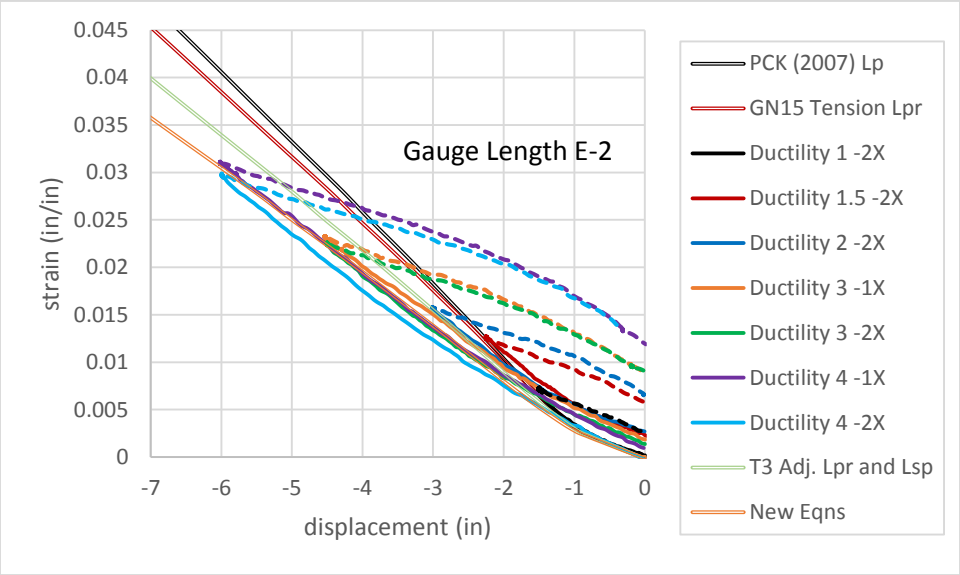

Figure 6-60. Test 3: Tension Strain-Disp. for Bar E (Gauge Length 2 Centered 4.65" above the Footing)

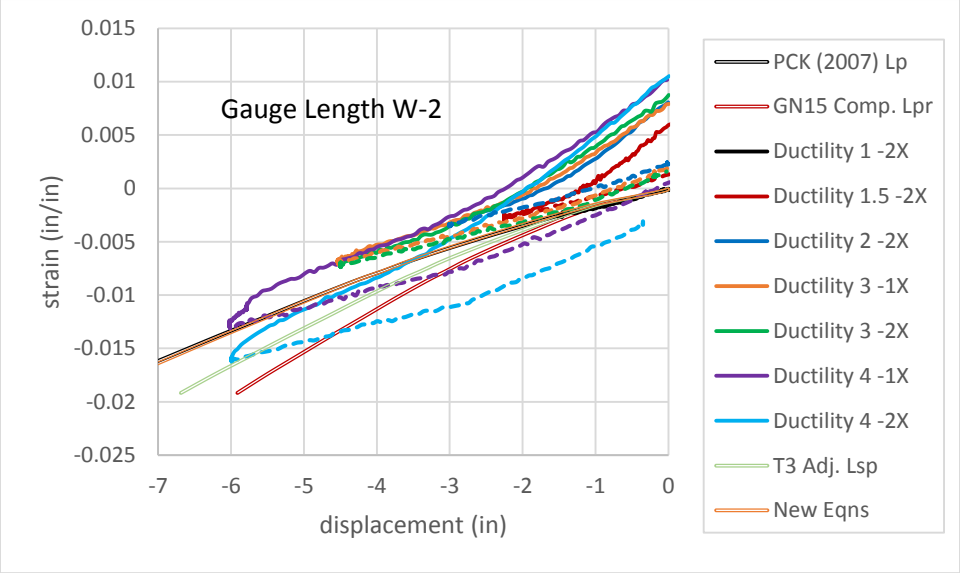

Figure 6-61. Test 3: Compression Strain-Disp. for Bar W (Gauge Length 2 Centered 5.58" above the Footing)

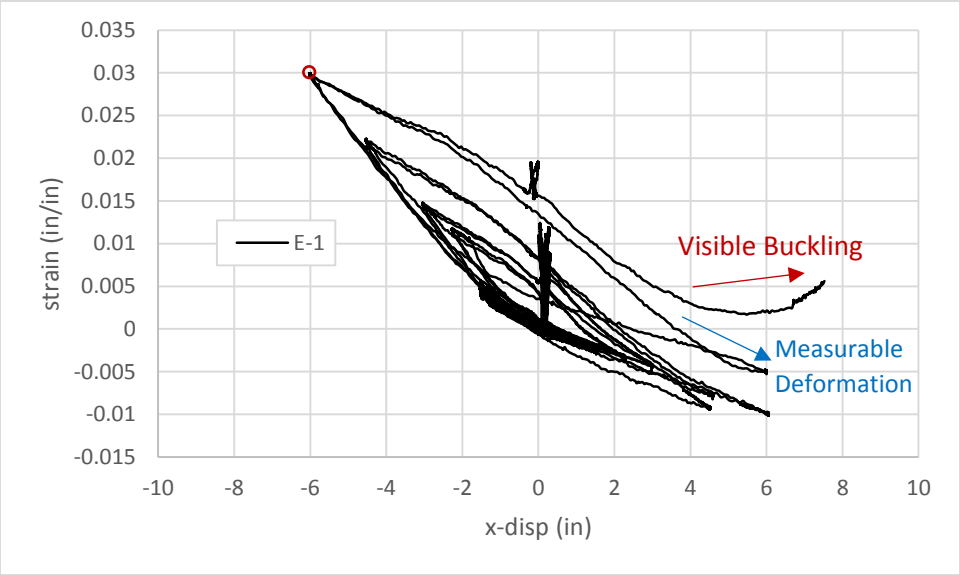

Figure 6-62. Test 3: Strain Hysteresis over the East Buckled Bar (Gauge Length 1 Centered 2.11" above the Footing)

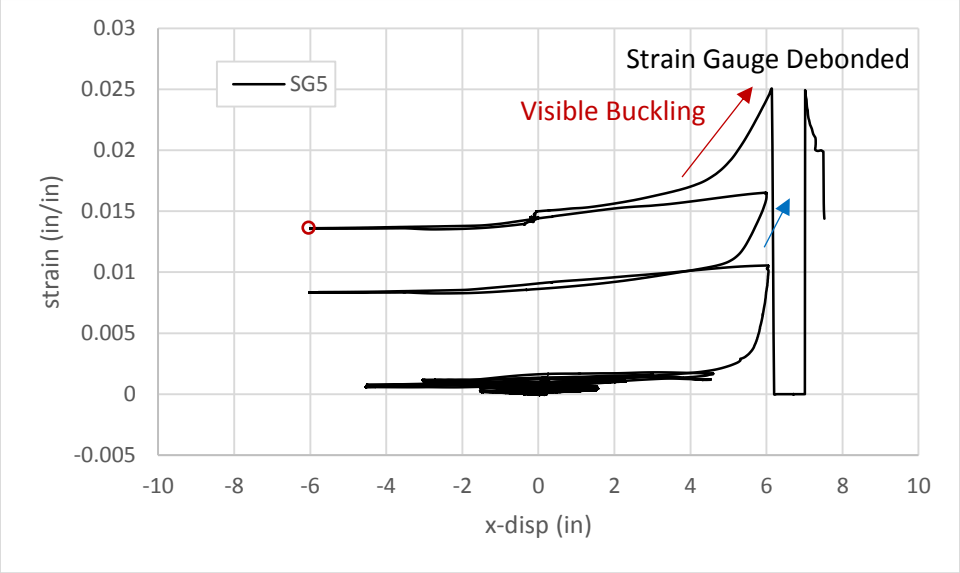

Figure 6-63. Test 3: East Spiral Strain Gauge Hysteresis for the First Layer above the Footing

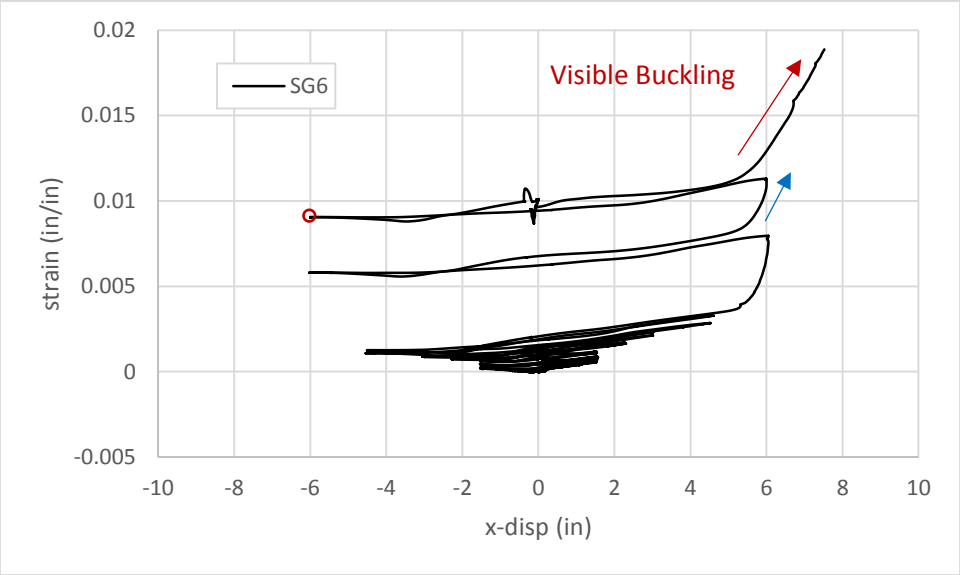

Figure 6-64. Test 3: East Spiral Strain Gauge Hysteresis for the Second Layer above the Footing

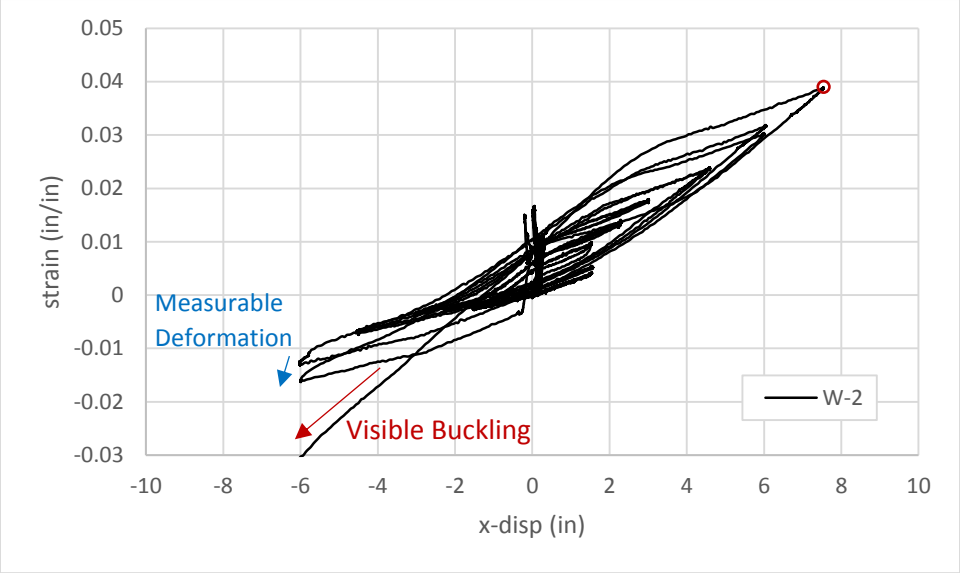

Figure 6-65. Test 3: Strain Hysteresis over the West Buckled Bar (Gauge Length 2 Centered 5.58" above the Footing)

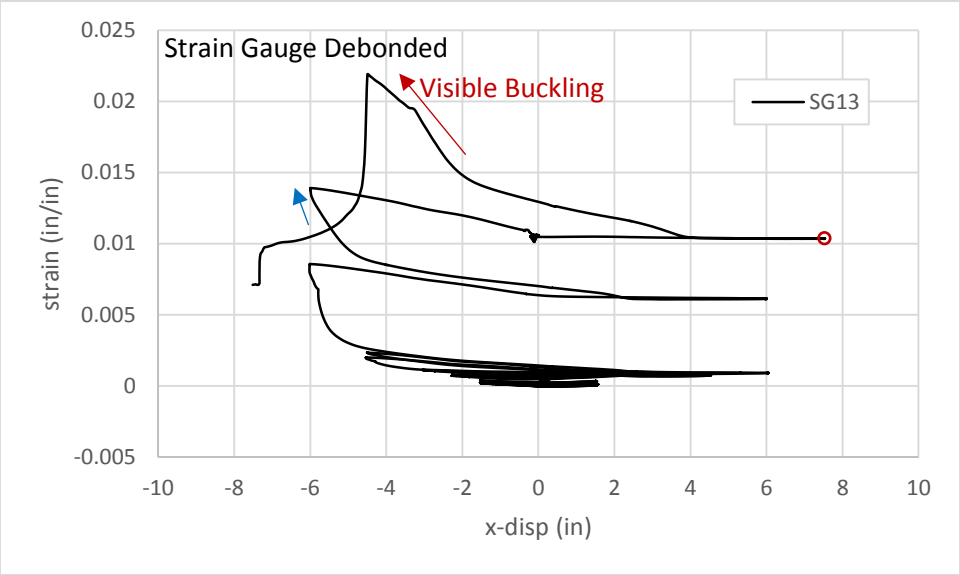

Figure 6-66. Test 3: West Spiral Strain Gauge Hysteresis for the First Layer above the Footing

Test 3 - Curvature and Strain Penetration Data

Curvature and stain penetration data for Test 3 is presented in the following section. The methods in which this data was generated are outlined in the summary for Test 1. Sample cross section curvature profiles are shown in Figure 6-67 and Figure 6-68. Vertical curvature profiles for respective loading directions appear in Figure 6-69 through Figure 6-73. Fixed-end rotations attributable to strain penetration of longitudinal reinforcement into the footing are shown in Figure 6-74 through Figure 6-76. Comparison of the measured displacements to those obtained via integration of the measured curvature profiles and extrapolation of the fixed-end rotation to the center of the applied lateral load are shown in Figure 6-77 and Figure 6-78.

The measured extent of plasticity is compared to design recommendations for the tensile triangular plastic hinge length in Figure 6-79. GN15 refers to the (Goodnight, Kowalsky and Nau 2015a) unidirectional tensile hinge length while New Equations refers to a new bidirectional plastic hinge method which was created based on this study. Details of the new plastic hinge method appear in a later chapter of this report. The measured equivalent strain penetration lengths are compared to design recommendations in Figure 6-80. GN15 refers to the (Goodnight, Kowalsky and Nau 2015a) unidirectional Lsp while PCK (2007) refers to the (Priestley, Calvi and Kowalsky 2007) definition of Lsp. Finally, the measured hysteretic response is compared to monotonic predictions in Figure 6-81 through Figure 6-84. The larger elastic displacements are not observed when sectional response is considered.

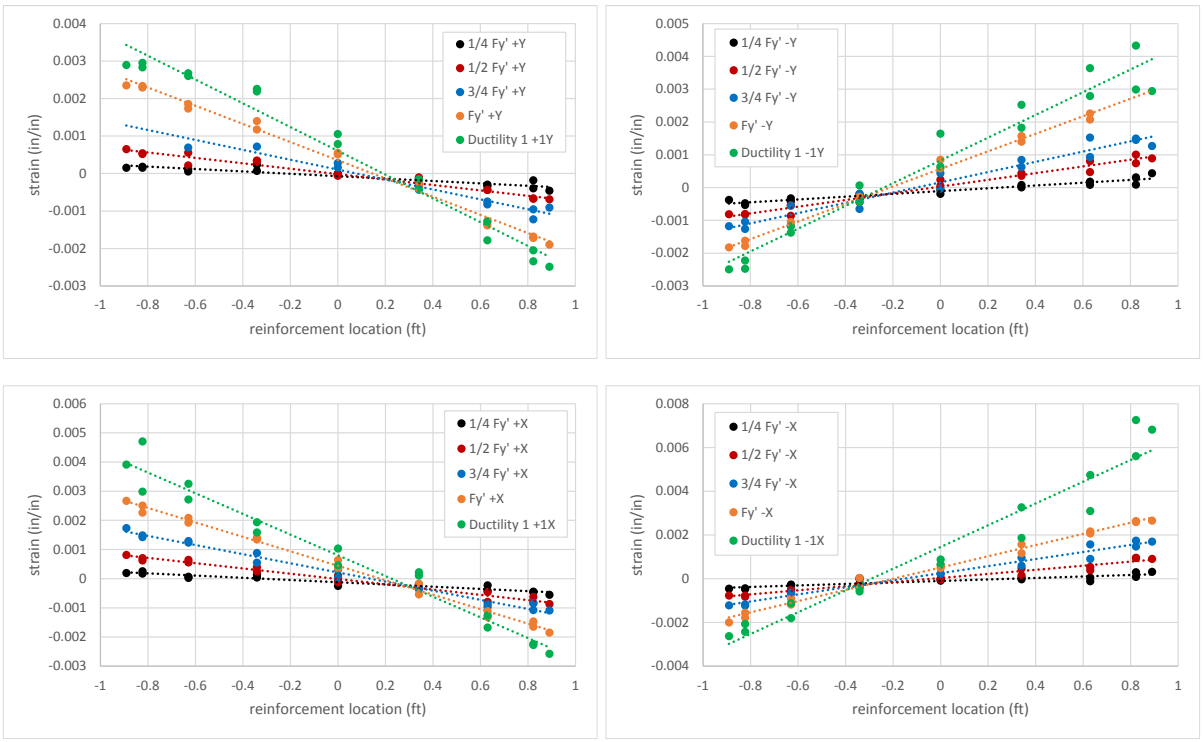

Figure 6-67. Test 3: Elastic Curvature Profiles for the Second Instrumented Section above the Footing

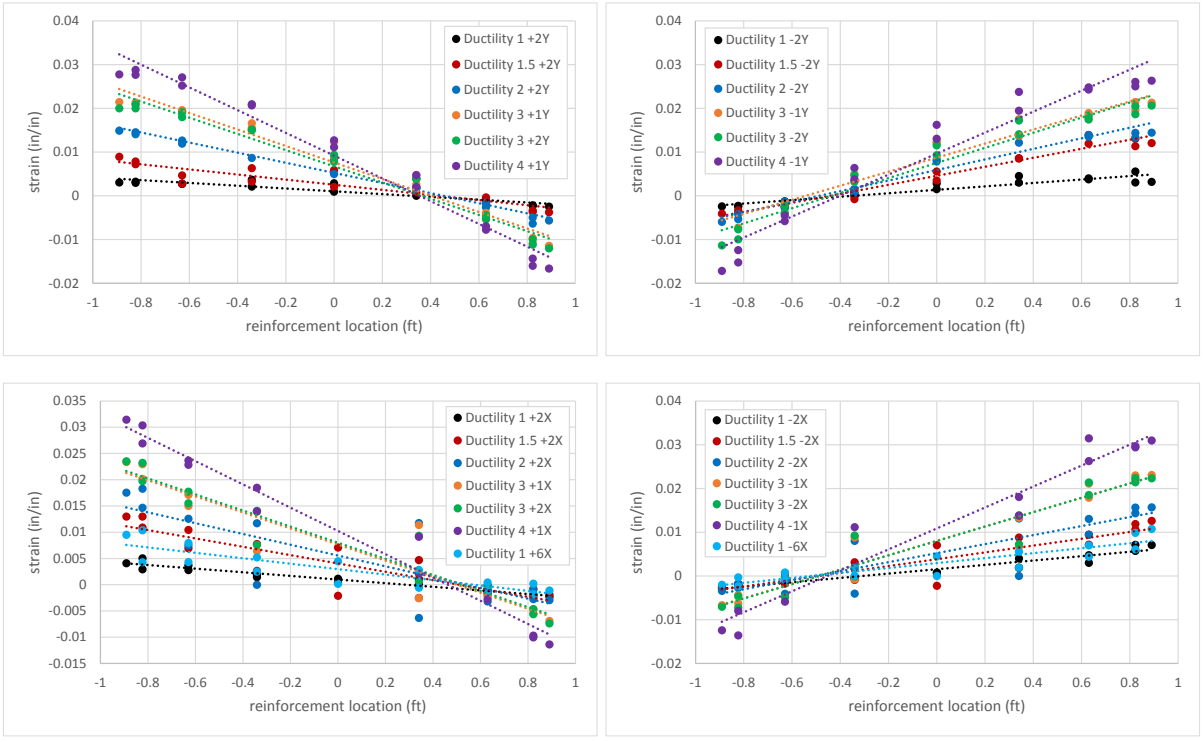

Figure 6-68. Test 3: Curvature Profiles for the Second Instrumented Section above the Footing

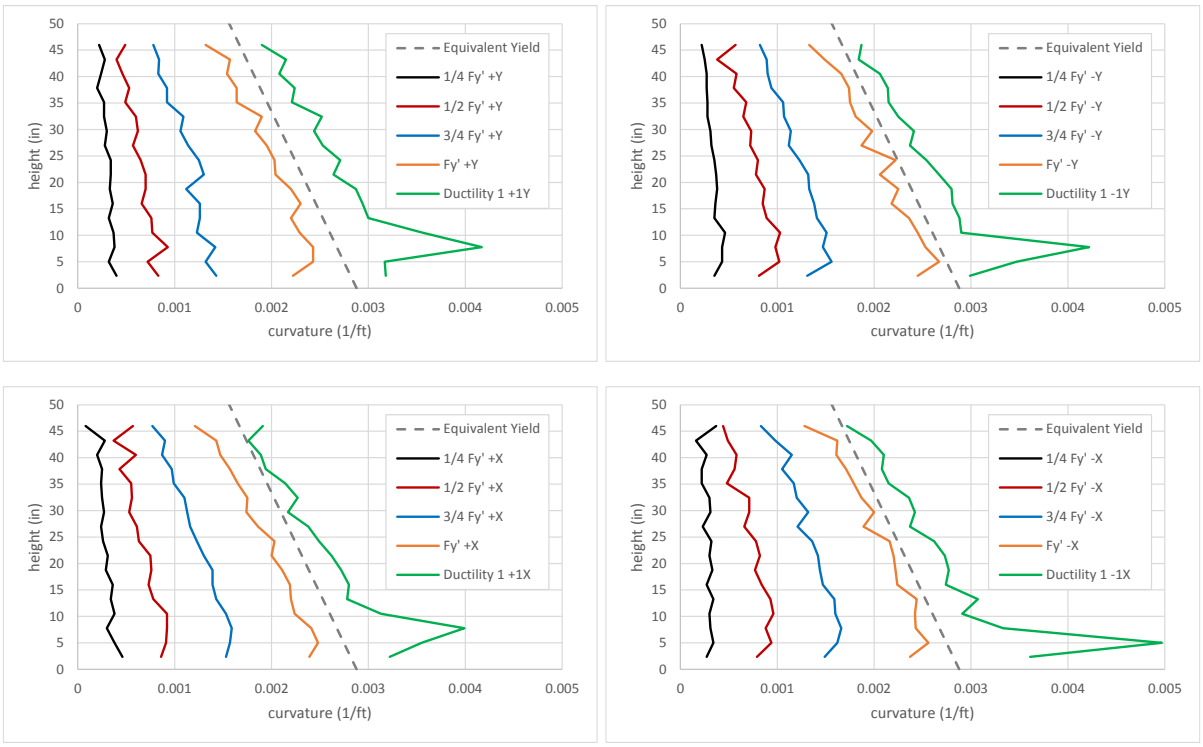

Figure 6-69. Test 3: Elastic Vertical Curvature Profiles

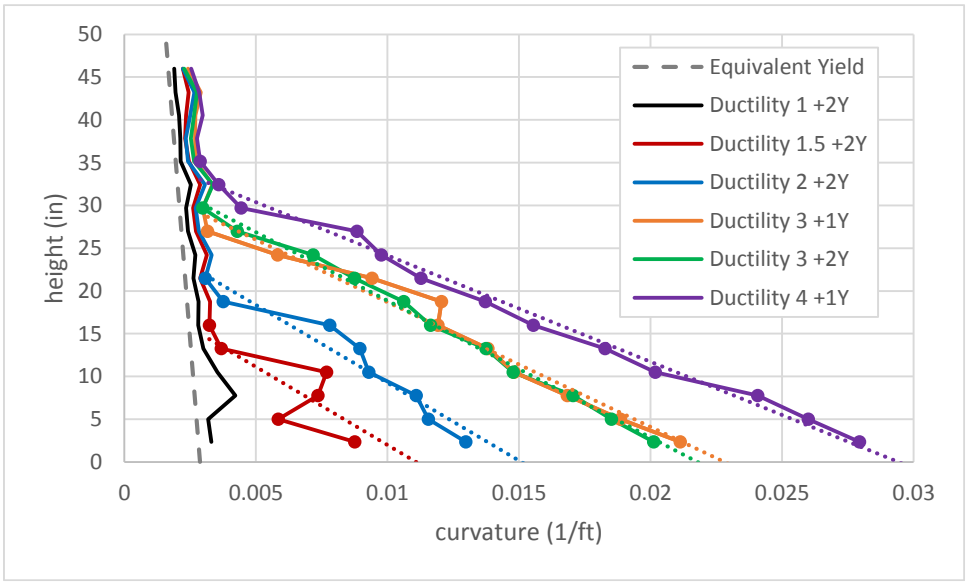

Figure 6-70. Test 3: Vertical Curvature Profiles for Loading in the +Y-direction

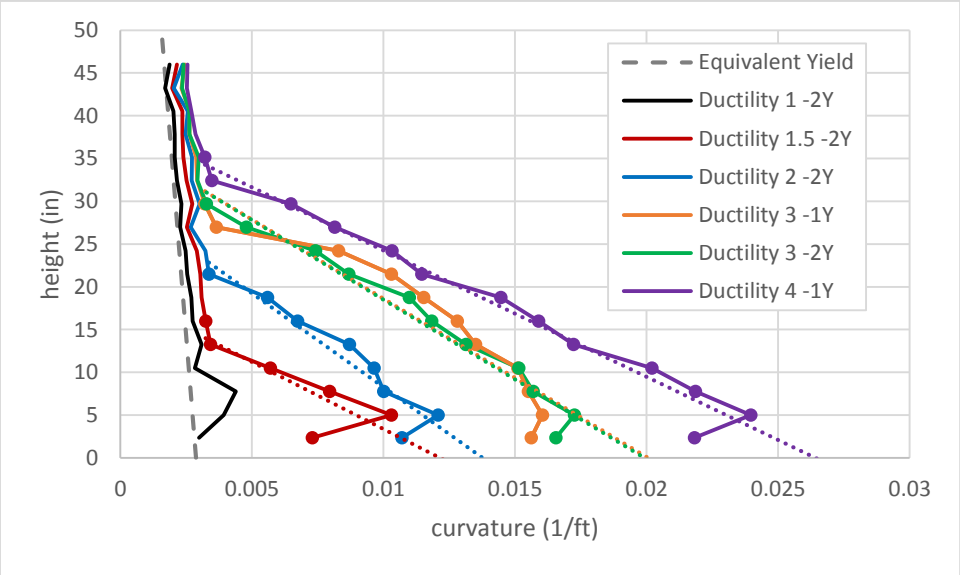

Figure 6-71. Test 3: Vertical Curvature Profiles for Loading in the -Y-direction

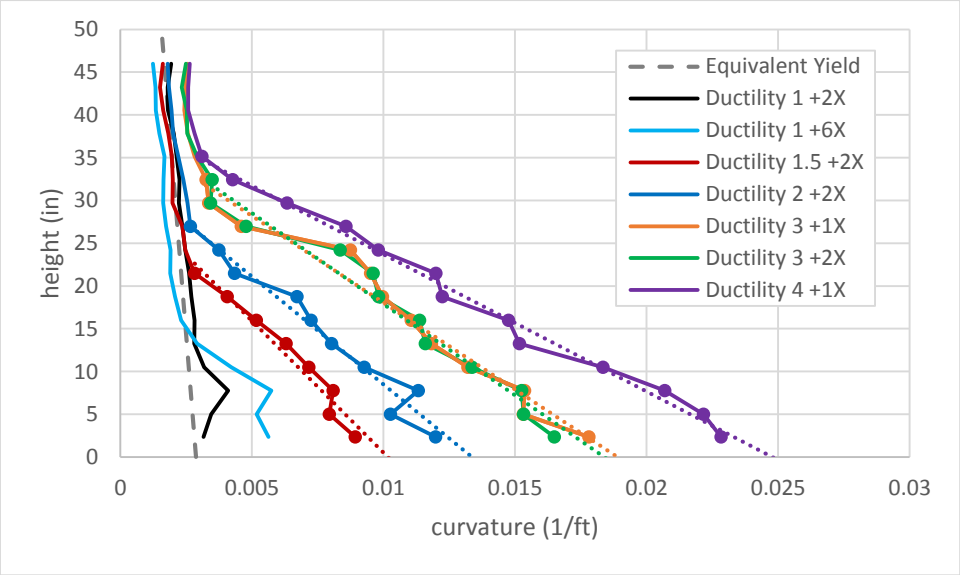

Figure 6-72. Test 3: Vertical Curvature Profiles for Loading in the +X-direction

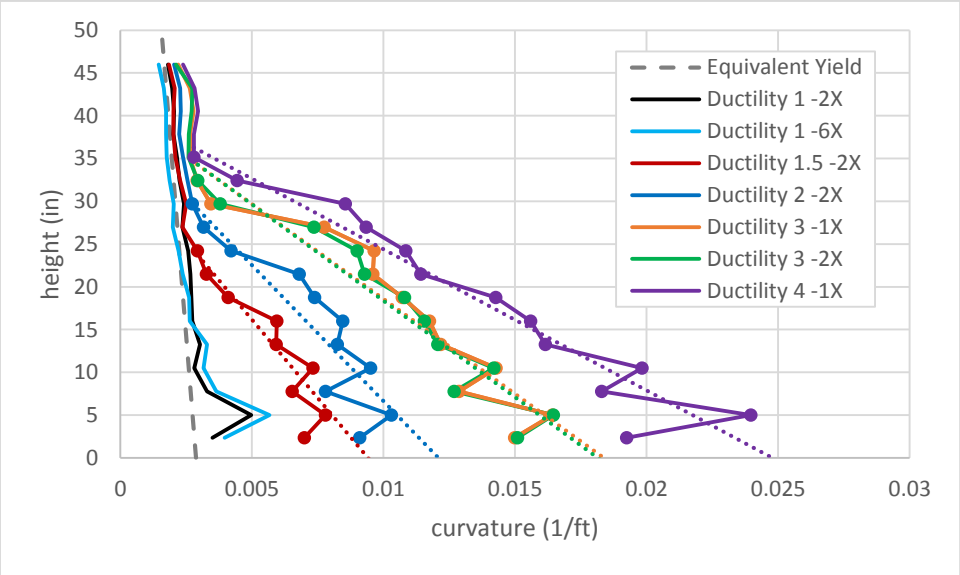

Figure 6-73. Test 3: Vertical Curvature Profiles for Loading in the -X-direction

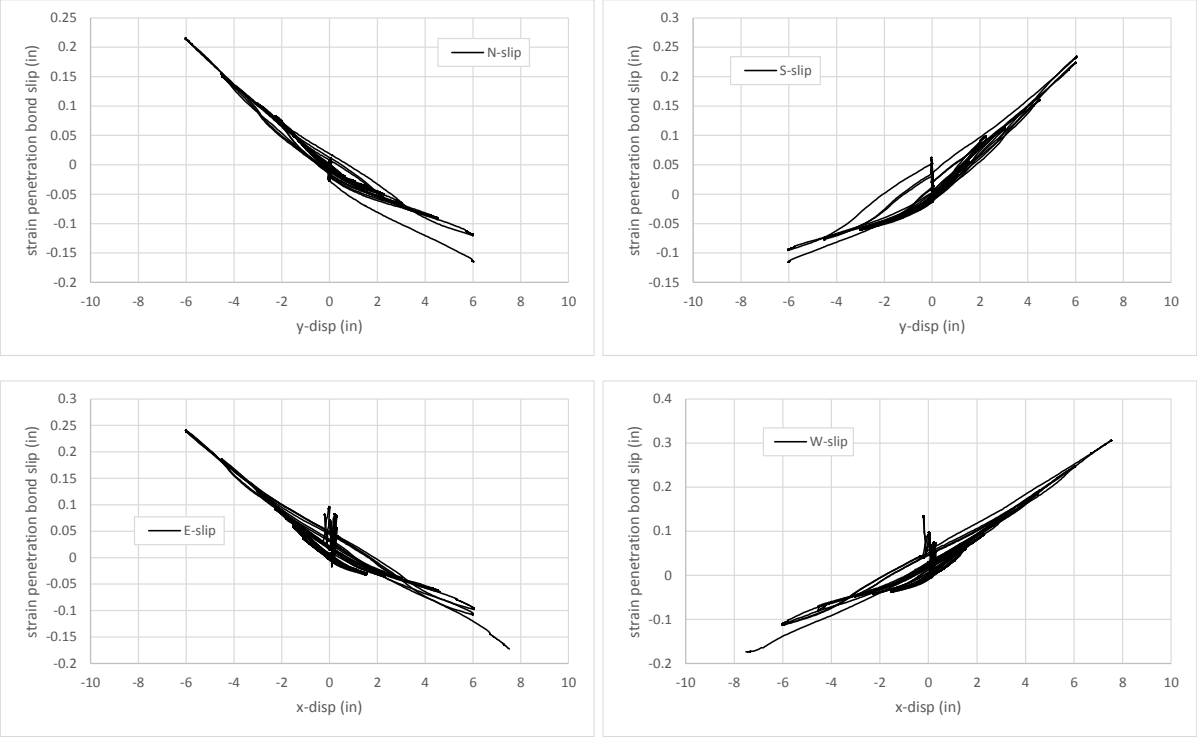

Figure 6-74. Test 3: Extreme Fiber Bar Strain Penetration Bond Slip Hysteresis

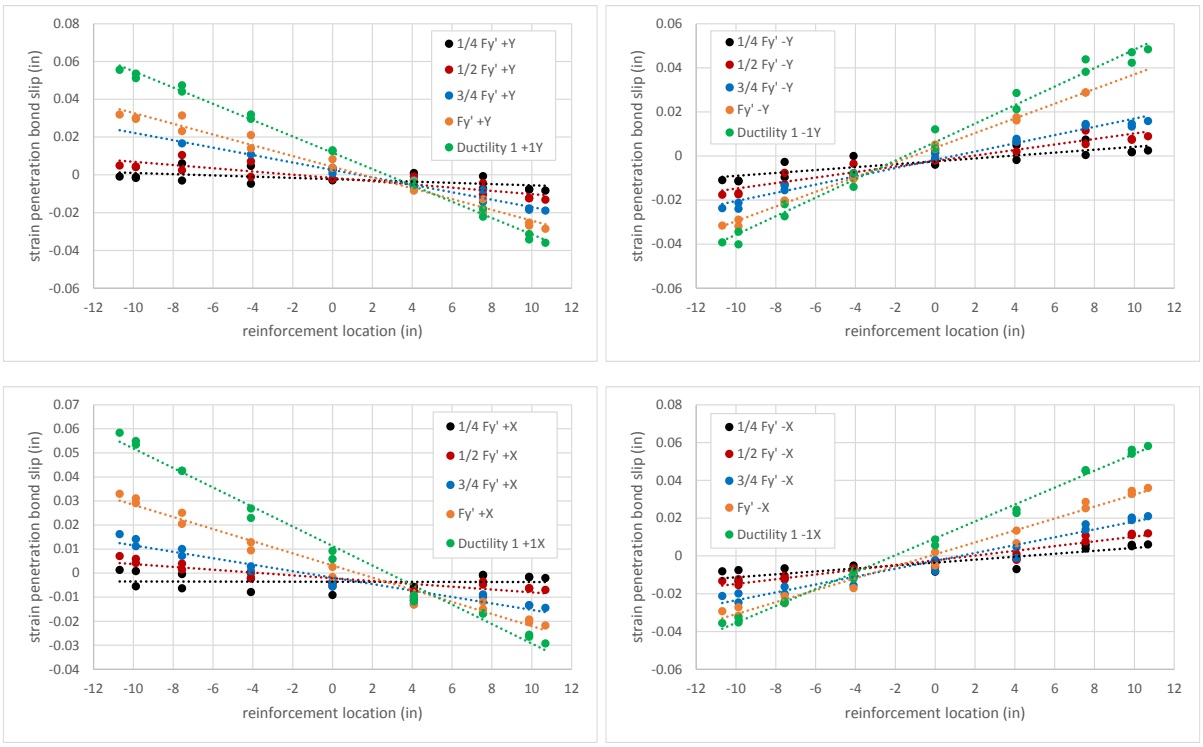

Figure 6-75. Test 3: Fixed End Rotations due to Strain Penetration during the Elastic Cycles

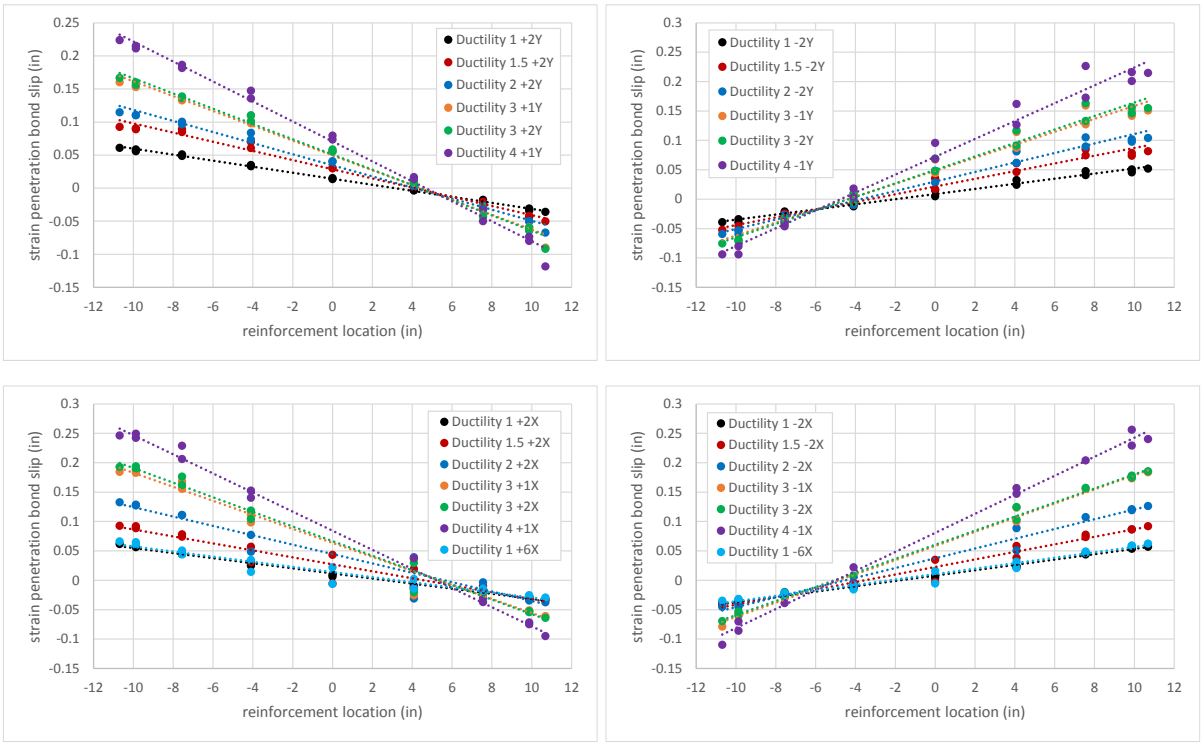

Figure 6-76. Test 3: Fixed-End Rotations due to Strain Penetration

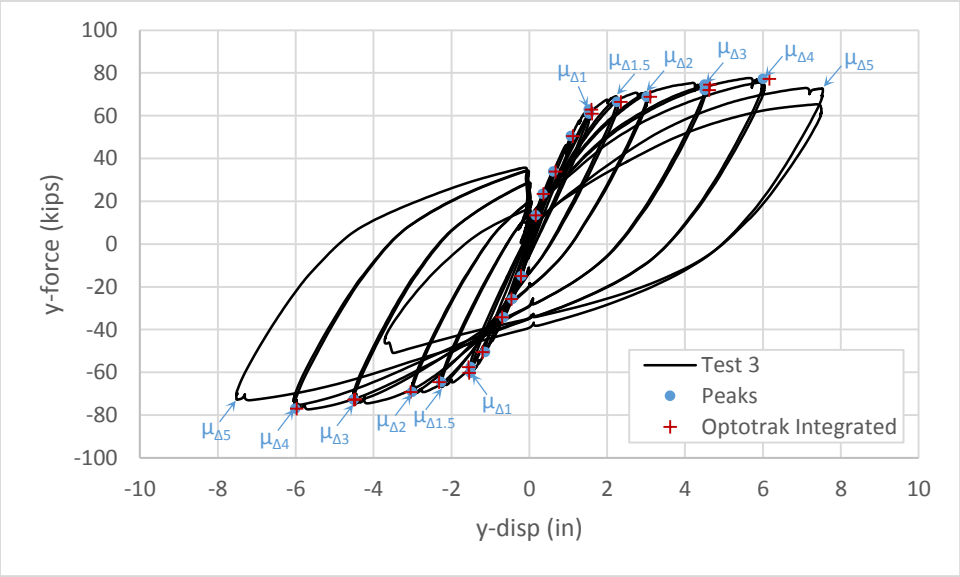

Figure 6-77. Test 3: Optotrak Integrated Flexural Disp. Compared to Measured String Pot. Disp.

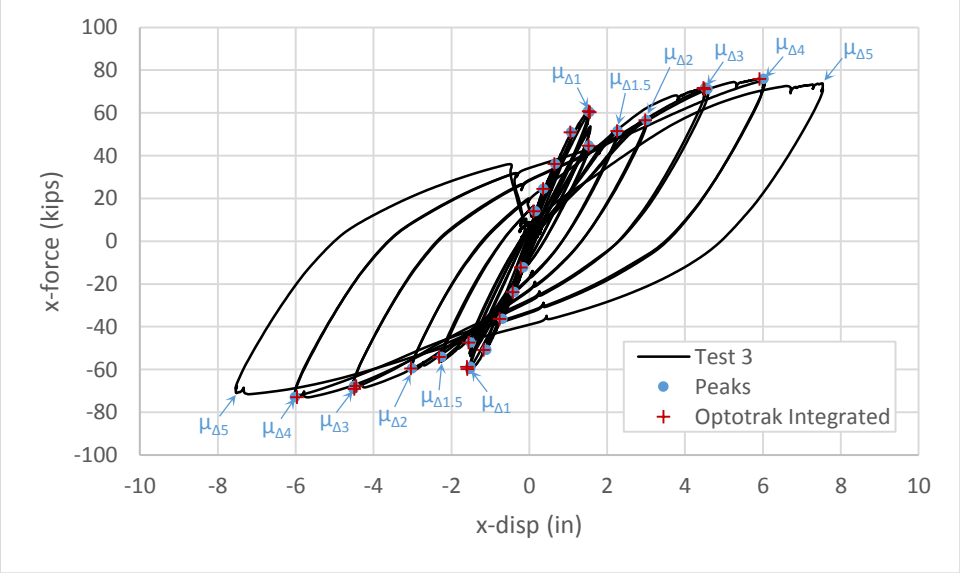

Figure 6-78. Test 3: Optotrak Integrated Flexural Disp. Compared to Measured String Pot. Disp.

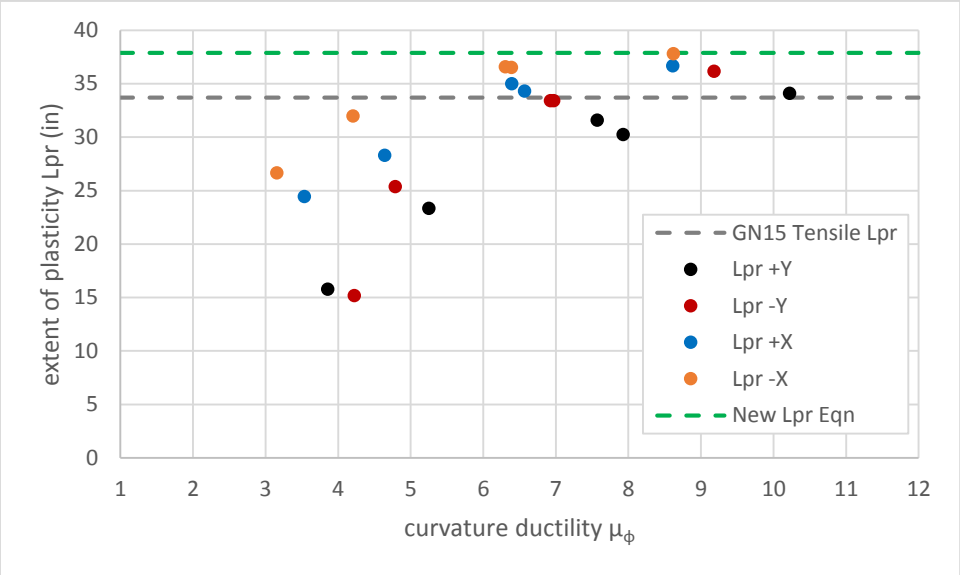

Figure 6-79. Test 3: Measured Extent of Plasticity Compared to Tensile Hinge Lengths

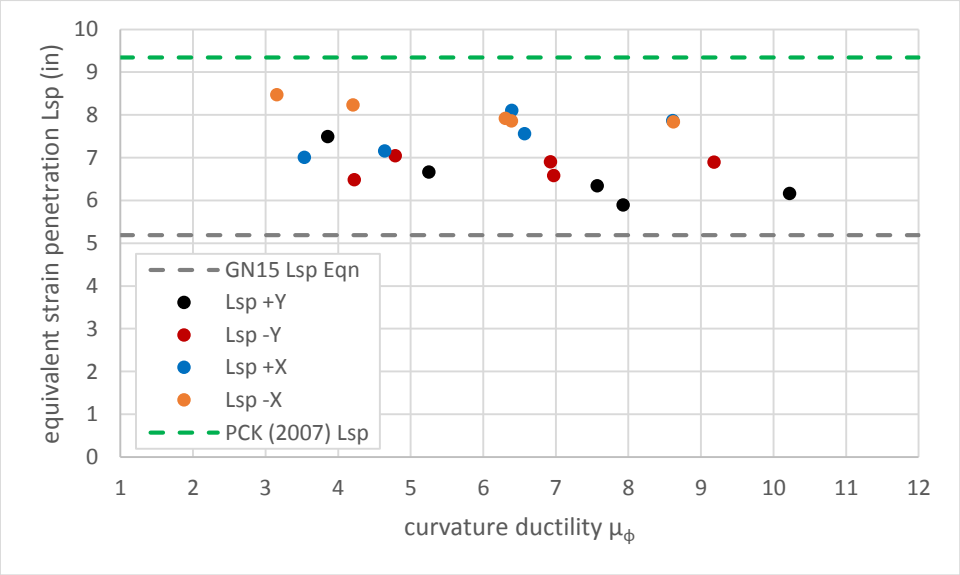

Figure 6-80. Test 3: Measured Equivalent Strain Penetration Lengths Compared to Design Expressions

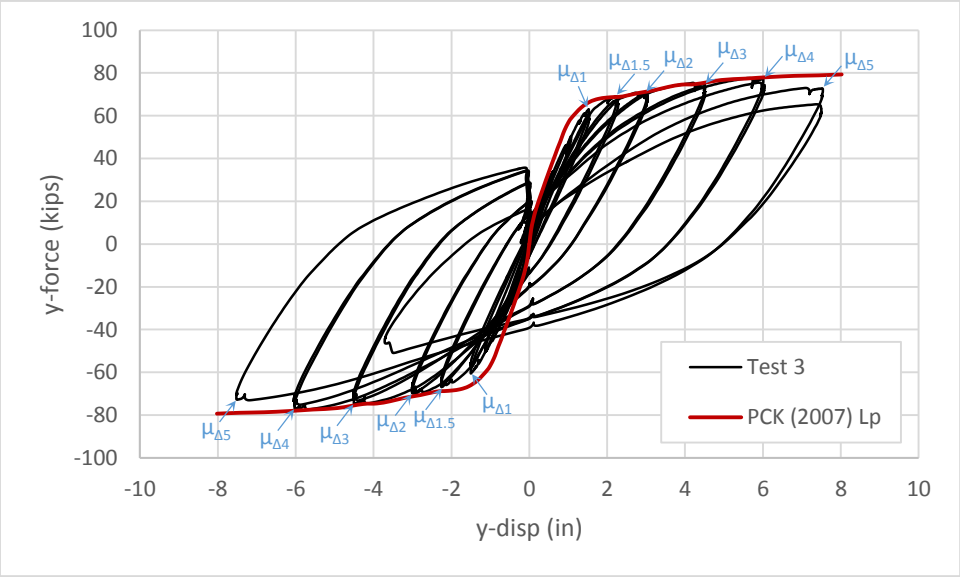

Figure 6-81. Test 3: Y-Direction Hysteretic Response Compared to PCK (2007) Hinge Length Monotonic Prediction

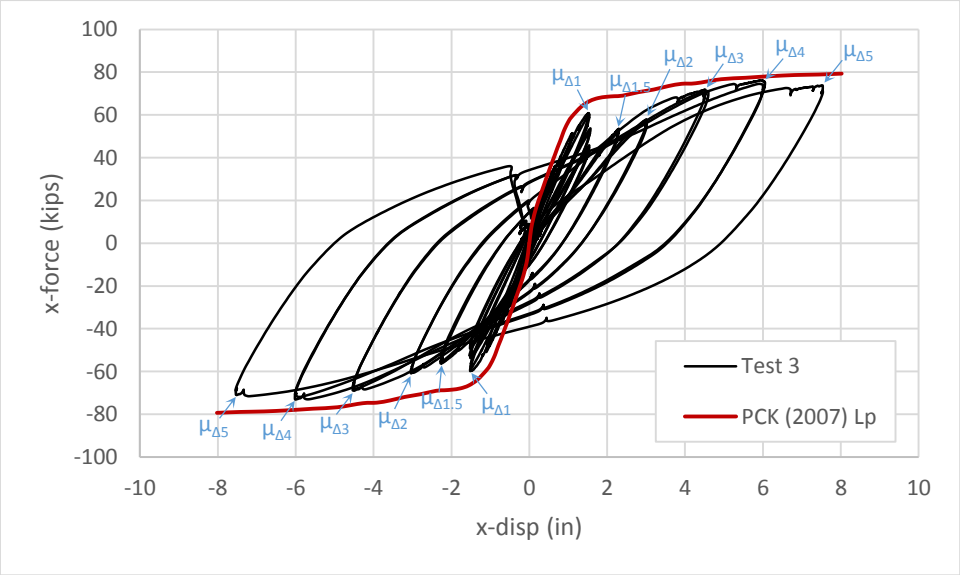

Figure 6-82. Test 3: X-Direction Hysteretic Response Compared to PCK (2007) Hinge Length Monotonic Prediction

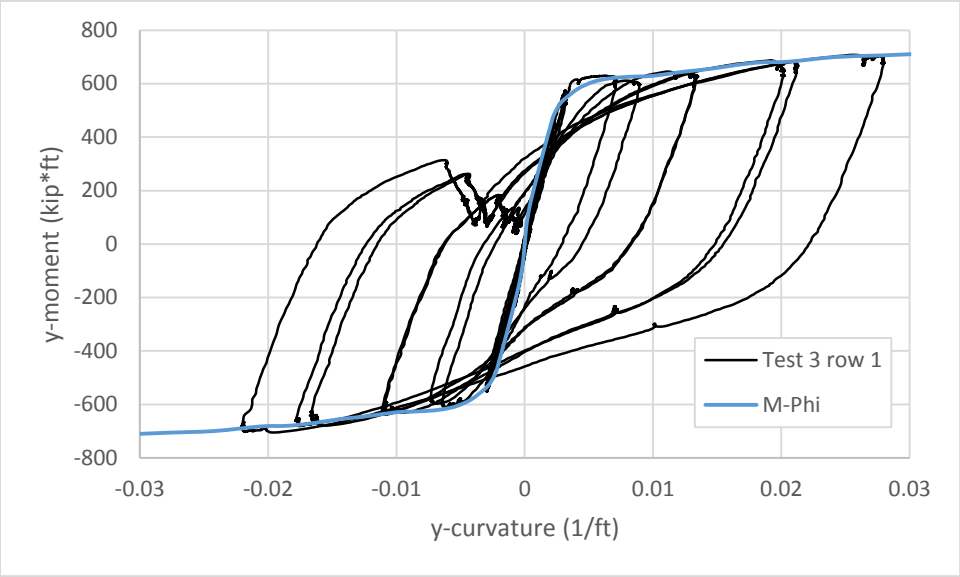

Figure 6-83. Test 3: Y-Direction Sectional Response Compared to Monotonic Moment Curvature Analysis

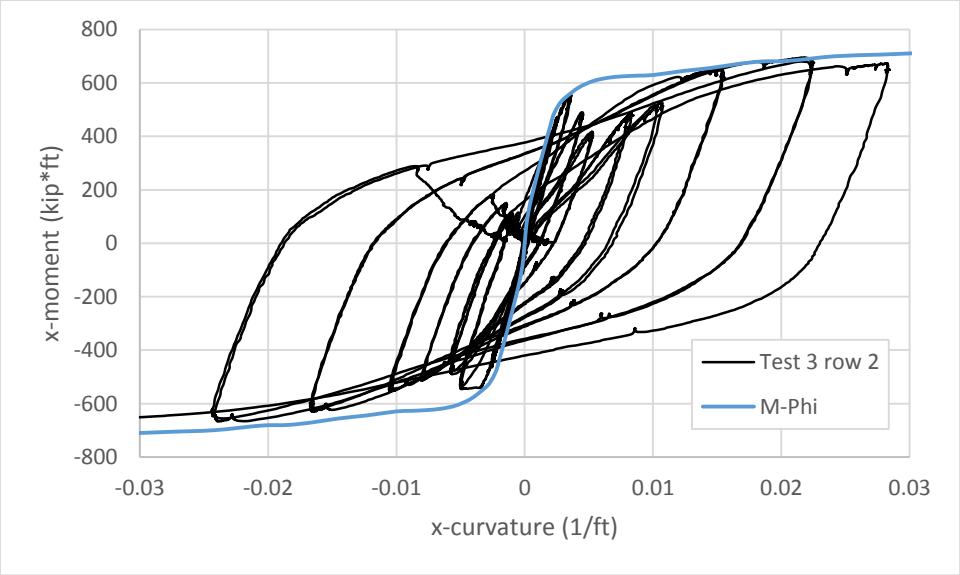

Figure 6-84. Test 3: X-Direction Sectional Response Compared to Monotonic Moment Curvature Analysis

Response Comparison for Nominally Identical Tests 1, 2, and 3

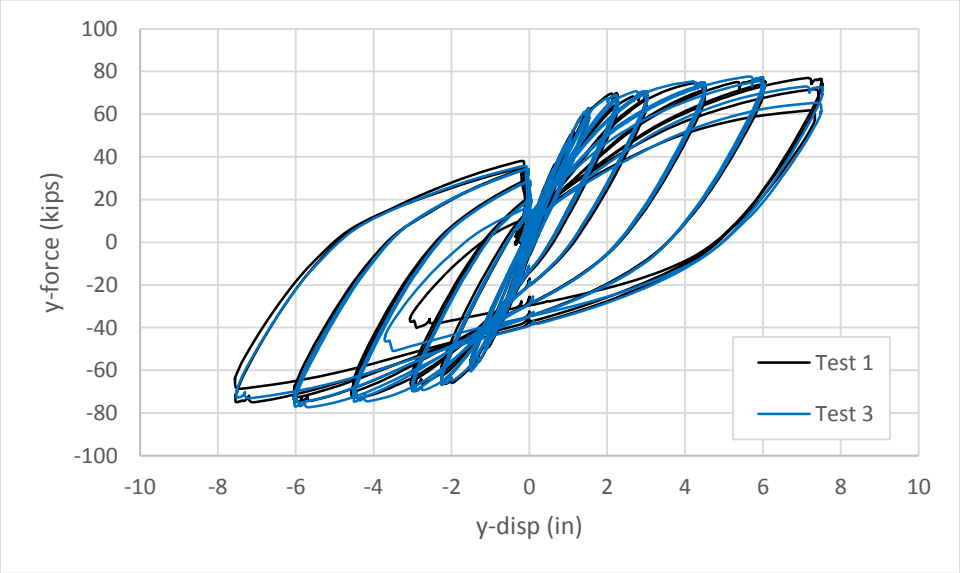

Figure 6-85. Test 1 "Symmetric" and Test 3 "Asymmetric" Two-Cycle-Set Hysteretic Comparison

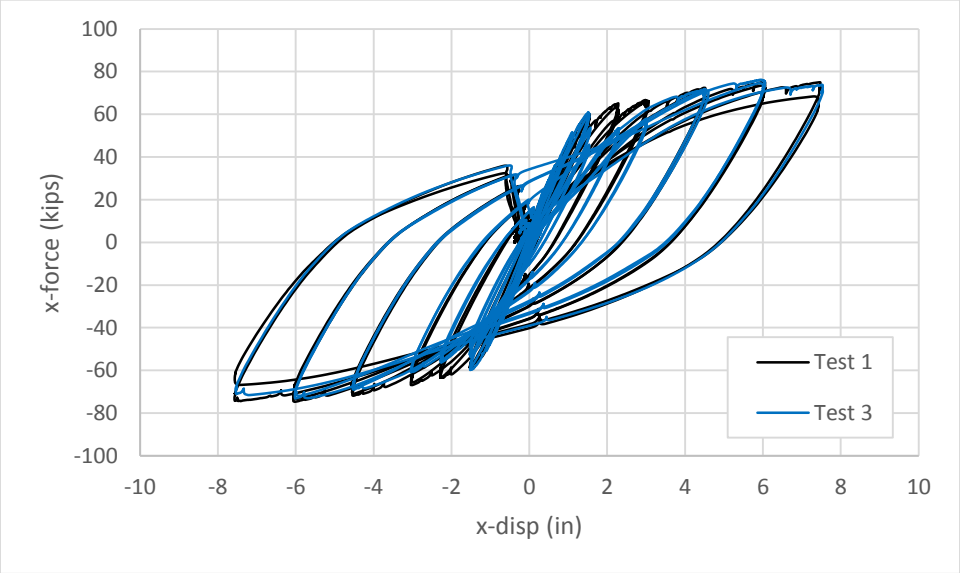

Figure 6-86. Test 1 "Symmetric" and Test 3 "Asymmetric" Two-Cycle-Set Hysteretic Comparison

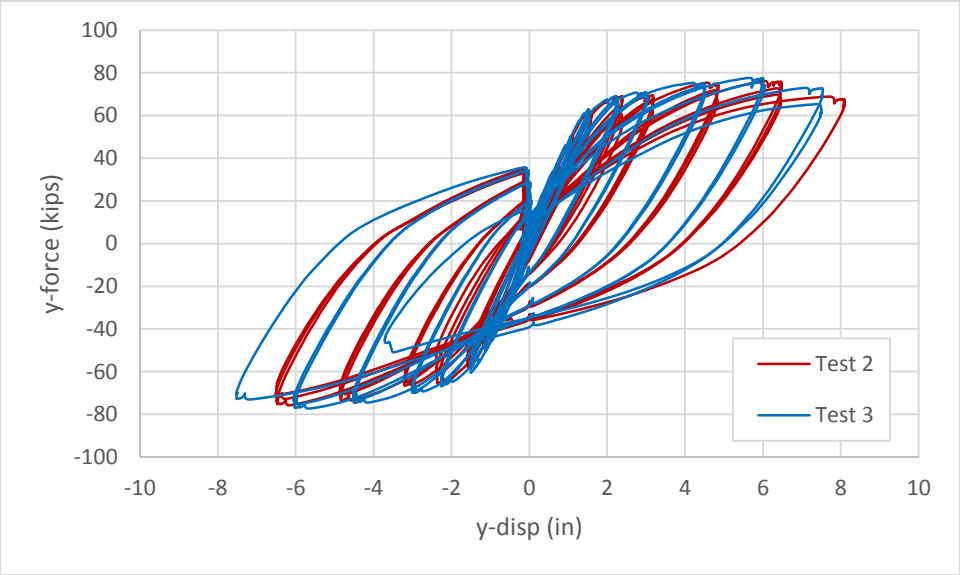

Figure 6-87. Test 2 Symmetric Three-Cycle-Set and Test 3 Asymmetric Two-Cycle-Set

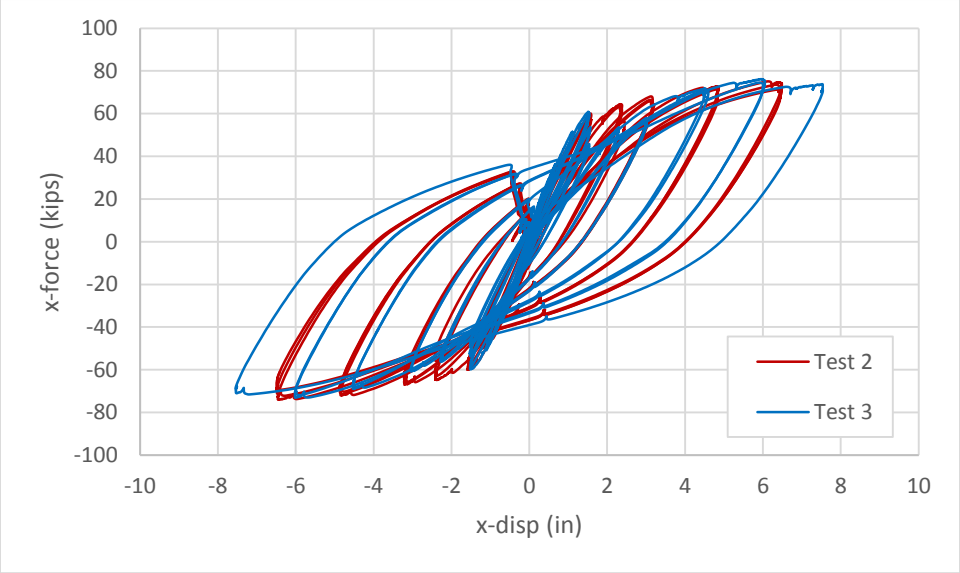

Figure 6-88. Test 2 Symmetric Three-Cycle-Set and Test 3 Asymmetric Two-Cycle-Set

Chapter 7 - Test 4 Summary Report

The fourth specimen had a 24" diameter circular cross-section reinforced with 16 #7 A706 longitudinal bars ($A_{st}/A_g = 2.1\%$) and a #3 spiral at 2" on center ($4A_{sp}/D's = 1\%$). The only difference between this specimen and Tests 1-3 was the transverse steel spacing and concrete strength, since the previous specimens had a #3 spiral at 2.75" for ($4A_{sp}/D's = 0.7\%$) and came from a separate concrete truck. Details of the test setup, instrumentation, and specimen design appear in Chapter 2. A material properties summary for the longitudinal and transverse steel from the first six experiments appears in Table 3-1 and Table 3-2. The column had a tested concrete strength of $f_c' = 7.68\ ksi$, while the footing had $f_c' = 10.33\ ksi$. The specimen had the same level of applied axial load ($191\ kips$). The fourth specimen was subjected to the Type-B Symmetric Two-Cycle-Set Bidirectional Load History shown in Figure 7-1. This figure includes a diagram of the column cross-section with the selected bar and crack labeling scheme. Displacements in the +Y-direction placed the South reinforcement in tension. Cracks due to loading in the +Y-direction were labeled as red. The orientation of the X and Y axes are shown in Figure 2-52 with regards to the test setup. The +Y-axis is perpendicular to and points away from the strong wall. Values of interests, damage observations, and a predictions summary for the fourth test appear in Table 7-1, Table 7-2, and Table 7-3. Photos of the specimen appear in Figure 7-4 and Figure 7-6. The tighter transverse steel spacing necessitated reducing the number of target markers placed on bars NW, NE, SE, and SW. This was accompanied with a more dense instrumentation of the most highly strained bars in the four extreme fiber regions of the column. The (Mander, Priestley and Park 1988) confined and unconfined concrete curves for Tests 1 and 4 appear in Figure 7-2, while a predicted response comparison is shown in Figure 7-3.

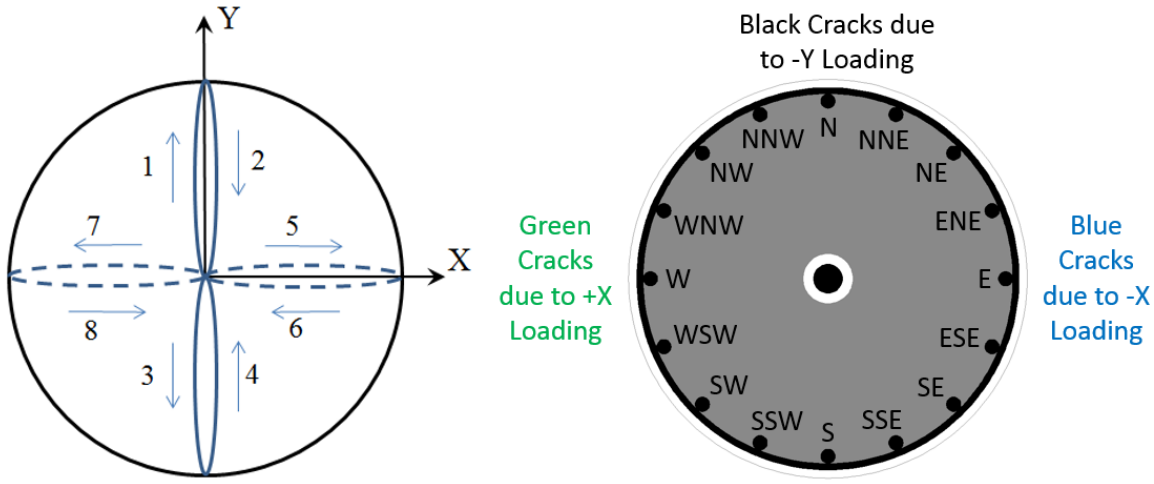

Type-B Symmetric Two-Cycle-Set Biaxial Load History

- Begins with elastic cycles (1-8) in ¼ yield increments until F_y'
- The equivalent yield displacement is then computed as $\Delta_y = \Delta_y'(M_n/M_y')$
- Two inelastic cycles (1-8) for each displacement ductility level $\mu_{\Delta n} = n \cdot \Delta_y$
- Cycle labeling system: $(\mu_{\Delta 6}^{-1Y} = -8.23\ in)$ Represents the first cycle of displacement ductility six in the -Y direction

Figure 7-1. Test 4: Load History and Labeling System for Reinforcement and Cracks

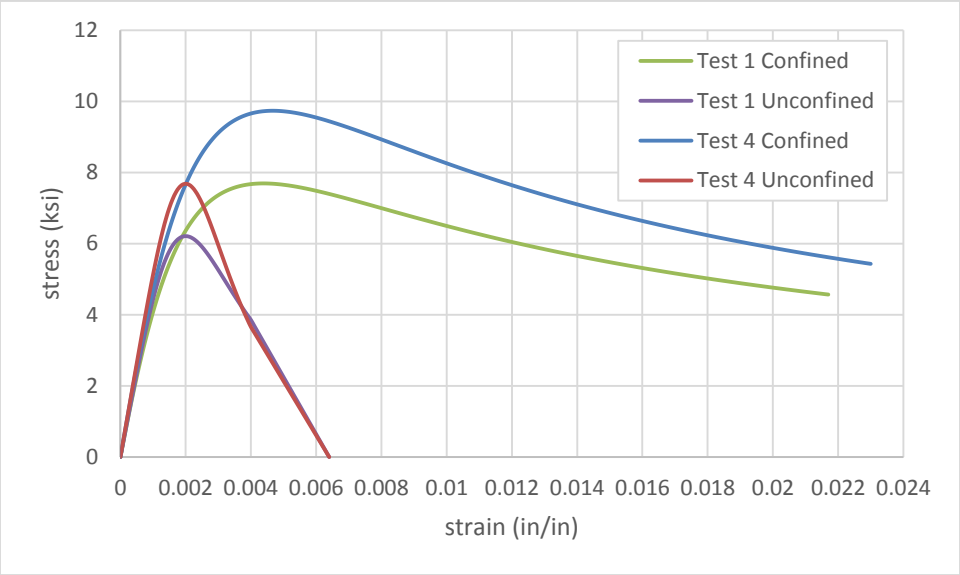

Figure 7-2. Comparison of Tests 1 and 4 (Mander, Priestley and Park 1988) Concrete Curves

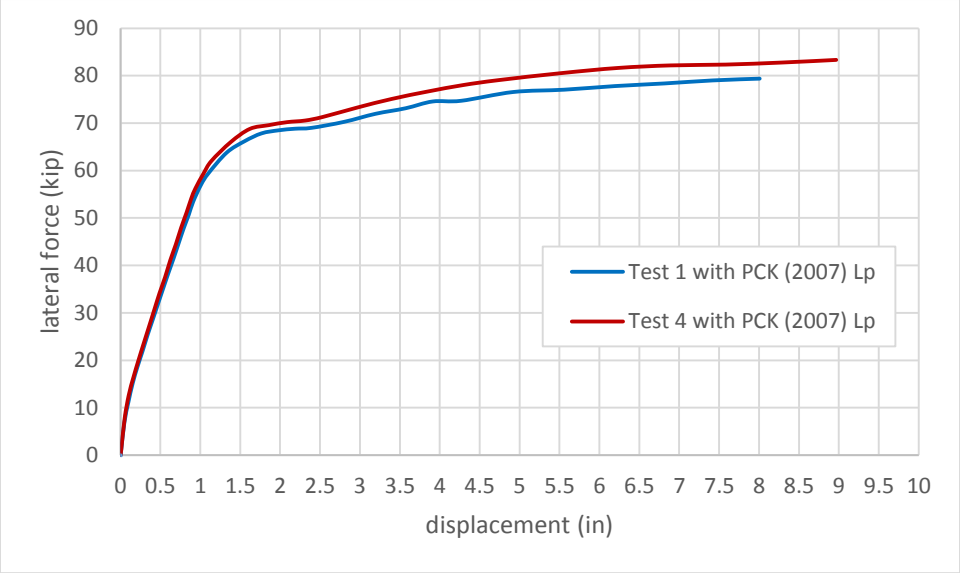

Figure 7-3. Monotonic Prediction Comparison for Tests 1 and 4

Table 7-1. Test 4: Values of Interest

Load History	Type-B Symmetric Two-Cycle-Set
Length, Diameter, and Aspect Ratio	$L = 109.4375\ in, D = 24\ in,\ (L/D = 4.56)$
Longitudinal Steel Detailing	$16\ \#7\ for\ \rho_l = A_{st}/A_g = 2.1\%$
Longitudinal Steel Properties	$f_y = 71.2\ ksi, f_u = 97.9\ ksi, \varepsilon_y = 0.00254$
Transverse Steel Detailing	$\#3\ @\ 2\ in\ for\ \rho_s = 4A_{sp}/D's = 1.0\%$
Transverse Steel Properties	$f_y = 67.6\ ksi, f_u = 105.6\ ksi, \varepsilon_y = 0.00448$
Column Concrete Strength	$f_c' = 7.68\ ksi$
Footing Concrete Strength	$f_c' = 10.33\ ksi$
Axial Load	$P = 191\ kips, \left(P/f_c'\ A_g = 6.0\%\right)$
Analytical First Yield Force	$F_y' = 51.48\ kips$
Experimental First Yield Disp.	$\Delta_y' = 1.01\ in$
Analytical Nominal Moment Capacity	$M_n = 640.31\ kip \cdot ft$
Equivalent Yield Displacement	$\Delta_y = \Delta_y'\left(M_n/M_y'\right) = 1.37\ in$
Maximum Lateral Force	$F_y = 78.04\ kips, F_x = 76.58\ kips$
Failure Mode	Loss in lateral strength due to buckling of nearly all column longitudinal bars, followed by a single fractured bar.

Table 7-2. Test 4: Damage Observations

Damage Observations:		
Cycle Peak at which First Cracking was Observed Visually:		
North	$\Delta_y = -0.5F_y' = -0.34\ in$	$F_y = -25.46\ kips$
South	$\Delta_y = 0.5F_y' = 0.30\ in$	$F_y = 25.76\ kips$
East	$\Delta_x = -0.5F_y' = -0.34\ in$	$F_x = -23.96\ kips$
West	$\Delta_x = 0.5F_y' = 0.34\ in$	$F_x = 24.67\ kips$
Cycle Peak at which Cover Concrete Crushing was Observed Visually:		
North	$\mu_{\Delta 2}^{+1Y} = 2.73\ in$	$\varepsilon_c = -0.00721$
South	$\mu_{\Delta 2}^{-1Y} = -2.73\ in$	$\varepsilon_c = -0.00753$
East	$\mu_{\Delta 2}^{+1X} = 2.73\ in$	$\varepsilon_c = -0.00506$
West	$\mu_{\Delta 2}^{-1X} = -2.74\ in$	$\varepsilon_c = -0.00502$
Exact Displacement and Cycle Label for Initial Spiral Yielding in the Confinement Zone:		
North	$\Delta_y = 3.92\ in\ during\ \mu_{\Delta 3}^{+1Y}$	$\varepsilon_c = -0.01622$
South	$\Delta_y = -4.01\ in\ during\ \mu_{\Delta 3}^{-2Y}$	$\varepsilon_c = -0.01294$
East	$\Delta_x = 4.77\ in\ during\ \mu_{\Delta 4}^{+1X}$	$\varepsilon_c = -0.00863$
West	$\Delta_x = -5.48\ in\ during\ \mu_{\Delta 4}^{-1X}$	$\varepsilon_c = -0.01256$
Peak Tensile Displacement Prior to Visual Bar Buckling During Subsequent Reversal of Load:		
North	$\mu_{\Delta 5}^{-1Y} = -6.84\ in, Observed\ at\ \mu_{\Delta 5}^{+2Y} = 6.85\ in$	$\varepsilon_s = 0.03856$
South	$\mu_{\Delta 6}^{+1Y} = 8.22\ in, Observed\ at\ \mu_{\Delta 6}^{-1Y} = -8.23\ in$	$\varepsilon_s = 0.04738$
East	$\mu_{\Delta 5}^{-1X} = -6.85\ in, Observed\ at\ \mu_{\Delta 5}^{+2X} = 6.85\ in$	$\varepsilon_s = 0.03886$
West	$\mu_{\Delta 6}^{+1X} = 8.20\ in, Observed\ at\ \mu_{\Delta 6}^{-1X} = -8.21\ in$	$\varepsilon_s = 0.04856$
Exact Displacement and Cycle Label for Fracture of Previously Buckled Reinforcement		
North	$\Delta_y = -4.75\ in\ during\ \mu_{\Delta 6}^{-2Y}$	Single North Extreme Bar

Table 7-3. Test 4: Damage Predictions

Damage Predictions with the New Bidirectional Plastic Hinge Model and New Strain Limits:		
Bar Buckling Predictions		
New Method	$\Delta_{bb}^{Lpr} = 7.80\ in$	$\varepsilon_s^{bb} = 0.04200$
Feng et al. (2015)	$\Delta_{bb}^{Lp} = 6.71\ in$	$\varepsilon_s^{bb} = 0.048$
Cover Crushing Prediction		
New Method	$\Delta_{cc}^{Lpr} = 2.13\ in$	$\varepsilon_c^{cc} = -0.004$
Spiral Yielding Prediction		
New Method	$\Delta_{sy}^{Lpr} = 5.21\ in$	$\varepsilon_c^{sy} = -0.01192 * M, (M = 0.8)$
Original Ultimate Concrete Compression Strain		
Mander et al. (1988)	$\Delta_{cu}^{Lpr} = 7.48\ in$	$\varepsilon_{cu} = -0.0153$

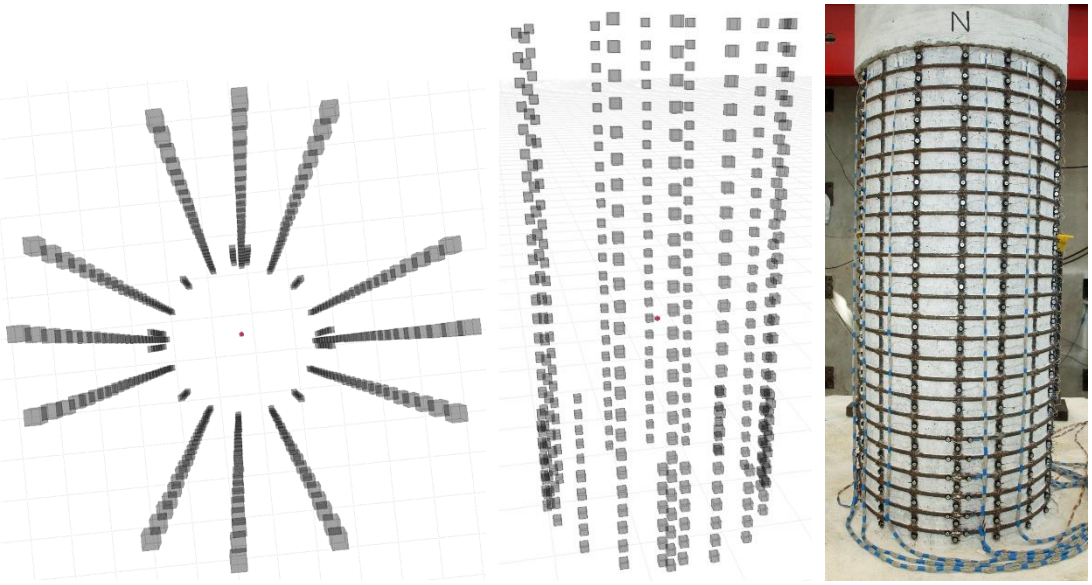

Figure 7-4. Test 4: 3D Rendering of Initial Optotrak Data, (Left) Cross Section and (Right) Profile

Figure 7-5. Test 4: Vertical and Horizontal Linear Potentiometers at Footing Interface

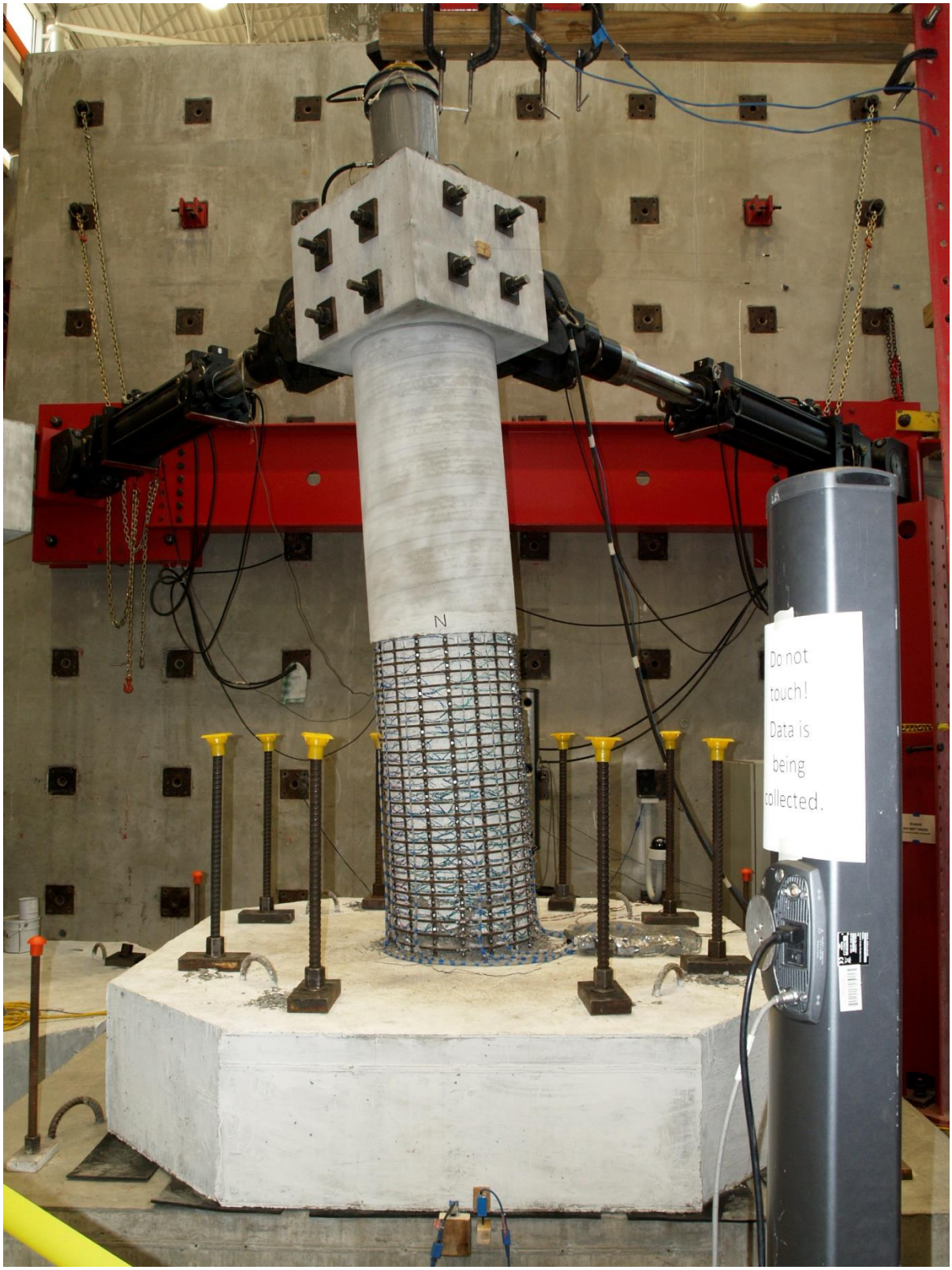

Figure 7-6. Test 4: Specimen Deformation at $\mu_{\Delta 6}^{+1x} = 8.20"$

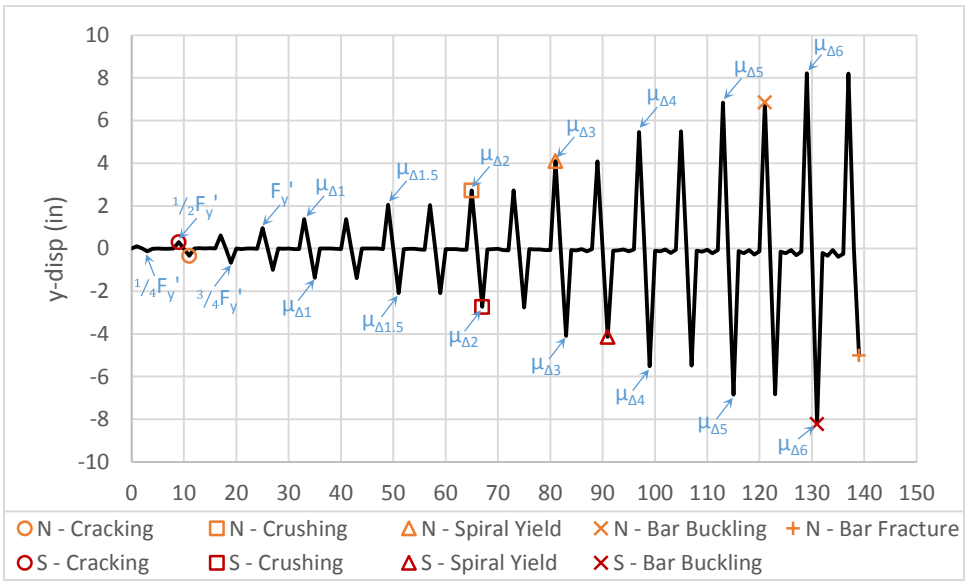

Figure 7-7. Test 4: Y-Displacement History

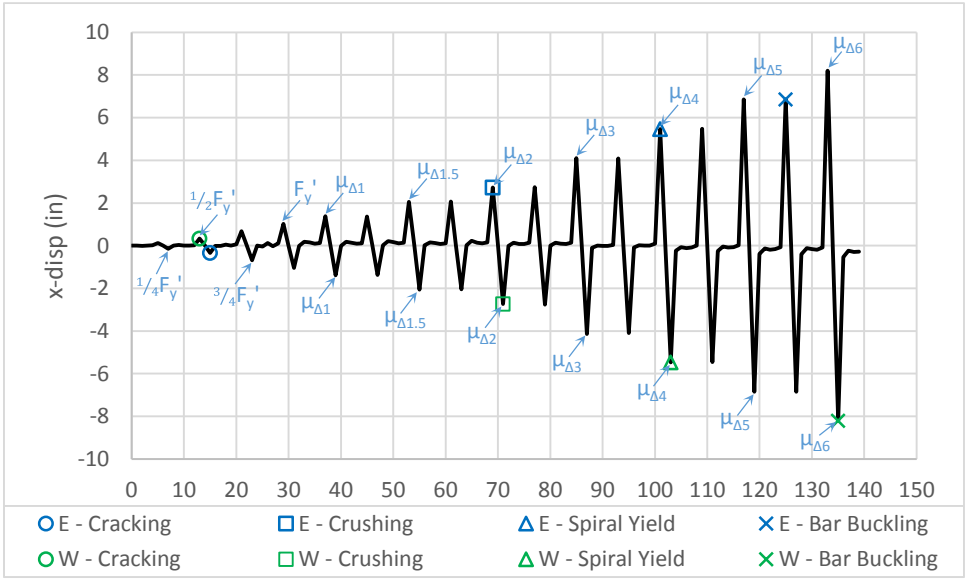

Figure 7-8. Test 4: X-Displacement History

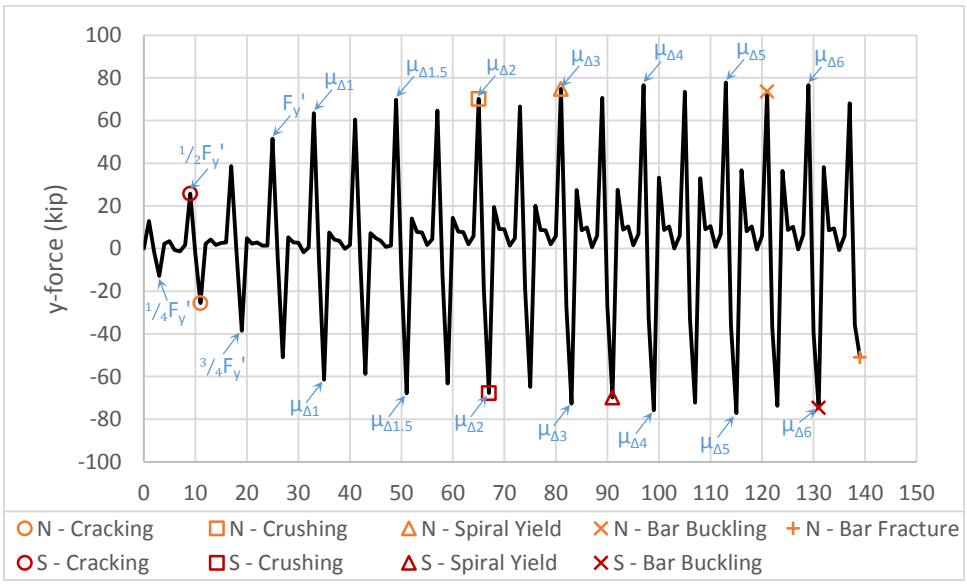

Figure 7-9. Test 4: Y-Force History

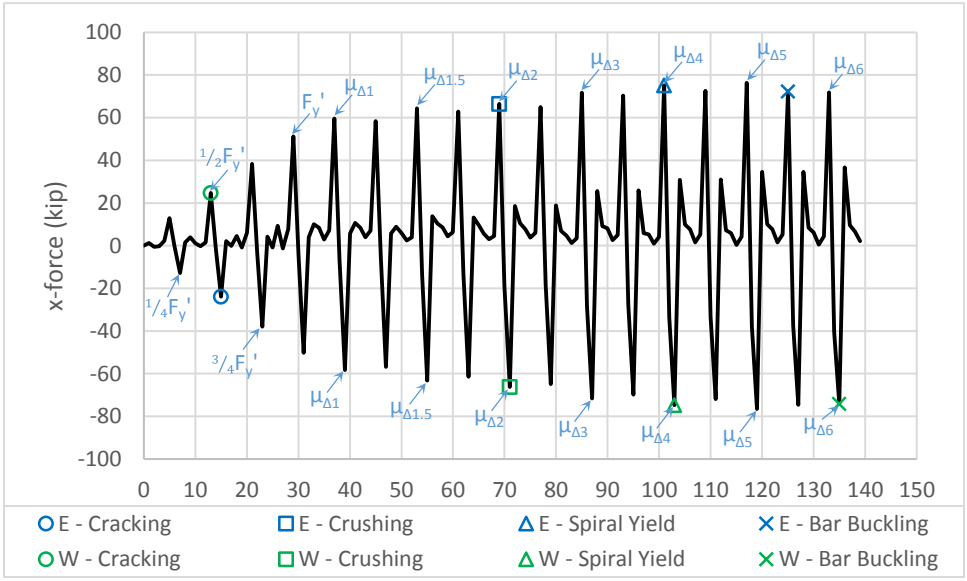

Figure 7-10. Test 4: X-Force History

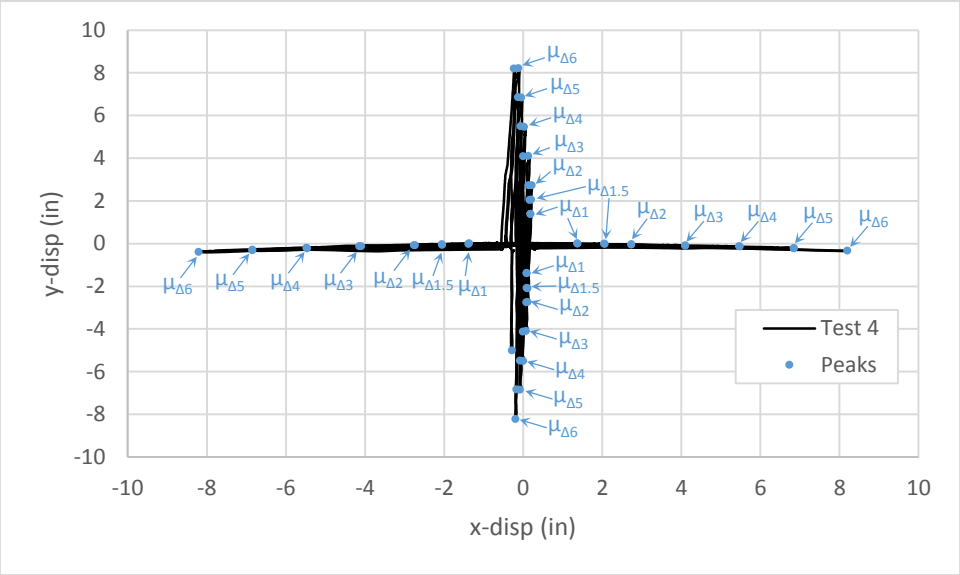

Figure 7-11. Test 4: Type-B Symmetric Two-Cycle-Set Displacement History

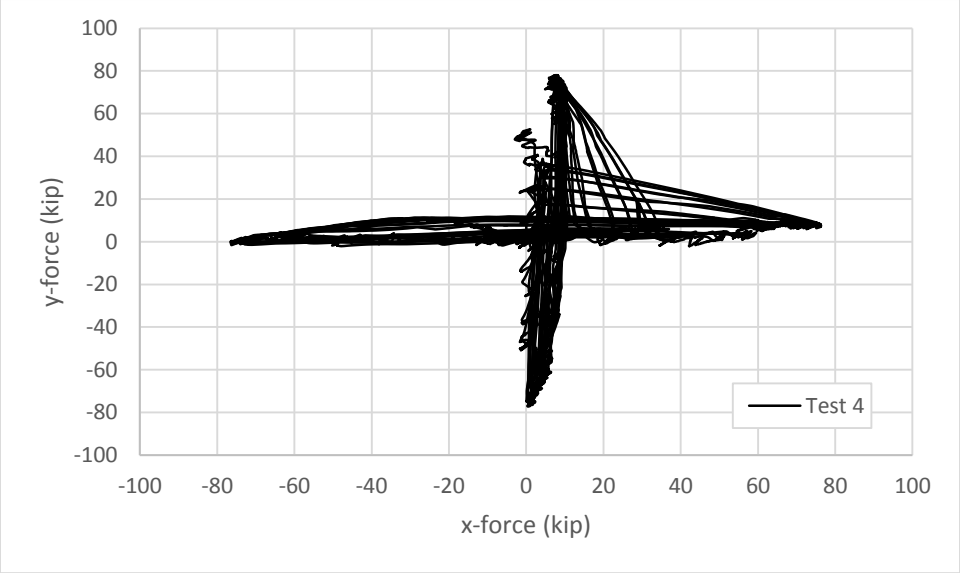

Figure 7-12. Test 4: Load Path

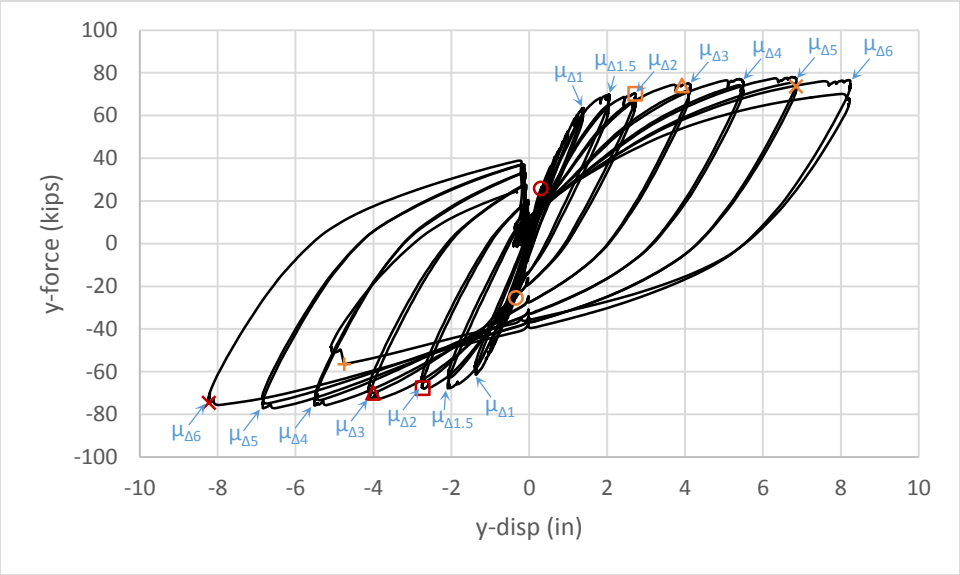

Figure 7-13. Test 4: Y-Direction Hysteretic Response

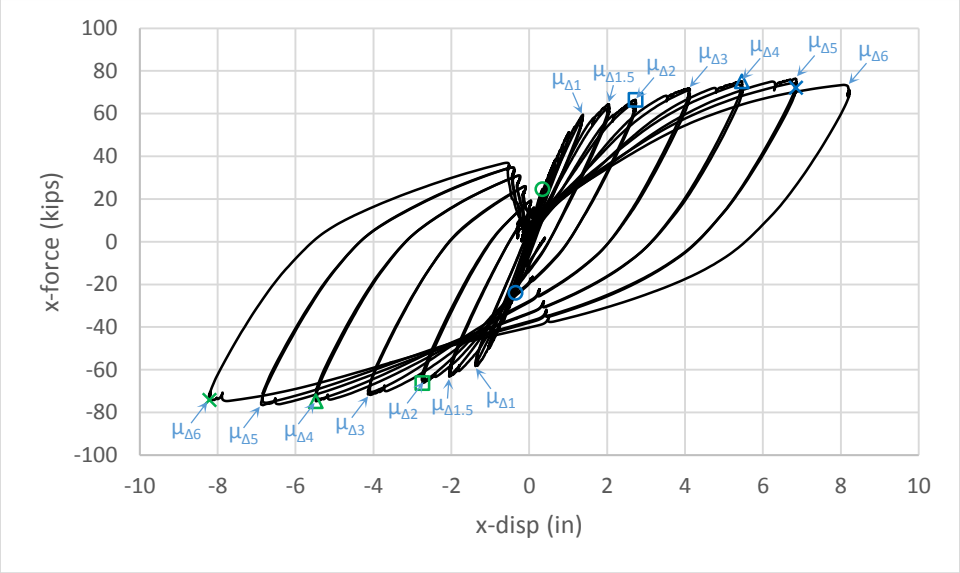

Figure 7-14. Test 4: X-Direction Hysteretic Response

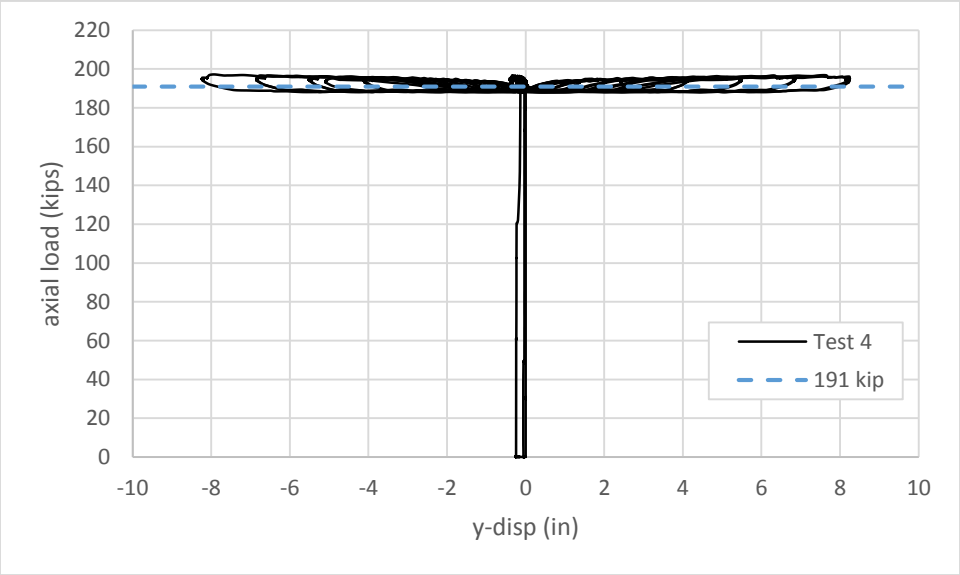

Figure 7-15. Test 4: Y-Direction Axial Load History

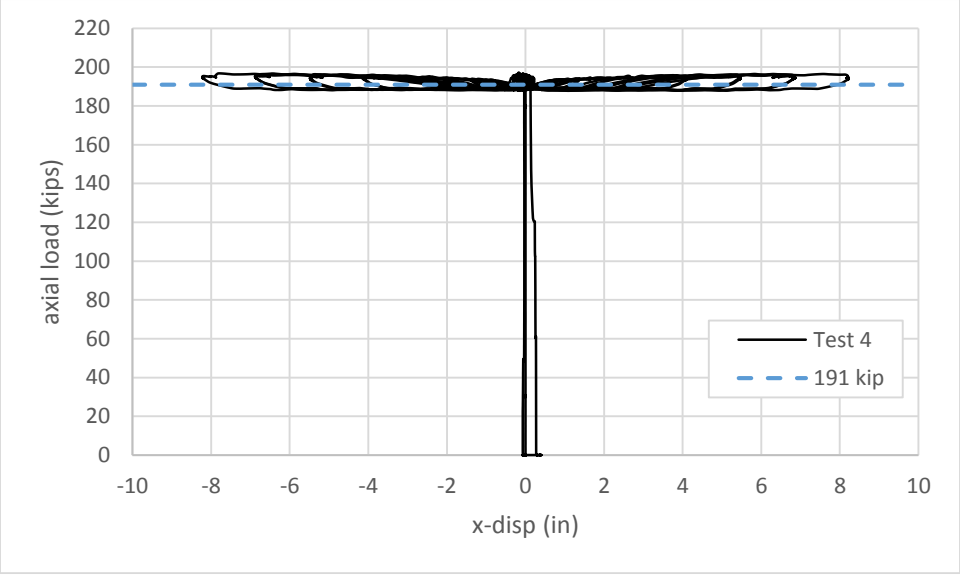

Figure 7-16. Test 4: X-Direction Axial Load History

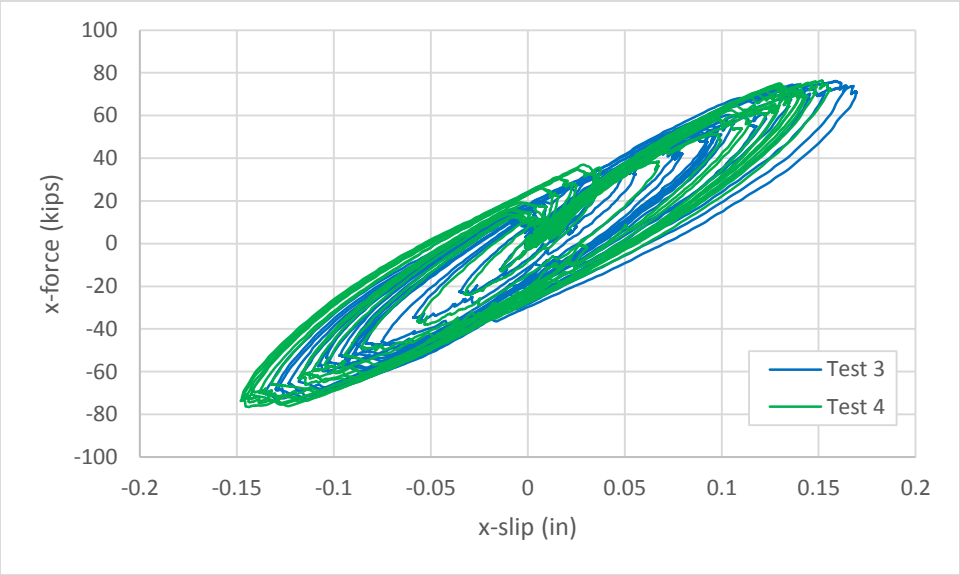

Figure 7-17. Test 4: X-Direction Horizontal Relative Footing Interface Displacement, see Figure 7-5

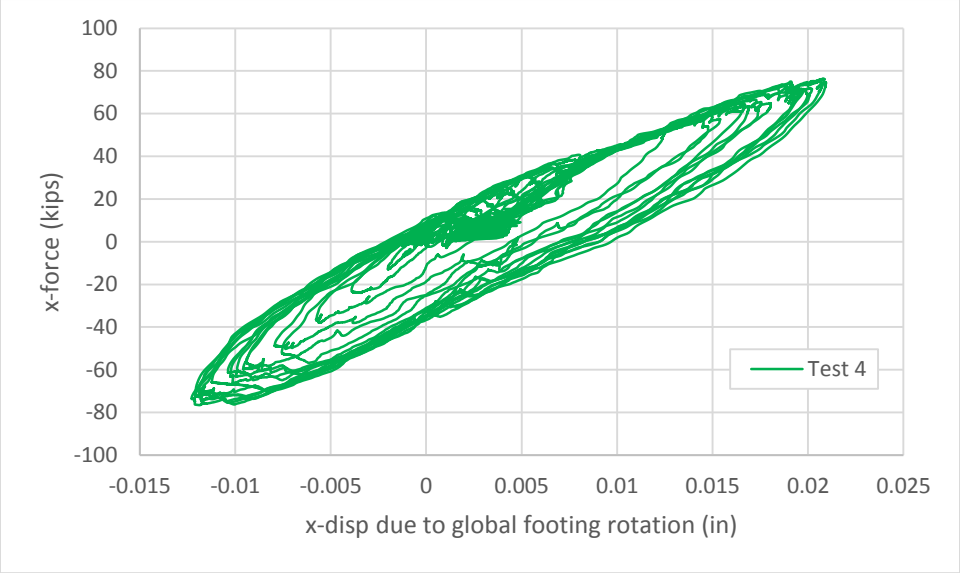

Figure 7-18. Test 4: X-Displacement due to Global Footing Rotation, see Figure 7-5

Test 4 - Experimental Observations

The test began with collection of the initial measurements prior to application of the axial load. A constant axial load of $191\ kips\ (P/f_c'\ A_g = 6.0\%)$ was then applied using a self-regulating axial load system described in Chapter 2. The imposed displacement histories in the Y and X-directions for the Symmetric Two-Cycle-Set Biaxial Load History of Figure 7-1 are shown in Figure 7-7 and Figure 7-8. The resulting column shear force histories in the Y and X-directions appear in Figure 7-9 and Figure 7-10. The full displacement history and resulting load path for Test 4 appear in Figure 7-11 and Figure 7-12. The Y and X-direction column hysteretic response appears in Figure 7-13 and Figure 7-14. The axial load history is shown in Figure 7-15 and Figure 7-16.

In Test 4, the relative displacement between the transfer and specimen footings was measured using linear potentiometers in the four primary directions, see Figure 7-5. A calculation channel was added to the data acquisition to subtract the relative footing displacement from the string potentiometer displacement, providing the total column deformation. This included both the horizontal slip at the footing interface as well as any global footing rotations which were extrapolated to the center of the applied lateral load, where the string potentiometers measured the total deformation. The data from this calculation channel was updated in real time, allowing for it to be used for the control of the actuators, which insured that the appropriate displacement amplitudes were reached in each cycle. As an example, the relative horizontal slip between the specimen and transfer footings is depicted in Figure 7-17, while the lateral displacement due to global footing rotation is shown in Figure 7-18. The force proportional relationship between relative horizontal footing slip and lateral displacement matches that of Test 3, which was used to correct the measured displacements of Test 2. Global footing rotation contributed only minimally to the total deformation, as shown in Figure 7-18. All deformation values reported in this summary are fully corrected based on the measured data.

The load history began with elastic cycles (1-8) in ¼ F_y' increments until the analytically predicted first yield force ($F_y' = 51.48\ kips$) was reached in each direction of loading. Cracks were first observed on all sides of the specimen during the ½ F_y' cycle, see Figure 7-19 and Figure 7-20. At the analytically predicted first yield force, displacements in the four primary directions were measured at $\Delta_y' = 0.97$" and $\Delta_y' = -0.99$" in Y-direction and $\Delta_y' = 1.02$" and $\Delta_y' = -1.04$" in X-direction, producing an average experimental first yield displacement of $\Delta_y' = 1.01$". This value exceeded the analytical prediction for the first yield displacement of 0.83", which will be further investigated upon review of the measured strains. Cracks observed on each side of the specimen at first yield are shown in Figure 7-21 and Figure 7-22. The equivalent yield displacement for the column was then computed as $\Delta_y = \Delta_y'(M_n/M_y') = 1.37\ in$, where $M_n = 640.31\ kip \cdot ft$ represents the analytical nominal moment capacity corresponding to an extreme fiber compression strain of $\varepsilon_c = 0.004$ or a steel tensile strain of $\varepsilon_s = 0.015$, whichever occurs first. The remainder of the Symmetric Two-Cycle-Set Load History consists of two cycles (1-8 from Figure 7-1) for each displacement ductility level $\mu_{\Delta n} = n \cdot \Delta_y$, where $n = 1, 1.5, 2, 3, 4, 5, 6\ etc.$

For each displacement ductility level, cracks were marked during the second cycle of loading and those which were visible under two primary directions were still marked with that direction's representative color from Figure 7-1. At displacement ductility one, the cracks remained horizontal, but increased in width and became more numerous as shown in Figure 7-23 and Figure 7-24. During

the first cycle of displacement ductility 1.5, the first signs of concrete flaking were observed in the four primary directions, see Figure 7-25 and Figure 7-26. This slight amount of concrete flaking usually precedes crushing, however the damage did not change during the second cycle of loading. In a given direction of loading, cracks on the shear face began to show some inclination in regions above the footing-column interface as shown in Figure 7-27 and Figure 7-28. Those near the footing-column interface remained horizontal. The photos of cracks on the North and South sides of the specimen were shown at the end of the displacement ductility level, so that cracks due to loading in the orthogonal direction appear in the photos.

During the first cycle of displacement ductility two, small amounts of concrete crushing were observed in the four primary directions, see Figure 7-29 and Figure 7-30. Photos of the crack profile on each side of the specimen at the conclusion of displacement ductility two appear in Figure 7-31 and Figure 7-32. Spiral reinforcement on the North side of the specimen yielded under confinement demands during $\mu_{\Delta 3}^{+1y} = 4.11"$. Photos of the compression zone in each primary loading direction during the first cycle of displacement ductility three appear in Figure 7-33 and Figure 7-34. Spiral yielding was measured on the South side of the specimen during $\mu_{\Delta 3}^{-2y} = -4.13"$. Crack profiles at the end of displacement ductility three are shown in Figure 7-35 and Figure 7-36. By this time, there was a distinct crack inclination on the shear faces of the specimen in a given direction of loading. Cracks in one direction were clearly interacting with cracks in the opposing directions, however even in the presence of adjacent horizontal cracks, the diagonal cracks on the shear faces continued to elongate and incline for the remainder of the experiment.

Spiral yielding was measured on East and West sides of the specimen was during $\mu_{\Delta 4}^{+1x} = 5.47"$ and $\mu_{\Delta 4}^{-1x} = -5.48"$. Photos of the four confinement regions during respective cycles of displacement ductility four appear in Figure 7-37 and Figure 7-38, while crack profiles at the end of the ductility level appear in Figure 7-39 and Figure 7-40. Significant yielding in spiral layers overlaying the extreme fiber reinforcement was measured during the first cycle of displacement ductility five, although the reinforcement remained visibly straight as shown in Figure 7-41 and Figure 7-42. The North extreme fiber bar buckled during $\mu_{\Delta 5}^{+2y} = 6.84"$, see Figure 7-43, while the South bars remained visibly straight during $\mu_{\Delta 5}^{-2y} = -6.83"$. The East extreme fiber bar buckled during $\mu_{\Delta 5}^{+2x} = 6.85"$, refer to Figure 7-44, while the West reinforcement remained visibly straight at $\mu_{\Delta 5}^{-2x} = -6.85"$.

The adjacent North reinforcing Bar NNE buckled during $\mu_{\Delta 6}^{+1y} = 8.22"$, followed by simultaneous buckling of Bars S, SSE, and SSW during $\mu_{\Delta 6}^{-1y} = -8.23"$ as shown in Figure 7-45. The adjacent East reinforcing Bars ENE and ESE buckled during $\mu_{\Delta 6}^{+1x} = 8.20"$, followed by buckling of Bars W, WNW, and WSW during $\mu_{\Delta 6}^{-1x} = -8.21"$ as shown in Figure 7-46. Bars NNW and NE buckled during $\mu_{\Delta 6}^{+2y} = 8.21"$, while the deformation in the previously buckled reinforcement increased significantly. The previously buckled North extreme fiber bar fractured at $-4.75"$ during $\mu_{\Delta 6}^{-2y}$ as shown in Figure 7-47. Bars SE and SW buckled during this cycle as well. The test was ended at this time, since fracture of the North bar resulted in significant strength loss as shown in Figure 7-13. Photos of each side of the specimen after instrumentation removal appear in Figure 7-48, Figure 7-49, and Figure 7-50. As with the previous specimens, the column was recentered and saved as a repair candidate for a separate research program sponsored by the AKDOT.

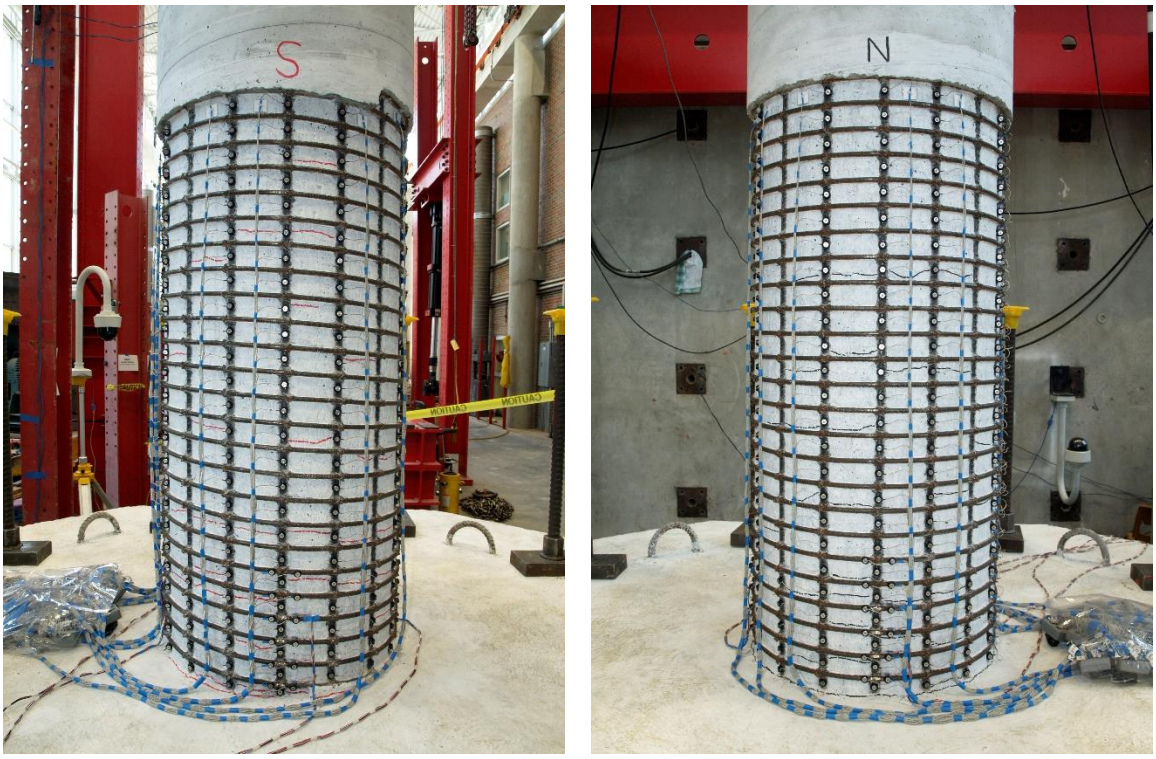

Figure 7-19. Test 4: First Cracking on the South and North Sides of the Specimen during $\Delta_y = 0.30$" and $\Delta_y = -0.34$"

Figure 7-20. Test 4: First Cracking on the West and East Sides of the Specimen during $\Delta_x = 0.34$" and $\Delta_x = -0.35$"

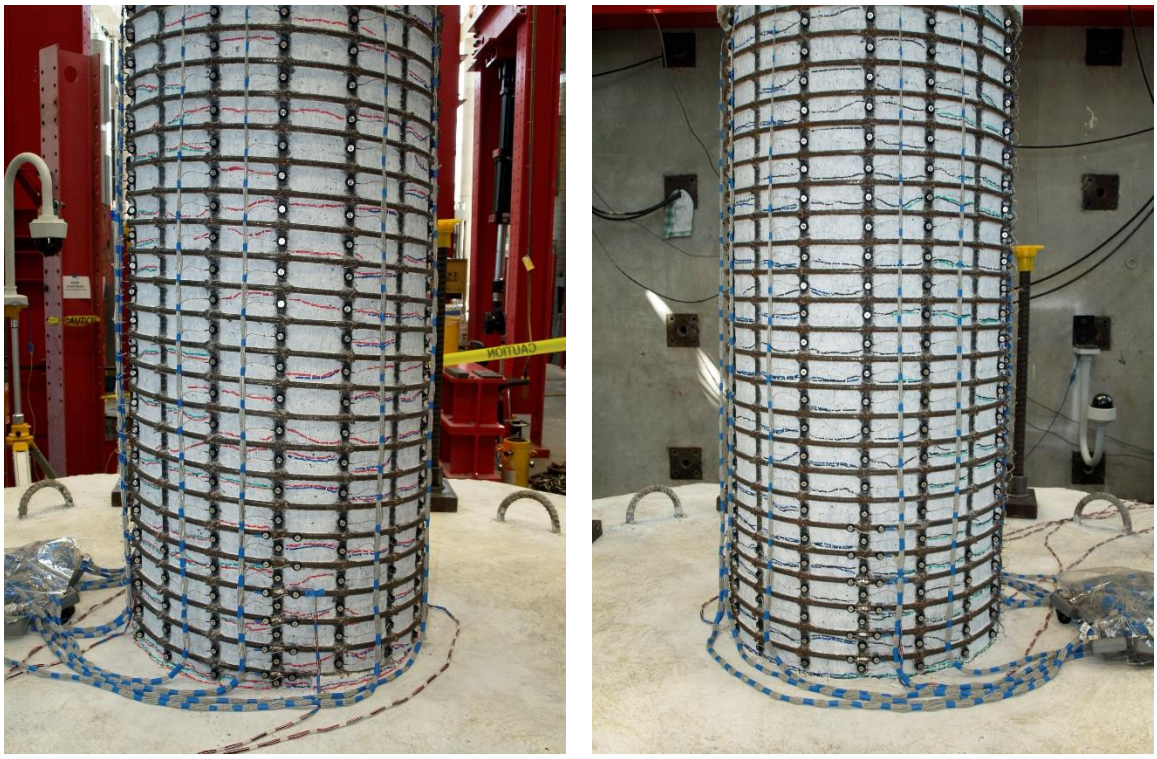

Figure 7-21. Test 4: Cracking on the South and North Sides during $\Delta'_y = 0.97$" and $\Delta'_y = -0.99$" in Y-Direction

Figure 7-22. Test 4: Cracking on the West and East Sides during $\Delta'_y = 1.02$" and $\Delta'_y = -1.04$" in X-Direction

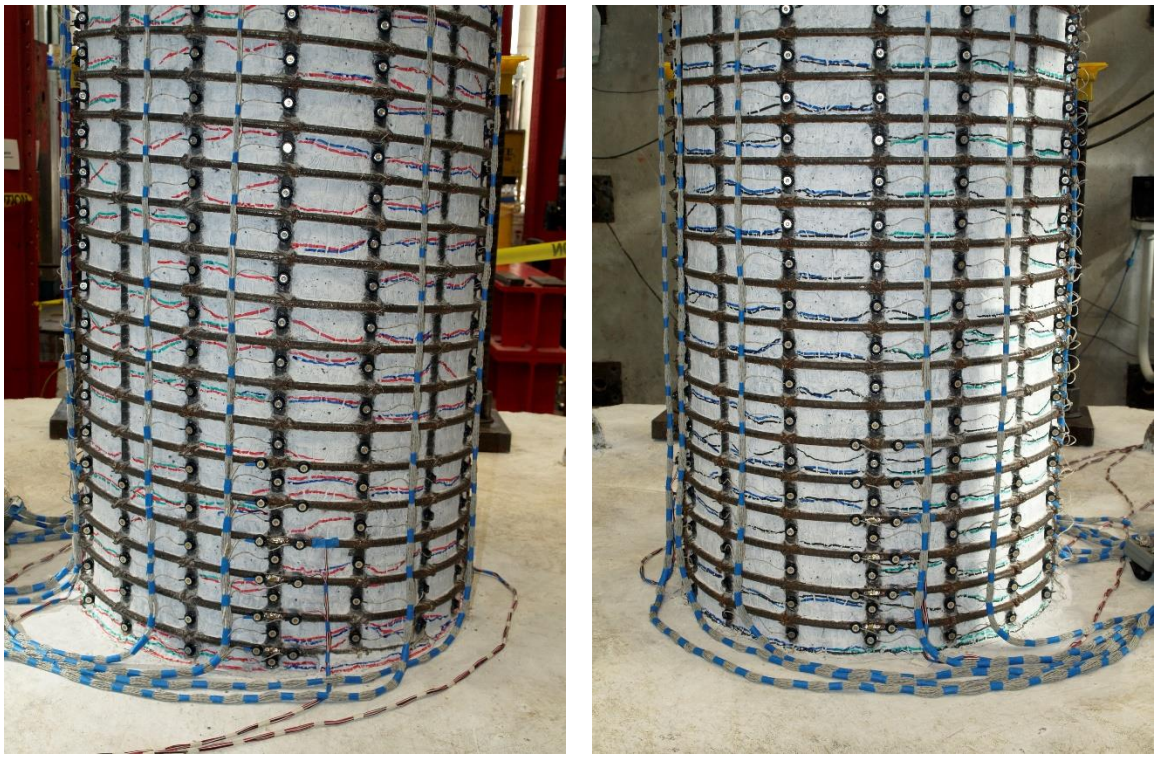

Figure 7-23. Test 4: Cracking on the (Left) South Side at $\mu_{\Delta 1}^{+2y} = 1.38"$ and (Right) North Side at $\mu_{\Delta 1}^{-2y} = -1.39"$

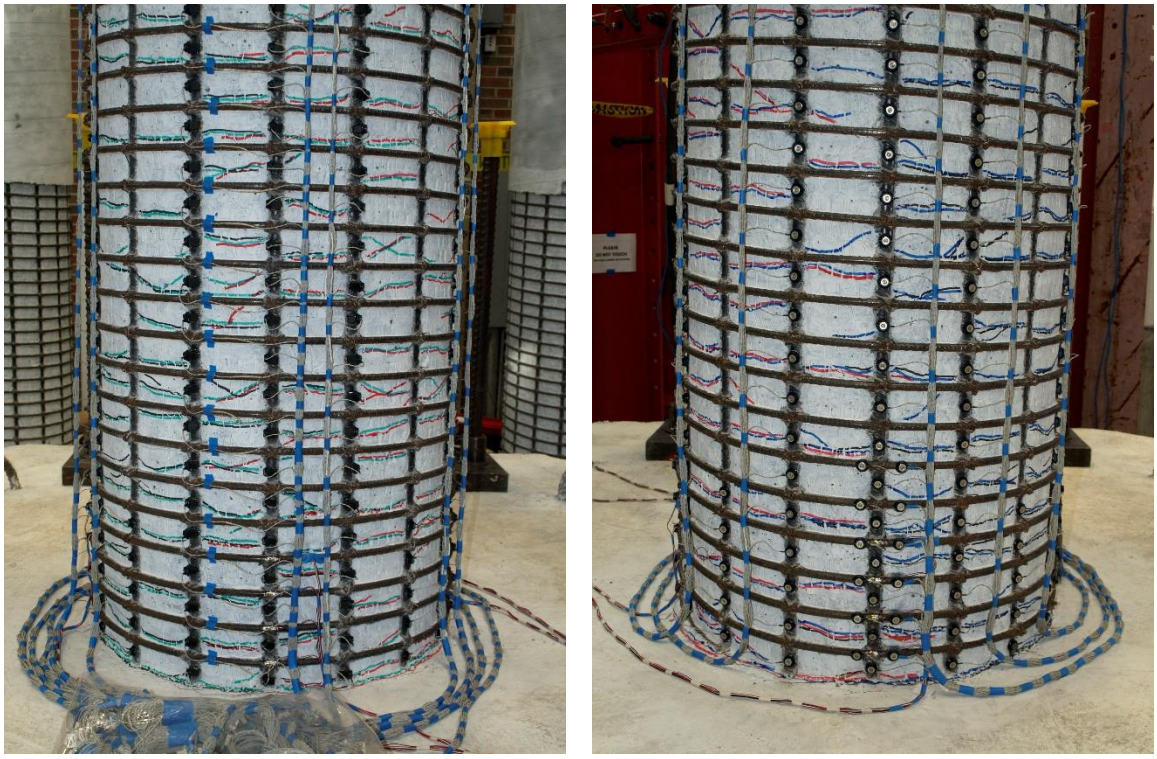

Figure 7-24. Test 4: Cracking on the (Left) West Side at $\mu_{\Delta 1}^{+2x} = 1.37"$ and (Right) East Side at $\mu_{\Delta 1}^{-2x} = -1.37"$

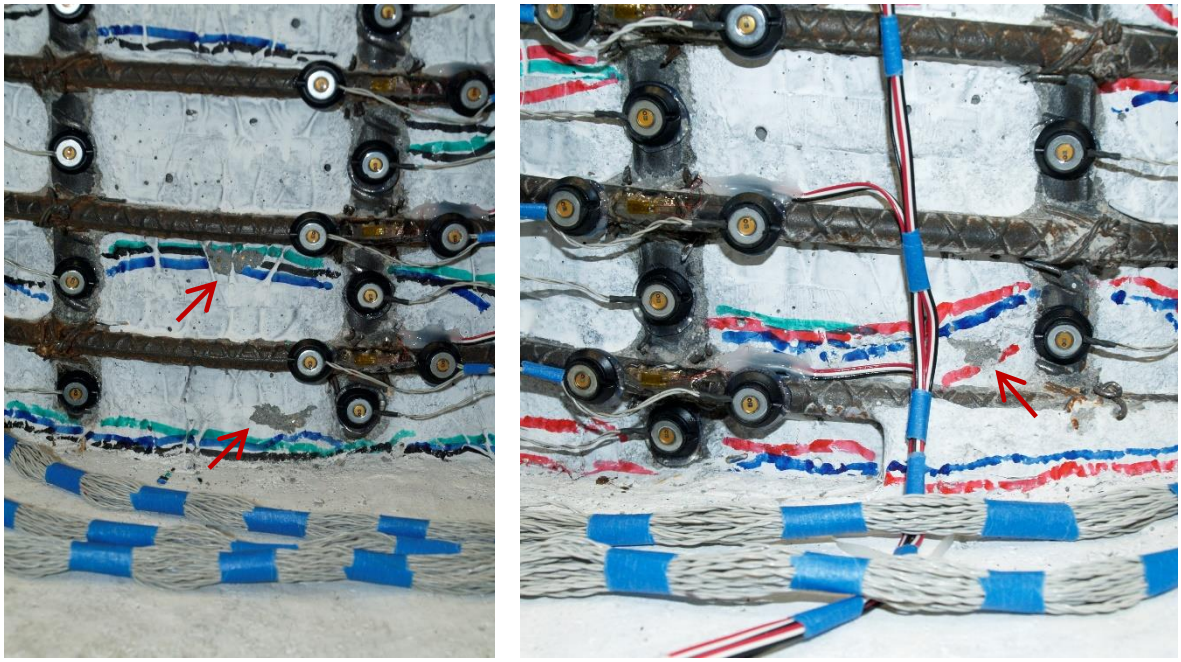

Figure 7-25. Test 4: Initial Concrete Flaking on (Left) North Side at $\mu_{\Delta 1.5}^{+1y} = 2.06$" and (Right) South Side at $\mu_{\Delta 1.5}^{-1y} = -2.09$"

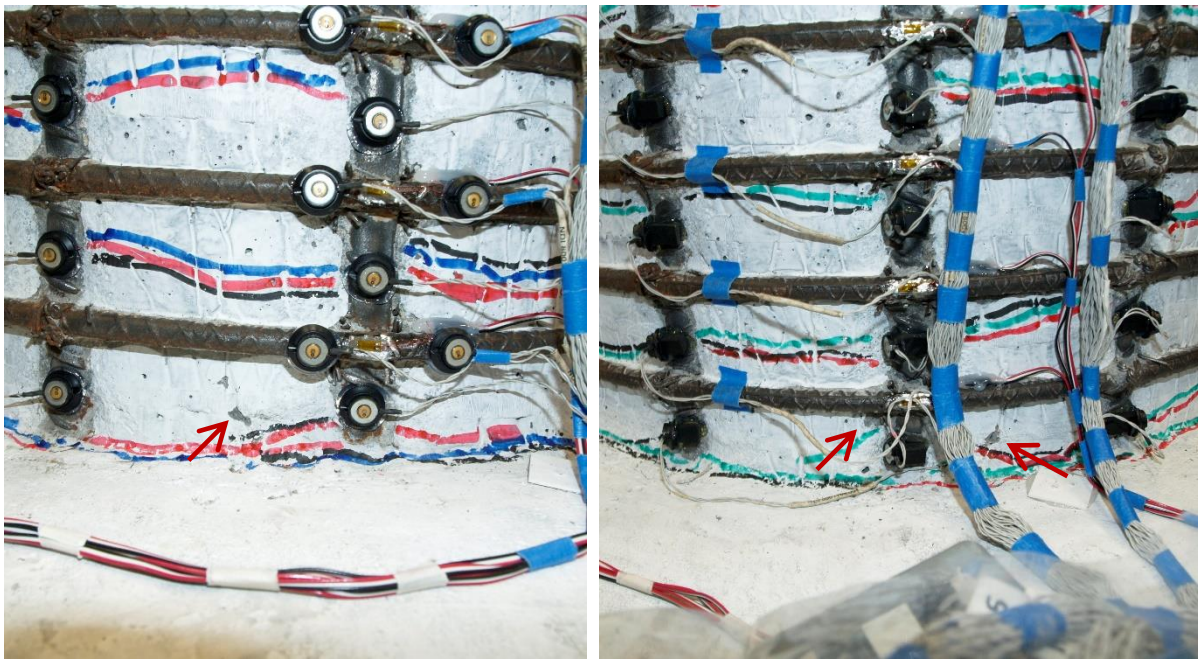

Figure 7-26. Test 4: Initial Concrete Flaking on (Left) East Side at $\mu_{\Delta 1.5}^{+1x} = 2.05$" and (Right) West Side at $\mu_{\Delta 1.5}^{-1x} = -2.05$"

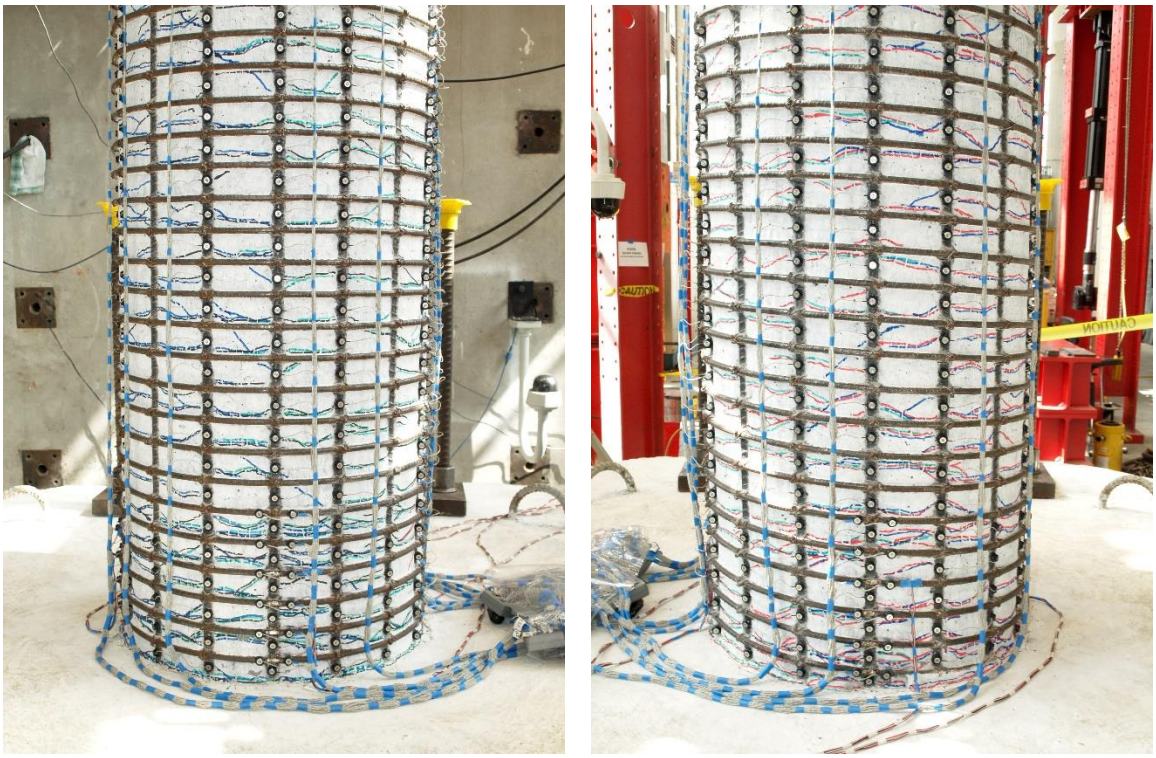

Figure 7-27. Test 4: (Left) North and (Right) South Sides of the Specimen at the End of $\mu_{\Delta 1.5}$

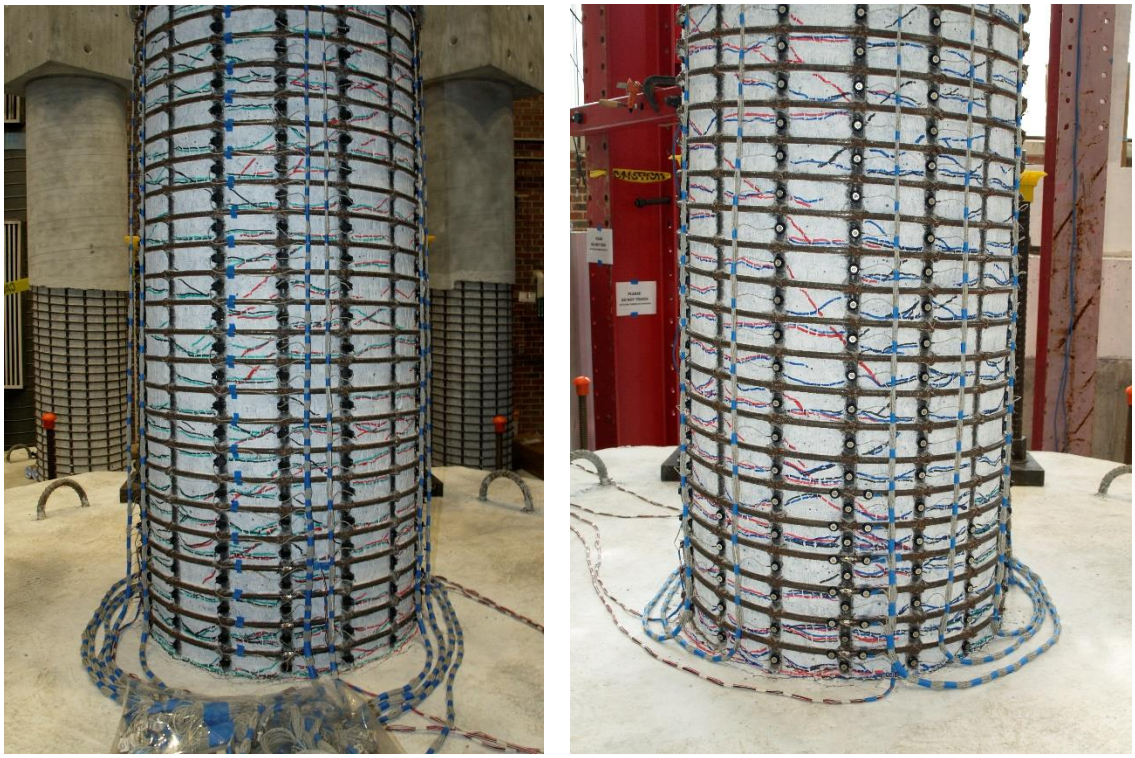

Figure 7-28. Test 4: Cracking on the (Left) West Side at $\mu_{\Delta 1.5}^{+2x} = 2.06$" and (Right) East Side at $\mu_{\Delta 1.5}^{-2x} = -2.05$"

Figure 7-29. Test 4: Concrete Crushing on the (Left) North Side at $\mu_{\Delta 2}^{+1y} = 2.73"$ and (Right) South Side at $\mu_{\Delta 2}^{-1y} = -2.73"$

Figure 7-30. Test 4: Concrete Crushing on the (Left) East Side at $\mu_{\Delta 2}^{+1x} = 2.73"$ and (Right) West Side at $\mu_{\Delta 2}^{-1x} = -2.74"$

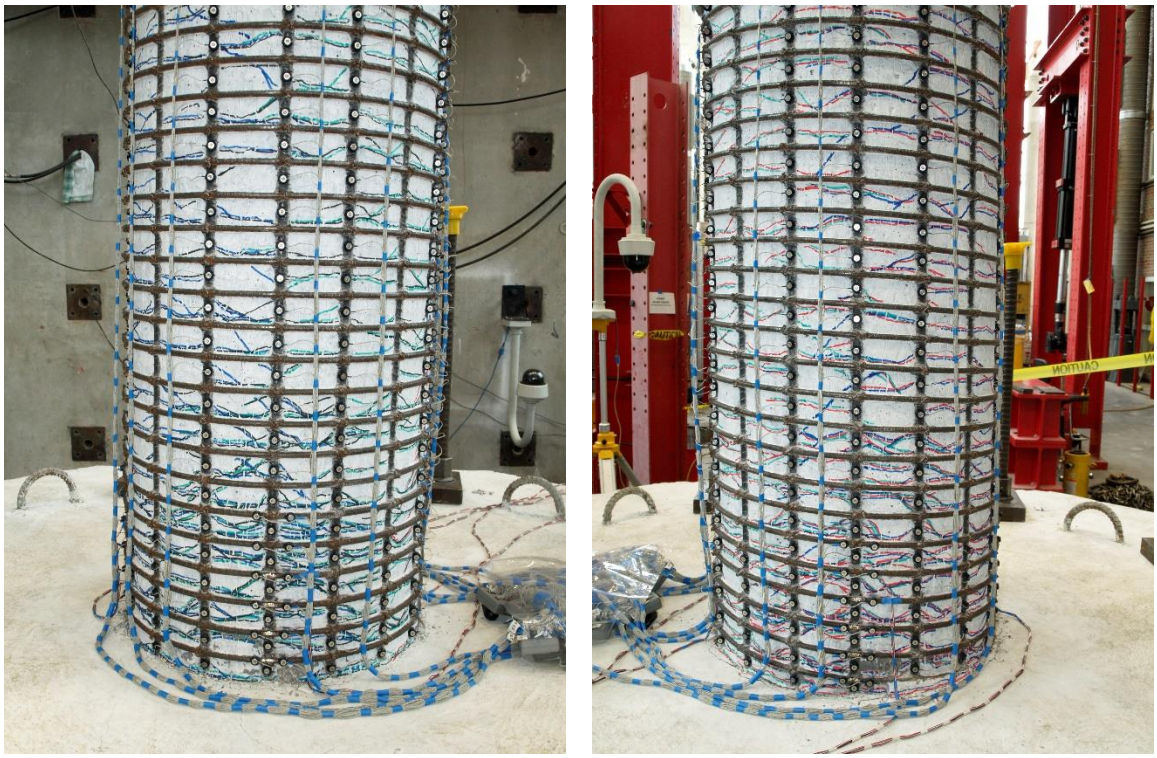

Figure 7-31. Test 4: (Left) North and (Right) South Sides of the Specimen at the End of $\mu_{\Delta 2}$

Figure 7-32. Test 4: Cracking on the (Left) West Side at $\mu_{\Delta 2}^{+2x} = 2.74$" and (Right) East Side at $\mu_{\Delta 2}^{-2x} = -2.76$"

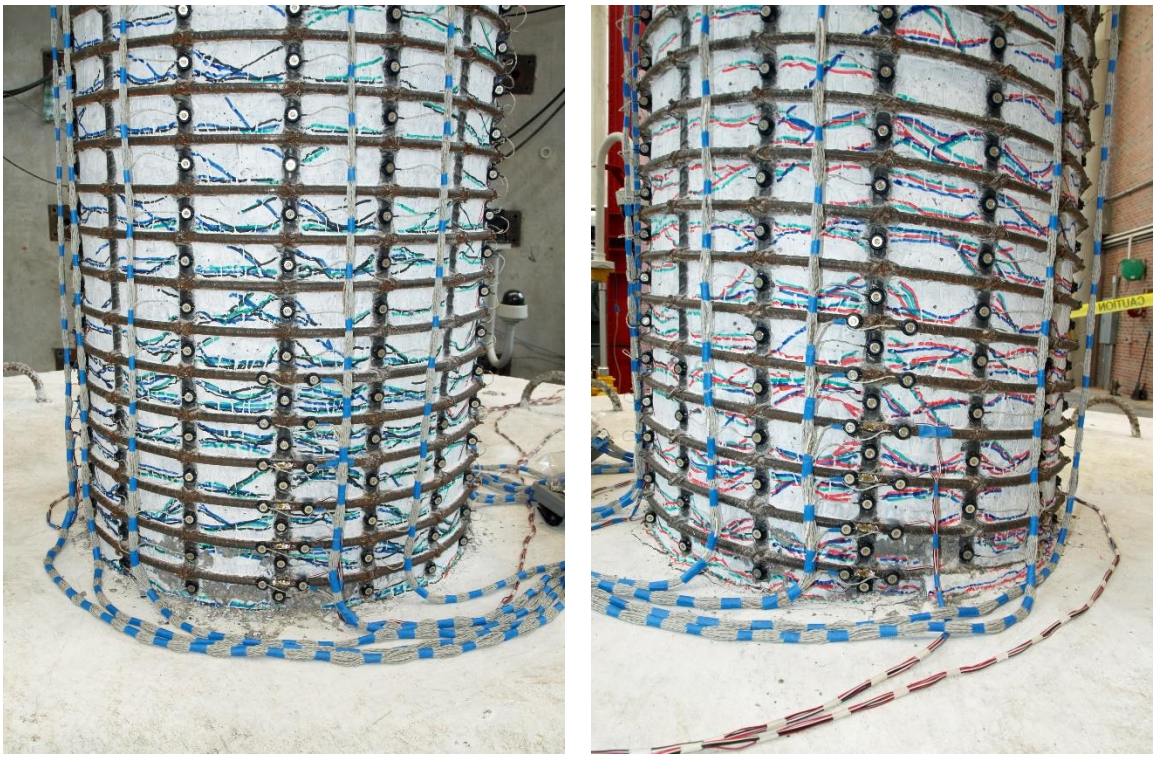

Figure 7-33. Test 4: Crushing on the (Left) North Side at $\mu_{\Delta 3}^{+1y} = 4.11"$ and (Right) South Side at $\mu_{\Delta 3}^{-1y} = -4.09"$

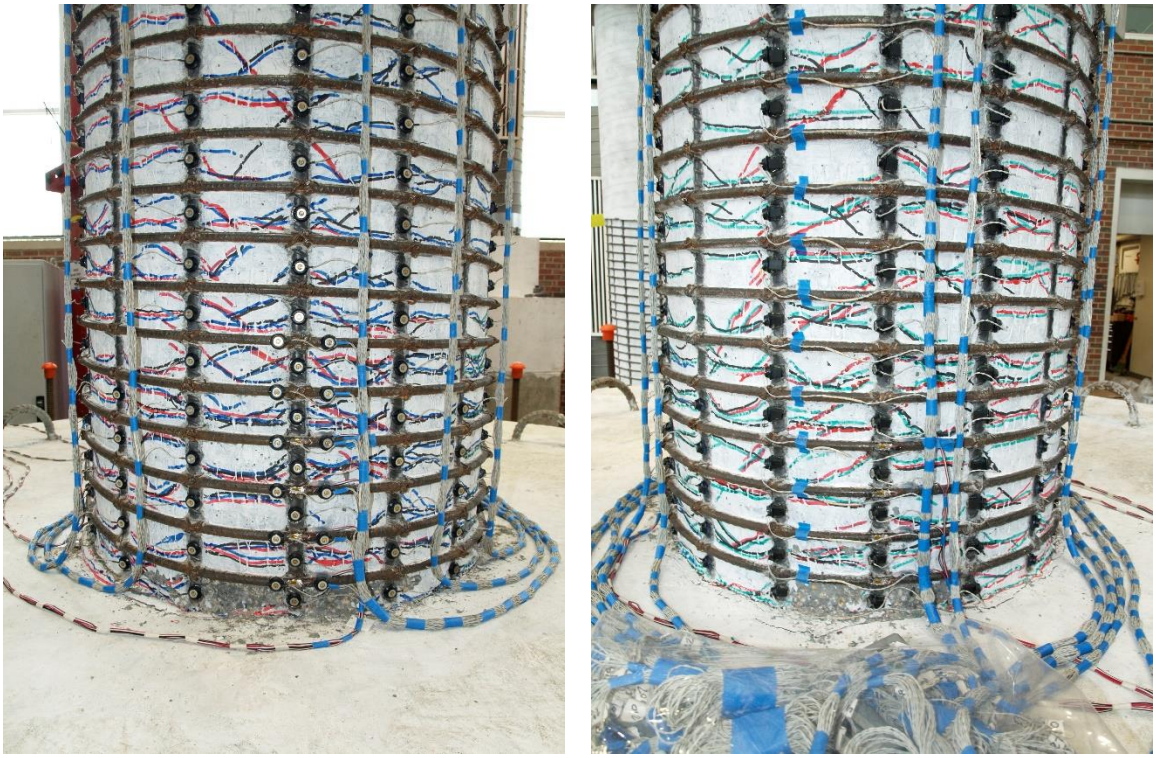

Figure 7-34. Test 4: Crushing on the (Left) East Side at $\mu_{\Delta 3}^{+1x} = 4.11"$ and (Right) West Side at $\mu_{\Delta 3}^{-1x} = -4.14"$

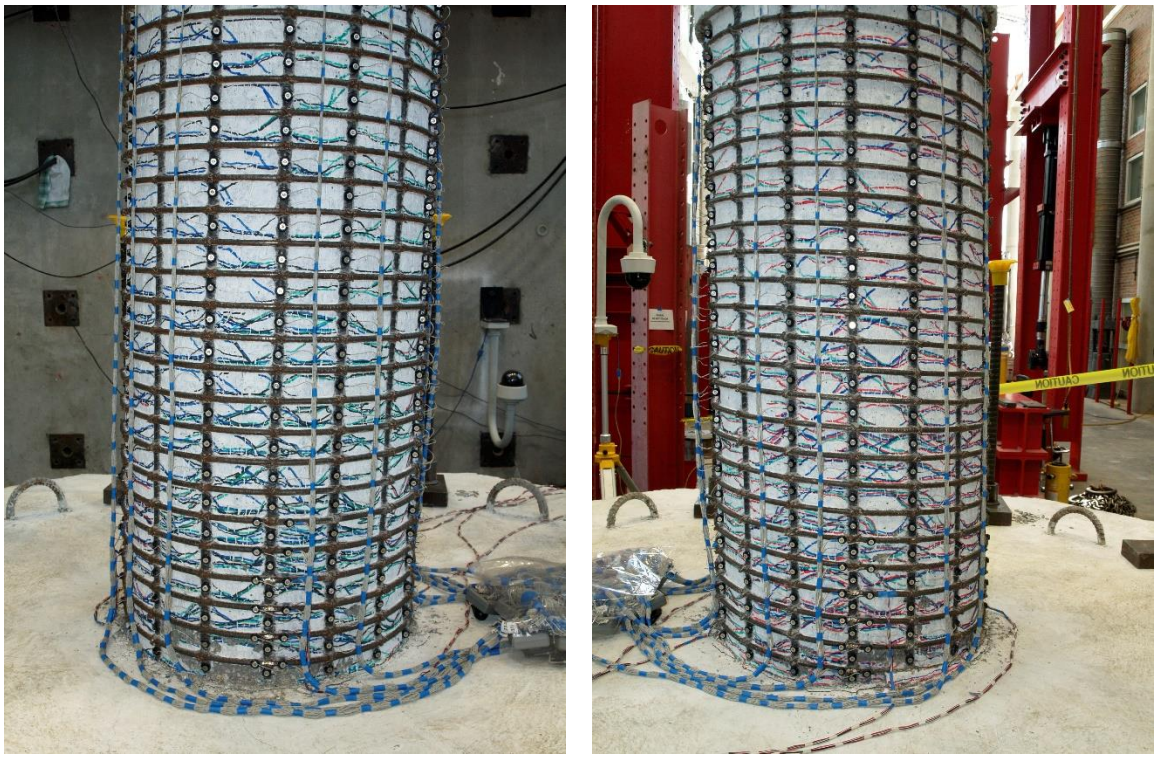

Figure 7-35. Test 4: (Left) North and (Right) South Sides of the Specimen at the End of $\mu_{\Delta 3}$

Figure 7-36. Test 4: Cracking on the (Left) West Side at $\mu_{\Delta 3}^{+2x} = 4.09$" and (Right) East Side at $\mu_{\Delta 3}^{-2x} = -4.09$"

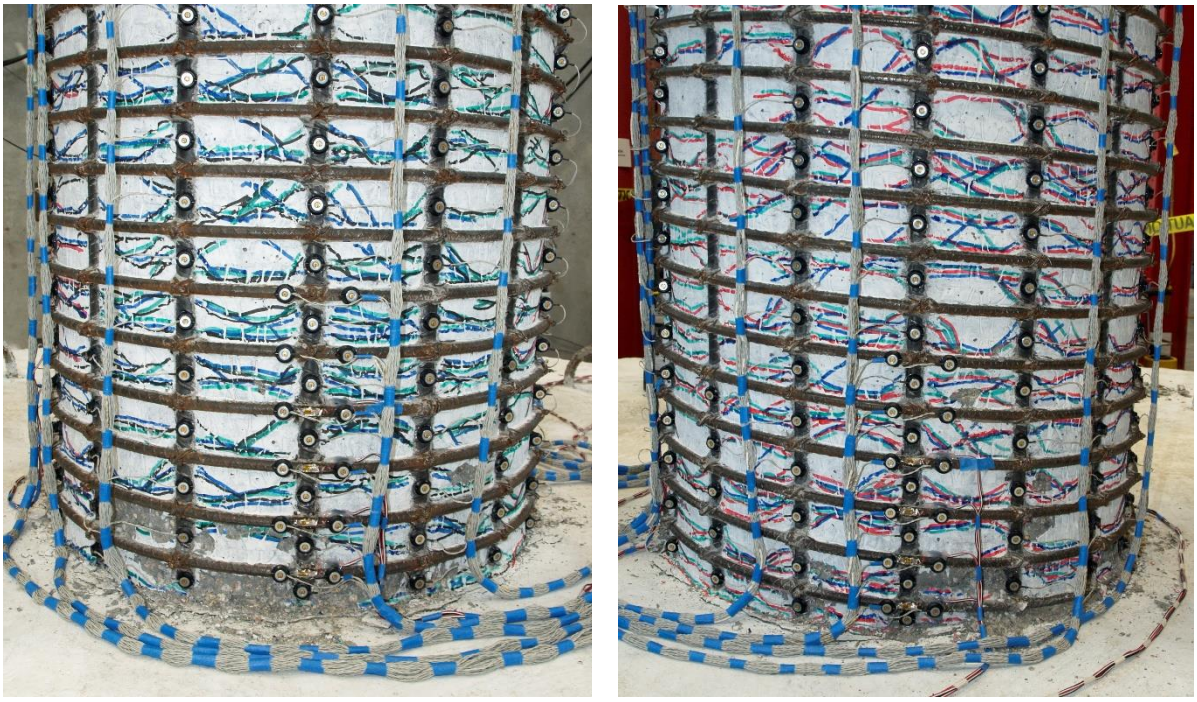

Figure 7-37. Test 4: Crushing on the (Left) North Side at $\mu_{\Delta 4}^{+1y} = 5.47"$ and (Right) South Side at $\mu_{\Delta 4}^{-1y} = -5.51"$

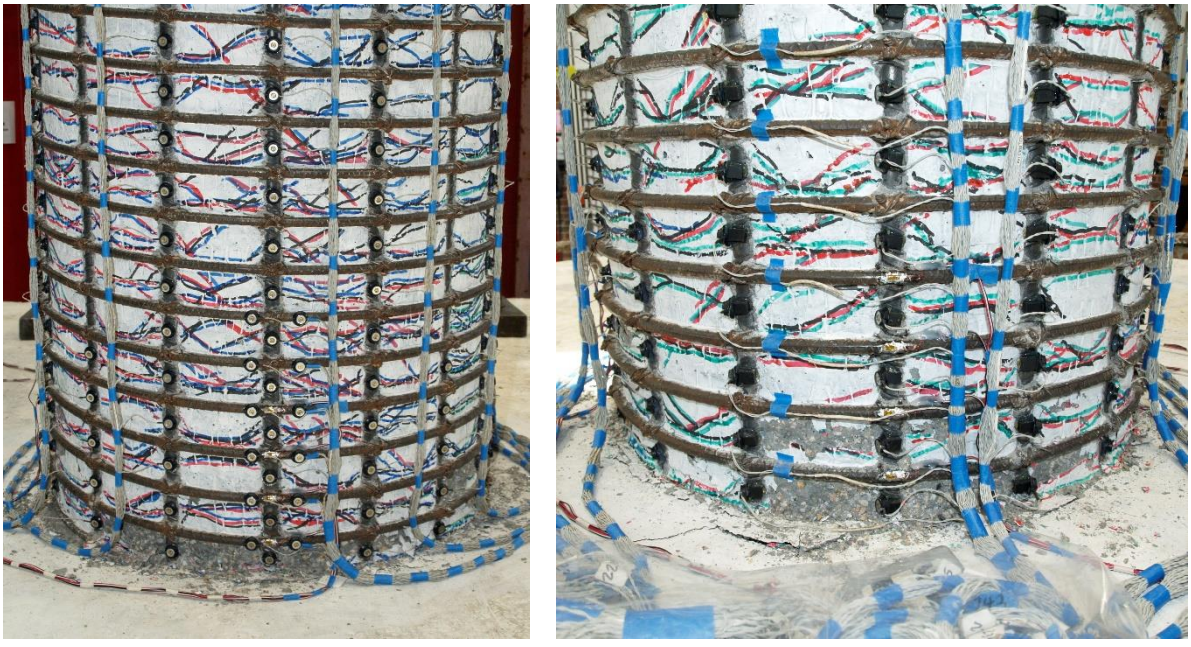

Figure 7-38. Test 4: Crushing on the (Left) East Side at $\mu_{\Delta 4}^{+1x} = 5.47"$ and (Right) West Side at $\mu_{\Delta 4}^{-1x} = -5.48"$

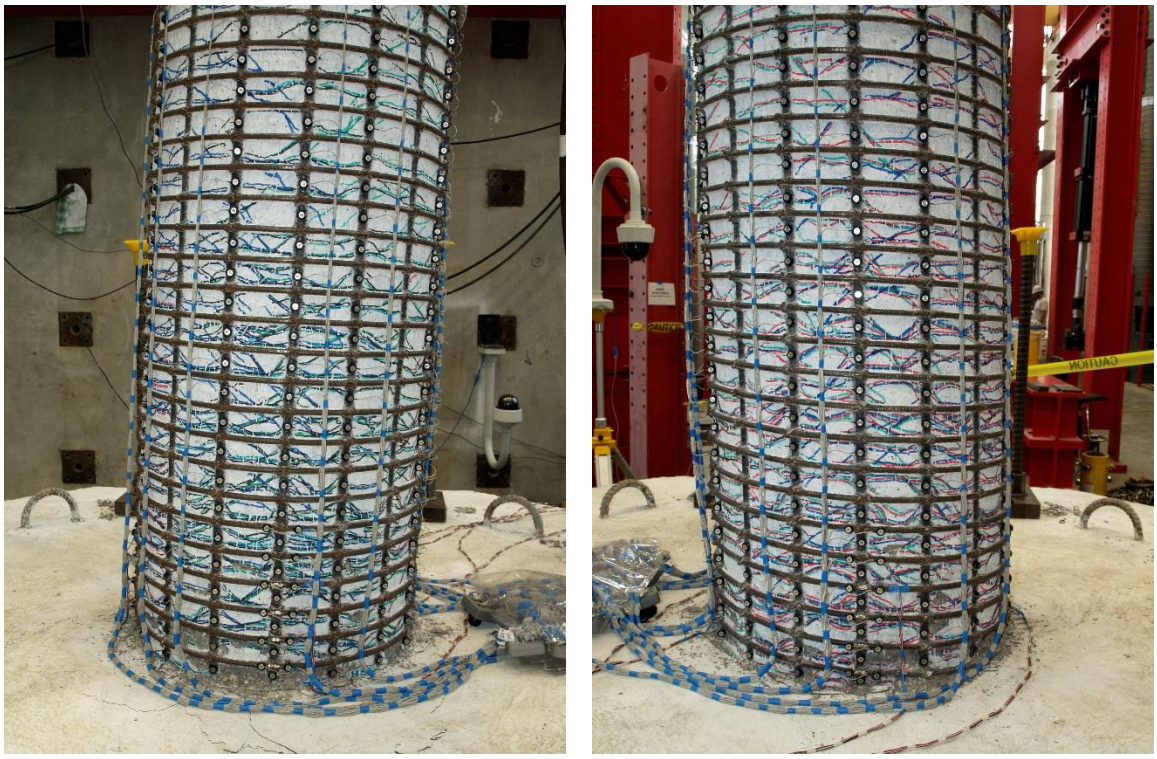

Figure 7-39. Test 4: (Left) North and (Right) South Sides of the Specimen at the End of $\mu_{\Delta 4}$

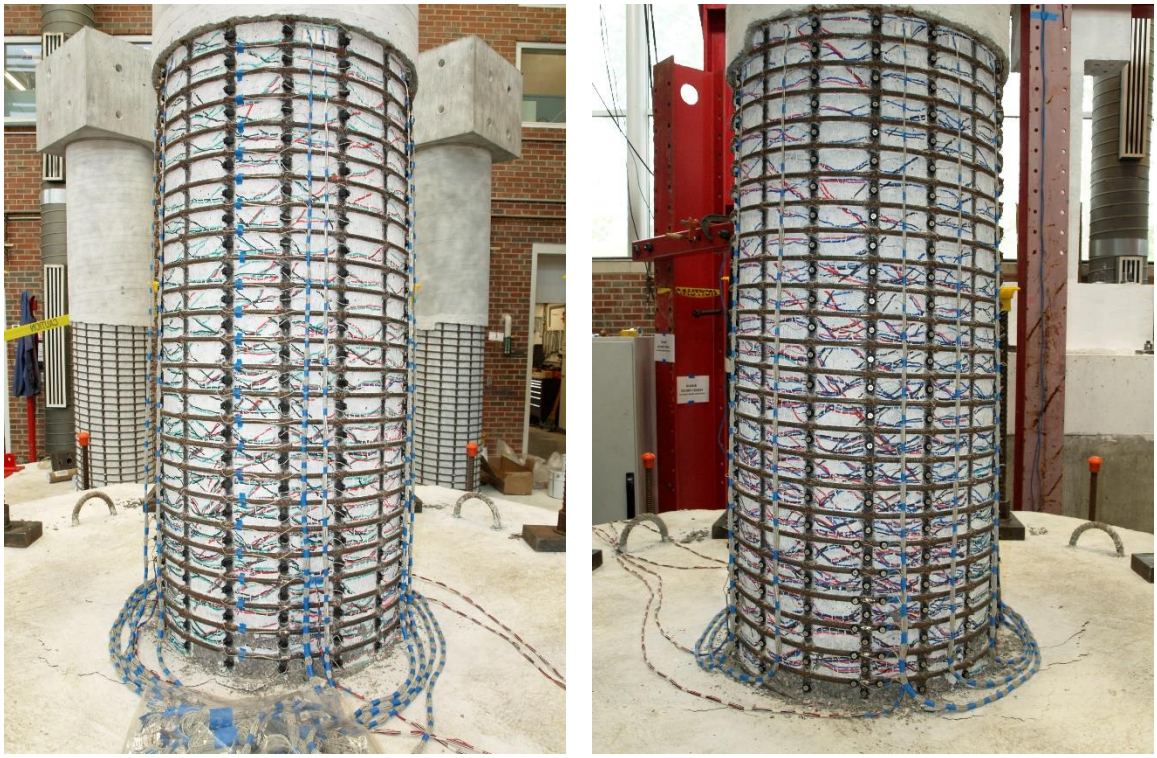

Figure 7-40. Test 4: Cracking on the (Left) West Side at $\mu_{\Delta 4}^{+2x} = 5.48$" and (Right) East Side at $\mu_{\Delta 4}^{-2x} = -5.46$"

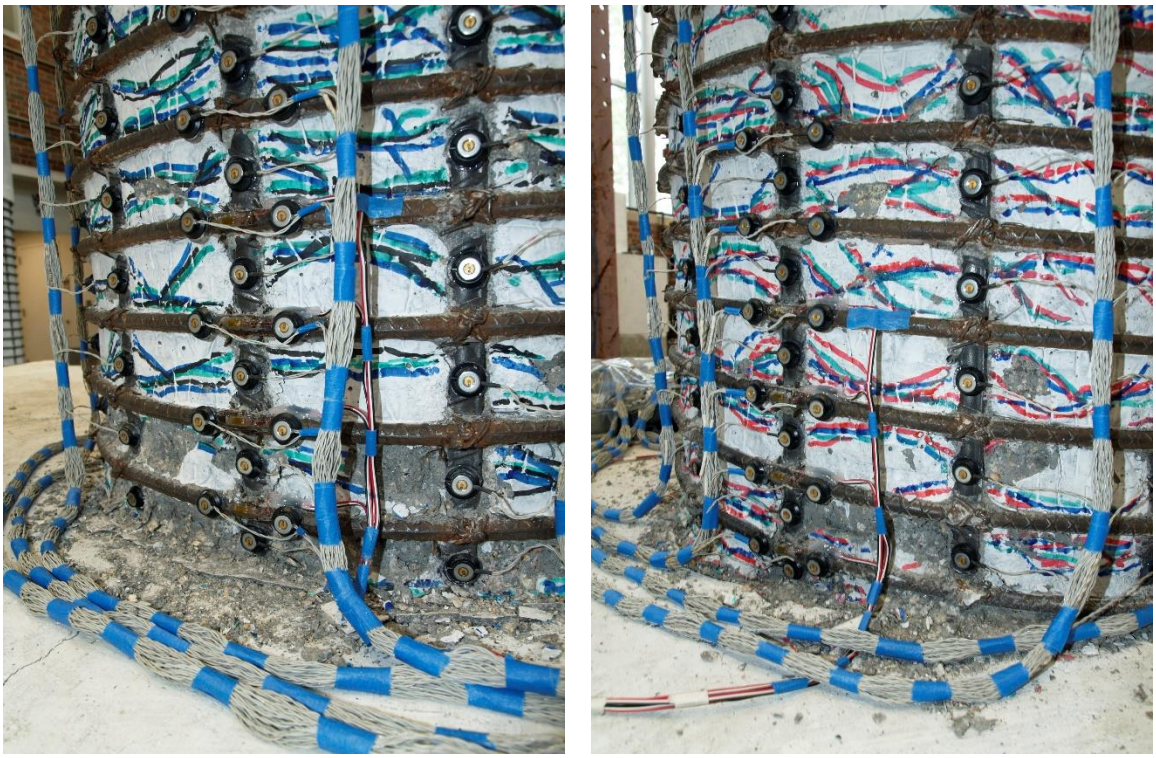

Figure 7-41. Test 4: Unbuckled Reinforcement on the (Left) North at $\mu_{\Delta 5}^{+1y} = 6.84"$ and (Right) South at $\mu_{\Delta 5}^{-1y} = -6.84"$

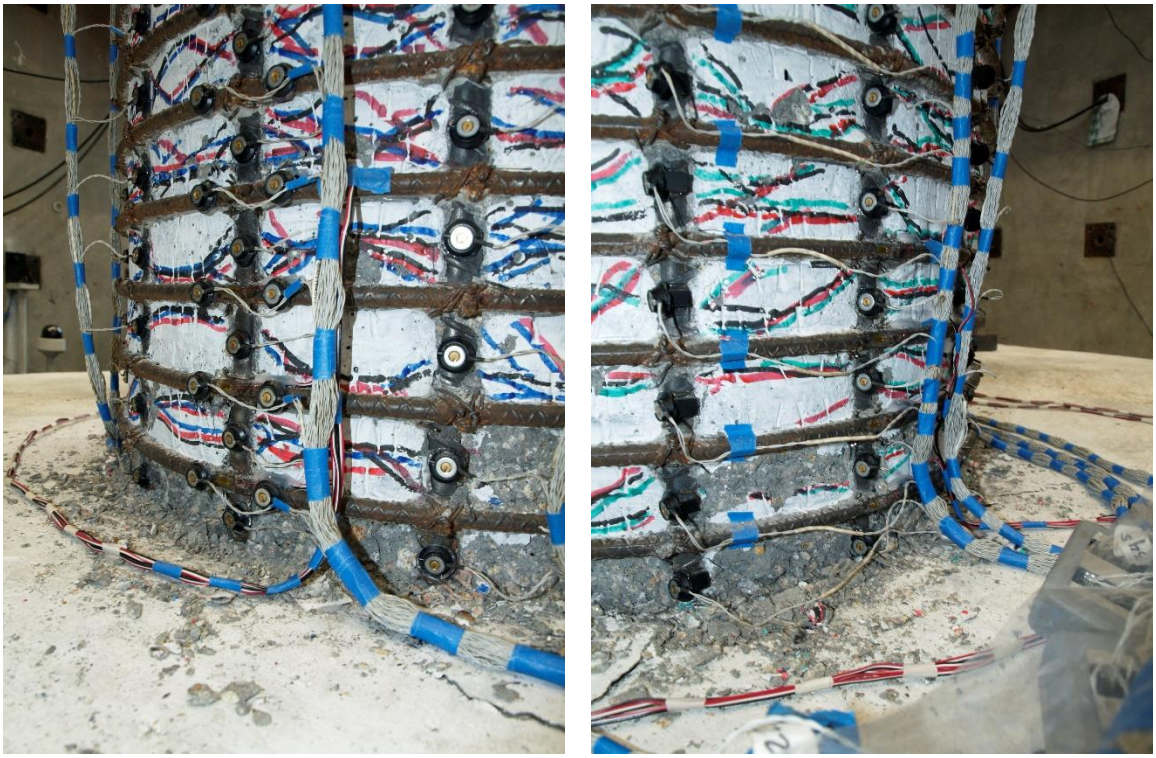

Figure 7-42. Test 4: Unbuckled Reinforcement on the (Left) East at $\mu_{\Delta 5}^{+1x} = 6.85"$ and (Left) West at $\mu_{\Delta 5}^{-1x} = -6.85"$

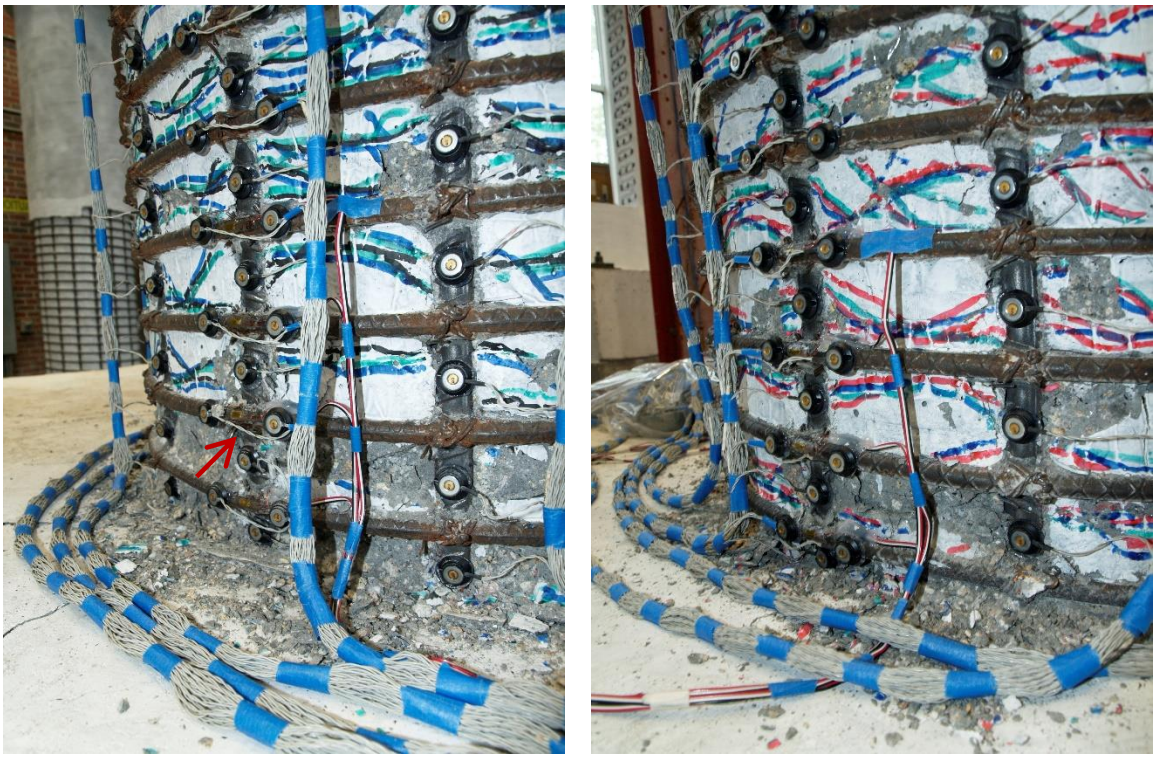

Figure 7-43. Test 4: (Left) Buckling of Bar N at $\mu_{\Delta 5}^{+2y} = 6.84$" and (Right) South Bars Remained Straight at $\mu_{\Delta 5}^{-2y} = -6.83$"

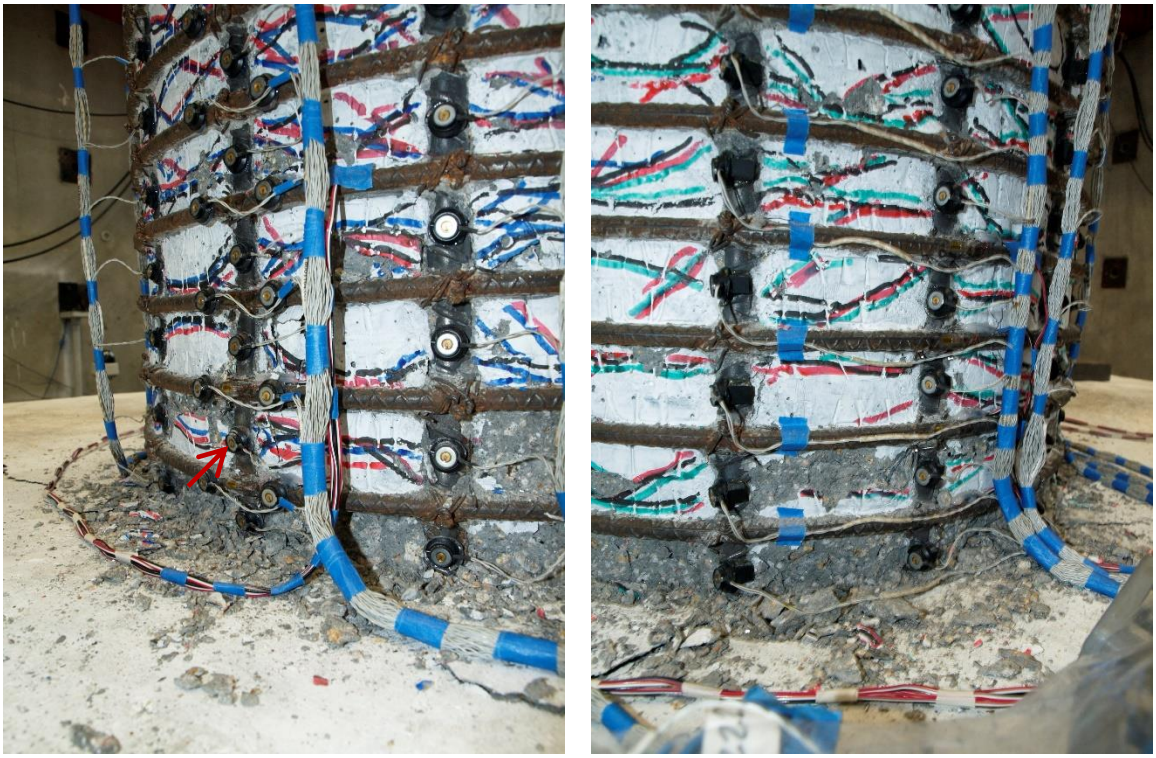

Figure 7-44. Test 4: (Left) Buckling of Bar E at $\mu_{\Delta 5}^{+2x} = 6.85$" and (Right) West Bars Remained Straight at $\mu_{\Delta 5}^{-2x} = -6.85$"

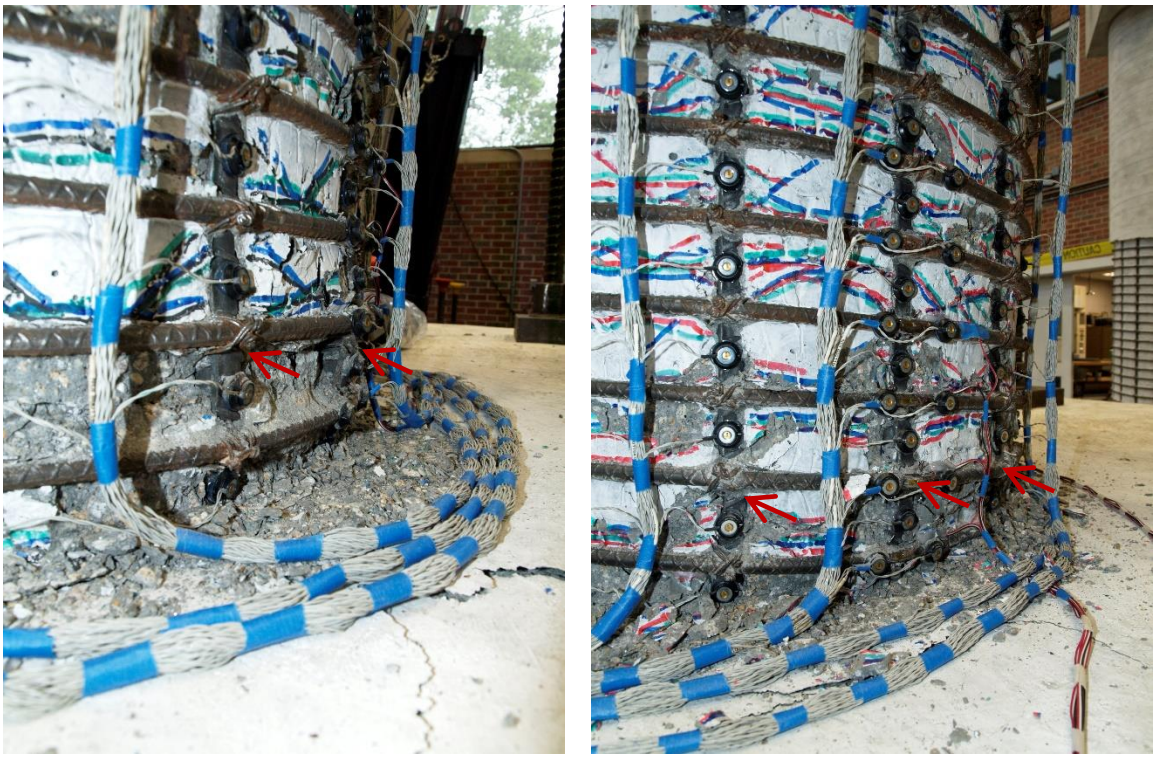

Figure 7-45. Test 4: Buckling of (Left) Bar NNE at $\mu_{\Delta 6}^{+1y} = 8.22$" and (Right) Bars S, SSE, and SSW at $\mu_{\Delta 6}^{-1y} = -8.23$"

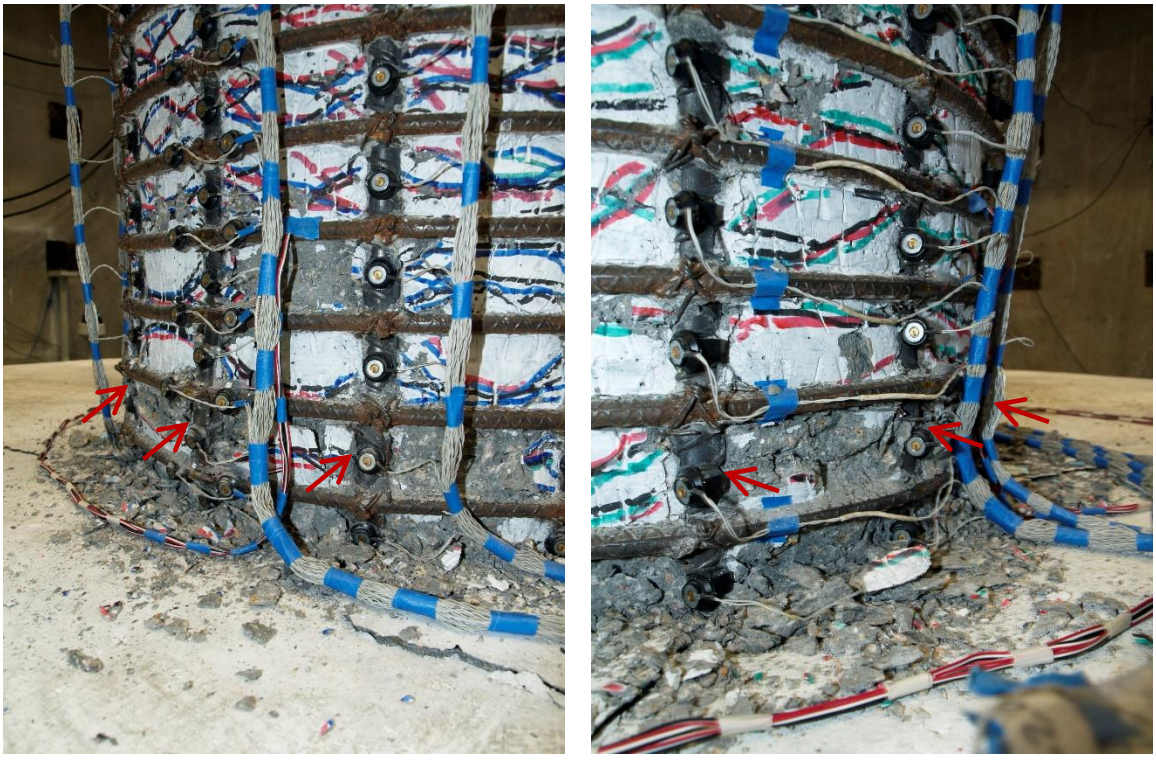

Figure 7-46. Test 4: Buckling of (Left) Bars ENE &ESE at $\mu_{\Delta 6}^{+1x} = 8.20$" and (Right) Bars W, WNW, & WSW at $\mu_{\Delta 6}^{-1x} = -8.21$"

Figure 7-47. Test 4: (Left) Buckling of Bars NNW & NE at $\mu_{\Delta 6}^{+2y} = 8.21$" and (Right) Fracture of Bar N at -4.75" during $\mu_{\Delta 6}^{-2y}$

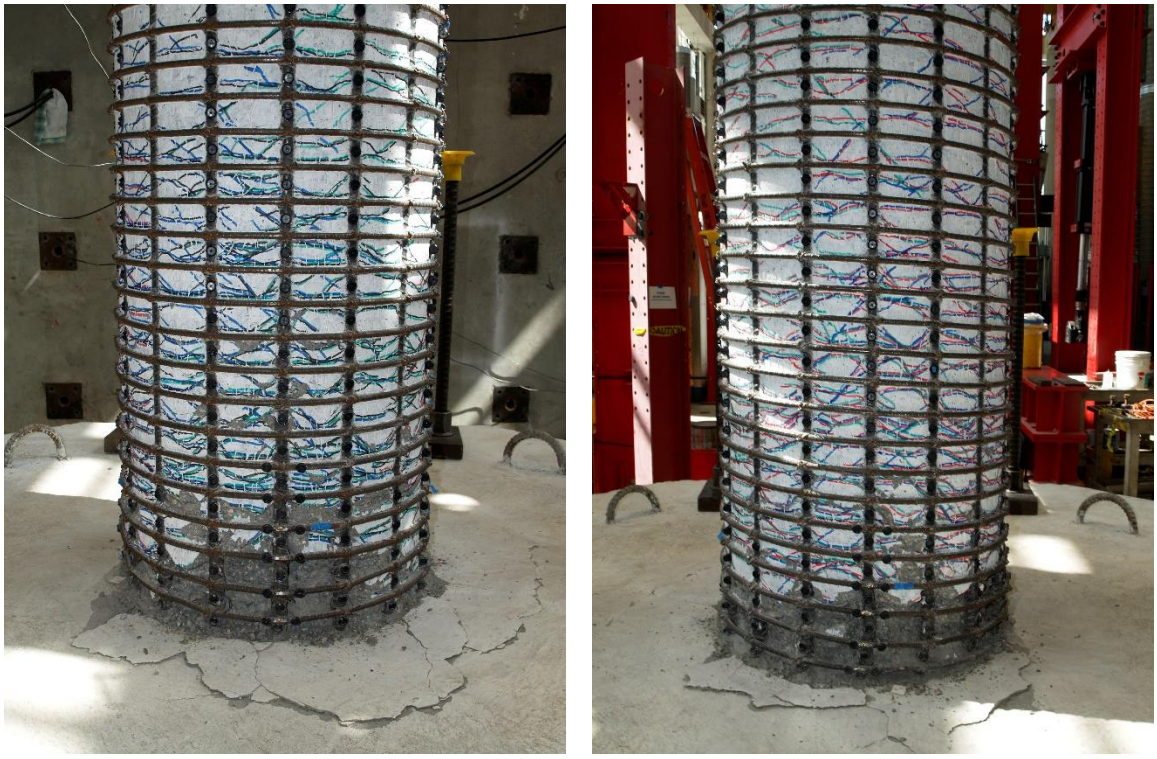

Figure 7-48. Test 4: (Left) North and (Right) South Sides of the Specimen after Instrumentation Removal

Figure 7-49. Test 4: (Left) East and (Right) West Sides of the Specimen after Instrumentation Removal

Figure 7-50. Test 4: Close Up of Damage on the North Side of the Specimen

Test 4 - Strain Data Analysis

North and South Bar Strains

Vertical strain profiles for North and South reinforcement during y-direction cycles are shown in Figure 7-51 and Figure 7-52. Strains in the lowest four spiral layers during compressive y-direction cycles on the North and South sides of the specimen appear in Figure 7-53 and Figure 7-54. The relationship between strain and displacement for either peak tensile or peak compressive gauge lengths appear in Figure 7-55 through Figure 7-59. These figures contain monotonic moment curvature predictions for respective plastic hinge methods. PCK (2007) Lp refers to the (Priestley, Calvi and Kowalsky 2007) plastic hinge method, GN15 Tension/Compression Lpr refers to the (Goodnight, Kowalsky and Nau 2015a) unidirectional modified plastic hinge method, TX Measured refer to using the measured extent of plasticity and average equivalent strain penetration length from this specific test, and New Equations refers to a new bidirectional plastic hinge method which was created based on this study. Details of the new plastic hinge method appear in a later chapter of this report.

The spiral strain gauge hysteresis for the first and second layers above the footing on the North side of the specimen are shown in Figure 7-61 and Figure 7-62. The first spiral layer goes off scale during $\mu_{\Delta 5}^{+2y} = 6.84$" as the North extreme fiber bar visibly buckled, see Figure 7-43. The second North spiral layer above the footing went off scale during $\mu_{\Delta 5}^{+1y} = 6.84$", even though the North reinforcement remained visibly straight as shown in Figure 7-41. The visual observation of bar buckling was confirmed upon inspection of the North longitudinal bar strain hysteresis in Figure 7-60; however, there was slight measurable outward deformation in the previous compressive cycle.

The spiral strain gauge hysteresis for the first and second layers above the footing on the South side of the specimen appear in Figure 7-64 and Figure 7-65. The first South spiral layer goes off scale during $\mu_{\Delta 6}^{-1y} = -8.23$" as three South bars buckled simultaneously, see Figure 7-45. The second spiral layer went off scale during $\mu_{\Delta 5}^{-2y} = -6.83$", even though the South bars remained visibly straight as shown in Figure 7-43. The visual observation of bar buckling was confirmed upon inspection of the South longitudinal bar strain hysteresis in Figure 7-63; however, there was significant measurable outward deformation in the previous compressive cycle. As previously noted, this measurable deformation was not discernable by eye.

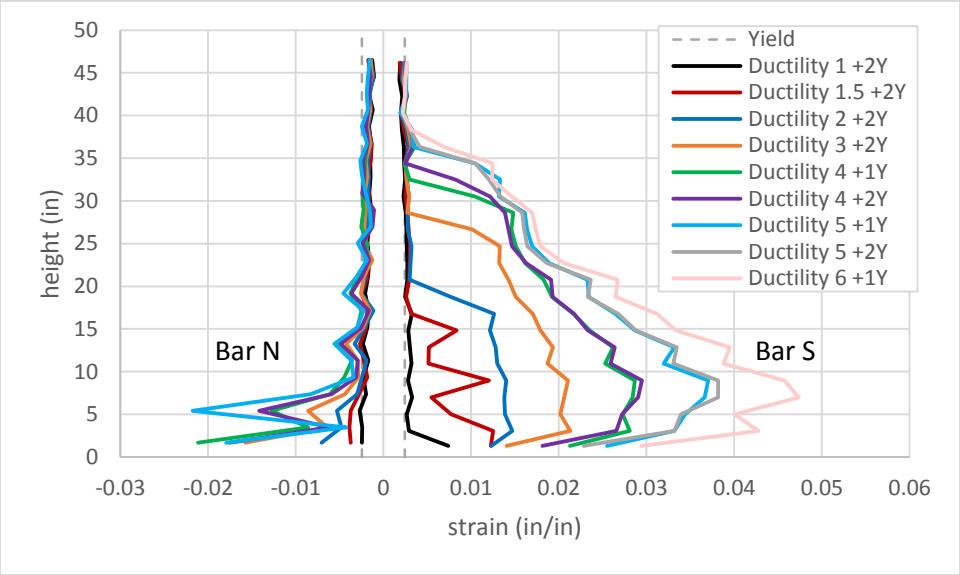

Figure 7-51. Test 4: Vertical Strain Profiles for Loading in the +Y-direction

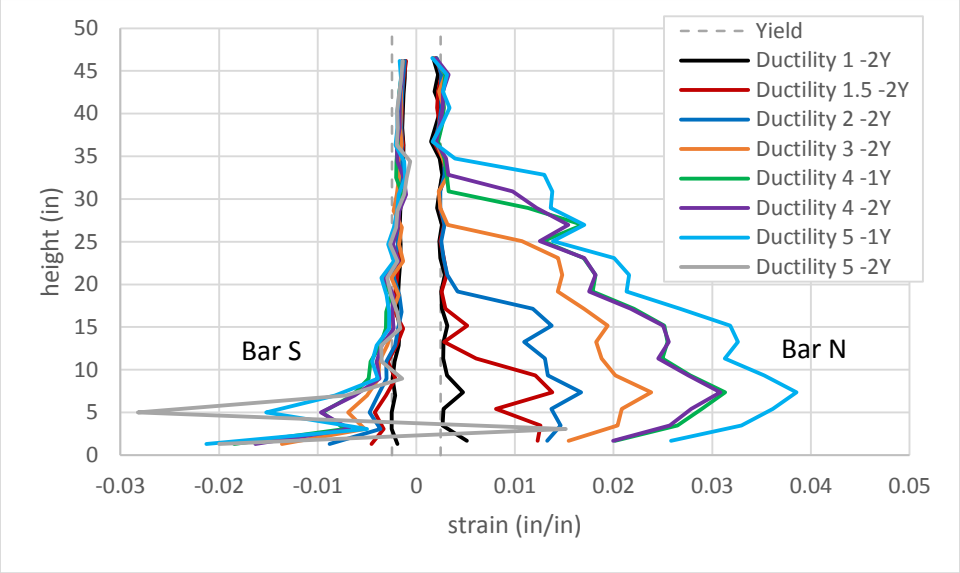

Figure 7-52. Test 4: Vertical Strain Profiles for Loading in the -Y-direction

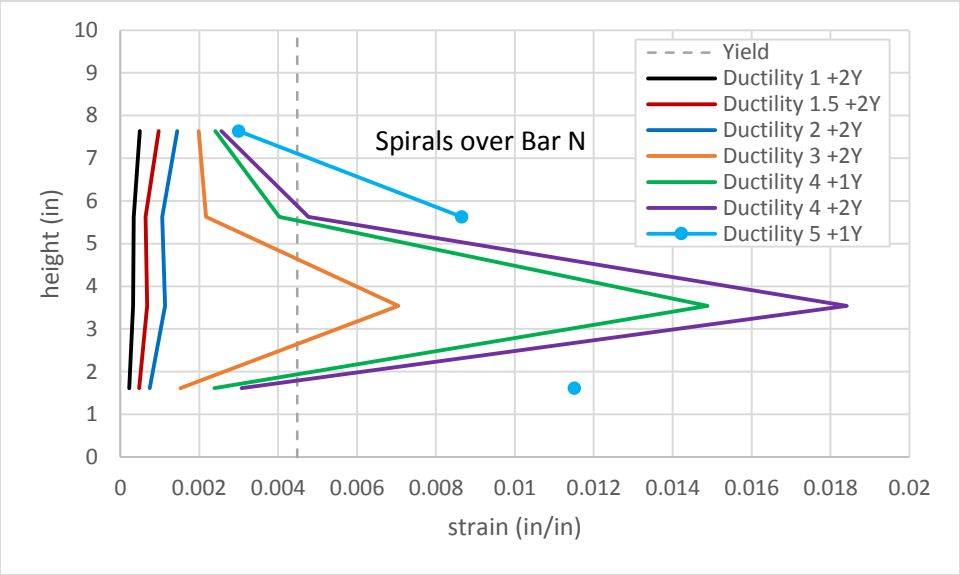

Figure 7-53. Test 4: Spiral Strains Measured Over the North Extreme Fiber Bar during +Y Cycles

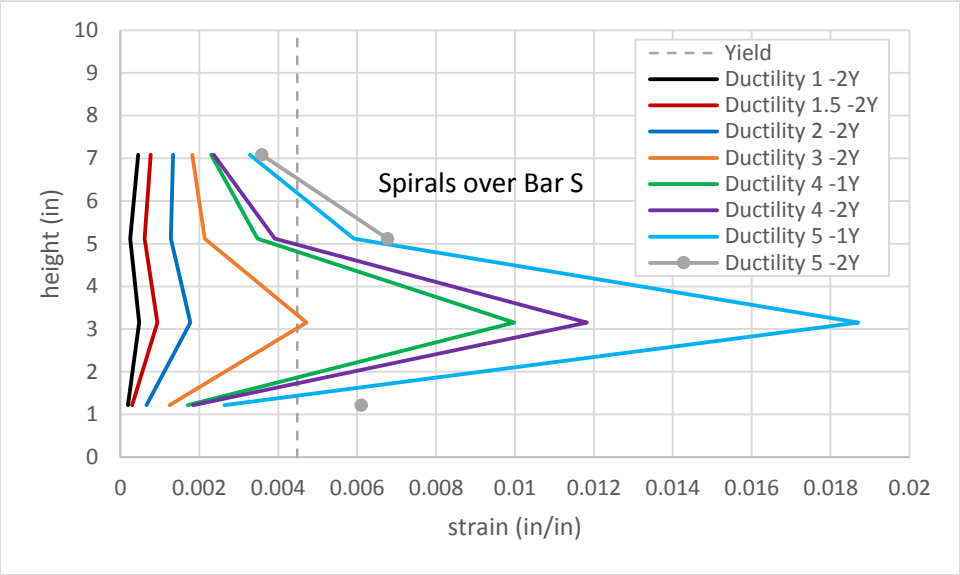

Figure 7-54. Test 4: Spiral Strains Measured Over the South Extreme Fiber Bar during –Y Cycles

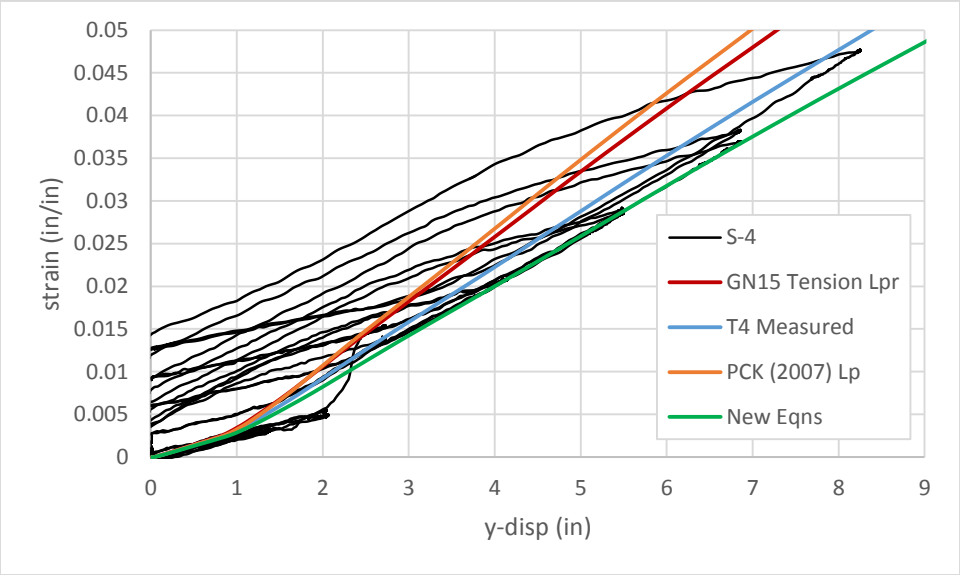

Figure 7-55. Test 4: Tension Strain-Disp. for Bar S (Gauge Length 4 Centered 6.99" above the Footing)

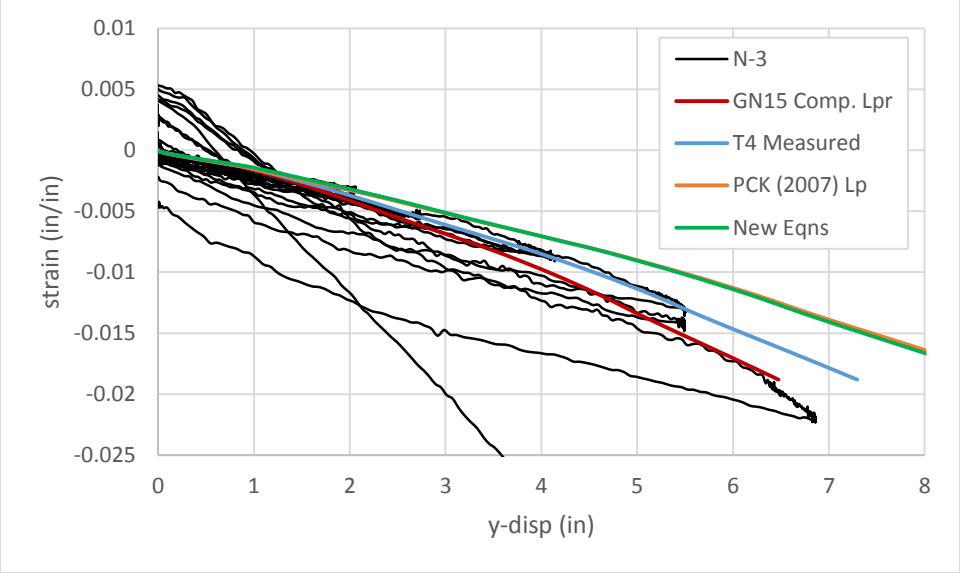

Figure 7-56. Test 4: Compression Strain-Disp. for Bar N (Gauge Length 3 Centered 5.40" above the Footing)

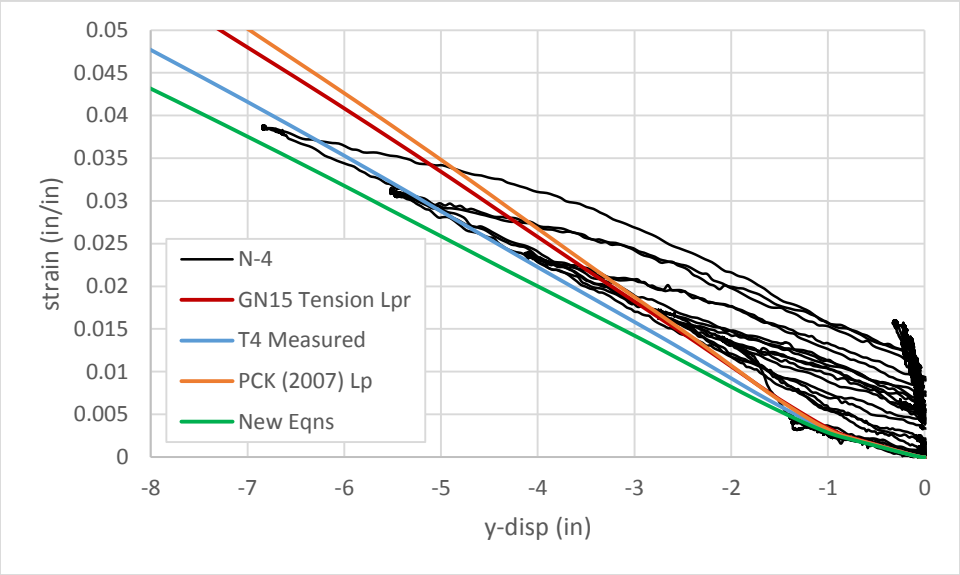

Figure 7-57. Test 4: Tension Strain-Disp. for Bar N (Gauge Length 4 Centered 7.37" above the Footing)

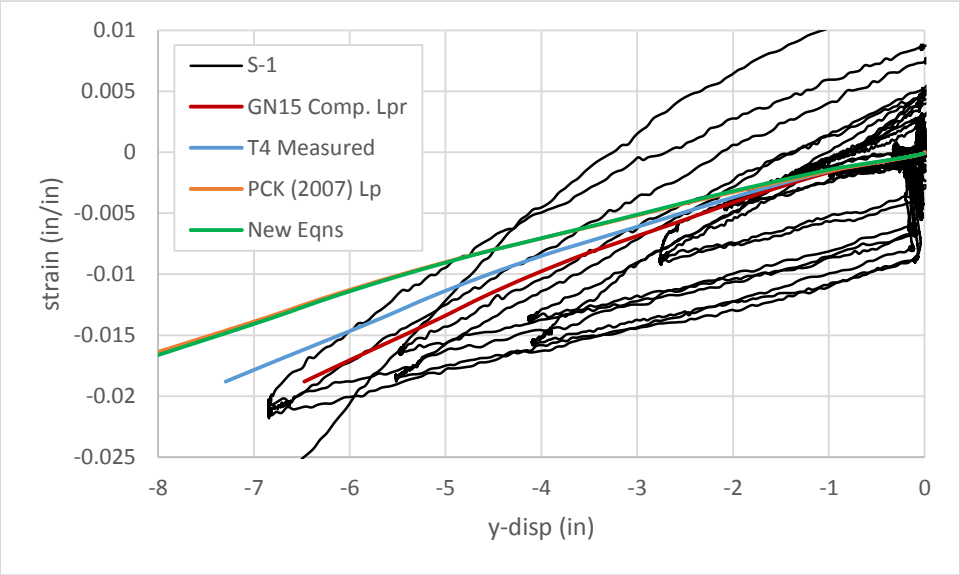

Figure 7-58. Test 4: Compression Strain-Disp. for Bar S (Gauge Length 1 Centered 1.32" above the Footing)

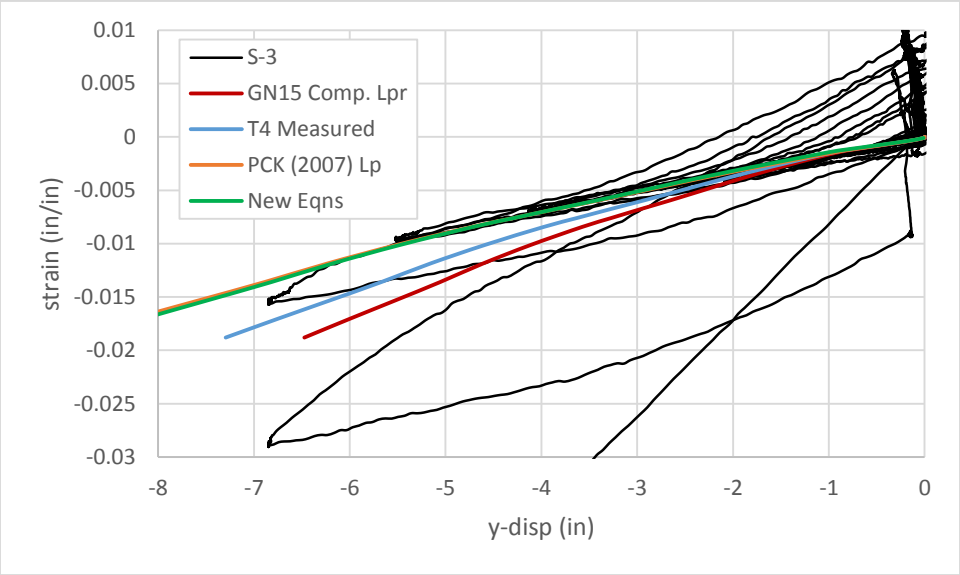

Figure 7-59. Test 4: Compression Strain-Disp. for Bar S (Gauge Length 3 Centered 5.02" above the Footing)

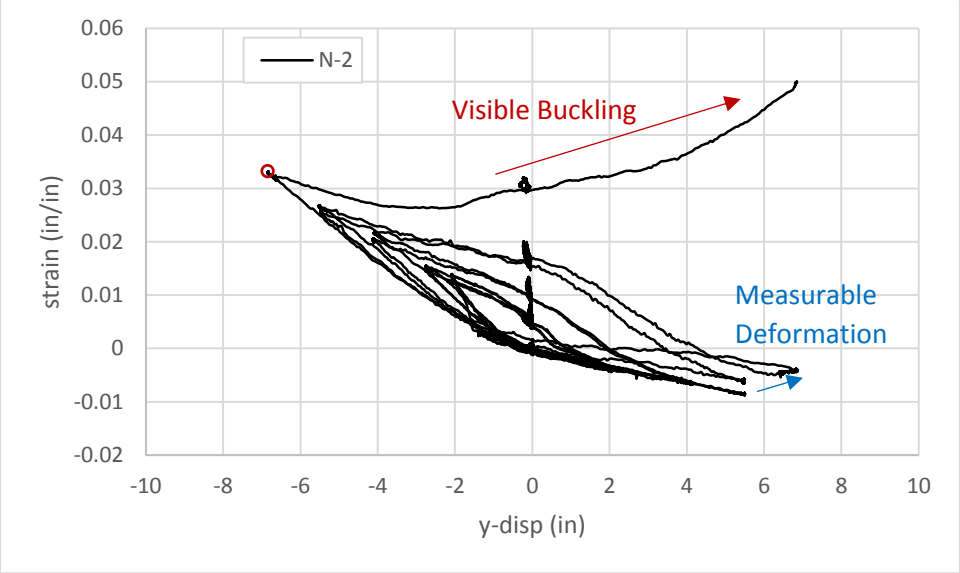

Figure 7-60. Test 4: Strain Hysteresis over the North Buckled Bar (Gauge Length 2 Centered 3.46" above the Footing)

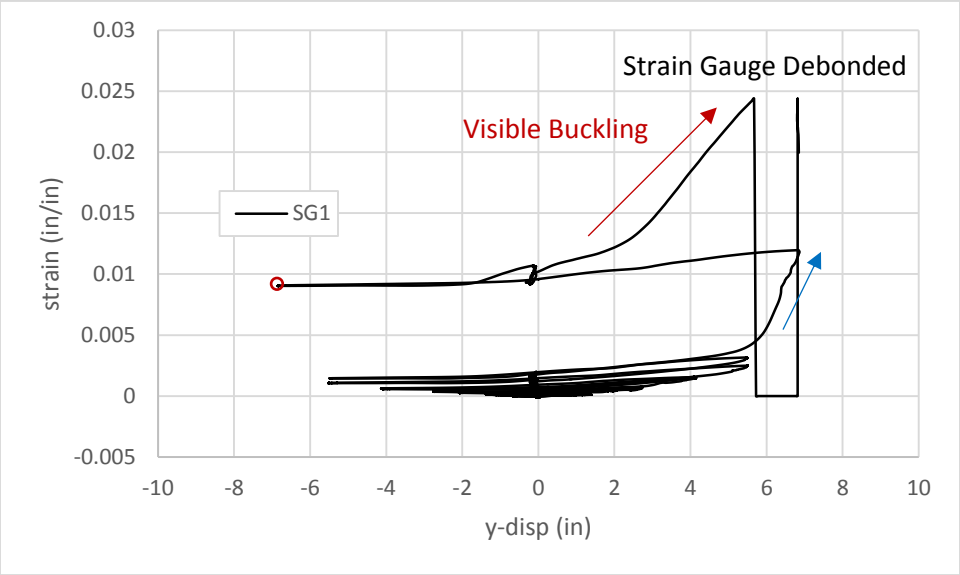

Figure 7-61. Test 4: North Spiral Strain Gauge Hysteresis for the First Layer above the Footing

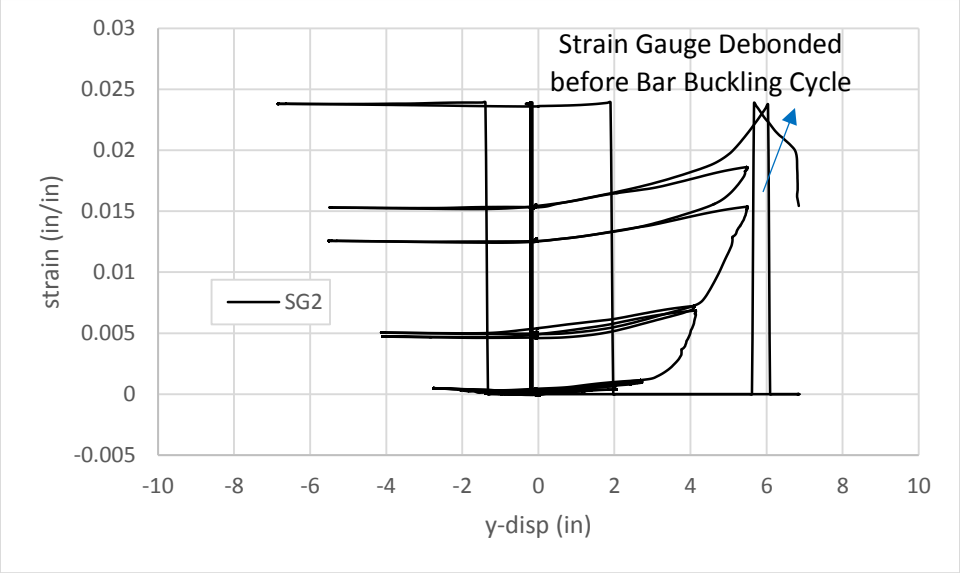

Figure 7-62. Test 4: North Spiral Strain Gauge Hysteresis for the Second Layer above the Footing

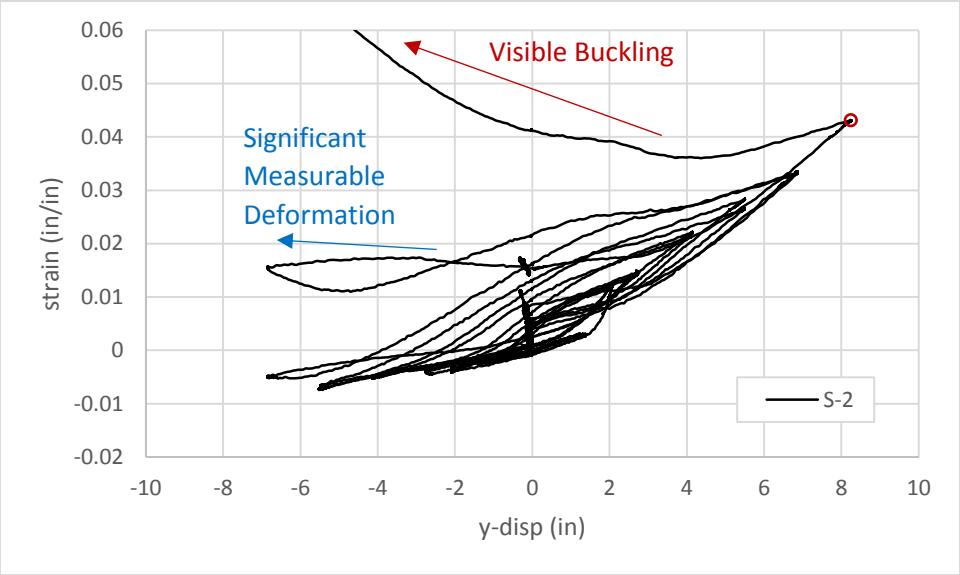

Figure 7-63. Test 4: Strain Hysteresis over the South Buckled Bar (Gauge Length 2 Centered 3.05" above the Footing)

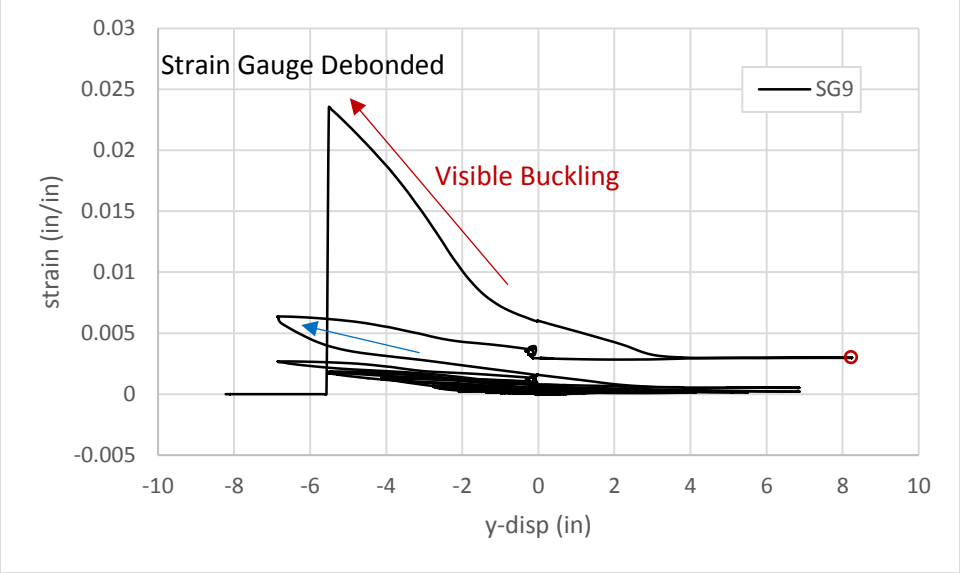

Figure 7-64. Test 4: South Spiral Strain Gauge Hysteresis for the First Layer above the Footing

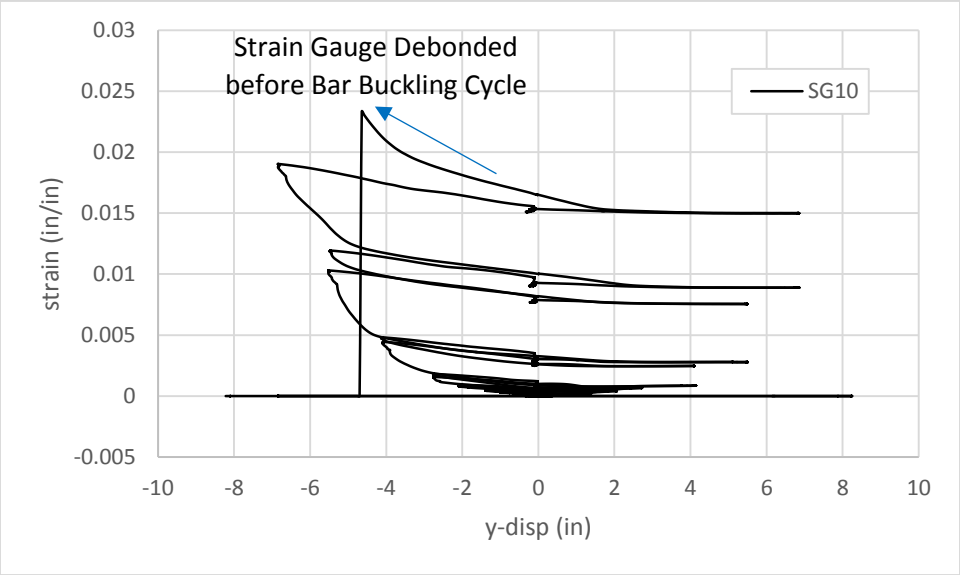

Figure 7-65. Test 4: South Spiral Strain Gauge Hysteresis for the Second Layer above the Footing

East and West Bar Strains

Vertical strain profiles for East and West reinforcement during x-direction cycles are shown in Figure 7-66 and Figure 7-67. Strains in the lowest four spiral layers during compressive x-direction cycles on the East and West sides of the specimen appear in Figure 7-68 and Figure 7-69. The relationship between strain and displacement for either peak tensile or peak compressive gauge lengths appear in Figure 7-70 through Figure 7-74. These figures contain monotonic moment curvature predictions for respective plastic hinge methods. PCK (2007) Lp refers to the (Priestley, Calvi and Kowalsky 2007) plastic hinge method, GN15 Tension/Compression Lpr refers to the (Goodnight, Kowalsky and Nau 2015a) unidirectional modified plastic hinge method, TX Measured refer to using the measured extent of plasticity and average equivalent strain penetration length from this specific test, and New Equations refers to a new bidirectional plastic hinge method which was created based on this study. Details of the new plastic hinge method appear in a later chapter of this report.

The spiral strain gauge hysteresis for the first and second layers above the footing on the East side of the specimen appear in Figure 7-76 and Figure 7-77. The strain gauge over the first spiral layer debonded during $\mu_{\Delta 5}^{+1x} = 6.85$", even though the East bars remained visibly straight as shown in Figure 7-42. The second spiral layer went off scale during $\mu_{\Delta 5}^{+2x} = 6.85$" as the East extreme fiber bar visibly buckled, see Figure 7-44. The visual observation of bar buckling was confirmed upon inspection of the East longitudinal bar strain hysteresis in Figure 7-75.

The spiral strain gauge hysteresis for the first and second layers above the footing on the West side of the specimen appear in Figure 7-79 and Figure 7-80. Both spiral layers went off scale during $\mu_{\Delta 6}^{-1x} = -8.21$" as three West bars buckled simultaneously, see Figure 7-46. The visual observation of bar buckling was confirmed upon inspection of the West longitudinal bar strain hysteresis in Figure 7-28.

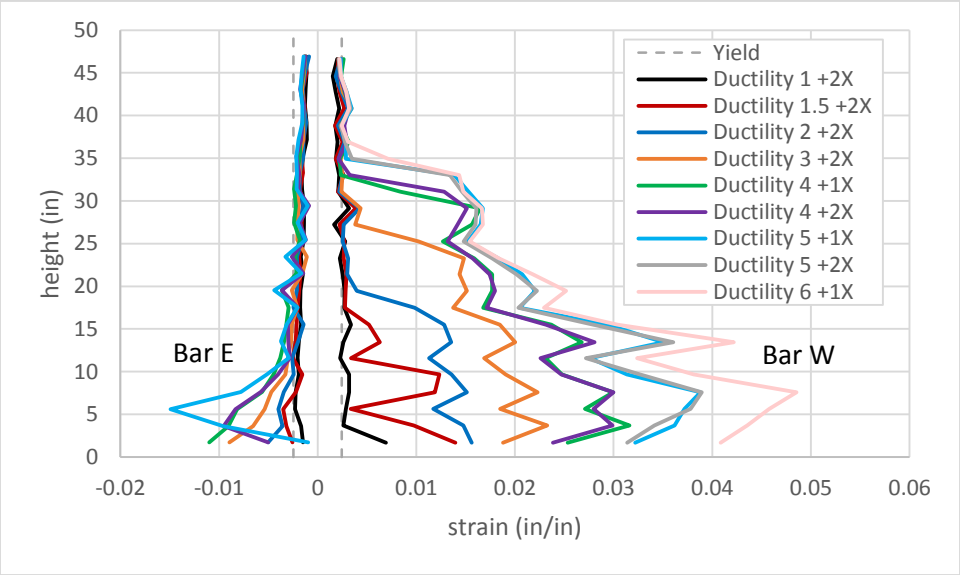

Figure 7-66. Test 4: Vertical Strain Profiles for Loading in the +X-direction

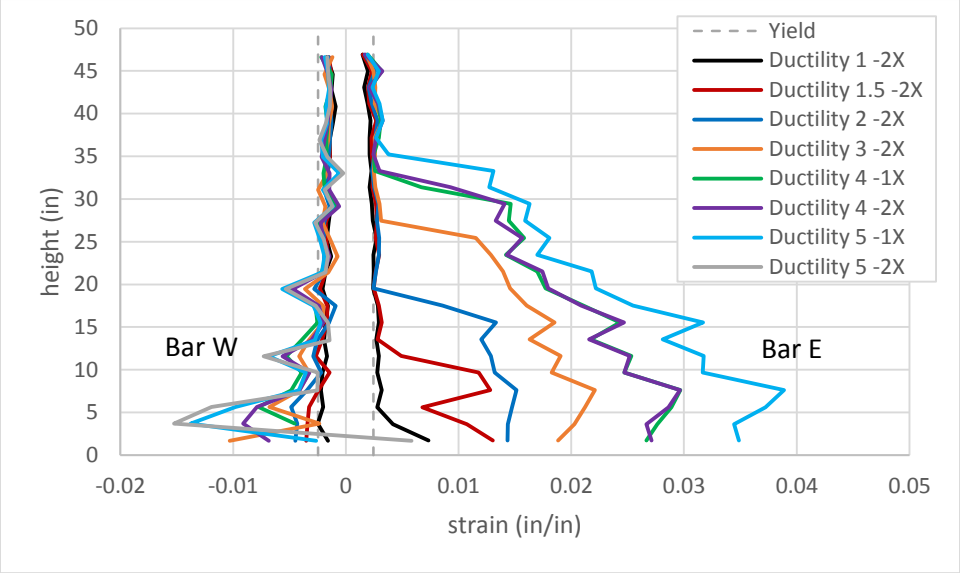

Figure 7-67. Test 4: Vertical Strain Profiles for Loading in the -X-direction

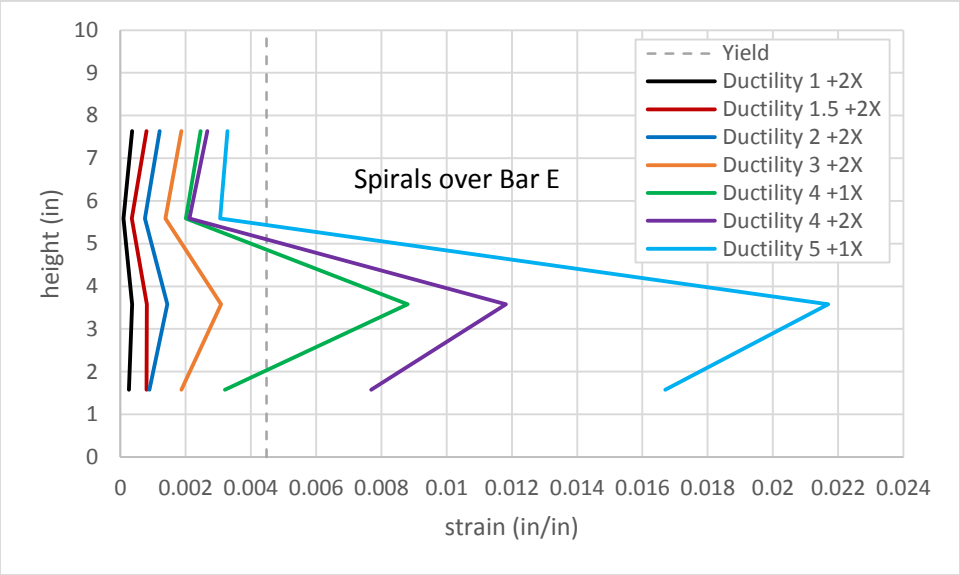

Figure 7-68. Test 4: Spiral Strains Measured Over the East Extreme Fiber Bar during +X Cycles

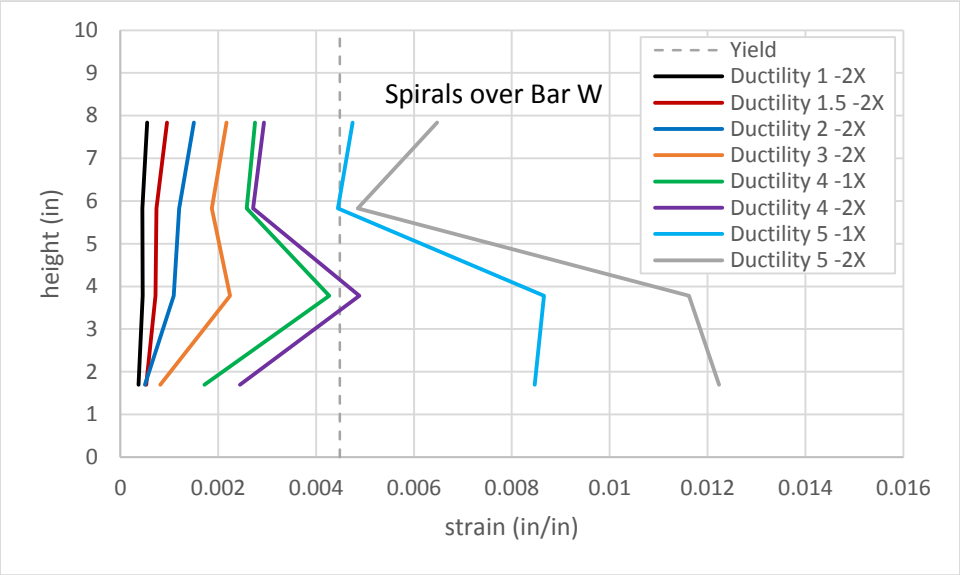

Figure 7-69. Test 4: Spiral Strains Measured Over the West Extreme Fiber Bar during -X Cycles

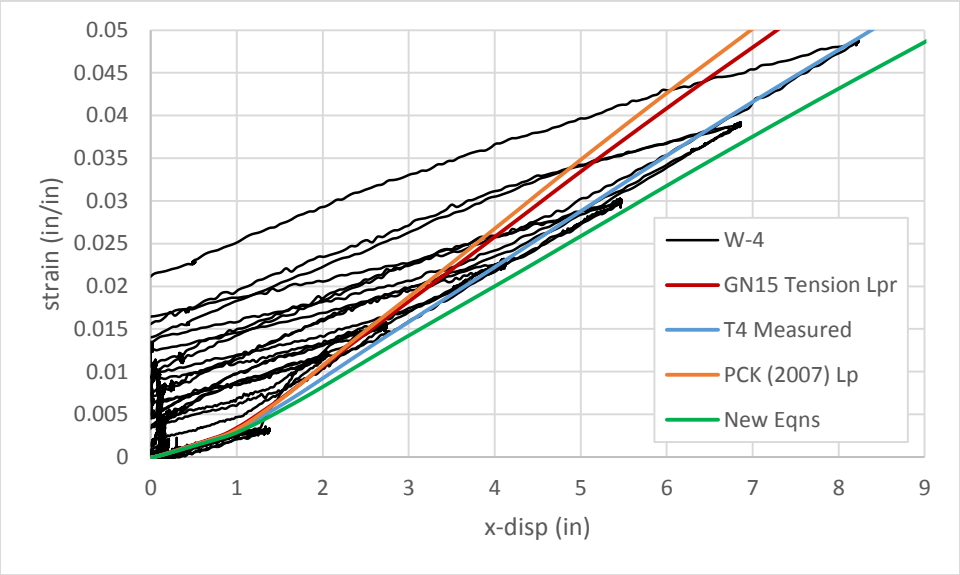

Figure 7-70. Test 4: Tension Strain-Disp. for Bar W (Gauge Length 4 Centered 7.57" above the Footing)

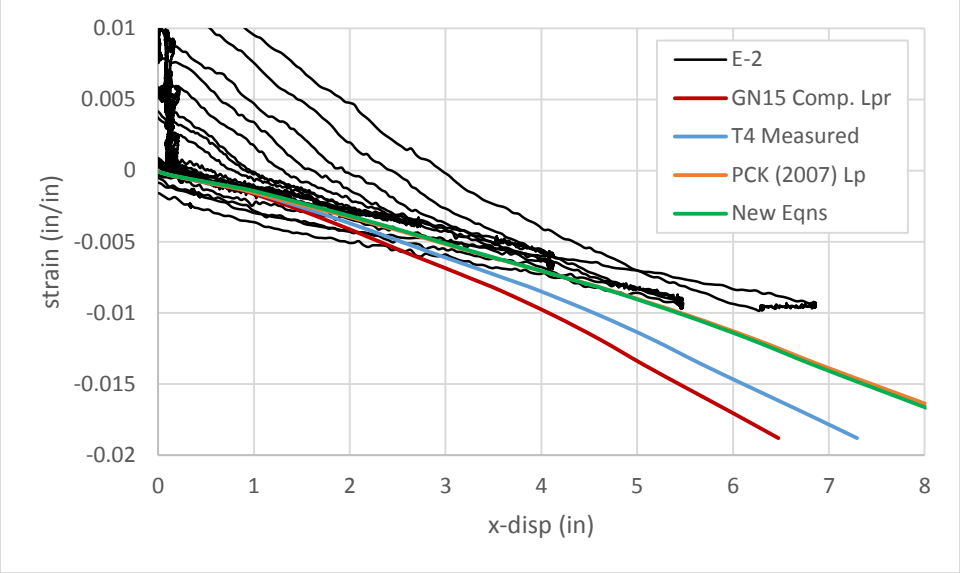

Figure 7-71. Test 4: Compression Strain-Disp. for Bar E (Gauge Length 2 Centered 3.62" above the Footing)

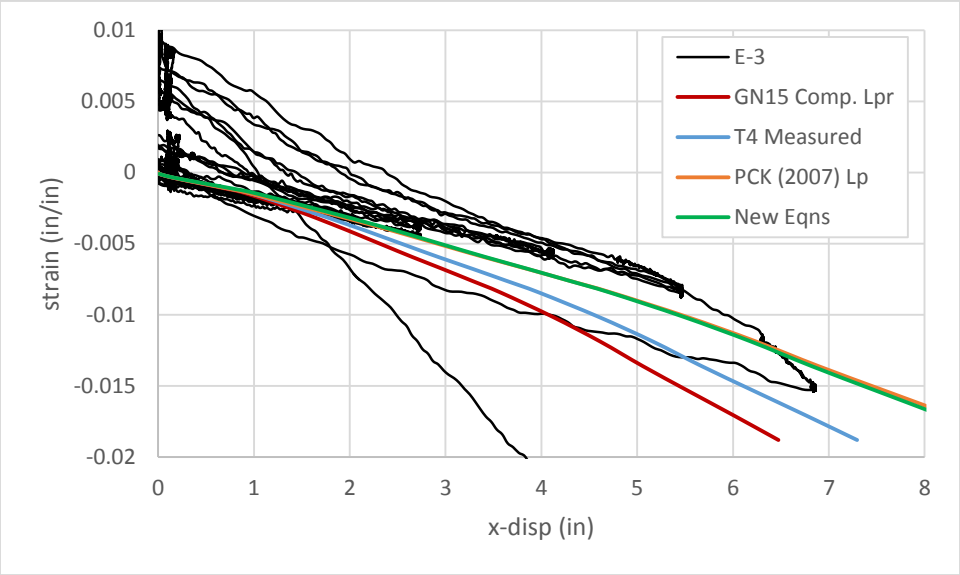

Figure 7-72. Test 4: Compression Strain-Disp. for Bar E (Gauge Length 3 Centered 5.61" above the Footing)

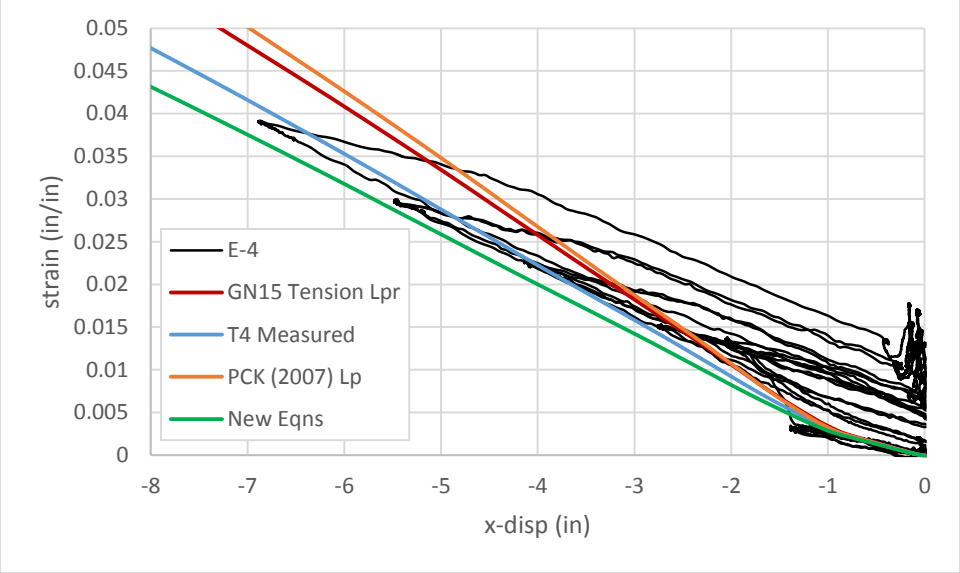

Figure 7-73. Test 4: Tension Strain-Disp. for Bar E (Gauge Length 4 Centered 7.63" above the Footing)

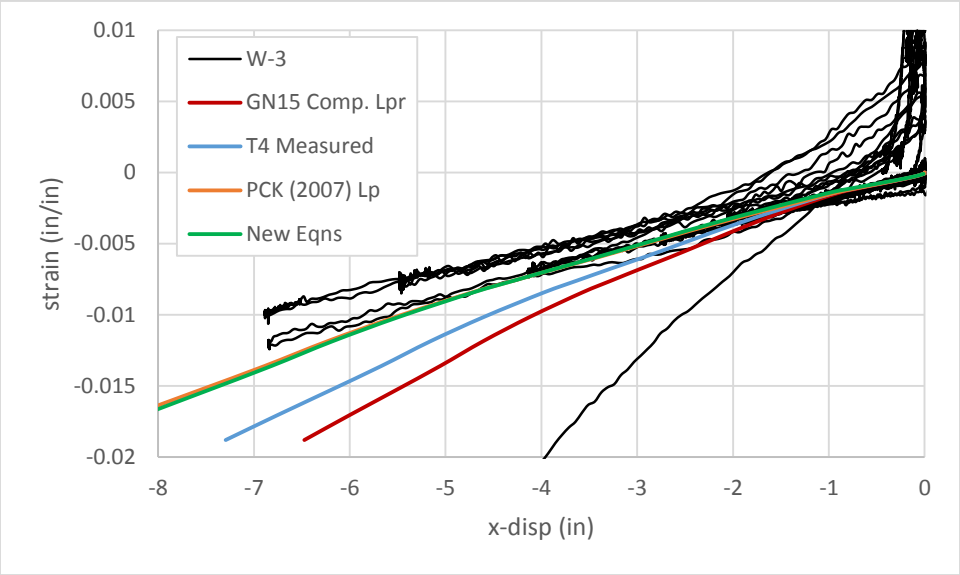

Figure 7-74. Test 4: Compression Strain-Disp. for Bar W (Gauge Length 3 Centered 5.62" above the Footing)

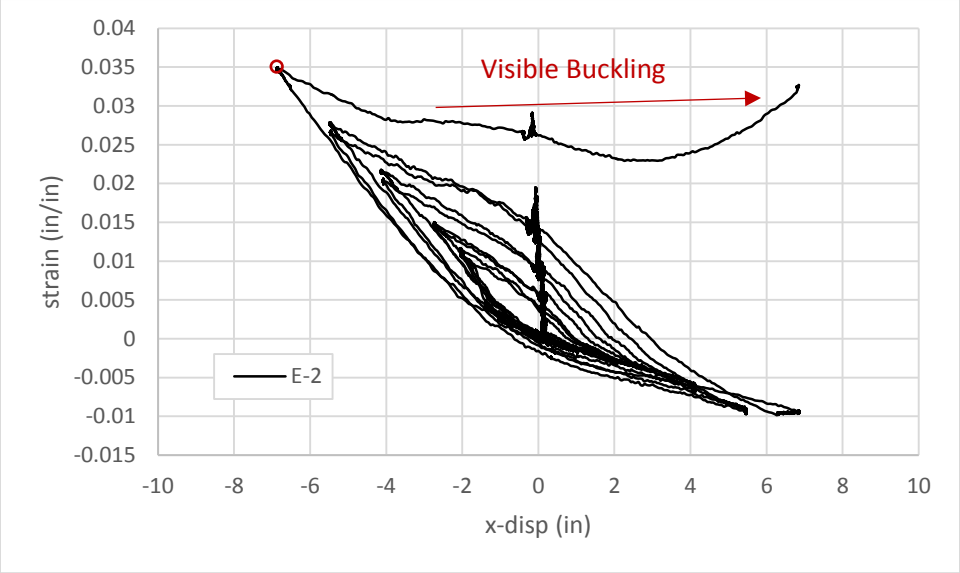

Figure 7-75. Test 4: Strain Hysteresis over the East Buckled Bar (Gauge Length 2 Centered 3.62" above the Footing)

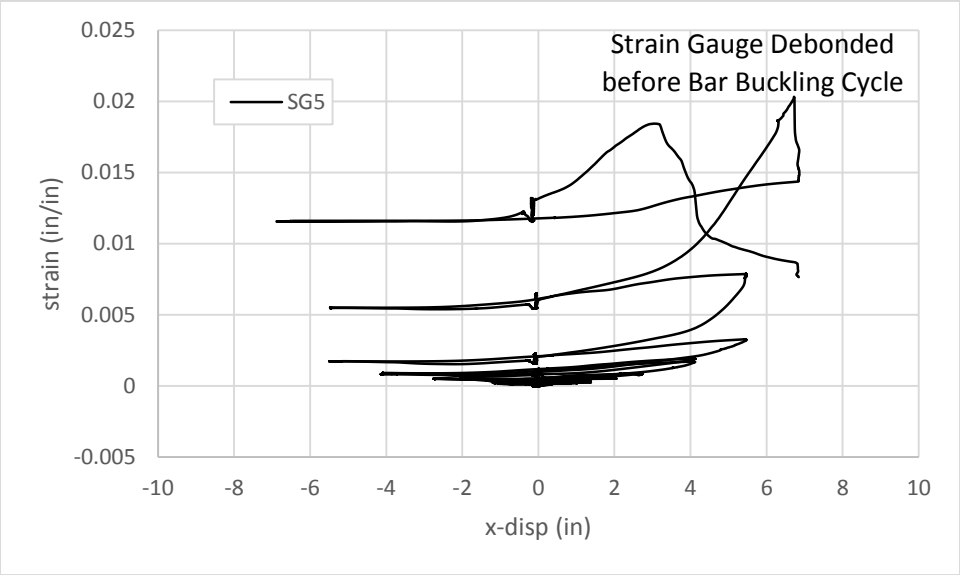

Figure 7-76. Test 4: East Spiral Strain Gauge Hysteresis for the First Layer above the Footing

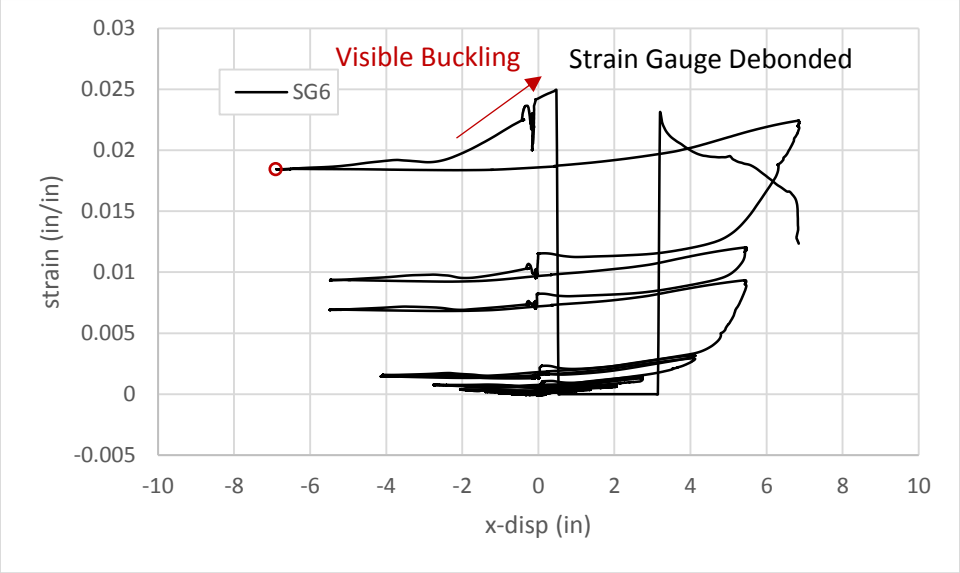

Figure 7-77. Test 4: East Spiral Strain Gauge Hysteresis for the Second Layer above the Footing

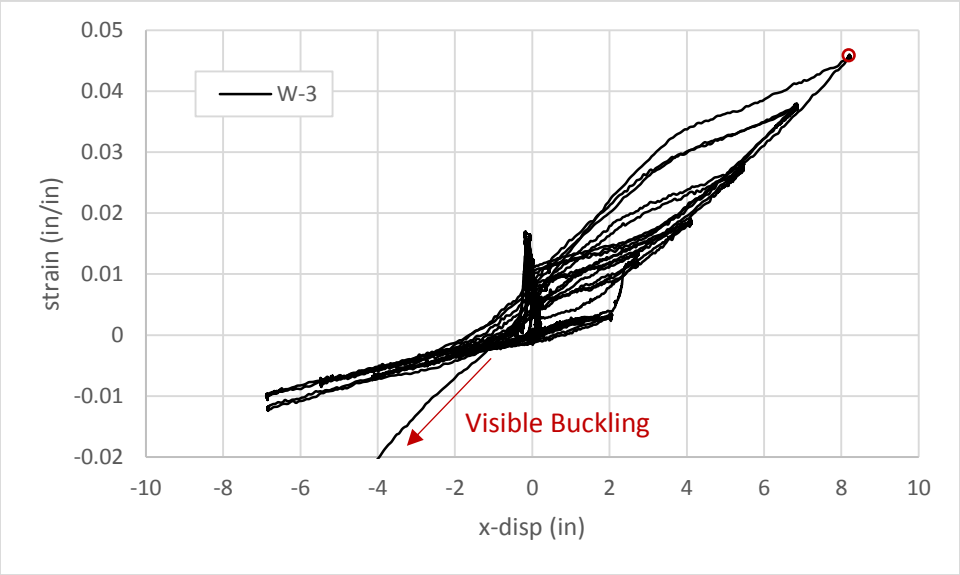

Figure 7-78. Test 4: Strain Hysteresis over the West Buckled Bar (Gauge Length 3 Centered 5.62" above the Footing)

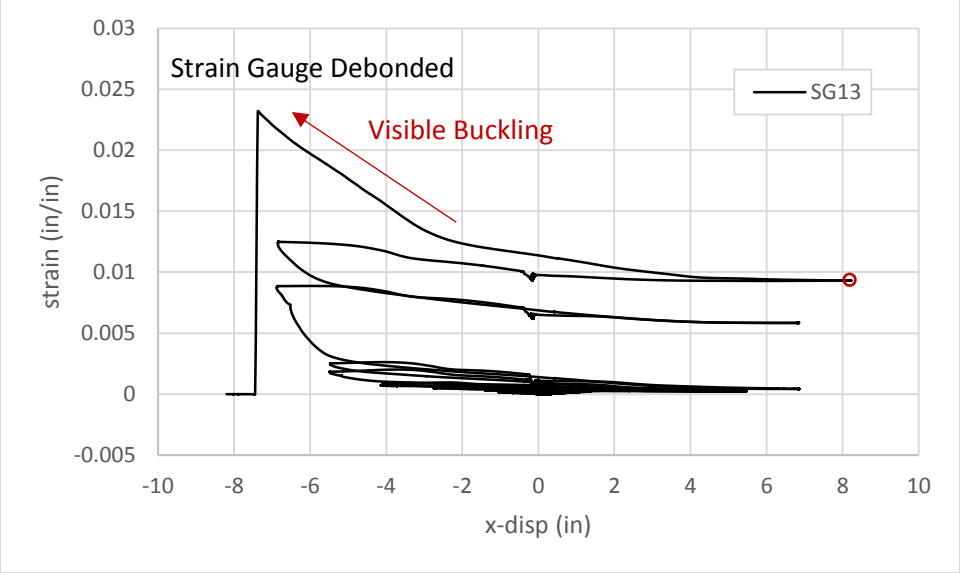

Figure 7-79. Test 4: West Spiral Strain Gauge Hysteresis for the First Layer above the Footing

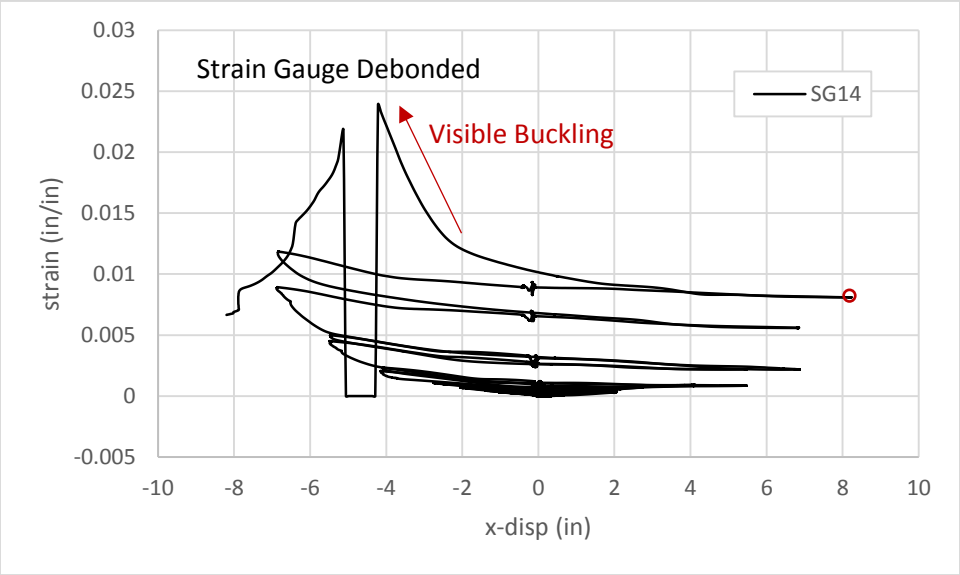

Figure 7-80. Test 4: West Spiral Strain Gauge Hysteresis for the Second Layer above the Footing

Test 4 - Curvature and Strain Penetration Data

Curvature and stain penetration data for Test 4 is presented in the following section. The methods in which this data was generated are outlined in the summary for Test 1. Sample cross section curvature profiles are shown in Figure 7-81 and Figure 7-82. Vertical curvature profiles for respective loading directions appear in Figure 7-83 through Figure 7-87. Fixed-end rotations attributable to strain penetration of longitudinal reinforcement into the footing are shown in Figure 7-88 through Figure 7-90. Comparison of the measured displacements to those obtained via integration of the measured curvature profiles and extrapolation of the fixed-end rotation to the center of the applied lateral load are shown in Figure 7-91 and Figure 7-92.

The measured extent of plasticity is compared to design recommendations for the tensile triangular plastic hinge length in Figure 7-93. GN15 refers to the (Goodnight, Kowalsky and Nau 2015a) unidirectional tensile hinge length while New Equations refers to a new bidirectional plastic hinge method which was created based on this study. Details of the new plastic hinge method appear in a later chapter of this report. The measured equivalent strain penetration lengths are compared to design recommendations in Figure 7-94. GN15 refers to the (Goodnight, Kowalsky and Nau 2015a) unidirectional Lsp while PCK (2007) refers to the (Priestley, Calvi and Kowalsky 2007) definition of Lsp. Finally, the measured hysteretic response is compared to monotonic predictions in Figure 7-95 through Figure 7-98. The larger elastic displacements are not observed when sectional response is considered.

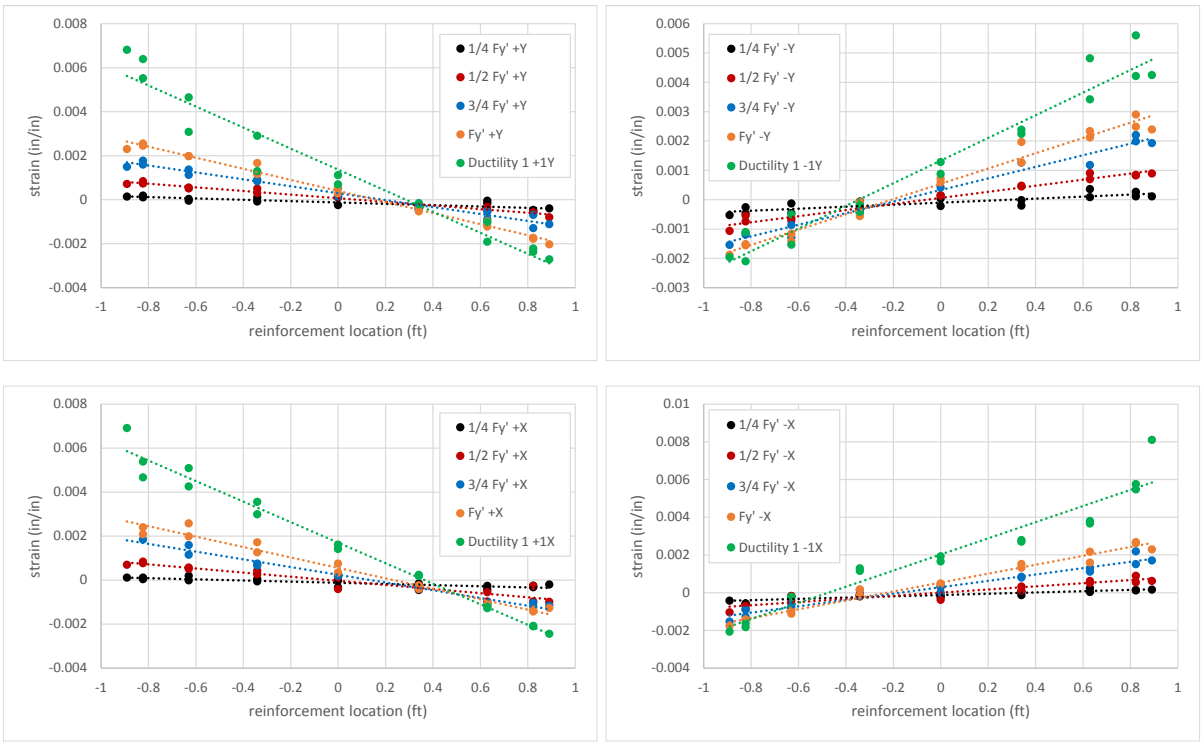

Figure 7-81. Test 4: Elastic Curvature Profiles for the First Instrumented Section above the Footing

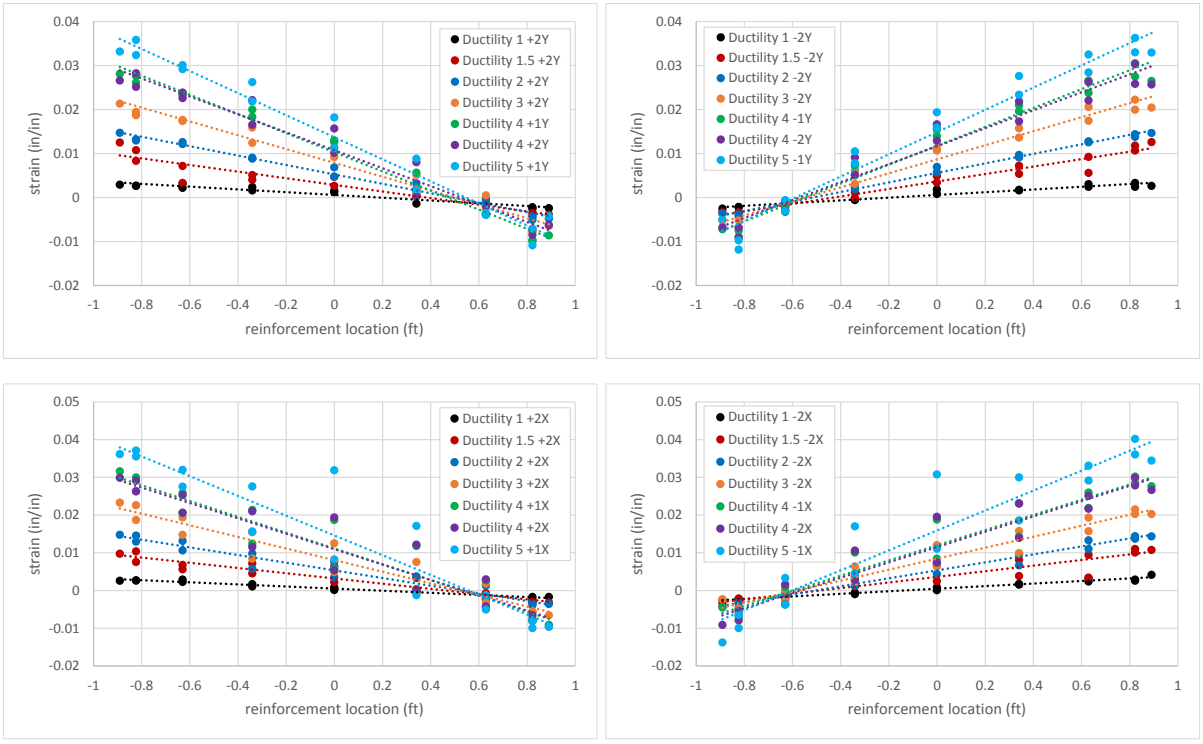

Figure 7-82. Test 4: Curvature Profiles for the Second Instrumented Section above the Footing

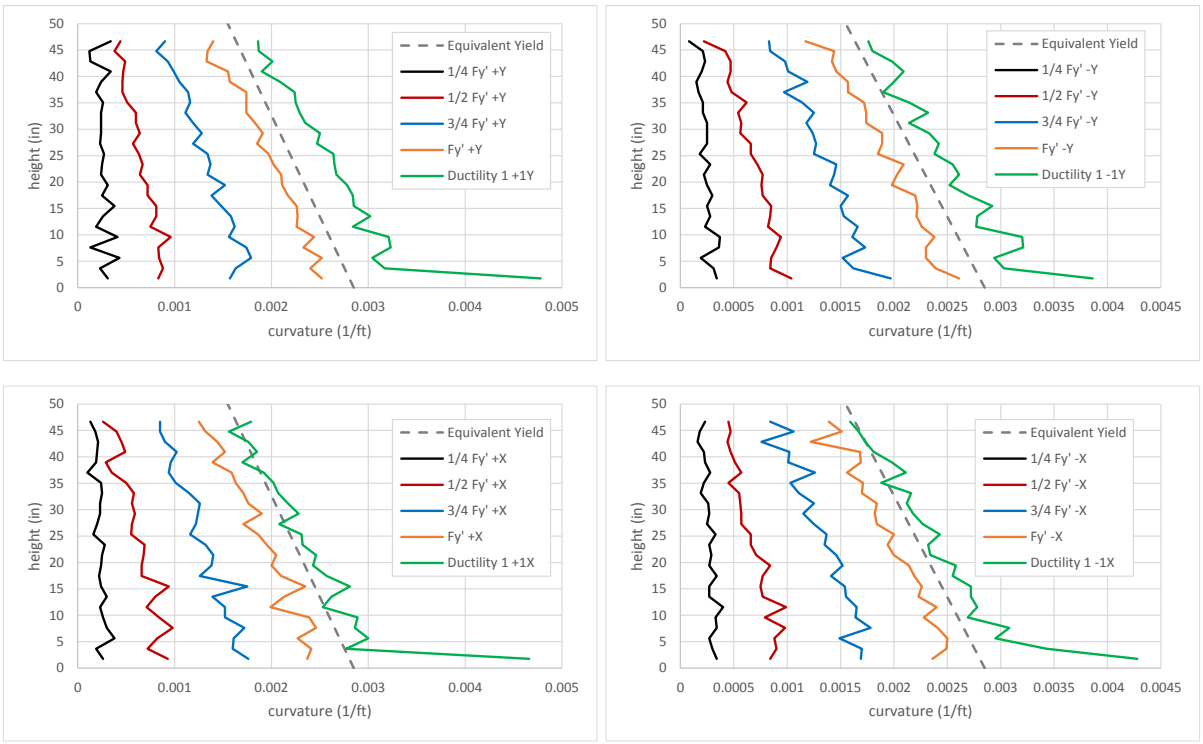

Figure 7-83. Test 4: Elastic Vertical Curvature Profiles

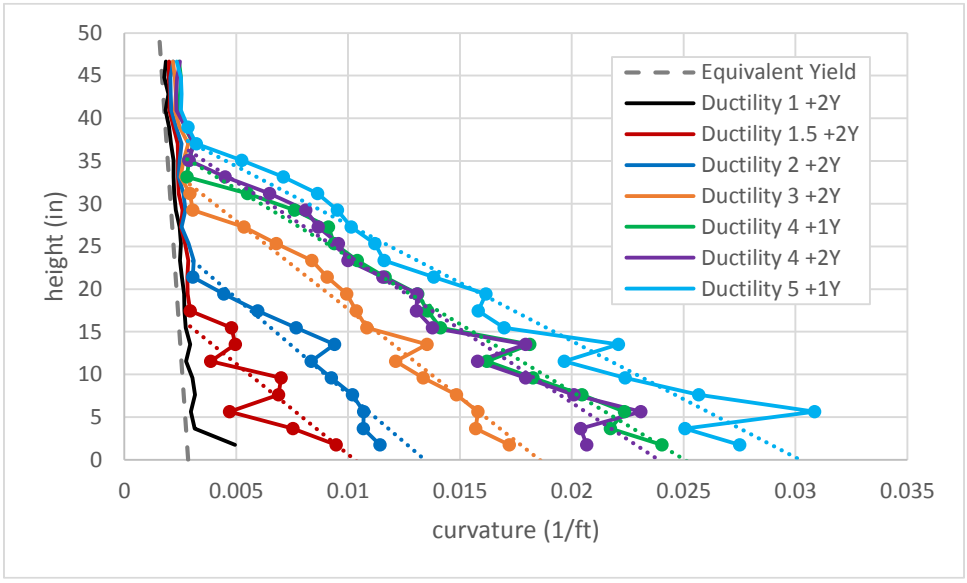

Figure 7-84. Test 4: Vertical Curvature Profiles for Loading in the +Y-direction

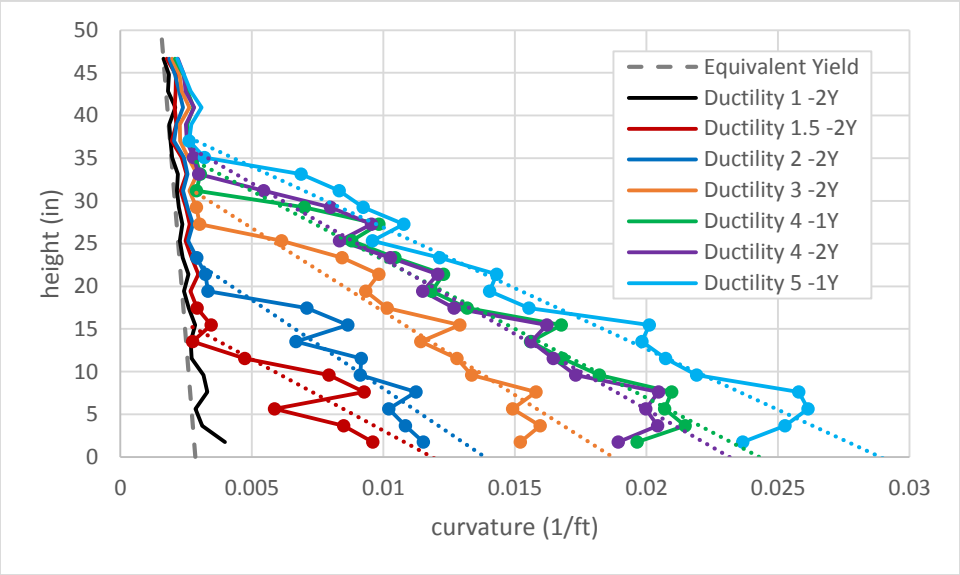

Figure 7-85. Test 4: Vertical Curvature Profiles for Loading in the -Y-direction

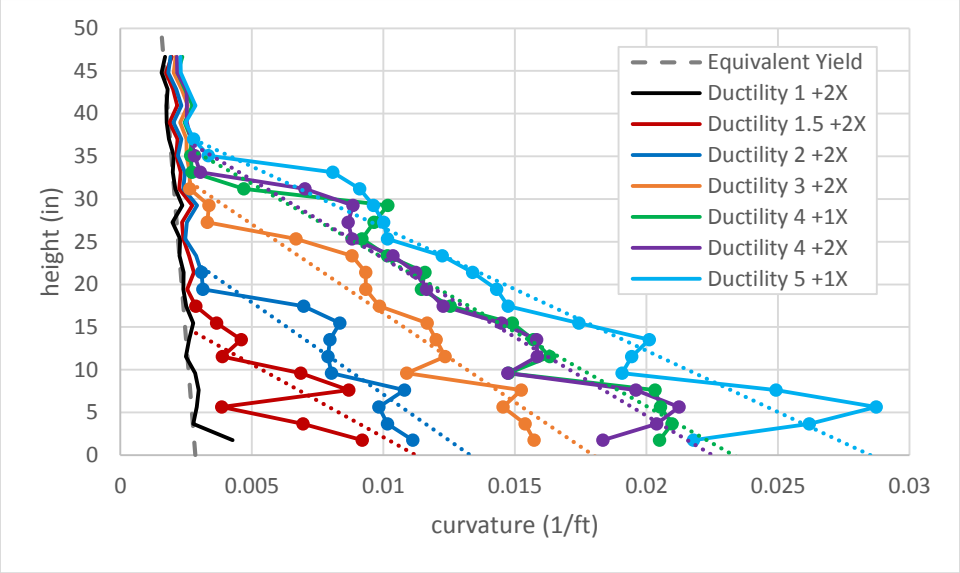

Figure 7-86. Test 4: Vertical Curvature Profiles for Loading in the +X-direction

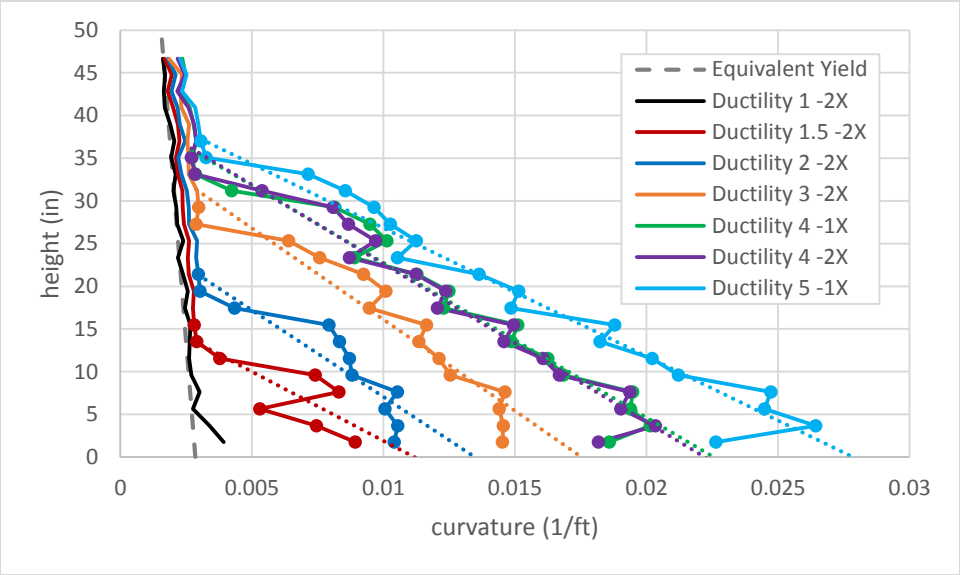

Figure 7-87. Test 4: Vertical Curvature Profiles for Loading in the -X-direction

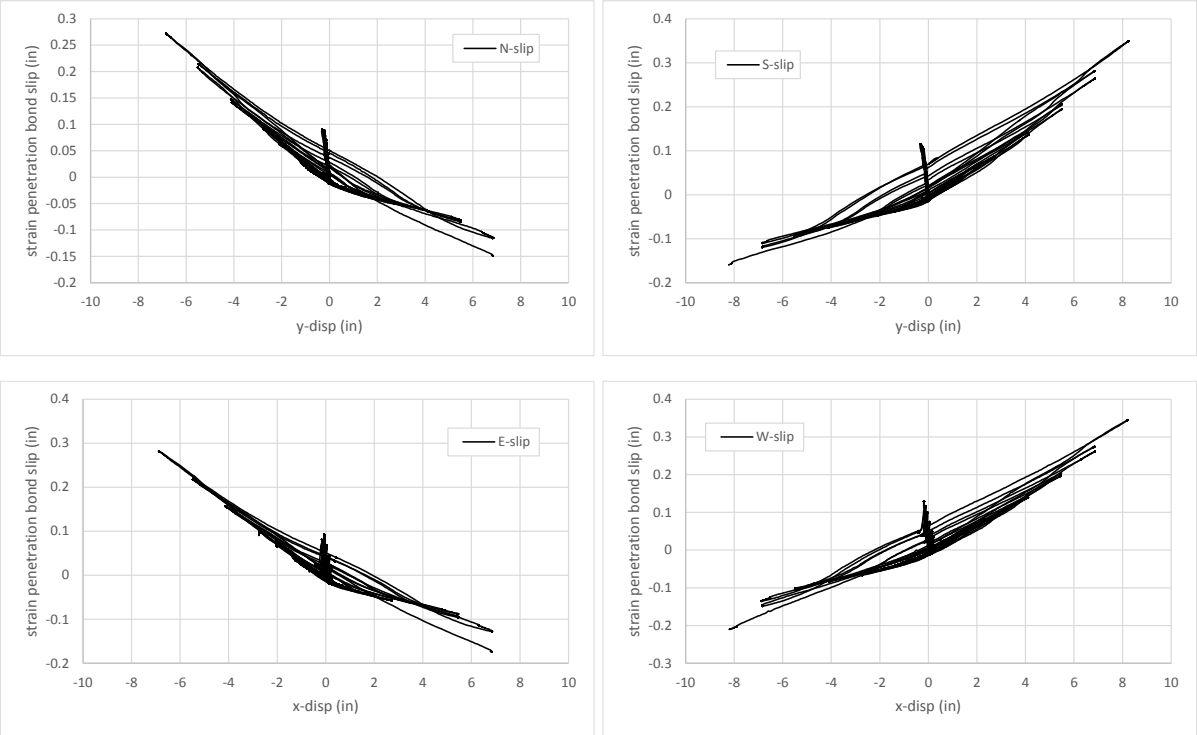

Figure 7-88. Test 4: Extreme Fiber Bar Strain Penetration Bond Slip Hysteresis

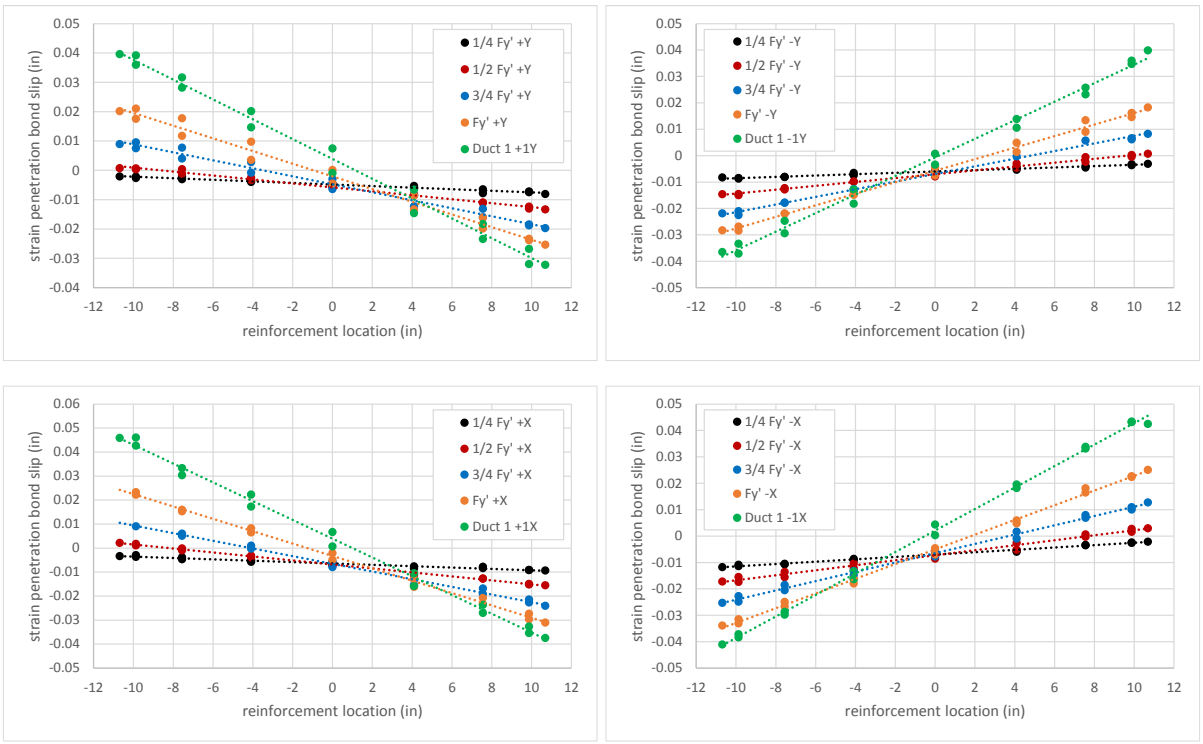

Figure 7-89. Test 4: Fixed End Rotations due to Strain Penetration during the Elastic Cycles

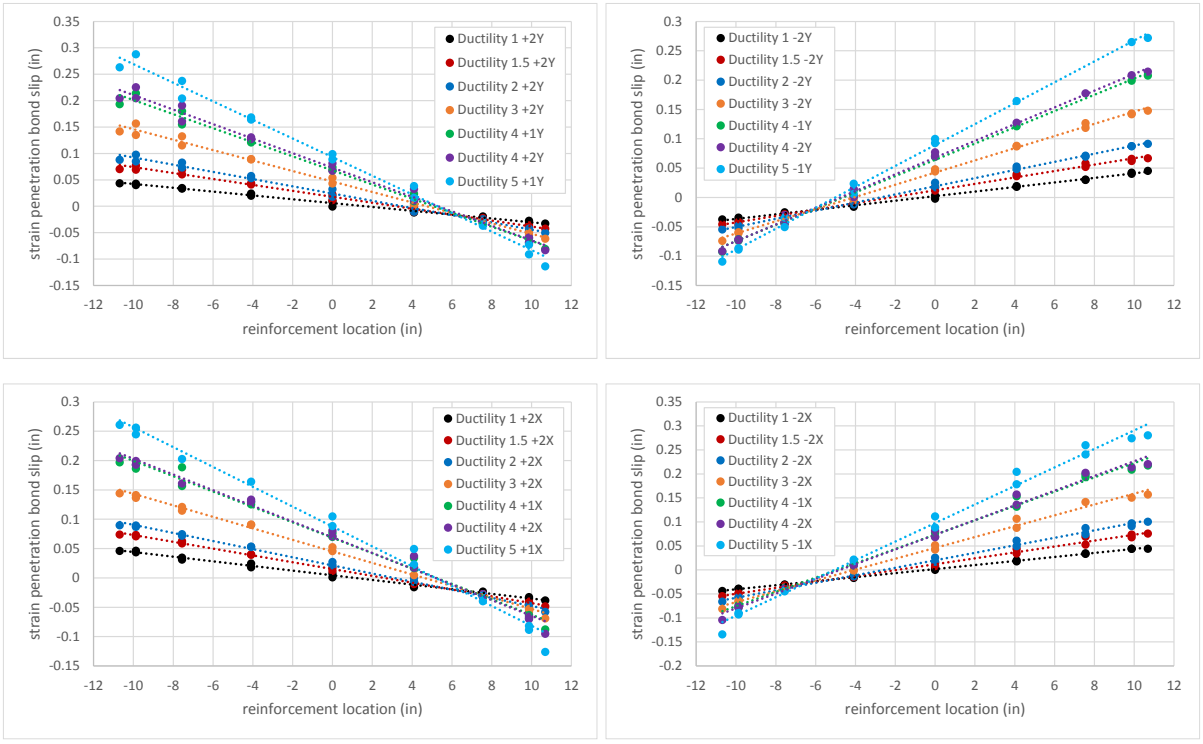

Figure 7-90. Test 4: Fixed End Rotations due to Strain Penetration

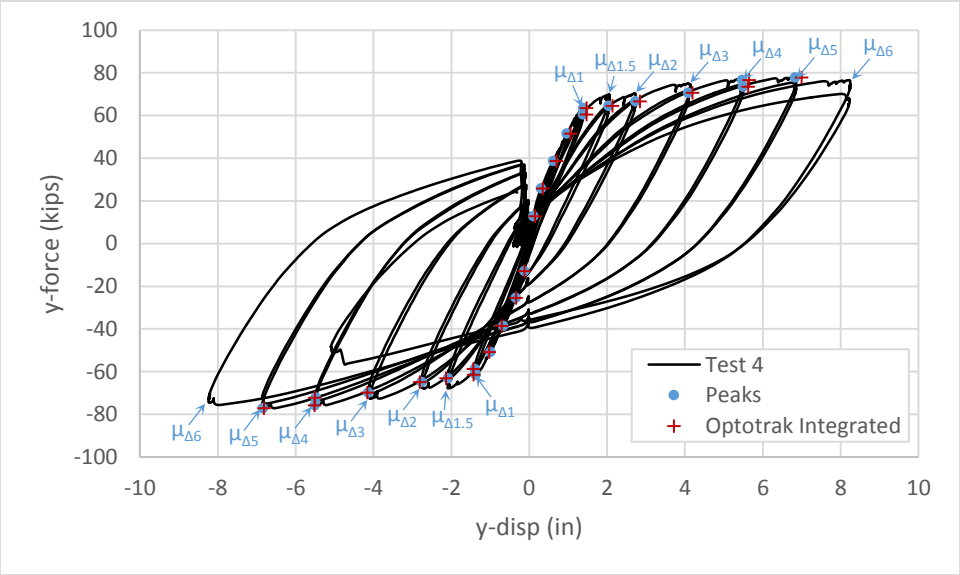

Figure 7-91. Test 4: Optotrak Integrated Flexural Disp. Compared to Measured String Pot. Disp.

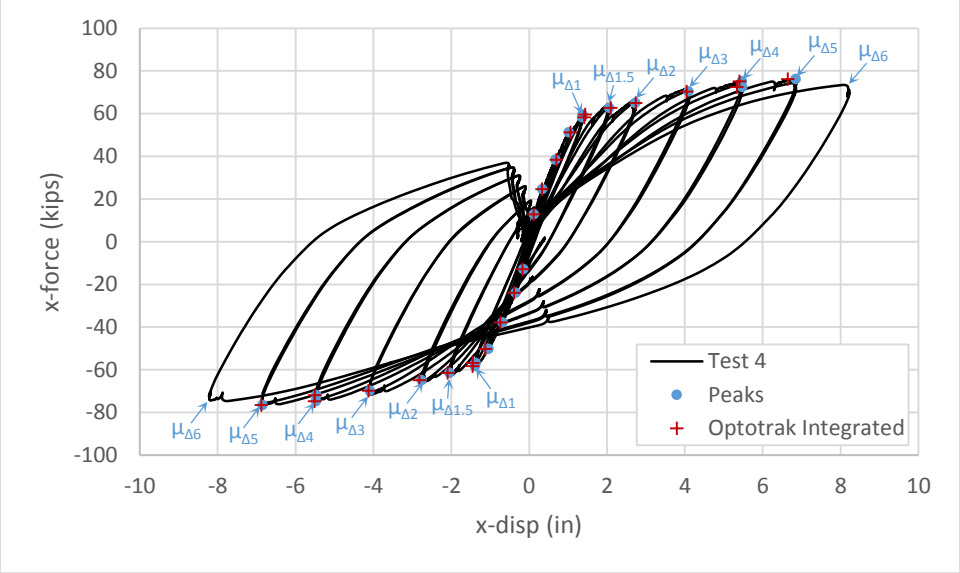

Figure 7-92. Test 4: Optotrak Integrated Flexural Disp. Compared to Measured String Pot. Disp.

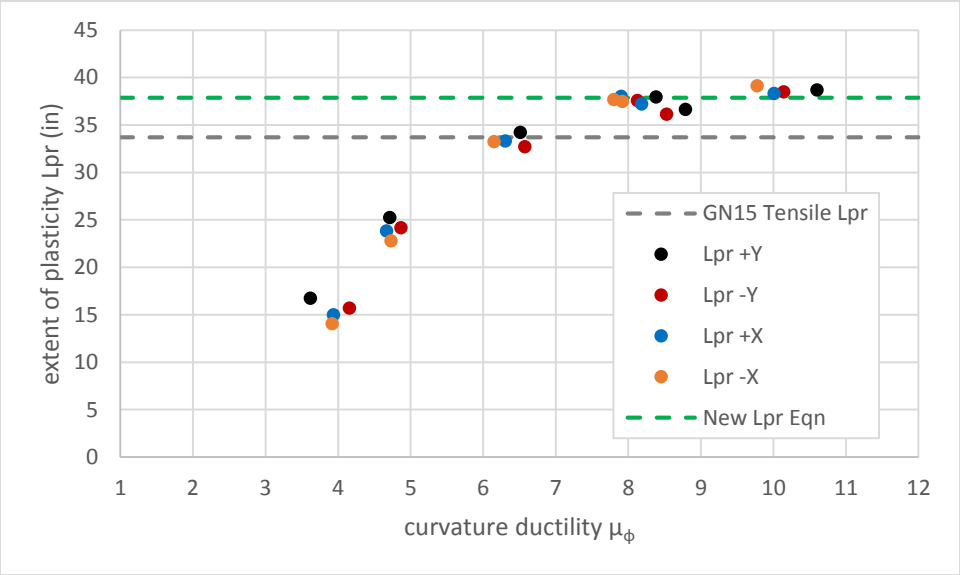

Figure 7-93. Test 4: Measured Extent of Plasticity Compared to Tensile Hinge Lengths

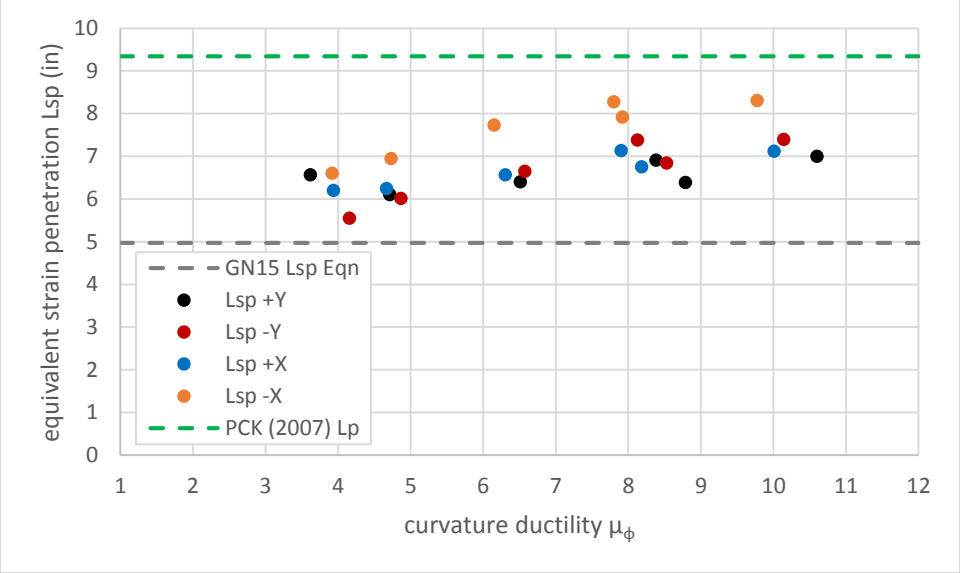

Figure 7-94. Test 4: Measured Equivalent Strain Penetration Lengths Compared to Design Expressions

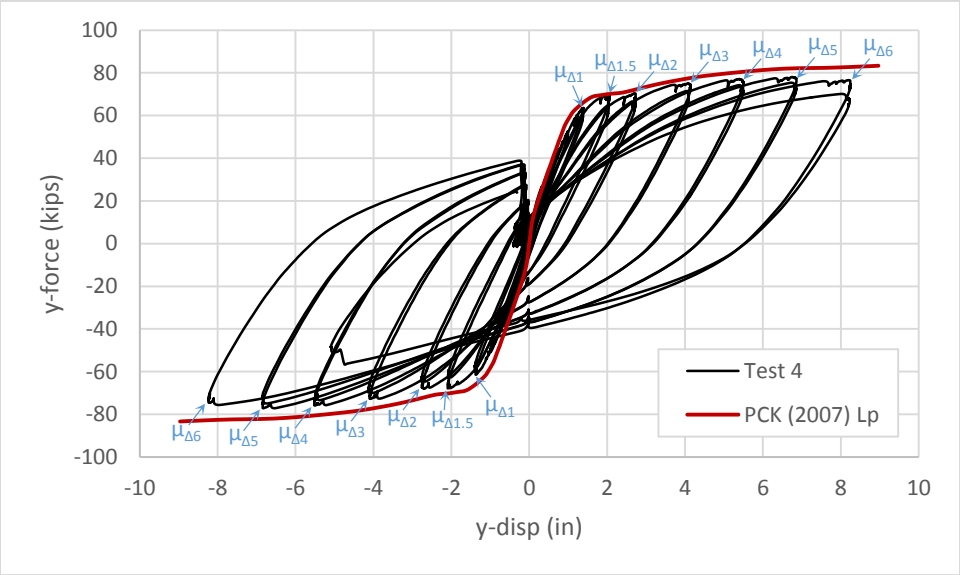

Figure 7-95. Test 4: Y-Direction Hysteretic Response Compared to PCK (2007) Hinge Length Monotonic Prediction

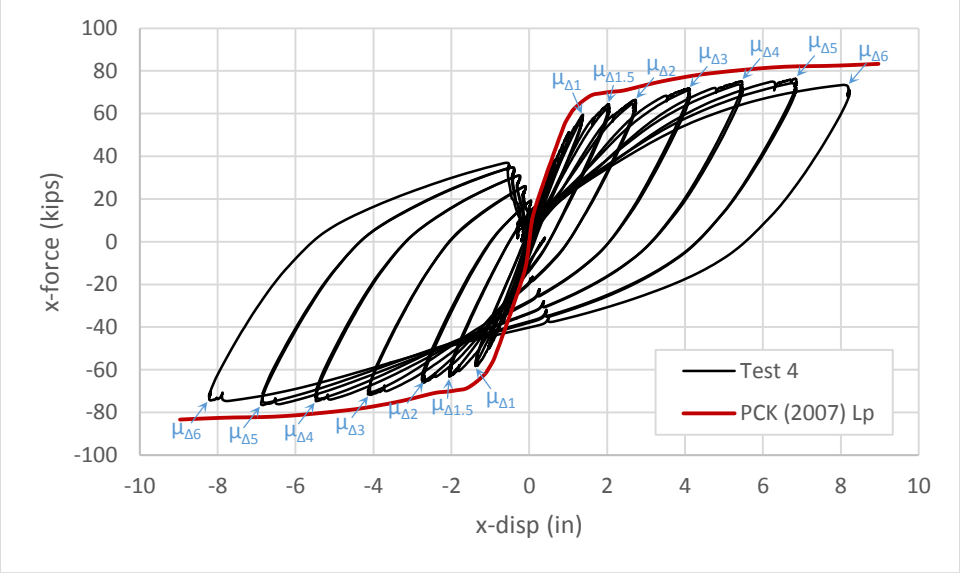

Figure 7-96. Test 4: X-Direction Hysteretic Response Compared to PCK (2007) Hinge Length Monotonic Prediction

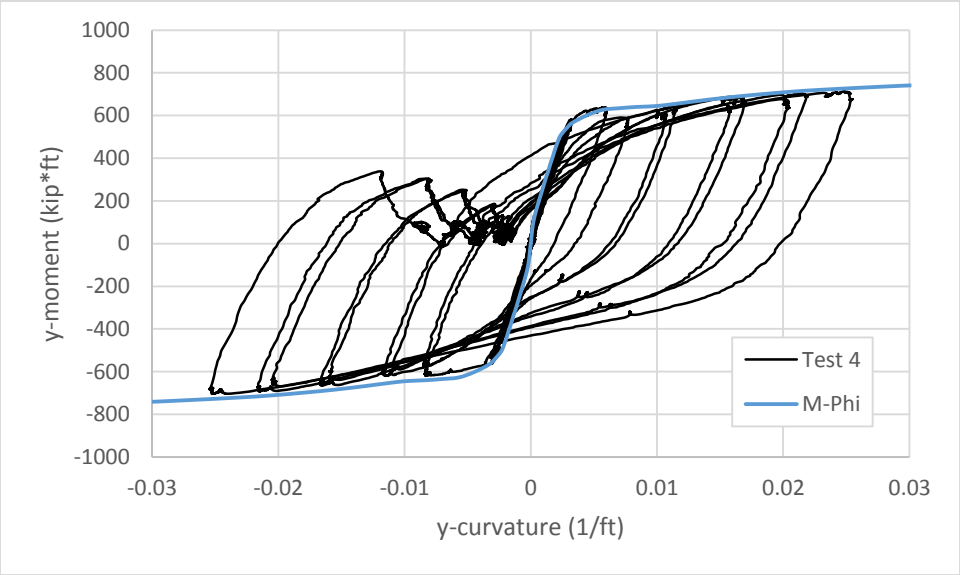

Figure 7-97. Test 4: Y-Direction Sectional Response Compared to Monotonic Moment Curvature Analysis

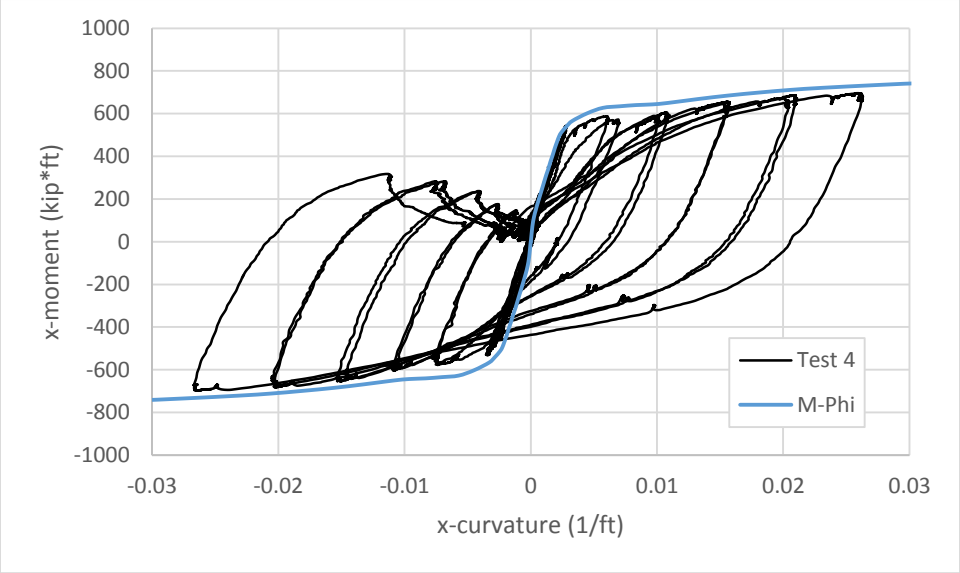

Figure 7-98. Test 4: X-Direction Sectional Response Compared to Monotonic Moment Curvature Analysis

Response Comparison for Test 1 (0.7%) and Test 4 (1% Transverse Volumetric Steel)

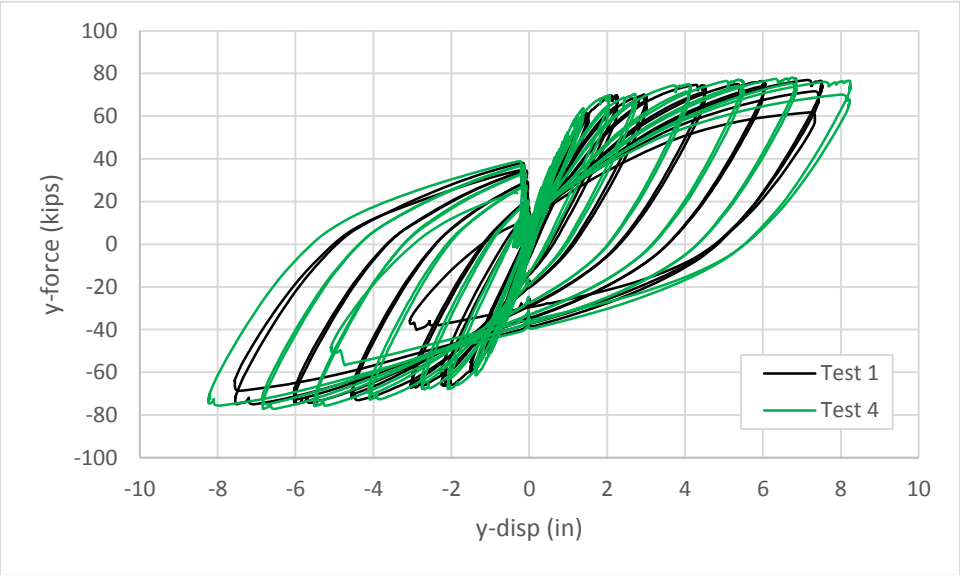

Figure 7-99. Tests 1 (0.7%) and 4 (1% Transverse Steel) Hysteretic Response Comparison in the Y-Direction

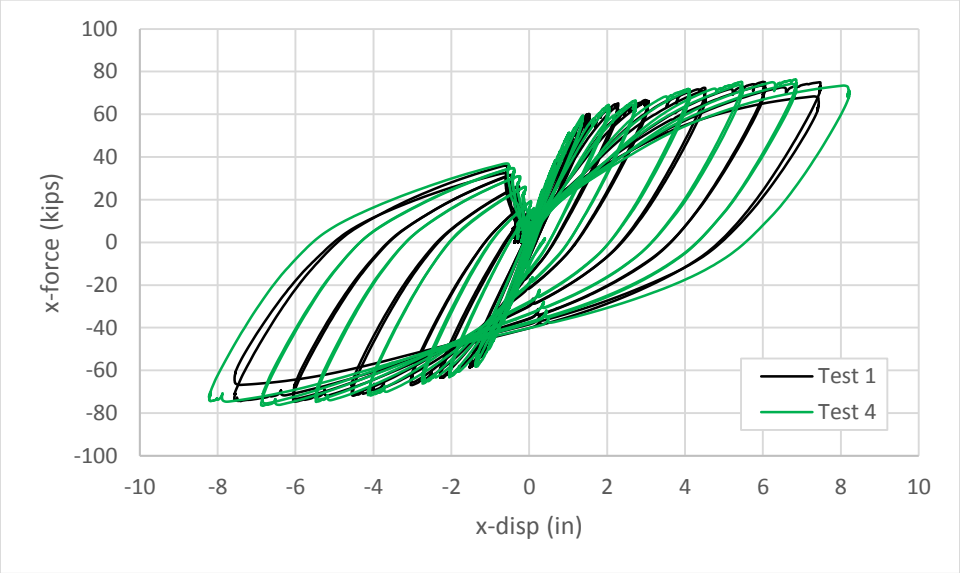

Figure 7-100. Tests 1 (0.7%) and 4 (1% Transverse Steel) Hysteretic Response Comparison in the X-Direction

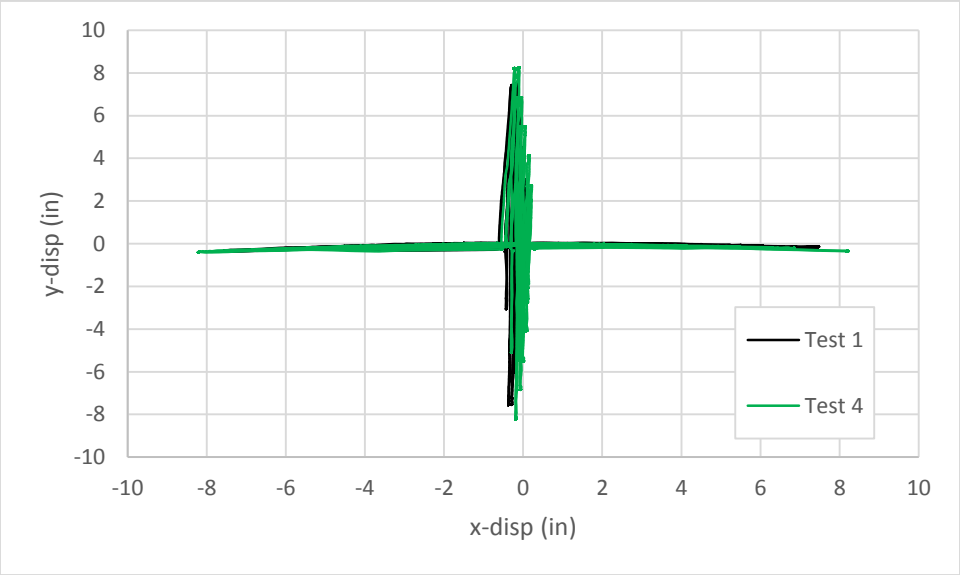

Figure 7-101. Tests 1 and 4 Symmetric Two-Cycle-Set Bidirectional Load History

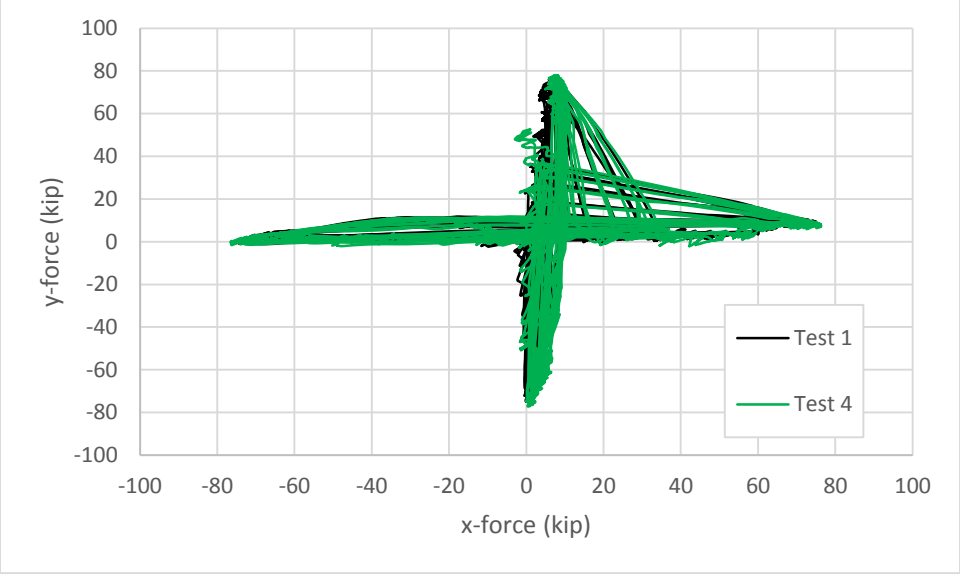

Figure 7-102. Tests 1 and 4 Load Path Comparison

Chapter 8 - Test 5 Summary Report

The fifth specimen had a 24" diameter circular cross-section reinforced with 16 #7 A706 longitudinal bars ($A_{st}/A_g = 2.1\%$) and a #3 spiral at 2" on center ($4A_{sp}/D's = 1\%$). The only difference between this specimen and Tests 1-3 was the transverse steel spacing and concrete strength. This specimen was nominally identical to that of Test 4, except that three cycles were ran at each displacement ductility level instead of only two. Details of the test setup, instrumentation, and specimen design appear in Chapter 2. A material properties summary for the longitudinal and transverse steel from the first six experiments appears in Table 3-1 and Table 3-2. The column had a tested concrete strength of $f_c' = 7.60\ ksi$, while the footing had $f_c' = 10.38\ ksi$. The specimen had the same level of applied axial load ($191\ kips$). The fifth specimen was subjected to the Type-B Symmetric Three-Cycle-Set Bidirectional Load History shown in Figure 8-1. This figure includes a diagram of the column cross-section with the selected bar and crack labeling scheme. Displacements in the +Y-direction placed the South reinforcement in tension. Cracks due to loading in the +Y-direction were labeled as red. The orientation of the X and Y axes are shown in Figure 2-52 with regards to the test setup. The +Y-axis is perpendicular to and points away from the strong wall. Values of interests, damage observations, and a predictions summary for the fifth test appear in Table 8-1, Table 8-2, and Table 8-3. A photo of the specimen instrumentation appears in Figure 8-2. The tighter transverse steel spacing necessitated reducing the number of target markers placed on bars NW, NE, SE, and SW. This was accompanied with a more dense instrumentation of the most highly strained bars in the four extreme fiber regions of the column.

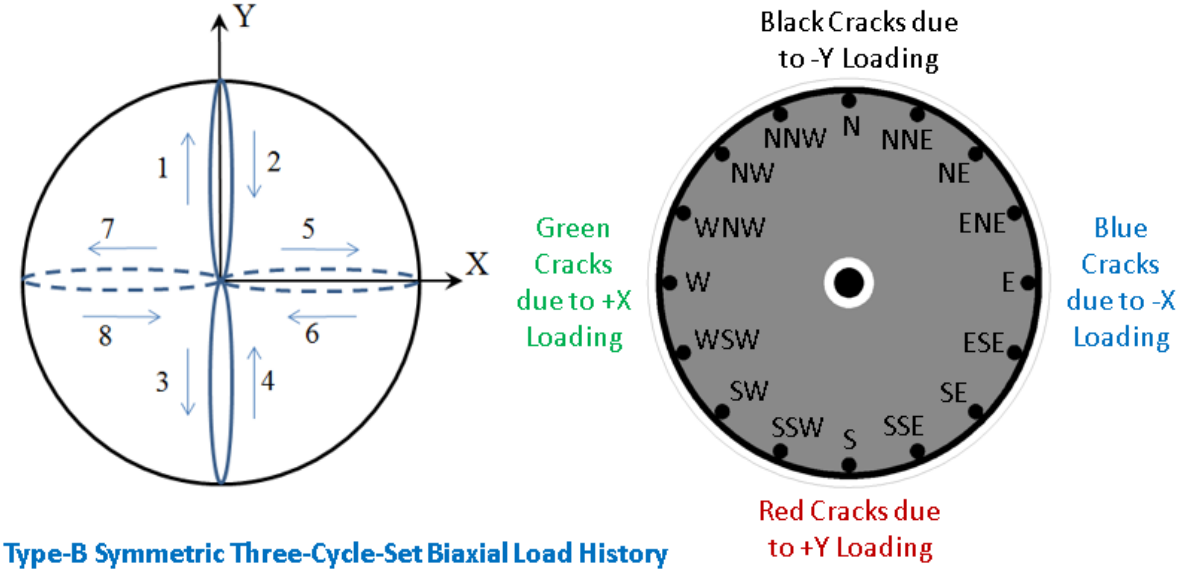

Type-B Symmetric Three-Cycle-Set Biaxial Load History

- Begins with elastic cycles (1-8) in ¼ yield increments until F_y'
- The equivalent yield displacement is then computed as $\Delta_y = \Delta_y' \left(M_n / M_y'\right)$
- Three inelastic cycles (1-8) for each displacement ductility level $\mu_{\Delta n} = n \cdot \Delta_y$
- Cycle labeling system: $\left(\mu_{\Delta 6}^{-1Y} = -8.20\ in\right)$ Represents the first cycle of displacement ductility six in the -Y direction

Figure 8-1. Test 5: Load History and Labeling System for Reinforcement and Cracks

Table 8-1. Test 5: Values of Interest

Load History	Type-B Symmetric Three-Cycle-Set
Length, Diameter, and Aspect Ratio	$L = 109.4375\ in, D = 24\ in,\ (L/D = 4.56)$
Longitudinal Steel Detailing	$16\ \#7\ for\ \rho_l = A_{st}/A_g = 2.1\%$
Longitudinal Steel Properties	$f_y = 71.2\ ksi, f_u = 97.9\ ksi, \varepsilon_y = 0.00254$
Transverse Steel Detailing	$\#3\ @\ 2\ in\ for\ \rho_s = 4A_{sp}/D's = 1.0\%$
Transverse Steel Properties	$f_y = 67.6\ ksi, f_u = 105.6\ ksi, \varepsilon_y = 0.00448$
Column Concrete Strength	$f_c' = 7.60\ ksi$
Footing Concrete Strength	$f_c' = 10.38\ ksi$
Axial Load	$P = 191\ kips, \left(P/f_c'\ A_g = 6.0\%\right)$
Analytical First Yield Force	$F_y' = 51.45\ kips$
Experimental First Yield Disp.	$\Delta_y' = 1.00\ in$
Analytical Nominal Moment Capacity	$M_n = 637.64\ kip \cdot ft$
Equivalent Yield Displacement	$\Delta_y = \Delta_y'\left(M_n/M_y'\right) = 1.37\ in$
Maximum Lateral Force	$F_y = 77.71\ kips, F_x = 76.30\ kips$
Failure Mode	Loss in lateral strength due to extensive buckling of all 16 reinforcing bars, followed by spiral fracture.

Table 8-2. Test 5: Damage Observations

Damage Observations:		
Cycle Peak at which First Cracking was Observed Visually:		
North	$\Delta_y = -0.5F_y' = -0.31\ in$	$F_y = -24.64\ kips$
South	$\Delta_y = 0.5F_y' = 0.34\ in$	$F_y = 26.37\ kips$
East	$\Delta_x = -0.5F_y' = -0.35\ in$	$F_x = -24.13\ kips$
West	$\Delta_x = 0.5F_y' = 0.34\ in$	$F_x = 25.26\ kips$
Cycle Peak at which Cover Concrete Crushing was Observed Visually:		
North	$\mu_{\Delta 2}^{+1Y} = 2.73\ in$	$\varepsilon_c = -0.00758$
South	$\mu_{\Delta 2}^{-1Y} = -2.73\ in$	$\varepsilon_c = -0.00677$
East	$\mu_{\Delta 1.5}^{+2X} = 2.05\ in$	$\varepsilon_c = -0.00417$
West	$\mu_{\Delta 2}^{-1X} = -2.72\ in$	$\varepsilon_c = -0.00565$
Exact Displacement and Cycle Label for Initial Spiral Yielding in the Confinement Zone:		
North	$\Delta_y = 5.45\ in\ during\ \mu_{\Delta 4}^{+1Y}$	$\varepsilon_c = -0.01904$
South	$\Delta_y = -5.16\ in\ during\ \mu_{\Delta 4}^{-2Y}$	$\varepsilon_c = -0.01166$
East	$\Delta_x = 5.47\ in\ during\ \mu_{\Delta 4}^{+1X}$	$\varepsilon_c = -0.00970$
West	$\Delta_x = -5.43\ in\ during\ \mu_{\Delta 4}^{-2X}$	$\varepsilon_c = -0.01131$
Peak Tensile Displacement Prior to Visual Bar Buckling During Subsequent Reversal of Load:		
North	$\mu_{\Delta 5}^{-2Y} = -6.85\ in, Observed\ at\ \mu_{\Delta 5}^{+3Y} = 6.81\ in$	$\varepsilon_s = 0.04041$
South	$\mu_{\Delta 6}^{+1Y} = 8.20\ in, Observed\ at\ \mu_{\Delta 6}^{-1Y} = -8.20\ in$	$\varepsilon_s = 0.04694$
East	$\mu_{\Delta 5}^{-1X} = -6.83\ in, Observed\ at\ \mu_{\Delta 5}^{+2X} = 6.84\ in$	$\varepsilon_s = 0.03670$
West	$\mu_{\Delta 5}^{+3X} = 6.83\ in, Observed\ at\ \mu_{\Delta 5}^{-3X} = -6.83\ in$	$\varepsilon_s = 0.04250$
Exact Displacement and Cycle Label for Fracture of Transverse Reinforcement		
Spiral	$\Delta_x = 7.13\ in\ during\ \mu_{\Delta 6}^{+2X}$	2nd Layer above Footing

Table 8-3. Test 5: Damage Predictions

Damage Predictions with the New Bidirectional Plastic Hinge Model and New Strain Limits:		
Bar Buckling Predictions		
New Method	$\Delta_{bb}^{Lpr} = 7.80\ in$	$\varepsilon_s^{bb} = 0.04200$
Feng et al. (2015)	$\Delta_{bb}^{Lp} = 6.72\ in$	$\varepsilon_s^{bb} = 0.048$
Cover Crushing Prediction		
New Method	$\Delta_{cc}^{Lpr} = 2.13\ in$	$\varepsilon_c^{cc} = -0.004$
Spiral Yielding Prediction		
New Method	$\Delta_{sy}^{Lpr} = 5.20\ in$	$\varepsilon_c^{sy} = -0.01192 * M, (M = 0.8)$
Original Ultimate Concrete Compression Strain		
Mander et al. (1988)	$\Delta_{cu}^{Lpr} = 7.53\ in$	$\varepsilon_{cu} = -0.0155$

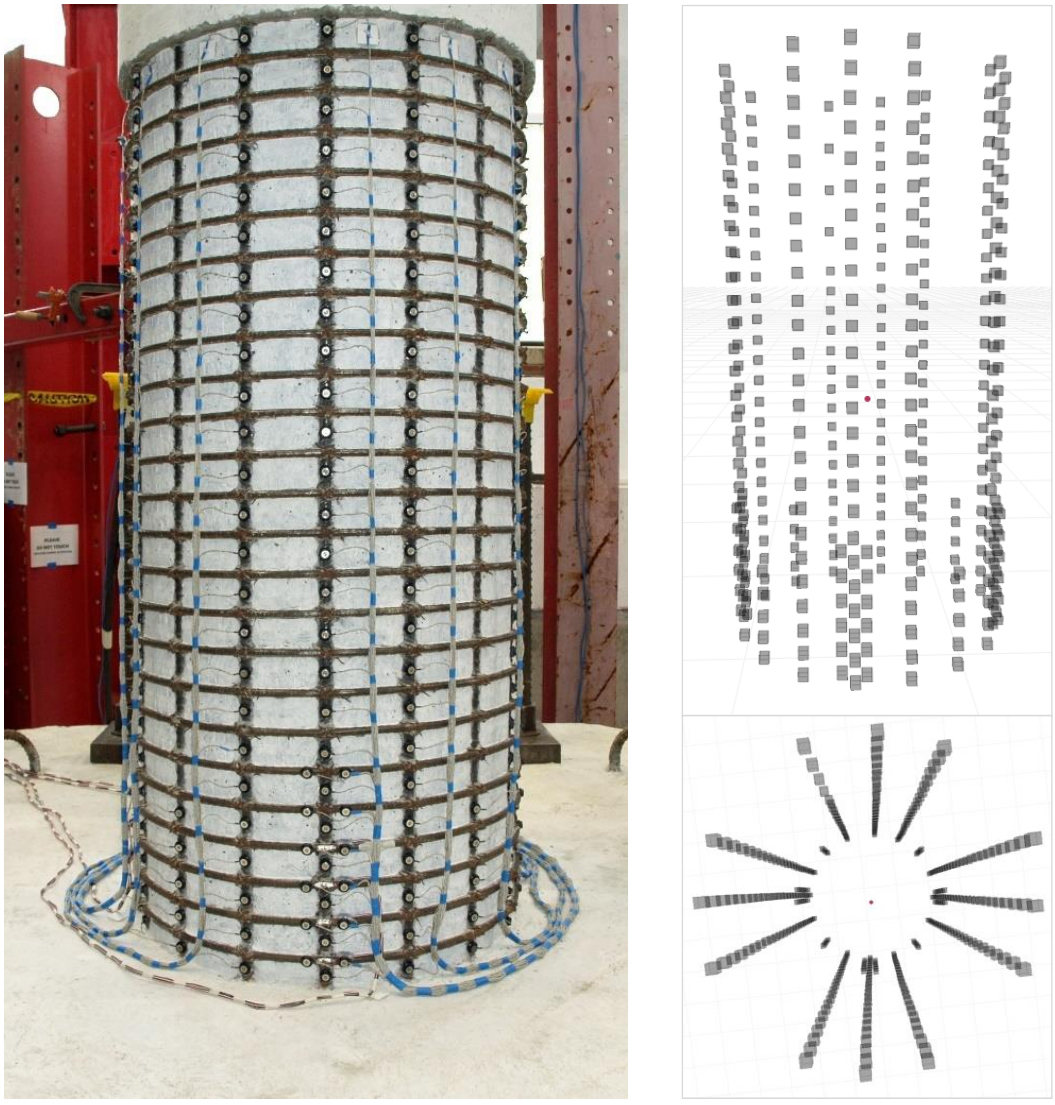

Figure 8-2. Test 5: Optotrak Target Marker and Strain Gauge Instrumentation on the East Side of the Specimen

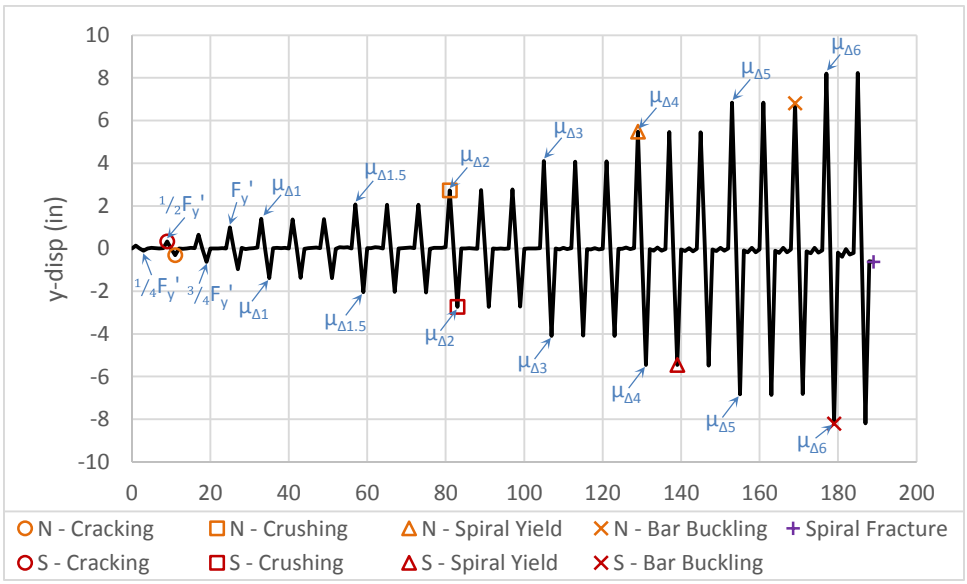

Figure 8-3. Test 5: Y-Displacement History

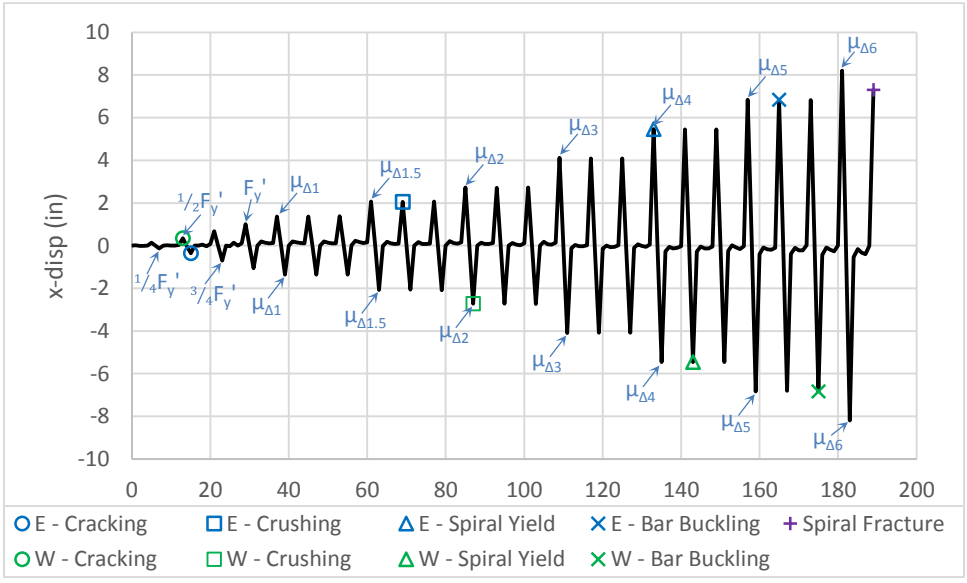

Figure 8-4. Test 5: X-Displacement History

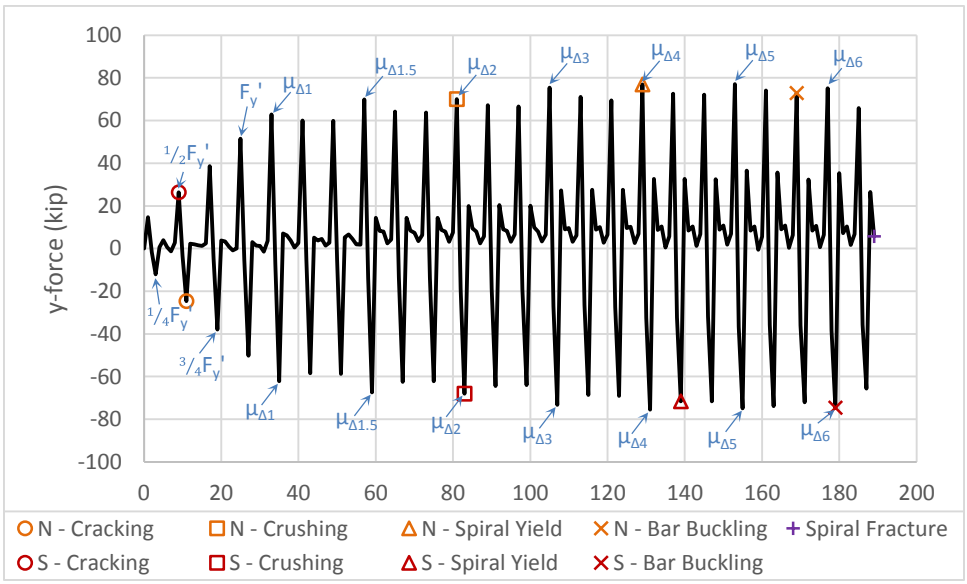

Figure 8-5. Test 5: Y-Force History

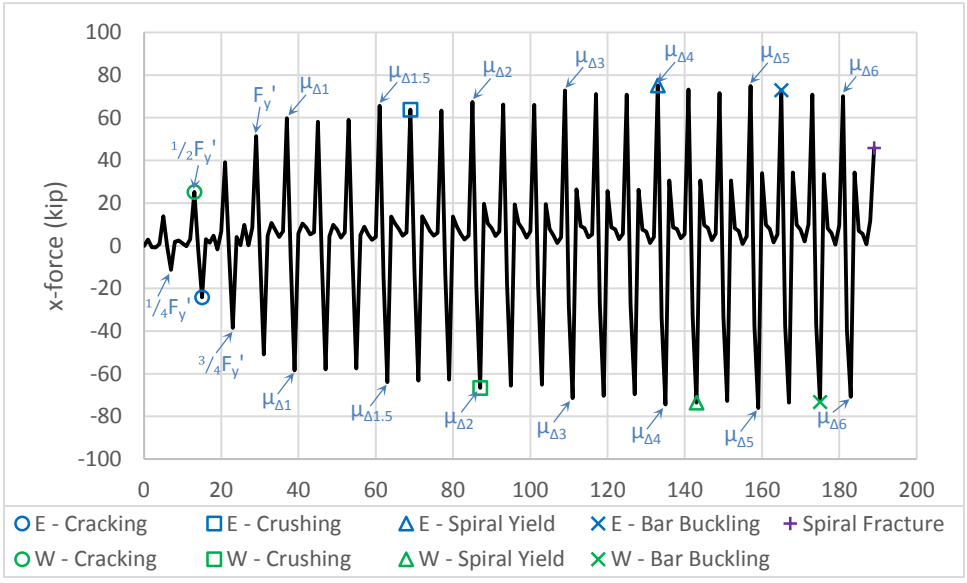

Figure 8-6. Test 5: X-Force History

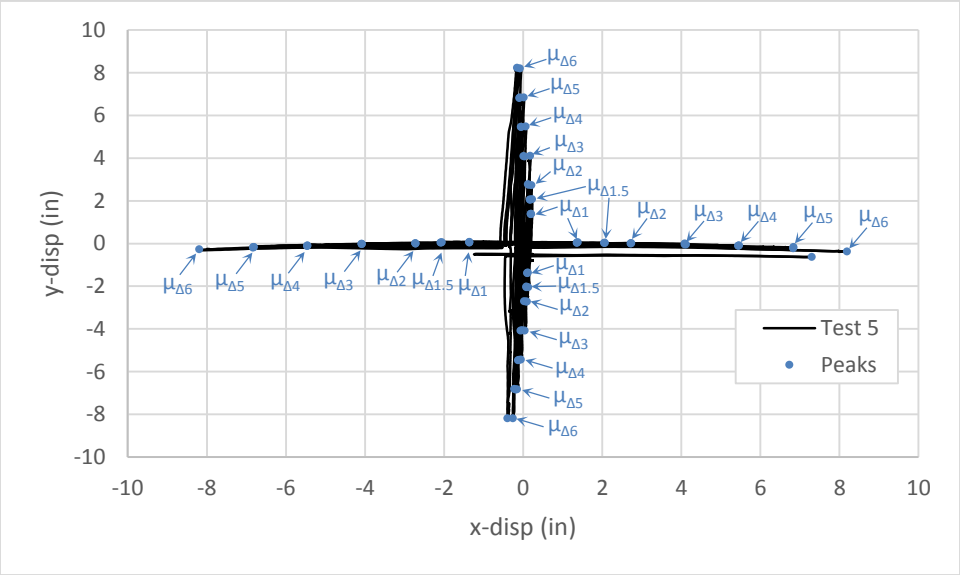

Figure 8-7. Test 5: Type-B Symmetric Three-Cycle-Set Displacement History

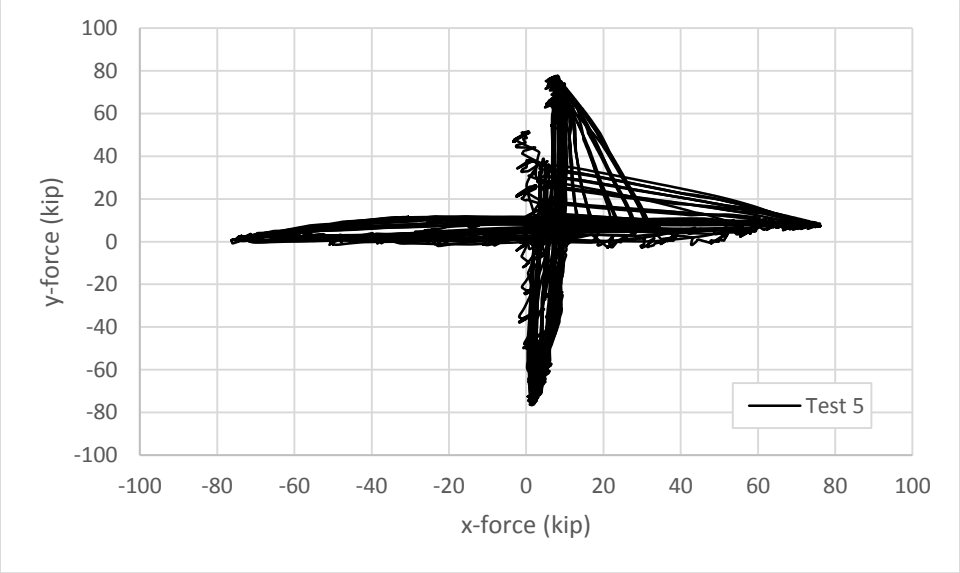

Figure 8-8. Test 5: Load Path

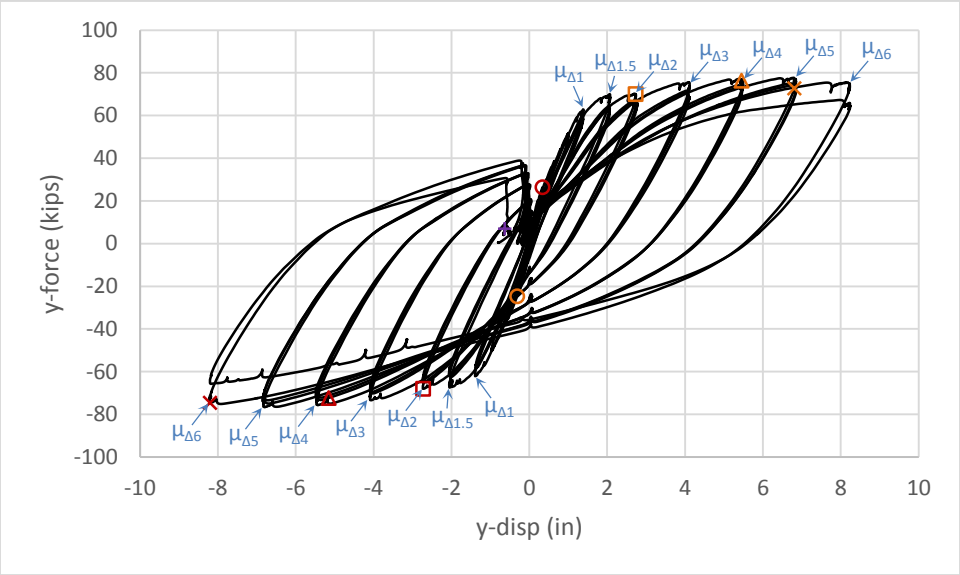

Figure 8-9. Test 5: Y-Direction Hysteretic Response

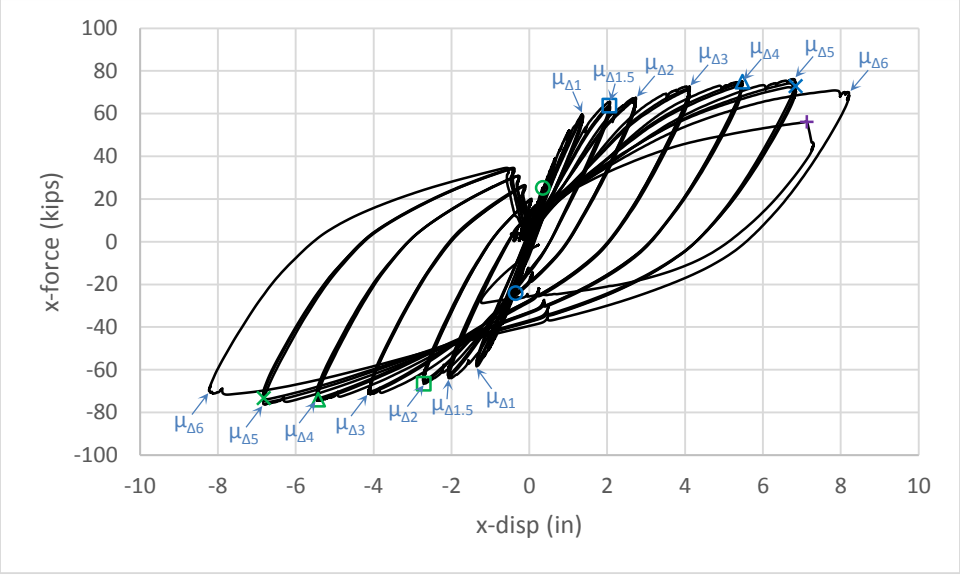

Figure 8-10. Test 5: X-Direction Hysteretic Response

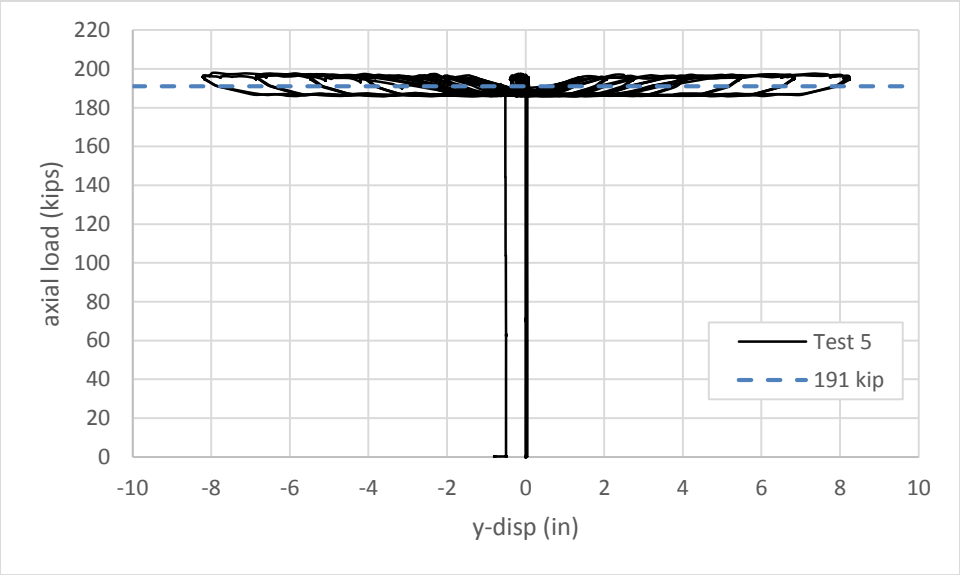

Figure 8-11. Test 5: Y-Direction Axial Force History

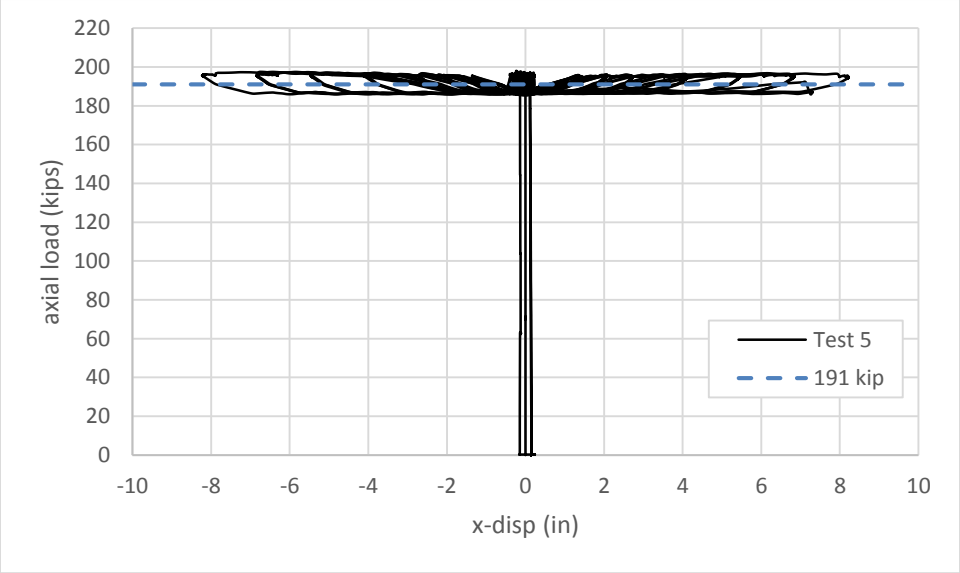

Figure 8-12. Test 5: X-Direction Axial Force History

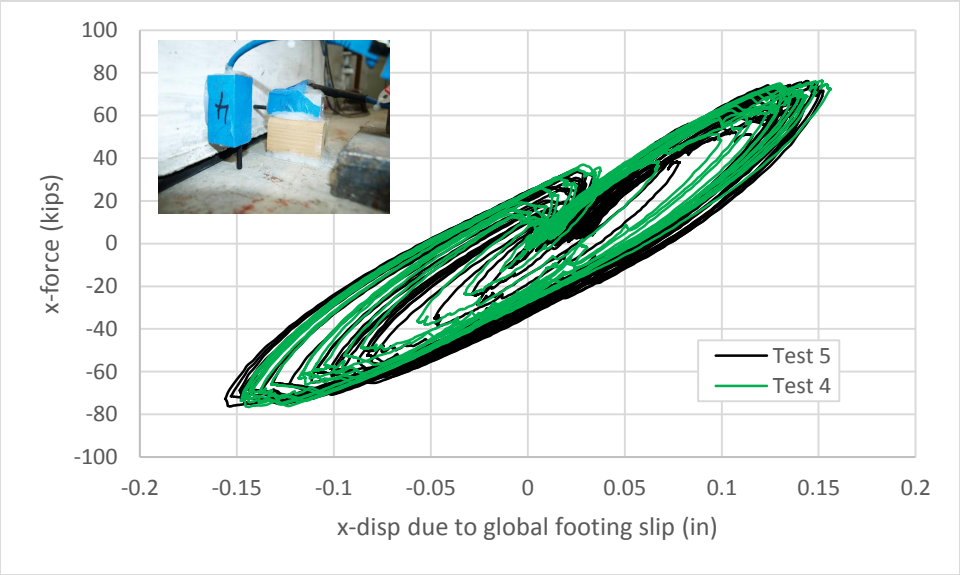

Figure 8-13. Test 5: X-Direction Horizontal Relative Footing Interface Displacement

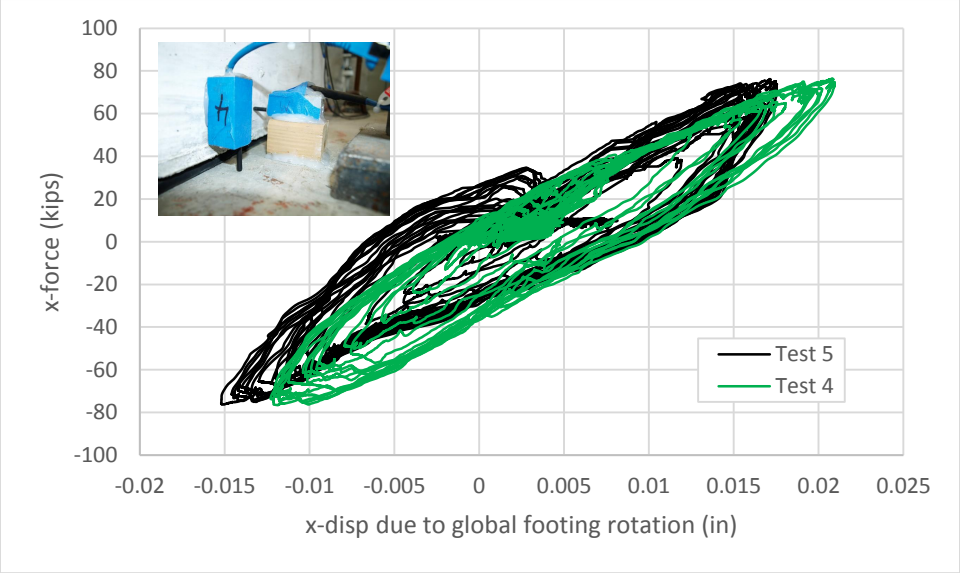

Figure 8-14. Test 5: X-Displacement due to Global Footing Rotation

Test 5 - Experimental Observations

The test began with collection of the initial measurements prior to application of the axial load. A constant axial load of 191 $kips$ $\left(P/f_c' A_g = 6.0\%\right)$ was then applied using a self-regulating axial load system described in Chapter 2. The imposed displacement histories in the Y and X-directions for the Symmetric Three-Cycle-Set Biaxial Load History of Figure 8-1 are shown in Figure 8-3 and Figure 8-4. The resulting column shear force histories in the Y and X-directions appear in Figure 8-5 and Figure 8-6. The full displacement history and resulting load path for Test 5 can be found in Figure 8-7 and Figure 8-8. The Y and X-direction column hysteretic response appears in Figure 8-9 and Figure 8-10. The axial load history is shown in Figure 8-11 and Figure 8-12.

In Test 5, the relative displacement between the transfer and specimen footings was measured using linear potentiometers in the four primary directions. A calculation channel was added to the data acquisition to subtract the relative footing displacement from the string potentiometer displacement, providing the total column deformation. This included both the horizontal slip at the footing interface as well as any global footing rotations which were extrapolated to the center of the applied lateral load. The data from this calculation channel was updated in real time, allowing for it to be used for the control of the actuators, which insured that the appropriate displacement amplitudes were reached in each cycle. For example, the relative horizontal slip between the specimen and transfer footings is shown in Figure 8-13, while the lateral displacement due to global footing rotation appears in Figure 8-14. The force proportional relationship between relative horizontal footing slip and lateral displacement matches that of Test 4. Global footing rotation contributed only minimally to the total deformation, and can be considered negligible. All deformation values reported in this summary are fully corrected based on the measured data.

The load history began with elastic cycles (1-8) in ¼ F_y' increments until the analytically predicted first yield force ($F_y' = 51.45\ kips$) was reached in each direction of loading. Cracks were first observed on all sides of the specimen during the ½ F_y' cycle, see Figure 8-15 and Figure 8-16. At the analytically predicted first yield force, displacements in the four primary directions were measured at $\Delta_y' = 1.00$" and $\Delta_y' = -0.96$" in Y-direction and $\Delta_y' = 1.00$" and $\Delta_y' = -1.05$" in X-direction, producing an average experimental first yield displacement of $\Delta_y' = 1.00$". This value exceeded the analytical prediction for the first yield displacement of 0.83", however it closely matched that measured in nominally identical Test 4 $\left(\Delta_y' = 1.01"\right)$. Cracks observed on each side of the specimen at first yield are shown in Figure 8-17 and Figure 8-18. The equivalent yield displacement for the column was then computed as $\Delta_y = \Delta_y'\left(M_n/M_y'\right) = 1.36"$, where $M_n = 637.64\ kip \cdot ft$ represents the analytical nominal moment capacity corresponding to an extreme fiber compression strain of $\varepsilon_c = 0.004$ or a steel tensile strain of $\varepsilon_s = 0.015$, whichever occurs first. The remainder of the Symmetric Three-Cycle-Set Load History consists of three cycles (1-8 from Figure 8-1) for each displacement ductility level $\mu_{\Delta n} = n \cdot \Delta_y$, where $n = 1, 1.5, 2, 3, 4, 5, 6\ etc.$

For each displacement ductility level, cracks were marked during the third cycle of loading and those which were visible under two primary directions were still marked with that direction's representative color from Figure 8-1. At displacement ductility one, the cracks remained horizontal, but increased in width and became more numerous as shown in Figure 8-19 and Figure 8-20. During the first cycle of displacement ductility 1.5, the first signs of concrete flaking were observed on the North and South sides of the specimen, see Figure 8-21. This slight amount of concrete flaking usually

precedes crushing. East concrete flaking was observed at $\mu_{\Delta 1.5}^{+1x} = 2.07$", followed by crushing during $\mu_{\Delta 1.5}^{+2x} = 2.05$", see Figure 8-22. Similarly, concrete crushing was observed on the North side at $\mu_{\Delta 1.5}^{+2y} = 2.05$", refer to Figure 8-22. In a given direction of loading, cracks on the shear face began to show some inclination in regions above the footing-column interface as shown in Figure 8-23 and Figure 8-24. Cracks near the footing-column interface remained horizontal. Photos of cracks on the North and South sides of the specimen are shown at the end of the displacement ductility level, therefore cracks due to loading in the orthogonal direction also appear.

Additional concrete crushing was observed on the North side at $\mu_{\Delta 2}^{+1y} = 2.73$", followed by South crushing during $\mu_{\Delta 2}^{-1y} = -2.73$", see Figure 8-25. Similarly, more concrete crushing occurred on the East side at $\mu_{\Delta 2}^{+1x} = 2.73$", followed by crushing on West side during $\mu_{\Delta 2}^{-1y} = -2.73$", see Figure 8-26. Photos of the crack profile on each side of the specimen at the conclusion of displacement ductility two appear in Figure 8-27 and Figure 8-28. Crack profiles at the end of displacement ductility three are shown in Figure 8-29 and Figure 8-30. By this time, there was a distinct crack inclination on the shear faces of the specimen in a given direction of loading. Cracks in one direction were clearly interacting with cracks in the opposing directions, however even in the presence of adjacent horizontal cracks, the diagonal cracks on the shear faces continued to elongate and incline for the remainder of the experiment.

Spiral reinforcement on the North side of the specimen yielded under confinement demands during $\mu_{\Delta 4}^{+1y} = 5.48$". Photos of the compression zone in each primary loading direction during early cycles of displacement ductility four appear in Figure 8-31 and Figure 8-32, while crack profiles at the end of the ductility level appear in Figure 8-33 and Figure 8-34. Spiral yielding was then measured on the East, South, and West sides of the specimen during $\mu_{\Delta 4}^{+1x} = 5.47$", $\mu_{\Delta 4}^{-2y} = -5.46$", and $\mu_{\Delta 4}^{-2x} = -5.46$",respectively. Successive compression cycles of displacement ductility four led to larger tension strains measured in confining steel, which is discussed in a later section of this summary. Significant yielding in spiral layers overlaying the extreme fiber reinforcement was measured during the first two cycles of displacement ductility five, although the North, South, and West reinforcement remained visibly straight as shown in Figure 8-35 and Figure 8-36. The East extreme fiber bar visibly buckled during $\mu_{\Delta 5}^{+2x} = 6.84$", refer to Figure 8-36.

Bars N and NNE buckled simultaneously during $\mu_{\Delta 5}^{+3y} = 6.81$", see Figure 8-37, while the South reinforcement remained visibly straight at $\mu_{\Delta 5}^{-3y} = -6.82$". Adjacent East Bars ENE and ESE buckled during $\mu_{\Delta 5}^{+3x} = 6.83$", followed by buckling of the West extreme fiber bar during $\mu_{\Delta 5}^{-3x} = -6.83$", see Figure 8-38. Deformation in the previously buckled North bars increased during $\mu_{\Delta 6}^{+1y} = 8.20$", followed by buckling of Bars S and SSE during $\mu_{\Delta 6}^{-1y} = -8.20$", see Figure 8-39. Adjacent East Bars NE and SE buckled during $\mu_{\Delta 6}^{+1x} = 8.19$" as shown in Figure 8-40. The deformation in the East reinforcement was more severe, since it had buckled one cycle earlier than that the other primary directions. Adjacent West Bars WNW and WSW buckled during $\mu_{\Delta 6}^{-1x} = -8.19$", followed by North Bars NNW and NW at $\mu_{\Delta 6}^{+2y} = 8.23$", refer to Figure 8-41.

Adjacent South Bars SSW and SW buckled during $\mu_{\Delta 6}^{-2y} = -8.19$", see Figure 8-42. All sixteen reinforcing bars had buckled at this time. The South bars had deformed sideways, Figure 8-43, pointing in the East direction. Extensive bar buckling led to strength loss during the second cycle of

displacement ductility six, see Figure 8-9. This strength loss increased rapidly once the second spiral layer fractured on the SE side of the specimen at 7.13" during $\mu_{\Delta 6}^{+2x}$, refer to Figure 8-10 and Figure 8-44. Immediately after spiral fracture, the column twisted counterclockwise about the base. This twist was still present after the column was recentered to the origin The knuckles which connected the two lateral actuators to the loading cap had a portion of their rotational capacity taken up by the twist, which could influence the subsequent repair and retesting of this column should it be selected as a repair candidate. Accurate estimates of the magnitude of the twist at the center of the lateral load can be made using the string potentiometer array. Spiral fracture led to a more significant loss in strength when compared to a single longitudinal bar fracture which had ended the previous specimens. Photos of the specimen after removal of the instrumentation and loose core concrete appear in Figure 8-45, Figure 8-46, and Figure 8-47.

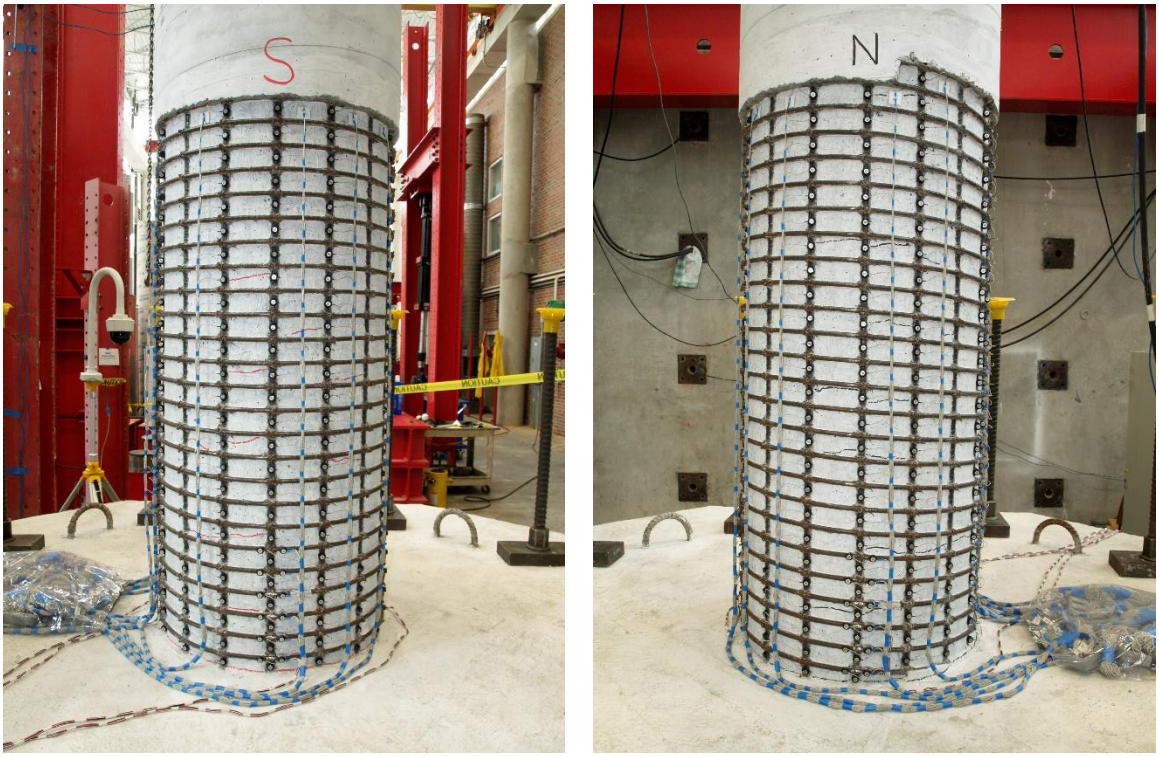

Figure 8-15. Test 5: First Cracking on the South and North Sides of the Specimen during $\Delta_y = 0.34$" and $\Delta_y = -0.31$"

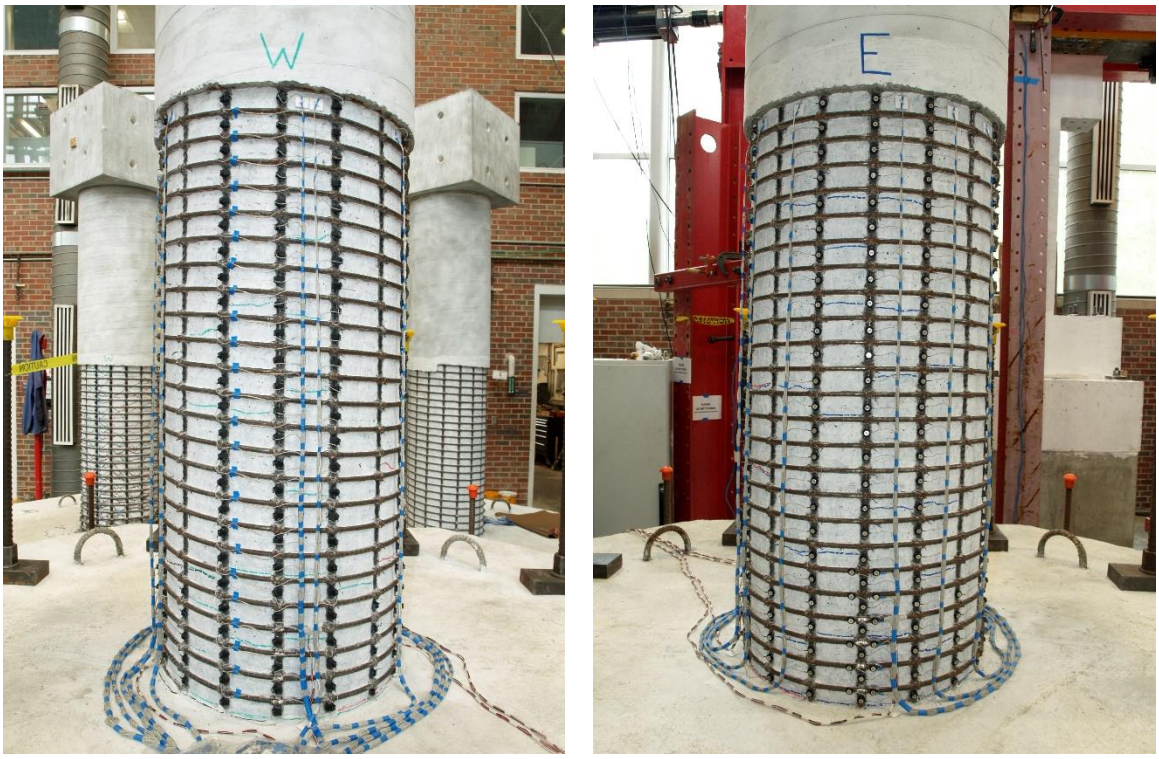

Figure 8-16. Test 5: First Cracking on the West and East Sides of the Specimen during $\Delta_x = 0.34$" and $\Delta_x = -0.35$"

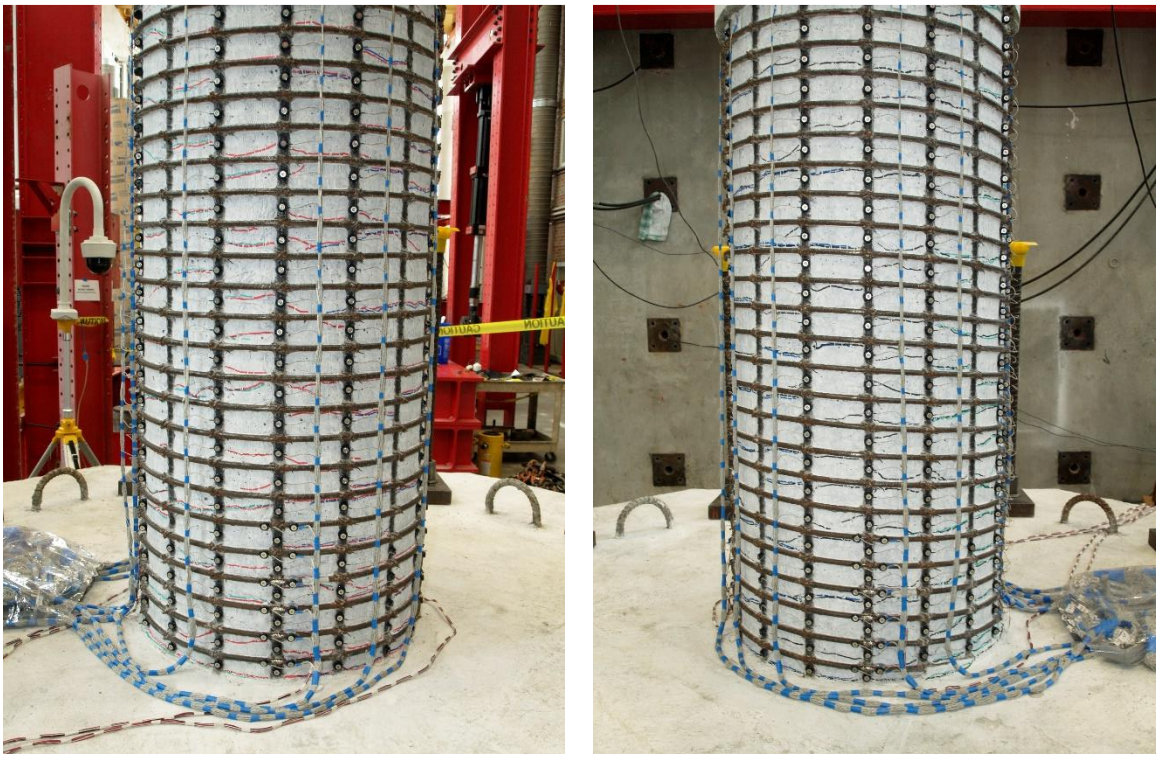

Figure 8-17. Test 5: Cracking on the South and North Sides during $\Delta'_y = 1.00$" and $\Delta'_y = -0.96$" in Y-Direction

Figure 8-18. Test 5: Cracking on the West and East Sides during $\Delta'_y = 1.00"$ and $\Delta'_y = -1.05"$ in X-Direction

Figure 8-19. Test 5: Cracking on the (Left) South Side at $\mu_{\Delta 1}^{+3y} = 1.38"$ and (Right) North Side at $\mu_{\Delta 1}^{-3y} = -1.38"$

Figure 8-20. Test 5: Cracking on the (Left) West Side at $\mu_{\Delta 1}^{+3x} = 1.38$" and (Right) East Side at $\mu_{\Delta 1}^{-3x} = -1.36$"

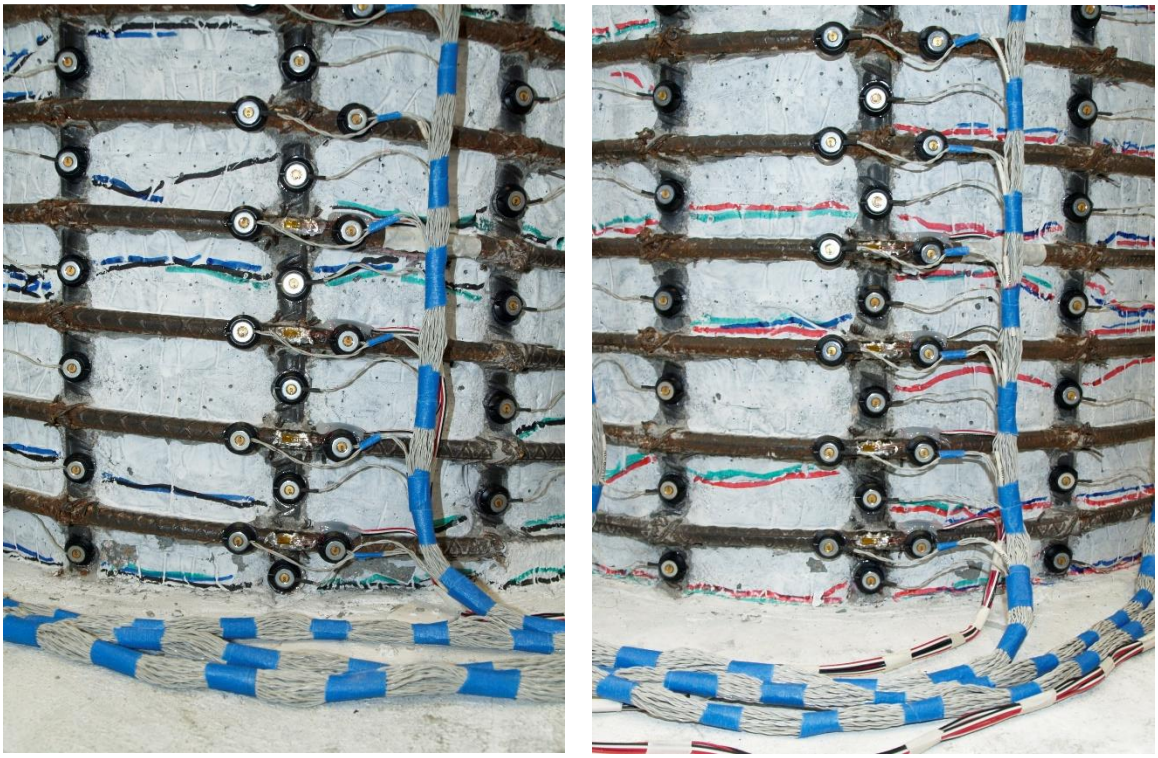

Figure 8-21. Test 5: Initial Concrete Flaking on (Left) North Side at $\mu_{\Delta 1.5}^{+1y} = 2.07$" and (Right) South Side at $\mu_{\Delta 1.5}^{-1y} = -2.05$"

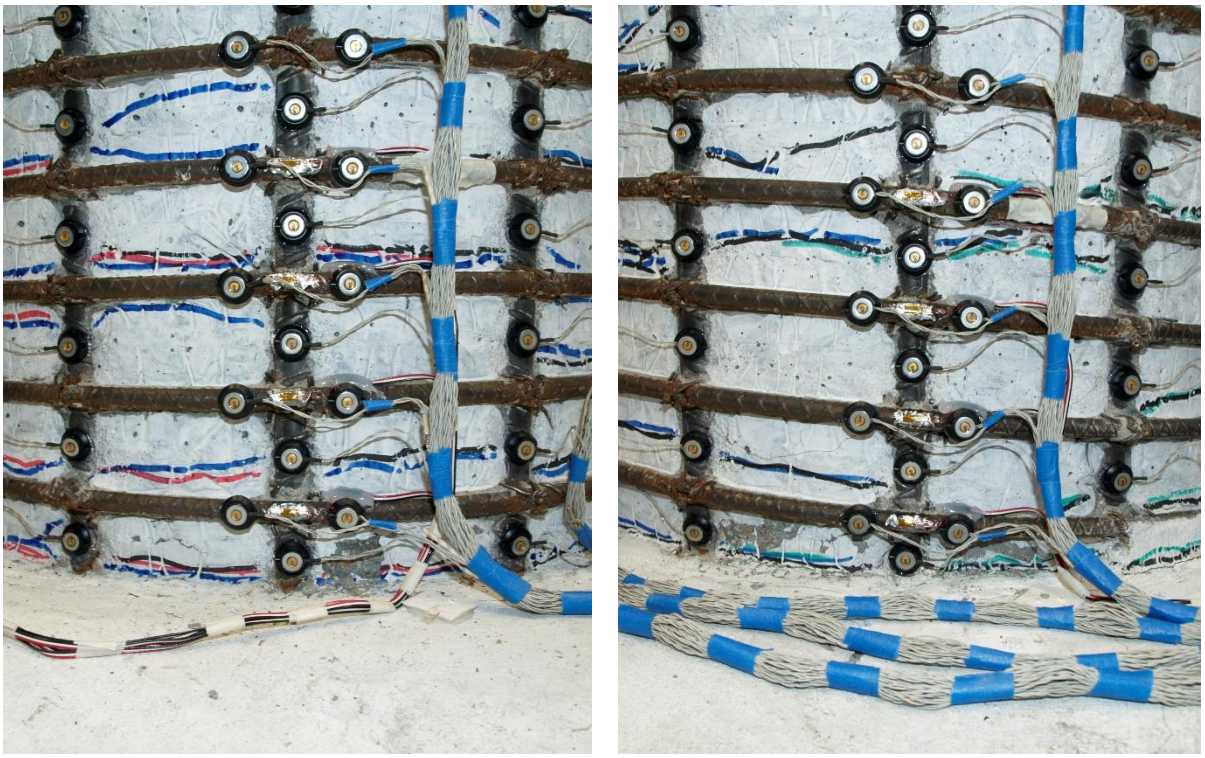

Figure 8-22. Test 5: (Left) East Concrete Crushing at $\mu_{\Delta 1.5}^{+2x} = 2.05$" and (Right) North Concrete Crushing at $\mu_{\Delta 1.5}^{+2y} = 2.05$"

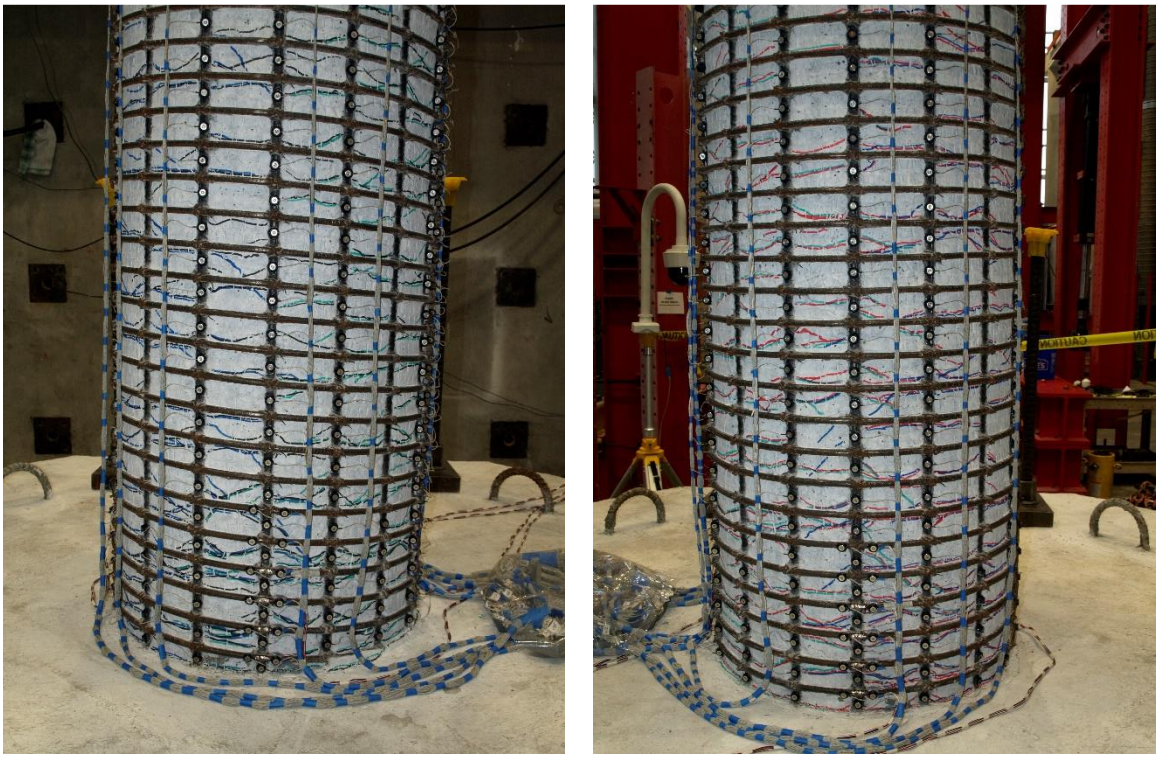

Figure 8-23. Test 5: (Left) North and (Right) South Sides of the Specimen at the End of $\mu_{\Delta 1.5}$

Figure 8-24. Test 5: Cracking on the (Left) West Side at $\mu_{\Delta 1.5}^{+3x} = 2.07$" and (Right) East Side at $\mu_{\Delta 1.5}^{-3x} = -2.09$"

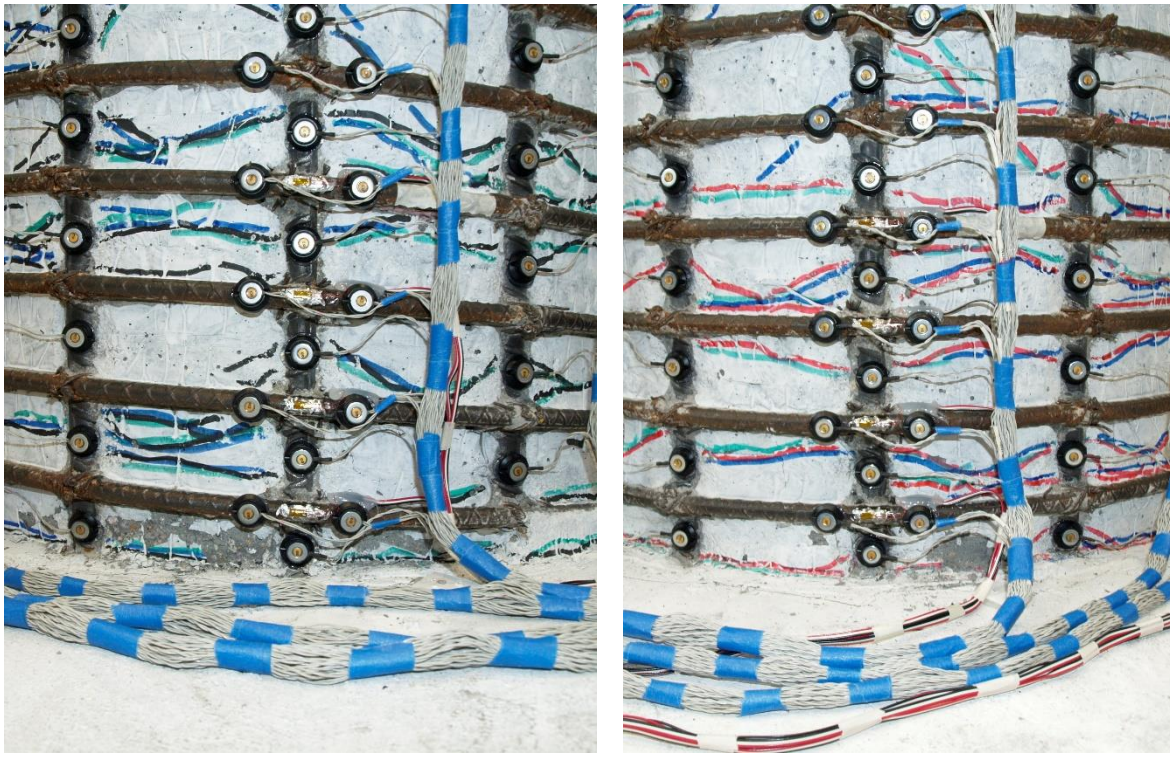

Figure 8-25. Test 5: Concrete Crushing on the (Left) North Side at $\mu_{\Delta 2}^{+1y} = 2.73$" and (Right) South Side at $\mu_{\Delta 2}^{-1y} = -2.73$"

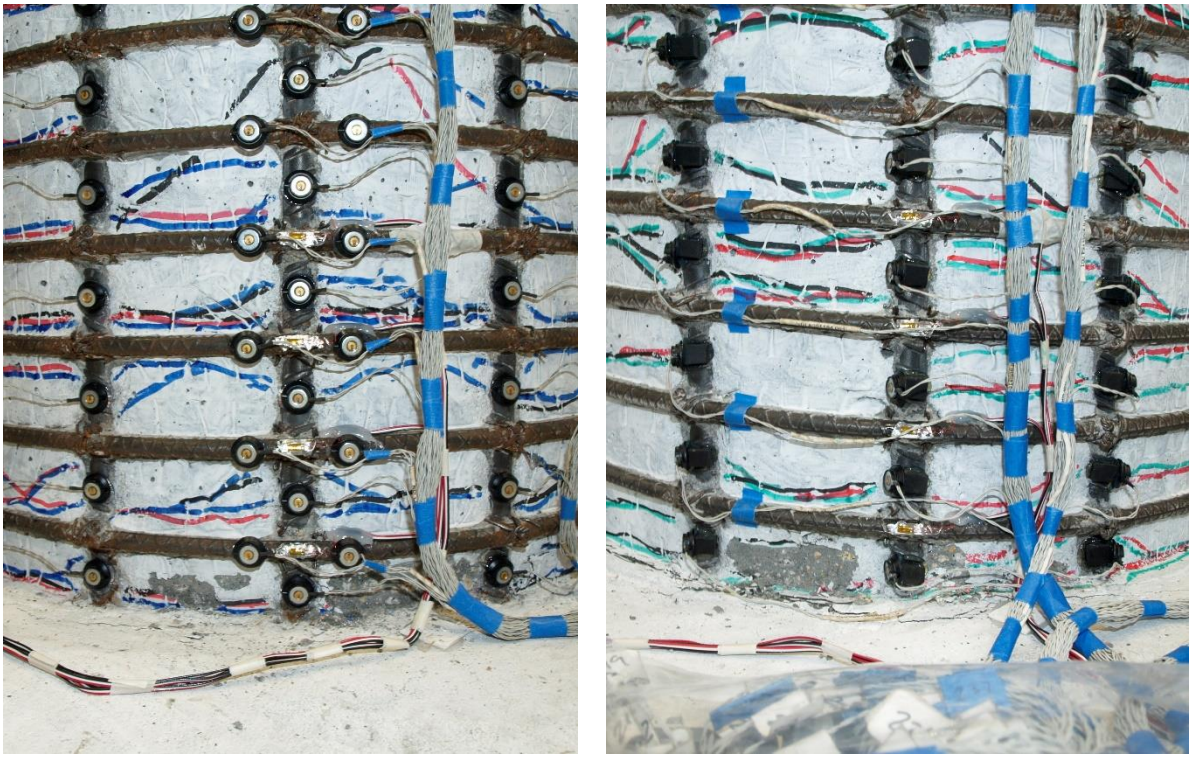

Figure 8-26. Test 5: Concrete Crushing on the (Left) East Side at $\mu_{\Delta 2}^{+1x} = 2.73$" and (Right) West Side at $\mu_{\Delta 2}^{-1x} = -2.72$"

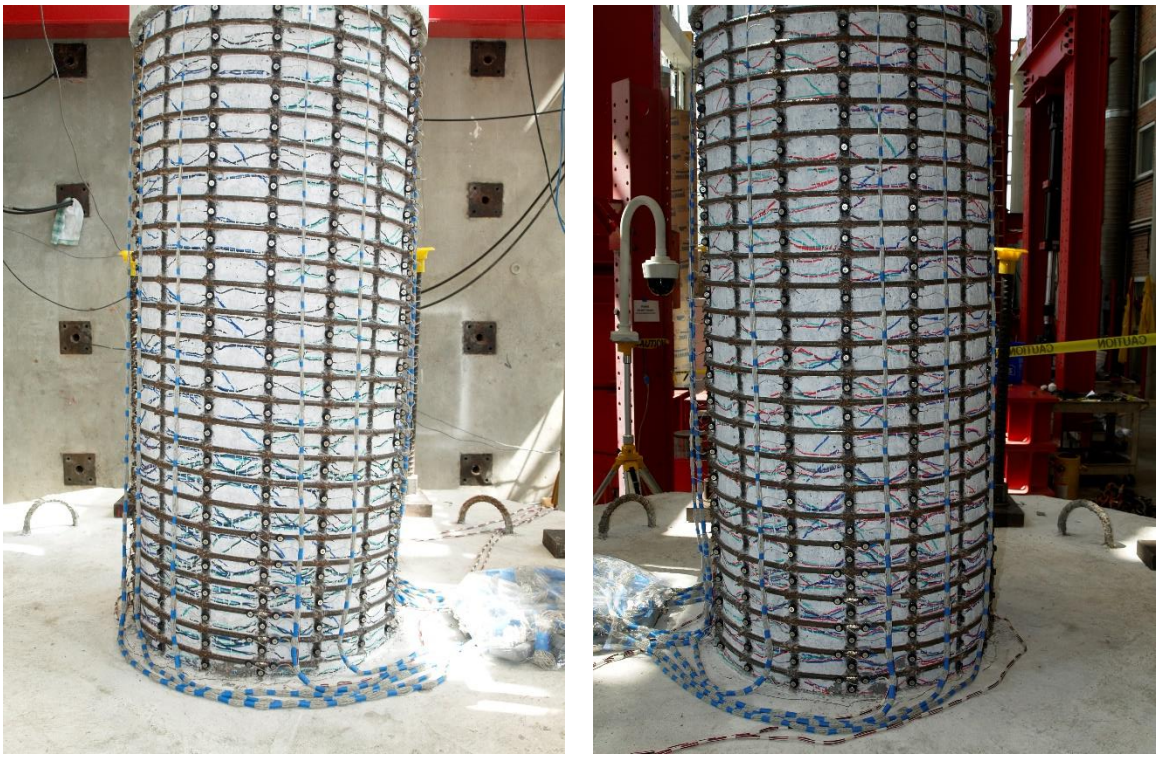

Figure 8-27. Test 5: (Left) North and (Right) South Sides of the Specimen at the End of $\mu_{\Delta 2}$

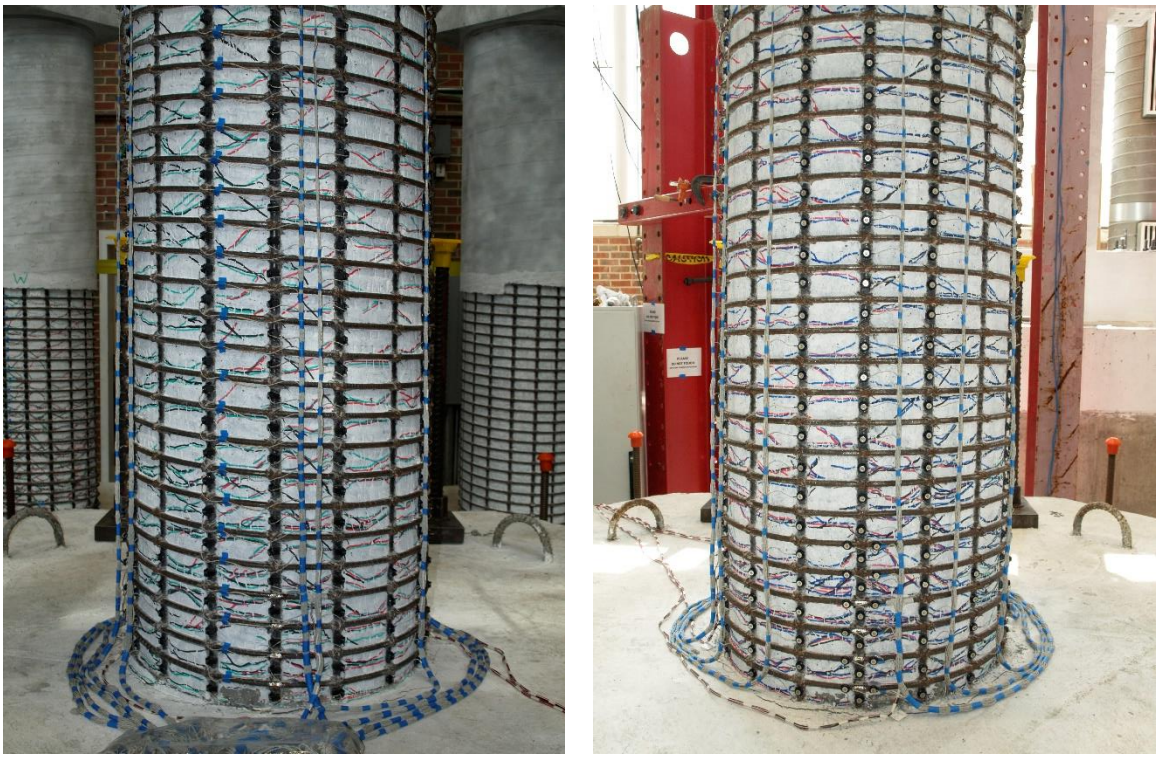

Figure 8-28. Test 5: Cracking on the (Left) West Side at $\mu_{\Delta 2}^{+3x} = 2.73$" and (Right) East Side at $\mu_{\Delta 2}^{-3x} = -2.73$"

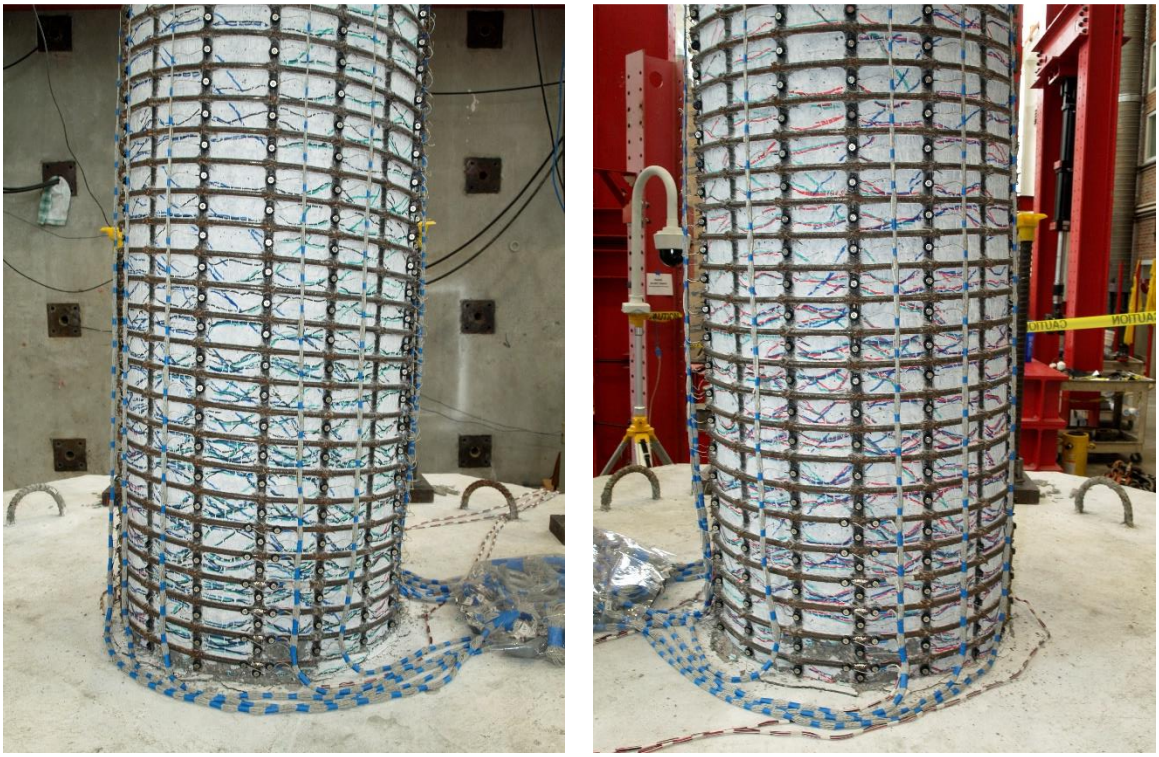

Figure 8-29. Test 5: (Left) North and (Right) South Sides of the Specimen at the End of $\mu_{\Delta 3}$

Figure 8-30. Test 5: Cracking on the (Left) West Side at $\mu_{\Delta 3}^{+3x} = 4.09$" and (Right) East Side at $\mu_{\Delta 3}^{-3x} = -4.08$"

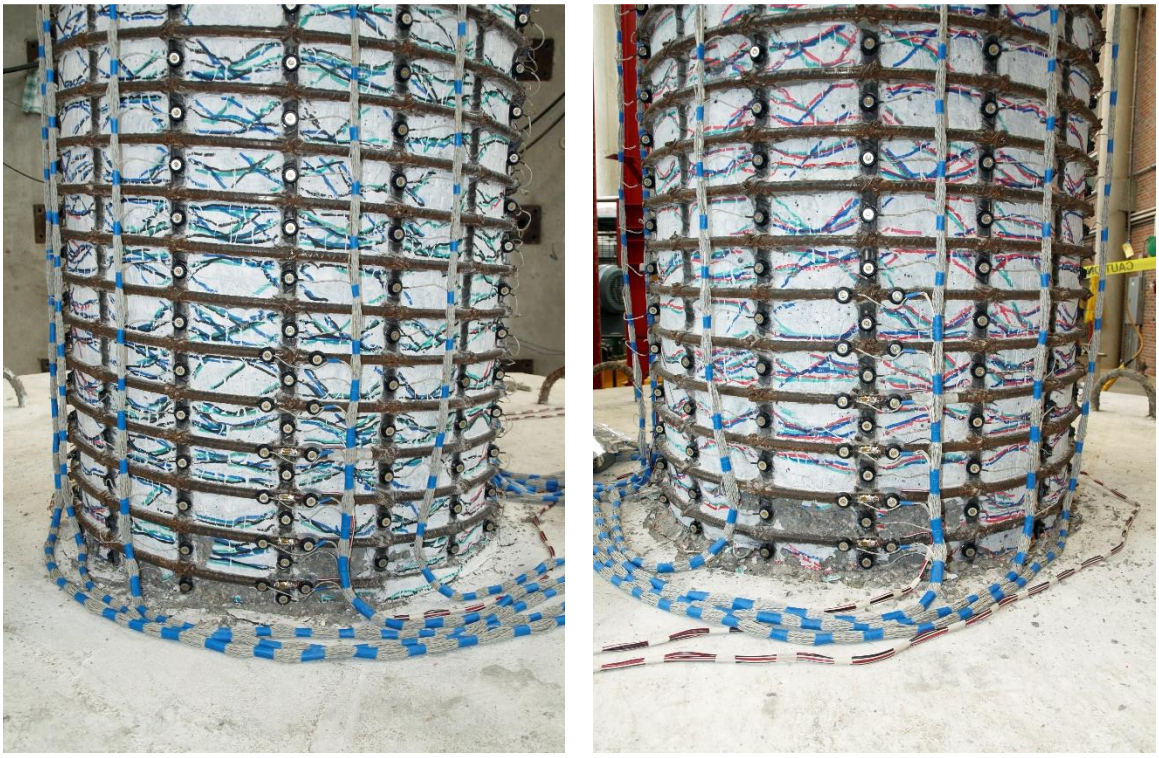

Figure 8-31. Test 5: Initial Spiral Yield on the (Left) North Side at $\mu_{\Delta 4}^{+1y} = 5.48$" and (Right) South Side at $\mu_{\Delta 4}^{-2y} = -5.46$"

Figure 8-32. Test 5: Initial Spiral Yield on the (Left) East Side at $\mu_{\Delta 4}^{+1x} = 5.47"$ and (Right) West Side at $\mu_{\Delta 4}^{-2x} = -5.46"$

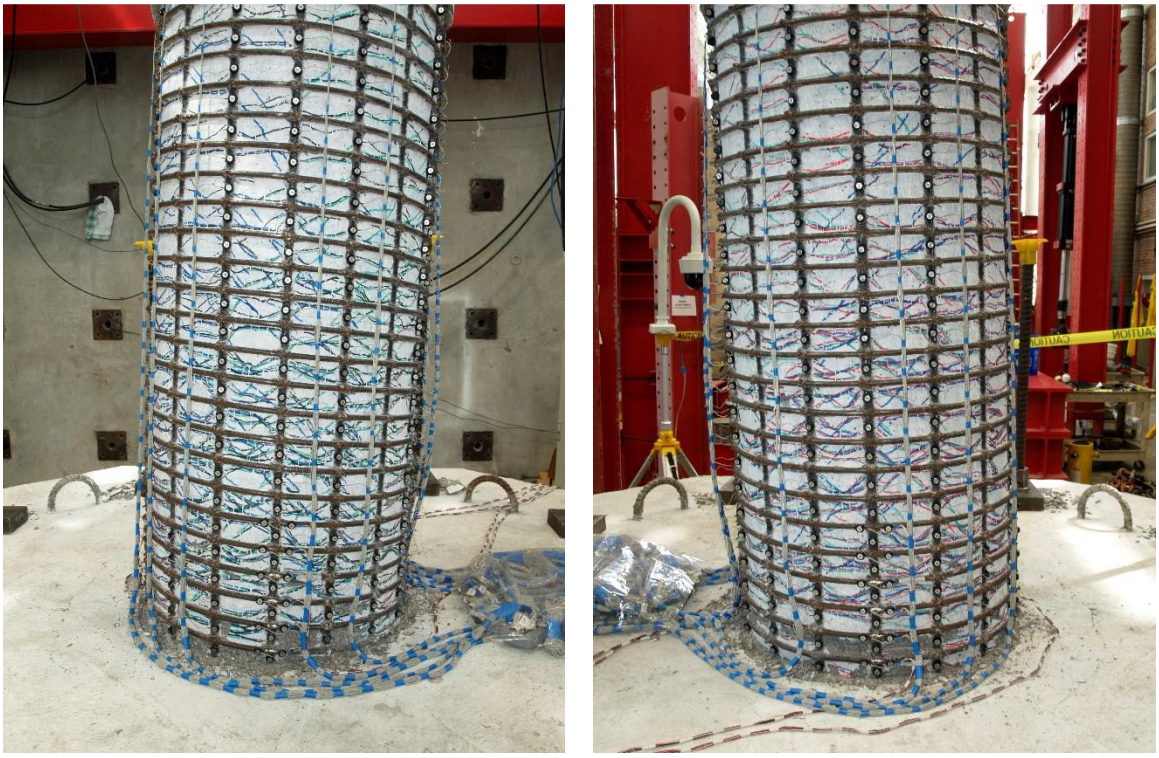

Figure 8-33. Test 5: (Left) North and (Right) South Sides of the Specimen at the End of $\mu_{\Delta 4}$

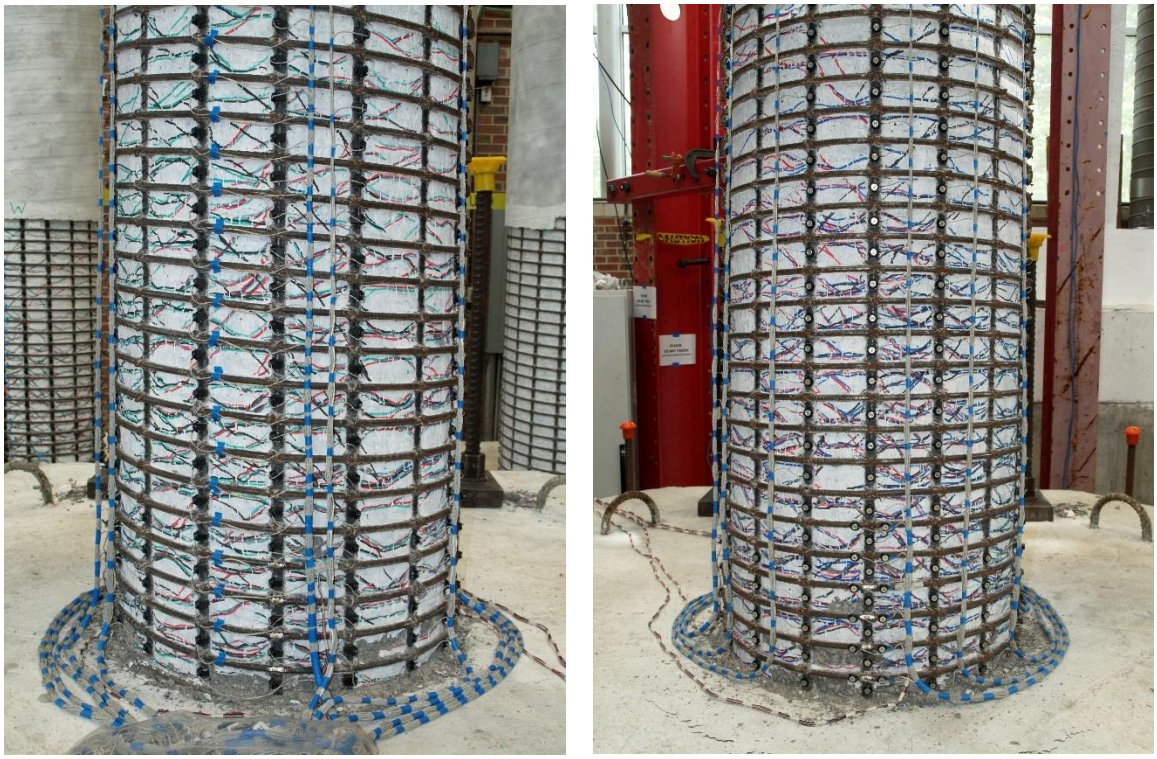

Figure 8-34. Test 5: Cracking on the (Left) West Side at $\mu_{\Delta 4}^{+3x} = 5.45$" and (Right) East Side at $\mu_{\Delta 4}^{-3x} = -5.45$"

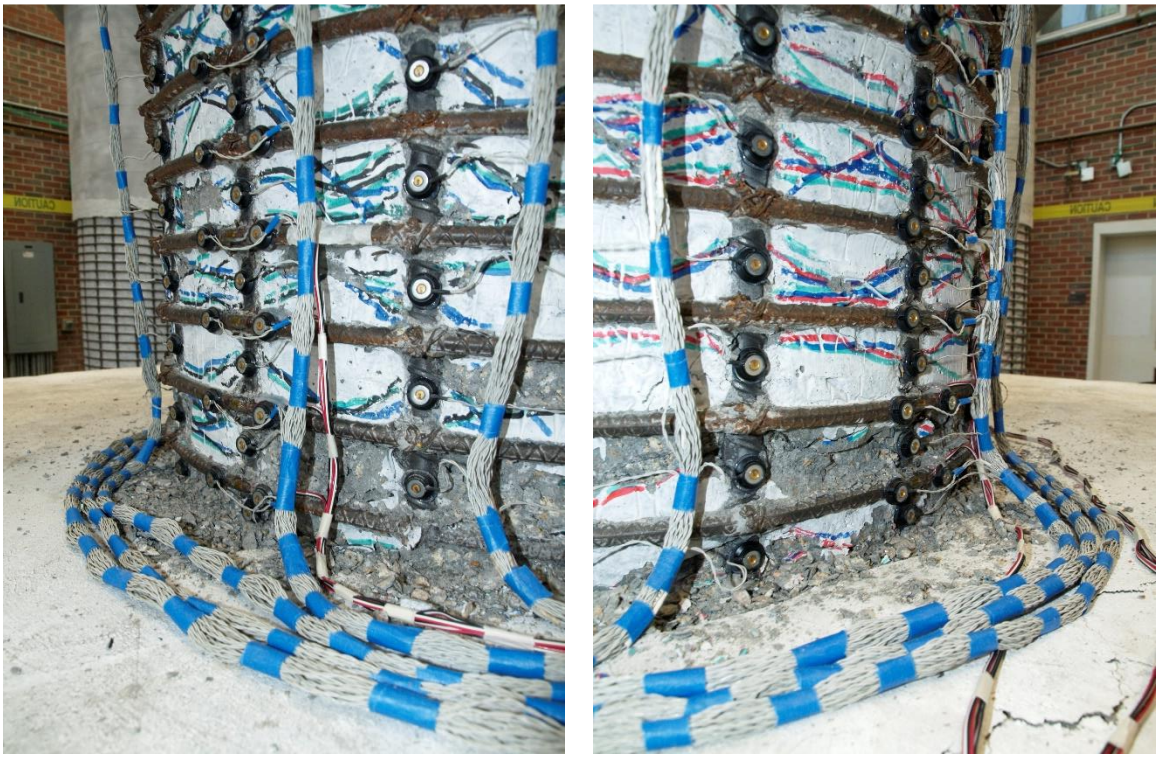

Figure 8-35. Test 5: Bars Remained Visibly Straight on (Left) North at $\mu_{\Delta 5}^{+2y} = 6.84$" and (Right) South at $\mu_{\Delta 5}^{-2y} = -6.85$"

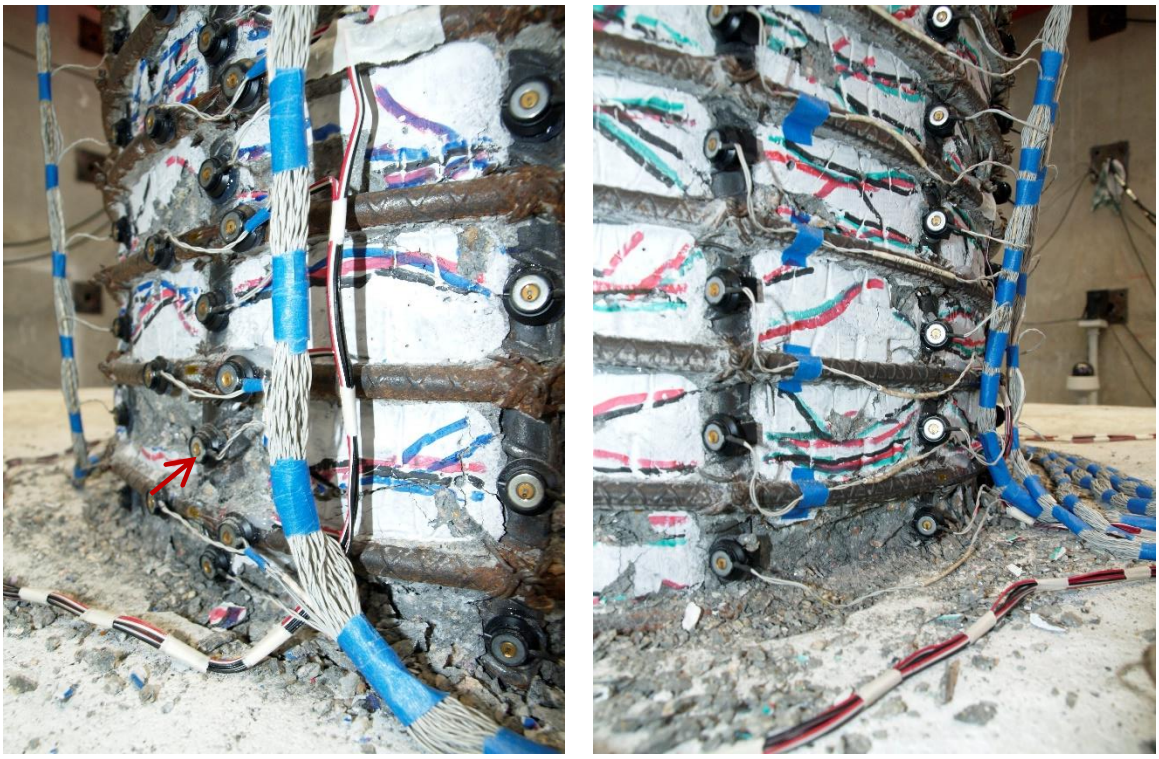

Figure 8-36. Test 5: (Left) East Bar Buckling at $\mu_{\Delta 5}^{+2x} = 6.84"$ and (Right) West Bars Visibly Straight at $\mu_{\Delta 5}^{-2x} = -6.81"$

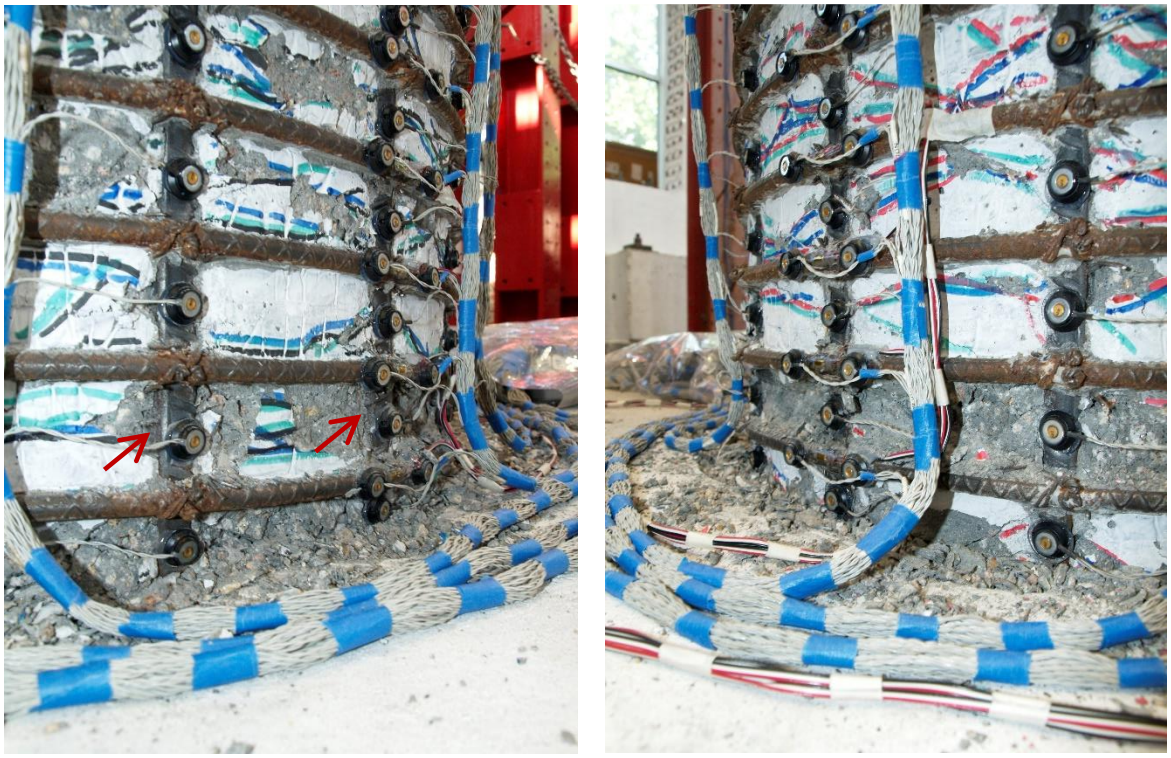

Figure 8-37. Test 5: (Left) Bar N and NNE Buckling at $\mu_{\Delta 5}^{+3y} = 6.81"$ and (Right) South Bars Straight at $\mu_{\Delta 5}^{-3y} = -6.82"$

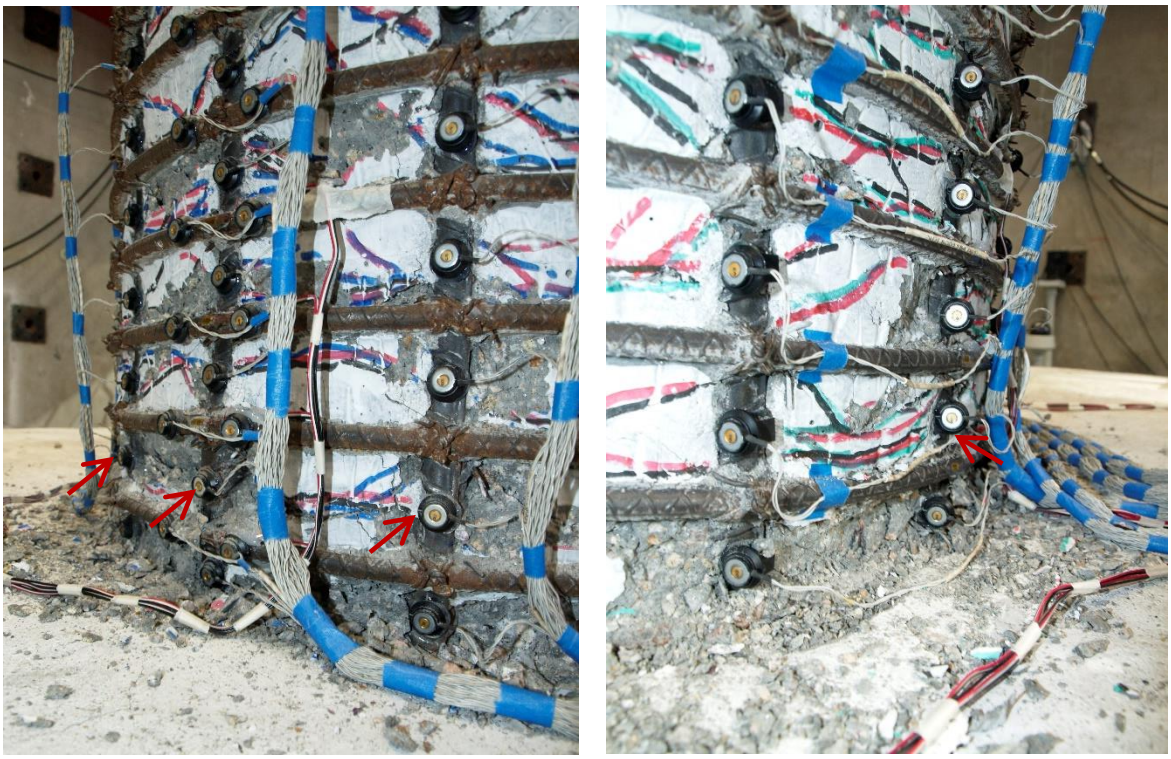

Figure 8-38. Test 5: (Left) Buckling of Bars ENE and ESE at $\mu_{\Delta 5}^{+3x} = 6.83$" and (Right) Buckling of Bar W at $\mu_{\Delta 5}^{-3x} = -6.83$"

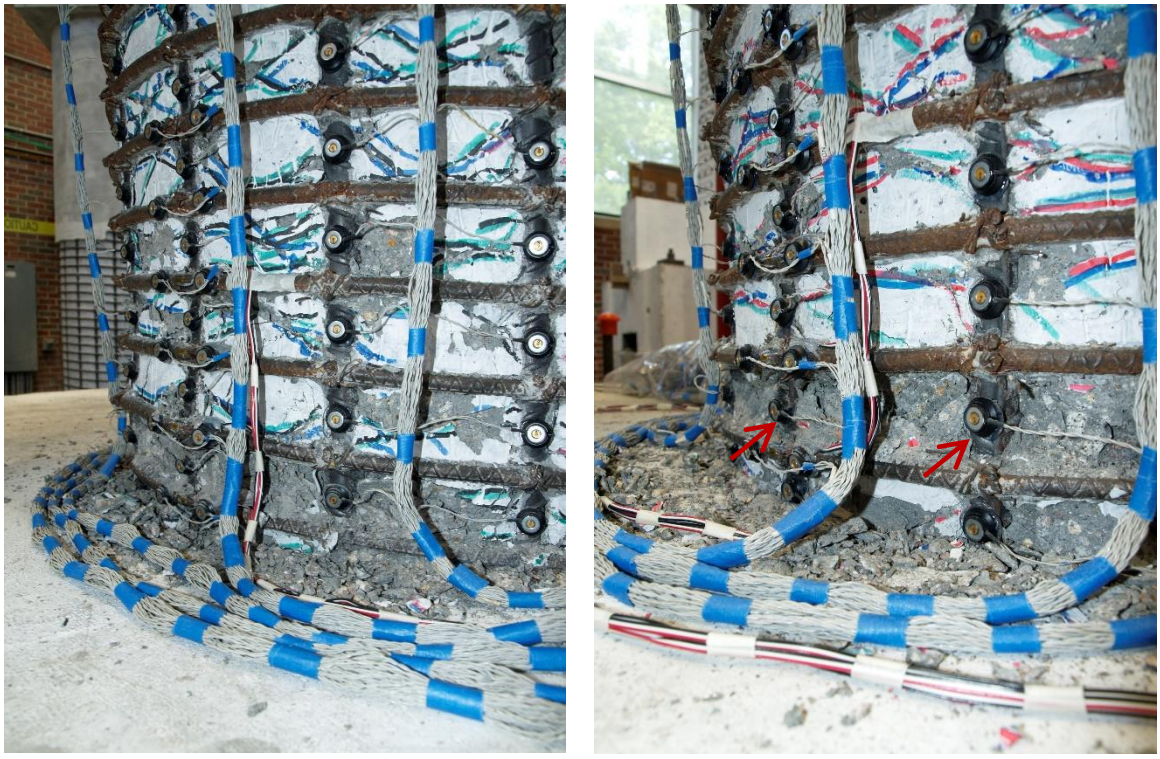

Figure 8-39. Test 5: (Left) North Side at $\mu_{\Delta 6}^{+1y} = 8.20$" and (Right) Buckling of Bars S and SSE at $\mu_{\Delta 6}^{-1y} = -8.20$"

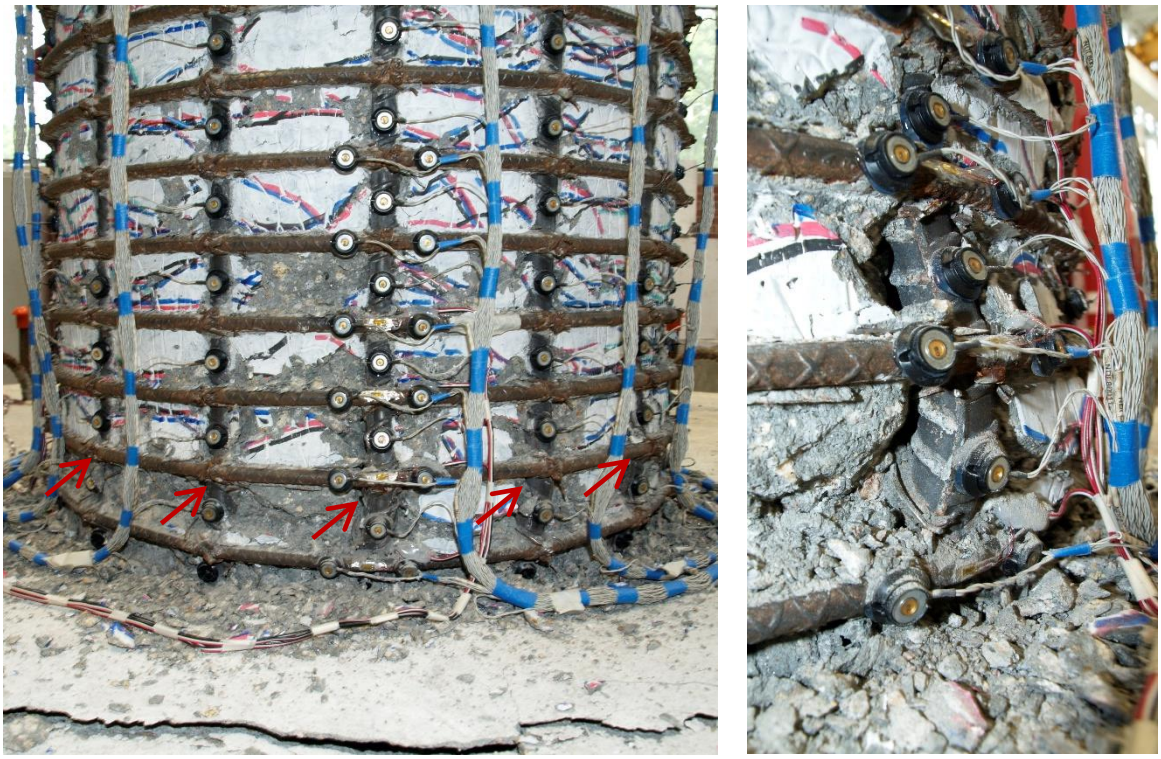

Figure 8-40. Test 5: (Left) Buckling of Bars NE and SE at $\mu_{\Delta 6}^{+1x} = 8.19$" and (Right) Deformation in the East Buckled Bar

Figure 8-41. Test 5: Buckling of Bars (Left) WNW and WSW at $\mu_{\Delta 6}^{-1x} = -8.19$" and (Right) NNW and NW at $\mu_{\Delta 6}^{+2y} = 8.23$"

Figure 8-42. Test 5: Buckling of Bars SSW and SW at $\mu_{\Delta 6}^{-2y} = -8.19$"

Figure 8-43. Test 5: Sideways Buckling of Bars on the SE side of the Specimen at $\mu_{\Delta 6}^{-2y} = -8.19$"

Figure 8-44. Test 5: Spiral Fracture at 7.13" during $\mu_{\Delta 6}^{+2x}$ Led to a Counterclockwise Twist of the Column about the Base

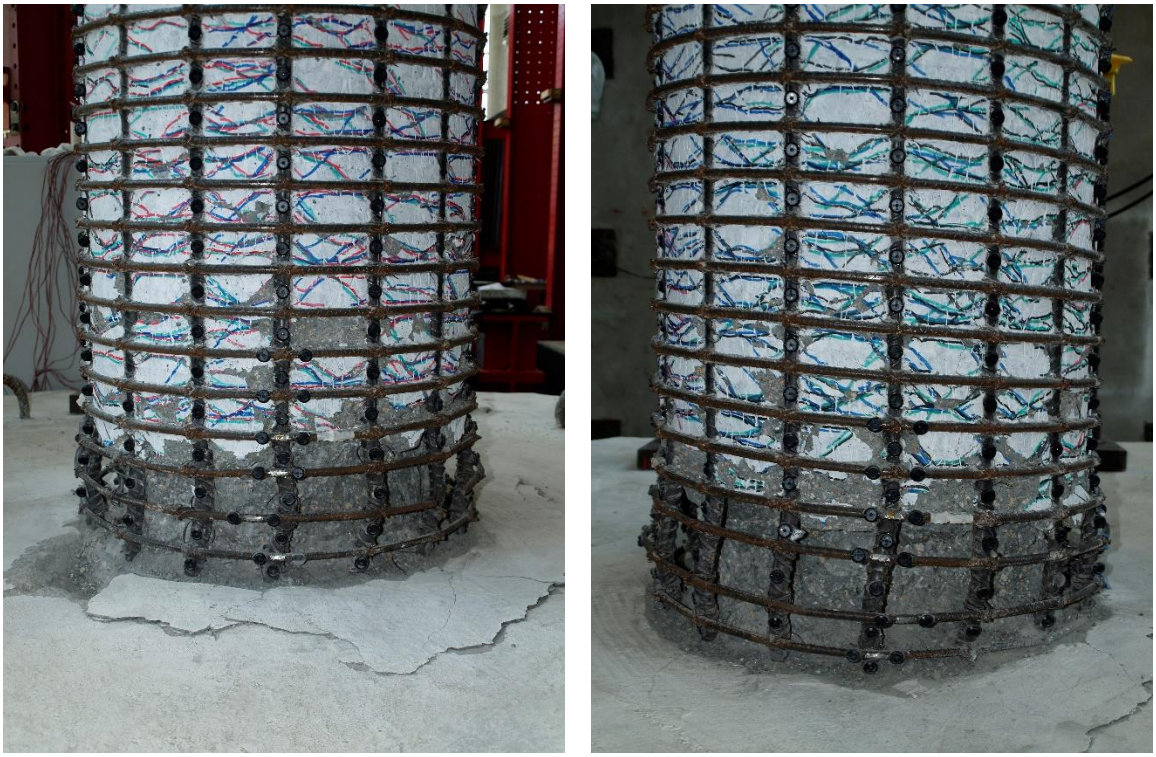

Figure 8-45. Test 5: (Left) South and (Right) North Sides of the Specimen after Instrumentation Removal

Figure 8-46. Test 5: (Left) West and (Right) East Sides of the Specimen after Instrumentation Removal

Figure 8-47. Test 5: Close-Up of SE Region where the Second Spiral Layer Fractured

Test 5 - Strain Data Analysis

North and South Bar Strains

Vertical strain profiles for North and South reinforcement during y-direction cycles are shown in Figure 8-48 and Figure 8-49. Strains in the lowest four spiral layers during compressive y-direction cycles on the North and South sides of the specimen appear in Figure 8-50 and Figure 8-51. The relationship between strain and displacement for either peak tensile or peak compressive gauge lengths appear in Figure 8-52 through Figure 8-55. These figures contain monotonic moment curvature predictions for respective plastic hinge methods. PCK (2007) Lp refers to the (Priestley, Calvi and Kowalsky 2007) plastic hinge method, GN15 Tension/Compression Lpr refers to the (Goodnight, Kowalsky and Nau 2015a) unidirectional modified plastic hinge method, TX Adjusted Lpr and Lsp refer to using the measured extent of plasticity and average equivalent strain penetration length from this specific test, and New Equations refers to a new bidirectional plastic hinge method which was created based on this study. Details of the new plastic hinge method appear in a later chapter of this report.

The spiral strain gauge hysteresis for the first and second layers above the footing on the North side of the specimen are shown in Figure 8-57 and Figure 8-58. Tension strains in the first spiral layer increased during $\mu_{\Delta 5}^{+3y} = 6.81$" as two North bars visibly buckled, see Figure 8-37. The second North spiral layer above the footing went off scale during $\mu_{\Delta 5}^{+2y} = 6.84$", even though the North reinforcement remained visibly straight as shown in Figure 8-35. The sharp increase in tension strain in the first two spiral layers during $\mu_{\Delta 5}^{+2y} = 6.84$" indicates some level of measurable outward deformation prior to visible buckling. The visual observation of bar buckling was confirmed upon inspection of the North longitudinal bar strain hysteresis in Figure 8-56; however, there was significant measurable outward deformation in the previous compressive cycle.

The spiral strain gauge hysteresis for the second and third layers above the footing on the South side of the specimen appear in Figure 8-60 and Figure 8-61. The second and third South spiral layers went off scale during $\mu_{\Delta 6}^{-1y} = -8.20$", when two South bars visibly buckled, see Figure 8-39. Measured strains in the first spiral layer were lower than those above as shown in Figure 8-51. The visual observation of bar buckling was confirmed upon inspection of the South longitudinal bar strain hysteresis in Figure 8-59.

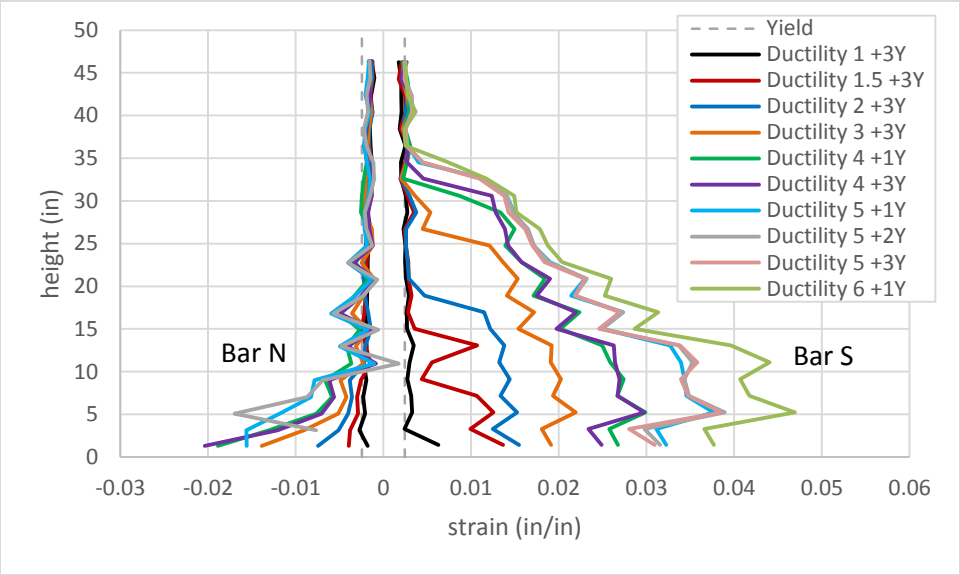

Figure 8-48. Test 5: Vertical Strain Profiles for Loading in the +Y-direction

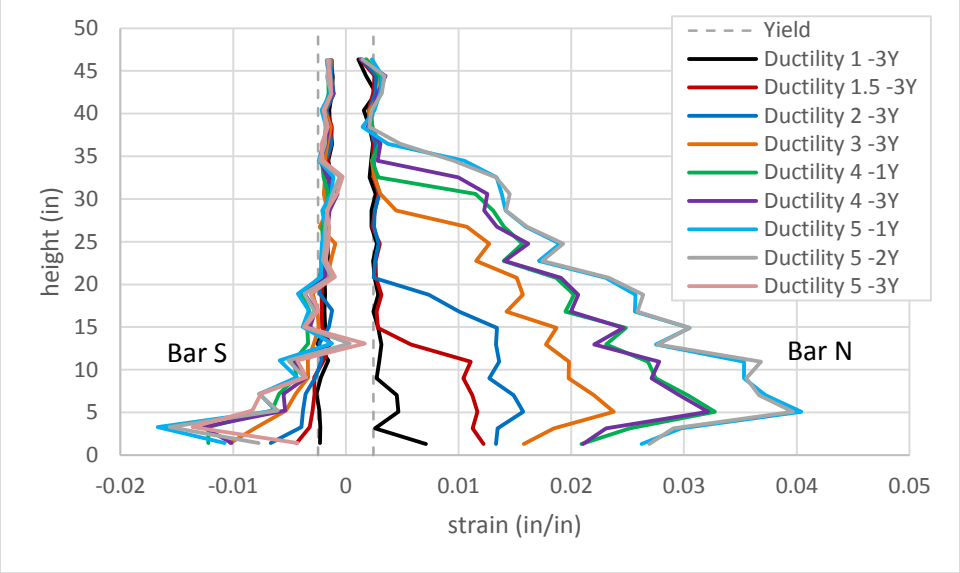

Figure 8-49. Test 5: Vertical Strain Profiles for Loading in the -Y-direction

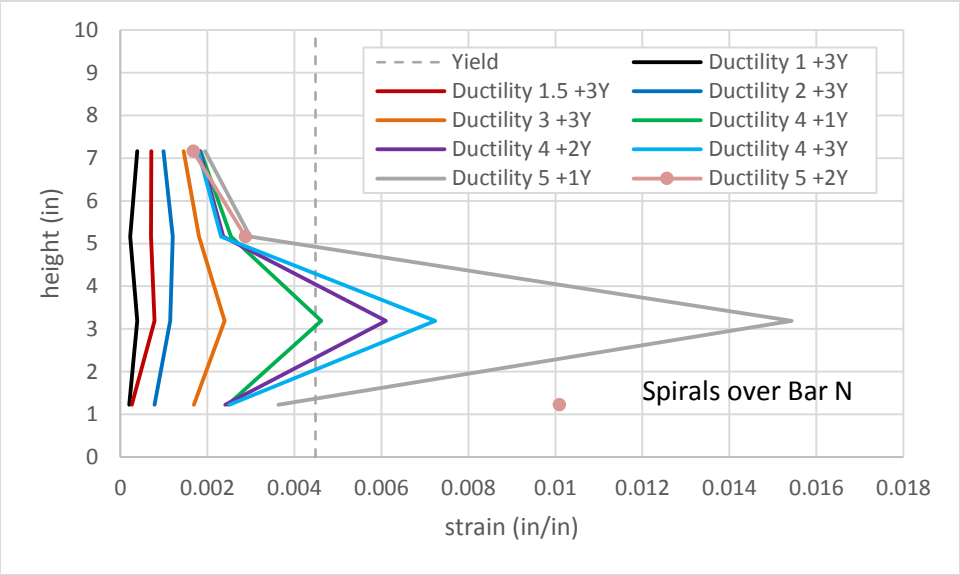

Figure 8-50. Test 5: Spiral Strains Measured Over the North Extreme Fiber Bar during +Y Cycles

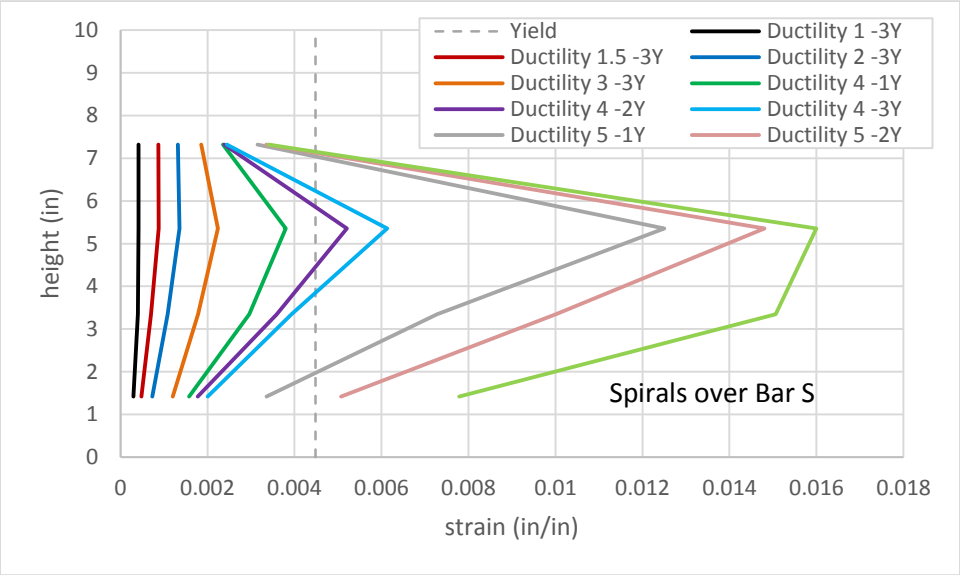

Figure 8-51. Test 5: Spiral Strains Measured Over the South Extreme Fiber Bar during -Y Cycles

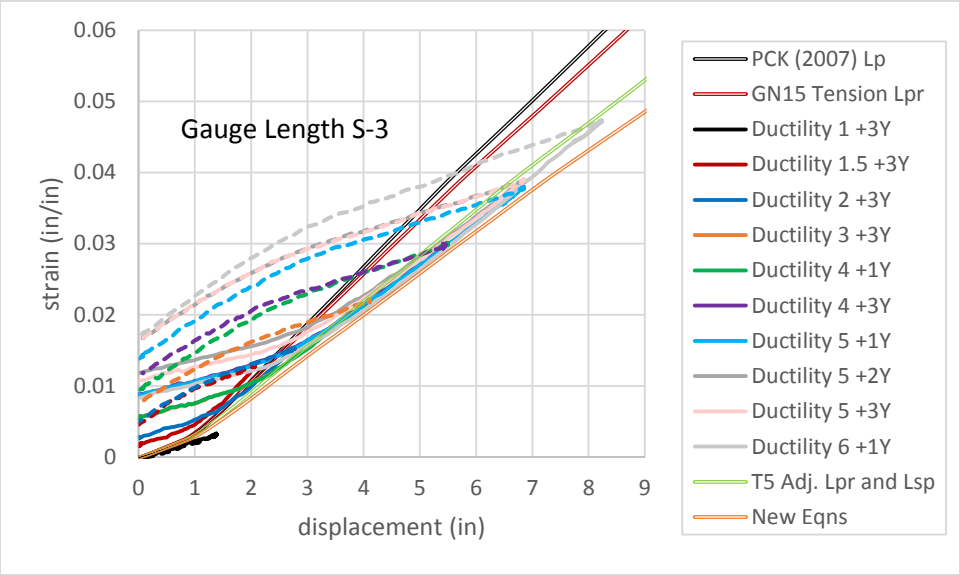

Figure 8-52. Test 5: Tension Strain-Disp. for Bar S (Gauge Length 3 Centered 5.23" above the Footing)

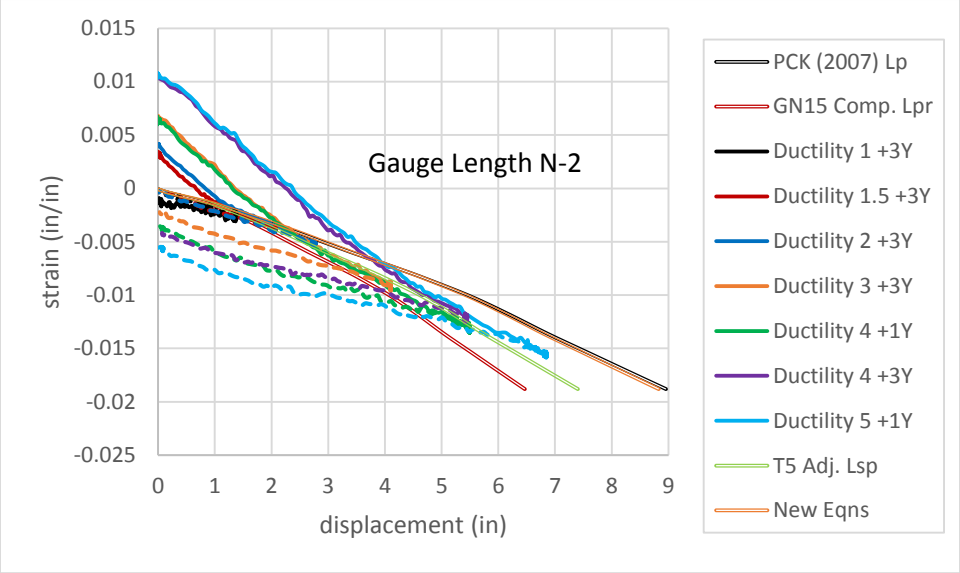

Figure 8-53. Test 5: Compression Strain-Disp. for Bar N (Gauge Length 2 Centered 3.14" above the Footing)

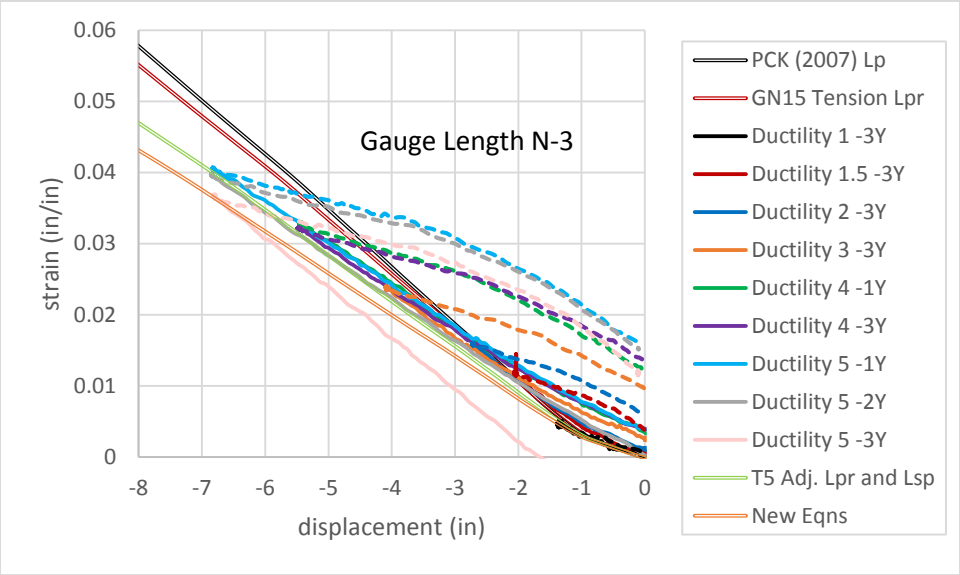

Figure 8-54. Test 5: Tension Strain-Disp. for Bar N (Gauge Length 3 Centered 5.07" above the Footing)

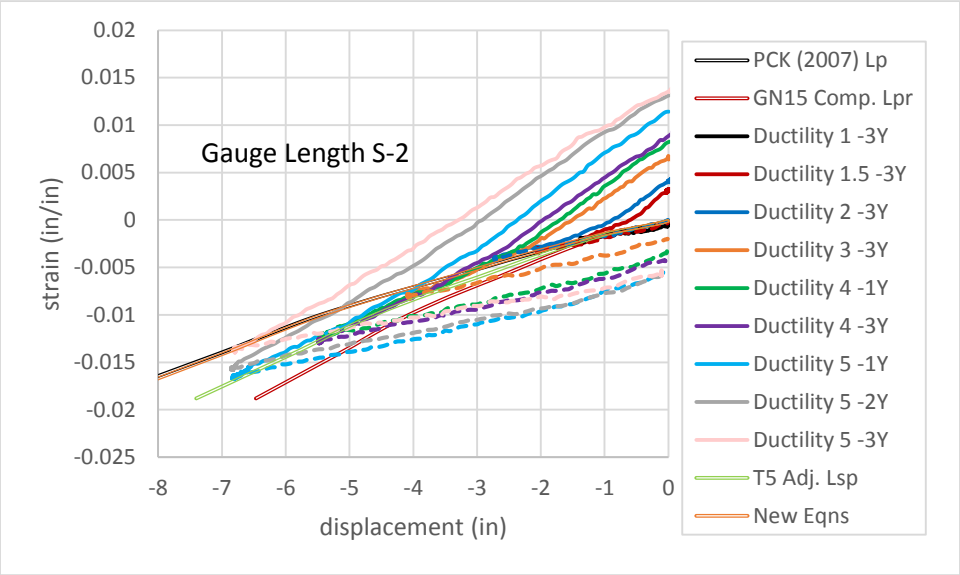

Figure 8-55. Test 5: Compression Strain-Disp. for Bar S (Gauge Length 2 Centered 3.27" above the Footing)

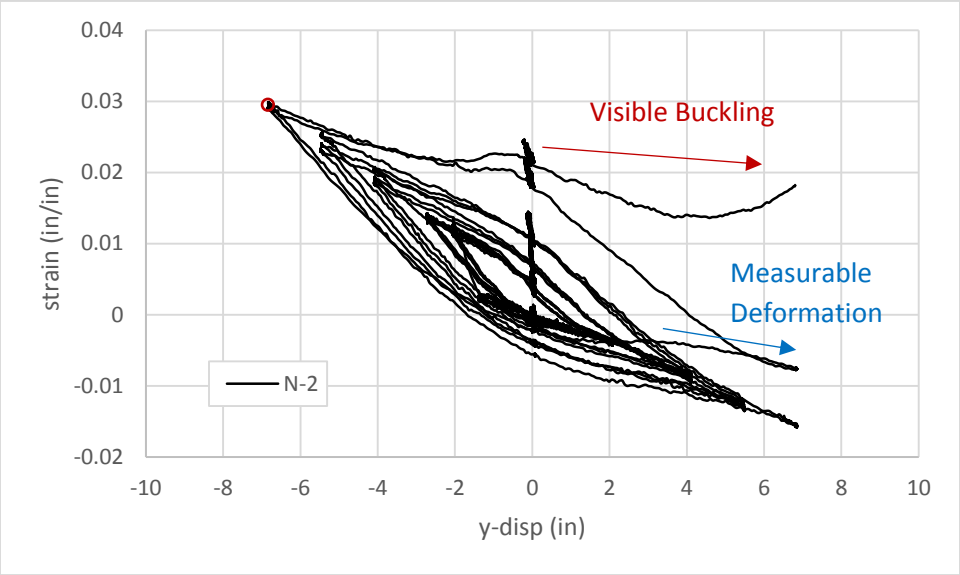

Figure 8-56. Test 5: Strain Hysteresis over the North Buckled Bar (Gauge Length 2 Centered 3.14" above the Footing)

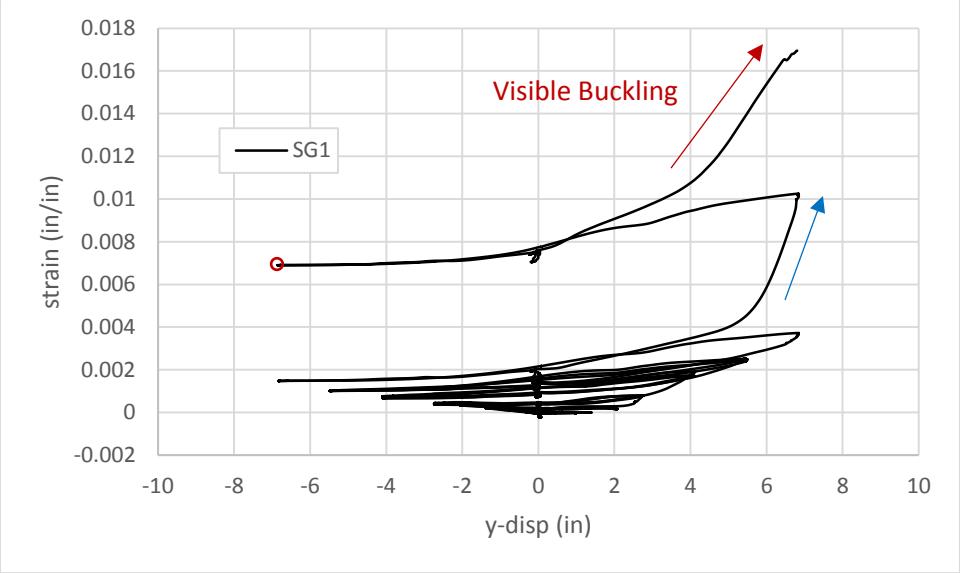

Figure 8-57. Test 5: North Spiral Strain Gauge Hysteresis for the First Layer above the Footing

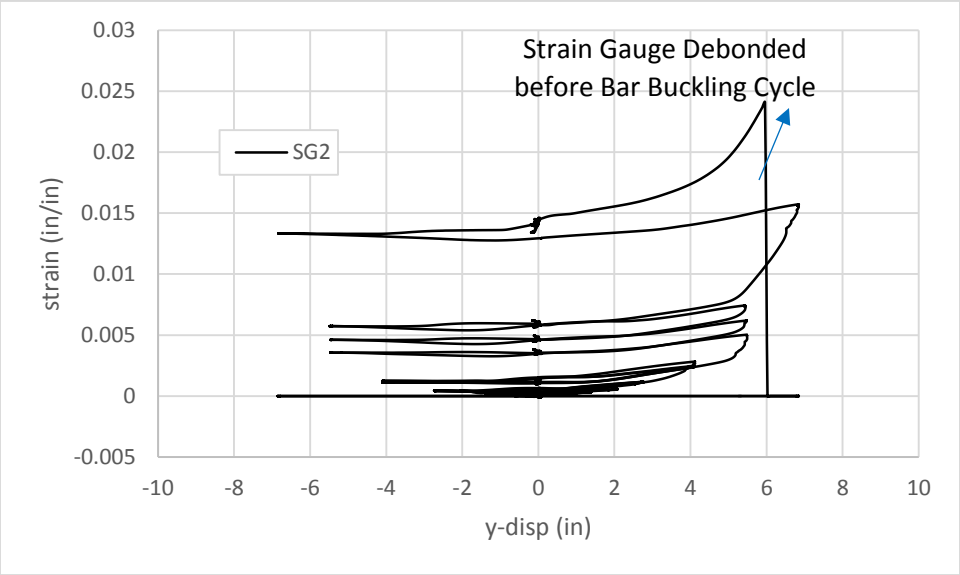

Figure 8-58. Test 5: North Spiral Strain Gauge Hysteresis for the Second Layer above the Footing

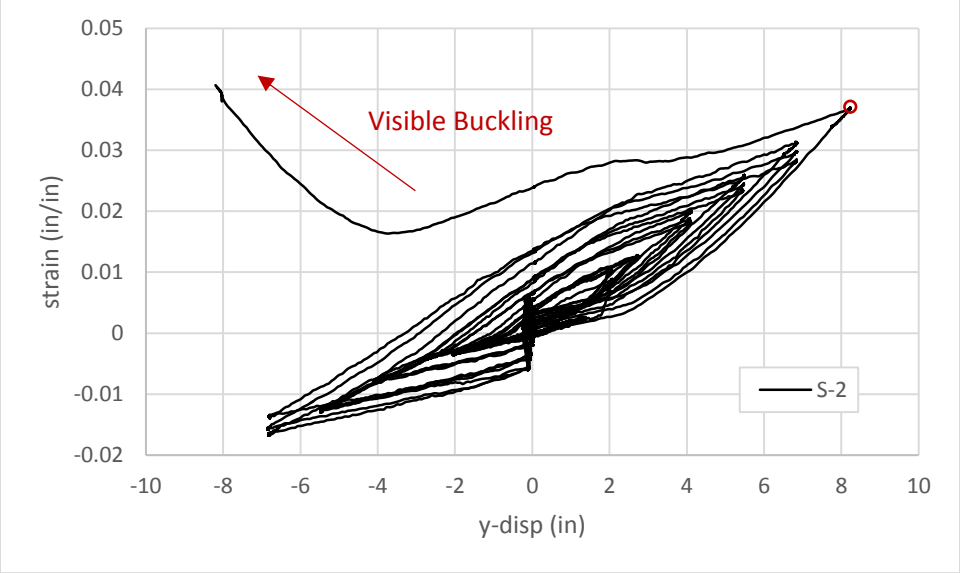

Figure 8-59. Test 5: Strain Hysteresis over the South Buckled Bar (Gauge Length 2 Centered 3.27" above the Footing)

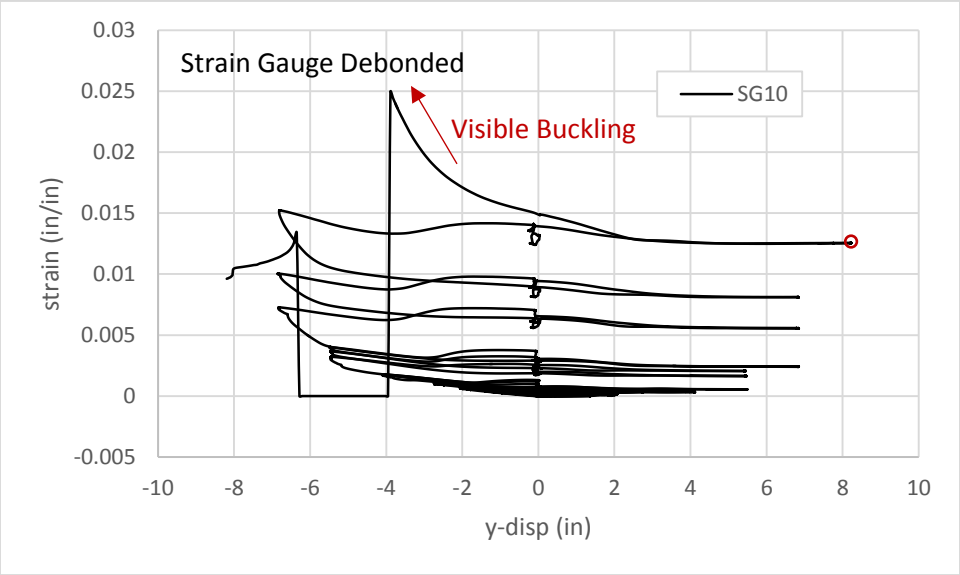

Figure 8-60. Test 5: South Spiral Strain Gauge Hysteresis for the Second Layer above the Footing

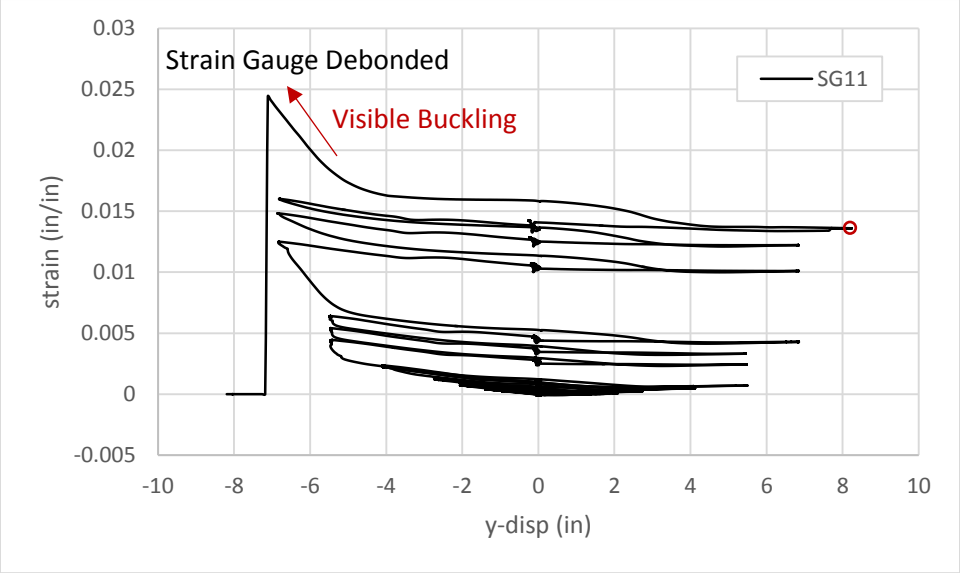

Figure 8-61. Test 5: South Spiral Strain Gauge Hysteresis for the Third Layer above the Footing

East and West Bar Strains

Vertical strain profiles for East and West reinforcement during x-direction cycles are shown in Figure 8-62 and Figure 8-63. Strains in the lowest four spiral layers during compressive x-direction cycles on the East and West sides of the specimen appear in Figure 8-64 and Figure 8-65. The relationship between strain and displacement for either peak tensile or peak compressive gauge lengths appear in Figure 8-66 through Figure 8-69. These figures contain monotonic moment curvature predictions for respective plastic hinge methods. PCK (2007) Lp refers to the (Priestley, Calvi and Kowalsky 2007) plastic hinge method, GN15 Tension/Compression Lpr refers to the (Goodnight, Kowalsky and Nau 2015a) unidirectional modified plastic hinge method, TX Adjusted Lpr and Lsp refer to using the measured extent of plasticity and average equivalent strain penetration length from this specific test, and New Equations refers to a new bidirectional plastic hinge method which was created based on this study. Details of the new plastic hinge method appear in a later chapter of this report.

The spiral strain gauge hysteresis for the first and second layers above the footing on the East side of the specimen appear in Figure 8-71 and Figure 8-72. The first spiral layer went off scale during $\mu_{\Delta 5}^{+2x} = 6.84$" as the East extreme fiber bar visibly buckled, see Figure 8-36. The strain gauge over the second spiral layer debonded during $\mu_{\Delta 5}^{+1x} = 6.84$", even though the East bars remained visibly straight. The visual observation of bar buckling was confirmed upon inspection of the East longitudinal bar strain hysteresis in Figure 8-70.

The spiral strain gauge hysteresis for the first and second layers above the footing on the West side of the specimen appear in Figure 8-74 and Figure 8-75. Both spiral layers went off scale during $\mu_{\Delta 5}^{-3x} = -6.83$" as the West extreme fiber bar buckled, see Figure 8-38. The visual observation of bar buckling was confirmed upon inspection of the West longitudinal bar strain hysteresis in Figure 8-73.

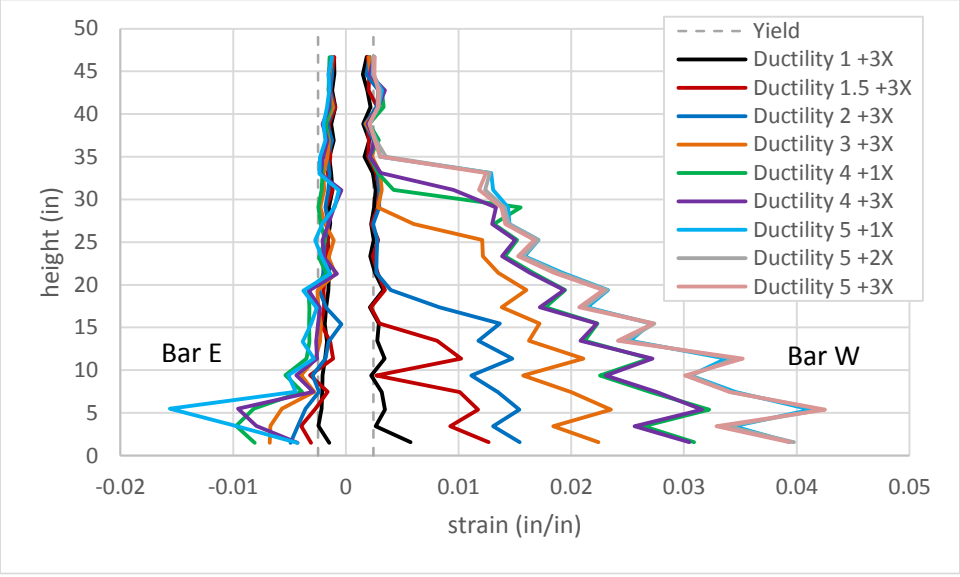

Figure 8-62. Test 5: Vertical Strain Profiles for Loading in the +X-direction

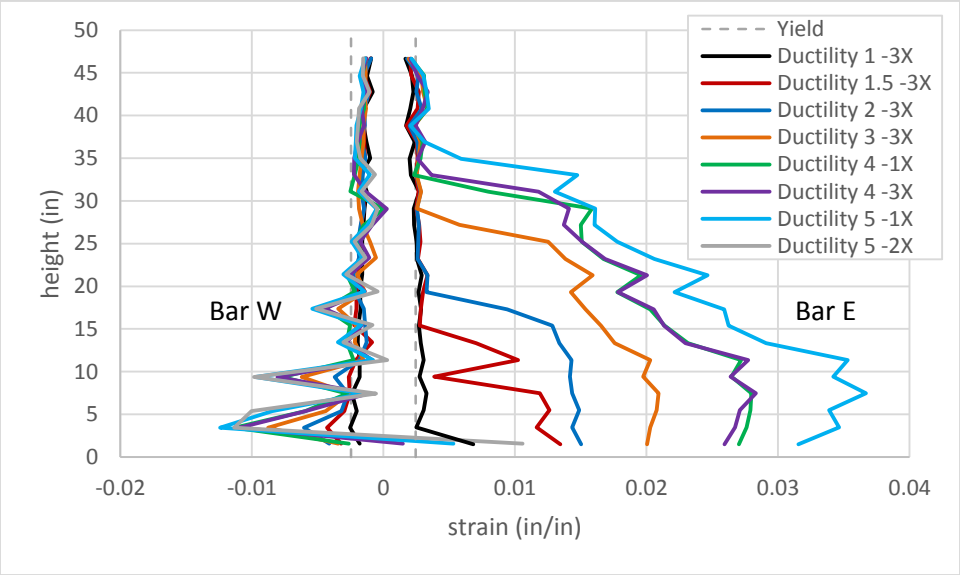

Figure 8-63. Test 5: Vertical Strain Profiles for Loading in the -X-direction

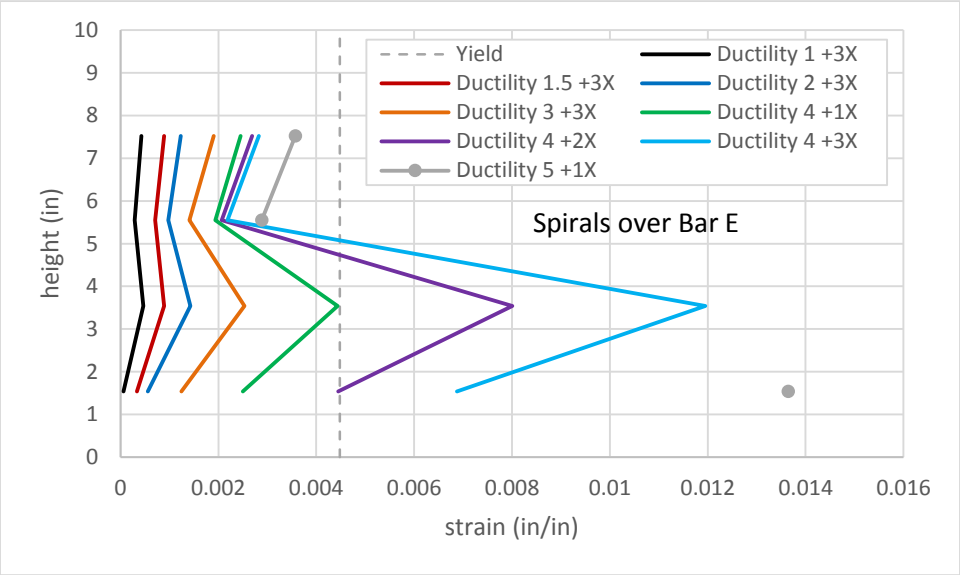

Figure 8-64. Test 5: Spiral Strains Measured Over the East Extreme Fiber Bar during +X Cycles

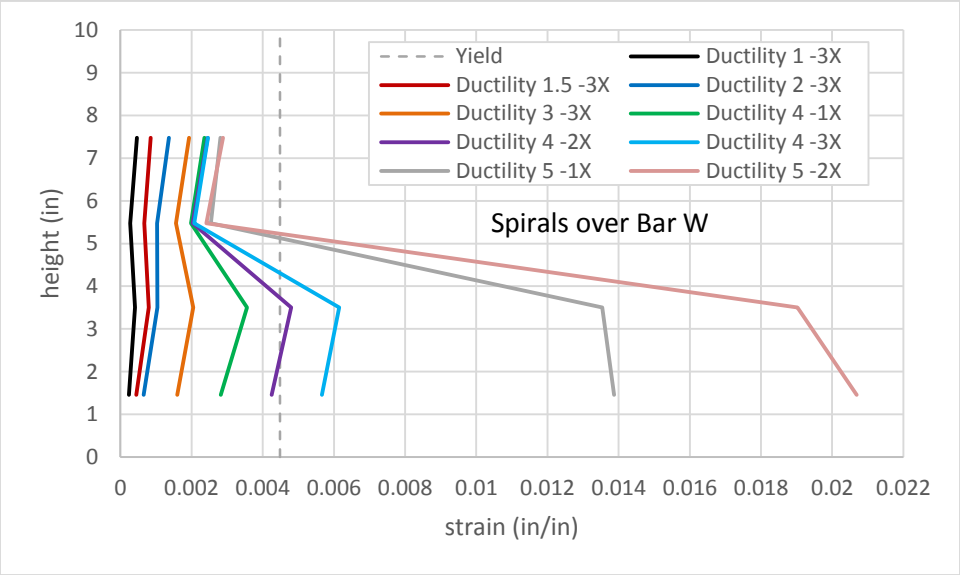

Figure 8-65. Test 5: Spiral Strains Measured Over the West Extreme Fiber Bar during -X Cycles

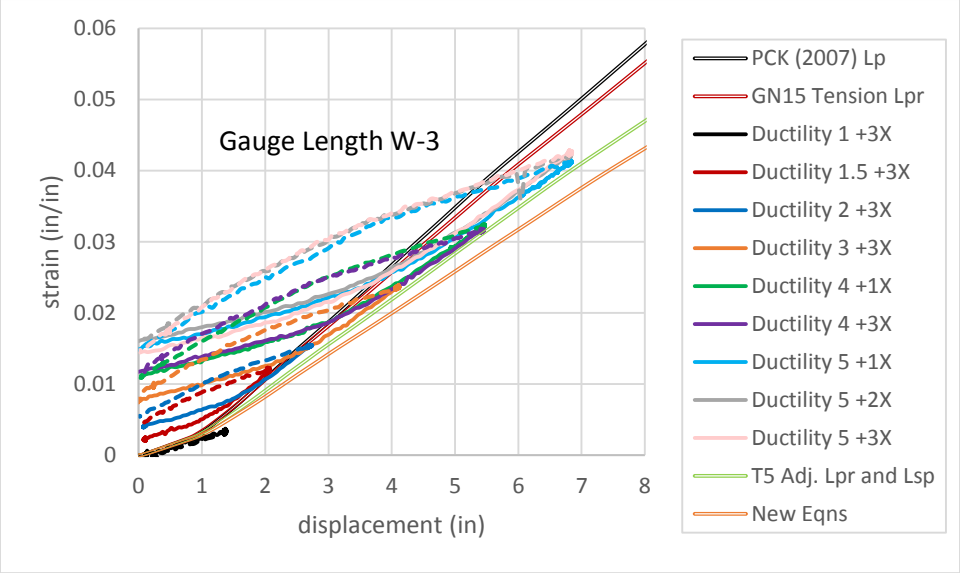

Figure 8-66. Test 5: Tension Strain-Disp. for Bar W (Gauge Length 3 Centered 5.39" above the Footing)

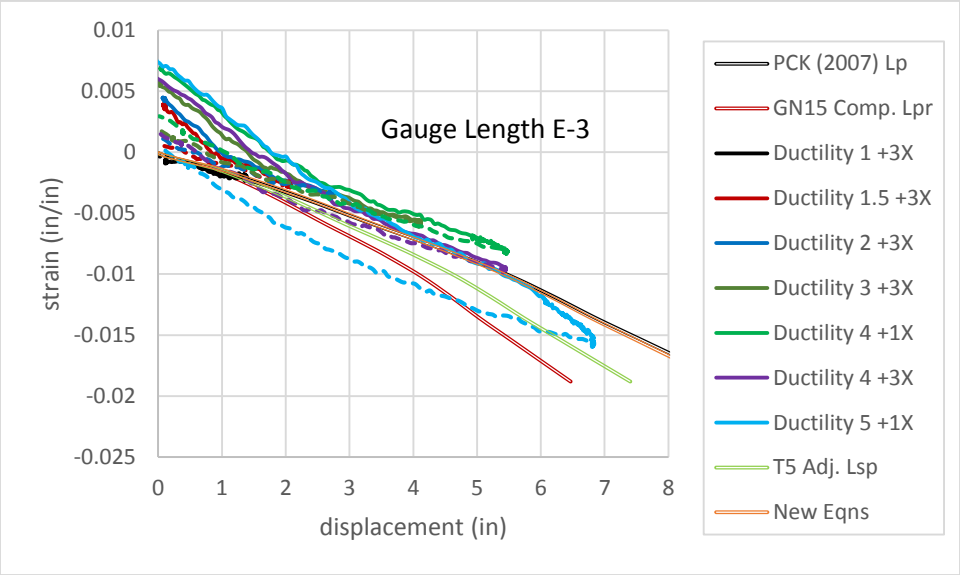

Figure 8-67. Test 5: Compression Strain-Disp. for Bar E (Gauge Length 3 Centered 5.39" above the Footing)

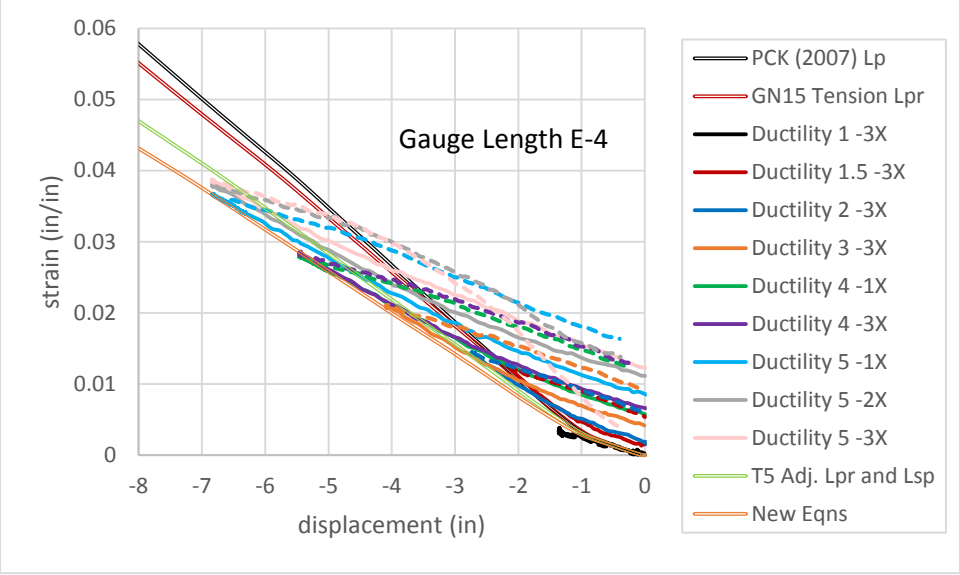

Figure 8-68. Test 5: Tension Strain-Disp. for Bar E (Gauge Length 4 Centered 7.46" above the Footing)

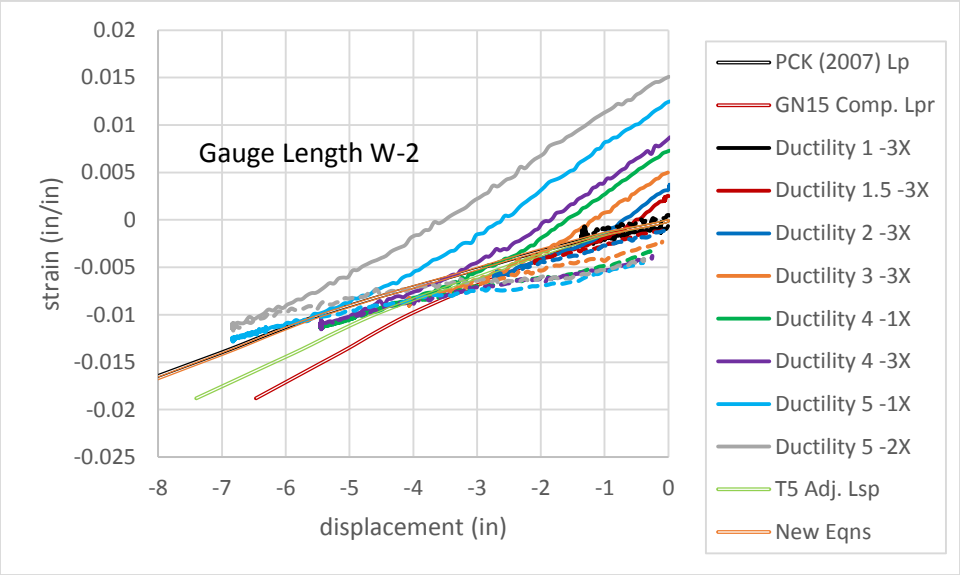

Figure 8-69. Test 5: Tension Strain-Disp. for Bar W (Gauge Length 2 Centered 3.42" above the Footing)

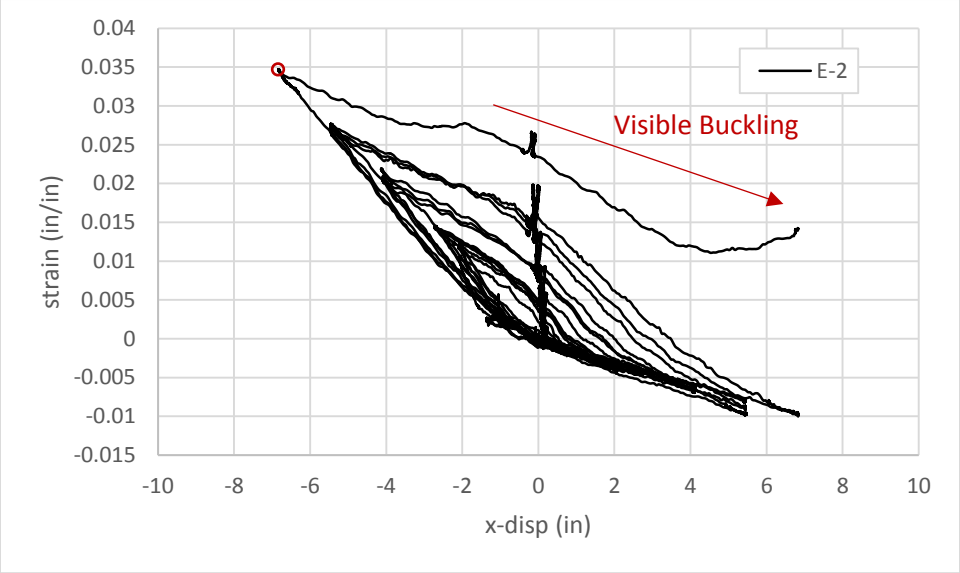

Figure 8-70. Test 5: Strain Hysteresis over the East Buckled Bar (Gauge Length 2 Centered 3.46" above the Footing)

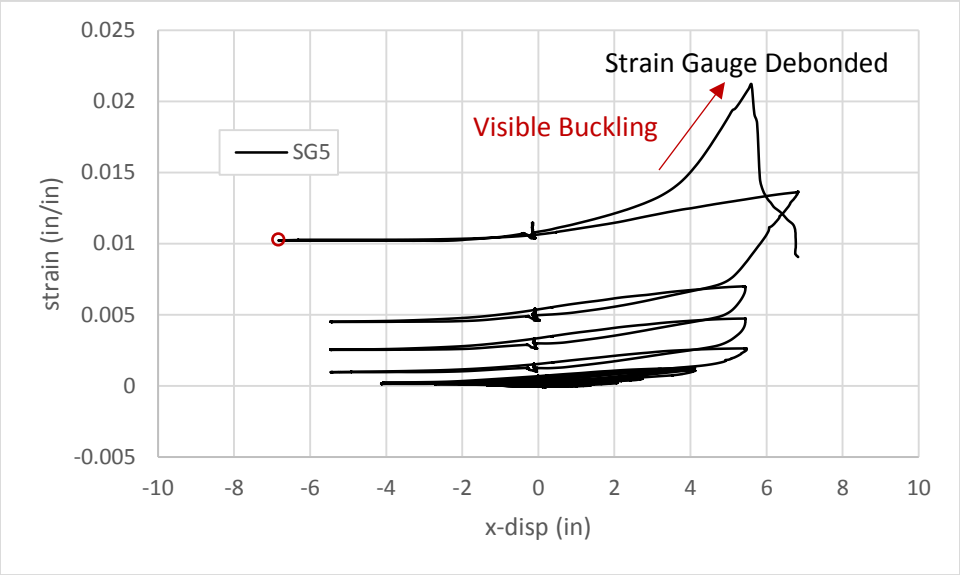

Figure 8-71. Test 5: East Spiral Strain Gauge Hysteresis for the First Layer above the Footing

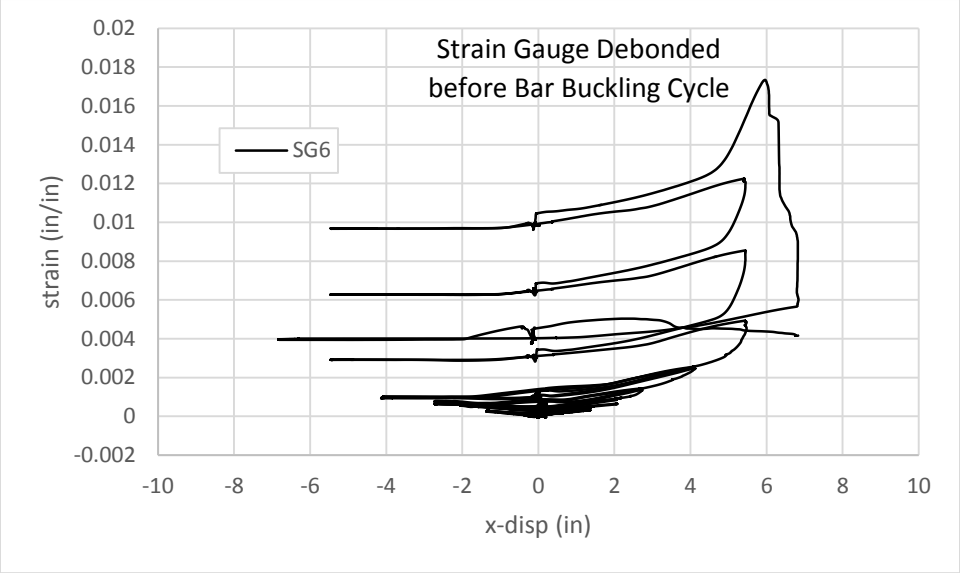

Figure 8-72. Test 5: East Spiral Strain Gauge Hysteresis for the Second Layer above the Footing

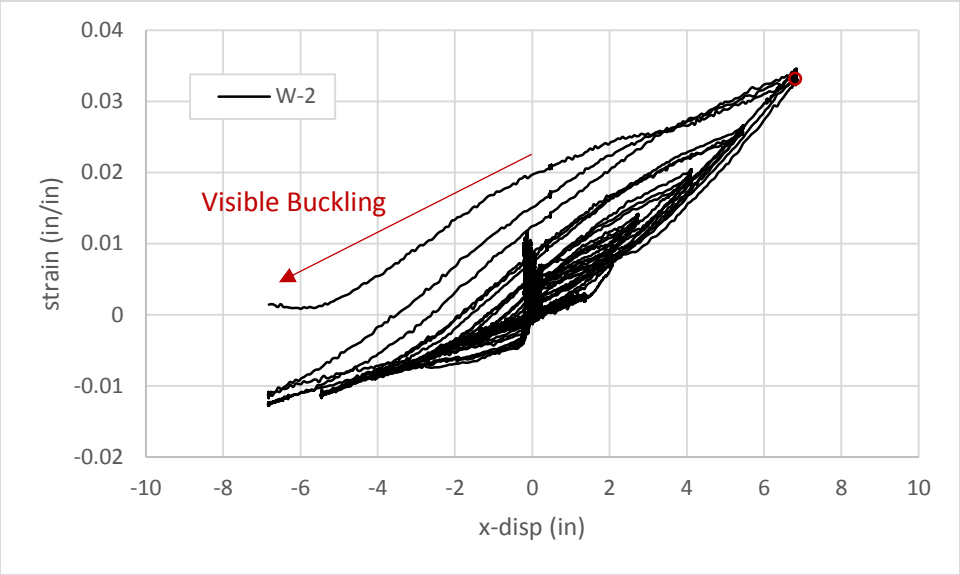

Figure 8-73. Test 5: Strain Hysteresis over the West Buckled Bar (Gauge Length 2 Centered 3.42" above the Footing)

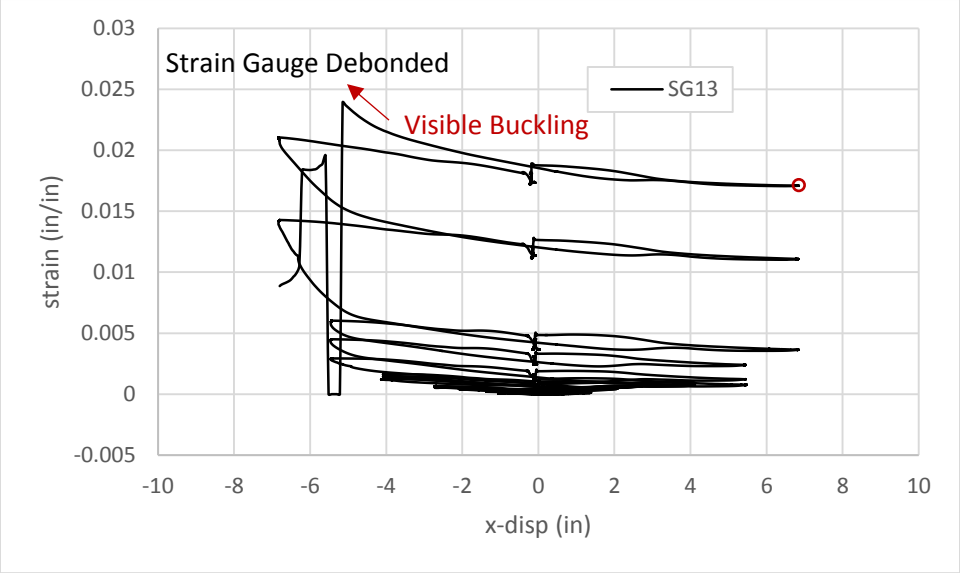

Figure 8-74. Test 5: West Spiral Strain Gauge Hysteresis for the First Layer above the Footing

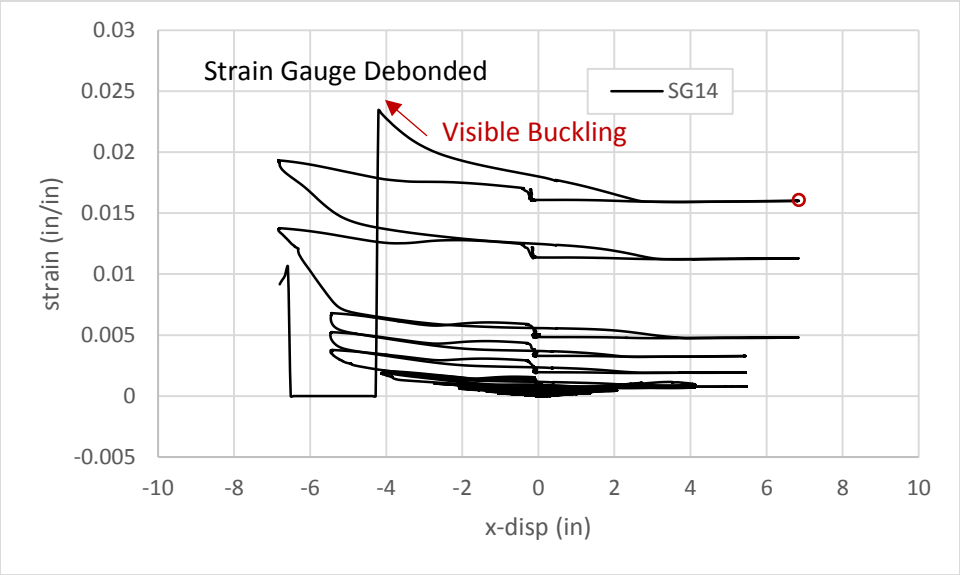

Figure 8-75. Test 5: West Spiral Strain Gauge Hysteresis for the Second Layer above the Footing

Test 5 - Curvature and Strain Penetration Data

Curvature and stain penetration data for Test 5 is presented in the following section. The methods in which this data was generated are outlined in the summary for Test 1. Sample cross section curvature profiles are shown in Figure 8-76 and Figure 8-77. Vertical curvature profiles for respective loading directions appear in Figure 8-78 through Figure 8-82. Fixed-end rotations attributable to strain penetration of longitudinal reinforcement into the footing are shown in Figure 8-83 through Figure 8-85. Comparison of the measured displacements to those obtained via integration of the measured curvature profiles and extrapolation of the fixed-end rotation to the center of the applied lateral load are shown in Figure 8-86 and Figure 8-87.

The measured extent of plasticity is compared to design recommendations for the tensile triangular plastic hinge length in Figure 8-88. GN15 refers to the (Goodnight, Kowalsky and Nau 2015a) unidirectional tensile hinge length while New Equations refers to a new bidirectional plastic hinge method which was created based on this study. Details of the new plastic hinge method appear in a later chapter of this report. The measured equivalent strain penetration lengths are compared to design recommendations in Figure 8-89. GN15 refers to the (Goodnight, Kowalsky and Nau 2015a) unidirectional Lsp while PCK (2007) refers to the (Priestley, Calvi and Kowalsky 2007) definition of Lsp. Finally, the measured hysteretic response is compared to monotonic predictions in Figure 8-90 through Figure 8-93. The larger elastic displacements are not observed when sectional response is considered.

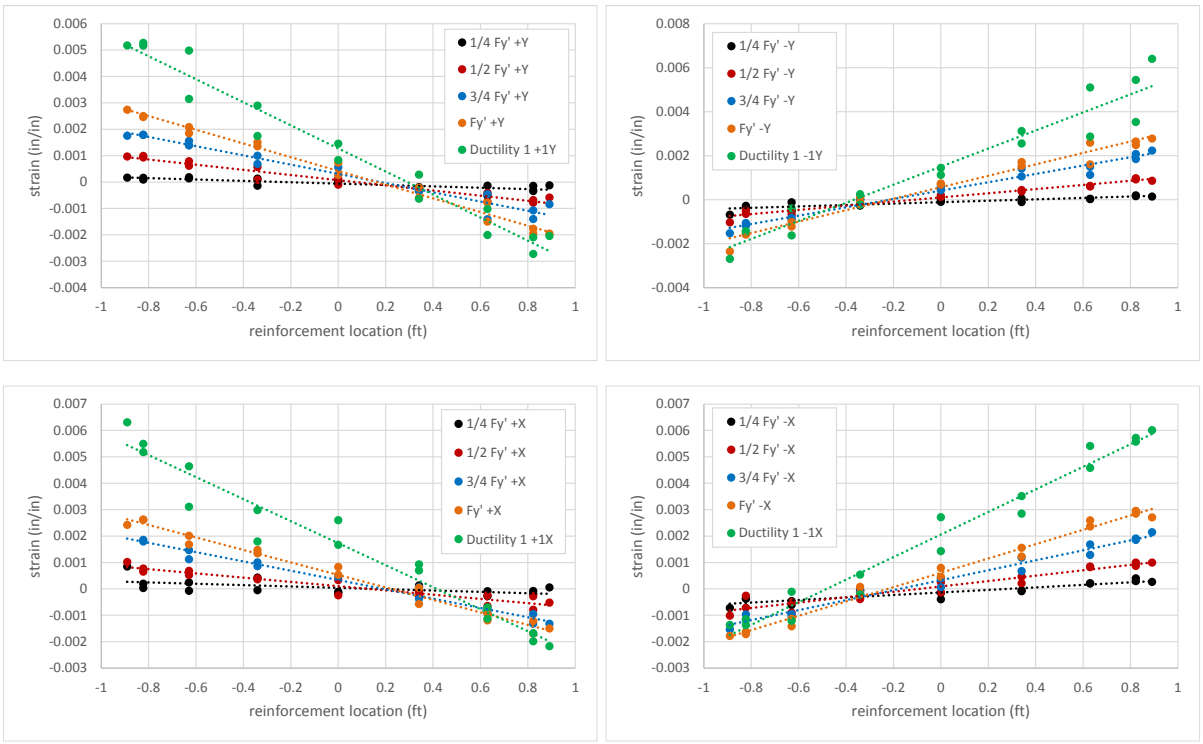

Figure 8-76. Test 5: Elastic Curvature Profiles for the First Instrumented Section above the Footing

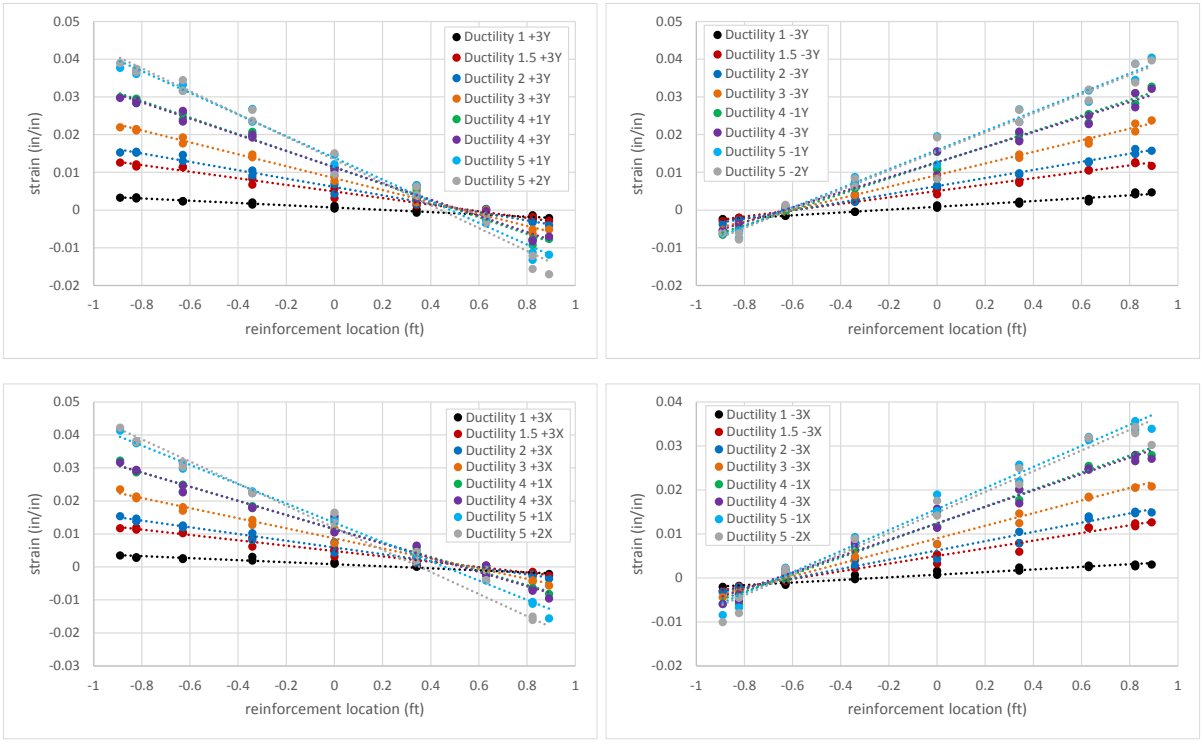

Figure 8-77. Test 5: Curvature Profiles for the Third Instrumented Section above the Footing

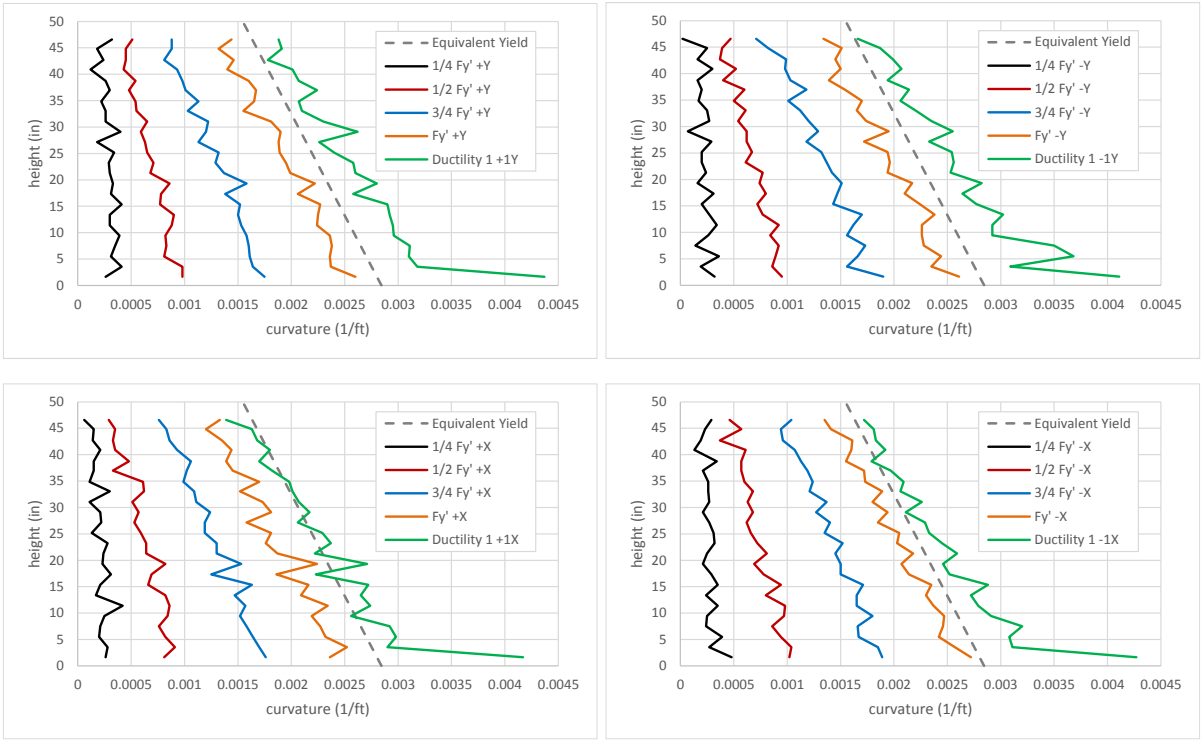

Figure 8-78. Test 5: Elastic Vertical Curvature Profiles

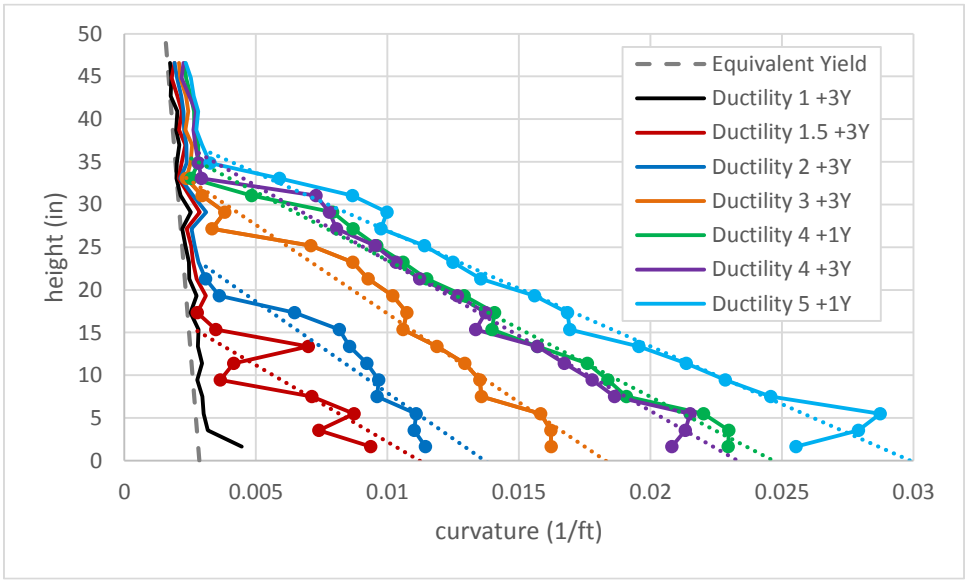

Figure 8-79. Test 5: Vertical Curvature Profiles for Loading in the +Y-direction

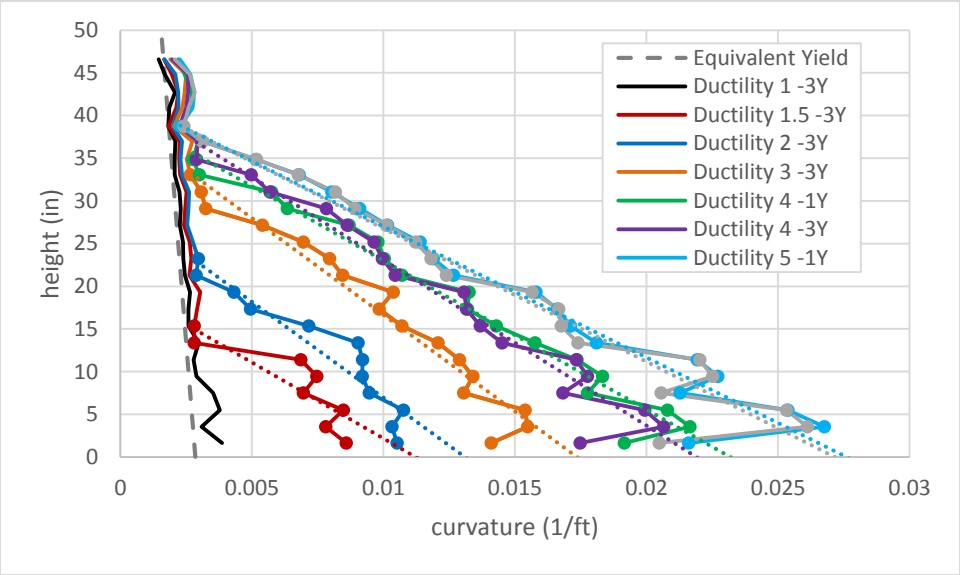

Figure 8-80. Test 5: Vertical Curvature Profiles for Loading in the -Y-direction

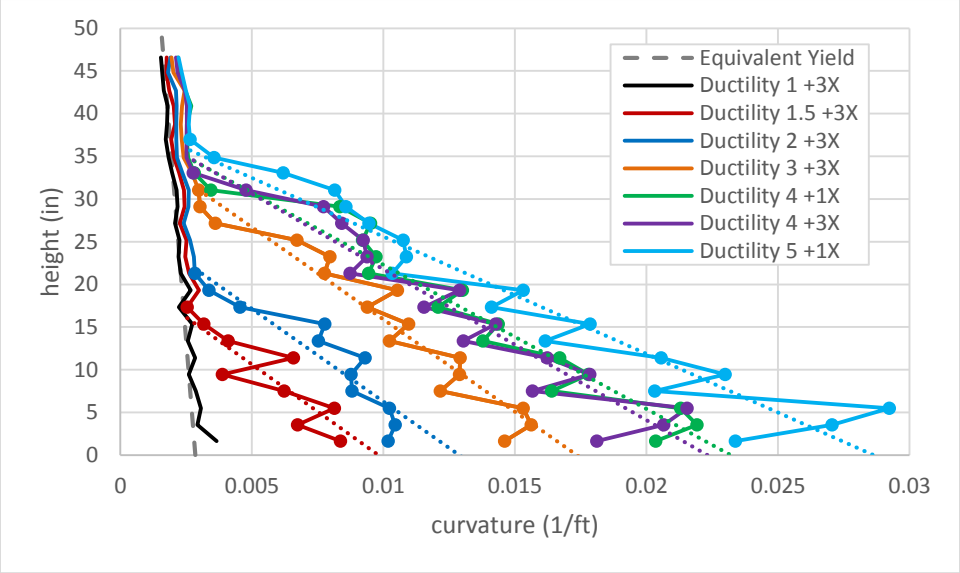

Figure 8-81. Test 5: Vertical Curvature Profiles for Loading in the +X-direction

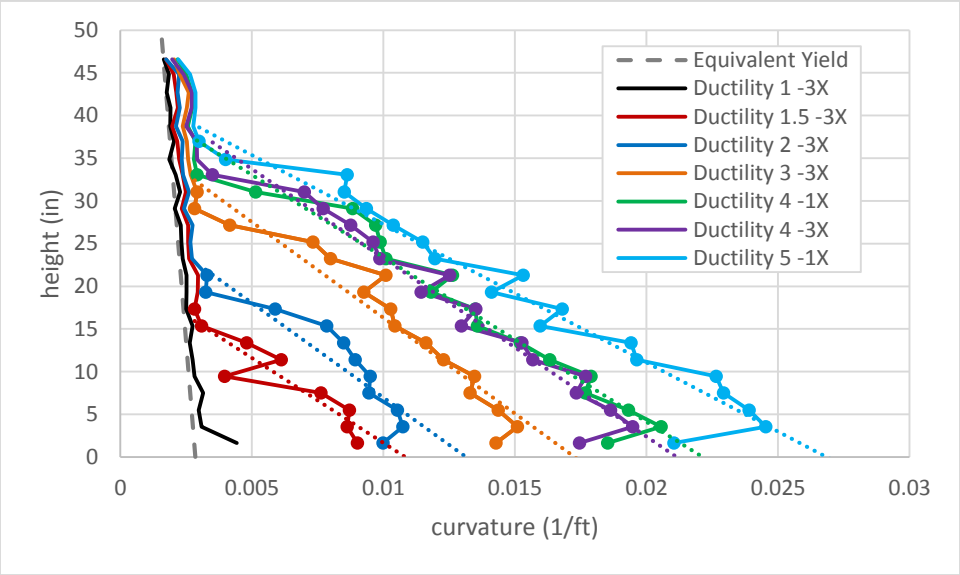

Figure 8-82. Test 5: Vertical Curvature Profiles for Loading in the -X-direction

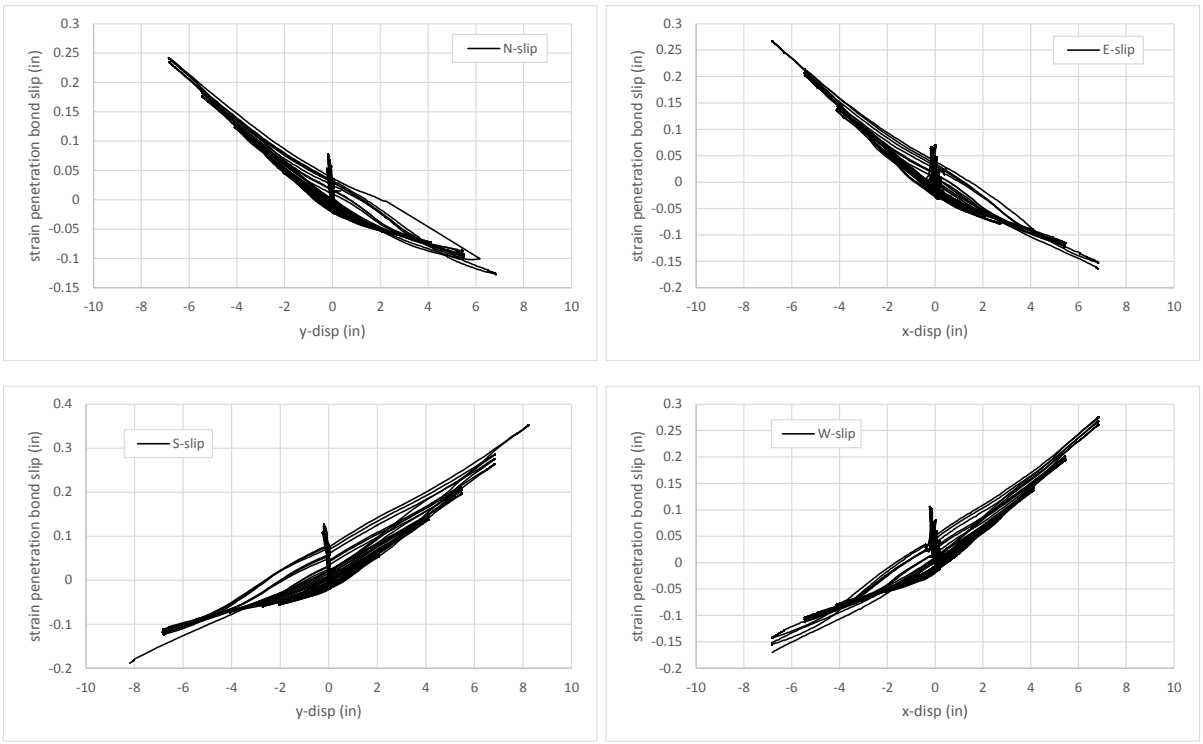

Figure 8-83. Test 5: Extreme Fiber Bar Strain Penetration Bond Slip Hysteresis

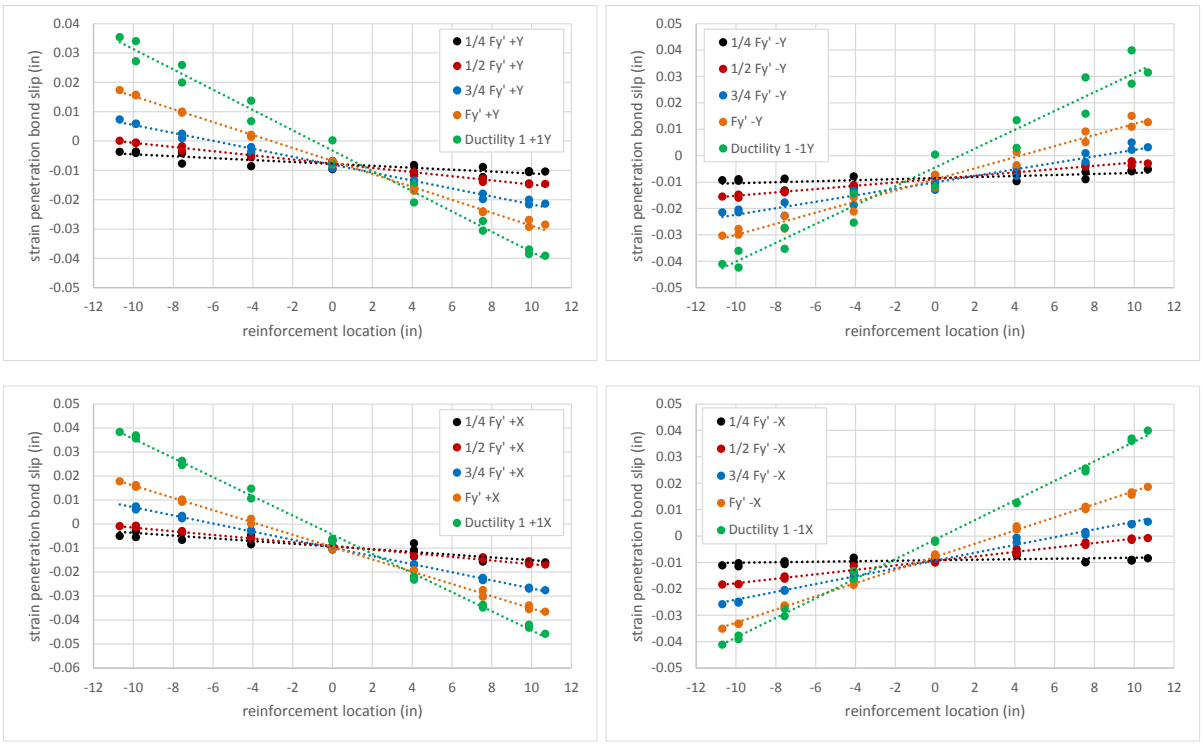

Figure 8-84. Test 5: Fixed End Rotations due to Strain Penetration during the Elastic Cycles

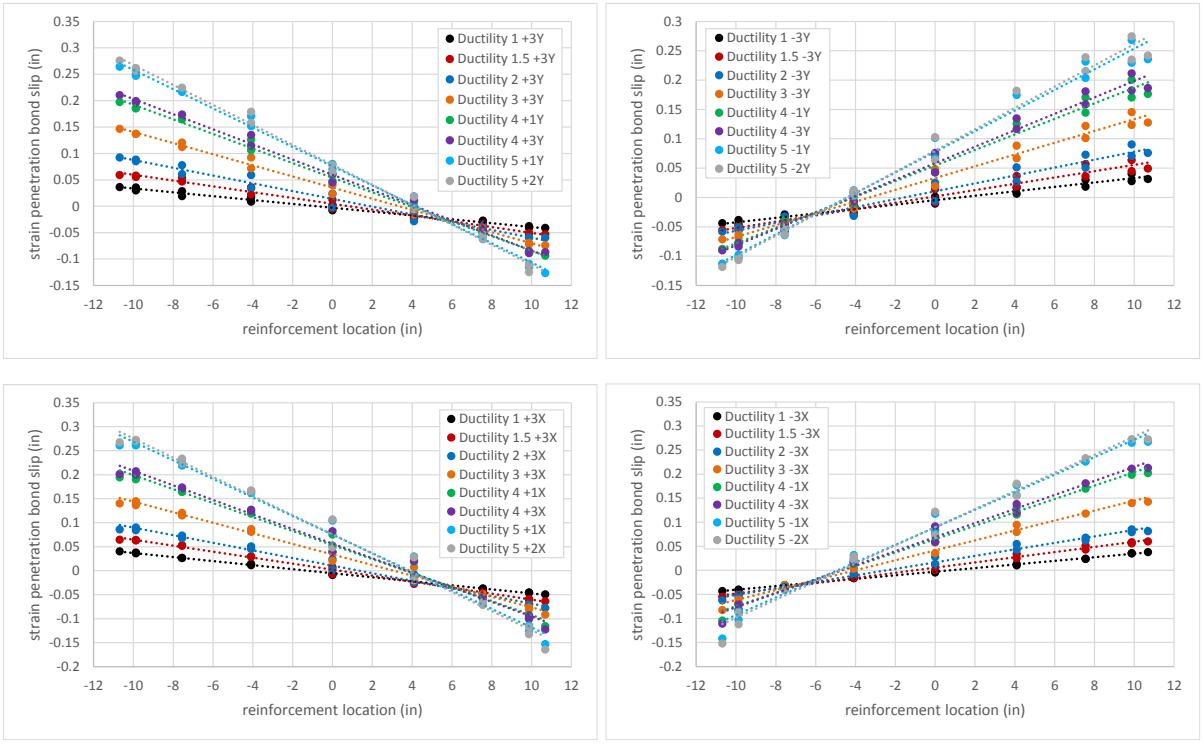

Figure 8-85. Test 5: Fixed End Rotations due to Strain Penetration

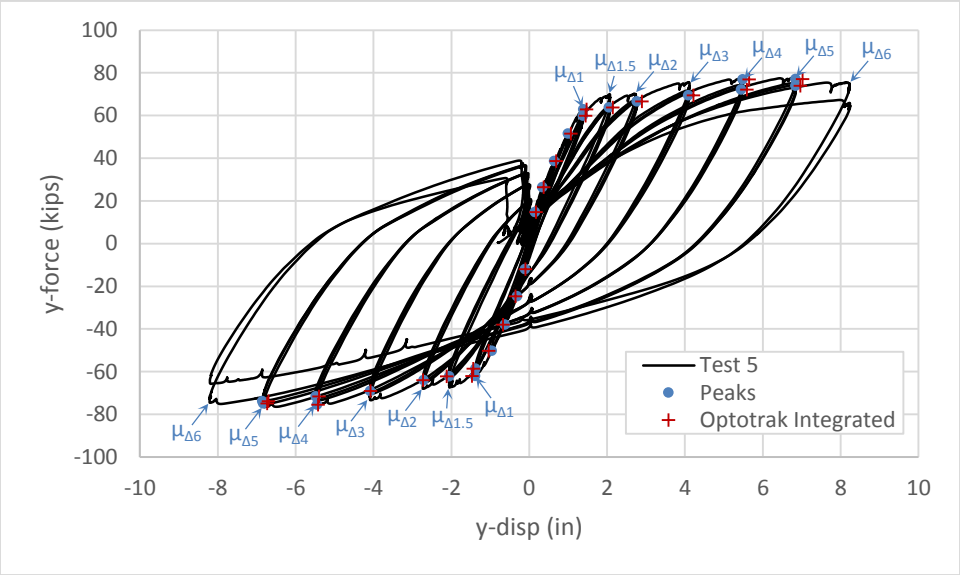

Figure 8-86. Test 5: Optotrak Integrated Flexural Disp. Compared to Measured String Pot. Disp.

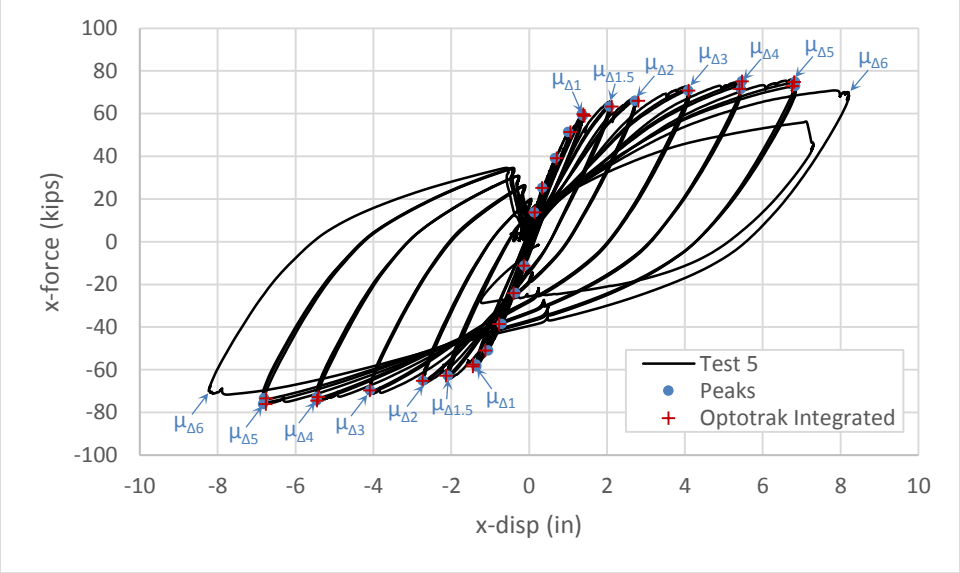

Figure 8-87. Test 5: Optotrak Integrated Flexural Disp. Compared to Measured String Pot. Disp.

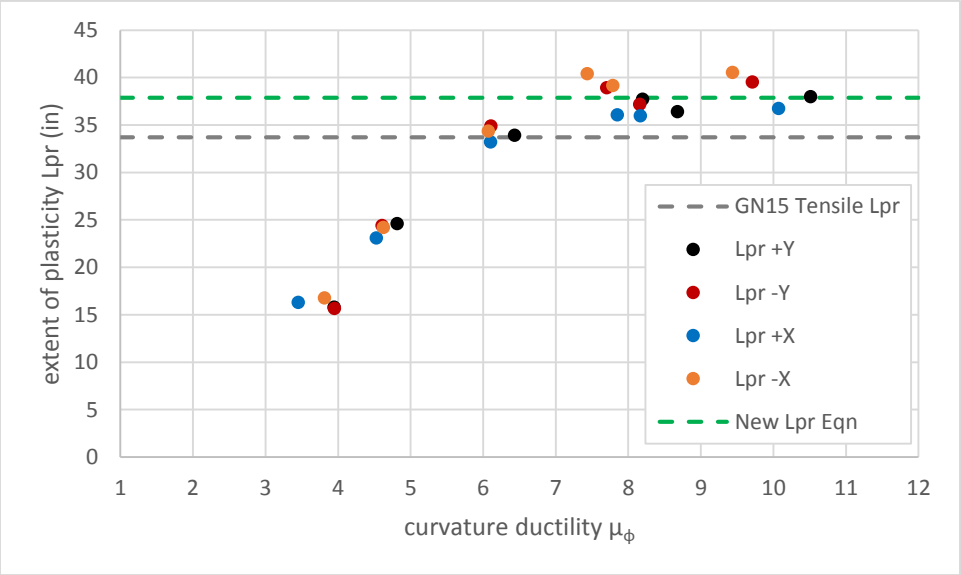

Figure 8-88. Test 5: Measured Extent of Plasticity Compared to Tensile Hinge Lengths

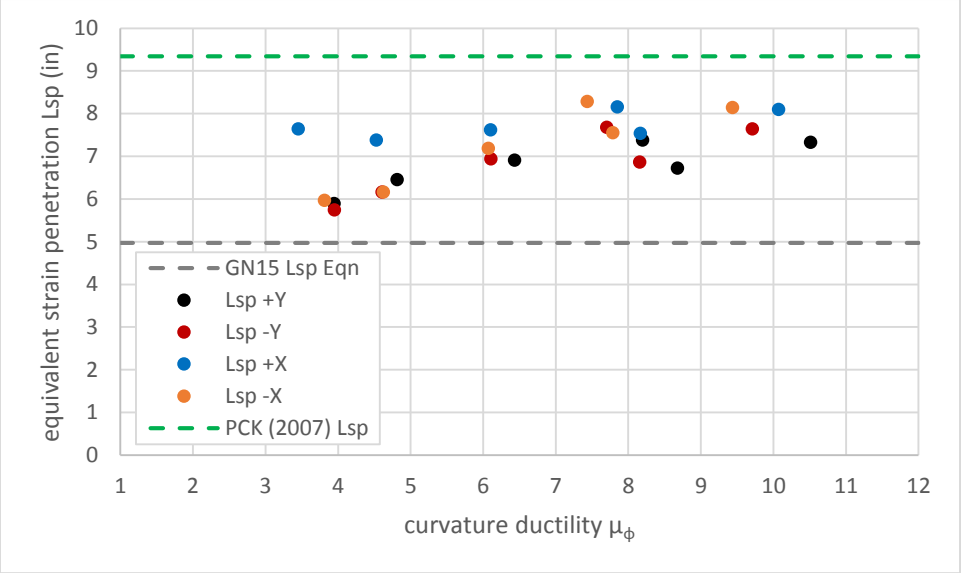

Figure 8-89. Test 5: Measured Equivalent Strain Penetration Lengths Compared to Design Expressions

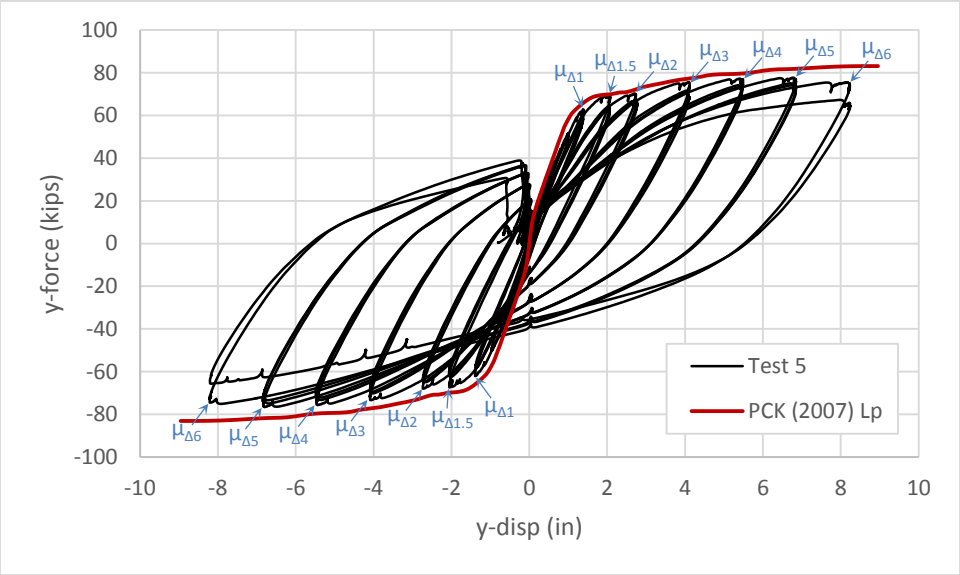

Figure 8-90. Test 5: Y-Direction Hysteretic Response Compared to PCK (2007) Hinge Length Monotonic Prediction

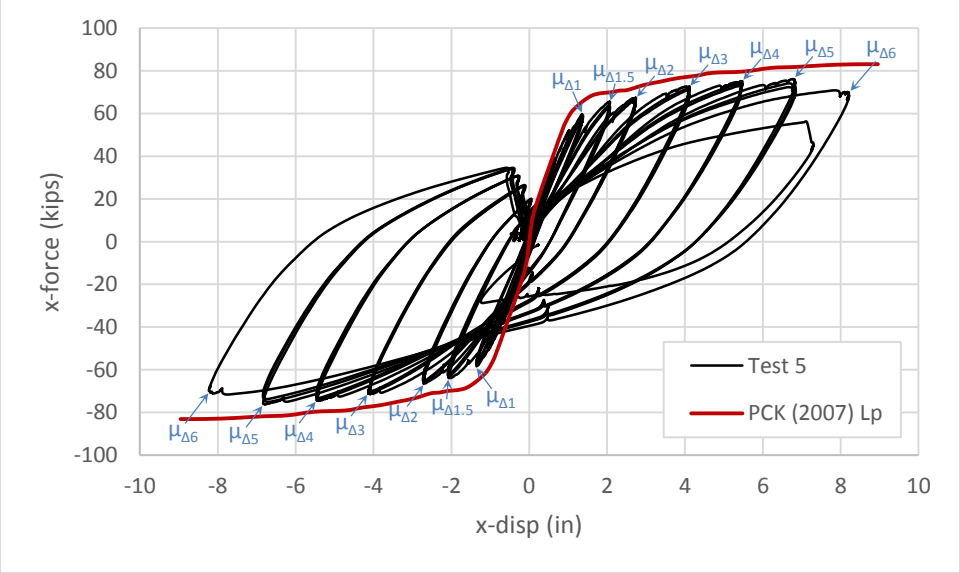

Figure 8-91. Test 5: X-Direction Hysteretic Response Compared to PCK (2007) Hinge Length Monotonic Prediction

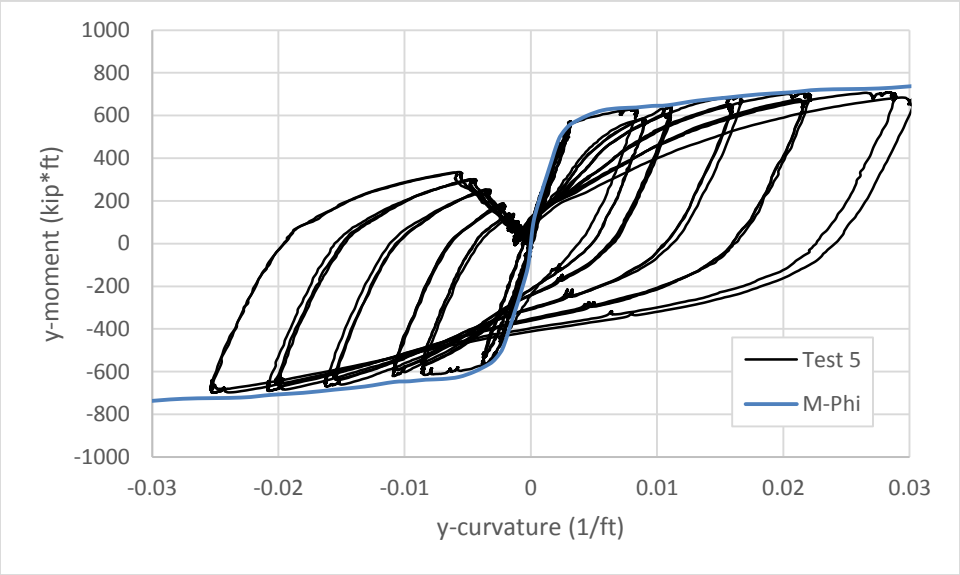

Figure 8-92. Test 5: Y-Direction Sectional Response Compared to Monotonic Moment Curvature Analysis

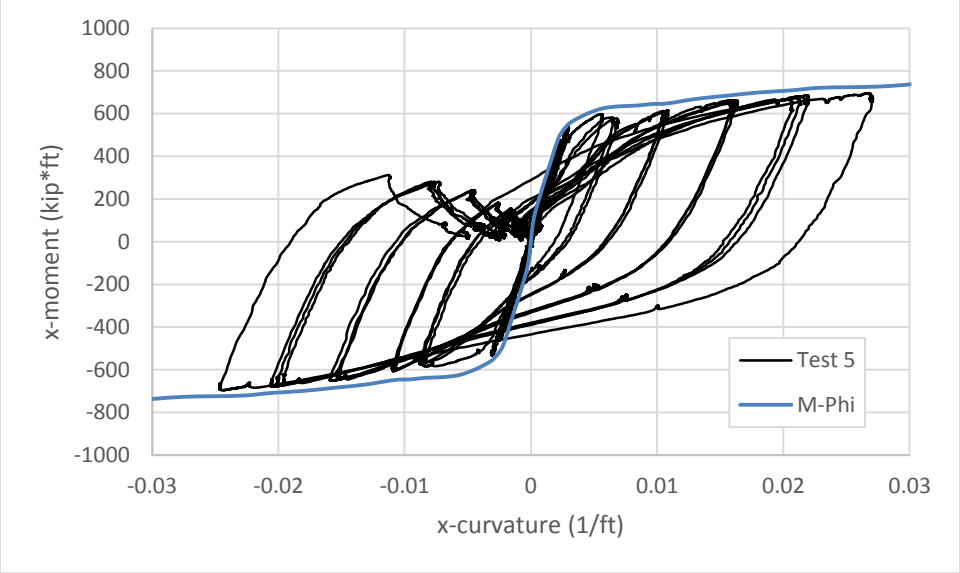

Figure 8-93. Test 5: X-Direction Sectional Response Compared to Monotonic Moment Curvature Analysis

Response Comparison for Tests 4 (Two-Cycle-Set) and 5 (Three-Cycle-Set)

Tests 4 and 5 were nominally identical with the exception that an additional cycle was ran at each displacement ductility level in Test 5. The increase from two to three cycles did not lead to an earlier propagation of damage. A hysteretic response comparison for Tests 4 and 5 appears in Figure 8-94 and Figure 8-95.

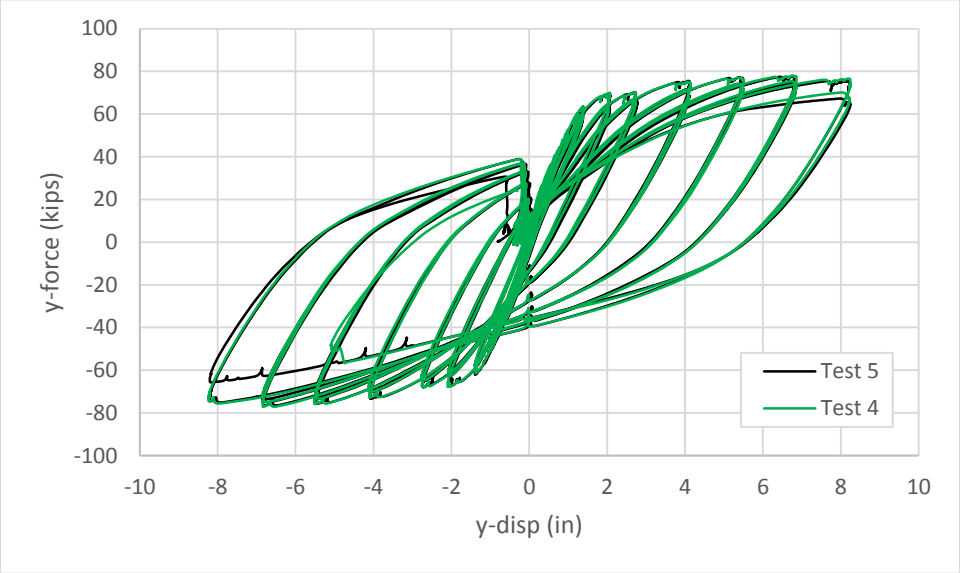

Figure 8-94. Y-Direction Hysteretic Comparison for Tests 4 (Two-Cycle-Set) and 5 (Three-Cycle-Set)

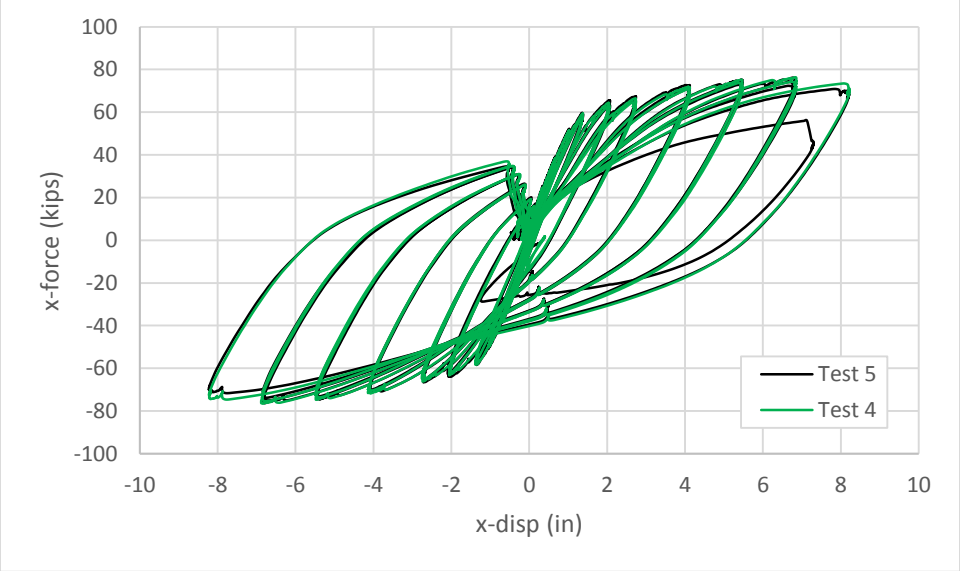

Figure 8-95. X-Direction Hysteretic Comparison for Tests 4 (Two-Cycle-Set) and 5 (Three-Cycle-Set)

Chapter 9 - Test 6 Summary Report

The sixth specimen had a 24" diameter circular cross-section reinforced with 16 #7 A706 longitudinal bars ($A_{st}/A_g = 2.1\%$) and a #3 spiral at 2" on center ($4A_{sp}/D's = 1\%$). This specimen was nominally identical to that of Tests 4 and 5, except an Asymmetric Two-Cycle-Set load history was employed where the ductility demands in the x-direction lagged behind those in the primary y-direction. Details of the test setup, instrumentation, and specimen design appear in Chapter 2. A material properties summary for the longitudinal and transverse steel from the first six experiments appears in Table 3-1 and Table 3-2. The column had a tested concrete strength of $f_c' = 7.81\ ksi$, while the footing had $f_c' = 9.67\ ksi$. The specimen had the same level of applied axial load ($191\ kips$). The sixth specimen was subjected to the Type-B Asymmetric Two-Cycle-Set Bidirectional Load History shown in Figure 9-1. This figure includes a diagram of the column cross-section with the selected bar and crack labeling scheme. Displacements in the +Y-direction placed the South reinforcement in tension. Cracks due to loading in the +Y-direction were labeled as red. The orientation of the X and Y axes are shown in Figure 2-52 with regards to the test setup. The +Y-axis is perpendicular to and points away from the strong wall. Values of interests, damage observations, and a predictions summary for the sixth test appear in Table 9-1, Table 9-2, and Table 9-3. A photo of the specimen instrumentation appears in Figure 9-2. The tighter transverse steel spacing necessitated reducing the number of target markers placed on bars NW, NE, SE, and SW. This was accompanied with a more dense instrumentation of the most highly strained bars in the four extreme fiber regions of the column.

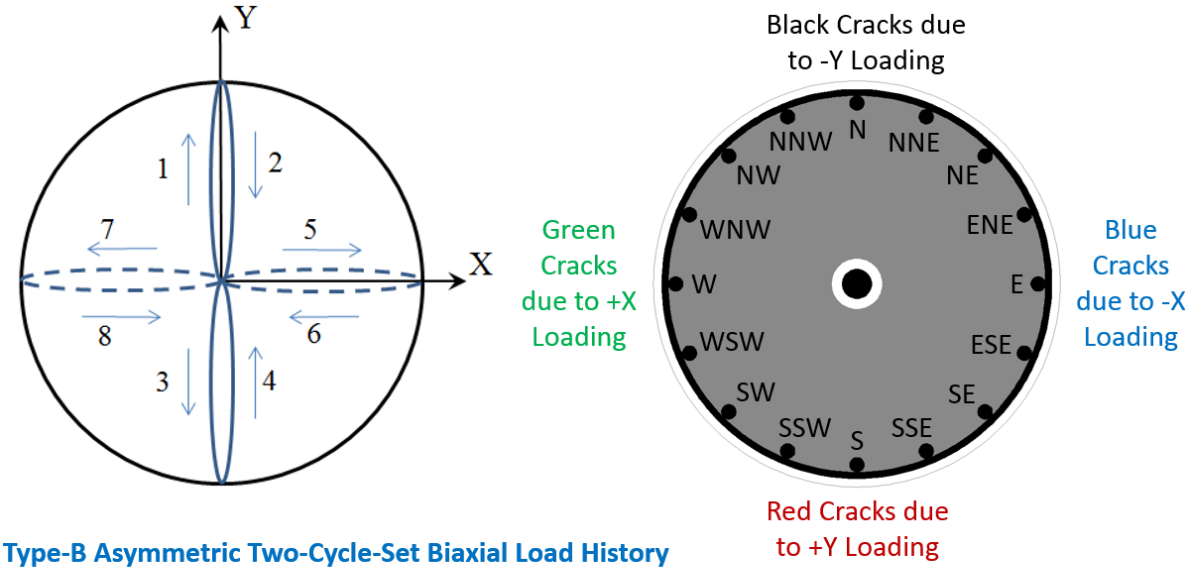

Type-B Asymmetric Two-Cycle-Set Biaxial Load History

- Begins with elastic cycles (1-8) in ¼ yield increments until F_y'
- The equivalent yield displacement is then computed as $\Delta_y = \Delta_y'(M_n/M_y')$
- Inelastic cycles (1-4) in the Y-direction followed by inelastic cycles (5-8) in the X-direction for each of the following displacement ductility levels $\mu_{\Delta n} = n \cdot \Delta_y$
  - $\mu_{\Delta 1}^{\pm Y}$ & $\mu_{\Delta 1}^{\pm X}$, $\mu_{\Delta 1.5}^{\pm Y}$ & $\mu_{\Delta 1}^{\pm X}$, $\mu_{\Delta 2}^{\pm Y}$ & $\mu_{\Delta 1}^{\pm X}$, $\mu_{\Delta 3}^{\pm Y}$ & $\mu_{\Delta 1.5}^{\pm X}$, $\mu_{\Delta 4}^{\pm Y}$ & $\mu_{\Delta 2}^{\pm X}$, etc. where $\mu_{\Delta}^{\pm X}$ lags by two displacement ductility levels until bar buckling is observed
- Cycle labeling system: $(\mu_{\Delta 4}^{-2Y} = -5.49\ in)$ Represents the second cycle of displacement ductility four in the -Y direction

Figure 9-1. Test 6: Load History and Labeling System for Reinforcement and Cracks

Table 9-1. Test 6: Values of Interest

Load History	Type-B Asymmetric Two-Cycle-Set
Length, Diameter, and Aspect Ratio	$L = 109.4375\ in, D = 24\ in,\ (L/D = 4.56)$
Longitudinal Steel Detailing	16 #7 $for\ \rho_l = A_{st}/A_g = 2.1\%$
Longitudinal Steel Properties	$f_y = 71.2\ ksi, f_u = 97.9\ ksi, \varepsilon_y = 0.00254$
Transverse Steel Detailing	#3 @ 2 $in\ for\ \rho_s = 4A_{sp}/D's = 1.0\%$
Transverse Steel Properties	$f_y = 67.6\ ksi, f_u = 105.6\ ksi, \varepsilon_y = 0.00448$
Column Concrete Strength	$f_c' = 7.81\ ksi$
Footing Concrete Strength	$f_c' = 9.67\ ksi$
Axial Load	$P = 191\ kips, \left(P/f_c'\ A_g = 5.9\%\right)$
Analytical First Yield Force	$F_y' = 51.72\ kips$
Experimental First Yield Disp.	$\Delta_y' = 1.03\ in$ Measured $\Delta_y' = 1.01\ in$ from Tests 4 and 5 used to find Δ_y
Analytical Nominal Moment Capacity	$M_n = 642.51\ kip \cdot ft$
Equivalent Yield Displacement	$\Delta_y = \Delta_y'\left(M_n/M_y'\right) = 1.40\ in$ with Measured Δ_y' $\Delta_y = 1.37\ in$ from Tests 4 and 5 defines load history
Maximum Lateral Force	$F_y = 79.92\ kips, F_x = 76.92\ kips$
Failure Mode	Loss in lateral strength due to buckling of 15 of 16 reinforcing bars, specimen saved without fracture as the first specimen which will be repaired.

Table 9-2. Test 6: Damage Observations

Damage Observations:		
Cycle Peak at which First Cracking was Observed Visually:		
North	$\Delta_y = -0.5F_y' = -0.39\ in$	$F_y = -25.36\ kips$
South	$\Delta_y = 0.5F_y' = 0.35\ in$	$F_y = 25.87\ kips$
East	$\Delta_x = -0.5F_y' = -0.32\ in$	$F_x = -25.23\ kips$
West	$\Delta_x = 0.5F_y' = 0.38\ in$	$F_x = 25.94\ kips$
Cycle Peak at which Cover Concrete Crushing was Observed Visually:		
North	$\mu_{\Delta 2}^{+1Y} = 2.73\ in$	$\varepsilon_c = -0.00727$
South	$\mu_{\Delta 2}^{-1Y} = -2.75\ in$	$\varepsilon_c = -0.00640$
East	$\mu_{\Delta 2}^{+2X} = 2.74\ in$	$\varepsilon_c = -0.00267$
West	$\mu_{\Delta 2}^{-1X} = -2.76\ in$	$\varepsilon_c = -0.00443$
Exact Displacement and Cycle Label for Initial Spiral Yielding in the Confinement Zone:		
North	$\Delta_y = 4.08\ in\ during\ \mu_{\Delta 3}^{+1Y}$	$\varepsilon_c = -0.02195$
South	$\Delta_y = -4.99\ in\ during\ \mu_{\Delta 4}^{-1Y}$	$\varepsilon_c = -0.01380$
East	$\Delta_x = 4.91\ in\ during\ \mu_{\Delta 4}^{+2X}$	$\varepsilon_c = -0.00509$
West	$\Delta_x = -5.34\ in\ during\ \mu_{\Delta 4}^{-2X}$	$\varepsilon_c = -0.00851$
Peak Tensile Displacement Prior to Visual Bar Buckling During Subsequent Reversal of Load:		
North	$\mu_{\Delta 5}^{-1Y} = -6.85\ in, Observed\ at\ \mu_{\Delta 5}^{+2Y} = 6.87\ in$	$\varepsilon_s = 0.03625$
South	$\mu_{\Delta 5}^{+2Y} = 6.87\ in, Observed\ at\ \mu_{\Delta 5}^{-2Y} = -6.84\ in$	$\varepsilon_s = 0.03668$
East	$\mu_{\Delta 5}^{-2X} = -6.84\ in, Observed\ at\ \mu_{\Delta 6}^{+1X} = 8.21\ in$	$\varepsilon_s = 0.03800$
West	$\mu_{\Delta 6}^{+1X} = 8.21\ in, Observed\ at\ \mu_{\Delta 6}^{-1X} = -8.21\ in$	$\varepsilon_s = 0.04369$

Table 9-3. Test 6: Damage Predictions

Damage Predictions with the New Bidirectional Plastic Hinge Model and New Strain Limits:		
Bar Buckling Predictions		
New Method	$\Delta_{bb}^{Lpr} = 7.79\ in$	$\varepsilon_s^{bb} = 0.04214$
Feng et al. (2015)	$\Delta_{bb}^{Lp} = 6.76\ in$	$\varepsilon_s^{bb} = 0.0485$
Cover Crushing Prediction		
New Method	$\Delta_{cc}^{Lpr} = 2.14\ in$	$\varepsilon_c^{cc} = -0.004$
Spiral Yielding Prediction		
New Method	$\Delta_{sy}^{Lpr} = 5.25\ in$	$\varepsilon_c^{sy} = -0.01192 * M, (M = 0.8)$
Original Ultimate Concrete Compression Strain		
Mander et al. (1988)	$\Delta_{cu}^{Lpr} = 7.45\ in$	$\varepsilon_{cu} = -0.0152$

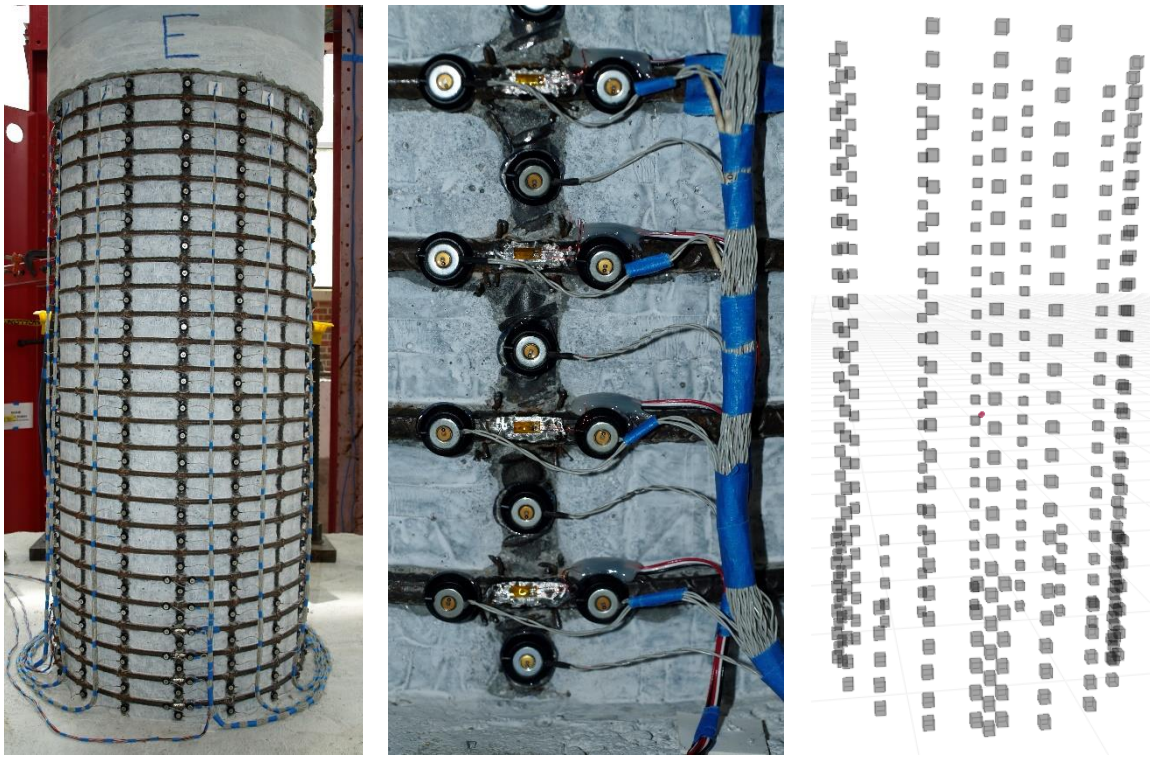

Figure 9-2. Test 6: Optotrak Target Marker and Strain Gauge Instrumentation on the East Side of the Specimen

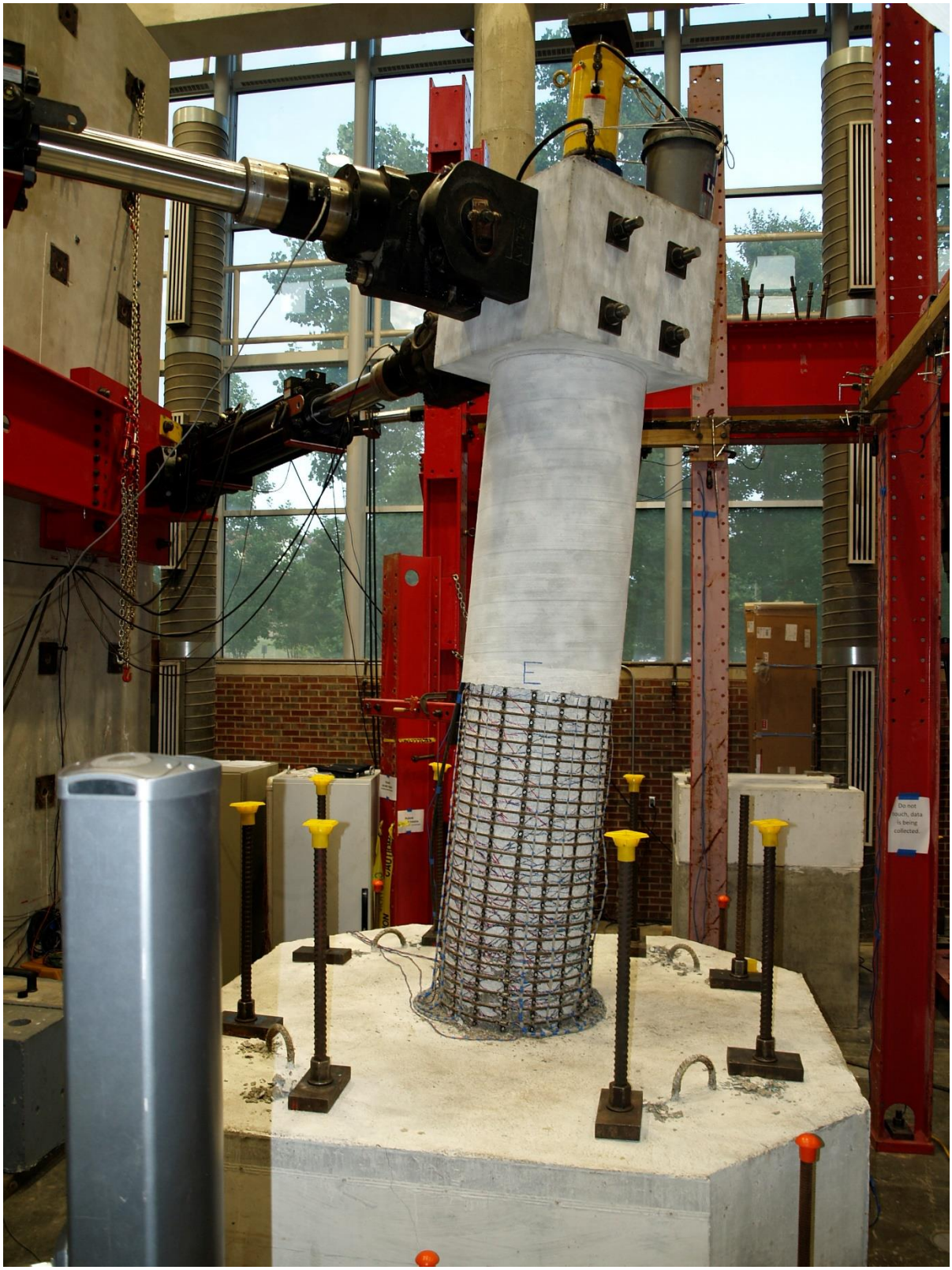

Figure 9-3. Test 6: Specimen Deformation at $\mu_{\Delta 6}^{+1y} = 8.22"$

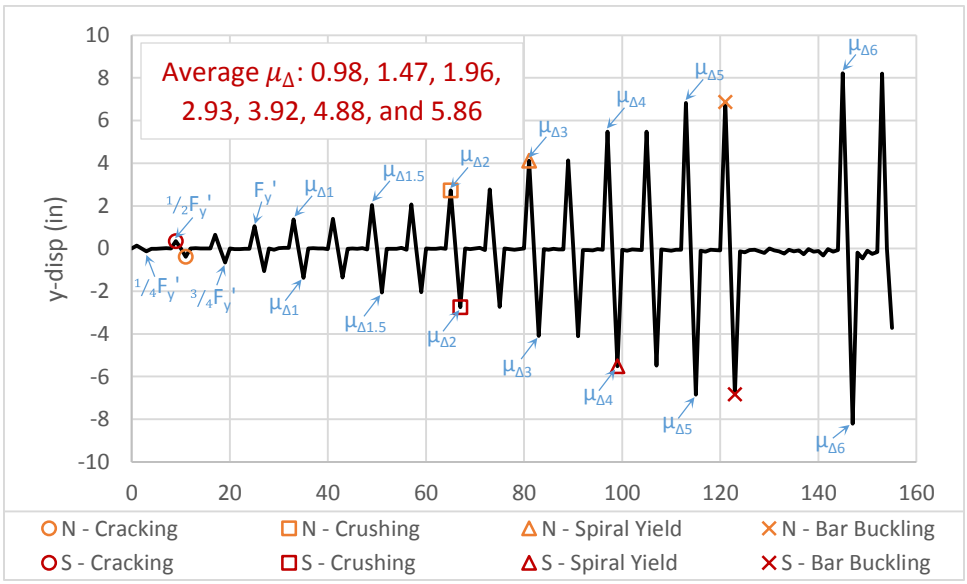

Figure 9-4. Test 6: Y-Displacement History

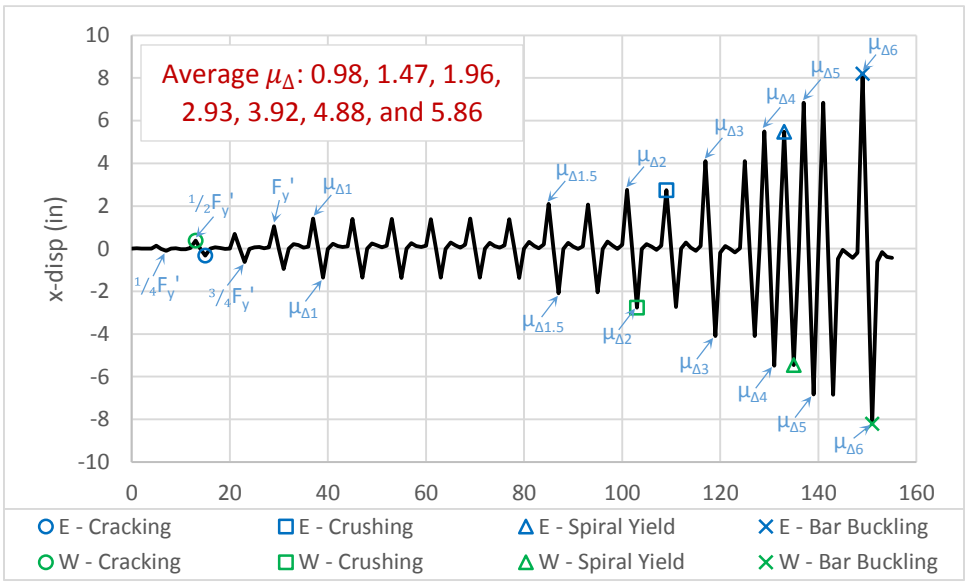

Figure 9-5. Test 6: X-Displacement History

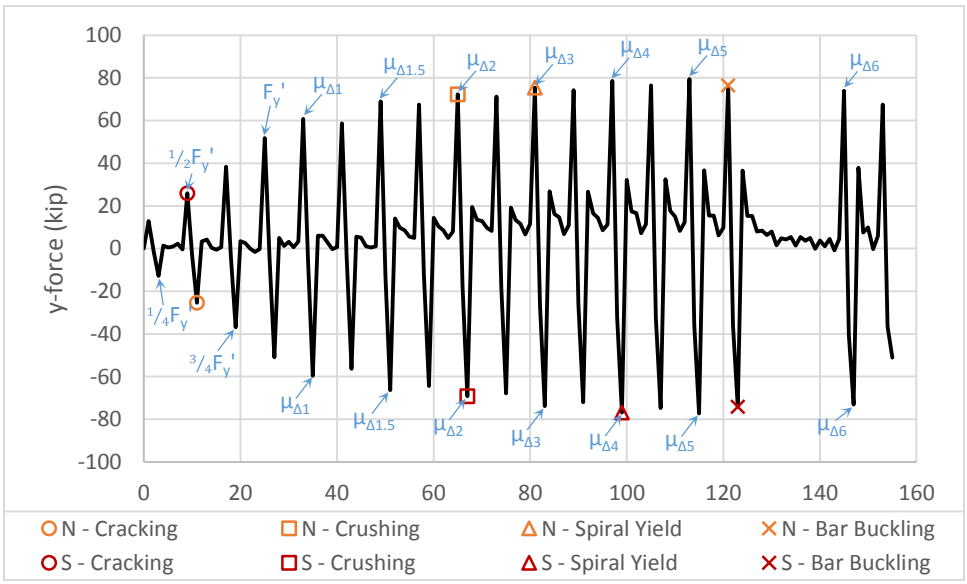

Figure 9-6. Test 6: Y-Force History

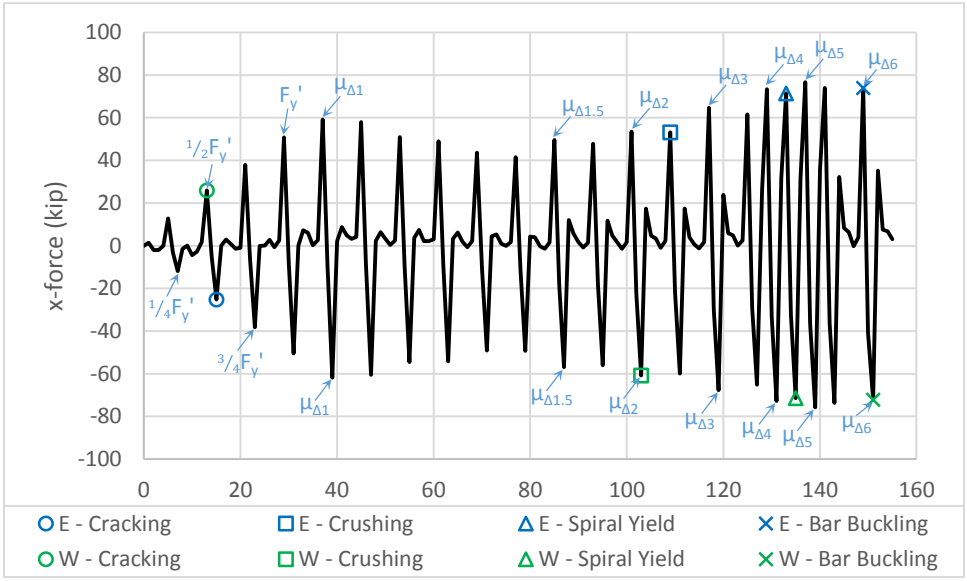

Figure 9-7. Test 6: X-Force History

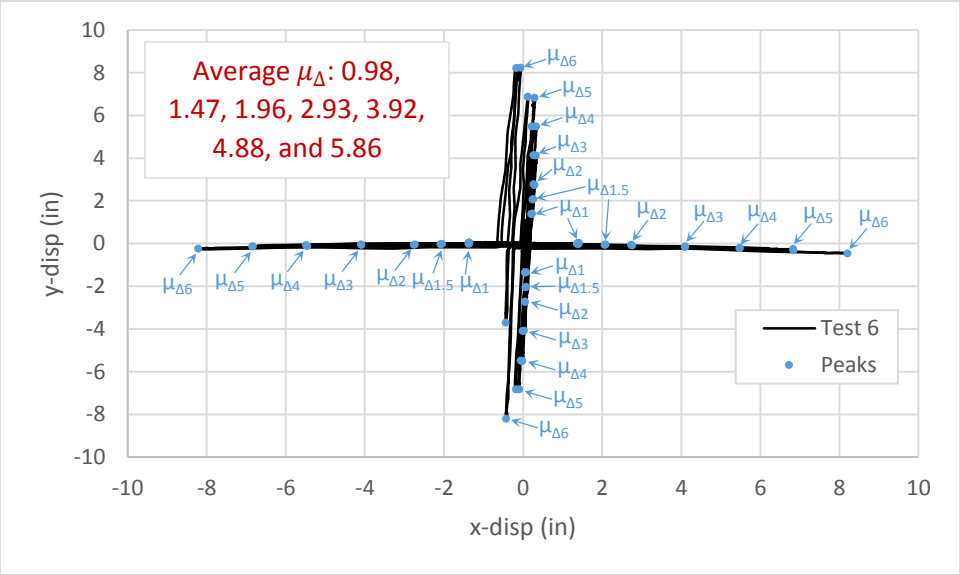

Figure 9-8. Test 6: Type-B Asymmetric Two-Cycle-Set Displacement History

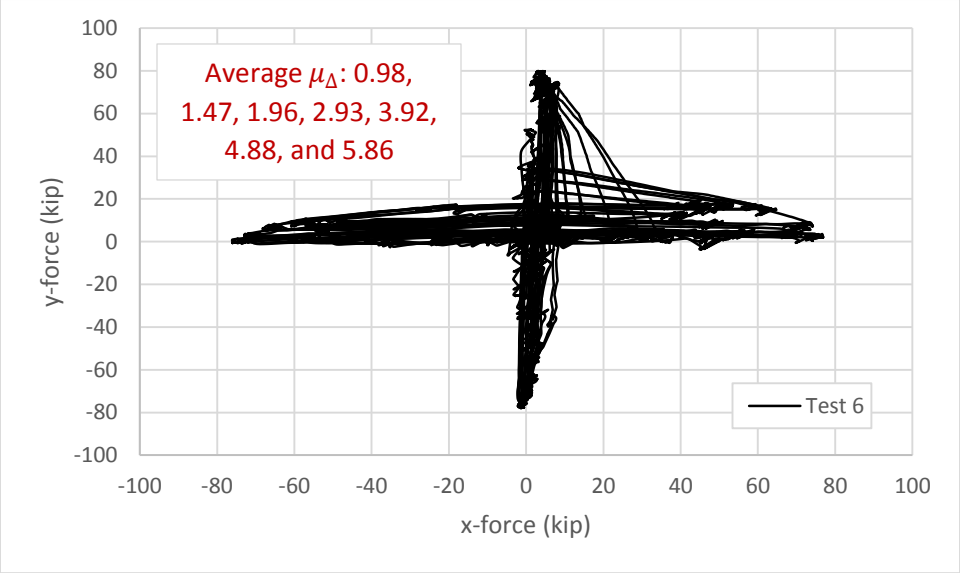

Figure 9-9. Test 6: Load Path

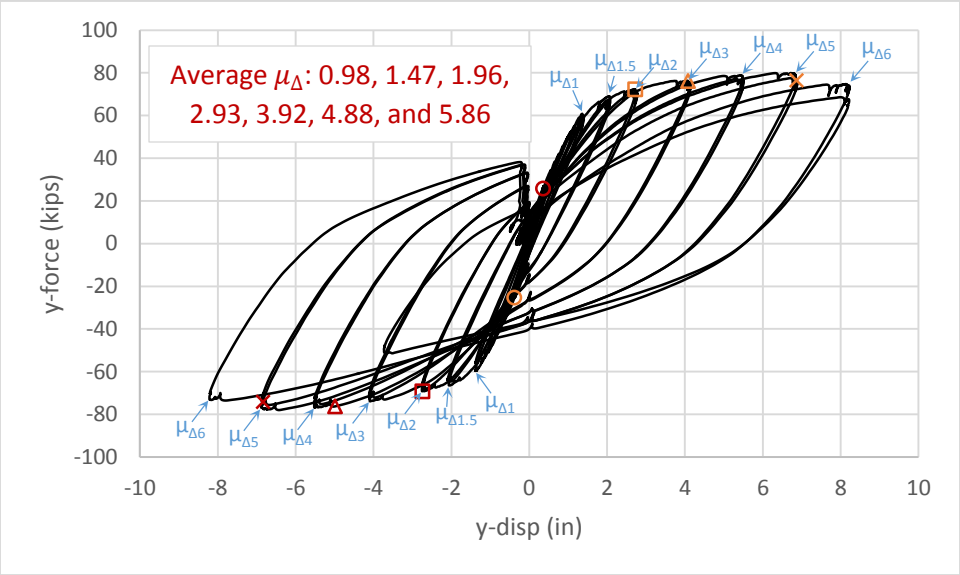

Figure 9-10. Test 6: Y-Direction Hysteretic Response

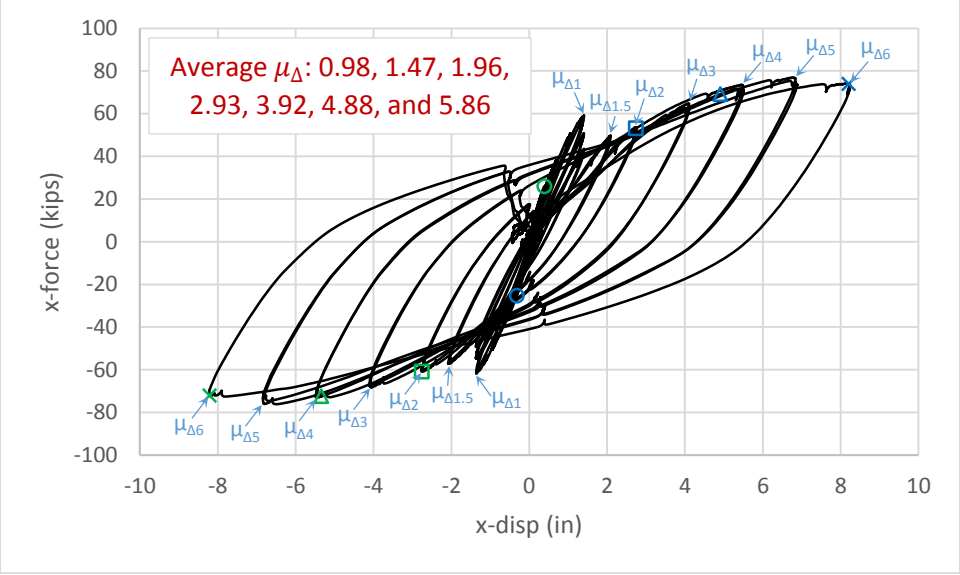

Figure 9-11. Test 6: X-Direction Hysteretic Response

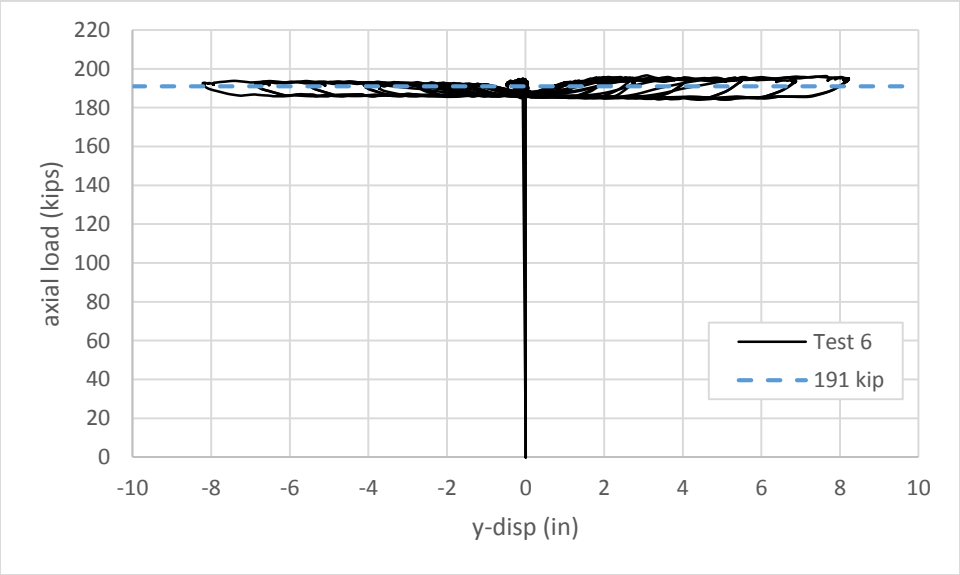

Figure 9-12. Test 6: Y-Direction Axial Force History

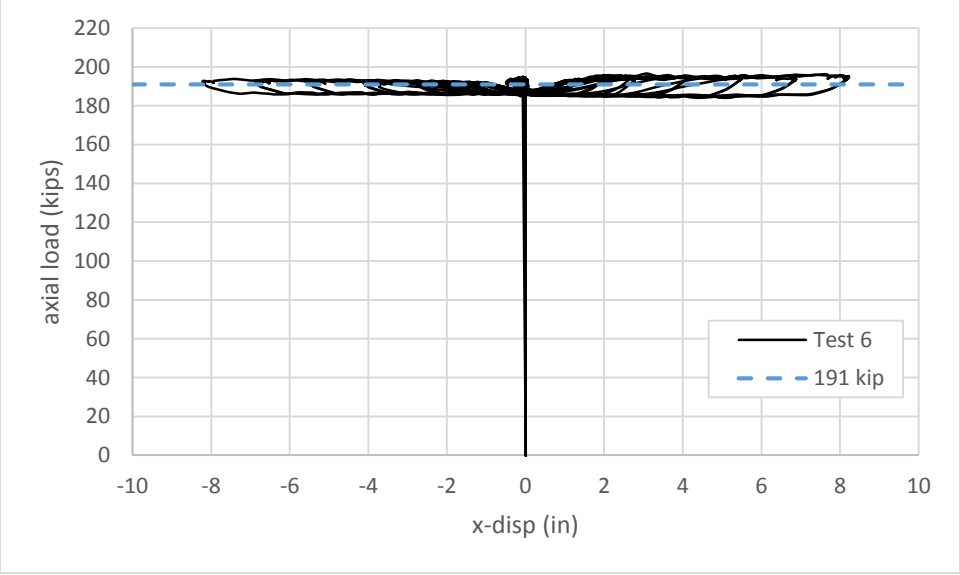

Figure 9-13. Test 6: X-Direction Axial Force History

Figure 9-14. Test 6: Linear Potentiometers at the Transfer Footing Interface, (Left) North and (Right) West Sides

Test 6 - Experimental Observations

The test began with collection of the initial measurements prior to application of the axial load. A constant axial load of $191\ kips\ \left(P/f_c'\ A_g = 5.9\%\right)$ was then applied using a self-regulating axial load system described in Chapter 2. The imposed displacement histories in the Y and X-directions for the Asymmetric Two-Cycle-Set Load History of Figure 9-1 are shown in Figure 9-4 and Figure 9-5. The resulting column shear force histories in the Y and X-directions appear in Figure 9-6 and Figure 9-7. The full displacement history and resulting load path can be found in Figure 9-8 and Figure 9-9. The Y and X-direction column hysteretic response appears in Figure 9-10 and Figure 9-11. The axial load history is shown in Figure 9-12 and Figure 9-13.

In Test 6, the relative displacement between the transfer and specimen footings was measured using linear potentiometers in the four primary directions, see Figure 9-14. A calculation channel was added to the data acquisition to subtract the relative footing displacement from the string potentiometer displacement, providing the total column deformation. This included both the horizontal slip at the footing interface as well as any global footing rotations which were extrapolated to the center of the applied lateral load. The data from this calculation channel was updated in real time, allowing for it to be used for the control of the actuators, which insured that the appropriate displacement amplitudes were reached in each cycle. All deformation values reported in this summary are fully corrected based on the measured data.

The load history began with elastic cycles (1-8) in ¼ F_y' increments until the analytically predicted first yield force ($F_y' = 51.72\ kips$) was reached in each direction of loading. Cracks were first observed on all sides of the specimen during the ½ F_y' cycle, see Figure 9-15 and Figure 9-16. At the analytically predicted first yield force, displacements in the four primary directions were measured at $\Delta_y' = 1.05$" and $\Delta_y' = -1.05$" in Y-direction and $\Delta_y' = 1.06$" and $\Delta_y' = -0.96$" in X-direction, producing an average experimental first yield displacement of $\Delta_y' = 1.03$". Cracks observed on each side of the specimen at first yield are shown in Figure 9-17 and Figure 9-18. The equivalent

yield displacement for the column was then computed as $\Delta_y = \Delta'_y\left(M_n/M'_y\right) = 1.40\ in$, where $M_n = 642.51\ kip \cdot ft$ represents the analytical nominal moment capacity corresponding to an extreme fiber compression strain of $\varepsilon_c = 0.004$ or a steel tensile strain of $\varepsilon_s = 0.015$, whichever occurs first. In an effort to make this specimen directly comparable to Tests 4 and 5, which utilized a Symmetric Two or Three-Cycle-Set bidirectional load history, the equivalent yield displacement of Test 4 and 5 ($\Delta_y = 1.37$") was used to define the displacement ductility levels ($\mu_{\Delta n} = n \cdot \Delta_y$) of the asymmetric load history selected for Test 6. The average measured displacement ductility of cycles ran in Test 6 referencing the actual equivalent yield displacement of ($\Delta_y = 1.40$") were as follows: 0.98, 1.47, 1.96, 2.93, 3.92, 4.88, and 5.86. This was expected to have little influence on the damage observations.

The following set of cycles began the asymmetric portion of the two-cycle-set displacement history where the displacement demands in the x-direction lagged behind those in the y-direction as shown in Figure 9-4 and Figure 9-5. Small amounts of concrete flaking, which generally precedes more noticeable concrete crushing, was observed on the South side of the specimen during $\mu_{\Delta 1.5}^{-1y} = -2.06$". Crack profiles on the South and North sides of the specimen at $\mu_{\Delta 1.5}^{+2y} = 2.07$" and $\mu_{\Delta 1.5}^{-2y} = -2.05$" appear in Figure 9-21. Photos of the East and West sides of the specimen at the conclusion of $\mu_{\Delta 1.5}^{\pm 2y}$ and $\mu_{\Delta 1}^{\pm 4x}$ are shown in Figure 9-22. The red and black cracks from $\mu_{\Delta 1.5}^{\pm 2y}$ show a distinct inclination on the shear faces the column. Even though the displacement ductility was not increased during $\mu_{\Delta 1}^{\pm 4x}$, the cracks due to loading in this direction spread, following those created during the larger orthogonal loading.

Concrete crushing was first observed on the North and South sides of the specimen during $\mu_{\Delta 2}^{+1y} = 2.73$" and $\mu_{\Delta 2}^{-1y} = -2.75$" respectively, as shown in Figure 9-23. Cracks on South and North sides of the specimen during $\mu_{\Delta 2}^{+2y} = 2.77$" and $\mu_{\Delta 2}^{-2y} = -2.73$" are shown in Figure 9-24. The crack profiles on the East and West sides of the specimen after $\mu_{\Delta 2}^{\pm 2y}$ and $\mu_{\Delta 1}^{\pm 6x}$ appear in Figure 9-25. Again, the inclination of cracks due to loading in the y-direction increased, however those due to loading in the x-direction remained horizontal on the shear faces due to the lower displacement demands. Spiral yielding was first measured on the North side of the specimen under confinement demands during $\mu_{\Delta 3}^{+1y} = 4.12$", see Figure 9-26. The visible effects of crushing were more prominent on the South side of the specimen during $\mu_{\Delta 3}^{-1y} = -4.09$", however, the transverse steel remained elastic. The crack profiles on the South and North sides of the specimen during $\mu_{\Delta 3}^{+2y} = 4.13$" and $\mu_{\Delta 3}^{-2y} = -4.10$" are depicted in Figure 9-27. Cracks on the East and West sides of the specimen after $\mu_{\Delta 3}^{\pm 2y}$ and $\mu_{\Delta 1.5}^{\pm 2x}$ are shown in Figure 9-28.

Spiral yielding under confinement demands was first measured on the South side of the specimen during $\mu_{\Delta 4}^{-1y} = -5.51$", see Figure 9-29. Concrete crushing was observed on the West and East sides of the specimen during $\mu_{\Delta 2}^{-1x} = -2.76$" and $\mu_{\Delta 2}^{+2x} = 2.74$", mirroring the displacement amplitude which initially caused crushing in the primary loading direction, see Figure 9-30. Cracks on South and North sides of the specimen during $\mu_{\Delta 4}^{+2y} = 5.48$" and $\mu_{\Delta 4}^{-2y} = -5.49$" are shown in Figure 9-31. The crack profiles on the East and West sides of the specimen after $\mu_{\Delta 4}^{\pm 2y}$ and $\mu_{\Delta 2}^{\pm 2x}$ appear in Figure 9-32. The same degree of inclination of cracks on the shear faces of the column during $\mu_{\Delta 2}^{\pm 2y}$ was not observed on the North and South sides of the column during $\mu_{\Delta 2}^{\pm 2x}$, due to the more

distributed horizontal cracking which occurred during the higher amplitude cycles of the primary loading direction.

The measured strain in spiral layers on the North and South sides of the specimen spiked during $\mu_{\Delta 5}^{+1y} = 6.82"$ and $\mu_{\Delta 5}^{-1y} = -6.85"$, however the extreme fiber reinforcement remained visibly straight as shown in Figure 9-33. North reinforcing bars N and NNE buckled simultaneously during $\mu_{\Delta 5}^{+2y} = 6.87"$, followed by buckling of the South extreme fiber bar during $\mu_{\Delta 5}^{-2y} = -6.84"$ as shown in Figure 9-34. The asymmetric portion of the displacement history was concluded after finishing $\mu_{\Delta 5}^{\pm 2y}$ and $\mu_{\Delta 3}^{\pm 2x}$, and cracks were no longer marked for the remainder of the load history which continued with direct cycling in the x-direction to evaluate the impact of the primary y-direction cycling on damage states in the secondary direction. Spiral yielding was first measured on the East side of the specimen during $\mu_{\Delta 4}^{+2x} = 5.48"$, followed by the West side during $\mu_{\Delta 4}^{-2x} = -5.46"$, see Figure 9-35. Note that spiral yielding was observed during $\mu_{\Delta 4}^{\pm 2x}$, while the North side yielded at $4.08"$ during $\mu_{\Delta 3}^{+1y}$ and the South side yielded at $-4.99"$ on the way to $\mu_{\Delta 4}^{-1y}$, highlighting the delay of this observation on the East and West sides of the specimen. The East and West reinforcement remained visibly straight during $\mu_{\Delta 5}^{+2x} = 6.84"$ and $\mu_{\Delta 5}^{-2x} = -6.84"$, respectively, even though the measured spiral strains increased significantly. Photos depicting the compression zone and extreme fiber reinforcement during these cycles appear in Figure 9-36 and Figure 9-37.

At this time, the peak ductility demands in each direction had reached $\mu_{\Delta 5}$, and it was decided that the loading should proceed symmetrically, with equal ductility demands in the y and x-directions. The adjacent North reinforcing bar NNW buckled during $\mu_{\Delta 6}^{+1y} = 8.22"$, followed by buckling of South bars SSW and SSE during $\mu_{\Delta 6}^{-1y} = -8.21"$, see Figure 9-38. Now, three bars had buckled on the North and South sides of the specimen, but East and West bar buckling had not yet been observed. East reinforcing bars E, ESE, and ENE buckled simultaneously during $\mu_{\Delta 6}^{+1x} = 8.21"$, followed by buckling of West bars W, WSW, and WNW during $\mu_{\Delta 6}^{-1x} = -8.21"$, see Figure 9-39. Photos depicting the deformed specimen at $\mu_{\Delta 6}^{+1y} = 8.22"$ and $\mu_{\Delta 6}^{+1x} = 8.21"$ are available in Figure 9-3 and Figure 9-41.

Bar NE buckled during $\mu_{\Delta 6}^{+2y} = 8.21"$, while the deformation in the previously buckled North bars increased as shown in Figure 9-40. The loading was then reversed in the y-direction and paused at $-3.72"$ on the way to $\mu_{\Delta 6}^{-2y}$. It was observed that South bars SE and SW had buckled, which means that only bar NW remained straight within the cross section. In comparison to the previous cycle to $\mu_{\Delta 6}^{-1y}$, there was a significant loss in strength due to the severity of buckling within the cross section. In an effort to prevent the twist of the column which resulted after fracturing the transverse steel in Test 5, the column was recentered and the test was ended at this time without fracture of reinforcing steel. This specimen was to be the first to be repaired using the plastic hinge relocation method, and serves as a proof of concept for a column with extensive buckling, but without fractured reinforcement. Photos of the specimen after removal of the instrumentation appear in Figure 9-42, Figure 9-43, and Figure 9-44. Note that cracks were no longer marked after bar buckling initiated during $\mu_{\Delta 5}^{\pm 2y}$ and $\mu_{\Delta 3}^{\pm 2x}$.

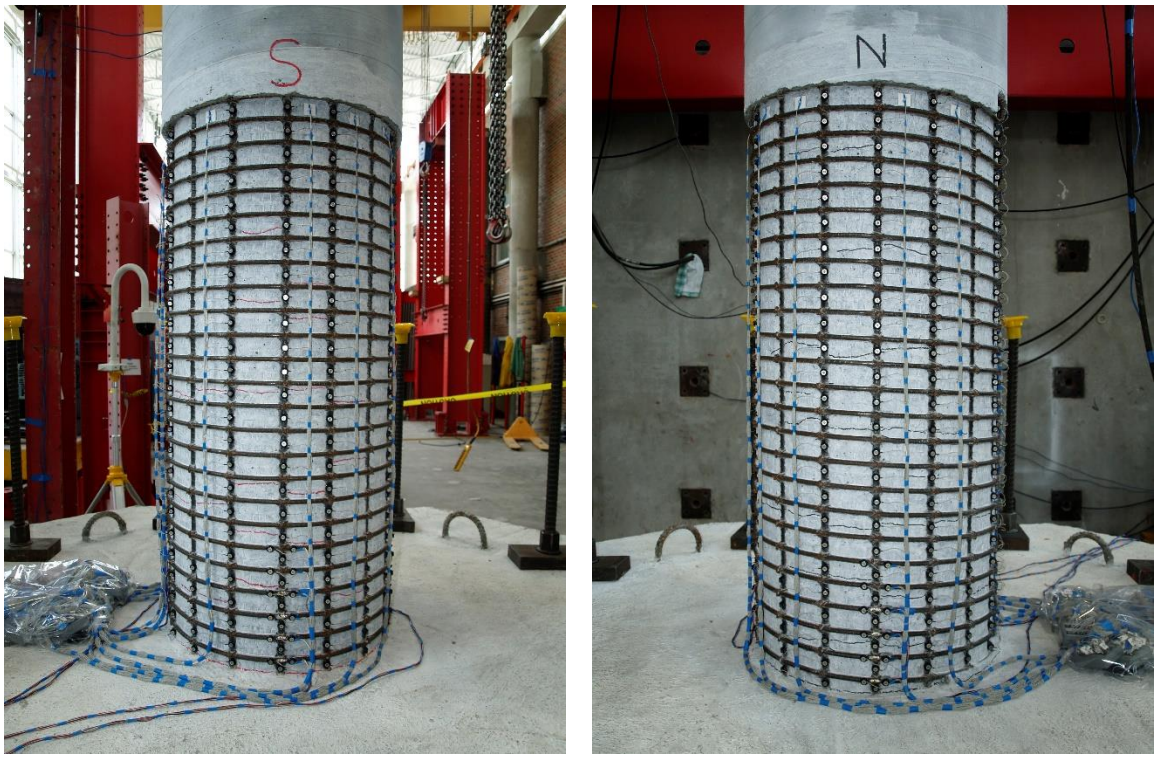

Figure 9-15. Test 6: First Cracking on the South and North Sides of the Specimen during $\Delta_y = 0.35$" and $\Delta_y = -0.36$"

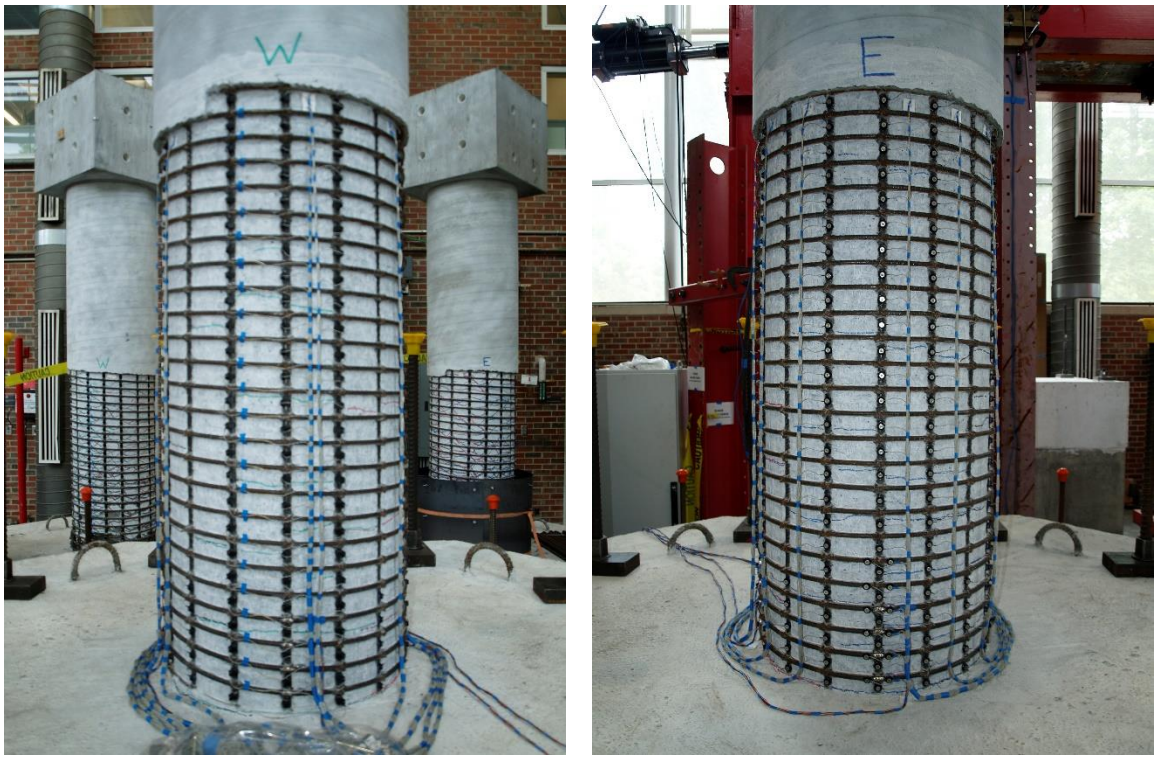

Figure 9-16. Test 6: First Cracking on the West and East Sides of the Specimen during $\Delta_x = 0.38$" and $\Delta_x = -0.32$"

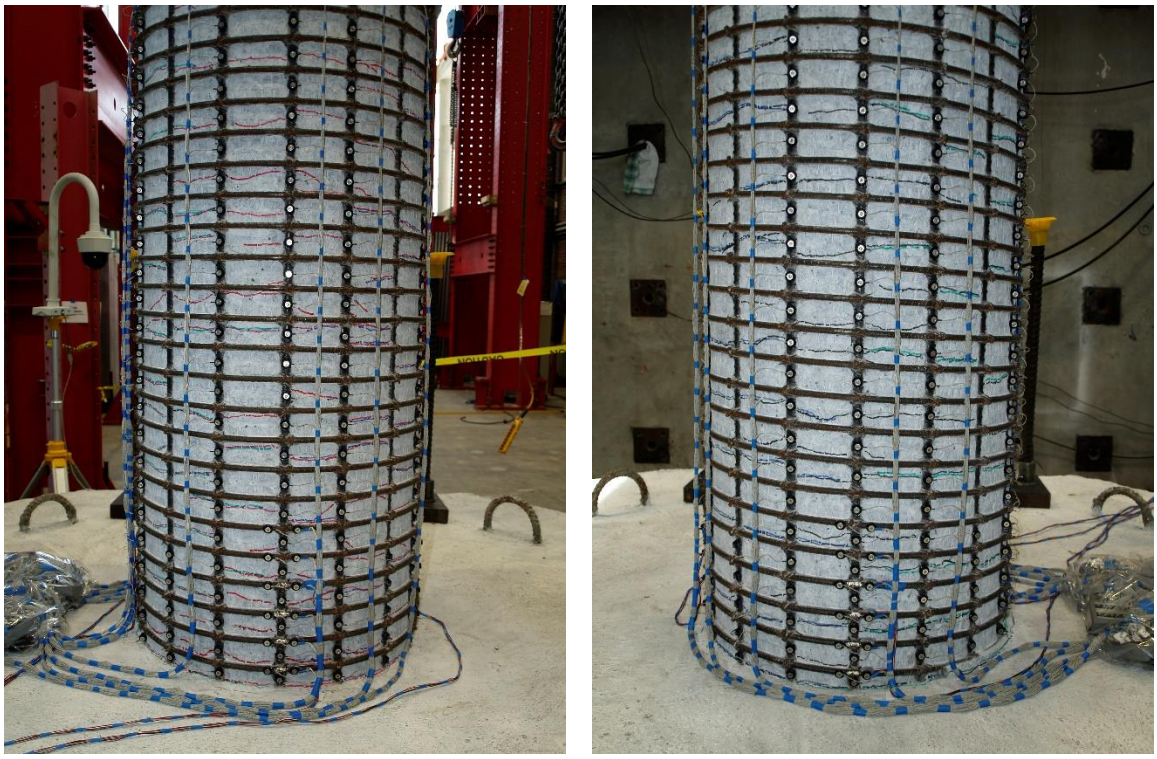

Figure 9-17. Test 6: Cracking on the South and North Sides during $\Delta'_y = 1.05"$ and $\Delta'_y = -1.05"$ in Y-Direction

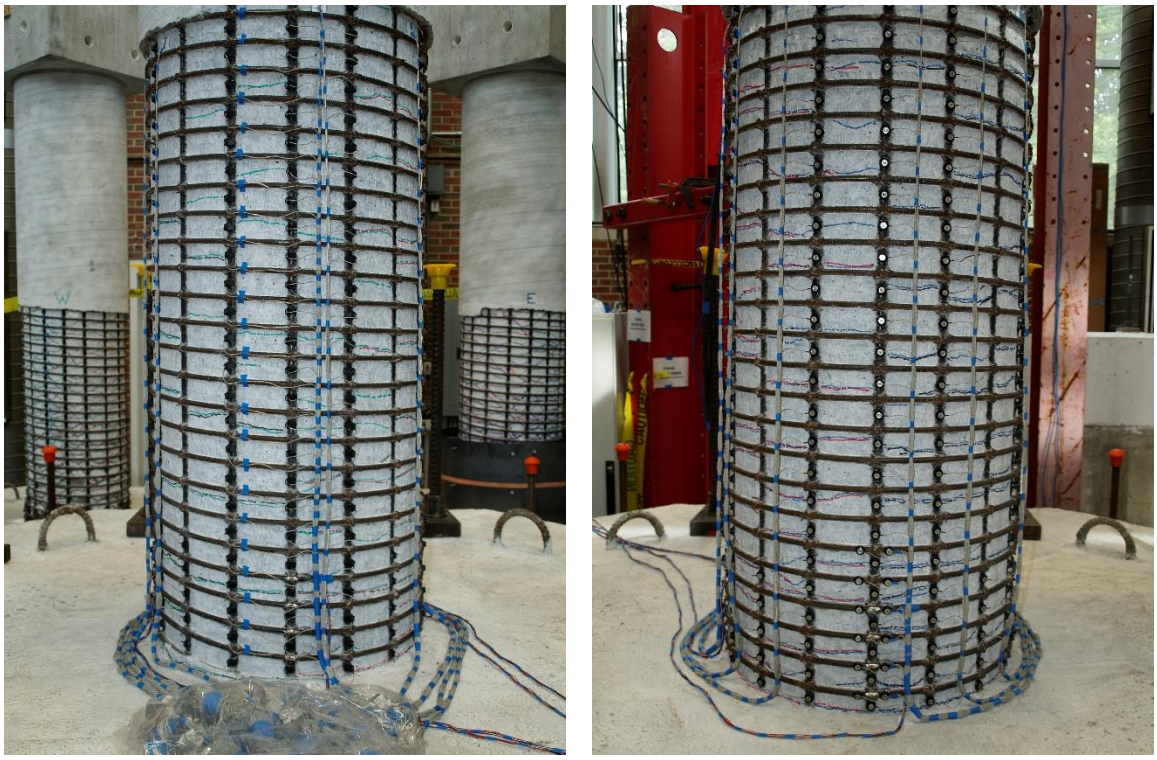

Figure 9-18. Test 6: Cracking on the West and East Sides during $\Delta'_y = 1.06"$ and $\Delta'_y = -0.96"$ in X-Direction

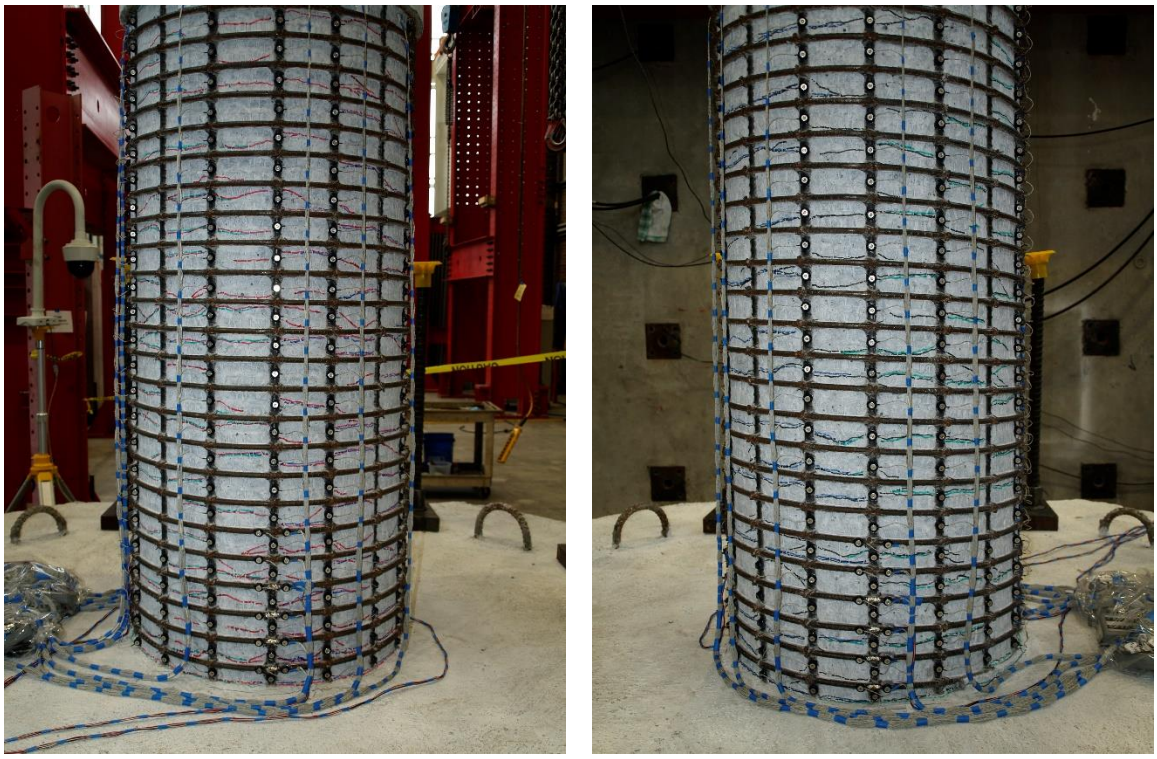

Figure 9-19. Test 6: Cracking on the (Left) South Side at $\mu_{\Delta 1}^{+2y} = 1.40$" and (Right) North Side at $\mu_{\Delta 1}^{-2y} = -1.36$"

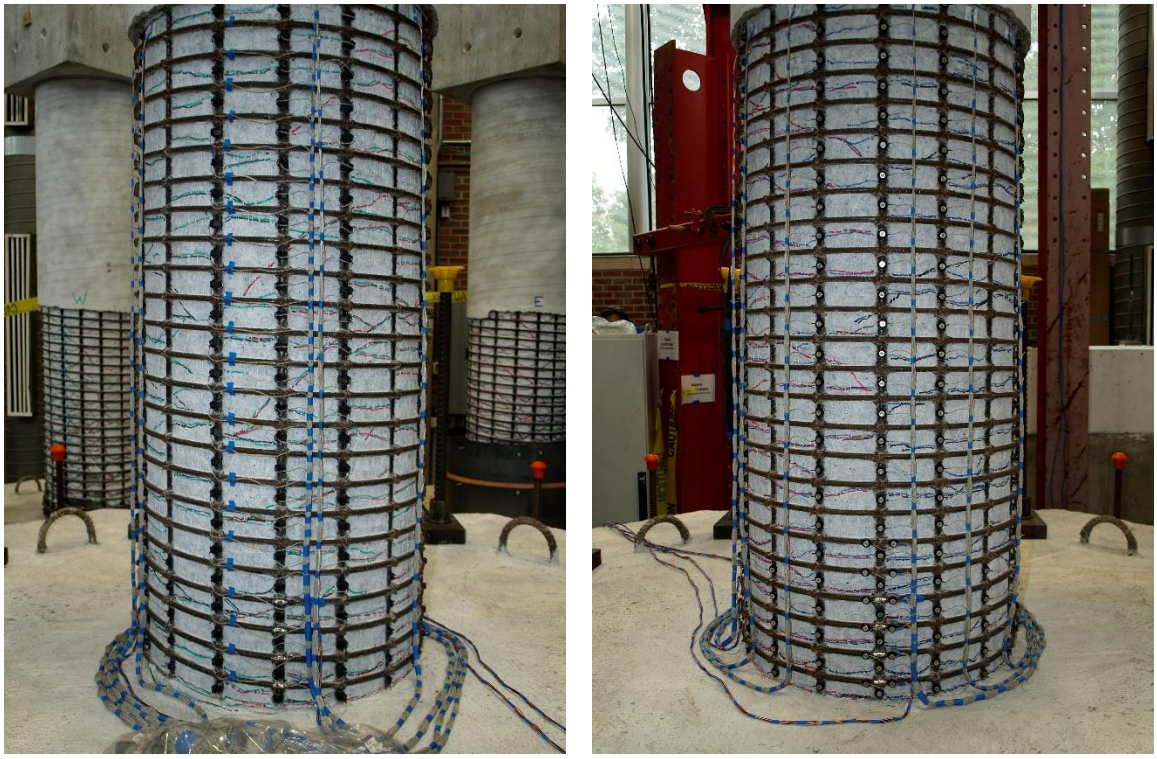

Figure 9-20. Test 6: Cracking on the (Left) West Side at $\mu_{\Delta 1}^{+2x} = 1.39$" and (Right) East Side at $\mu_{\Delta 1}^{-2x} = -1.36$"

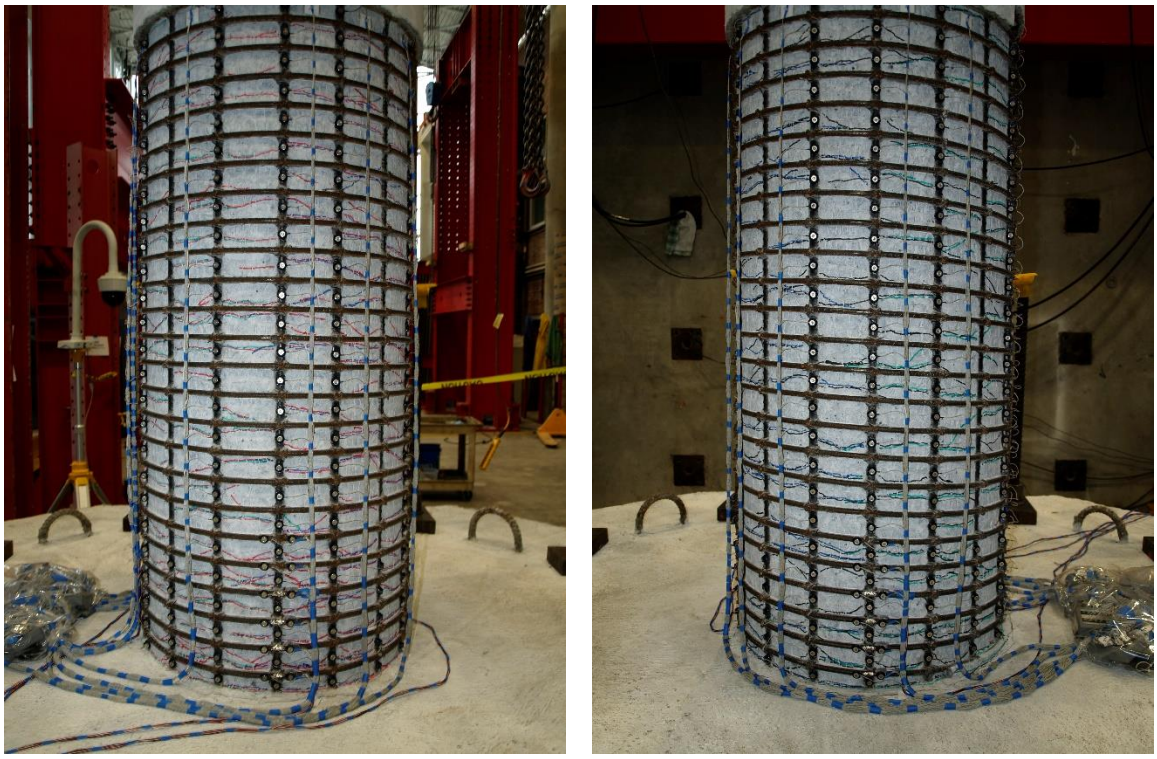

Figure 9-21. Test 6: Cracking on the (Left) South Side at $\mu_{\Delta 1.5}^{+2y} = 2.07"$ and (Right) North Side at $\mu_{\Delta 1.5}^{-2y} = -2.05"$

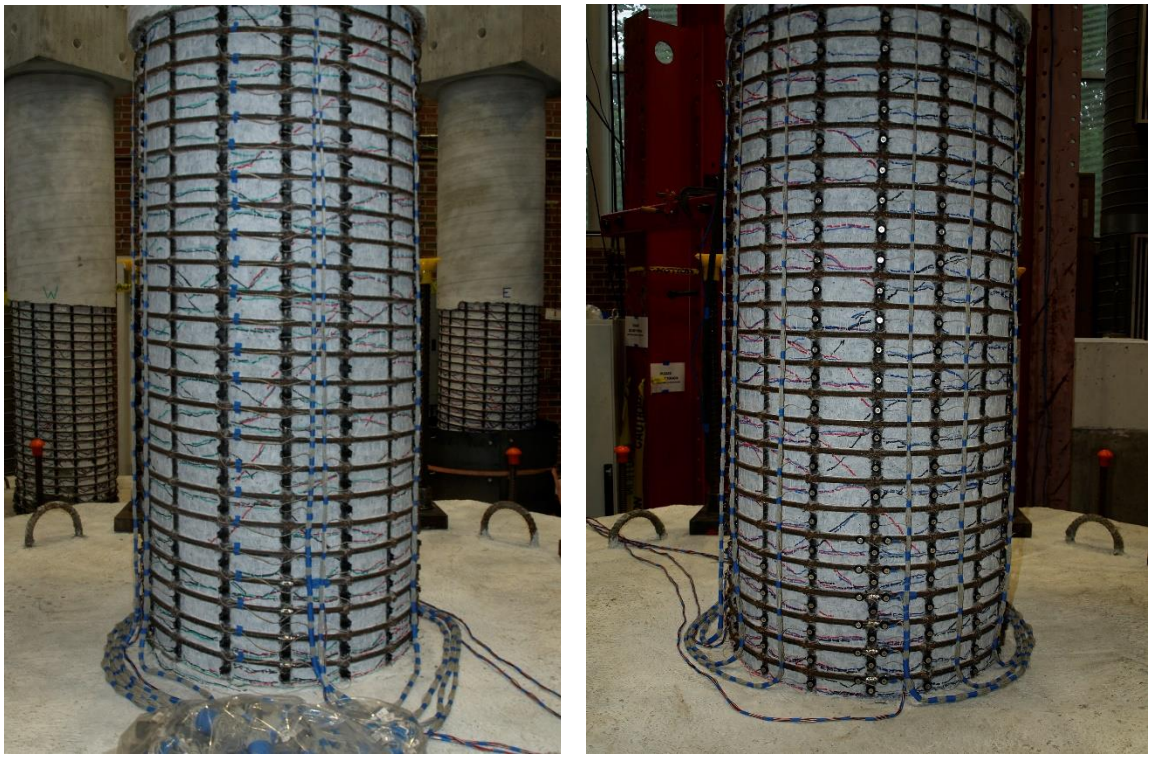

Figure 9-22. Test 6: Cracking on the (Left) West and (Right) East Sides after $\mu_{\Delta 1.5}^{\pm 2y}$ and $\mu_{\Delta 1}^{\pm 4x}$

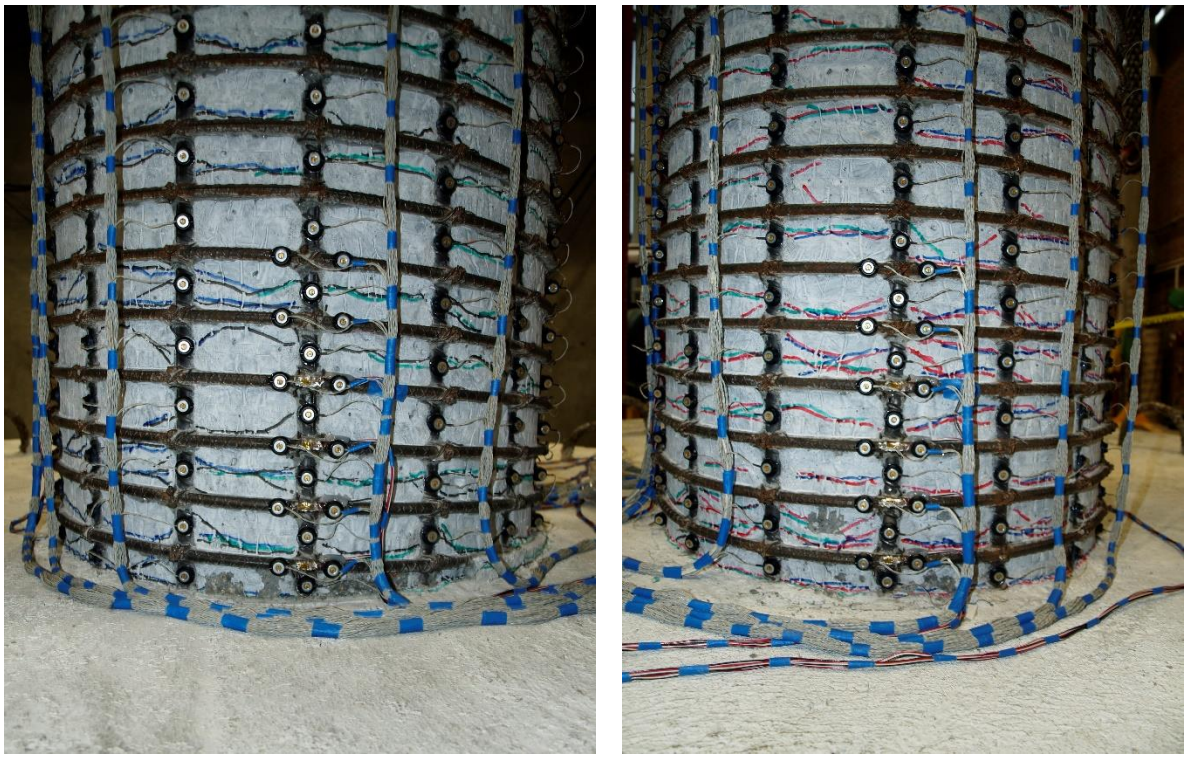

Figure 9-23. Test 6: (Left) North Concrete Crushing at $\mu_{\Delta 2}^{+1y} = 2.73"$ and (Right) South Concrete Crushing at $\mu_{\Delta 2}^{-1y} = -2.75"$

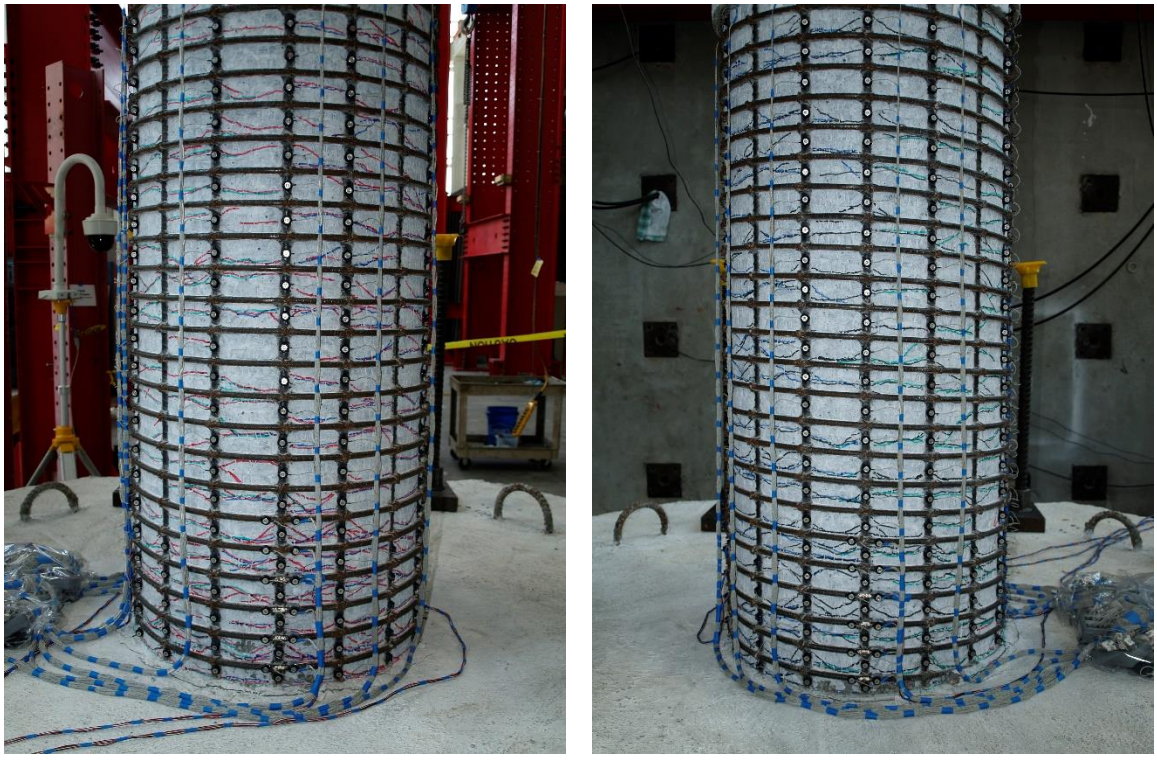

Figure 9-24. Test 6: Cracking on the (Left) South Side at $\mu_{\Delta 2}^{+2y} = 2.77"$ and (Right) North Side at $\mu_{\Delta 2}^{-2y} = -2.73"$

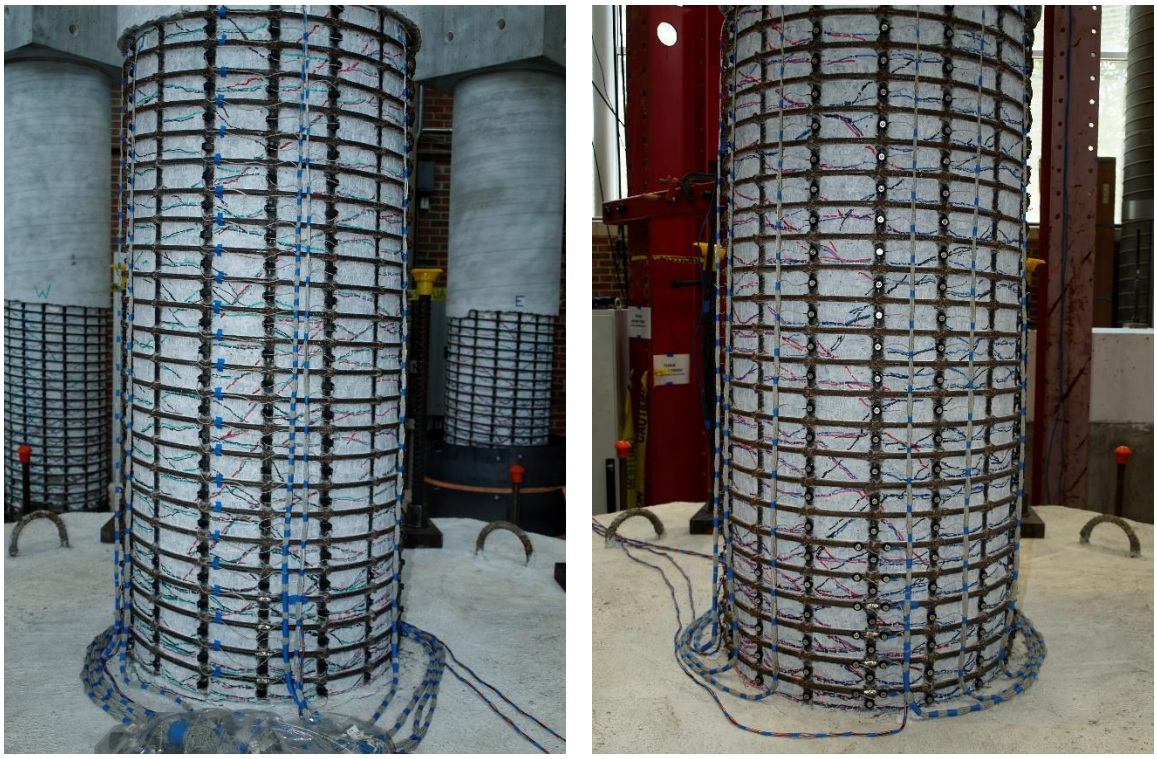

Figure 9-25. Test 6: Cracking on the (Left) West and (Right) East Sides after $\mu_{\Delta 2}^{\pm 2y}$ and $\mu_{\Delta 1}^{\pm 6x}$

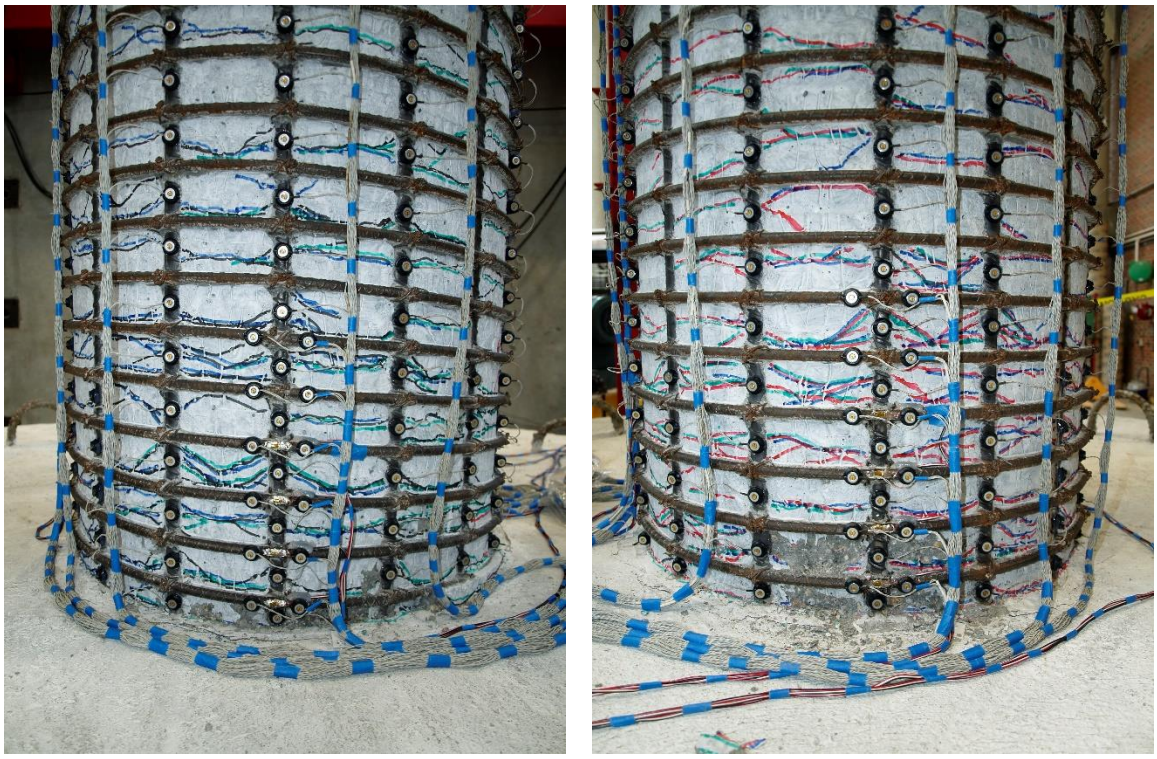

Figure 9-26. Test 6: (Left) Initial North Spiral Yielding during $\mu_{\Delta 3}^{+1y} = 4.12"$ and (Right) South Crushing at $\mu_{\Delta 3}^{-1y} = -4.09"$

Figure 9-27. Test 6: Cracking on the (Left) South Side at $\mu_{\Delta 3}^{+2y} = 4.13"$ and (Right) North Side at $\mu_{\Delta 3}^{-2y} = -4.10"$

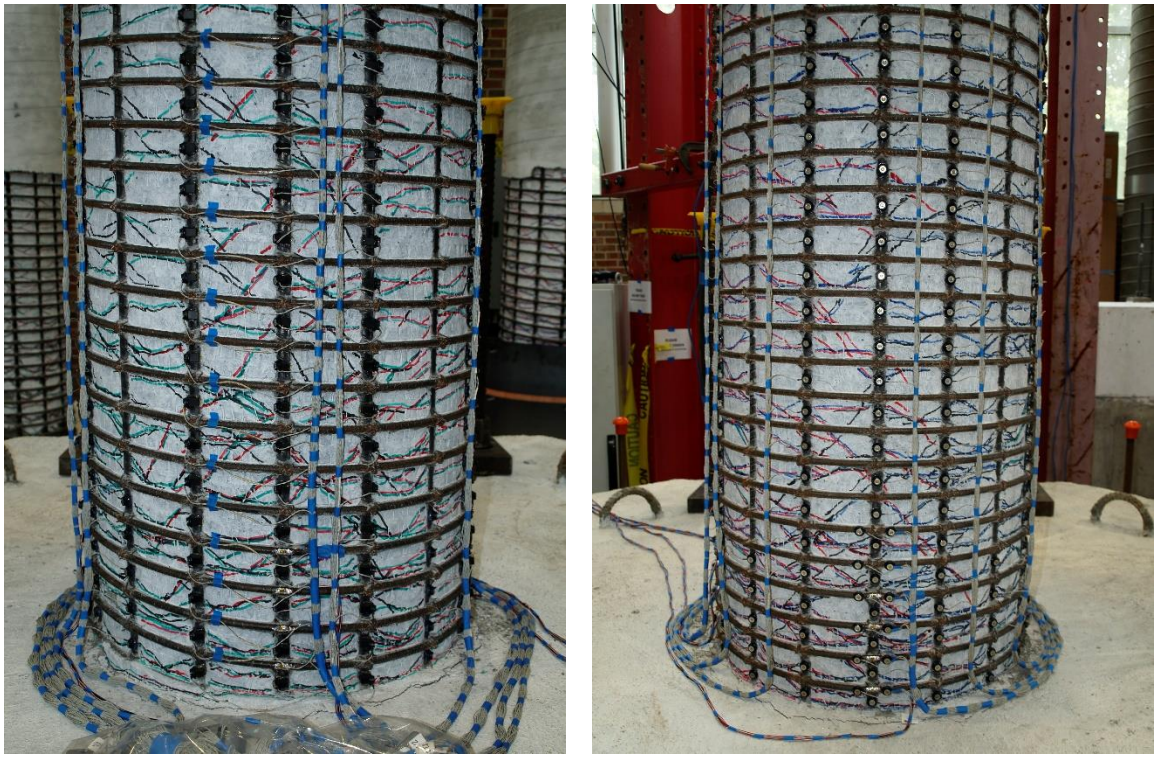

Figure 9-28. Test 6: Cracking on the (Left) West and (Right) East Sides after $\mu_{\Delta 3}^{\pm 2y}$ and $\mu_{\Delta 1.5}^{\pm 2x}$

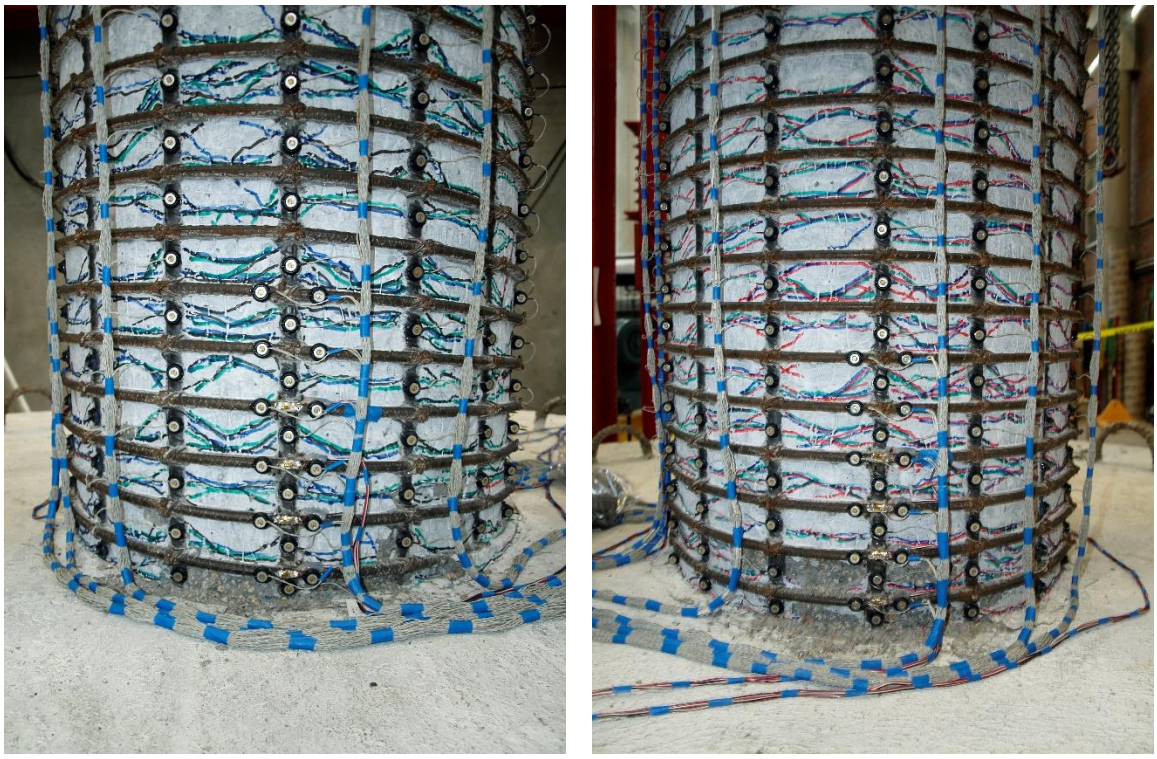

Figure 9-29. Test 6: (Left) North Crushing at $\mu_{\Delta 4}^{+1y} = 5.48"$ and (Right) Initial South Spiral Yielding during $\mu_{\Delta 4}^{-1y} = -5.51"$

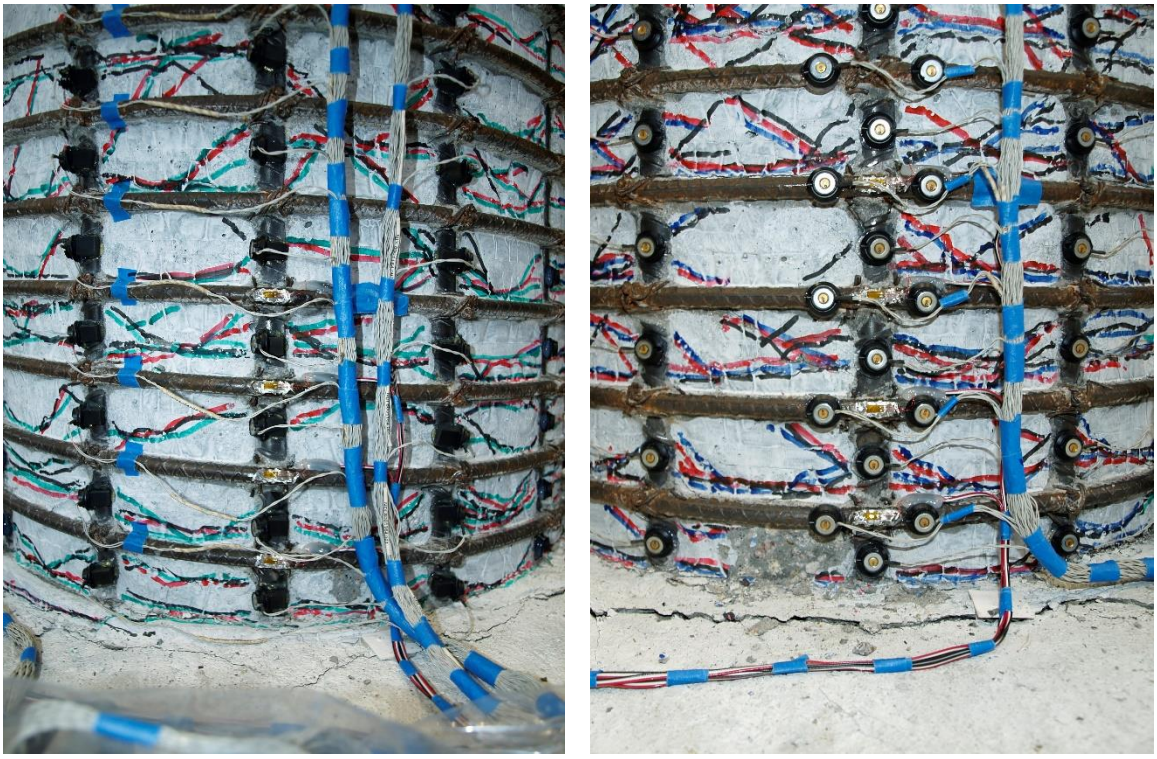

Figure 9-30. Test 6: (Left) West Concrete Crushing at $\mu_{\Delta 2}^{-1x} = -2.76"$ and (Right) East Concrete Crushing at $\mu_{\Delta 2}^{+2x} = 2.74"$

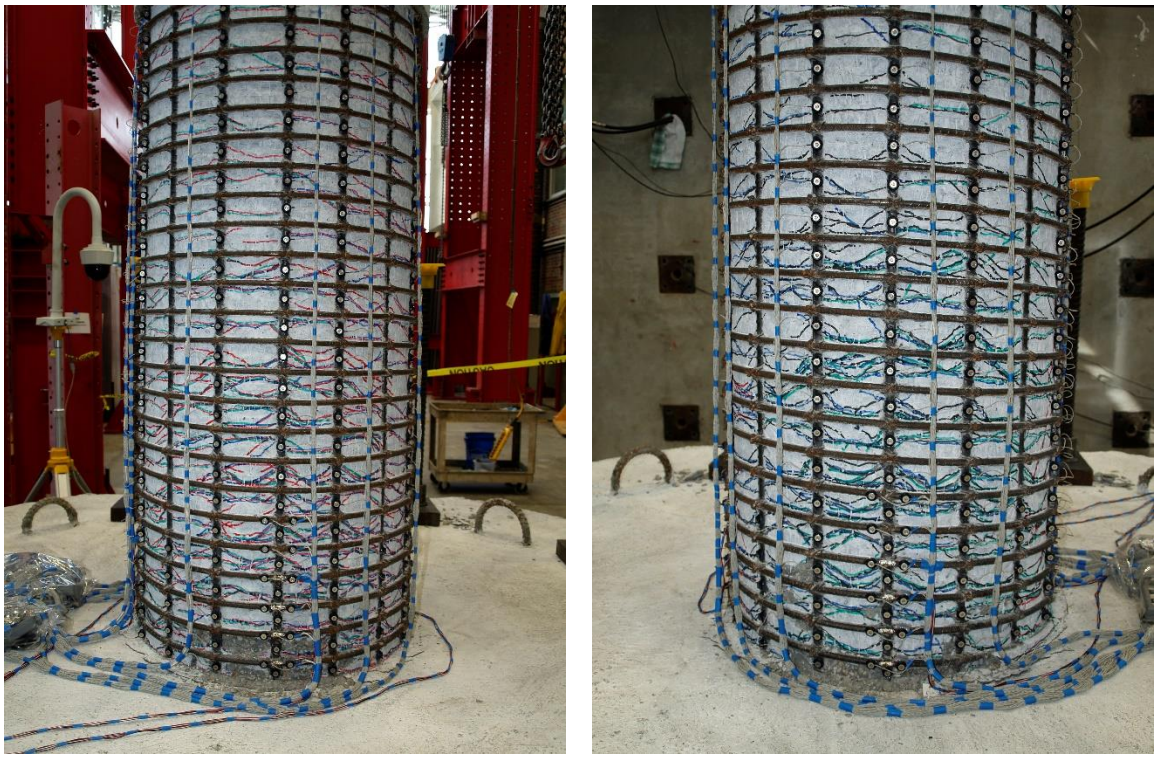

Figure 9-31. Test 6: Cracking on the (Left) South Side at $\mu_{\Delta 4}^{+2y} = 5.48"$ and (Right) North Side at $\mu_{\Delta 4}^{-2y} = -5.49"$

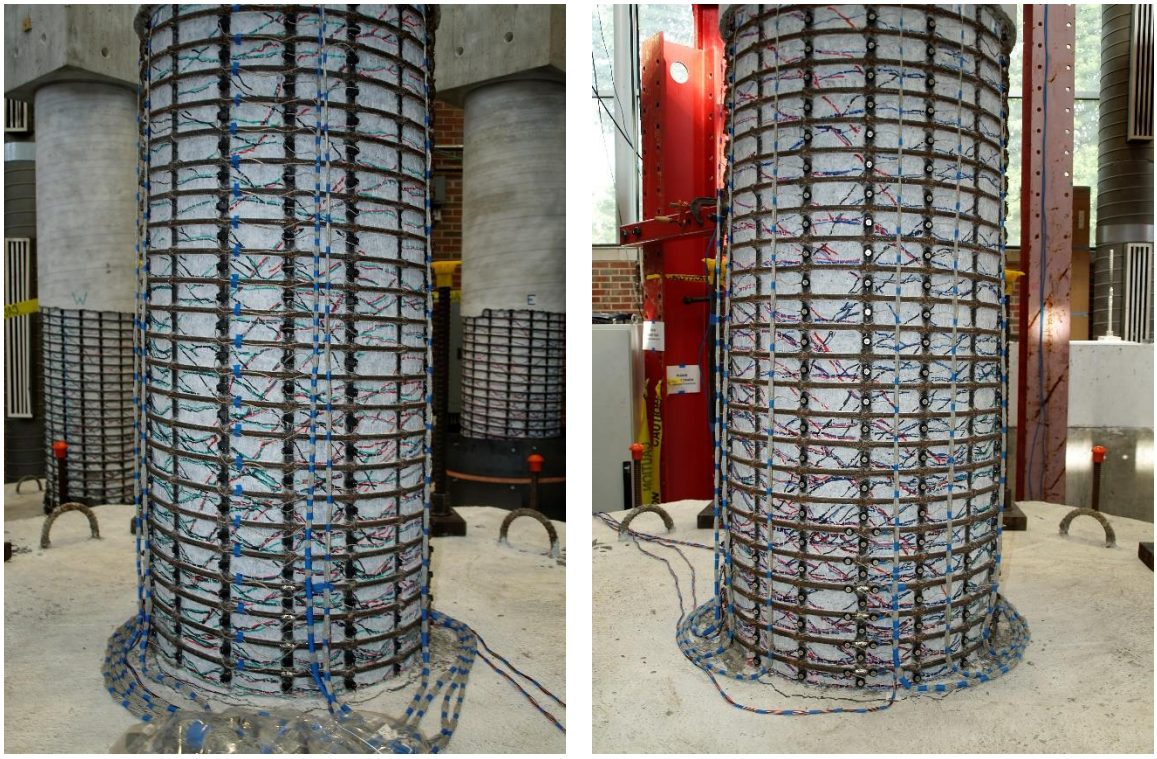

Figure 9-32. Test 6: Cracking on the (Left) West and (Right) East Sides after $\mu_{\Delta 4}^{\pm 2y}$ and $\mu_{\Delta 2}^{\pm 2x}$

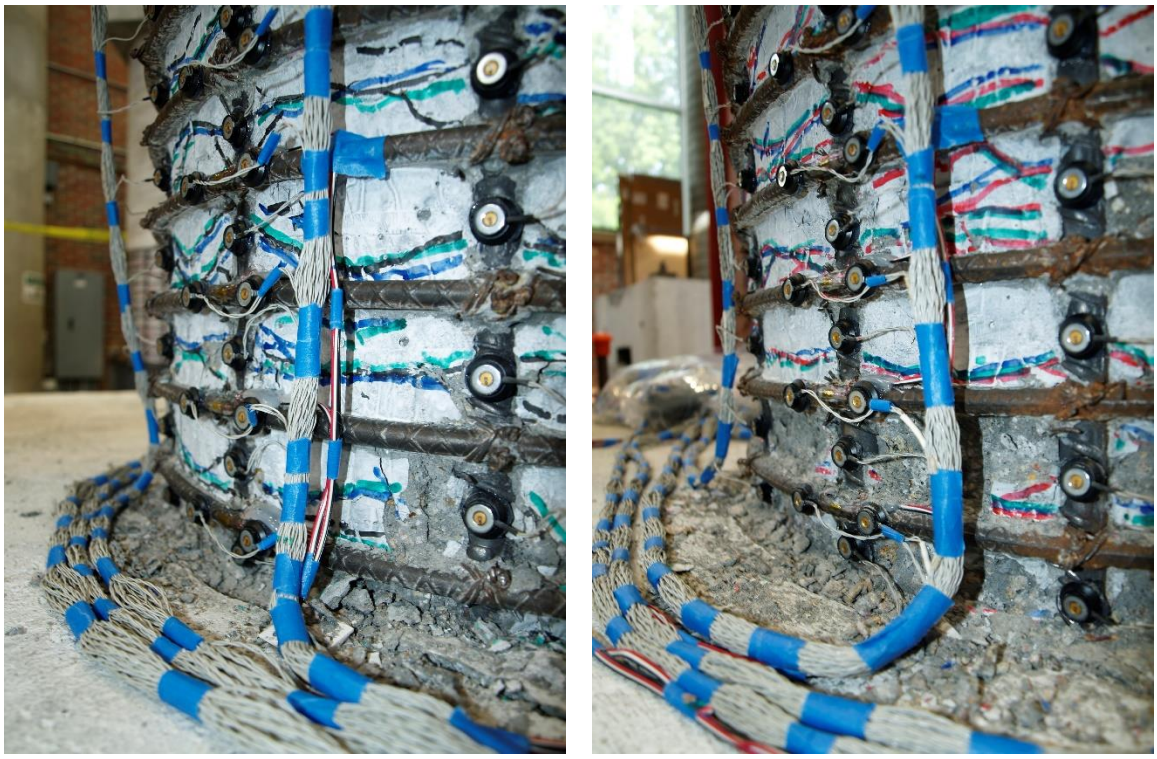

Figure 9-33. Test 6: Reinforcement Remained Straight on (Left) North at $\mu_{\Delta 5}^{+1y} = 6.82$" and (Right) South at $\mu_{\Delta 5}^{-1y} = -6.85$"

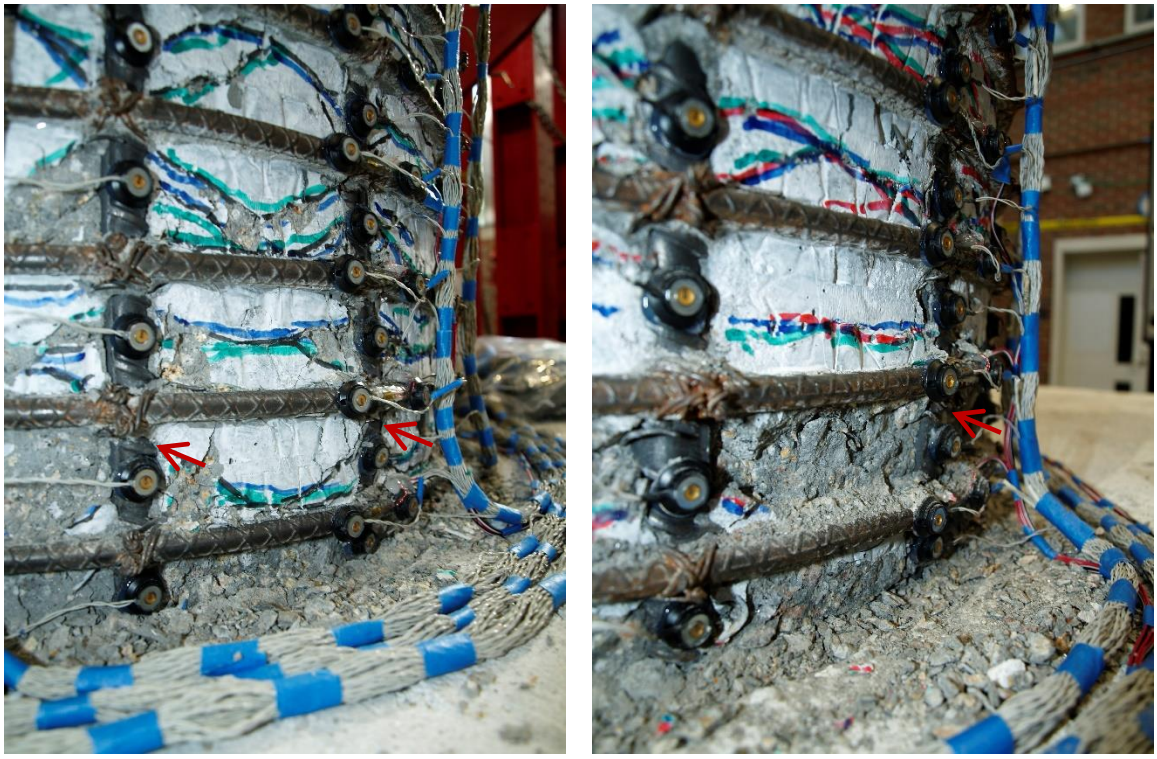

Figure 9-34. Test 6: Buckling of (Left) Bars N and NNE at $\mu_{\Delta 5}^{+2y} = 6.87$" and (Right) Bar S at $\mu_{\Delta 5}^{-2y} = -6.84$"

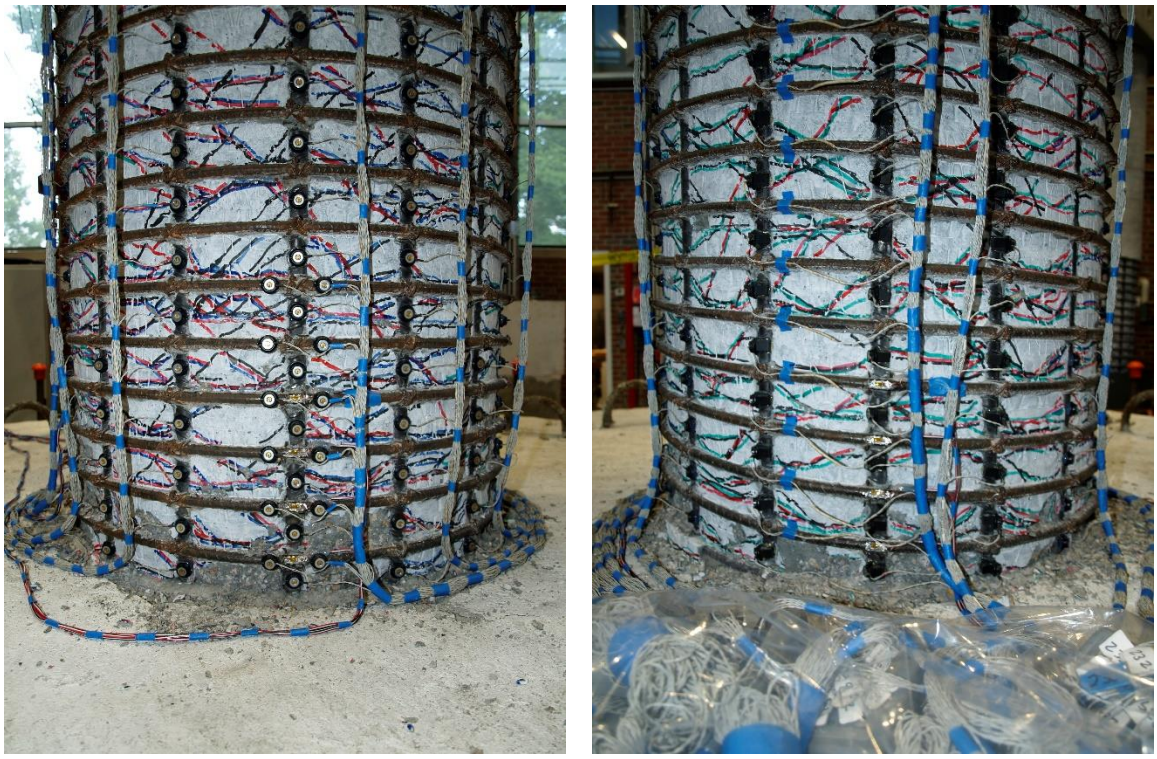

Figure 9-35. Test 6: Initial Spiral Yielding on the (Left) East Side at $\mu_{\Delta 4}^{+2x} = 5.48"$ and (Right) West Side at $\mu_{\Delta 4}^{-2x} = -5.46"$

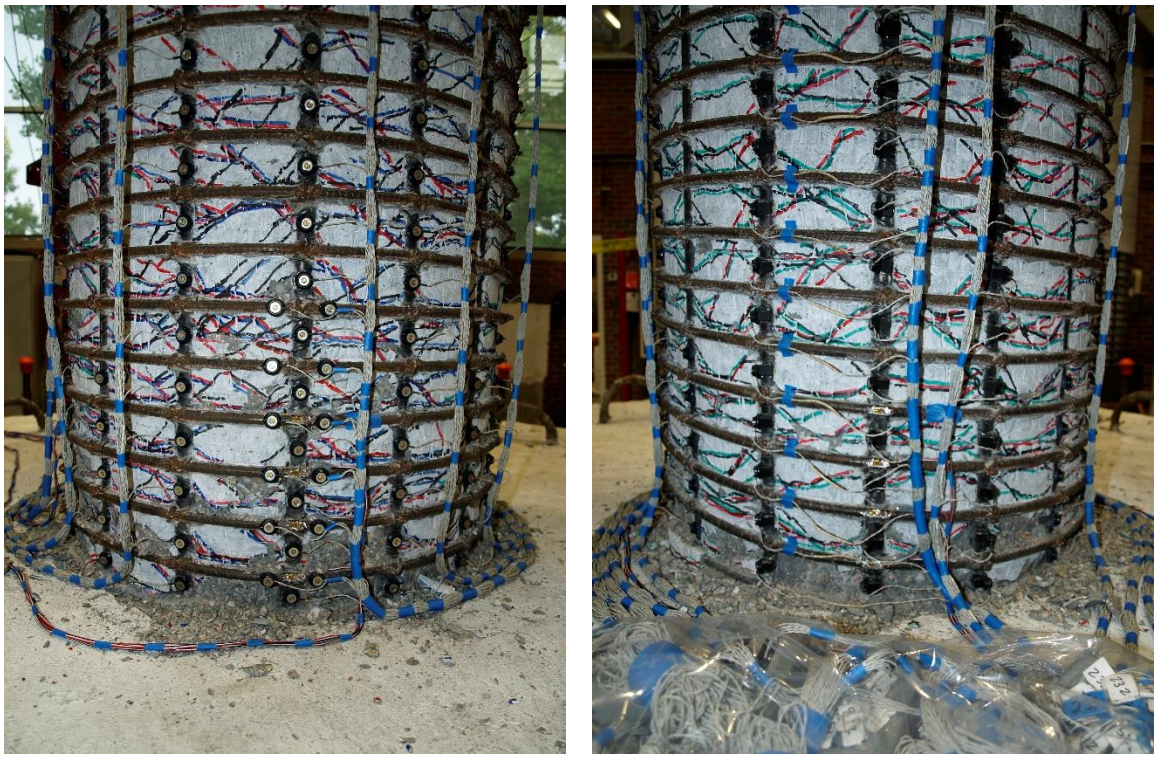

Figure 9-36. Test 6: Crushing on the (Left) East Side at $\mu_{\Delta 5}^{+2x} = 6.84"$ and (Right) West Side at $\mu_{\Delta 5}^{-2x} = -6.84"$

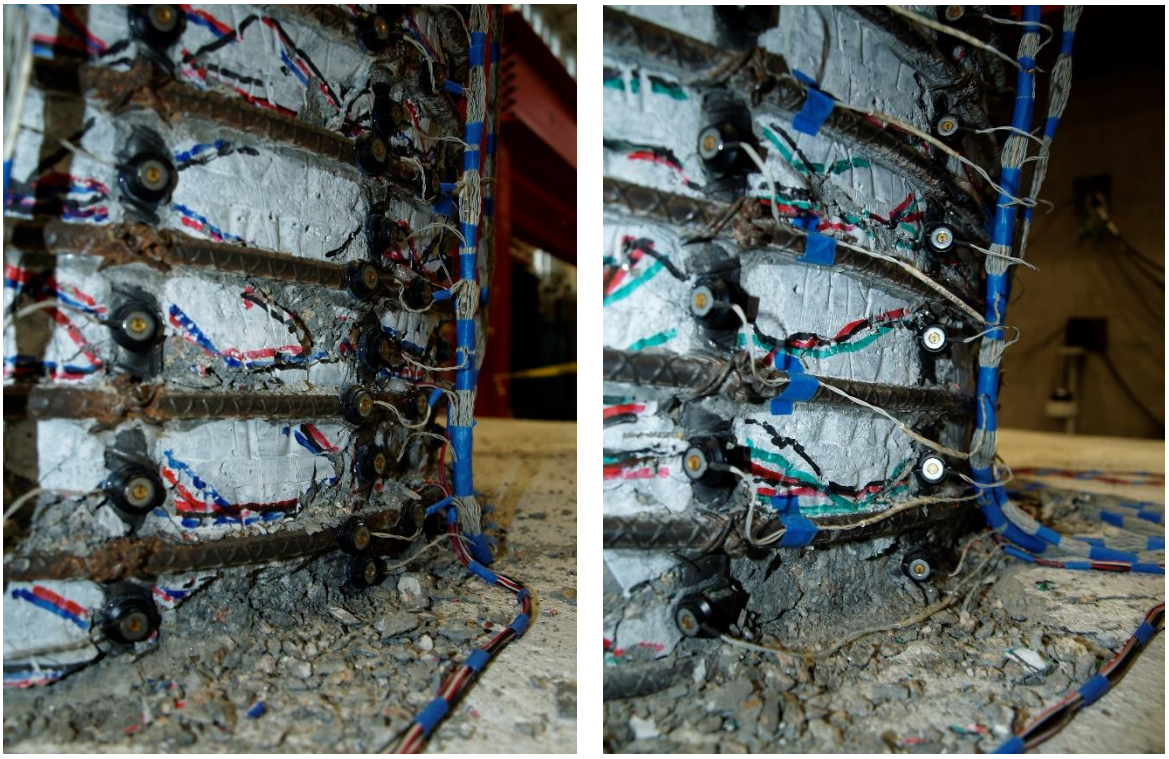

Figure 9-37. Test 6: Reinforcement Remained Straight on (Left) East at $\mu_{\Delta 5}^{+2x} = 6.84"$ and (Right) West at $\mu_{\Delta 5}^{-2x} = -6.84"$

Figure 9-38. Test 6: Buckling of (Left) Bar NNW at $\mu_{\Delta 6}^{+1y} = 8.22"$ and (Right) Bars SSW and SSE at $\mu_{\Delta 6}^{-1y} = -8.21"$

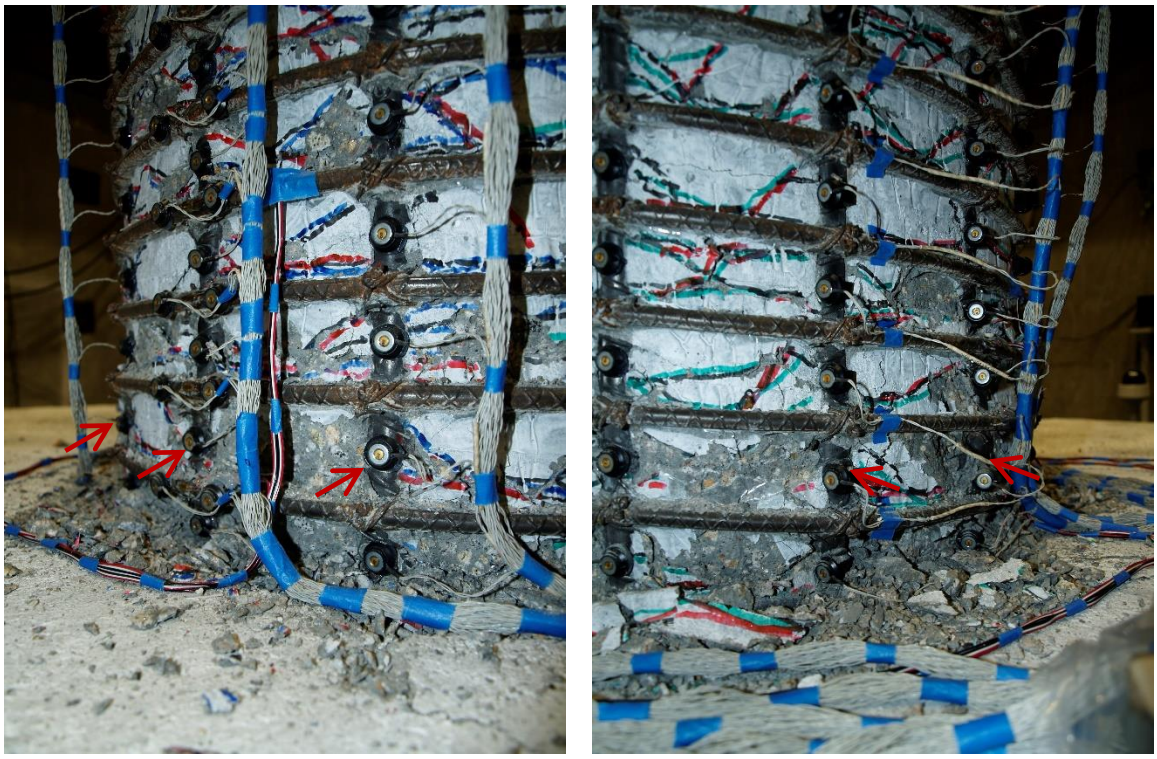

Figure 9-39. Test 6: Buckling of Bars (Left) E, ESE, & ENE at $\mu_{\Delta 6}^{+1x} = 8.21"$ and (Right) W, WSW, & WNW at $\mu_{\Delta 6}^{-1x} = -8.21"$

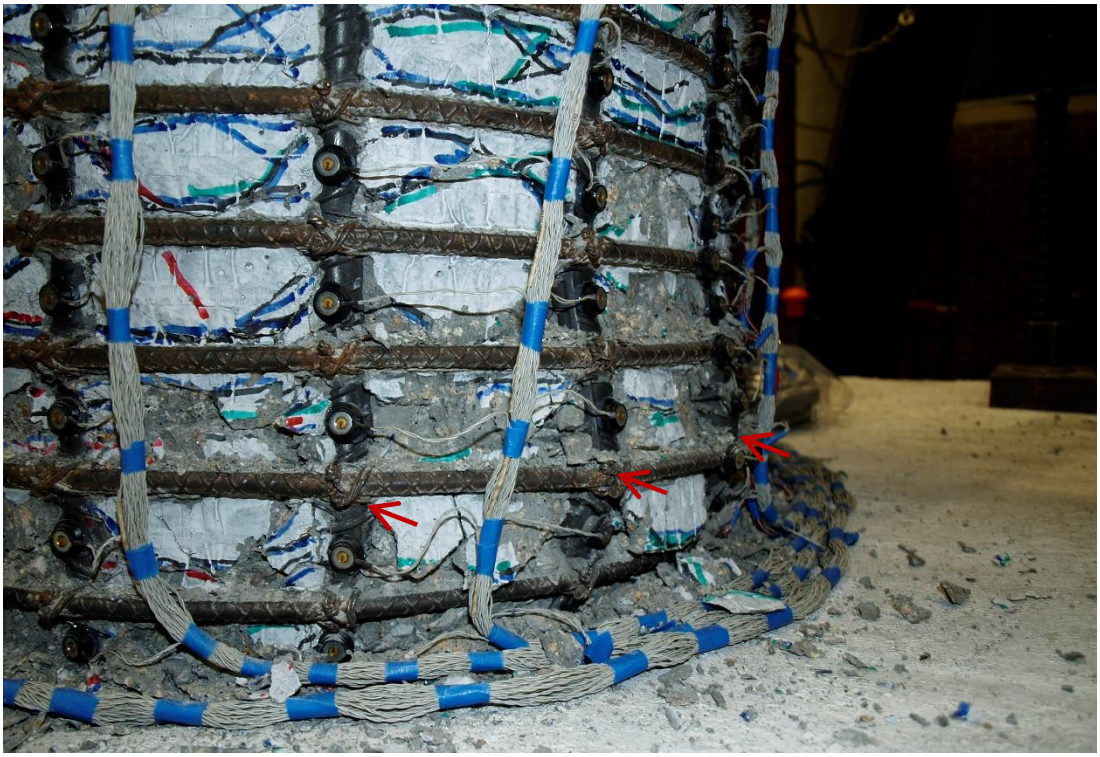

Figure 9-40. Test 6: Buckling of Bar NE during $\mu_{\Delta 6}^{+2y} = 8.21"$

Figure 9-41. Test 6: Specimen Deformation at $\mu_{\Delta 6}^{+1x} = 8.21"$

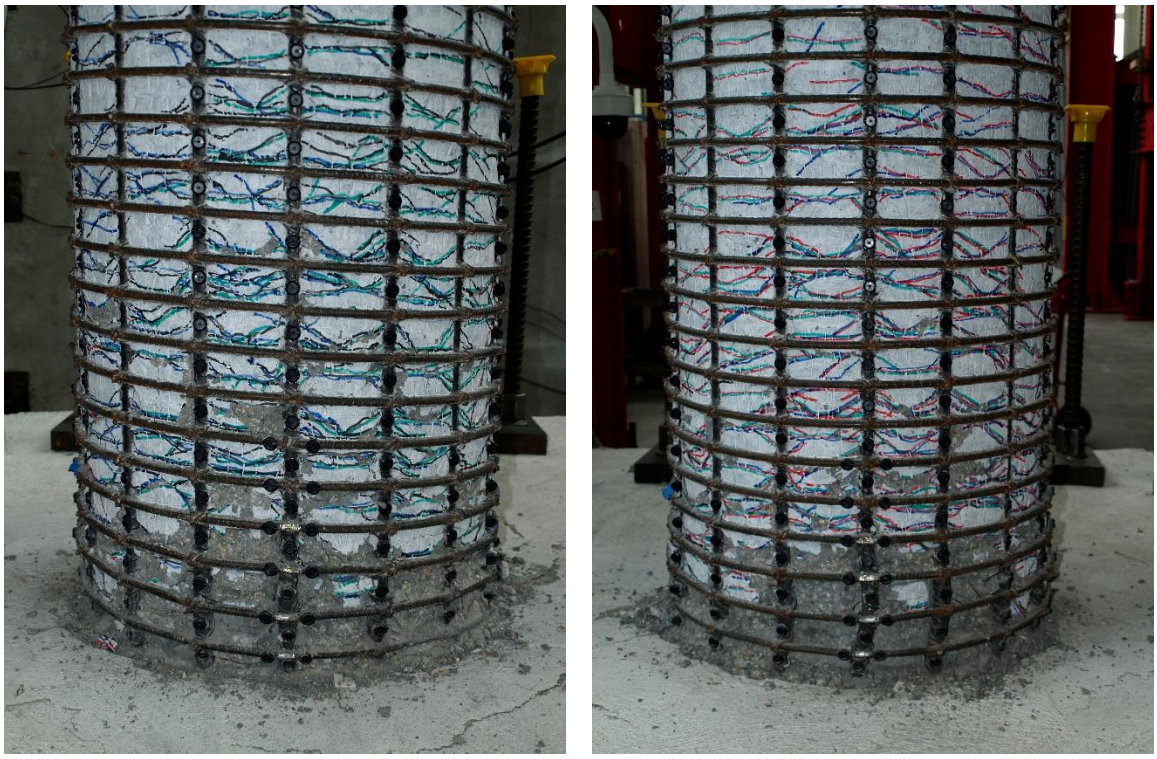

Figure 9-42. Test 6: (Left) North and (Right) South Sides of the Specimen after Instrumentation Removal

Figure 9-43. Test 6: (Left) North and (Right) South Sides of the Specimen after Instrumentation Removal

Figure 9-44. Test 6: (Left) West and (Right) East Sides of the Specimen after Instrumentation Removal

Test 6 - Strain Data Analysis

North and South Bar Strains

Vertical strain profiles for North and South reinforcement during y-direction cycles are shown in Figure 9-45 and Figure 9-46. Strains in the lowest four spiral layers during compressive y-direction cycles on the North and South sides of the specimen appear in Figure 9-47 and Figure 9-48. The relationship between strain and displacement for either peak tensile or peak compressive gauge lengths appear in Figure 9-49 through Figure 9-53. These figures contain monotonic moment curvature predictions for respective plastic hinge methods. PCK (2007) Lp refers to the (Priestley, Calvi and Kowalsky 2007) plastic hinge method, GN15 Tension/Compression Lpr refers to the (Goodnight, Kowalsky and Nau 2015a) unidirectional modified plastic hinge method, TX Measured refer to using the measured extent of plasticity and average equivalent strain penetration length from this specific test, and New Equations refers to a new bidirectional plastic hinge method which was created based on this study. Details of the new plastic hinge method appear in a later chapter of this report.

The spiral strain gauge hysteresis for the second and third layers above the footing on the North side of the specimen are shown in Figure 9-56 and Figure 9-57. The second North spiral layer above the footing went off scale during $\mu_{\Delta 5}^{+1y} = 6.82"$, even though the North reinforcement remained visibly straight as shown in Figure 9-33. Tension strains in the second spiral layer increased during $\mu_{\Delta 5}^{+2y} = 6.87"$ as two North bars visibly buckled, see Figure 9-34. The sharp increase in tension strain in the first two spiral layers during $\mu_{\Delta 5}^{+1y} = 6.82"$, as well as the cycle by cycle increase in spiral

tension strain during $\mu_{\Delta 4}$ in the second spiral layer indicates some level of measurable outward deformation prior to visible buckling. The visual observation of bar buckling was confirmed upon inspection of the North longitudinal bar strain hystereses in Figure 9-54 and Figure 9-55; however, there was significant measurable outward deformation in the previous compressive cycle.

The spiral strain gauge hysteresis for the first and second layers above the footing on the South side of the specimen are shown in Figure 9-60 and Figure 9-61. Tension strains in the first spiral layer increased during $\mu_{\Delta 5}^{-2y} = -6.84$" as the South extreme fiber bar visibly buckled, see Figure 9-34. The strain gauge over the second South spiral layer above the footing went off scale during $\mu_{\Delta 5}^{-1y} = -6.85$", even though the reinforcement remained visibly straight, see Figure 9-33. A similar cycle by cycle increase in the measured spiral tension strain in the second layer was observed during $\mu_{\Delta 4}$. The visual observation of bar buckling was confirmed upon inspection of the South longitudinal bar strain hystereses in Figure 9-58 and Figure 9-59; however, there was significant measurable outward deformation in the previous compressive cycle.

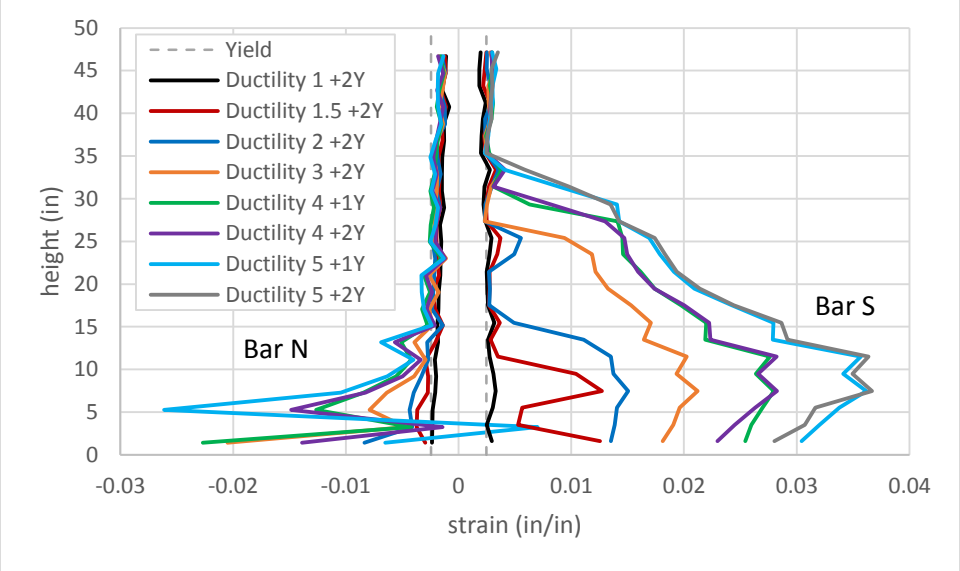

Figure 9-45. Test 6: Vertical Strain Profiles for Loading in the +Y-direction

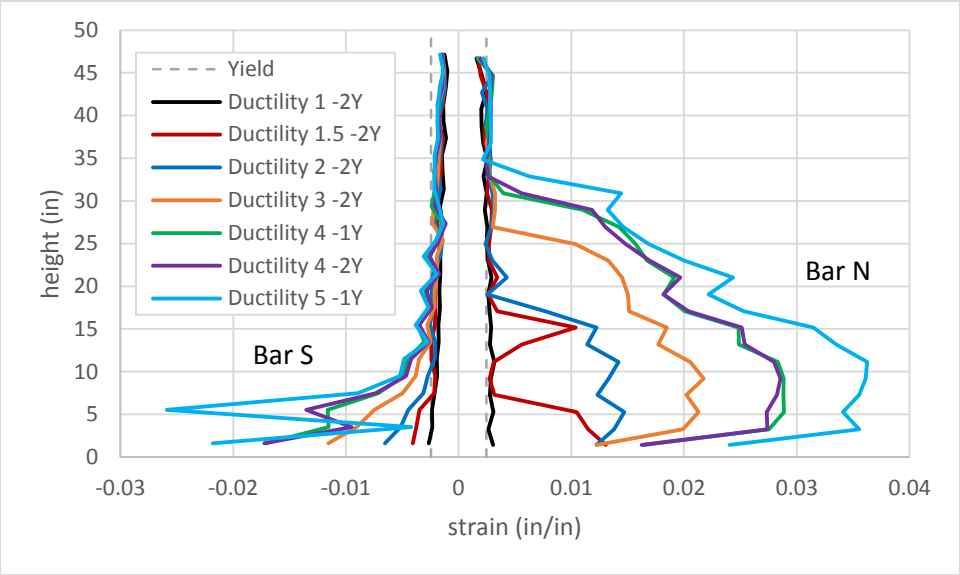

Figure 9-46. Test 6: Vertical Strain Profiles for Loading in the -Y-direction

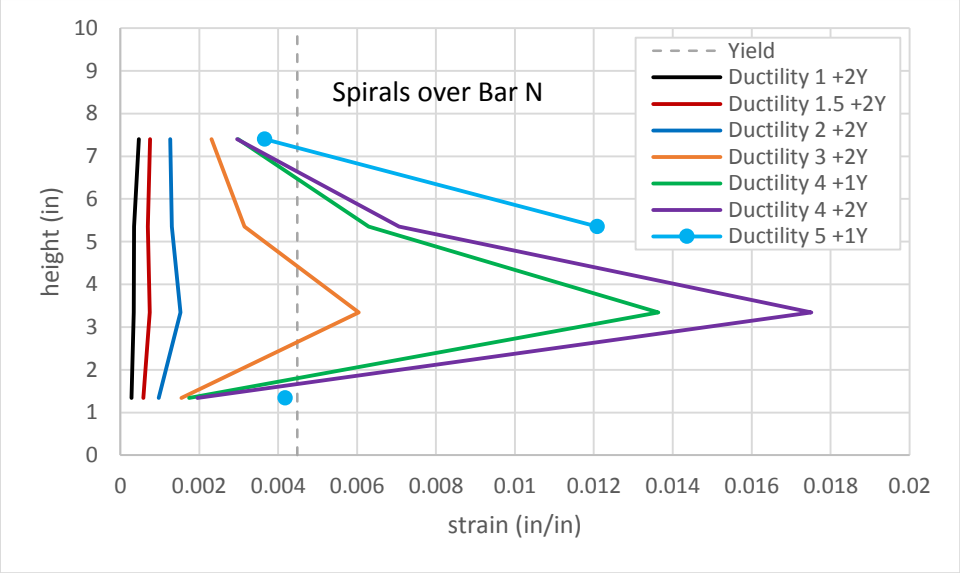

Figure 9-47. Test 6: Spiral Strains Measured Over the North Extreme Fiber Bar during +Y Cycles

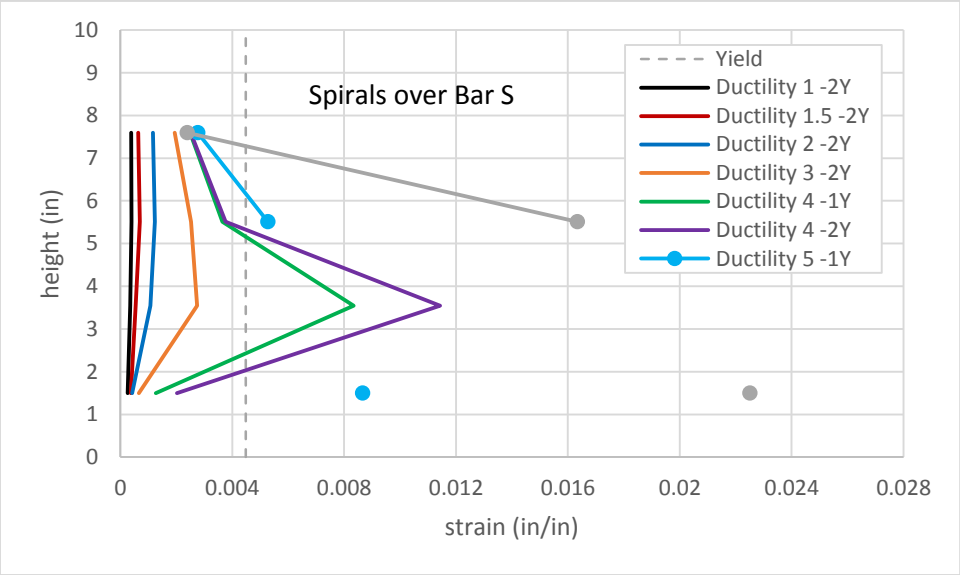

Figure 9-48. Test 6: Spiral Strains Measured Over the South Extreme Fiber Bar during -Y Cycles

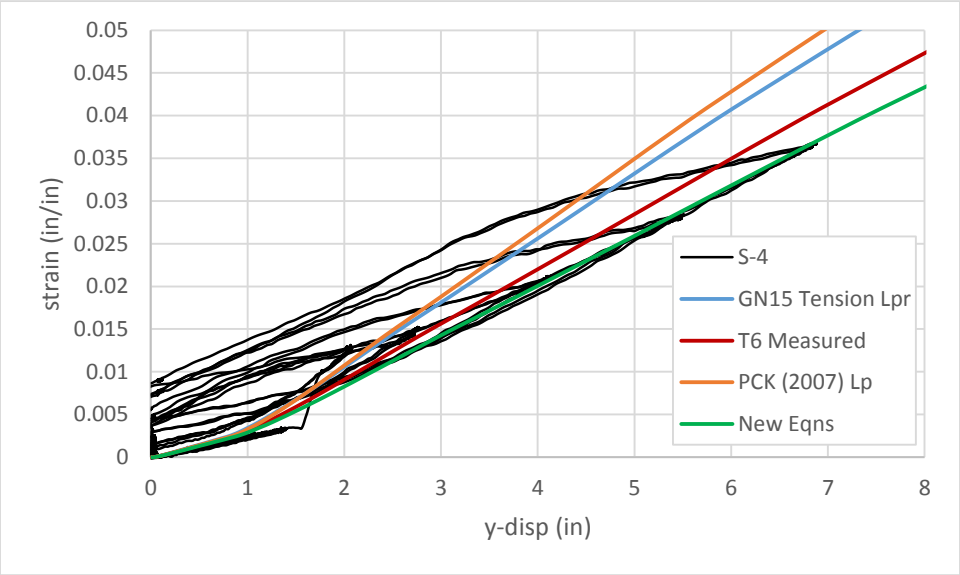

Figure 9-49. Test 6: Tension Strain-Disp. for Bar S (Gauge Length 4 Centered 7.46" above the Footing)

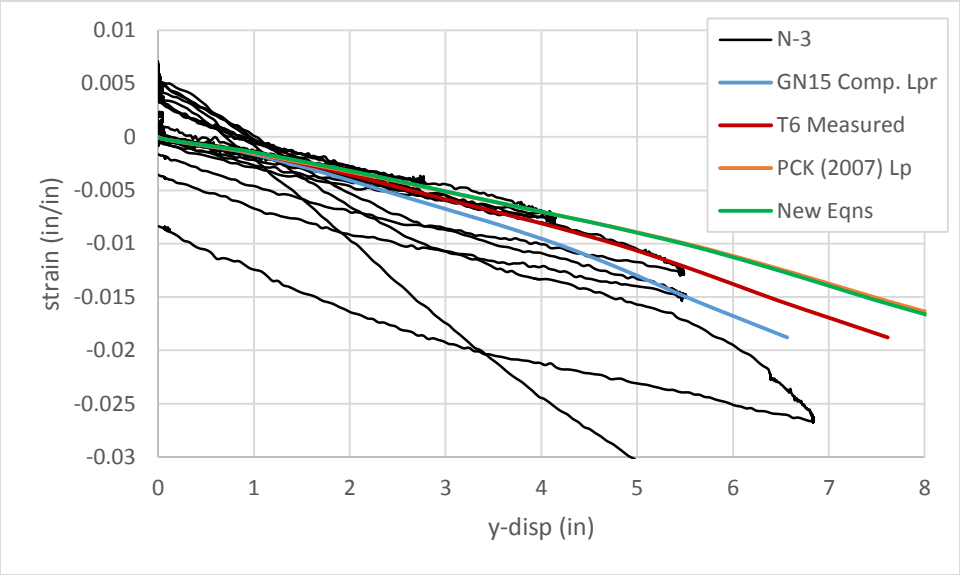

Figure 9-50. Test 6: Compression Strain-Disp. for Bar N (Gauge Length 3 Centered 5.28" above the Footing)

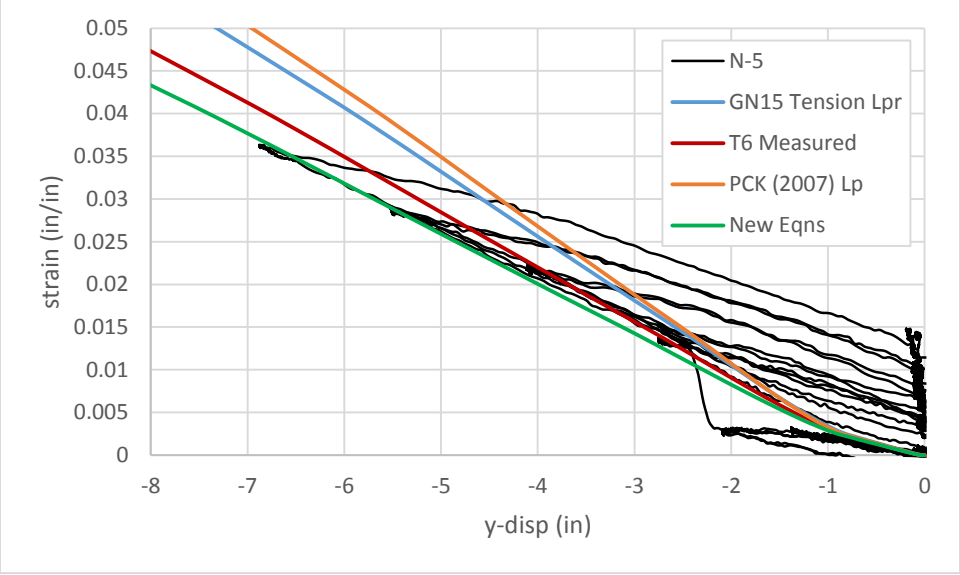

Figure 9-51. Test 6: Tension Strain-Disp. for Bar N (Gauge Length 5 Centered 9.20" above the Footing)

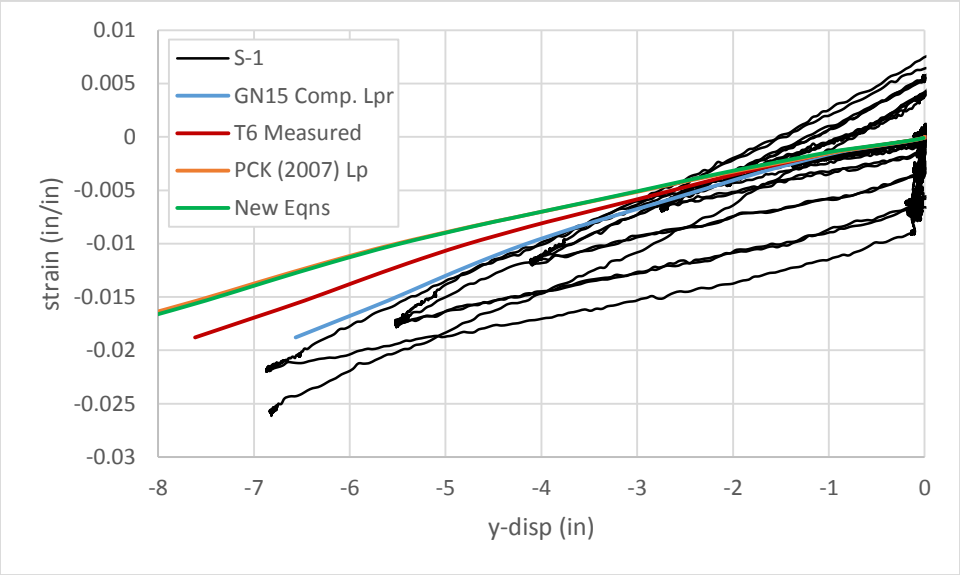

Figure 9-52. Test 6: Compression Strain-Disp. for Bar S (Gauge Length 1 Centered 1.59" above the Footing)

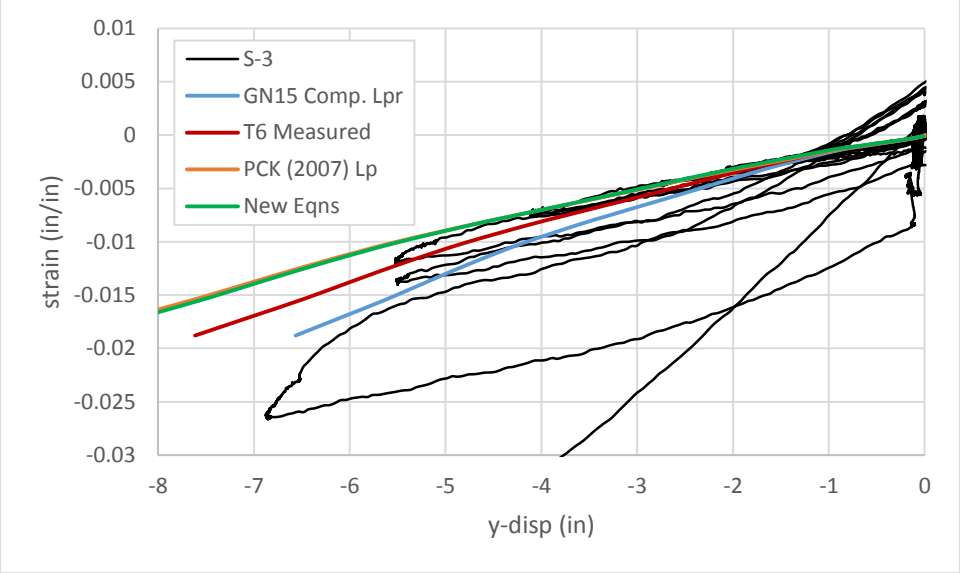

Figure 9-53. Test 6: Compression Strain-Disp. for Bar S (Gauge Length 3 Centered 5.52" above the Footing)

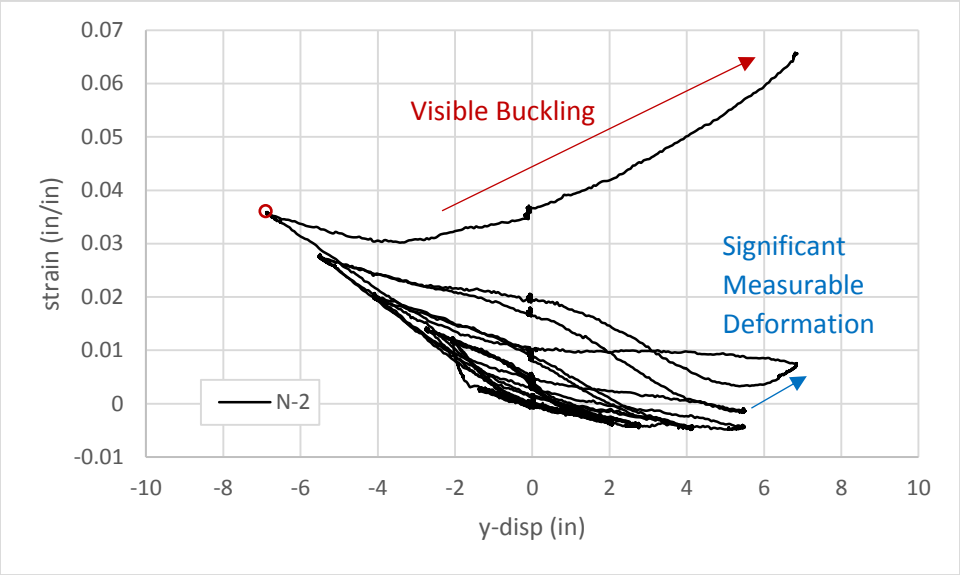

Figure 9-54. Test 6: Strain Hysteresis over the North Buckled Bar (Gauge Length 2 Centered 3.26" above the Footing)

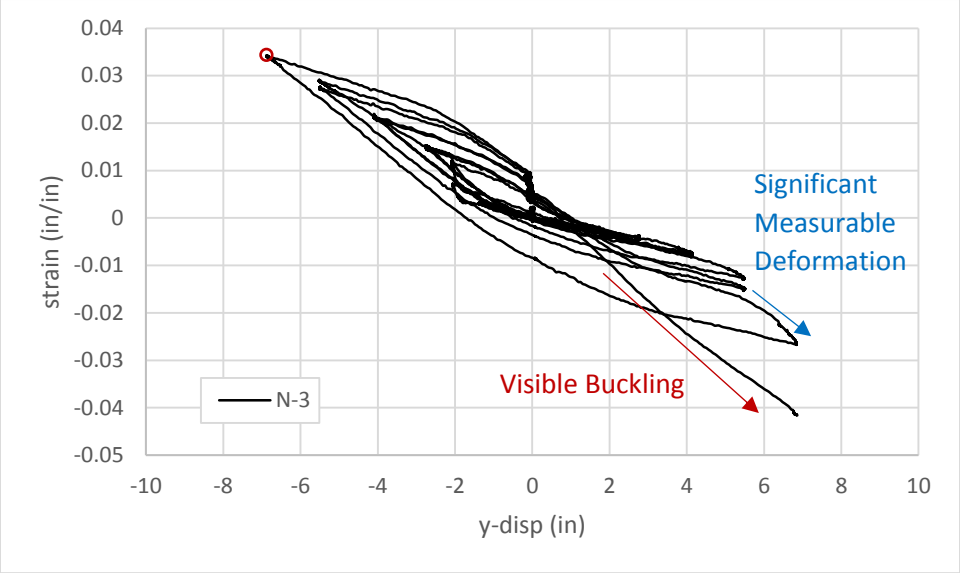

Figure 9-55. Test 6: Strain Hysteresis over the North Buckled Bar (Gauge Length 3 Centered 5.28" above the Footing)

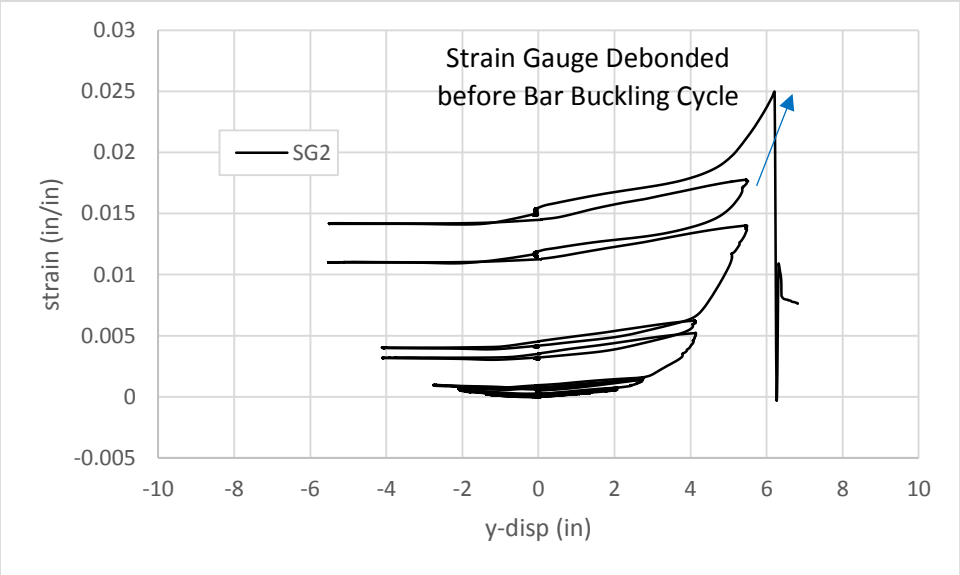

Figure 9-56. Test 6: North Spiral Strain Gauge Hysteresis for the Second Layer above the Footing

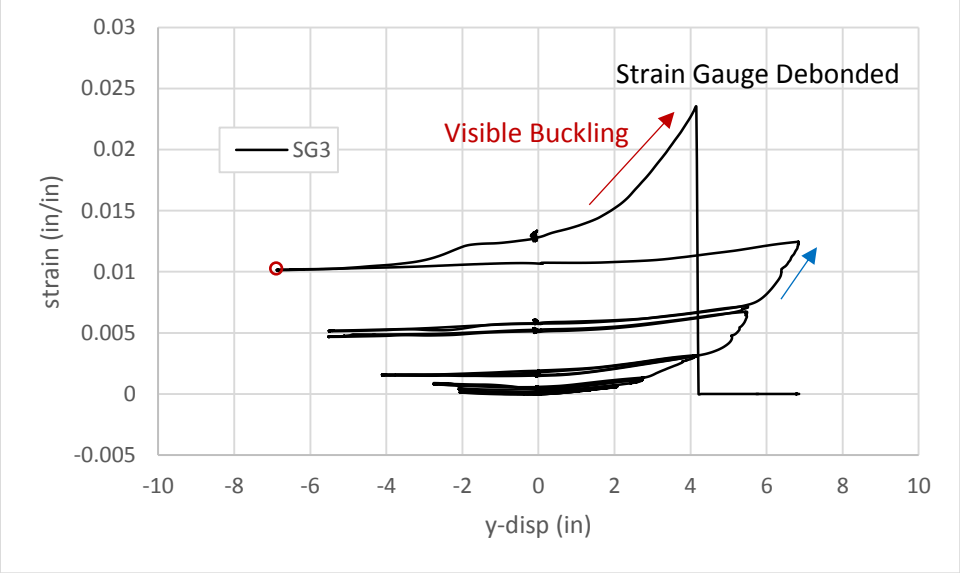

Figure 9-57. Test 6: North Spiral Strain Gauge Hysteresis for the Third Layer above the Footing

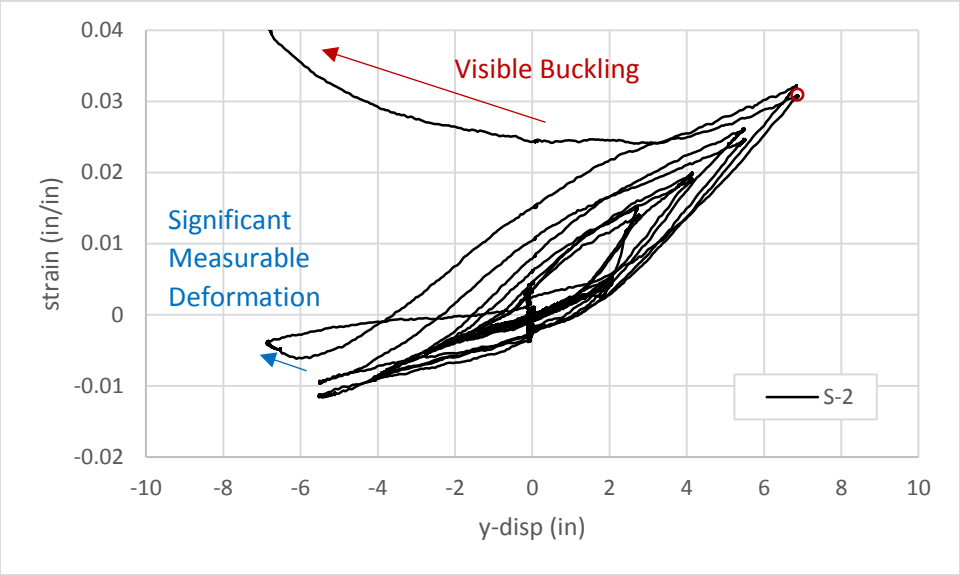

Figure 9-58. Test 6: Strain Hysteresis over the South Buckled Bar (Gauge Length 2 Centered 3.53" above the Footing)

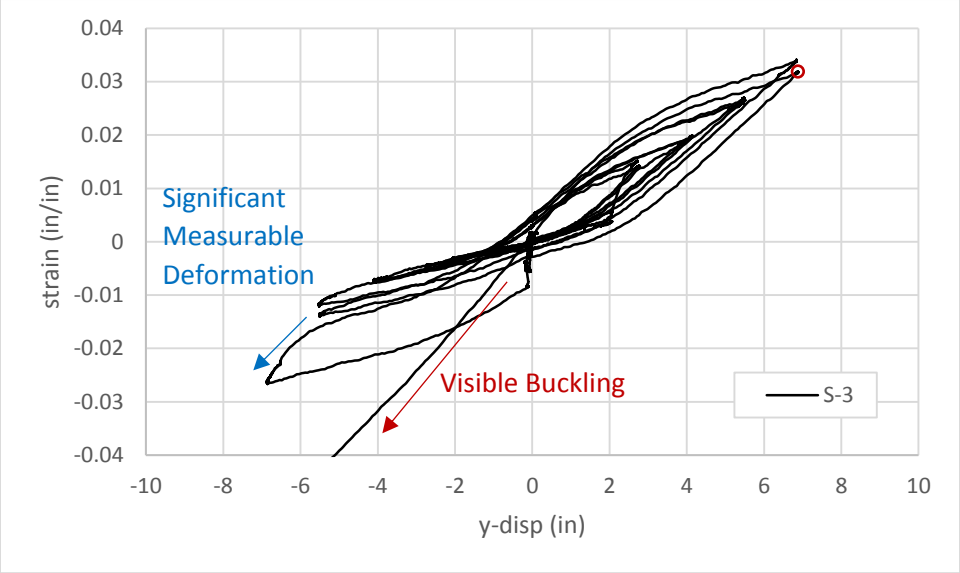

Figure 9-59. Test 6: Strain Hysteresis over the South Buckled Bar (Gauge Length 3 Centered 5.52" above the Footing)

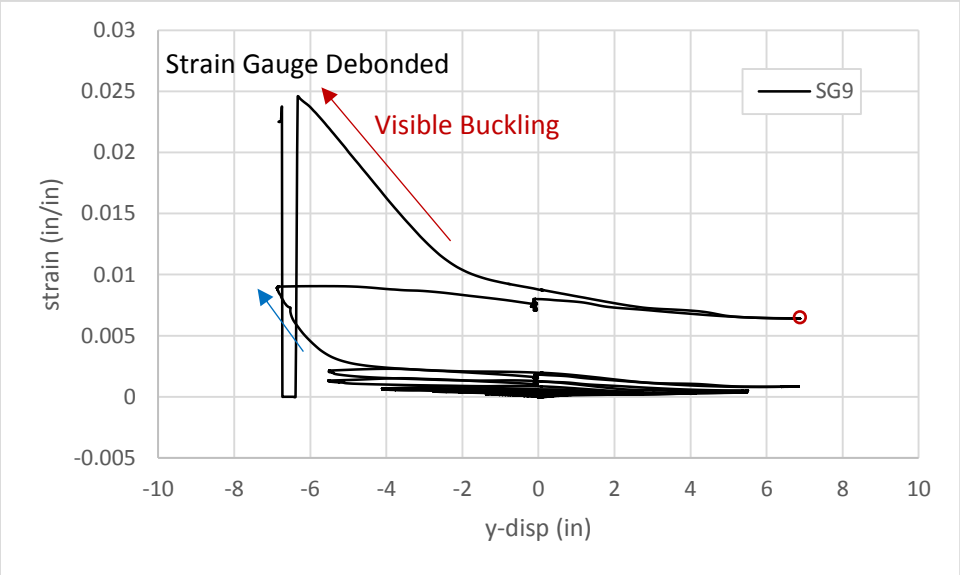

Figure 9-60. Test 6: South Spiral Strain Gauge Hysteresis for the First Layer above the Footing

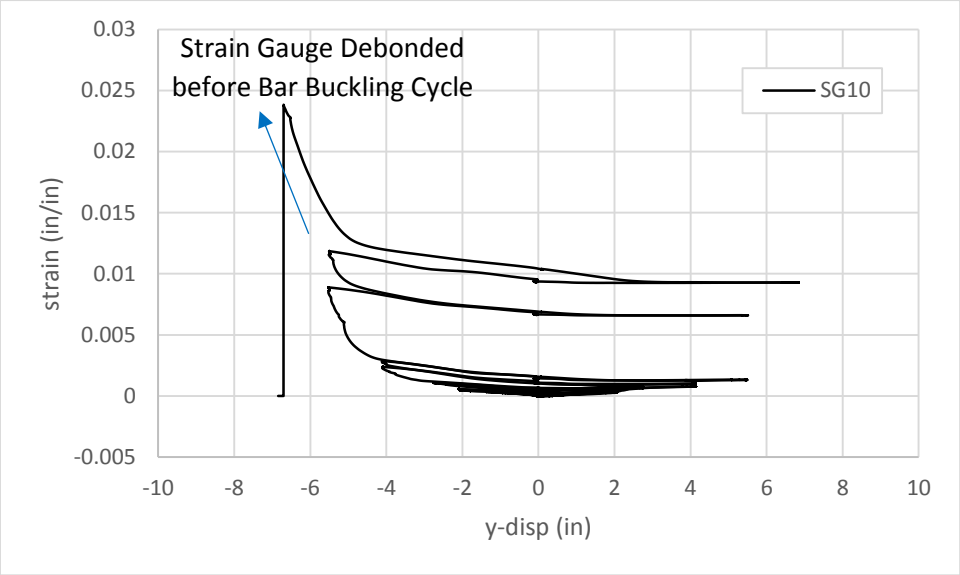

Figure 9-61. Test 6: South Spiral Strain Gauge Hysteresis for the Second Layer above the Footing

East and West Bar Strains

Vertical strain profiles for East and West reinforcement during x-direction cycles are shown in Figure 9-62 and Figure 9-63. Strains in the lowest four spiral layers during compressive x-direction cycles on the East and West sides of the specimen appear in Figure 9-64 and Figure 9-65. The relationship between strain and displacement for either peak tensile or peak compressive gauge lengths appear in Figure 9-66 through Figure 9-70. These figures contain monotonic moment curvature predictions for respective plastic hinge methods. PCK (2007) Lp refers to the (Priestley, Calvi and Kowalsky 2007) plastic hinge method, GN15 Tension/Compression Lpr refers to the (Goodnight, Kowalsky and Nau 2015a) unidirectional modified plastic hinge method, TX Measured refer to using the measured extent of plasticity and average equivalent strain penetration length from this specific test, and New Equations refers to a new bidirectional plastic hinge method which was created based on this study. Details of the new plastic hinge method appear in a later chapter of this report.

Spiral strain gauge and Optotrak strain hysteresis for the first and second East spiral layers above the footing appear in Figure 9-72 and Figure 9-73. The second strain gauge above the footing was not functioning properly, so the Optotrak strains are included. The measured strains in the first spiral match until this layer yielded during $\mu_{\Delta 5}^{+1y} = 6.82$". After spiral yielding the left and right portions of the spiral on either side of the extreme fiber bar begin to straighten out, which influences the measured arc-strains computed over the approximate 2" Optotrak gauge length. Tension strains in the first East spiral layer increased during successive $\mu_{\Delta 5}$ cycles, even though the reinforcement remained visibly straight at $\mu_{\Delta 5}^{+2x} = 6.84$", see Figure 9-37. Both spiral layers had a spike in measured tension strains during $\mu_{\Delta 6}^{+1x} = 8.21$" as three East bars buckled simultaneously, see Figure 9-39. The visual observation of bar buckling was confirmed upon inspection of the East longitudinal bar strain hystereses in Figure 9-71.

The spiral strain gauge hysteresis for the first and second layers above the footing on the West side of the specimen are shown in Figure 9-76 and Figure 9-77. Both spiral layers went off scale during $\mu_{\Delta 5}^{-2x} = -6.84$", even through the West reinforcement remained visibly straight, see Figure 9-37. The visual observation of bar buckling was confirmed upon inspection of the East longitudinal bar strain hystereses in Figure 9-74 and Figure 9-75; however, there was significant measurable outward deformation in the previous compressive cycle.

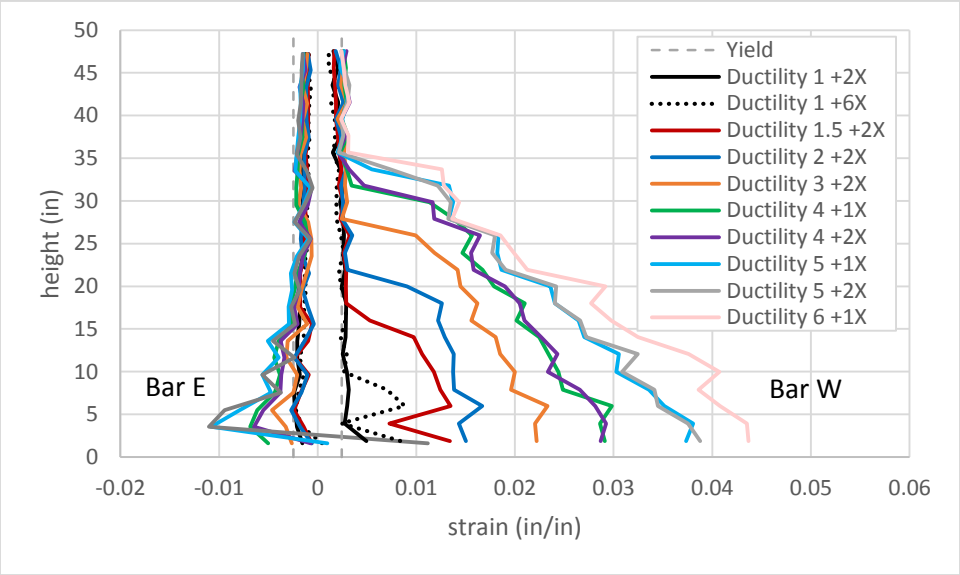

Figure 9-62. Test 6: Vertical Strain Profiles for Loading in the +X-direction

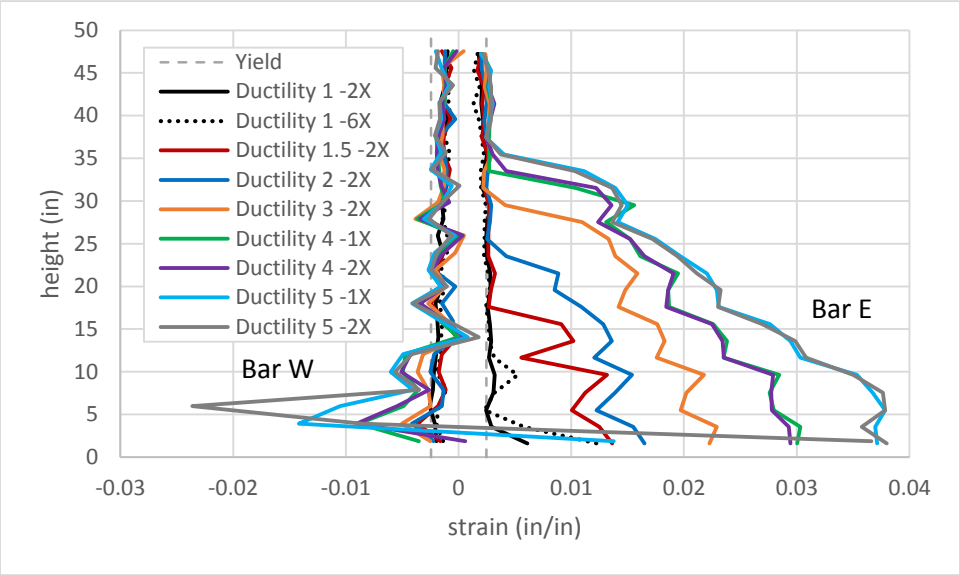

Figure 9-63. Test 6: Vertical Strain Profiles for Loading in the -X-direction

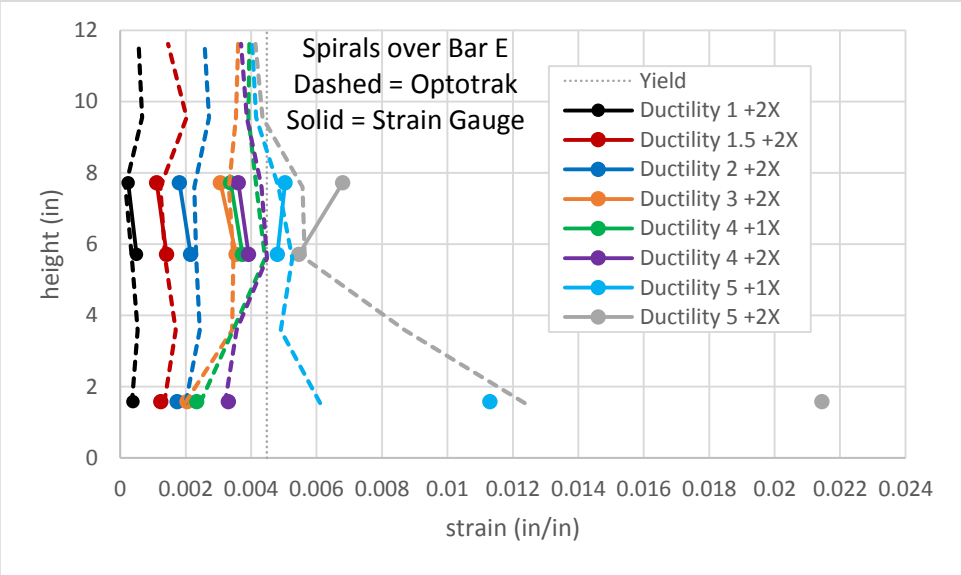

Figure 9-64. Test 6: Spiral Strains Measured Over the East Extreme Fiber Bar during +X Cycles

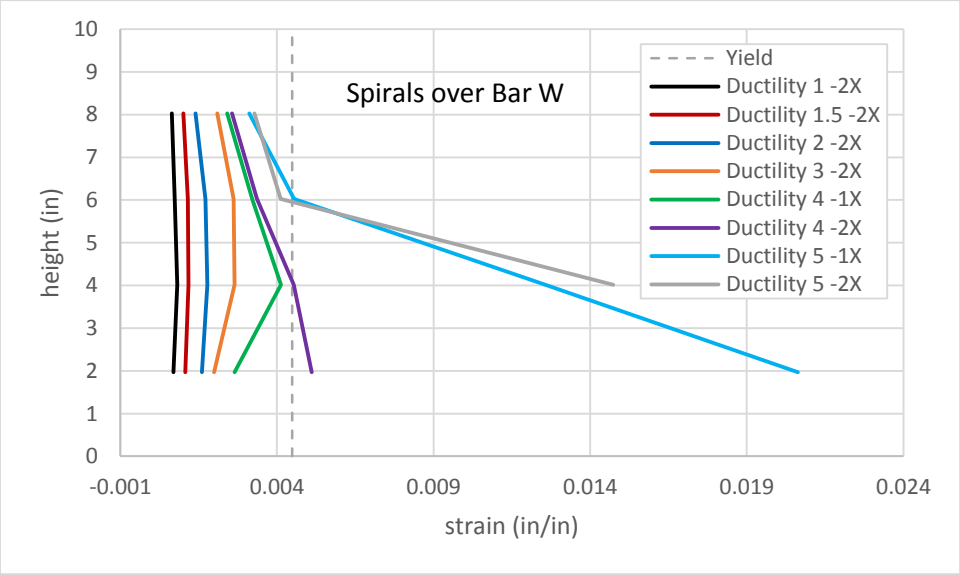

Figure 9-65. Test 6: Spiral Strains Measured Over the West Extreme Fiber Bar during -X Cycles

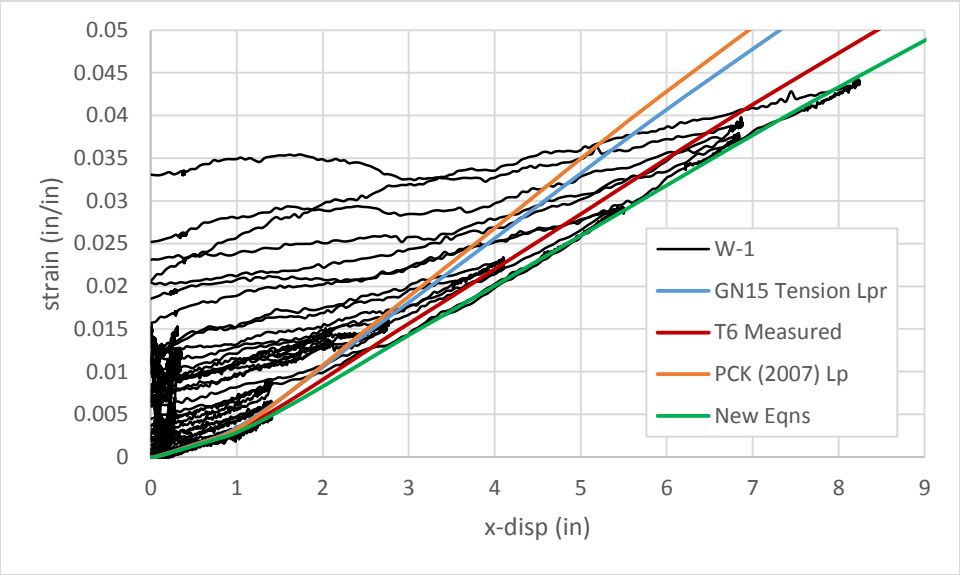

Figure 9-66. Test 6: Tension Strain-Disp. for Bar W (Gauge Length 1 Centered 1.88" above the Footing)

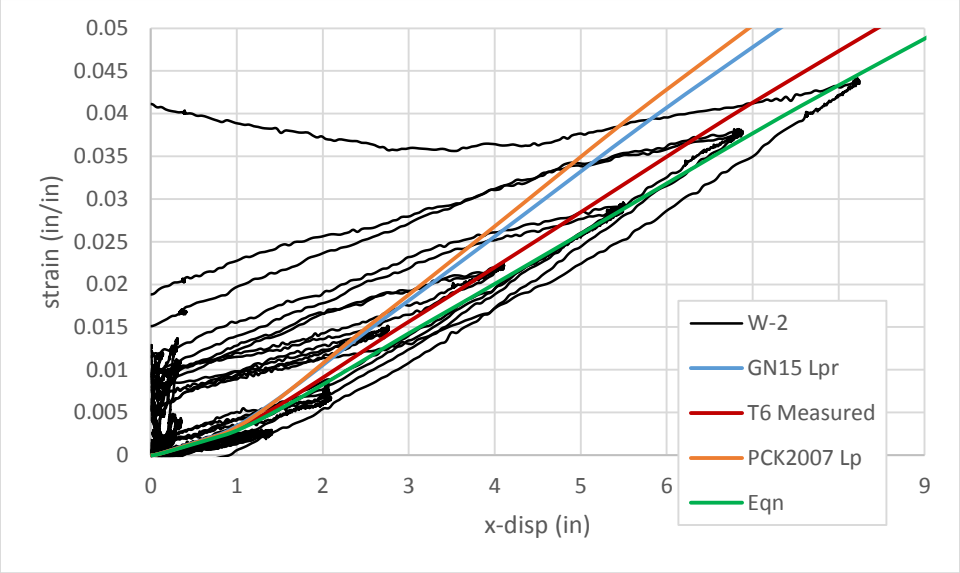

Figure 9-67. Test 6: Tension Strain-Disp. for Bar W (Gauge Length 2 Centered 3.92" above the Footing)

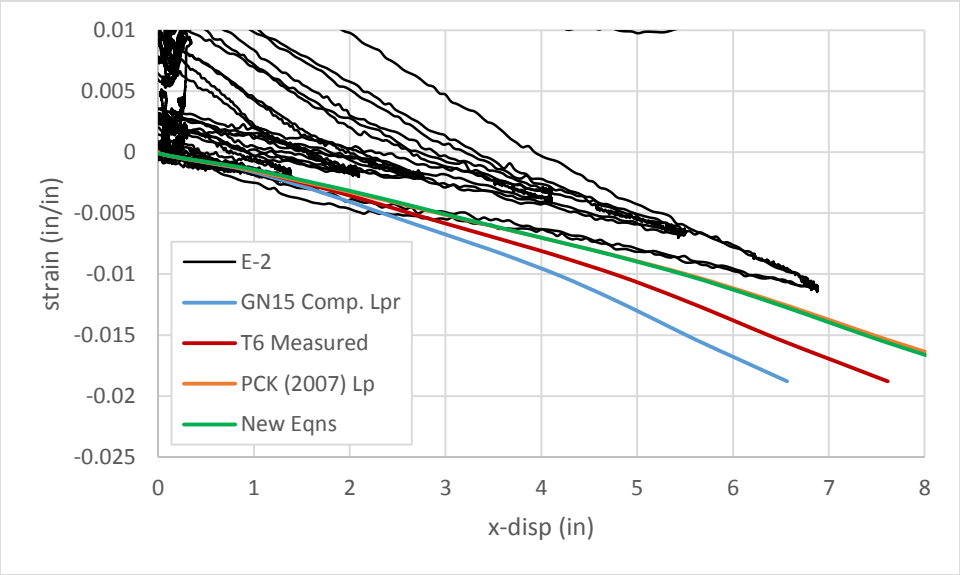

Figure 9-68. Test 6: Compression Strain-Disp. for Bar E (Gauge Length 2 Centered 3.54" above the Footing)

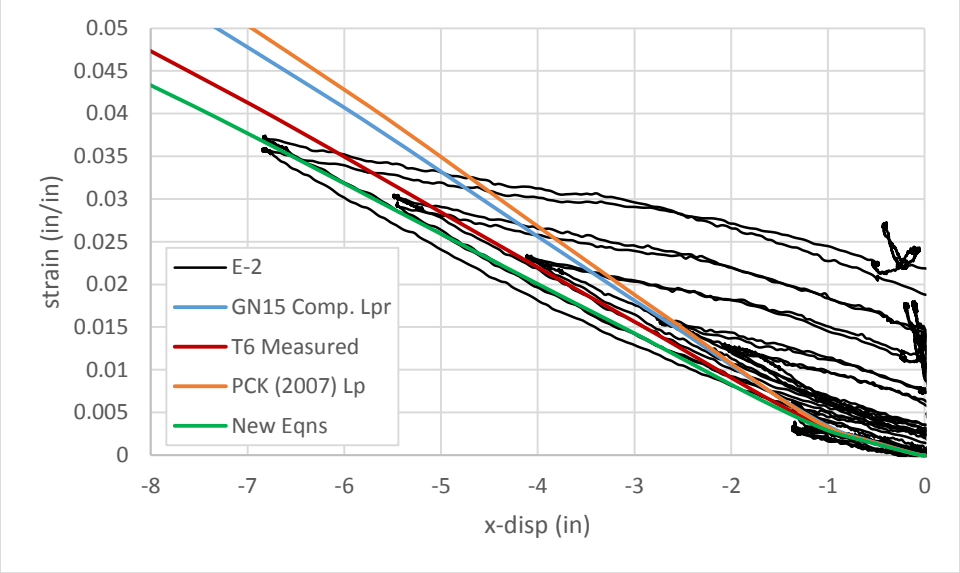

Figure 9-69. Test 6: Tension Strain-Disp. for Bar E (Gauge Length 2 Centered 3.54" above the Footing)

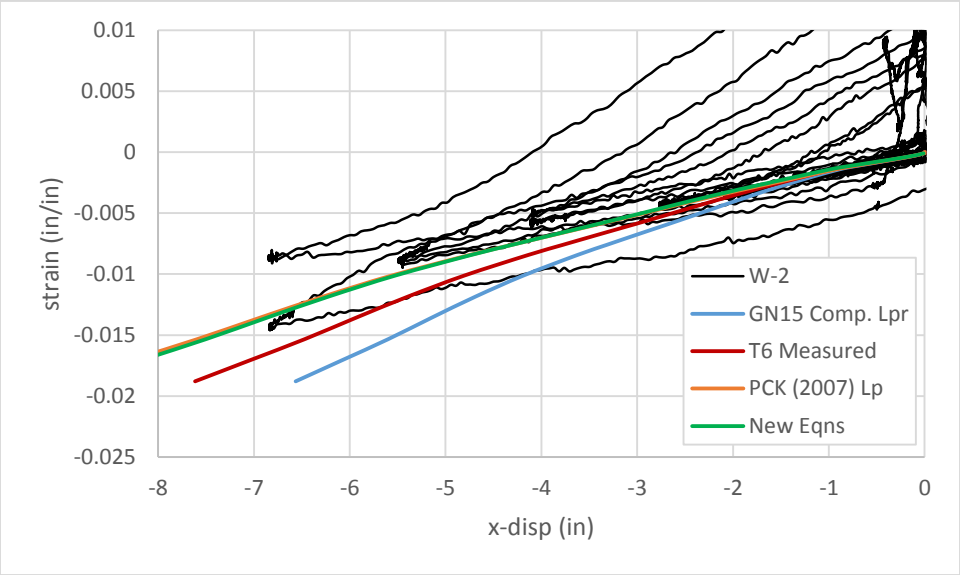

Figure 9-70. Test 6: Compression Strain-Disp. for Bar W (Gauge Length 2 Centered 3.92" above the Footing)

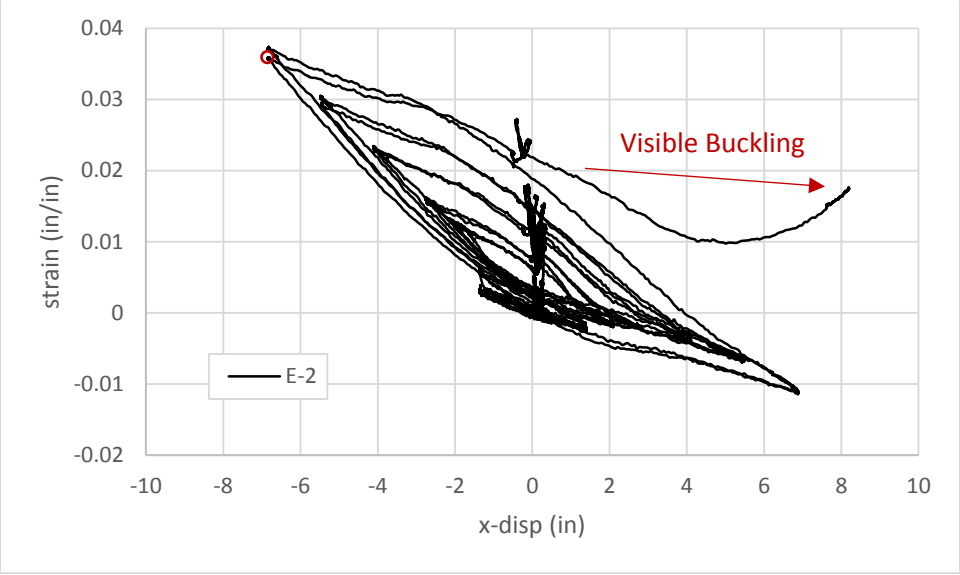

Figure 9-71. Test 6: Strain Hysteresis over the East Buckled Bar (Gauge Length 2 Centered 3.54" above the Footing)

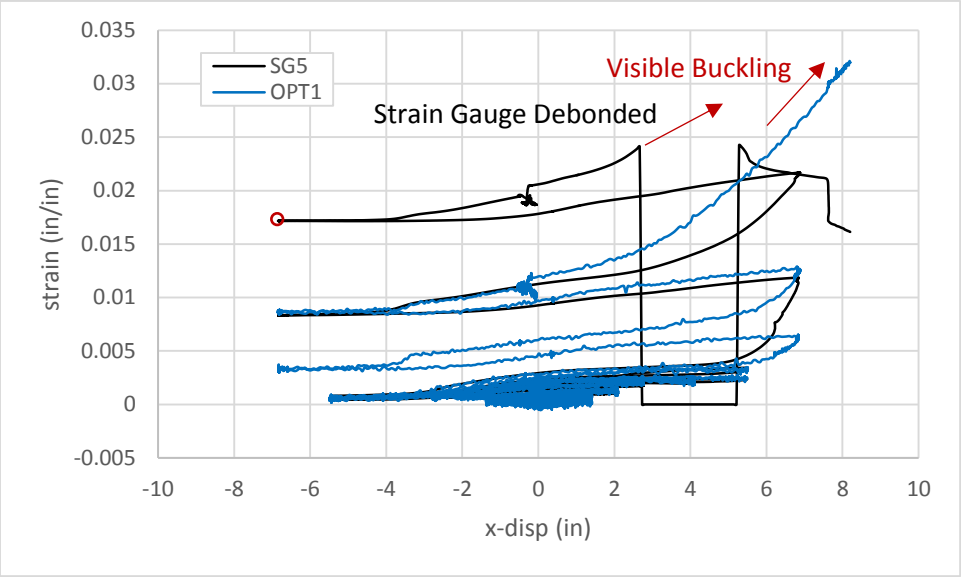

Figure 9-72. Test 6: East Spiral Strain Gauge (Black) and Optotrak (Blue) Hysteresis for the First Layer above the Footing

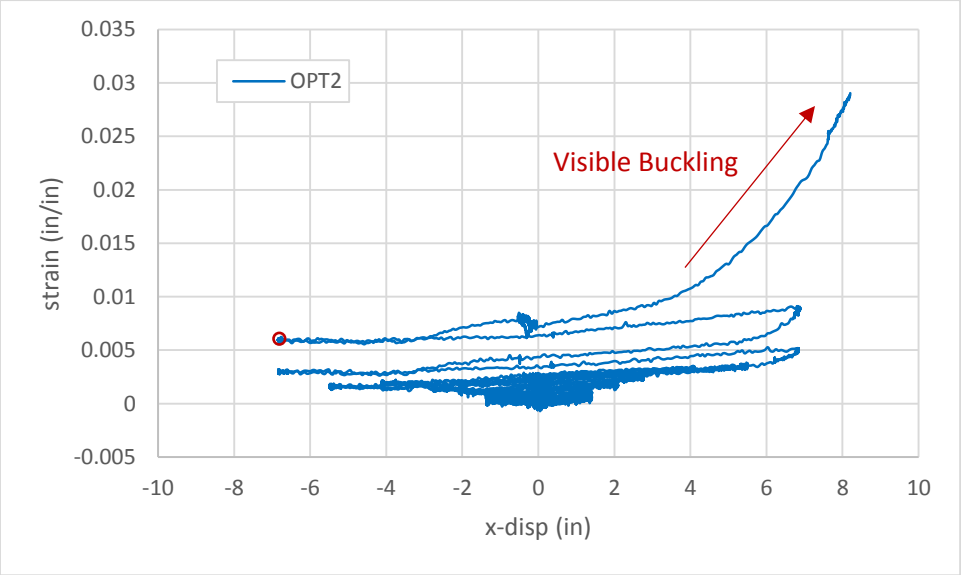

Figure 9-73. Test 6: East Spiral Optotrak Strain Hysteresis for the Second Layer above the Footing

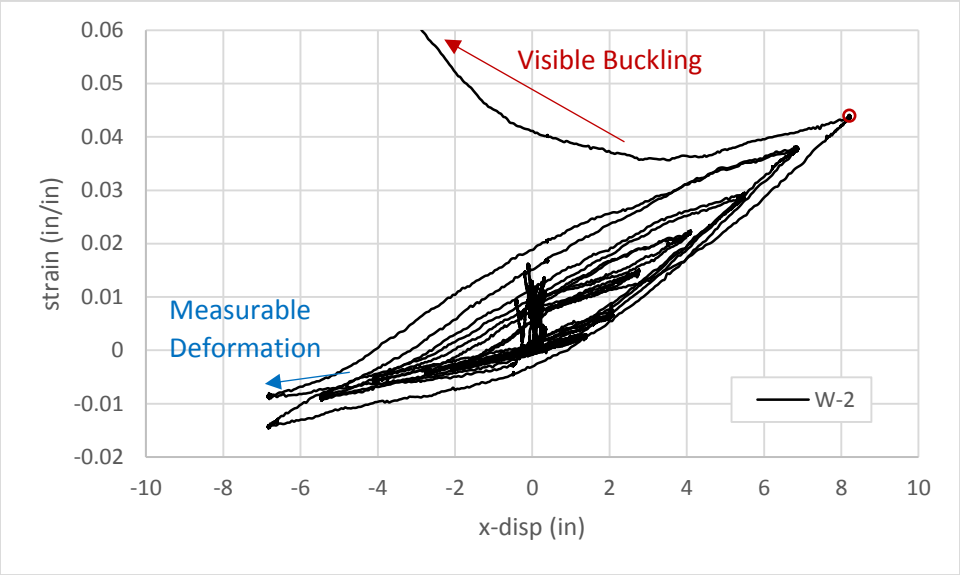

Figure 9-74. Test 6: Strain Hysteresis over the West Buckled Bar (Gauge Length 2 Centered 3.92" above the Footing)

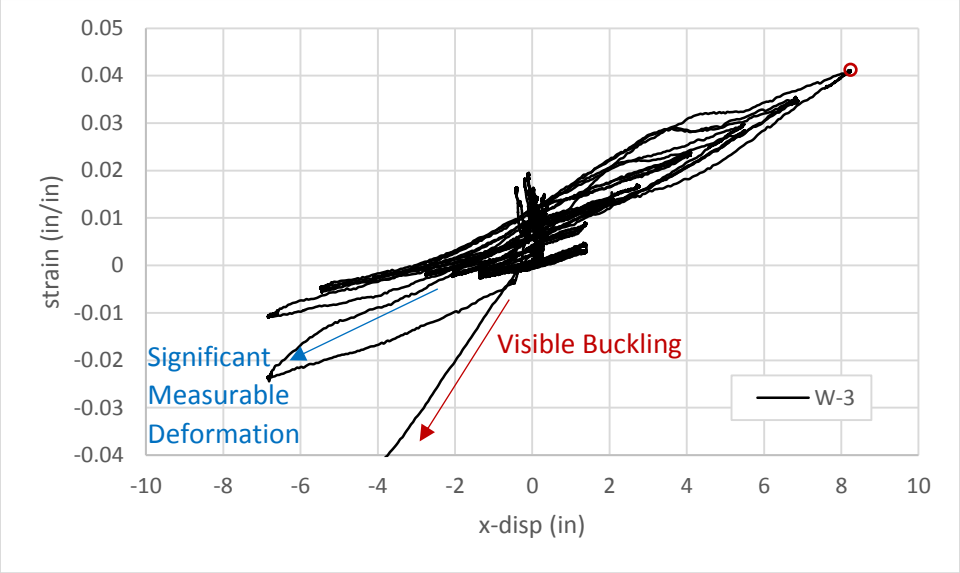

Figure 9-75. Test 6: Strain Hysteresis over the West Buckled Bar (Gauge Length 3 Centered 5.99" above the Footing)

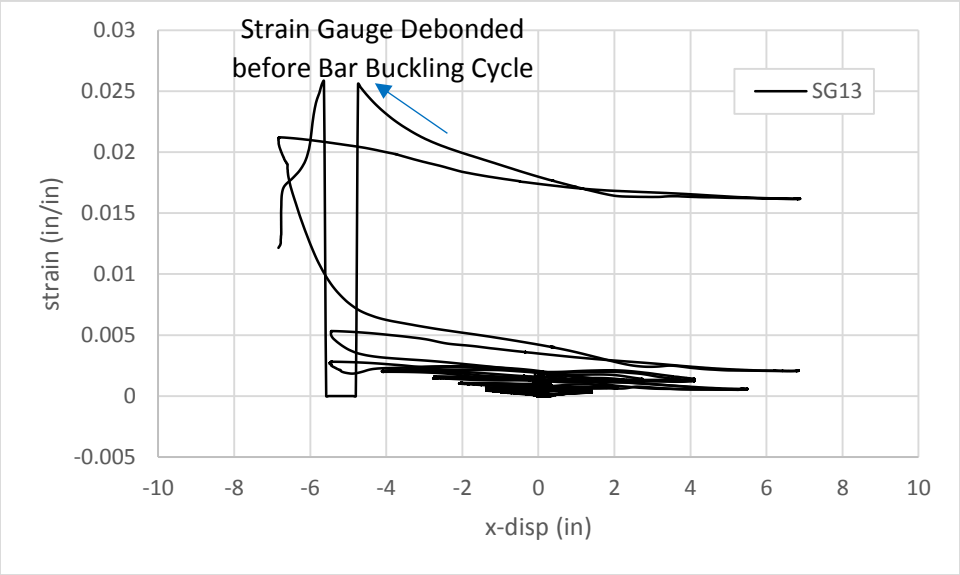

Figure 9-76. Test 6: West Spiral Strain Gauge Hysteresis for the First Layer above the Footing

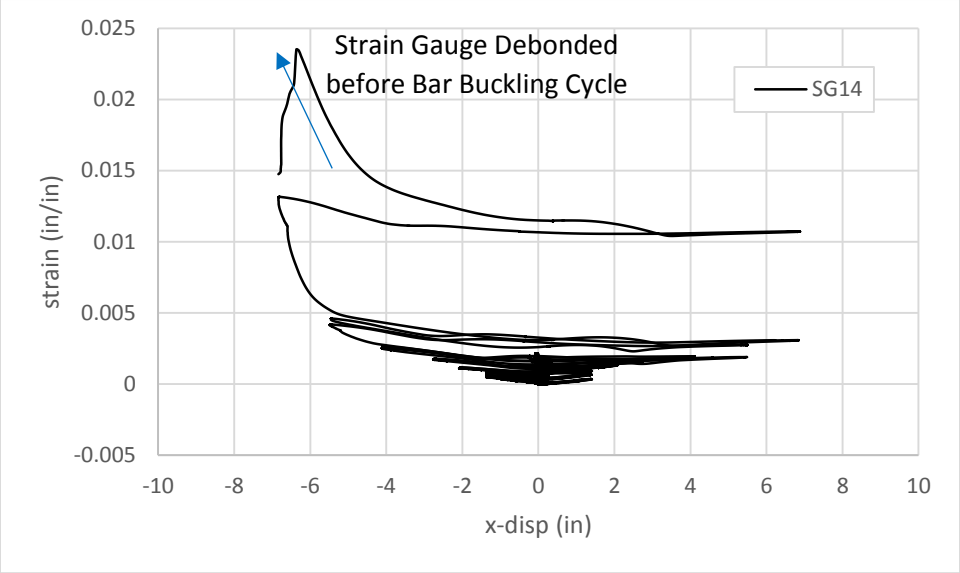

Figure 9-77. Test 6: West Spiral Strain Gauge Hysteresis for the Second Layer above the Footing

Test 6 - Curvature and Strain Penetration Data

Curvature and stain penetration data for Test 6 is presented in the following section. The methods in which this data was generated are outlined in the summary for Test 1. Sample cross section curvature profiles are shown in Figure 9-78 and Figure 9-79. Vertical curvature profiles for respective loading directions appear in Figure 9-80 through Figure 9-84. Fixed-end rotations attributable to strain penetration of longitudinal reinforcement into the footing are shown in Figure 9-85 through Figure 9-87. Comparison of the measured displacements to those obtained via integration of the measured curvature profiles and extrapolation of the fixed-end rotation to the center of the applied lateral load are shown in Figure 9-88 and Figure 9-89.

The measured extent of plasticity is compared to design recommendations for the tensile triangular plastic hinge length in Figure 9-90. GN15 refers to the (Goodnight, Kowalsky and Nau 2015a) unidirectional tensile hinge length while New Equations refers to a new bidirectional plastic hinge method which was created based on this study. Details of the new plastic hinge method appear in a later chapter of this report. The measured equivalent strain penetration lengths are compared to design recommendations in Figure 9-91. GN15 refers to the (Goodnight, Kowalsky and Nau 2015a) unidirectional Lsp while PCK (2007) refers to the (Priestley, Calvi and Kowalsky 2007) definition of Lsp. Finally, the measured hysteretic response is compared to monotonic predictions in Figure 9-92 and Figure 9-93.

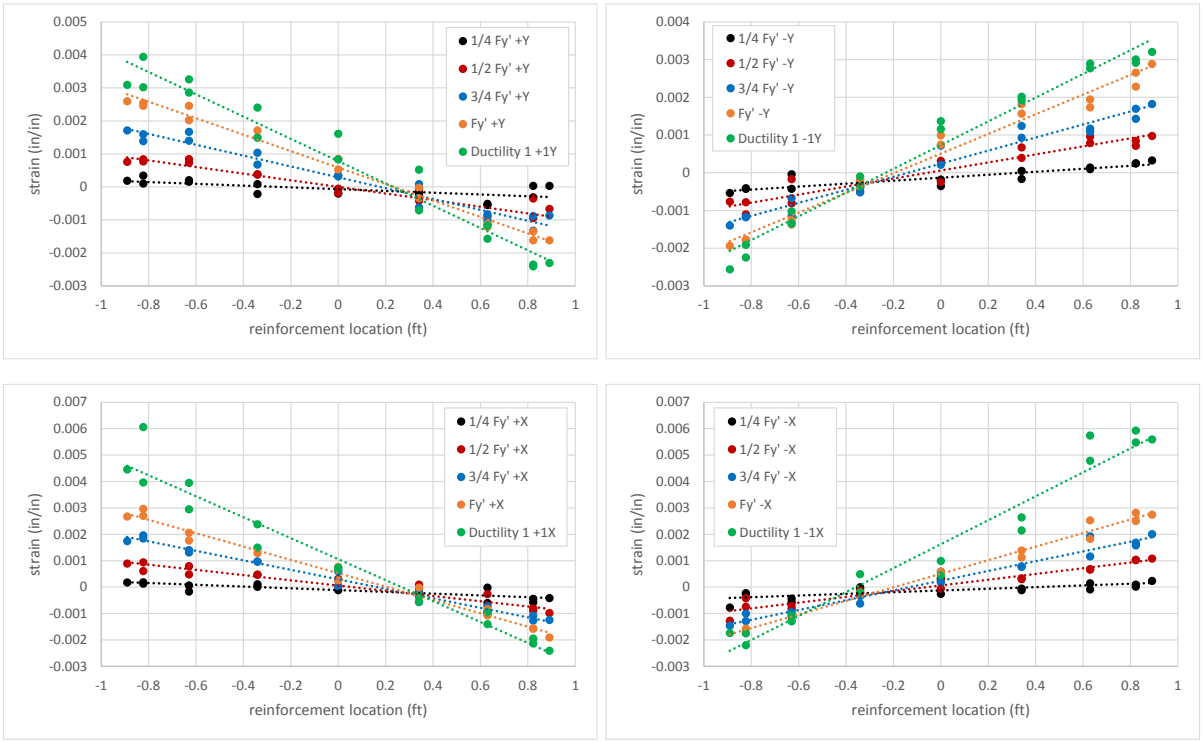

Figure 9-78. Test 6: Elastic Curvature Profiles for the First Instrumented Section above the Footing

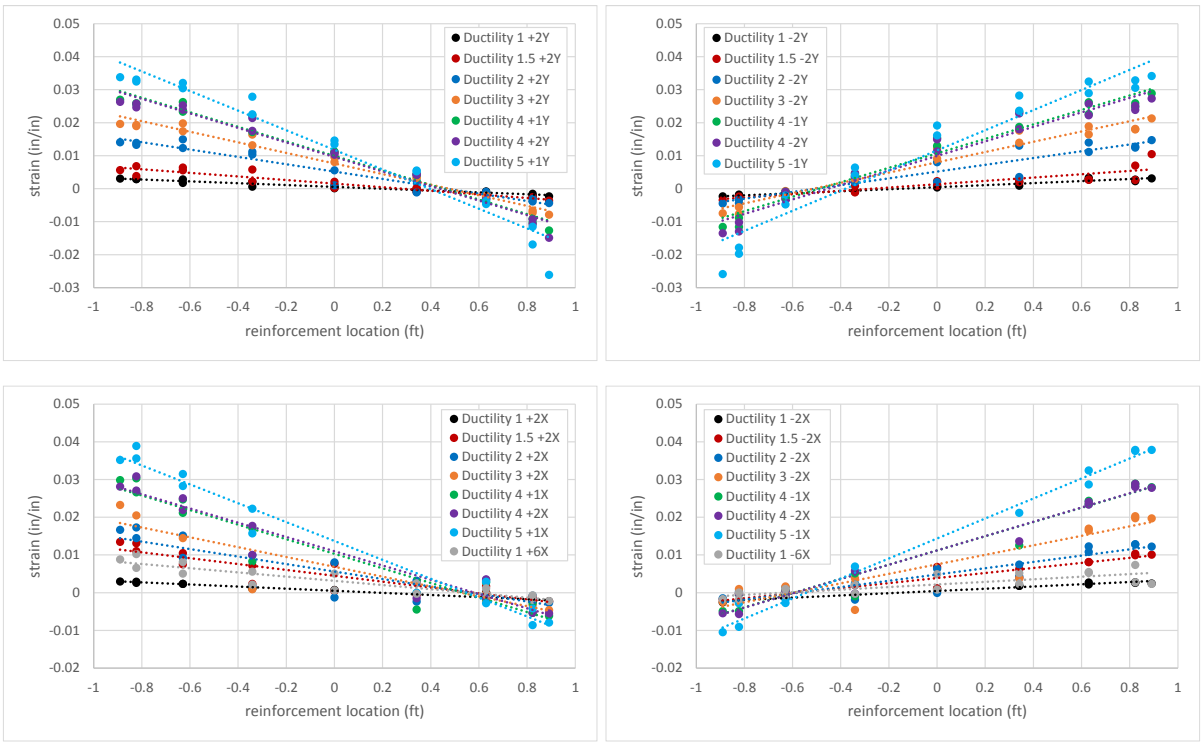

Figure 9-79. Test 6: Curvature Profiles for the Third Instrumented Section above the Footing

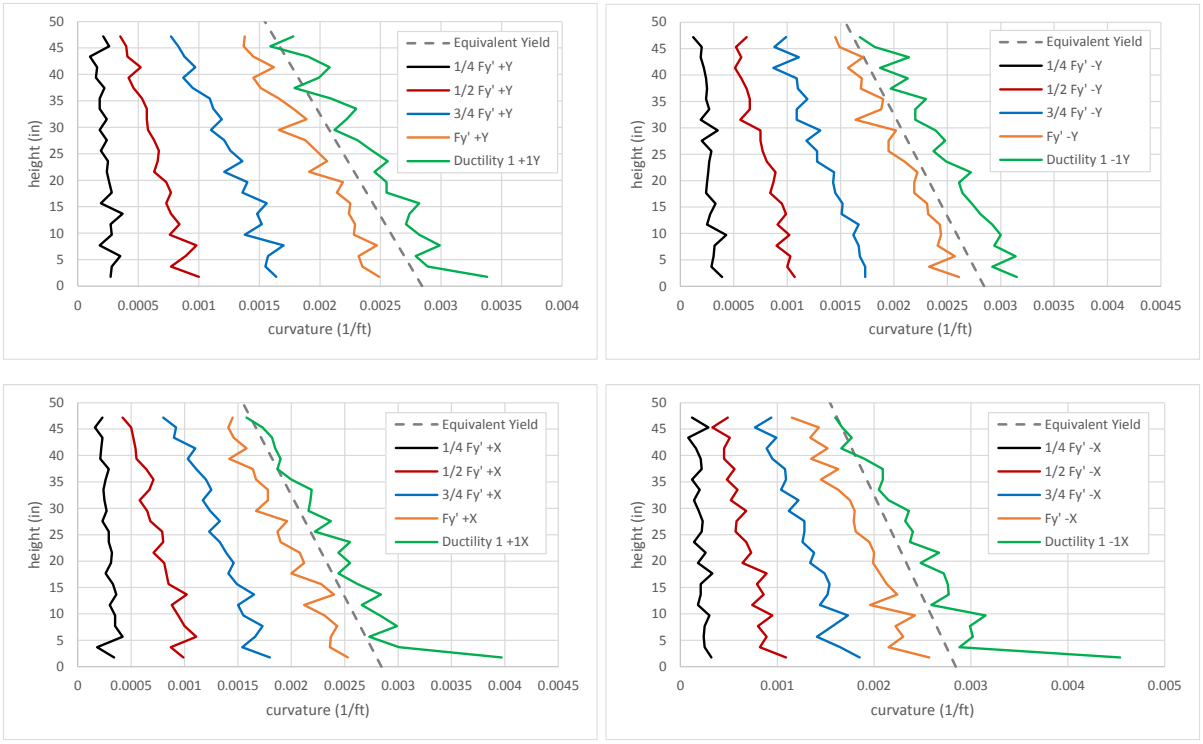

Figure 9-80. Test 6: Elastic Vertical Curvature Profiles

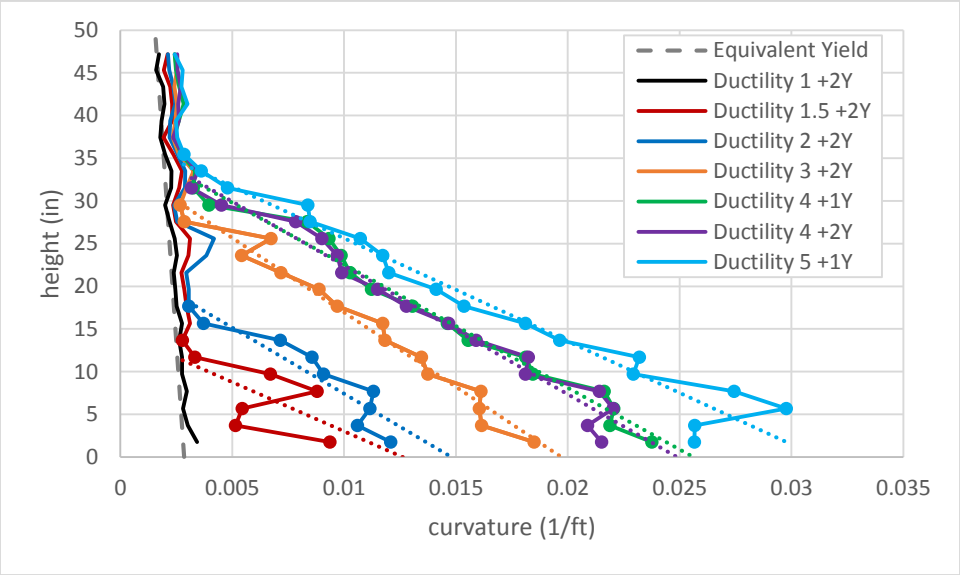

Figure 9-81. Test 6: Vertical Curvature Profiles for Loading in the +Y-direction

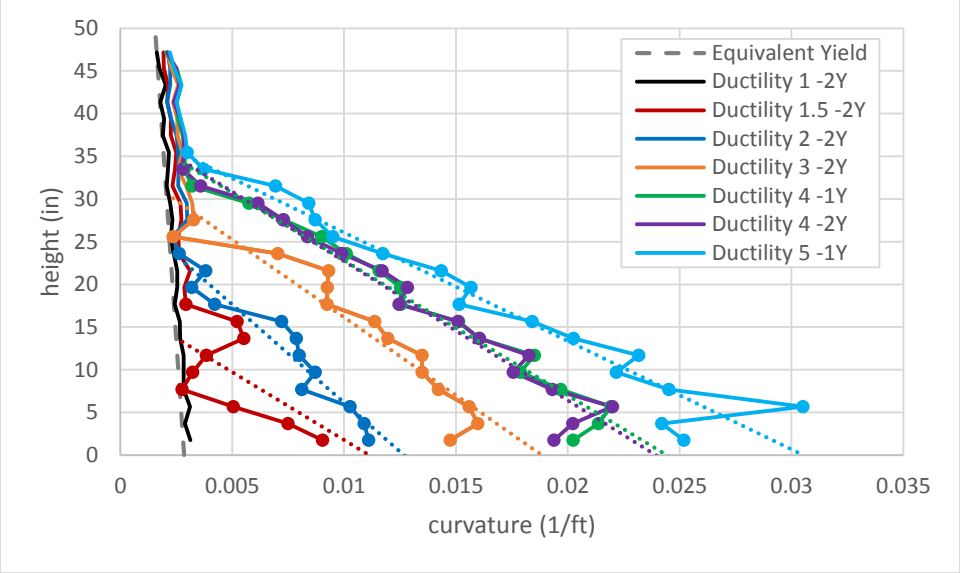

Figure 9-82. Test 6: Vertical Curvature Profiles for Loading in the -Y-direction

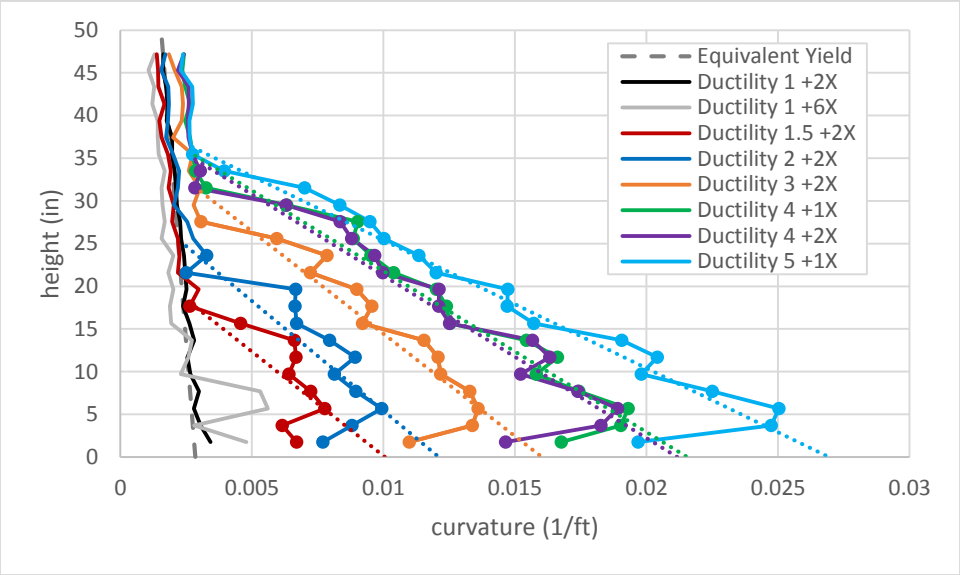

Figure 9-83. Test 6: Vertical Curvature Profiles for Loading in the +X-direction

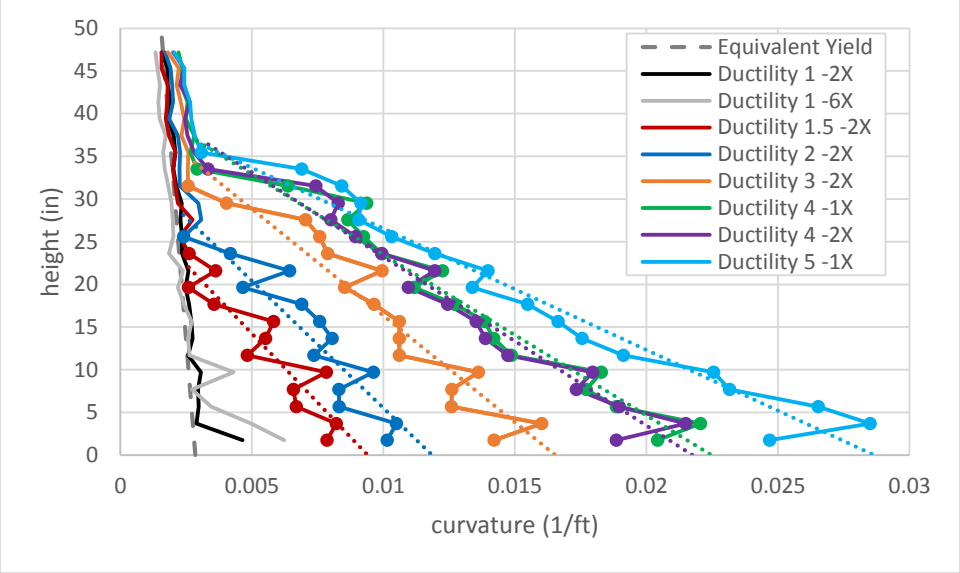

Figure 9-84. Test 6: Vertical Curvature Profiles for Loading in the -X-direction

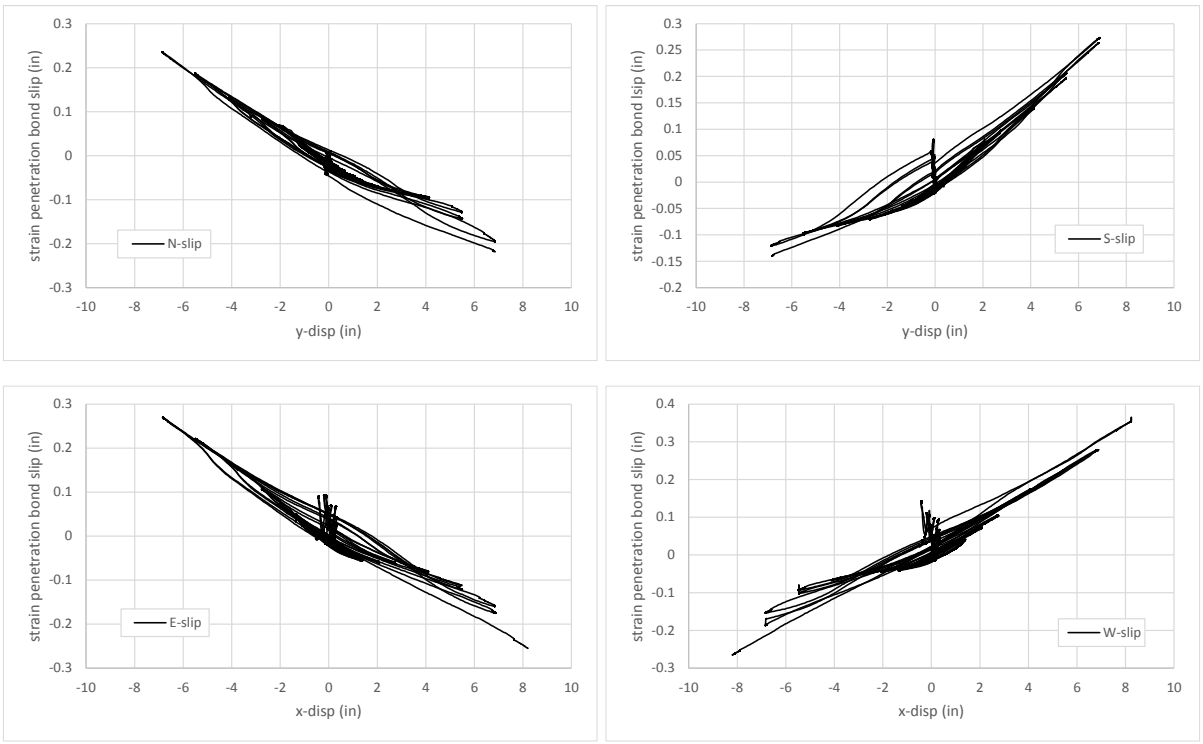

Figure 9-85. Test 6: Extreme Fiber Bar Strain Penetration Bond Slip Hysteresis

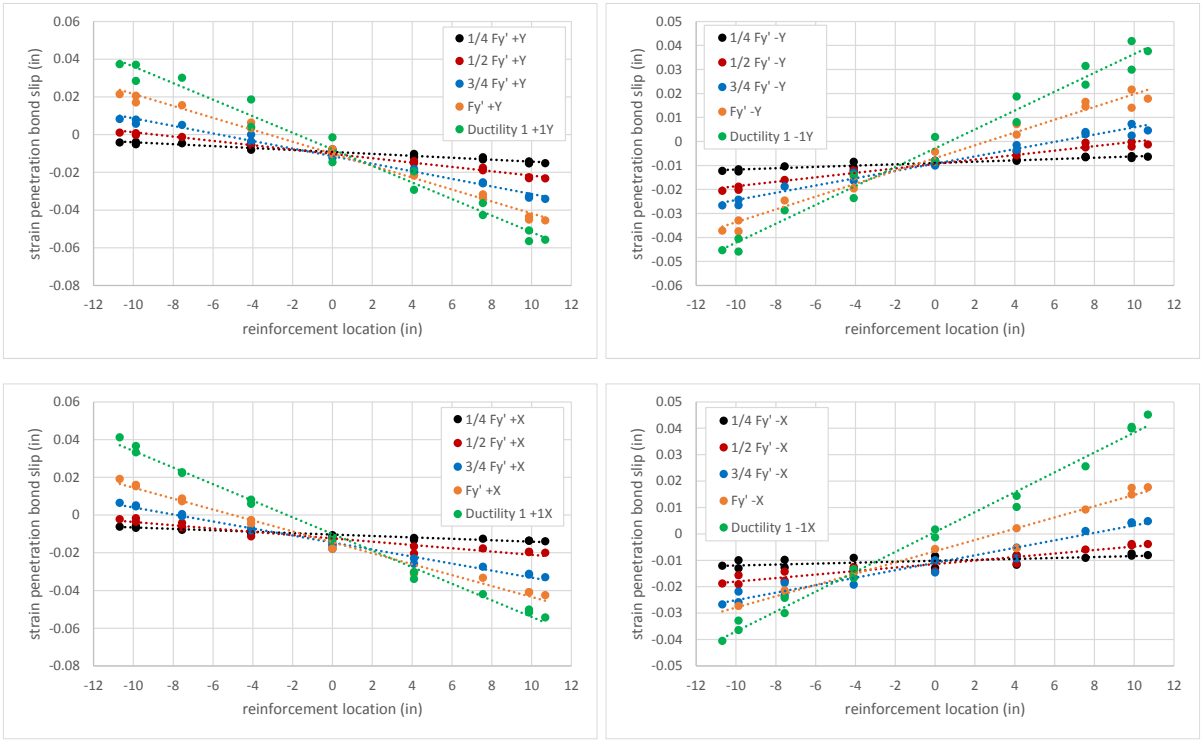

Figure 9-86. Test 6: Fixed End Rotations due to Strain Penetration during the Elastic Cycles

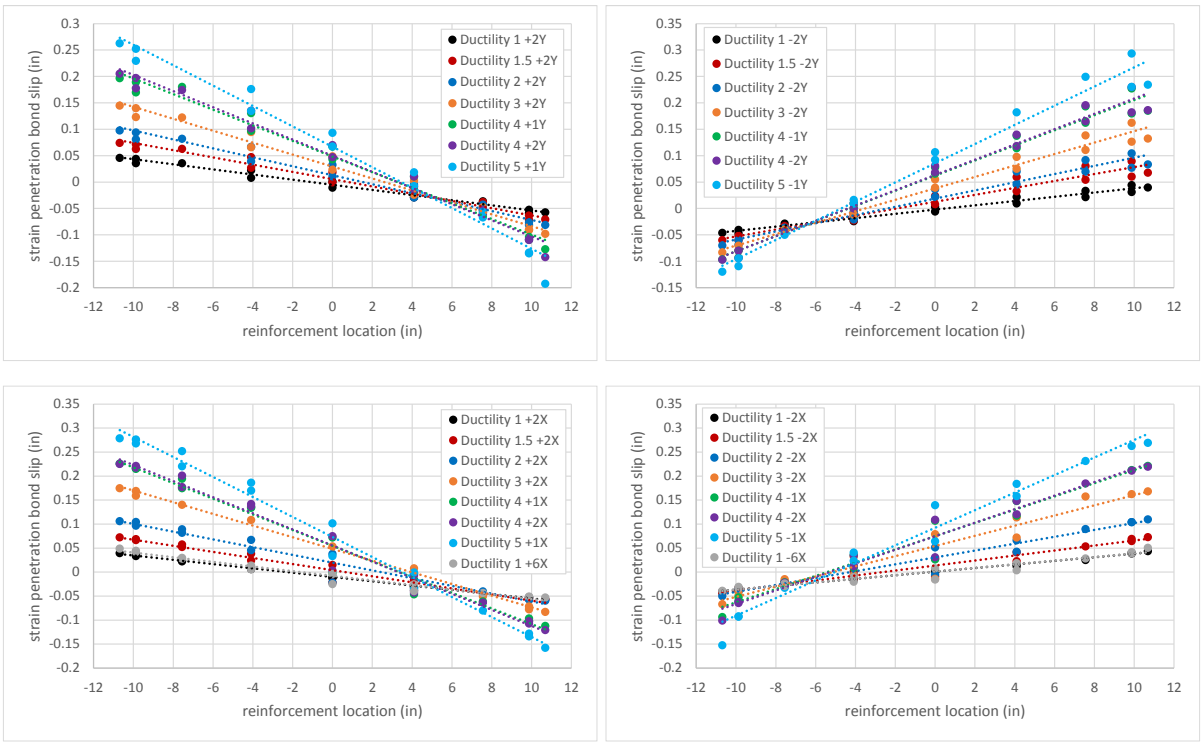

Figure 9-87. Test 6: Fixed End Rotations due to Strain Penetration

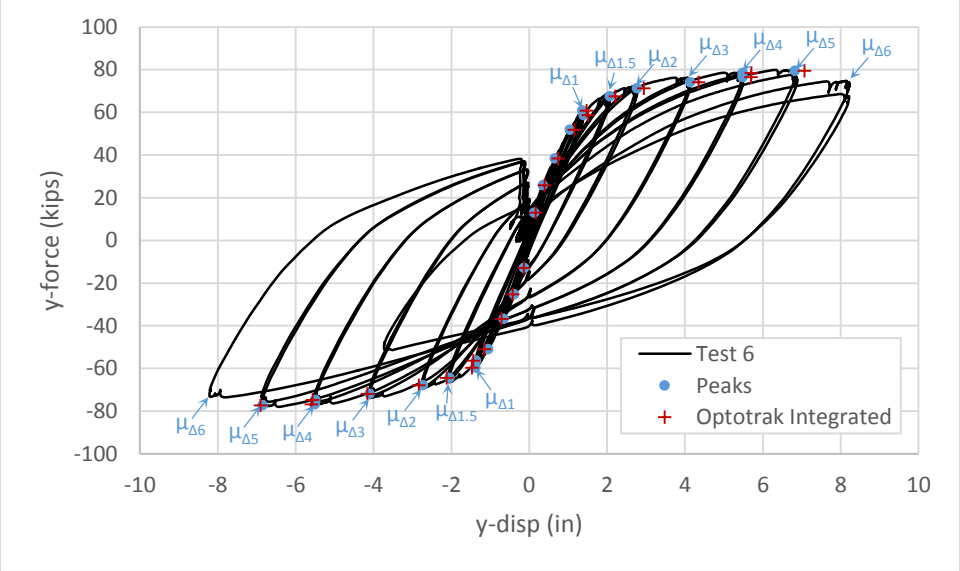

Figure 9-88. Test 6: Optotrak Integrated Flexural Disp. Compared to Measured String Pot. Disp.

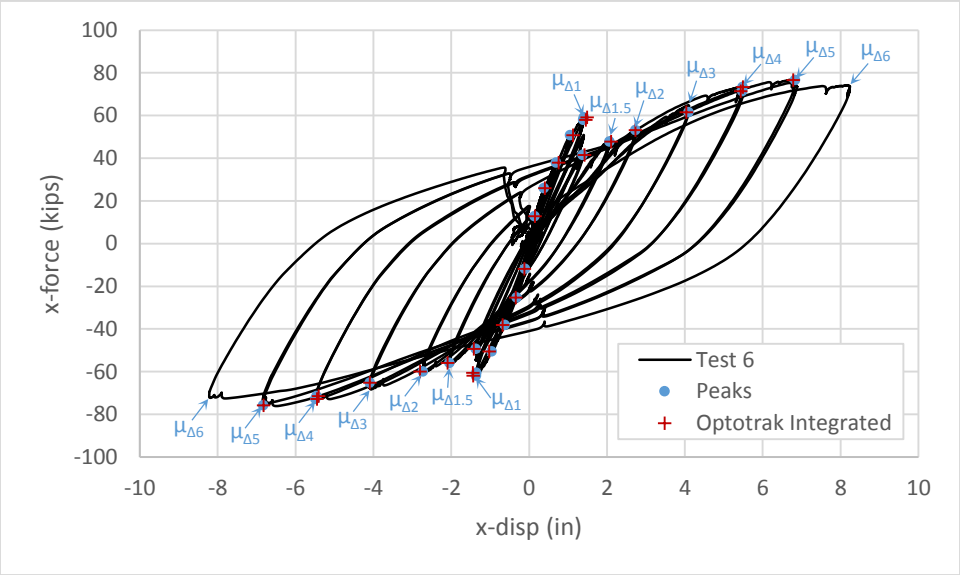

Figure 9-89. Test 6: Optotrak Integrated Flexural Disp. Compared to Measured String Pot. Disp.

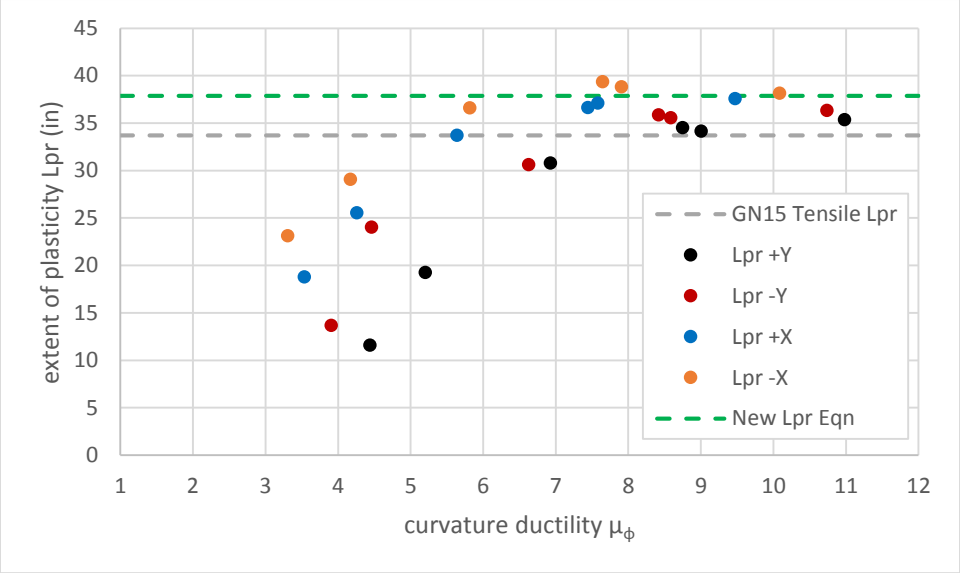

Figure 9-90. Test 6: Measured Extent of Plasticity Compared to Tensile Hinge Lengths

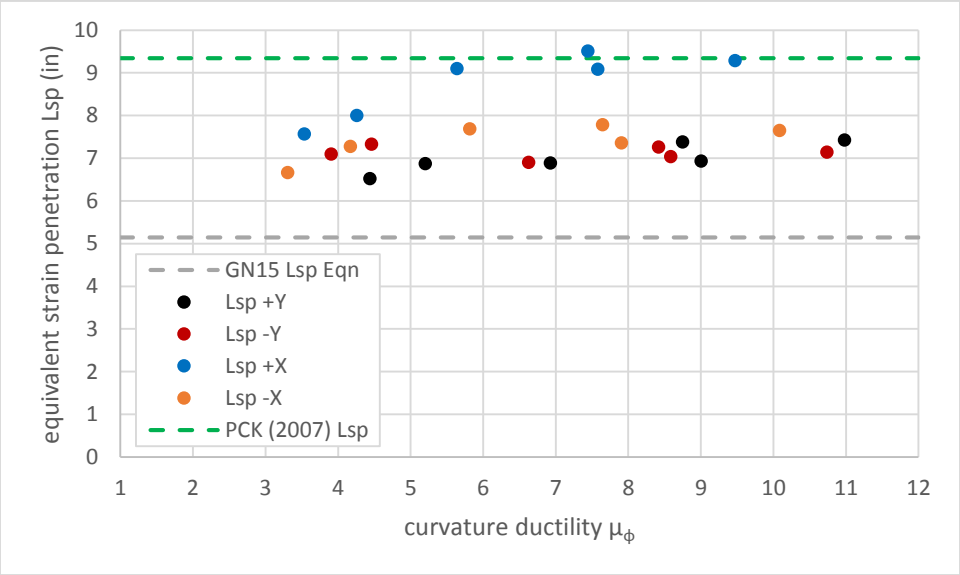

Figure 9-91. Test 6: Measured Equivalent Strain Penetration Lengths Compared to Design Expressions

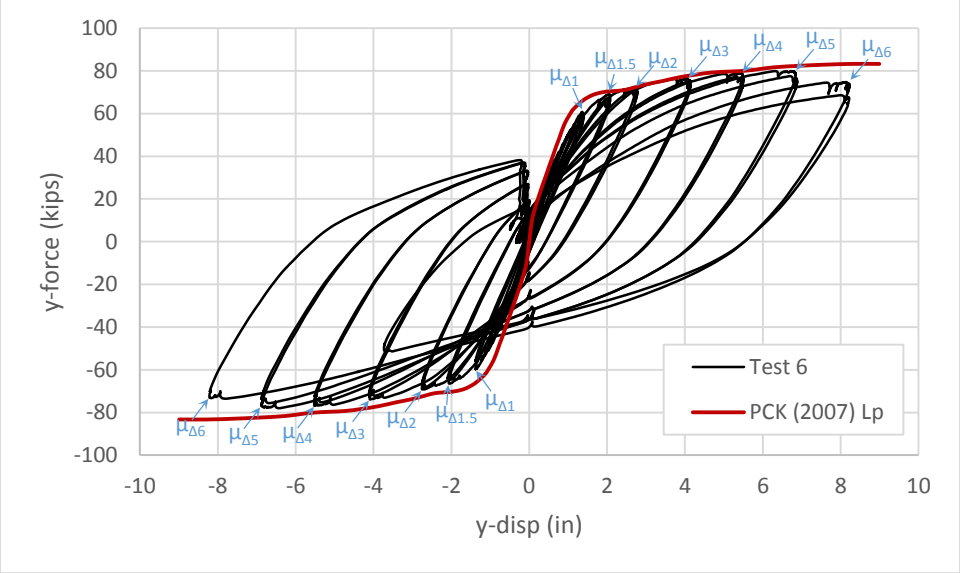

Figure 9-92. Test 6: Y-Direction Hysteretic Response Compared to PCK (2007) Hinge Length Monotonic Prediction

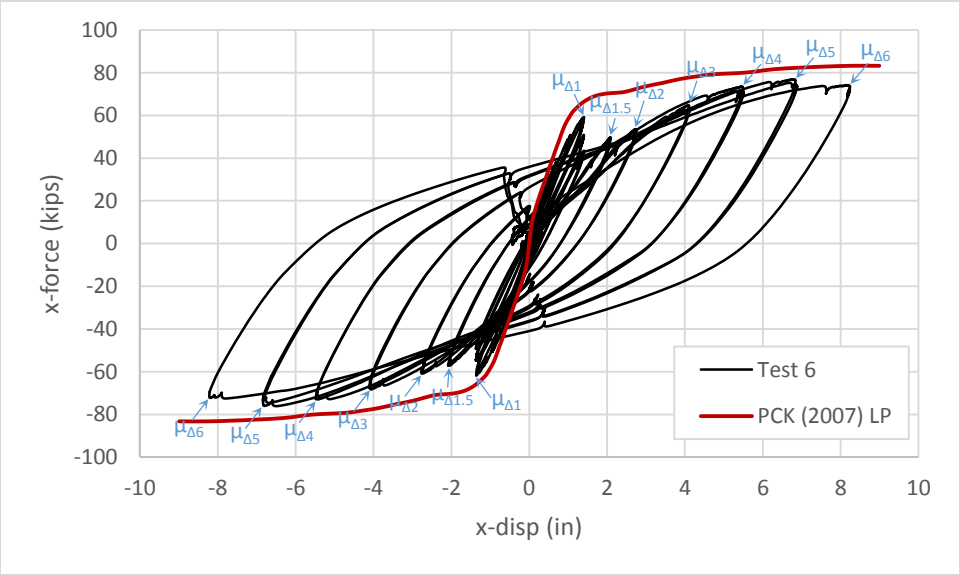

Figure 9-93. Test 6: X-Direction Hysteretic Response Compared to PCK (2007) Hinge Length Monotonic Prediction

Response Comparison to Previous Experiments

Comparison of Tests 4 (Symmetric) and 6 (Asymmetric Two-Cycle-Set)

Test 6 was nominally identical to Test 4, with the exception that the x-direction ductility demands lagged behind those in the y-direction until visible buckling was observed on the North and South sides of the specimen during $\mu_{\Delta 5}^{\pm 2y}$ and $\mu_{\Delta 3}^{\pm 2x}$. The load history of Test 6continued with cycles in the x-direction only until $\mu_{\Delta 5}^{\pm 2x}$, and finally a symmetric application of load in the two primary directions for $\mu_{\Delta 6}$.Test 4 utilized a standard symmetric two-cycle-set load history with balanced ductility demands in each direction. In terms of limit states, cover crushing occurred in both tests during $\mu_{\Delta 2}$. In Test 4, spiral yielding occurred on the North and East sides during $\mu_{\Delta 3}$, followed by the South and Wests sides during $\mu_{\Delta 4}$. In Tests 6, spiral yielding only occurred on the North side during $\mu_{\Delta 3}$, and on all other sides during $\mu_{\Delta 4}$. In Test 4, bar buckling was observed on the North and East sides during $\mu_{\Delta 5}$, followed by the South and West sides during $\mu_{\Delta 6}$. In Test 6, bar bucking as observed on the North and South sides during $\mu_{\Delta 5}$, followed by the East and West sides during $\mu_{\Delta 6}$. Overall, the change is displacement history did not appear to influence the limit state displacements, however the strains have yet to be processed to investigate this topic more thoroughly.

A hysteretic response comparison for Tests 4 and 6 appears in Figure 9-94 and Figure 9-95. At first glance, the y-direction response appears to be identical, however, it is clear that the first +y and -y cycle of each ductility level produced larger forces along the envelop portion of the curve as the loading proceeded beyond that of the prior peak displacement. This is due to the fact that the lower ductility demands in the orthogonal direction produced smaller residual strains. At the peak of each cycle, the influence of these prior residual strains is reduced, since the strain demands have increased sufficiently beyond the prior values. Both Tests had equal ductility demands at the conclusion of $\mu_{\Delta 5}$, and the measured response during the symmetric application of $\mu_{\Delta 6}$ is similar down to the level of

strength lost at the peak of each cycle. Test 4 was concluded after the previously buckled North extreme fiber bar fractured at -4.75" during $\mu_{\Delta 6}^{-2y}$. During this cycle, the strength loss of Test 6 mirrored that of Test 4, but the loading was stopped at -3.72" without fracturing any reinforcement. The x-direction hysteretic response comparison of Figure 9-95 highlights the difference in the two load histories. Up until $\mu_{\Delta 1}^{\pm 2}$ the response matches for both tests, since the loading was applied symmetrically. Beyond this point, the x-direction ductility demands lagged behind those in the y-direction in the following proportions: $\mu_{\Delta 1.5}^{\pm 2y}$ and $\mu_{\Delta 1}^{\pm 4x}$, $\mu_{\Delta 2}^{\pm 2y}$ and $\mu_{\Delta 1}^{\pm 6x}$, $\mu_{\Delta 3}^{\pm 2y}$ and $\mu_{\Delta 1.5}^{\pm 2x}$, $\mu_{\Delta 4}^{\pm 2y}$ and $\mu_{\Delta 2}^{\pm 2x}$, and $\mu_{\Delta 5}^{\pm 2y}$ and $\mu_{\Delta 3}^{\pm 2x}$. The apparent loss in strength here is only a loss in stiffness, due to the hysteretic characteristics of the North and South reinforcement, which was exposed to higher ductility demands in the prior y-direction cycling. Once the loading was switched to direct x-direction cycling from $\mu_{\Delta 4}$ to $\mu_{\Delta 5}$ the strength at the peak of the cycle resembled that of Test 4.

Comparison of Tests 3 ($\rho_s = 0.7\%$) and 6 ($\rho_s = 1\%$) both with Asymmetric Two-Cycle-Set

Test 6 was reinforced with a #3 spiral at 2" spacing for ($\rho_s = 1\%$) while Test 3 had a #3 spiral at 2.75" spacing for ($\rho_s = 0.7\%$). Test 6 also had a slightly higher concrete compressive strength, $f_c' = 7.81\ ksi$ compared to $6.24\ ksi$. The Asymmetric Two-Cycle-Set load history utilized for each specimen is shown in Figure 9-98 and Figure 9-99, while the hysteretic response is comparison appears in Figure 9-96 and Figure 9-97. The noted observations in the previous section produced comparable results between the two tests.

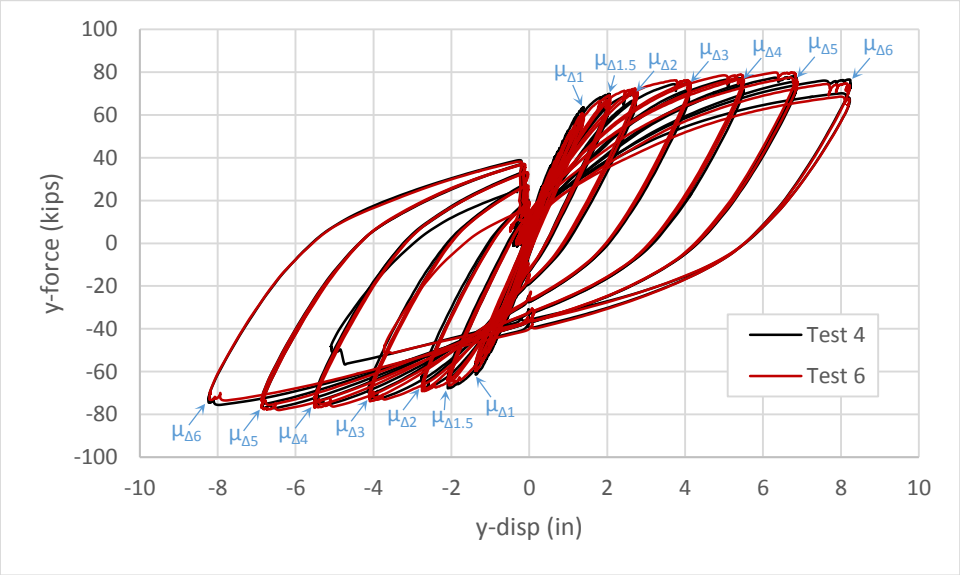

Figure 9-94. Y-Direction Hysteretic Comparison for Tests 4 (Symmetric) and 6 (Asymmetric) Two-Cycle-Set

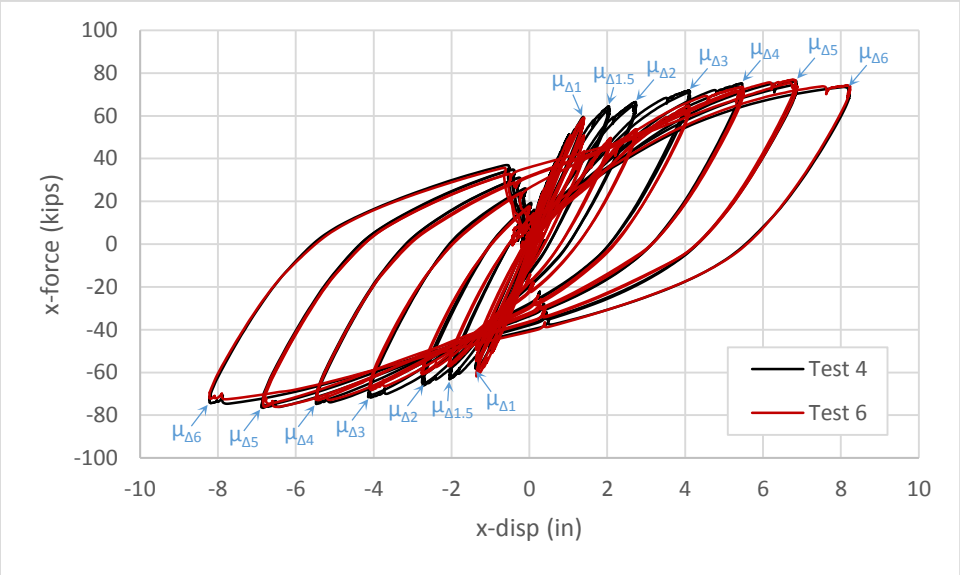

Figure 9-95. X-Direction Hysteretic Comparison for Tests 4 (Symmetric) and 6 (Asymmetric) Two-Cycle-Set

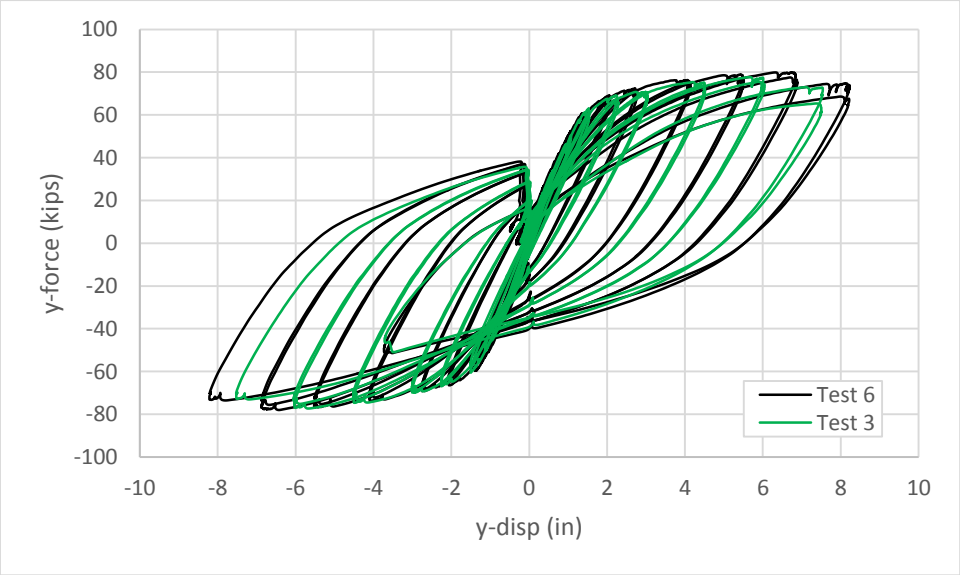

Figure 9-96. Y-Direction Hysteretic Comparison for Tests 3 (Asymmetric) and 6 (Asymmetric) Two-Cycle-Set

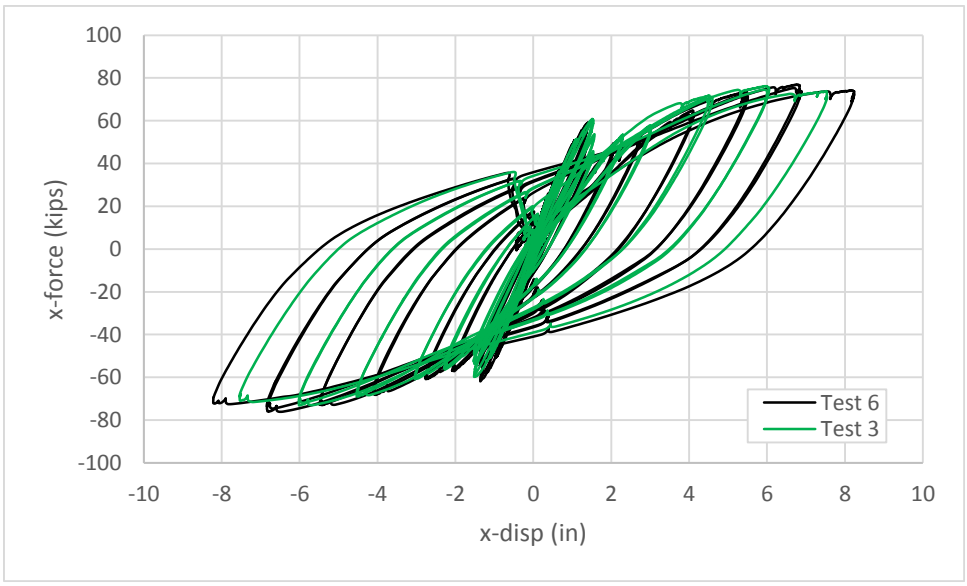

Figure 9-97. X-Direction Hysteretic Comparison for Tests 3 (Asymmetric) and 6 (Asymmetric) Two-Cycle-Set

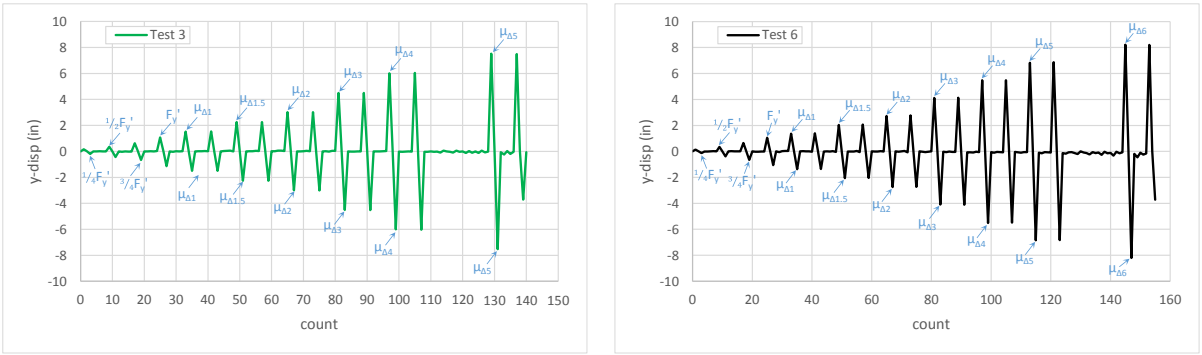

Figure 9-98. Y-Direction Asymmetric Two-Cycle-Set Displacement History Comparison for Tests 3 and 6

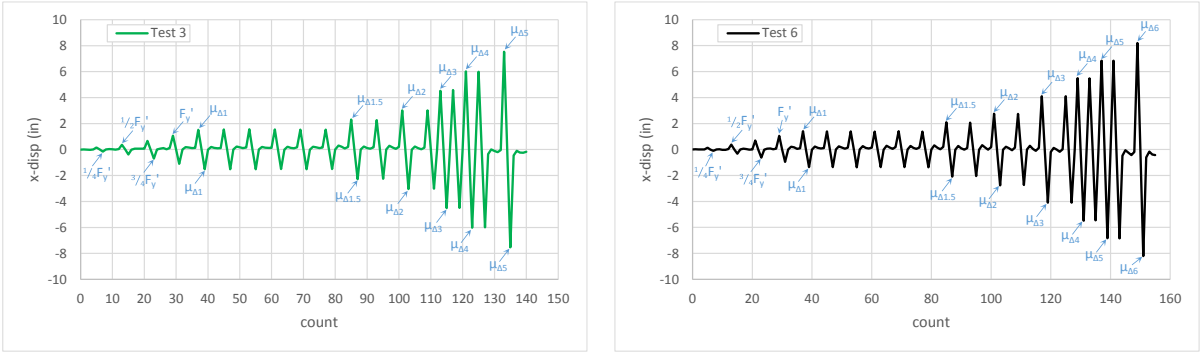

Figure 9-99. X-Direction Asymmetric Two-Cycle-Set Displacement History Comparison for Tests 3 and 6

Chapter 10 – Test 7 Summary Report

The seventh specimen had a 24" diameter circular cross-section reinforced with 16 #6 A706 longitudinal bars ($A_{st}/A_g = 1.6\%$) and a #3 spiral at 1.5" on center ($4A_{sp}/D's = 1.3\%$). The specimen was nominally identical to those chosen for Tests 8 and 9 which contained 1% and 0.7% transverse steel, respectively. The column selected for Test 10 was nominally identical to that of Test 7, except it contained 2.1% longitudinal steel. Details of the test setup, instrumentation, and specimen design appear in Chapter 2. A material properties summary for the longitudinal and transverse steel from the final six experiments appears in Table 3-3 through Table 3-5. The column had a tested concrete strength of $f_c' = 5.79\ ksi$, while the footing had $f_c' = 7.17\ ksi$. The same constant compressive axial load of $191\ kips$ was applied to all the specimens. The seventh specimen was subjected to the Type-B Symmetric Two-Cycle-Set Bidirectional Load History shown in Figure 10-1. This figure includes a diagram of the column cross-section with the selected bar and crack labeling scheme. Displacements in the +Y-direction placed the South reinforcement in tension. Cracks due to loading in the +Y-direction were labeled as red. The orientation of the X and Y axes are shown in Figure 2-52 with regards to the test setup. The +Y-axis is perpendicular to and points away from the strong wall. Values of interests, damage observations, and a predictions summary for the seventh test appear in Table 10-1, Table 10-2, and Table 10-3. A photo of the deformed specimen appears in Figure 10-2. The tighter transverse steel spacing necessitated reducing the number of target markers placed on bars NW, NE, SE, and SW. This was accompanied with a more dense instrumentation of the most highly strained bars in the four extreme fiber regions of the column.

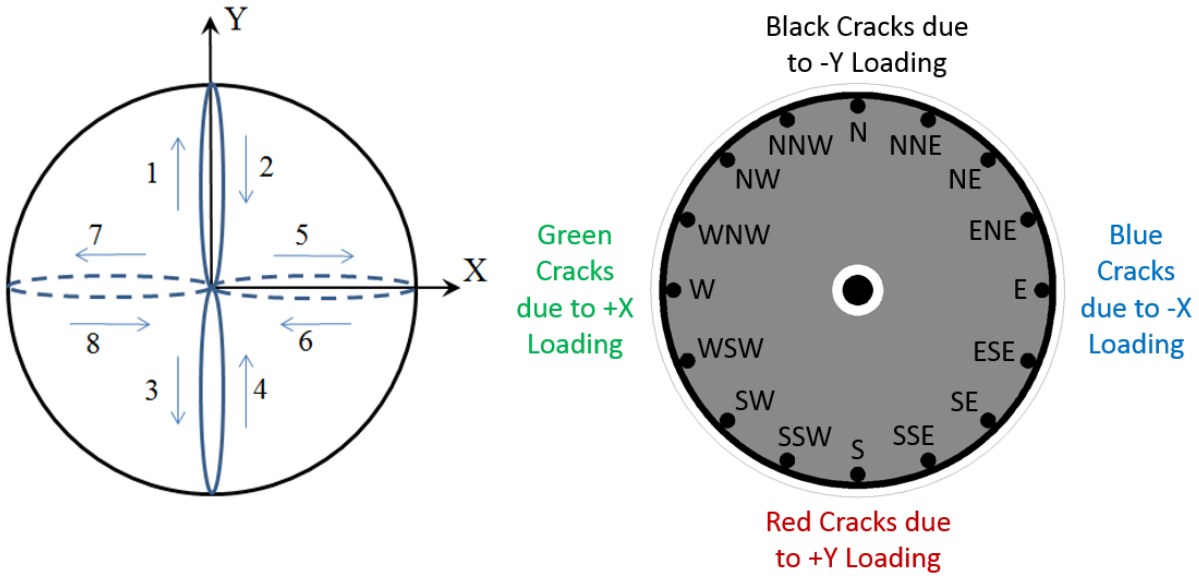

Figure 10-1. Test 7: Load History Orientation and Labeling System for Reinforcement and Cracks

Table 10-1. Test 7: Values of Interest

Load History	Type-B Symmetric Two-Cycle-Set
Length, Diameter, and Aspect Ratio	$L = 109.4375\ in, D = 24\ in,\ (L/D = 4.56)$
Longitudinal Steel Detailing	$16\ \#6\ for\ \rho_l = A_{st}/A_g = 1.6\%$
Longitudinal Steel Properties	$f_y = 70.33\ ksi, f_u = 98.68\ ksi, \varepsilon_y = 0.00283$
Transverse Steel Detailing	$\#3\ @\ 1.5\ in\ for\ \rho_s = 4A_{sp}/D's = 1.3\%$
Transverse Steel Properties	$f_y = 63.89\ ksi, f_u = 93.64\ ksi, \varepsilon_y = 0.00418$
Column Concrete Strength	$f_c' = 5.79\ ksi$
Footing Concrete Strength	$f_c' = 7.17\ ksi$
Axial Load	$P = 191\ kips, \left(P/f_c'\ A_g = 7.9\%\right)$
Analytical First Yield Force	$F_y' = 40.92\ kips$
Experimental First Yield Disp.	$\Delta_y' = 0.91\ in$
Analytical Nominal Moment Capacity	$M_n = 505.79\ kip \cdot ft$
Equivalent Yield Displacement	$\Delta_y = \Delta_y'\left(M_n/M_y'\right) = 1.23\ in$
Maximum Lateral Force	$F_y = 65.30\ kips, F_x = 63.20\ kips$
Failure Mode	Fracture of Previously Buckled Reinforcement

Table 10-2. Test 7: Damage Observations

Damage Observations:		
Cycle Peak at which First Cracking was Observed Visually:		
North	$\Delta_y = -0.5F_y' = -0.29\ in$	$F_y = -20.44\ kips$
South	$\Delta_y = 0.5F_y' = 0.21\ in$	$F_y = 20.48\ kips$
East	$\Delta_x = -0.5F_y' = -0.28\ in$	$F_x = -19.90\ kips$
West	$\Delta_x = 0.5F_y' = 0.28\ in$	$F_x = 20.44\ kips$
Cycle Peak at which Cover Concrete Crushing was Observed Visually:		
North	$\mu_{\Delta 2}^{+2Y} = 2.49\ in$	$\varepsilon_c = -0.00553$
South	$\mu_{\Delta 1.5}^{-1Y} = -1.91\ in$	$\varepsilon_c = -0.00510$
East	$\mu_{\Delta 1.5}^{+1X} = 1.89\ in$	$\varepsilon_c = -0.00364$
West	$\mu_{\Delta 2}^{-1X} = -2.48\ in$	$\varepsilon_c = -0.00461$
Exact Displacement and Cycle Label for Initial Spiral Yielding in the Confinement Zone:		
North	$\Delta_y = 7.26\ in\ during\ \mu_{\Delta 6}^{+1Y}$	$\varepsilon_c = -0.02610$
South	$\Delta_y = -5.88\ in\ during\ \mu_{\Delta 6}^{-1Y}$	$\varepsilon_c = -0.01669$
East	$\Delta_x = 4.83\ in\ during\ \mu_{\Delta 4}^{+1X}$	$\varepsilon_c = -0.01129$
West	$\Delta_x = -5.48\ in\ during\ \mu_{\Delta 5}^{-1X}$	$\varepsilon_c = -0.01452$
Peak Tensile Displacement Prior to Visual Bar Buckling During Subsequent Reversal of Load:		
North	$\mu_{\Delta 6}^{-2Y} = -7.44\ in, Observed\ at\ \mu_{\Delta 7}^{+1Y} = 8.67\ in$	$\varepsilon_s = 0.04510$
South	$South\ Bar\ Buckling\ Not\ Observed$	
East	$\mu_{\Delta 5}^{-2X} = -6.17\ in, Observed\ at\ \mu_{\Delta 6}^{+1X} = 7.40\ in$	$\varepsilon_s = 0.04355$
West	$\mu_{\Delta 6}^{+2X} = 7.48\ in, Observed\ at\ \mu_{\Delta 6}^{-2X} = -7.39\ in$	$\varepsilon_s = 0.04799$
Exact Displacement and Cycle Label for Fracture of Previously Buckled Reinforcement		
North	$\Delta_y = -8.19\ in\ during\ \mu_{\Delta 7}^{-2Y}$	Single North Extreme Bar

Table 10-3. Test 7: Damage Predictions

Damage Predictions with the New Bidirectional Plastic Hinge Model and New Strain Limits:		
Bar Buckling Predictions		
New Method	$\Delta_{bb}^{Lpr} = 7.45\ in$	$\varepsilon_s^{bb} = 0.04356$
Feng et al. (2015)	$\Delta_{bb}^{Lp} = 7.61\ in$	$\varepsilon_s^{bb} = 0.0631$
Cover Crushing Prediction		
New Method	$\Delta_{cc}^{Lpr} = 1.97\ in$	$\varepsilon_c^{cc} = -0.004$
Spiral Yielding Prediction		
New Method	$\Delta_{sy}^{Lpr} = 5.38\ in$	$\varepsilon_c^{sy} = -0.01384 * M, (M = 0.8)$
Original Ultimate Concrete Compression Strain		
Mander et al. (1988)	$\Delta_{cu}^{Lpr} = 9.43\ in$	$\varepsilon_{cu} = -0.0211$

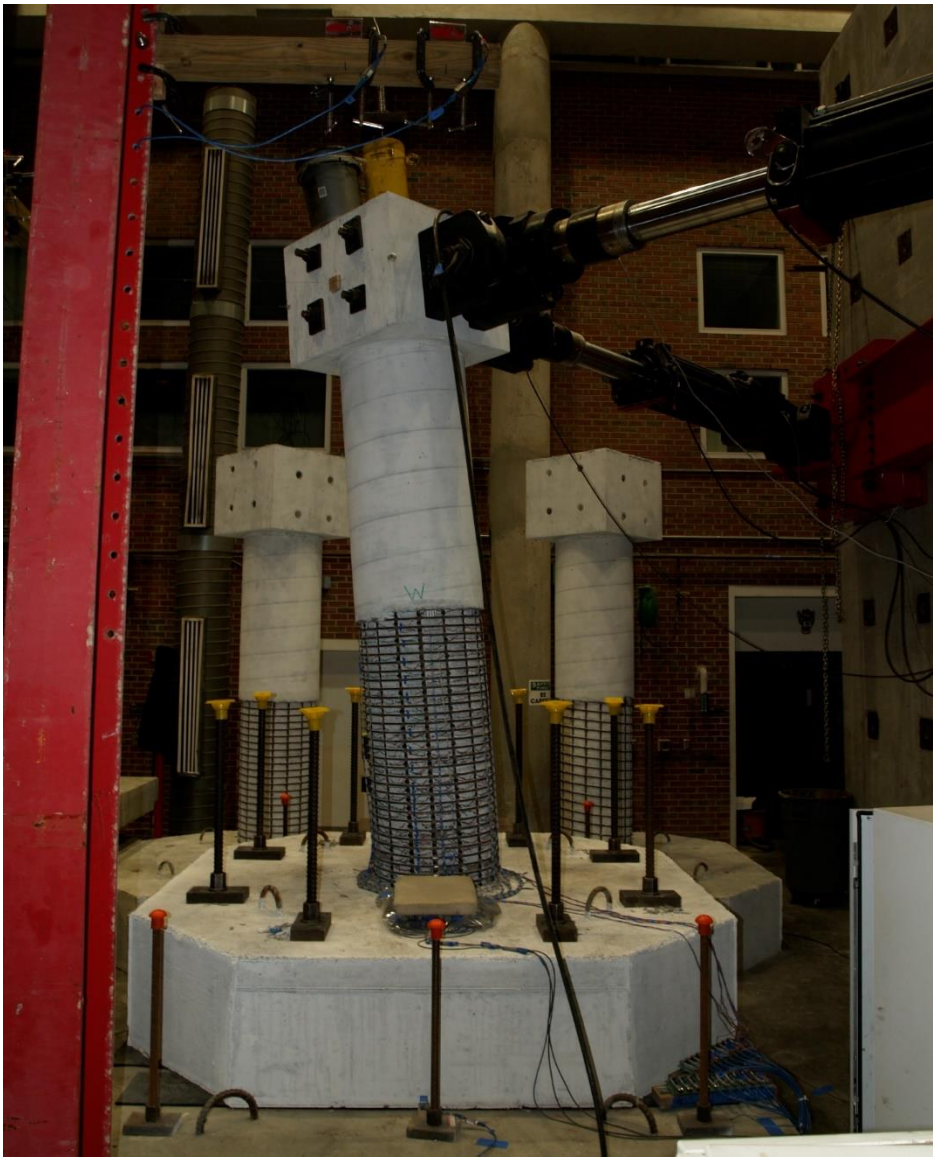

Figure 10-2. Test 7: Deformed Specimen at $\mu_{\Delta 7}^{+1y} = 8.67$"

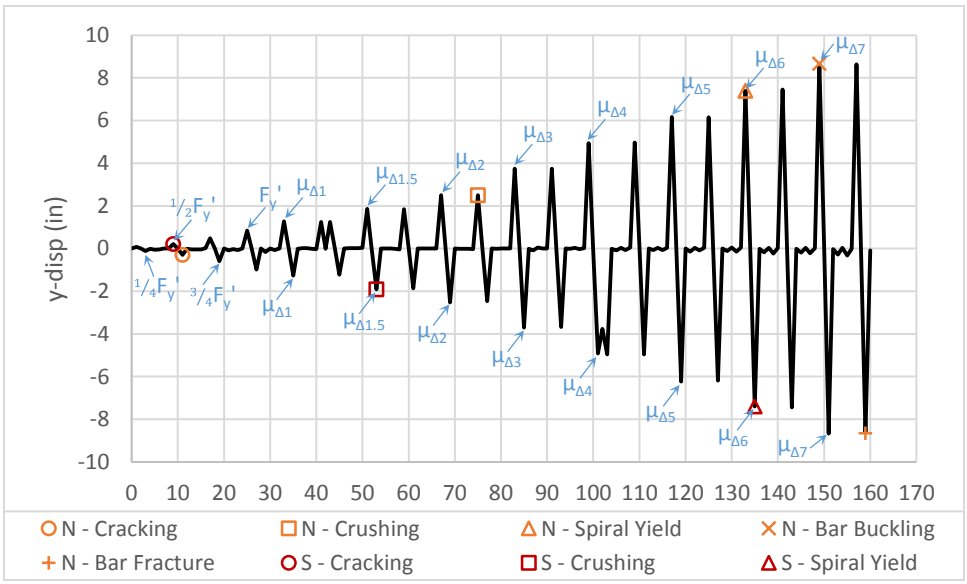

Figure 10-3. Test 7: Y-Displacement History

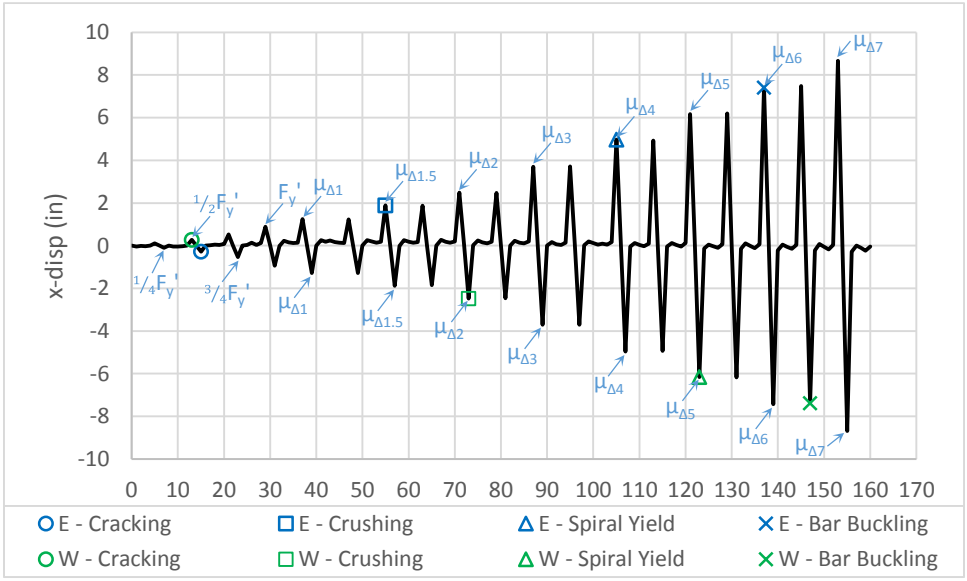

Figure 10-4. Test 7: X-Displacement History

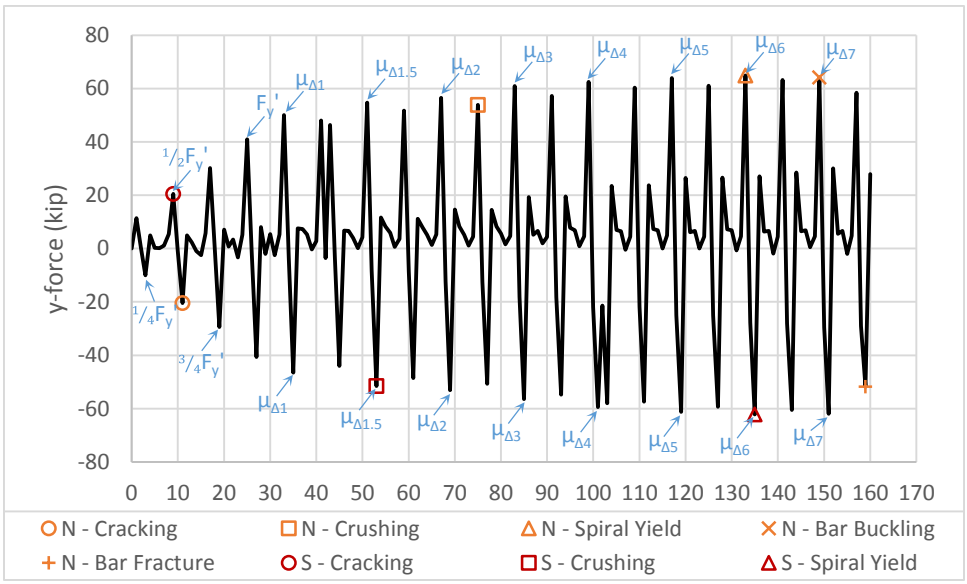

Figure 10-5. Test 7: Y-Force History

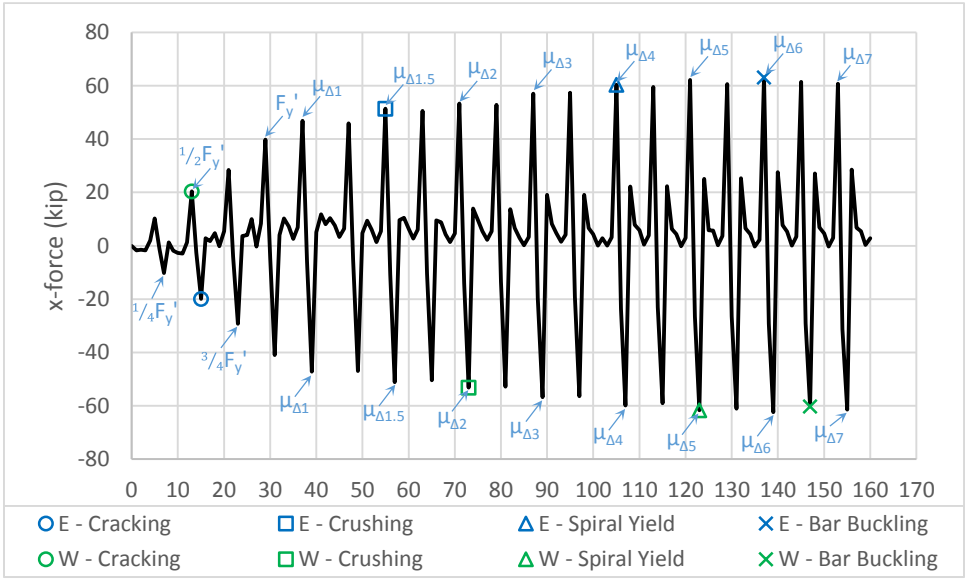

Figure 10-6. Test 7: X-Force History

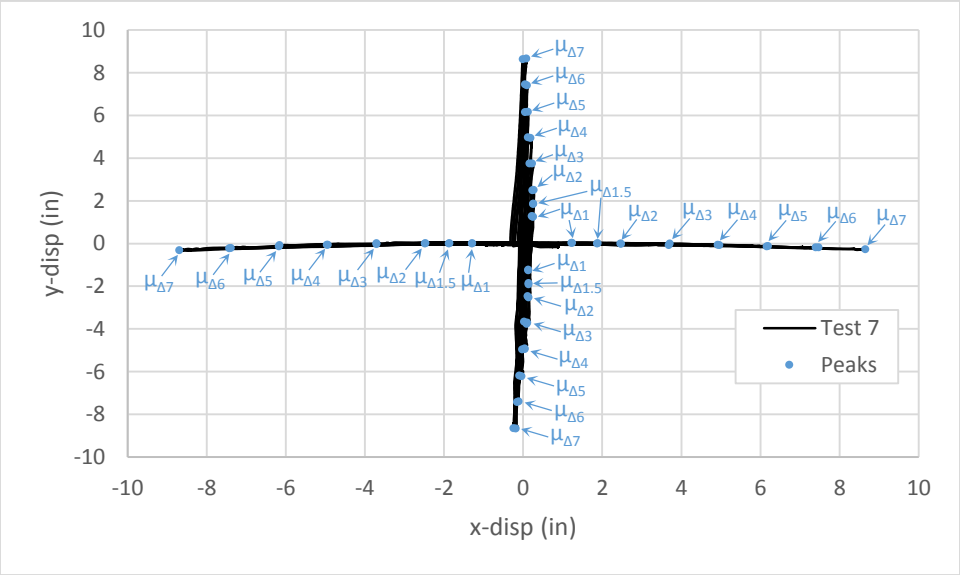

Figure 10-7. Test 7: Type-B Symmetric Two-Cycle-Set Displacement History

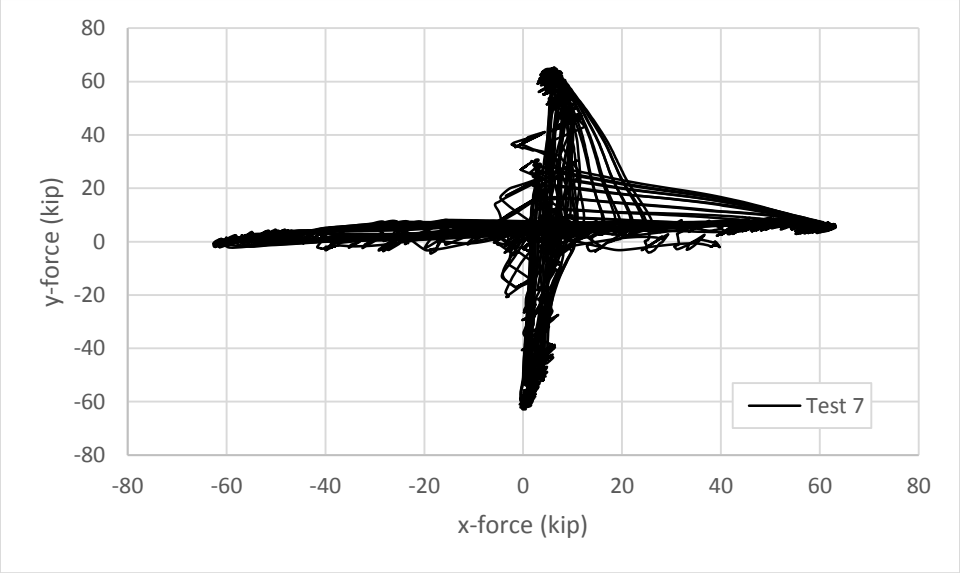

Figure 10-8. Test 7: Load Path

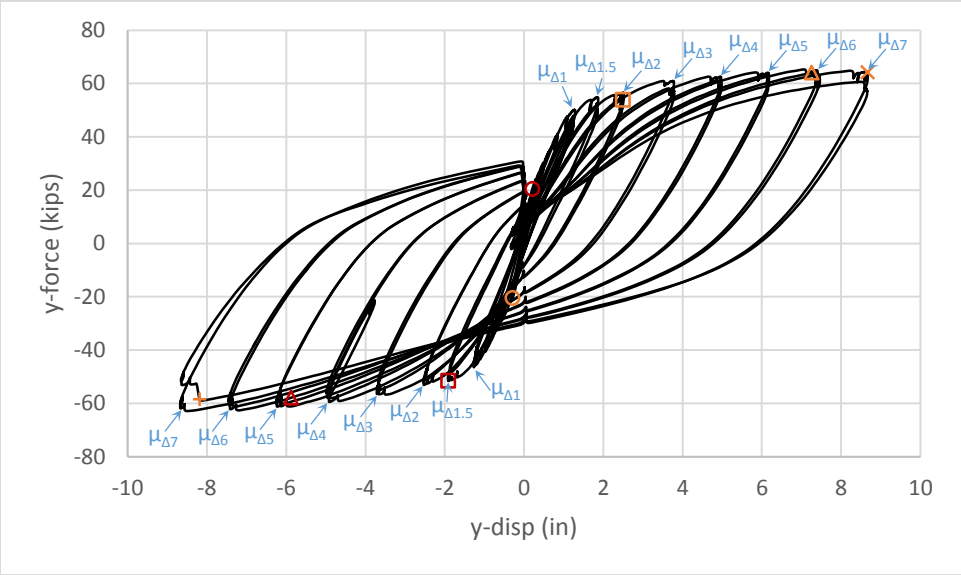

Figure 10-9. Test 7: Y-Direction Hysteretic Response

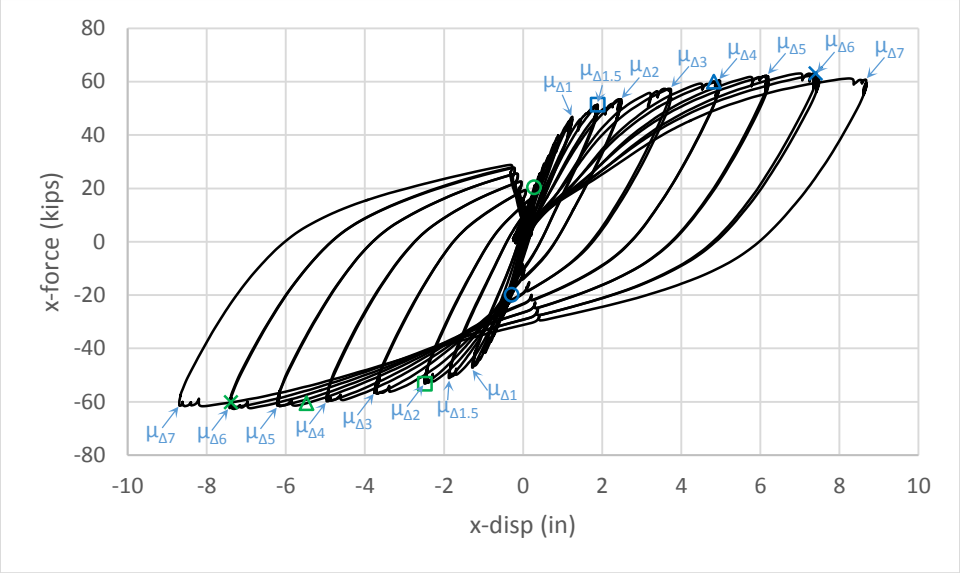

Figure 10-10. Test 7: X-Direction Hysteretic Response

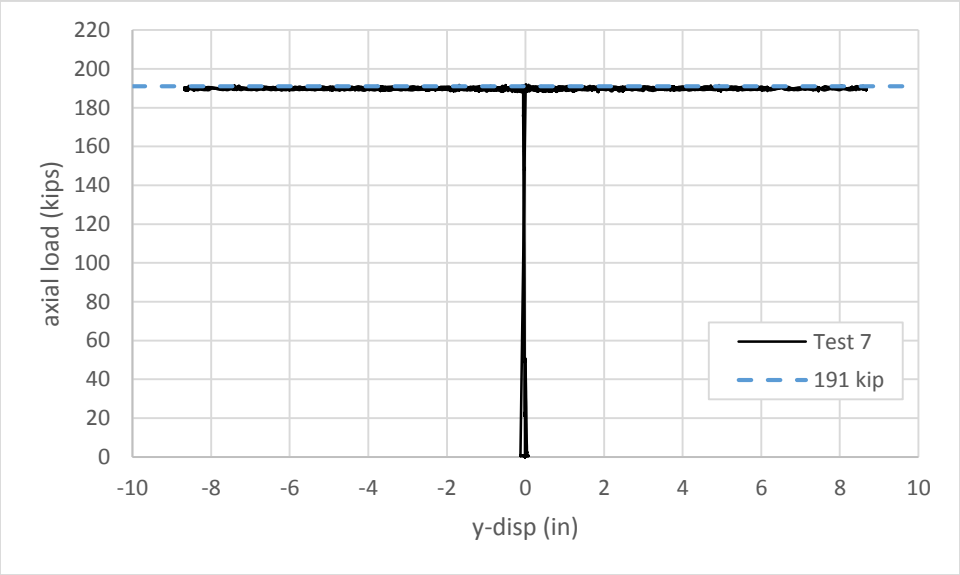

Figure 10-11. Test 7: Y-Direction Axial Force History

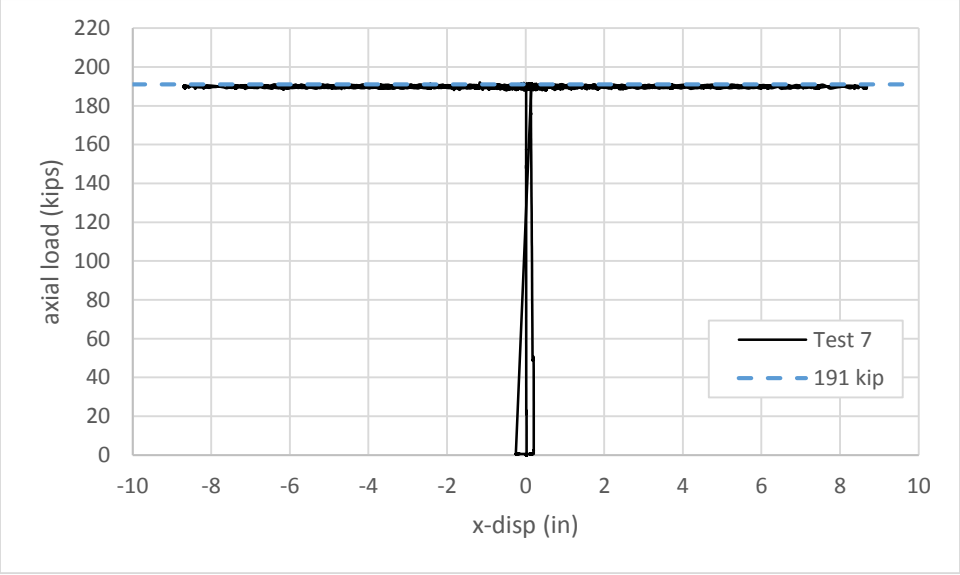

Figure 10-12. Test 7: X-Direction Axial Force History

Test 7 - Experimental Observations

Tests 7-9 evaluated 24" diameter columns $(L/D = 4.56)$ with $\rho_l = A_{st}/A_g = 1.6\%$ longitudinal steel and transverse volumetric ratios of either $\rho_s = 4A_{sp}/D's = 1.3\%, 1.0\%, or\ 0.7\%$. Values of interests and damage observations for Load Path Test 7 are presented in Table 10-1 and Table 10-2. Test 7 evaluated a 24" diameter column $(L/D = 4.56)$ with $\rho_l = A_{st}/A_g = 1.6\%$ longitudinal steel and a transverse volumetric ratio of $\rho_s = 4A_{sp}/D's = 1.3\%$. The test began with the application of a constant axial load of $191\ kips\ \left(P/f_c'\ A_g = 7.9\%\right)$. The imposed displacement histories in the Y and X-directions for the Symmetric Two-Cycle-Set Biaxial Load History shown in Figure 10-3 and Figure 10-4. The resulting column shear force histories in the Y and X-directions appear in Figure 10-5 and Figure 10-6. The full displacement history and resulting load path for Test 7 appear in Figure 10-7 and Figure 10-8. The Y and X-direction column hysteretic response appears Figure 10-9 and Figure 10-10. The axial load history is shown in Figure 10-11 and Figure 10-12.

The load history began with elastic ¼ F_y' cycle increments until the analytically predicted first yield force $(F_y' = 40.72\ kips)$ was reached in each direction of loading. Cracks were first observed on all sides of the specimen during the ½ F_y' cycle. At the analytically predicted first yield force, an average experimental first yield displacement of $\Delta_y' = 0.91"$ was measured in the four primary directions. The equivalent yield displacement for the column was then computed as $\Delta_y = \Delta_y'\left(M_n/M_y'\right) = 1.23\ in$, where $M_n = 505.79\ kip \cdot ft$ represents the analytical nominal moment capacity corresponding to an extreme fiber compression strain of $\varepsilon_c = 0.004$ or a steel tensile strain of $\varepsilon_s = 0.015$, whichever occurs first. The remainder of the Symmetric Two-Cycle-Set Load History consists of two cycles for each displacement ductility level $\mu_{\Delta n} = n \cdot \Delta_y$, where $n = 1, 1.5, 2, 3, 4, 5, 6\ etc$. Cracks observed on each side of the specimen at equivalent yield are shown in Figure 10-13 and Figure 10-14.

Concrete Crushing was observed on the South side at $\mu_{\Delta 1.5}^{-1y} = -1.91"$ and the East Side at $\mu_{\Delta 1.5}^{+1x} = 1.89"$, as depicted in Figure 10-15. Concrete crushing was then observed on the West side at $\mu_{\Delta 2}^{-1x} = -2.48"$, followed by the North side at $\mu_{\Delta 2}^{+2y} = 2.49"$, see Figure 10-16. Confinement steel yielded on the East side during $\mu_{\Delta 4}^{+1x} = 4.96"$, followed by spiral yielding at $\mu_{\Delta 5}^{-1x} = -6.16"$ on the West side of the specimen, refer to Figure 10-17. Spirals on the North Side yielded during $\mu_{\Delta 6}^{+1y} = 7.40"$, followed by the South side at $\mu_{\Delta 6}^{-1y} = -7.40"$ as shown in Figure 10-18.

The East extreme fiber bar visibly buckled during $\mu_{\Delta 6}^{+1x} = 7.40"$, followed by the West extreme fiber bar during $\mu_{\Delta 6}^{-2x} = -7.39"$, see Figure 10-19 The North extreme fiber bar visibly buckled during $\mu_{\Delta 7}^{+1y} = 8.67"$ as shown in Figure 10-20. Adjacent West bars WNW and WSW buckled during $\mu_{\Delta 7}^{+1x} = 8.66"$. Two additional North Bars NNE and NNW buckled during $\mu_{\Delta 7}^{+2y} = 8.63"$. At $-8.19"$ during the subsequent reversal to $\mu_{\Delta 7}^{-2y}$, the previously buckled North extreme fiber bar fractured, see Figure 10-20. Bar buckling on the South side of the specimen was never observed. Photos of the specimen after the test appear in Figure 10-21 and Figure 10-22.

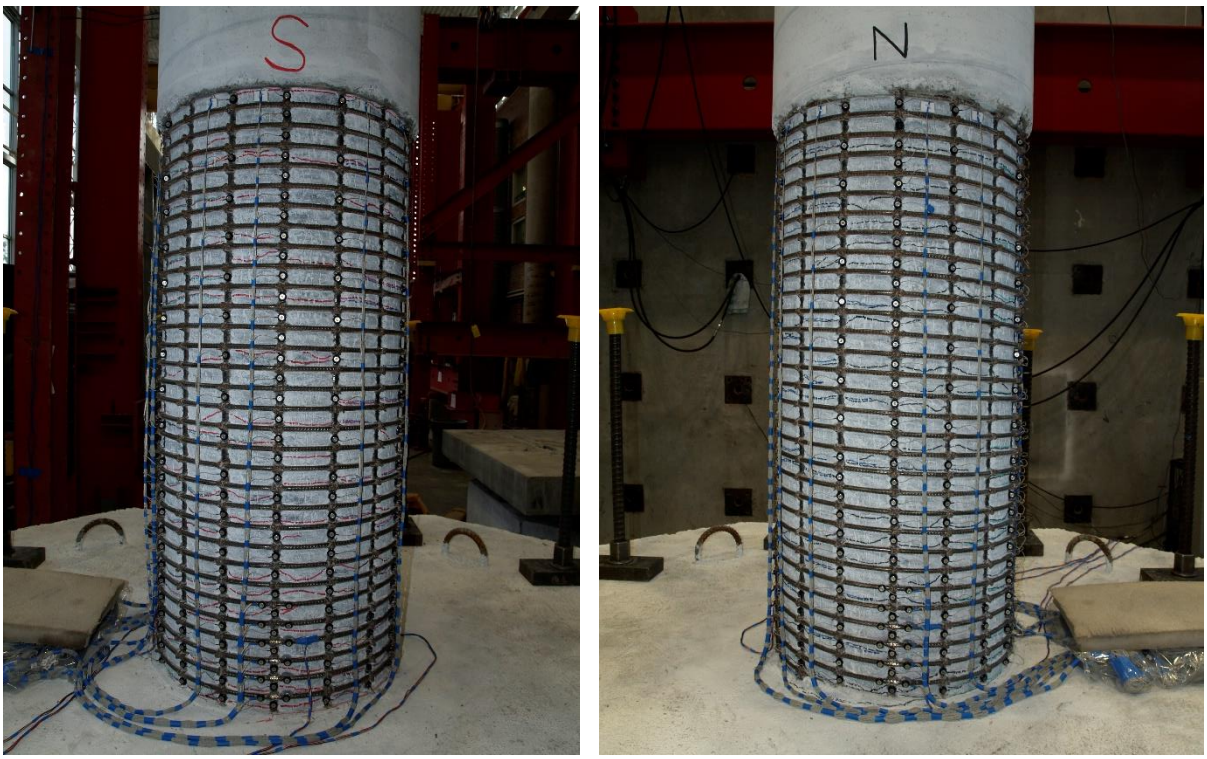

Figure 10-13. Test 7: Cracking on the (Left) South Side at $\mu_{\Delta 1}^{+2y} = 1.25$" and (Right) North Side at $\mu_{\Delta 1}^{-2y} = -1.23$"

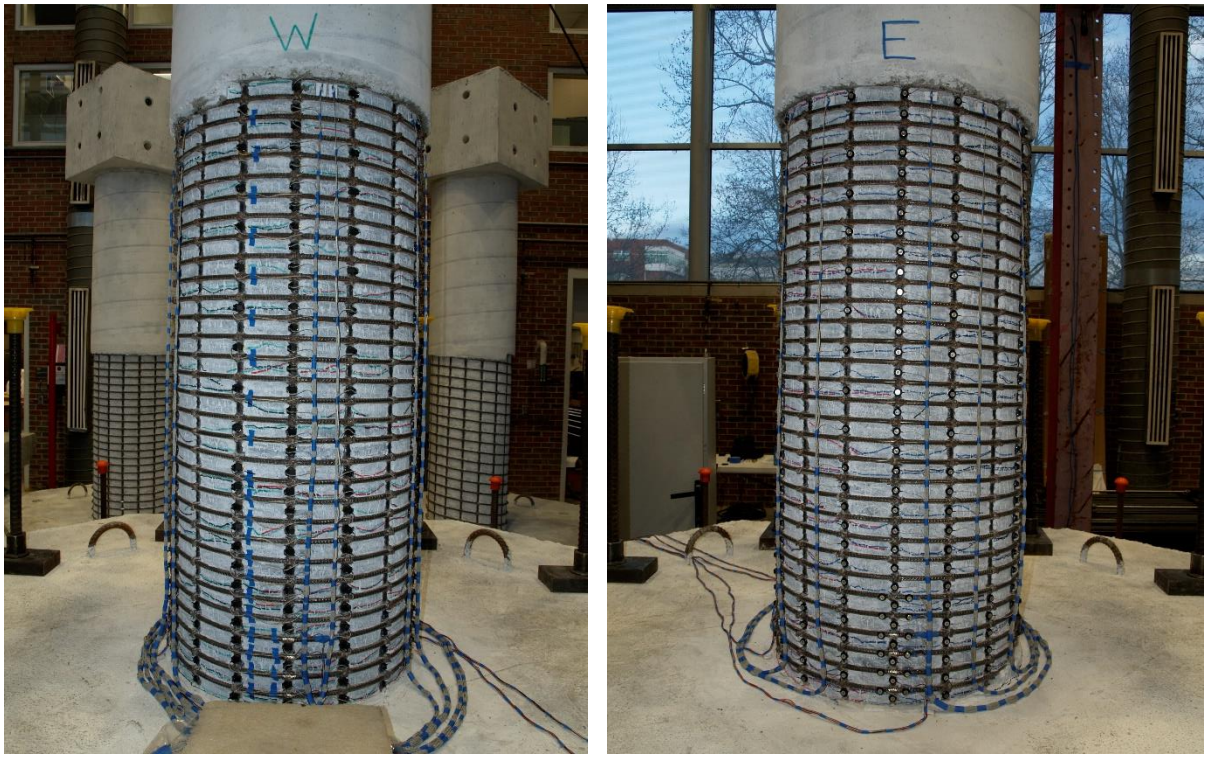

Figure 10-14. Test 7: Cracking on the (Left) West Side at $\mu_{\Delta 1}^{+2x} = 1.23$" and (Right) East Side at $\mu_{\Delta 1}^{-2x} = -1.28$"

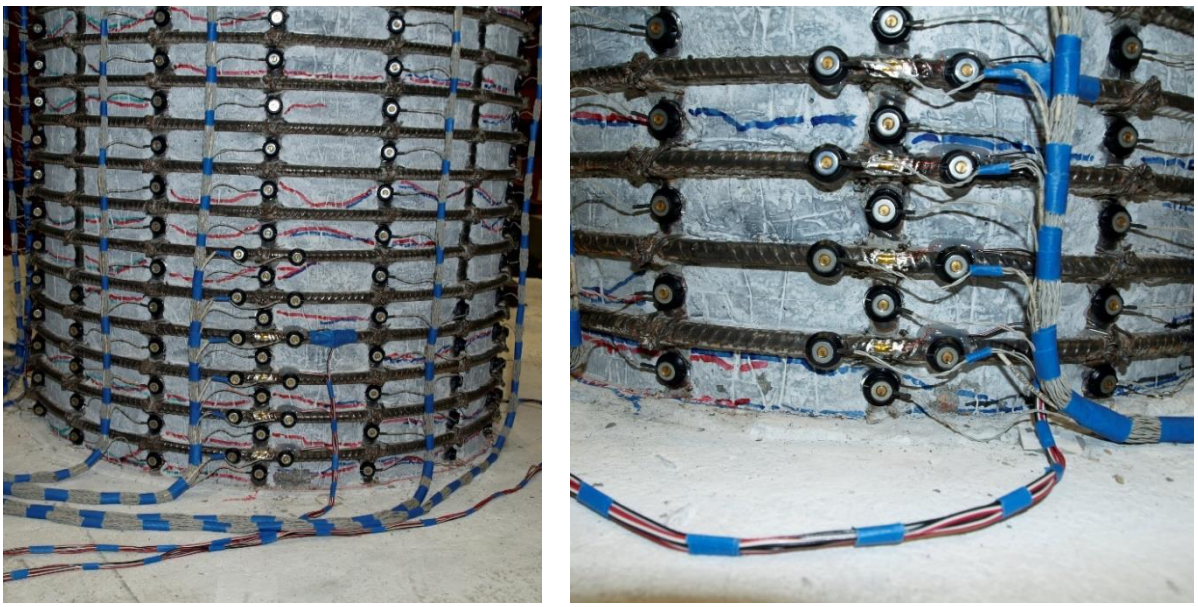

Figure 10-15. Test 7: Concrete Crushing on the (Left) South Side at $\mu_{\Delta 1.5}^{-1y} = -1.91$" and (Right) East Side at $\mu_{\Delta 1.5}^{+1x} = 1.89$"

Figure 10-16. Test 7: Concrete Crushing on the (Left) West Side at $\mu_{\Delta 2}^{-1x} = -2.48$" and (Right) North Side at $\mu_{\Delta 2}^{+2y} = 2.49$"

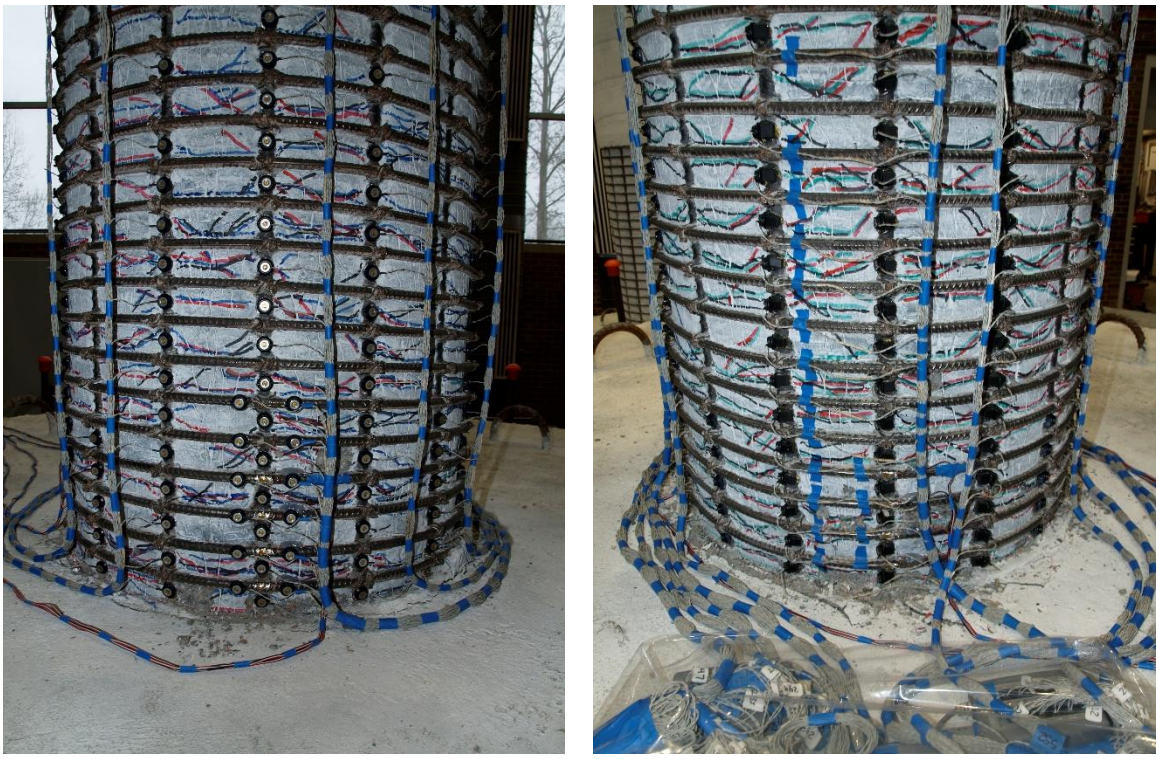

Figure 10-17. Test 7: Spiral Yielding on the (Left) East Side at $\mu_{\Delta 4}^{+1x} = 4.96"$ and (Right) West Side at $\mu_{\Delta 5}^{-1x} = -6.16"$

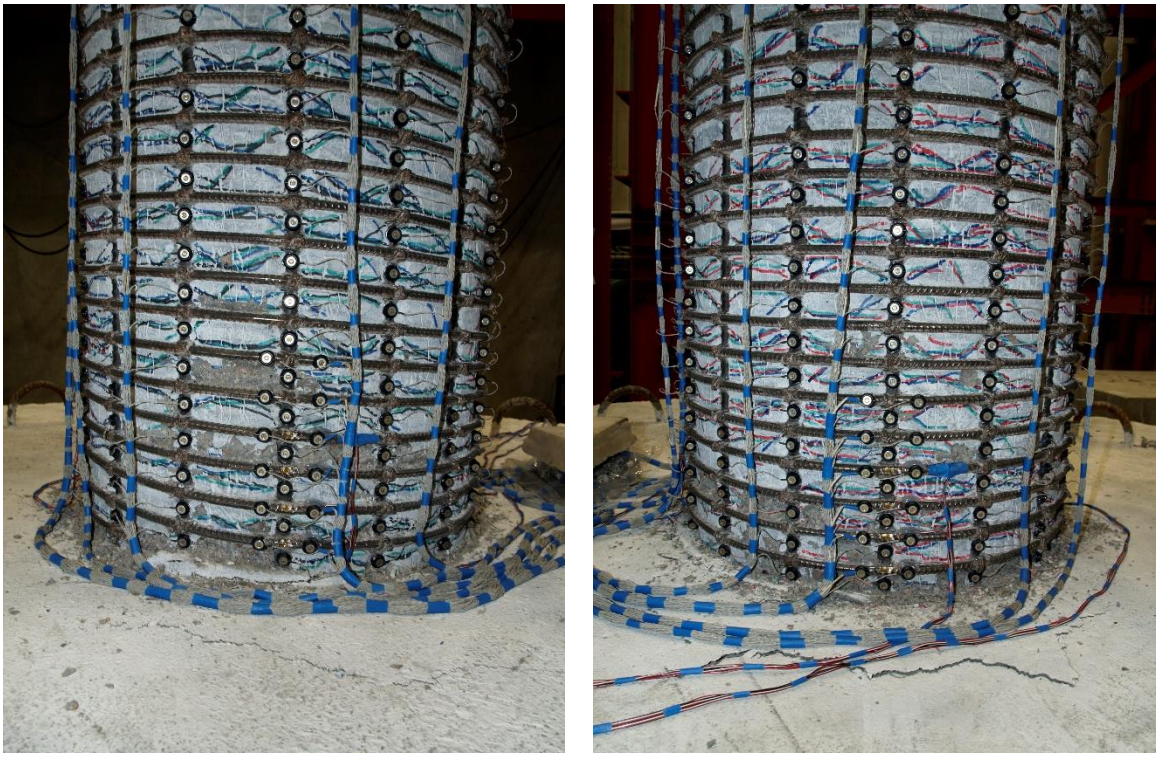

Figure 10-18. Test 7: Spiral Yielding on the (Left) North Side at $\mu_{\Delta 6}^{+1y} = 7.40"$ and (Right) South Side at $\mu_{\Delta 6}^{-1y} = -7.40"$

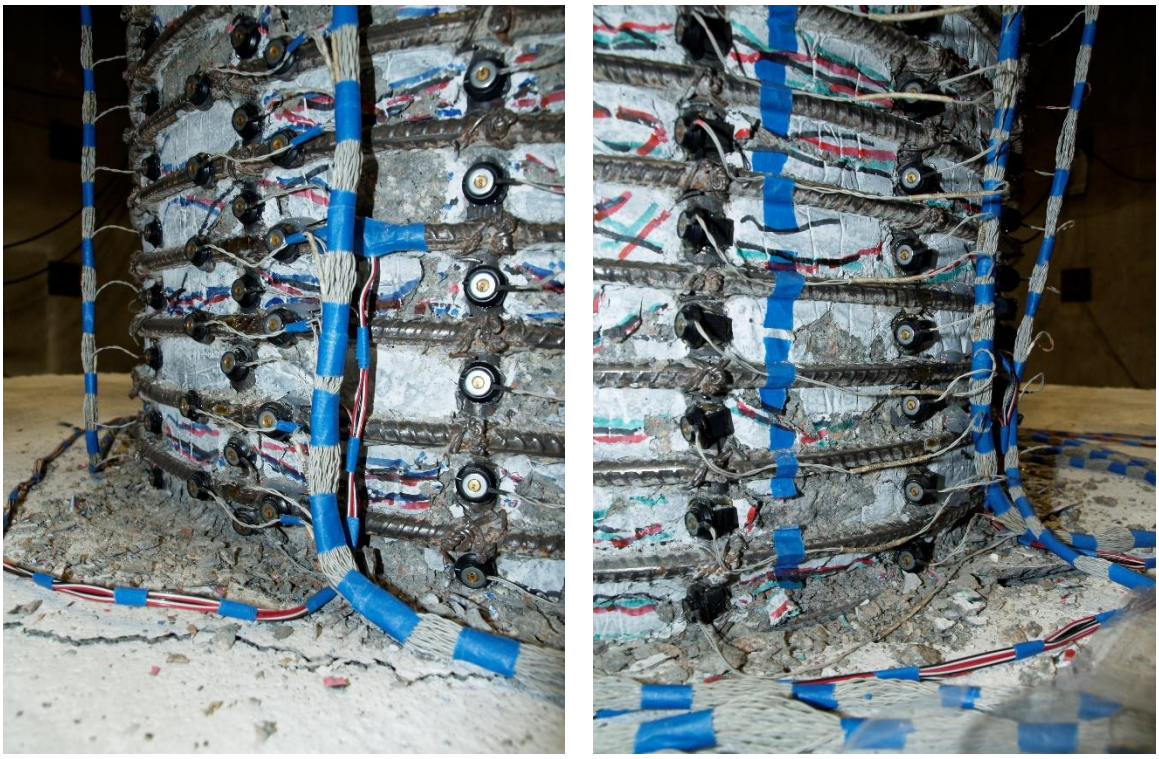

Figure 10-19. Test 7: Bar Buckling on the (Left) East Side at $\mu_{\Delta 6}^{+1x} = 7.40"$ and (Right) West Side at $\mu_{\Delta 6}^{-2x} = -7.39"$

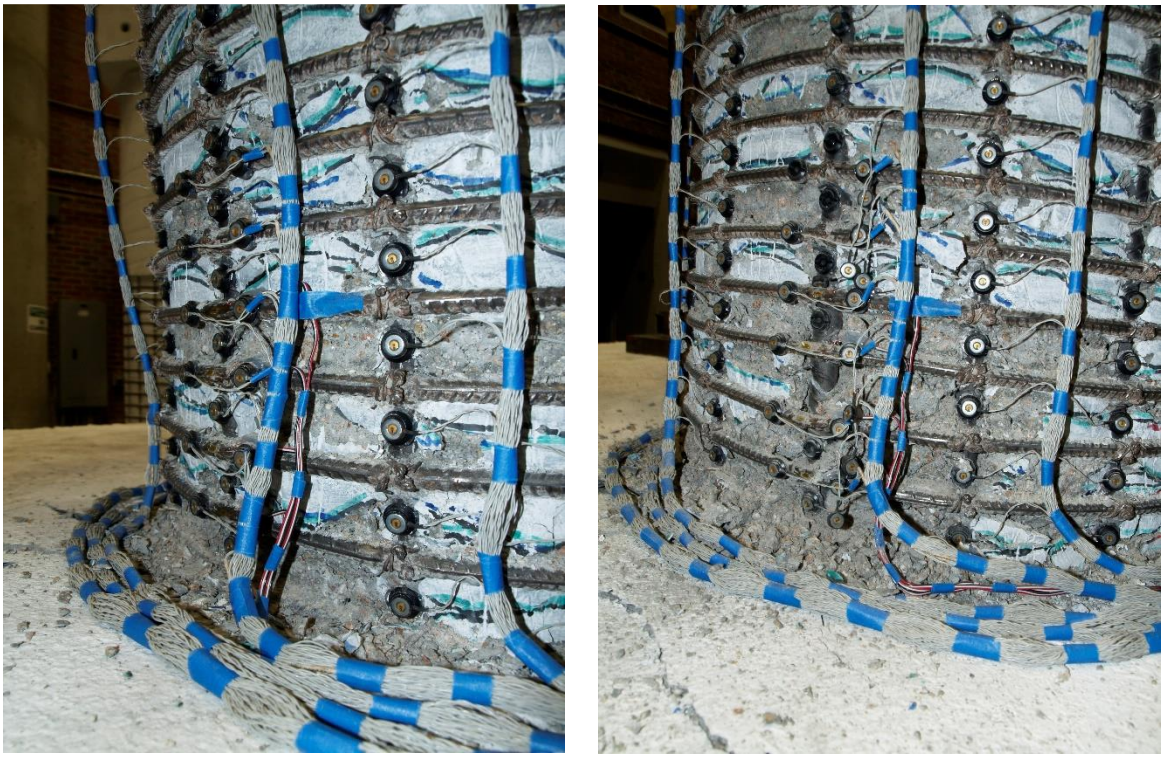

Figure 10-20. Test 7: (Left) North Bar Buckling at $\mu_{\Delta 7}^{+1y} = 8.67"$ and (Right) North Bar Fracture at $-8.19"$ during $\mu_{\Delta 7}^{-2y}$

Figure 10-21. Test 7: (Left) North and (Right) South Sides of the Specimen after the Test

Figure 10-22. Test 7: (Left) East and (Right) West Sides of the Specimen after the Test

Test 7 - Strain Data Analysis

North and South Bar Strains

Vertical strain profiles for North and South reinforcement during y-direction cycles are shown in Figure 10-23 and Figure 10-24. Strains in the lowest four spiral layers during compressive y-direction cycles on the North and South sides of the specimen appear in Figure 10-25 and Figure 10-26. The relationship between strain and displacement for either peak tensile or peak compressive gauge lengths appear in Figure 10-27 through Figure 10-31. These figures contain monotonic moment curvature predictions for respective plastic hinge methods. PCK (2007) Lp refers to the (Priestley, Calvi and Kowalsky 2007) plastic hinge method, GN15 Tension/Compression Lpr refers to the (Goodnight, Kowalsky and Nau 2015a) unidirectional modified plastic hinge method, TX Measured refer to using the measured extent of plasticity and average equivalent strain penetration length from this specific test, and New Equations refers to a new bidirectional plastic hinge method which was created based on this study. Details of the new plastic hinge method appear in a later chapter of this report.

The spiral strain gauge hysteresis for the third layer above the footing on the North side of the specimen is shown in Figure 10-33. Tension strains in the third spiral layer increased during $\mu_{\Delta 7}^{+1y} = 8.67$" as the North extreme fiber bar visibly buckled, see Figure 10-20. The visual observation of bar buckling was confirmed upon inspection of the North longitudinal bar strain hysteresis in Figure 10-32; however, there was slight measurable outward deformation in the previous compressive cycle.

The spiral strain gauge hysteresis for the second layer above the footing on the South side of the specimen is shown in Figure 10-36. The South reinforcement never visibly buckled; however, there was slight measurable outward deformation in the final compressive cycle as shown in Figure 10-35.

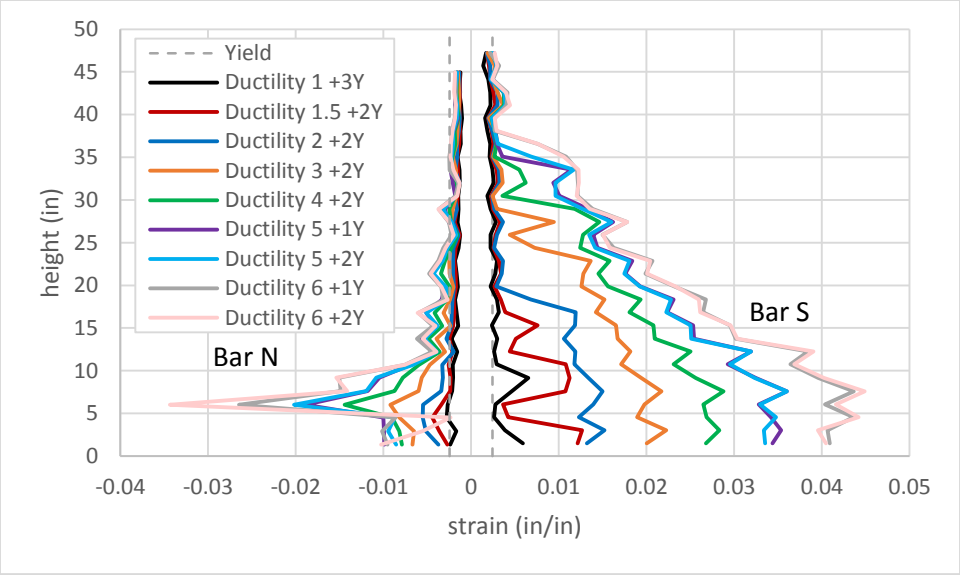

Figure 10-23. Test 7: Vertical Strain Profiles for Loading in the +Y-direction

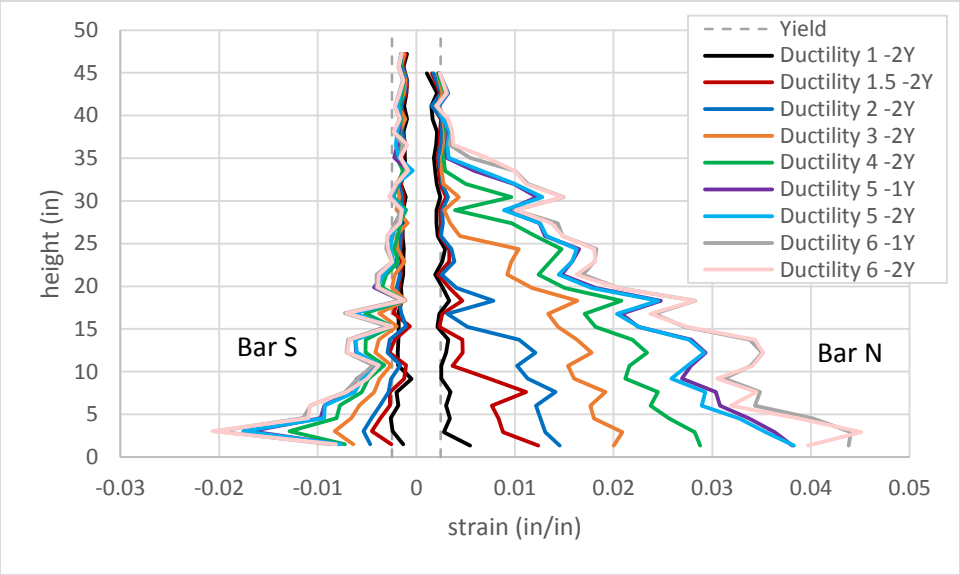

Figure 10-24. Test 7: Vertical Strain Profiles for Loading in the -Y-direction

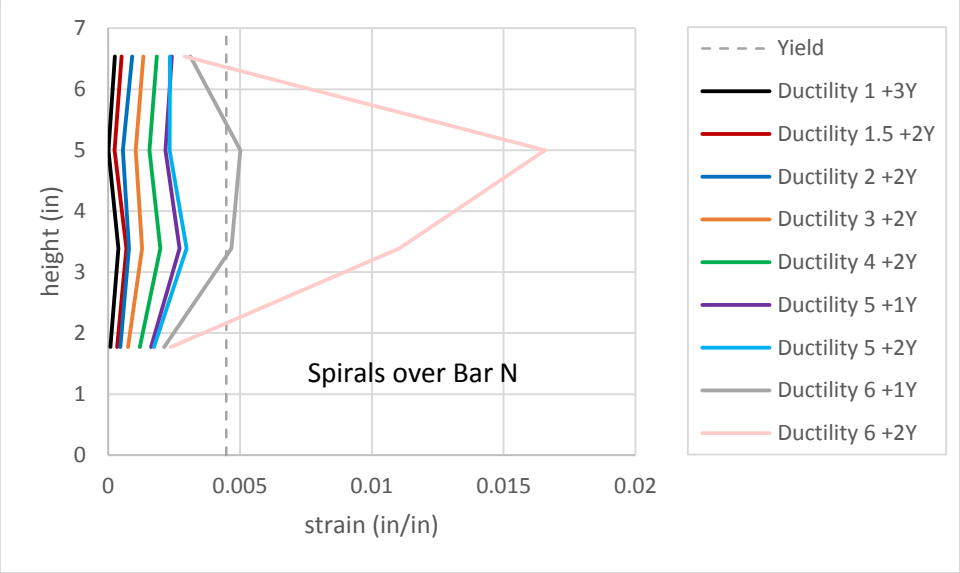

Figure 10-25. Test 7: Spiral Strains Measured Over the North Extreme Fiber Bar during +Y Cycles

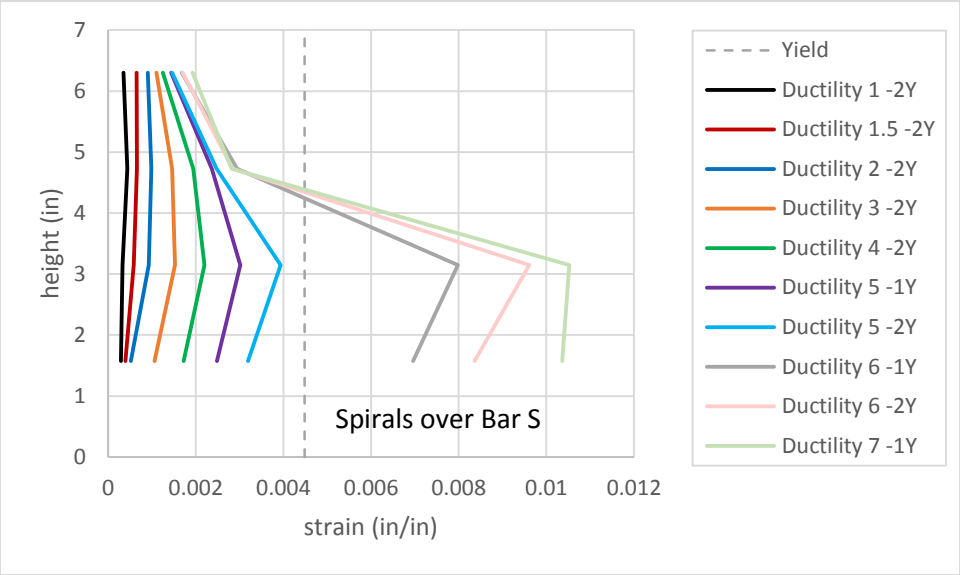

Figure 10-26. Test 7: Spiral Strains Measured Over the South Extreme Fiber Bar during -Y Cycles

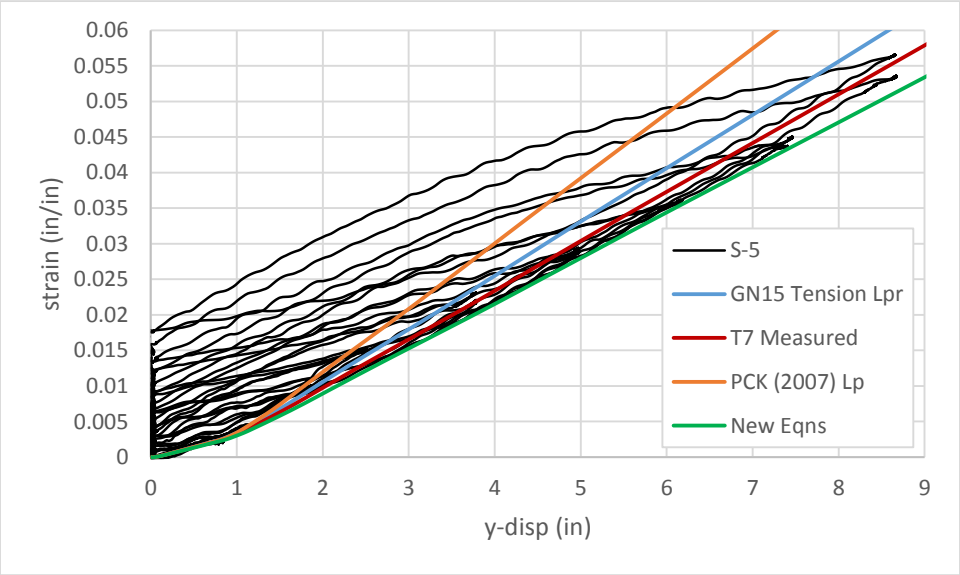

Figure 10-27. Test 7: Tension Strain-Disp. for Bar S (Gauge Length 5 Centered 7.59" above the Footing)

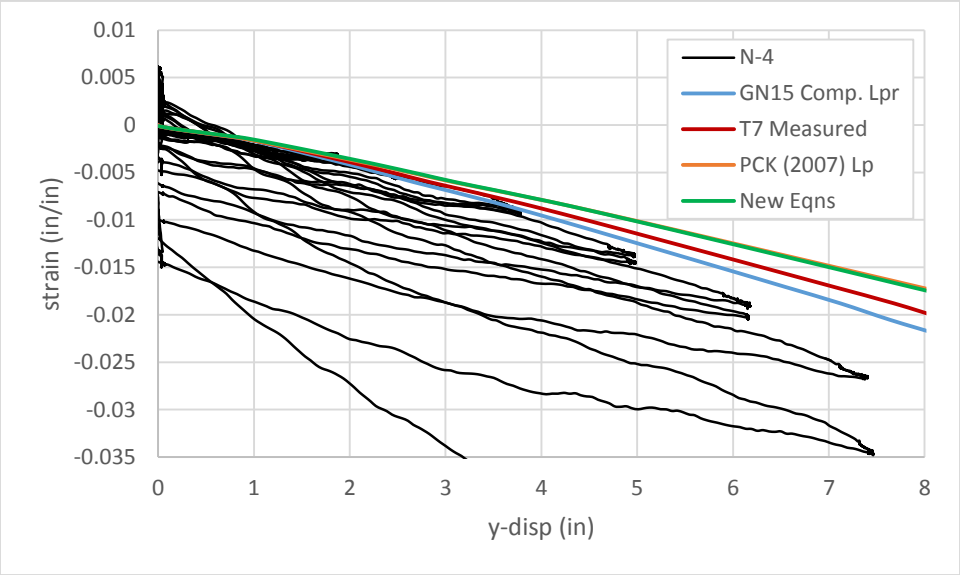

Figure 10-28. Test 7: Compression Strain-Disp. for Bar N (Gauge Length 4 Centered 6.03" above the Footing)

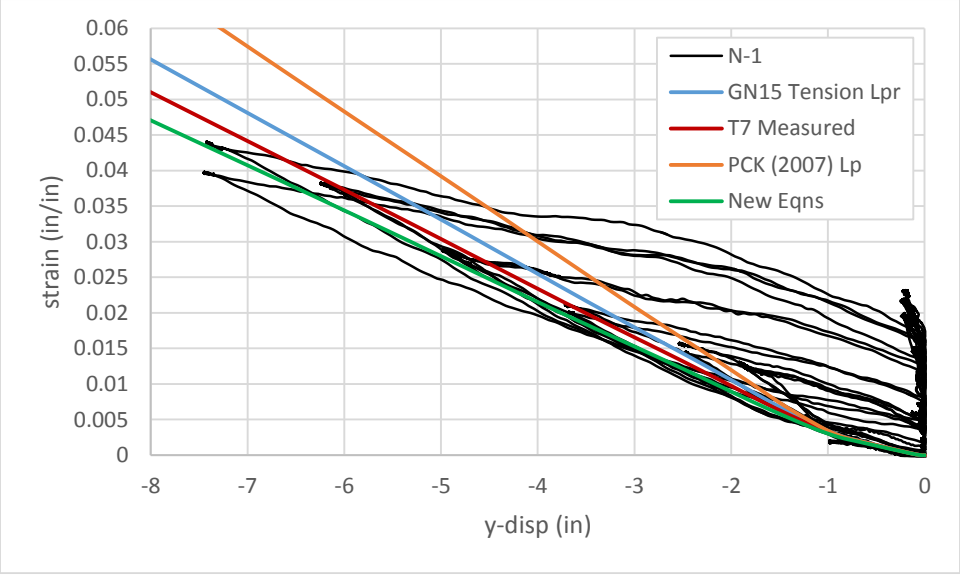

Figure 10-29. Test 7: Tension Strain-Disp. for Bar N (Gauge Length 1 Centered 1.35" above the Footing)

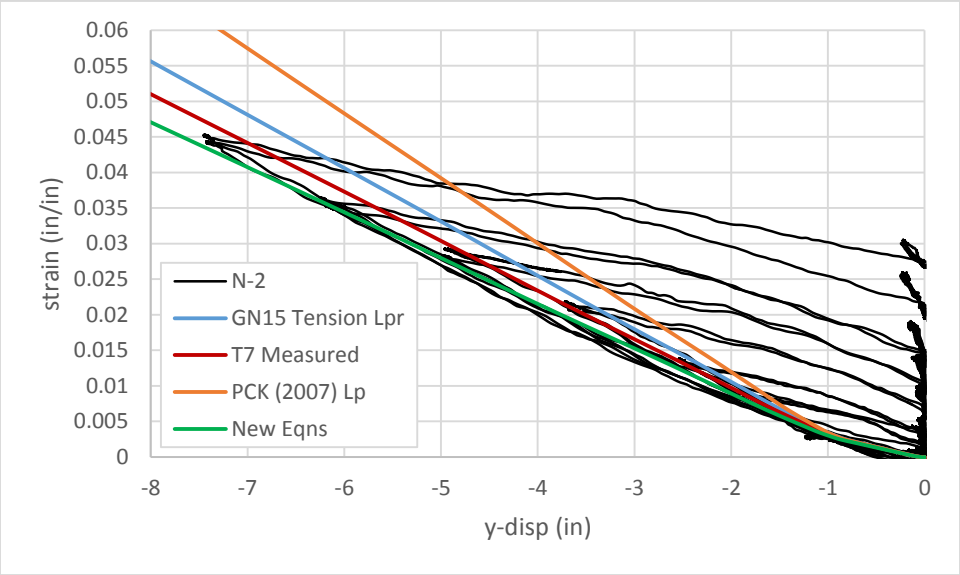

Figure 10-30. Test 7: Tension Strain-Disp. for Bar N (Gauge Length 2 Centered 2.93" above the Footing)

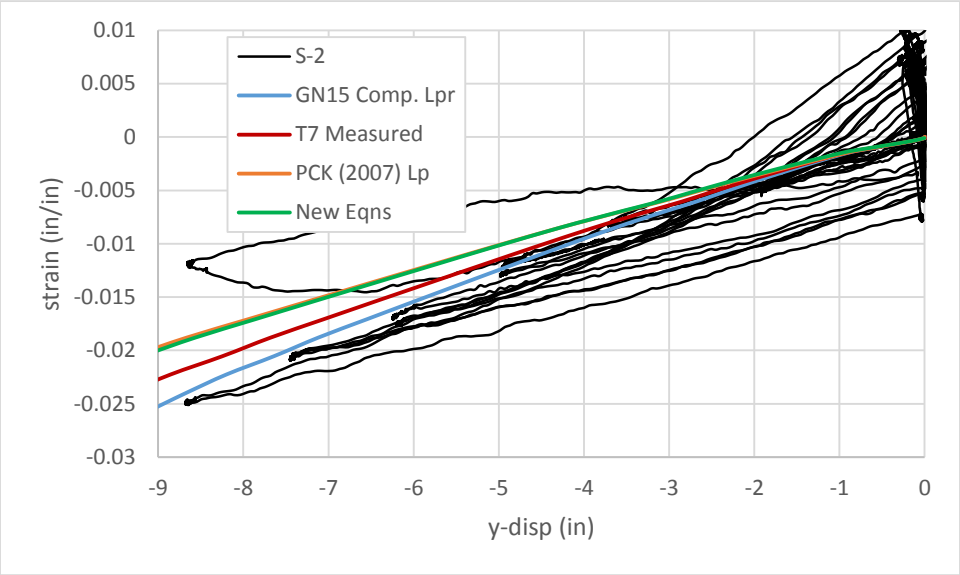

Figure 10-31. Test 7: Compression Strain-Disp. for Bar S (Gauge Length 2 Centered 3.03" above the Footing)

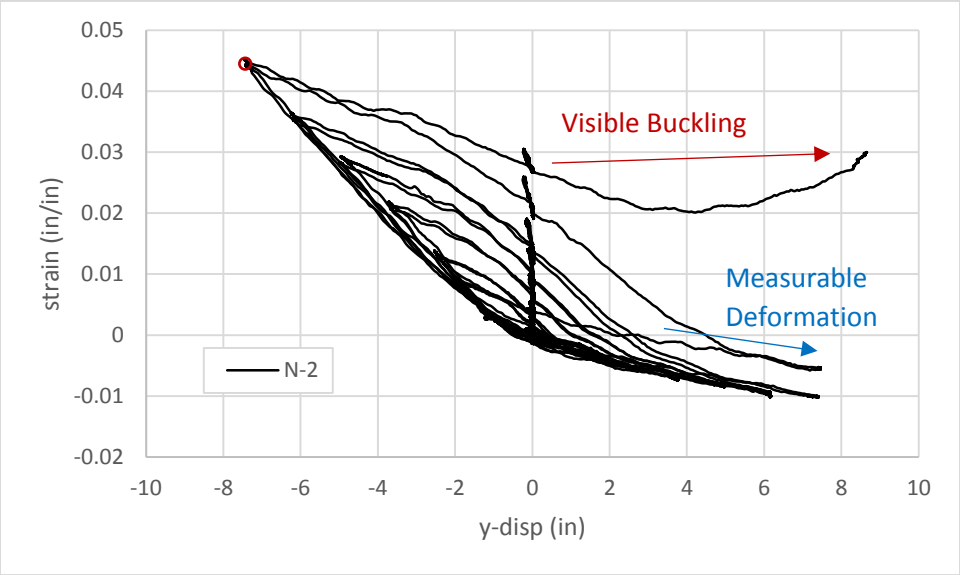

Figure 10-32. Test 7: Strain Hysteresis over the North Buckled Bar (Gauge Length 2 Centered 2.93" above the Footing)

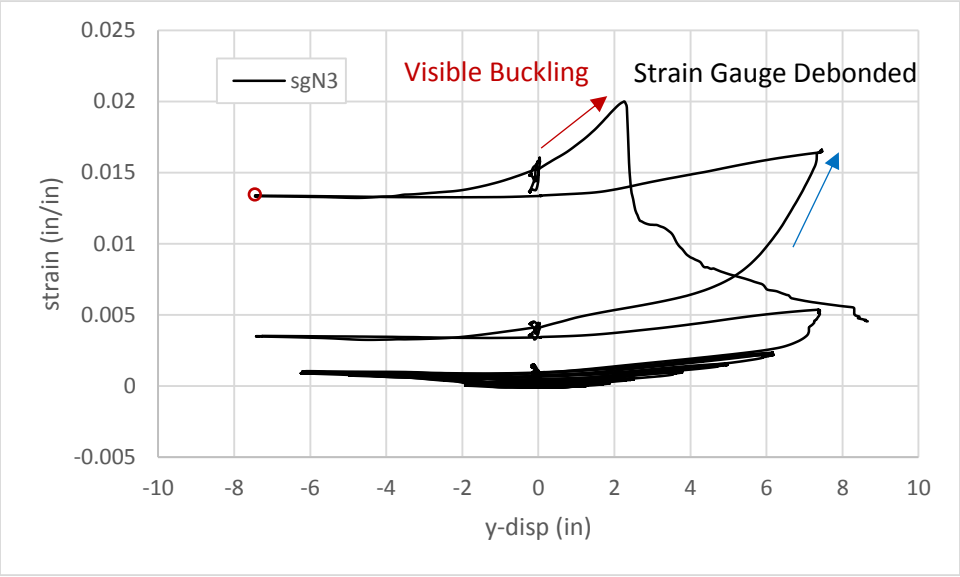

Figure 10-33. Test 7: Spiral Strain Hysteresis for the 3rd North Layer above the Footing

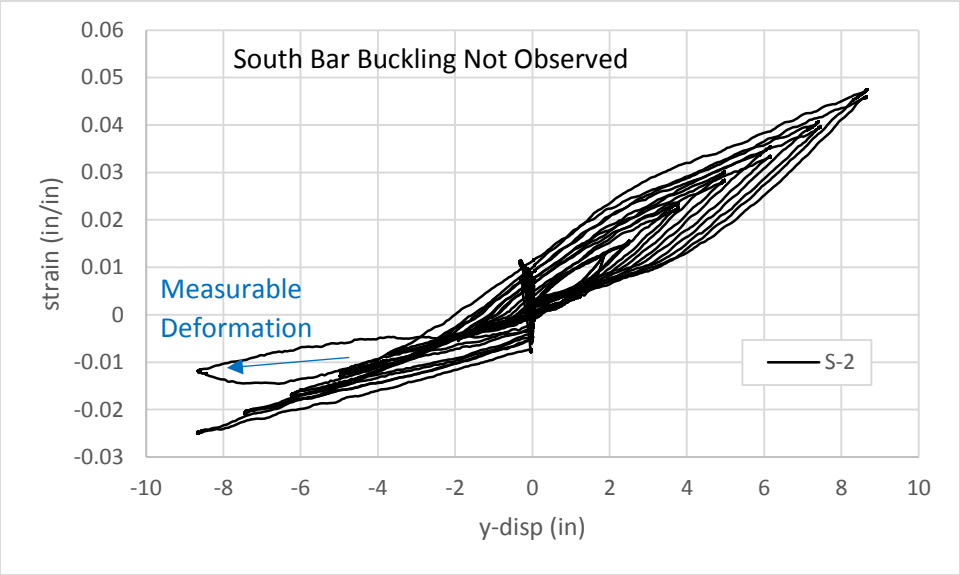

Figure 10-34. Test 7: Strain Hysteresis over the South Bar (Gauge Length 2 Centered 3.03" above the Footing)

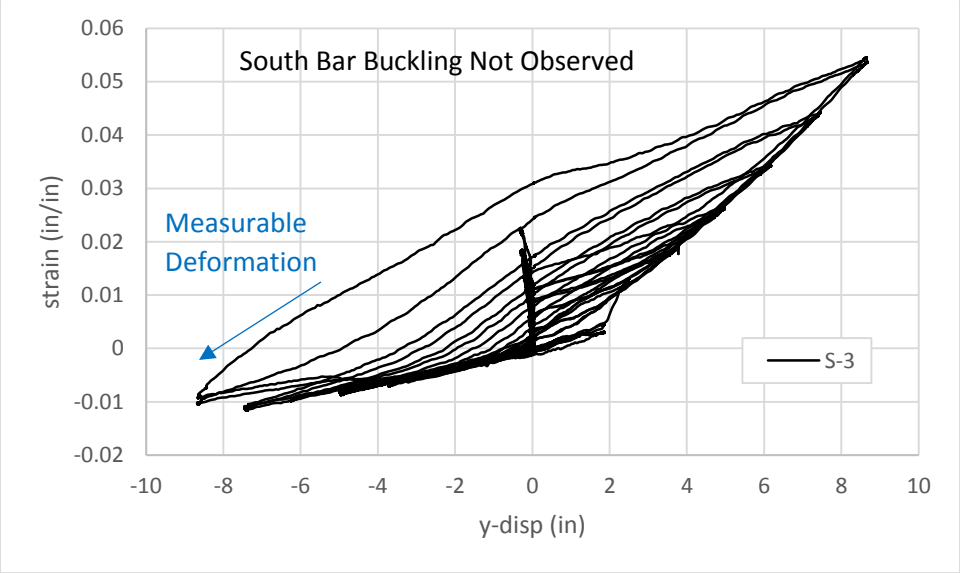

Figure 10-35. Test 7: Strain Hysteresis over the South Bar (Gauge Length 3 Centered 4.55" above the Footing)

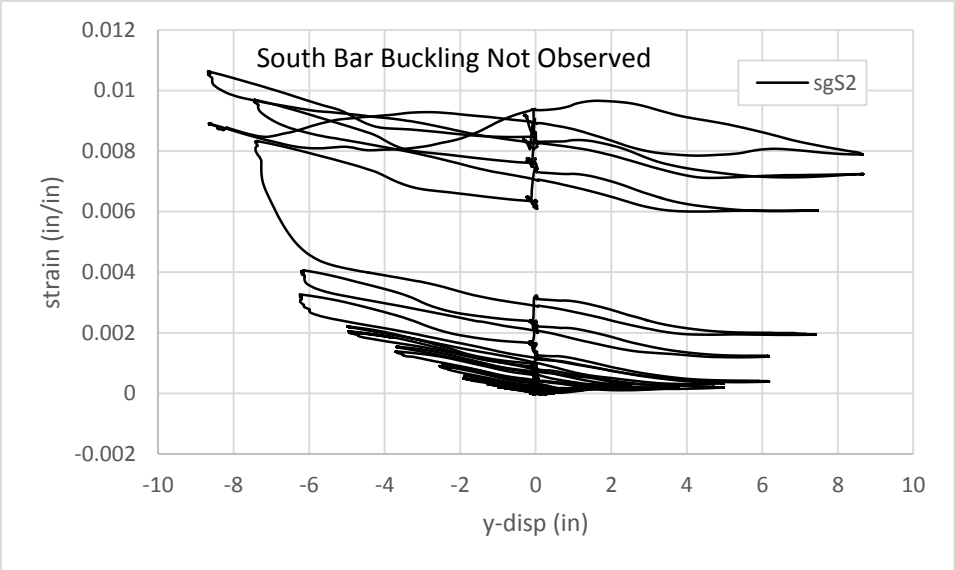

Figure 10-36. Test 7: Spiral Strain Hysteresis for the 2nd South Layer above the Footing

East and West Bar Strains

Vertical strain profiles for East and West reinforcement during x-direction cycles are shown in Figure 10-37 and Figure 10-38. Strains in the lowest four spiral layers during compressive x-direction cycles on the East and West sides of the specimen appear in Figure 10-39 and Figure 10-40. The relationship between strain and displacement for either peak tensile or peak compressive gauge lengths appear in Figure 10-41 through Figure 10-46. These figures contain monotonic moment curvature predictions for respective plastic hinge methods. PCK (2007) Lp refers to the (Priestley, Calvi and Kowalsky 2007) plastic hinge method, GN15 Tension/Compression Lpr refers to the (Goodnight, Kowalsky and Nau 2015a) unidirectional modified plastic hinge method, TX Measured refer to using the measured extent of plasticity and average equivalent strain penetration length from this specific test, and New Equations refers to a new bidirectional plastic hinge method which was created based on this study. Details of the new plastic hinge method appear in a later chapter of this report.

Spiral strain gauge and Optotrak strain hysteresis for the second and third East spiral layers above the footing appear in Figure 10-49 and Figure 10-50. The strain gauge over the second East spiral layer went off scale during $\mu_{\Delta 5}^{+2x} = 6.19"$, even though the reinforcement remained visibly straight. The third spiral layer had a spike in measured tension strains during $\mu_{\Delta 6}^{+1x} = 7.40"$, when the East extreme fiber bar buckled, see Figure 10-19. The visual observation of bar buckling was confirmed upon inspection of the East longitudinal bar strain hystereses in Figure 10-47 and Figure 10-48; however, there was significant measurable outward deformation in the previous compressive cycle.

Spiral strain gauge and Optotrak strain hysteresis for the first and second West spiral layers above the footing appear in Figure 10-53 and Figure 10-54. Strain gauges over both layers went off scale during $\mu_{\Delta 6}^{-1x} = -7.43"$, even though the reinforcement remained visibly straight. The visual observation of bar buckling was confirmed upon inspection of the West longitudinal bar strain hystereses in Figure 10-51 and Figure 10-52; however, there was significant measurable outward deformation in the previous compressive cycles.

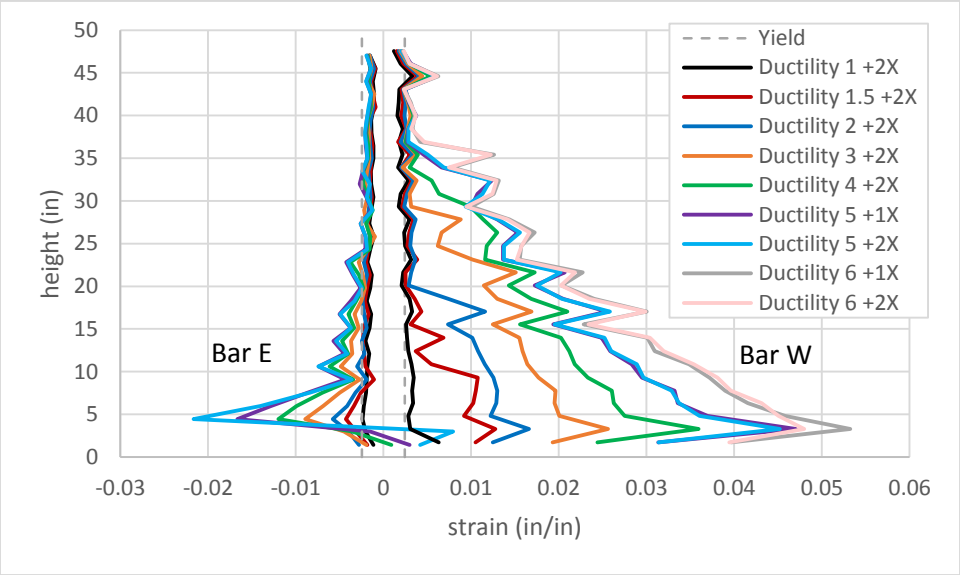

Figure 10-37. Test 7: Vertical Strain Profiles for Loading in the +X-direction

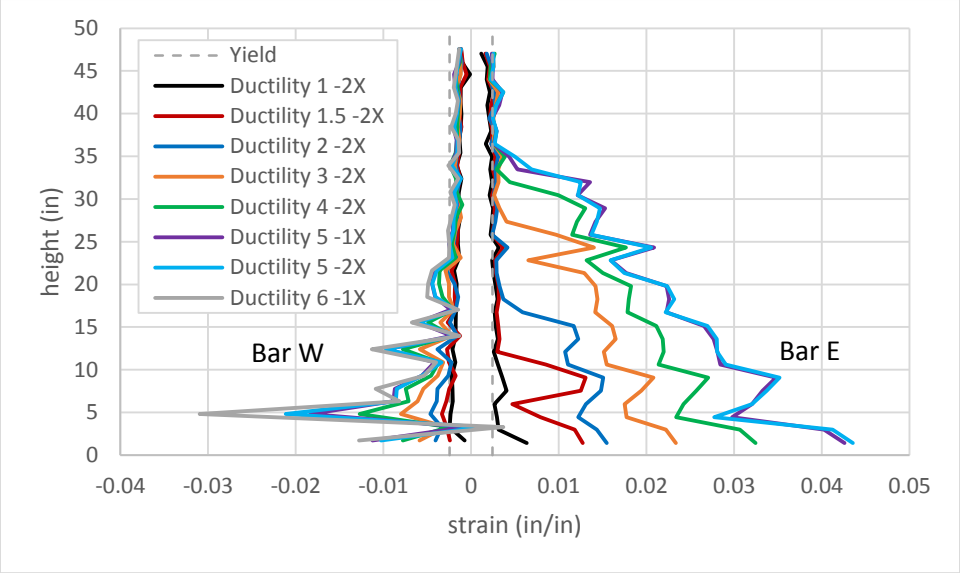

Figure 10-38. Test 7: Vertical Strain Profiles for Loading in the -X-direction

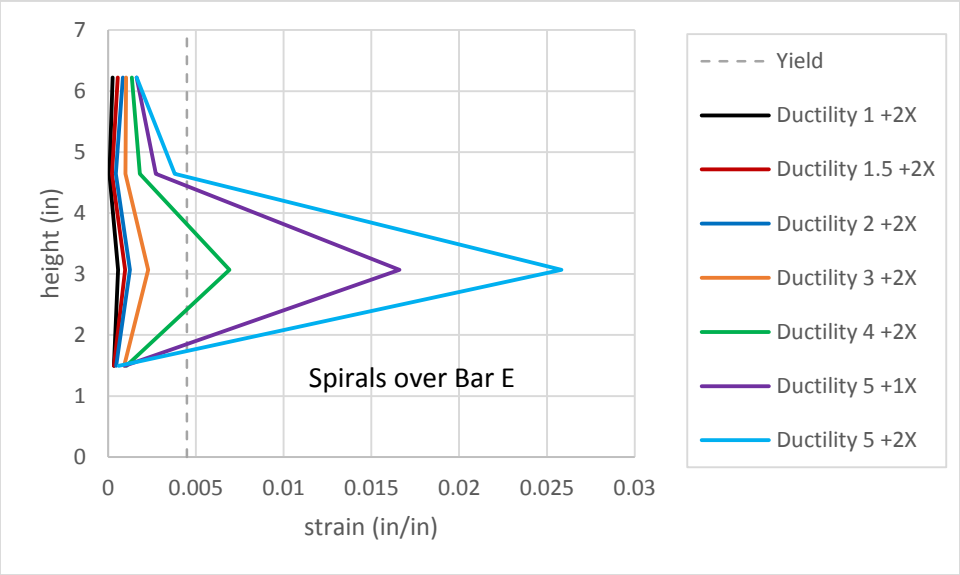

Figure 10-39. Test 7: Spiral Strains Measured Over the East Extreme Fiber Bar during +X Cycles

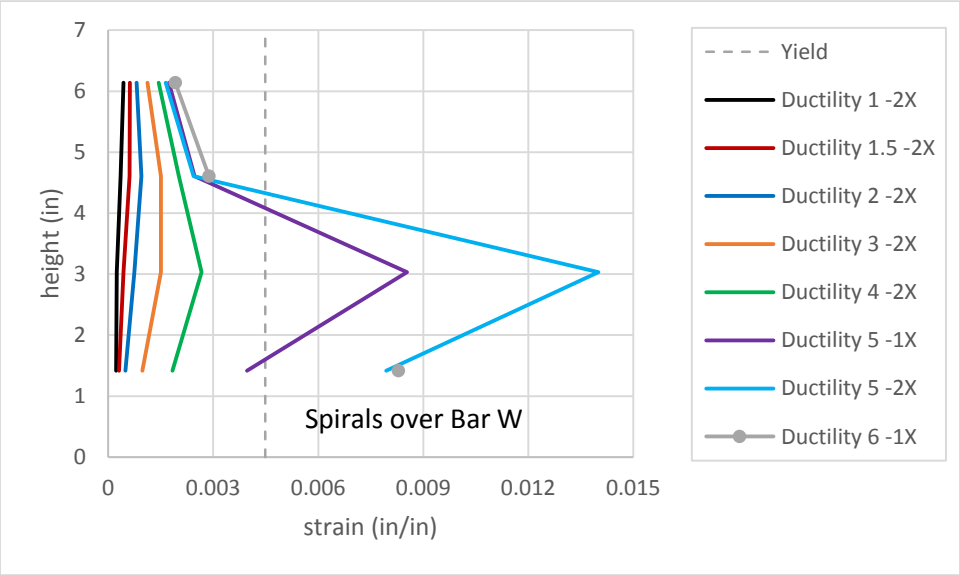

Figure 10-40. Test 7: Spiral Strains Measured Over the West Extreme Fiber Bar during -X Cycles

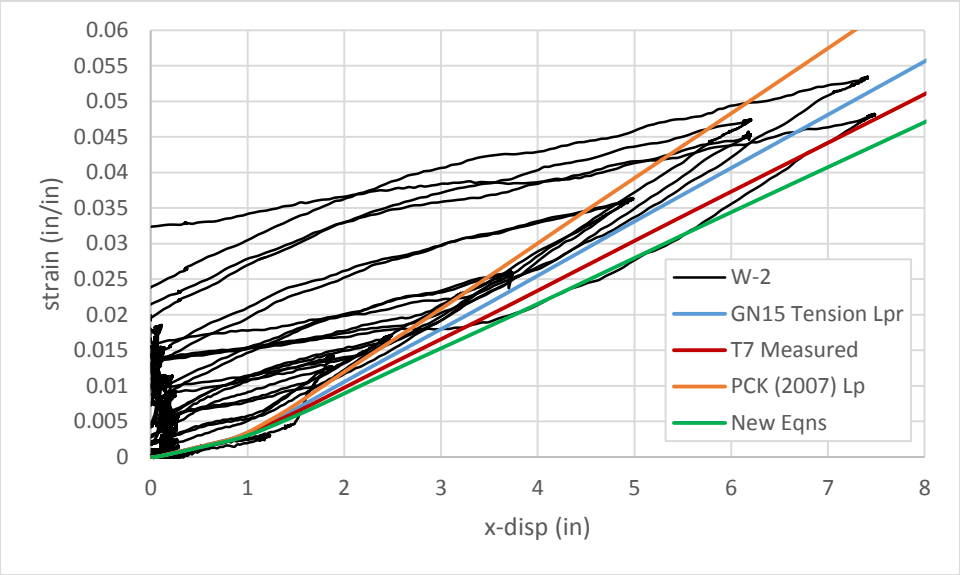

Figure 10-41. Test 7: Tension Strain-Disp. for Bar W (Gauge Length 2 Centered 3.30" above the Footing)

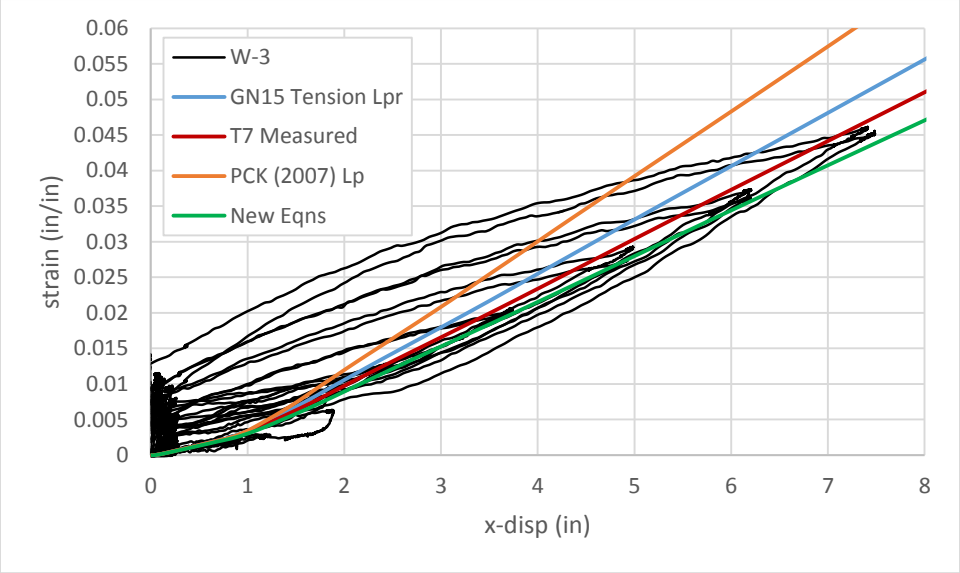

Figure 10-42. Test 7: Tension Strain-Disp. for Bar W (Gauge Length 3 Centered 4.83" above the Footing)

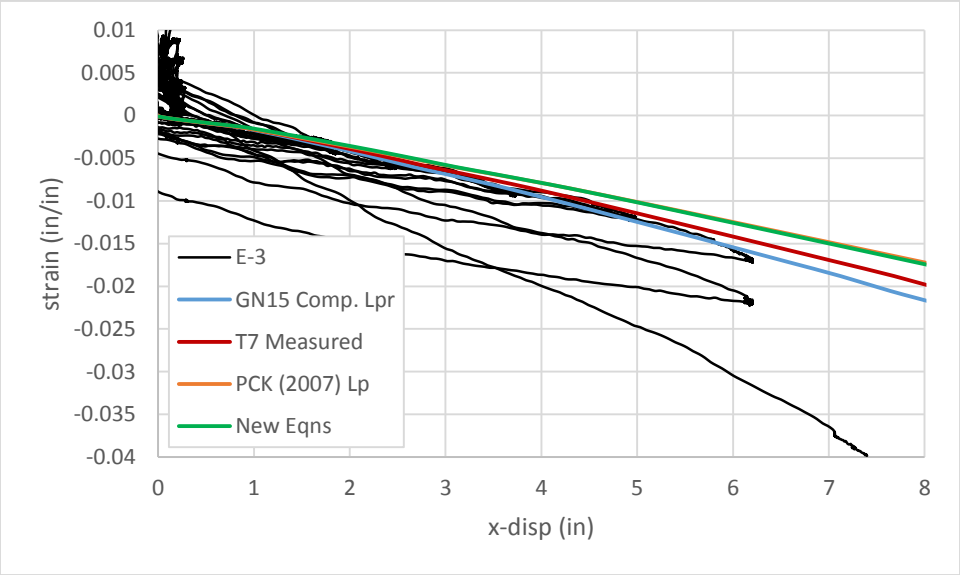

Figure 10-43. Test 7: Compression Strain-Disp. for Bar E (Gauge Length 3 Centered 4.46" above the Footing)

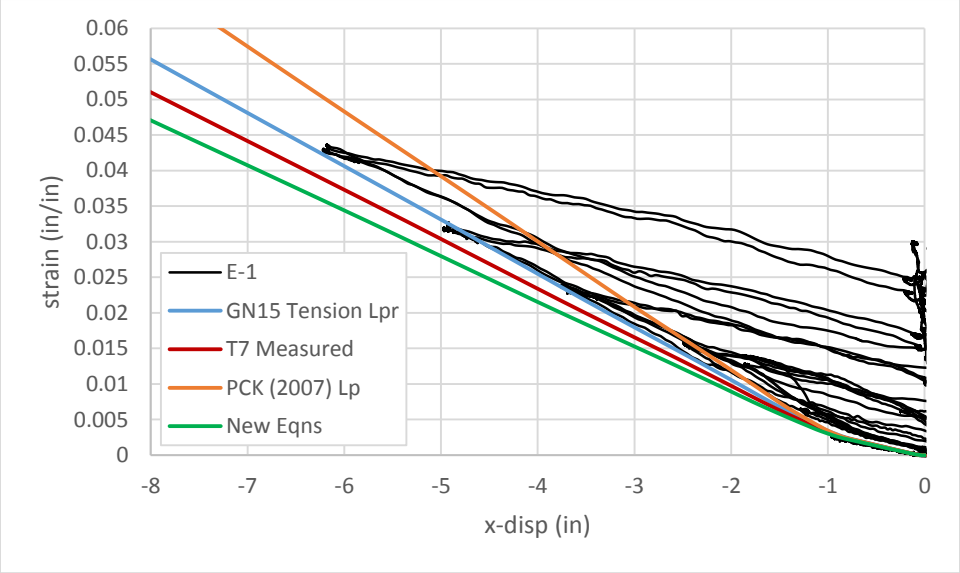

Figure 10-44. Test 7: Tension Strain-Disp. for Bar E (Gauge Length 1 Centered 1.43" above the Footing)

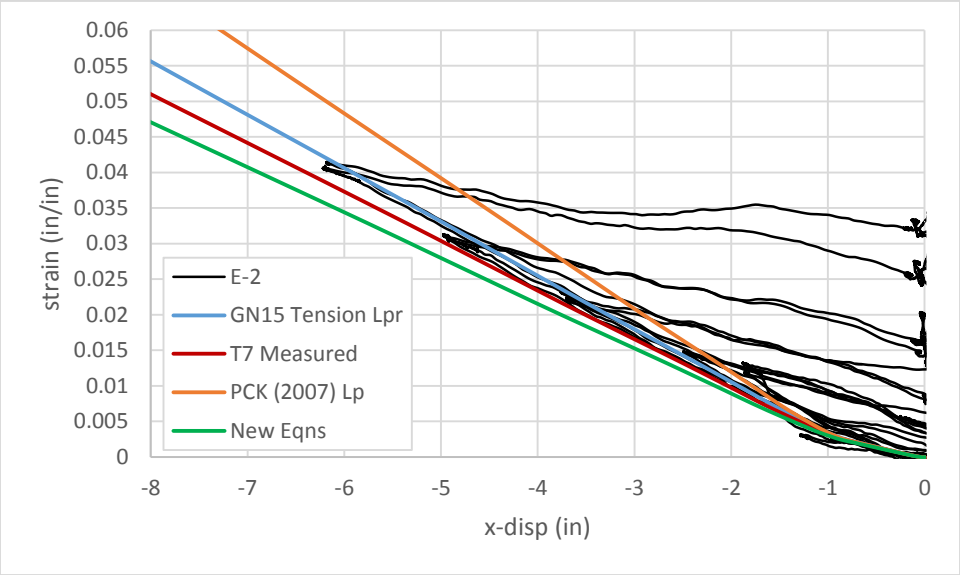

Figure 10-45. Test 7: Tension Strain-Disp. for Bar E (Gauge Length 2 Centered 2.97" above the Footing)

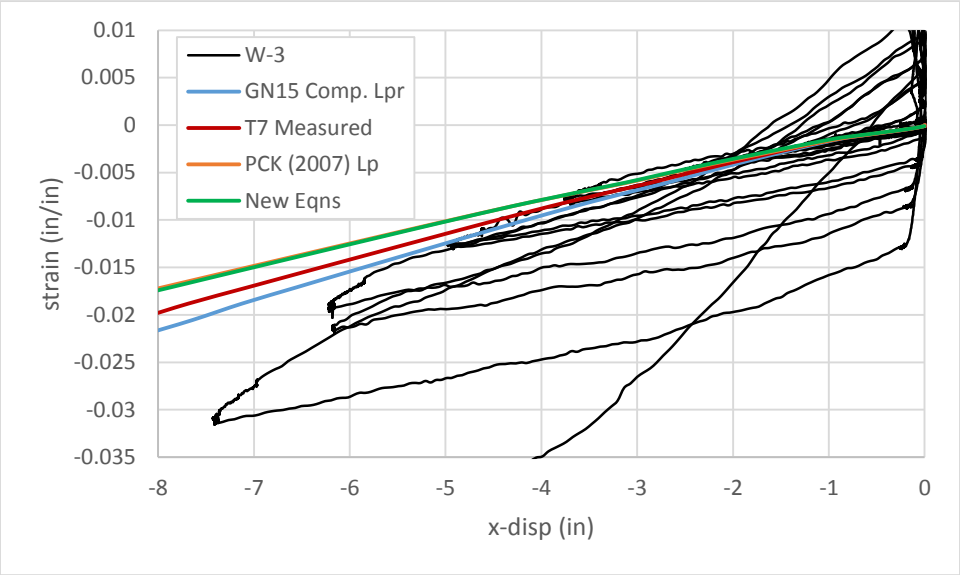

Figure 10-46. Test 7: Compression Strain-Disp. for Bar W (Gauge Length 3 Centered 4.83" above the Footing)

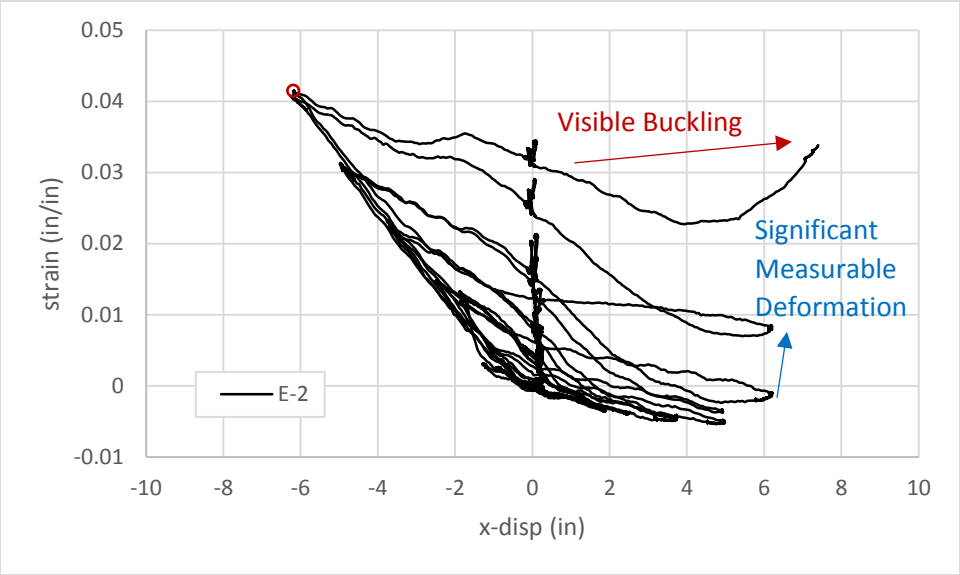

Figure 10-47. Test 7: Strain Hysteresis over the East Buckled Bar (Gauge Length 2 Centered 2.97" above the Footing)

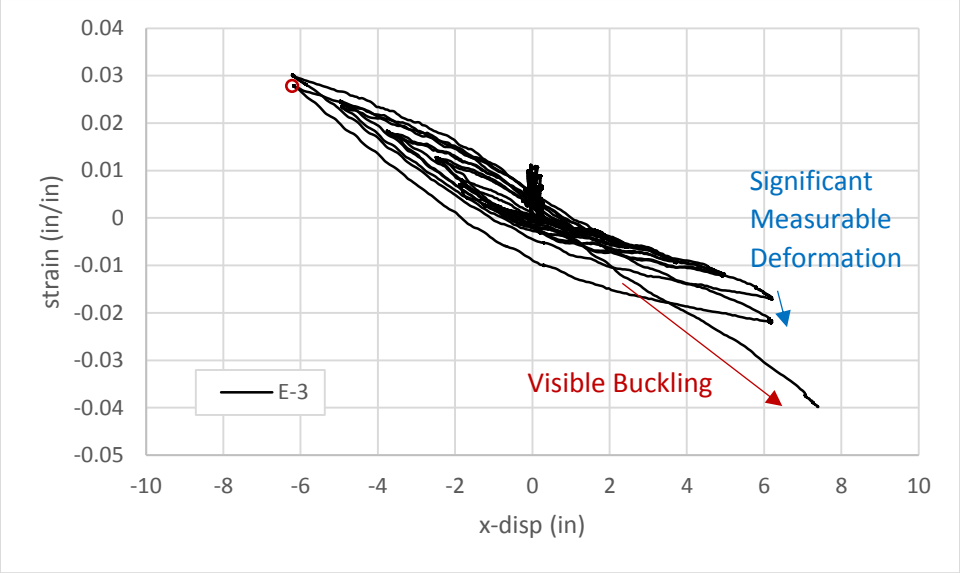

Figure 10-48. Test 7: Strain Hysteresis over the East Buckled Bar (Gauge Length 3 Centered 4.46" above the Footing)

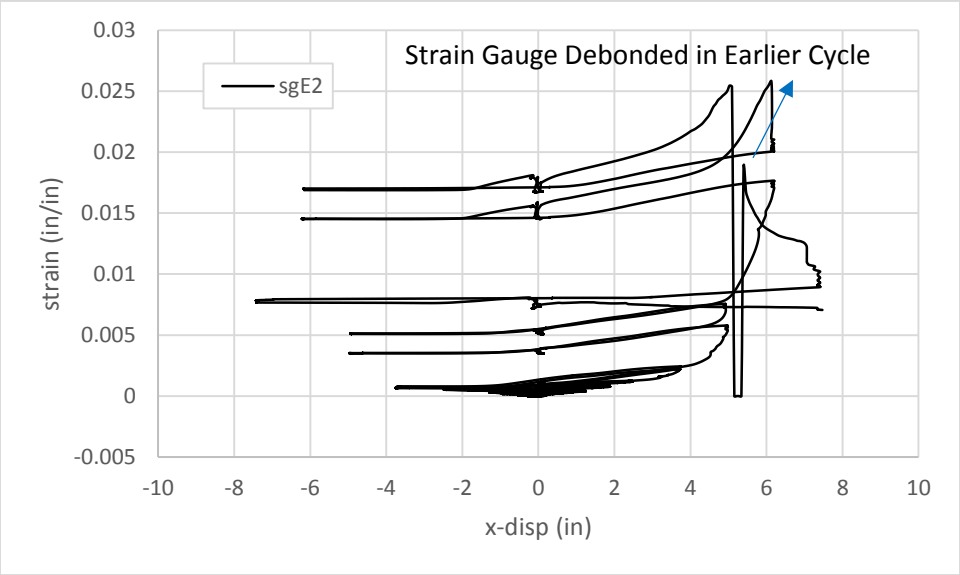

Figure 10-49. Test 7: Spiral Strain Hysteresis for the 2nd East Layer above the Footing

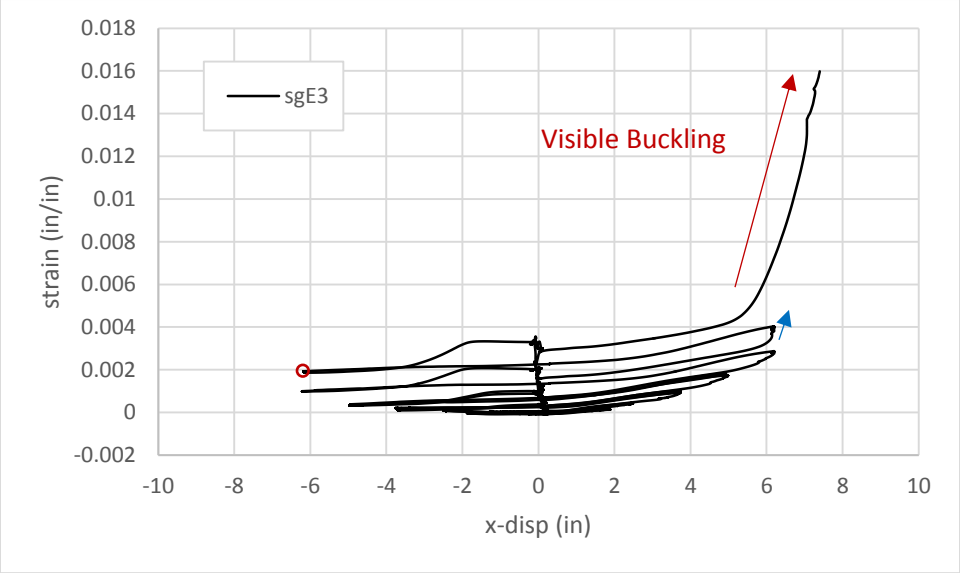

Figure 10-50. Test 7: Spiral Strain Hysteresis for the 3rd East Layer above the Footing

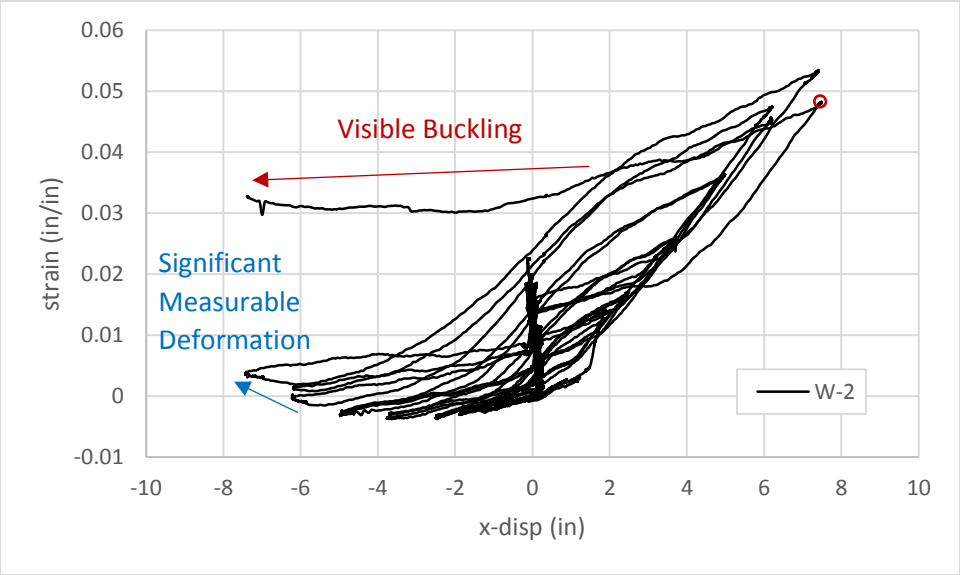

Figure 10-51. Test 7: Strain Hysteresis over the West Buckled Bar (Gauge Length 2 Centered 3.30" above the Footing)

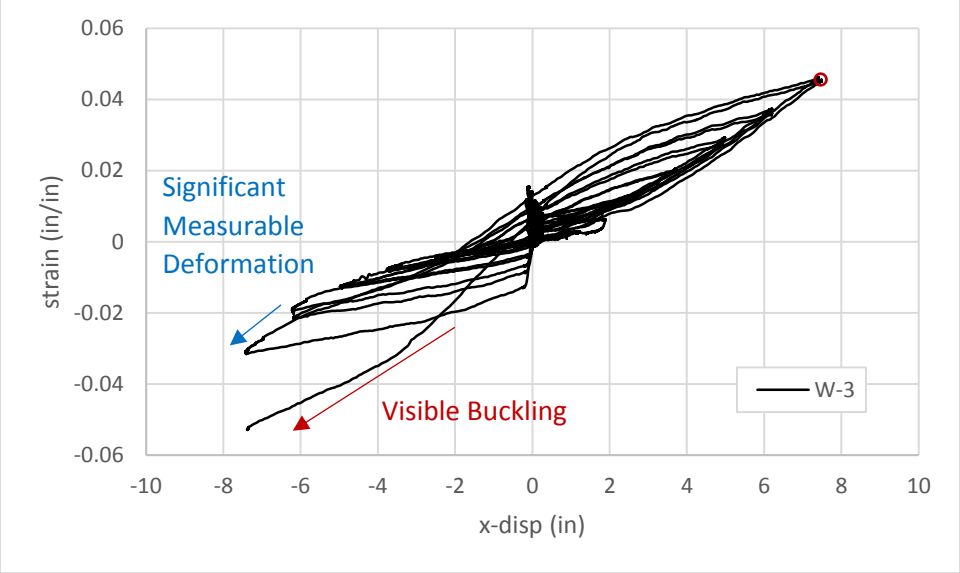

Figure 10-52. Test 7: Strain Hysteresis over the West Buckled Bar (Gauge Length 3 Centered 4.83" above the Footing)

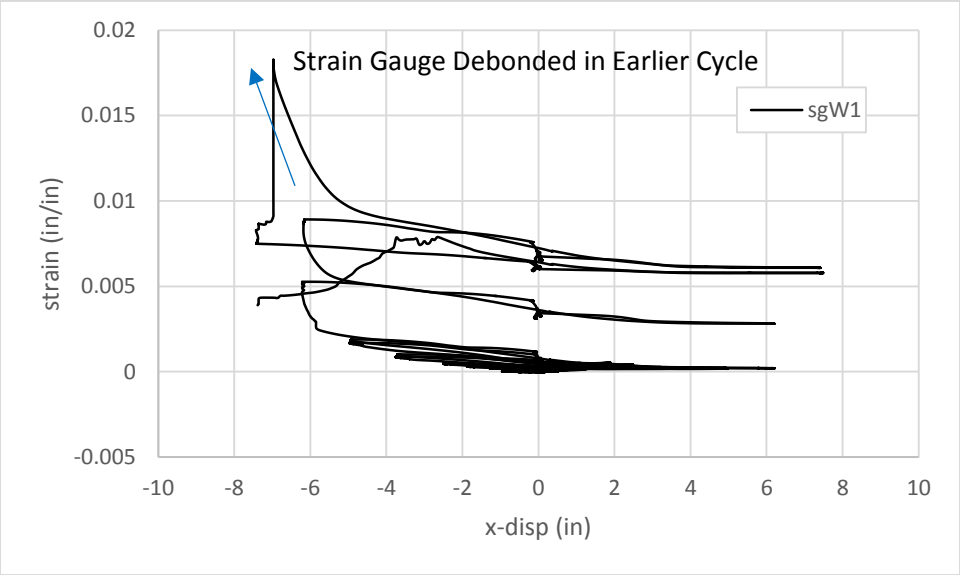

Figure 10-53. Test 7: Spiral Strain Hysteresis for the 1st West Layer above the Footing

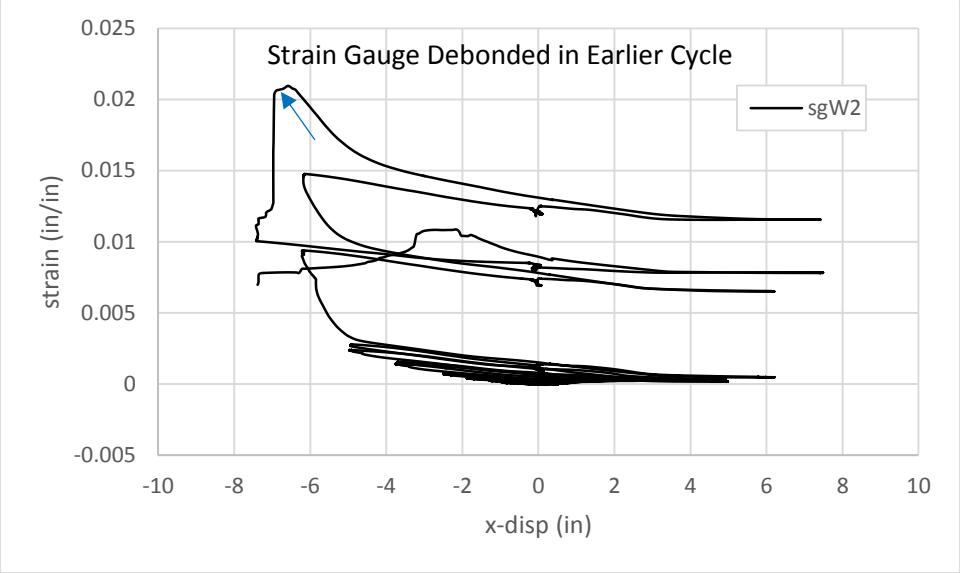

Figure 10-54. Test 7: Spiral Strain Hysteresis for the 2nd West Layer above the Footing

Test 7 - Curvature and Strain Penetration Data

Curvature and stain penetration data for Test 7 is presented in the following section. The methods in which this data was generated are outlined in the summary for Test 1. Sample cross section curvature profiles are shown in Figure 10-55 and Figure 10-56. Vertical curvature profiles for respective loading directions appear in Figure 10-57 through Figure 10-61. Fixed-end rotations attributable to strain penetration of longitudinal reinforcement into the footing are shown in Figure 10-62 through Figure 10-64. Comparison of the measured displacements to those obtained via integration of the measured curvature profiles and extrapolation of the fixed-end rotation to the center of the applied lateral load are shown in Figure 10-65 and Figure 10-66.

The measured extent of plasticity is compared to design recommendations for the tensile triangular plastic hinge length in Figure 10-67. GN15 refers to the (Goodnight, Kowalsky and Nau 2015a) unidirectional tensile hinge length while New Equations refers to a new bidirectional plastic hinge method which was created based on this study. Details of the new plastic hinge method appear in a later chapter of this report. The measured equivalent strain penetration lengths are compared to design recommendations in Figure 10-68. GN15 refers to the (Goodnight, Kowalsky and Nau 2015a) unidirectional Lsp while PCK (2007) refers to the (Priestley, Calvi and Kowalsky 2007) definition of Lsp. Finally, the measured hysteretic response is compared to monotonic predictions in Figure 10-69 and Figure 10-70.

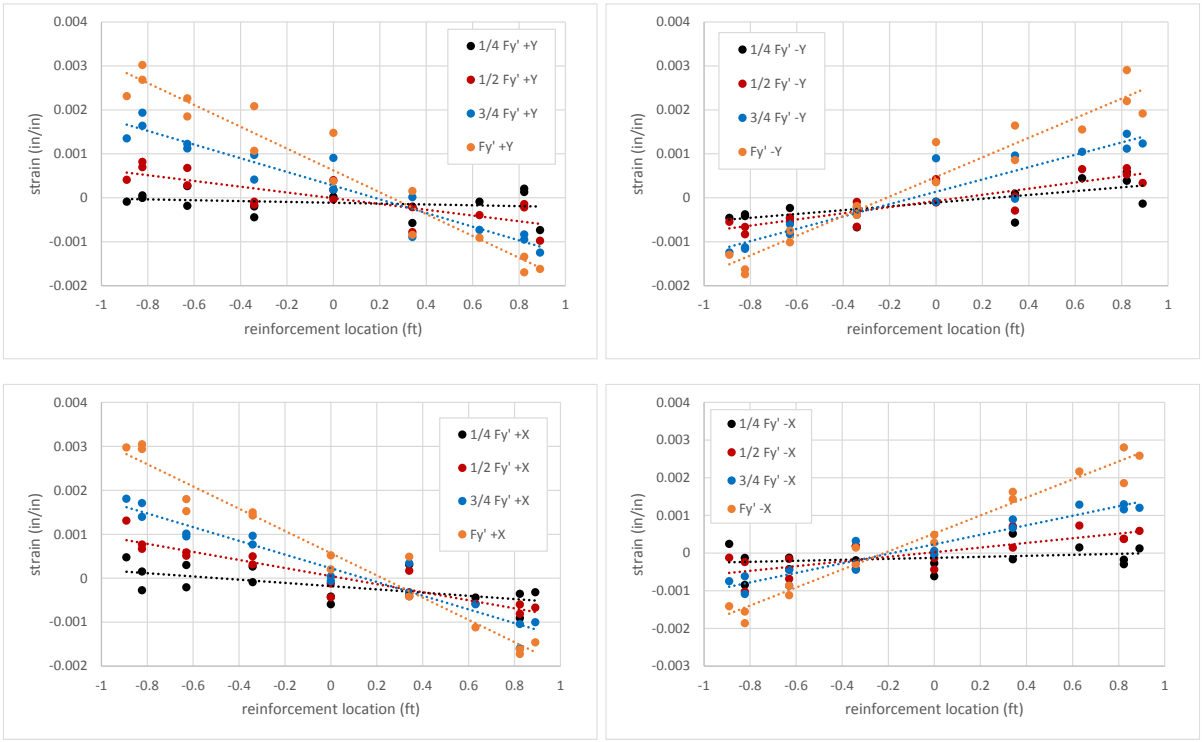

Figure 10-55. Test 7: Elastic Curvature Profiles for the First Instrumented Section above the Footing

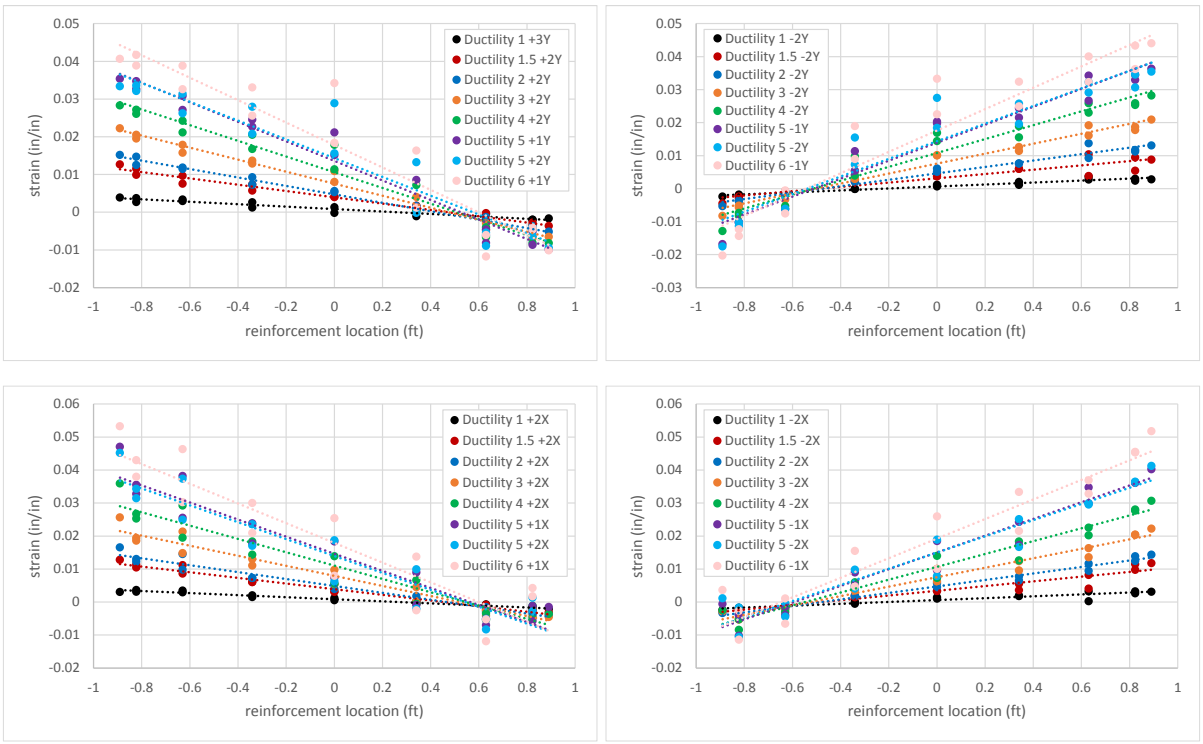

Figure 10-56. Test 7: Curvature Profiles for the Second Instrumented Section above the Footing

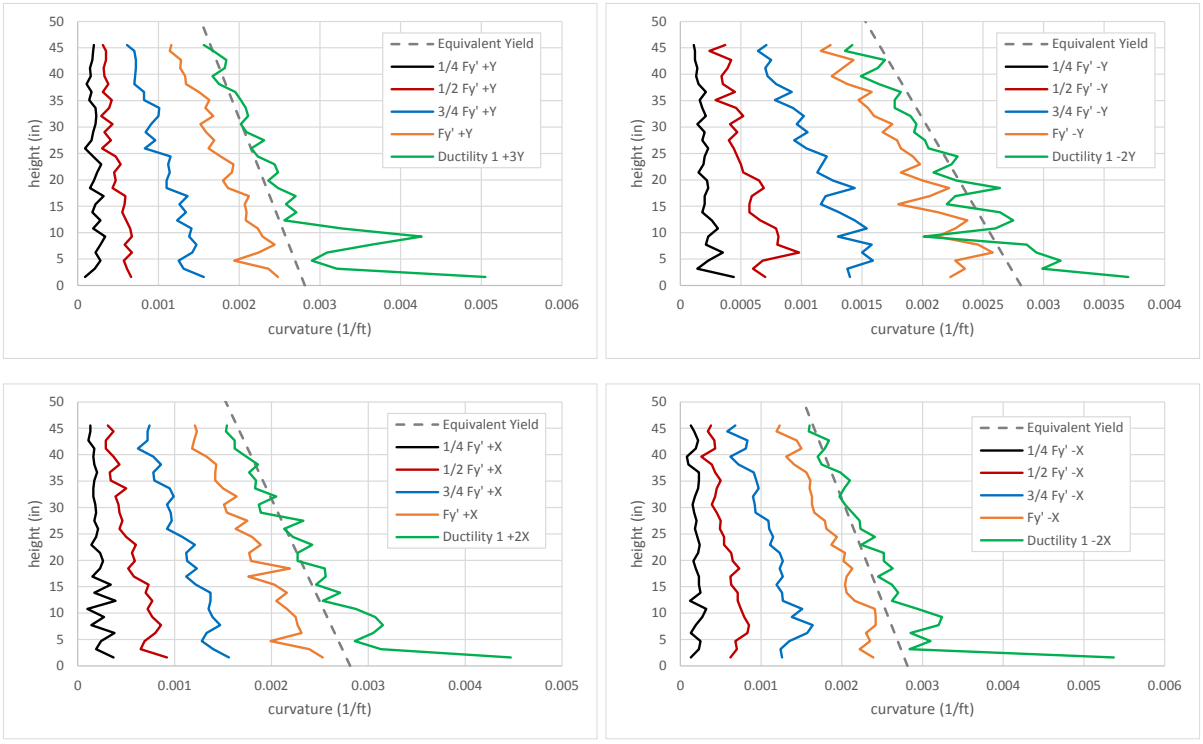

Figure 10-57. Test 7: Elastic Vertical Curvature Profiles

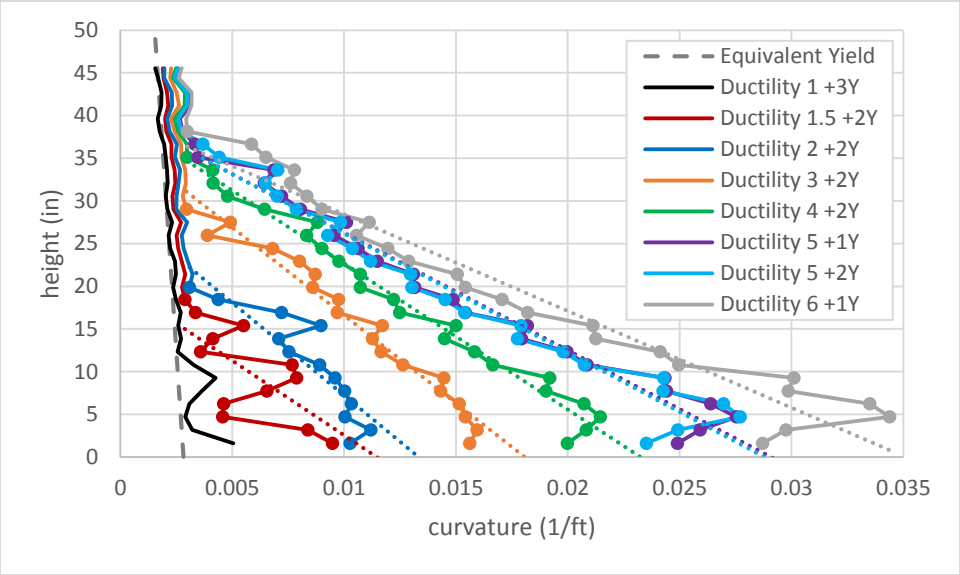

Figure 10-58. Test 7: Vertical Curvature Profiles for Loading in the +Y-direction

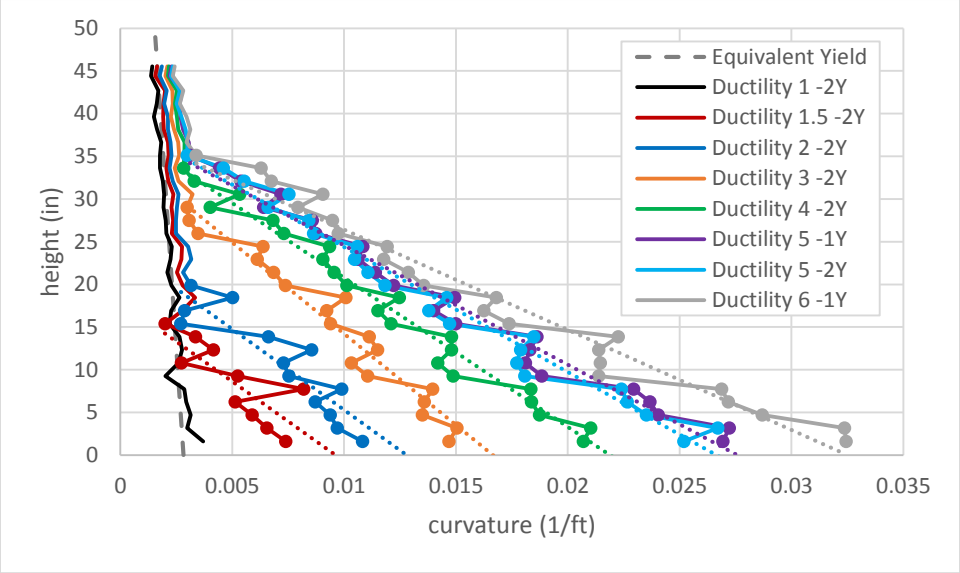

Figure 10-59. Test 7: Vertical Curvature Profiles for Loading in the -Y-direction

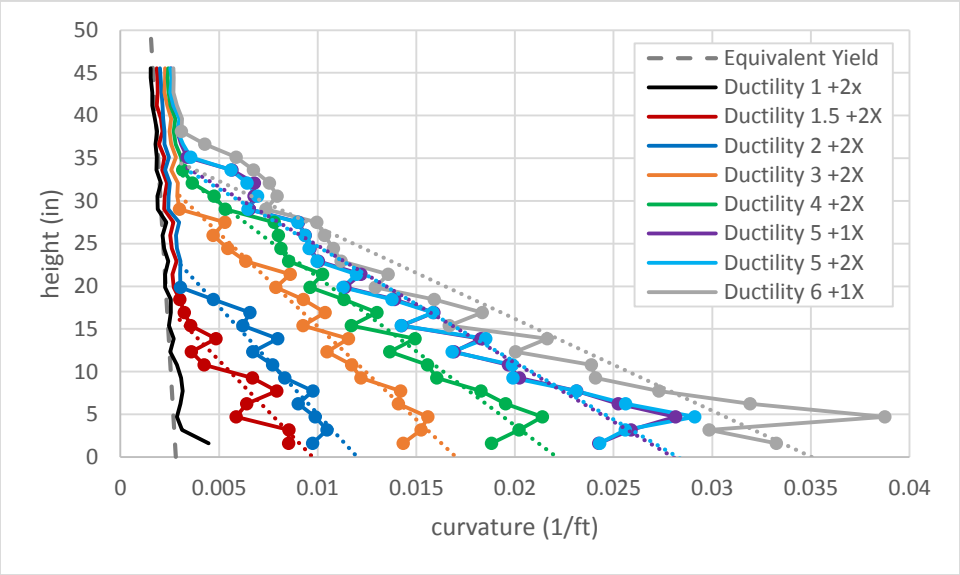

Figure 10-60. Test 7: Vertical Curvature Profiles for Loading in the +X-direction

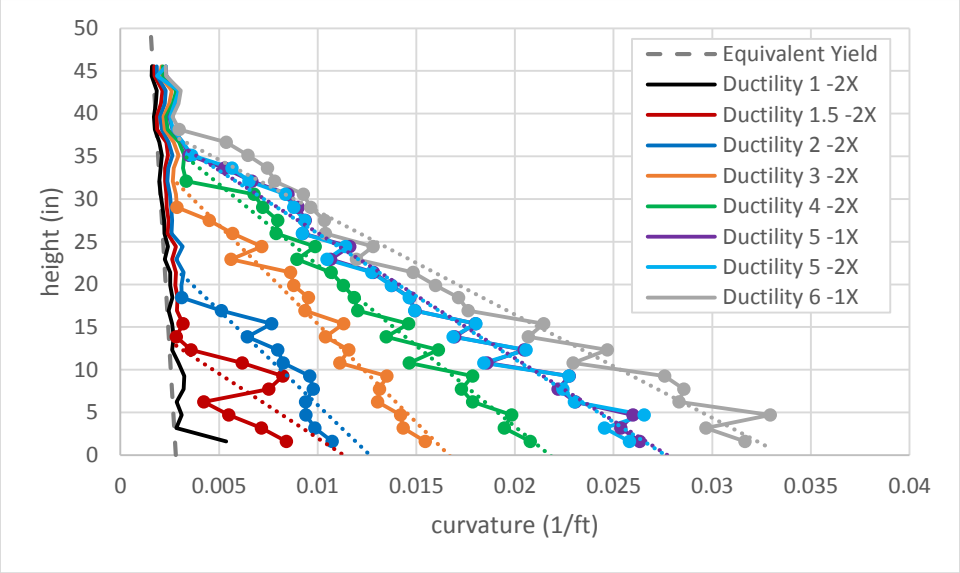

Figure 10-61. Test 7: Vertical Curvature Profiles for Loading in the -X-direction

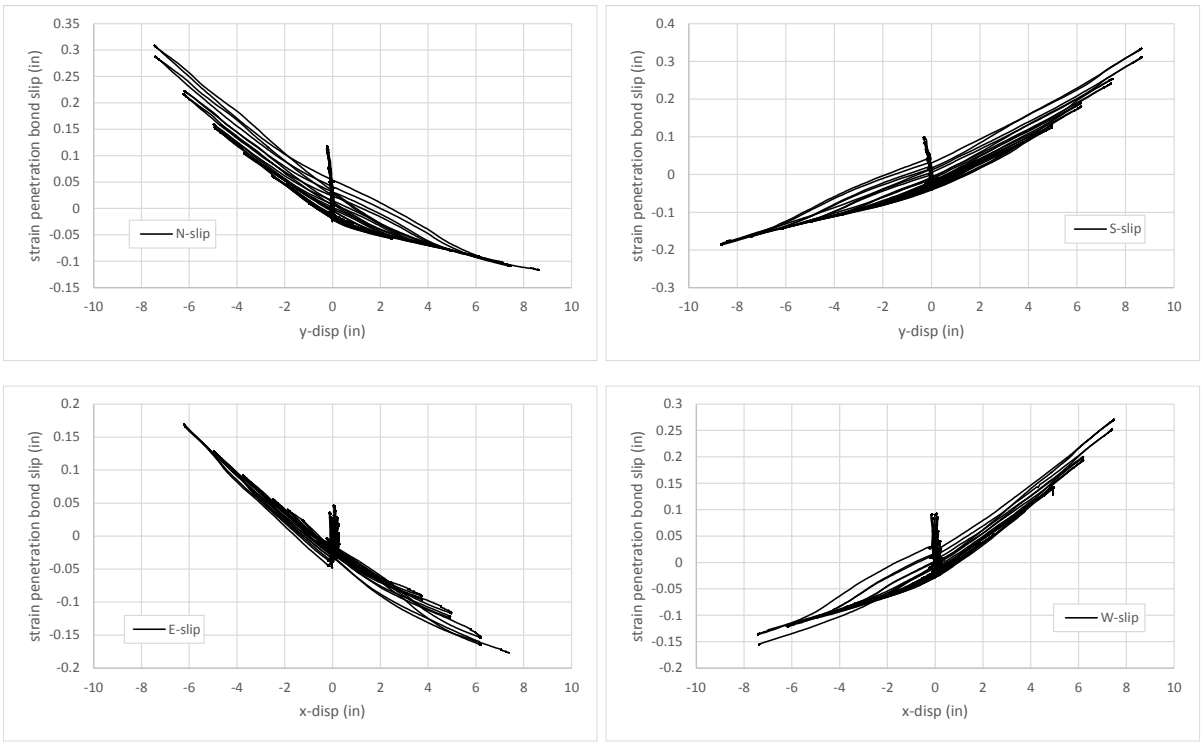

Figure 10-62. Test 7: Extreme Fiber Bar Strain Penetration Bond Slip Hysteresis

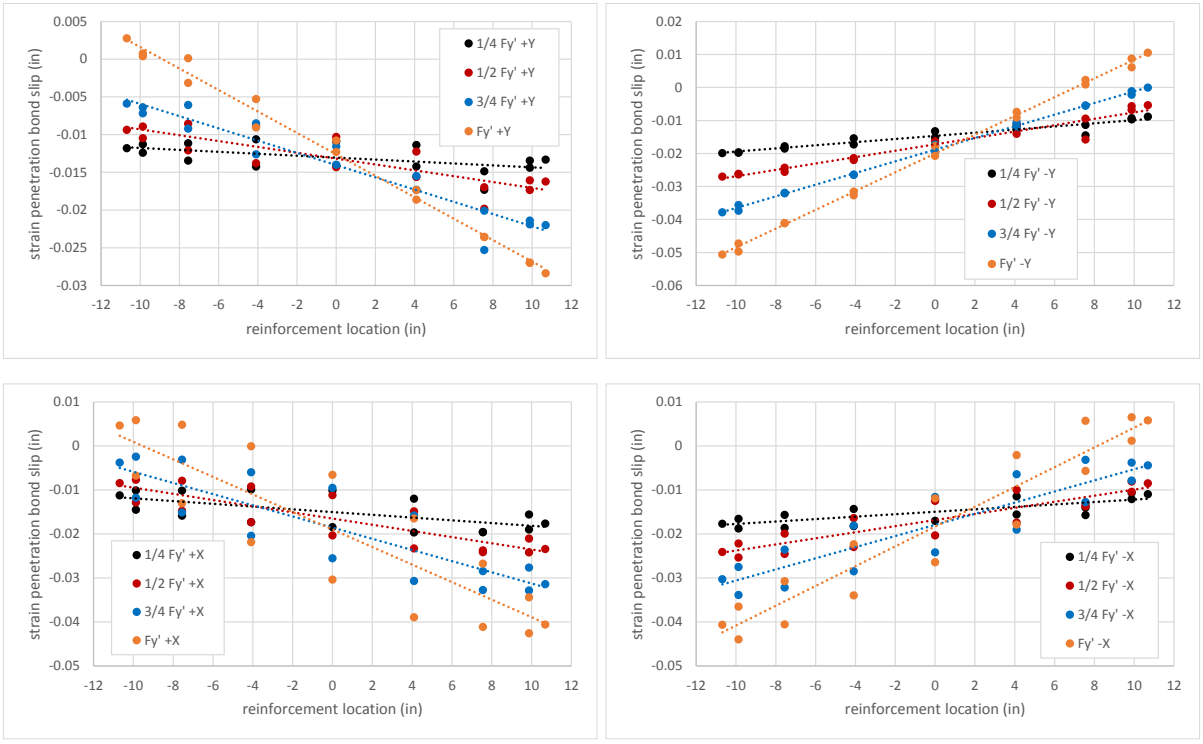

Figure 10-63. Test 7: Fixed End Rotations due to Strain Penetration during the Elastic Cycles

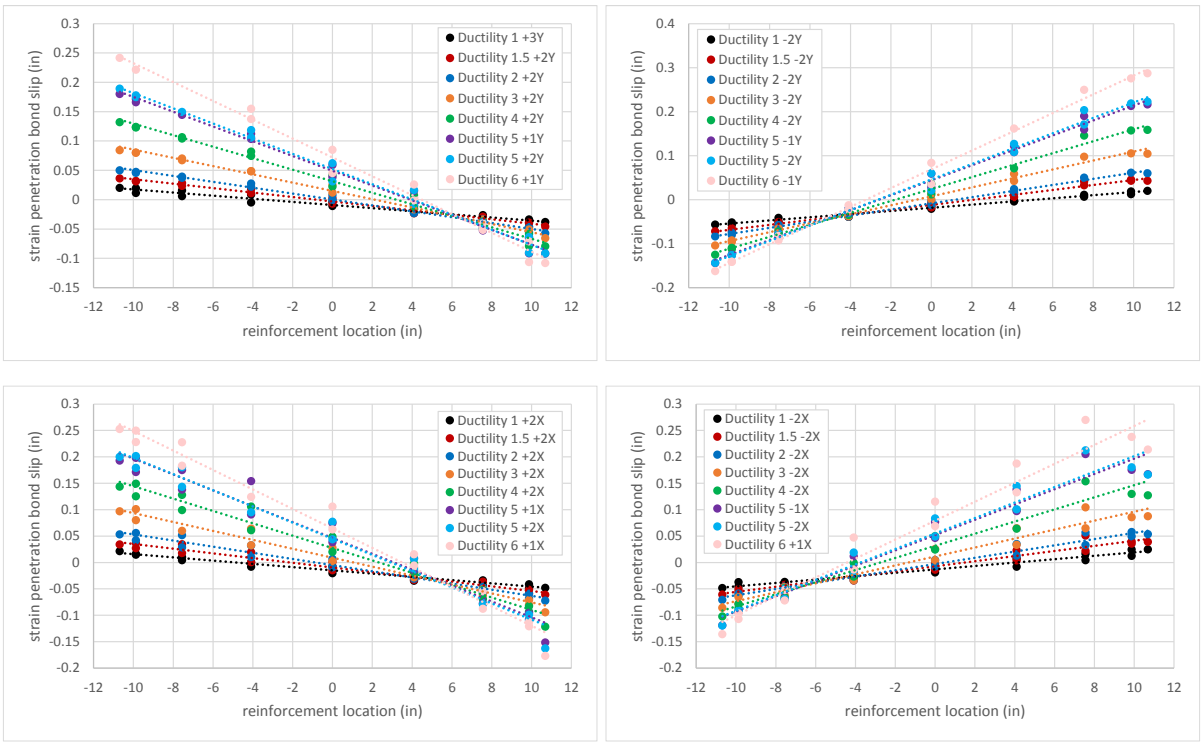

Figure 10-64. Test 7: Fixed End Rotations due to Strain Penetration

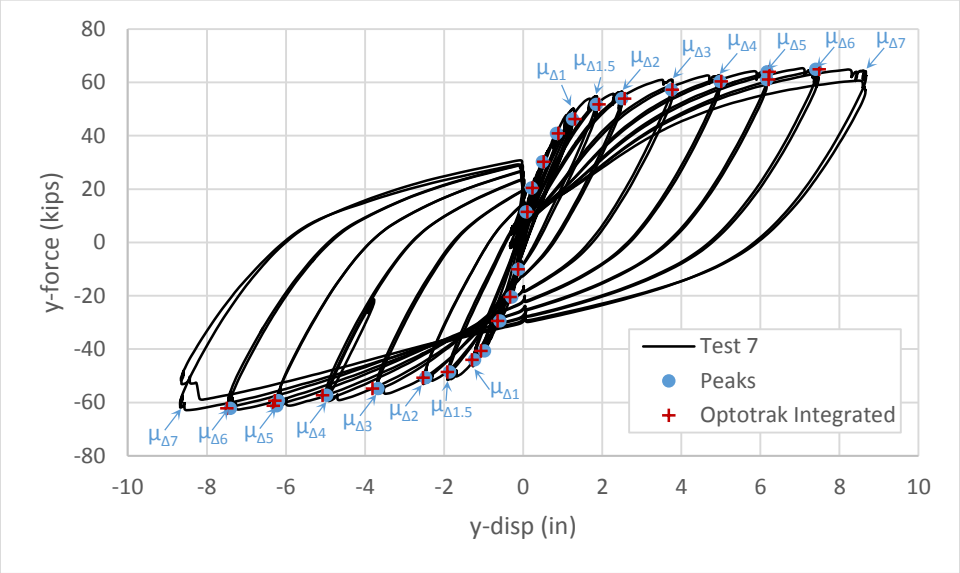

Figure 10-65. Test 7: Optotrak Integrated Flexural Disp. Compared to Measured String Pot. Disp.

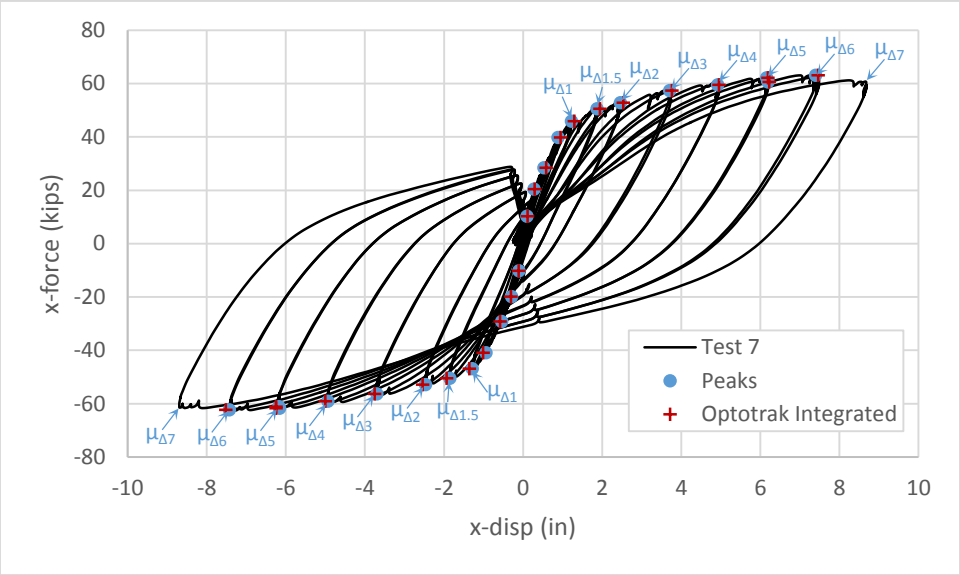

Figure 10-66. Test 7: Optotrak Integrated Flexural Disp. Compared to Measured String Pot. Disp.

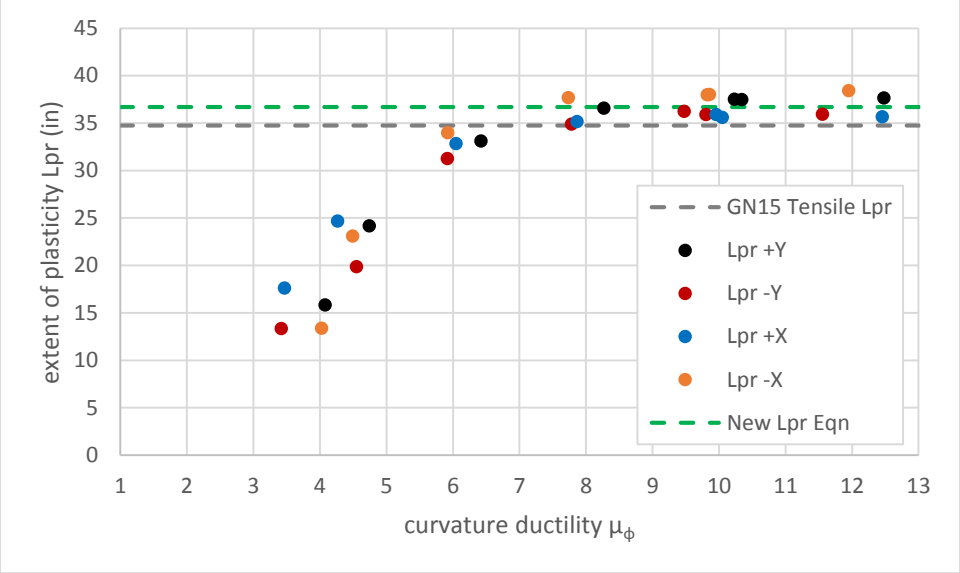

Figure 10-67. Test 7: Measured Extent of Plasticity Compared to Tensile Hinge Lengths

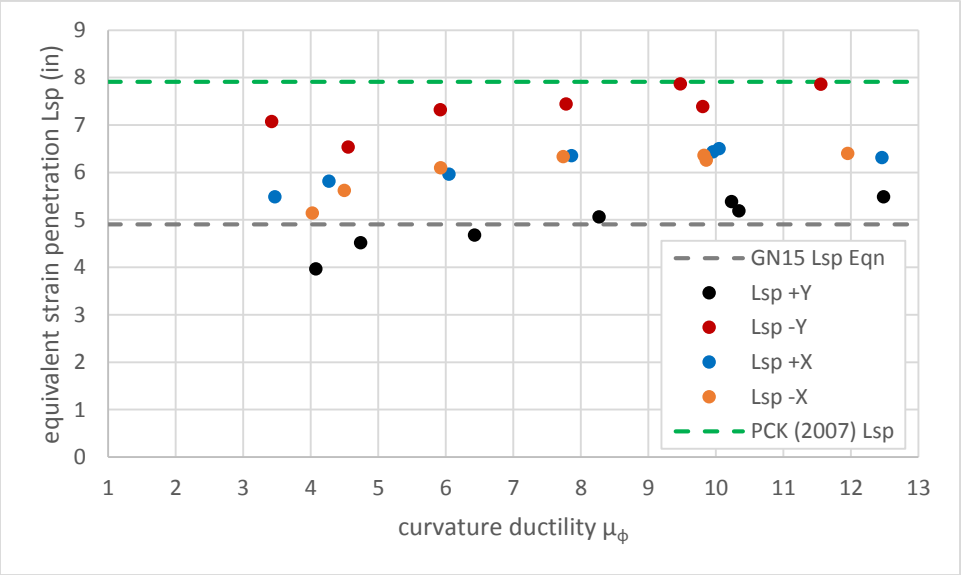

Figure 10-68. Test 7: Measured Equivalent Strain Penetration Lengths Compared to Design Expressions

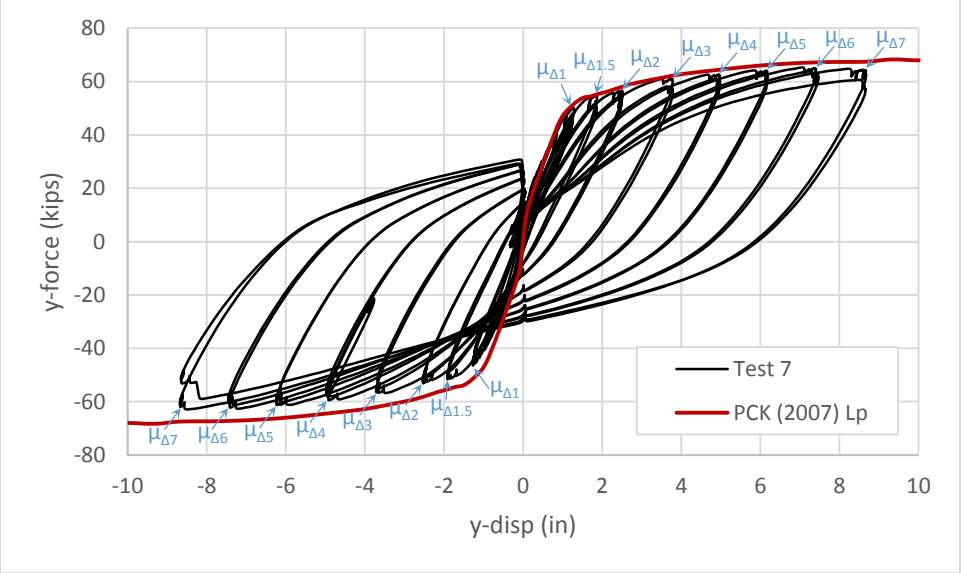

Figure 10-69. Test 7: Y-Direction Hysteretic Response Compared to PCK (2007) Hinge Length Monotonic Prediction

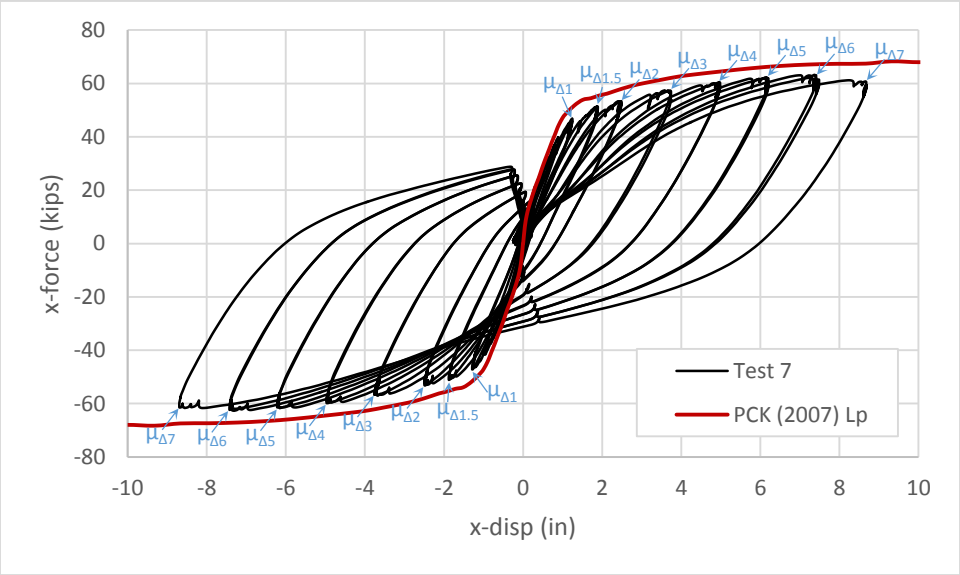

Figure 10-70. Test 7: X-Direction Hysteretic Response Compared to PCK (2007) Hinge Length Monotonic Prediction

Chapter 11 – Test 8 Summary Report

The eighth specimen had a 24" diameter circular cross-section reinforced with 16 #6 A706 longitudinal bars ($A_{st}/A_g = 1.6\%$) and a #3 spiral at 2" on center ($4A_{sp}/D's = 1\%$). The specimen was nominally identical to those chosen for Tests 7 and 9 which contained 1.3% and 0.7% transverse steel, respectively. The columns selected for Tests 4-6 were nominally identical to that of Test 8, except they contained 2.1% longitudinal steel. Details of the test setup, instrumentation, and specimen design appear in Chapter 2. A material properties summary for the longitudinal and transverse steel from the final six experiments appears in Table 3-3 through Table 3-5. The column had a tested concrete strength of $f_c' = 6.24\ ksi$, while the footing had $f_c' = 8.57\ ksi$. The same constant compressive axial load of $191\ kips$ was applied to all the specimens. The eighth specimen was subjected to the Type-B Symmetric Two-Cycle-Set Bidirectional Load History shown in Figure 11-1. This figure includes a diagram of the column cross-section with the selected bar and crack labeling scheme. Displacements in the +Y-direction placed the South reinforcement in tension. Cracks due to loading in the +Y-direction were labeled as red. The orientation of the X and Y axes are shown in Figure 2-52 with regards to the test setup. The +Y-axis is perpendicular to and points away from the strong wall. Values of interests, damage observations, and a predictions summary for the eighth test appear in Table 11-1, Table 11-2, and Table 11-3. A photo of the deformed specimen appears in Figure 11-2. The tighter transverse steel spacing necessitated reducing the number of target markers placed on bars NW, NE, SE, and SW. This was accompanied with a more dense instrumentation of the most highly strained bars in the four extreme fiber regions of the column.

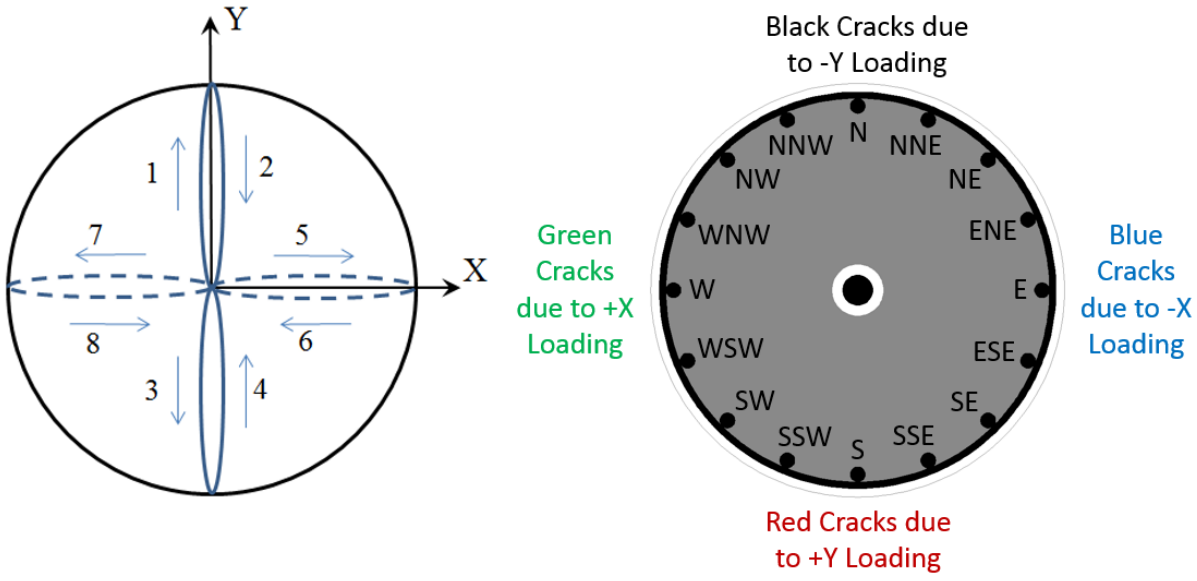

Figure 11-1. Test 8: Load History Orientation and Labeling System for Reinforcement and Cracks

Table 11-1. Test 8: Values of Interest

Load History	Type-B Symmetric Two-Cycle-Set
Length, Diameter, and Aspect Ratio	$L = 109.4375\ in, D = 24\ in,\ (L/D = 4.56)$
Longitudinal Steel Detailing	$16\ \#6\ for\ \rho_l = A_{st}/A_g = 1.6\%$
Longitudinal Steel Properties	$f_y = 70.33\ ksi, f_u = 98.68\ ksi, \varepsilon_y = 0.00283$
Transverse Steel Detailing	$\#3\ @\ 2\ in\ for\ \rho_s = 4A_{sp}/D's = 1.0\%$
Transverse Steel Properties	$f_y = 63.89\ ksi, f_u = 93.64\ ksi, \varepsilon_y = 0.00418$
Column Concrete Strength	$f_c' = 6.24\ ksi$
Footing Concrete Strength	$f_c' = 8.57\ ksi$
Axial Load	$P = 191\ kips, \left(P/f_c'\ A_g = 7.4\%\right)$
Analytical First Yield Force	$F_y' = 41.36\ kips$
Experimental First Yield Disp.	$\Delta_y' = 0.91\ in$
Analytical Nominal Moment Capacity	$M_n = 507.47\ kip \cdot ft$
Equivalent Yield Displacement	$\Delta_y = \Delta_y'\left(M_n/M_y'\right) = 1.22\ in$
Maximum Lateral Force	$F_y = 65.02\ kips, F_x = 62.86\ kips$
Failure Mode	Fracture of Previously Buckled Reinforcement

Table 11-2. Test 8: Damage Observations

Damage Observations:		
Cycle Peak at which First Cracking was Observed Visually:		
North	$\Delta_y = -0.5F_y' = -0.29\ in$	$F_y = -21.67\ kips$
South	$\Delta_y = 0.5F_y' = 0.25\ in$	$F_y = 19.56\ kips$
East	$\Delta_x = -0.5F_y' = -0.27\ in$	$F_x = -19.28\ kips$
West	$\Delta_x = 0.5F_y' = 0.27\ in$	$F_x = 19.99\ kips$
Cycle Peak at which Cover Concrete Crushing was Observed Visually:		
North	$\mu_{\Delta 1.5}^{+1Y} = 1.87\ in$	$\varepsilon_c = -0.00431$
South	$\mu_{\Delta 1.5}^{-1Y} = -1.88\ in$	$\varepsilon_c = -0.00403$
East	$\mu_{\Delta 2}^{+1X} = 2.46\ in$	$\varepsilon_c = -0.00596$
West	$\mu_{\Delta 2}^{-1X} = -2.46\ in$	$\varepsilon_c = -0.00571$
Exact Displacement and Cycle Label for Initial Spiral Yielding in the Confinement Zone:		
North	$\Delta_y = 5.89\ in\ during\ \mu_{\Delta 5}^{+1Y}$	$\varepsilon_c = -0.01696$
South	$\Delta_y = -5.79\ in\ during\ \mu_{\Delta 5}^{-1Y}$	$\varepsilon_c = -0.01395$
East	$\Delta_x = 4.71\ in\ during\ \mu_{\Delta 4}^{+1X}$	$\varepsilon_c = -0.01330$
West	$\Delta_x = -4.94\ in\ during\ \mu_{\Delta 5}^{-1X}$	$\varepsilon_c = -0.01519$
Peak Tensile Displacement Prior to Visual Bar Buckling During Subsequent Reversal of Load:		
North	$\mu_{\Delta 6}^{-1Y} = -7.37\ in, Observed\ at\ \mu_{\Delta 6}^{+2Y} = 7.31\ in$	$\varepsilon_s = 0.04037$
South	$\mu_{\Delta 6}^{+2Y} = 7.31\ in, Observed\ at\ \mu_{\Delta 6}^{-2Y} = -7.34\ in$	$\varepsilon_s = 0.04242$
East	$\mu_{\Delta 5}^{-2X} = -6.11\ in, Observed\ at\ \mu_{\Delta 6}^{+1X} = 7.32\ in$	$\varepsilon_s = 0.03542$
West	$\mu_{\Delta 6}^{+1X} = 7.32\ in, Observed\ at\ \mu_{\Delta 6}^{-1X} = -7.36\ in$	$\varepsilon_s = 0.04354$
Exact Displacement and Cycle Label for Fracture of Previously Buckled Reinforcement		
East	$\Delta_x = -5.03\ in\ during\ \mu_{\Delta 7}^{-1X}$	Single East Extreme Bar

Table 11-3. Test 8: Damage Predictions

Damage Predictions with the New Bidirectional Plastic Hinge Model and New Strain Limits:		
Bar Buckling Predictions		
New Method	$\Delta_{bb}^{Lpr} = 6.71\ in$	$\varepsilon_s^{bb} = 0.03904$
Feng et al. (2015)	$\Delta_{bb}^{Lp} = 6.46\ in$	$\varepsilon_s^{bb} = 0.0526$
Cover Crushing Prediction		
New Method	$\Delta_{cc}^{Lpr} = 1.98\ in$	$\varepsilon_c^{cc} = -0.004$
Spiral Yielding Prediction		
New Method	$\Delta_{sy}^{Lpr} = 5.33\ in$	$\varepsilon_c^{sy} = -0.01384 * M, (M = 0.8)$
Original Ultimate Concrete Compression Strain		
Mander et al. (1988)	$\Delta_{cu}^{Lpr} = 7.50\ in$	$\varepsilon_{cu} = -0.0169$

Figure 11-2. Test 8: Deformed Specimen at $\mu_{\Delta 7}^{+1x} = 8.53"$

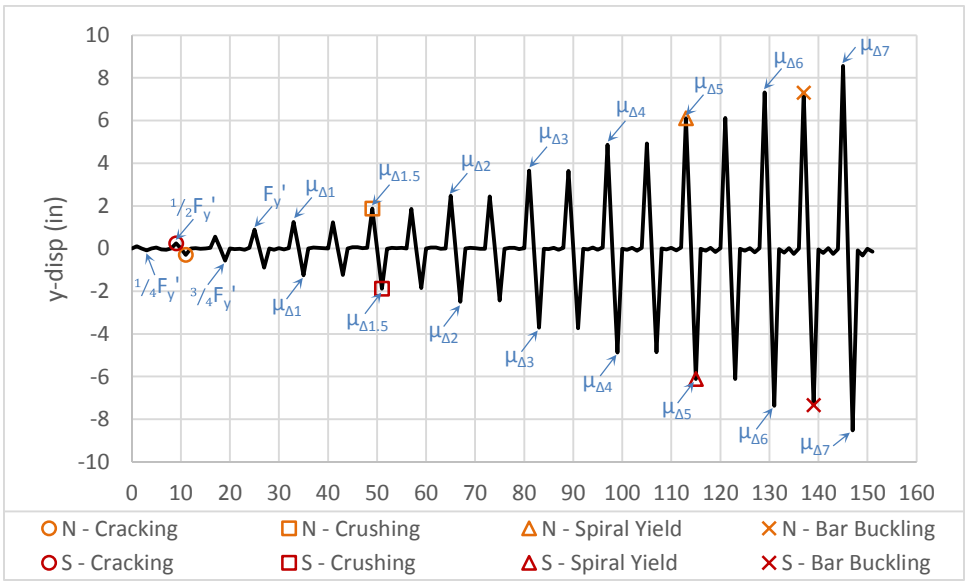

Figure 11-3. Test 8: Y-Displacement History

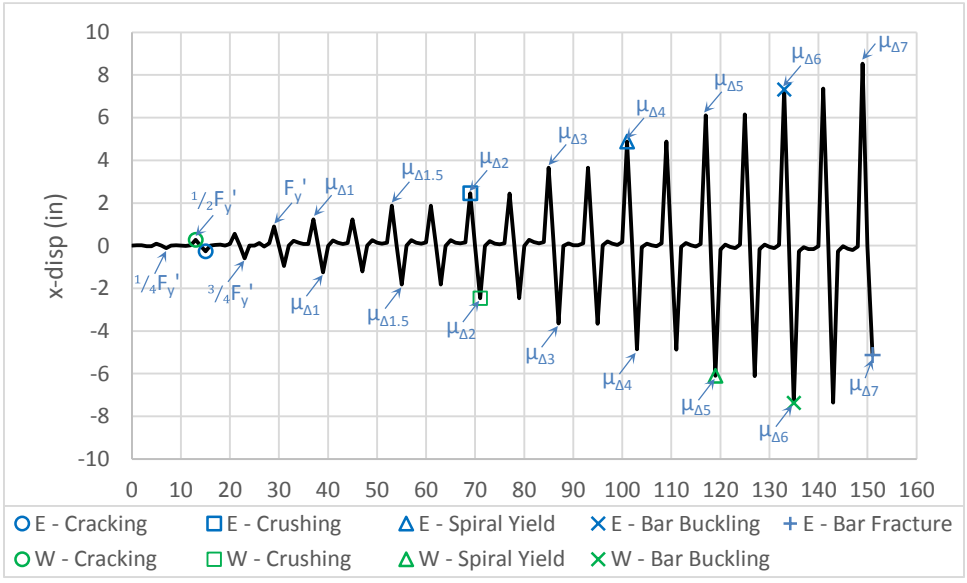

Figure 11-4. Test 8: X-Displacement History

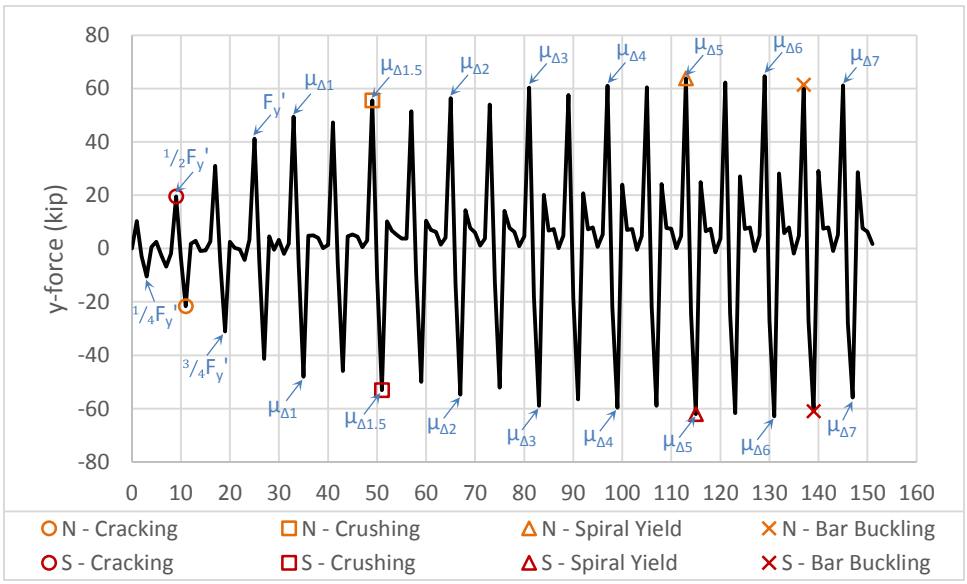

Figure 11-5. Test 8: Y-Force History

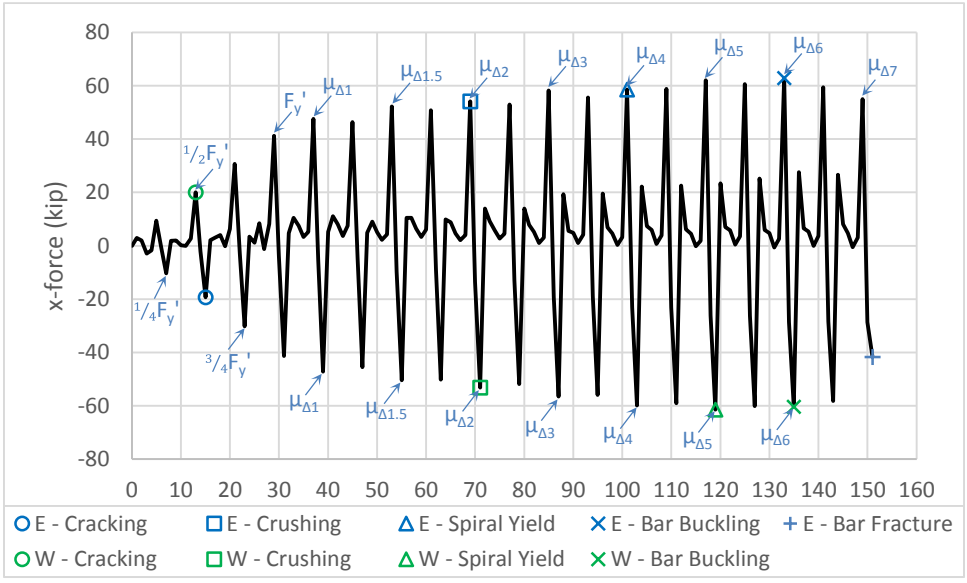

Figure 11-6. Test 8: X-Force History

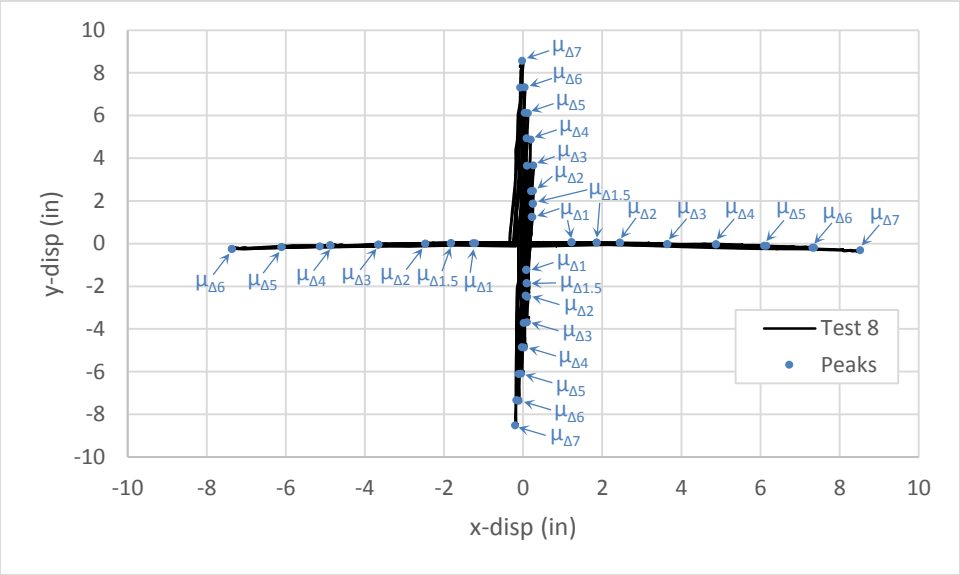

Figure 11-7. Test 8: Type-B Symmetric Two-Cycle-Set Displacement History

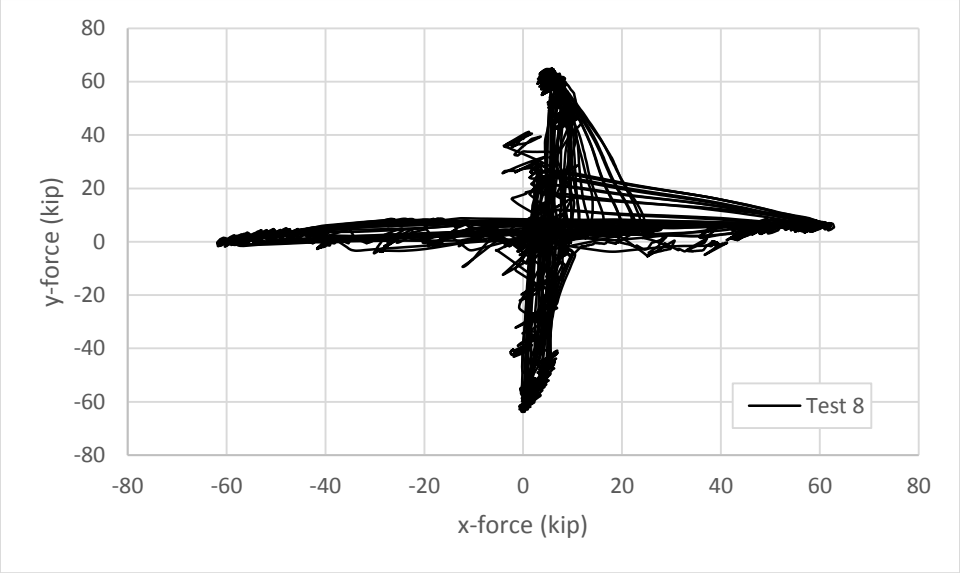

Figure 11-8. Test 8: Load Path

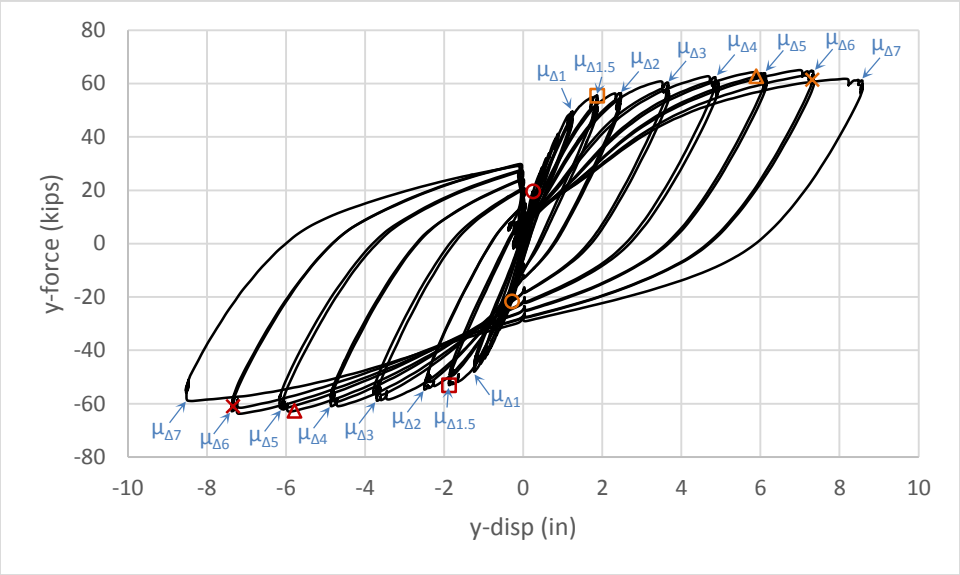

Figure 11-9. Test 8: Y-Direction Hysteretic Response

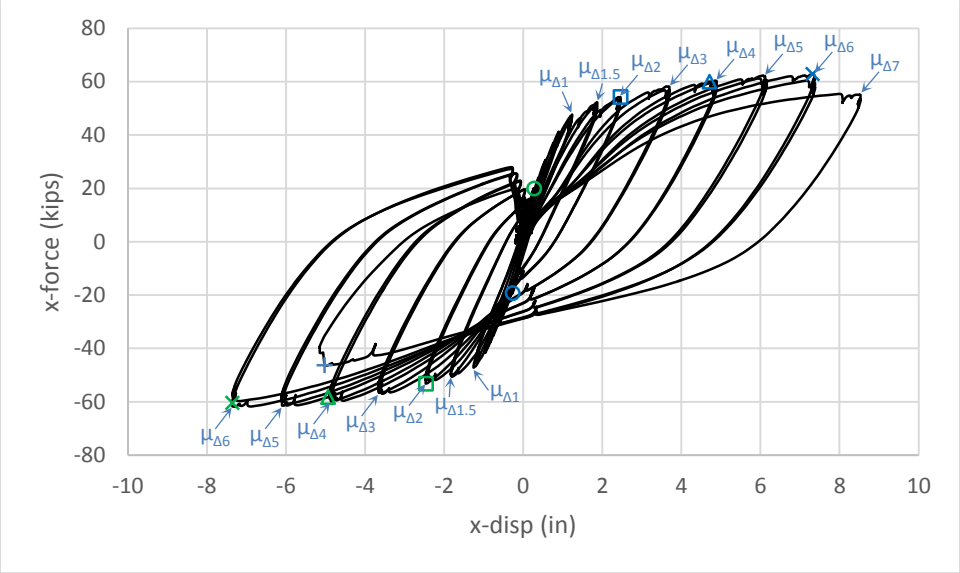

Figure 11-10. Test 8: X-Direction Hysteretic Response

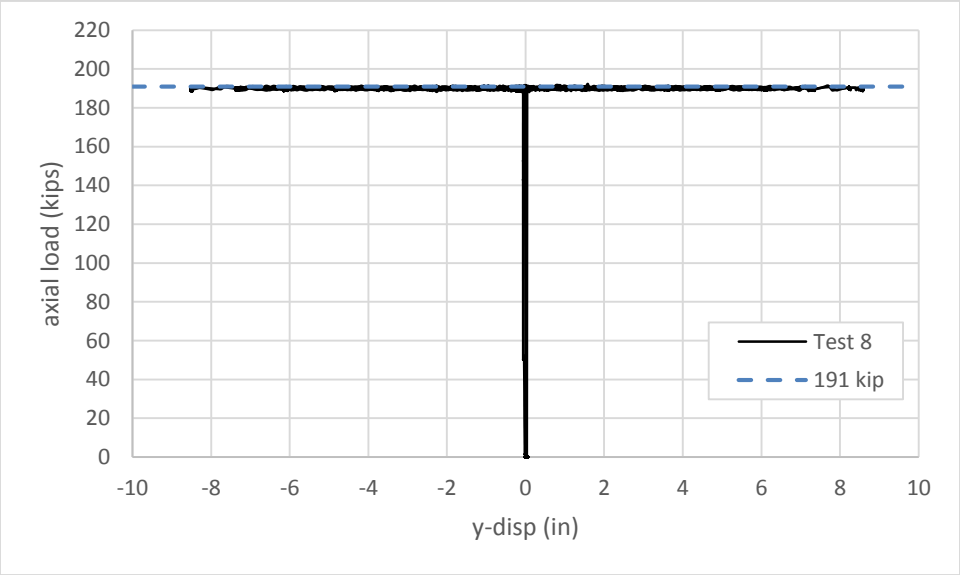

Figure 11-11. Test 8: Y-Direction Axial Force History

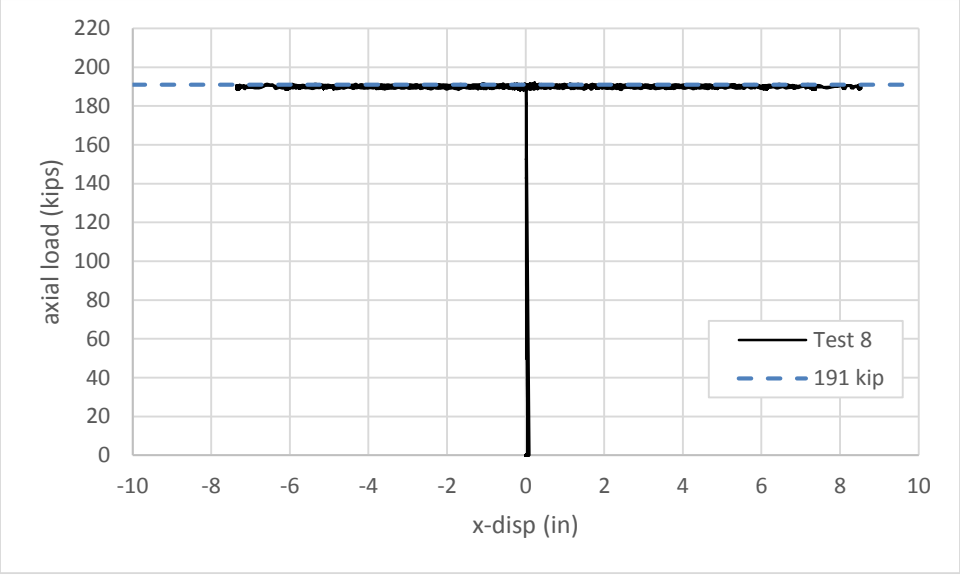

Figure 11-12. Test 8: X-Direction Axial Force History

Test 8 - Experimental Observations

Values of interests and damage observations for Load Path Test 8 are presented in Table 11-1 and Table 11-2. Test 8 evaluated a 24" diameter column $(L/D = 4.56)$ with $\rho_l = A_{st}/A_g = 1.6\%$ longitudinal steel and a transverse volumetric ratio of $\rho_s = 4A_{sp}/D's = 1.0\%$. The test began with the application of a constant axial load of $191\ kips\ \left(P/f_c'\ A_g = 7.4\%\right)$. The imposed displacement histories in the Y and X-directions for the Symmetric Two-Cycle-Set Biaxial Load History shown in Figure 11-3 and Figure 11-4. The resulting column shear force histories in the Y and X-directions appear in Figure 11-5 and Figure 11-6. The full displacement history and resulting load path for Test 8 appear in Figure 11-7 and Figure 11-8. The Y and X-direction column hysteretic response appears Figure 11-9 and Figure 11-10. The axial load history is shown in Figure 11-11 and Figure 11-12.

The load history began with elastic ¼ F_y' cycle increments until the analytically predicted first yield force $(F_y' = 41.36\ kips)$ was reached in each direction of loading. Cracks were first observed on all sides of the specimen during the ½ F_y' cycle. At the analytically predicted first yield force, an average experimental first yield displacement of $\Delta_y' = 0.91$" was measured in the four primary directions. The equivalent yield displacement for the column was then computed as $\Delta_y = \Delta_y'\left(M_n/M_y'\right) = 1.22\ in$, where $M_n = 507.47\ kip \cdot ft$ represents the analytical nominal moment capacity corresponding to an extreme fiber compression strain of $\varepsilon_c = 0.004$ or a steel tensile strain of $\varepsilon_s = 0.015$, whichever occurs first. The remainder of the Symmetric Two-Cycle-Set Load History consists of two cycles for each displacement ductility level $\mu_{\Delta n} = n \cdot \Delta_y$, where $n = 1, 1.5, 2, 3, 4, 5, 6\ etc$. Cracks observed on each side of the specimen at equivalent yield are shown in Figure 11-13 and Figure 11-14.

Concrete Crushing was observed on the North side during $\mu_{\Delta 1.5}^{+1y} = 1.87$", followed by the South side during $\mu_{\Delta 1.5}^{-1y} = -1.88$", as shown in Figure 11-15. Cover Concrete crushing occurred on the East side during $\mu_{\Delta 2}^{+1x} = 2.46$" and then on the West side during $\mu_{\Delta 2}^{-1x} = -2.46$", see Figure 11-16. Compressive demands on the East side of the specimen during $\mu_{\Delta 4}^{+1x} = 4.88$" led to initial spiral yielding, followed by yielding of North spirals during $\mu_{\Delta 5}^{+1y} = 6.11$", refer to Figure 11-17. Spirals on the South Side yielded during $\mu_{\Delta 5}^{-1y} = -6.11$", followed by the West side at $\mu_{\Delta 5}^{-1x} = -6.10$", see Figure 11-18.

The East extreme fiber bar visibly buckled during $\mu_{\Delta 6}^{+1x} = 7.32$", followed by the West extreme fiber bar during $\mu_{\Delta 6}^{-1x} = -7.36$" as shown in Figure 11-19. The North extreme fiber bar visibly buckled during $\mu_{\Delta 6}^{+2y} = 7.31$", then the South bar buckled during $\mu_{\Delta 6}^{-2y} = -7.34$", refer to Figure 11-20. The adjacent East bar ESE buckled during $\mu_{\Delta 6}^{+2x} = 7.36$". The adjacent West bar WSW then buckled during $\mu_{\Delta 6}^{-2x} = -7.35$". The adjacent North bar NNW buckled during $\mu_{\Delta 7}^{+1y} = 8.56$". Three additional South reinforcing bars SSE, SSW, and SW buckled during $\mu_{\Delta 7}^{-1y} = -8.53$". East Bars SE, NE, ENE then buckled during $\mu_{\Delta 7}^{+1x} = 8.53$" as shown in Figure 11-21. The previously buckled East extreme fiber bar then fractured at -5.03" during the subsequent reversal to $\mu_{\Delta 7}^{-1X}$. Even at this displacement, it was clear that Bars NW, WNW and NNE had all buckled, confirming that all 16 bars within the cross section had buckled. Photos of the specimen after the test appear in Figure 11-22 and Figure 11-23.

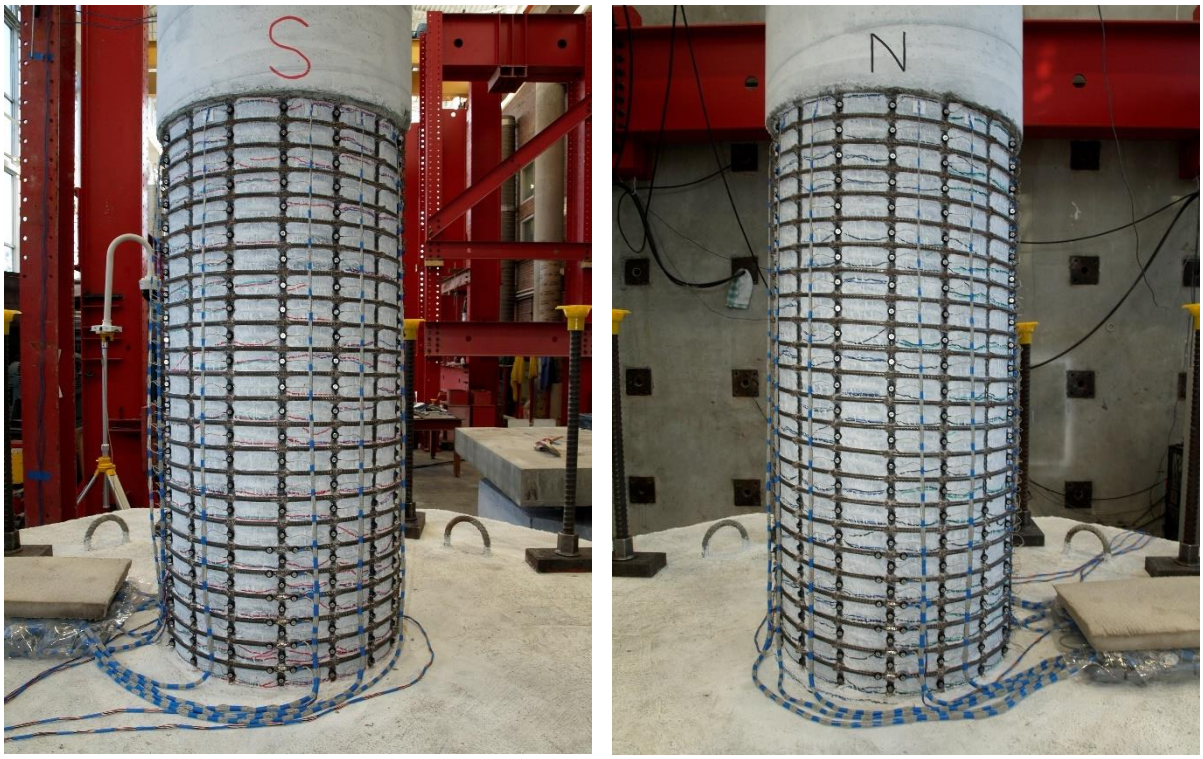

Figure 11-13. Test 8: Crack Profiles on the (Left) South Side at $\mu_{\Delta 1}^{+2y} = 1.24$" and (Right) North Side at $\mu_{\Delta 1}^{-2y} = -1.23$"

Figure 11-14. Test 8: Crack Profiles on the (Left) West Side at $\mu_{\Delta 1}^{+2x} = 1.22$" and (Right) East Side at $\mu_{\Delta 1}^{-2x} = -1.21$"

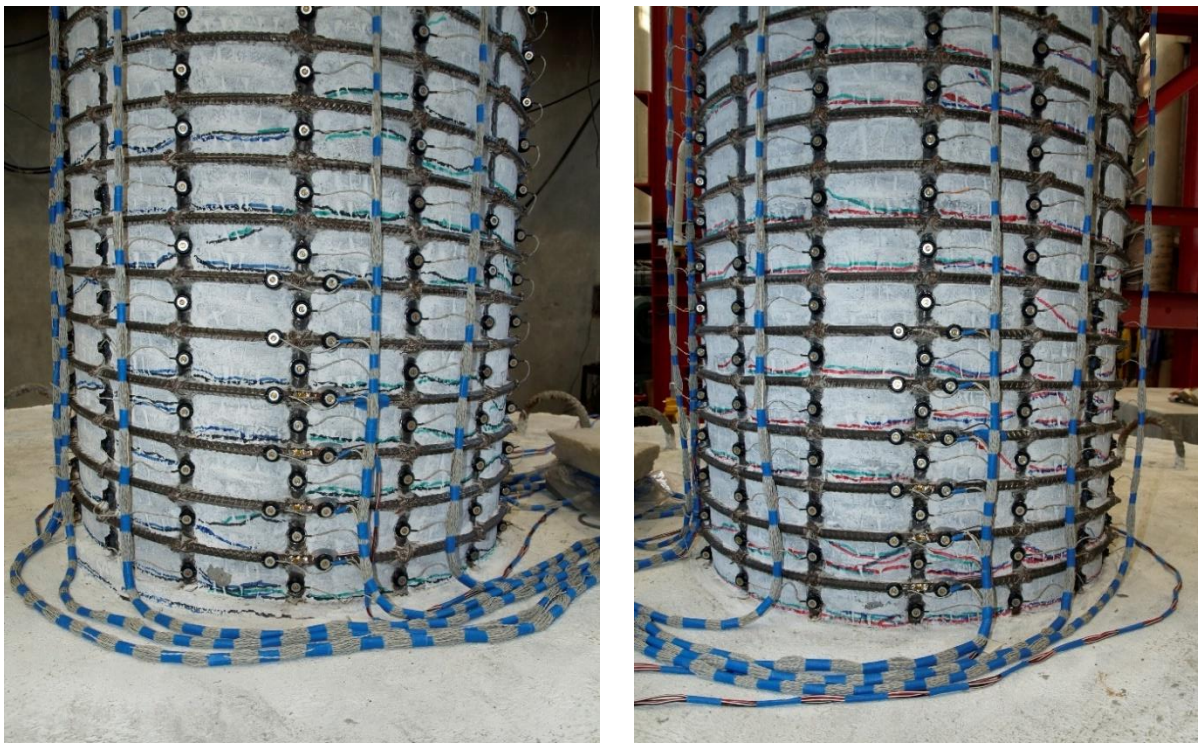

Figure 11-15. Test 8: Concrete Crushing on the (Left) North Side at $\mu_{\Delta 1.5}^{+1y} = 1.87"$ and (Right) South Side at $\mu_{\Delta 1.5}^{-1y} = -1.88"$

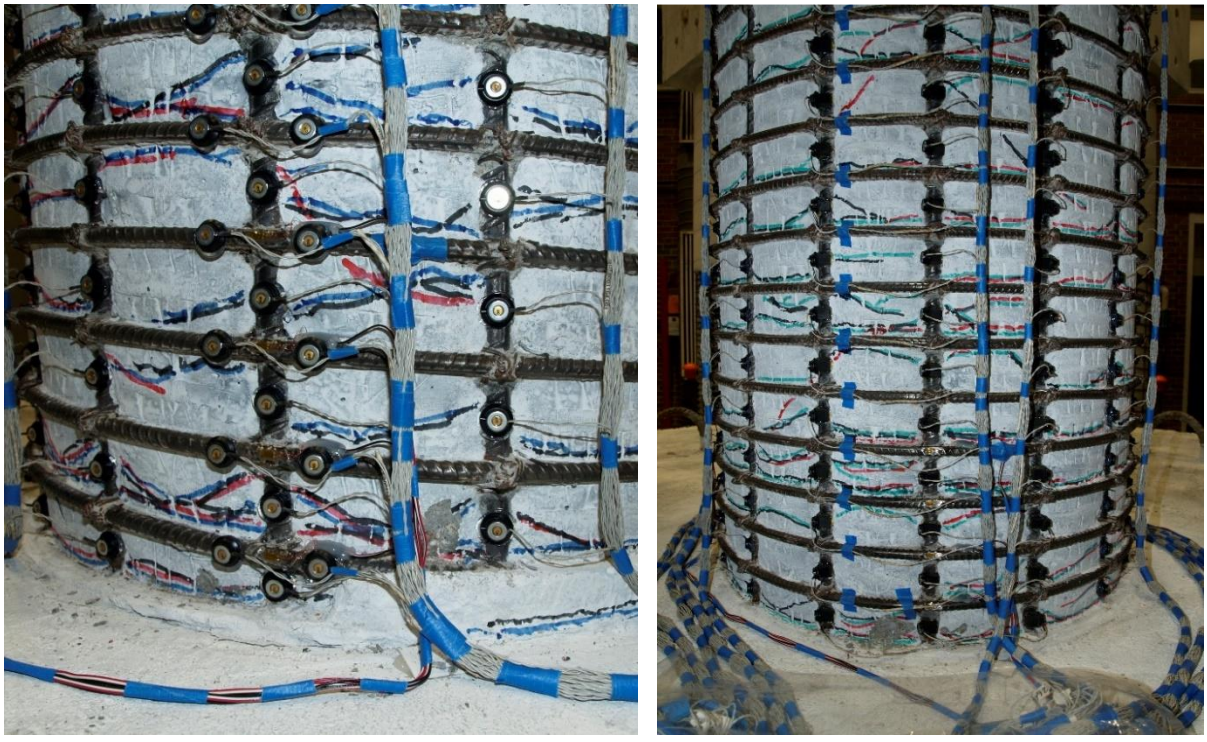

Figure 11-16. Test 8: Concrete Crushing on the (Left) East Side at $\mu_{\Delta 2}^{+1x} = 2.46"$ and (Right) West Side at $\mu_{\Delta 2}^{-1x} = -2.46"$

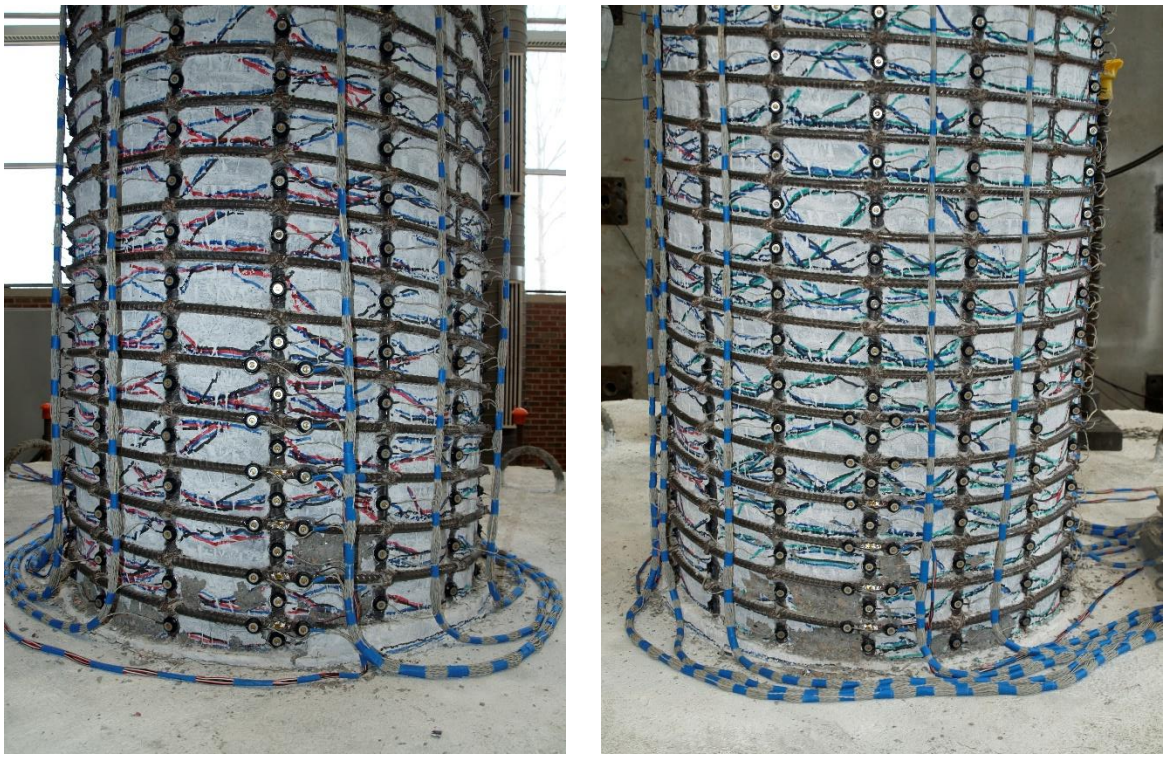

Figure 11-17. Test 8: Spiral Yielding on the (Left) East Side at $\mu_{\Delta 4}^{+1x} = 4.88"$ and (Right) North Side at $\mu_{\Delta 5}^{+1y} = 6.11"$

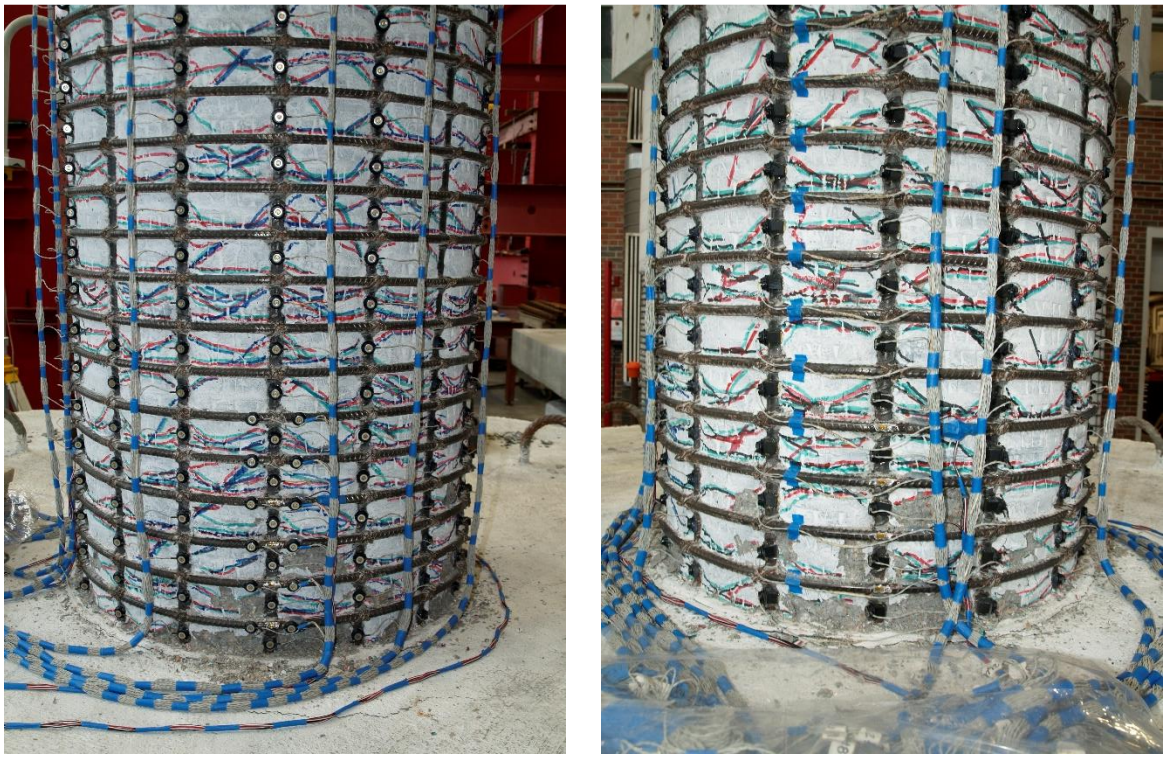

Figure 11-18. Test 8: Spiral Yielding on the (Left) South Side at $\mu_{\Delta 5}^{-1y} = -6.11"$ and (Right) West Side at $\mu_{\Delta 5}^{-1x} = -6.10"$

Figure 11-19. Test 8: Bar Buckling on the (Left) East Side at $\mu_{\Delta 6}^{+1x} = 7.32"$ and (Right) West Side at $\mu_{\Delta 6}^{-1x} = -7.36"$

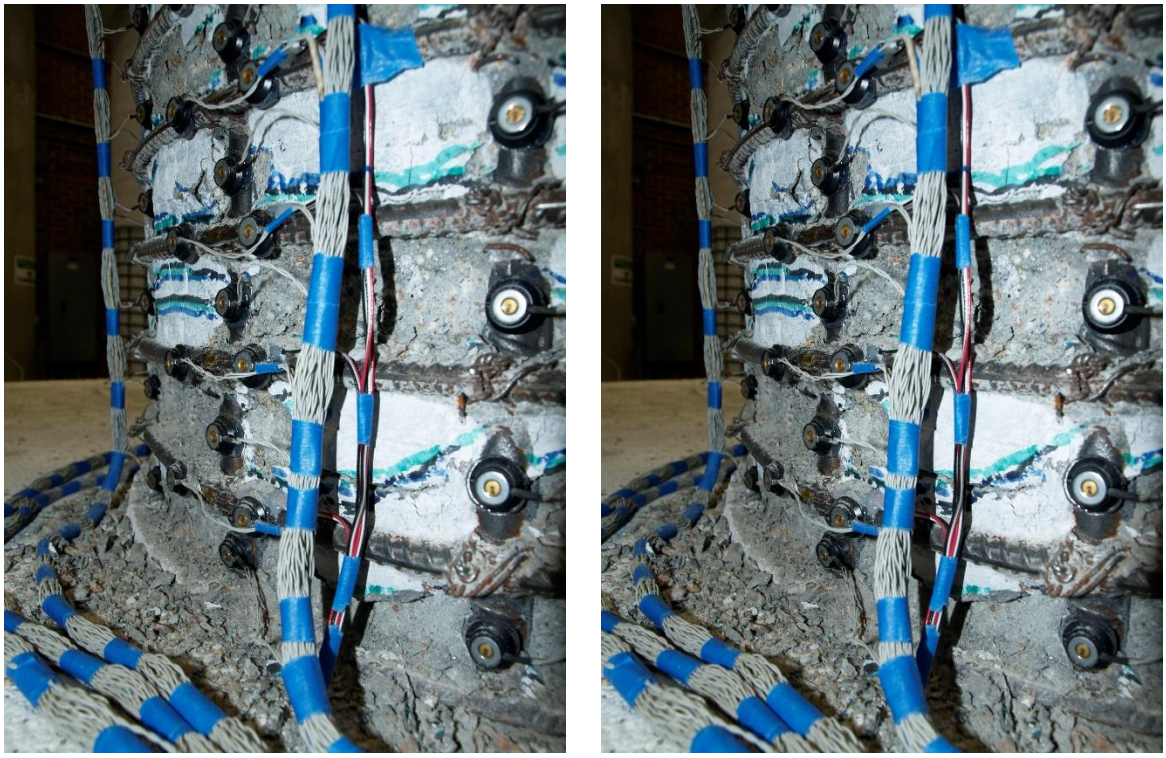

Figure 11-20. Test 8: Bar Buckling on the (Left) North Side at $\mu_{\Delta 6}^{+2y} = 7.31"$ and (Right) South Side at $\mu_{\Delta 6}^{-2y} = -7.34"$

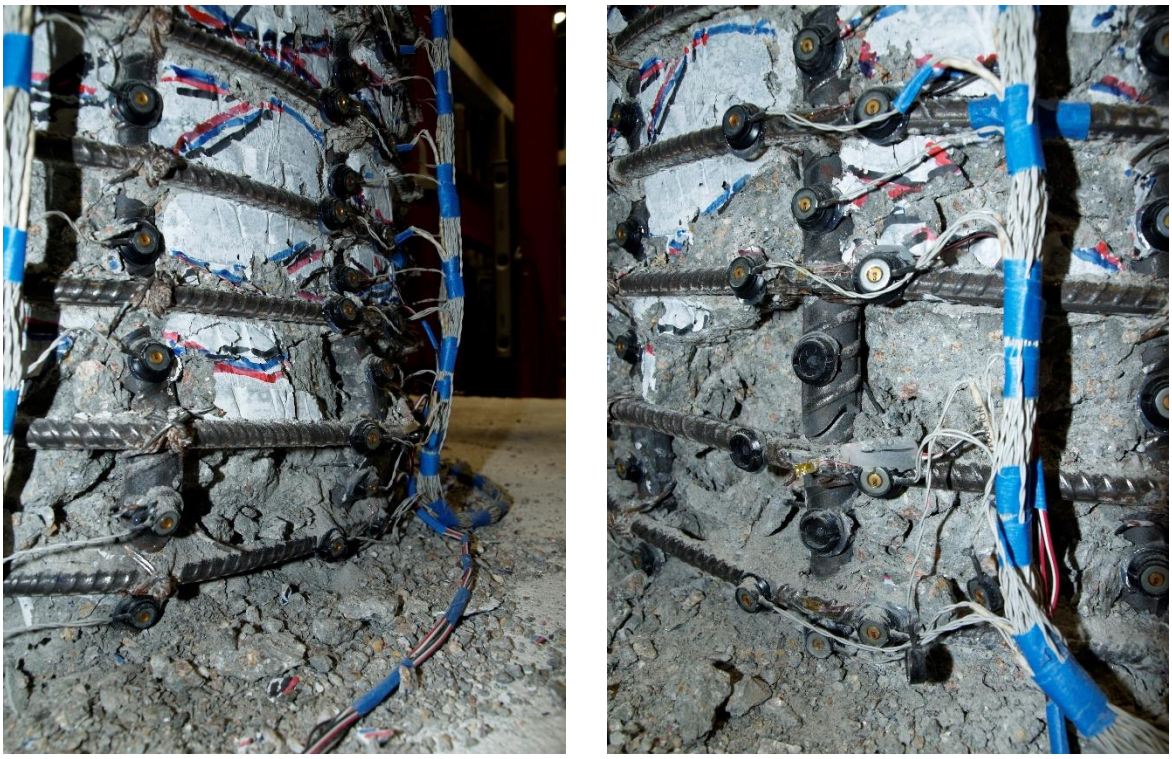

Figure 11-21. Test 8: (Left) East Side Buckled Deformation at $\mu_{\Delta 7}^{+1x} = 8.53"$ and (Right) East Bar Fracture during $\mu_{\Delta 7}^{-1X}$

Figure 11-22. Test 8: (Left) South and (Right) North Sides of the Column after the Test

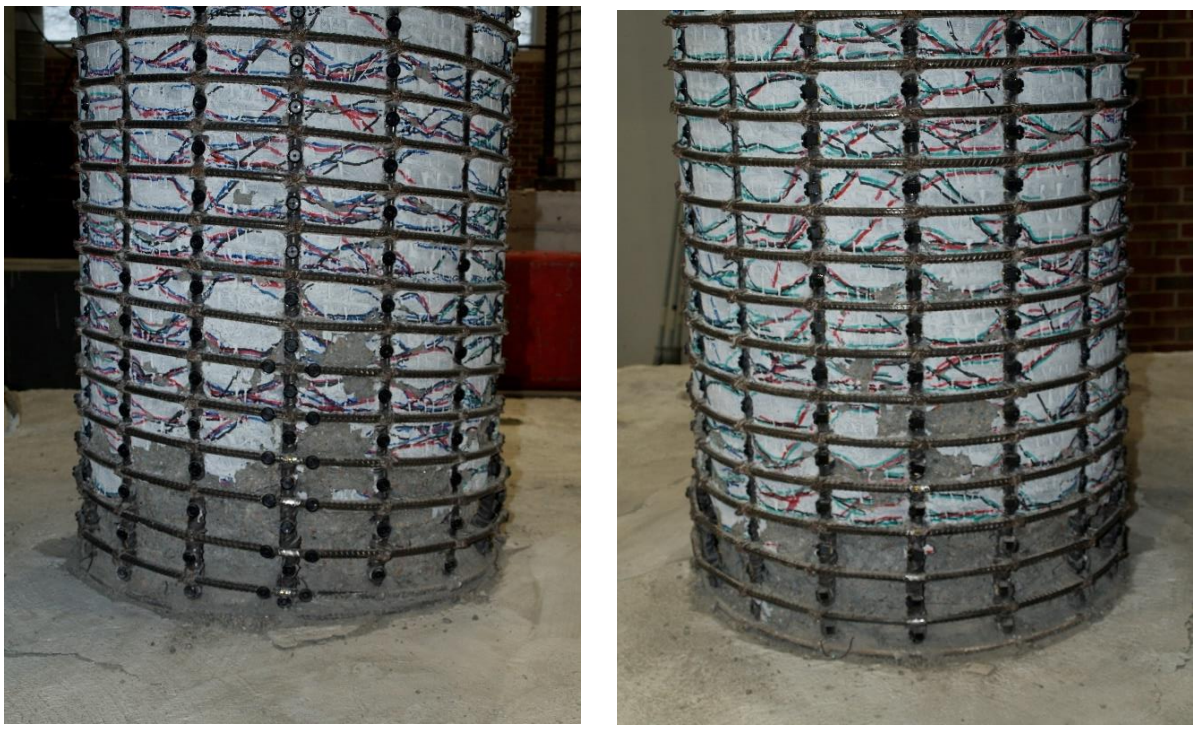

Figure 11-23. Test 8: (Left) East and (Right) West Sides of the Column after the Test

Test 8 - Strain Data Analysis

North and South Bar Strains

Vertical strain profiles for North and South reinforcement during y-direction cycles are shown in Figure 11-24 and Figure 11-25. Strains in the lowest four spiral layers during compressive y-direction cycles on the North and South sides of the specimen appear in Figure 11-26 and Figure 11-27. The relationship between strain and displacement for either peak tensile or peak compressive gauge lengths appear in Figure 11-28 through Figure 11-31. These figures contain monotonic moment curvature predictions for respective plastic hinge methods. PCK (2007) Lp refers to the (Priestley, Calvi and Kowalsky 2007) plastic hinge method, GN15 Tension/Compression Lpr refers to the (Goodnight, Kowalsky and Nau 2015a) unidirectional modified plastic hinge method, TX Measured refer to using the measured extent of plasticity and average equivalent strain penetration length from this specific test, and New Equations refers to a new bidirectional plastic hinge method which was created based on this study. Details of the new plastic hinge method appear in a later chapter of this report.

The spiral strain gauge hysteresis for the second layer above the footing on the North side of the specimen is shown in Figure 11-33. Tension strains in this layer increased during $\mu_{\Delta 6}^{+2y} = 7.31"$ as the North extreme fiber bar visibly buckled, see Figure 11-20. The visual observation of bar buckling was confirmed upon inspection of the North longitudinal bar strain hysteresis in Figure 11-32.

The spiral strain gauge hysteresis for the second layer above the footing on the South side of the specimen is shown in Figure 11-35. Tension strains in this layer increased during $\mu_{\Delta 6}^{-2y} = -7.34"$ as the South extreme fiber bar visibly buckled, see Figure 11-20. The visual observation of bar buckling was confirmed upon inspection of the South longitudinal bar strain hysteresis in Figure 11-34.

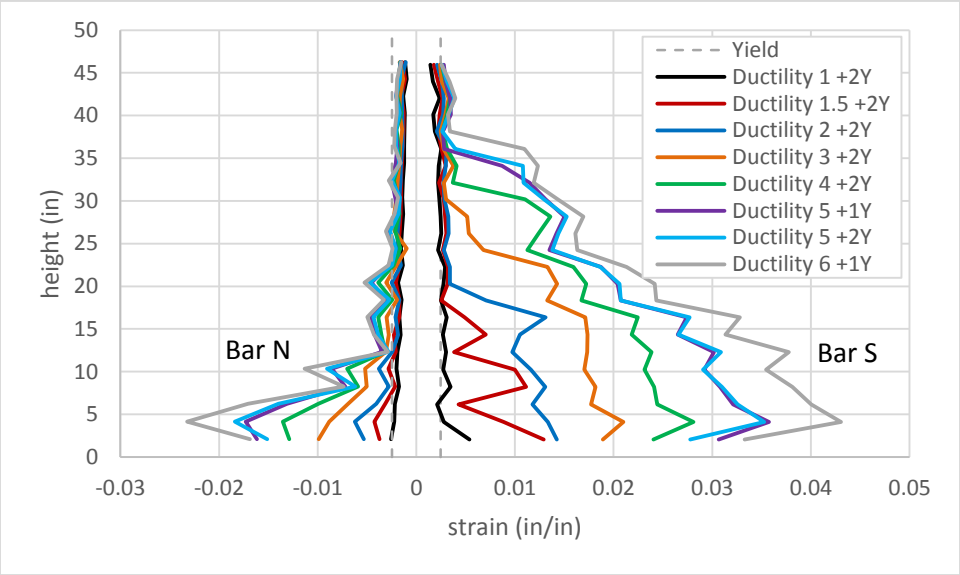

Figure 11-24. Test 8: Vertical Strain Profiles for Loading in the +Y-direction

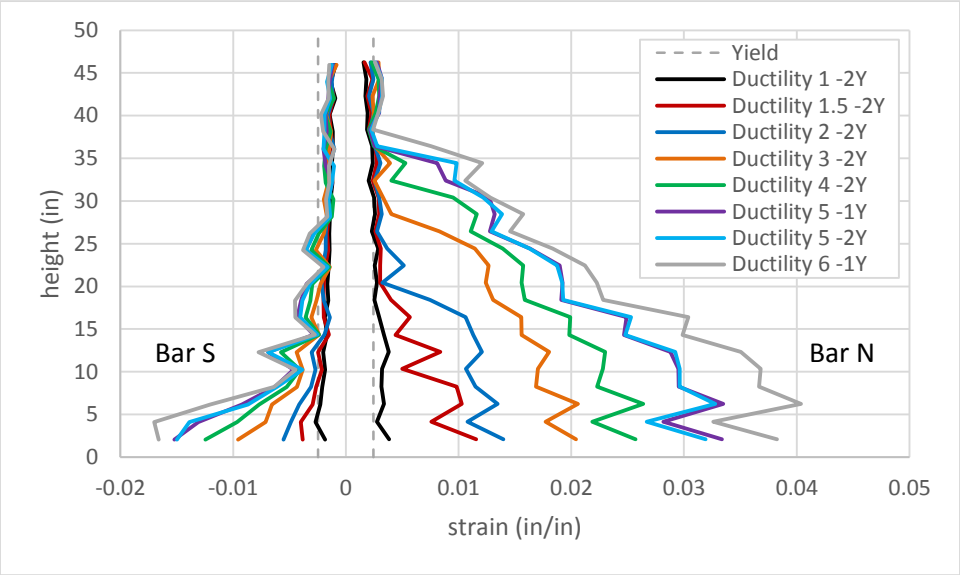

Figure 11-25. Test 8: Vertical Strain Profiles for Loading in the -Y-direction

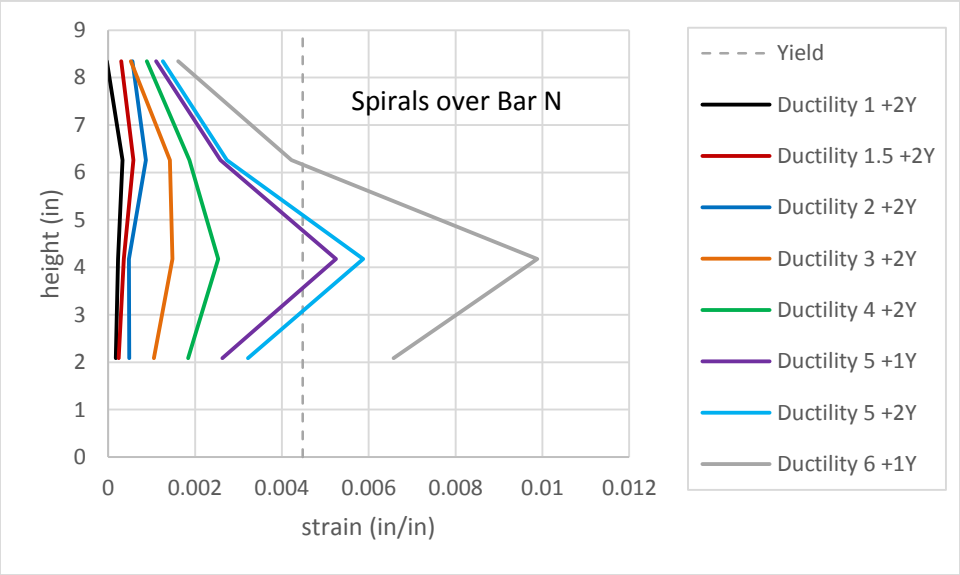

Figure 11-26. Test 8: Spiral Strains Measured Over the North Extreme Fiber Bar during +Y Cycles

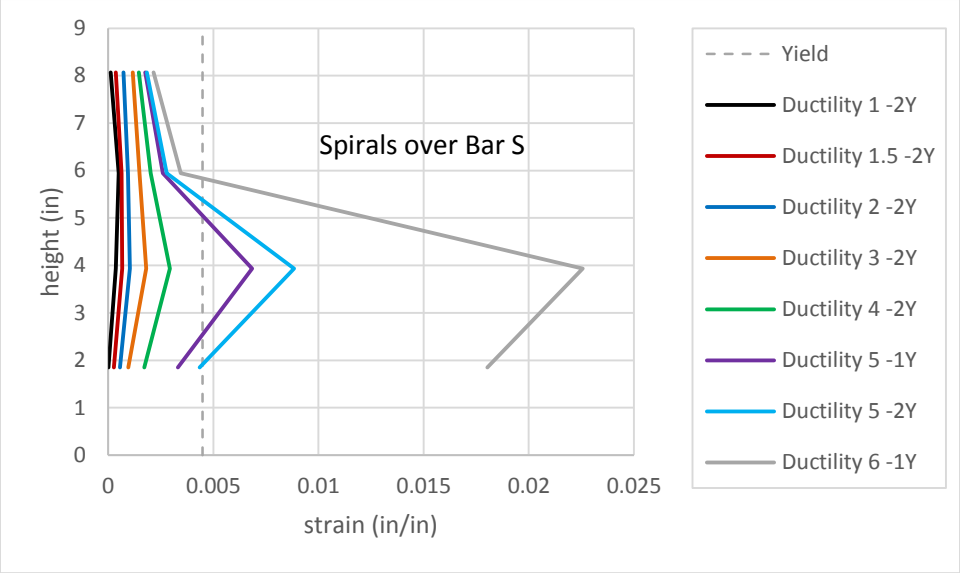

Figure 11-27. Test 8: Spiral Strains Measured Over the South Extreme Fiber Bar during -Y Cycles

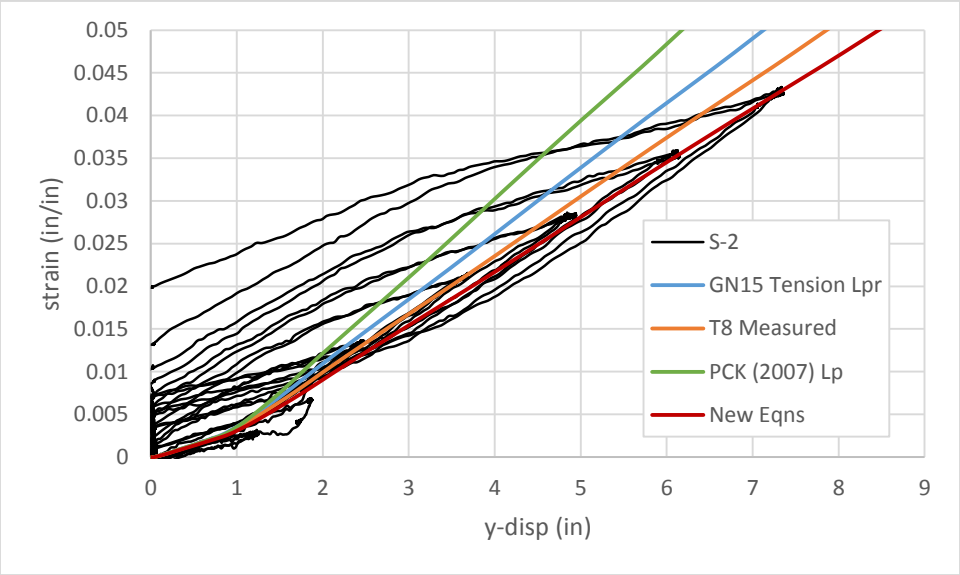

Figure 11-28. Test 8: Tension Strain-Disp. for Bar S (Gauge Length 2 Centered 4.11" above the Footing)

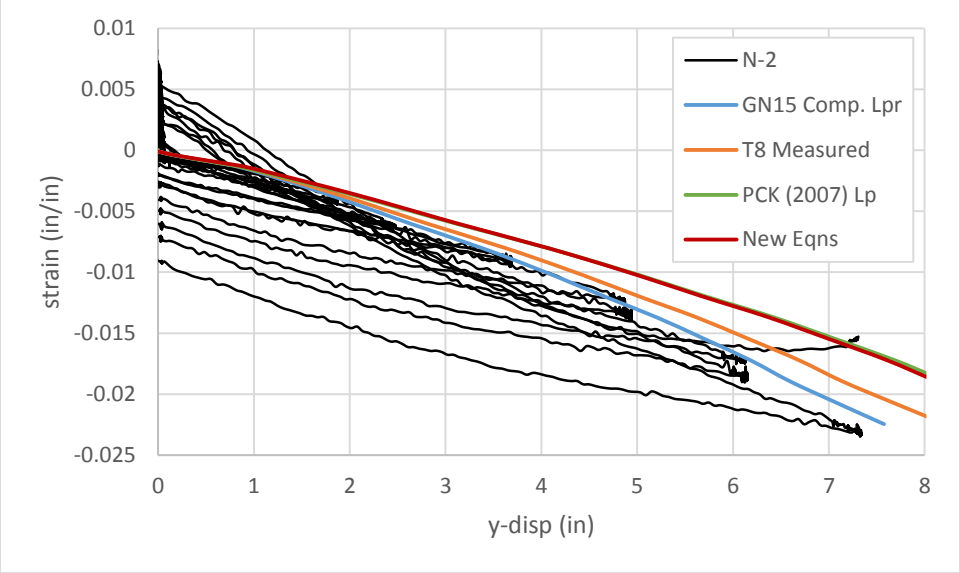

Figure 11-29. Test 8: Compression Strain-Disp. for Bar N (Gauge Length 2 Centered 4.15" above the Footing)

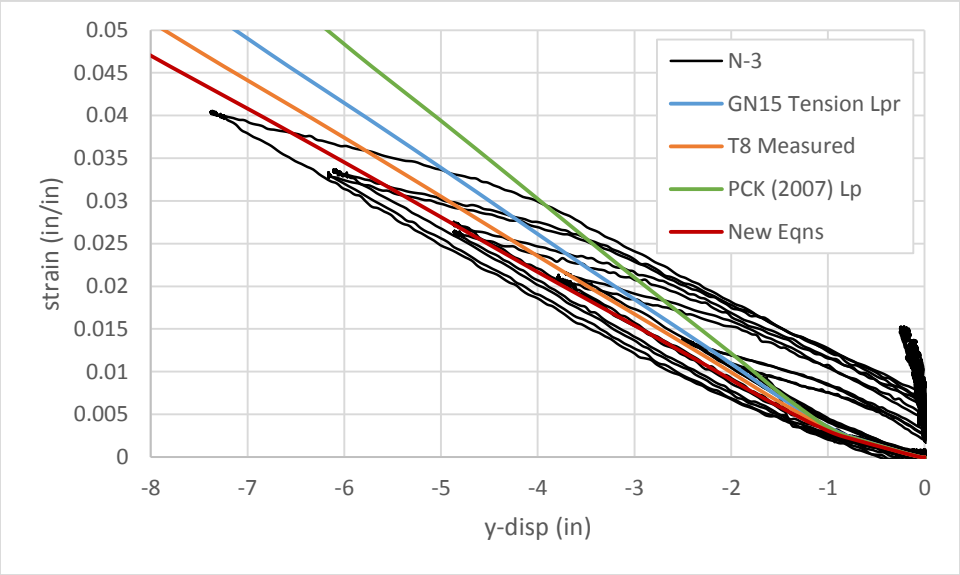

Figure 11-30. Test 8: Tension Strain-Disp. for Bar N (Gauge Length 3 Centered 6.23" above the Footing)

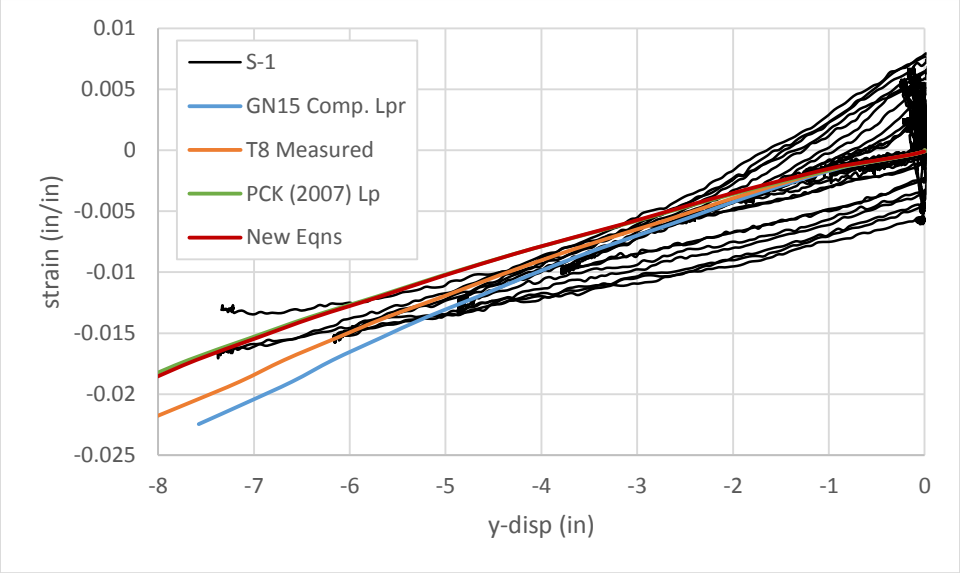

Figure 11-31. Test 8: Compression Strain-Disp. for Bar S (Gauge Length 1 Centered 2.06" above the Footing)

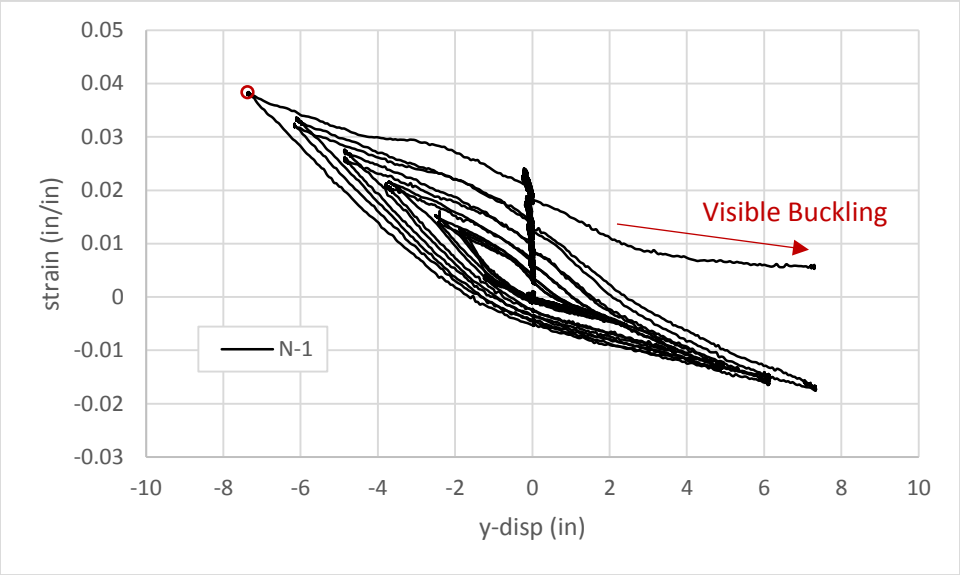

Figure 11-32. Test 8: Strain Hysteresis over the North Buckled Bar (Gauge Length 1 Centered 2.08" above the Footing)

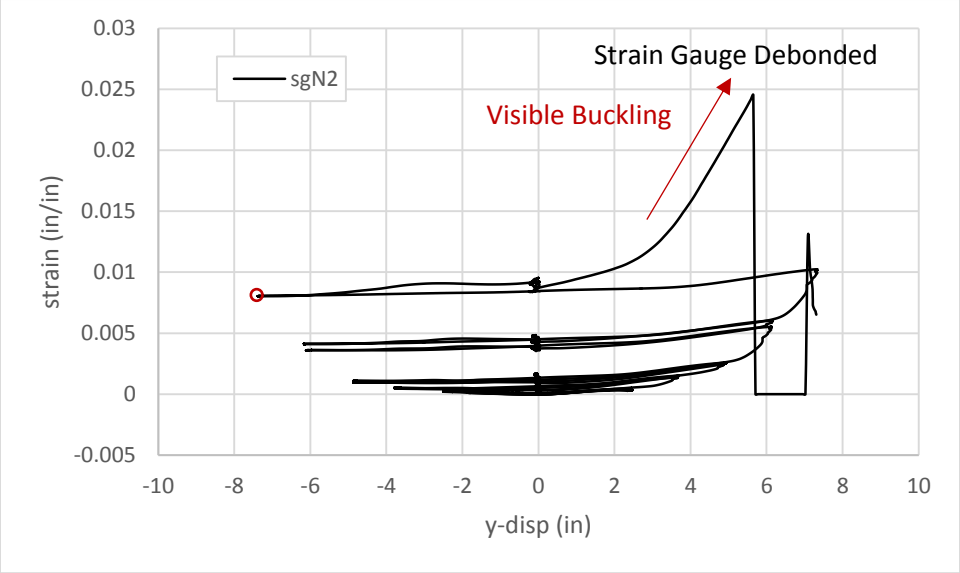

Figure 11-33. Test 8: Spiral Strain Hysteresis for the 2nd North Layer above the Footing

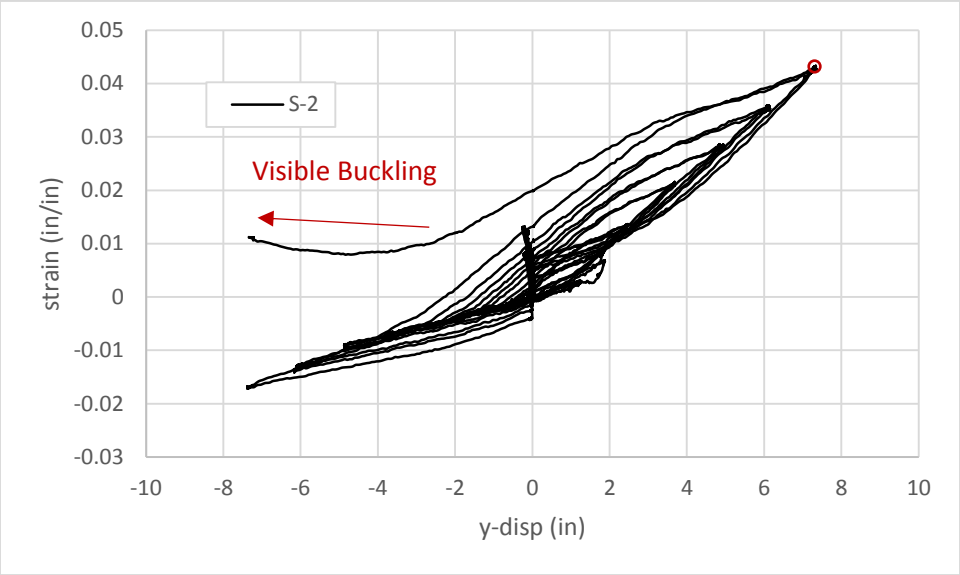

Figure 11-34. Test 8: Strain Hysteresis over the South Buckled Bar (Gauge Length 2 Centered 4.11" above the Footing)

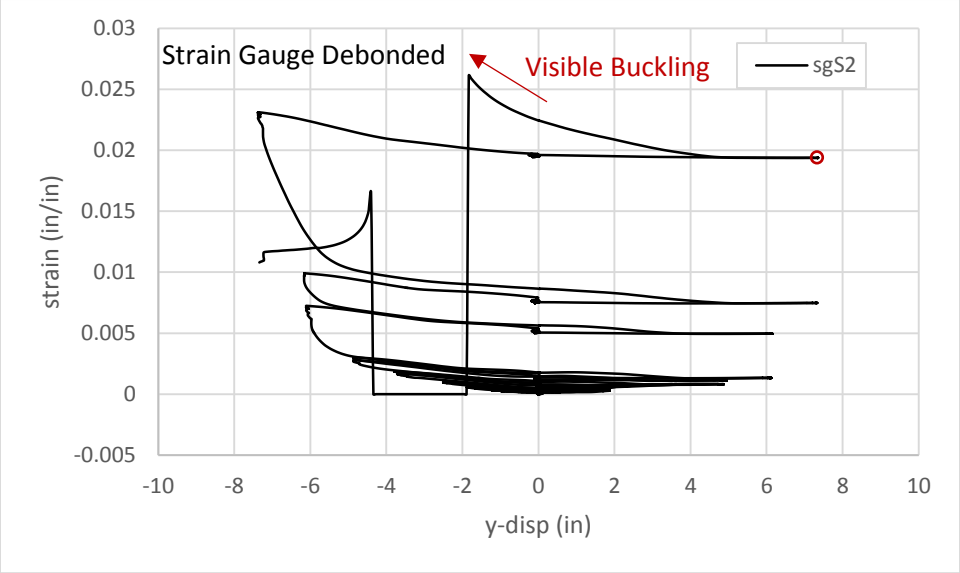

Figure 11-35. Test 8: Spiral Strain Hysteresis for the 2nd South Layer above the Footing

East and West Bar Strains

Vertical strain profiles for East and West reinforcement during x-direction cycles are shown in Figure 11-36 and Figure 11-37. Strains in the lowest four spiral layers during compressive x-direction cycles on the East and West sides of the specimen appear in Figure 11-38 and Figure 11-39. The relationship between strain and displacement for either peak tensile or peak compressive gauge lengths appear in Figure 11-40 through Figure 11-45. These figures contain monotonic moment curvature predictions for respective plastic hinge methods. PCK (2007) Lp refers to the (Priestley, Calvi and Kowalsky 2007) plastic hinge method, GN15 Tension/Compression Lpr refers to the (Goodnight, Kowalsky and Nau 2015a) unidirectional modified plastic hinge method, TX Measured refer to using the measured extent of plasticity and average equivalent strain penetration length from this specific test, and New Equations refers to a new bidirectional plastic hinge method which was created based on this study. Details of the new plastic hinge method appear in a later chapter of this report.

Spiral strain gauge and Optotrak strain hysteresis for the second and third East layers above the footing appear in Figure 11-48 and Figure 11-49. Both layers had a spike in measured tension strains during $\mu_{\Delta 6}^{+1x} = 7.32$", when the East extreme fiber bar buckled, see Figure 11-19. The visual observation of bar buckling was confirmed upon inspection of the East longitudinal bar strain hystereses in Figure 11-46 and Figure 11-47; however, there was significant measurable outward deformation in the previous compressive cycle.

Spiral strain gauge and Optotrak strain hysteresis for the first and second West layers above the footing appear in Figure 11-51 and Figure 11-52. Both layers had a spike in measured tension strains during $\mu_{\Delta 6}^{-1x} = -7.36$", when the West extreme fiber bar buckled, see Figure 11-19. The visual observation of bar buckling was confirmed upon inspection of the West longitudinal bar strain hysteresis in Figure 11-50; however, there was measurable outward deformation in the previous compressive cycle.

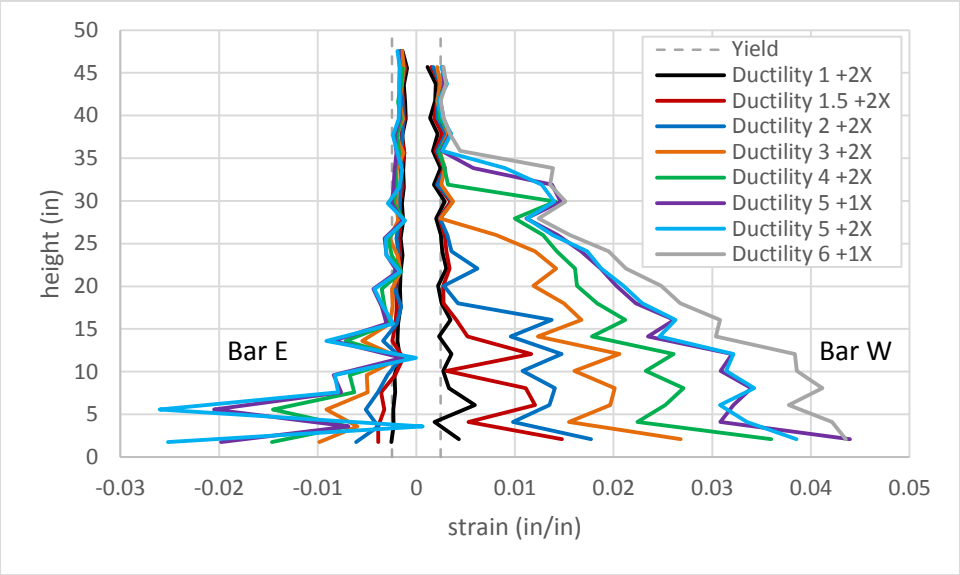

Figure 11-36. Test 8: Vertical Strain Profiles for Loading in the +X-direction

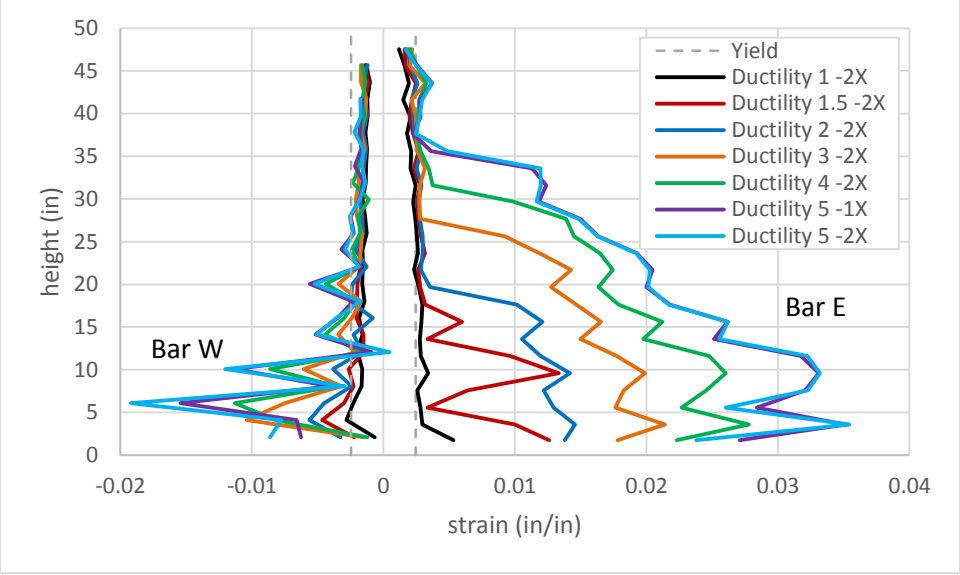

Figure 11-37. Test 8: Vertical Strain Profiles for Loading in the -X-direction

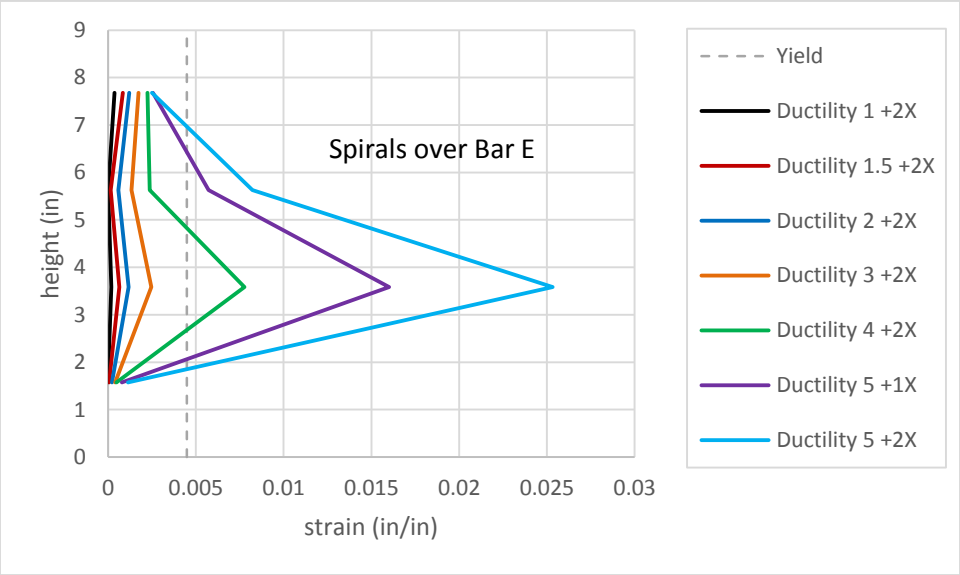

Figure 11-38. Test 8: Spiral Strains Measured Over the East Extreme Fiber Bar during +X Cycles

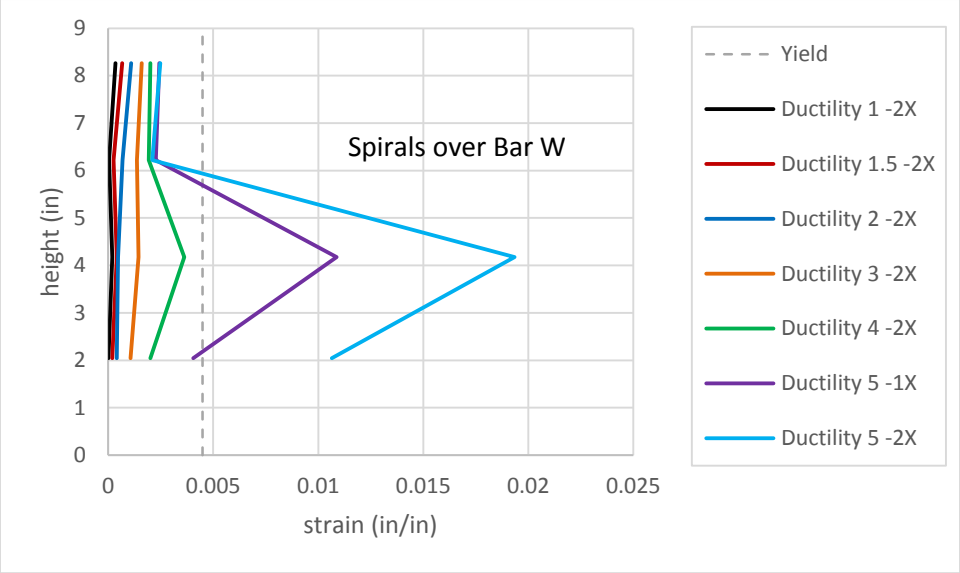

Figure 11-39. Test 8: Spiral Strains Measured Over the West Extreme Fiber Bar during -X Cycles

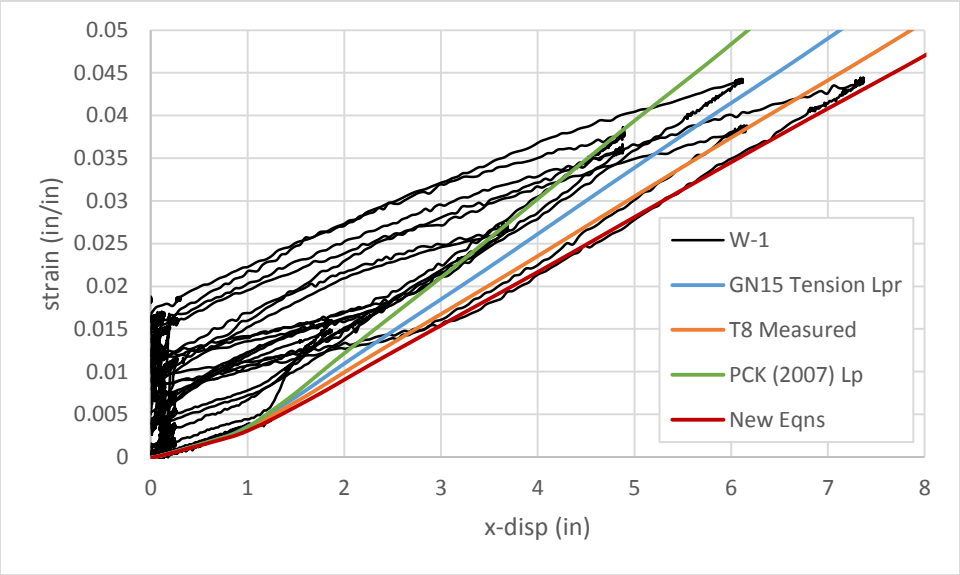

Figure 11-40. Test 8: Tension Strain-Disp. for Bar W (Gauge Length 1 Centered 2.10" above the Footing)

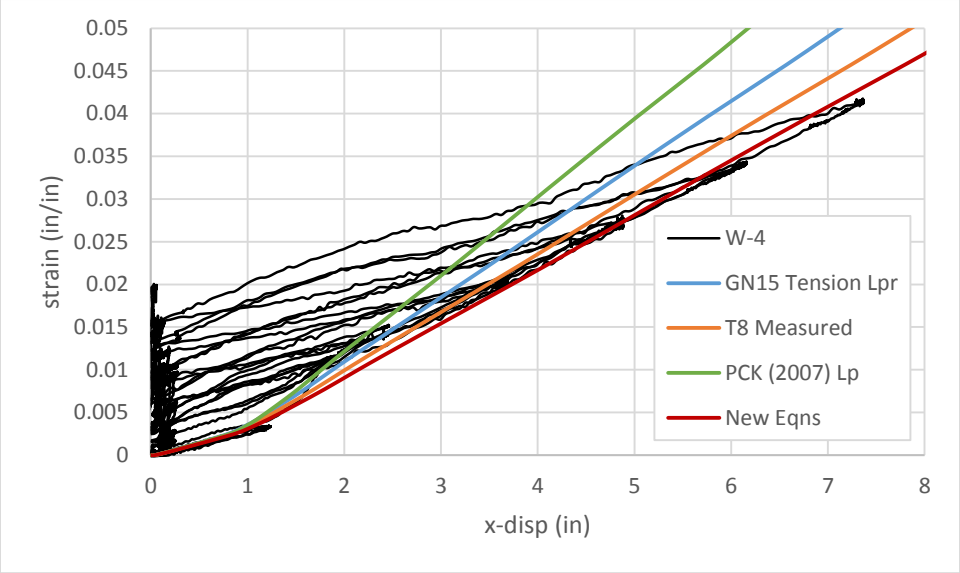

Figure 11-41. Test 8: Tension Strain-Disp. for Bar W (Gauge Length 4 Centered 8.08" above the Footing)

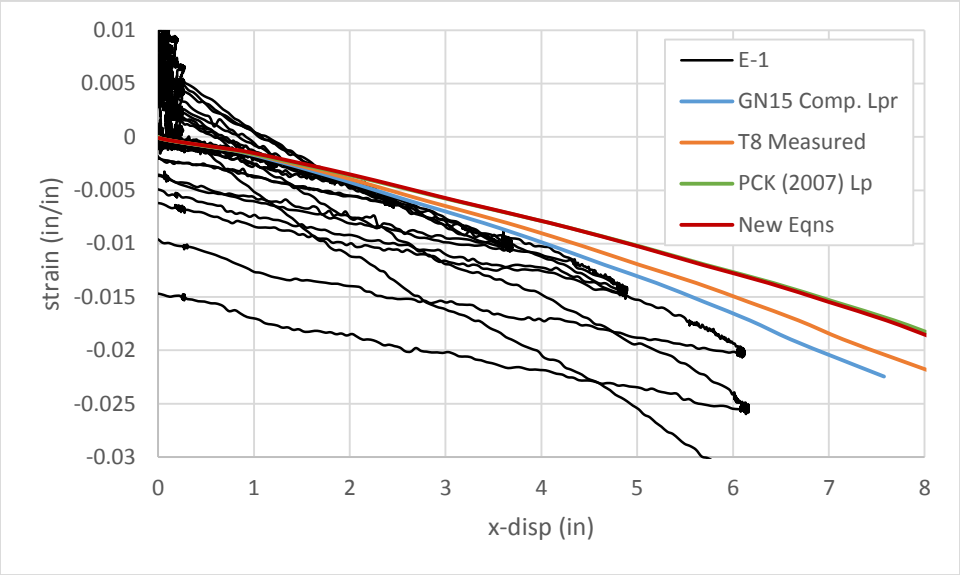

Figure 11-42. Test 8: Compression Strain-Disp. for Bar E (Gauge Length 1 Centered 1.76" above the Footing)

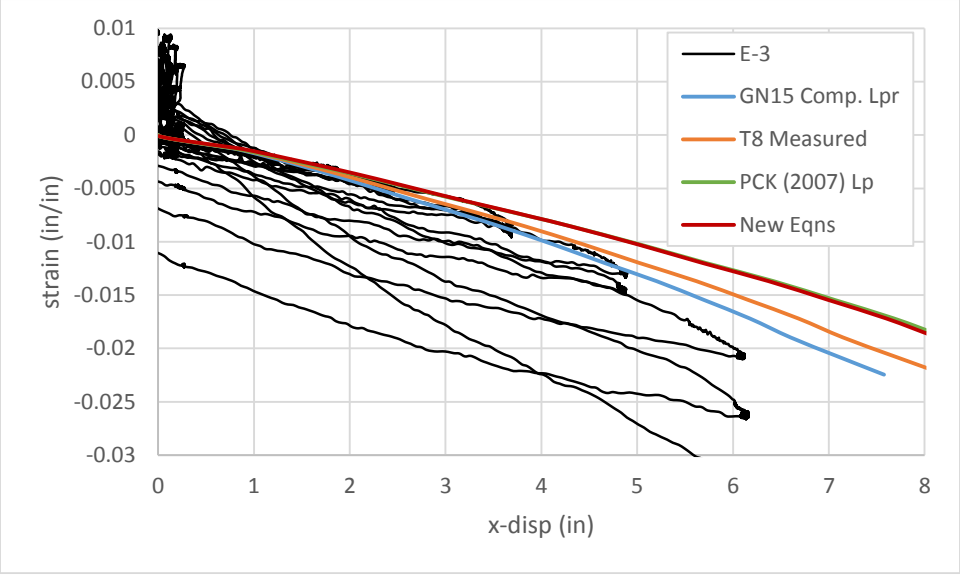

Figure 11-43. Test 8: Compression Strain-Disp. for Bar E (Gauge Length 3 Centered 5.57" above the Footing)

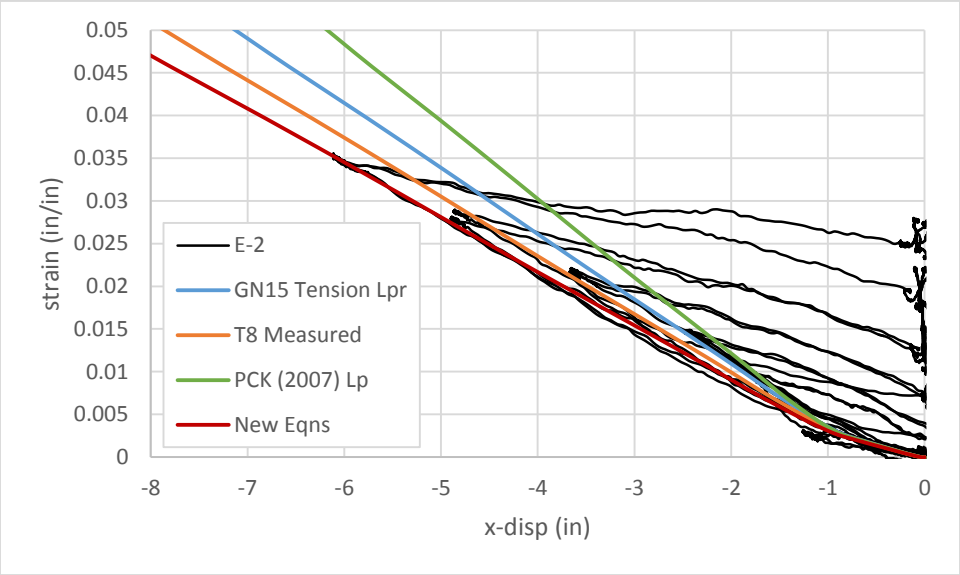

Figure 11-44. Test 8: Tension Strain-Disp. for Bar E (Gauge Length 4 Centered 8.08" above the Footing)

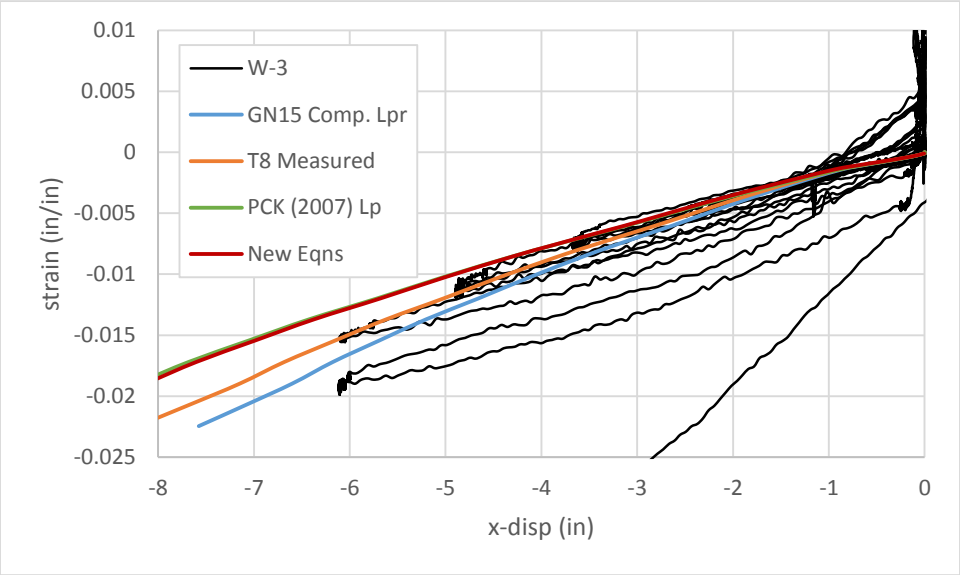

Figure 11-45. Test 8: Compression Strain-Disp. for Bar W (Gauge Length 3 Centered 6.07" above the Footing)

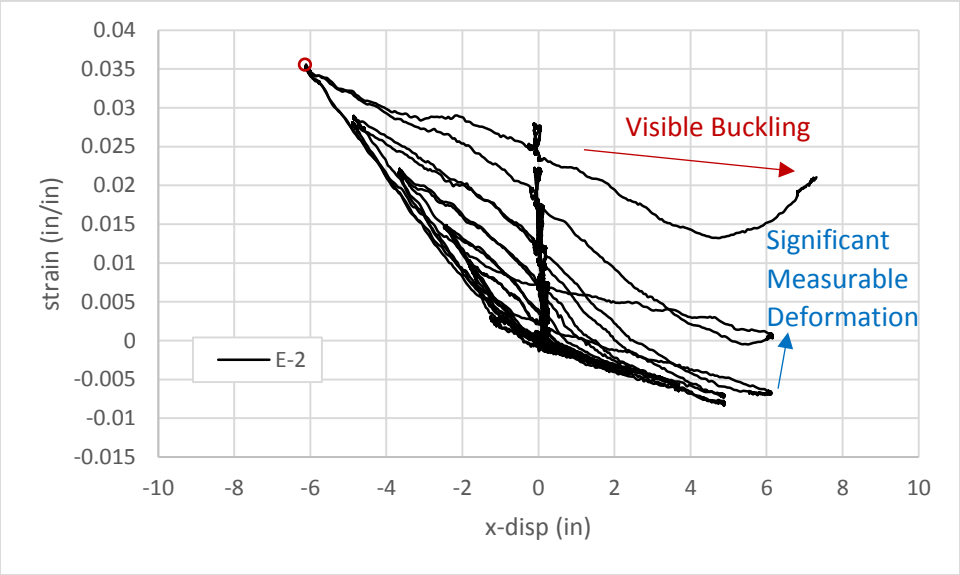

Figure 11-46. Test 8: Strain Hysteresis over the East Buckled Bar (Gauge Length 2 Centered 3.58" above the Footing)

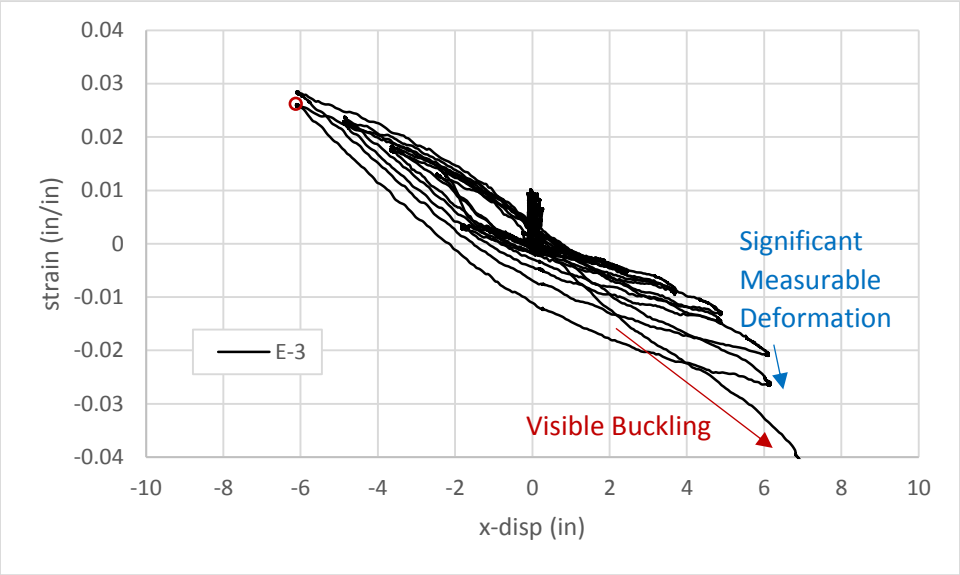

Figure 11-47. Test 8: Strain Hysteresis over the East Buckled Bar (Gauge Length 3 Centered 5.57" above the Footing)

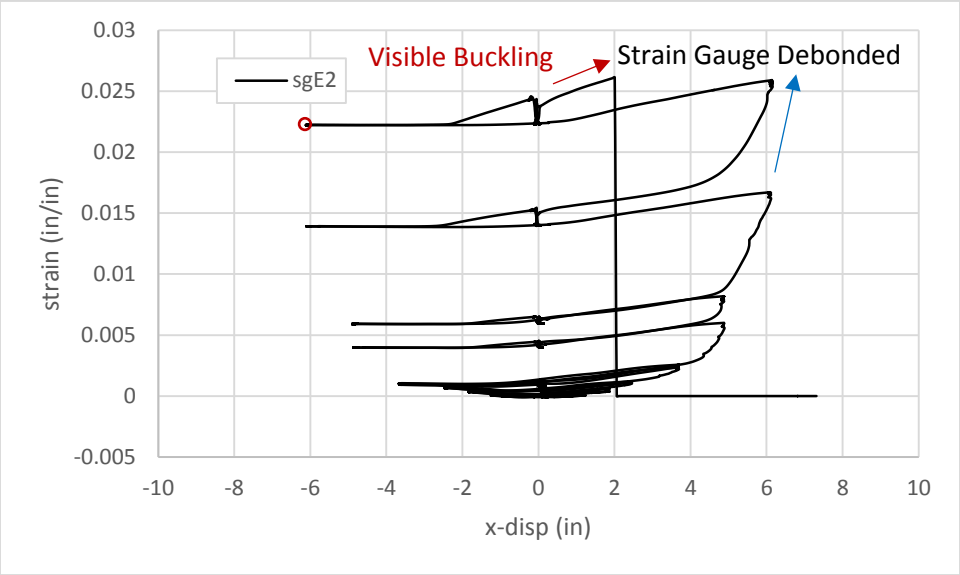

Figure 11-48. Test 8: Spiral Strain Hysteresis for the 2nd East Layer above the Footing

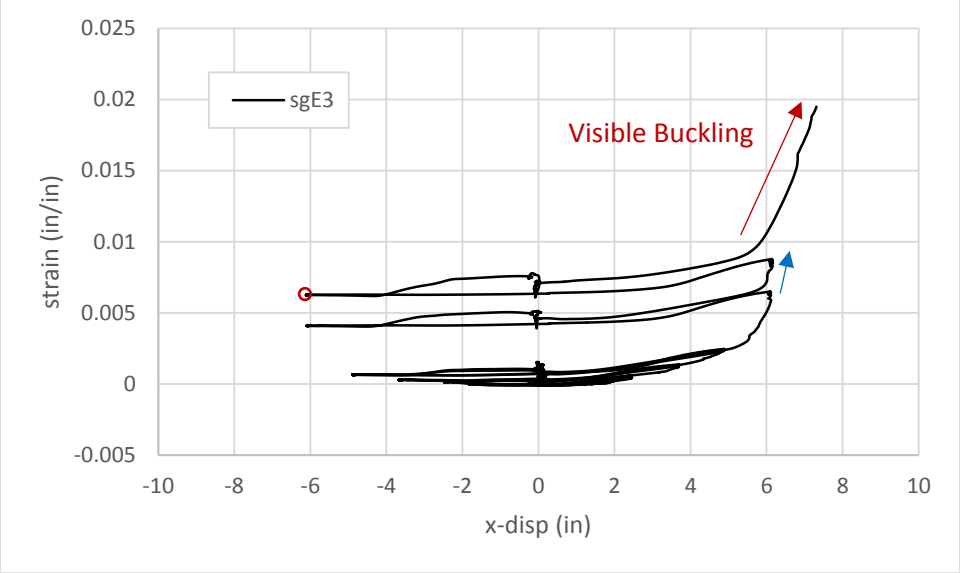

Figure 11-49. Test 8: Spiral Strain Hysteresis for the 3rd East Layer above the Footing

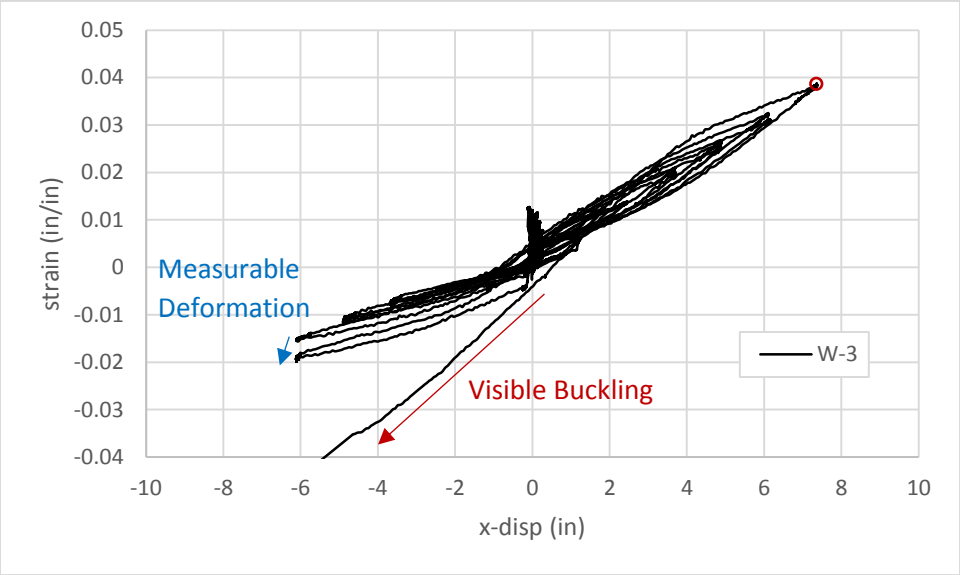

Figure 11-50. Test 8: Strain Hysteresis over the West Buckled Bar (Gauge Length 3 Centered 6.07" above the Footing)

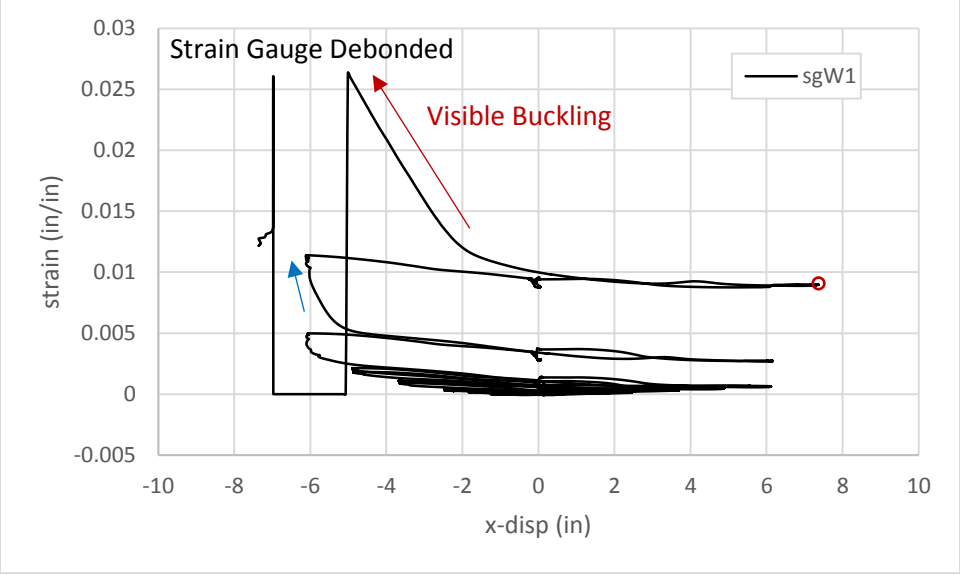

Figure 11-51. Test 8: Spiral Strain Hysteresis for the 1st West Layer above the Footing

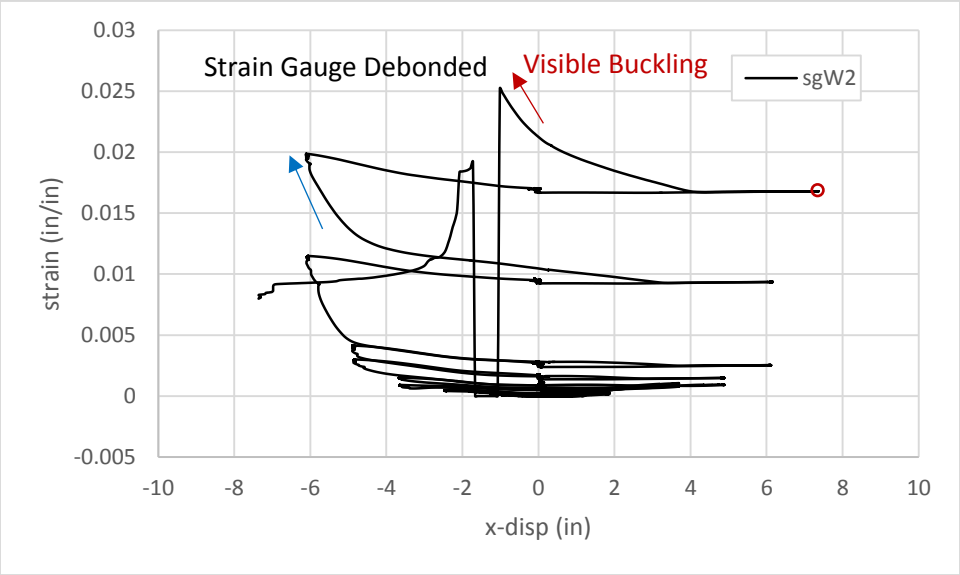

Figure 11-52. Test 8: Spiral Strain Hysteresis for the 2nd West Layer above the Footing

Test 8 - Curvature and Strain Penetration Data

Curvature and stain penetration data for Test 8 is presented in the following section. The methods in which this data was generated are outlined in the summary for Test 1. Sample cross section curvature profiles are shown in Figure 11-53 and Figure 11-54. Vertical curvature profiles for respective loading directions appear in Figure 11-55 through Figure 11-59. Fixed-end rotations attributable to strain penetration of longitudinal reinforcement into the footing are shown in Figure 11-60 through Figure 11-62. Comparison of the measured displacements to those obtained via integration of the measured curvature profiles and extrapolation of the fixed-end rotation to the center of the applied lateral load are shown in Figure 11-63 and Figure 11-64.

The measured extent of plasticity is compared to design recommendations for the tensile triangular plastic hinge length in Figure 11-65. GN15 refers to the (Goodnight, Kowalsky and Nau 2015a) unidirectional tensile hinge length while New Equations refers to a new bidirectional plastic hinge method which was created based on this study. Details of the new plastic hinge method appear in a later chapter of this report. The measured equivalent strain penetration lengths are compared to design recommendations in Figure 11-66. GN15 refers to the (Goodnight, Kowalsky and Nau 2015a) unidirectional Lsp while PCK (2007) refers to the (Priestley, Calvi and Kowalsky 2007) definition of Lsp. Finally, the measured hysteretic response is compared to monotonic predictions in Figure 11-67 and Figure 11-68.

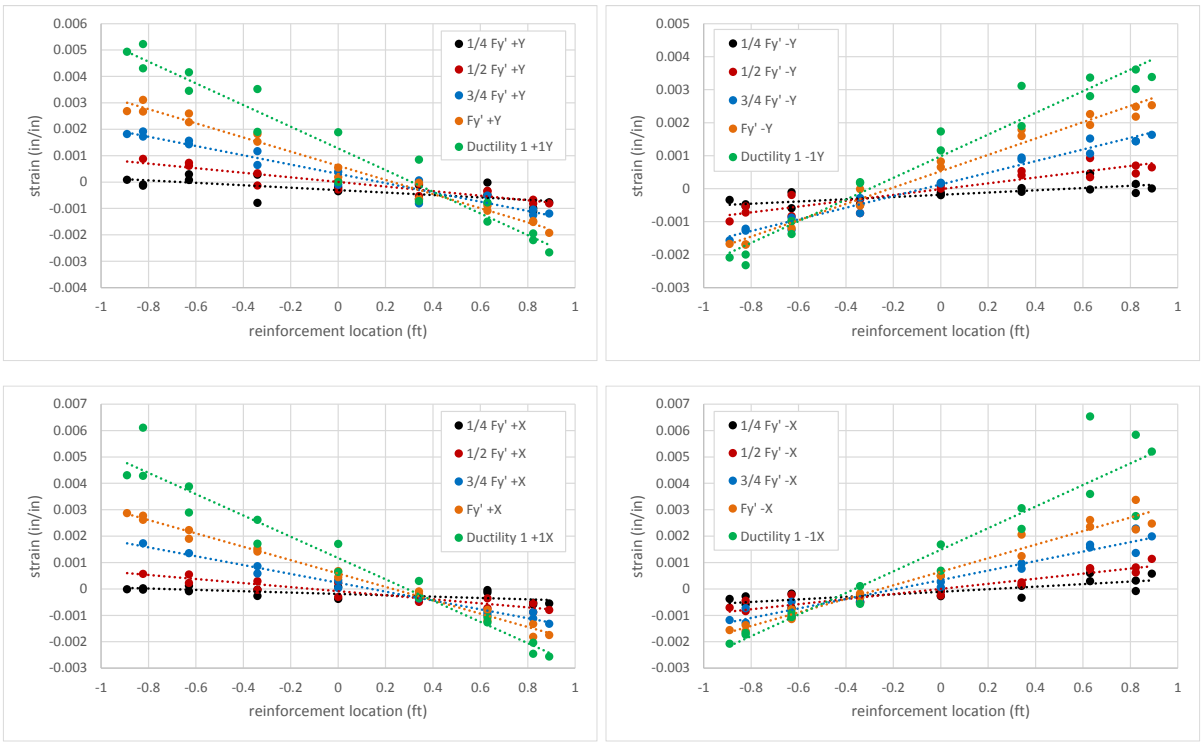

Figure 11-53. Test 8: Elastic Curvature Profiles for the First Instrumented Section above the Footing

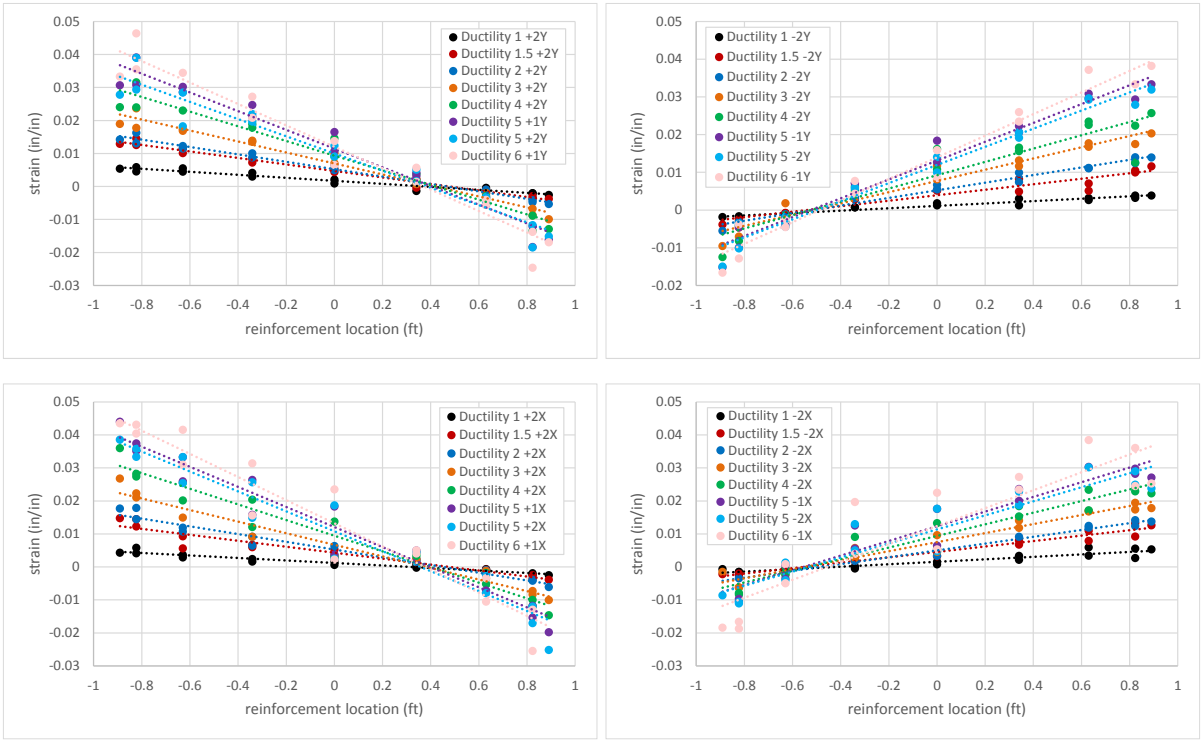

Figure 11-54. Test 8: Curvature Profiles for the First Instrumented Section above the Footing

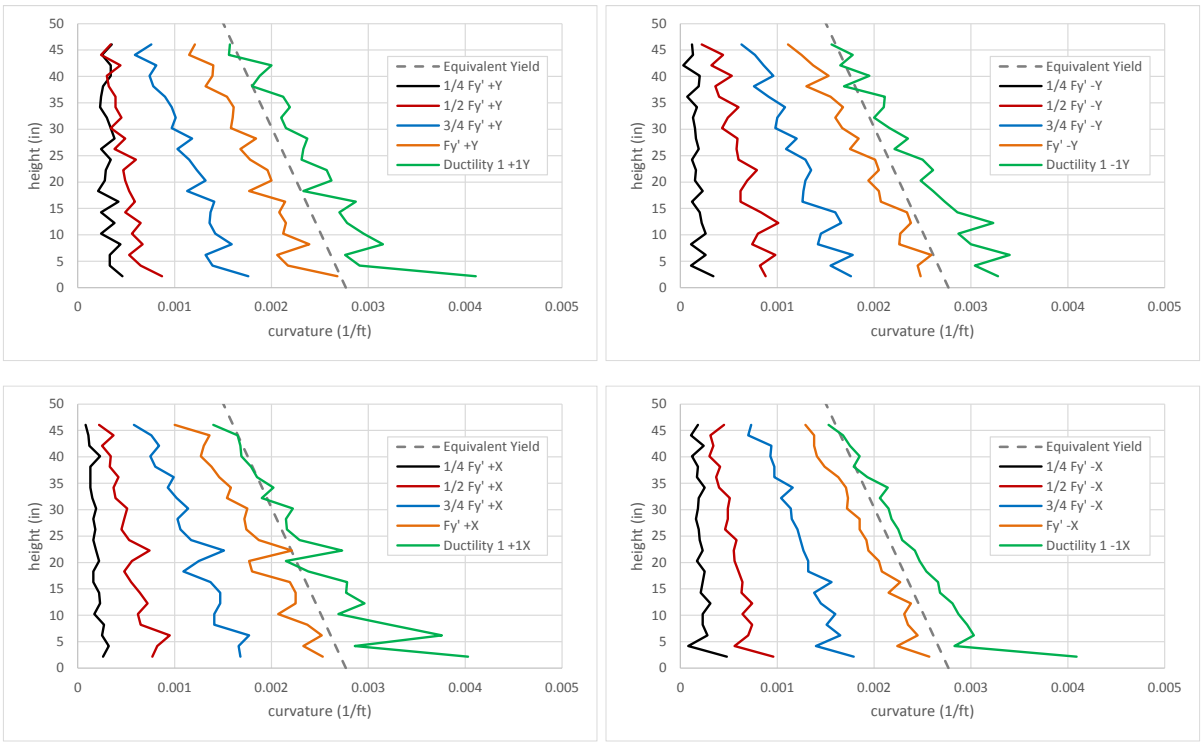

Figure 11-55. Test 8: Elastic Vertical Curvature Profiles

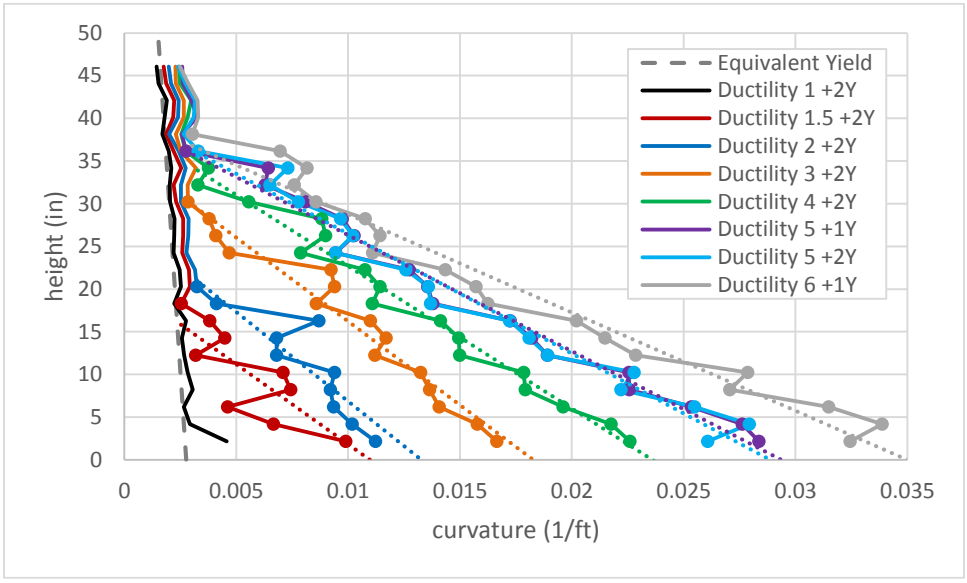

Figure 11-56. Test 8: Vertical Curvature Profiles for Loading in the +Y-direction

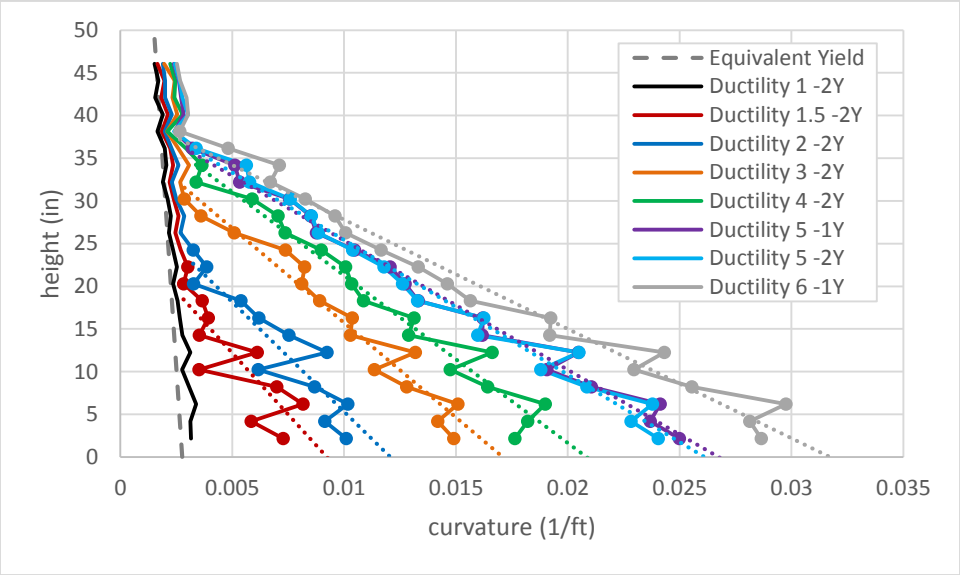

Figure 11-57. Test 8: Vertical Curvature Profiles for Loading in the -Y-direction

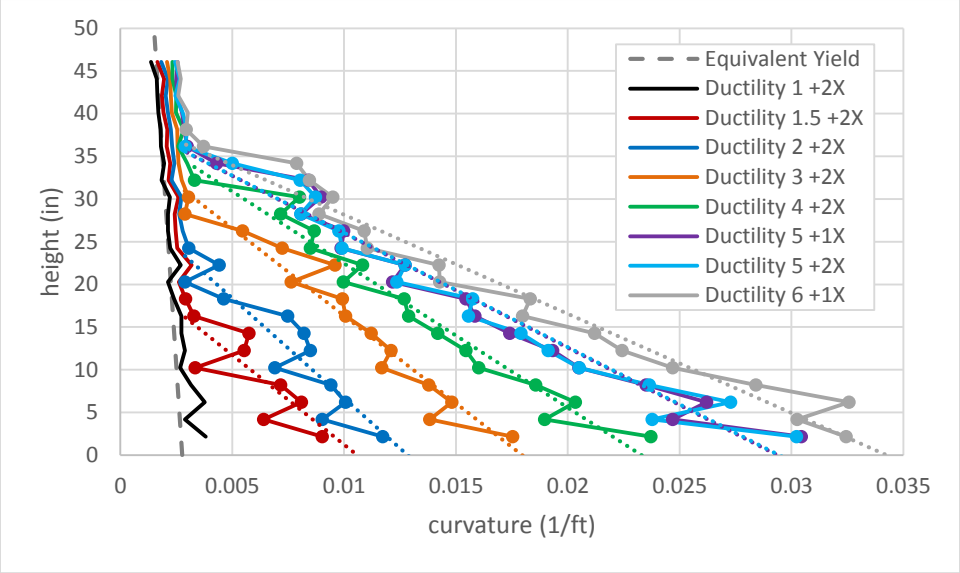

Figure 11-58. Test 8: Vertical Curvature Profiles for Loading in the +X-direction

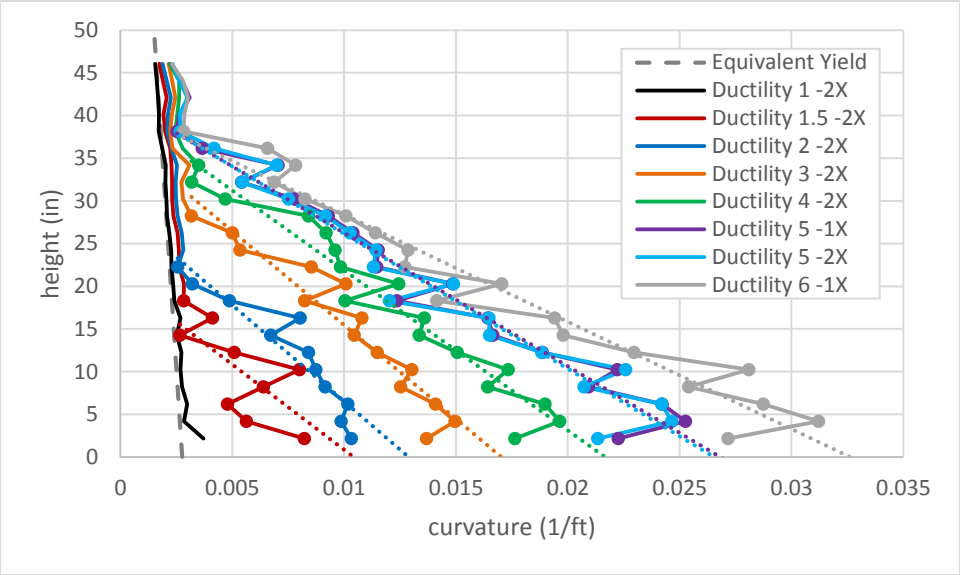

Figure 11-59. Test 8: Vertical Curvature Profiles for Loading in the -X-direction

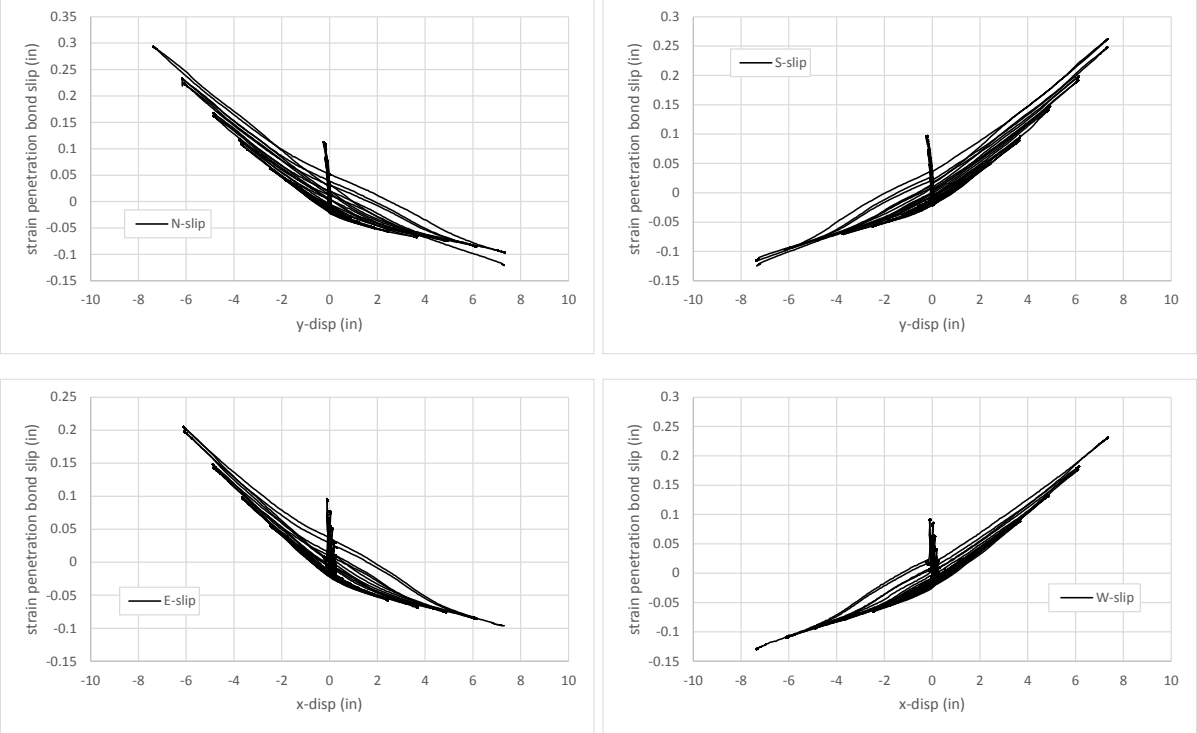

Figure 11-60. Test 8: Extreme Fiber Bar Strain Penetration Bond Slip Hysteresis

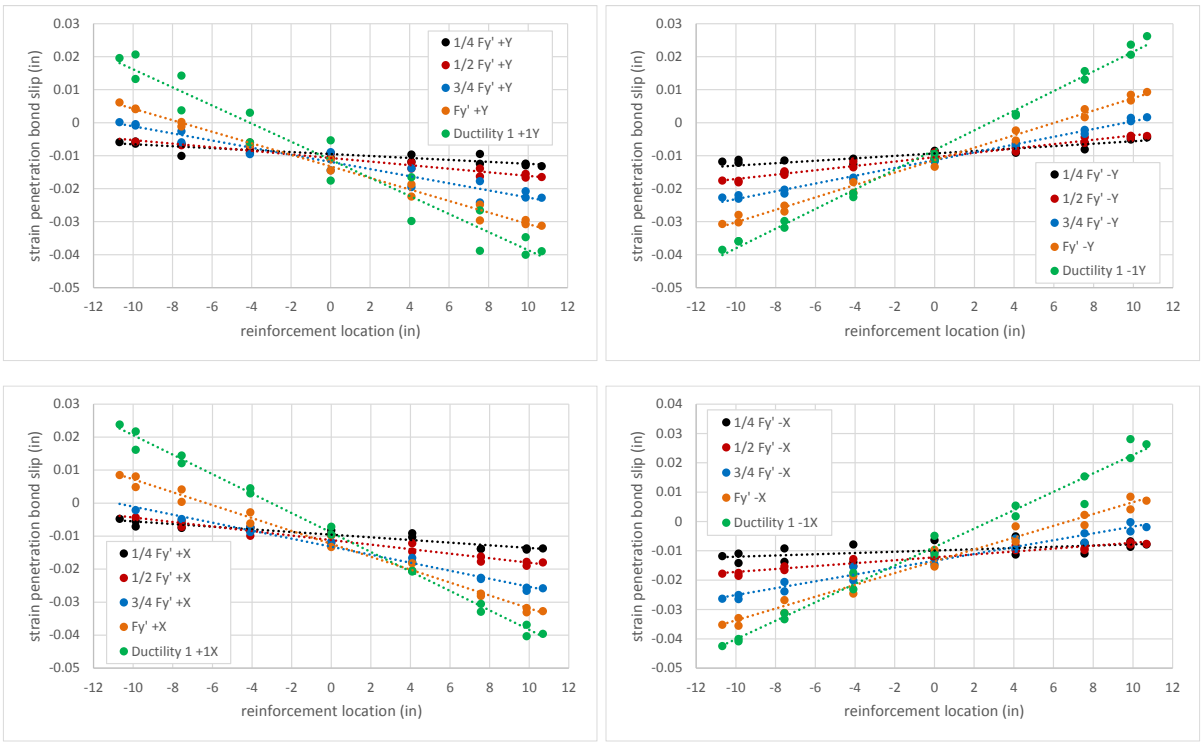

Figure 11-61. Test 8: Fixed End Rotations due to Strain Penetration during the Elastic Cycles

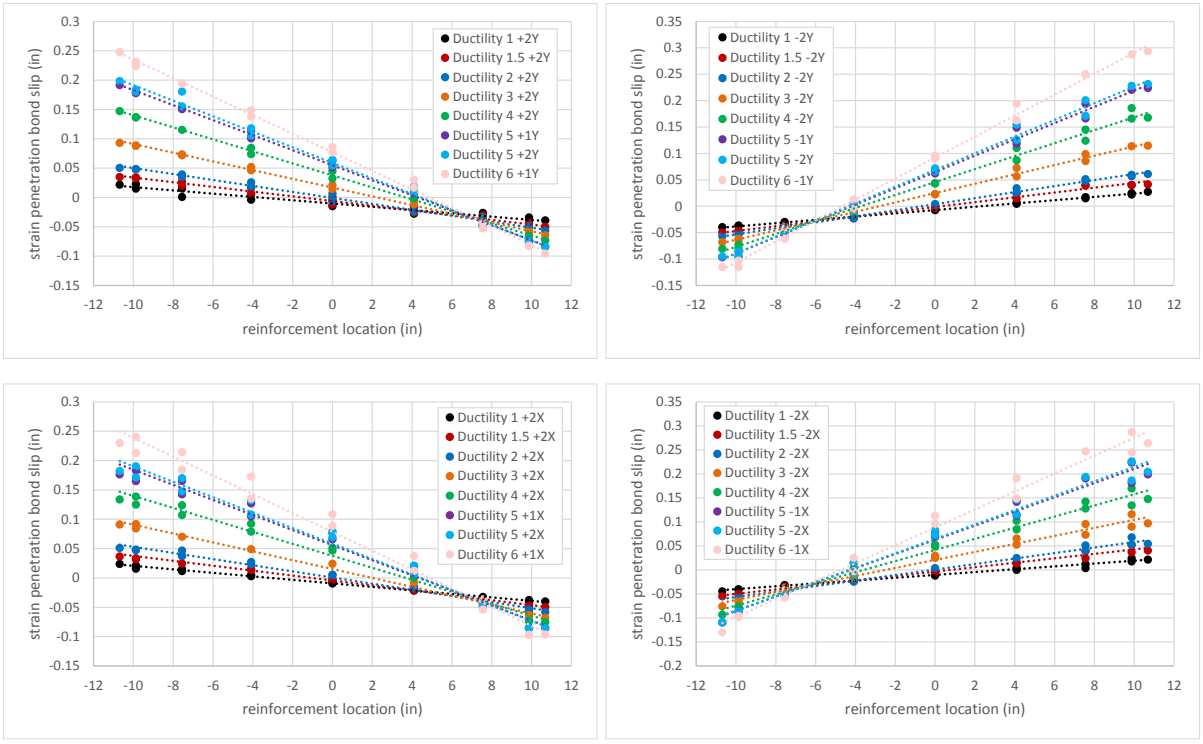

Figure 11-62. Test 8: Fixed End Rotations due to Strain Penetration

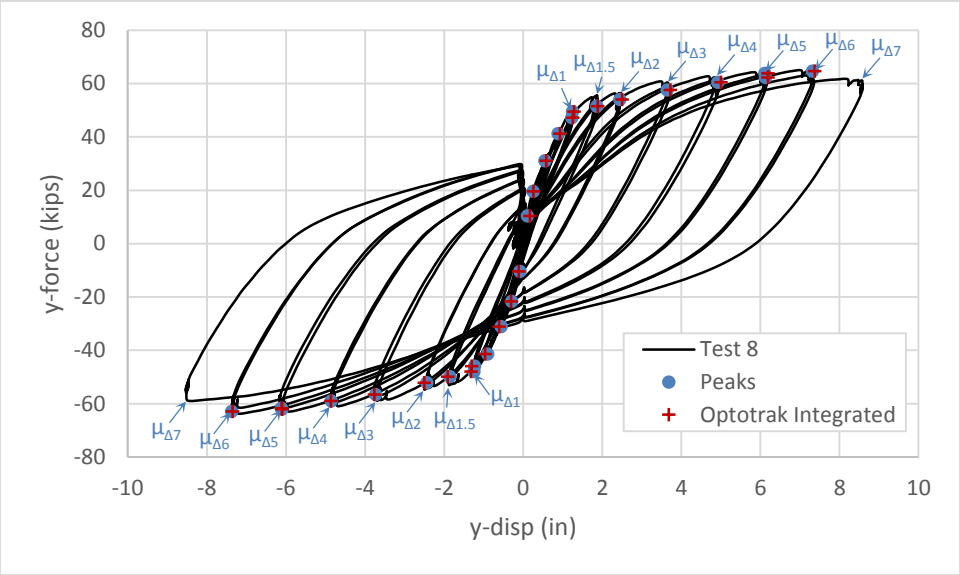

Figure 11-63. Test 8: Optotrak Integrated Flexural Disp. Compared to Measured String Pot. Disp.

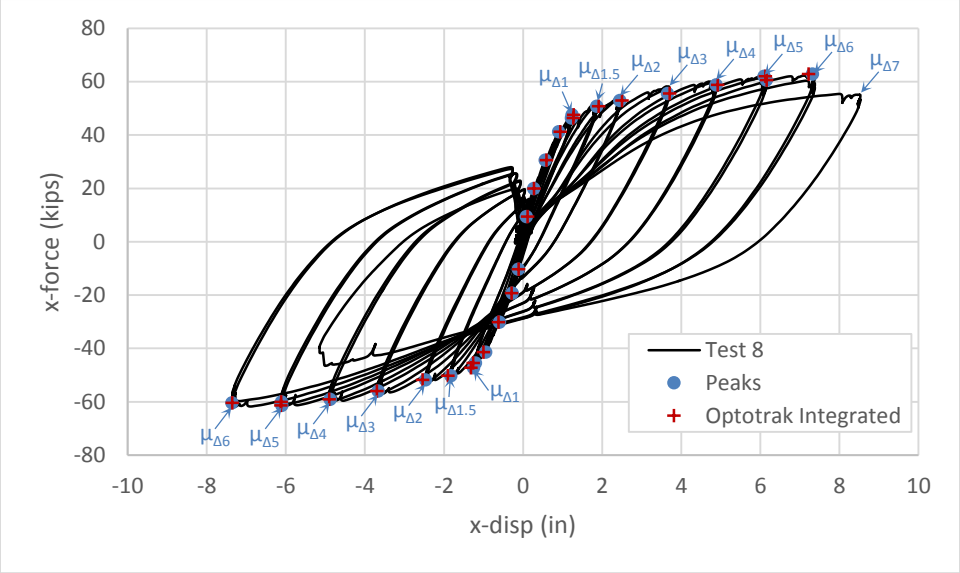

Figure 11-64. Test 8: Optotrak Integrated Flexural Disp. Compared to Measured String Pot. Disp.

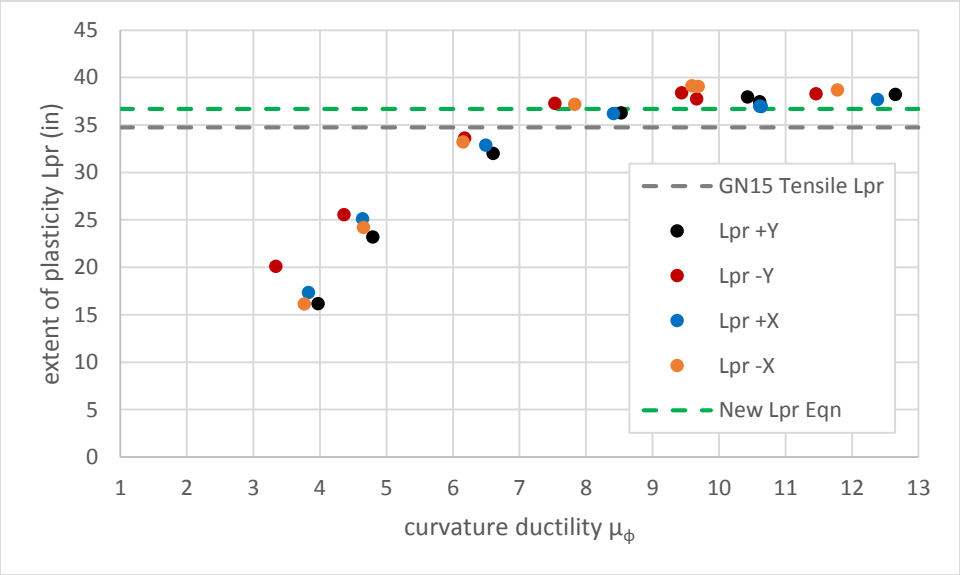

Figure 11-65. Test 8: Measured Extent of Plasticity Compared to Tensile Hinge Lengths

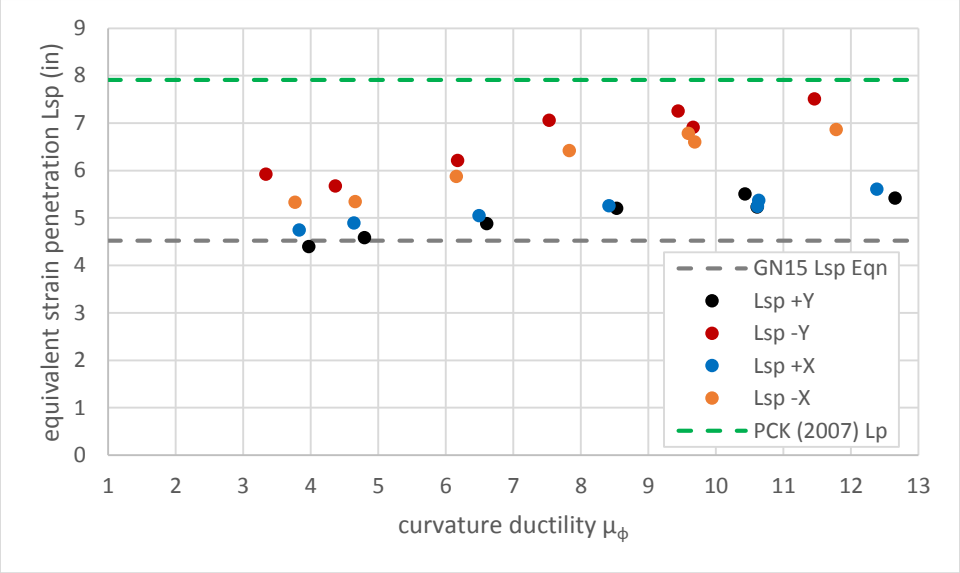

Figure 11-66. Test 8: Measured Equivalent Strain Penetration Lengths Compared to Design Expressions

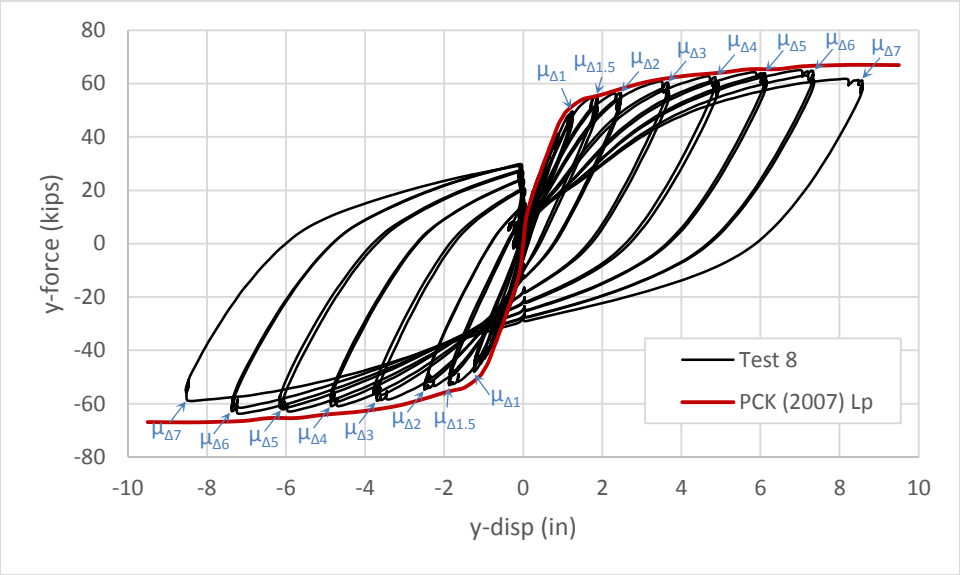

Figure 11-67. Test 8: Y-Direction Hysteretic Response Compared to PCK (2007) Hinge Length Monotonic Prediction

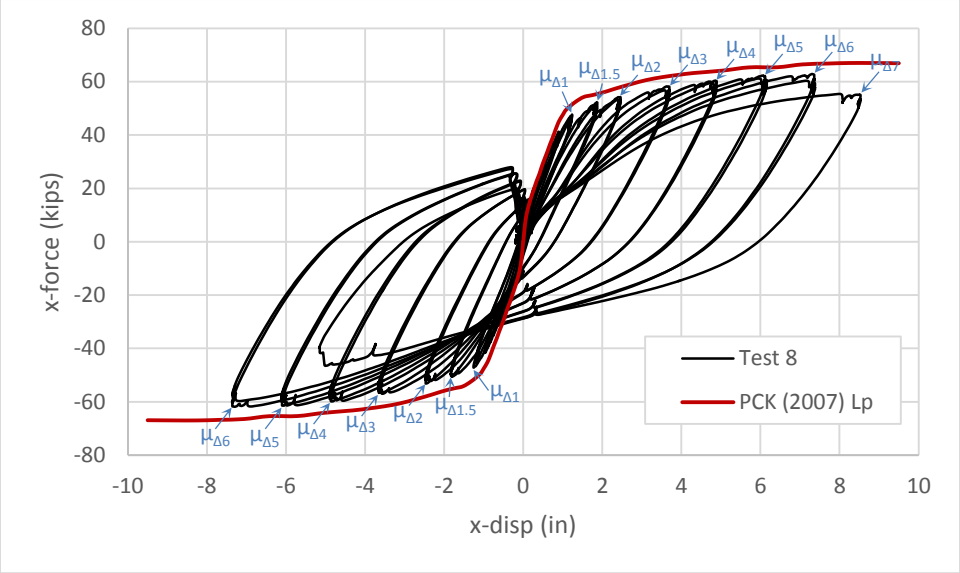

Figure 11-68. Test 8: X-Direction Hysteretic Response Compared to PCK (2007) Hinge Length Monotonic Prediction

Response Comparison for Test 7 (1.3%) and Test 8 (1% Transverse Volumetric Steel)

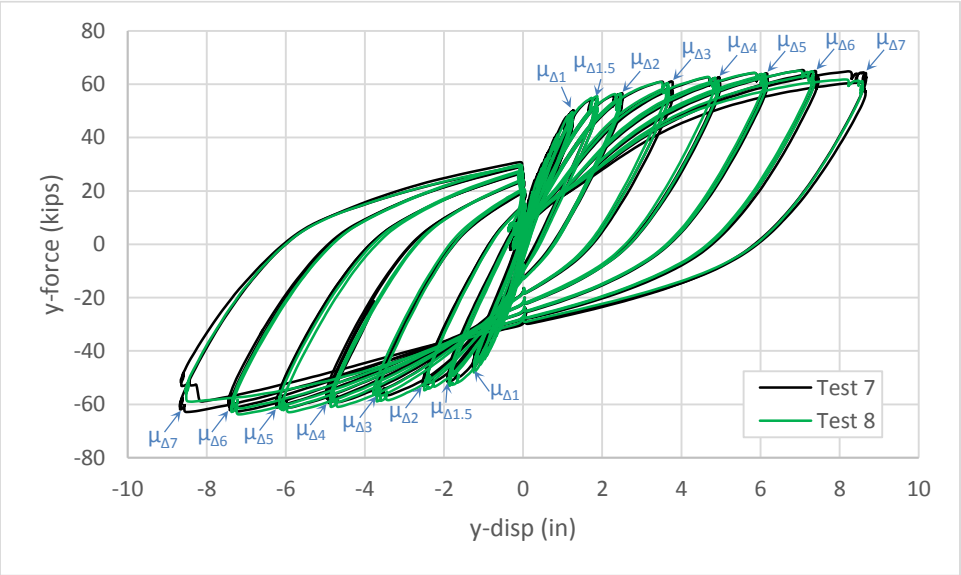

Figure 11-69. Tests 7 (1.3%) and 8 (1% Transverse Steel) Hysteretic Response Comparison in the Y-Direction

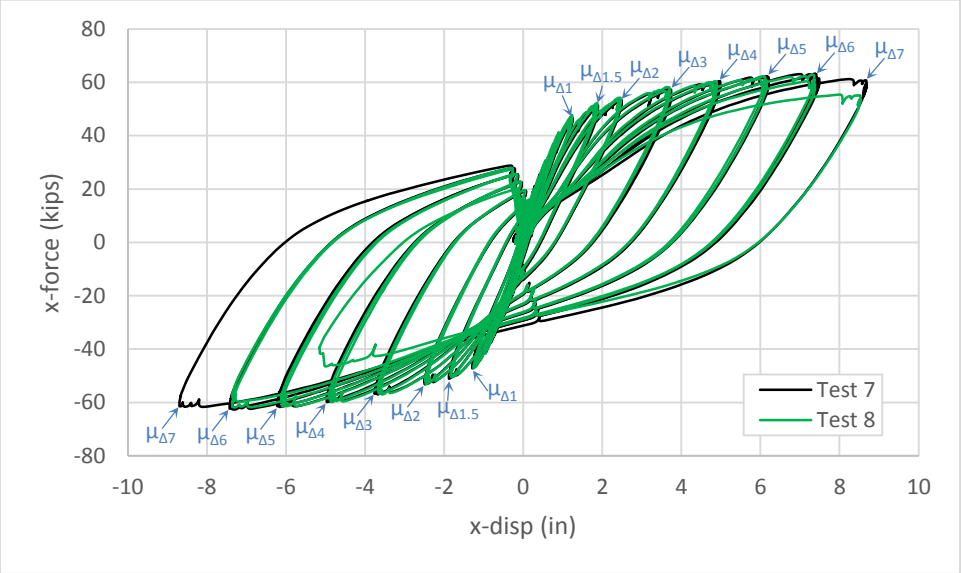

Figure 11-70. Tests 7 (1.3%) and 8 (1% Transverse Steel) Hysteretic Response Comparison in the X-Direction

Chapter 12 – Test 9 Summary Report

The ninth specimen had a 24" diameter circular cross-section reinforced with 16 #6 A706 longitudinal bars ($A_{st}/A_g = 1.6\%$) and a #3 spiral at 2.75" on center ($4A_{sp}/D's = 0.7\%$). The specimen was nominally identical to those chosen for Tests 7 and 8 which contained 1.3% and 1% transverse steel, respectively. The columns selected for Tests 1-3 were nominally identical to that of Test 9, except they contained 2.1% longitudinal steel. Details of the test setup, instrumentation, and specimen design appear in Chapter 2. A material properties summary for the longitudinal and transverse steel from the final six experiments appears in Table 3-3 through Table 3-5. The column had a tested concrete strength of $f_c' = 6.29\ ksi$, while the footing had $f_c' = 8.34\ ksi$. The same constant compressive axial load of $191\ kips$ was applied to all the specimens. The ninth specimen was subjected to the Type-B Symmetric Two-Cycle-Set Bidirectional Load History shown in Figure 12-1. This figure includes a diagram of the column cross-section with the selected bar and crack labeling scheme. Displacements in the +Y-direction placed the South reinforcement in tension. Cracks due to loading in the +Y-direction were labeled as red. The orientation of the X and Y axes are shown in Figure 2-52 with regards to the test setup. The +Y-axis is perpendicular to and points away from the strong wall. Values of interests, damage observations, and a predictions summary for the ninth test appear in Table 12-1, Table 12-2, and Table 12-3. A photo of the deformed specimen appears in Figure 12-2.

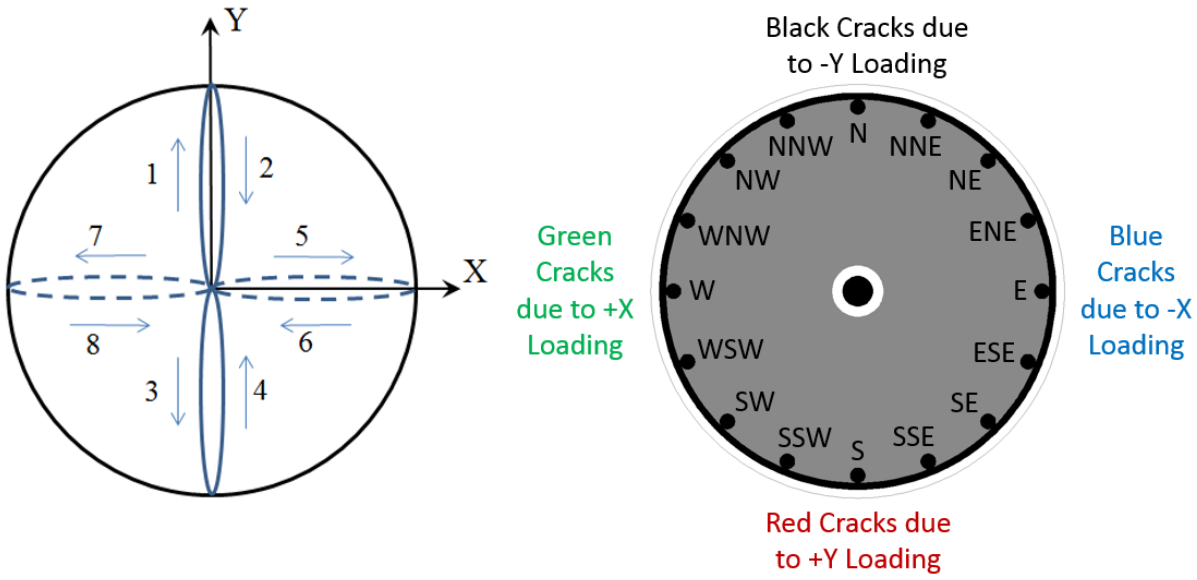

Figure 12-1. Test 9: Load History Orientation and Labeling System for Reinforcement and Cracks

Table 12-1. Test 9: Values of Interest

Load History	Type-B Symmetric Two-Cycle-Set
Length, Diameter, and Aspect Ratio	$L = 109.4375\ in, D = 24\ in,\ (L/D = 4.56)$
Longitudinal Steel Detailing	$16\ \#6\ for\ \rho_l = A_{st}/A_g = 1.6\%$
Longitudinal Steel Properties	$f_y = 70.33\ ksi, f_u = 98.68\ ksi, \varepsilon_y = 0.00283$
Transverse Steel Detailing	$\#3\ @\ 2.75\ in\ for\ \rho_s = 4A_{sp}/D's = 0.7\%$
Transverse Steel Properties	$f_y = 63.89\ ksi, f_u = 93.64\ ksi, \varepsilon_y = 0.00418$
Column Concrete Strength	$f_c' = 6.29\ ksi$
Footing Concrete Strength	$f_c' = 8.34\ ksi$
Axial Load	$P = 191\ kips, \left(P/f_c'\ A_g = 7.3\%\right)$
Analytical First Yield Force	$F_y' = 41.34\ kips$
Experimental First Yield Disp.	$\Delta_y' = 0.95\ in$
Analytical Nominal Moment Capacity	$M_n = 508.07\ kip \cdot ft$
Equivalent Yield Displacement	$\Delta_y = \Delta_y'\left(M_n/M_y'\right) = 1.28\ in$
Maximum Lateral Force	$F_y = 63.22\ kips, F_x = 61.87\ kips$
Failure Mode	Fracture of Previously Buckled Reinforcement

Table 12-2. Test 9: Damage Observations

Damage Observations:		
Cycle Peak at which First Cracking was Observed Visually:		
North	$\Delta_y = -0.5F_y' = -0.31\ in$	$F_y = -20.44\ kips$
South	$\Delta_y = 0.5F_y' = 0.30\ in$	$F_y = 20.69\ kips$
East	$\Delta_x = -0.5F_y' = -0.30\ in$	$F_x = -19.59\ kips$
West	$\Delta_x = 0.5F_y' = 0.33\ in$	$F_x = 20.46\ kips$
Cycle Peak at which Cover Concrete Crushing was Observed Visually:		
North	$\mu_{\Delta 2}^{+1Y} = 2.57\ in$	$\varepsilon_c = -0.00610$
South	$\mu_{\Delta 1.5}^{-1Y} = -1.90\ in$	$\varepsilon_c = -0.00470$
East	$\mu_{\Delta 2}^{+1X} = 2.57\ in$	$\varepsilon_c = -0.00661$
West	$\mu_{\Delta 2}^{-1X} = -2.58\ in$	$\varepsilon_c = -0.00598$
Exact Displacement and Cycle Label for Initial Spiral Yielding in the Confinement Zone:		
North	$\Delta_y = 5.10\ in\ during\ \mu_{\Delta 4}^{+1Y}$	$\varepsilon_c = -0.01170$
South	$\Delta_y = -4.82\ in\ during\ \mu_{\Delta 4}^{-1Y}$	$\varepsilon_c = -0.01175$
East	$\Delta_x = 4.27\ in\ during\ \mu_{\Delta 4}^{+1X}$	$\varepsilon_c = -0.01150$
West	$\Delta_x = -4.68\ in\ during\ \mu_{\Delta 4}^{-2X}$	$\varepsilon_c = -0.01786$
Peak Tensile Displacement Prior to Visual Bar Buckling During Subsequent Reversal of Load:		
North	$\mu_{\Delta 5}^{-1Y} = -6.40\ in, Observed\ at\ \mu_{\Delta 5}^{+2Y} = 6.41\ in$	$\varepsilon_s = 0.03443$
South	$\mu_{\Delta 5}^{+2Y} = 6.41\ in, Observed\ at\ \mu_{\Delta 5}^{-2Y} = -6.40\ in$	$\varepsilon_s = 0.03517$
East	$\mu_{\Delta 5}^{-1X} = -6.38\ in, Observed\ at\ \mu_{\Delta 5}^{+2X} = 6.41\ in$	$\varepsilon_s = 0.03618$
West	$\mu_{\Delta 5}^{+2X} = 6.41\ in, Observed\ at\ \mu_{\Delta 5}^{-2X} = -6.40\ in$	$\varepsilon_s = 0.03790$
Exact Displacement and Cycle Label for Fracture of Previously Buckled Reinforcement		
East	$\Delta_x = -6.16\ in\ during\ \mu_{\Delta 6}^{-1X}$	Single East Extreme Bar

Table 12-3. Test 9: Damage Predictions

Damage Predictions with the New Bidirectional Plastic Hinge Model and New Strain Limits:		
Bar Buckling Predictions		
New Method	$\Delta_{bb}^{Lpr} = 5.97\ in$	$\varepsilon_s^{bb} = 0.03396$
Feng et al. (2015)	$\Delta_{bb}^{Lp} = 5.40\ in$	$\varepsilon_s^{bb} = 0.04232$
Cover Crushing Prediction		
New Method	$\Delta_{cc}^{Lpr} = 1.98\ in$	$\varepsilon_c^{cc} = -0.004$
Spiral Yielding Prediction		
New Method	$\Delta_{sy}^{Lpr} = 5.06\ in$	$\varepsilon_c^{sy} = -0.01384 * M, (M = 0.8)$
Original Ultimate Concrete Compression Strain		
Mander et al. (1988)	$\Delta_{cu}^{Lpr} = 6.05\ in$	$\varepsilon_{cu} = -0.0139$

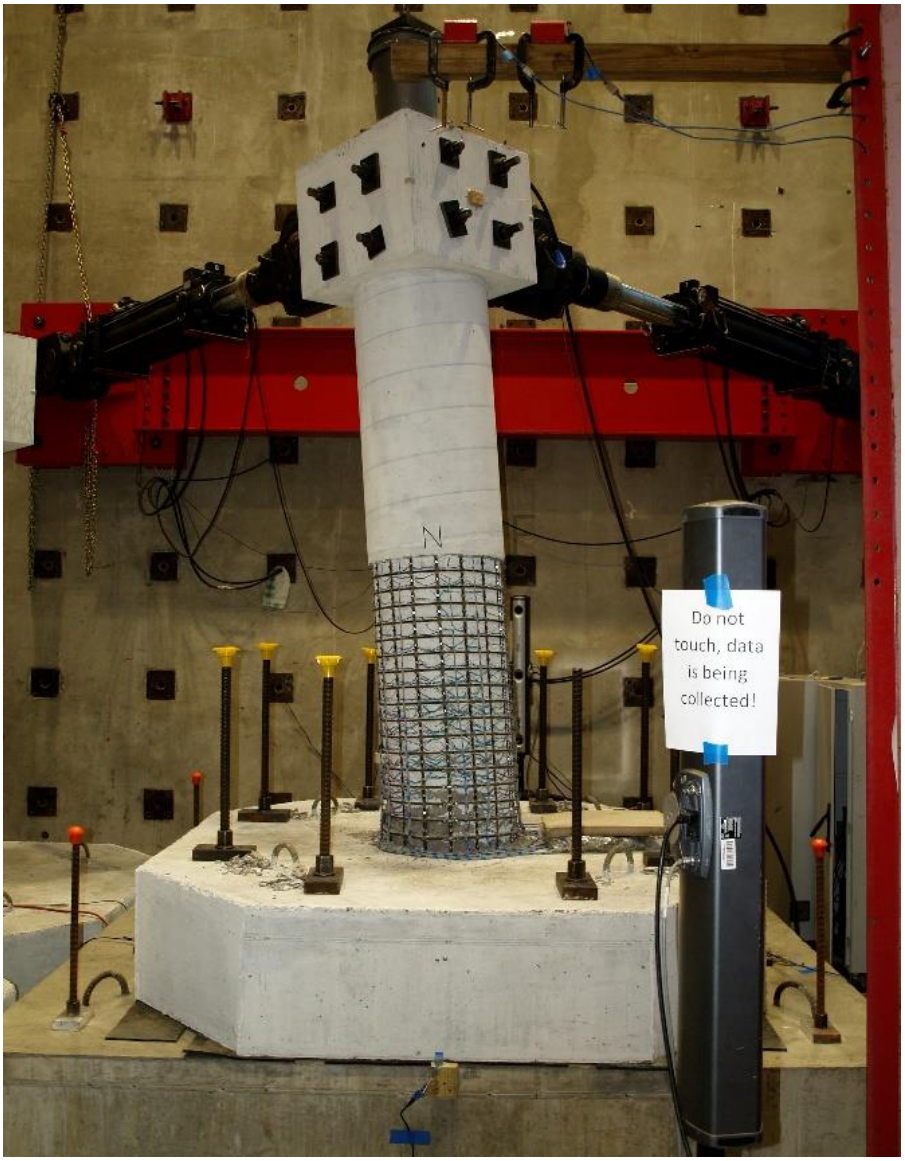

Figure 12-2. Test 9: Deformed Specimen at $\mu_{\Delta 6}^{+1x} = 7.68$"

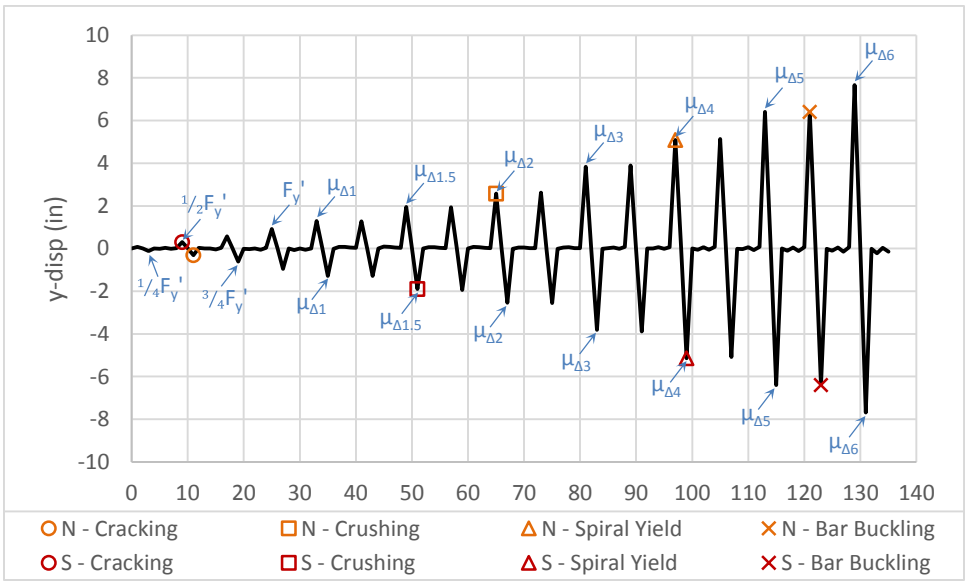

Figure 12-3. Test 9: Y-Displacement History

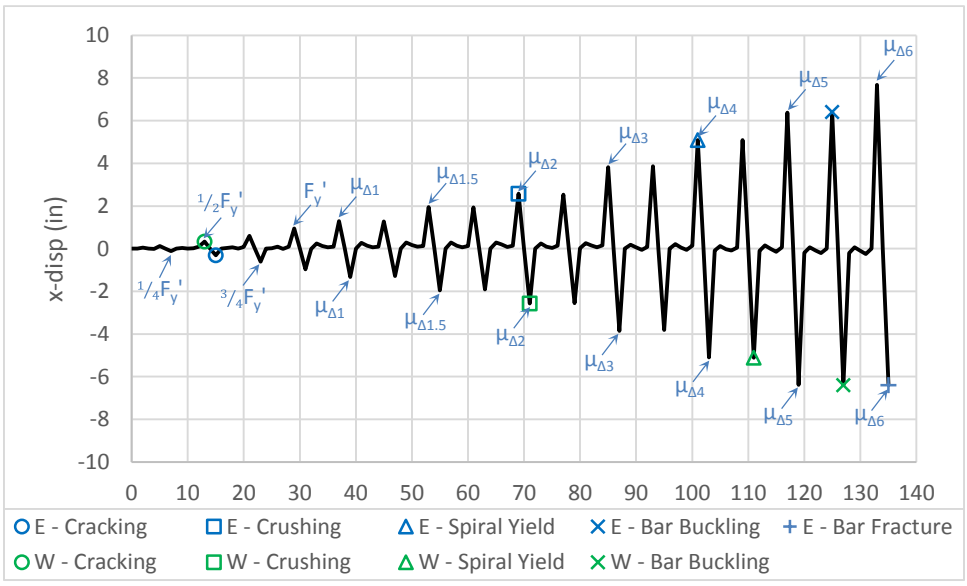

Figure 12-4. Test 9: X-Displacement History

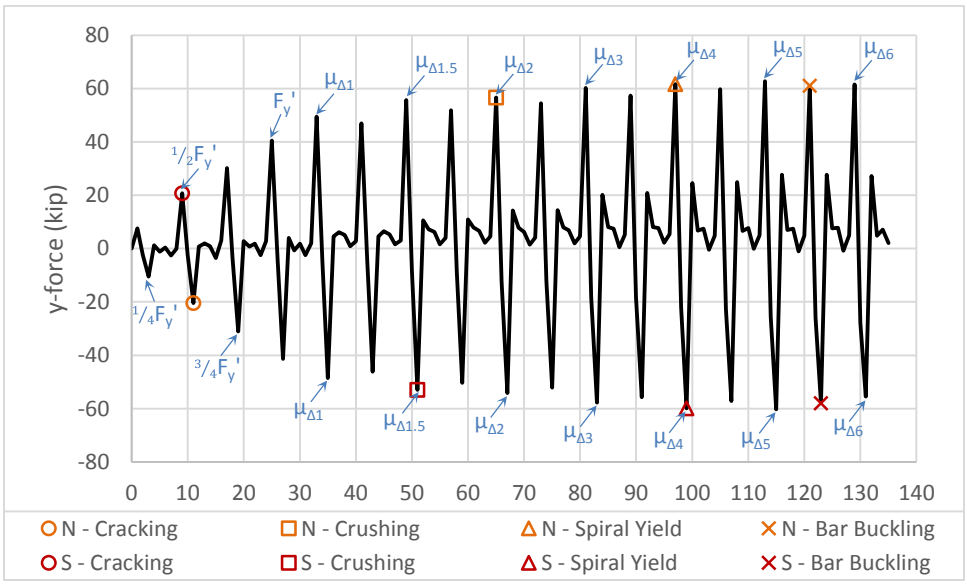

Figure 12-5. Test 9: Y-Force History

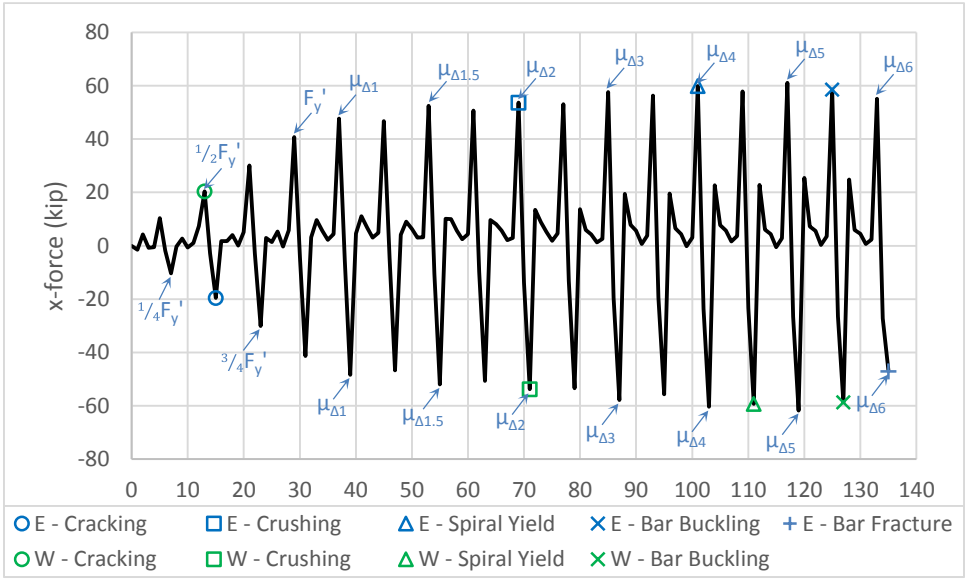

Figure 12-6. Test 9: X-Force History

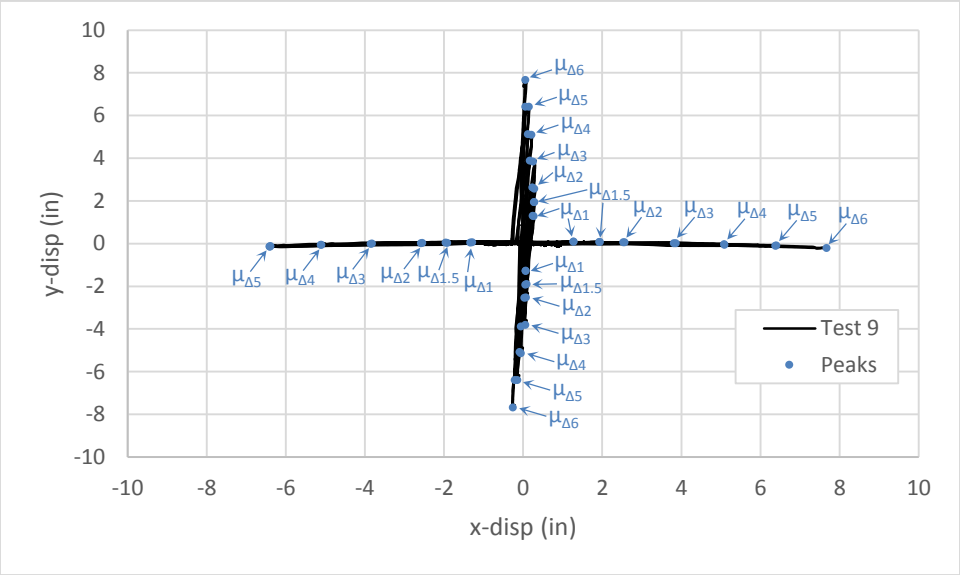

Figure 12-7. Test 9: Type-B Symmetric Two-Cycle-Set Displacement History

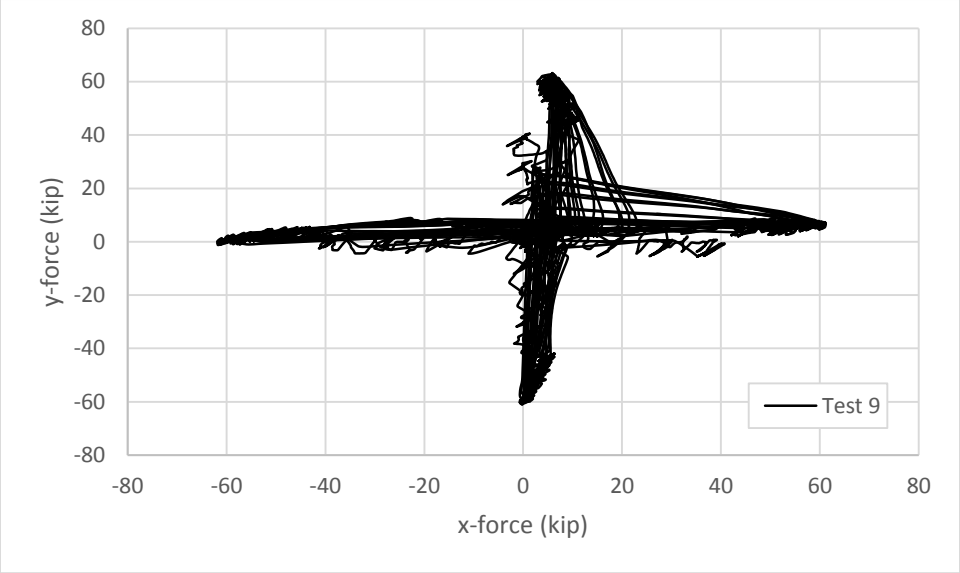

Figure 12-8. Test 9: Load Path

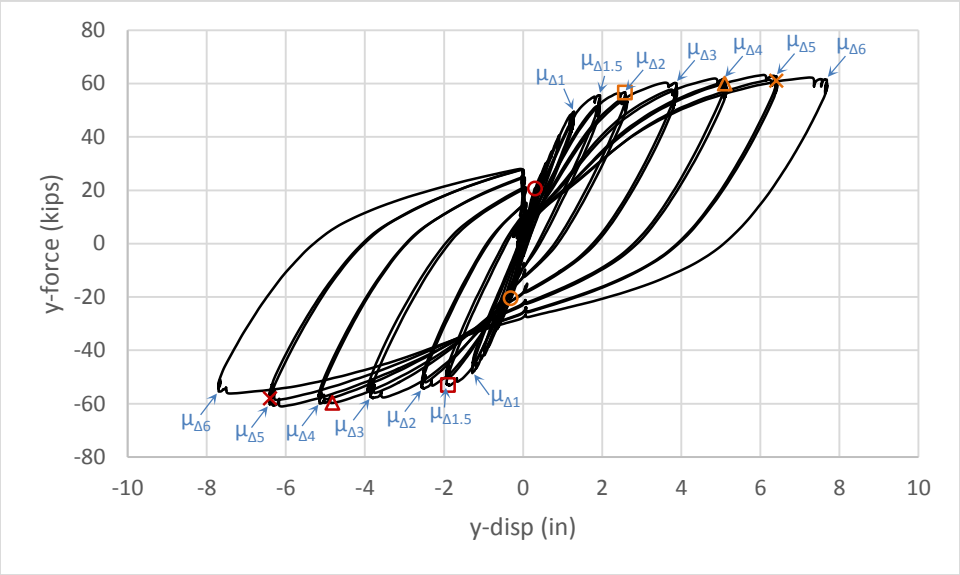

Figure 12-9. Test 9: Y-Direction Hysteretic Response

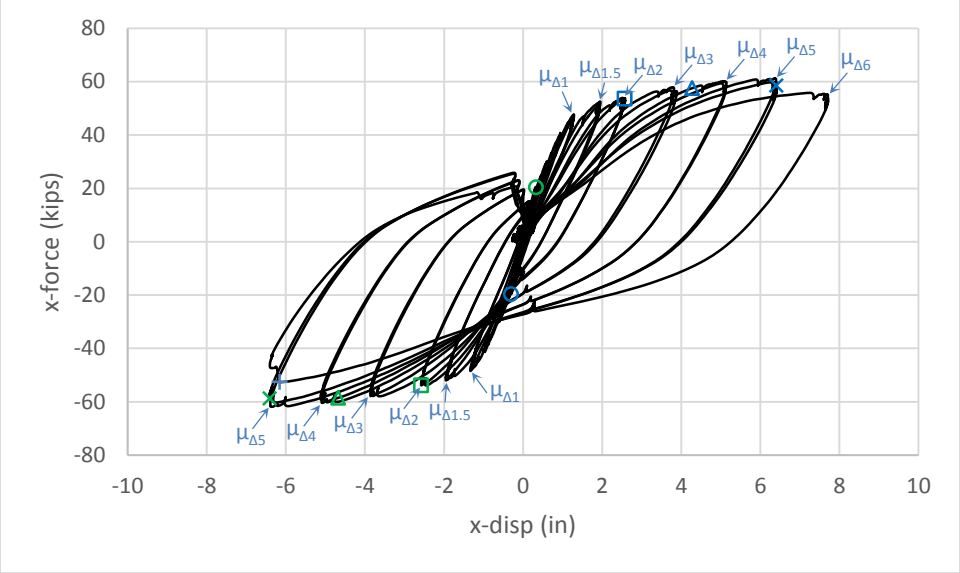

Figure 12-10. Test 9: X-Direction Hysteretic Response

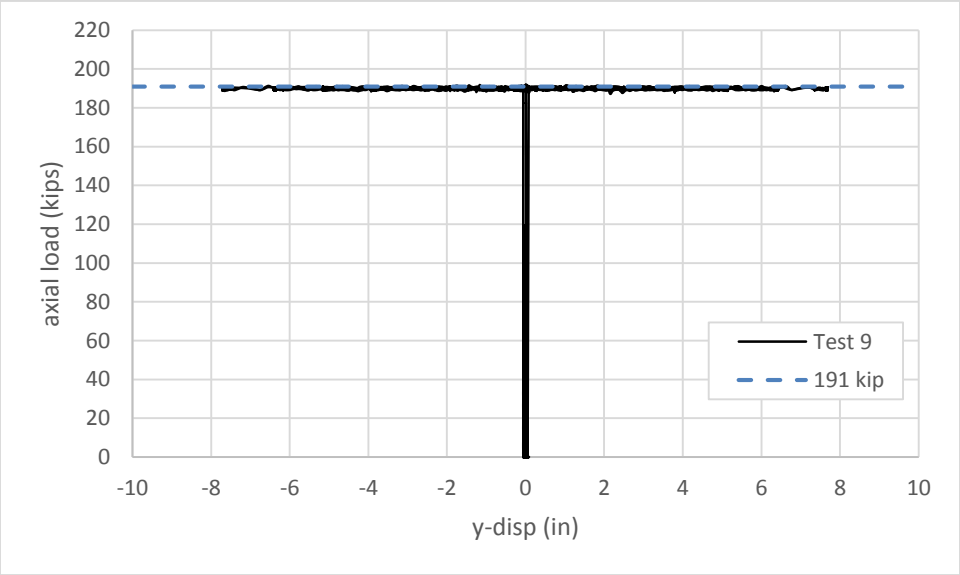

Figure 12-11. Test 9: Y-Direction Axial Force History

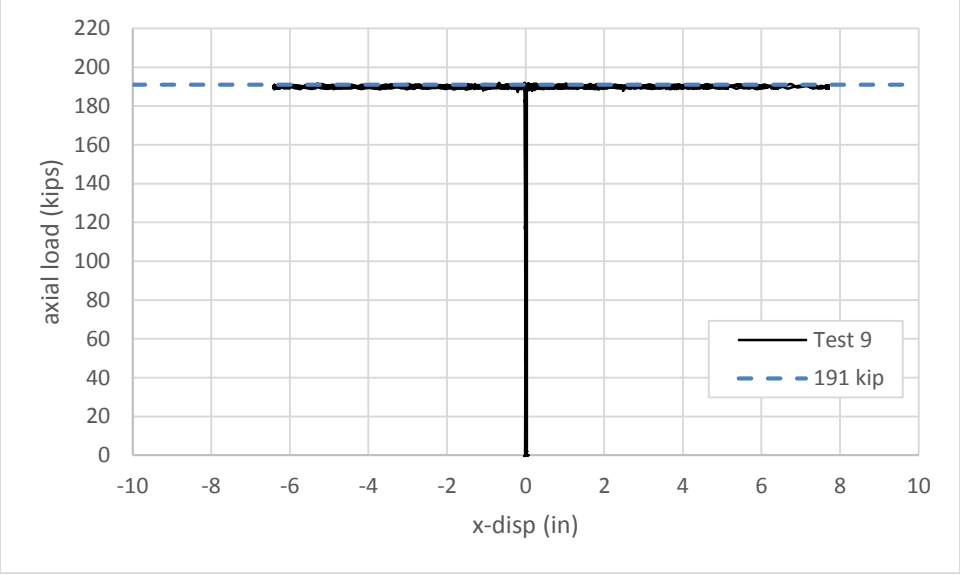

Figure 12-12. Test 9: X-Direction Axial Force History

Test 9 - Experimental Observations

Values of interests and damage observations for Load Path Test 9 are presented in Table 12-1 and Table 12-2. Test 9 evaluated a 24" diameter column $(L/D = 4.56)$ with $\rho_l = A_{st}/A_g = 1.6\%$ longitudinal steel and a transverse volumetric ratio of $\rho_s = 4A_{sp}/D's = 0.7\%$. The test began with the application of a constant axial load of $191\ kips\ \left(P/f_c'\ A_g = 7.3\%\right)$. The imposed displacement histories in the Y and X-directions for the Symmetric Two-Cycle-Set Biaxial Load History shown in Figure 12-3 and Figure 12-4. The resulting column shear force histories in the Y and X-directions appear in Figure 12-5 and Figure 12-6. The full displacement history and resulting load path for Test 9 appear in Figure 12-7 and Figure 12-8. The Y and X-direction column hysteretic response appears Figure 12-9 and Figure 12-10. Spiral strains on respective sides of the specimen during compressions cycles are depicted in Figure 12-11 through Figure 12-12.

The load history began with elastic ¼ F_y' cycle increments until the analytically predicted first yield force $(F_y' = 41.34\ kips)$ was reached in each direction of loading. Cracks were first observed on all sides of the specimen during the ½ F_y' cycle. At the analytically predicted first yield force, an average experimental first yield displacement of $\Delta_y' = 0.95$" was measured in the four primary directions. The equivalent yield displacement for the column was then computed as $\Delta_y = \Delta_y'\left(M_n/M_y'\right) = 1.28\ in$, where $M_n = 508.07\ kip \cdot ft$ represents the analytical nominal moment capacity corresponding to an extreme fiber compression strain of $\varepsilon_c = 0.004$ or a steel tensile strain of $\varepsilon_s = 0.015$, whichever occurs first. The remainder of the Symmetric Two-Cycle-Set Load History consists of two cycles for each displacement ductility level $\mu_{\Delta n} = n \cdot \Delta_y$, where $n = 1, 1.5, 2, 3, 4, 5, 6\ etc$. Cracks observed on each side of the specimen at equivalent yield are shown in Figure 12-13 and Figure 12-14.

Concrete crushing was observed on the South side of the specimen during $\mu_{\Delta 1.5}^{-1y} = -1.90$", followed by the North side during $\mu_{\Delta 2}^{+1y} = 2.57$" as shown in Figure 12-15. Cover concrete crushing was observed on the East side during$\mu_{\Delta 2}^{+1x} = 2.57$", and then on the West side during $\mu_{\Delta 2}^{-1x} = -2.58$", see Figure 12-16. Compressive demand on the North side of the specimen led to spiral yielding during $\mu_{\Delta 4}^{+1y} = 5.10$", followed by South spiral yielding during $\mu_{\Delta 4}^{-1y} = -5.14$", refer to Figure 12-17. Spiral yielding was measured on the East side during $\mu_{\Delta 4}^{+1x} = 5.10$", and then on the West side during $\mu_{\Delta 4}^{-2x} = -5.11$", see Figure 12-18.

The adjacent North Bar NNE visibly buckled during $\mu_{\Delta 5}^{+2y} = 6.41$", followed by buckling of South Bars S and SSW during $\mu_{\Delta 5}^{-2y} = -6.40$", as shown in Figure 12-19. The North extreme fiber bar remained visibly straight at $\mu_{\Delta 5}^{+2y} = 6.41$". The East extreme fiber bar visibly buckled during $\mu_{\Delta 5}^{+2x} = 6.41$", followed by buckling of the West Bar during $\mu_{\Delta 5}^{-2x} = -6.40$", see Figure 12-20. The North extreme fiber bar then buckled during $\mu_{\Delta 6}^{+1y} = 7.66$", as depicted in Figure 12-21. The adjacent South bar SSE buckled during $\mu_{\Delta 6}^{-1y} = 7.66$". Adjacent East Bars ENE and ESE buckled during $\mu_{\Delta 6}^{+1x} = 7.68$", as shown in Figure 12-21. The previously buckled East extreme fiber bar fractured -6.16" during the subsequent reversal to $\mu_{\Delta 6}^{-1X}$, see Figure 12-22. At this displacement, it was clear that Bars WNW, WSW, and SW had also buckled. Photos of the specimen after the test appear in Figure 12-23 and Figure 12-24.

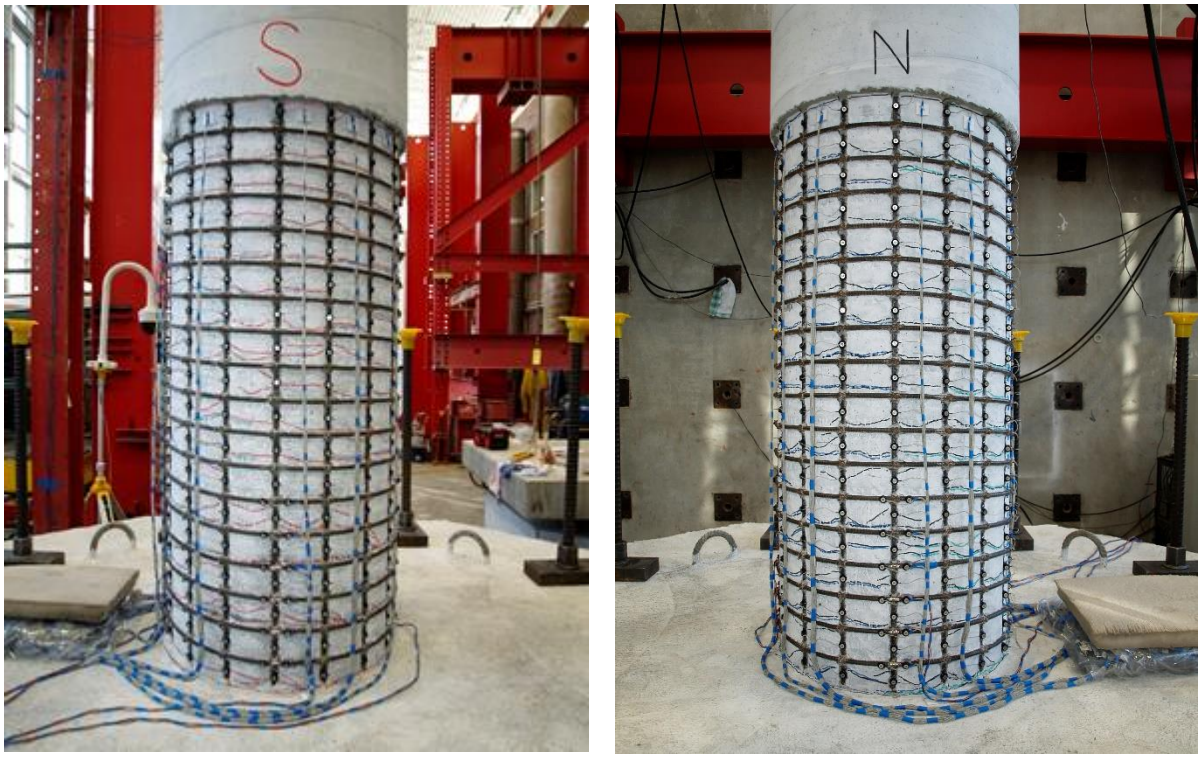

Figure 12-13. Test 9: Cracking on the (Left) South Side at $\mu_{\Delta 1}^{+2y} = 1.28$" and (Right) North Side at $\mu_{\Delta 1}^{-2y} = -1.28$"

Figure 12-14. Test 9: Cracking on the (Left) West Side at $\mu_{\Delta 1}^{+2x} = 1.27$" and (Right) East Side at $\mu_{\Delta 1}^{-2x} = -1.28$"

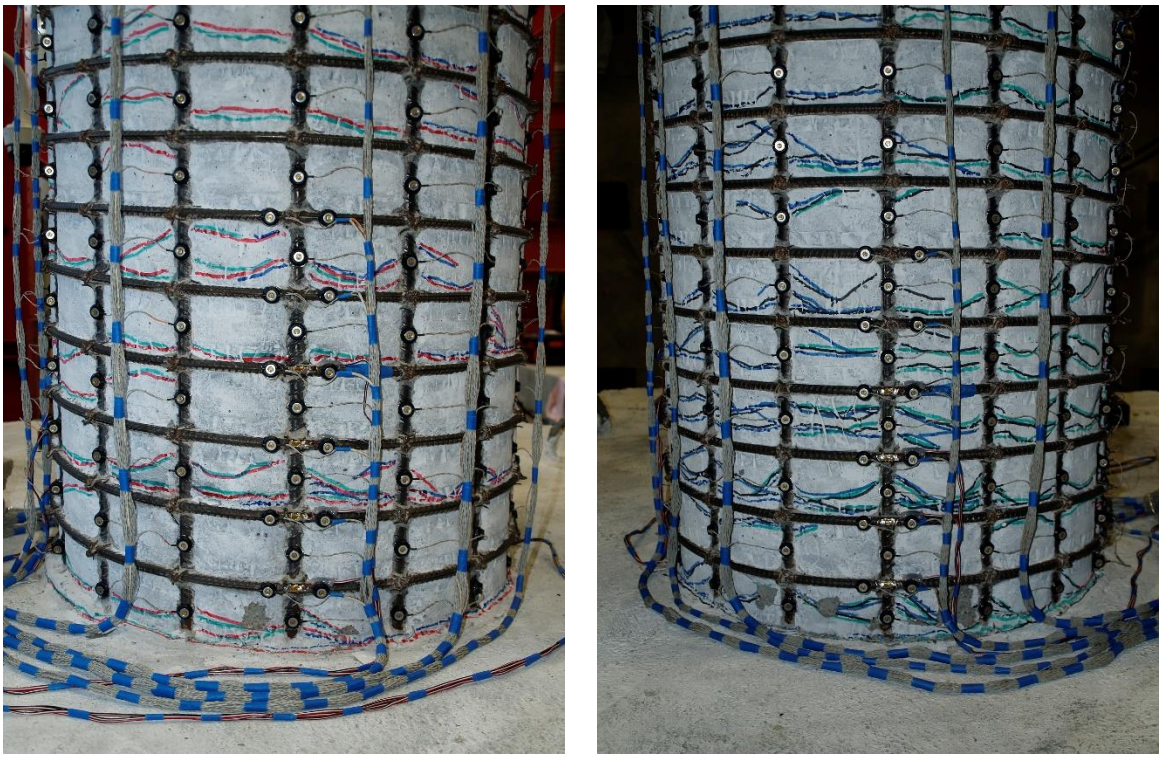

Figure 12-15. Test 9: Concrete Crushing on the (Left) South Side at $\mu_{\Delta 1.5}^{-1y} = -1.90"$ and (Right) North Side at $\mu_{\Delta 2}^{+1y} = 2.57"$

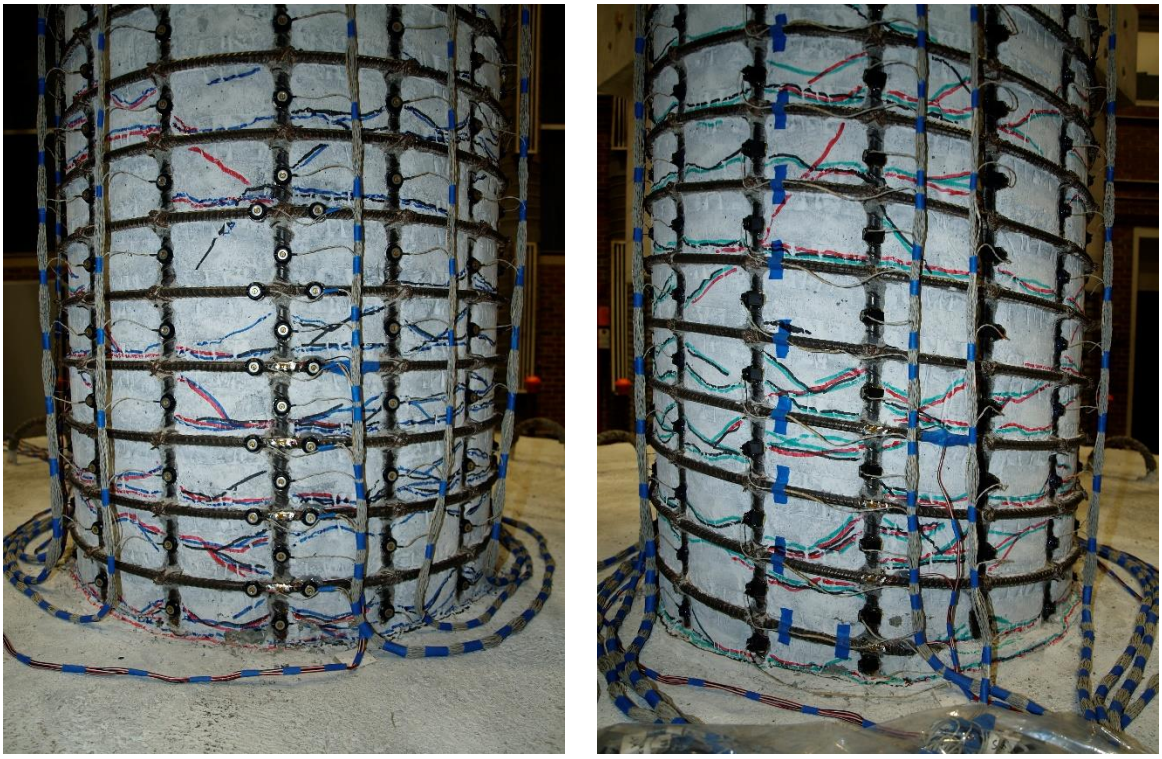

Figure 12-16. Test 9: Concrete Crushing on the (Left) East Side at $\mu_{\Delta 2}^{+1x} = 2.57"$ and (Right) West Side at $\mu_{\Delta 2}^{-1x} = -2.58"$

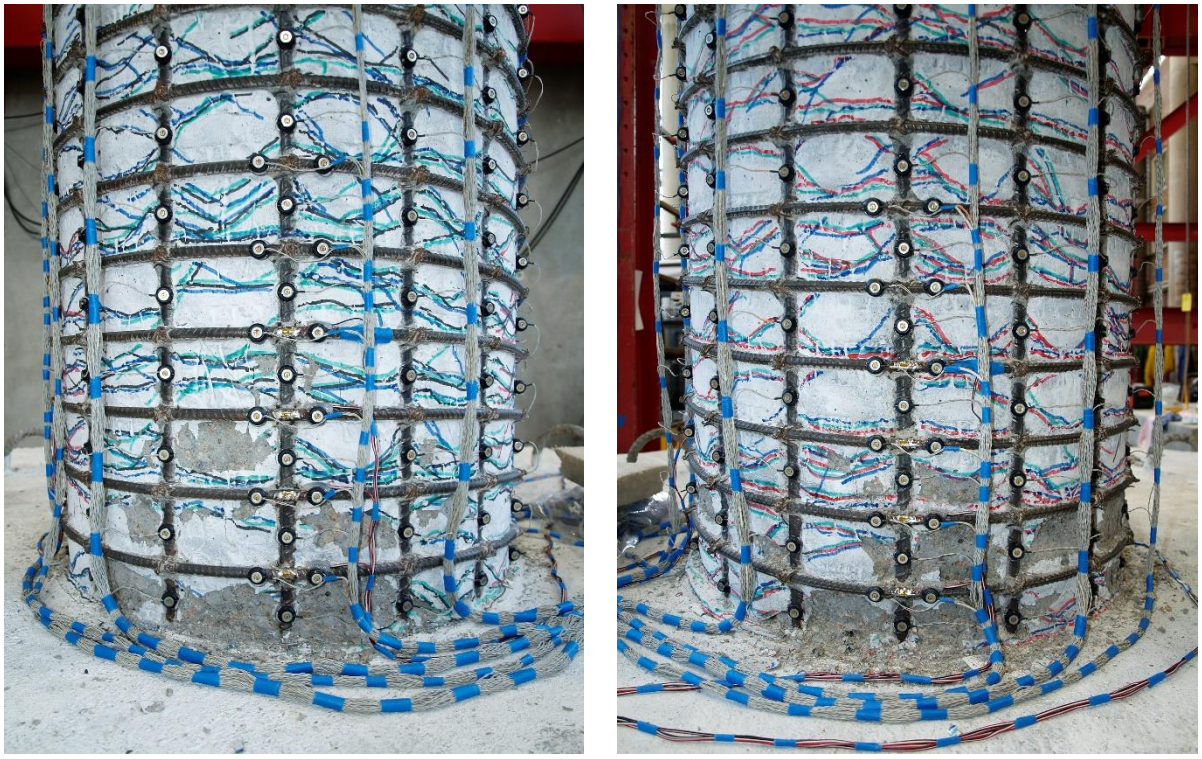

Figure 12-17. Test 9: Spiral Yielding on the (Left) North Side at $\mu_{\Delta 4}^{+1y} = 5.10"$ and (Right) South Side at $\mu_{\Delta 4}^{-1y} = -5.14"$

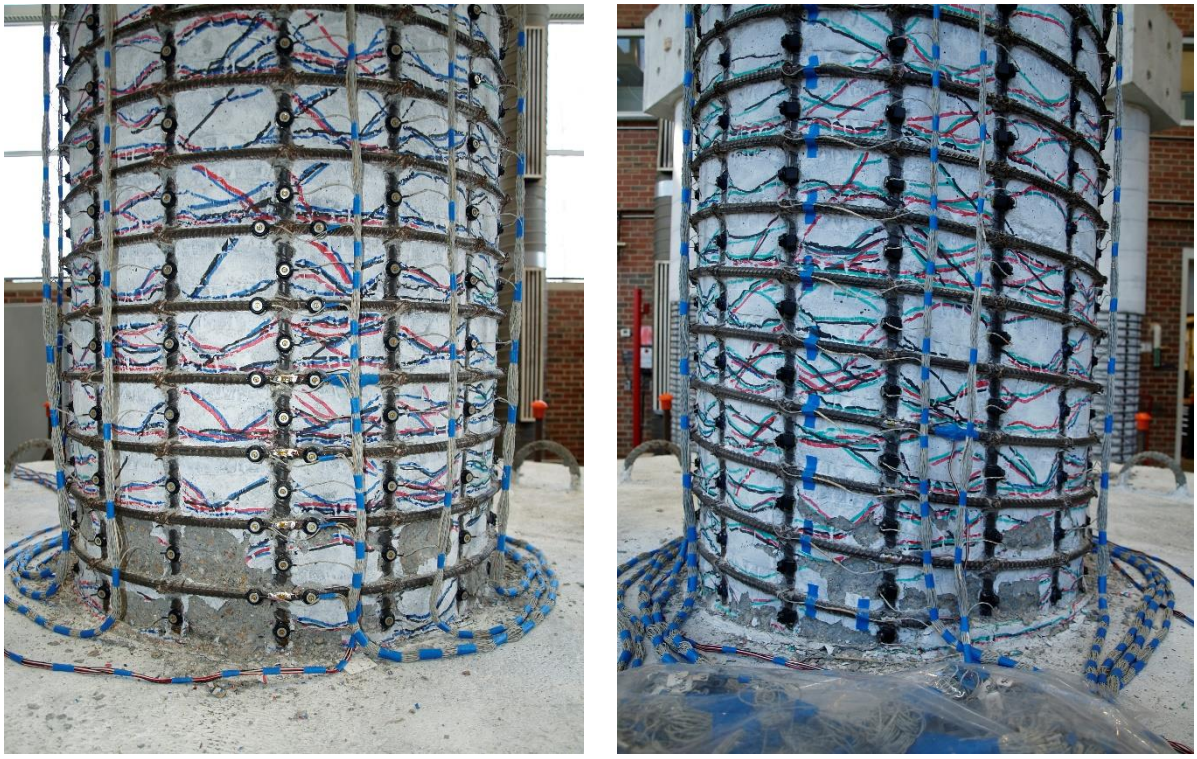

Figure 12-18. Test 9: Spiral Yielding on the (Left) East Side at $\mu_{\Delta 4}^{+1x} = 5.10"$ and (Right) West Side at $\mu_{\Delta 4}^{-2x} = -5.11"$

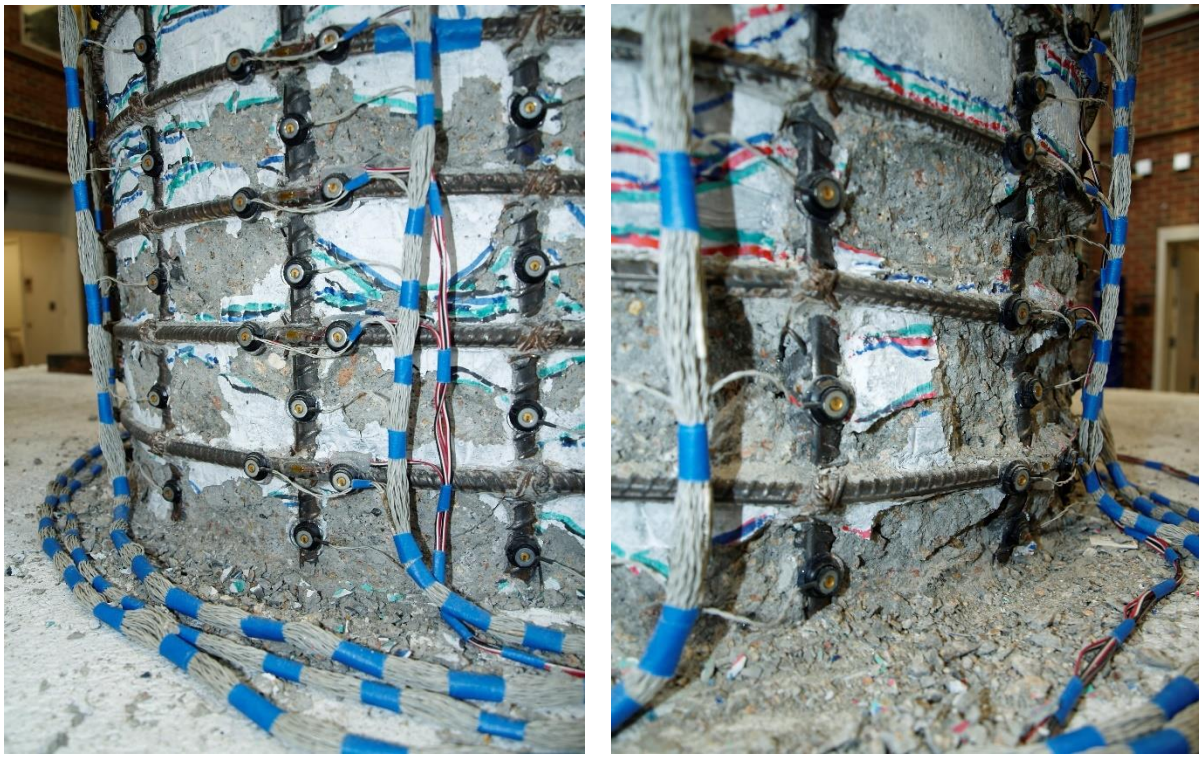

Figure 12-19. Test 9: Buckling of (Left) Adjacent Bar NNE at $\mu_{\Delta 5}^{+2y} = 6.41"$ and (Right) Bars S and SSW at $\mu_{\Delta 5}^{-2y} = -6.40"$

Figure 12-20. Test 9: (Left) Buckling of the East Bar at $\mu_{\Delta 5}^{+2x} = 6.41"$ and (Right) Buckling of the West Bar at $\mu_{\Delta 5}^{-2x} = -6.40"$

Figure 12-21. Test 9: Buckling of (Left) North Bar at $\mu_{\Delta 6}^{+1y} = 7.66"$ and (Right) Adjacent Bars ENE and ESE at $\mu_{\Delta 6}^{+1x} = 7.68"$

Figure 12-22. Test 9: (Left) Specimen at $\mu_{\Delta 6}^{+1x} = 7.68"$ and (Right) East Bar Fracture at $-6.16"$ during $\mu_{\Delta 6}^{-1X}$

Figure 12-23. Test 9: (Left) North and (Right) West Sides of the Specimen after the Test

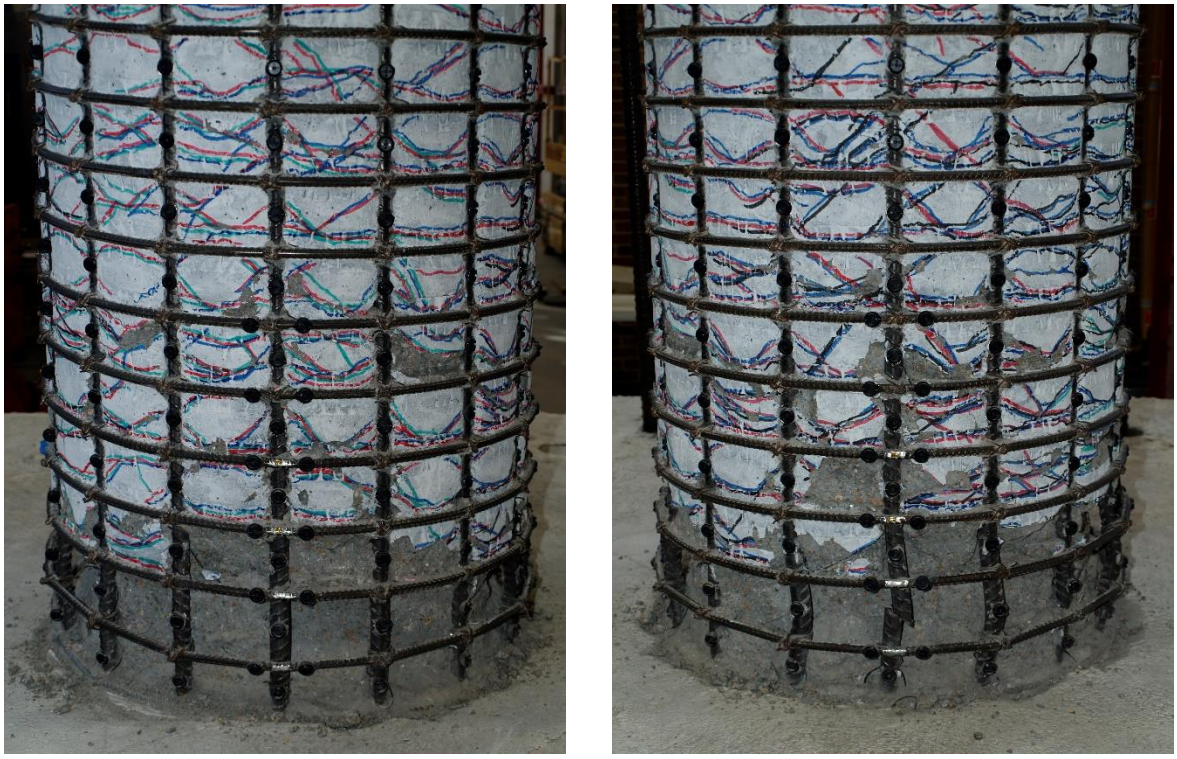

Figure 12-24. Test 9: (Left) South and (Right) East Sides of the Specimen after the Test

Test 9 - Strain Data Analysis

North and South Bar Strains

Vertical strain profiles for North and South reinforcement during y-direction cycles are shown in Figure 12-25 and Figure 12-26. Strains in the lowest four spiral layers during compressive y-direction cycles on the North and South sides of the specimen appear in Figure 12-27 and Figure 12-28. The relationship between strain and displacement for either peak tensile or peak compressive gauge lengths appear in Figure 12-29 through Figure 12-34. These figures contain monotonic moment curvature predictions for respective plastic hinge methods. PCK (2007) Lp refers to the (Priestley, Calvi and Kowalsky 2007) plastic hinge method, GN15 Tension/Compression Lpr refers to the (Goodnight, Kowalsky and Nau 2015a) unidirectional modified plastic hinge method, TX Measured refer to using the measured extent of plasticity and average equivalent strain penetration length from this specific test, and New Equations refers to a new bidirectional plastic hinge method which was created based on this study. Details of the new plastic hinge method appear in a later chapter of this report.

The spiral strain gauge hysteresis for the first and second layers above the footing on the North side of the specimen are shown in Figure 12-36 and Figure 12-37. The second North spiral layer went off scale during $\mu_{\Delta 5}^{+2y} = 6.41$" as the adjacent North bar NNE visibly buckled, see Figure 12-19. Measured strains in the first North spiral layer spiked during $\mu_{\Delta 6}^{+1y} = 7.66$" as the North extreme fiber bar visibly buckled, see Figure 12-21. The visual observation of extreme fiber bar buckling was confirmed upon inspection of the North longitudinal bar strain hysteresis in Figure 12-35; however, there was slight measurable outward deformation in the previous compressive cycle when the adjacent Bar NNE buckled. The first occurrence of North bar buckling during $\mu_{\Delta 5}^{+2y} = 6.41$" is the important observation which is compared to the strain limit recommendations in this study.

The spiral strain gauge hysteresis for the first and second layers above the footing on the South side of the specimen appear in Figure 12-39 and Figure 12-40. The first South spiral layer went off scale during $\mu_{\Delta 5}^{-1y} = -6.40$" even though the South reinforcement remained visibly straight. Measured strains in the second spiral layer increased during $\mu_{\Delta 5}^{-2y} = -6.40$", when the South bars S and SSW visibly buckled as shown in Figure 12-19. The visual observation of bar buckling was confirmed upon inspection of the South longitudinal bar strain hysteresis in Figure 12-38; however, there was slight measurable outward deformation in the previous compressive cycle.

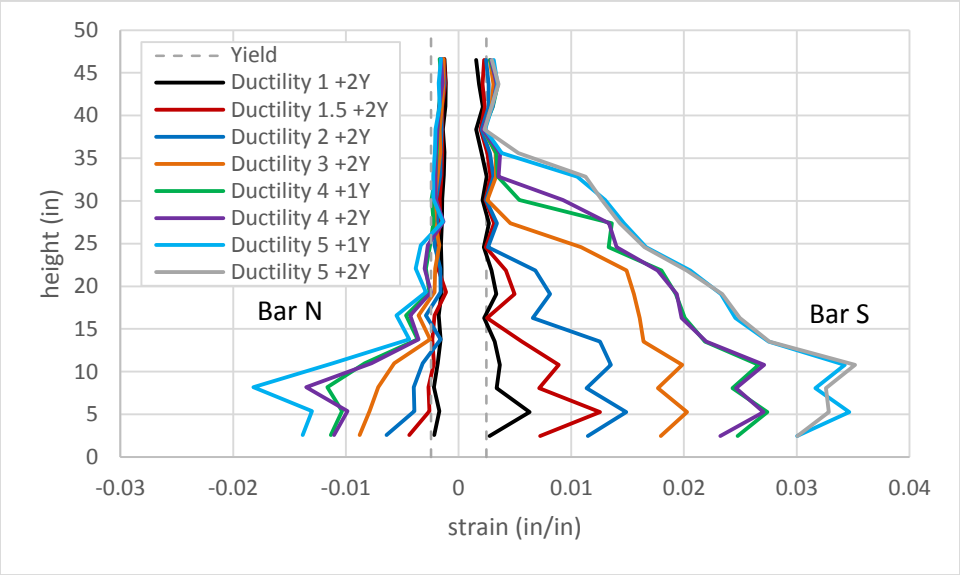

Figure 12-25. Test 9: Vertical Strain Profiles for Loading in the +Y-direction

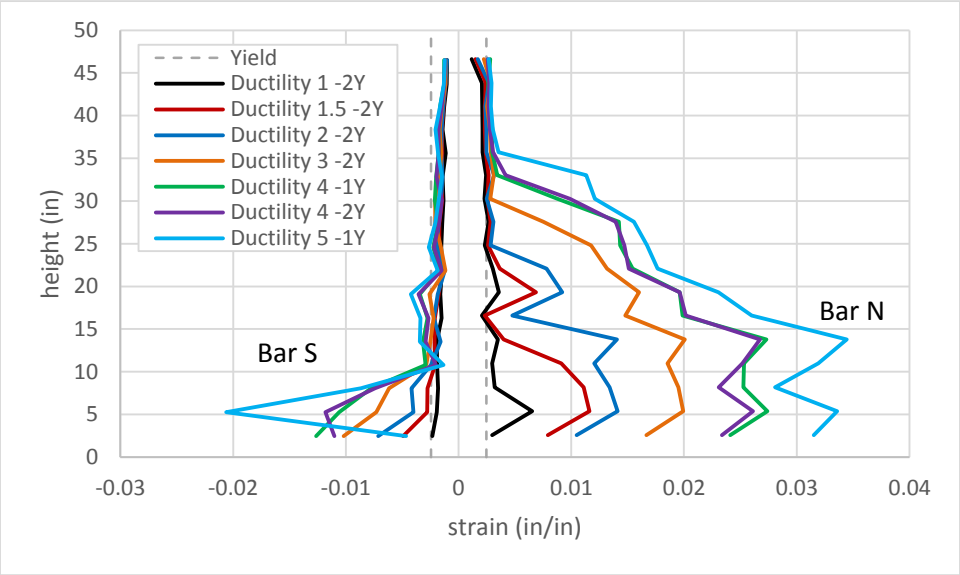

Figure 12-26. Test 9: Vertical Strain Profiles for Loading in the -Y-direction

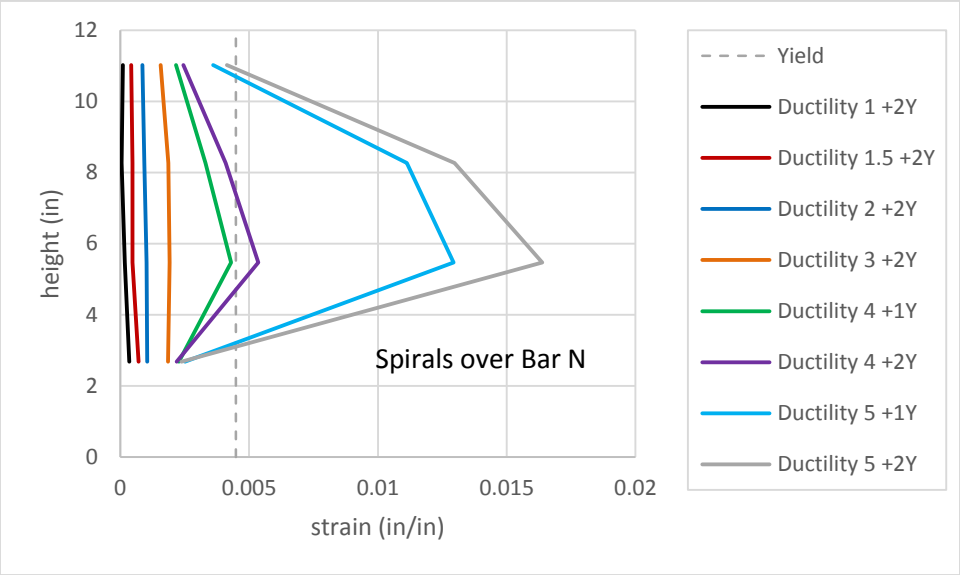

Figure 12-27. Test 9: Spiral Strains Measured Over the North Extreme Fiber Bar during +Y Cycles

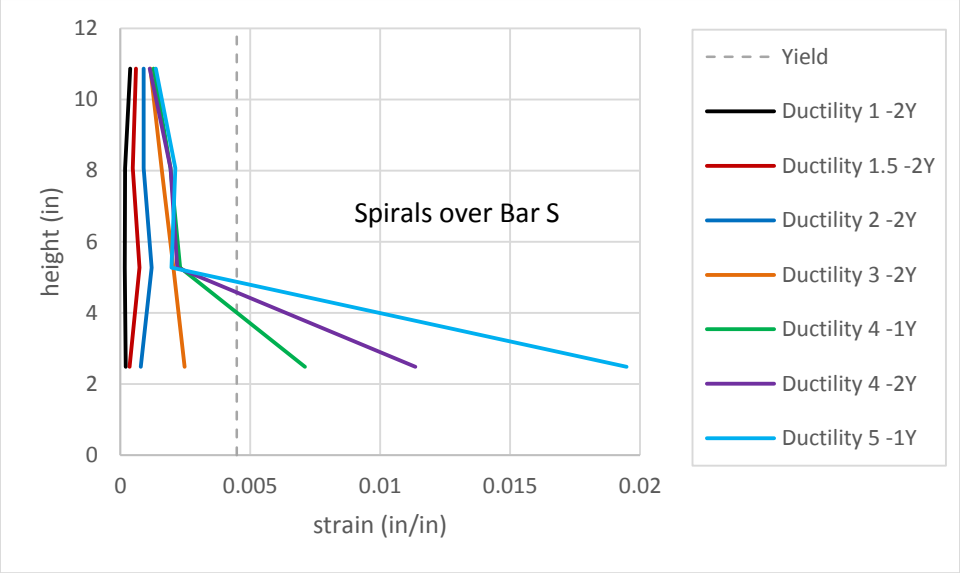

Figure 12-28. Test 9: Spiral Strains Measured Over the North Extreme Fiber Bar during -Y Cycles

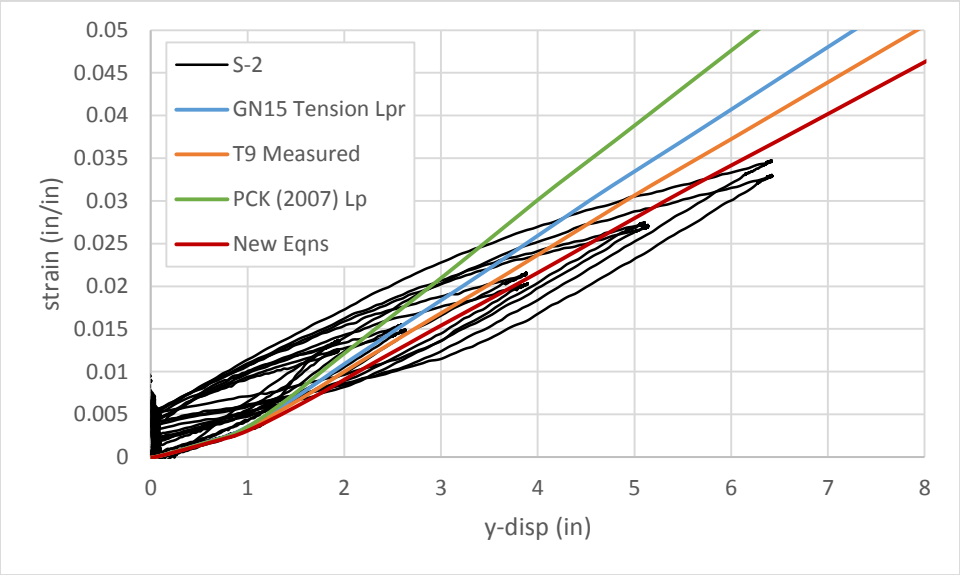

Figure 12-29. Test 9: Tension Strain-Disp. for Bar S (Gauge Length 2 Centered 5.26" above the Footing)

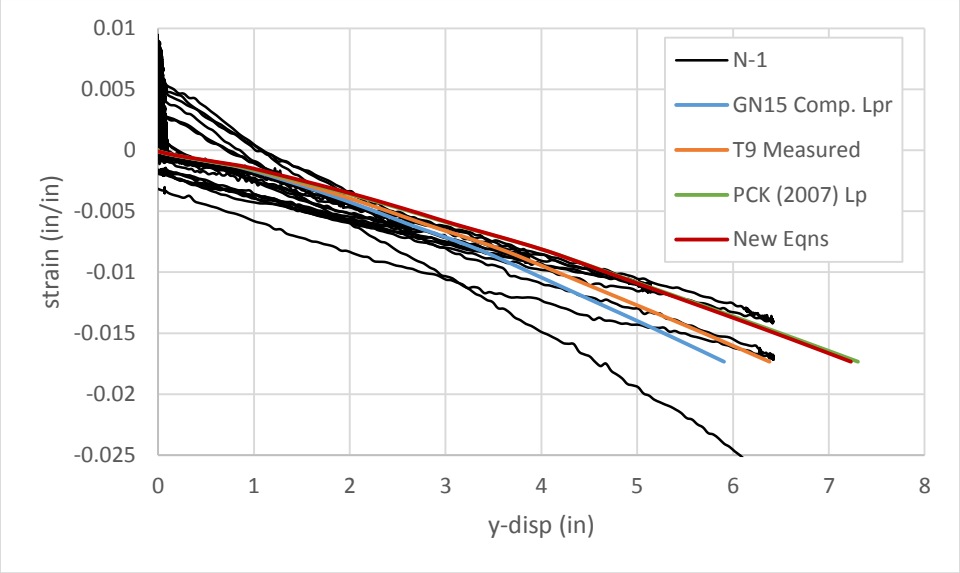

Figure 12-30. Test 9: Compression Strain-Disp. for Bar N (Gauge Length 1 Centered 2.57" above the Footing)

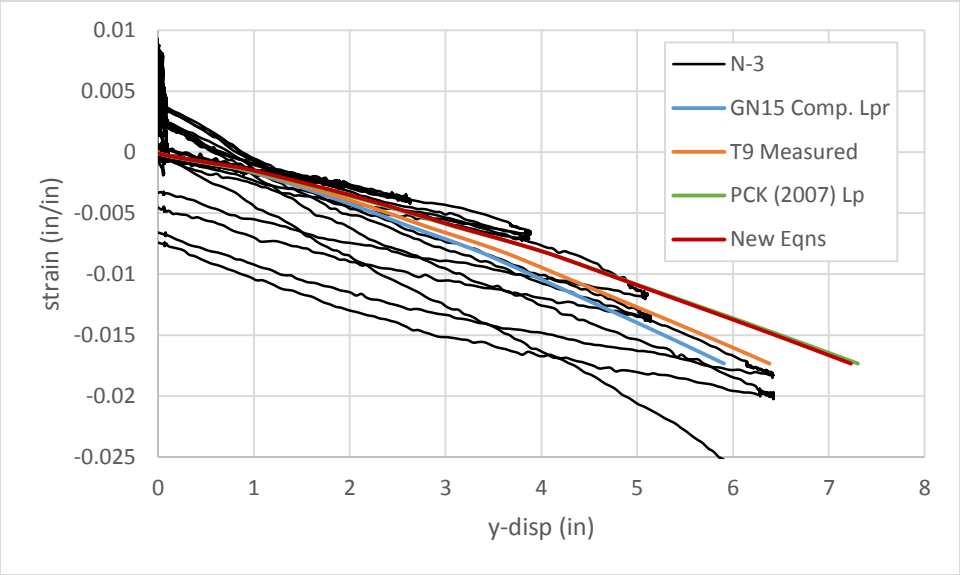

Figure 12-31. Test 9: Compression Strain-Disp. for Bar N (Gauge Length 3 Centered 8.17" above the Footing)

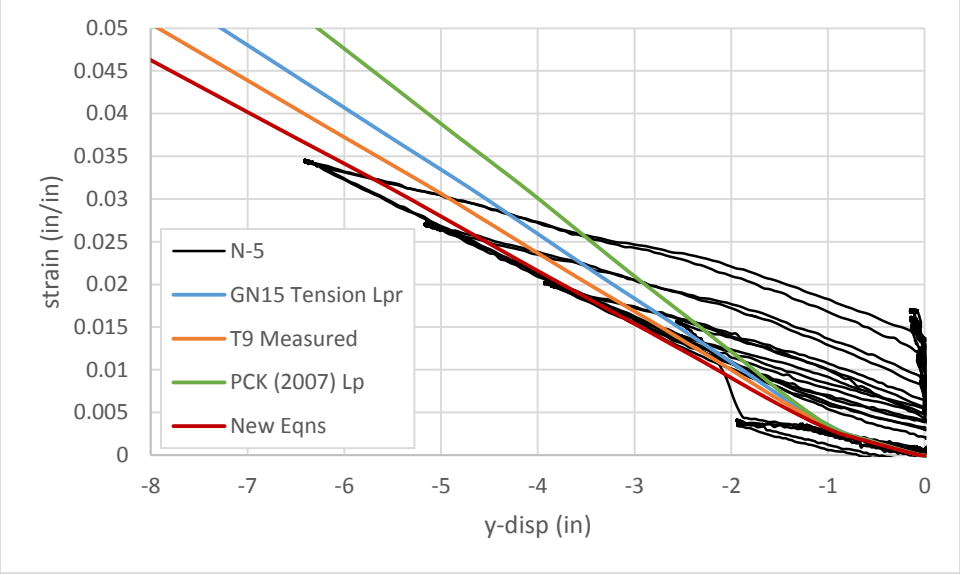

Figure 12-32. Test 9: Tension Strain-Disp. for Bar N (Gauge Length 5 Centered 13.78" above the Footing)

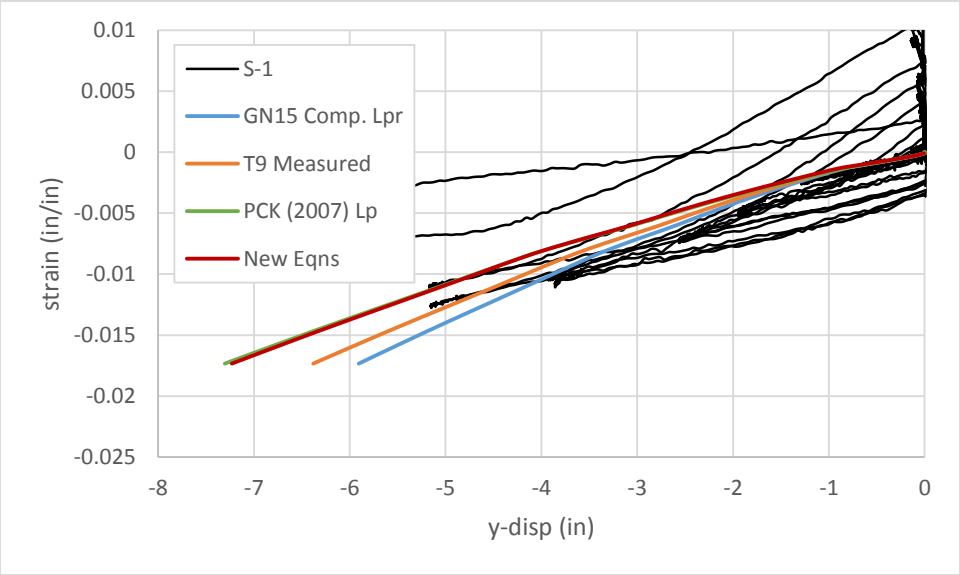

Figure 12-33. Test 9: Compression Strain-Disp. for Bar S (Gauge Length 1 Centered 2.47" above the Footing)

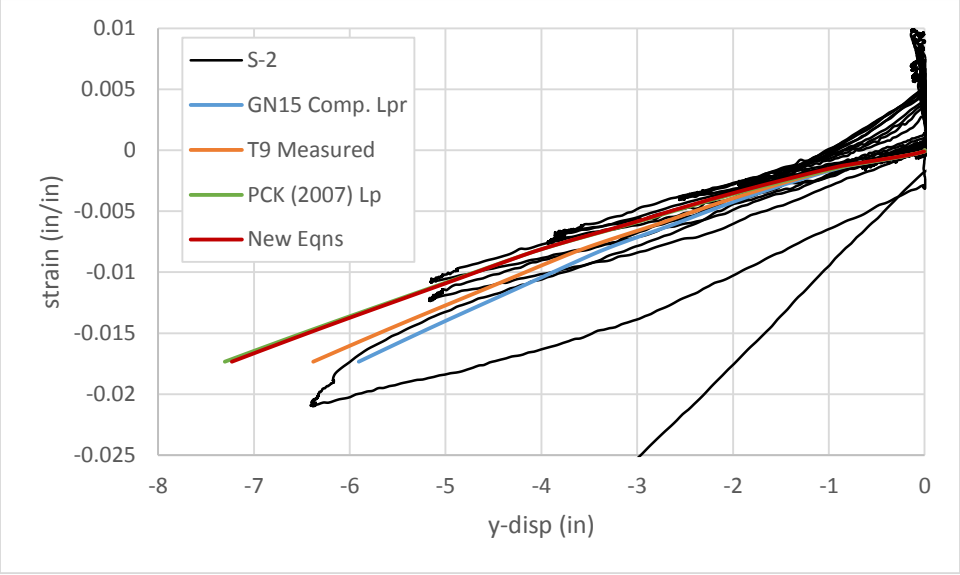

Figure 12-34. Test 9: Compression Strain-Disp. for Bar S (Gauge Length 2 Centered 5.26" above the Footing)

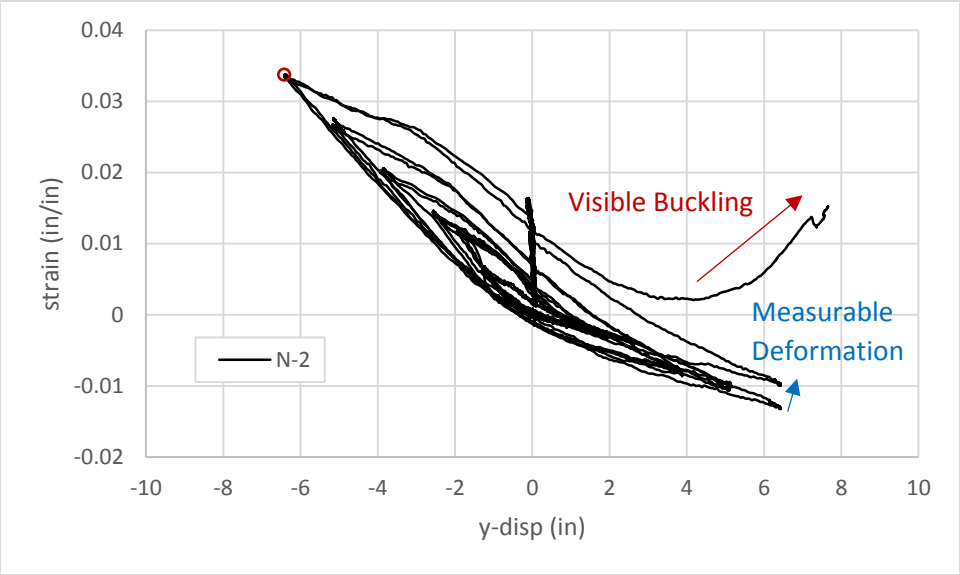

Figure 12-35. Test 9: Strain Hysteresis over the North Buckled Bar (Gauge Length 2 Centered 5.38" above the Footing)

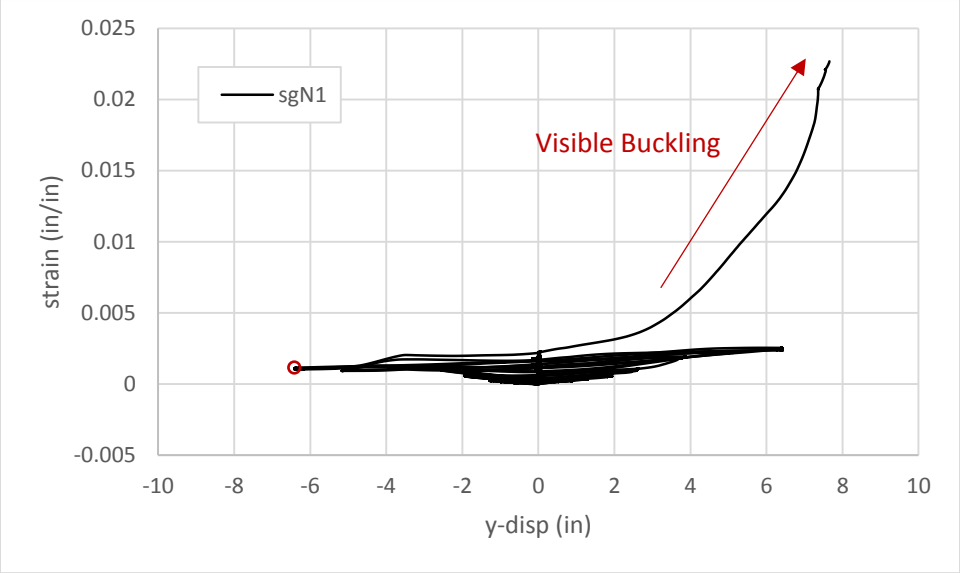

Figure 12-36. Test 9: Spiral Strain Hysteresis for the 1st North Layer above the Footing

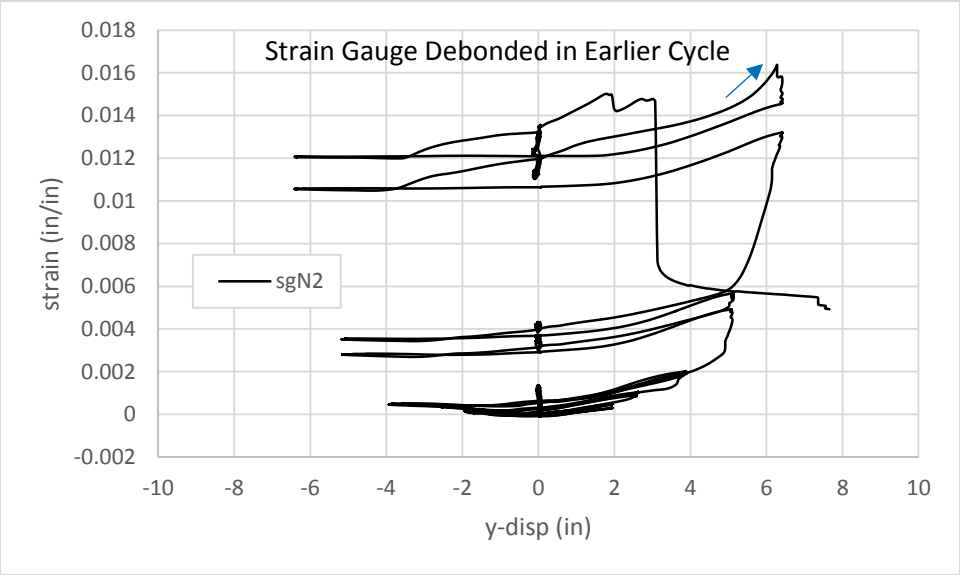

Figure 12-37. Test 9: Spiral Strain Hysteresis for the 2nd North Layer above the Footing

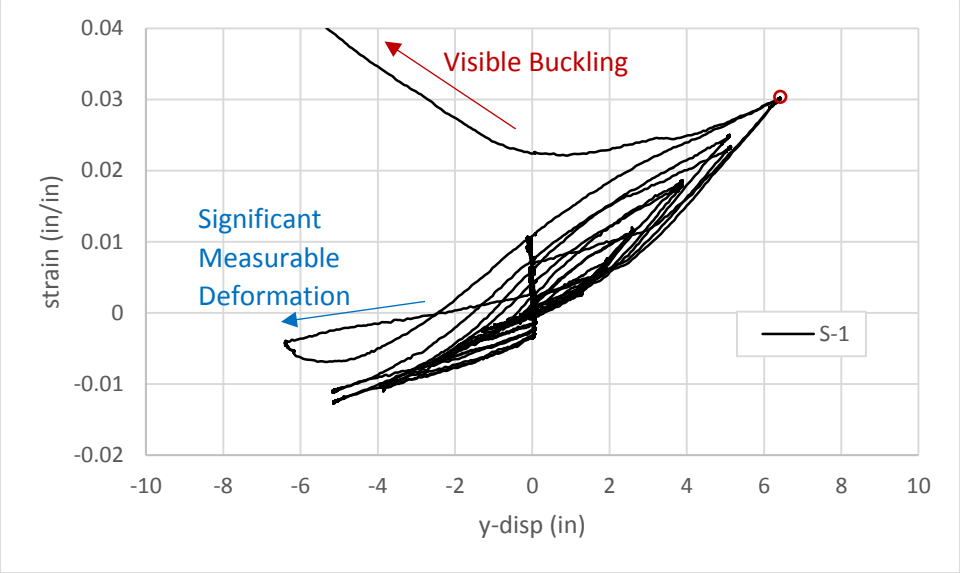

Figure 12-38. Test 9: Strain Hysteresis over the South Buckled Bar (Gauge Length 1 Centered 2.47" above the Footing)

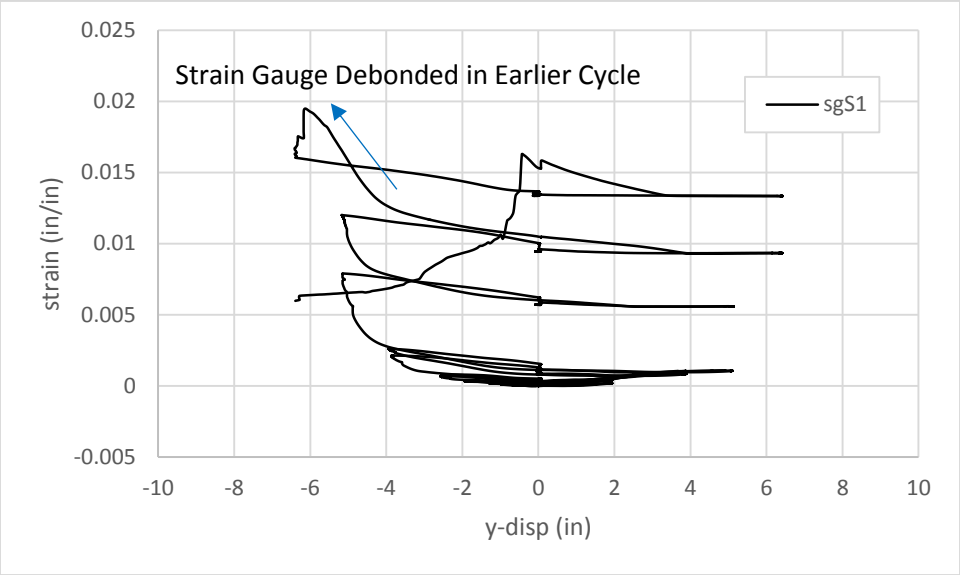

Figure 12-39. Test 9: Spiral Strain Hysteresis for the 1st South Layer above the Footing

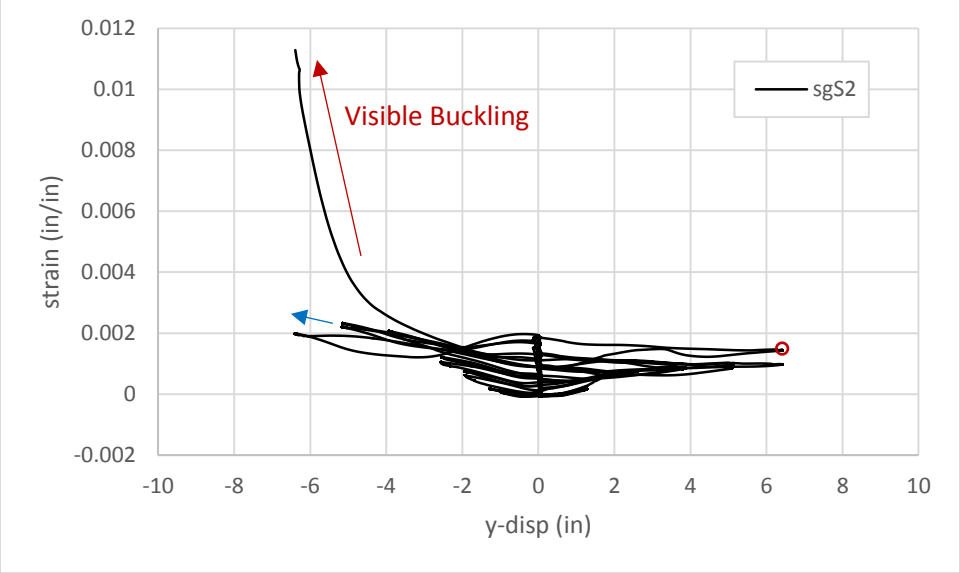

Figure 12-40. Test 9: Spiral Strain Hysteresis for the 2nd South Layer above the Footing

East and West Bar Strains

Vertical strain profiles for East and West reinforcement during x-direction cycles are shown in Figure 12-41 and Figure 12-42. Strains in the lowest four spiral layers during compressive x-direction cycles on the East and West sides of the specimen appear in Figure 12-43 and Figure 12-44. The relationship between strain and displacement for either peak tensile or peak compressive gauge lengths appear in Figure 12-45 through Figure 12-50. These figures contain monotonic moment curvature predictions for respective plastic hinge methods. PCK (2007) Lp refers to the (Priestley, Calvi and Kowalsky 2007) plastic hinge method, GN15 Tension/Compression Lpr refers to the (Goodnight, Kowalsky and Nau 2015a) unidirectional modified plastic hinge method, TX Measured refer to using the measured extent of plasticity and average equivalent strain penetration length from this specific test, and New Equations refers to a new bidirectional plastic hinge method which was created based on this study. Details of the new plastic hinge method appear in a later chapter of this report.

Spiral strain gauge hystereses for the first and second East layers above the footing appear in Figure 12-52 and Figure 12-53. Strain gauges over both layers went off scale during $\mu_{\Delta 5}^{+1x} = 6.38"$, even though the East reinforcement remained visibly straight. The East extreme fiber bar visibly buckled during $\mu_{\Delta 5}^{+2x} = 6.41"$ as shown in Figure 12-20. The visual observation of bar buckling was confirmed upon inspection of the East longitudinal bar strain hysteresis in Figure 12-51.

A spiral strain gauge hysteresis for the second West layer above the footing appears in Figure 12-55. The second spiral layer goes off scale during $\mu_{\Delta 5}^{-2x} = -6.40"$ as the West extreme fiber bar buckled, see Figure 12-20. The visual observation of bar buckling was confirmed upon inspection of the West longitudinal bar strain hysteresis in Figure 12-54; however, there was slight measurable outward deformation in the previous compressive cycle.

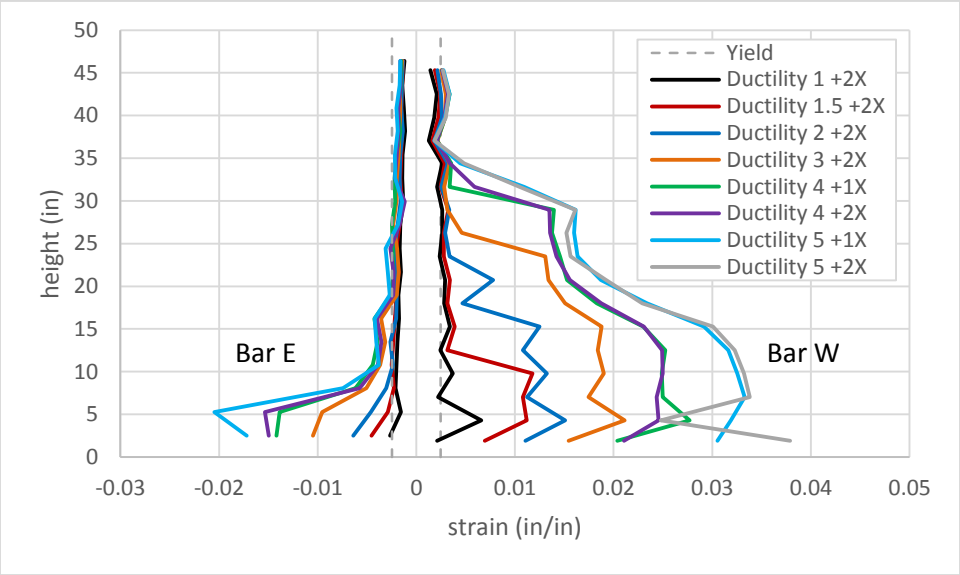

Figure 12-41. Test 9: Vertical Strain Profiles for Loading in the +X-direction

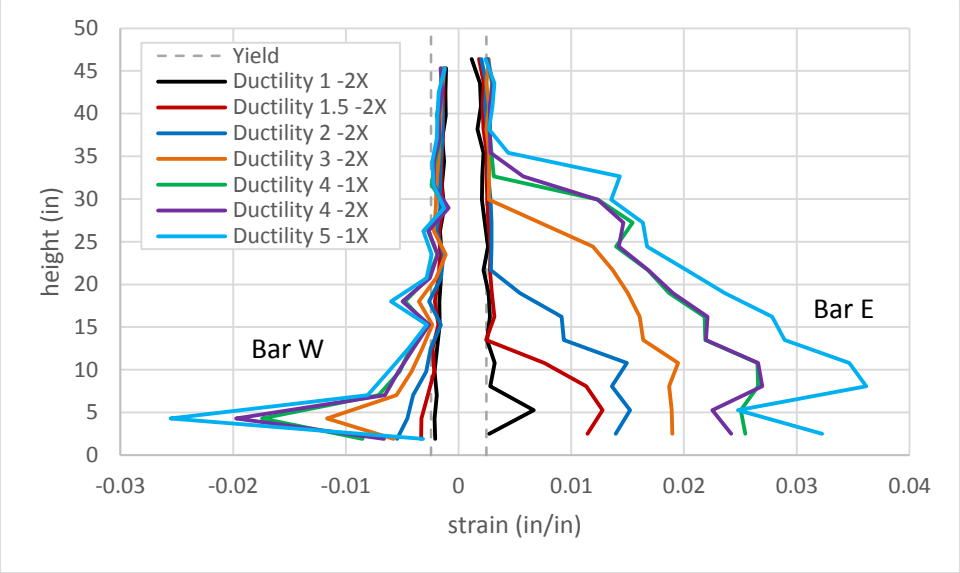

Figure 12-42. Test 9: Vertical Strain Profiles for Loading in the -X-direction

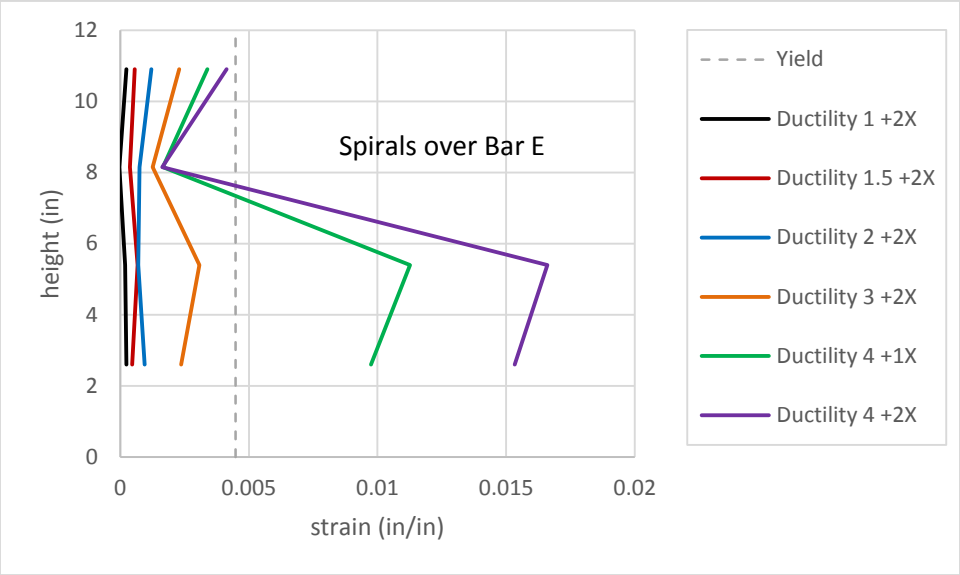

Figure 12-43. Test 9: Spiral Strains Measured Over the East Extreme Fiber Bar during +X Cycles

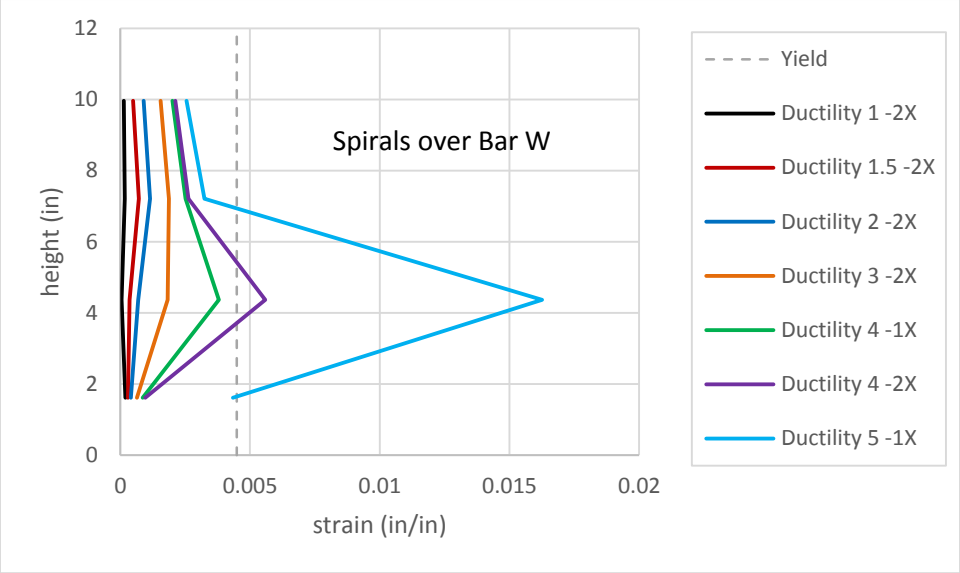

Figure 12-44. Test 9: Spiral Strains Measured Over the East Extreme Fiber Bar during -X Cycles

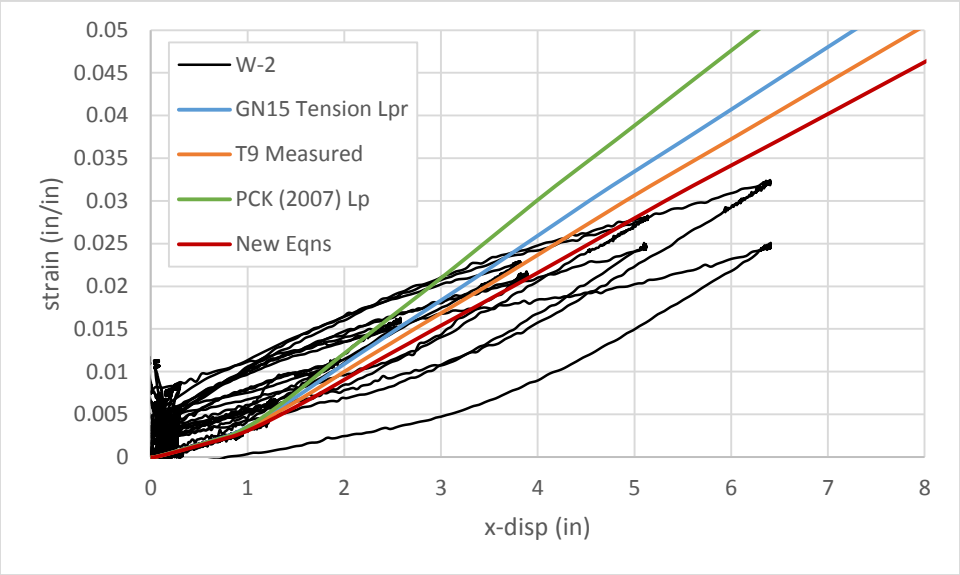

Figure 12-45. Test 9: Tension Strain-Disp. for Bar W (Gauge Length 2 Centered 4.30" above the Footing)

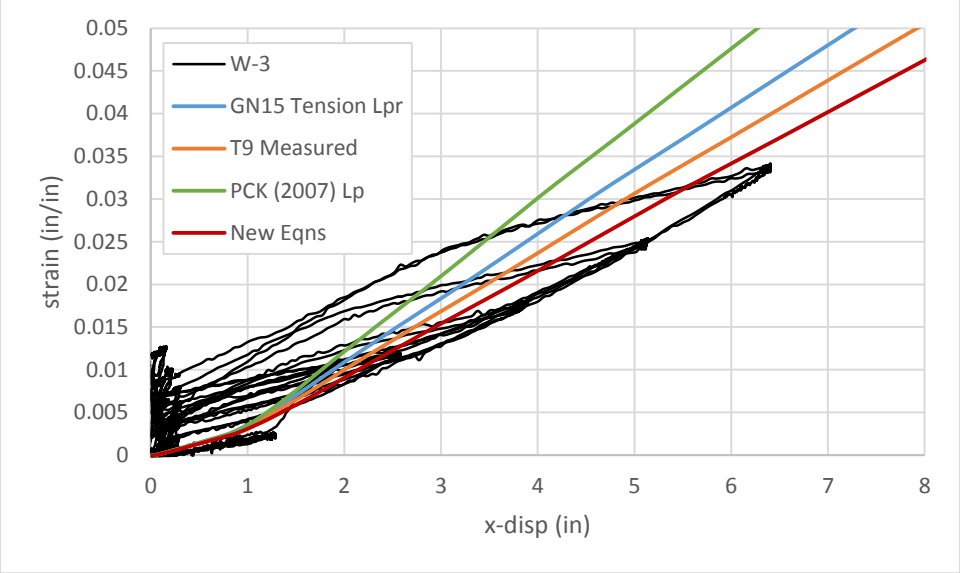

Figure 12-46. Test 9: Tension Strain-Disp. for Bar W (Gauge Length 3 Centered 7.02" above the Footing)

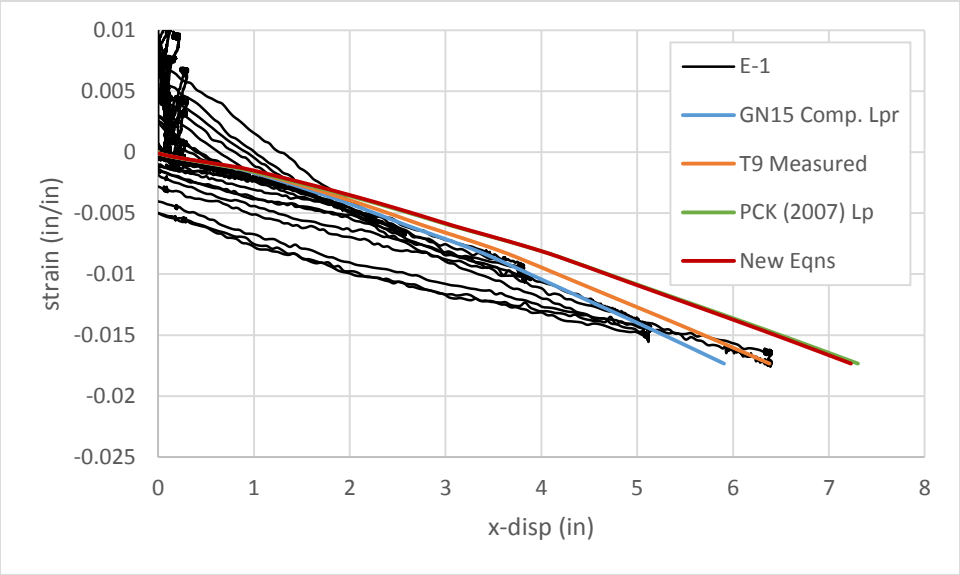

Figure 12-47. Test 9: Compression Strain-Disp. for Bar E (Gauge Length 1 Centered 2.50" above the Footing)

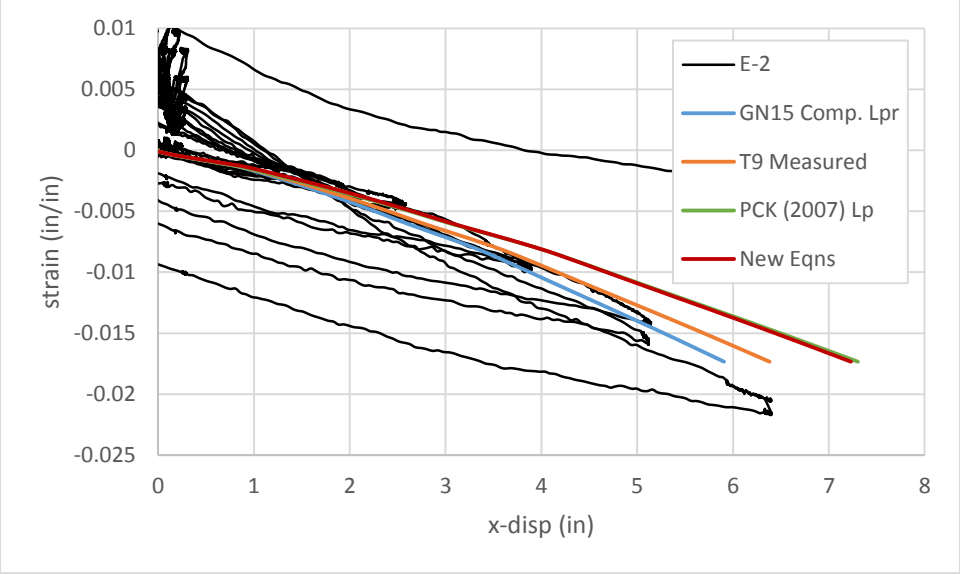

Figure 12-48. Test 9: Compression Strain-Disp. for Bar E (Gauge Length 2 Centered 5.28" above the Footing)

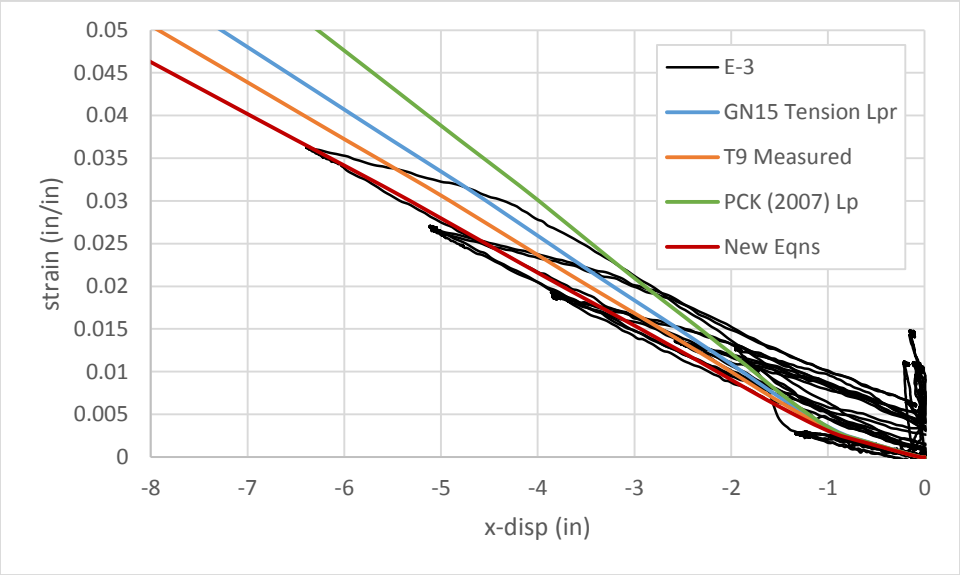

Figure 12-49. Test 9: Tension Strain-Disp. for Bar E (Gauge Length 3 Centered 8.07" above the Footing)

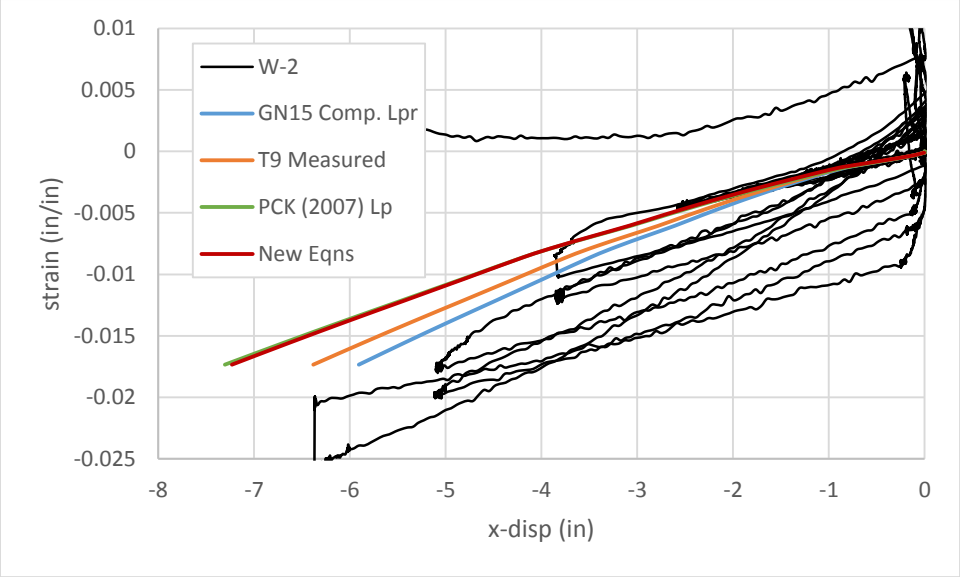

Figure 12-50. Test 9: Compression Strain-Disp. for Bar W (Gauge Length 2 Centered 4.30" above the Footing)

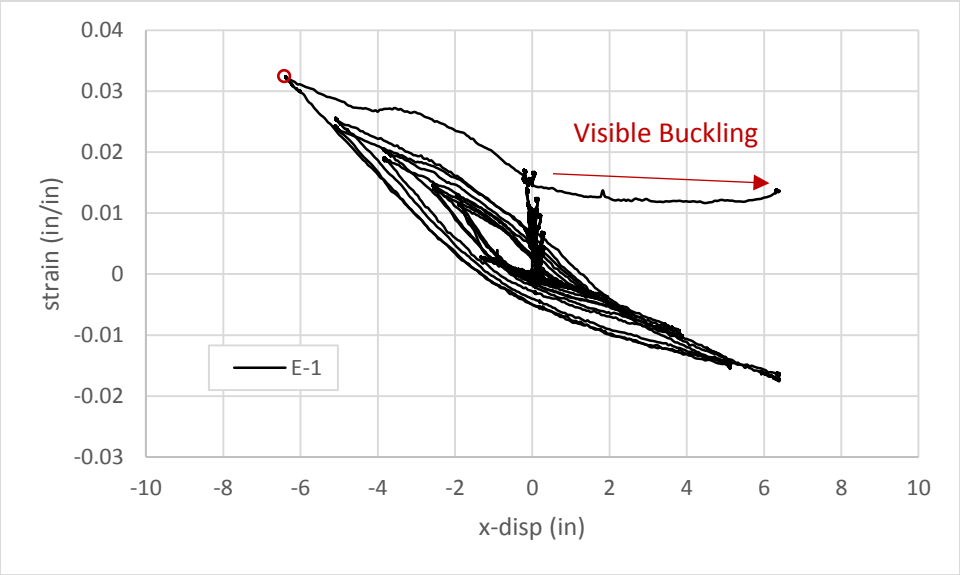

Figure 12-51. Test 9: Strain Hysteresis over the East Buckled Bar (Gauge Length 1 Centered 2.50" above the Footing)

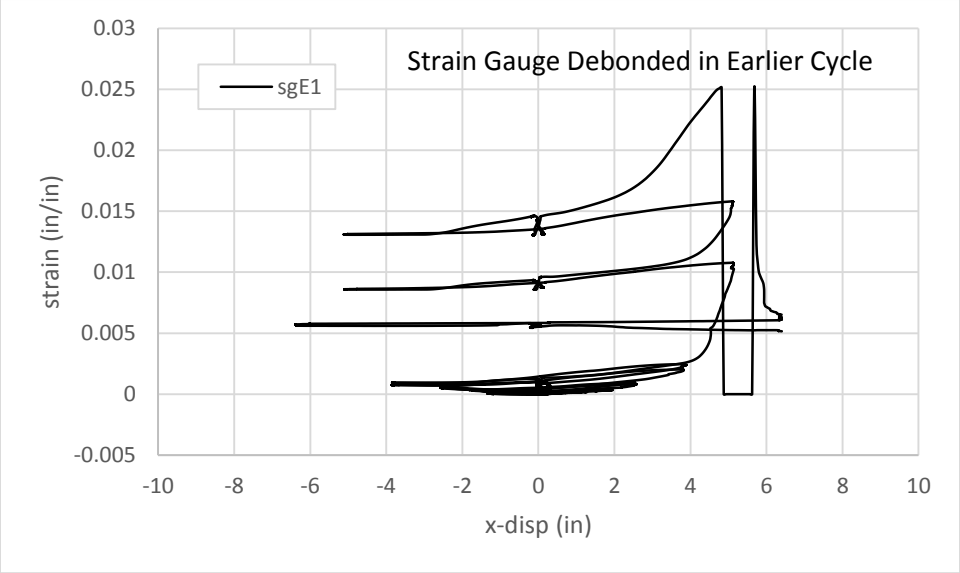

Figure 12-52. Test 9: Spiral Strain Hysteresis for the 1st East Layer above the Footing

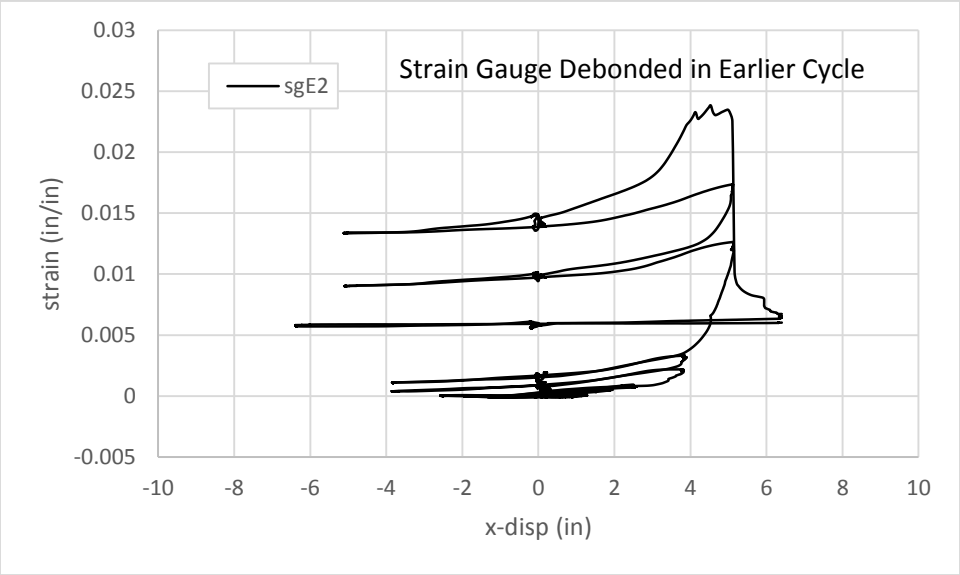

Figure 12-53. Test 9: Spiral Strain Hysteresis for the 2nd East Layer above the Footing

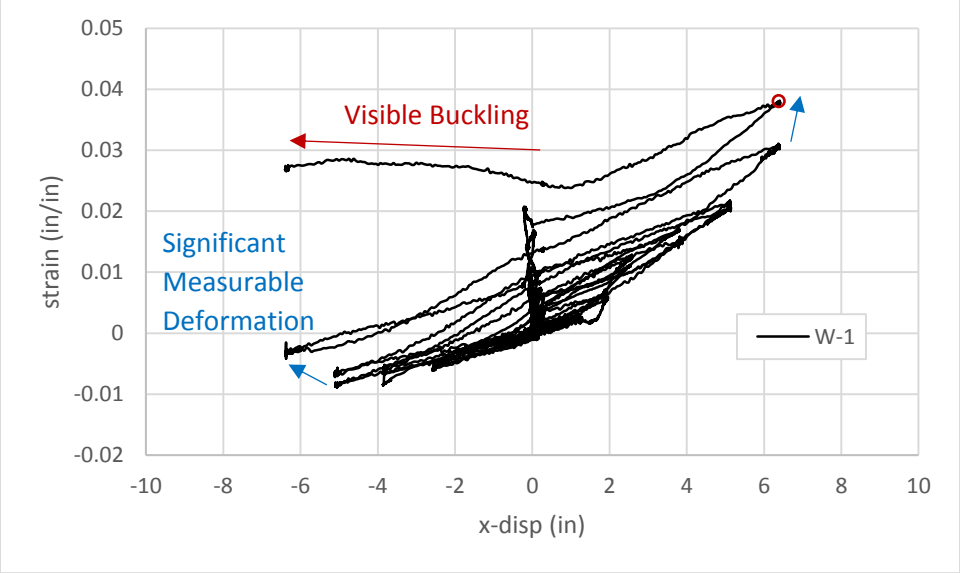

Figure 12-54. Test 9: Strain Hysteresis over the West Buckled Bar (Gauge Length 1 Centered 1.92" above the Footing)

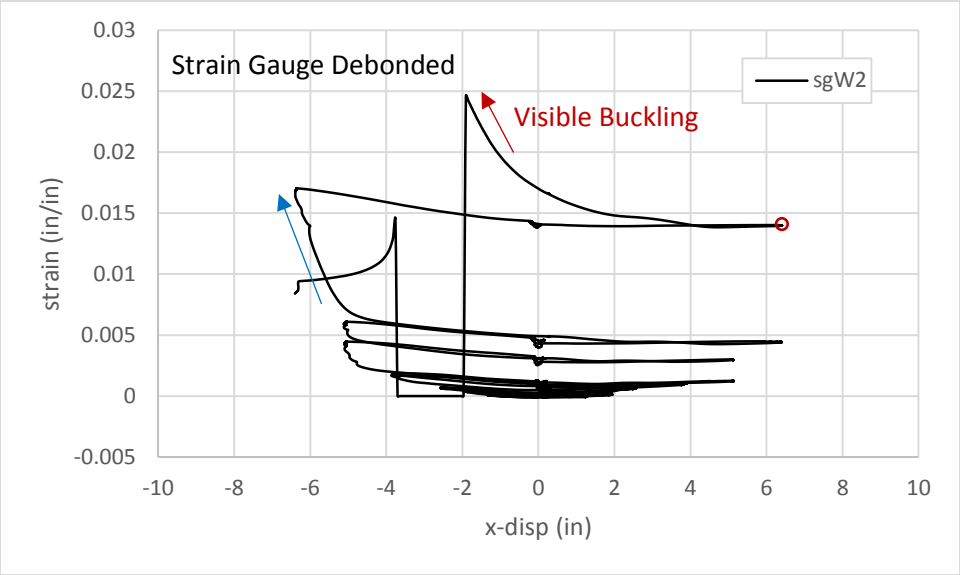

Figure 12-55. Test 9: Spiral Strain Hysteresis for the 2nd West Layer above the Footing

Test 9 - Curvature and Strain Penetration Data

Curvature and stain penetration data for Test 9 is presented in the following section. The methods in which this data was generated are outlined in the summary for Test 1. Sample cross section curvature profiles are shown in Figure 12-56 and Figure 12-57. Vertical curvature profiles for respective loading directions appear in Figure 12-58 through Figure 12-62. Fixed-end rotations attributable to strain penetration of longitudinal reinforcement into the footing are shown in Figure 12-63 through Figure 12-65. Comparison of the measured displacements to those obtained via integration of the measured curvature profiles and extrapolation of the fixed-end rotation to the center of the applied lateral load are shown in Figure 12-66 and Figure 12-67.

The measured extent of plasticity is compared to design recommendations for the tensile triangular plastic hinge length in Figure 12-68. GN15 refers to the (Goodnight, Kowalsky and Nau 2015a) unidirectional tensile hinge length while New Equations refers to a new bidirectional plastic hinge method which was created based on this study. Details of the new plastic hinge method appear in a later chapter of this report. The measured equivalent strain penetration lengths are compared to design recommendations in Figure 12-69. GN15 refers to the (Goodnight, Kowalsky and Nau 2015a) unidirectional Lsp while PCK (2007) refers to the (Priestley, Calvi and Kowalsky 2007) definition of Lsp. Finally, the measured hysteretic response is compared to monotonic predictions in Figure 12-70 and Figure 12-71.

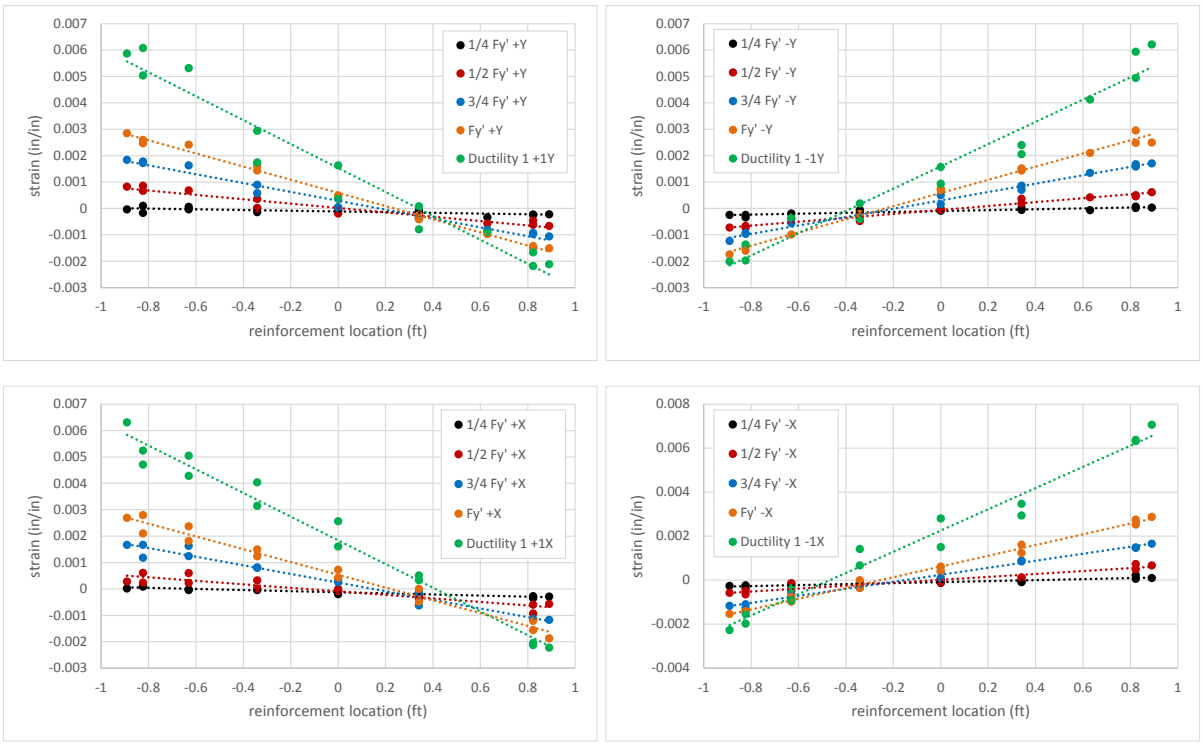

Figure 12-56. Test 9: Elastic Curvature Profiles for the Second Instrumented Section above the Footing

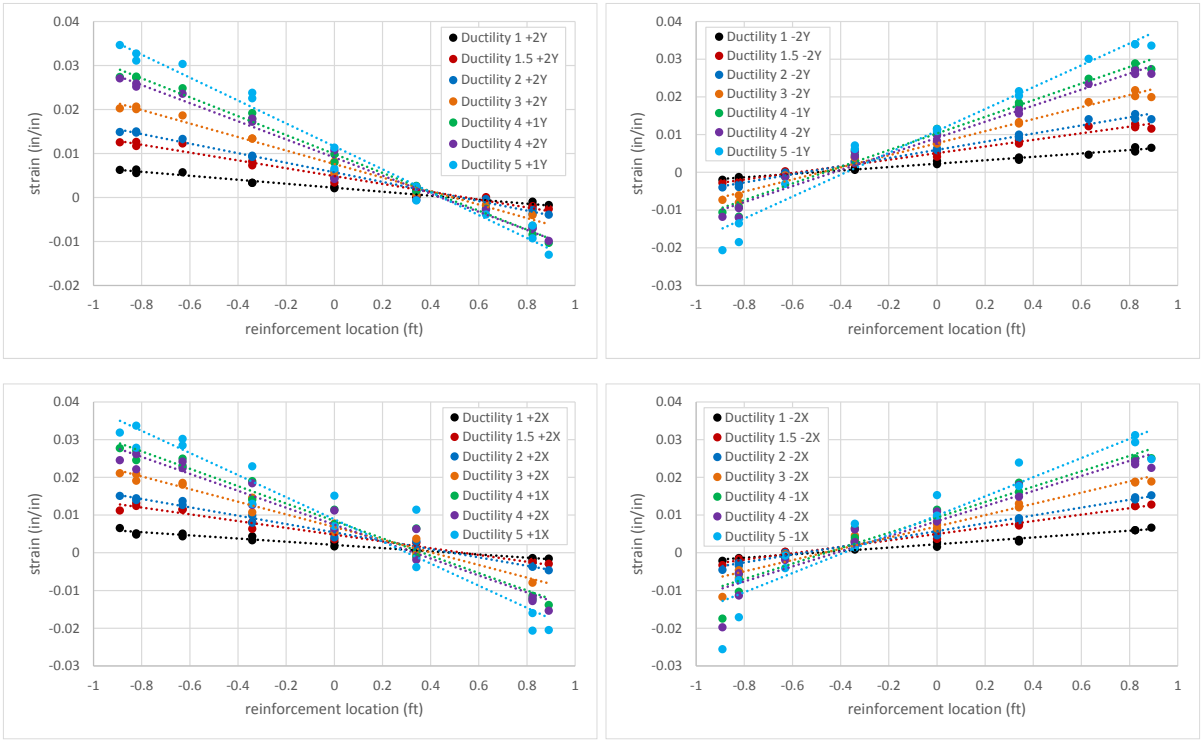

Figure 12-57. Test 9: Curvature Profiles for the Second Instrumented Section above the Footing

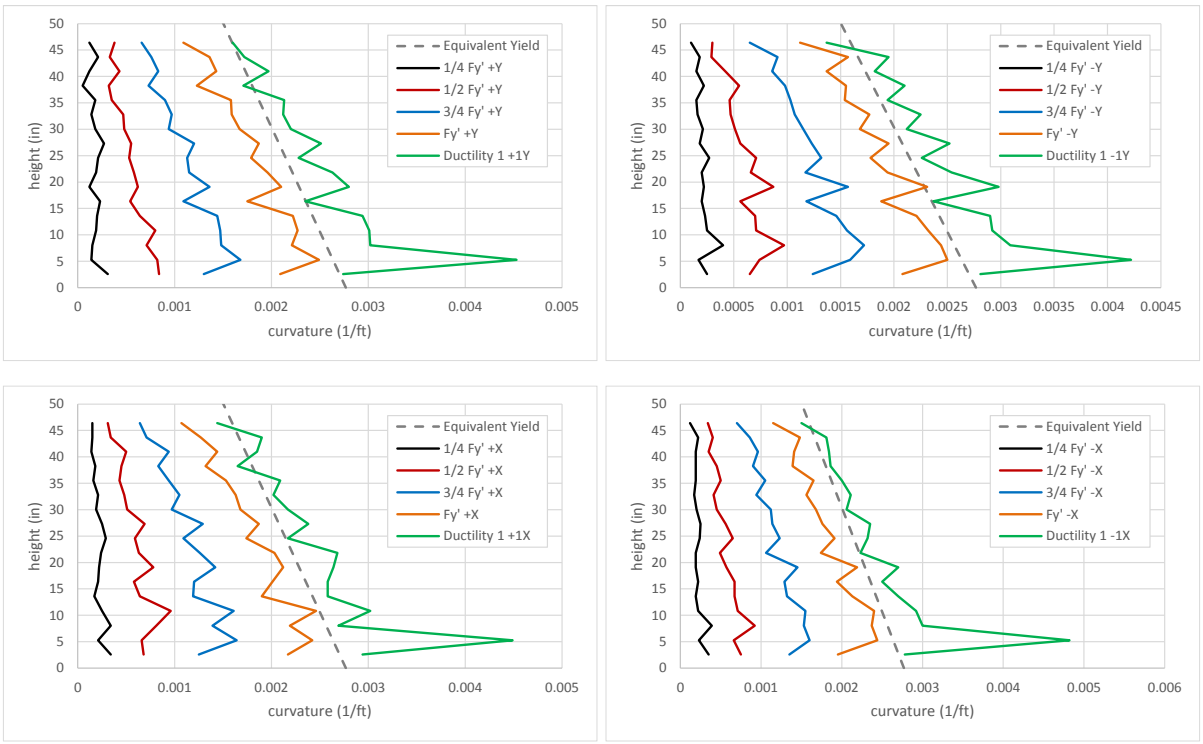

Figure 12-58. Test 9: Elastic Vertical Curvature Profiles

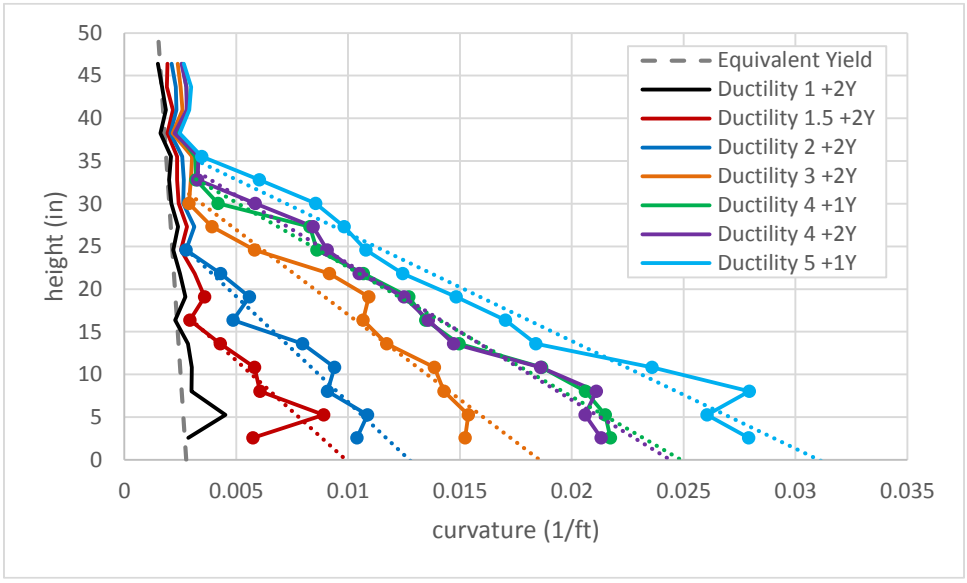

Figure 12-59. Test 9: Vertical Curvature Profiles for Loading in the +Y-direction

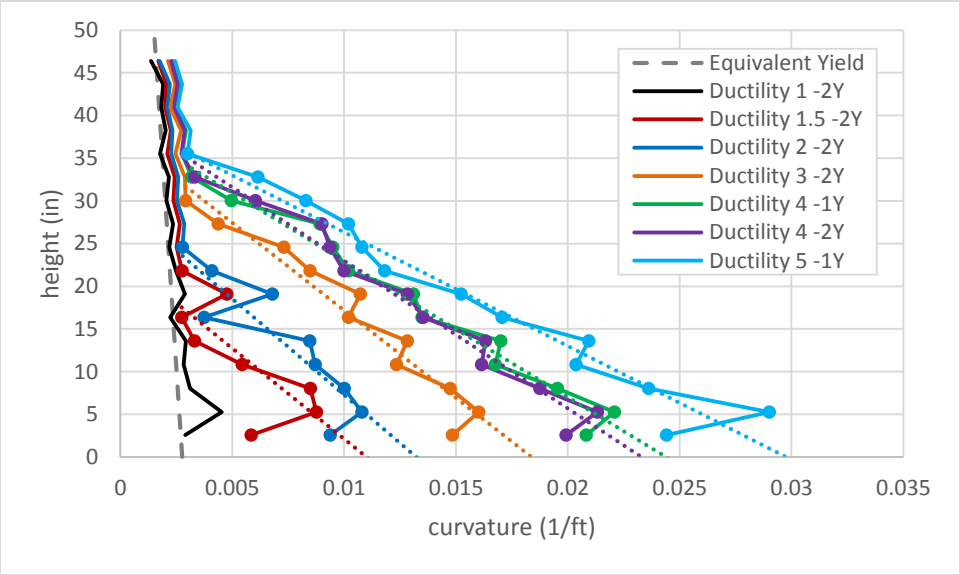

Figure 12-60. Test 9: Vertical Curvature Profiles for Loading in the -Y-direction

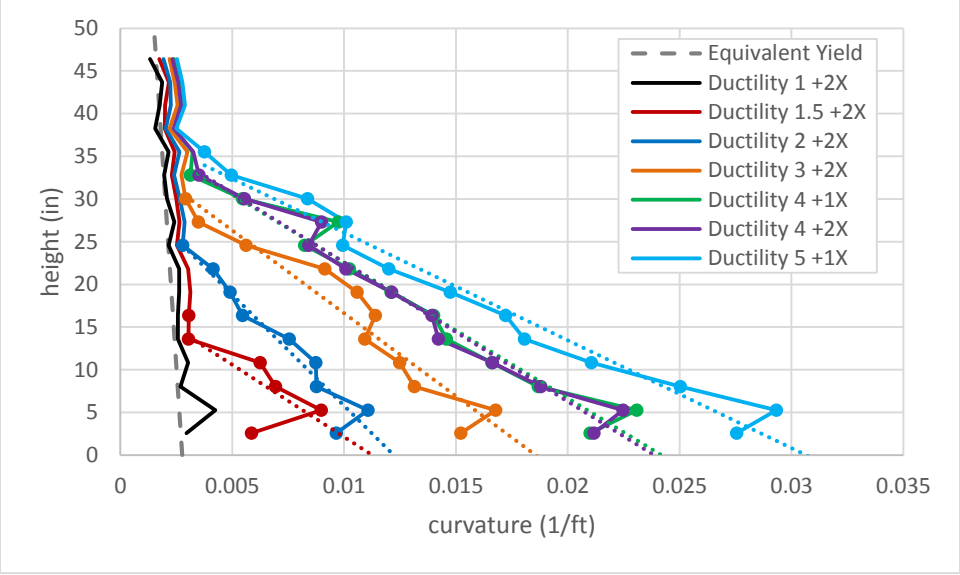

Figure 12-61. Test 9: Vertical Curvature Profiles for Loading in the +X-direction

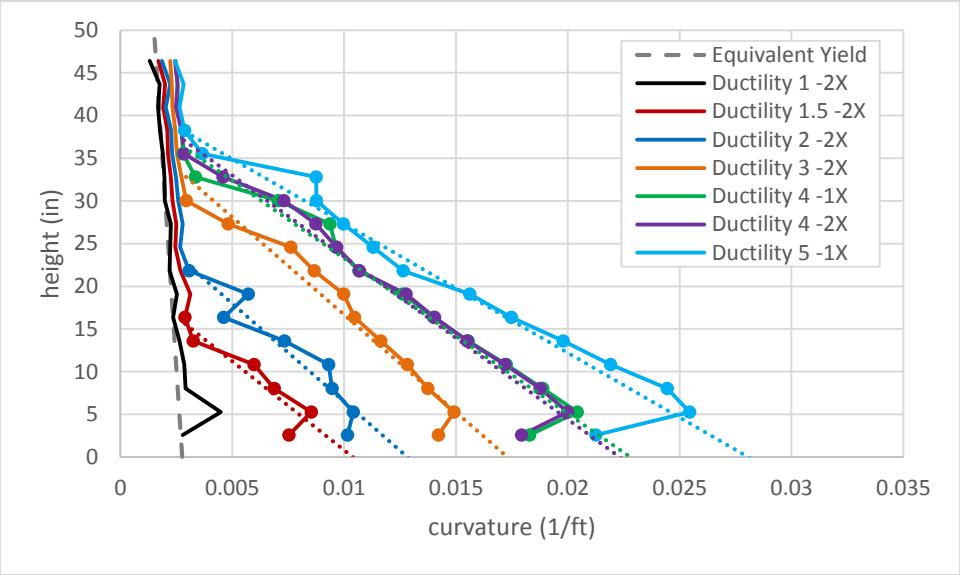

Figure 12-62. Test 9: Vertical Curvature Profiles for Loading in the -X-direction

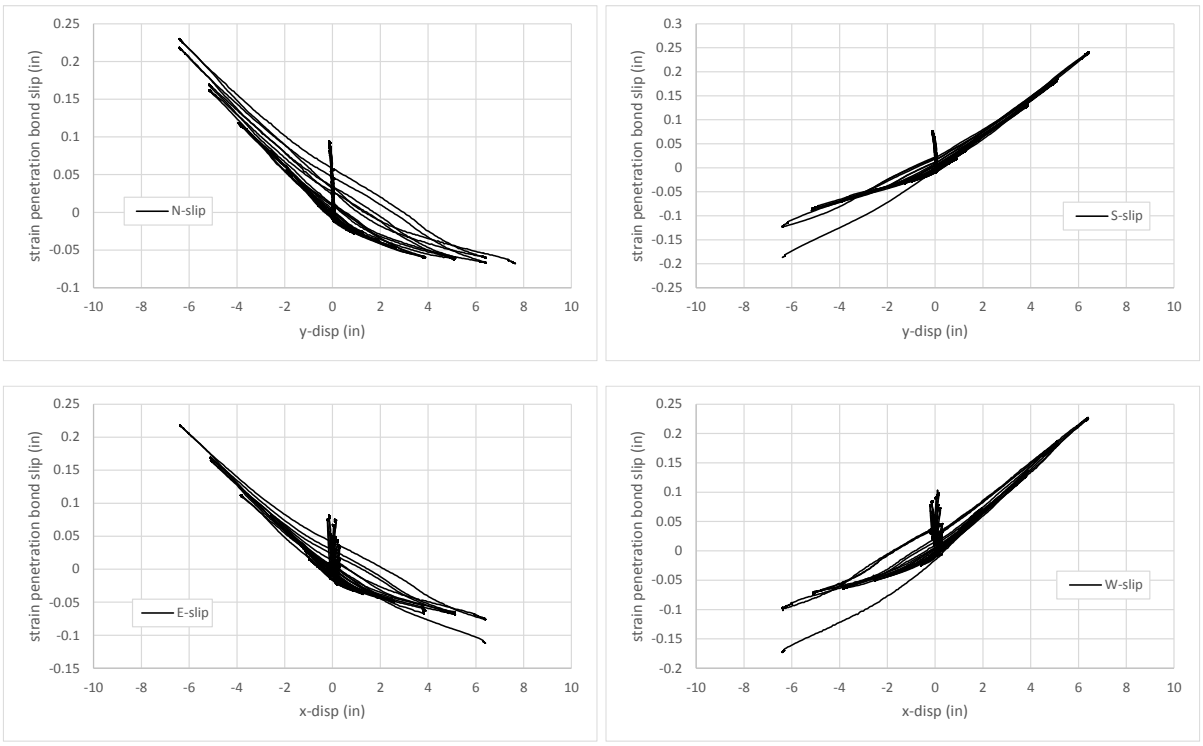

Figure 12-63. Test 9: Extreme Fiber Bar Strain Penetration Bond Slip Hysteresis

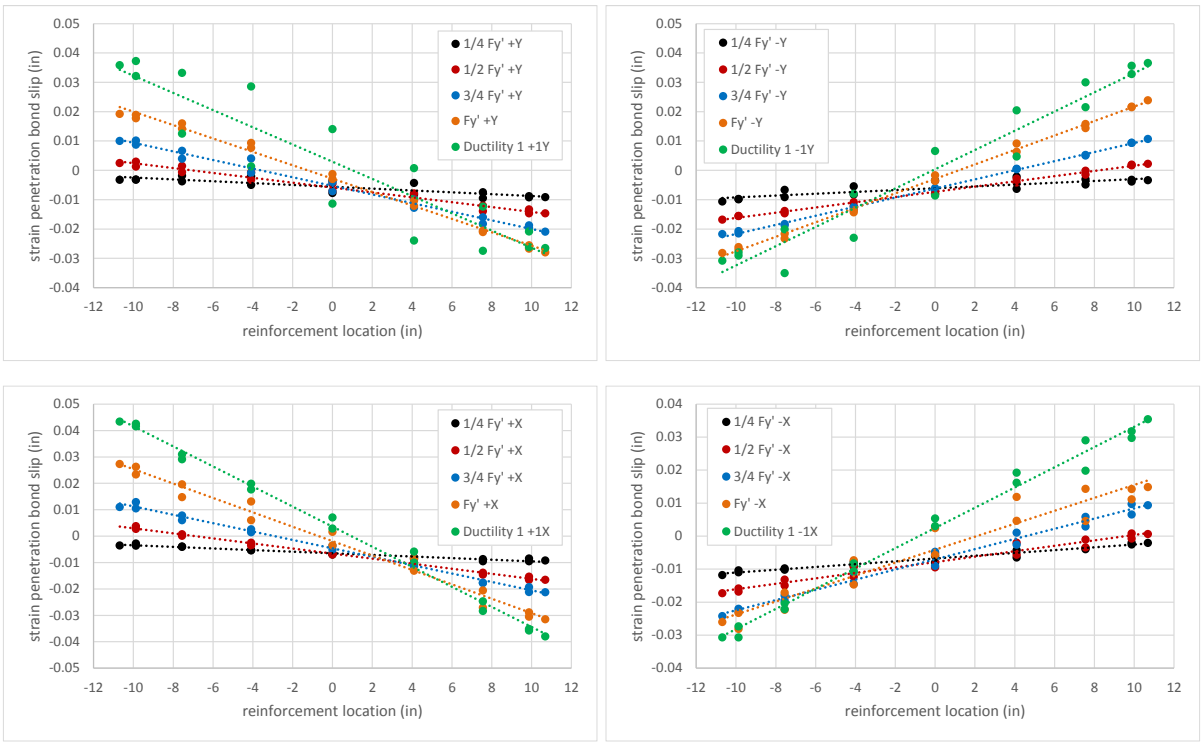

Figure 12-64. Test 9: Fixed End Rotations due to Strain Penetration during the Elastic Cycles

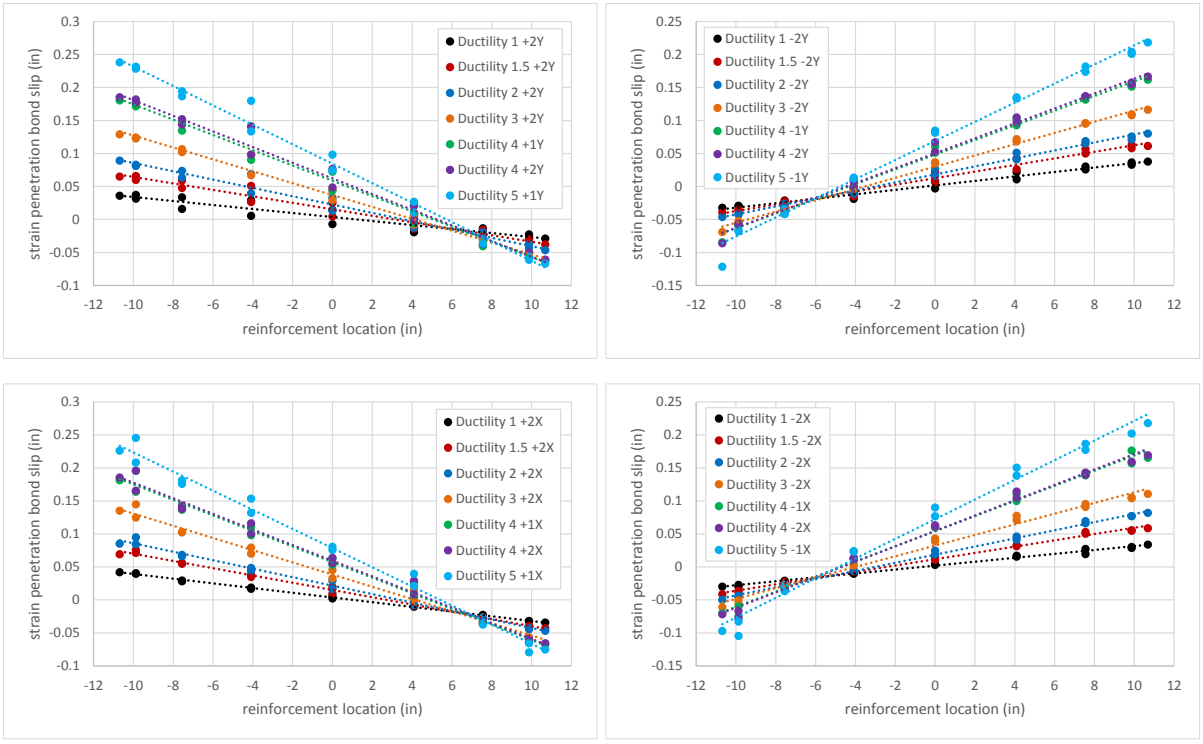

Figure 12-65. Test 9: Fixed End Rotations due to Strain Penetration

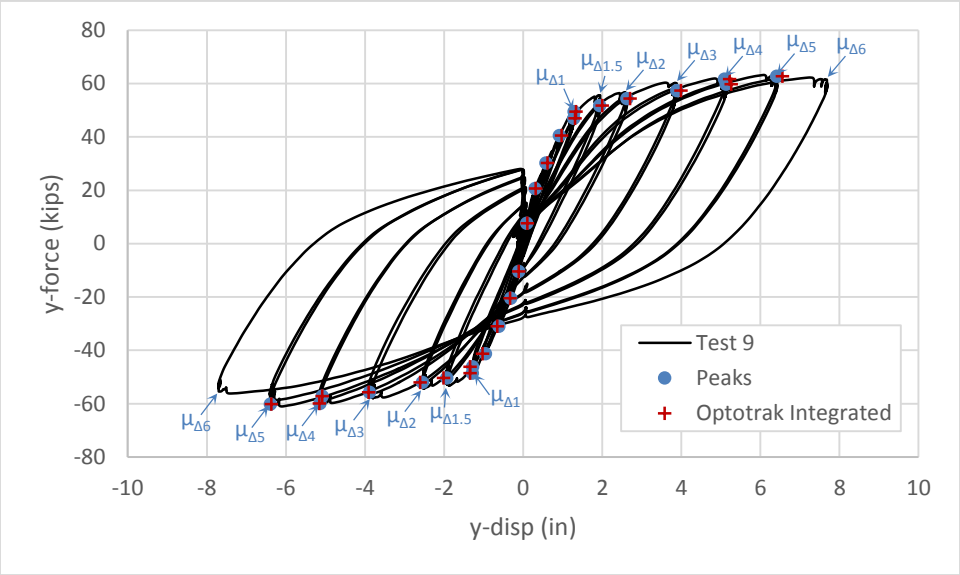

Figure 12-66. Test 9: Optotrak Integrated Flexural Disp. Compared to Measured String Pot. Disp.

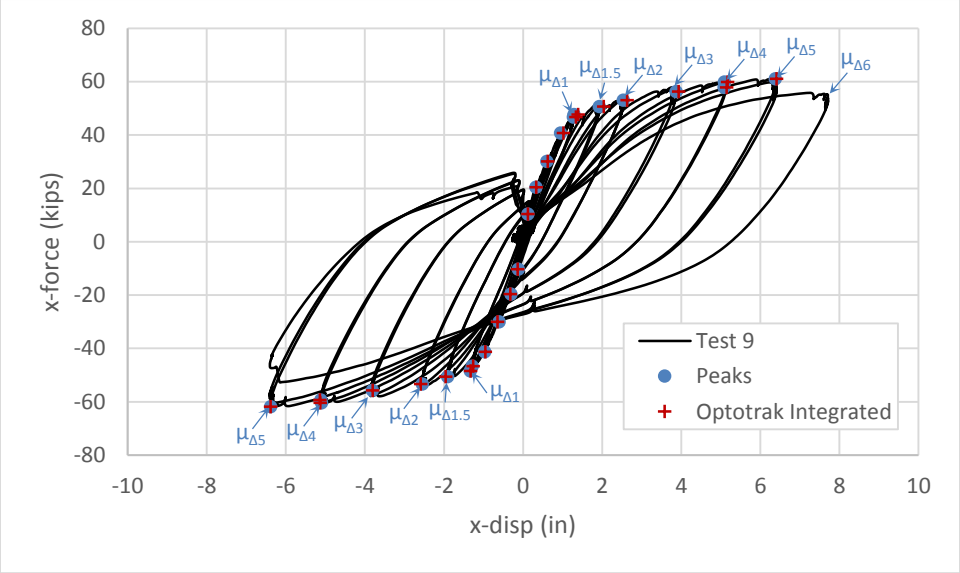

Figure 12-67. Test 9: Optotrak Integrated Flexural Disp. Compared to Measured String Pot. Disp.

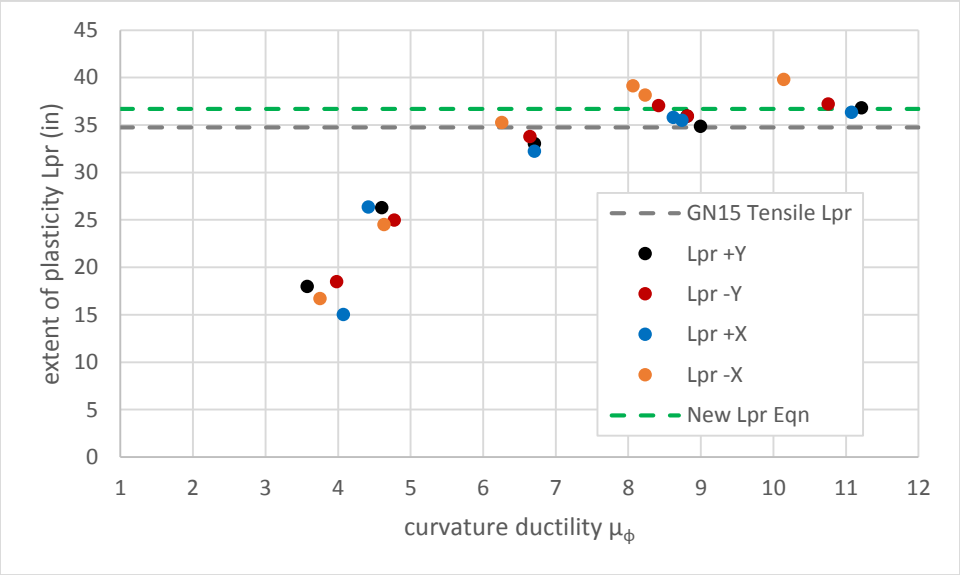

Figure 12-68. Test 9: Measured Extent of Plasticity Compared to Tensile Hinge Lengths

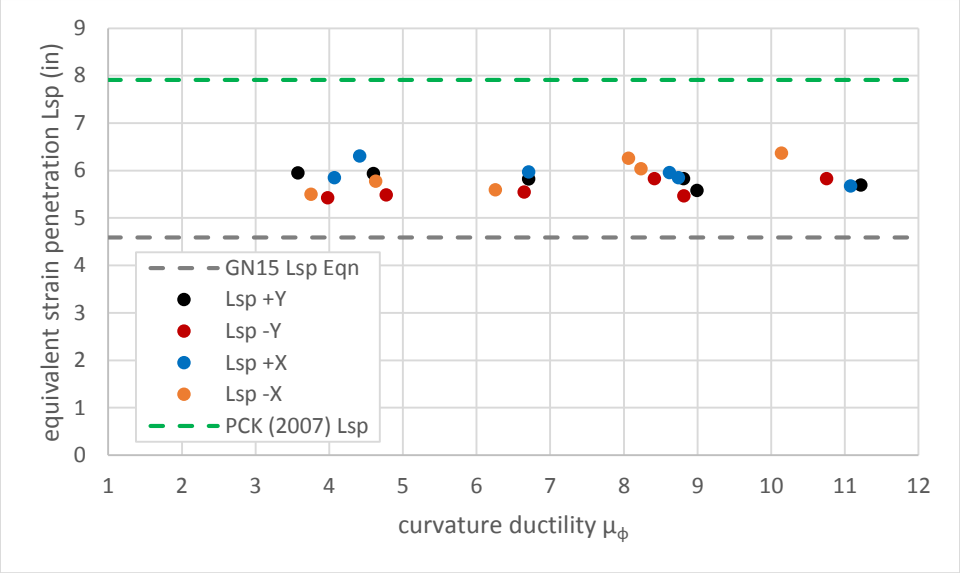

Figure 12-69. Test 9: Measured Equivalent Strain Penetration Lengths Compared to Design Expressions

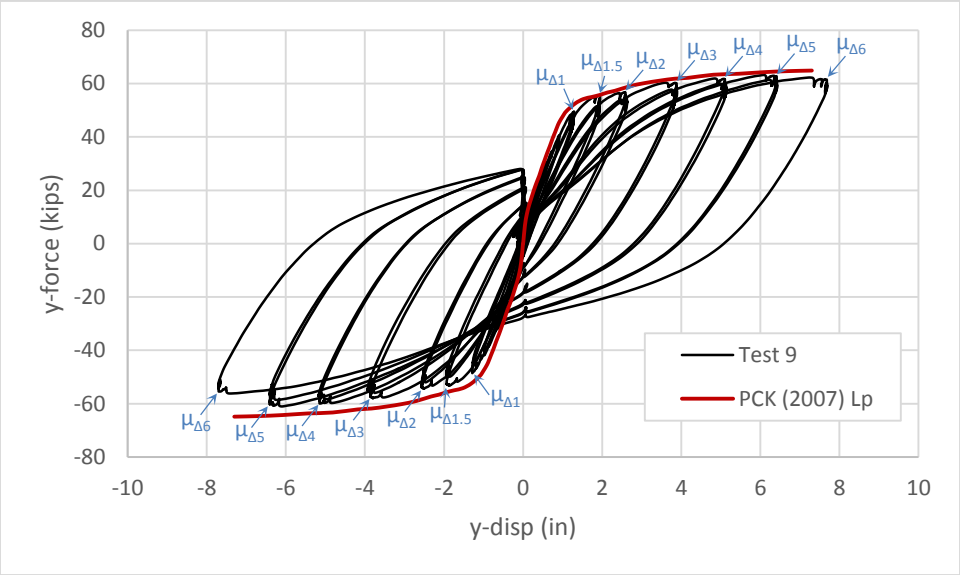

Figure 12-70. Test 9: Y-Direction Hysteretic Response Compared to PCK (2007) Hinge Length Monotonic Prediction

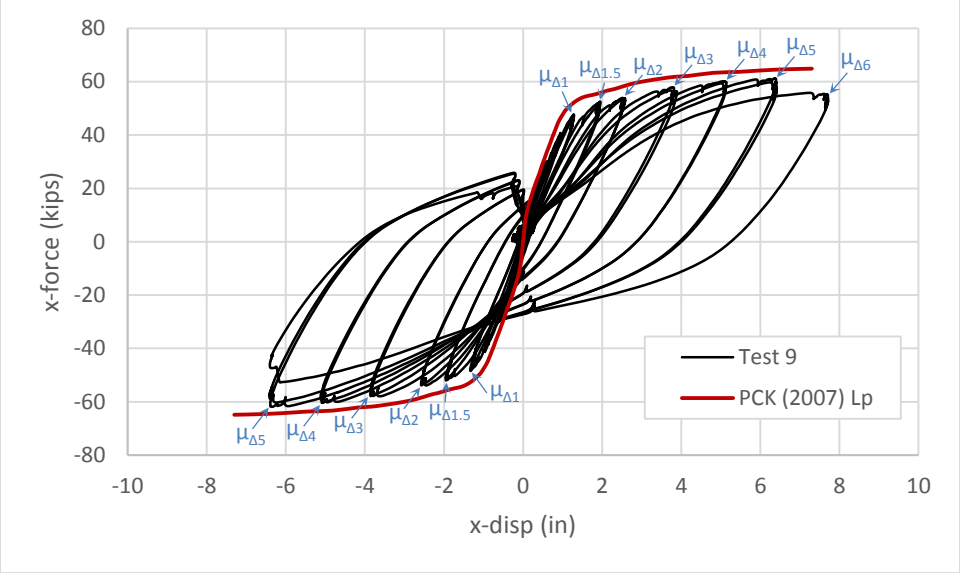

Figure 12-71. Test 9: X-Direction Hysteretic Response Compared to PCK (2007) Hinge Length Monotonic Prediction

Response Comparison to Previous Experiments

Comparison of Tests 7 (1.3%) and 9 (0.7% Transverse Volumetric Steel)

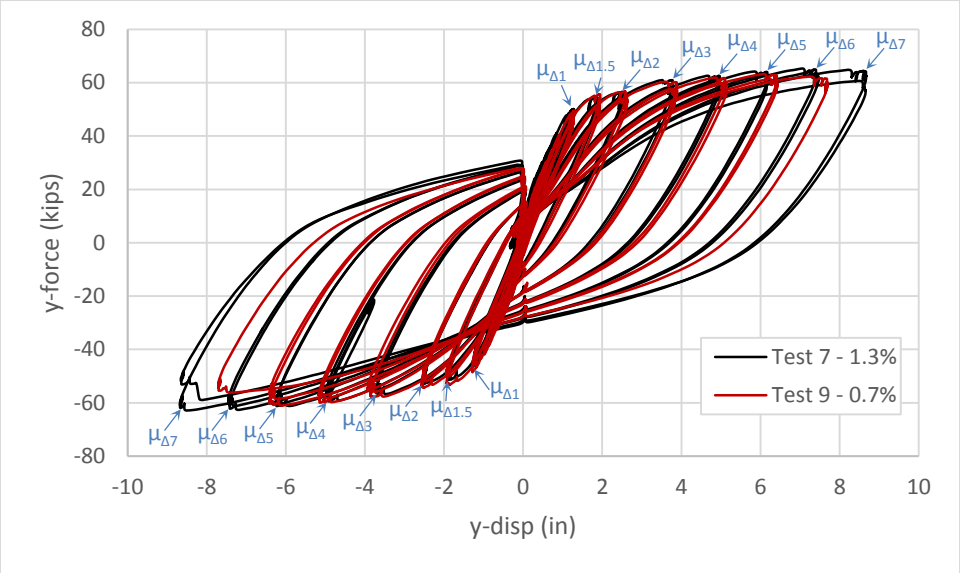

Figure 12-72. Tests 7 (1.3%) and 9 (0.7% Transverse Steel) Hysteretic Response Comparison in the Y-Direction

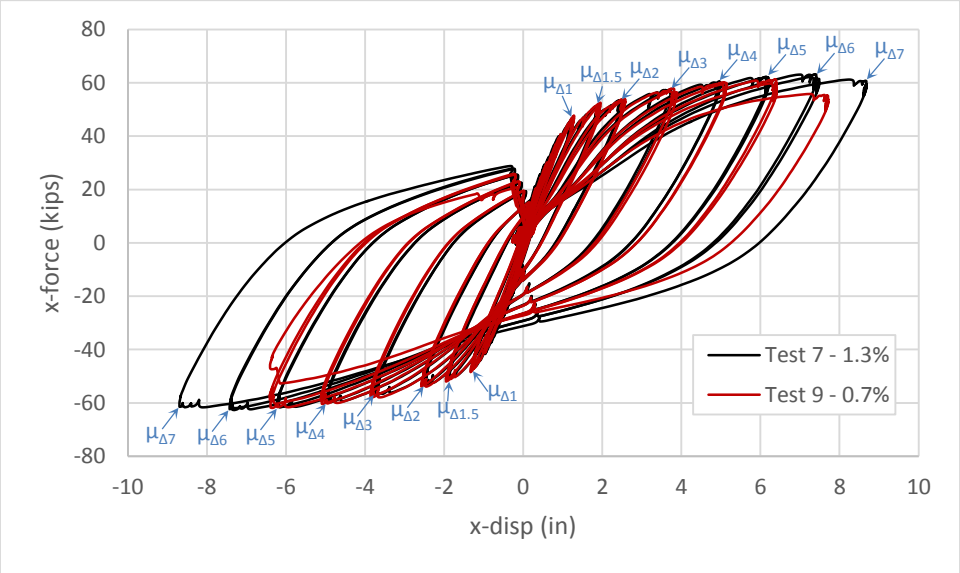

Figure 12-73. Tests 7 (1.3%) and 9 (0.7% Transverse Steel) Hysteretic Response Comparison in the X-Direction

Comparison of Tests 8 (1%) and 9 (0.7% Transverse Volumetric Steel)

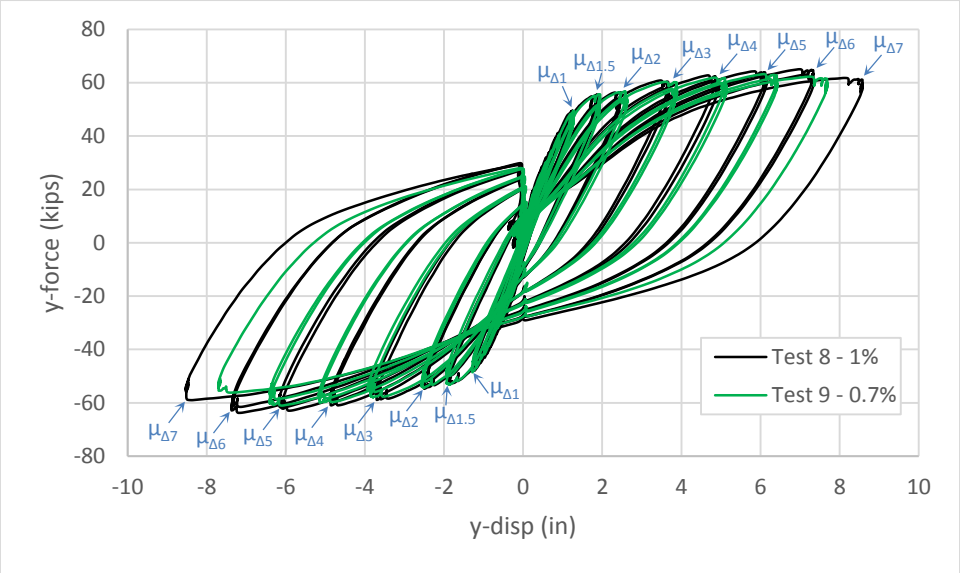

Figure 12-74. Tests 8 (1%) and 9 (0.7% Transverse Steel) Hysteretic Response Comparison in the Y-Direction

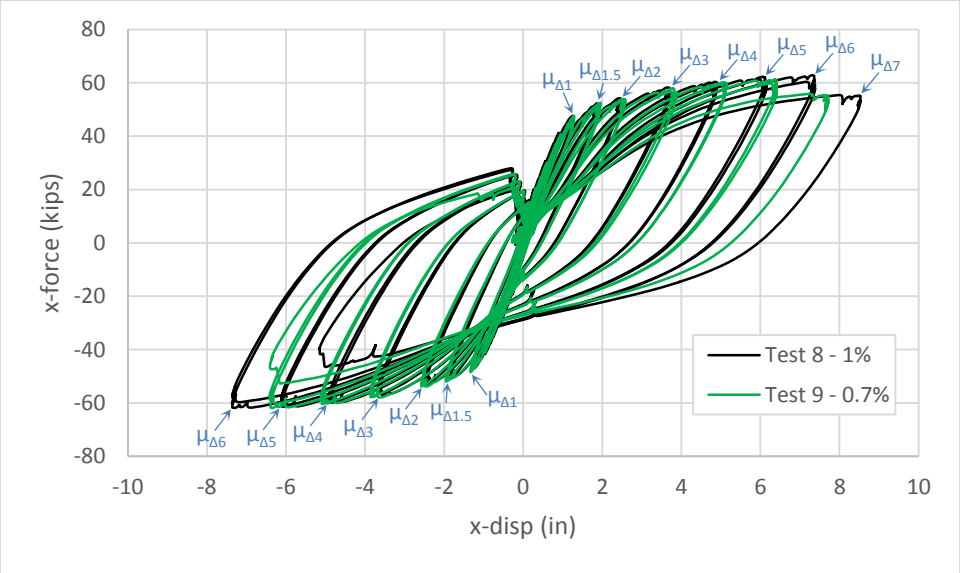

Figure 12-75. Tests 8 (1%) and 9 (0.7% Transverse Steel) Hysteretic Response Comparison in the X-Direction

Chapter 13 – Test 10 Summary Report

The tenth specimen had a 24" diameter circular cross-section reinforced with 16 #7 A706 longitudinal bars ($A_{st}/A_g = 2.1\%$) and a #3 spiral at 1.5" on center ($4A_{sp}/D's = 1.3\%$). Test 10 was designed to be comparable to previously tested columns 1-3 and 4-6 which had 0.7% and 1% transverse volumetric steel ratios, respectively. These experiments each had 2.1% longitudinal steel. Tests 1, 4, and 10 were subjected to the symmetric two-cycle-set loading protocol, Tests 2 and 5 used a three-cycle-set, and Tests 3 and 6 had an asymmetric application of the two-cycle set. Details of the test setup, instrumentation, and specimen design appear in Chapter 2. A material properties summary for the longitudinal and transverse steel from the final six experiments appears in Table 3-3 through Table 3-5. The column had a tested concrete strength of $f_c' = 6.13\ ksi$, while the footing had $f_c' = 7.52\ ksi$. The same constant compressive axial load of $191\ kips$ was applied to all the specimens. The tenth specimen was subjected to the Type-B Symmetric Two-Cycle-Set Bidirectional Load History shown in Figure 13-1. This figure includes a diagram of the column cross-section with the selected bar and crack labeling scheme. Displacements in the +Y-direction placed the South reinforcement in tension. Cracks due to loading in the +Y-direction were labeled as red. The orientation of the X and Y axes are shown in Figure 2-52 with regards to the test setup. The +Y-axis is perpendicular to and points away from the strong wall. Values of interests, damage observations, and a predictions summary for the tenth test appear in Table 13-1, Table 13-2, and Table 13-3. A photo of the deformed specimen appears in Figure 13-2.

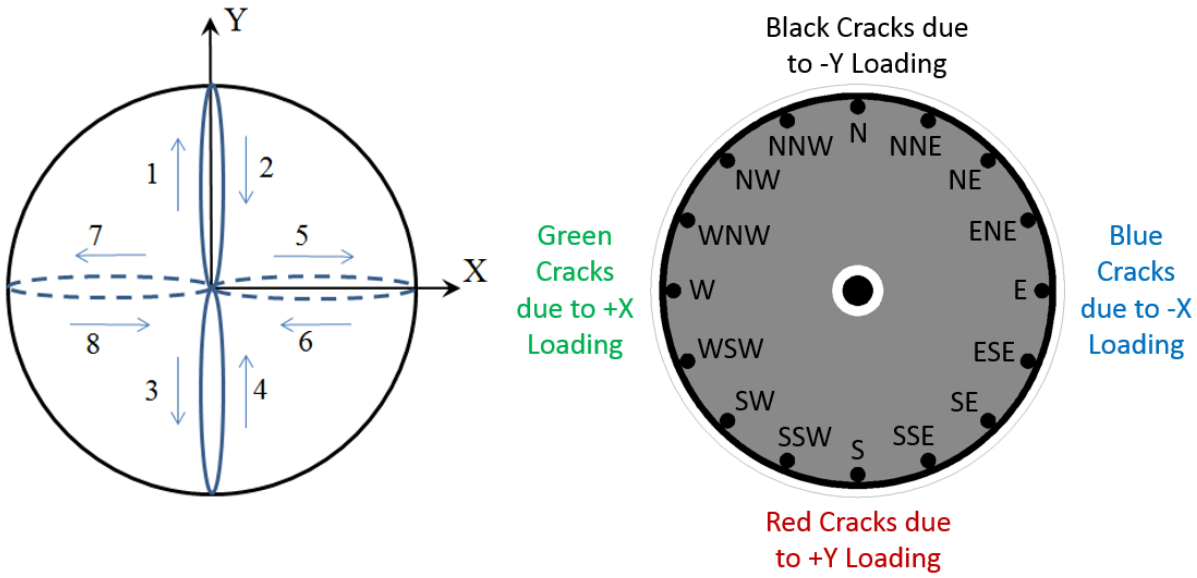

Figure 13-1. Test 10: Load History Orientation and Labeling System for Reinforcement and Cracks

Table 13-1. Test 10: Values of Interest

Load History	Type-B Symmetric Two-Cycle-Set
Length, Diameter, and Aspect Ratio	$L = 109.4375\ in, D = 24\ in,\ (L/D = 4.56)$
Longitudinal Steel Detailing	$16\ \#7\ for\ \rho_l = A_{st}/A_g = 2.1\%$
Longitudinal Steel Properties	$f_y = 69.63\ ksi, f_u = 96.66\ ksi, \varepsilon_y = 0.002708$
Transverse Steel Detailing	$\#3\ @\ 1.5\ in\ for\ \rho_s = 4A_{sp}/D's = 1.3\%$
Transverse Steel Properties	$f_y = 63.89\ ksi, f_u = 93.64\ ksi, \varepsilon_y = 0.00418$
Column Concrete Strength	$f_c' = 6.13\ ksi$
Footing Concrete Strength	$f_c' = 7.52\ ksi$
Axial Load	$P = 191\ kips, \left(P/f_c'\ A_g = 7.5\%\right)$
Analytical First Yield Force	$F_y' = 49.61\ kips$
Experimental First Yield Disp.	$\Delta_y' = 0.99\ in$
Analytical Nominal Moment Capacity	$M_n = 616.79\ kip \cdot ft$
Equivalent Yield Displacement	$\Delta_y = \Delta_y'\left(M_n/M_y'\right) = 1.36\ in$
Maximum Lateral Force	$F_y = 79.86\ kips, F_x = 76.99\ kips$
Failure Mode	Fracture of Previously Buckled Reinforcement

Table 13-2. Test 10: Damage Observations

Damage Observations:		
Cycle Peak at which First Cracking was Observed Visually:		
North	$\Delta_y = -0.5F_y' = -0.32\ in$	$F_y = -24.86\ kips$
South	$\Delta_y = 0.5F_y' = 0.30\ in$	$F_y = 23.84\ kips$
East	$\Delta_x = -0.5F_y' = -0.36\ in$	$F_x = -24.79\ kips$
West	$\Delta_x = 0.5F_y' = 0.35\ in$	$F_x = 24.83\ kips$
Cycle Peak at which Cover Concrete Crushing was Observed Visually:		
North	$\mu_{\Delta 1.5}^{+1Y} = 2.03\ in$	$\varepsilon_c = -0.00377$
South	$\mu_{\Delta 1.5}^{-2Y} = -2.05\ in$	$\varepsilon_c = -0.00503$
East	$\mu_{\Delta 2}^{+1X} = 2.72\ in$	$\varepsilon_c = -0.00682$
West	$\mu_{\Delta 2}^{-1X} = -2.74\ in$	$\varepsilon_c = -0.00491$
Exact Displacement and Cycle Label for Initial Spiral Yielding in the Confinement Zone:		
North	$\Delta_y = 4.64\ in\ during\ \mu_{\Delta 4}^{+1Y}$	$\varepsilon_c = -0.01610$
South	$\Delta_y = -5.79\ in\ during\ \mu_{\Delta 6}^{-1Y}$	$\varepsilon_c = -0.01674$
East	$\Delta_x = 5.46\ in\ during\ \mu_{\Delta 4}^{+1X}$	$\varepsilon_c = -0.01786$
West	$\Delta_x = -6.42\ in\ during\ \mu_{\Delta 5}^{-1X}$	$\varepsilon_c = -0.01405$
Peak Tensile Displacement Prior to Visual Bar Buckling During Subsequent Reversal of Load:		
North	$\mu_{\Delta 5}^{-2Y} = -6.82\ in, Observed\ at\ \mu_{\Delta 6}^{+1Y} = 8.15\ in$	$\varepsilon_s = 0.03839$
South	$\mu_{\Delta 6.5}^{+1Y} = 8.82\ in, Observed\ at\ \mu_{\Delta 6.5}^{-1Y} = -8.81\ in$	$\varepsilon_s = 0.05251$
East	$\mu_{\Delta 5}^{-2X} = -6.76\ in, Observed\ at\ \mu_{\Delta 6}^{+1X} = 8.13\ in$	$\varepsilon_s = 0.03703$
West	$West\ Bar\ Buckling\ Not\ Observed$	
Exact Displacement and Cycle Label for Fracture of Previously Buckled Reinforcement		
North	$\Delta_y = -8.00\ in\ during\ \mu_{\Delta 6.5}^{-1Y}$	Single North Extreme Bar

Table 13-3. Test 10: Damage Predictions

Damage Predictions with the New Bidirectional Plastic Hinge Model and New Strain Limits:		
Bar Buckling Predictions		
New Method	$\Delta_{bb}^{Lpr} = 8.23\ in$	$\varepsilon_s^{bb} = 0.04412$
Feng et al. (2015)	$\Delta_{bb}^{Lp} = 7.68\ in$	$\varepsilon_s^{bb} = 0.05585$
Cover Crushing Prediction		
New Method	$\Delta_{cc}^{Lpr} = 2.01\ in$	$\varepsilon_c^{cc} = -0.004$
Spiral Yielding Prediction		
New Method	$\Delta_{sy}^{Lpr} = 4.79\ in$	$\varepsilon_c^{sy} = -0.01192 * M, (M = 0.8)$
Original Ultimate Concrete Compression Strain		
Mander et al. (1988)	$\Delta_{cu}^{Lpr} = 9.12\ in$	$\varepsilon_{cu} = -0.0202$

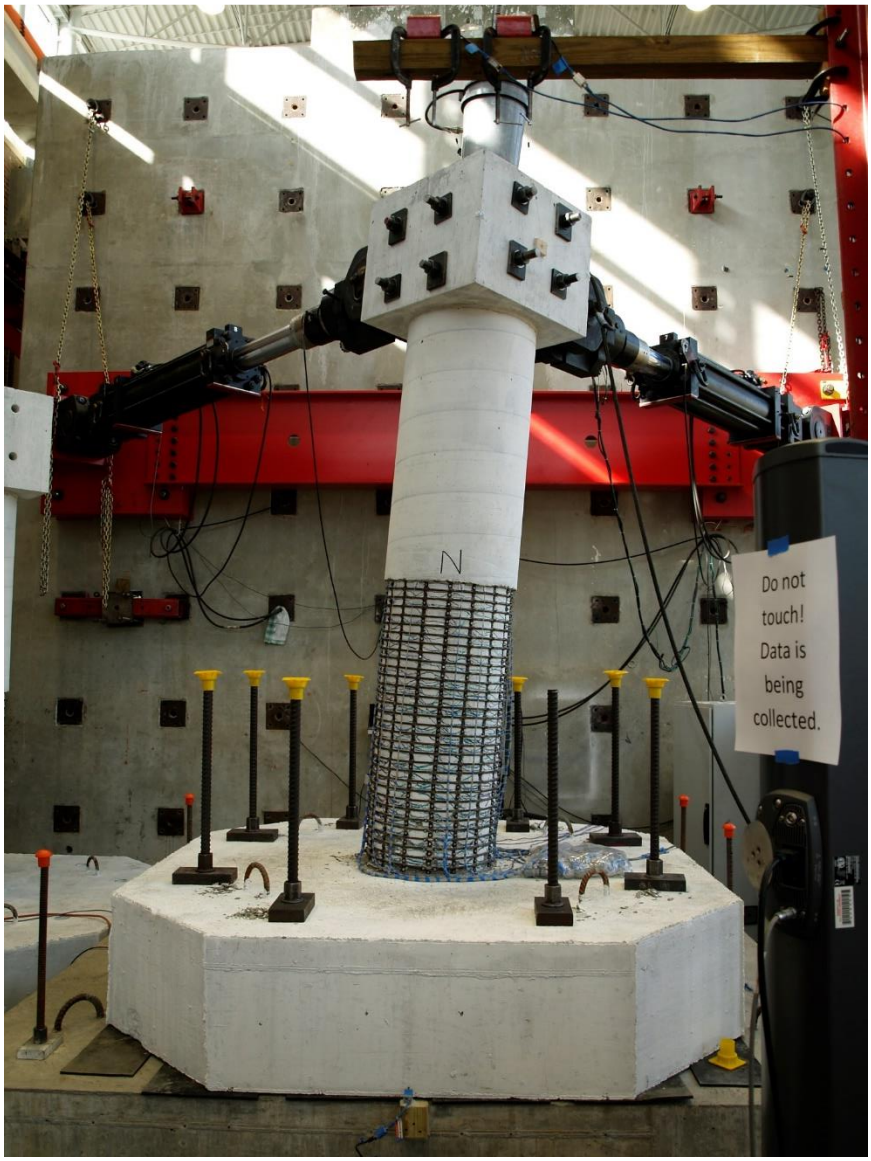

Figure 13-2. Test 10: Specimen Deformation at $\mu_{\Delta 6}^{-1x} = -8.13$"

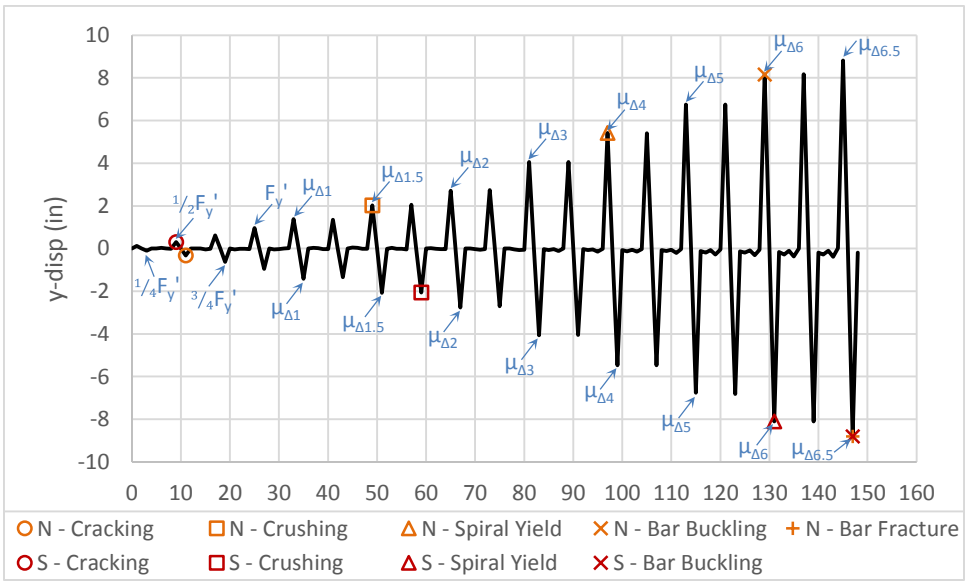

Figure 13-3. Test 10: Y-Displacement History

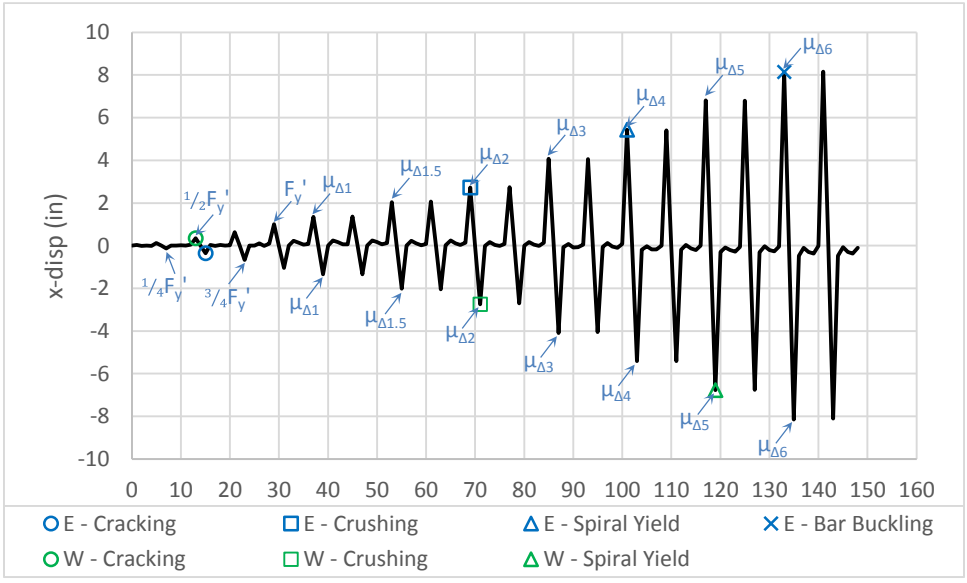

Figure 13-4. Test 10: X-Displacement History

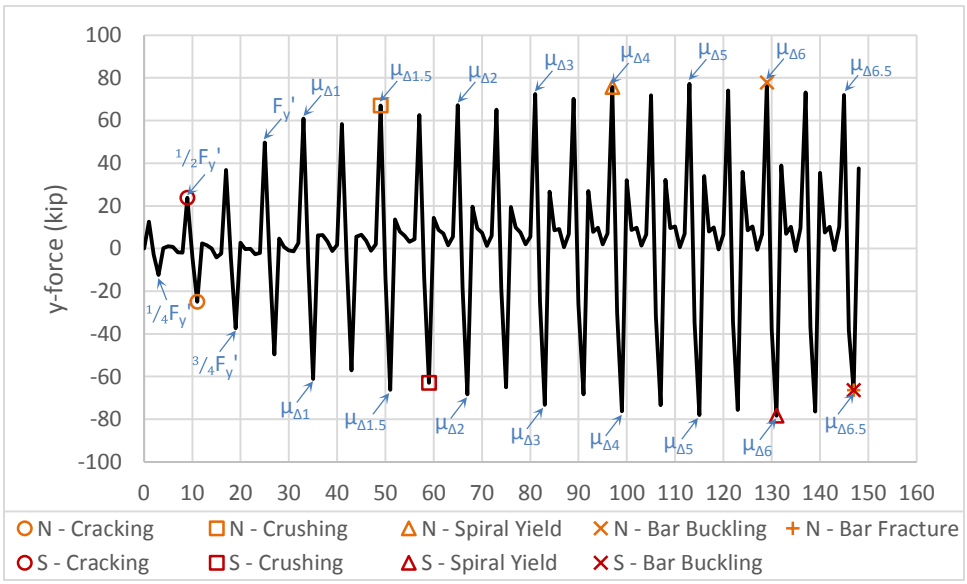

Figure 13-5. Test 10: Y-Force History

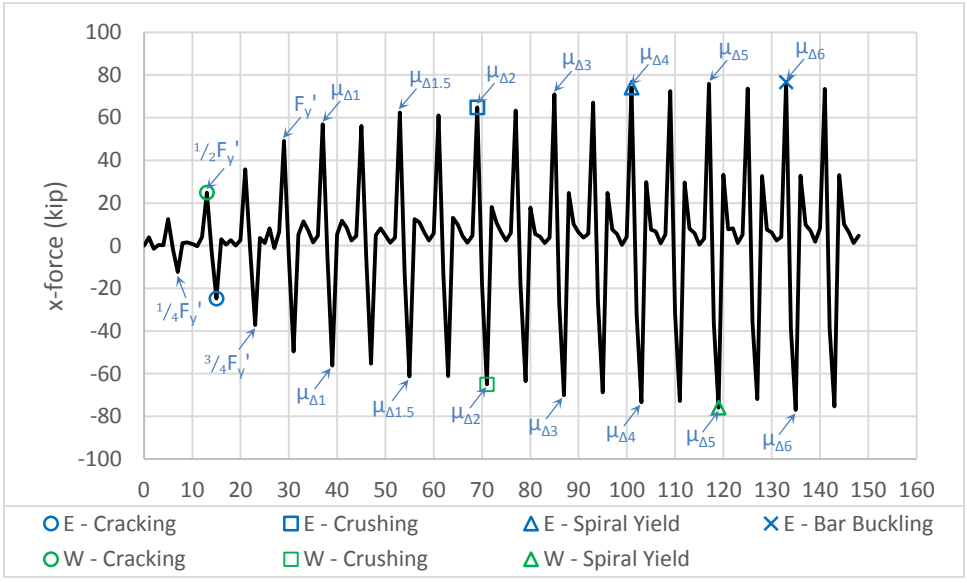

Figure 13-6. Test 10: X-Force History

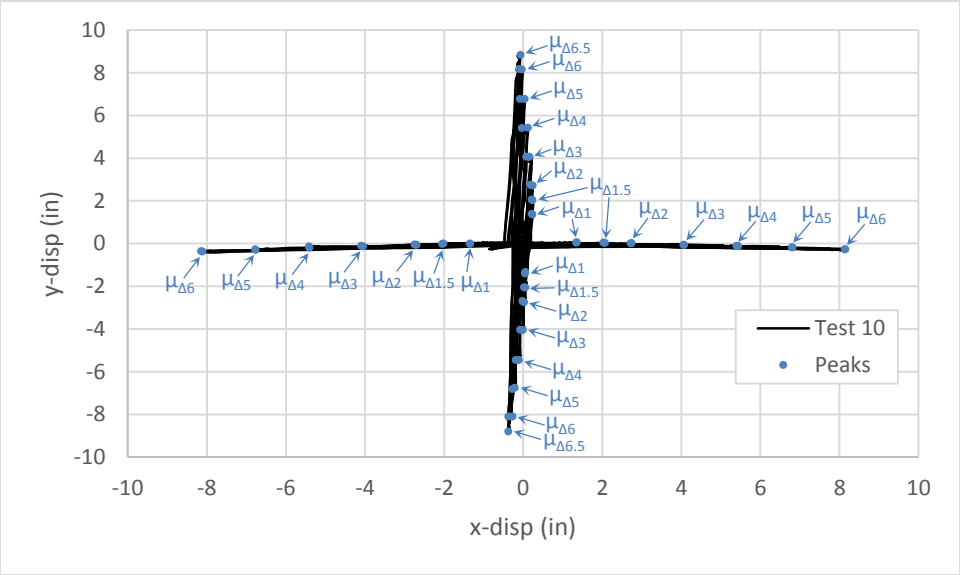

Figure 13-7. Test 10: Type-B Symmetric Two-Cycle-Set Displacement History

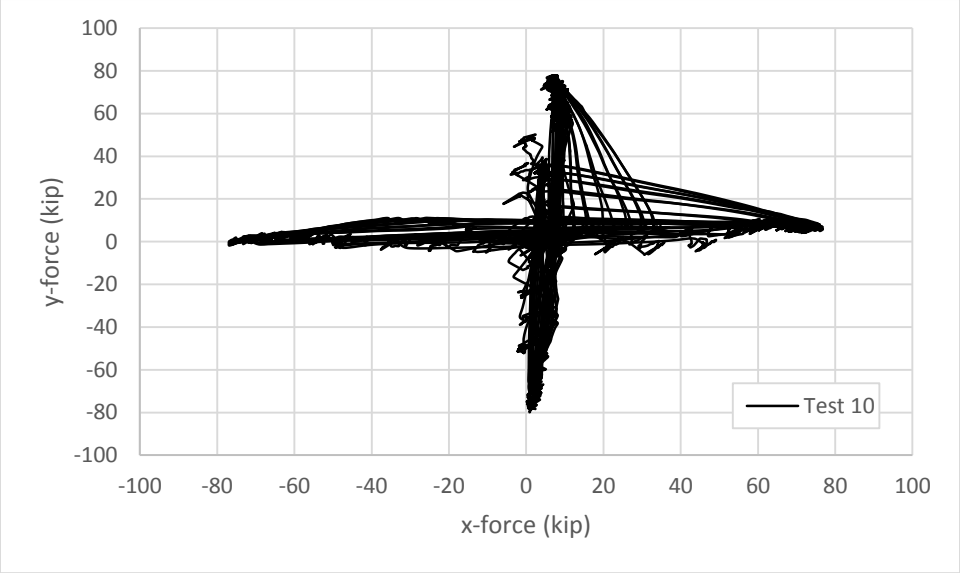

Figure 13-8. Test 10: Load Path

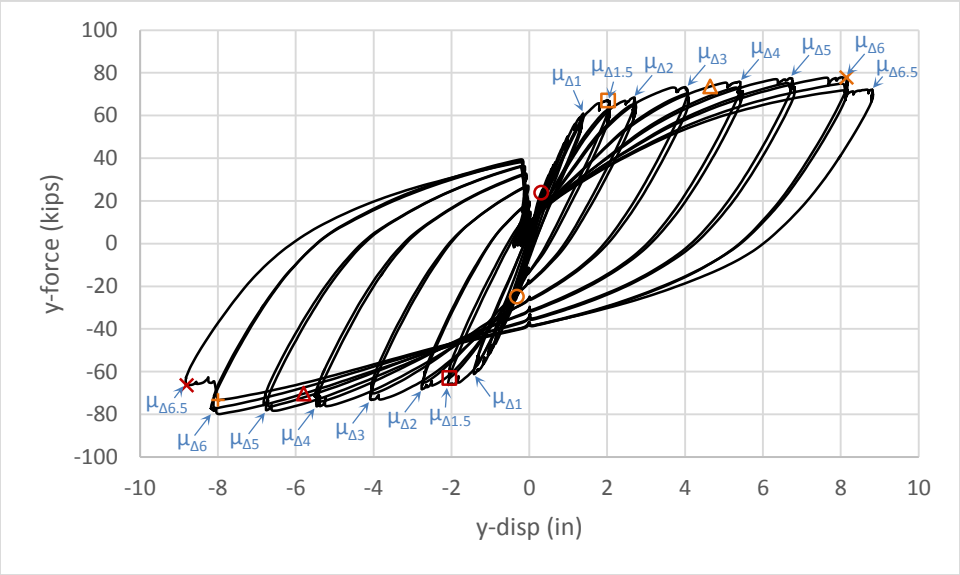

Figure 13-9. Test 10: Y-Direction Hysteretic Response

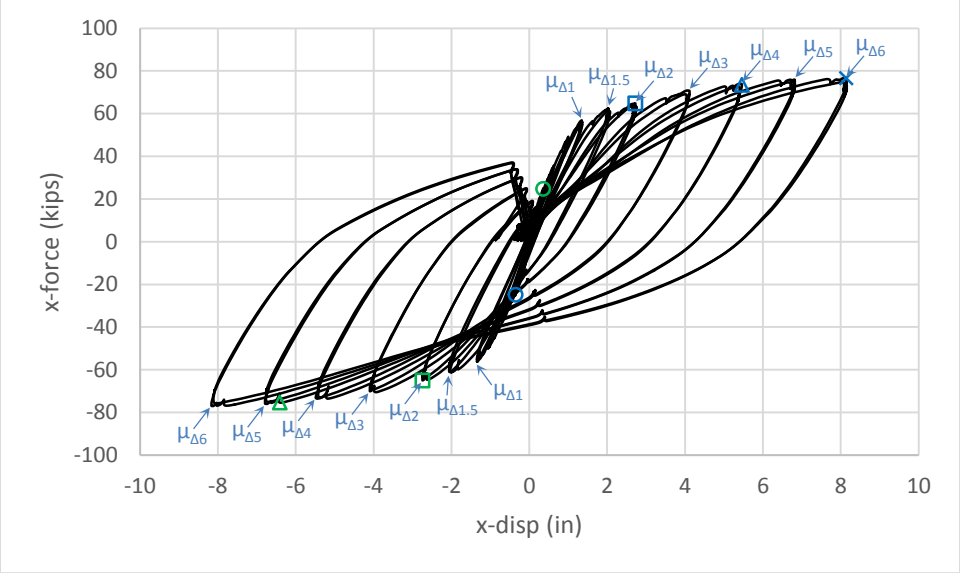

Figure 13-10. Test 10: X-Direction Hysteretic Response

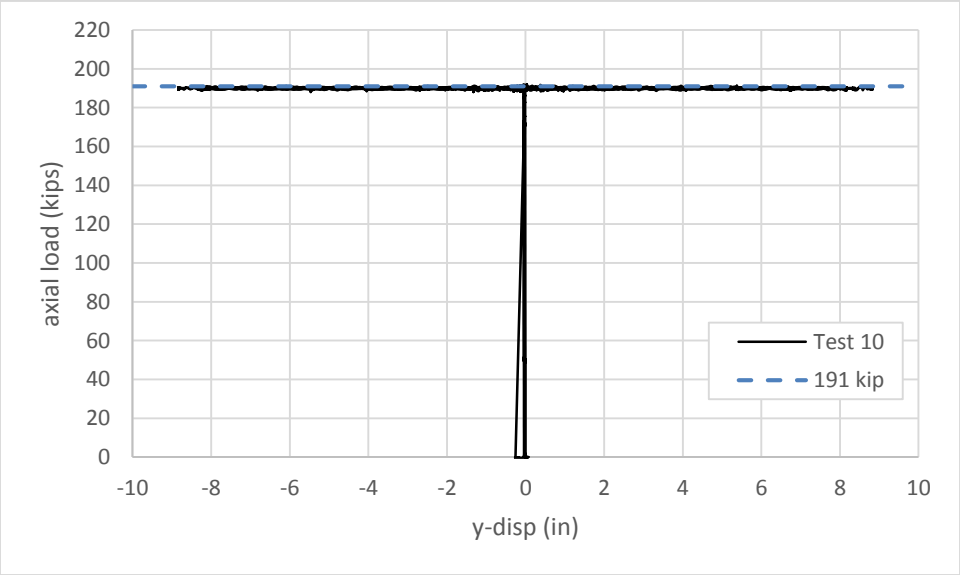

Figure 13-11. Test 10: Y-Direction Axial Force History

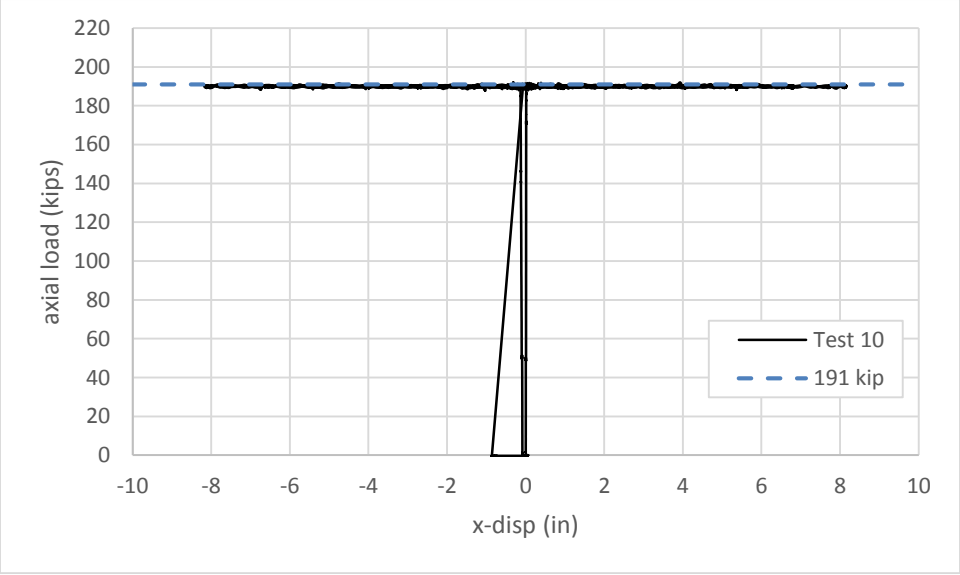

Figure 13-12. Test 10: X-Direction Axial Force History

Test 10 - Experimental Observations

Values of interests and damage observations for Load Path Test 10 are presented in Table 13-1 and Table 13-2. Test 10 evaluated a 24" diameter column $(L/D = 4.56)$ with $\rho_l = A_{st}/A_g = 2.1\%$ longitudinal steel and a transverse volumetric ratio of $\rho_s = 4A_{sp}/D's = 1.3\%$. The test began with the application of a constant axial load of $191\ kips\ \left(P/f_c'\ A_g = 7.5\%\right)$. The imposed displacement histories in the Y and X-directions for the Symmetric Two-Cycle-Set Bidirectional Load History shown in Figure 13-3 and Figure 13-4. The resulting column shear force histories in the Y and X-directions appear in Figure 13-5 and Figure 13-6. The full displacement history and resulting load path for Test 10 appear in Figure 13-7 and Figure 13-8. The Y and X-direction column hysteretic response appears Figure 13-9 and Figure 13-10. The axial force history appears in Figure 13-11 and Figure 13-12.

The load history began with elastic ¼ F_y' cycle increments until the analytically predicted first yield force $(F_y' = 49.61\ kips)$ was reached in each direction of loading. Cracks were first observed on all sides of the specimen during the ½ F_y' cycle. At the analytically predicted first yield force, an average experimental first yield displacement of $\Delta_y' = 0.99$" was measured in the four primary directions. The equivalent yield displacement for the column was then computed as $\Delta_y = \Delta_y'\left(M_n/M_y'\right) = 1.36\ in$, where $M_n = 616.79\ kip \cdot ft$ represents the analytical nominal moment capacity corresponding to an extreme fiber compression strain of $\varepsilon_c = 0.004$ or a steel tensile strain of $\varepsilon_s = 0.015$, whichever occurs first. The remainder of the Symmetric Two-Cycle-Set Load History consists of two cycles for each displacement ductility level $\mu_{\Delta n} = n \cdot \Delta_y$, where $n = 1, 1.5, 2, 3, 4, 5, 6\ etc$. Cracks observed on each side of the specimen at equivalent yield are shown in Figure 13-13 and Figure 13-14.

Concrete crushing was observed on the North side at $\mu_{\Delta 1.5}^{+1y} = 2.03$" and the South side at $\mu_{\Delta 1.5}^{-2y} = -2.05$", see Figure 13-15. Concrete crushing was observed on the East side at $\mu_{\Delta 2}^{+1x} = 2.72$", followed by the West side at $\mu_{\Delta 2}^{-1x} = -2.74$", see Figure 13-16. Confinement steel on the North side of the specimen yielded during $\mu_{\Delta 4}^{+1y} = 5.41$", while spirals on the East side yielded during $\mu_{\Delta 4}^{+1x} = 5.44$", refer to Figure 13-17. Spirals on the West side yielded during $\mu_{\Delta 5}^{-1x} = -6.77$", followed by the South side at $\mu_{\Delta 6}^{-1y} = -8.11$", as shown in Figure 13-18. Crack profiles on each side of the specimen at the conclusion of $\mu_{\Delta 5}$ appear in Figure 13-19 and Figure 13-20. The North extreme fiber bar visibly buckled during $\mu_{\Delta 6}^{+1y} = 8.15$", followed by the East extreme fiber bar during $\mu_{\Delta 6}^{+1x} = 8.13$", see Figure 13-21. The buckled deformation of the East bar was barely distinguishable by eye, but it had increased during the subsequent cycle to $\mu_{\Delta 6}^{+2x} = 8.15$", as shown in Figure 13-22. The adjacent North Bar NNW buckled during $\mu_{\Delta 6}^{+2y} = 8.17$", followed by Bar NNE during $\mu_{\Delta 6.5}^{+1y} = 8.82$", see Figure 13-22 and Figure 13-23. A photo of the specimen at $\mu_{\Delta 6}^{-1x} = -8.13$" appears in Figure 13-2.

It was clear that a full ductility level increase would not be necessary to fracture the previously buckled reinforcement, so it was decided that the load history would progress from $\mu_{\Delta 6} = 8.13$" to $\mu_{\Delta 6.5} = 8.81$". The previously buckled North extreme fiber bar fractured at -8.00" during $\mu_{\Delta 6.5}^{-1y}$, see Figure 13-24 and Figure 13-9, resulting in a significant loss in strength. South Bars SSE, S, and SSW buckled during $\mu_{\Delta 6.5}^{-1y} = -8.81$", see Figure 13-23. Bar Buckling on the West side of the specimen was never observed, since the specimen was saved for repair after the first bar fracture. Photos of the specimen after the test appear in Figure 13-25 and Figure 13-26.

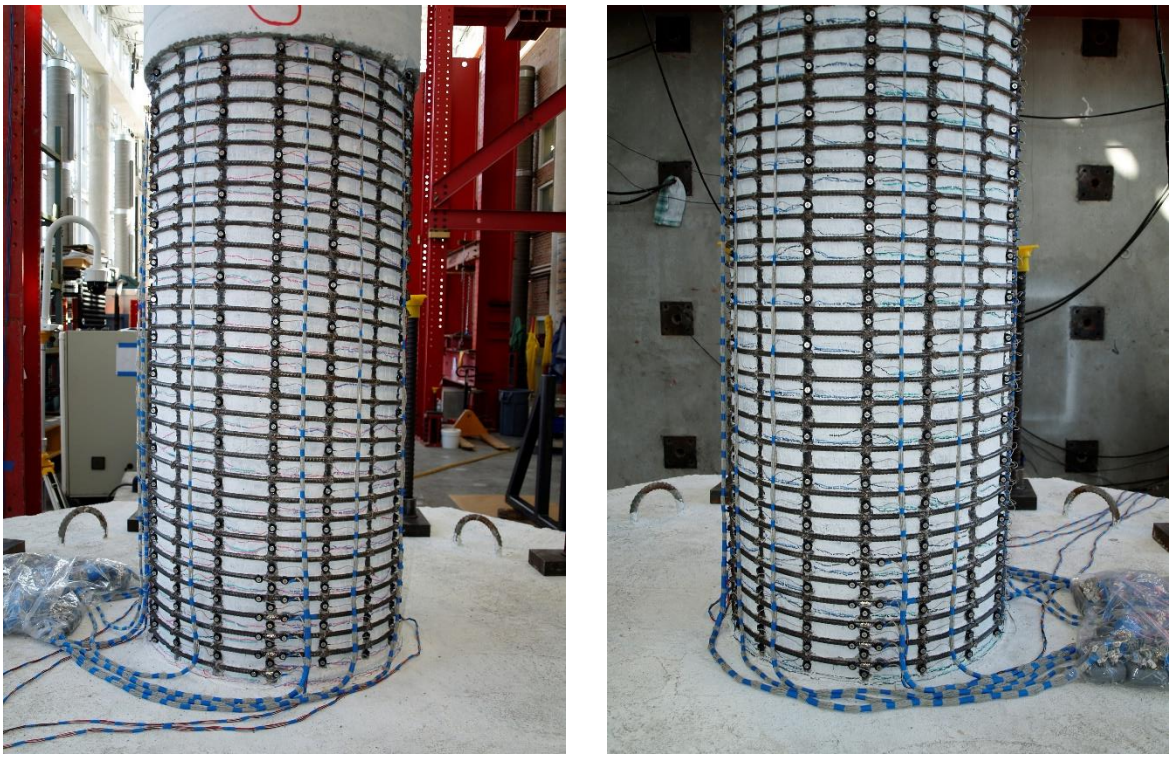

Figure 13-13. Test 10: Cracking on the (Left) South Side at $\mu_{\Delta 1}^{+2y} = 1.35$" and (Right) North Side at $\mu_{\Delta 1}^{-2y} = -1.34$"

Figure 13-14. Test 10: Cracking on the (Left) West Side at $\mu_{\Delta 1}^{+2x} = 1.36$" and (Right) East Side at $\mu_{\Delta 1}^{-2x} = -1.35$"

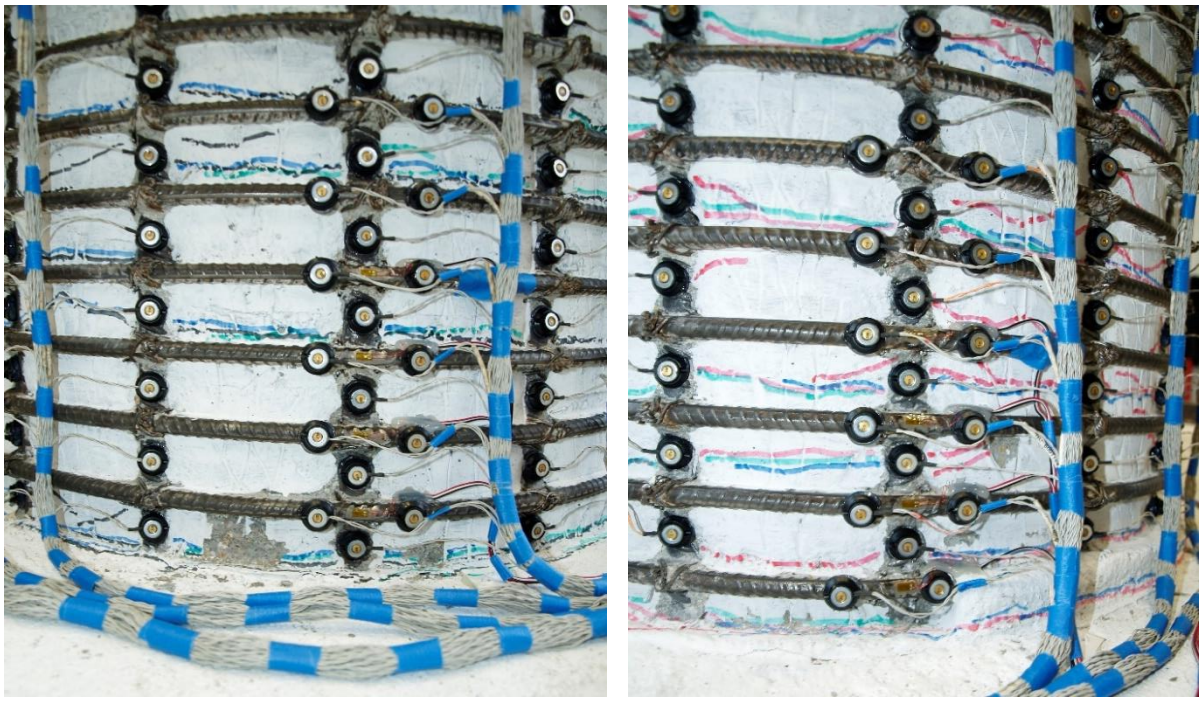

Figure 13-15. Test 10: Concrete Crushing on the (Left) North Side at $\mu_{\Delta 1.5}^{+1y} = 2.03$" and (Right) South Side at $\mu_{\Delta 1.5}^{-2y} = -2.05$"

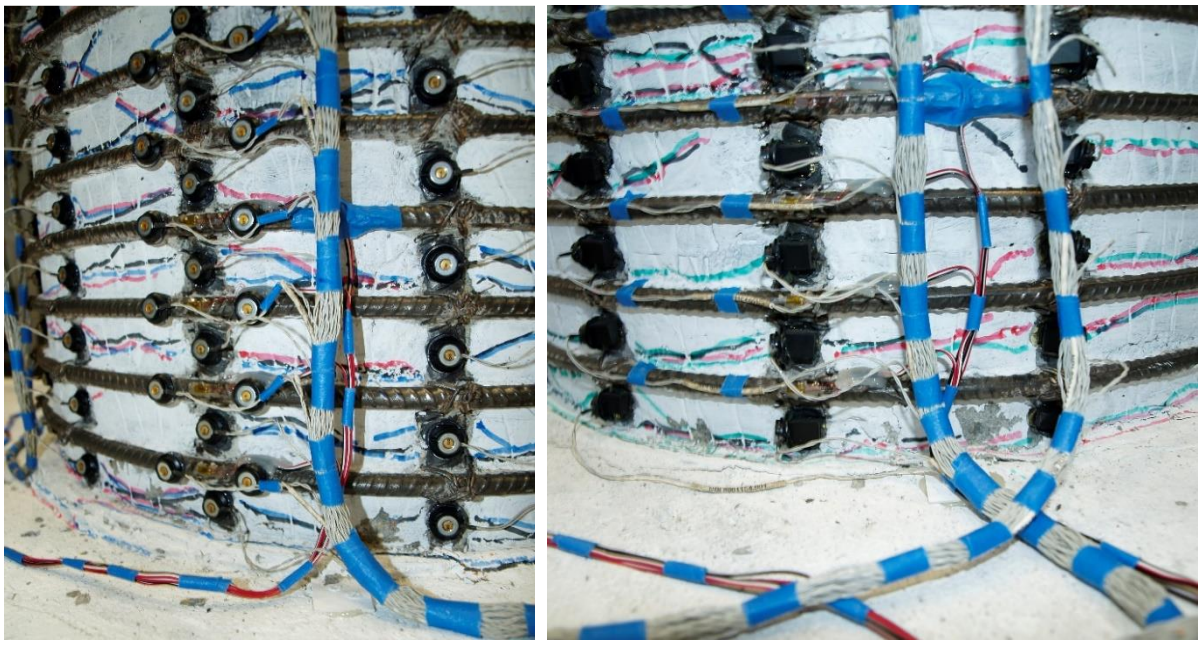

Figure 13-16. Test 10: Concrete Crushing on the (Left) East Side at $\mu_{\Delta 2}^{+1x} = 2.72$" and (Right) West Side at $\mu_{\Delta 2}^{-1x} = -2.74$"

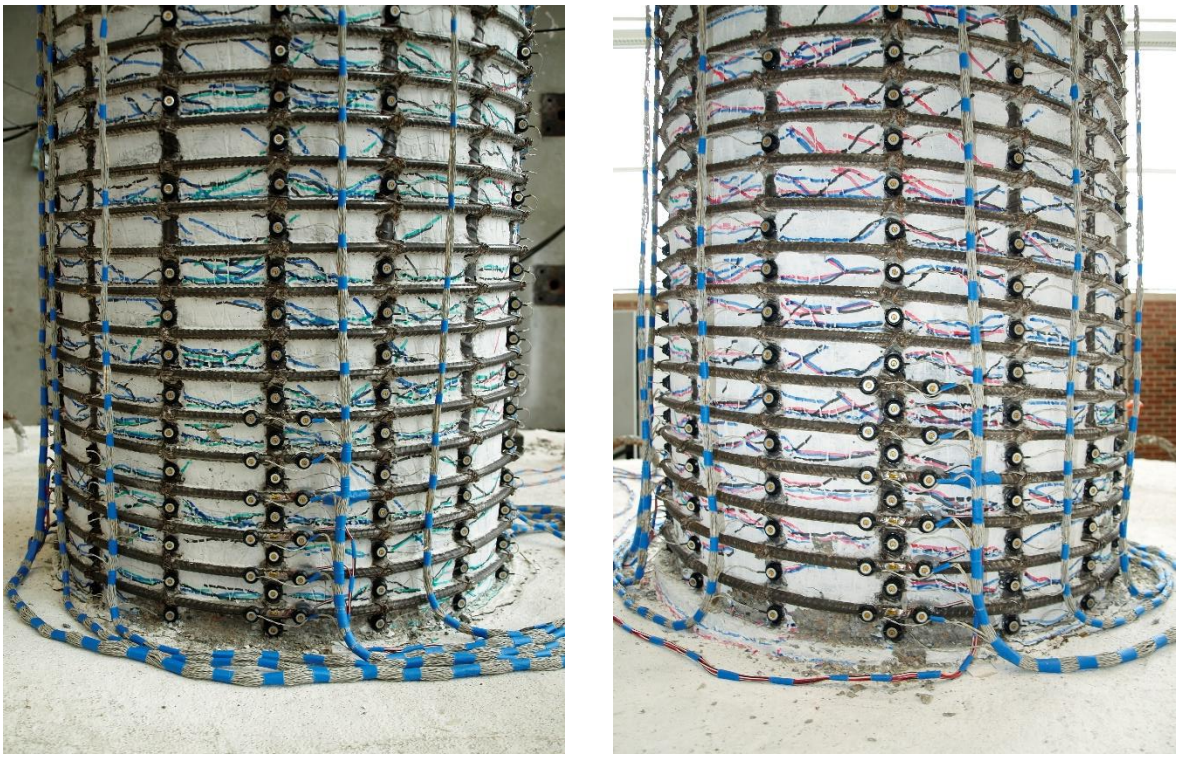

Figure 13-17. Test 10: Spiral Yielding on the (Left) North Side at $\mu_{\Delta 4}^{+1y} = 5.41"$ and (Right) East Side at $\mu_{\Delta 4}^{+1x} = 5.44"$

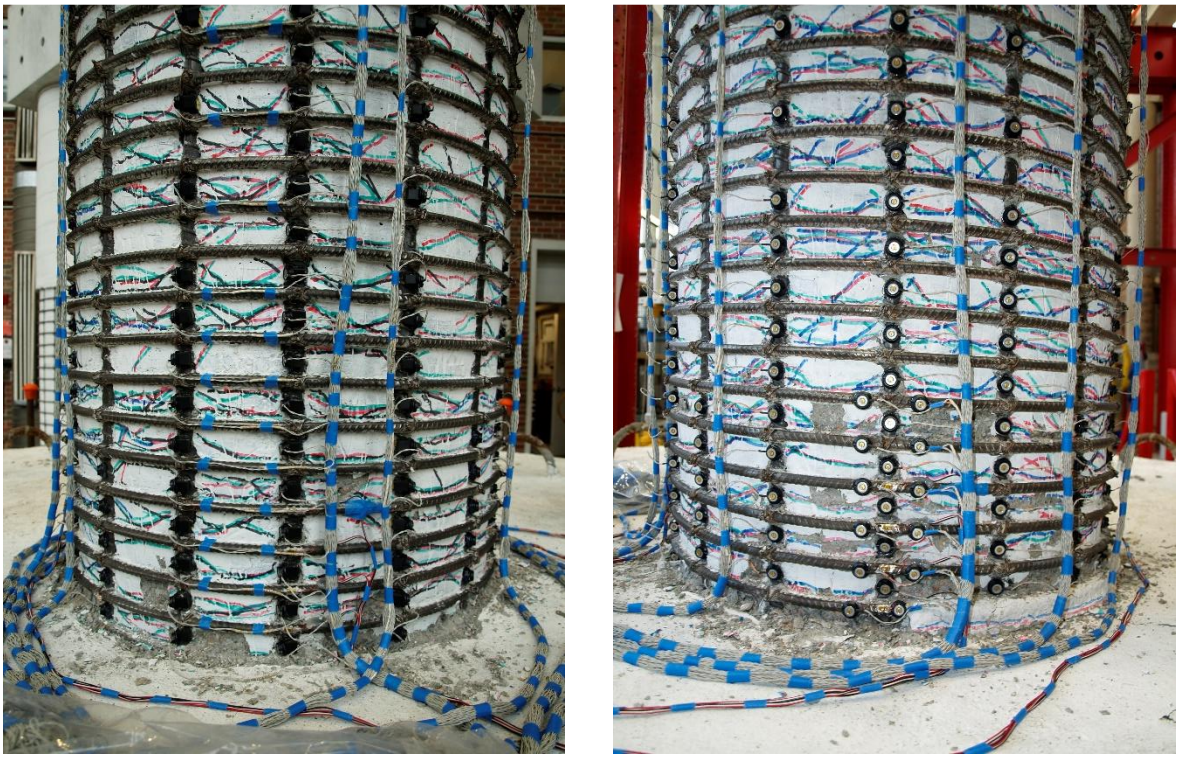

Figure 13-18. Test 10: Spiral Yielding on the (Left) West Side at $\mu_{\Delta 5}^{-1x} = -6.77"$ and (Right) South Side at $\mu_{\Delta 6}^{-1y} = -8.11"$

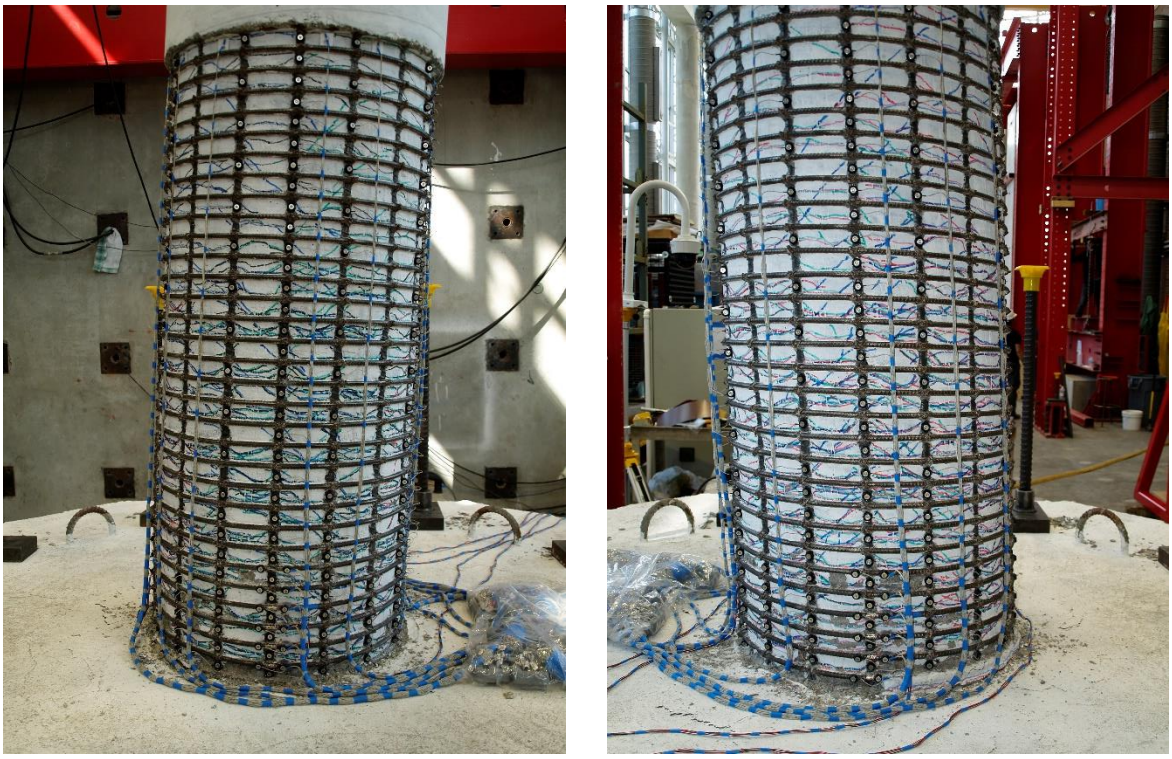

Figure 13-19. Test 10: Crack Profiles at the end of $\mu_{\Delta 5}$ on the (Left) North Side and (Right) South Side of the Column

Figure 13-20. Test 10: Crack Profiles at the end of $\mu_{\Delta 5}$ on the (Left) East Side and (Right) West Side of the Column

Figure 13-21. Test 10: Bar Buckling on the (Left) North Side at $\mu_{\Delta 6}^{+1y} = 8.15$" and (Right) East Side at $\mu_{\Delta 6}^{+1x} = 8.13$"

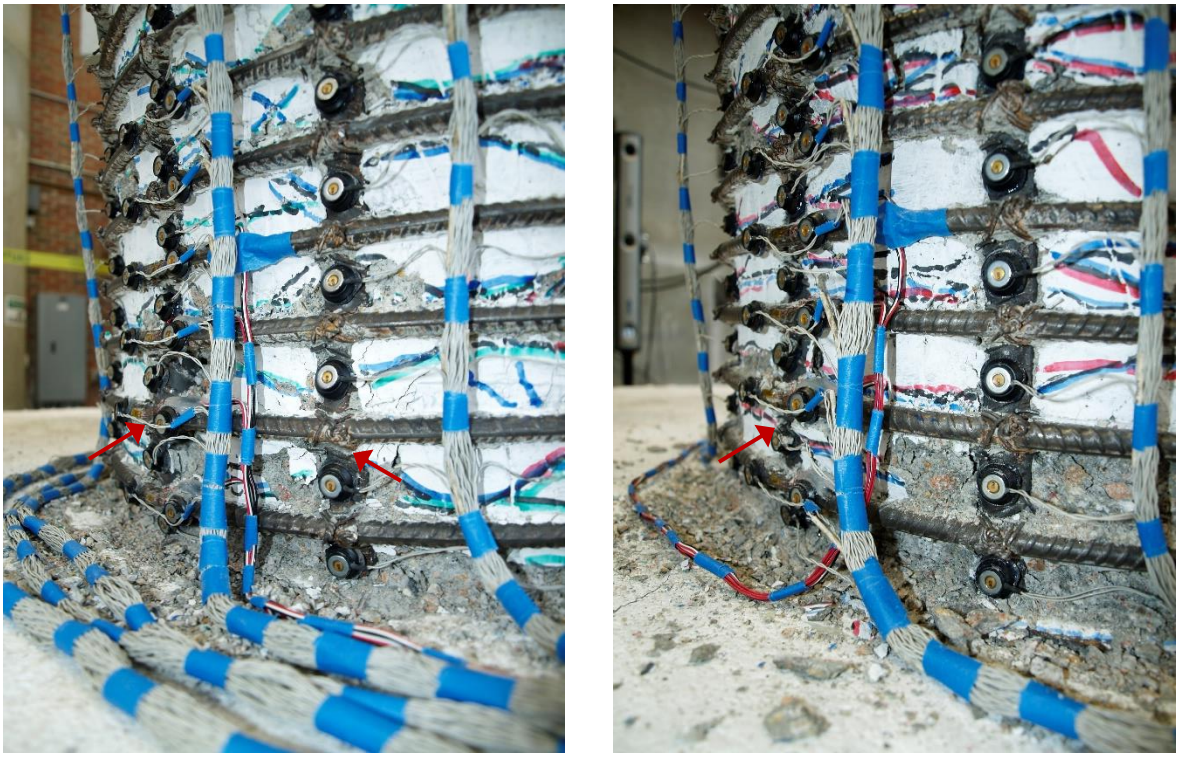

Figure 13-22. Test 10: (Left) Buckling of Bar NNW at $\mu_{\Delta 6}^{+2y} = 8.17$" and (Right) More Deformation in Bar E at $\mu_{\Delta 6}^{+2x} = 8.15$"

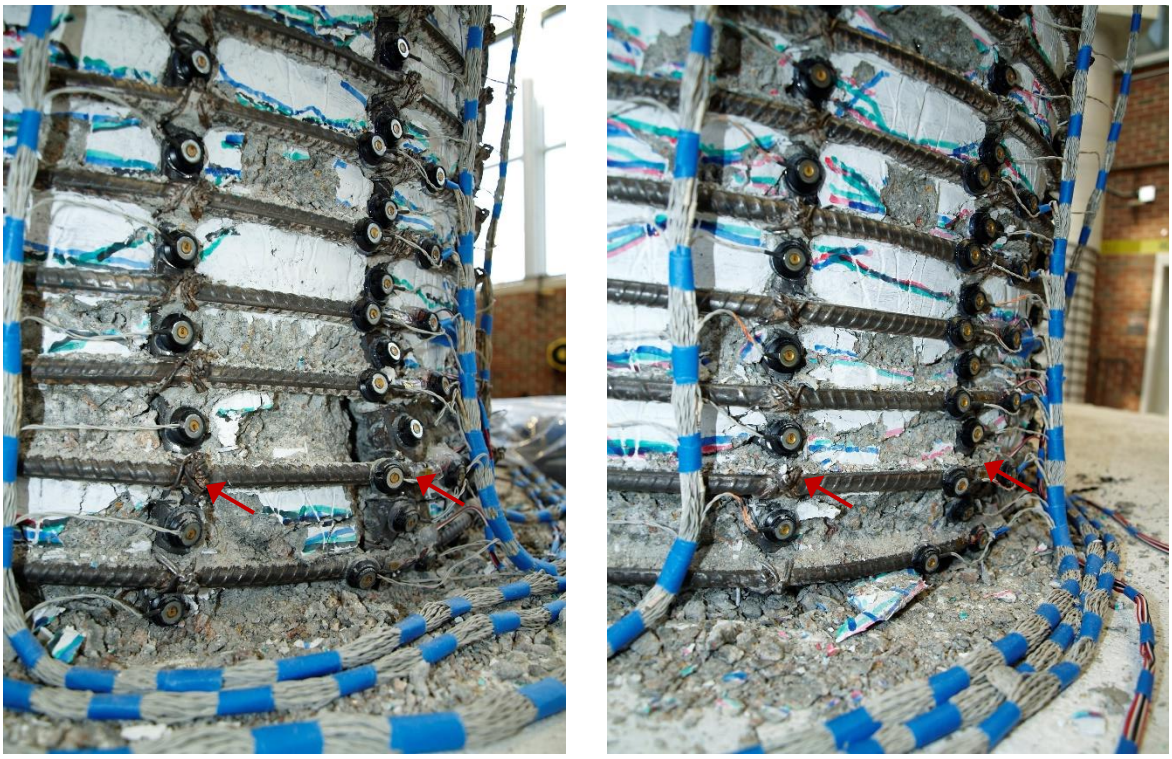

Figure 13-23. Test 10: Buckling of (Left) Bar NNE at $\mu_{\Delta 6.5}^{+1y} = 8.82$" (Right) Bars SSE, S, and SSW at $\mu_{\Delta 6.5}^{-1y} = -8.81$"

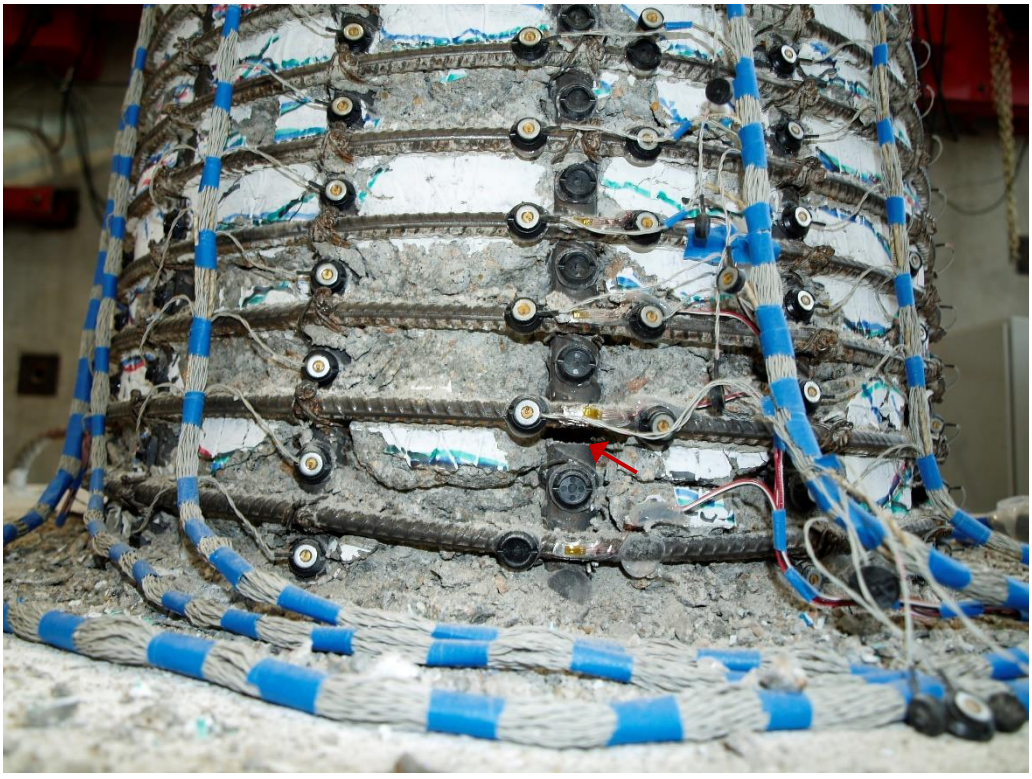

Figure 13-24. Test 10: North Bar Fracture at -8.00" during $\mu_{\Delta 6.5}^{-1y}$

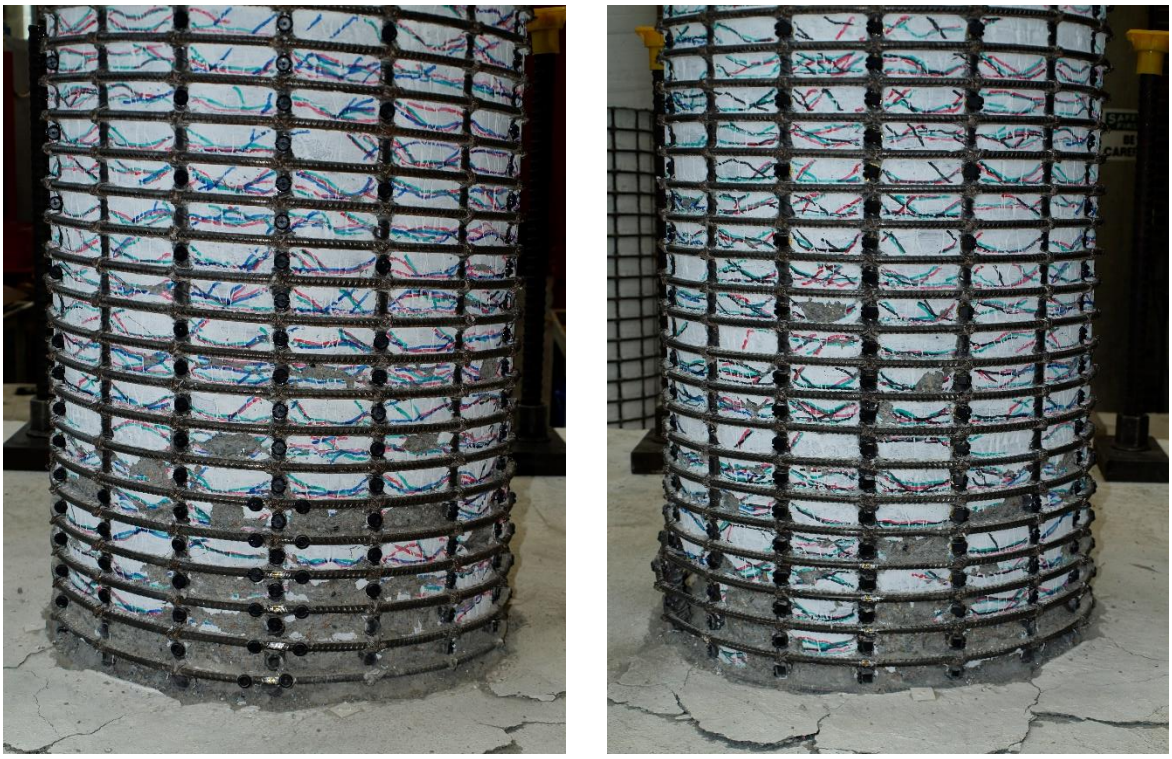

Figure 13-25. Test 10: (Left) South and (Right) West Sides of the Specimen after the Test

Figure 13-26. Test 10: (Left) North and (Right) East Sides of the Specimen after the Test

Test 10 - Strain Data Analysis

North and South Bar Strains

Vertical strain profiles for North and South reinforcement during y-direction cycles are shown in Figure 13-27 and Figure 13-28. Strains in the lowest four spiral layers during compressive y-direction cycles on the North and South sides of the specimen appear in Figure 13-29 and Figure 13-30. The relationship between strain and displacement for either peak tensile or peak compressive gauge lengths appear in Figure 13-31 through Figure 13-35. These figures contain monotonic moment curvature predictions for respective plastic hinge methods. PCK (2007) Lp refers to the (Priestley, Calvi and Kowalsky 2007) plastic hinge method, GN15 Tension/Compression Lpr refers to the (Goodnight, Kowalsky and Nau 2015a) unidirectional modified plastic hinge method, TX Measured refer to using the measured extent of plasticity and average equivalent strain penetration length from this specific test, and New Equations refers to a new bidirectional plastic hinge method which was created based on this study. Details of the new plastic hinge method appear in a later chapter of this report.

The spiral strain gauge hystereses for the first and second layers above the footing on the North side of the specimen is shown in Figure 13-38 and Figure 13-39. The strain gauge over the second layer went off scale during $\mu_{\Delta 5}^{+2y} = 6.76$", even though the North reinforcement remained visibly straight. Tension strains the first layer increased during $\mu_{\Delta 6}^{+1y} = 8.15$" as the North extreme fiber bar visibly buckled, see Figure 13-21. The visual observation of bar buckling was confirmed upon inspection of the North longitudinal bar strain hysteresis in Figure 13-36 and Figure 13-37; however, there was significant measurable outward deformation in the previous compressive cycle.

The spiral strain gauge hysteresis for the second layer above the footing on the South side of the specimen is shown in Figure 13-41. Tension strains in this layer increased during $\mu_{\Delta 6.5}^{-1y} = -8.81$" as three South bars buckled simultaneously, see Figure 13-23. The visual observation of bar buckling was confirmed upon inspection of the South longitudinal bar strain hysteresis in Figure 13-40; however, there was slight measurable outward deformation in the previous compressive cycle.

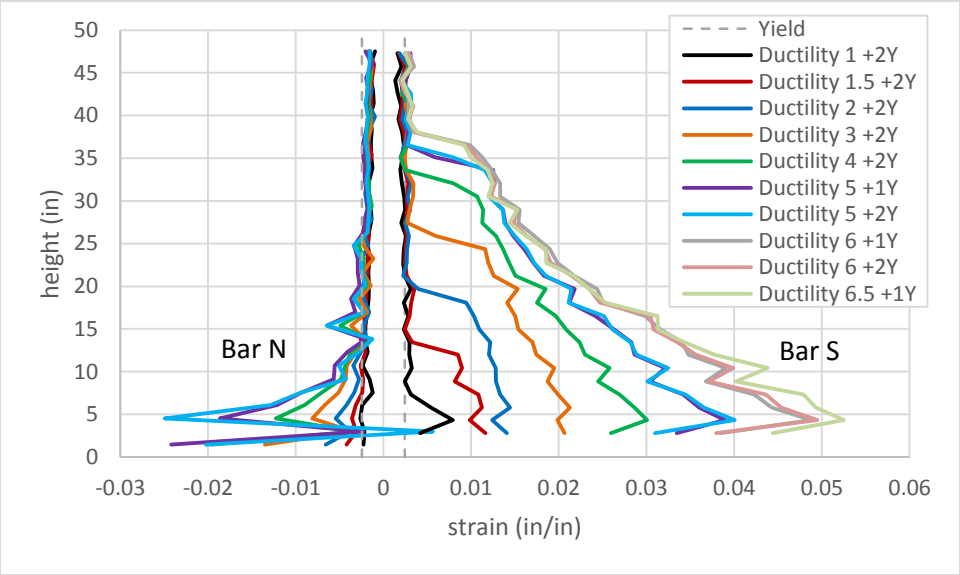

Figure 13-27. Test 10: Vertical Strain Profiles for Loading in the +Y-direction

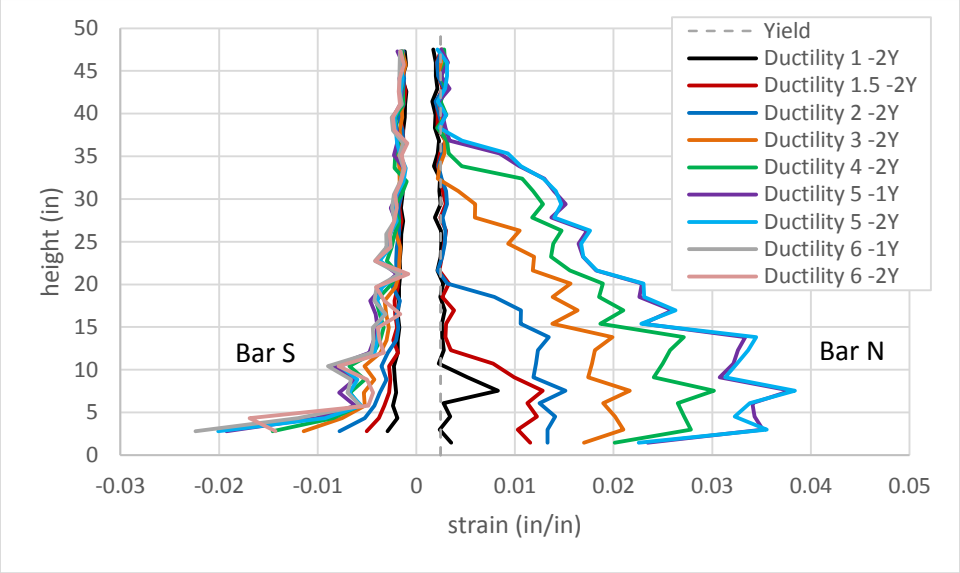

Figure 13-28. Test 10: Vertical Strain Profiles for Loading in the -Y-direction

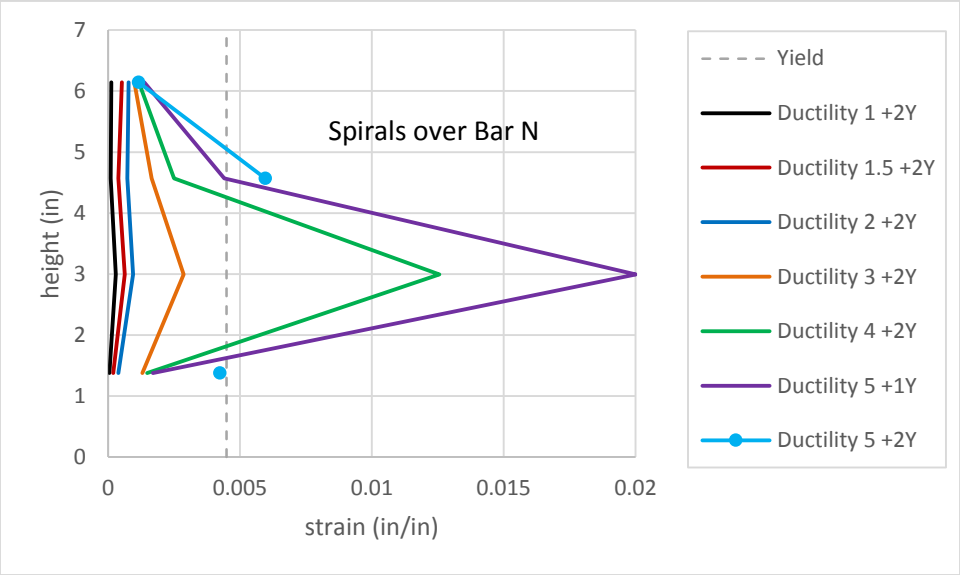

Figure 13-29. Test 10: Spiral Strains Measured Over the North Extreme Fiber Bar during +Y Cycles

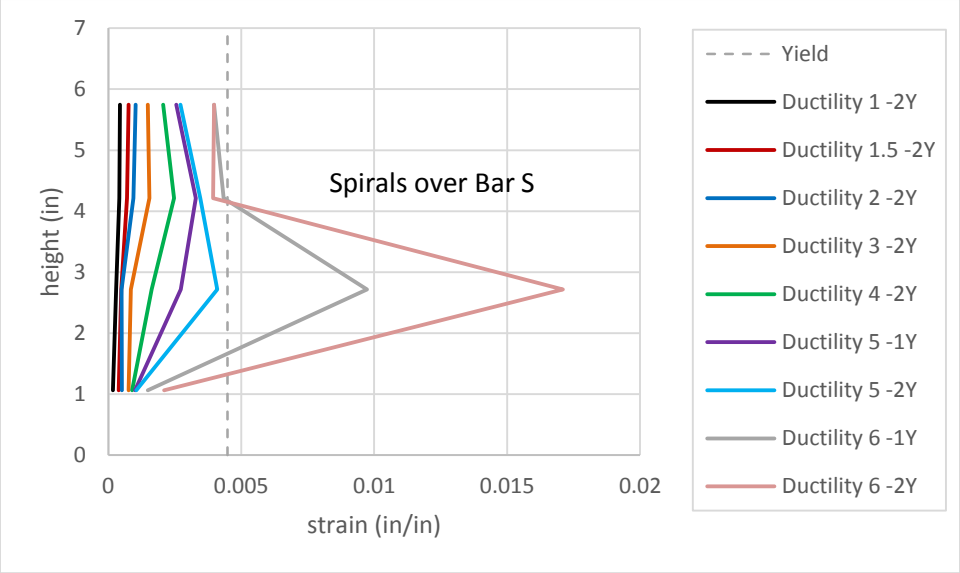

Figure 13-30. Test 10: Spiral Strains Measured Over the South Extreme Fiber Bar during -Y Cycles

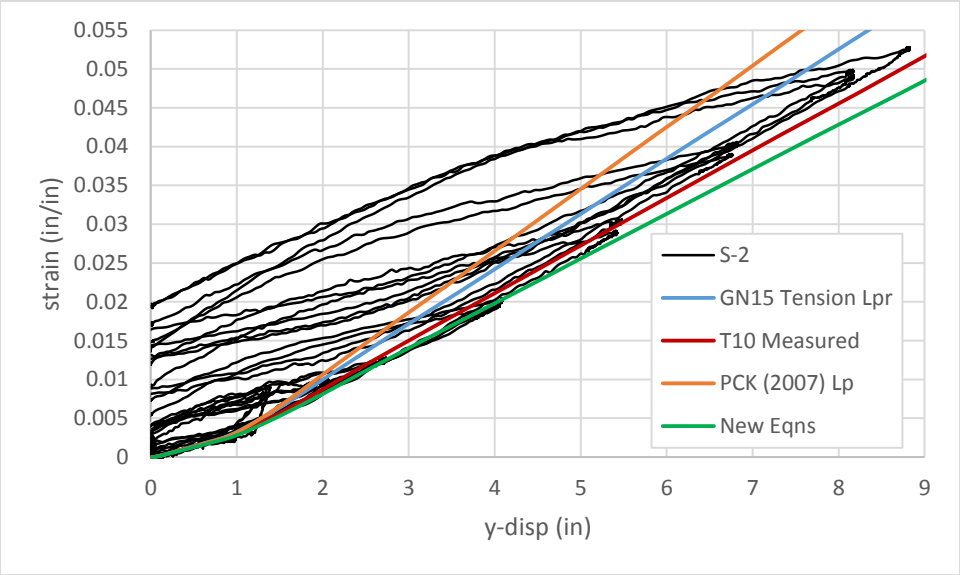

Figure 13-31. Test 10: Tension Strain-Disp. for Bar S (Gauge Length 2 Centered 4.33" above the Footing)

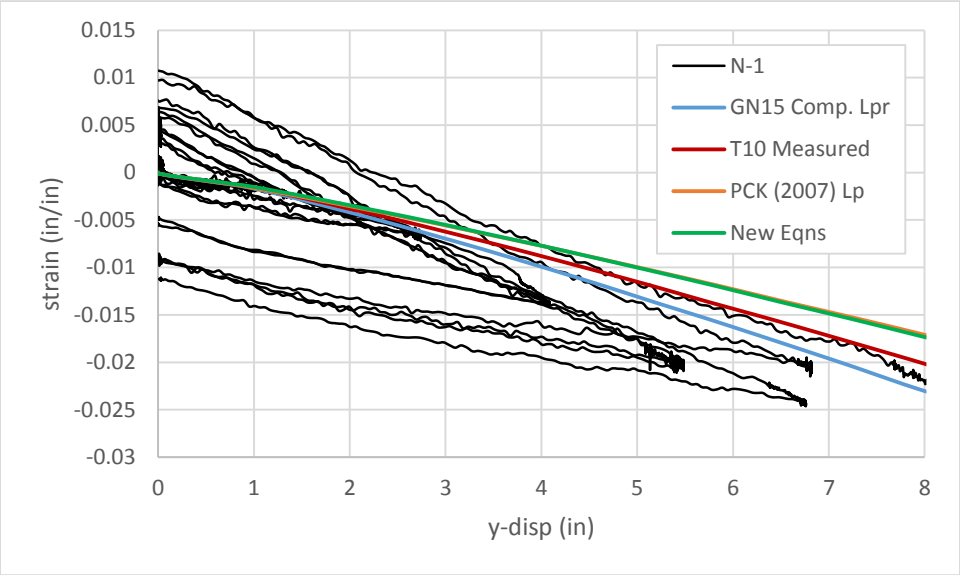

Figure 13-32. Test 10: Compression Strain-Disp. for Bar N (Gauge Length 1 Centered 1.46" above the Footing)

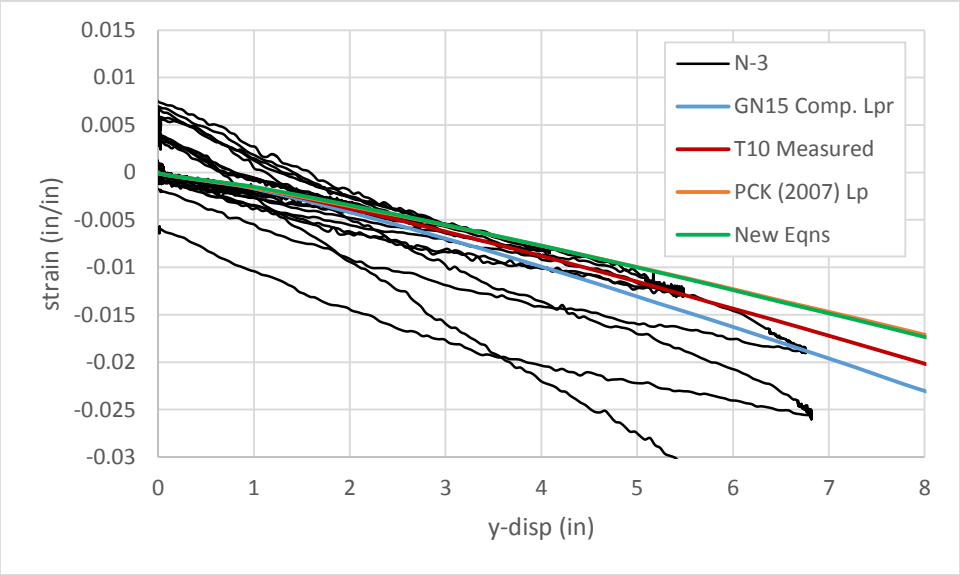

Figure 13-33. Test 10: Compression Strain-Disp. for Bar N (Gauge Length 3 Centered 4.53" above the Footing)

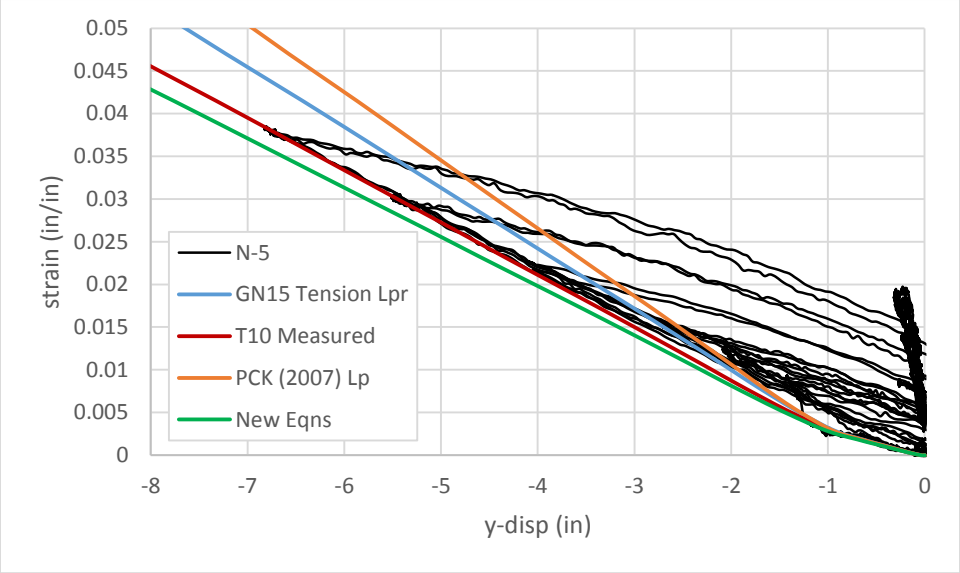

Figure 13-34. Test 10: Tension Strain-Disp. for Bar N (Gauge Length 5 Centered 7.56" above the Footing)

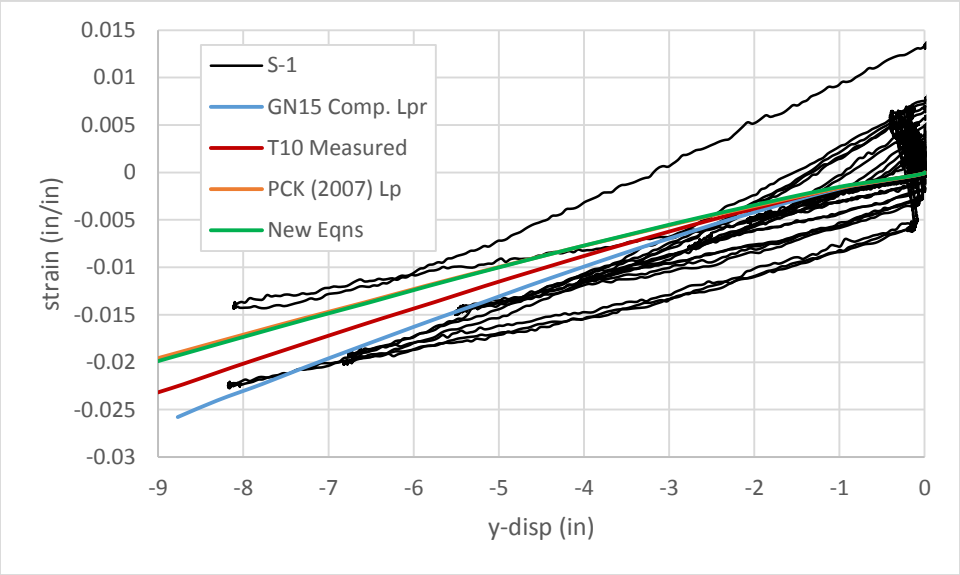

Figure 13-35. Test 10: Compression Strain-Disp. for Bar S (Gauge Length 1 Centered 2.80" above the Footing)

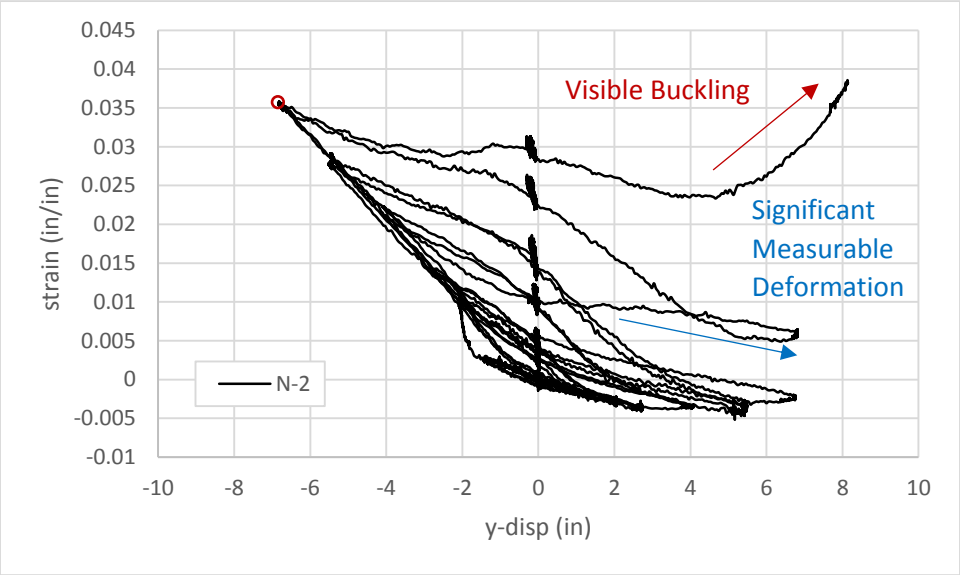

Figure 13-36. Test 10: Strain Hysteresis over the North Buckled Bar (Gauge Length 2 Centered 2.98" above the Footing)

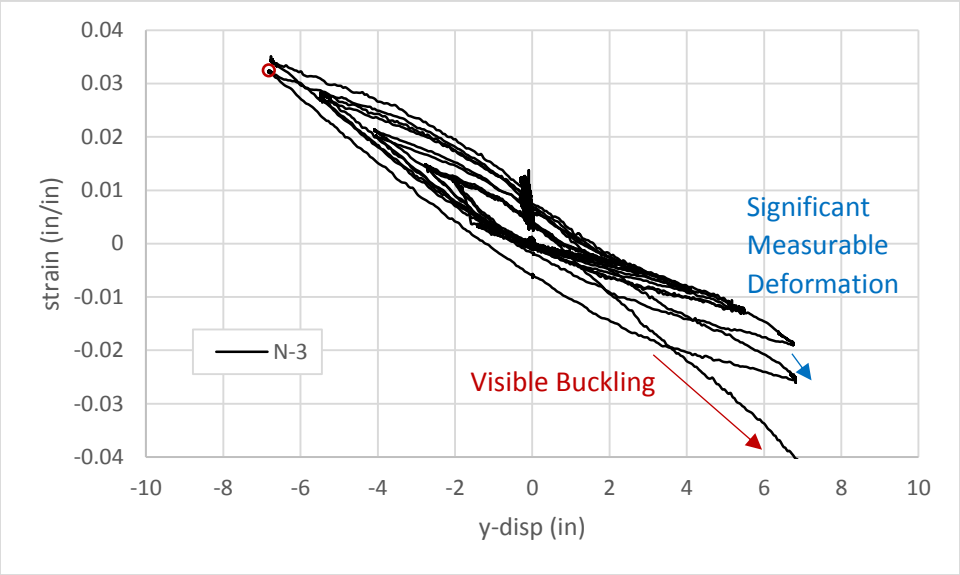

Figure 13-37. Test 10: Strain Hysteresis over the North Buckled Bar (Gauge Length 3 Centered 4.53" above the Footing)

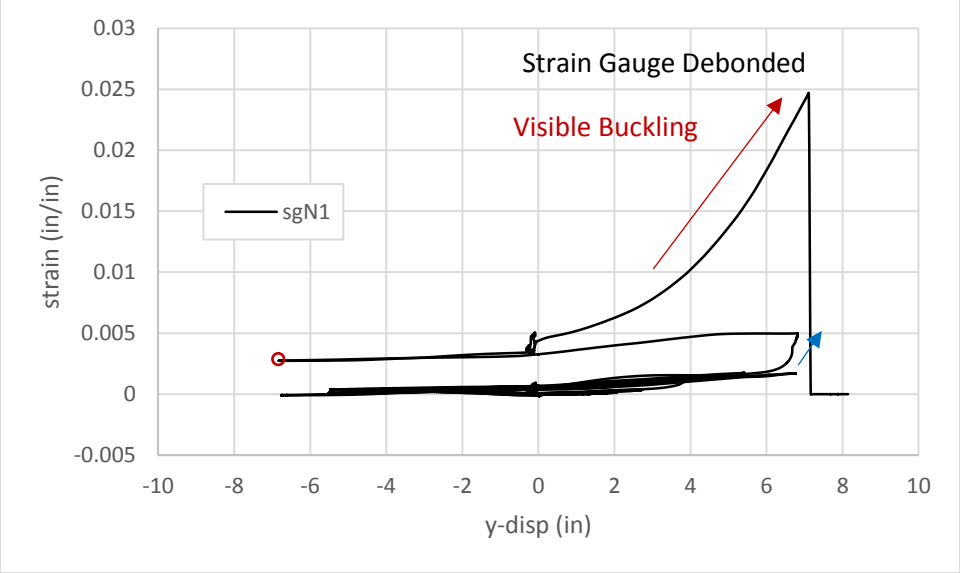

Figure 13-38. Test 10: Spiral Strain Hysteresis for the 1st North Layer above the Footing

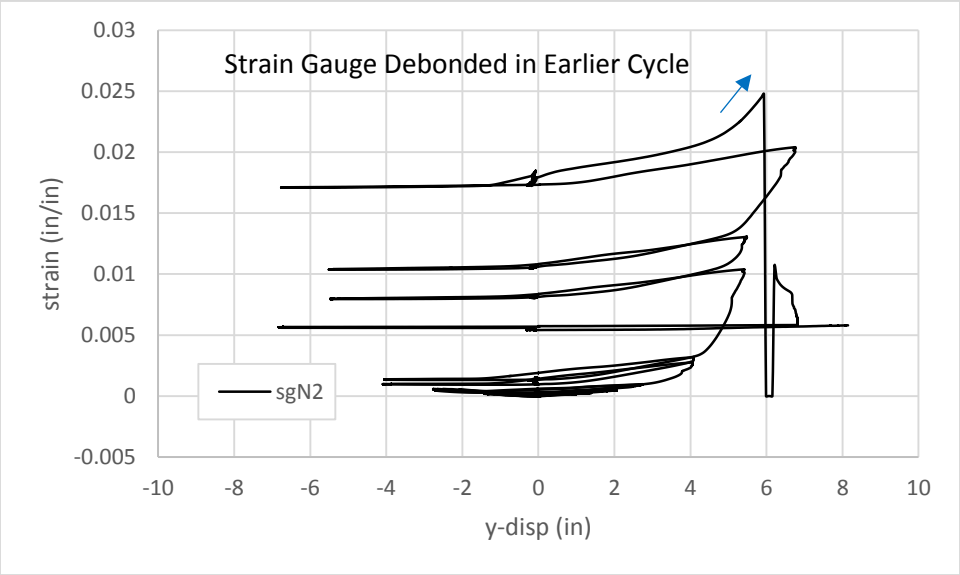

Figure 13-39. Test 10: Spiral Strain Hysteresis for the 2nd North Layer above the Footing

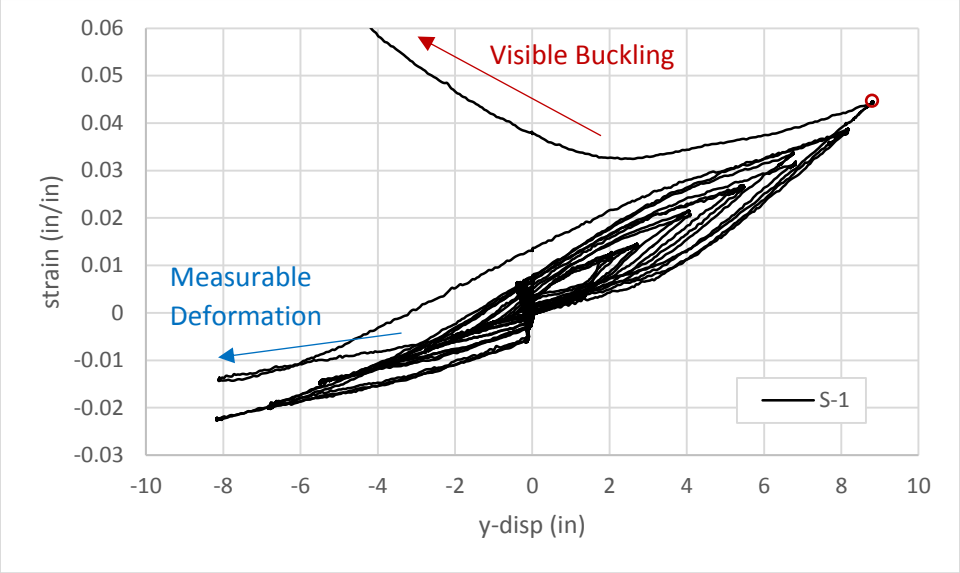

Figure 13-40. Test 10: Strain Hysteresis over the South Buckled Bar (Gauge Length 1 Centered 2.80" above the Footing)

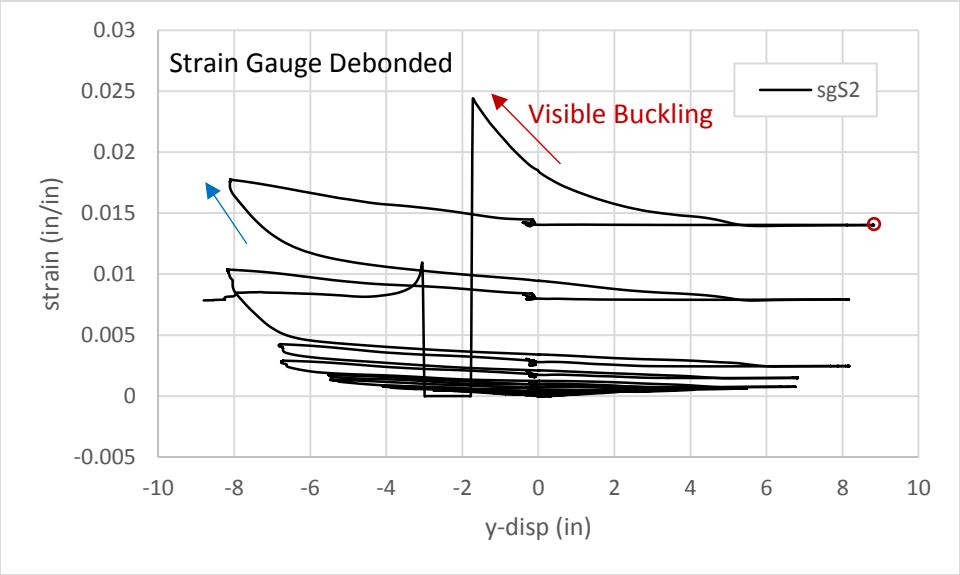

Figure 13-41. Test 10: Spiral Strain Hysteresis for the 2nd South Layer above the Footing

East and West Bar Strains

Vertical strain profiles for East and West reinforcement during x-direction cycles are shown in Figure 13-42 and Figure 13-43. Strains in the lowest four spiral layers during compressive x-direction cycles on the East and West sides of the specimen appear in Figure 13-44 and Figure 13-45. The relationship between strain and displacement for either peak tensile or peak compressive gauge lengths appear in Figure 13-46 through Figure 13-50. These figures contain monotonic moment curvature predictions for respective plastic hinge methods. PCK (2007) Lp refers to the (Priestley, Calvi and Kowalsky 2007) plastic hinge method, GN15 Tension/Compression Lpr refers to the (Goodnight, Kowalsky and Nau 2015a) unidirectional modified plastic hinge method, TX Measured refer to using the measured extent of plasticity and average equivalent strain penetration length from this specific test, and New Equations refers to a new bidirectional plastic hinge method which was created based on this study. Details of the new plastic hinge method appear in a later chapter of this report.

The spiral strain gauge hystereses for the first and second layers above the footing on the East side of the specimen is shown in Figure 13-52 and Figure 13-53. The strain gauge over the second layer went off scale during $\mu_{\Delta 5}^{+2x} = 6.80$", even though the East reinforcement remained visibly straight. Tension strains in the second spiral layer increased during $\mu_{\Delta 6}^{+1x} = 8.13$" as the East extreme fiber bar visibly buckled, see Figure 13-21. The visual observation of bar buckling was confirmed upon inspection of the East longitudinal bar strain hysteresis in Figure 13-51; however, there was slight measurable outward deformation in the previous compressive cycle.

The spiral strain gauge hysteresis for the second layer above the footing on the West side of the specimen is shown in Figure 13-56. The South reinforcement never visibly buckled; however, there was slight measurable outward deformation in the final compressive cycle as shown in Figure 13-54 and Figure 13-55.

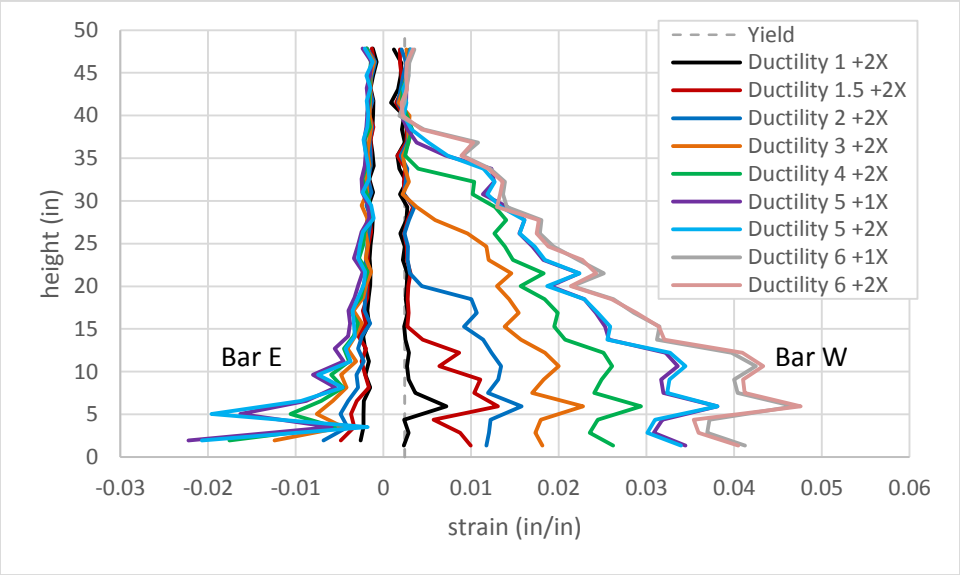

Figure 13-42. Test 10: Vertical Strain Profiles for Loading in the +X-direction

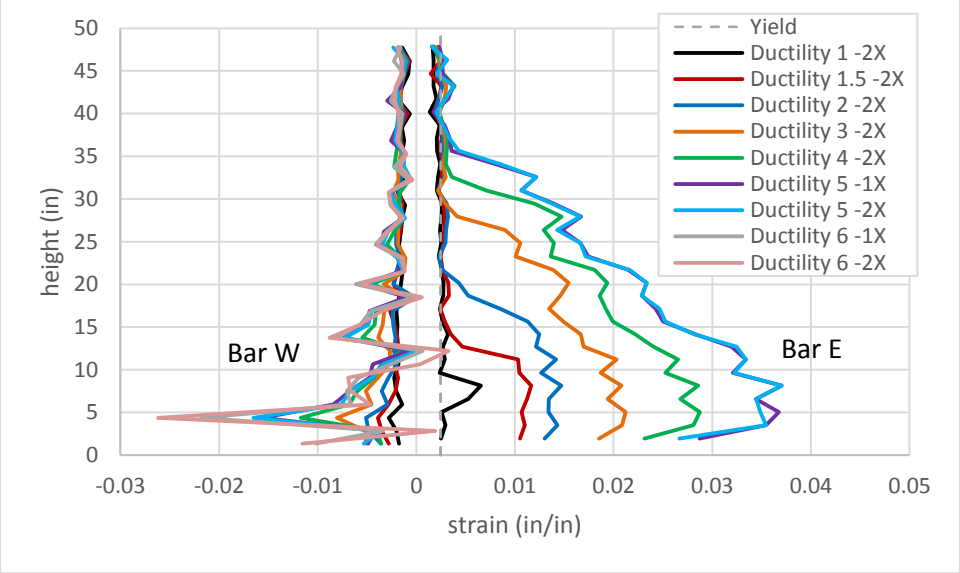

Figure 13-43. Test 10: Vertical Strain Profiles for Loading in the -X-direction

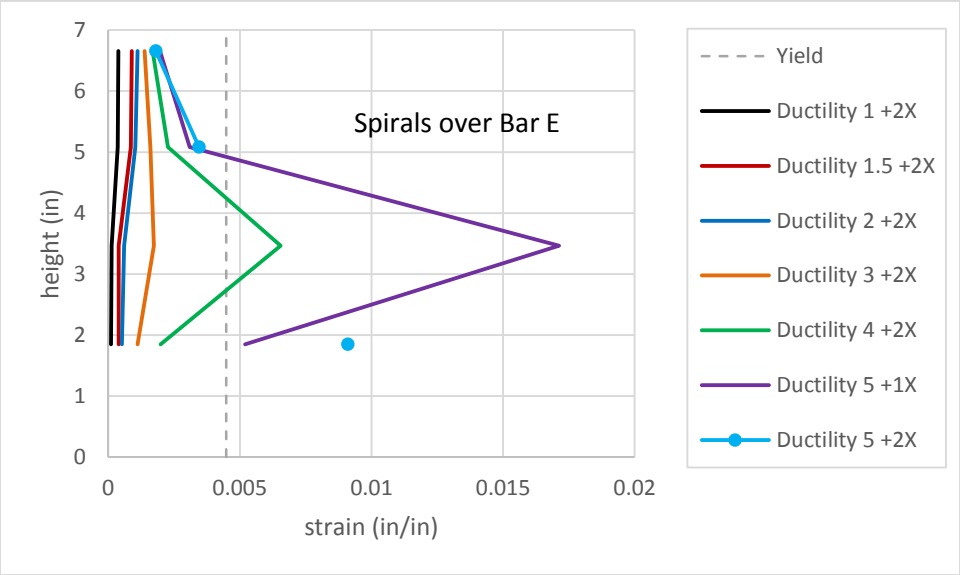

Figure 13-44. Test 10: Spiral Strains Measured Over the East Extreme Fiber Bar during +X Cycles

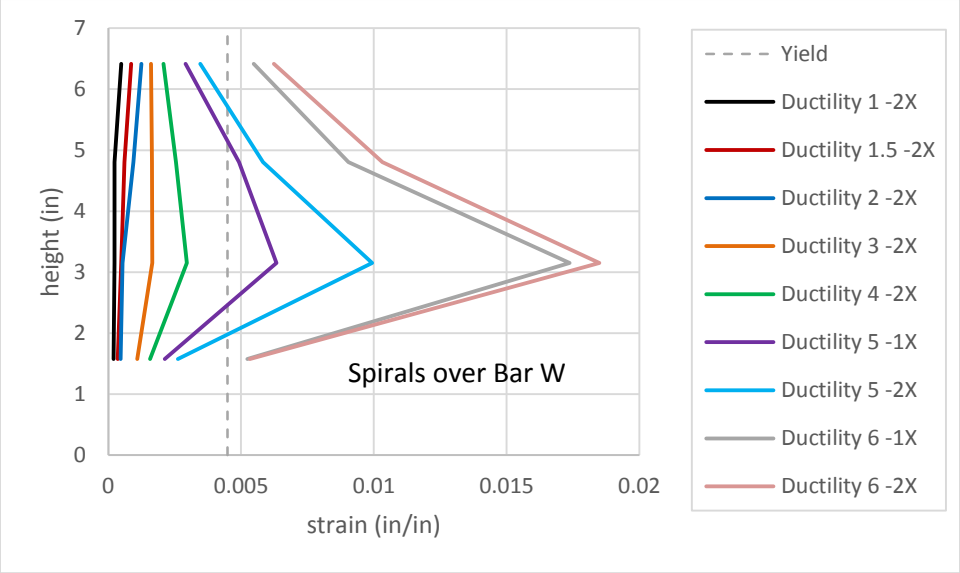

Figure 13-45. Test 10: Spiral Strains Measured Over the West Extreme Fiber Bar during -X Cycles

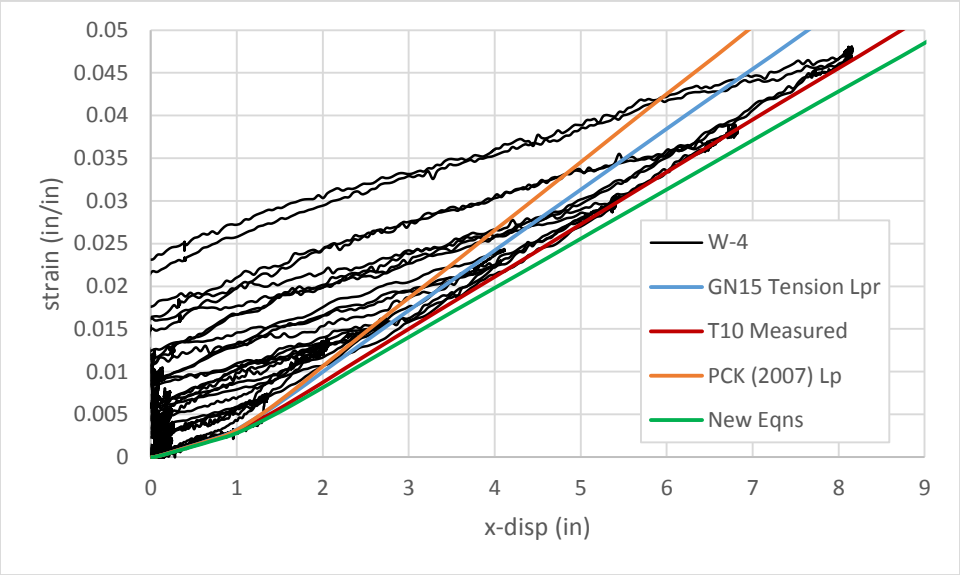

Figure 13-46. Test 10: Tension Strain-Disp. for Bar W (Gauge Length 4 Centered 5.95" above the Footing)

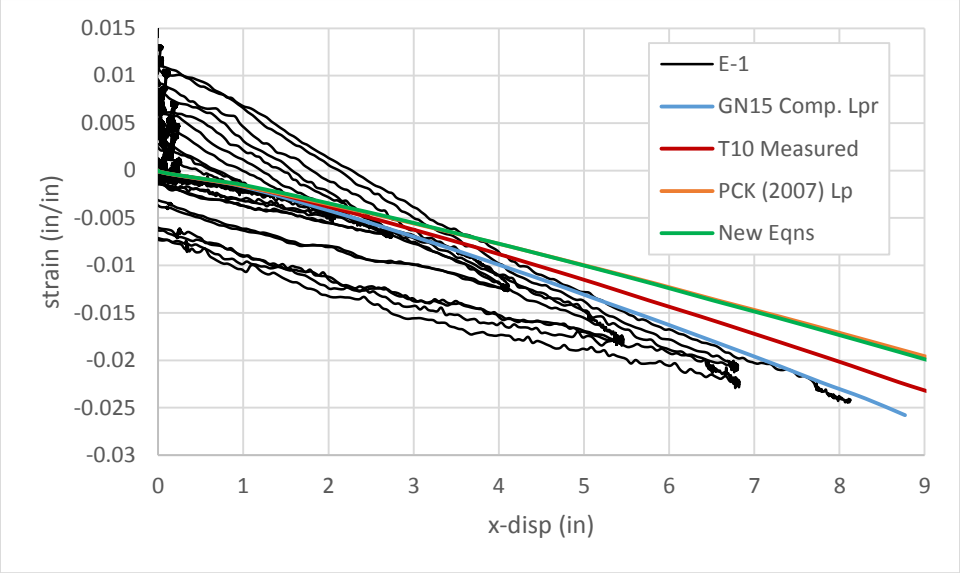

Figure 13-47. Test 10: Compression Strain-Disp. for Bar E (Gauge Length 3 Centered 1.93" above the Footing)

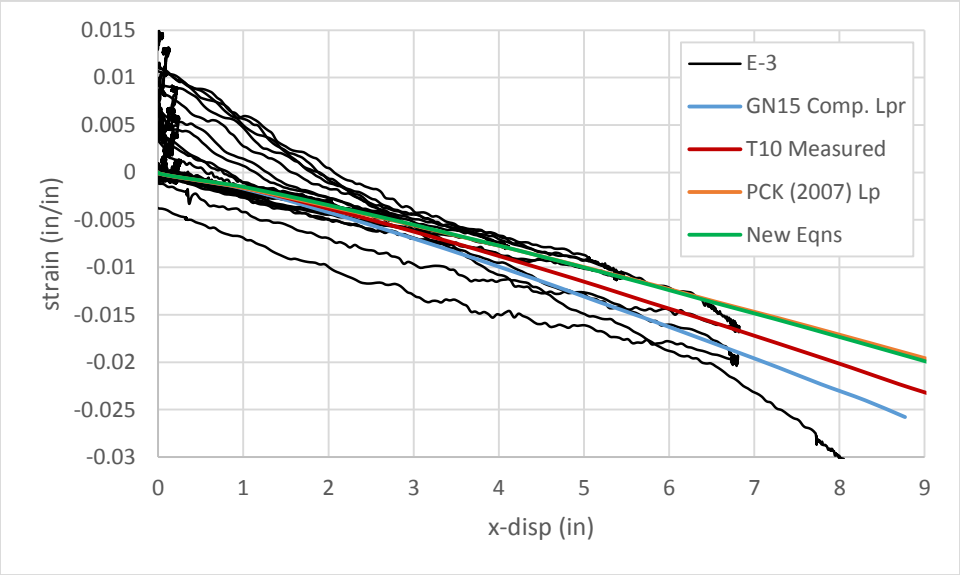

Figure 13-48. Test 10: Compression Strain-Disp. for Bar E (Gauge Length 3 Centered 5.04" above the Footing)

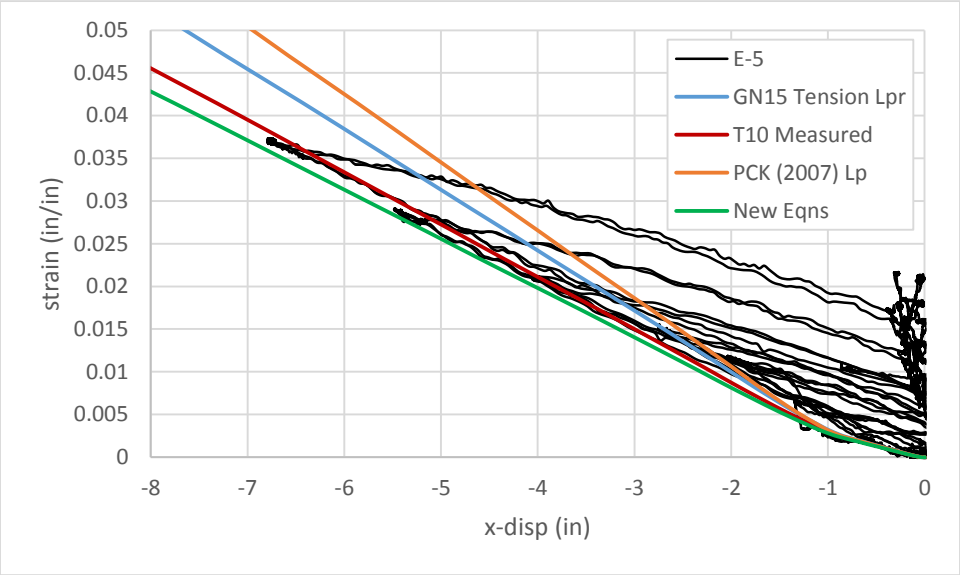

Figure 13-49. Test 10: Tension Strain-Disp. for Bar E (Gauge Length 5 Centered 8.14" above the Footing)

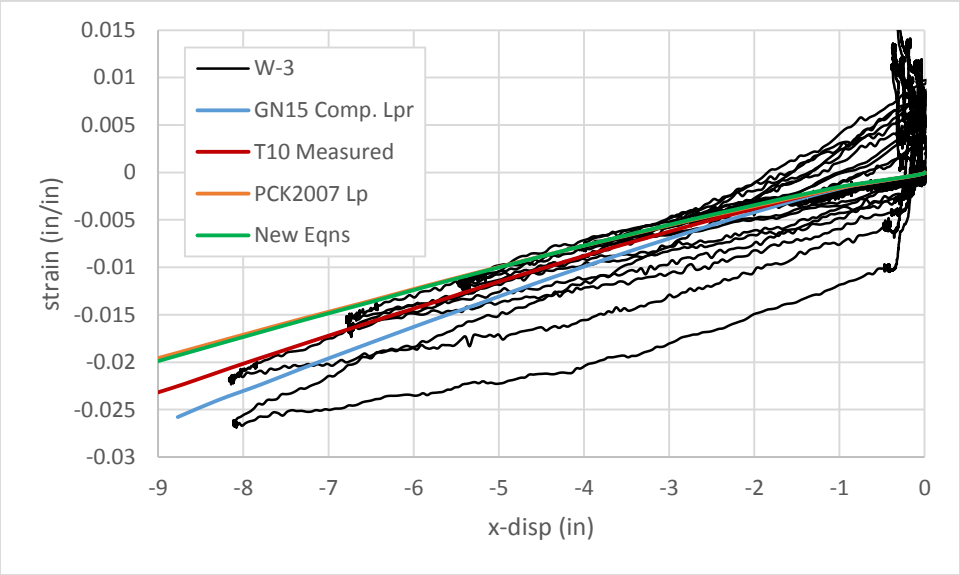

Figure 13-50. Test 10: Compression Strain-Disp. for Bar W (Gauge Length 3 Centered 4.38" above the Footing)

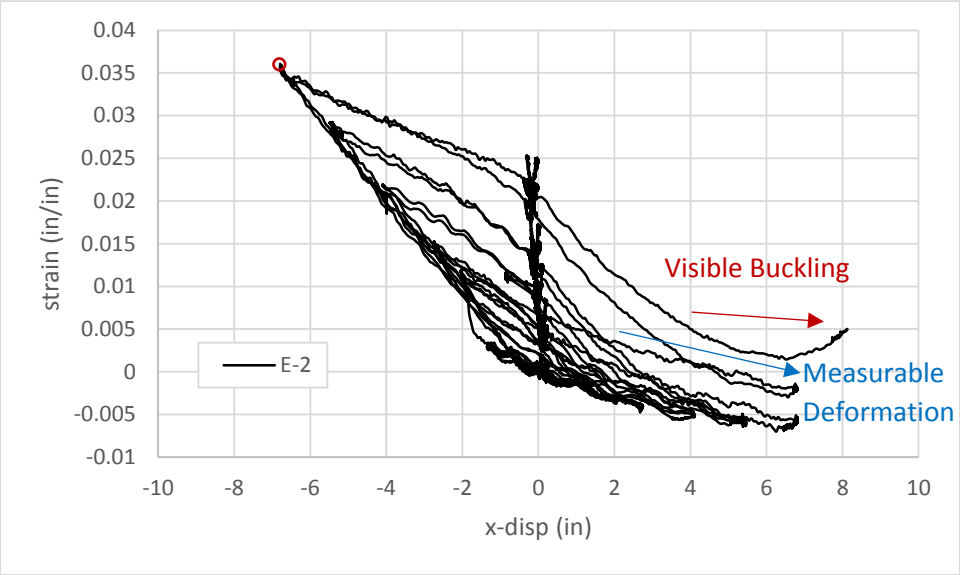

Figure 13-51. Test 10: Strain Hysteresis over the East Buckled Bar (Gauge Length 2 Centered 3.51" above the Footing)

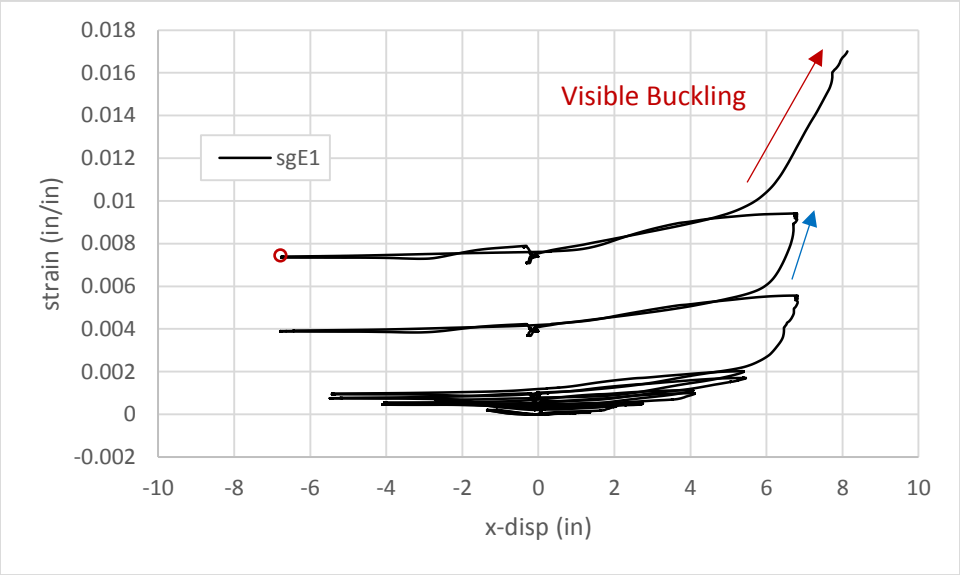

Figure 13-52. Test 10: Spiral Strain Hysteresis for the 1st East Layer above the Footing

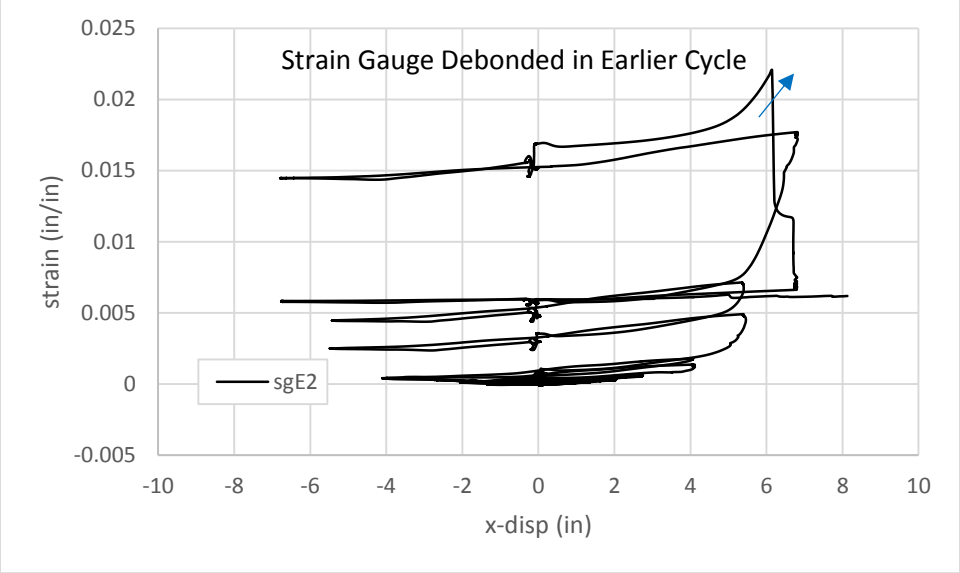

Figure 13-53. Test 10: Spiral Strain Hysteresis for the 2nd East Layer above the Footing

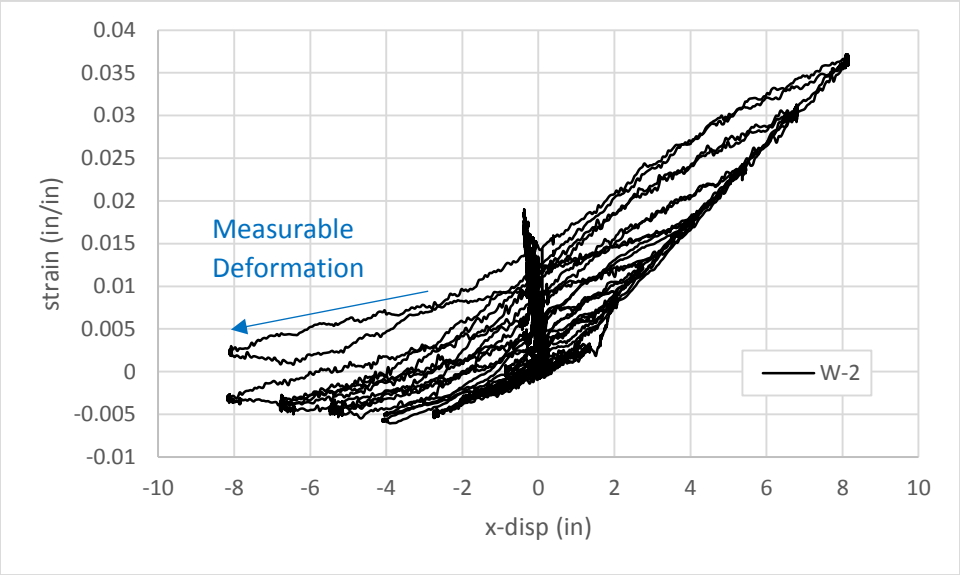

Figure 13-54. Test 10: Strain Hysteresis over the West Buckled Bar (Gauge Length 2 Centered 2.84" above the Footing)

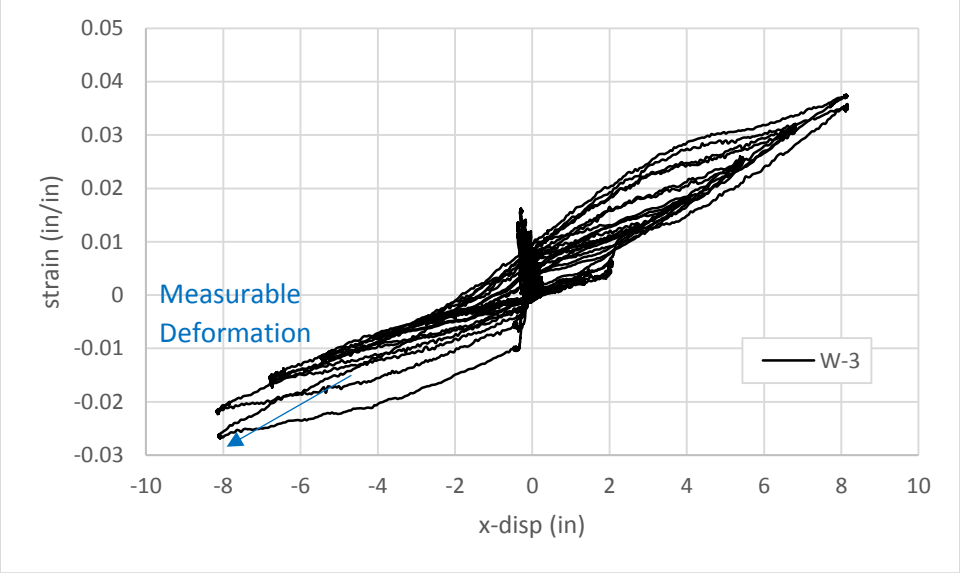

Figure 13-55. Test 10: Strain Hysteresis over the West Buckled Bar (Gauge Length 2 Centered 4.38" above the Footing)

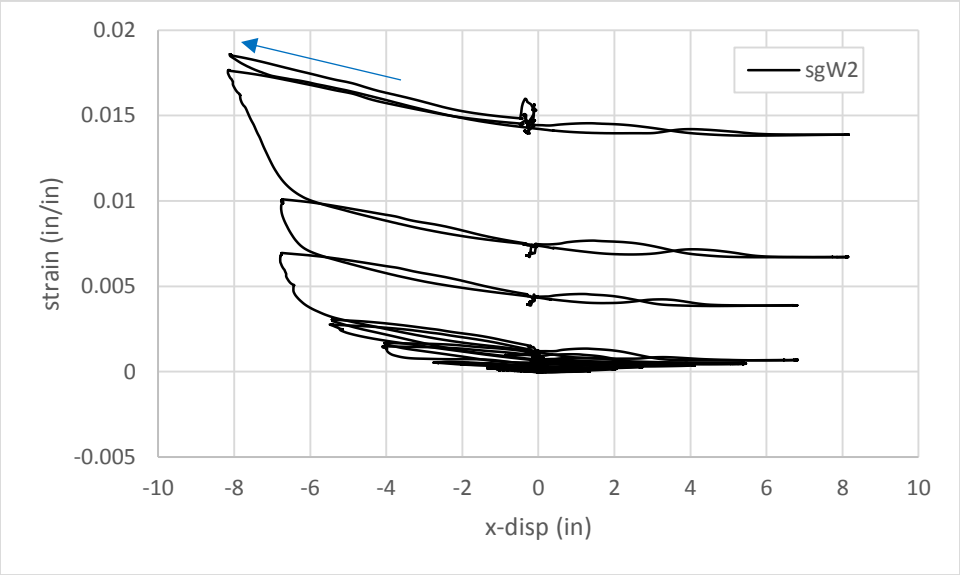

Figure 13-56. Test 10: Spiral Strain Hysteresis for the 2nd West Layer above the Footing

Test 10 - Curvature and Strain Penetration Data

Curvature and stain penetration data for Test 10 is presented in the following section. The methods in which this data was generated are outlined in the summary for Test 1. Sample cross section curvature profiles are shown in Figure 13-57 and Figure 13-58. Vertical curvature profiles for respective loading directions appear in Figure 13-59 through Figure 13-63. Fixed-end rotations attributable to strain penetration of longitudinal reinforcement into the footing are shown in Figure 13-64 through Figure 13-66. Comparison of the measured displacements to those obtained via integration of the measured curvature profiles and extrapolation of the fixed-end rotation to the center of the applied lateral load are shown in Figure 13-67 and Figure 13-68.

The measured extent of plasticity is compared to design recommendations for the tensile triangular plastic hinge length in Figure 13-69. GN15 refers to the (Goodnight, Kowalsky and Nau 2015a) unidirectional tensile hinge length while New Equations refers to a new bidirectional plastic hinge method which was created based on this study. Details of the new plastic hinge method appear in a later chapter of this report. The measured equivalent strain penetration lengths are compared to design recommendations in Figure 13-70. GN15 refers to the (Goodnight, Kowalsky and Nau 2015a) unidirectional Lsp while PCK (2007) refers to the (Priestley, Calvi and Kowalsky 2007) definition of Lsp. Finally, the measured hysteretic response is compared to monotonic predictions in Figure 13-71 and Figure 13-72.

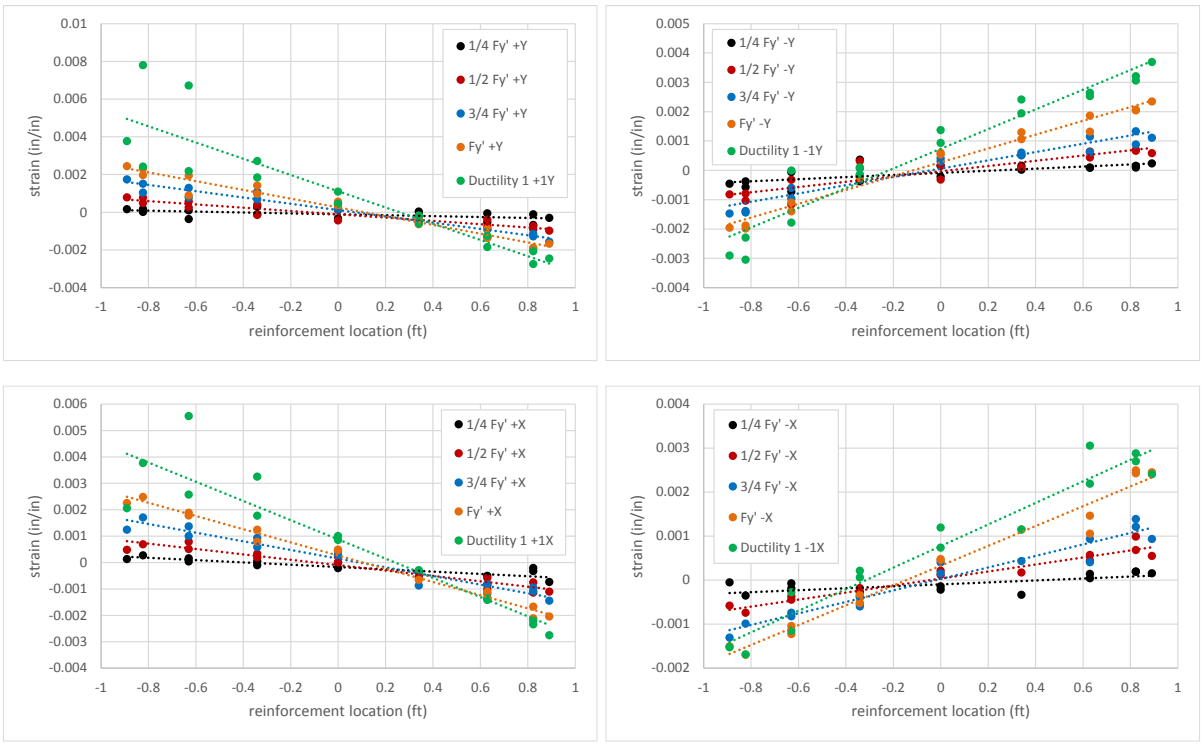

Figure 13-57. Test 10: Elastic Curvature Profiles for the First Instrumented Section above the Footing

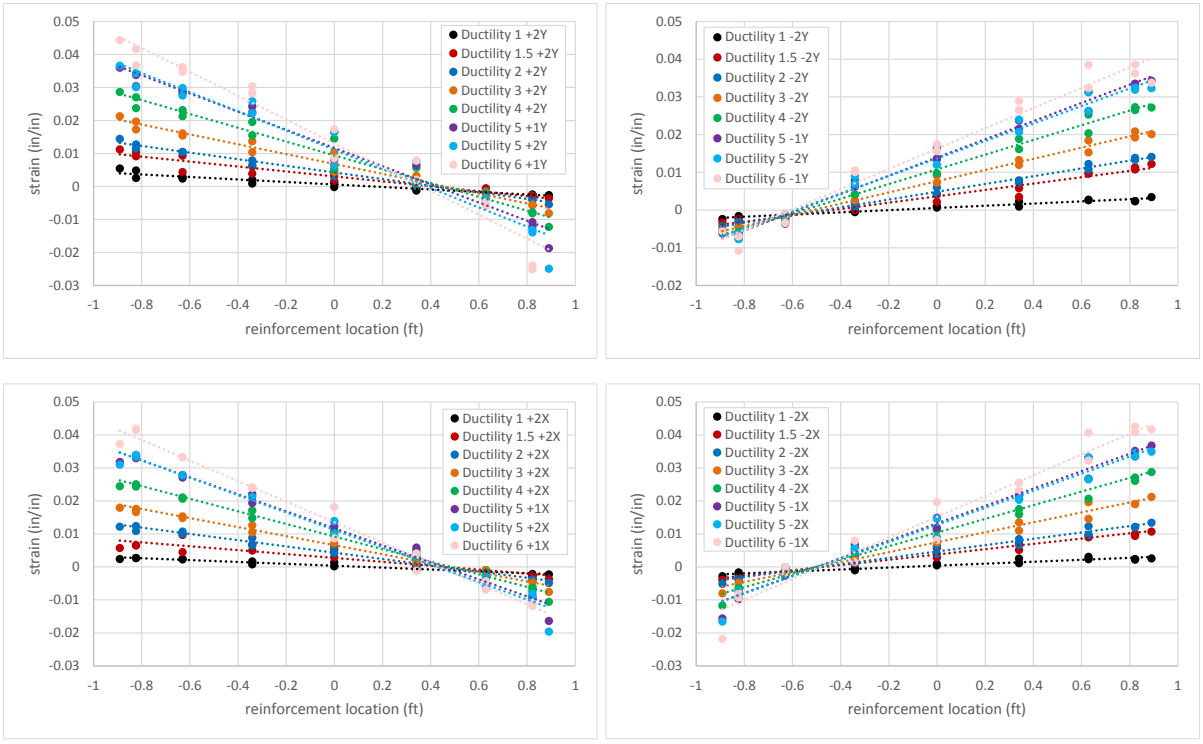

Figure 13-58. Test 10: Curvature Profiles for the Third Instrumented Section above the Footing

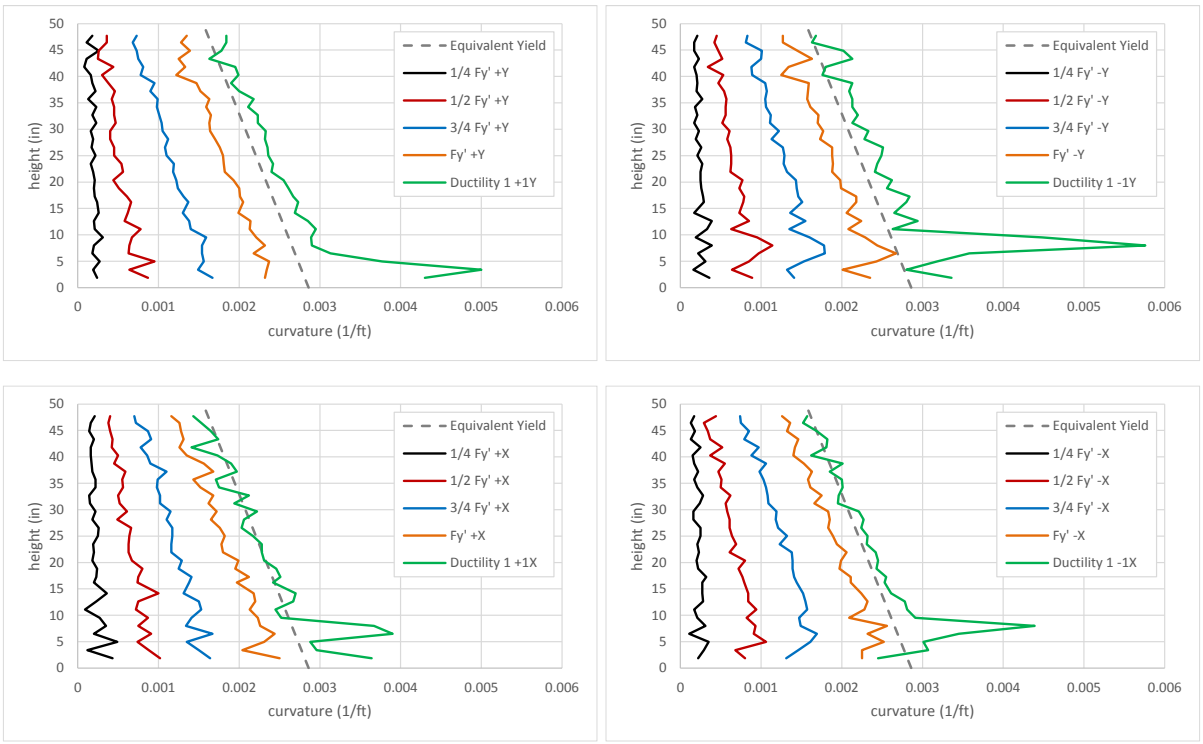

Figure 13-59. Test 10: Elastic Vertical Curvature Profiles

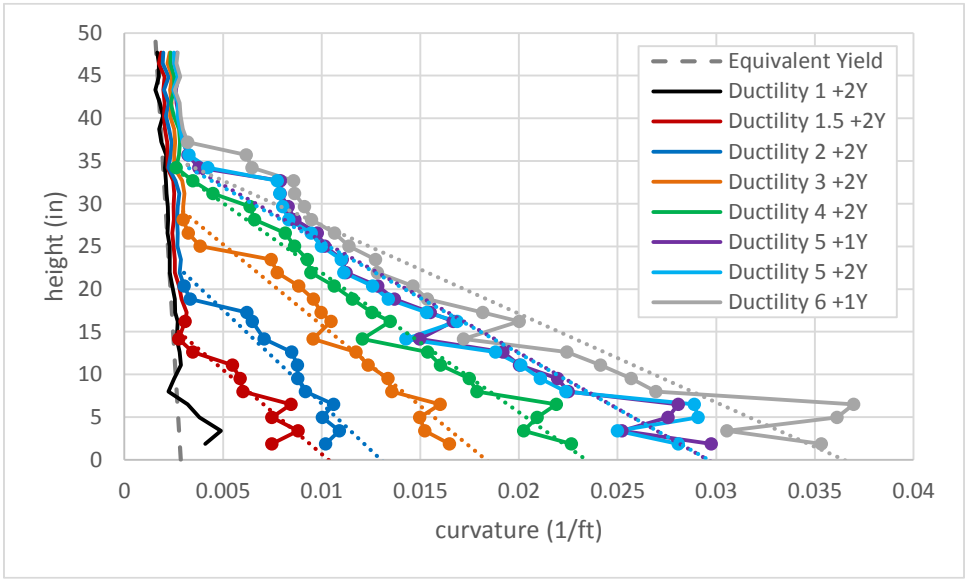

Figure 13-60. Test 10: Vertical Curvature Profiles for Loading in the +Y-direction

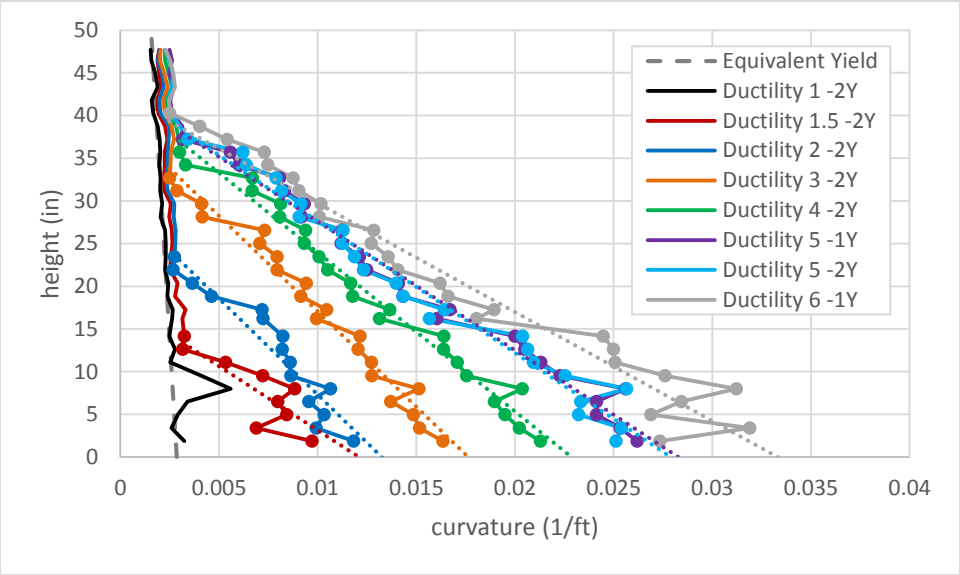

Figure 13-61. Test 10: Vertical Curvature Profiles for Loading in the -Y-direction

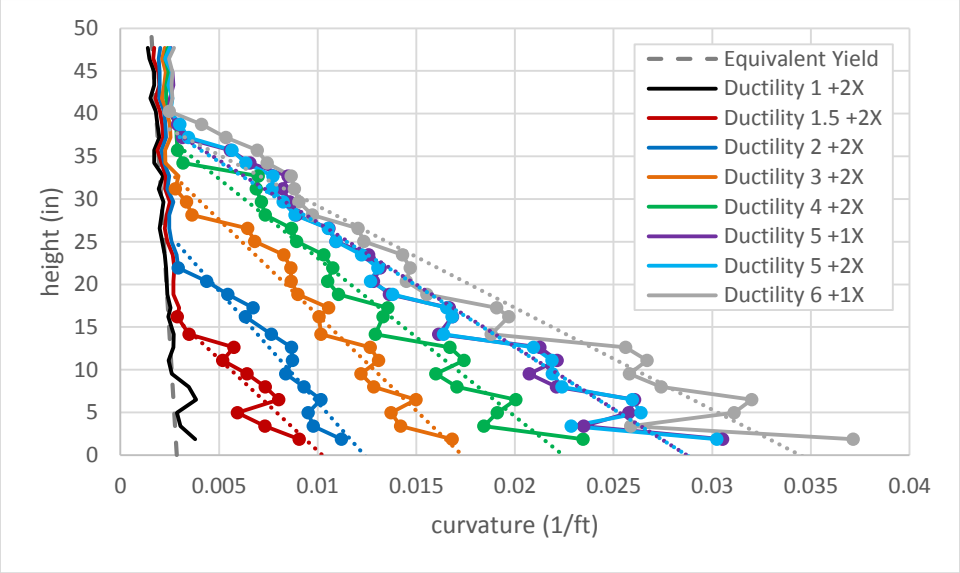

Figure 13-62. Test 10: Vertical Curvature Profiles for Loading in the +X-direction

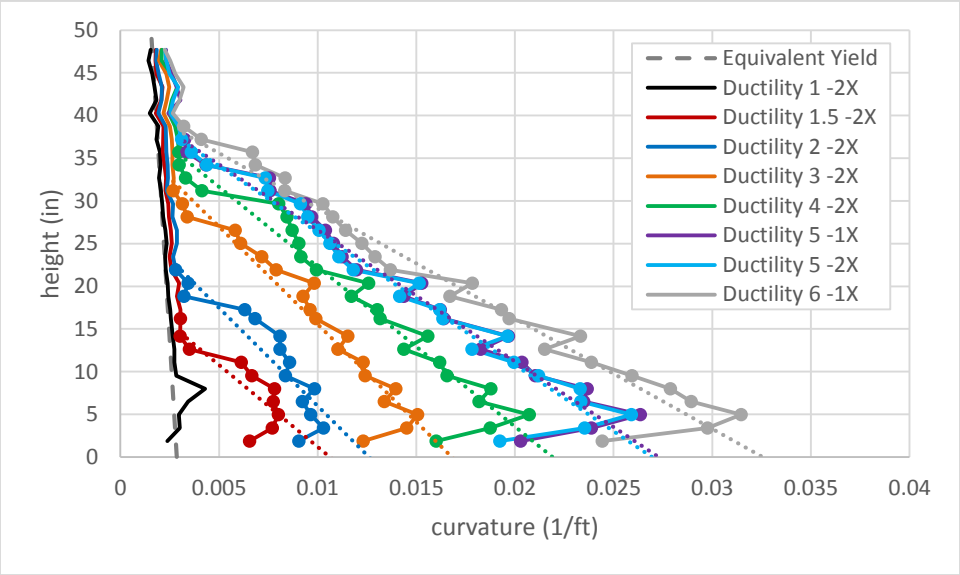

Figure 13-63. Test 10: Vertical Curvature Profiles for Loading in the -X-direction

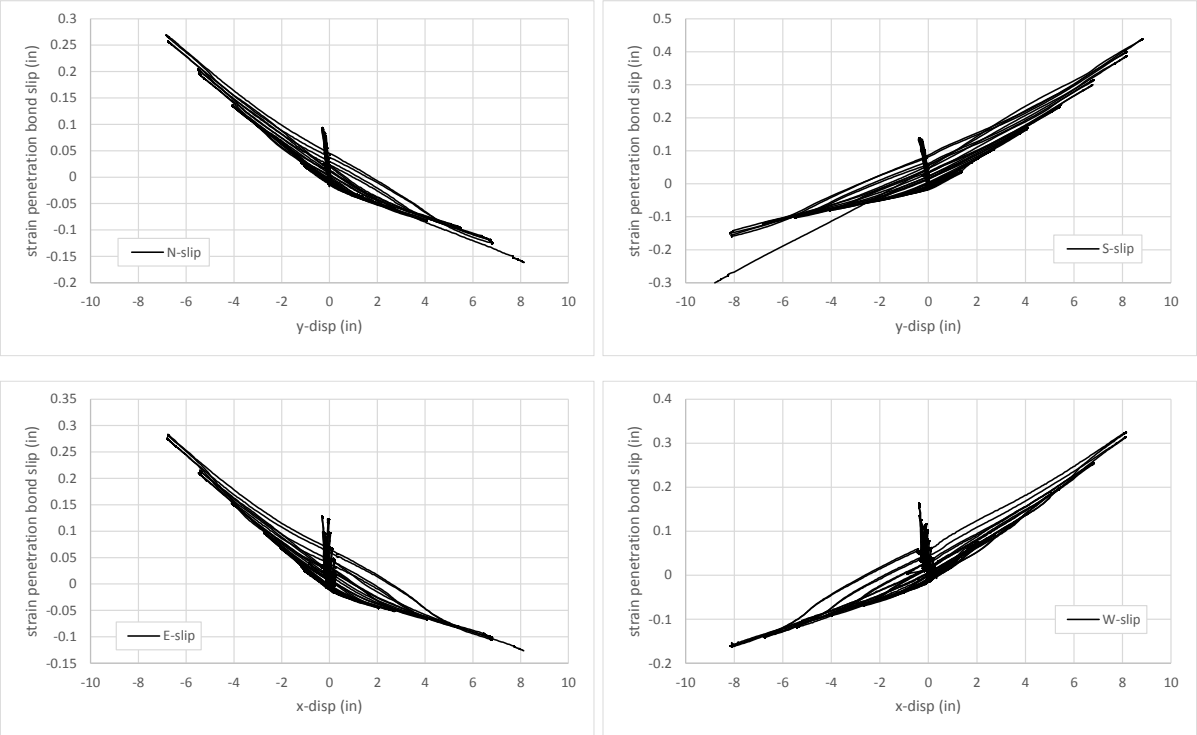

Figure 13-64. Test 10: Extreme Fiber Bar Strain Penetration Bond Slip Hysteresis

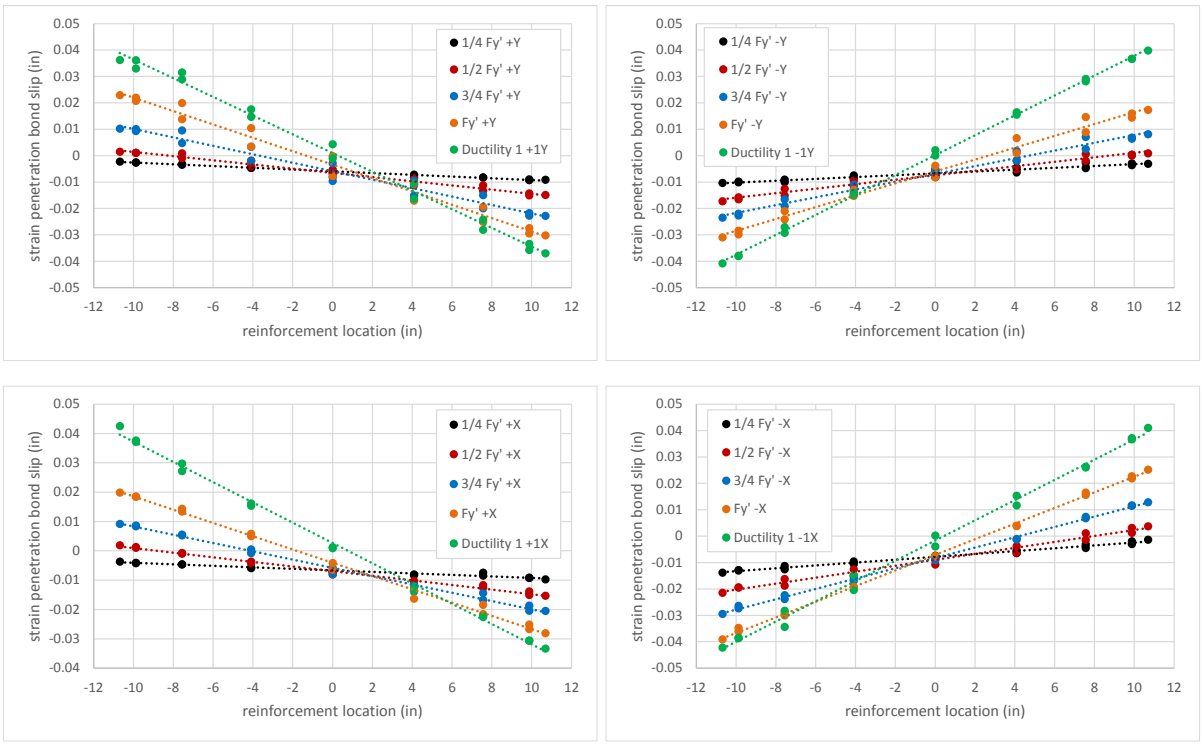

Figure 13-65. Test 10: Fixed End Rotations due to Strain Penetration during the Elastic Cycles

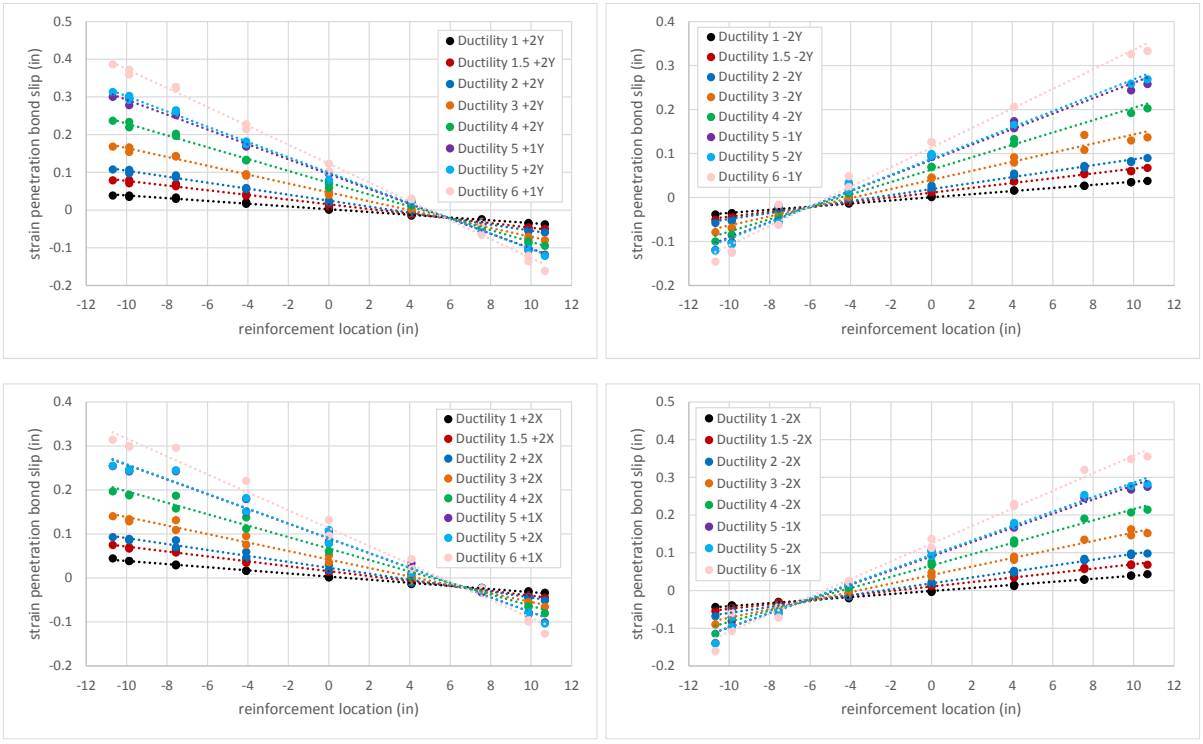

Figure 13-66. Test 10: Fixed End Rotations due to Strain Penetration

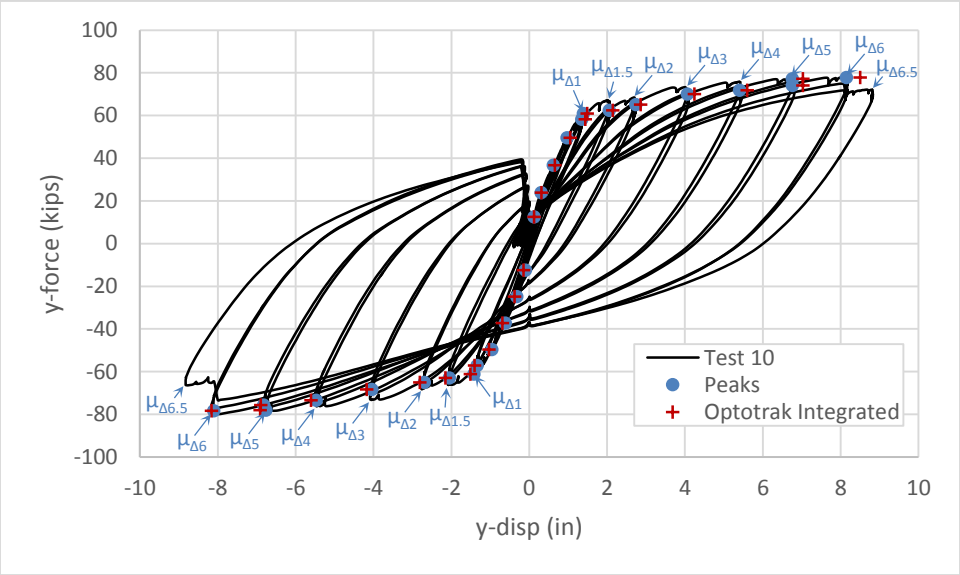

Figure 13-67. Test 10: Optotrak Integrated Flexural Disp. Compared to Measured String Pot. Disp.

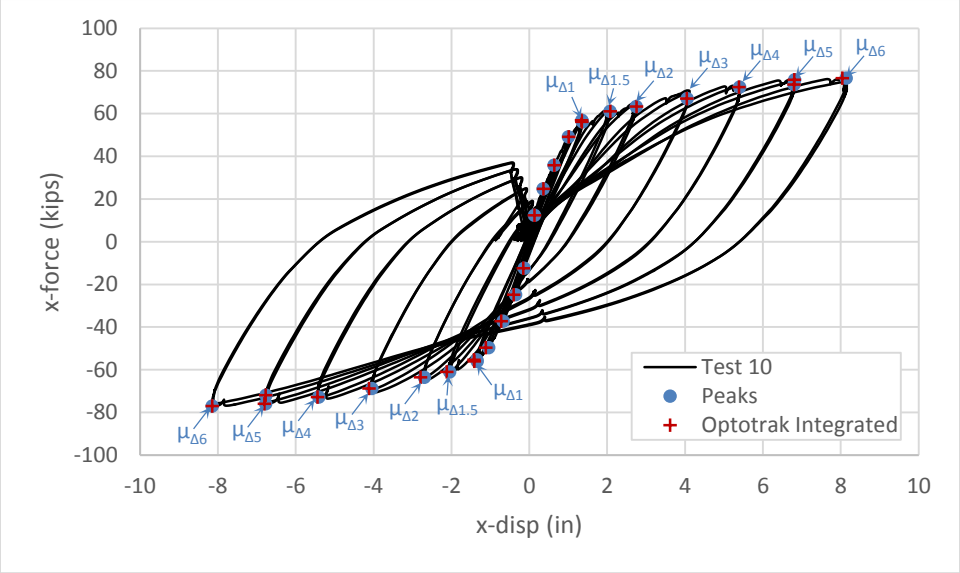

Figure 13-68. Test 10: Optotrak Integrated Flexural Disp. Compared to Measured String Pot. Disp.

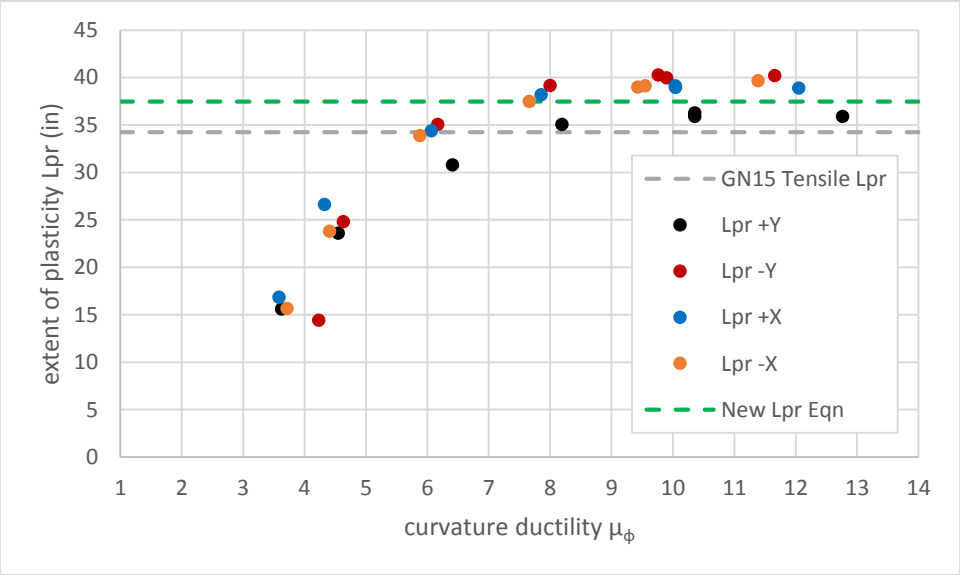

Figure 13-69. Test 10: Measured Extent of Plasticity Compared to Tensile Hinge Lengths

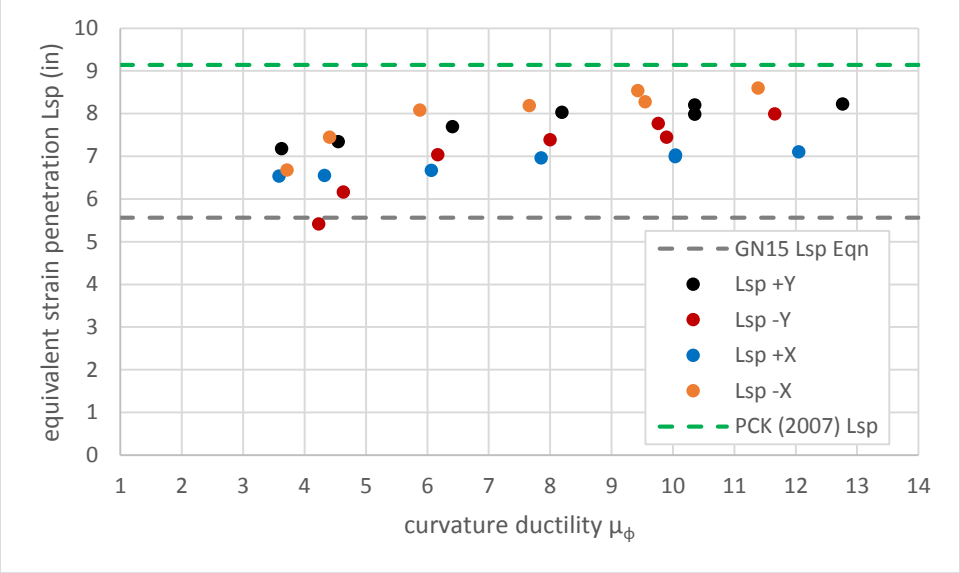

Figure 13-70. Test 10: Measured Equivalent Strain Penetration Lengths Compared to Design Expressions

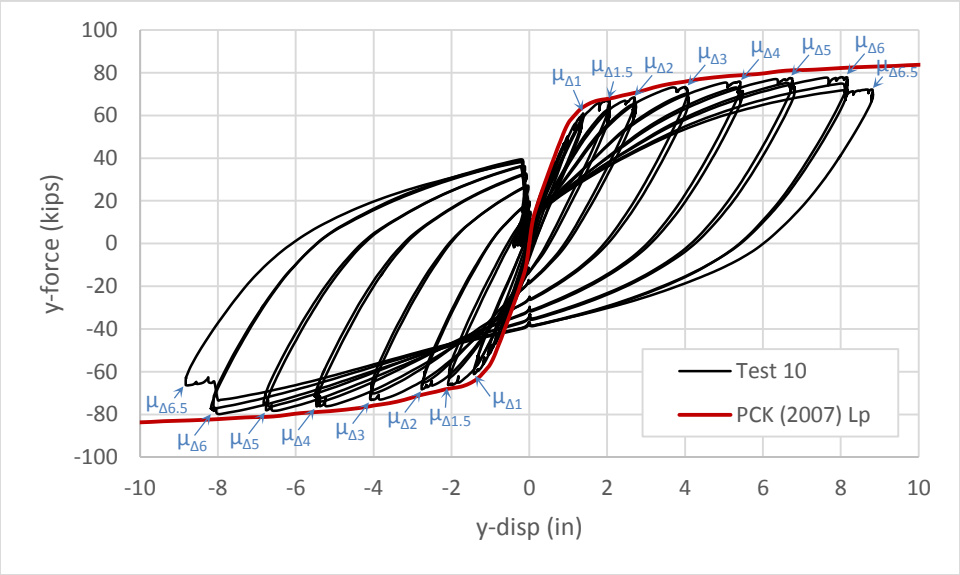

Figure 13-71. Test 10: Y-Direction Hysteretic Response Compared to PCK (2007) Hinge Length Monotonic Prediction

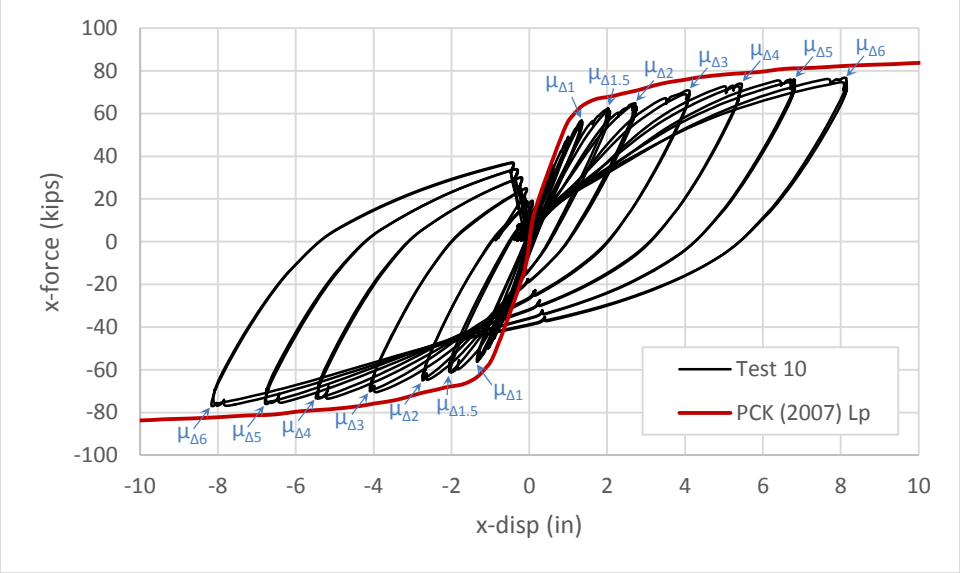

Figure 13-72. Test 10: Y-Direction Hysteretic Response Compared to PCK (2007) Hinge Length Monotonic Prediction

Response Comparison to Previous Experiments

Comparison of Tests 10 (1.3%) and 4 (1% Transverse Volumetric Steel)

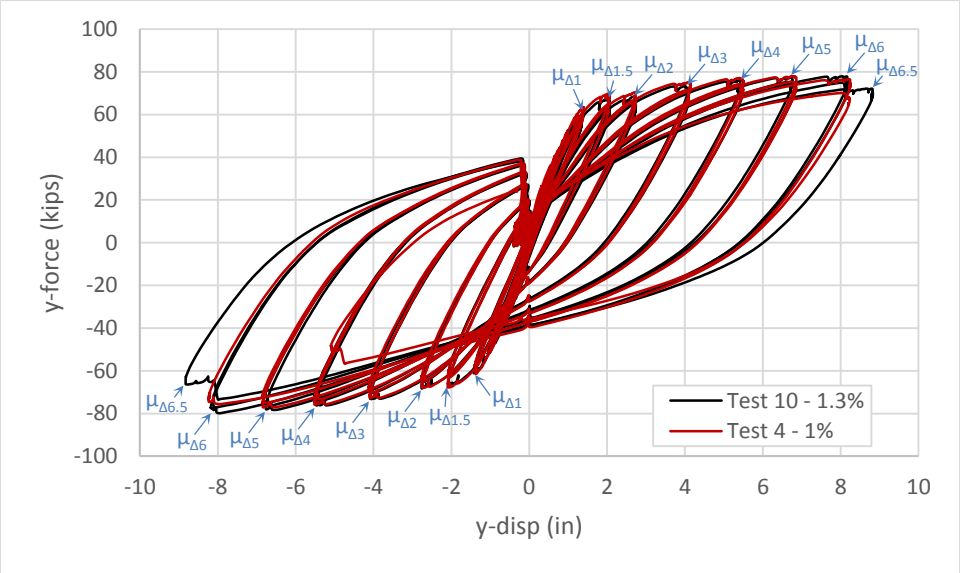

Figure 13-73. Tests 10 (1.3%) and 4 (1% Transverse Steel) Hysteretic Response Comparison in the Y-Direction

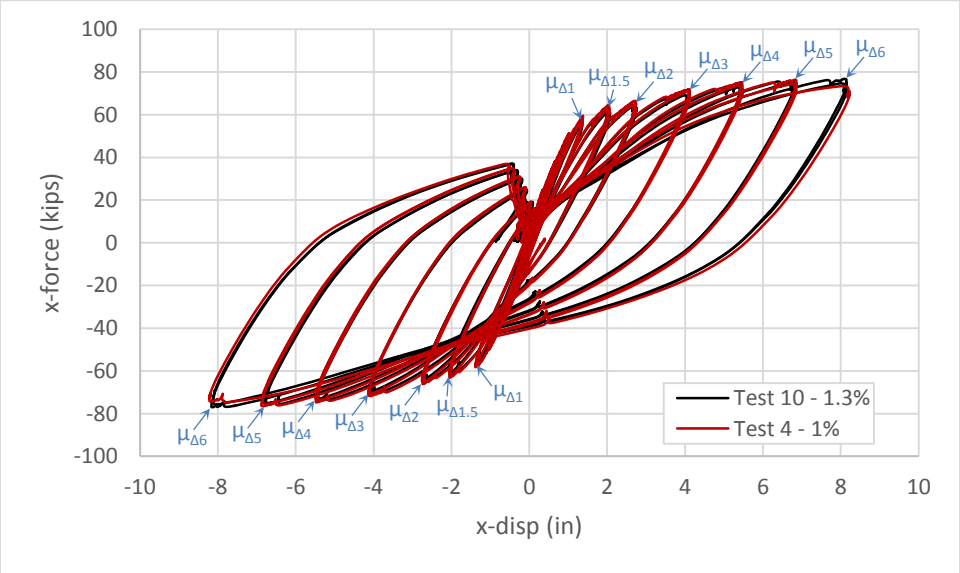

Figure 13-74. Tests 10 (1.3%) and 4 (1% Transverse Steel) Hysteretic Response Comparison in the X-Direction

Comparison of Tests 10 (2.1%) and 7 (1.6% Longitudinal Steel)

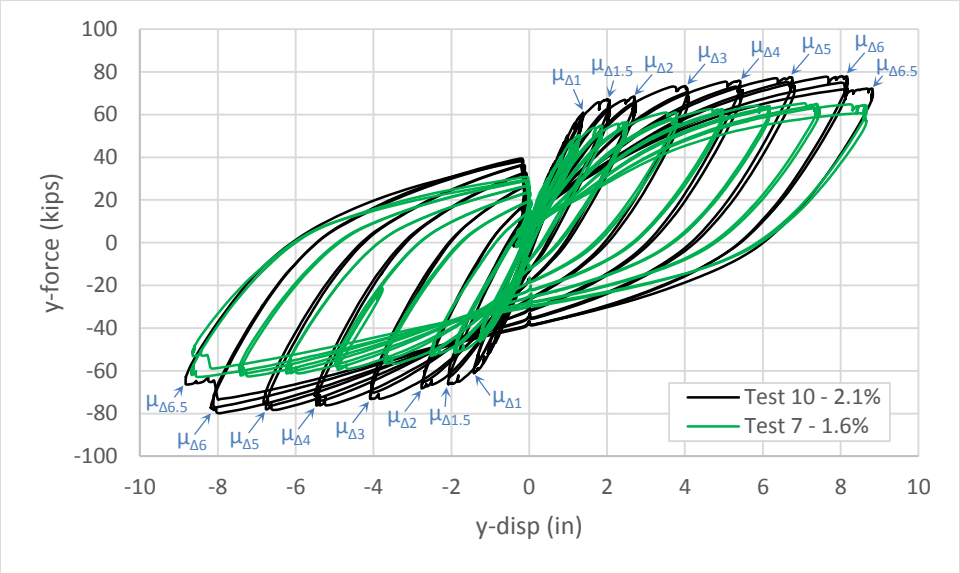

Figure 13-75. Tests 10 (2.1%) and 7 (1.6% Longitudinal Steel) Hysteretic Response Comparison in the Y-Direction

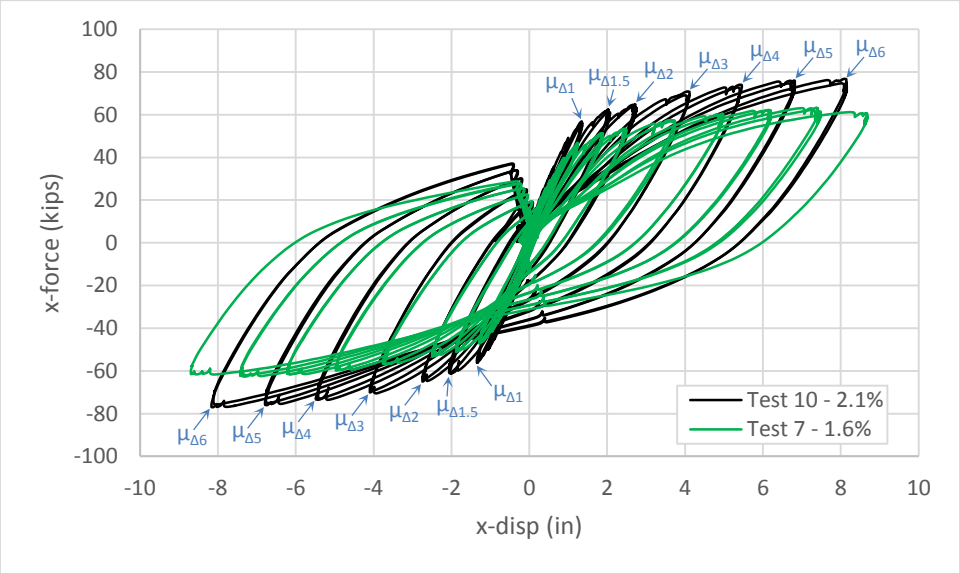

Figure 13-76. Tests 10 (2.1%) and 7 (1.6% Longitudinal Steel) Hysteretic Response Comparison in the X-Direction

Chapter 14 – Test 11 Summary Report

Subduction Megathrust Load Path Selected for Tests 11 and 12

The final two columns in the Load Path research program utilized a bidirectional adaptation of a megathrust loading protocol recommended in (Bazaez and Dusicka 2016). Test 11 evaluated a 24" diameter column ($L/D = 4.56$) with $\rho_l = A_{st}/A_g = 1.6\%$ longitudinal steel, a transverse volumetric ratio of $\rho_s = 4A_{sp}/D's = 1.0\%$, and a constant axial load of $191\ kips$ $\left(P/f_c' A_g = 7.5\%\right)$. Values of interests for Test 11 appear in Table 14-1. Test 12 was nominally identical, except it had a transverse volumetric ratio of 0.7%. These specimens are directly comparable to Tests 8 and 9 which were subjected to symmetric two-cycle-set load histories.

The scaling of the Megathrust load history for Test 11 was based on the ultimate deformation capacity of nominally identical Test 8, which utilized two-cycle-set loading. The orientation of the load history, imposed displacements, and resulting hysteretic response for Test 8 appear in Figure 14-1 and Figure 14-4 through Figure 14-7. In the two-cycle-set load history of Test 8, bar buckling was observed during displacement ductility six, followed by fracture of a previously buckled bar during displacement ductility seven. The megathrust loading protocol recommended by (Bazaez and Dusicka 2016) is shown in Figure 14-2 and Figure 14-3. The load history recommended in the literature reaches a peak response of ductility eight, adjustments to the megathrust load history for Test 11 are shown in Figure 14-2 and Figure 14-3. Comparisons of the scaled bidirectional megathrust loading protocol and either the symmetric two or three-cycle-set loading history appear in Figure 14-8 through Figure 14-11. In comparison, the scaled megathrust load path contains far more reversals at low ductility, but comparably fewer reversals at high ductility levels.

The specimen selected for Test 12 was nominally identical to that of Test 9, which had bar buckling during displacement ductility five, followed by fracture of a previously buckled bar during displacement ductility six as shown in Figure 14-12 through Figure 14-15. The same scaled megathrust load history from Test 11 was utilized in Test 12, except post-peak cycling began following displacement ductility six, which represented the ultimate displacement capacity of the nominally identical specimen of Test 9. The first yield displacement of Test 8 was used to define the ductility levels and thus cycle displacement amplitudes of Tests 11 and 12. Test 9 had a slightly larger, but comparable, equivalent yield displacement.

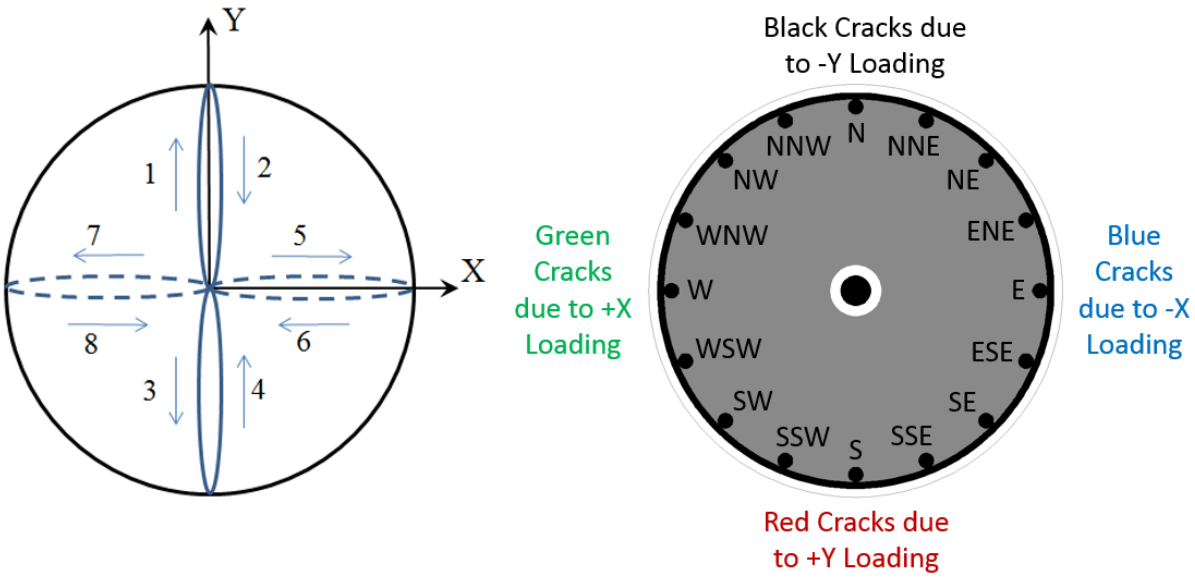

Figure 14-1. Test 11: Bidirectional Load History Orientation and Bar Naming System

Table 14-1. Test 11: Values of Interests

Load History	Scaled Bidirectional Megathrust
Length, Diameter, and Aspect Ratio	$L = 109.4375\ in, D = 24\ in,\ (L/D = 4.56)$
Longitudinal Steel Detailing	$16\ \#6\ for\ \rho_l = A_{st}/A_g = 1.6\%$
Longitudinal Steel Properties	$f_y = 70.33\ ksi, f_u = 98.68\ ksi, \varepsilon_y = 0.00283$
Transverse Steel Detailing	$\#3\ @\ 2\ in\ for\ \rho_s = 4A_{sp}/D's = 1.0\%$
Transverse Steel Properties	$f_y = 63.89\ ksi, f_u = 93.64\ ksi, \varepsilon_y = 0.00418$
Column Concrete Strength	$f_c' = 6.11\ ksi$
Footing Concrete Strength	$f_c' = 6.45\ ksi$
Axial Load	$P = 191\ kips, \left(P/f_c'\ A_g = 7.5\%\right)$
Analytical First Yield Force	$F_y' = 41.26\ kips$
Experimental First Yield Disp.	$\Delta_y' = 0.91\ in$ *(Value from Nominally Identical Test 8)*
Analytical Nominal Moment Capacity	$M_n = 505.56\ kip \cdot ft$
Equivalent Yield Displacement	$\Delta_y = \Delta_y'\left(M_n/M_y'\right) = 1.22\ in$ with Δ_y' from Test 8

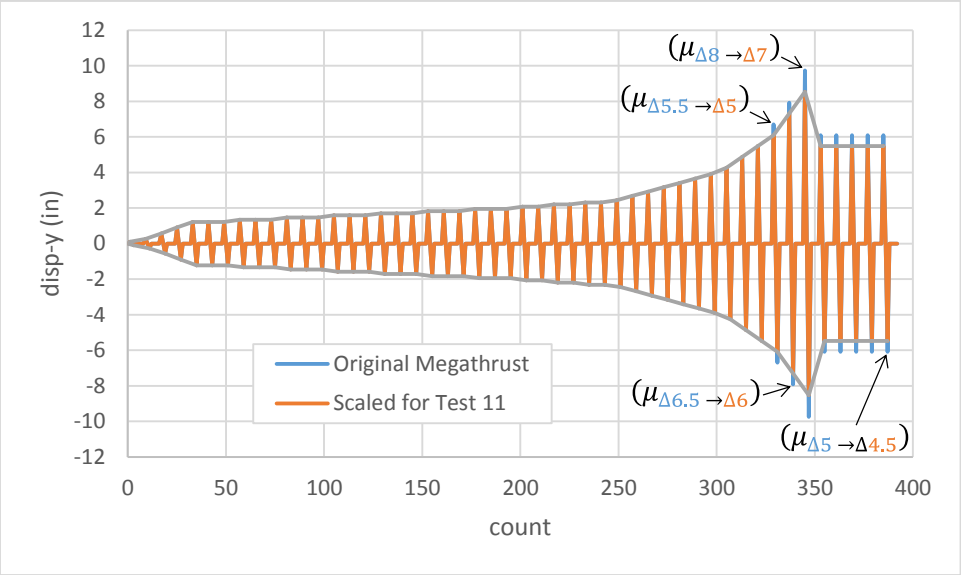

Figure 14-2. Original Megathrust LH Compared to Scaled LH in Test 11 (Y-Direction Displacements)

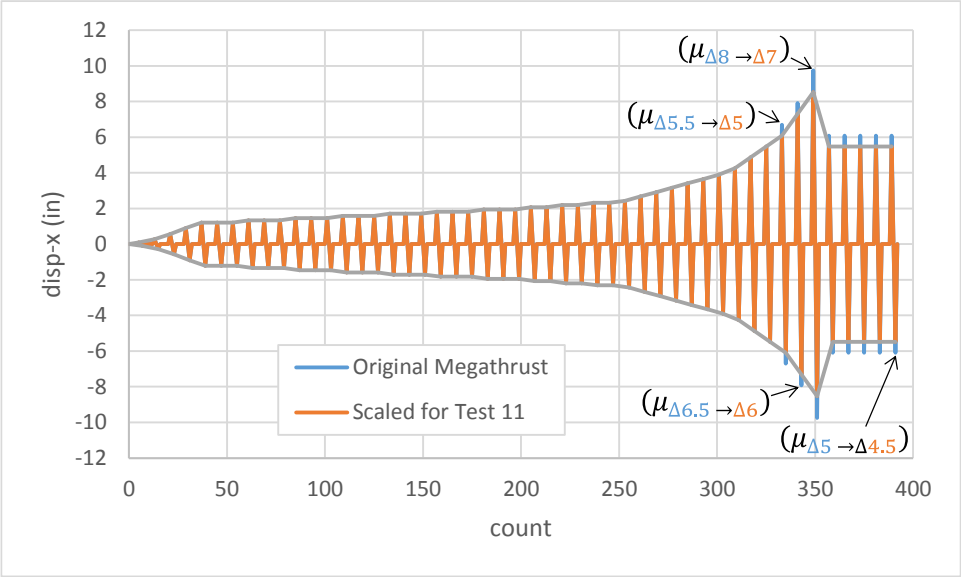

Figure 14-3. Original Megathrust LH Compared to Scaled LH in Test 11 (X-Direction Displacements)

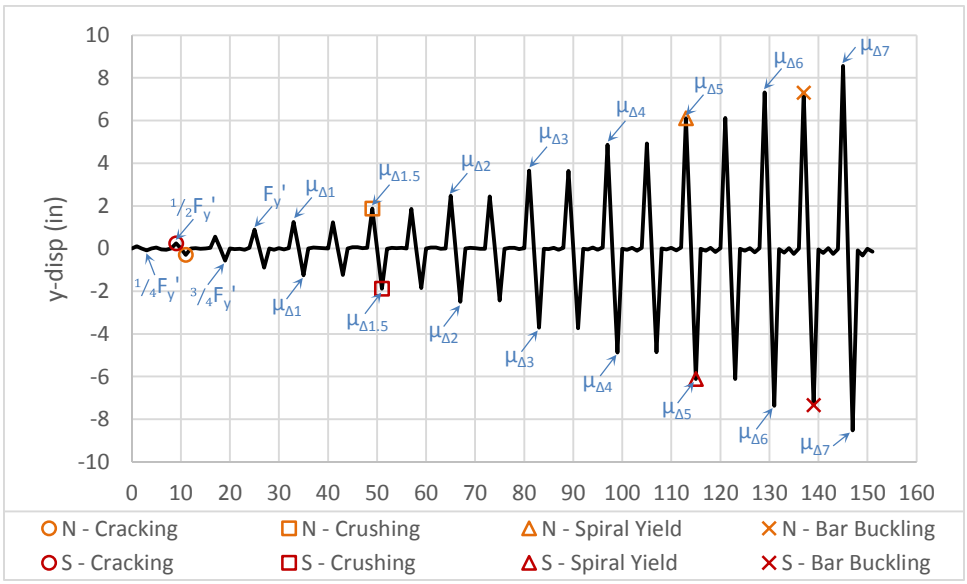

Figure 14-4. Test 8: Y-Displacement History (Bidirectional Symmetric 2-Cycle-Set) 1% Transverse Steel

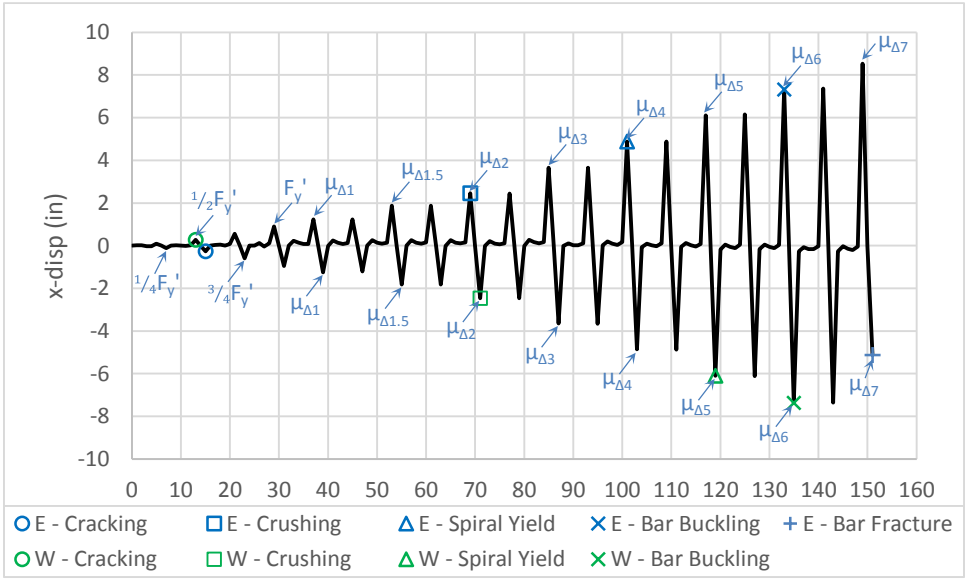

Figure 14-5. Test 8: X-Displacement History (Bidirectional Symmetric 2-Cycle-Set) 1% Transverse Steel

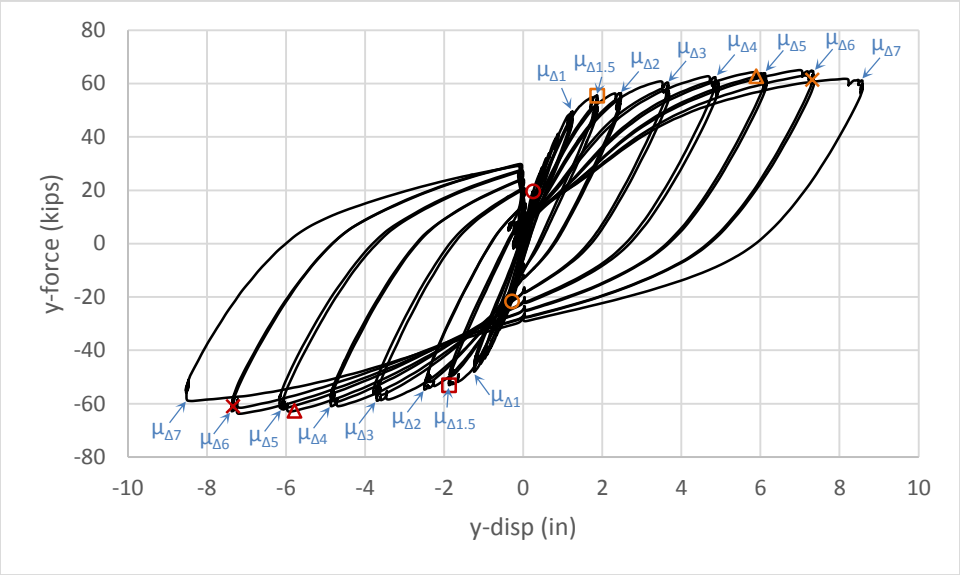

Figure 14-6. Test 8: Y-Direction Hysteretic Response (Bidirectional Symmetric 2-Cycle-Set) 1% Transverse Steel

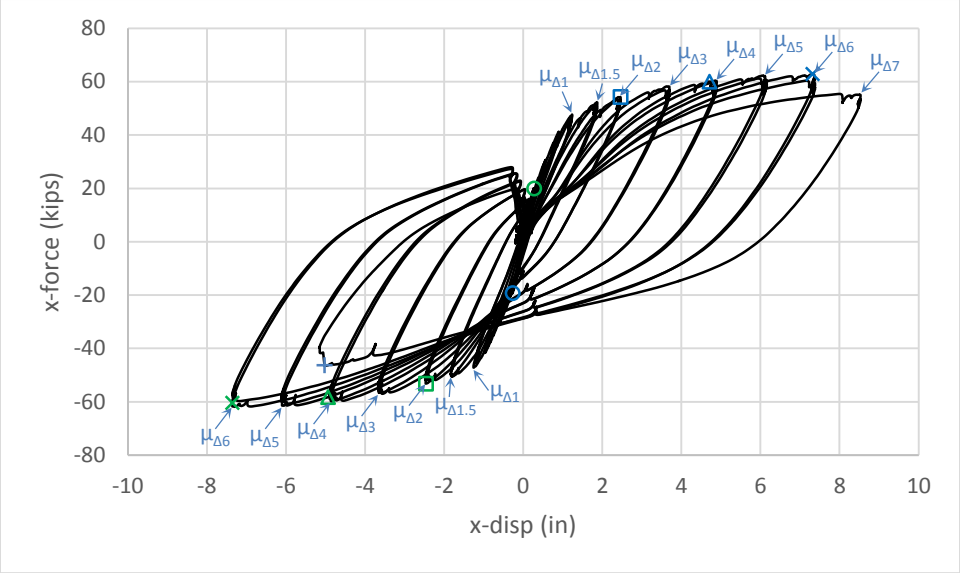

Figure 14-7. Test 8: X-Direction Hysteretic Response (Bidirectional Symmetric 2-Cycle-Set) 1% Transverse Steel

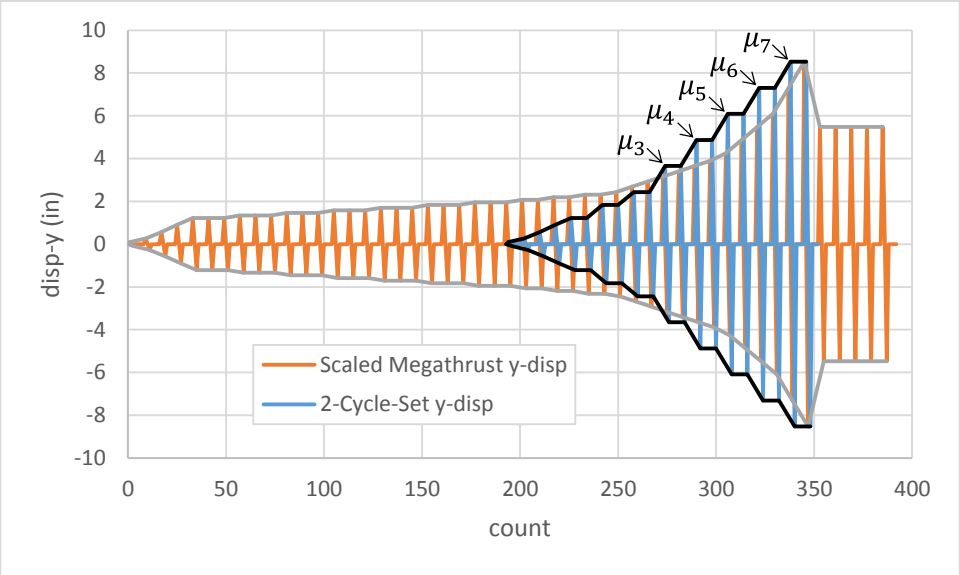

Figure 14-8. Scaled Megathrust Y-Direction Load Path Compared to Symmetric 2-Cycle-Set

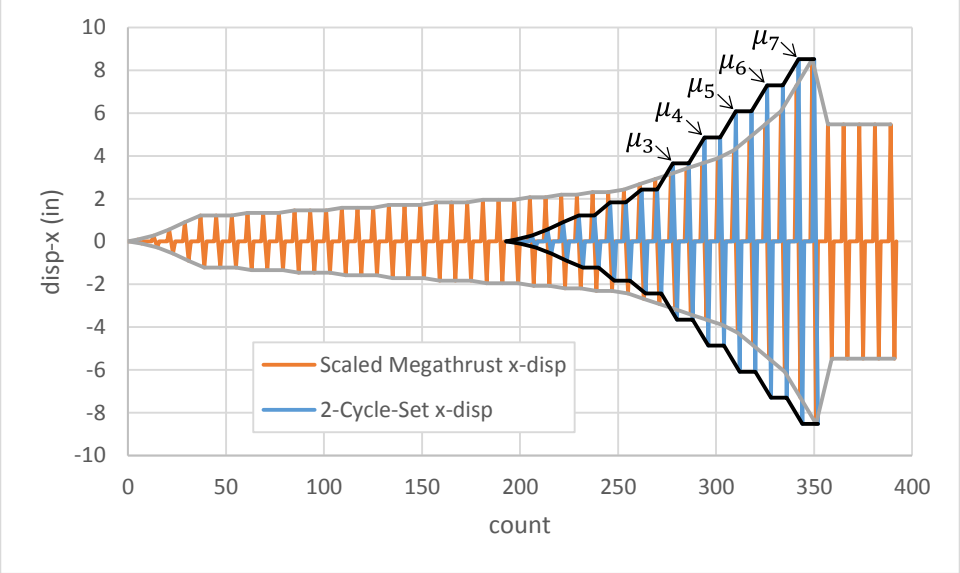

Figure 14-9. Scaled Megathrust X-Direction Load Path Compared to Symmetric 2-Cycle-Set

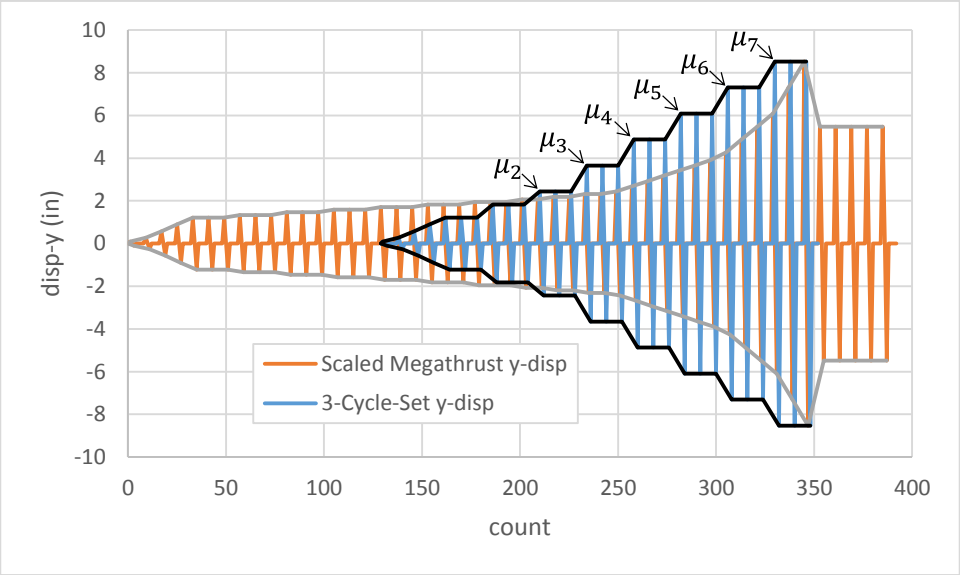

Figure 14-10. Scaled Megathrust Y-Direction Load Path Compared to Symmetric 3-Cycle-Set

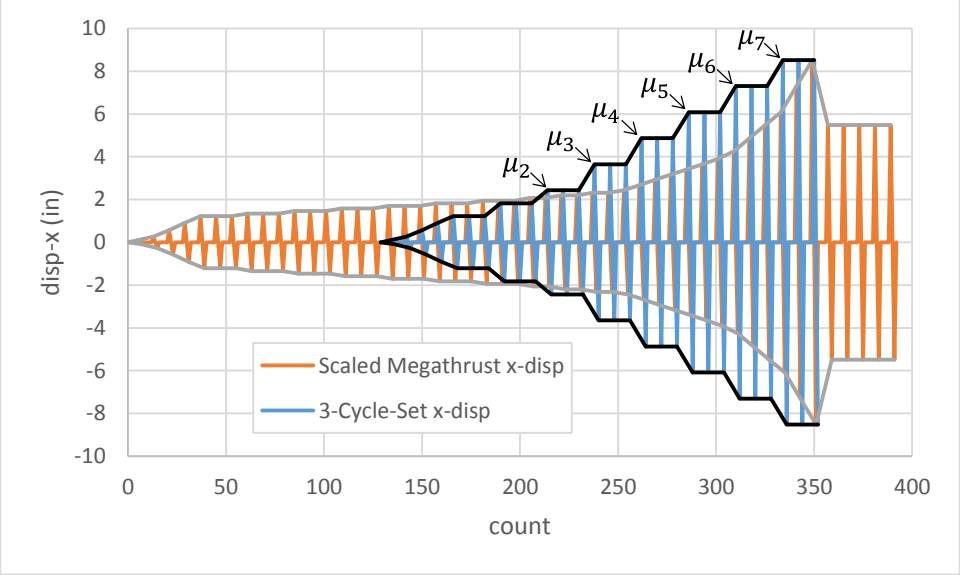

Figure 14-11. Scaled Megathrust X-Direction Load Path Compared to Symmetric 3-Cycle-Set

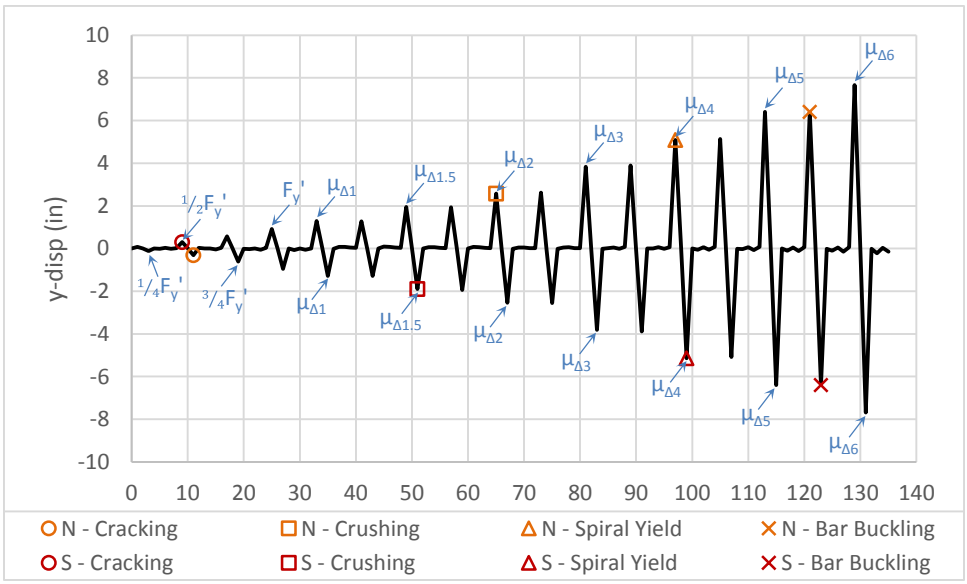

Figure 14-12. Test 9: Y-Displacement History (Bidirectional Symmetric 2-Cycle-Set) 0.7% Transverse Steel

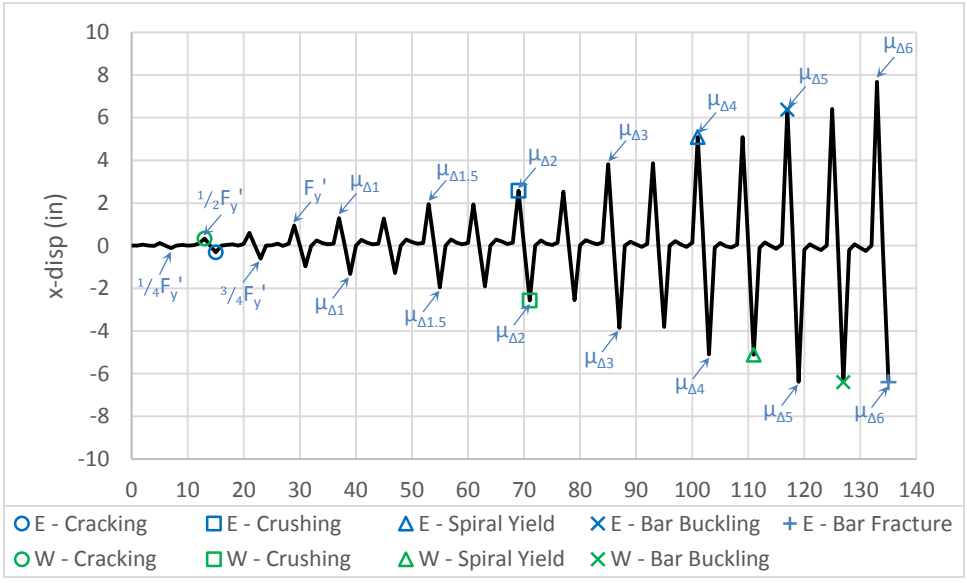

Figure 14-13. Test 9: X-Displacement History (Bidirectional Symmetric 2-Cycle-Set) 0.7% Transverse Steel

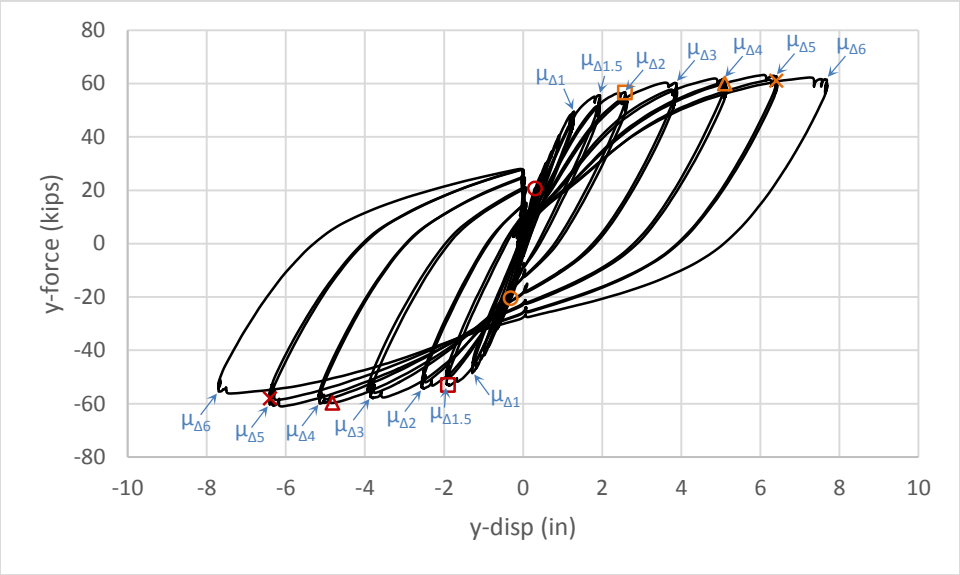

Figure 14-14. Test 9: Y-Direction Hysteretic Response (Bidirectional Symmetric 2-Cycle-Set) 0.7% Transverse Steel

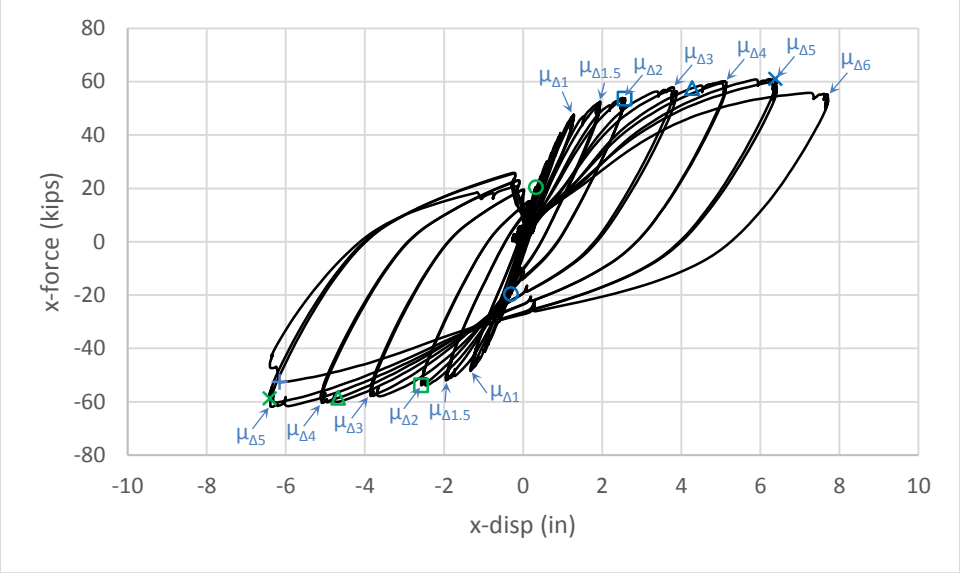

Figure 14-15. Test 9: X-Direction Hysteretic Response (Bidirectional Symmetric 2-Cycle-Set) 0.7% Transverse Steel

Test 11 - Experimental Observations

The eleventh specimen had a 24" diameter circular cross-section reinforced with 16 #6 A706 longitudinal bars ($A_{st}/A_g = 1.6\%$) and a #3 spiral at 1" on center ($4A_{sp}/D's = 1\%$). Details of the test setup, instrumentation, and specimen design appear in Chapter 2. A material properties summary for the longitudinal and transverse steel from the final six experiments appears in Table 3-3 through Table 3-5. The column had a tested concrete strength of $f_c' = 6.11\ ksi$, while the footing had $f_c' = 6.45\ ksi$. The same constant compressive axial load of $191\ kips$ was applied to all the specimens.

Test 11 utilized a scaled bidirectional adaptation of the megathrust loading protocol recommended in (Bazaez and Dusicka 2016). The test was designed to be comparable to that of nominally identical Test 8. The imposed displacement history appears in Figure 14-1, Figure 14-2, and Figure 14-3. This figure includes a diagram of the column cross-section with the selected bar and crack labeling scheme. Displacements in the +Y-direction placed the South reinforcement in tension. Cracks profiles were not marked during Test 11 due to the increased number of cycles in the load history and the need to finish the experiment within two days. The orientation of the X and Y axes are shown in Figure 2-52 with regards to the test setup. The +Y-axis is perpendicular to and points away from the strong wall. Values of interests, damage observations, and a predictions summary for the eleventh test appear in Table 14-2, Table 14-3, and Table 14-4. A photo of the deformed specimen appears in Figure 14-16.

Table 14-2. Test 11: Values of Interest

Load History	Scaled Bidirectional Megathrust
Length, Diameter, and Aspect Ratio	$L = 109.4375\ in, D = 24\ in,\ (L/D = 4.56)$
Longitudinal Steel Detailing	$16\ \#6\ for\ \rho_l = A_{st}/A_g = 1.6\%$
Longitudinal Steel Properties	$f_y = 70.33\ ksi, f_u = 98.68\ ksi, \varepsilon_y = 0.00283$
Transverse Steel Detailing	$\#3\ @\ 2\ in\ for\ \rho_s = 4A_{sp}/D's = 1.0\%$
Transverse Steel Properties	$f_y = 63.89\ ksi, f_u = 93.64\ ksi, \varepsilon_y = 0.00418$
Column Concrete Strength	$f_c' = 6.11\ ksi$
Footing Concrete Strength	$f_c' = 6.45\ ksi$
Axial Load	$P = 191\ kips, \left(P/f_c'\ A_g = 7.5\%\right)$
Analytical First Yield Force	$F_y' = 41.26\ kips$
Experimental First Yield Disp.	$\Delta_y' = 0.91\ in$ *(Value from Nominally Identical Test 8)*
Analytical Nominal Moment Capacity	$M_n = 505.56\ kip \cdot ft$
Equivalent Yield Displacement	$\Delta_y = \Delta_y'\left(M_n/M_y'\right) = 1.22\ in$ with Δ_y' from Test 8

Table 14-3. Test 11: Damage Observations

Damage Observations:		
Cycle Peak at which First Cracking was Observed Visually:		
North	$\Delta_y = -0.5F_y' = -0.30\ in$	$F_y = -20.64\ kips$
South	$\Delta_y = 0.5F_y' = 0.30\ in$	$F_y = 20.63\ kips$
East	$\Delta_x = -0.5F_y' = -0.30\ in$	$F_x = -20.53\ kips$
West	$\Delta_x = 0.5F_y' = 0.31\ in$	$F_x = 20.68\ kips$
Cycle Peak at which Cover Concrete Crushing was Observed Visually:		
North	$\mu_{\Delta 2.4}^{+1Y} = 2.96\ in$	$\varepsilon_c = -0.00539$
South	$\mu_{\Delta 2.2}^{-1Y} = -2.69\ in$	$\varepsilon_c = -0.00658$
East	$\mu_{\Delta 2.2}^{+1X} = 2.67\ in$	$\varepsilon_c = -0.00479$
West	$\mu_{\Delta 2.2}^{-1X} = -2.73\ in$	$\varepsilon_c = -0.00511$
Exact Displacement and Cycle Label for Initial Spiral Yielding in the Confinement Zone:		
North	$\Delta_y = 6.04\ in\ during\ \mu_{\Delta 5}^{+1Y}$	$\varepsilon_c = -0.01321$
South	$\Delta_y = -6.19\ in\ during\ \mu_{\Delta 6}^{-1Y}$	$\varepsilon_c = -0.01518$
East	$\Delta_x = 6.14\ in\ during\ \mu_{\Delta 6}^{+1X}$	$\varepsilon_c = -0.01817$
West	$\Delta_x = -6.06\ in\ during\ \mu_{\Delta 5}^{-1X}$	$\varepsilon_c = -0.01182$
Peak Tensile Displacement Prior to Visual Bar Buckling During Subsequent Reversal of Load:		
North	$\mu_{\Delta 6}^{-1Y} = -7.32\ in, Observed\ at\ \mu_{\Delta 7}^{+1Y} = 8.55\ in$	$\varepsilon_s = 0.04405$
South	$\mu_{\Delta 7}^{+1Y} = 8.55\ in, Observed\ at\ \mu_{\Delta 4.5p}^{-1Y} = -5.51\ in$	$\varepsilon_s = 0.04929$
East	$\mu_{\Delta 6}^{-1X} = -7.28\ in, Observed\ at\ \mu_{\Delta 7}^{+1X} = 8.49\ in$	$\varepsilon_s = 0.04354$
West	$\mu_{\Delta 7}^{+1X} = 8.49\ in, Observed\ at\ \mu_{\Delta 7}^{-1X} = -8.51\ in$	$\varepsilon_s = 0.05053$
Exact Displacement and Cycle Label for Fracture of Previously Buckled Reinforcement		
East	$\Delta_x = -4.56\ in\ during\ \mu_{\Delta 4.5p}^{-1X}$	Single East Extreme Bar

Table 14-4. Test 11: Damage Predictions

Damage Predictions with the New Bidirectional Plastic Hinge Model and New Strain Limits:		
Bar Buckling Predictions		
New Method	$\Delta_{bb}^{Lpr} = 6.71\ in$	$\varepsilon_s^{bb} = 0.03890$
Feng et al. (2015)	$\Delta_{bb}^{Lp} = 6.41\ in$	$\varepsilon_s^{bb} = 0.05194$
Cover Crushing Prediction		
New Method	$\Delta_{cc}^{Lpr} = 1.97\ in$	$\varepsilon_c^{cc} = -0.004$
Spiral Yielding Prediction		
New Method	$\Delta_{sy}^{Lpr} = 5.28\ in$	$\varepsilon_c^{sy} = -0.01384 * M, (M = 0.8)$
Original Ultimate Concrete Compression Strain		
Mander et al. (1988)	$\Delta_{cu}^{Lpr} = 7.49\ in$	$\varepsilon_{cu} = -0.0172$

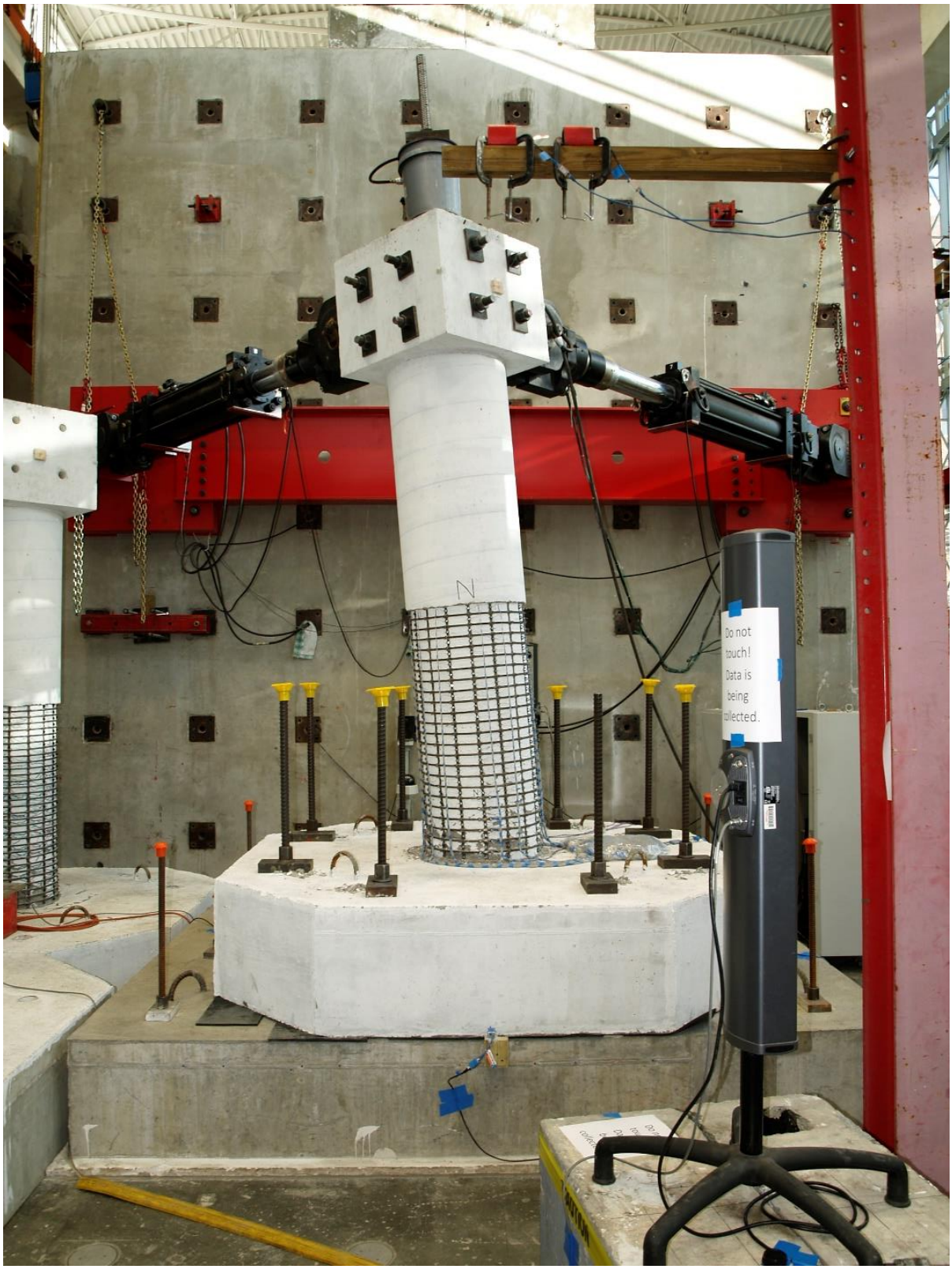

Figure 14-16. Test 11: Deformed Specimen at $\mu_{\Delta 7}^{+1x} = 8.49$"

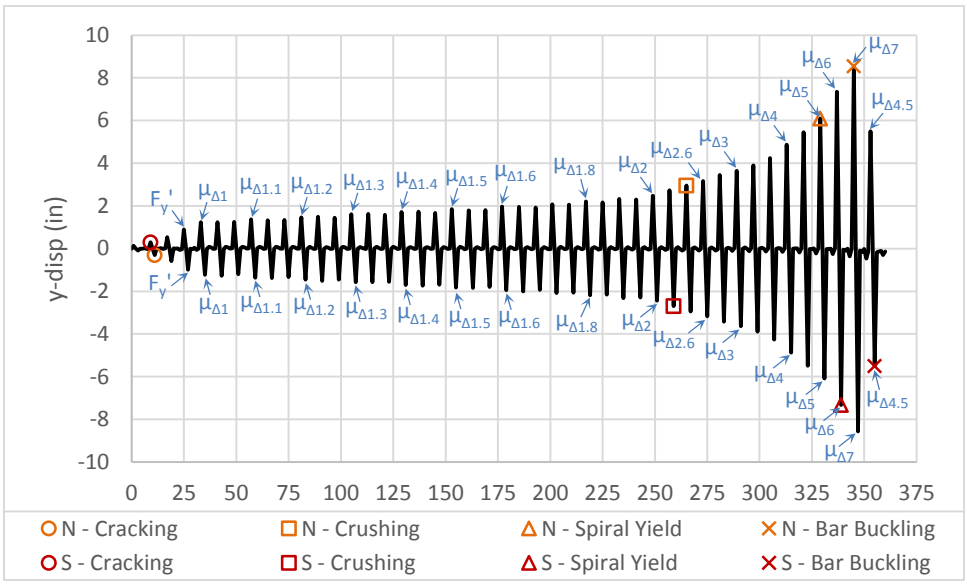

Figure 14-17. Test 11: Y-Displacement History

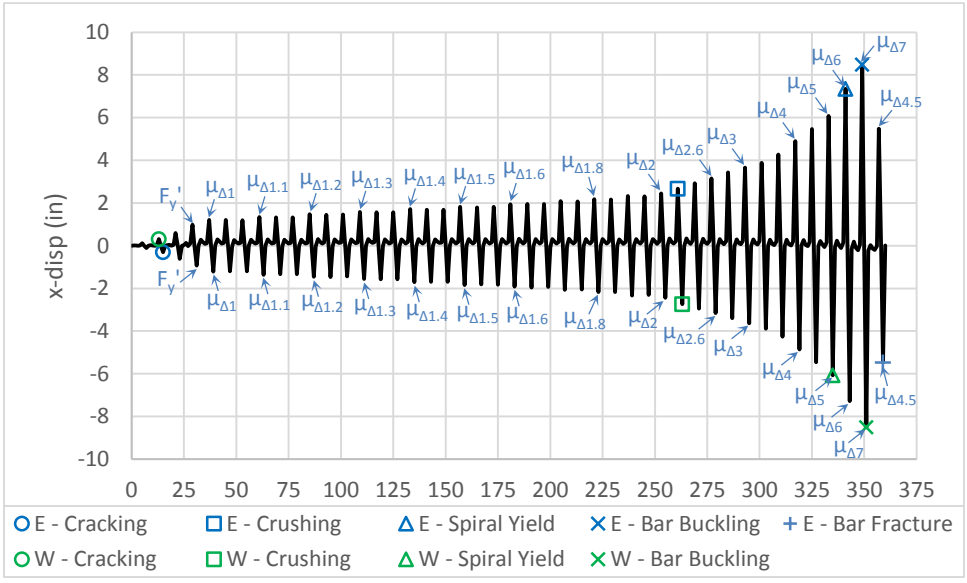

Figure 14-18. Test 11: X-Displacement History

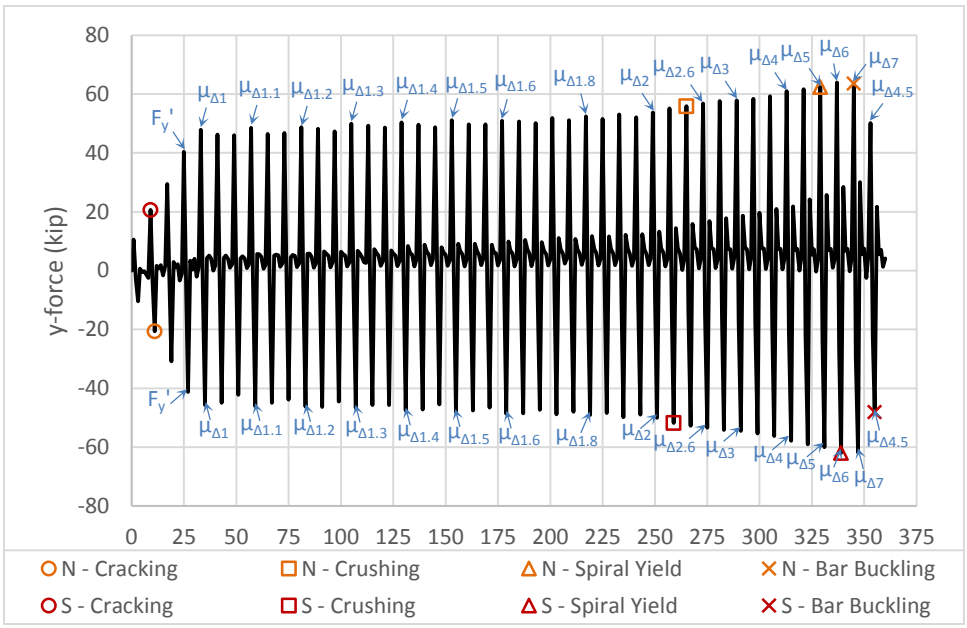

Figure 14-19. Test 11: Y-Force History

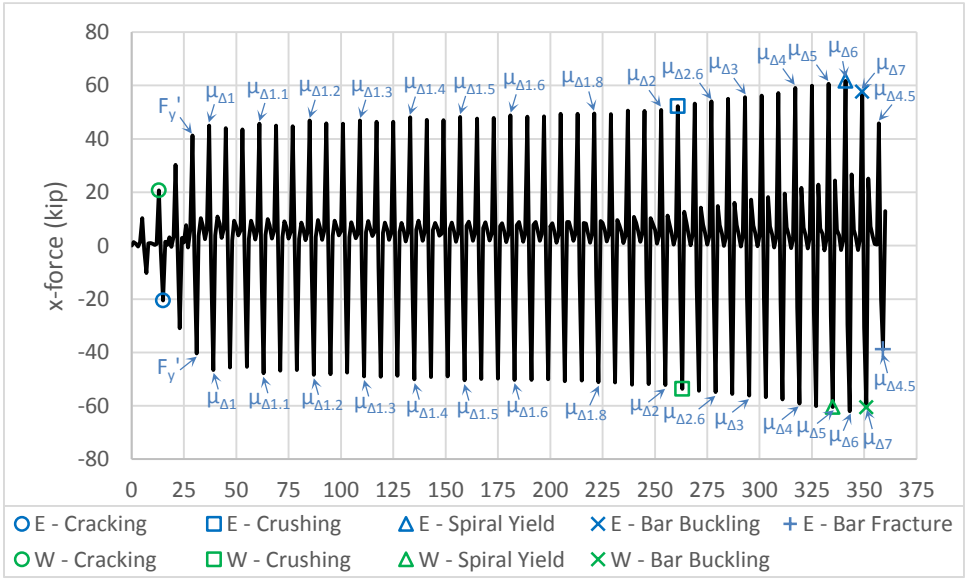

Figure 14-20. Test 11: X-Force History

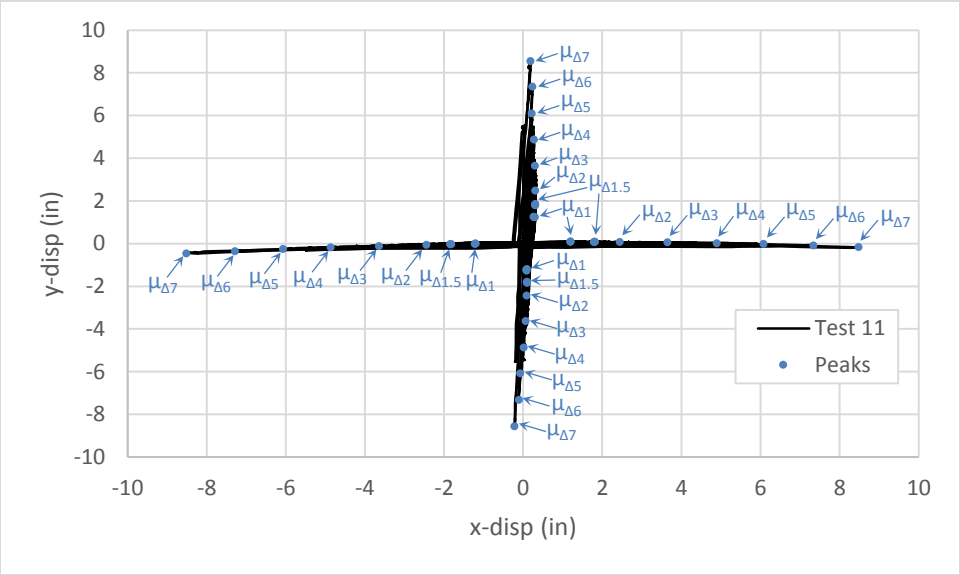

Figure 14-21. Test 11: Scaled Megathrust Loading Protocol from (Bazaez and Dusicka 2016)

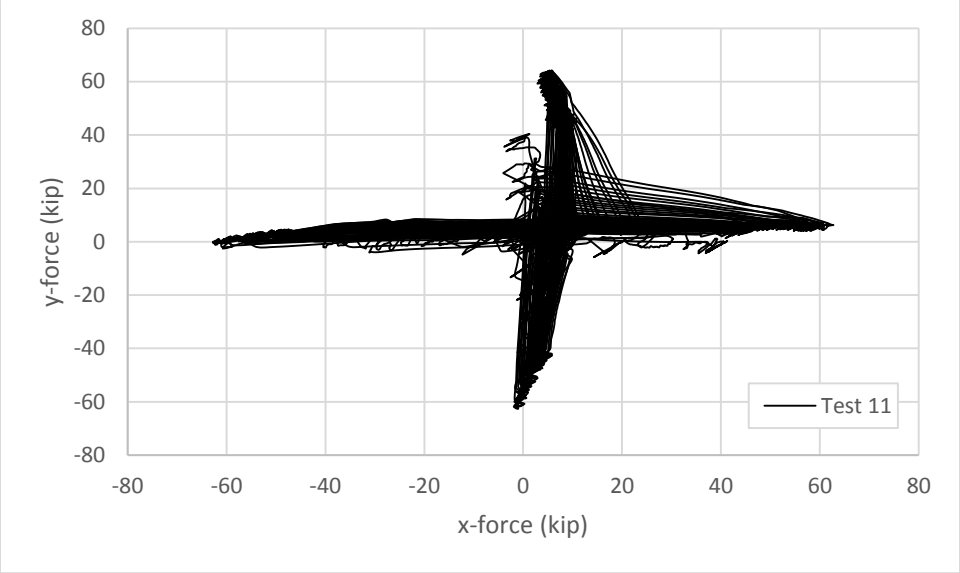

Figure 14-22. Test 11: Load Path

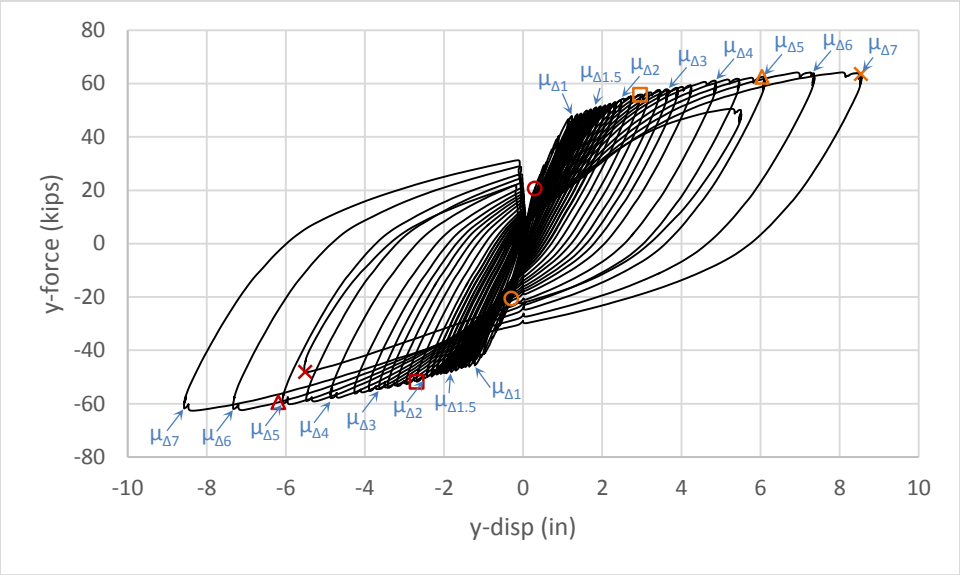

Figure 14-23. Test 11: Y-Direction Hysteretic Response

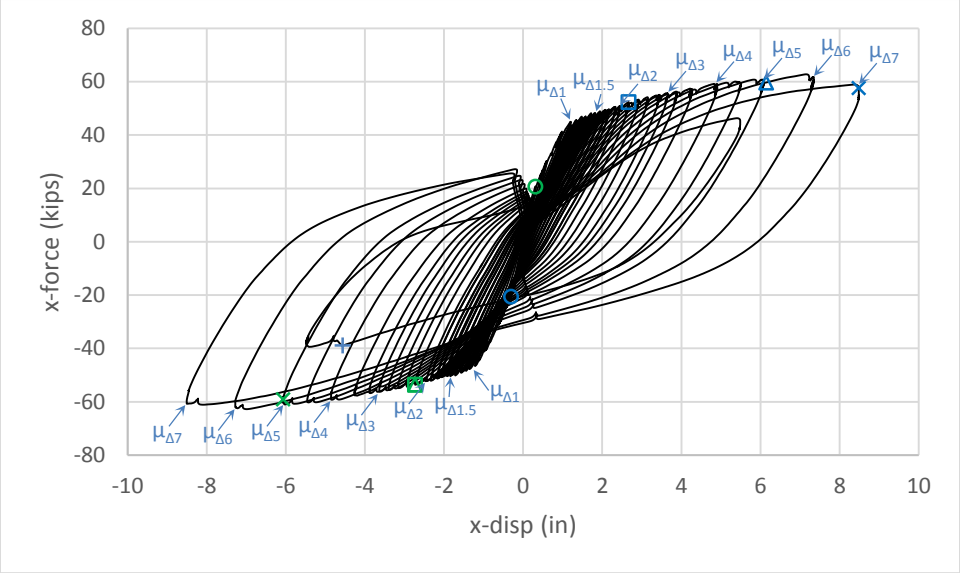

Figure 14-24. Test 11: X-Direction Hysteretic Response

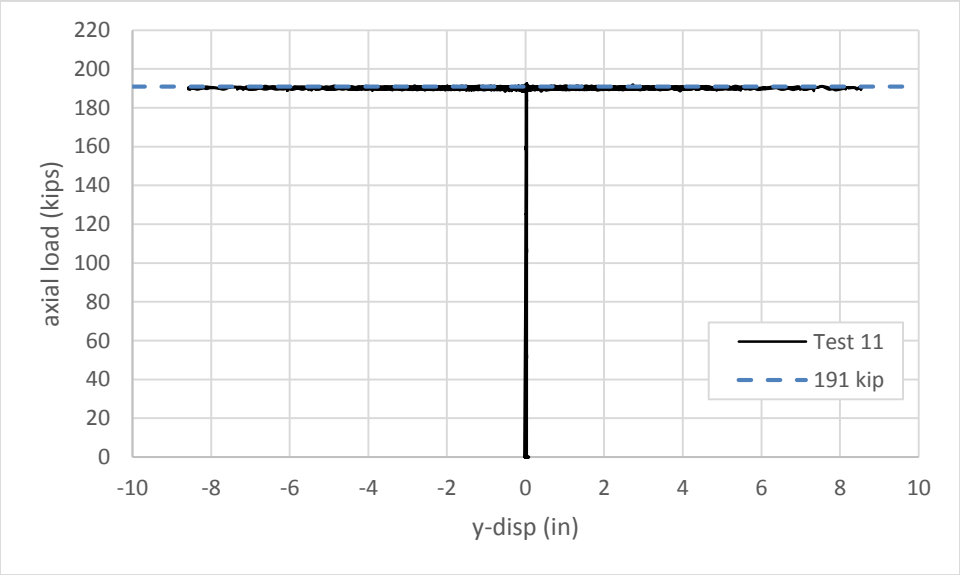

Figure 14-25. Test 11: Y-Direction Axial Force History

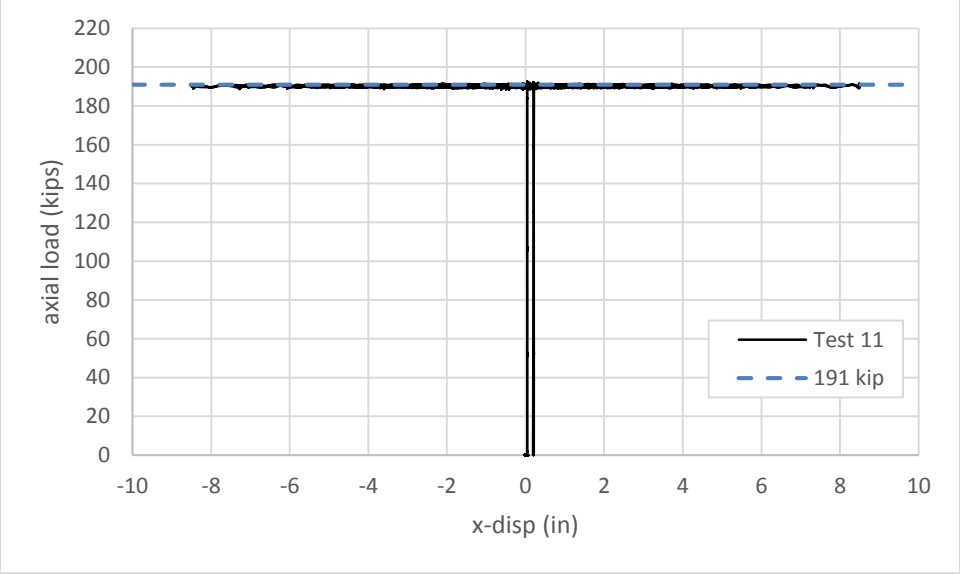

Figure 14-26. Test 11: X-Direction Axial Force History

Values of interests and damage observations for Load Path Test 11 are presented in Table 13-1 and Table 13-2. Test 11 evaluated a 24" diameter column $(L/D = 4.56)$ with $\rho_l = A_{st}/A_g = 1.6\%$ longitudinal steel and a transverse volumetric ratio of $\rho_s = 4A_{sp}/D's = 1\%$. The test began with the application of a constant axial load of $191\ kips\ \left(P/f_c'\ A_g = 7.5\%\right)$. The imposed displacement histories in the Y and X-directions for the scaled bidirectional adaptation of the megathrust loading protocol recommended in (Bazaez and Dusicka 2016) are shown in Figure 14-17 and Figure 14-18. The resulting column shear force histories in the Y and X-directions appear in Figure 14-19 and Figure 14-20. The full displacement history and resulting load path for Test 11 appear in Figure 14-21 and Figure 14-22. The Y and X-direction column hysteretic response appears Figure 14-23 and Figure 14-24. The axial force history appears in Figure 14-25 and Figure 14-26.

The load history began with elastic ¼ F_y' cycle increments until the analytically predicted first yield force $(F_y' = 41.26\ kips)$ was reached in each direction of loading. Cracks were first observed on all sides of the specimen during the ½ F_y' cycle. At the analytically predicted first yield force, an average experimental first yield displacement of $\Delta_y' = 0.95$" was measured in the four primary directions. The equivalent yield displacement for the column was then computed as $\Delta_y = \Delta_y'\left(M_n/M_y'\right) = 1.28\ in$, where $M_n = 505.56\ kip \cdot ft$ represents the analytical nominal moment capacity corresponding to an extreme fiber compression strain of $\varepsilon_c = 0.004$ or a steel tensile strain of $\varepsilon_s = 0.015$, whichever occurs first. To allow for direct comparison, the first yield displacement of $\Delta_y' = 0.91$" and resulting equivalent yield displacement of $\Delta_y = \Delta_y'\left(M_n/M_y'\right) = 1.22$" from Test 8 was used to define the cycle peaks in the load history of Test 11. The remainder of the scaled megathrust load history consists of equal magnitude bidirectional cycles at increments of the equivalent yield displacement $\mu_{\Delta n} = n \cdot \Delta_y$. Cracks profiles were not marked during Test 11 due to the increased number of cycles in the load history and the need to finish the experiment within two days.

Concrete crushing was observed on the South side of the specimen during $\mu_{\Delta 2.2}^{-1y} = -2.69$", followed by the East side at $\mu_{\Delta 2.2}^{+1x} = 2.67$" as shown in Figure 14-27 and Figure 14-28. Concrete crushing was observed on the West side during $\mu_{\Delta 2.2}^{-1x} = -2.73$", and then on the North side at $\mu_{\Delta 2.4}^{+1y} = 2.96$", see Figure 14-29 and Figure 14-30. Photos of the four extreme fiber regions during compressive cycles of $\mu_{\Delta 4}$ appear in Figure 14-31 and Figure 14-32. Confinement demands led to initial spiral yielding on the North side during $\mu_{\Delta 5}^{+1y} = 6.09$", followed by the West side during $\mu_{\Delta 5}^{-1x} = -6.07$", see Figure 14-33. Initial spiral yielding was measured on the South side during $\mu_{\Delta 6}^{-1y} = -7.32$", and then on the East side during $\mu_{\Delta 6}^{+1x} = 7.35$", see Figure 14-34.

The North extreme fiber bar visibly buckled during $\mu_{\Delta 7}^{+1y} = 8.55$", while the South reinforcement remained visibly straight at $\mu_{\Delta 7}^{-1y} = -8.57$", see Figure 14-35. East reinforcing bars NE, NNE, E and ENE buckled simultaneously during $\mu_{\Delta 7}^{+1x} = 8.49$" as shown in Figure 14-36. West reinforcing bars NW, WNW, and W buckled during $\mu_{\Delta 7}^{-1x} = -8.51$", see Figure 14-37. This concluded the ascending branch of the megathrust loading protocol, where now loading resumes with five repeated post-peak cycles at $\mu_{\Delta 4.5\mathrm{p}}$ which represent the remainder of the simulated earthquake load history.

Bar NNW buckled during $\mu_{\Delta 4.5\mathrm{p}}^{+1\mathrm{y}} = 5.50"$, followed by buckling of adjacent South bars SSE and SE at $\mu_{\Delta 4.5\mathrm{p}}^{-1\mathrm{y}} = -5.51"$, see Figure 14-38. The buckled deformation in the East reinforcing bars increased significantly during $\mu_{\Delta 4.5\mathrm{p}}^{+1\mathrm{x}} = 5.48"$ as shown in Figure 14-39. The previously buckled East extreme fiber bar fractured at $\Delta_x = -4.56"$ during $\mu_{\Delta 4.5\mathrm{p}}^{-1\mathrm{x}} = -5.48"$ as shown in Figure 14-41. At this displacement, it was clear that the adjacent West bars WSW and SW had buckled, see Figure 14-40. Photos of the specimen after removal of the instrumentation appear in Figure 14-42 and Figure 14-43.

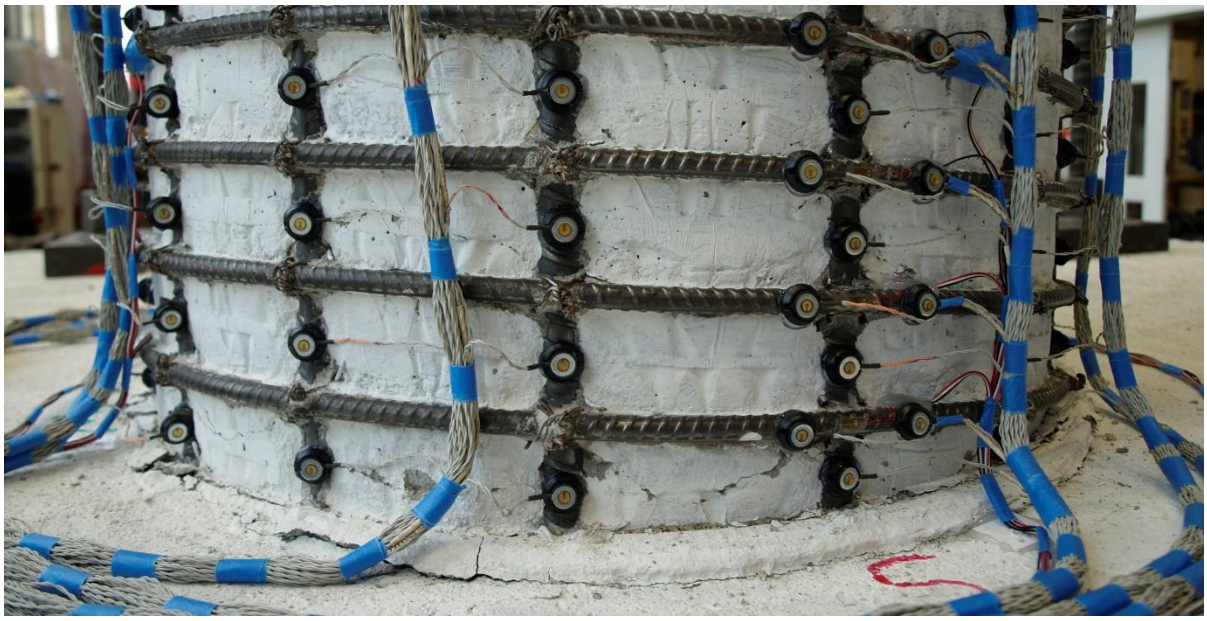

Figure 14-27. Test 11: Concrete Crushing on the South Side of the Specimen during $\mu_{\Delta 2.2}^{-1y} = -2.69"$

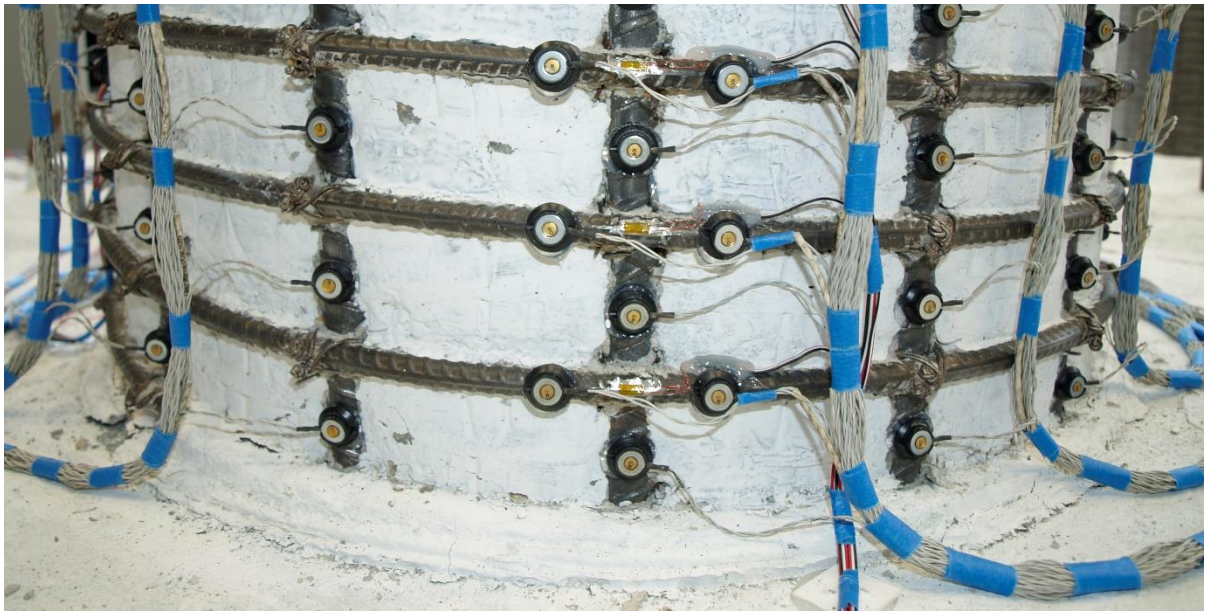

Figure 14-28. Test 11: Concrete Crushing on the East Side of the Specimen during $\mu_{\Delta 2.2}^{+1x} = 2.67$"

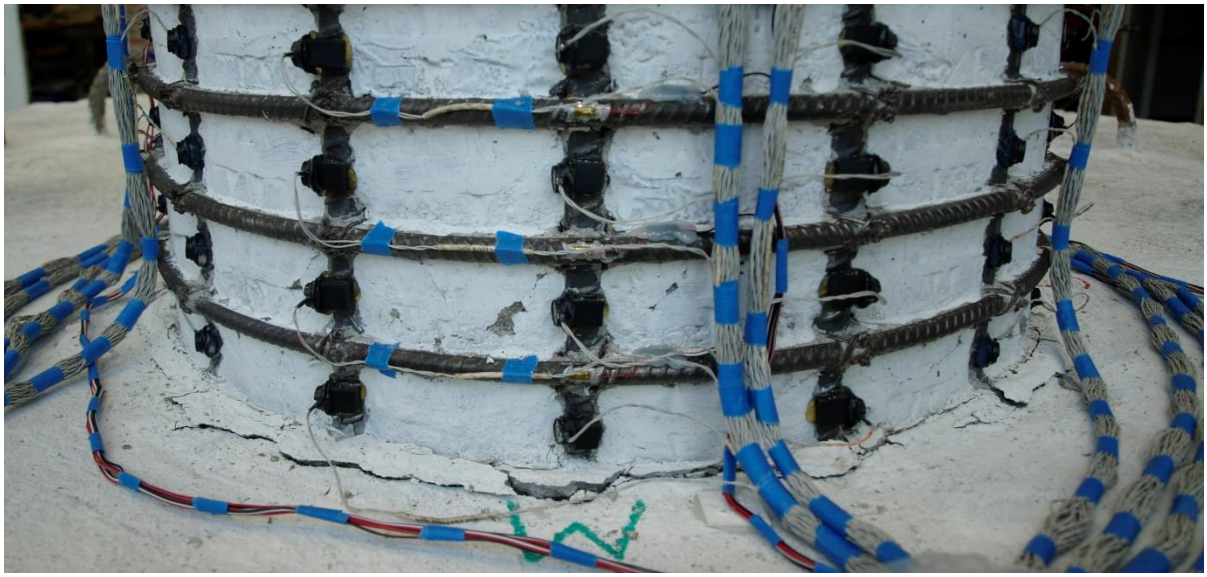

Figure 14-29. Test 11: Concrete Crushing on the West Side of the Specimen during $\mu_{\Delta 2.2}^{-1x} = -2.73$"

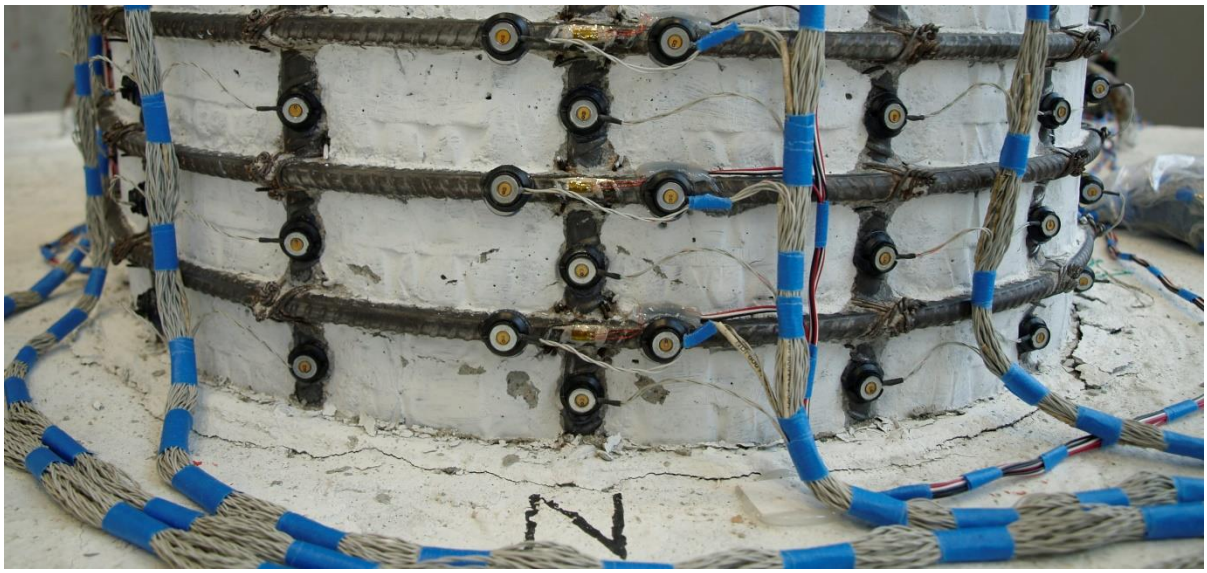

Figure 14-30. Test 11: Concrete Crushing on the North Side of the Specimen during $\mu_{\Delta 2.4}^{+1y} = 2.96$"

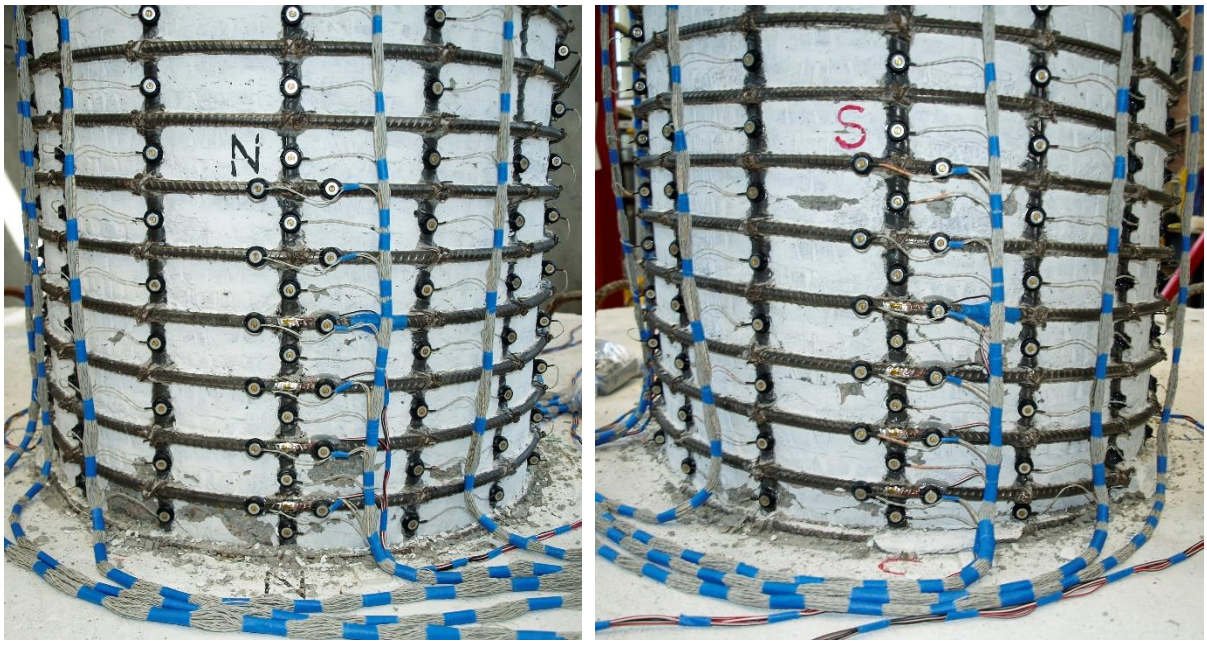

Figure 14-31. Test 11: (Left) North and (Right) South Sides of the Specimen during Compressive Cycles of $\mu_{\Delta 4}$

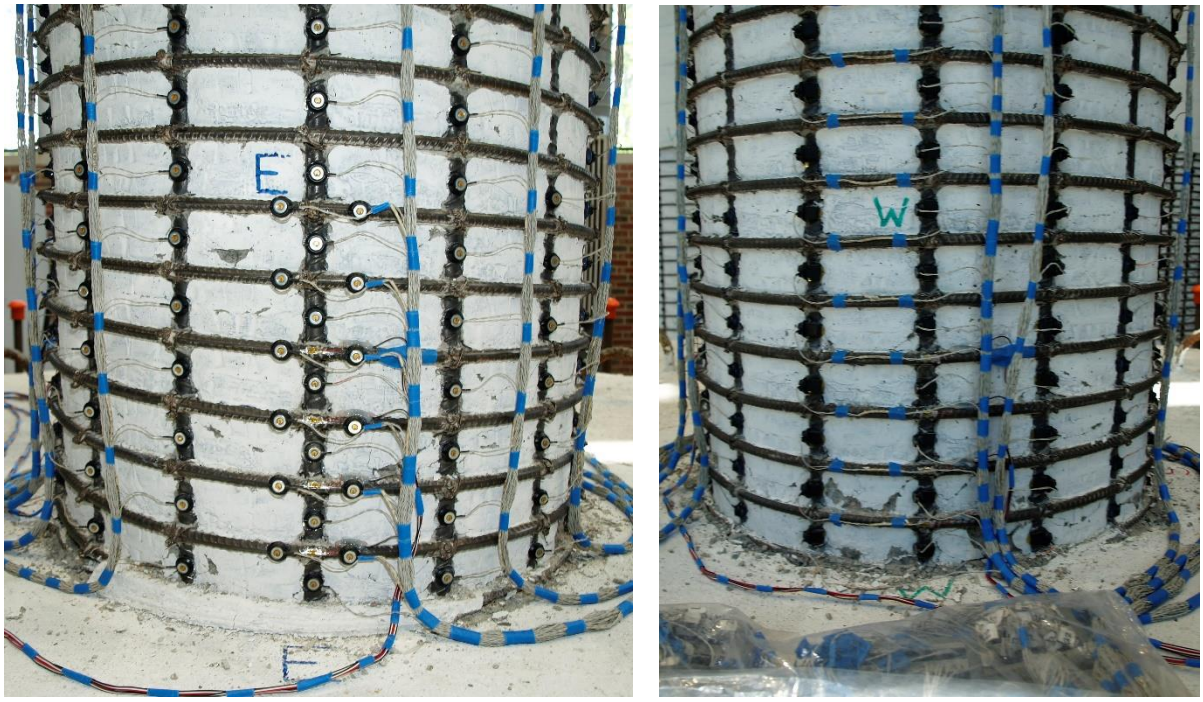

Figure 14-32. Test 11: (Left) East and (Right) West Sides of the Specimen during Compressive Cycles of $\mu_{\Delta 4}$

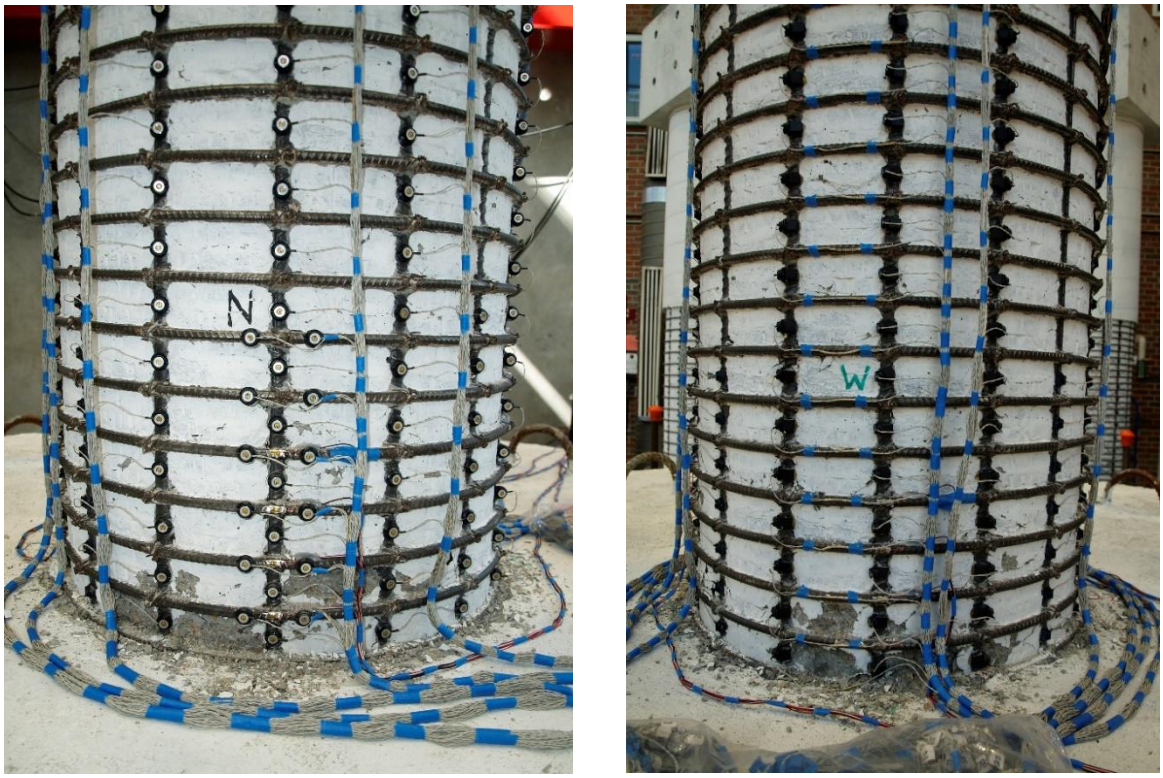

Figure 14-33. Test 11: Spiral Yielding on the (Left) North Side at $\mu_{\Delta 5}^{+1y} = 6.09"$ and (Right) West Side at $\mu_{\Delta 5}^{-1x} = -6.07"$

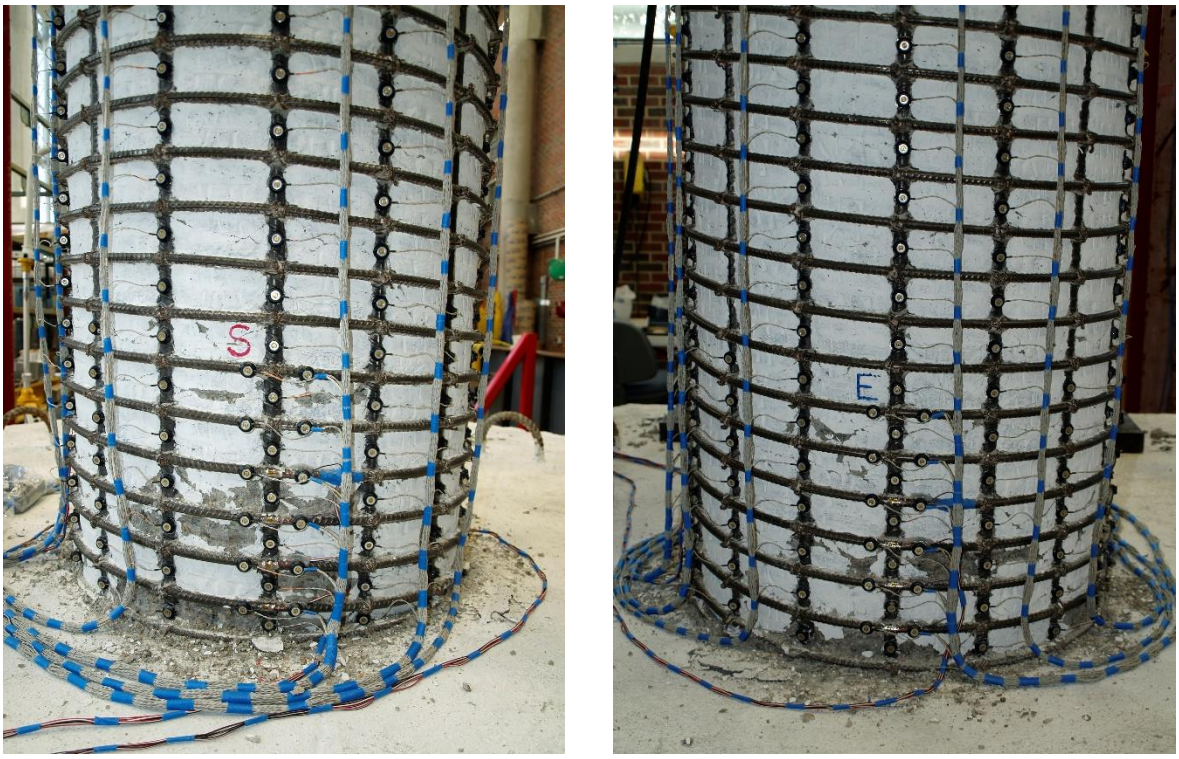

Figure 14-34. Test 11: Spiral Yielding on the (Left) South Side at $\mu_{\Delta 6}^{-1y} = -7.32$" and (Right) East Side at $\mu_{\Delta 6}^{+1x} = 7.35$"

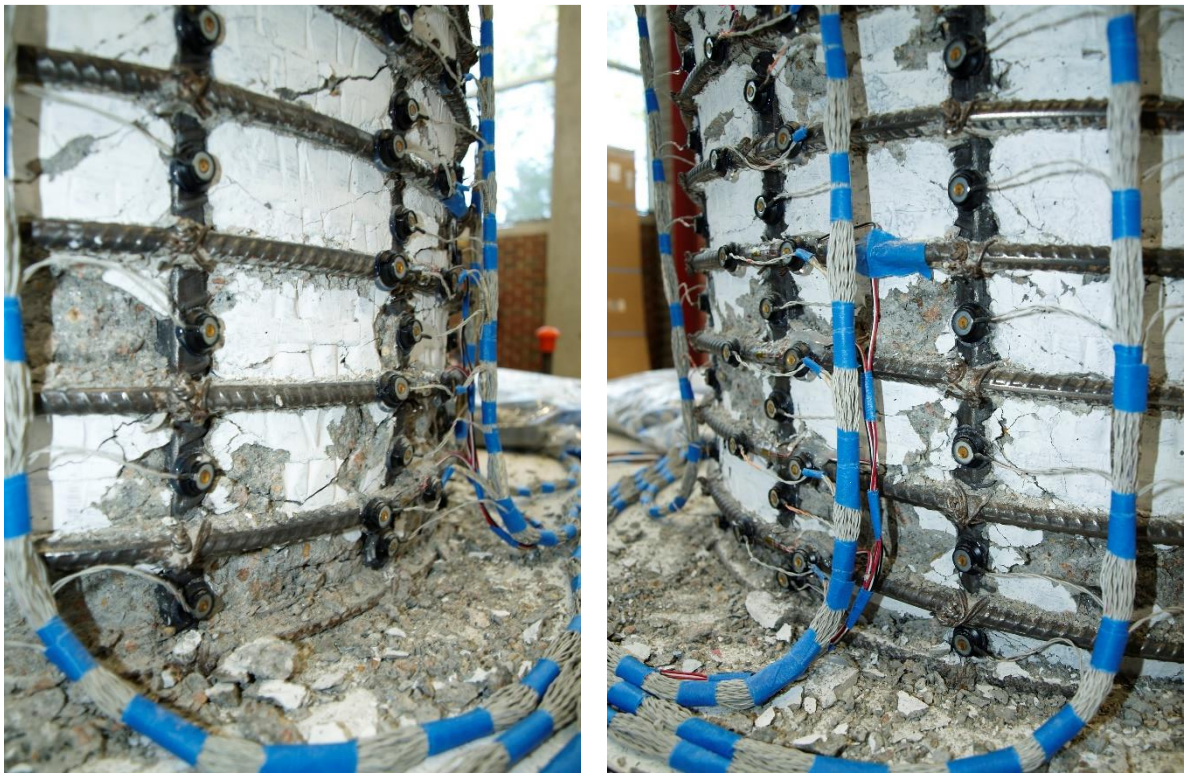

Figure 14-35. Test 11: (Left) North Bar Buckling at $\mu_{\Delta 7}^{+1y} = 8.55$" and (Right) South Remained Straight at $\mu_{\Delta 7}^{-1y} = -8.57$"

Figure 14-36. Test 11: Buckling of East bars NE, NNE, E and ENE during $\mu_{\Delta 7}^{+1x} = 8.49$"

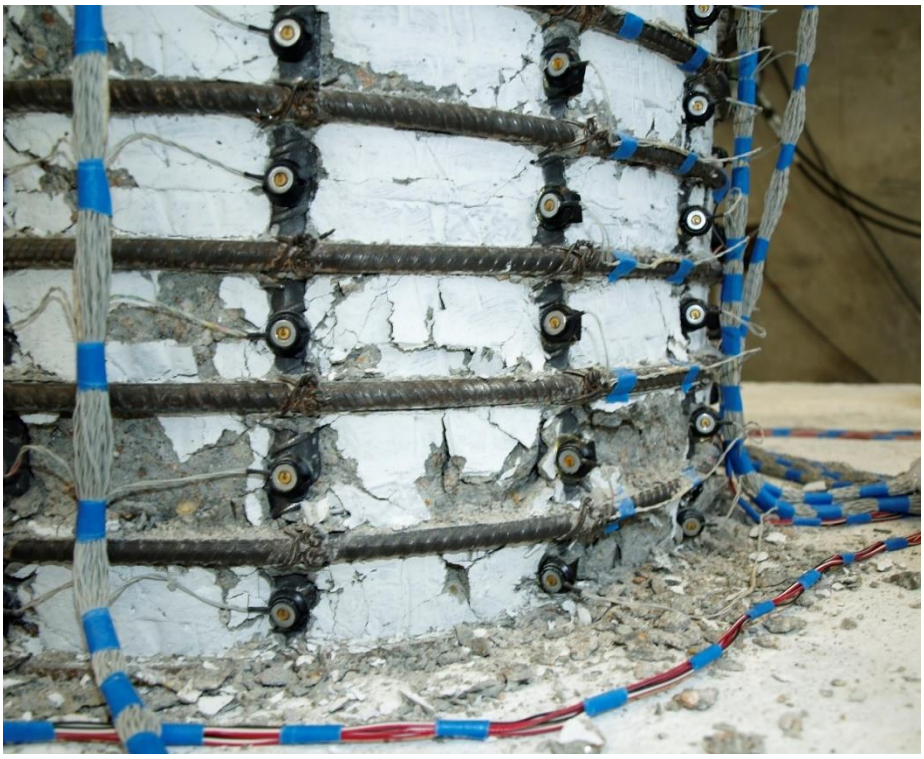

Figure 14-37. Test 11: Buckling of West bars NW, WNW, and W during $\mu_{\Delta 7}^{-1x} = -8.51$"

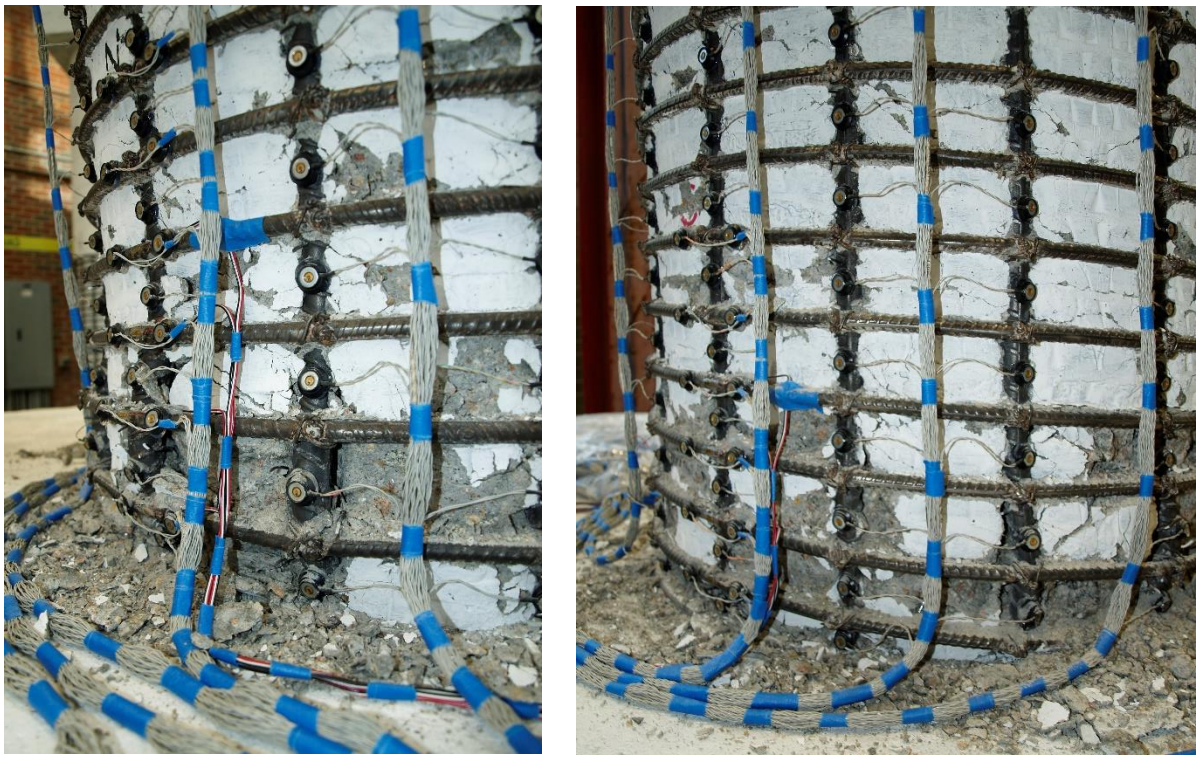

Figure 14-38. Test: Buckling of Bars (Left) NNW during $\mu_{\Delta 4.5p}^{+1y} = 5.50"$ (Right) SE and SSE during $\mu_{\Delta 4.5p}^{-1y} = -5.51"$

Figure 14-39. Test 11: Buckled Deformation on the East Side at $\mu_{\Delta 4.5p}^{+1x} = 5.48"$

Figure 14-40. Test 11: Buckling of Adjacent West Bars WSW and SW during $\mu_{\Delta 4.5p}^{-1x} = -5.48$"

Figure 14-41. Test 11: Fracture of the East Extreme Fiber Bar at $\Delta_x = -4.56$" during $\mu_{\Delta 4.5p}^{-1x} = -5.48$"

Figure 14-42. Test 11: (Left) North and (Right) East Sides of the Specimen after the Test

Figure 14-43. Test 11: (Left) South and (Right) West Sides of the Specimen after the Test

Test 11 - Strain Data Analysis

North and South Bar Strains

Vertical strain profiles for North and South reinforcement during y-direction cycles are shown in Figure 14-44 and Figure 14-45. Strains in the lowest four spiral layers during compressive y-direction cycles on the North and South sides of the specimen appear in Figure 14-46 and Figure 14-47. The relationship between strain and displacement for either peak tensile or peak compressive gauge lengths appear in Figure 14-48 through Figure 14-52. These figures contain monotonic moment curvature predictions for respective plastic hinge methods. PCK (2007) Lp refers to the (Priestley, Calvi and Kowalsky 2007) plastic hinge method, GN15 Tension/Compression Lpr refers to the (Goodnight, Kowalsky and Nau 2015a) unidirectional modified plastic hinge method, TX Measured refer to using the measured extent of plasticity and average equivalent strain penetration length from this specific test, and New Equations refers to a new bidirectional plastic hinge method which was created based on this study. Details of the new plastic hinge method appear in a later chapter of this report.

The spiral strain gauge hysteresis for the second layer above the footing on the North side of the specimen is shown in Figure 14-54. Tension strains in this layer increased during $\mu_{\Delta 7}^{+1y} = 8.55$" as the North extreme fiber bar visibly buckled, see Figure 14-35. The visual observation of bar buckling was confirmed upon inspection of the North longitudinal bar strain hysteresis in Figure 14-53.

The spiral strain gauge hysteresis for the second layer above the footing on the South side of the specimen is shown in Figure 14-57. The South extreme fiber bar never visibly buckled, but adjacent Bars SSE and SE buckled during $\mu_{\Delta 4.5p}^{-1y} = -5.51$", which was the first compressive post-peak cycle following $\mu_{\Delta 7}^{-1y} = -8.57$". These bars represent the first occurrence of bar buckling in the South region, but measured strain hysteresis for the extreme fiber bar are examined here, since only extreme fiber spiral strains were measured. The strain hystereses in Figure 14-55 and Figure 14-56 for the South extreme fiber bar is plotted through $\mu_{\Delta 7}^{-1y} = -8.57$". Although visible bar buckling was not observed, the hysteresis indicate that there was some degree of measurable outward deformation of the South bar during the peak compressive cycle. This slight measurable deformation was not accompanied by a spike in measured spiral tension strains as shown in Figure 14-57.

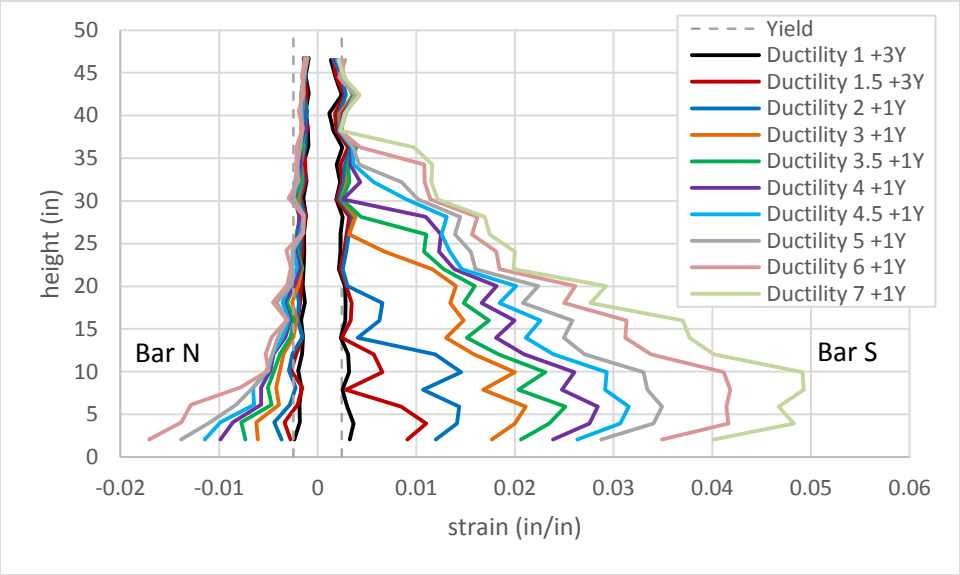

Figure 14-44. Test 11: Vertical Strain Profiles for Loading in the +Y-direction

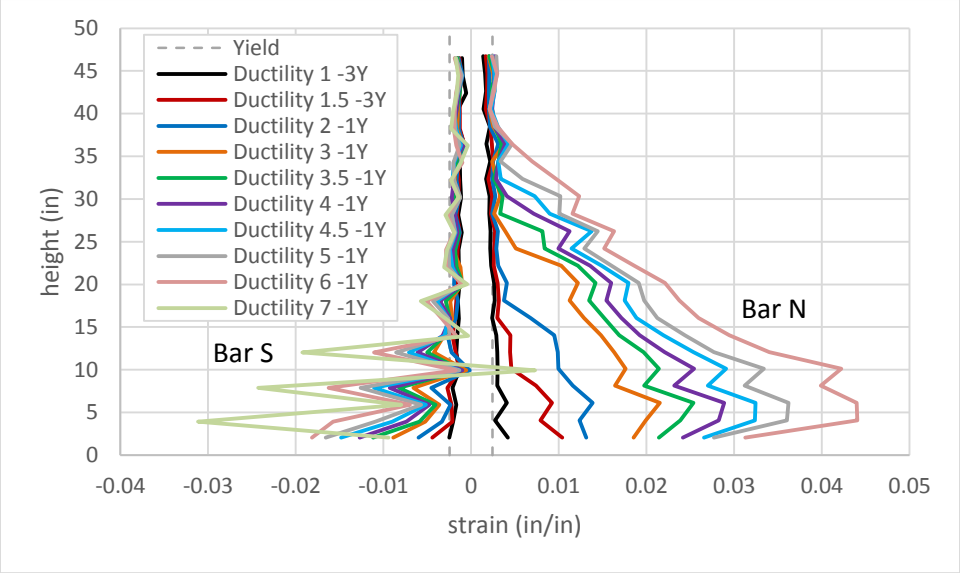

Figure 14-45. Test 11: Vertical Strain Profiles for Loading in the -Y-direction

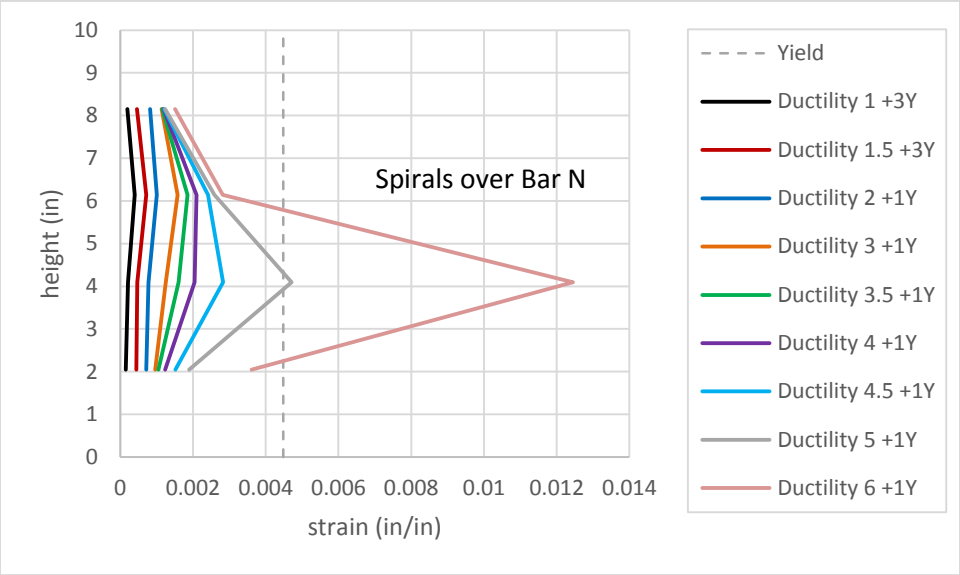

Figure 14-46. Test 11: Spiral Strains Measured Over the North Extreme Fiber Bar during +Y Cycles

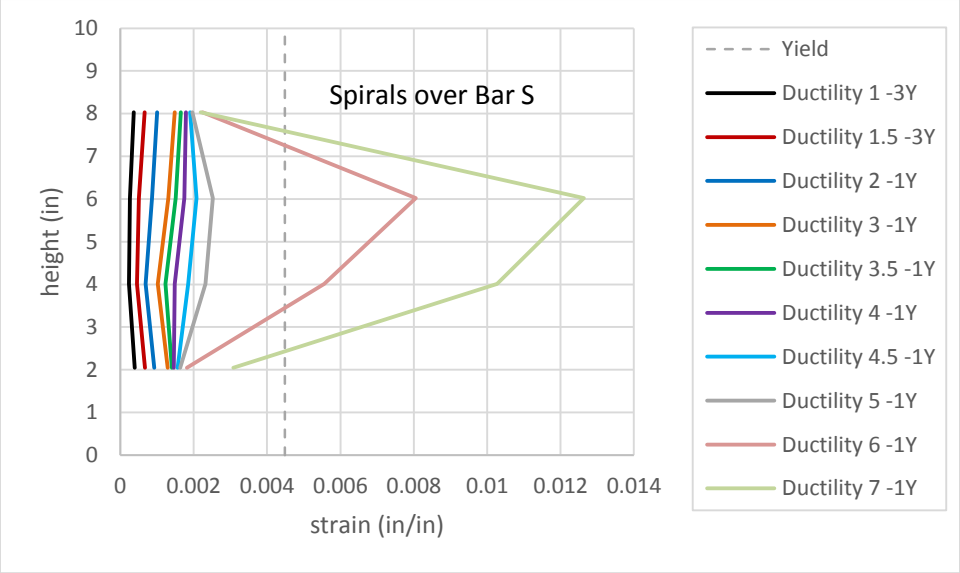

Figure 14-47. Test 11: Spiral Strains Measured Over the South Extreme Fiber Bar during -Y Cycles

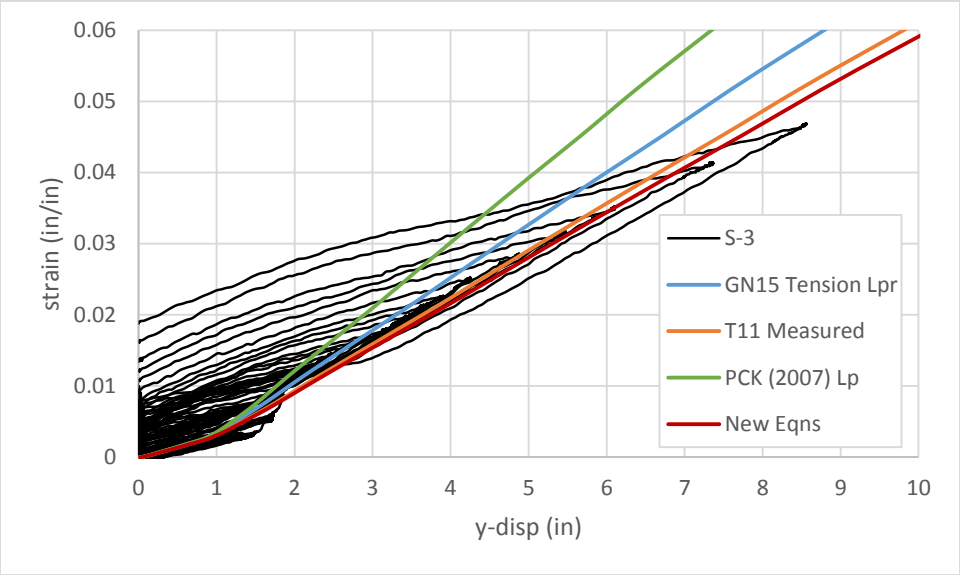

Figure 14-48. Test 11: Tension Strain-Disp. for Bar S (Gauge Length 3 Centered 5.89" above the Footing)

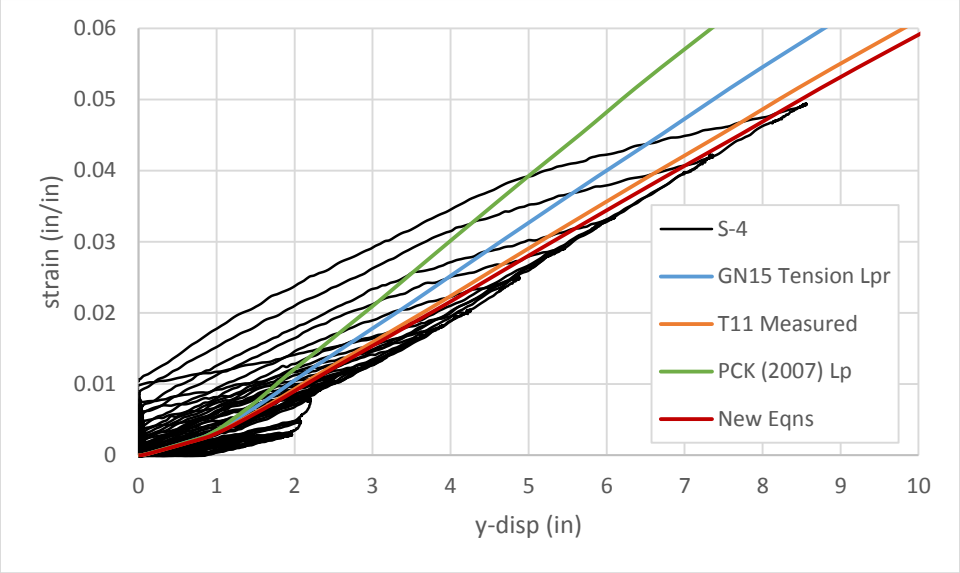

Figure 14-49. Test 11: Tension Strain-Disp. for Bar S (Gauge Length 4 Centered 7.88" above the Footing)

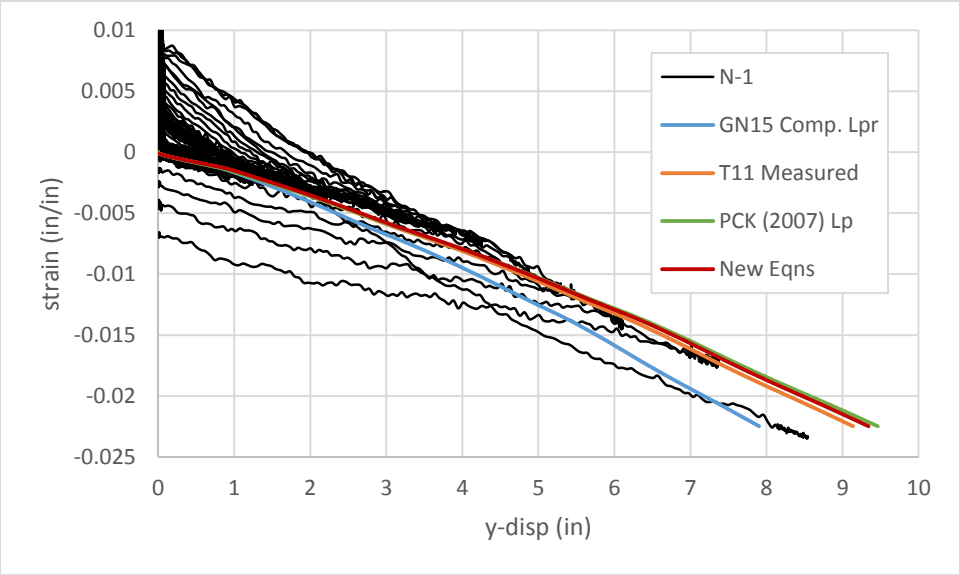

Figure 14-50. Test 11: Compression Strain-Disp. for Bar N (Gauge Length 1 Centered 2.06" above the Footing)

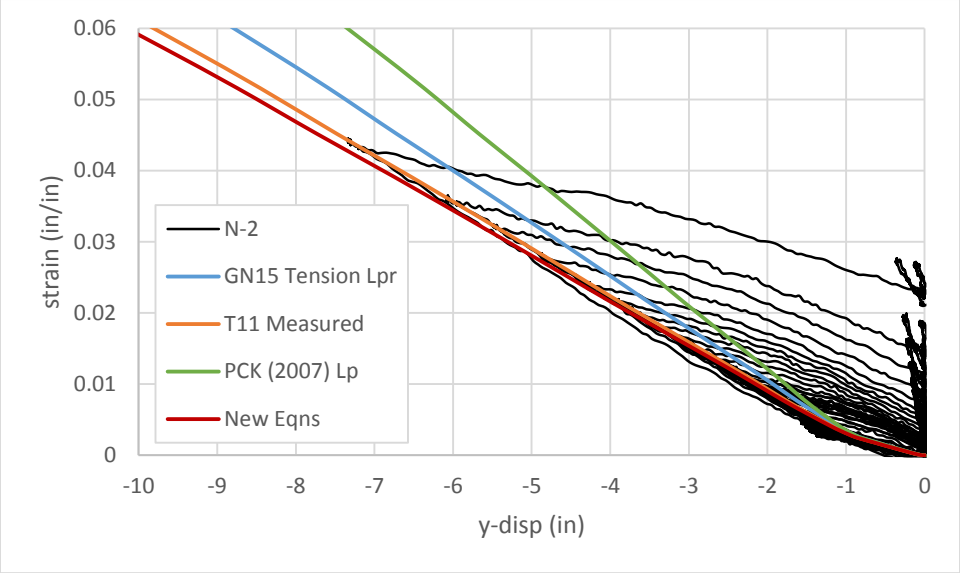

Figure 14-51. Test 11: Tension Strain-Disp. for Bar N (Gauge Length 2 Centered 4.07" above the Footing)

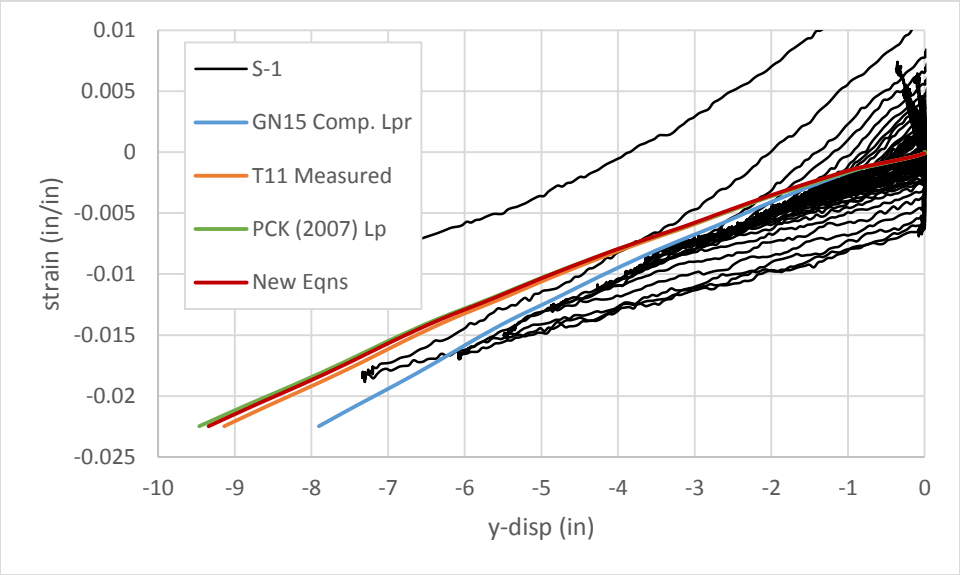

Figure 14-52. Test 11: Compression Strain-Disp. for Bar S (Gauge Length 1 Centered 2.05" above the Footing)

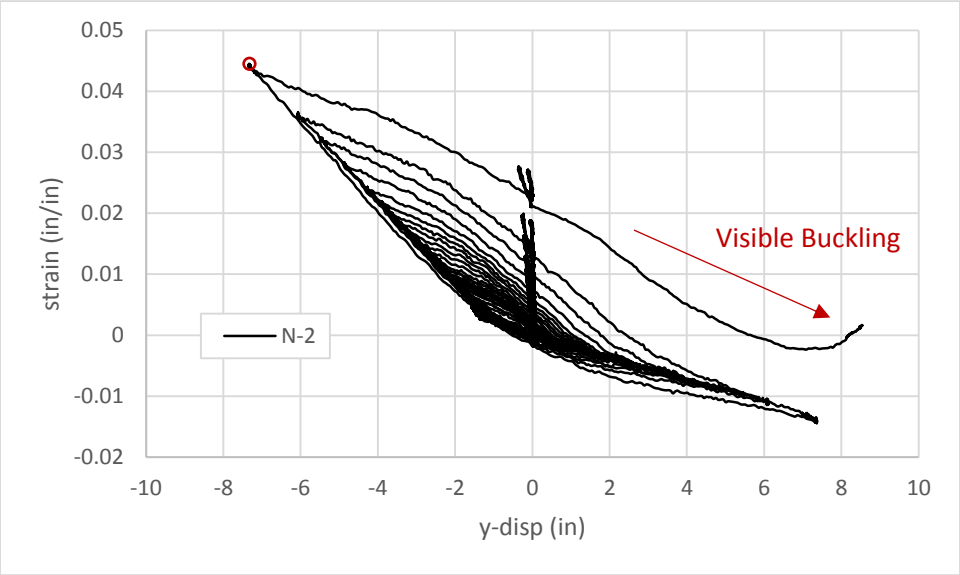

Figure 14-53. Test 11: Strain Hysteresis over the North Buckled Bar (Gauge Length 2 Centered 4.07" above the Footing)

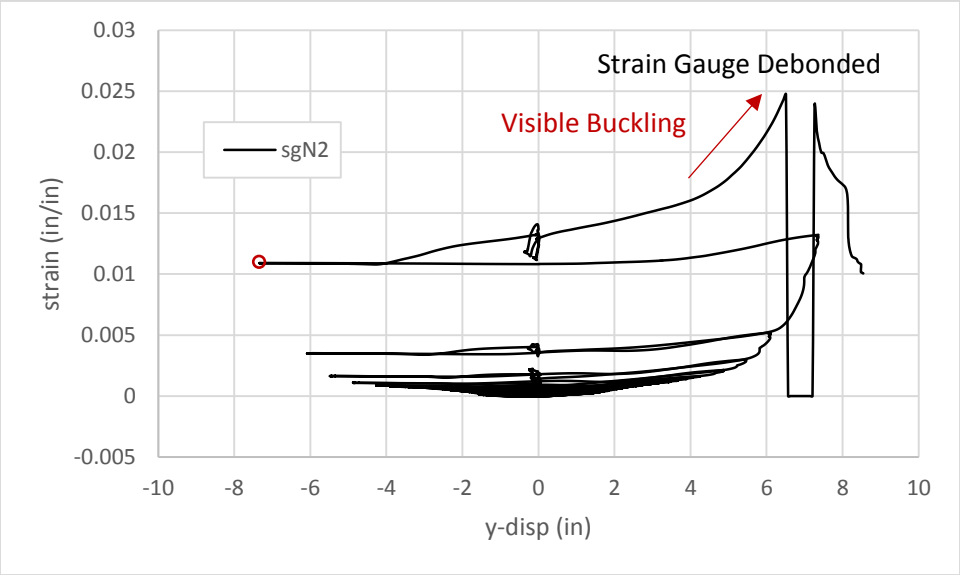

Figure 14-54. Test 11: Spiral Strain Hysteresis for the 2nd North Layer above the Footing

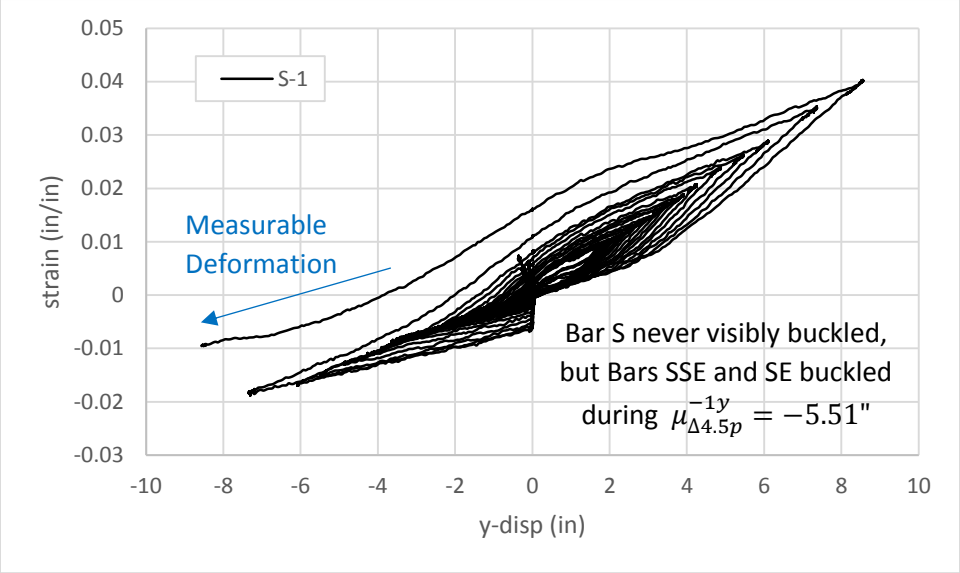

Figure 14-55. Test 11: Strain Hysteresis for the South Bar (Gauge Length 1 Centered 2.05" above the Footing)

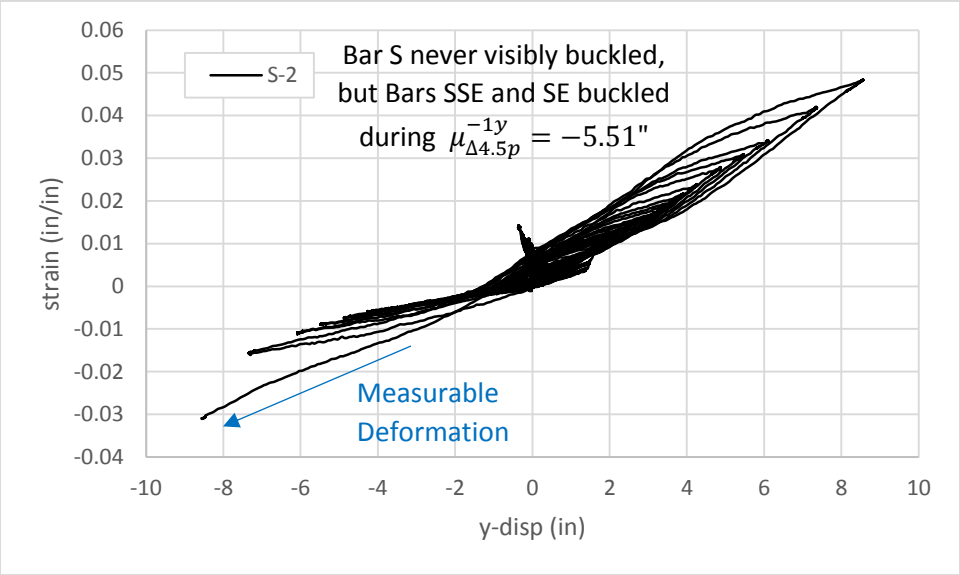

Figure 14-56. Test 11: Strain Hysteresis for the South Bar (Gauge Length 2 Centered 3.92" above the Footing)

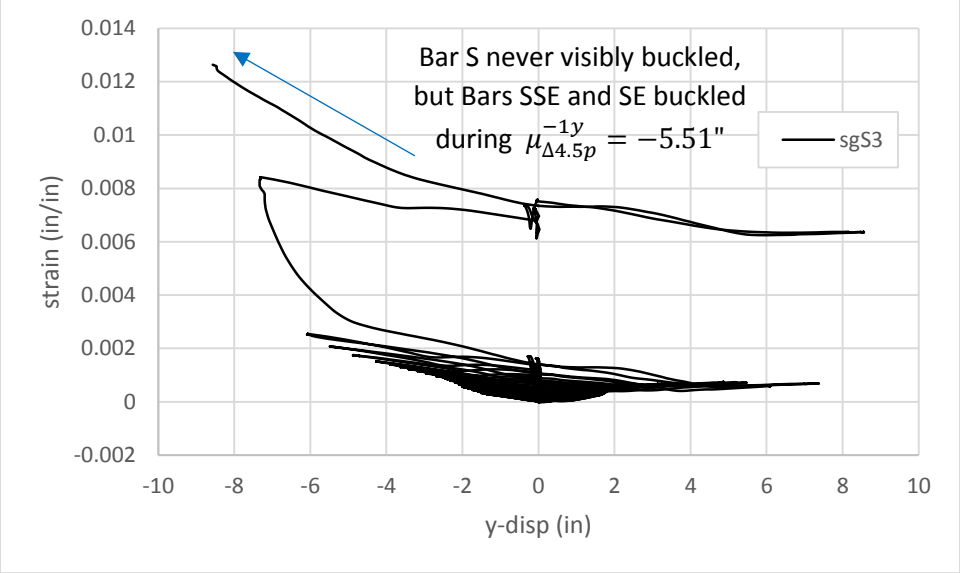

Figure 14-57. Test 11: Spiral Strain Hysteresis for the 3rd South Layer above the Footing

East and West Bar Strains

Vertical strain profiles for East and West reinforcement during x-direction cycles are shown in Figure 14-58 and Figure 14-59. Strains in the lowest four spiral layers during compressive x-direction cycles on the East and West sides of the specimen appear in Figure 14-60 and Figure 14-61. The relationship between strain and displacement for either peak tensile or peak compressive gauge lengths appear in Figure 14-62 through Figure 14-67. These figures contain monotonic moment curvature predictions for respective plastic hinge methods. PCK (2007) Lp refers to the (Priestley, Calvi and Kowalsky 2007) plastic hinge method, GN15 Tension/Compression Lpr refers to the (Goodnight, Kowalsky and Nau 2015a) unidirectional modified plastic hinge method, TX Measured refer to using the measured extent of plasticity and average equivalent strain penetration length from this specific test, and New Equations refers to a new bidirectional plastic hinge method which was created based on this study. Details of the new plastic hinge method appear in a later chapter of this report.

The spiral strain gauge hystereses for the first and second layers above the footing on the East side of the specimen is shown in Figure 14-69 and Figure 14-70. The strain gauge over the first layer went off scale during $\mu_{\Delta 6}^{+1x} = 7.35$", even though the East reinforcement remained visibly straight. Tension strains the second layer increased during $\mu_{\Delta 7}^{+1x} = 8.49$" as the four East bars buckled simultaneously, see Figure 14-36. The visual observation of bar buckling was confirmed upon inspection of the East longitudinal bar strain hysteresis in Figure 14-68.

The spiral strain gauge hysteresis for the first layer above the footing on the West side of the specimen is shown in Figure 14-73. Tension strains in this layer increased during $\mu_{\Delta 7}^{-1x} = -8.51$" as three West bars buckled simultaneously, see Figure 14-37. The visual observation of bar buckling was confirmed upon inspection of the West longitudinal bar strain hystereses in Figure 14-71 and Figure 14-72.

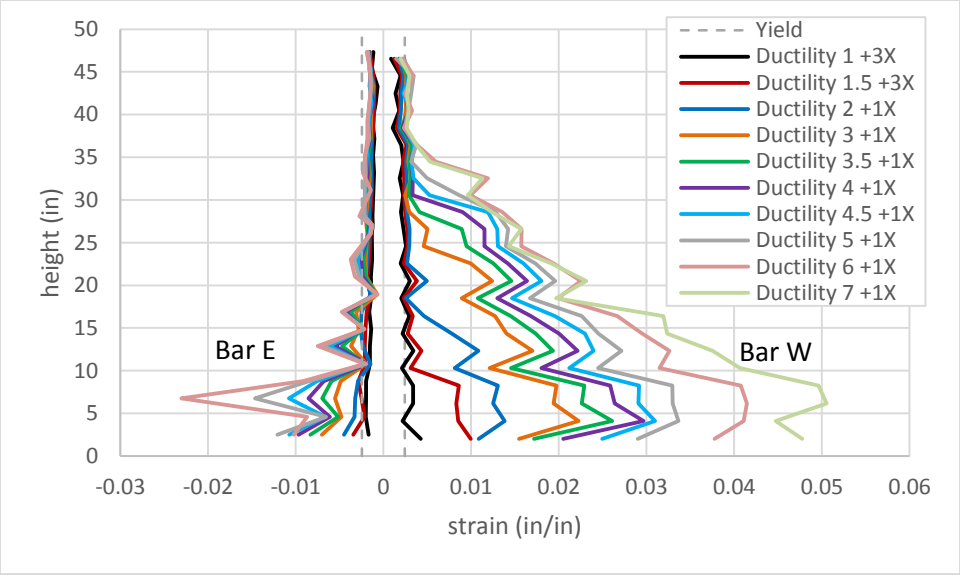

Figure 14-58. Test 11: Vertical Strain Profiles for Loading in the +X-direction

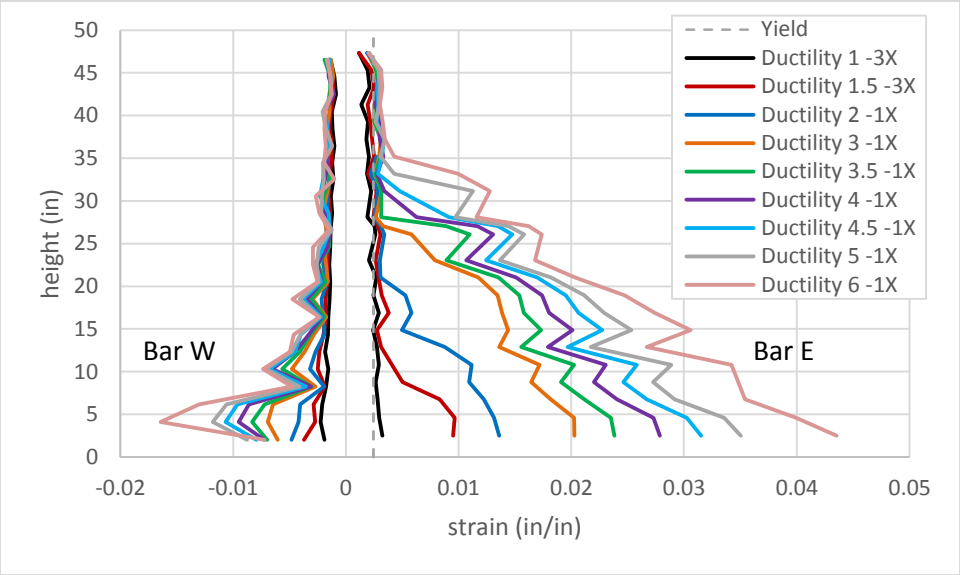

Figure 14-59. Test 11: Vertical Strain Profiles for Loading in the -X-direction

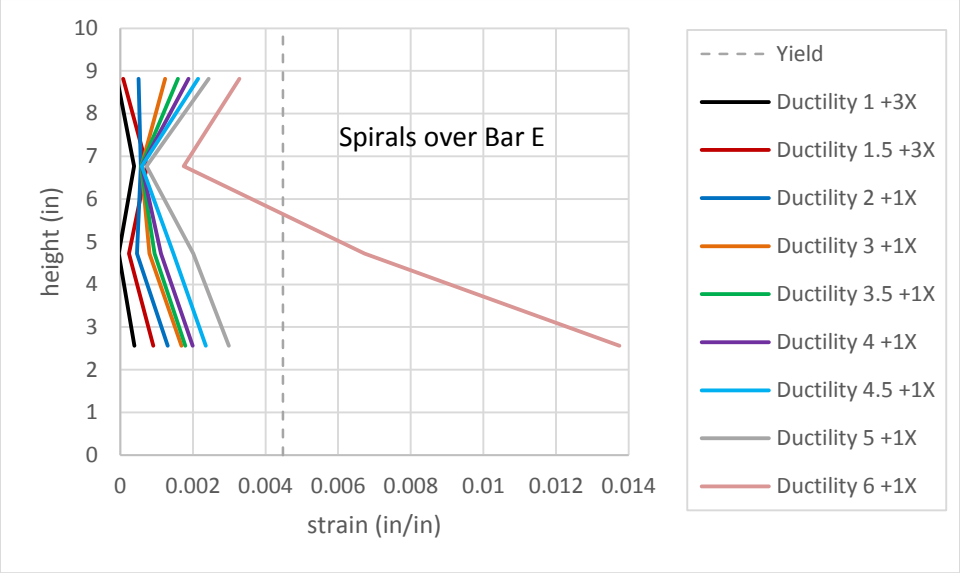

Figure 14-60. Test 11: Spiral Strains Measured Over the East Extreme Fiber Bar during +X Cycles

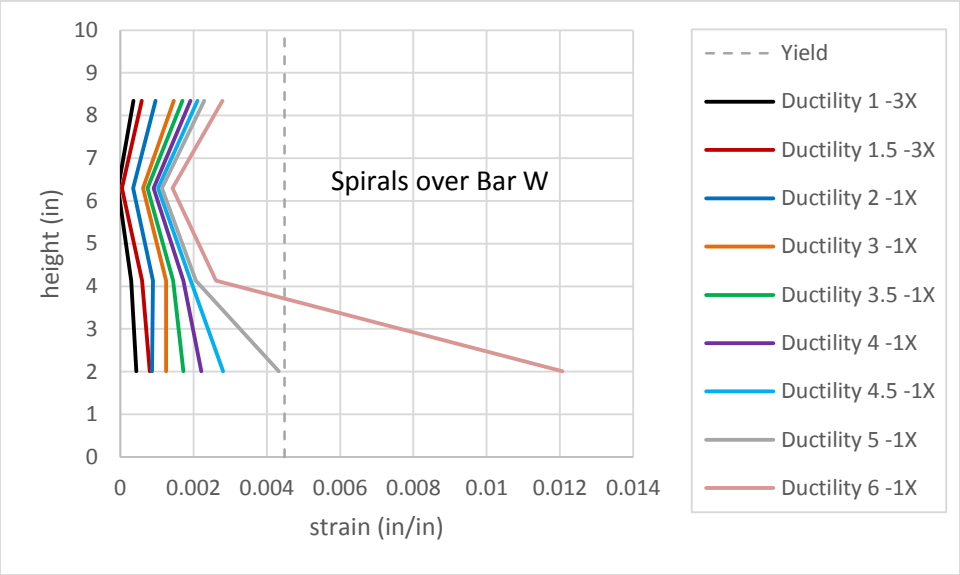

Figure 14-61. Test 11: Spiral Strains Measured Over the East Extreme Fiber Bar during -X Cycles

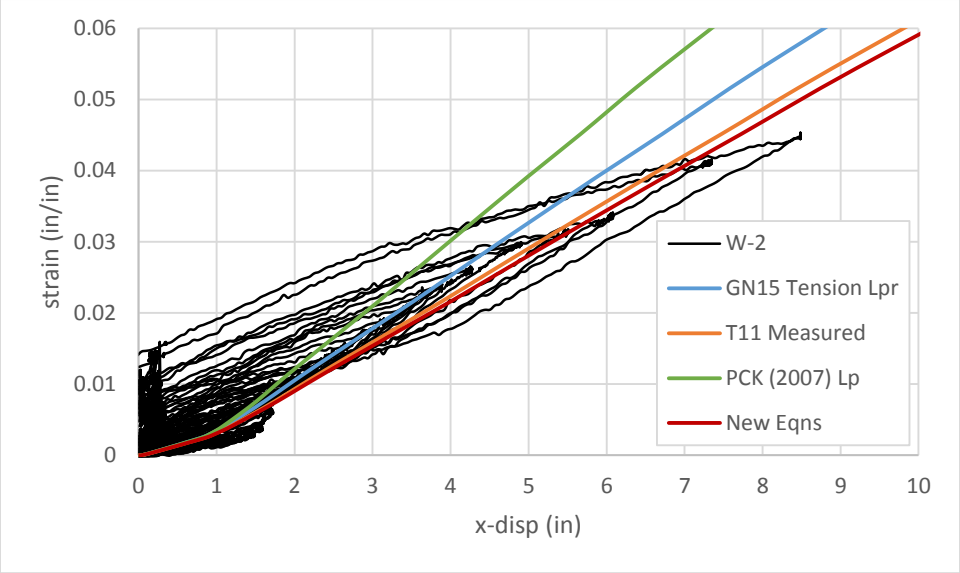

Figure 14-62. Test 11: Tension Strain-Disp. for Bar W (Gauge Length 2 Centered 4.13" above the Footing)

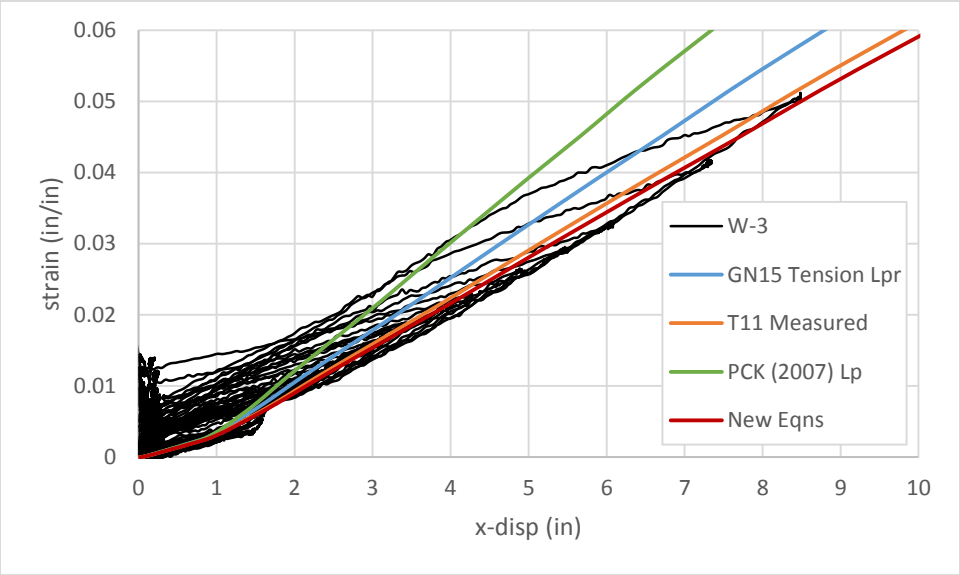

Figure 14-63. Test 11: Tension Strain-Disp. for Bar W (Gauge Length 3 Centered 6.18" above the Footing)

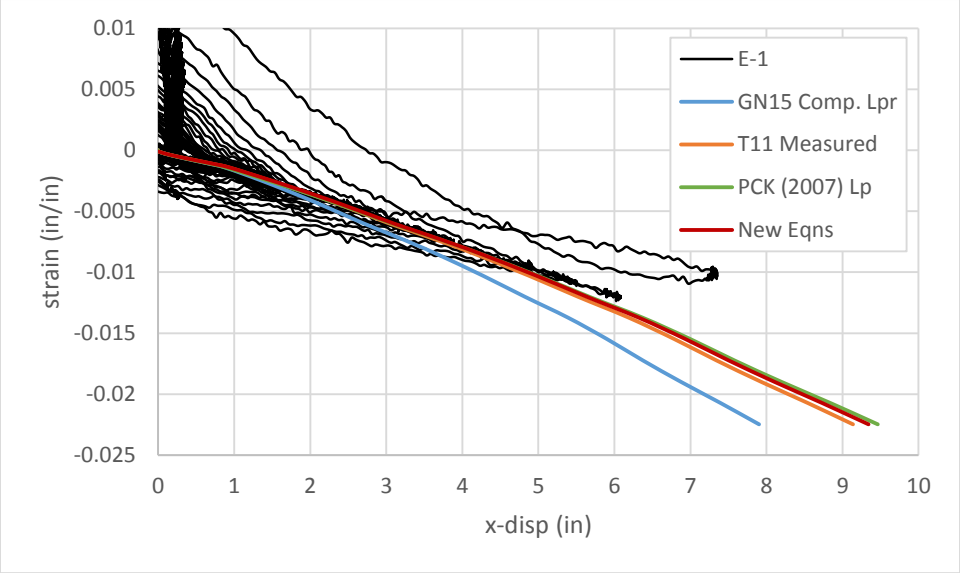

Figure 14-64. Test 11: Compression Strain-Disp. for Bar E (Gauge Length 1 Centered 2.51" above the Footing)

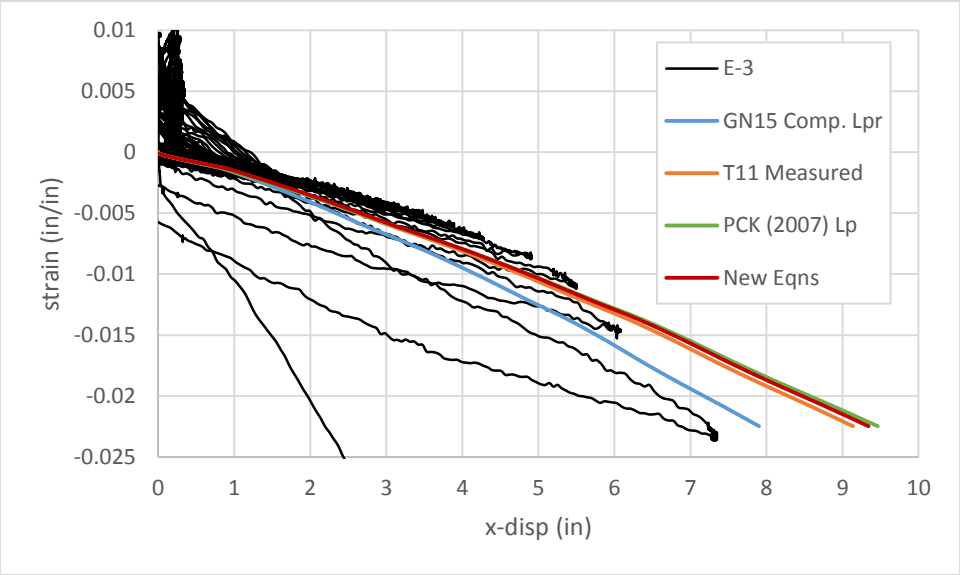

Figure 14-65. Test 11: Compression Strain-Disp. for Bar E (Gauge Length 3 Centered 6.74" above the Footing)

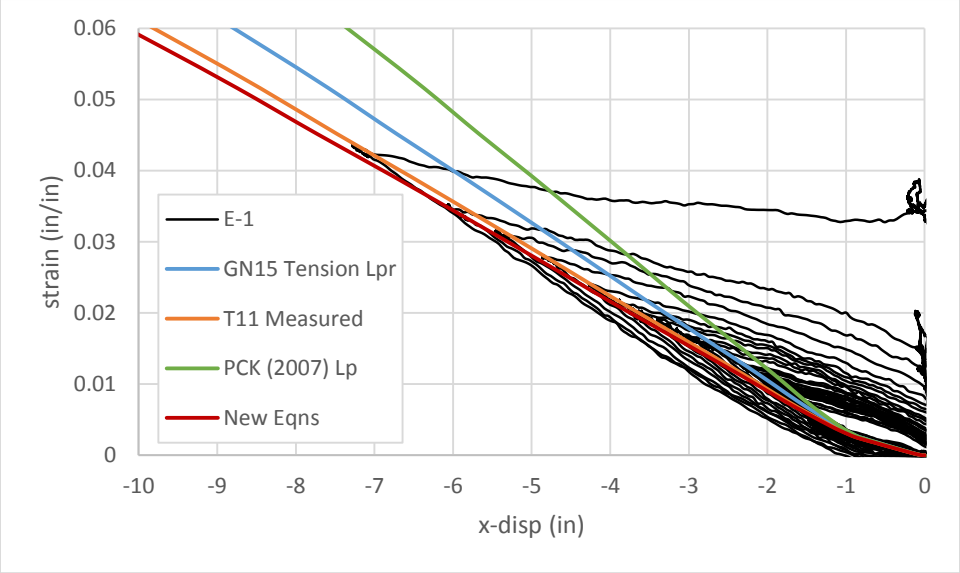

Figure 14-66. Test 11: Tension Strain-Disp. for Bar E (Gauge Length 1 Centered 2.51" above the Footing)

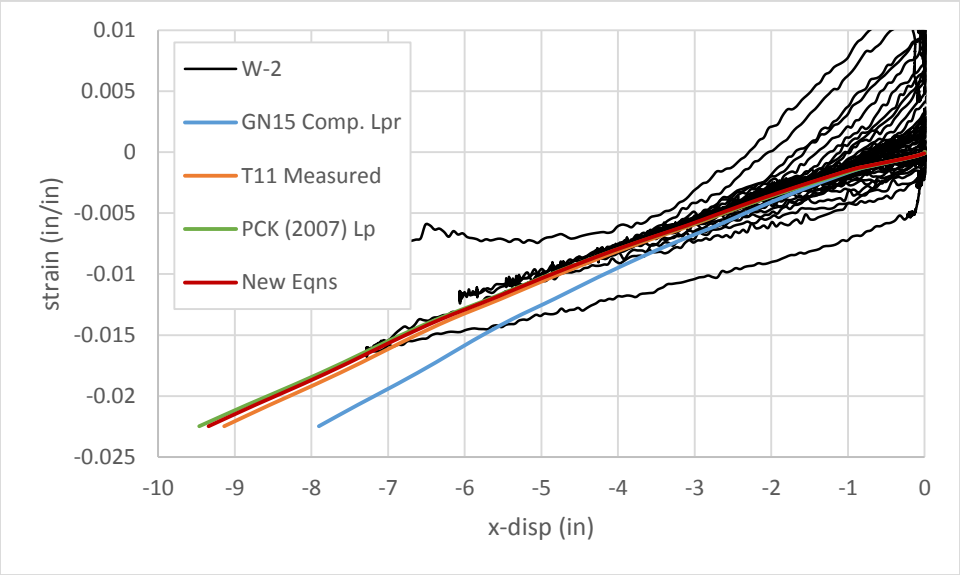

Figure 14-67. Test 11: Compression Strain-Disp. for Bar W (Gauge Length 2 Centered 4.13" above the Footing)

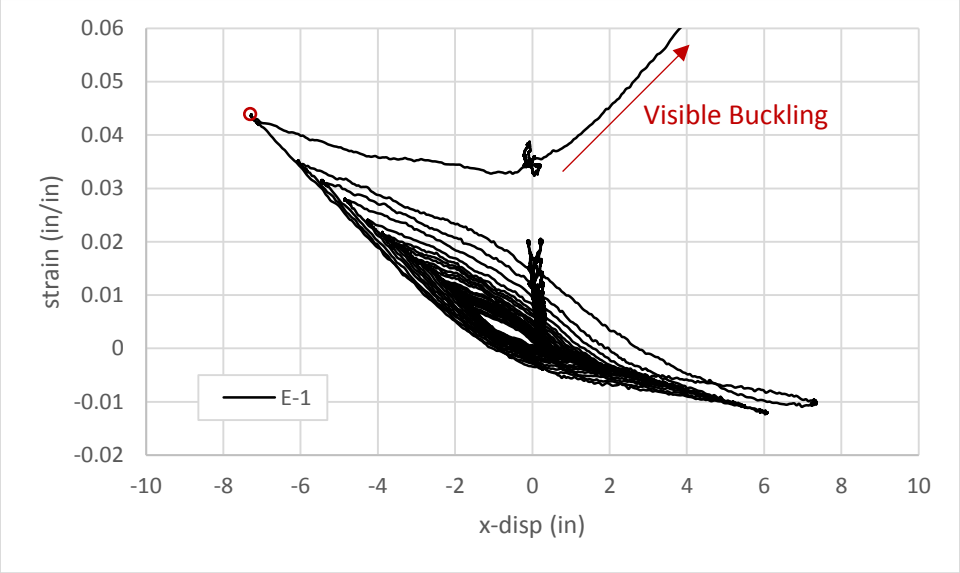

Figure 14-68. Test 11: Strain Hysteresis over the East Buckled Bar (Gauge Length 1 Centered 2.51" above the Footing)

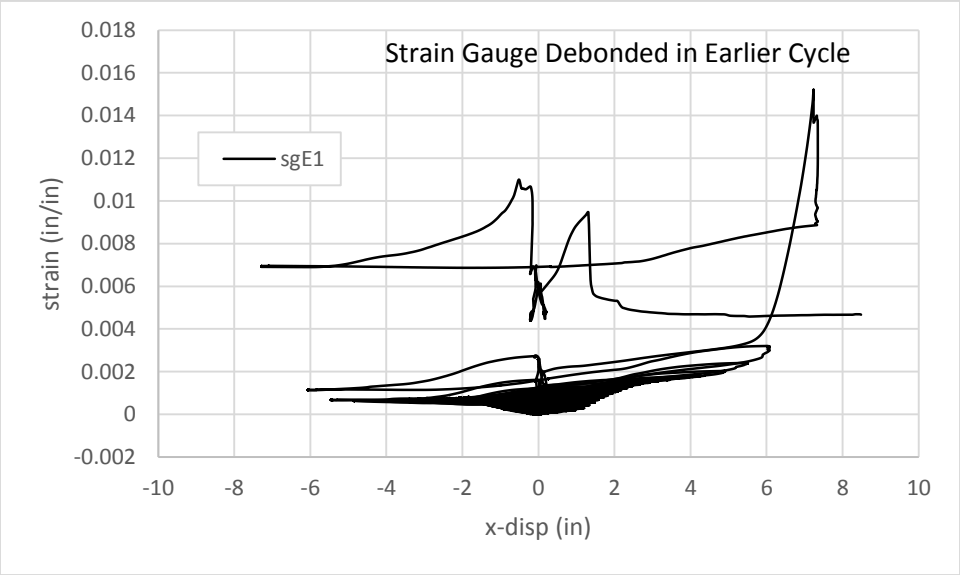

Figure 14-69. Test 11: Spiral Strain Hysteresis for the 1st East Layer above the Footing

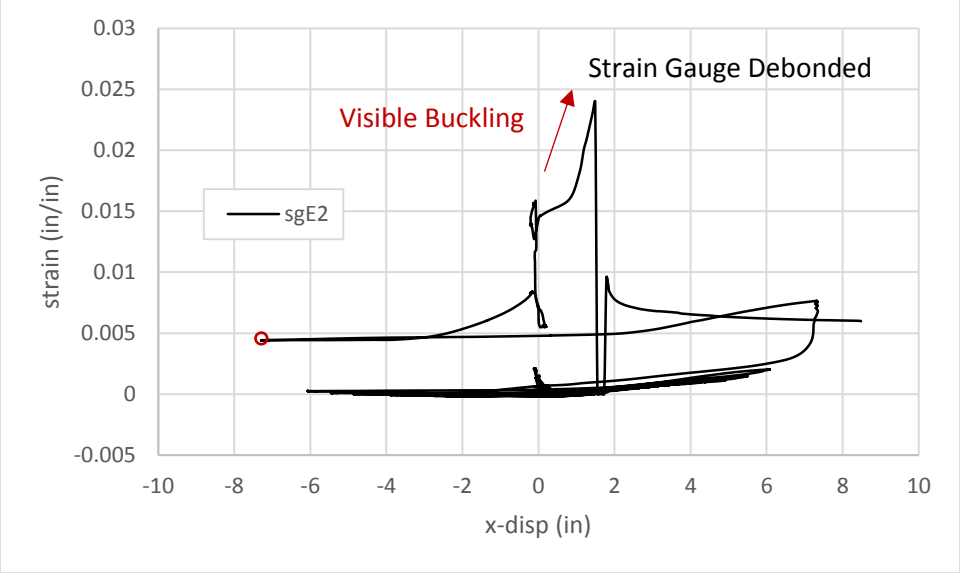

Figure 14-70. Test 11: Spiral Strain Hysteresis for the 2nd East Layer above the Footing

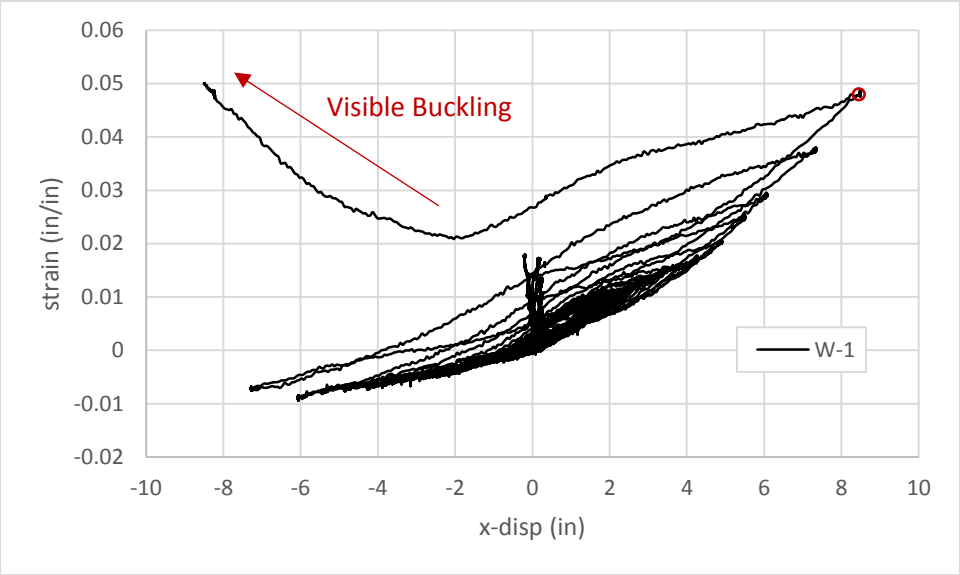

Figure 14-71. Test 11: Strain Hysteresis over the West Buckled Bar (Gauge Length 1 Centered 2.02" above the Footing)

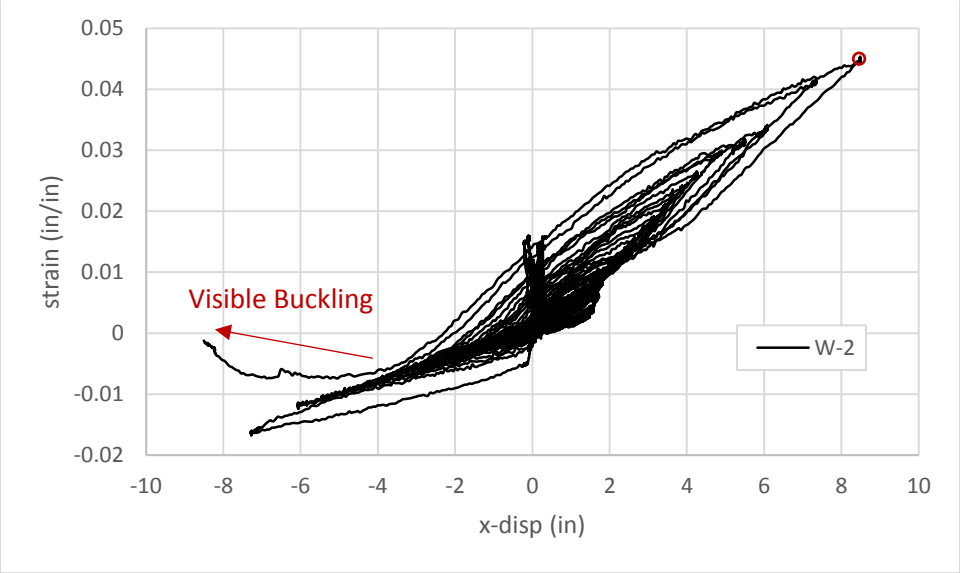

Figure 14-72. Test 11: Strain Hysteresis over the West Buckled Bar (Gauge Length 2 Centered 4.13" above the Footing)

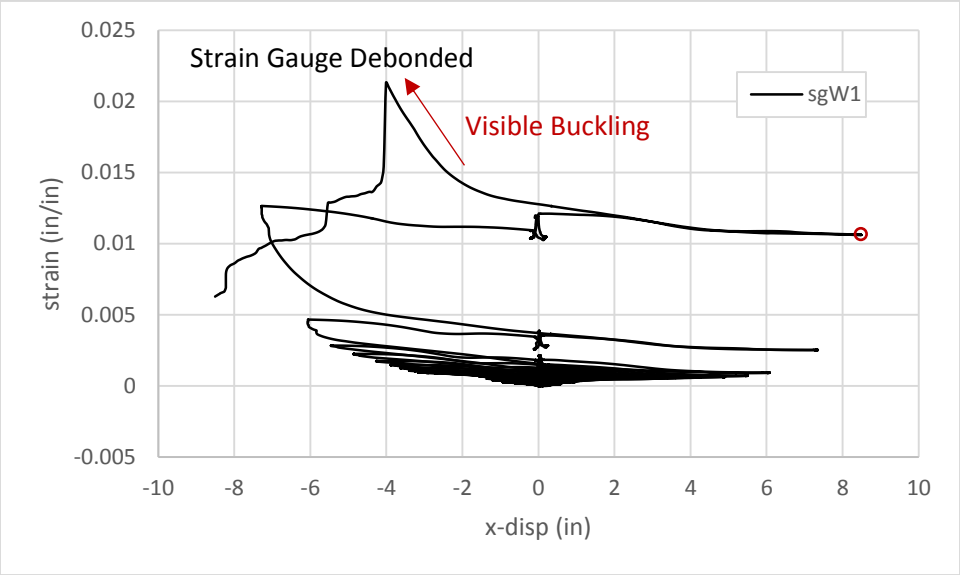

Figure 14-73. Test 11: Spiral Strain Hysteresis for the 1st West Layer above the Footing

Test 11 - Curvature and Strain Penetration Data

Curvature and stain penetration data for Test 11 is presented in the following section. The methods in which this data was generated are outlined in the summary for Test 1. Sample cross section curvature profiles are shown in Figure 14-74 and Figure 14-75. Vertical curvature profiles for respective loading directions appear in Figure 14-76 through Figure 14-80. Fixed-end rotations attributable to strain penetration of longitudinal reinforcement into the footing are shown in Figure 14-81 through Figure 14-83. Comparison of the measured displacements to those obtained via integration of the measured curvature profiles and extrapolation of the fixed-end rotation to the center of the applied lateral load are shown in Figure 14-84 and Figure 14-85.

The measured extent of plasticity is compared to design recommendations for the tensile triangular plastic hinge length in Figure 14-86. GN15 refers to the (Goodnight, Kowalsky and Nau 2015a) unidirectional tensile hinge length while New Equations refers to a new bidirectional plastic hinge method which was created based on this study. Details of the new plastic hinge method appear in a later chapter of this report. The measured equivalent strain penetration lengths are compared to design recommendations in Figure 14-87. GN15 refers to the (Goodnight, Kowalsky and Nau 2015a) unidirectional Lsp while PCK (2007) refers to the (Priestley, Calvi and Kowalsky 2007) definition of Lsp. Finally, the measured hysteretic response is compared to monotonic predictions in Figure 14-88 and Figure 14-89.

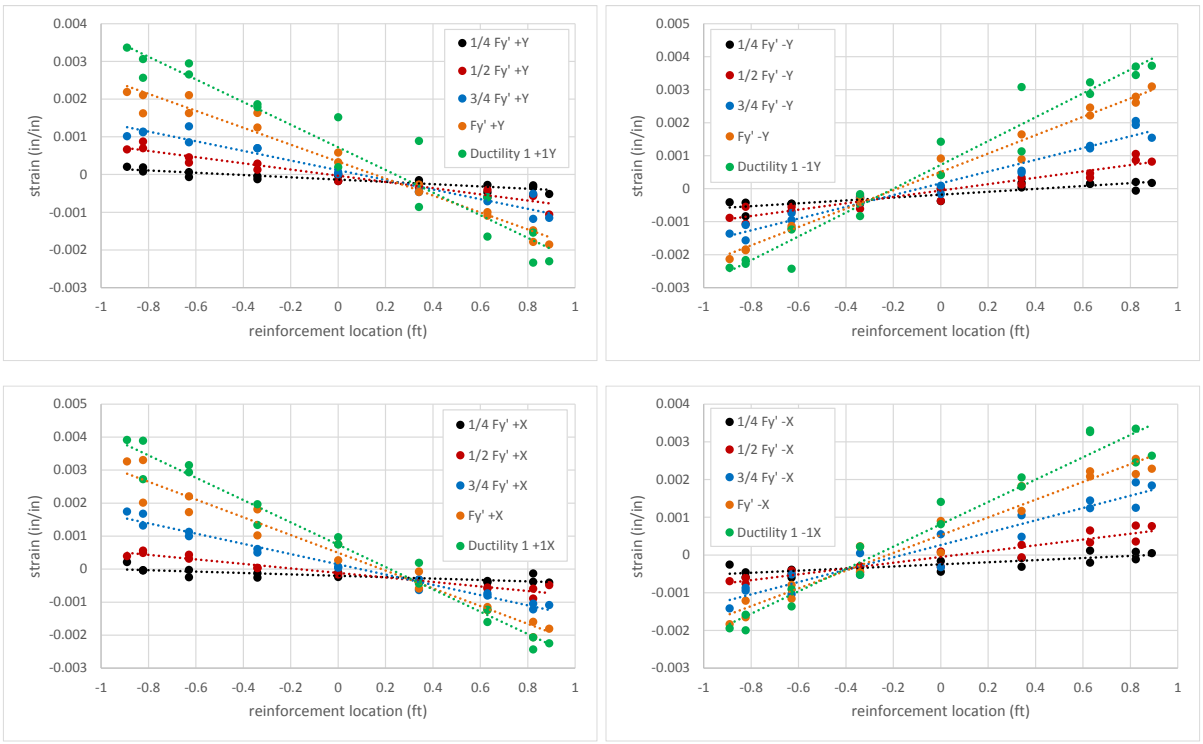

Figure 14-74. Test 11: Elastic Curvature Profiles for the First Instrumented Section above the Footing

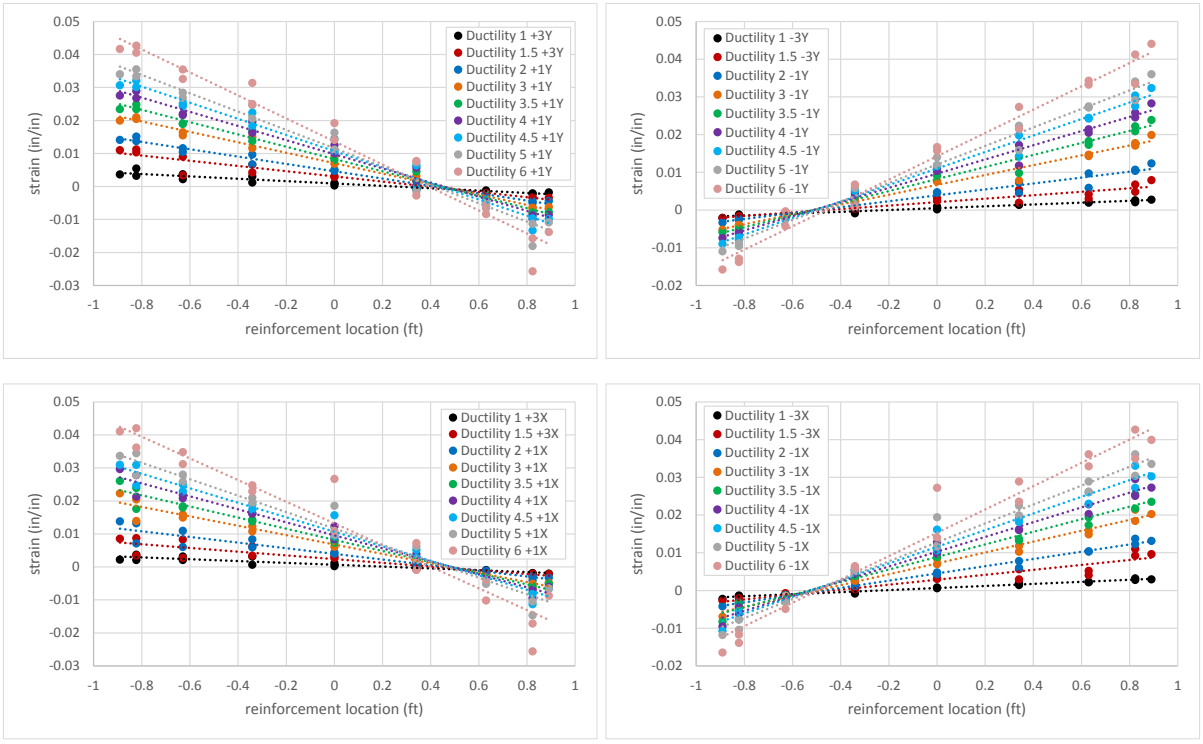

Figure 14-75. Test 11: Curvature Profiles for the Second Instrumented Section above the Footing

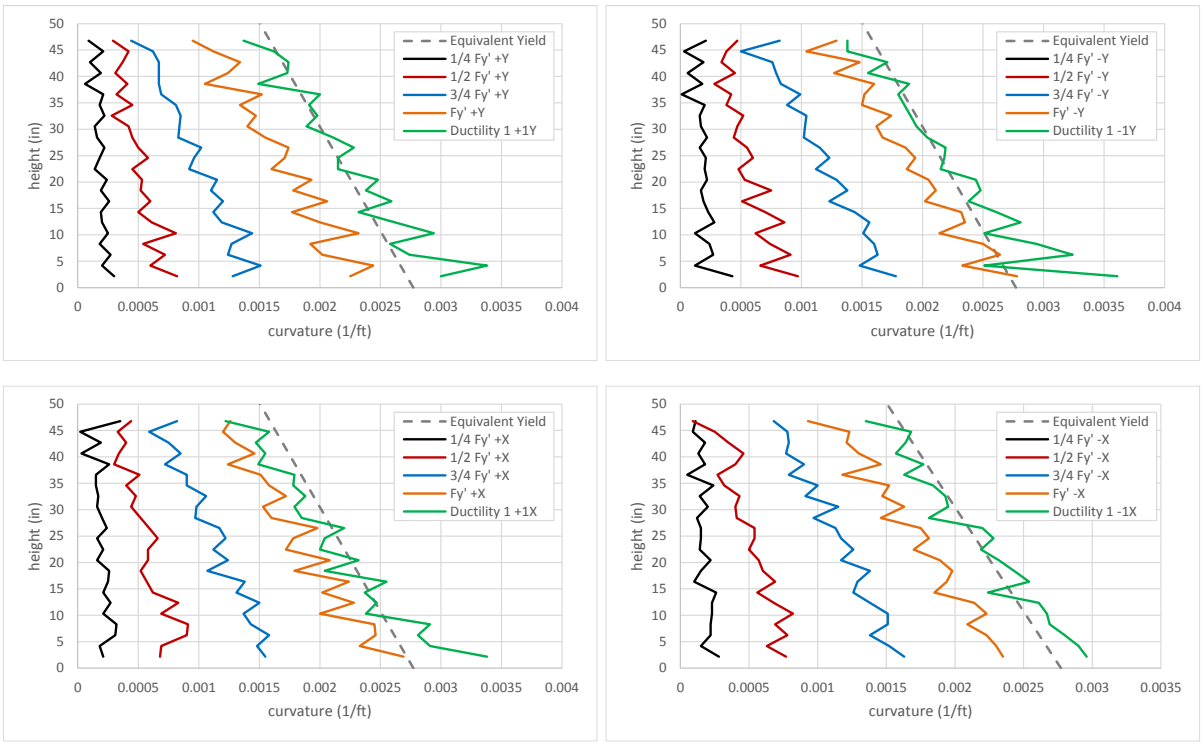

Figure 14-76. Test 11: Elastic Vertical Curvature Profiles

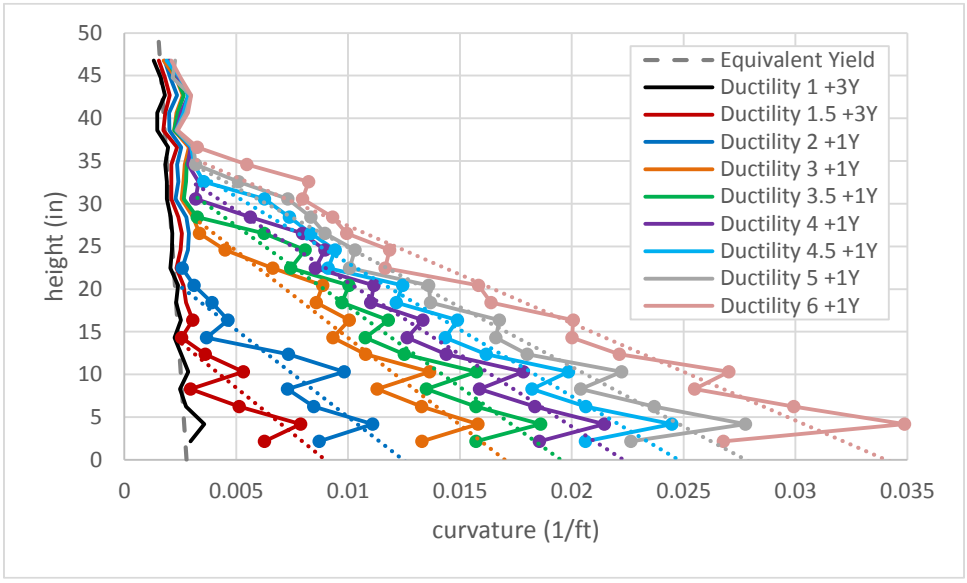

Figure 14-77. Test 11: Vertical Curvature Profiles for Loading in the +Y-direction

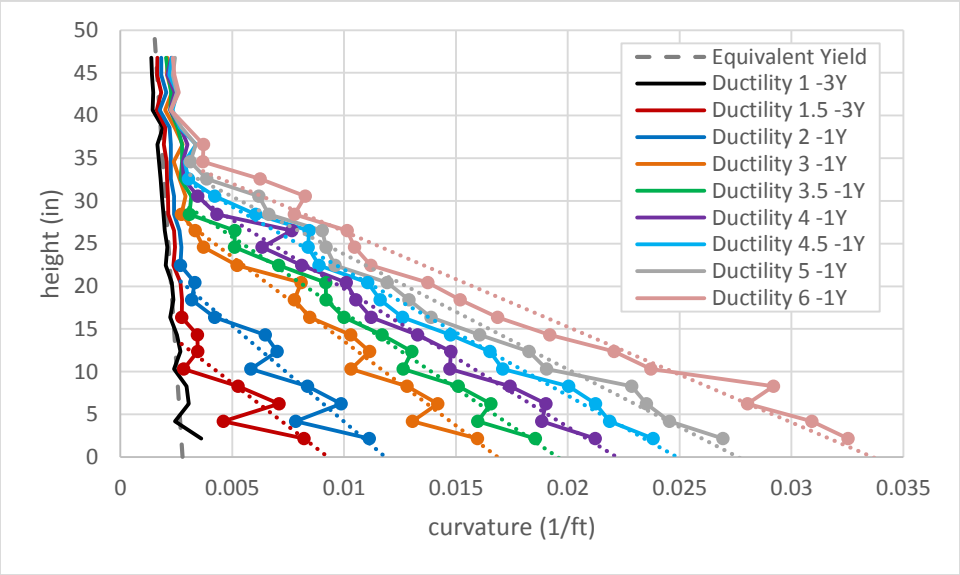

Figure 14-78. Test 11: Vertical Curvature Profiles for Loading in the -Y-direction

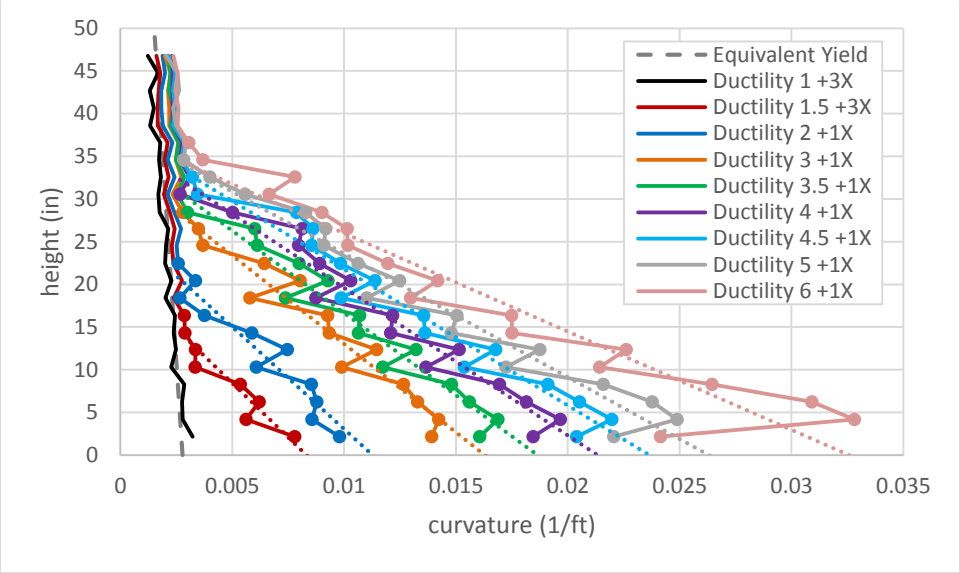

Figure 14-79. Test 11: Vertical Curvature Profiles for Loading in the +X-direction

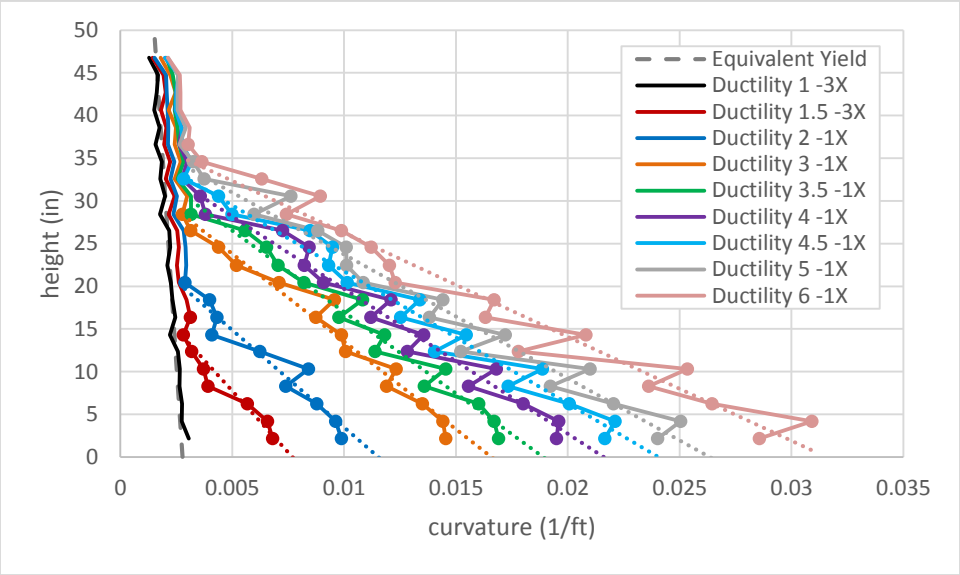

Figure 14-80. Test 11: Vertical Curvature Profiles for Loading in the -X-direction

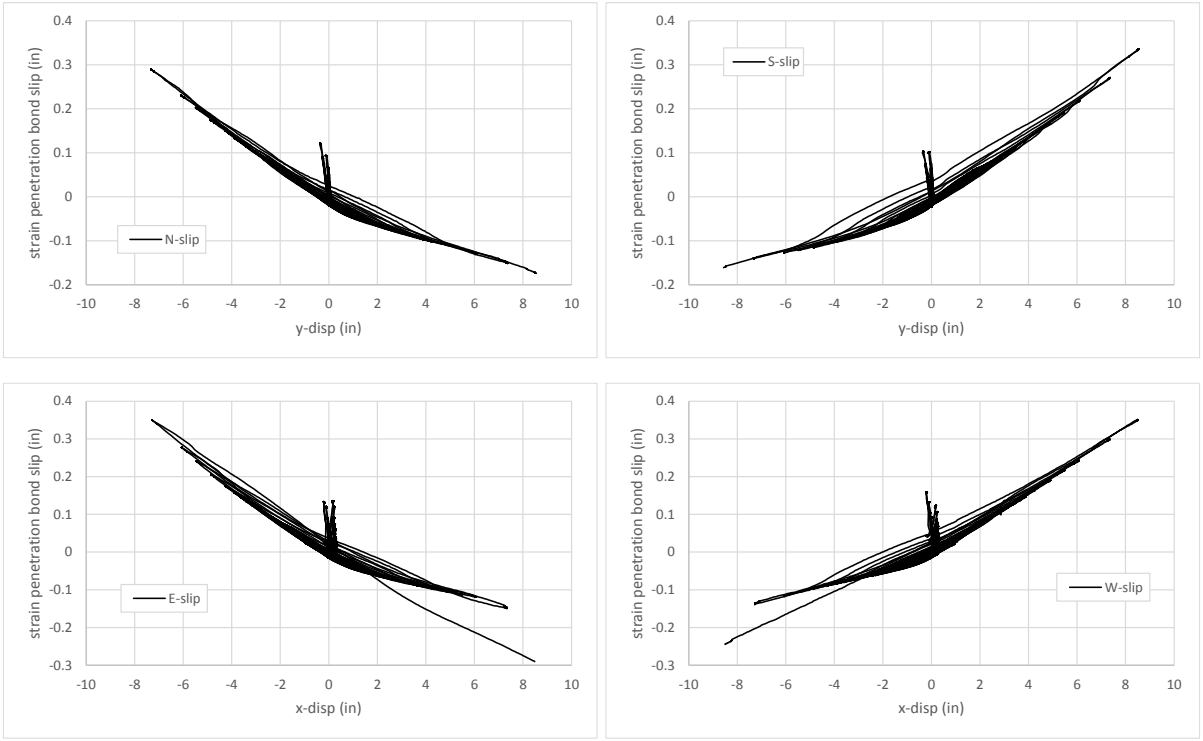

Figure 14-81. Test 11: Extreme Fiber Bar Strain Penetration Bond Slip Hysteresis

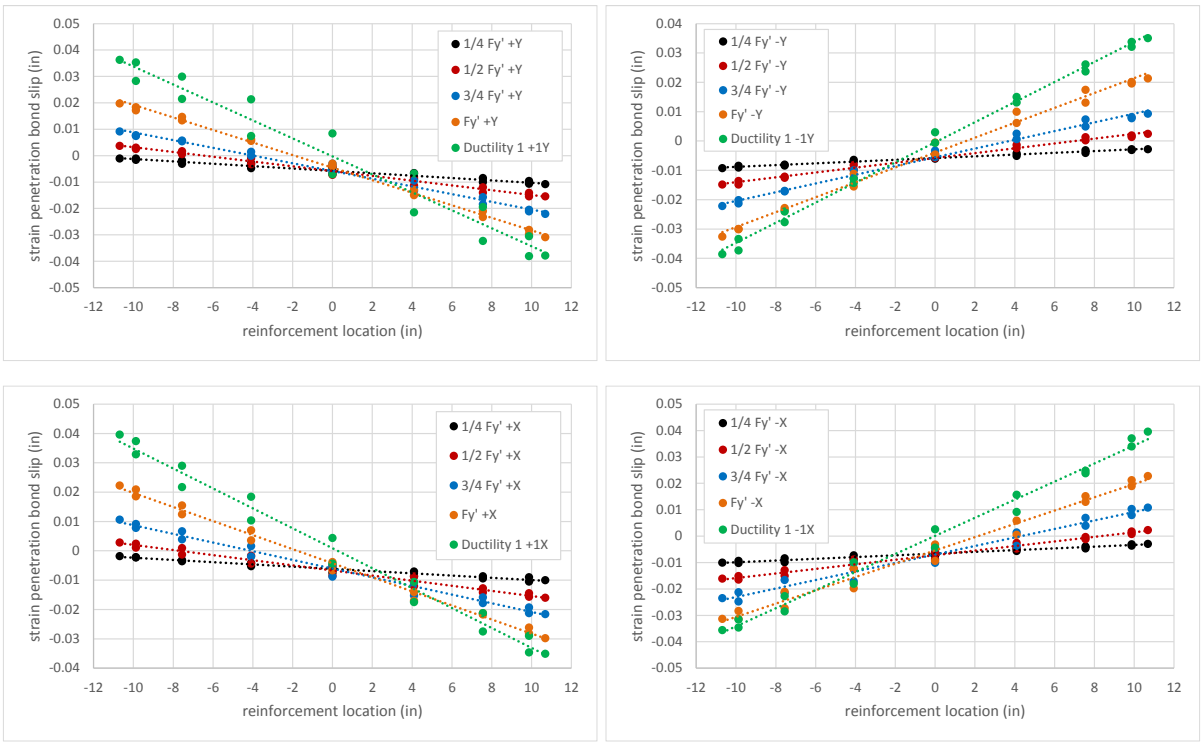

Figure 14-82. Test 11: Fixed End Rotations due to Strain Penetration during the Elastic Cycles

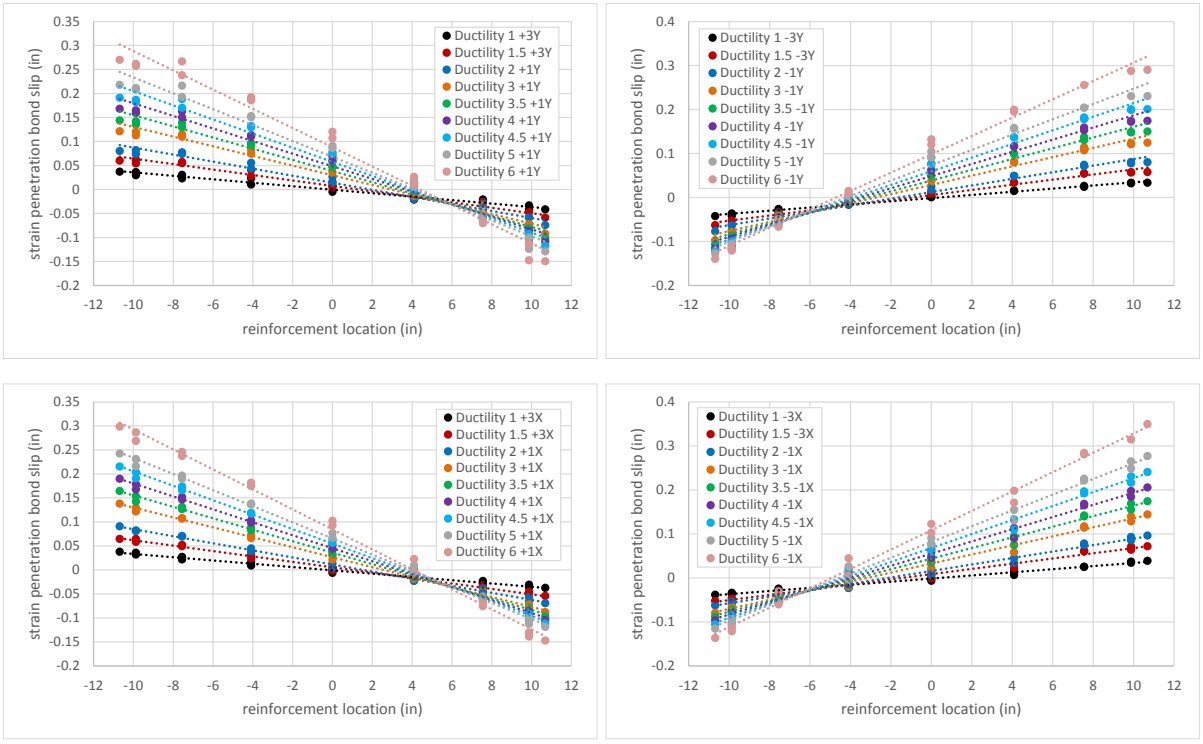

Figure 14-83. Test 11: Fixed End Rotations due to Strain Penetration

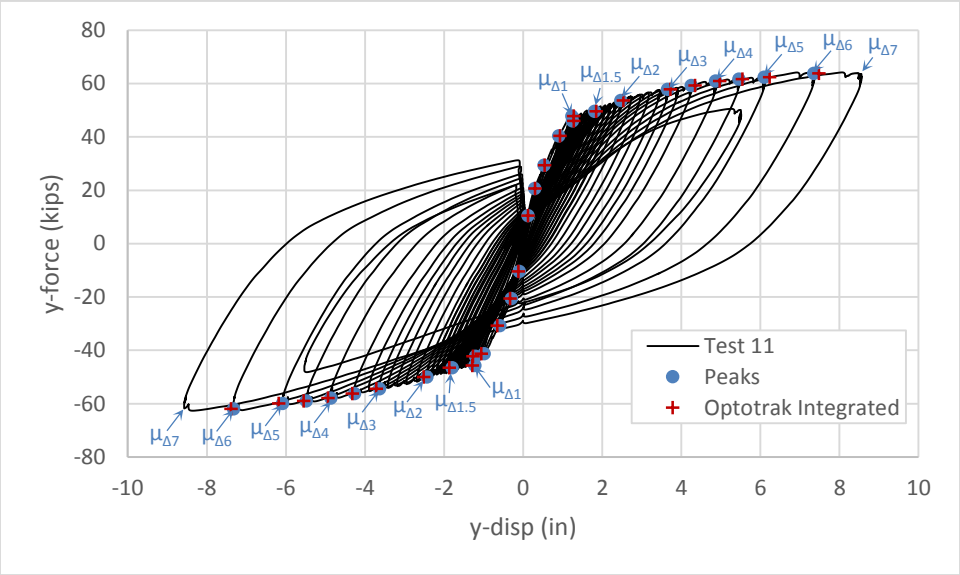

Figure 14-84. Test 11: Optotrak Integrated Flexural Disp. Compared to Measured String Pot. Disp.

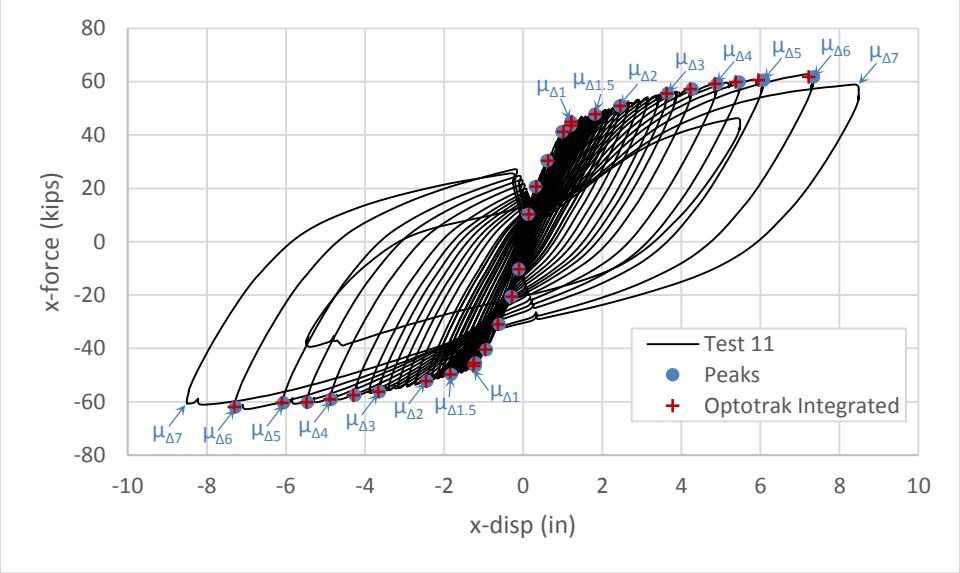

Figure 14-85. Test 11: Optotrak Integrated Flexural Disp. Compared to Measured String Pot. Disp.

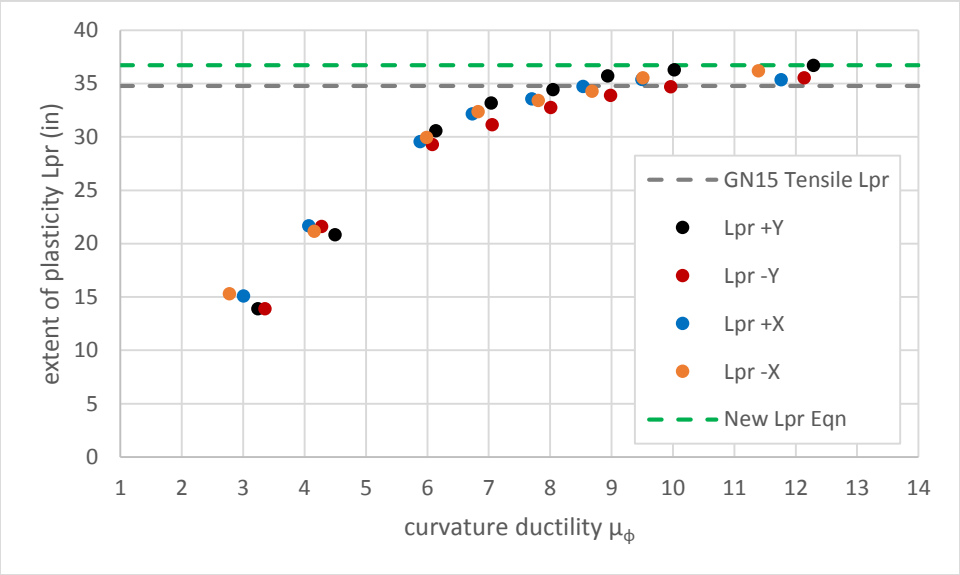

Figure 14-86. Test 11: Measured Extent of Plasticity Compared to Tensile Hinge Lengths

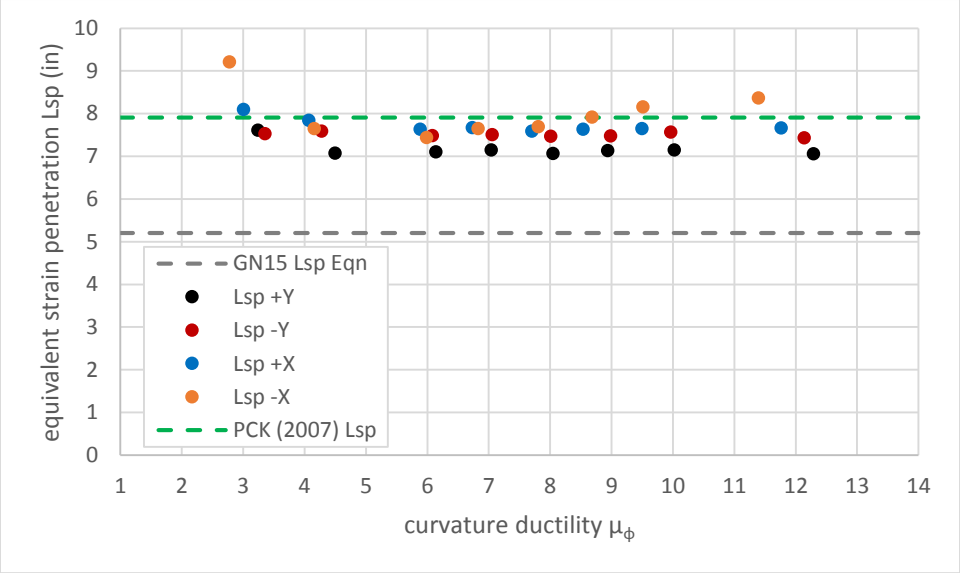

Figure 14-87. Test 11: Measured Equivalent Strain Penetration Lengths Compared to Design Expressions

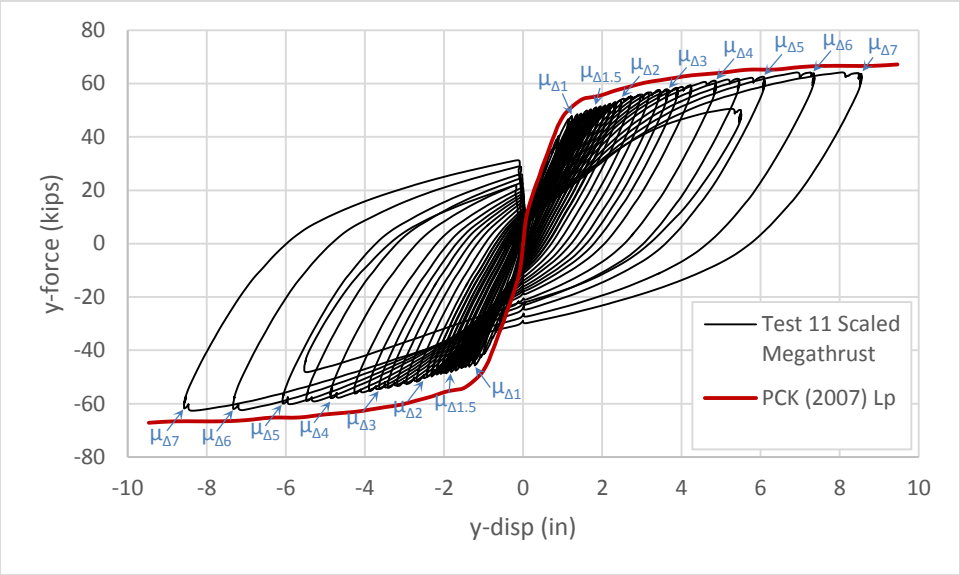

Figure 14-88. Test 11: Y-Direction Hysteretic Response Compared to PCK (2007) Hinge Length Monotonic Prediction

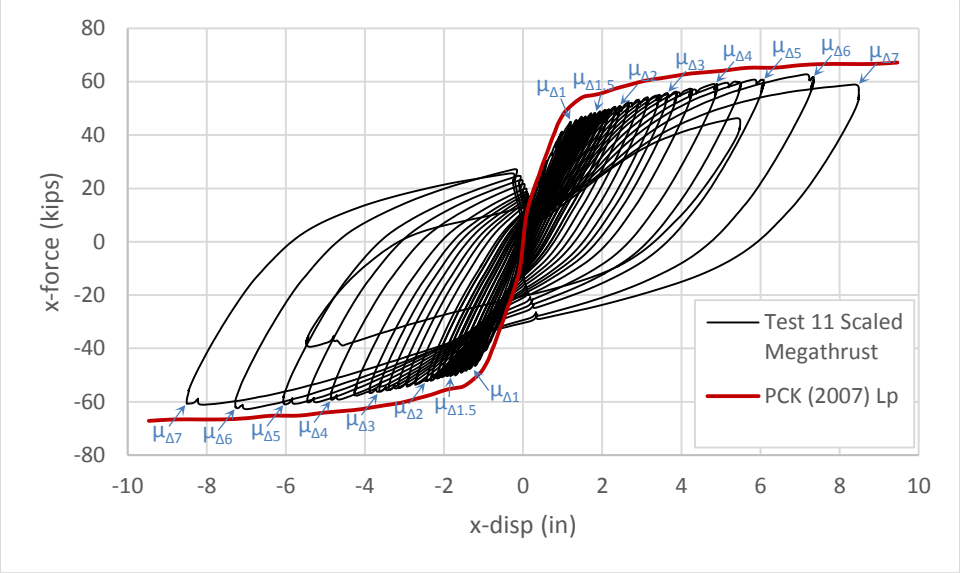

Figure 14-89. Test 11: X-Direction Hysteretic Response Compared to PCK (2007) Hinge Length Monotonic Prediction

Response Comparison of Tests 8 (Sym. 2-Cycle-Set) and 11 (Scaled Megathrust)

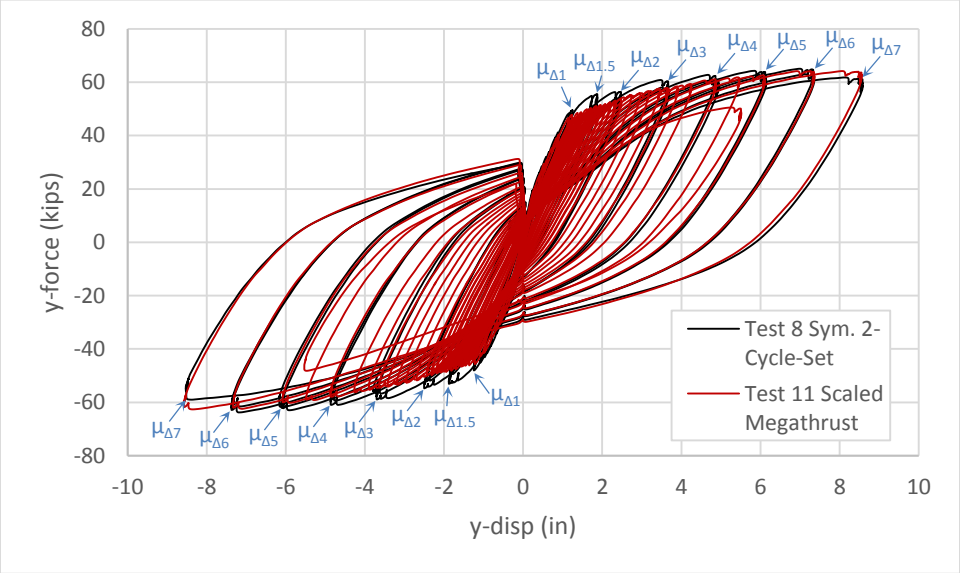

Figure 14-90. Y-Direction Hysteretic Comparison for Tests 8 (2-Cycle-Set) and 11 (Megathrust)

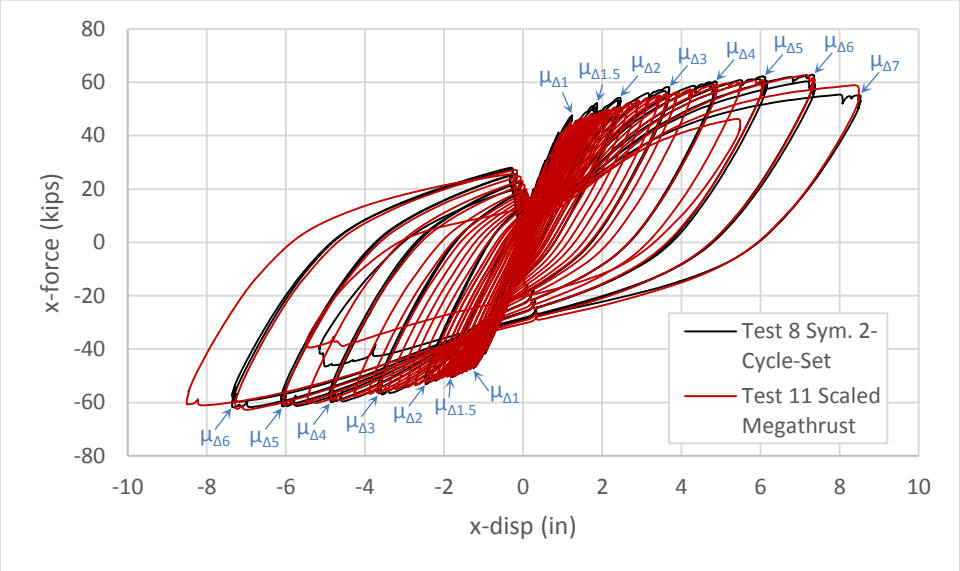

Figure 14-91. X-Direction Hysteretic Comparison for Tests 8 (2-Cycle-Set) and 11 (Megathrust)

Chapter 15 – Test 12 Summary Report

Tests 11 and 12 utilized scaled bidirectional adaptations of the megathrust loading protocol recommended in (Bazaez and Dusicka 2016).The tests were designed to be comparable to nominally identical symmetric two-cycle-set load history Tests 8 and 9 which had 1% and 0.7% volumetric steel, respectively. The specimen selected for Test 12 was nominally identical to that of Test 9, which had bar buckling during displacement ductility five, followed by fracture of a previously buckled bar during displacement ductility six as shown in Figure 14-12 through Figure 14-15. The same scaled megathrust load history from Test 11 in Figure 14-2 and Figure 14-3 was utilized in Test 12, except post-peak cycling began following displacement ductility six, which represented the ultimate displacement capacity of nominally identical Test 9. The first yield displacement of Test 8 was used to define the ductility levels and thus cycle displacement amplitudes of Tests 11 and 12. Test 9 had a slightly larger, but comparable, equivalent yield displacement.

The twelfth specimen had a 24" diameter circular cross-section reinforced with 16 #6 A706 longitudinal bars ($A_{st}/A_g = 1.6\%$) and a #3 spiral at 2.75" on center ($4A_{sp}/D's = 0.7\%$). Details of the test setup, instrumentation, and specimen design appear in Chapter 2. A material properties summary for the longitudinal and transverse steel from the final six experiments appears in Table 3-3 through Table 3-5. The column had a tested concrete strength of $f_c' = 6.23\ ksi$, while the footing had $f_c' = 6.61\ ksi$. The same constant compressive axial load of $191\ kips$ was applied to all the specimens. The axis of the imposed bidirectional load history is shown in Figure 15-1. This figure includes a diagram of the column cross-section with the selected bar and crack labeling scheme. Displacements in the +Y-direction placed the South reinforcement in tension. Cracks due to loading in the +Y-direction were labeled as red. The orientation of the X and Y axes are shown in Figure 2-52 with regards to the test setup. The +Y-axis is perpendicular to and points away from the strong wall. Values of interests, damage observations, and a predictions summary for the twelfth test appear in Table 15-1, Table 15-2, and Table 15-3. A photo of the test setup appears in Figure 15-2.

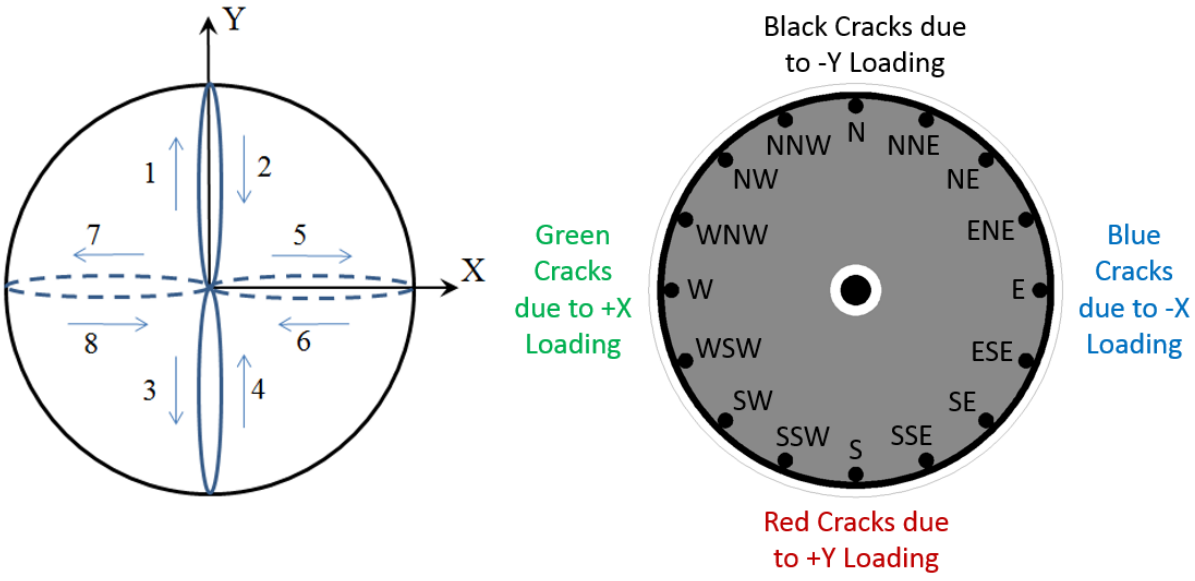

Figure 15-1. Test 12: Bidirectional Load History Orientation and Bar Naming System

Table 15-1. Test 12: Values of Interest

Load History	Scaled Bidirectional Megathrust
Length, Diameter, and Aspect Ratio	$L = 109.4375\ in, D = 24\ in,\ (L/D = 4.56)$
Longitudinal Steel Detailing	$16\ \#6\ for\ \rho_l = A_{st}/A_g = 1.6\%$
Longitudinal Steel Properties	$f_y = 70.33\ ksi, f_u = 98.68\ ksi, \varepsilon_y = 0.00283$
Transverse Steel Detailing	$\#3\ @\ 2.75\ in\ for\ \rho_s = 4A_{sp}/D's = 0.7\%$
Transverse Steel Properties	$f_y = 63.89\ ksi, f_u = 93.64\ ksi, \varepsilon_y = 0.00418$
Column Concrete Strength	$f_c' = 6.23\ ksi$
Footing Concrete Strength	$f_c' = 6.61\ ksi$
Axial Load	$P = 191\ kips, \left(P/f_c'\ A_g = 7.4\%\right)$
Analytical First Yield Force	$F_y' = 41.28\ kips$
Experimental First Yield Disp.	$\Delta_y' = 0.91\ in$ *(Value from Nominally Identical Test 8)*
Analytical Nominal Moment Capacity	$M_n = 505.51\ kip \cdot ft$
Equivalent Yield Displacement	$\Delta_y = \Delta_y'\left(M_n/M_y'\right) = 1.22\ in$ with Δ_y' from Test 8

Table 15-2. Test 12: Damage Observations

Damage Observations:		
Cycle Peak at which First Cracking was Observed Visually:		
North	$\Delta_y = -0.5F_y' = -0.30\ in$	$F_y = -20.67\ kips$
South	$\Delta_y = 0.5F_y' = 0.26\ in$	$F_y =\ kips$
East	$\Delta_x = -0.5F_y' = -0.33\ in$	$F_x = -\ kips$
West	$\Delta_x = 0.5F_y' = 0.26\ in$	$F_x =\ kips$
Cycle Peak at which Cover Concrete Crushing was Observed Visually:		
North	$\mu_{\Delta 2.4}^{+1Y} = 2.93\ in$	$\varepsilon_c = -0.00624$
South	$\mu_{\Delta 2.2}^{-1Y} = -2.68\ in$	$\varepsilon_c = -0.00483$
East	$\mu_{\Delta 1.8}^{+1X} = 2.19\ in$	$\varepsilon_c = -0.00427$
West	$\mu_{\Delta 1.7}^{-1X} = -2.11\ in$	$\varepsilon_c = -0.00373$
Exact Displacement and Cycle Label for Initial Spiral Yielding in the Confinement Zone:		
North	$\Delta_y = 5.23\ in\ during\ \mu_{\Delta 4.5}^{+1Y}$	$\varepsilon_c = -0.01240$
South	$\Delta_y = -4.73\ in\ during\ \mu_{\Delta 4}^{-1Y}$	$\varepsilon_c = -0.01101$
East	$\Delta_x = 5.42\ in\ during\ \mu_{\Delta 4.5}^{+1X}$	$\varepsilon_c = -0.01002$
West	$\Delta_x = -5.34\ in\ during\ \mu_{\Delta 4.5}^{-1X}$	$\varepsilon_c = -0.01436$
Peak Tensile Displacement Prior to Visual Bar Buckling During Subsequent Reversal of Load:		
North	$\mu_{\Delta 5}^{-1Y} = -6.08\ in, Observed\ at\ \mu_{\Delta 6}^{+1Y} = 7.30\ in$	$\varepsilon_s = 0.03283$
South	$\mu_{\Delta 5}^{+1Y} = 6.10\ in, Observed\ at\ \mu_{\Delta 5}^{-1Y} = -6.08\ in$	$\varepsilon_s = 0.03150$
East	$\mu_{\Delta 5}^{-1X} = -6.06\ in, Observed\ at\ \mu_{\Delta 6}^{+1X} = 7.35\ in$	$\varepsilon_s = 0.03298$
West	$\mu_{\Delta 5}^{+1X} = 6.09\ in, Observed\ at\ \mu_{\Delta 5}^{-1X} = -6.06\ in$	$\varepsilon_s = 0.03382$
Exact Displacement and Cycle Label for Fracture of Previously Buckled Reinforcement		
South	$\Delta_y = 3.30\ in\ during\ \mu_{\Delta 4.5p}^{+2Y}$	Single South Extreme Bar

Table 15-3. Test 12: Damage Predictions

Damage Predictions with the New Bidirectional Plastic Hinge Model and New Strain Limits:		
Bar Buckling Predictions		
New Method	$\Delta_{bb}^{Lpr} = 5.96\ in$	$\varepsilon_s^{bb} = 0.03382$
Feng et al. (2015)	$\Delta_{bb}^{Lp} = 5.39\ in$	$\varepsilon_s^{bb} = 0.04222$
Cover Crushing Prediction		
New Method	$\Delta_{cc}^{Lpr} = 1.97\ in$	$\varepsilon_c^{cc} = -0.004$
Spiral Yielding Prediction		
New Method	$\Delta_{sy}^{Lpr} = 5.04\ in$	$\varepsilon_c^{sy} = -0.01384 * M, (M = 0.8)$
Original Ultimate Concrete Compression Strain		
Mander et al. (1988)	$\Delta_{cu}^{Lpr} = 6.11\ in$	$\varepsilon_{cu} = -0.0141$

Figure 15-2.Test 12: Experimental Setup

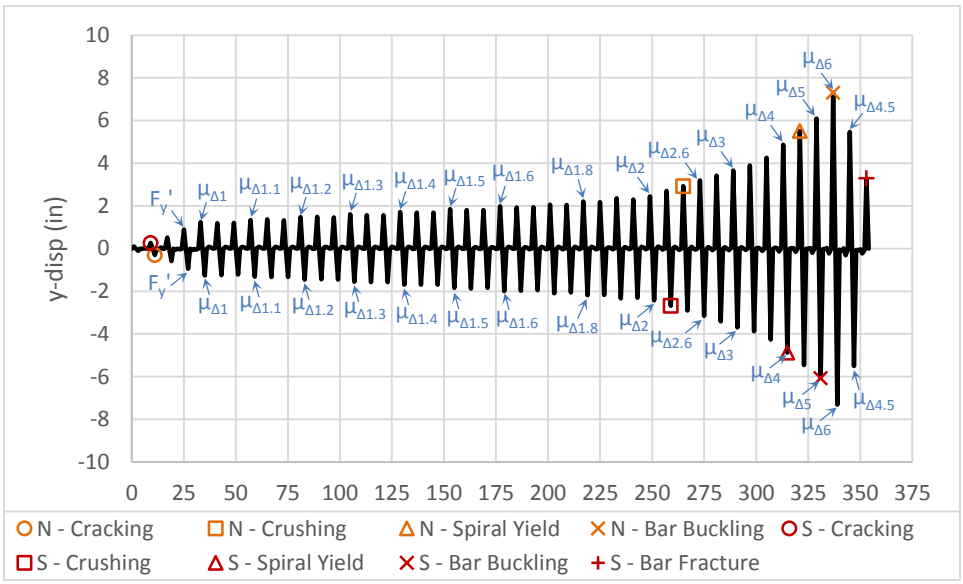

Figure 15-3. Test 12: Y-Displacement History

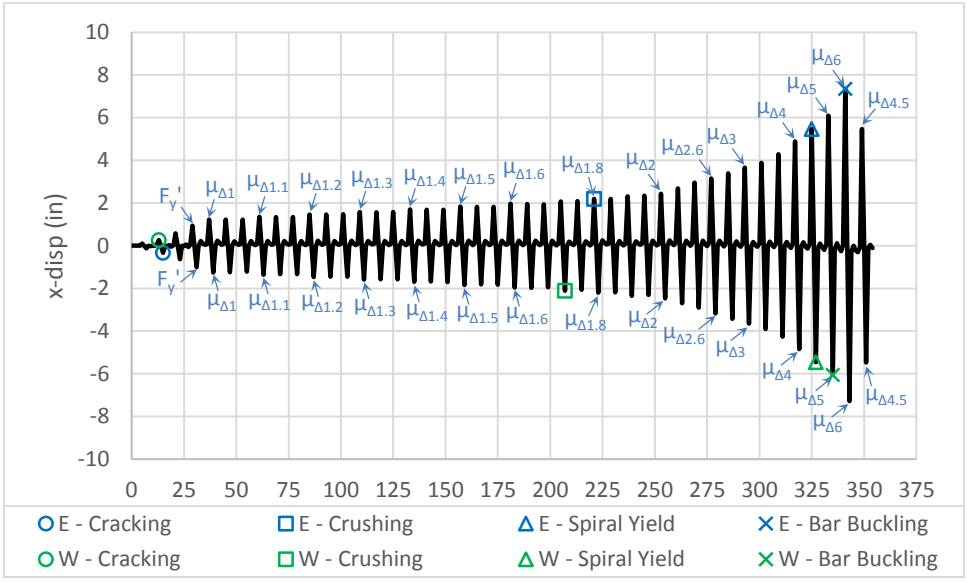

Figure 15-4. Test 12: X-Displacement History

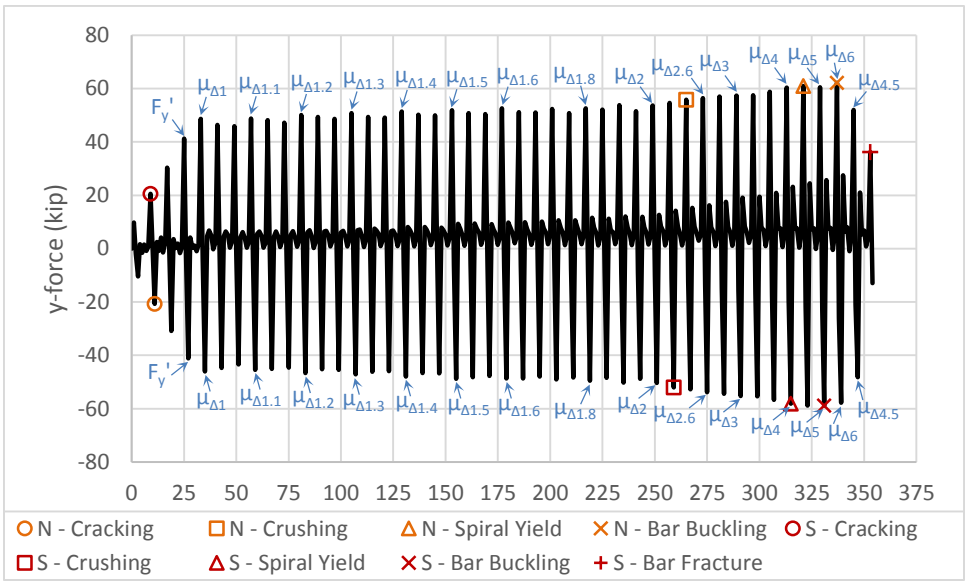

Figure 15-5. Test 12: Y-Force History

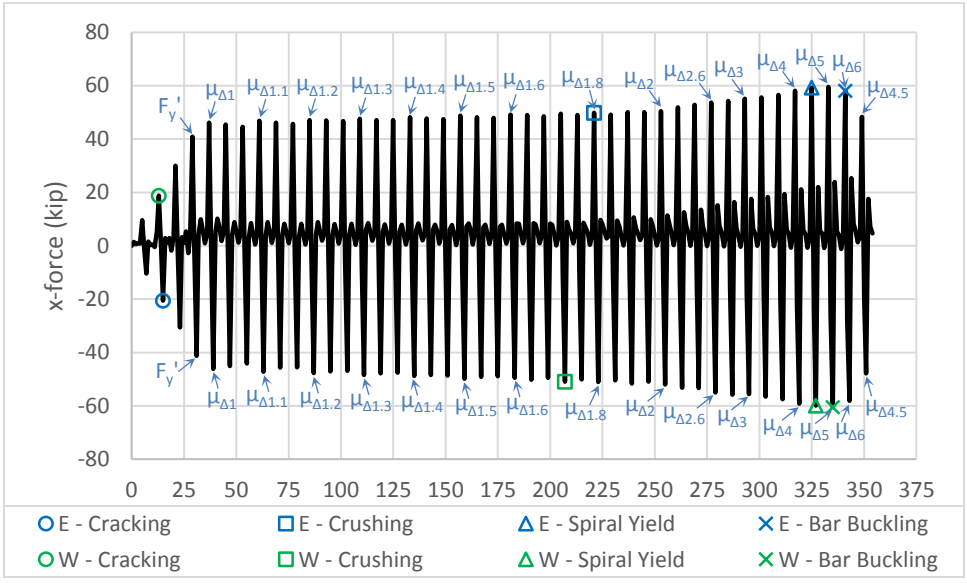

Figure 15-6. Test 12: X-Force History

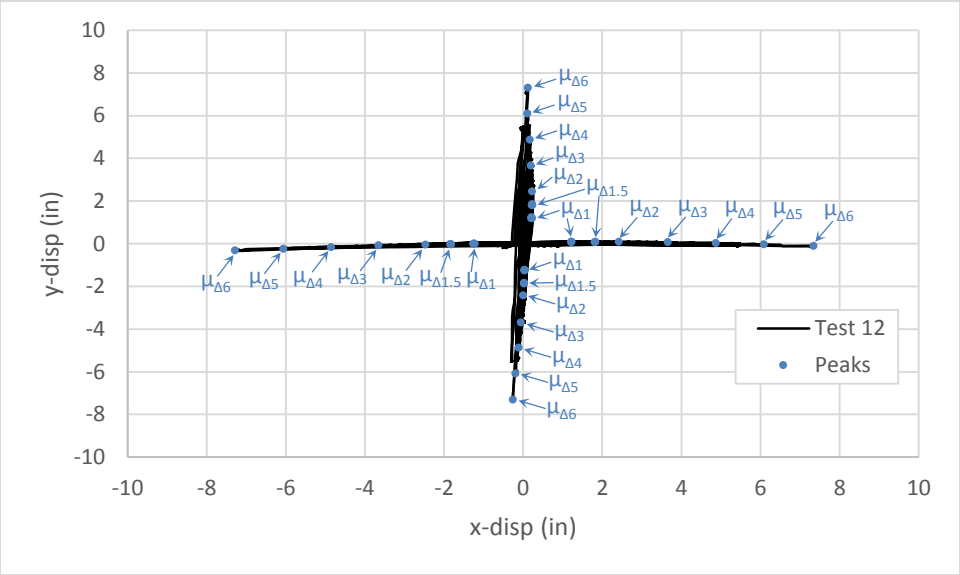

Figure 15-7. Test 12: Scaled Megathrust Loading Protocol from (Bazaez and Dusicka 2016)

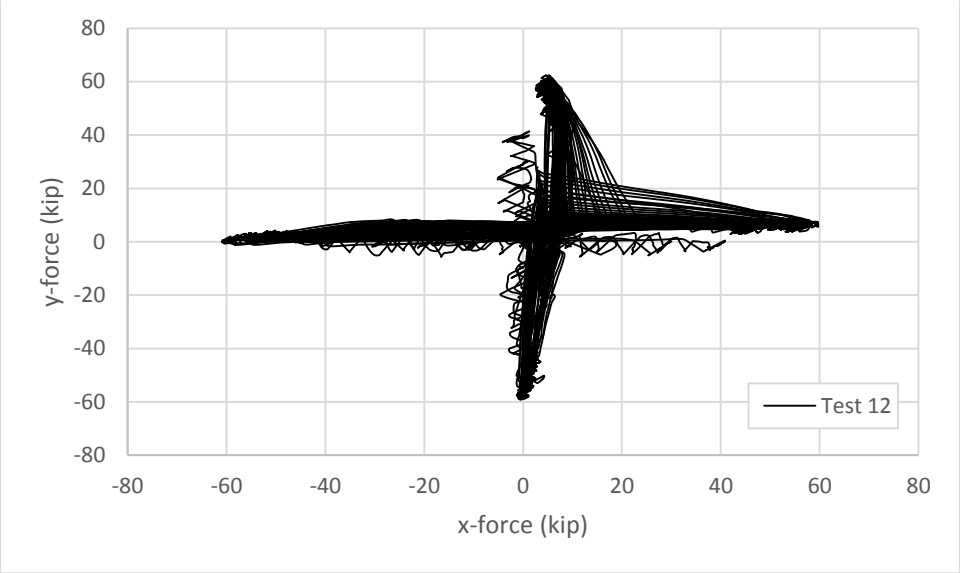

Figure 15-8. Test 12: Load Path

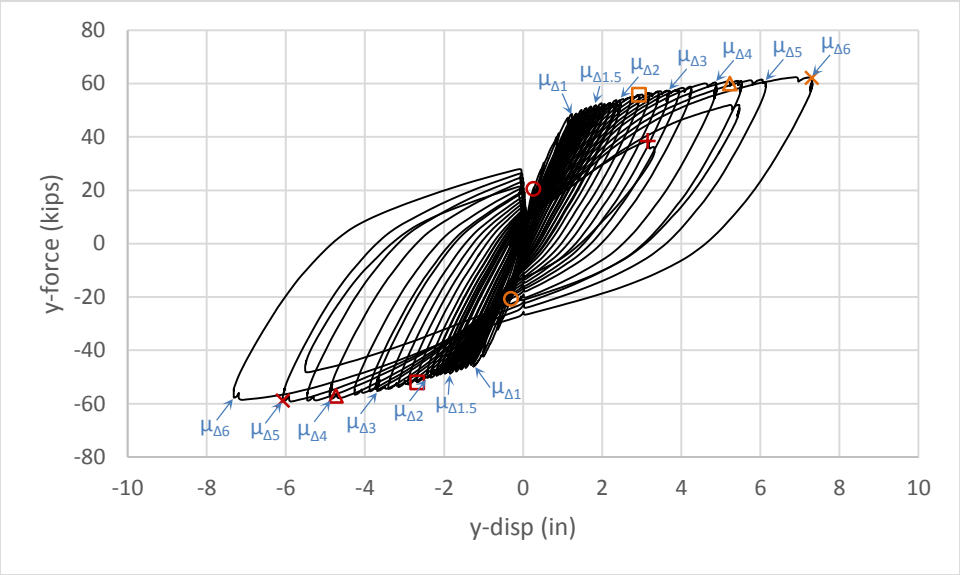

Figure 15-9. Test 12: Y-Direction Hysteretic Response

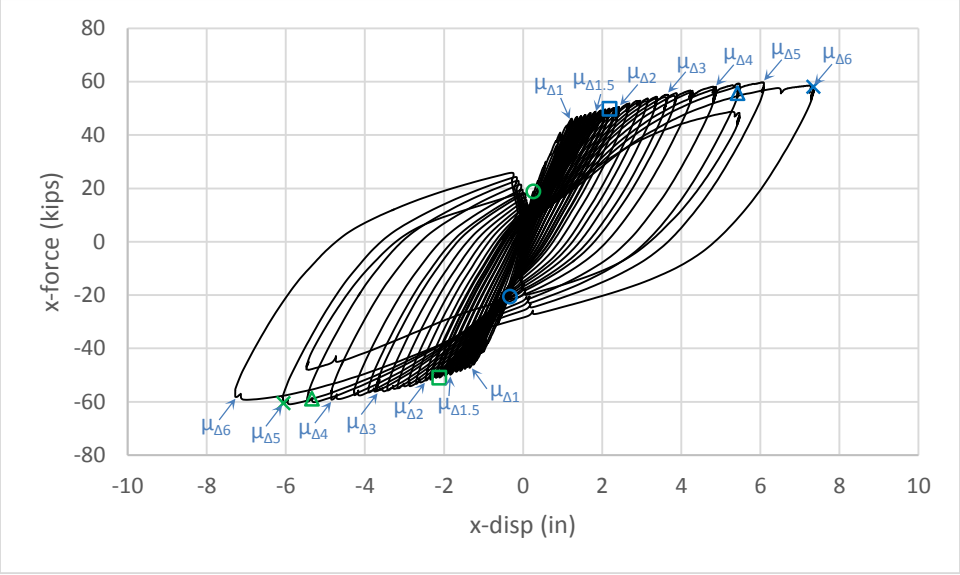

Figure 15-10. Test 12: X-Direction Hysteretic Response

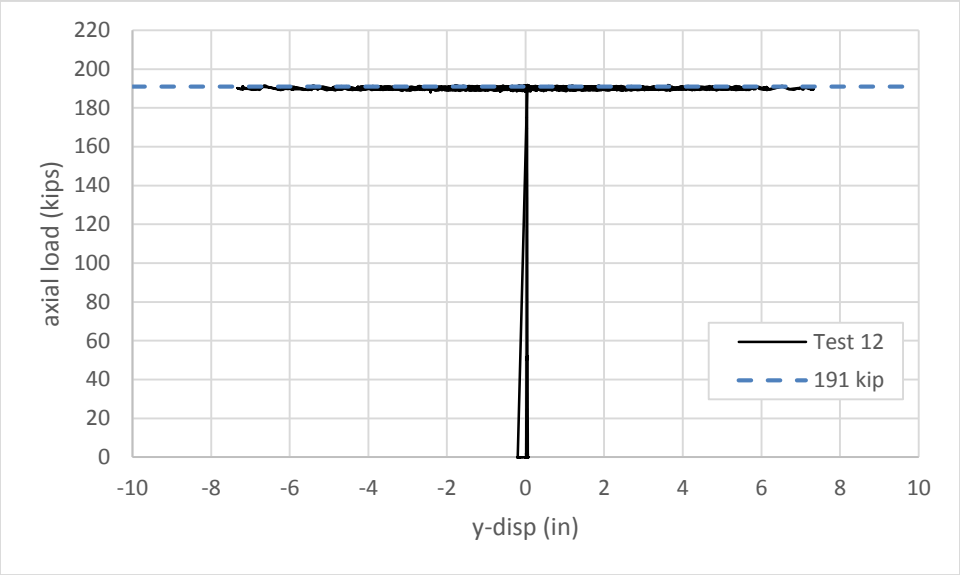

Figure 15-11. Test 12: Y-Direction Axial Force History

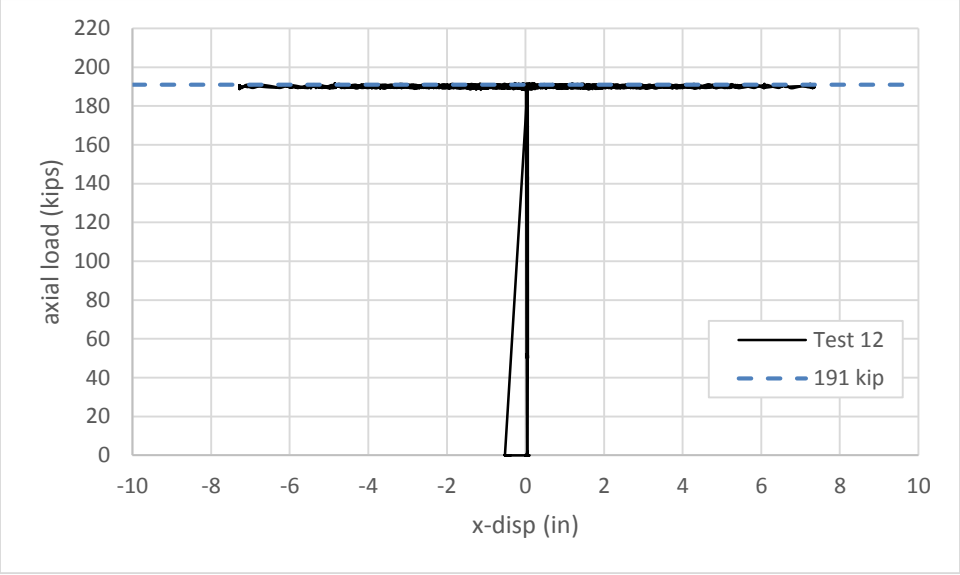

Figure 15-12. Test 12: X-Direction Axial Force History

Test 12 - Experimental Observations

Values of interests and damage observations for Load Path Test 12 are presented in Table 15-1 and Table 15-2. Test 12 evaluated a 24" diameter column $(L/D = 4.56)$ with $\rho_l = A_{st}/A_g = 1.6\%$ longitudinal steel and a transverse volumetric ratio of $\rho_s = 4A_{sp}/D's = 0.7\%$. The test began with the application of a constant axial load of $191\ kips\ \left(P/f_c'\ A_g = 7.4\%\right)$. The imposed displacement histories in the Y and X-directions for the scaled bidirectional adaptation of the megathrust loading protocol recommended in (Bazaez and Dusicka 2016) are shown in Figure 15-3 and Figure 15-4. The resulting column shear force histories in the Y and X-directions appear in Figure 15-5 and Figure 15-6. The full displacement history and resulting load path for Test 12 appear in Figure 15-7 and Figure 15-8. The Y and X-direction column hysteretic response appears Figure 15-9 and Figure 15-10. The axial force history appears in Figure 15-11 and Figure 15-12.

The load history began with elastic ¼ F_y' cycle increments until the analytically predicted first yield force $(F_y' = 41.28\ kips)$ was reached in each direction of loading. Cracks were first observed on all sides of the specimen during the ½ F_y' cycle. At the analytically predicted first yield force, an average experimental first yield displacement of $\Delta_y' = 0.95$" was measured in the four primary directions. The equivalent yield displacement for the column was then computed as $\Delta_y = \Delta_y'\left(M_n/M_y'\right) = 1.27\ in$, where $M_n = 505.51\ kip \cdot ft$ represents the analytical nominal moment capacity corresponding to an extreme fiber compression strain of $\varepsilon_c = 0.004$ or a steel tensile strain of $\varepsilon_s = 0.015$, whichever occurs first. To allow for direct comparison, the first yield displacement of $\Delta_y' = 0.91$" and resulting equivalent yield displacement of $\Delta_y = \Delta_y'\left(M_n/M_y'\right) = 1.22$" from Test 8 was used to define the cycle peaks in the load history of Tests 11 and 12. The remainder of the scaled megathrust load history consists of equal magnitude bidirectional cycles at increments of the equivalent yield displacement $\mu_{\Delta n} = n \cdot \Delta_y$.

Concrete crushing was observed on the West side of the specimen during $\mu_{\Delta 1.7}^{-1x} = -2.11$", followed by crushing on the East side at $\mu_{\Delta 1.8}^{+1x} = 2.19$", see Figure 15-13 and Figure 15-14. Crack profiles were first marked during $\mu_{\Delta 2}$ as shown in Figure 15-15 and Figure 15-16. Concrete crushing was observed on the South side of the specimen during $\mu_{\Delta 2.2}^{-1y} = -2.68$", and then on the North side at $\mu_{\Delta 2.4}^{+1y} = 2.93$", see Figure 15-17 and Figure 15-18. Crack profiles during $\mu_{\Delta 3}$ and $\mu_{\Delta 4}$ appear in Figure 15-19 through Figure 15-22. Confinement demands led to initial spiral yielding on the South side of the specimen during $\mu_{\Delta 4}^{-1y} = -4.87$", followed by the North side during $\mu_{\Delta 4.5}^{+1y} = 5.52$" as shown in Figure 15-23. Spiral yielding was measure don the East side during $\mu_{\Delta 4.5}^{+1x} = 5.47$", and then on the West side during $\mu_{\Delta 4.5}^{-1x} = -5.46$", see Figure 15-24.

South reinforcing bars S and SSE visibly buckled during $\mu_{\Delta 5}^{-1y} = -6.08$", followed by buckling of the West extreme fiber bar during $\mu_{\Delta 5}^{-1x} = -6.06$" as shown in Figure 15-25. The North extreme fiber bar buckled during $\mu_{\Delta 6}^{+1y} = 7.30$", and buckling of adjacent South bar SSW was observed at $\mu_{\Delta 6}^{-1y} = -7.31$", see Figure 15-26. East bars E, ESE, and ENE buckled simultaneously during $\mu_{\Delta 6}^{-1x} = -7.28$", and then adjacent West bars WNW and WSW buckled during the subsequent reversal to 0" as shown in Figure 15-27. Once a complete cycle at $\mu_{\Delta 6}$ was completed, post-peak loading at $\mu_{\Delta 4.5p}$ commenced. Adjacent North bars NE, NNE, and NNW buckled during $\mu_{\Delta 4.5\mathrm{p}}^{+1y} = 5.47$", followed by buckling of bars SE and SW during $\mu_{\Delta 4.5\mathrm{p}}^{-1y} = -5.50$", see Figure 15-28. Additional deformation in the

East and West bars during $\mu_{\Delta 4.5\mathrm{p}}^{\pm 1\mathrm{x}}$ is shown in Figure 15-29. The previously buckled South extreme fiber bar fractured at 3.30" during $\mu_{\Delta 4.5\mathrm{p}}^{+2\mathrm{y}}$ as depicted in Figure 15-30 and Figure 15-9.

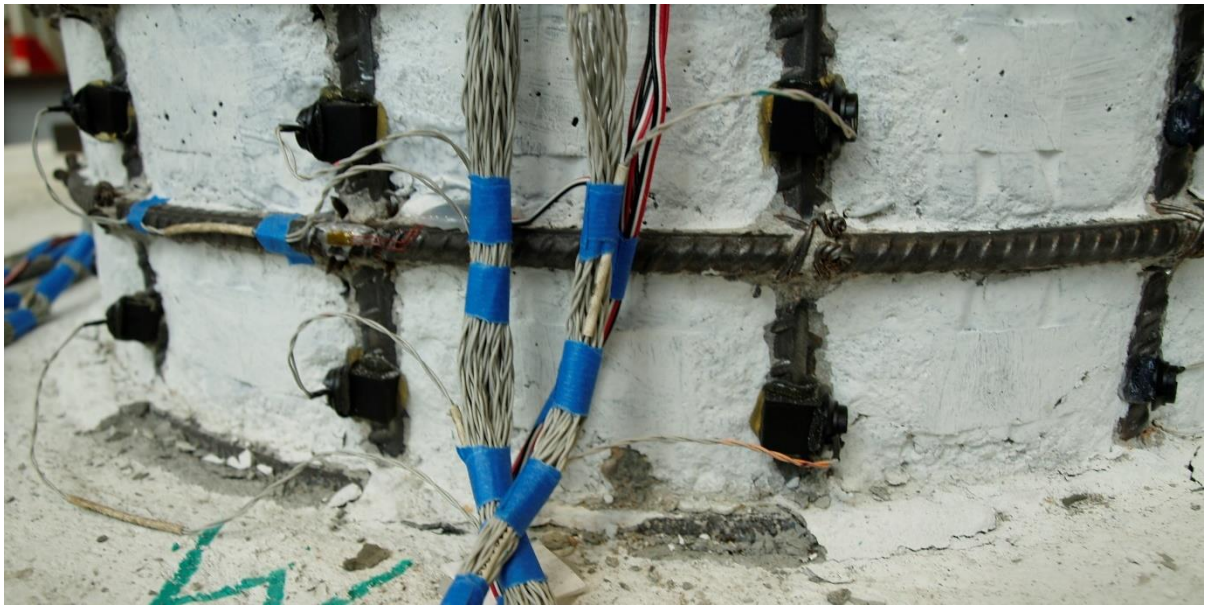

Figure 15-13. Test 12: Concrete Crushing on the West Side of the Specimen during $\mu_{\Delta 1.7}^{-1x} = -2.11$"

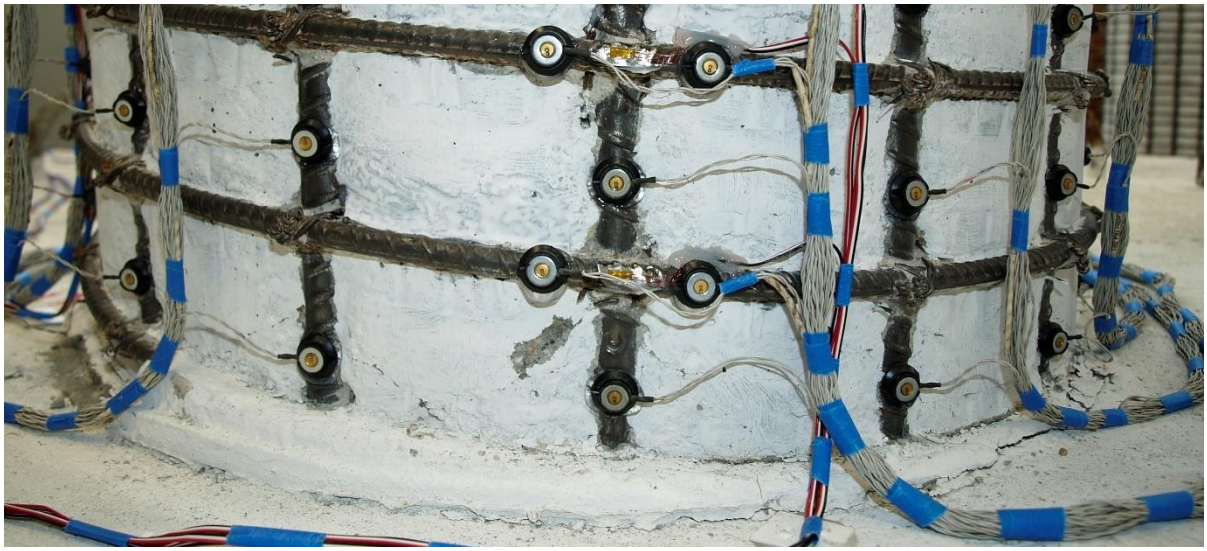

Figure 15-14. Test 12: Concrete Crushing on the East Side of the Specimen during $\mu_{\Delta 1.8}^{+1x} = 2.19$"

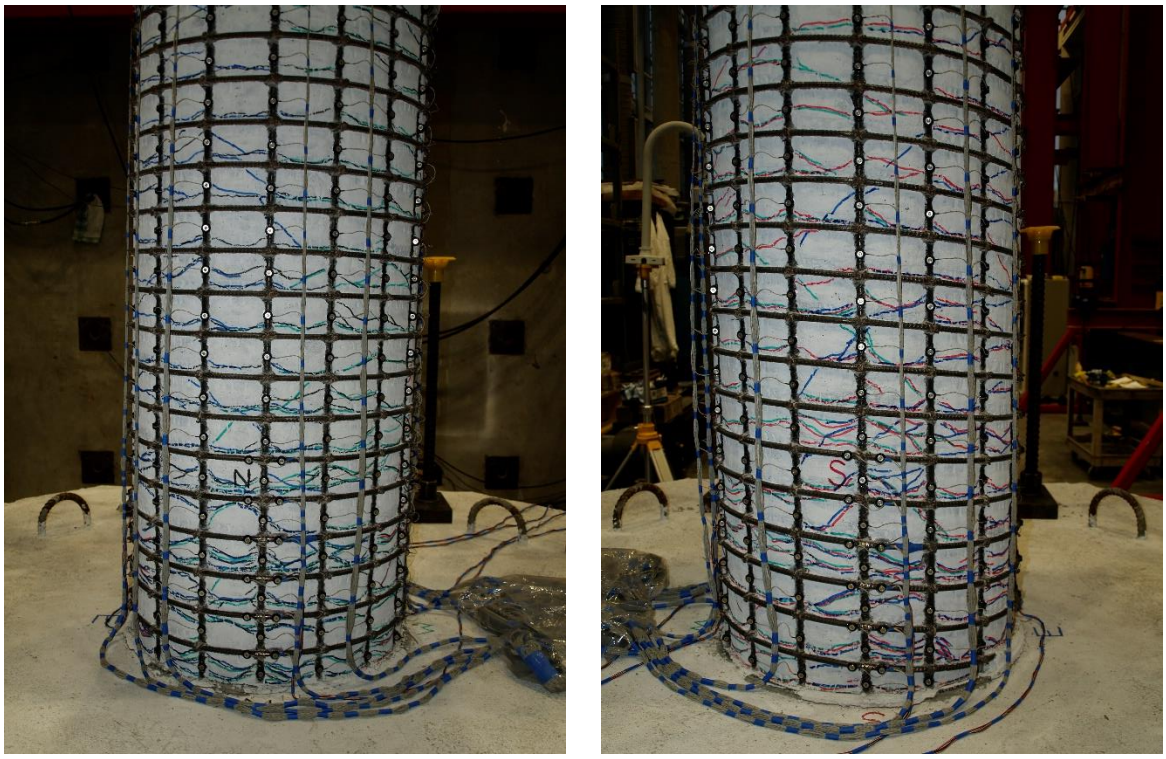

Figure 15-15. Test 12: (Left) North and (Right) South Sides of the Specimen at the End of $\mu_{\Delta 2}$

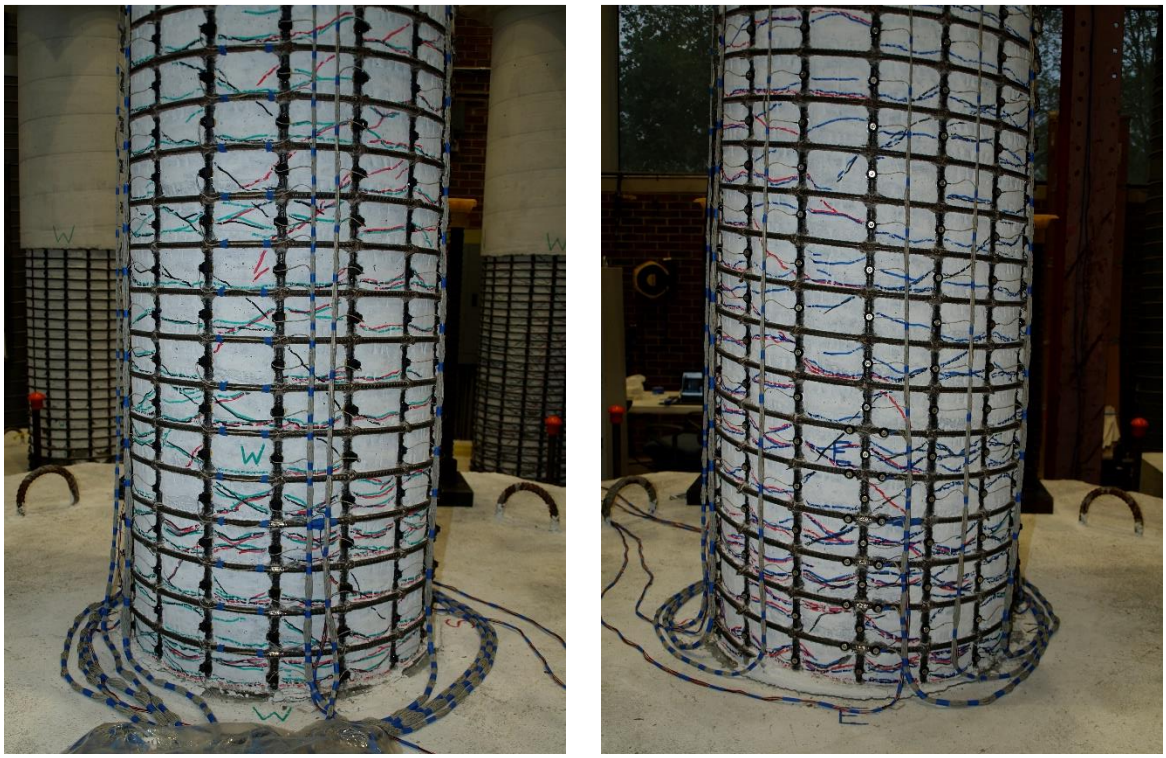

Figure 15-16. Test 12: (Left) West Side at $\mu_{\Delta 2}^{+1x} = 2.43$" and (Right) East Side at $\mu_{\Delta 2}^{-1x} = -2.46$"

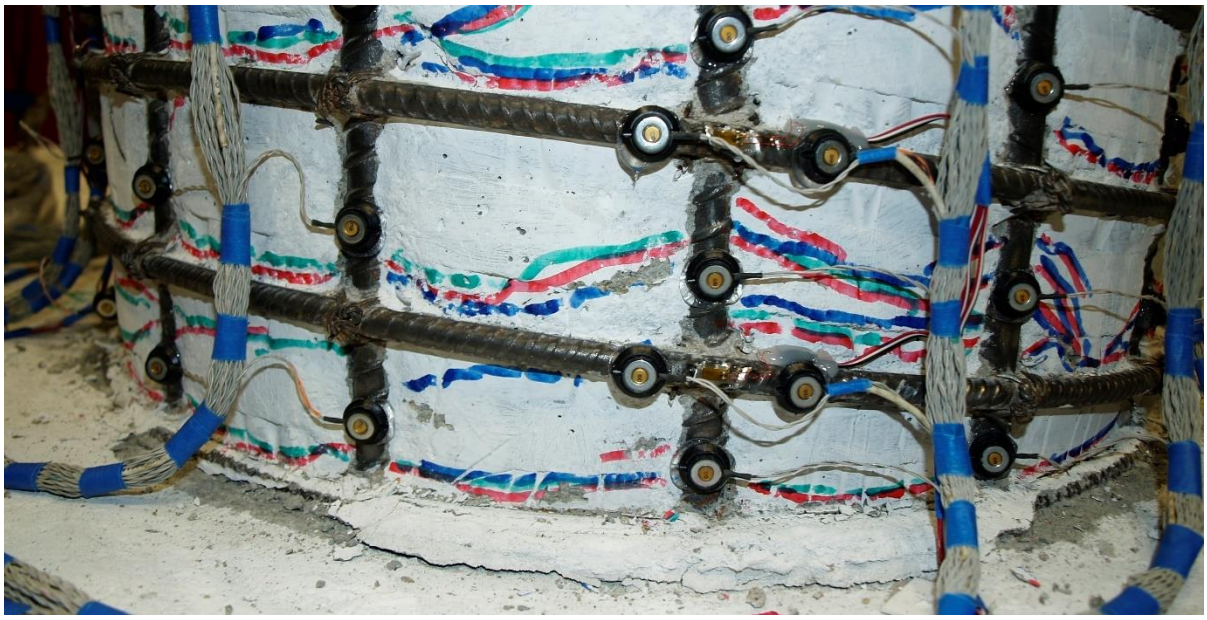

Figure 15-17. Test 12: Concrete Crushing on the South Side of the Specimen during $\mu_{\Delta 2.2}^{-1y} = -2.68$"

Figure 15-18. Test 12: Concrete Crushing on the North Side of the Specimen during $\mu_{\Delta 2.4}^{+1y} = 2.93$"

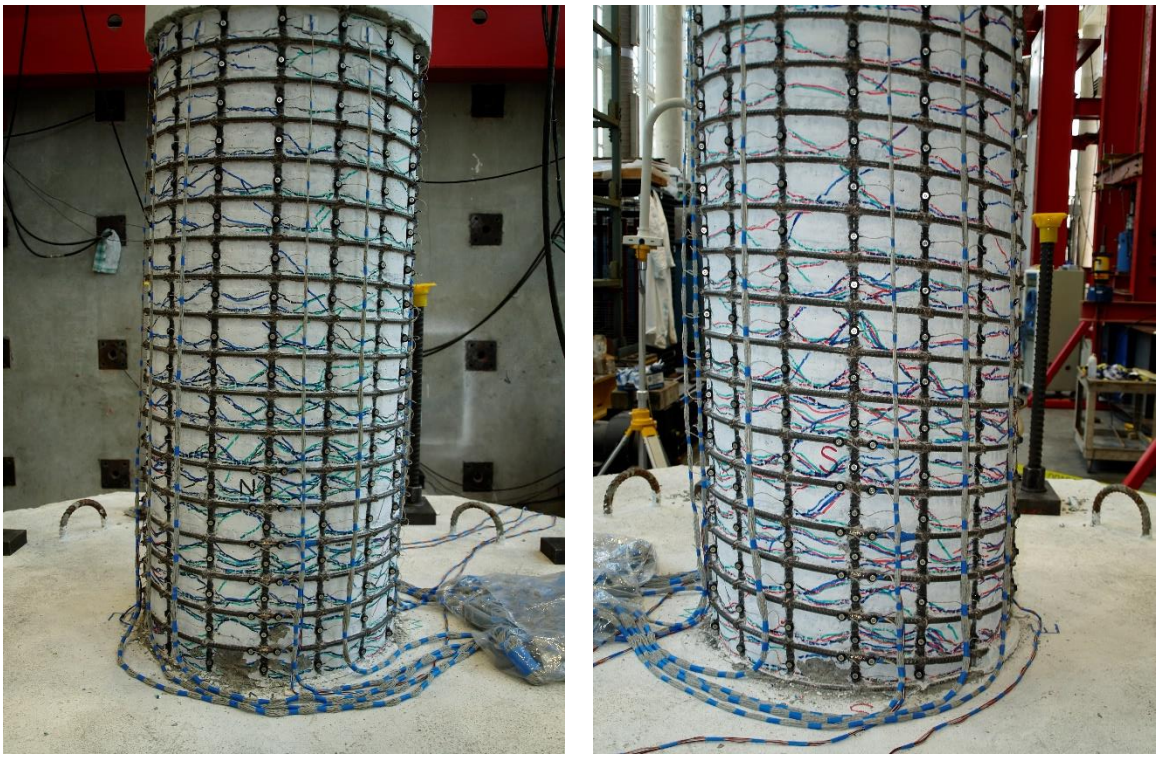

Figure 15-19. Test 12: (Left) North and (Right) South Sides of the Specimen at the End of $\mu_{\Delta 3}$

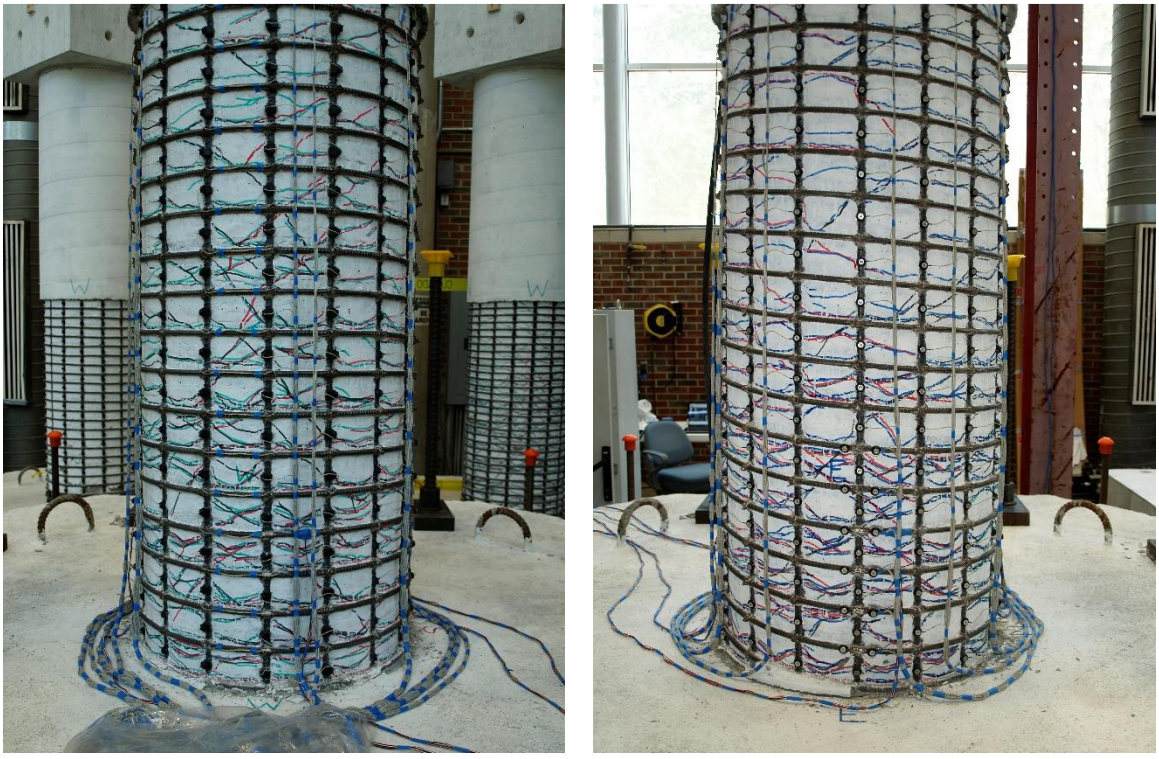

Figure 15-20. Test 12: (Left) West Side at $\mu_{\Delta 3}^{+1x} = 3.66"$ and (Right) East Side at $\mu_{\Delta 3}^{-1x} = -3.65"$

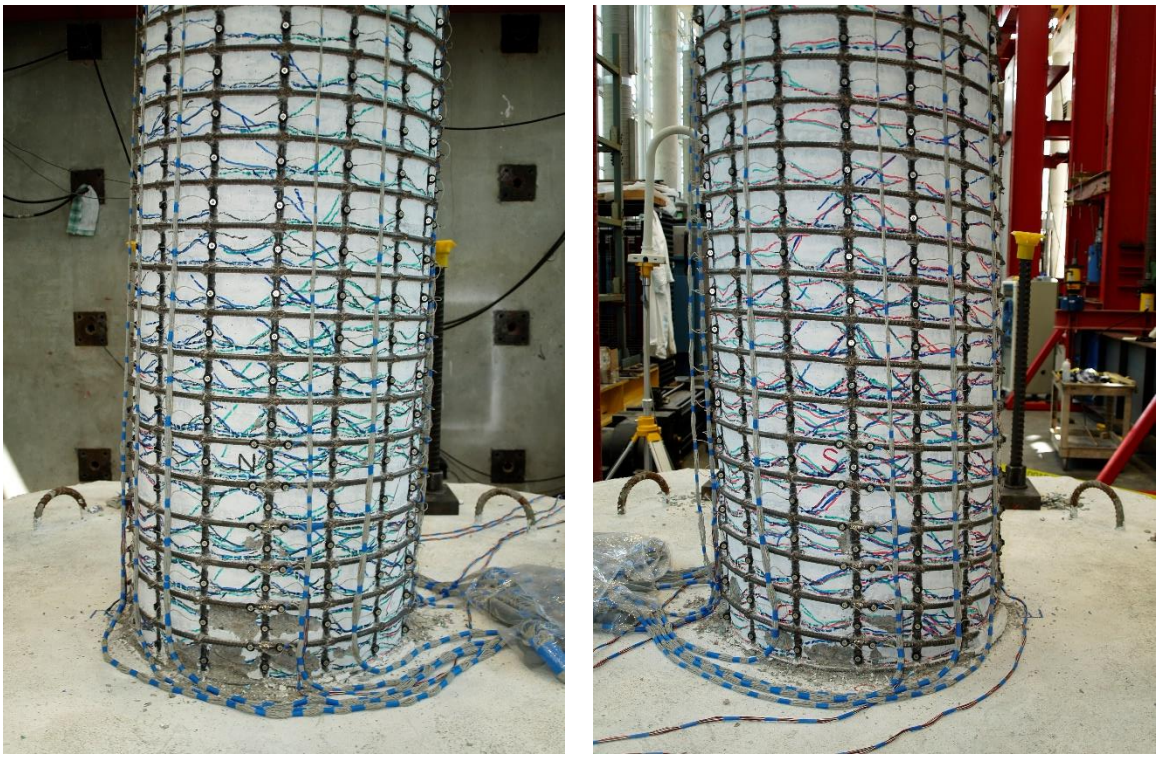

Figure 15-21. Test 12: (Left) North and (Right) South Sides of the Specimen at the End of $\mu_{\Delta 4}$

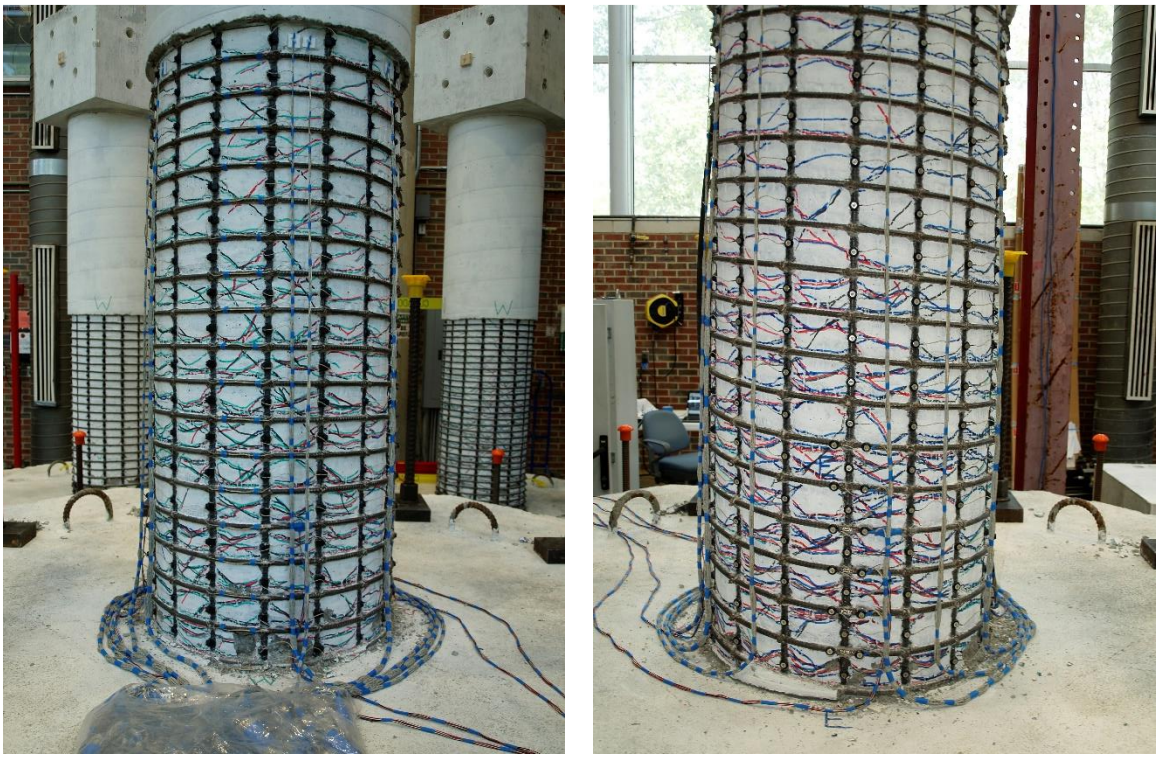

Figure 15-22. Test 12: (Left) West Side at $\mu_{\Delta 4}^{+1x} = 4.88$" and (Right) East Side at $\mu_{\Delta 4}^{-1x} = -4.85$"

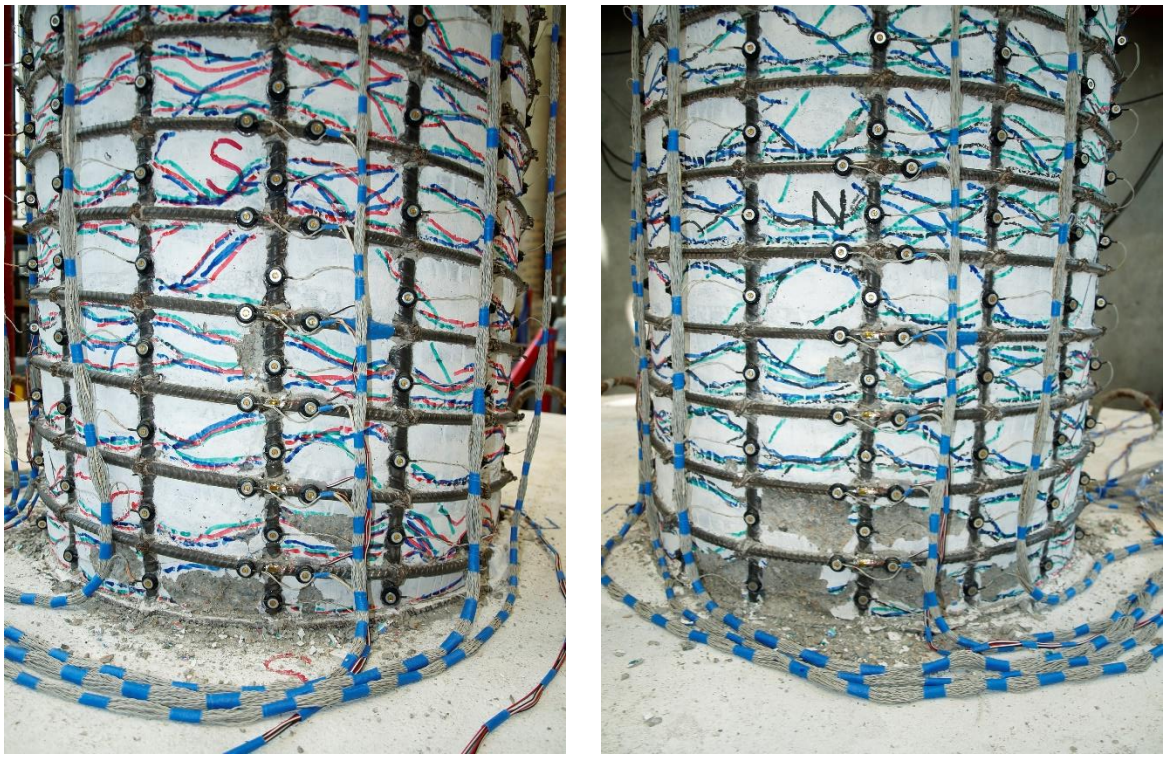

Figure 15-23. Test 12: Spiral Yielding on the (Left) South Side at $\mu_{\Delta 4}^{-1y} = -4.87"$ and (Right) North Side at $\mu_{\Delta 4.5}^{+1y} = 5.52"$

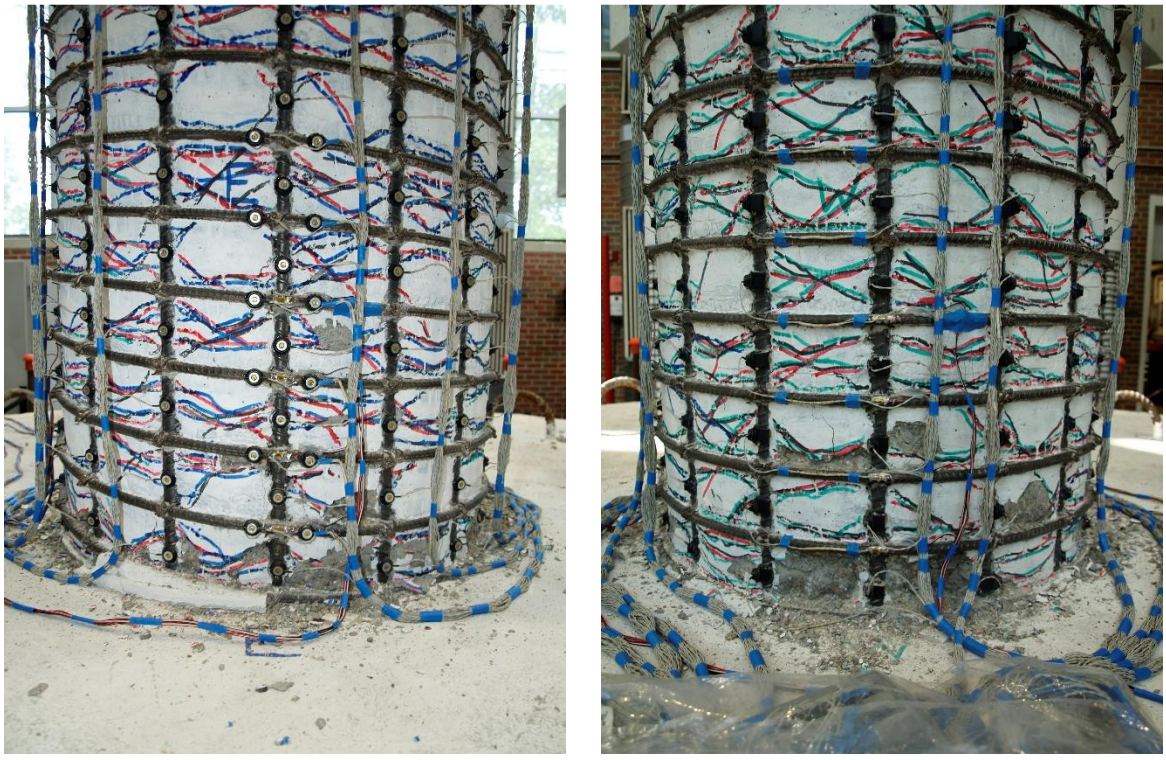

Figure 15-24. Test 12: Spiral Yielding on the (Left) East Side at $\mu_{\Delta 4.5}^{+1x} = 5.47"$ and (Right) West Side at $\mu_{\Delta 4.5}^{-1x} = -5.46"$

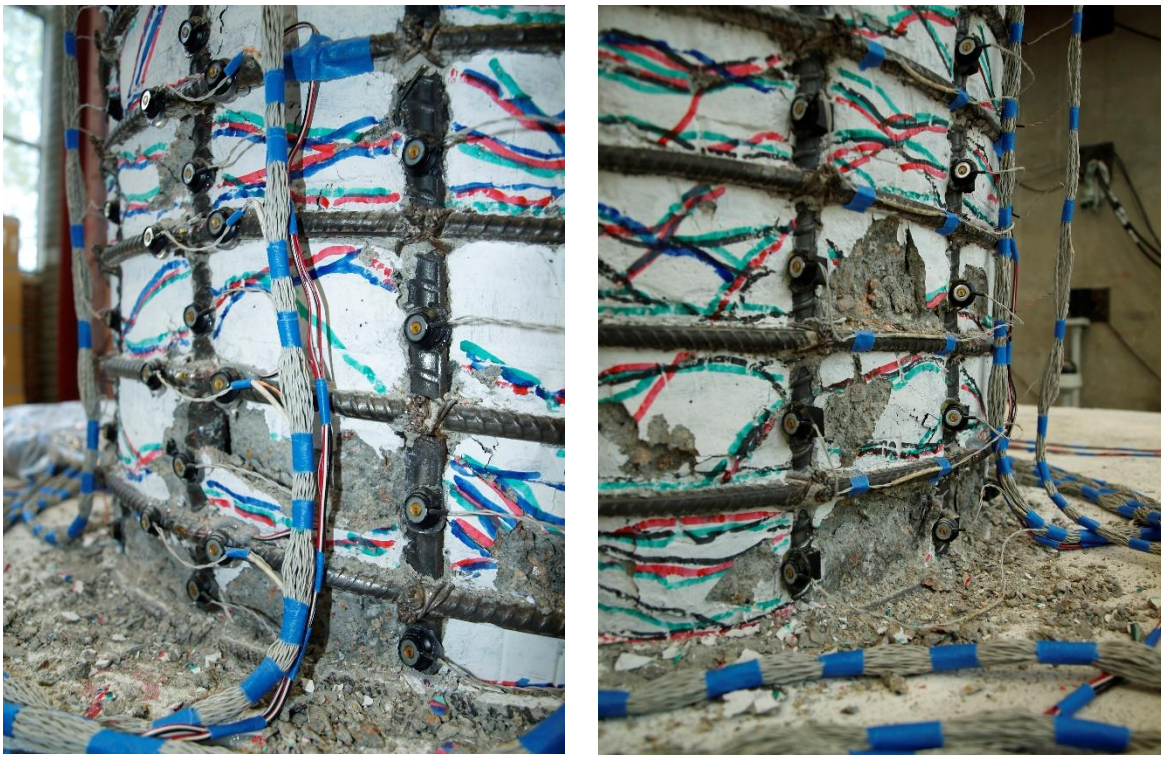

Figure 15-25. Test 12: Buckling of (Left) Bars S and SSE at $\mu_{\Delta 5}^{-1y} = -6.08"$ and (Right) Bar W at $\mu_{\Delta 5}^{-1x} = -6.06"$

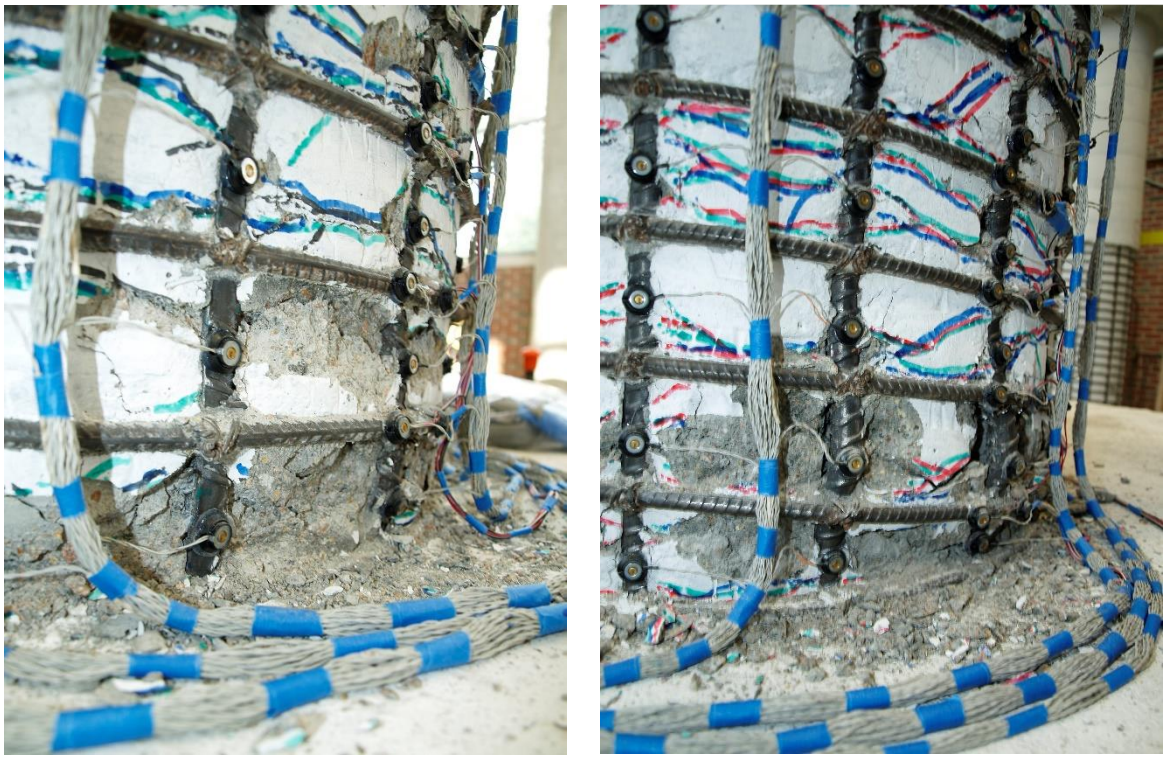

Figure 15-26. Test 12: Buckling of (Left) Bar N at $\mu_{\Delta 6}^{+1y} = 7.30"$ and (Right) Adjacent South Bar SSW at $\mu_{\Delta 6}^{-1y} = -7.31"$

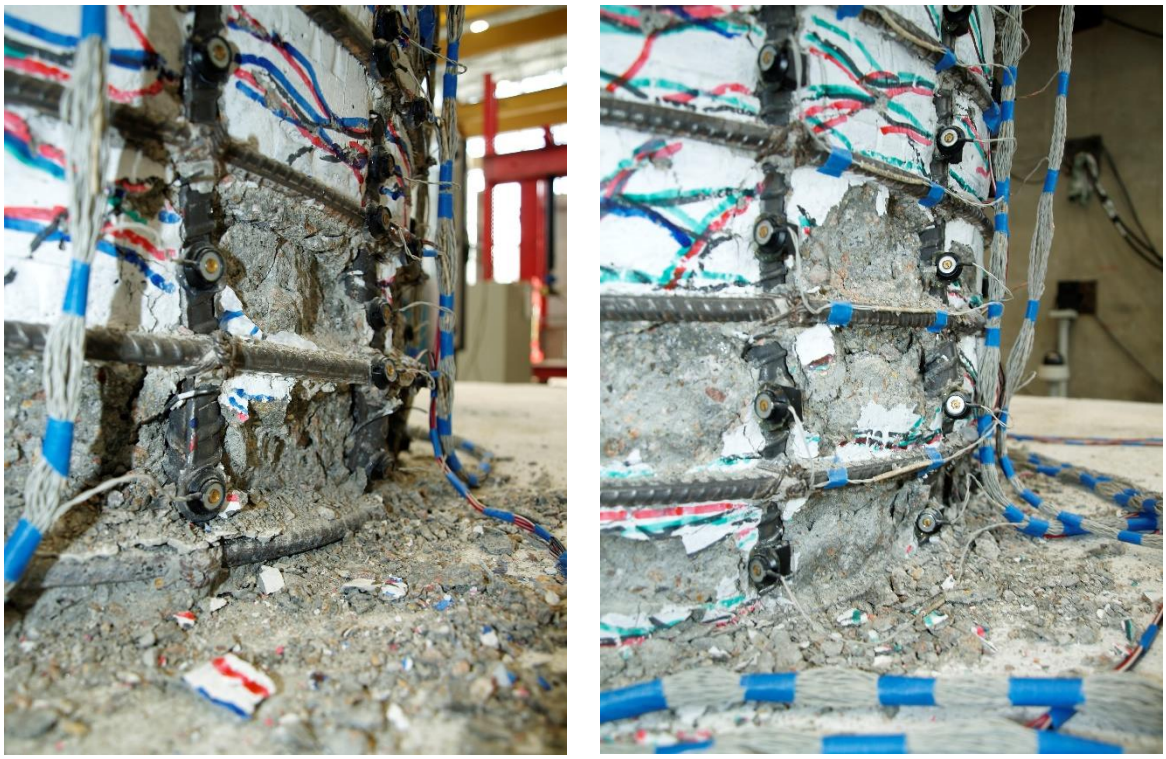

Figure 15-27. Test 12: Buckling of Bars (Left) E, ENE, & ESE at $\mu_{\Delta 6}^{-1x} = -7.28$" & (Right) WNW & WSW during Reversal to 0"

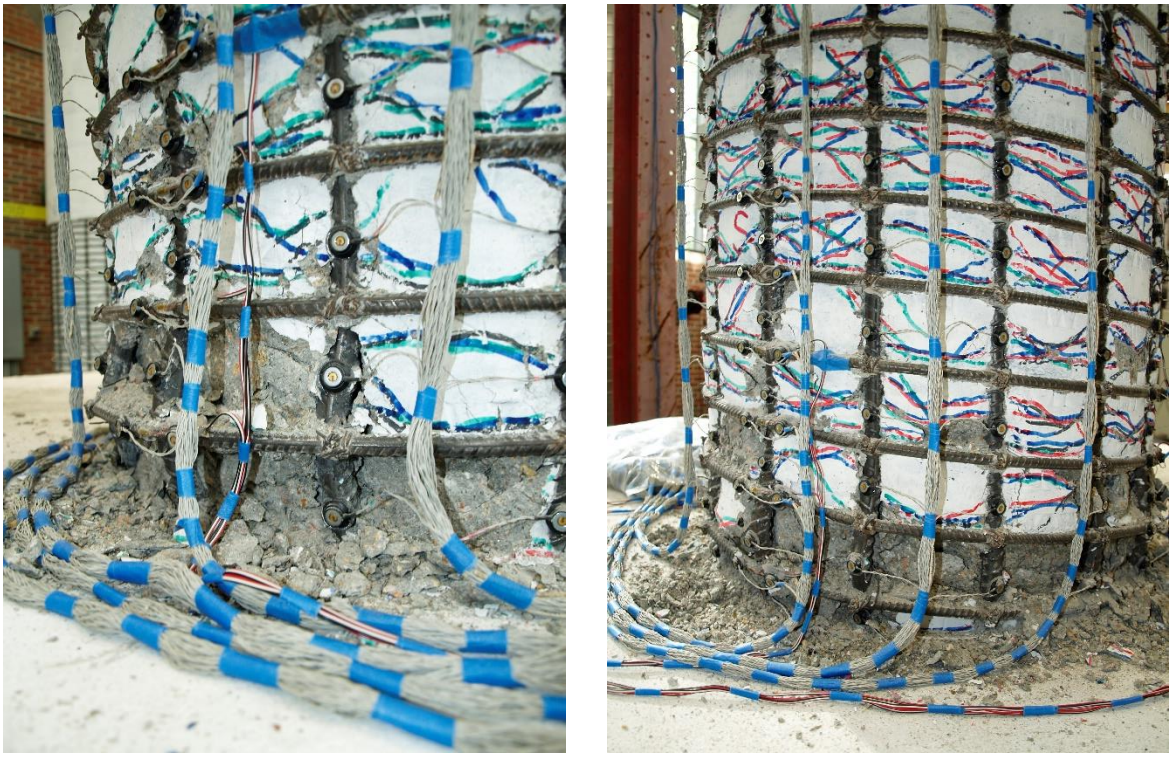

Figure 15-28. Test 12: Buckling of Bars (Left) NE, NNE, & NNW at $\mu_{\Delta 4.5p}^{+1y} = 5.47$" and (Right) SE & SW at $\mu_{\Delta 4.5p}^{-1y} = -5.50$"

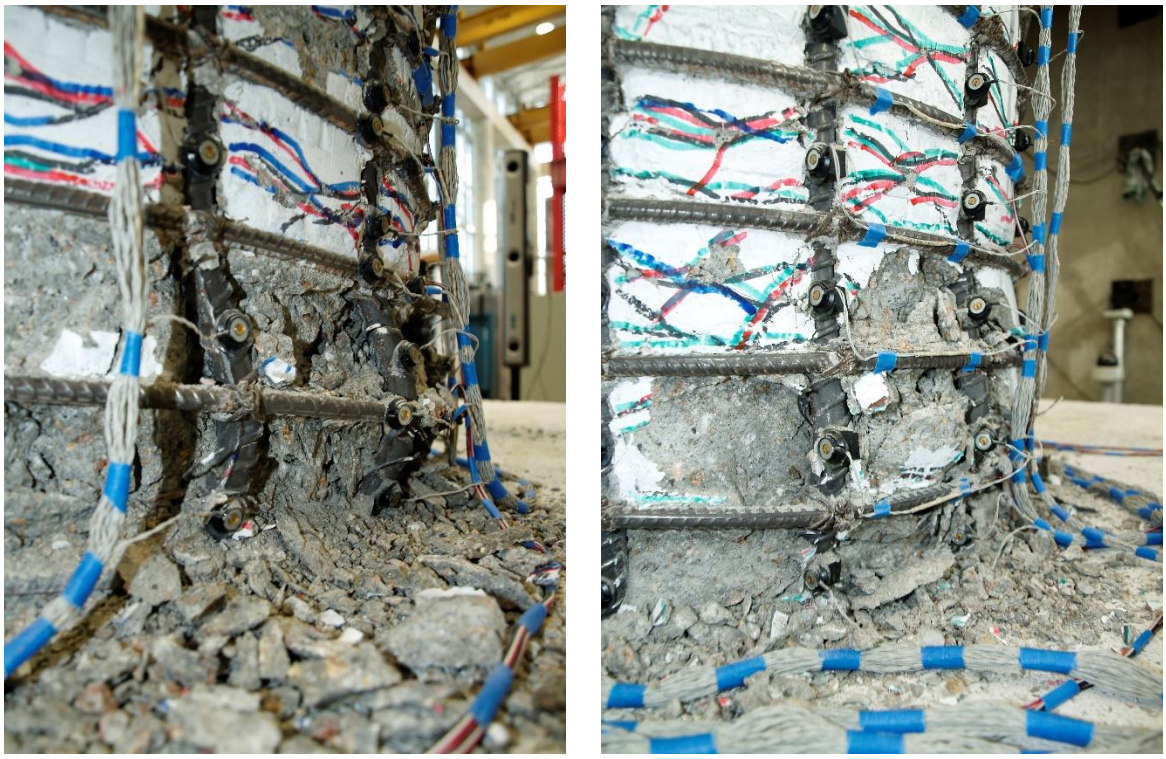

Figure 15-29. Test 12: Additional Deformation in (Left) East and (Right) West Bars during $\mu_{\Delta 4.5p}^{\pm 1x}$

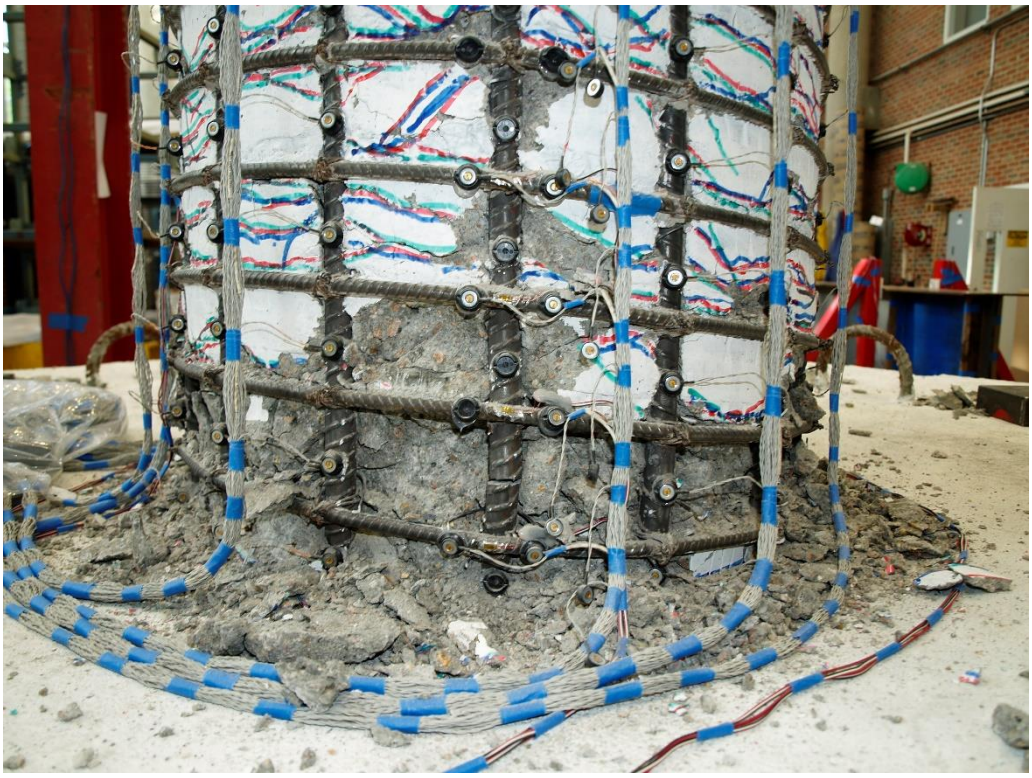

Figure 15-30. Test 12: Fracture of the Previously Buckled South Bar at $3.30"$ *during* $\mu_{\Delta 4.5p}^{+2y}$

Test 12 - Strain Data Analysis

North and South Bar Strains

Vertical strain profiles for North and South reinforcement during y-direction cycles are shown in Figure 15-31 and Figure 15-32. Strains in the lowest four spiral layers during compressive y-direction cycles on the North and South sides of the specimen appear in Figure 15-33 and Figure 15-34. The relationship between strain and displacement for either peak tensile or peak compressive gauge lengths appear in Figure 15-35 through Figure 15-39. These figures contain monotonic moment curvature predictions for respective plastic hinge methods. PCK (2007) Lp refers to the (Priestley, Calvi and Kowalsky 2007) plastic hinge method, GN15 Tension/Compression Lpr refers to the (Goodnight, Kowalsky and Nau 2015a) unidirectional modified plastic hinge method, TX Measured refer to using the measured extent of plasticity and average equivalent strain penetration length from this specific test, and New Equations refers to a new bidirectional plastic hinge method which was created based on this study. Details of the new plastic hinge method appear in a later chapter of this report.

The spiral strain gauge hysteresis for the first layer above the footing on the North side of the specimen is shown in Figure 15-42. Tension strains in this layer increased during $\mu_{\Delta 6}^{+1y} = 7.30$" as the North extreme fiber bar visibly buckled, see Figure 15-26. The visual observation of bar buckling was confirmed upon inspection of the North longitudinal bar strain hystereses in Figure 15-40 and Figure 15-41; however, there was measurable outward deformation in the previous compressive cycle.

The spiral strain gauge hysteresis for the second layer above the footing on the South side of the specimen is shown in Figure 15-44. Tension strains in this layer increased during $\mu_{\Delta 5}^{-1y} = -6.08$" as South reinforcing bars S and SSE visibly buckled, see Figure 15-25. The visual observation of bar buckling was confirmed upon inspection of the South longitudinal bar strain hysteresis in Figure 15-43.

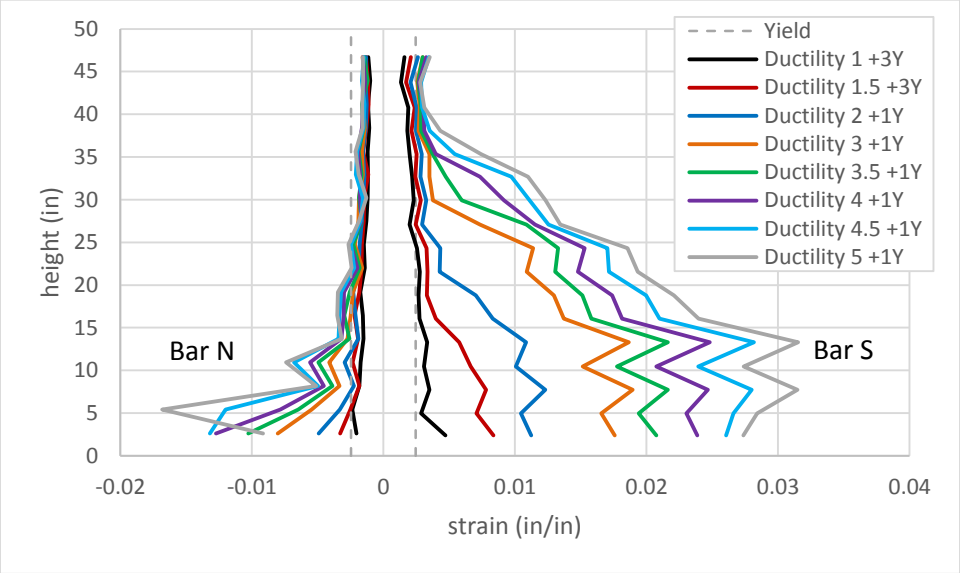

Figure 15-31. Test 12: Vertical Strain Profiles for Loading in the +Y-direction

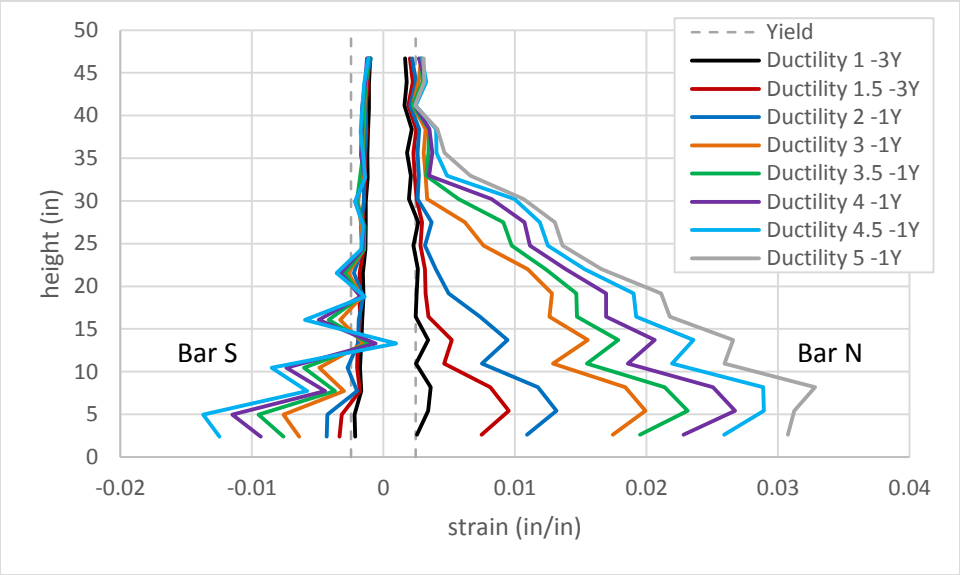

Figure 15-32. Test 12: Vertical Strain Profiles for Loading in the -Y-direction

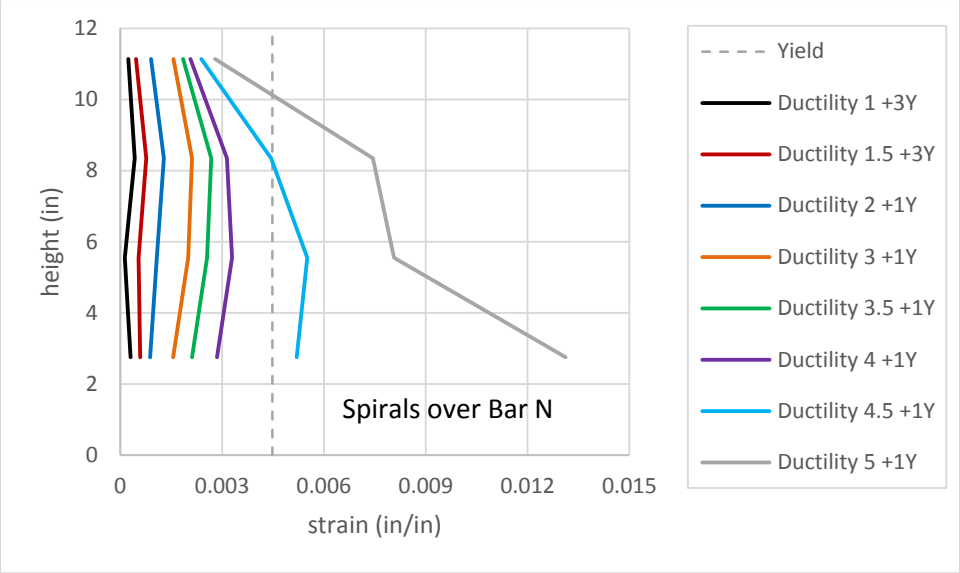

Figure 15-33. Test 12: Spiral Strains Measured Over the North Extreme Fiber Bar during +Y Cycles

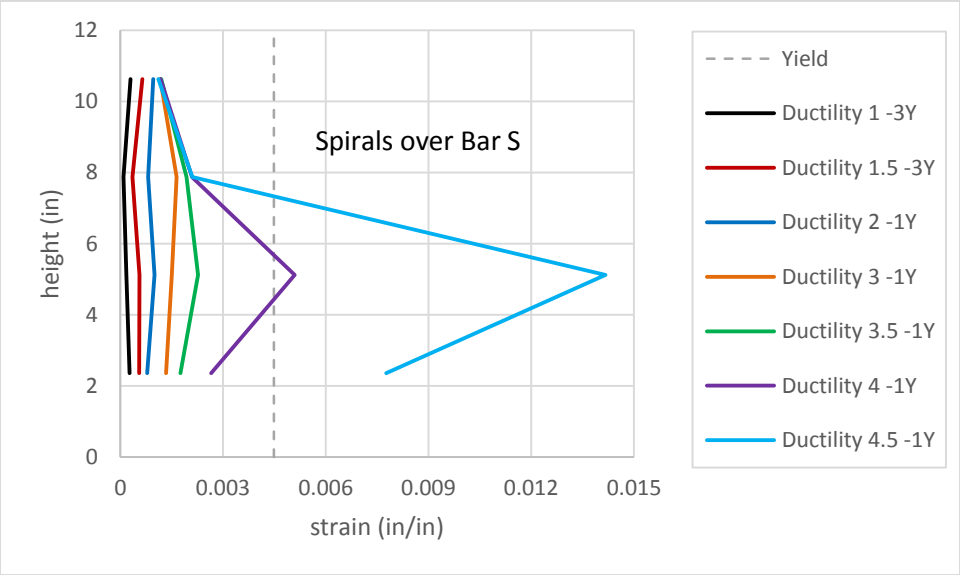

Figure 15-34. Test 12: Spiral Strains Measured Over the South Extreme Fiber Bar during -Y Cycles

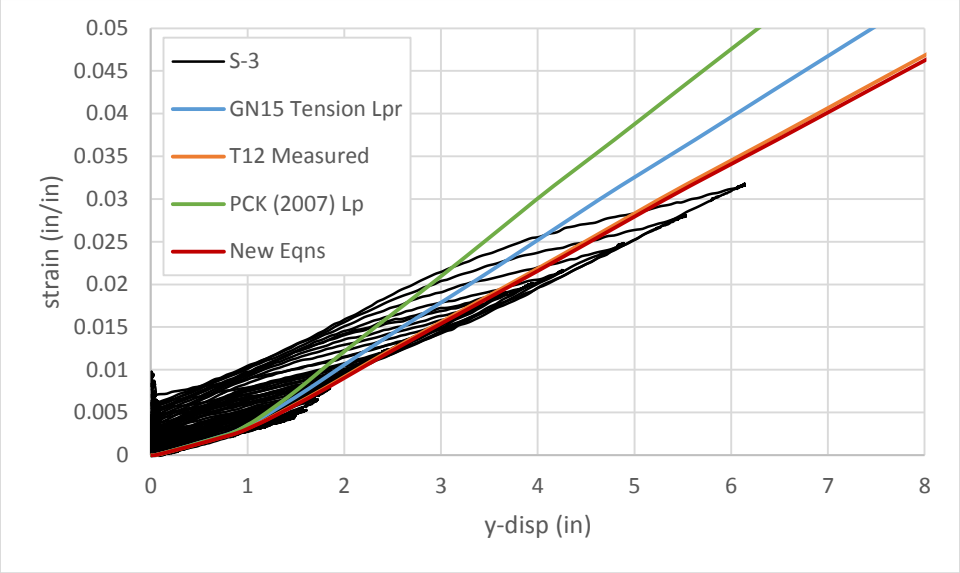

Figure 15-35. Test 12: Tension Strain-Disp. for Bar S (Gauge Length 3 Centered 7.72" above the Footing)

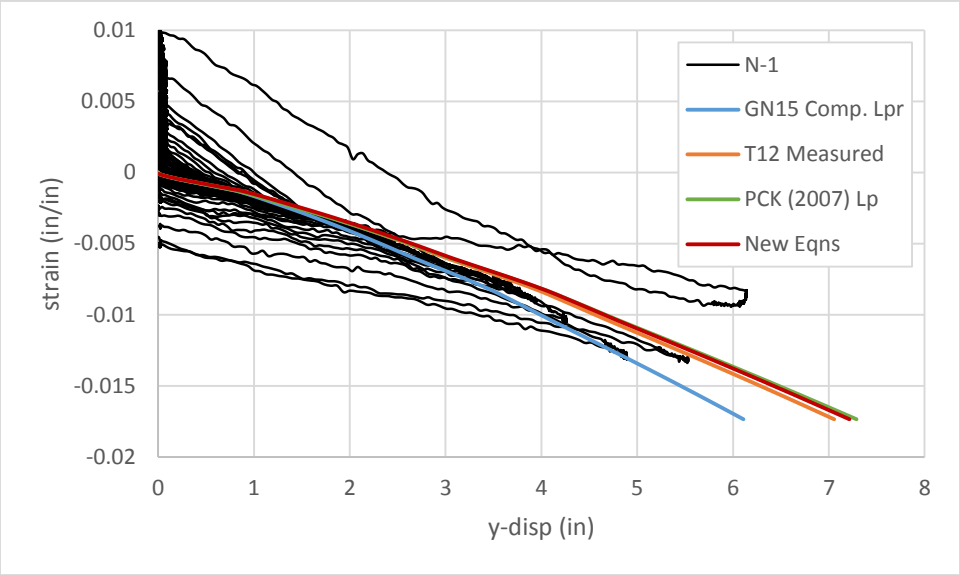

Figure 15-36. Test 12: Compression Strain-Disp. for Bar N (Gauge Length 1 Centered 2.60" above the Footing)

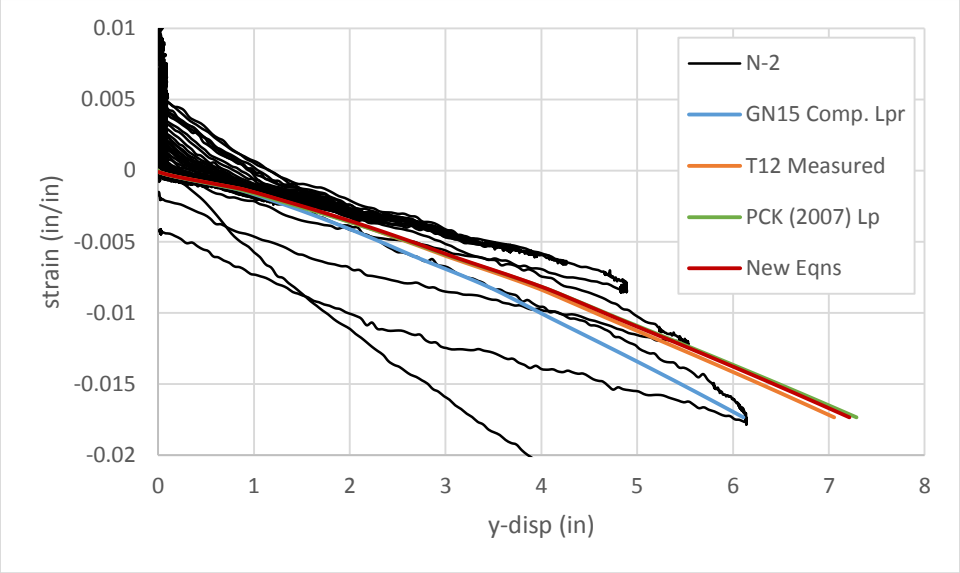

Figure 15-37. Test 12: Compression Strain-Disp. for Bar N (Gauge Length 2 Centered 5.41" above the Footing)

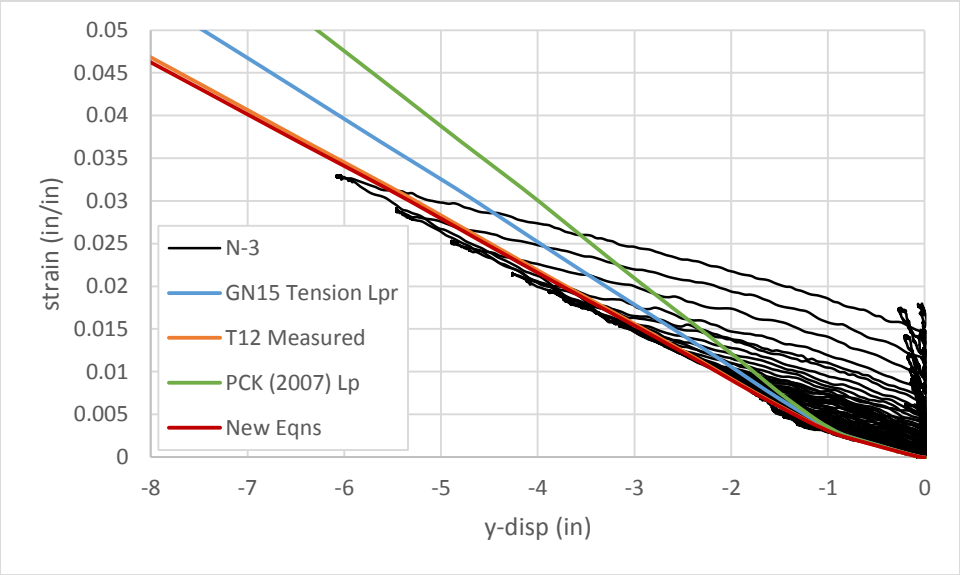

Figure 15-38. Test 12: Tension Strain-Disp. for Bar N (Gauge Length 3 Centered 8.19" above the Footing)

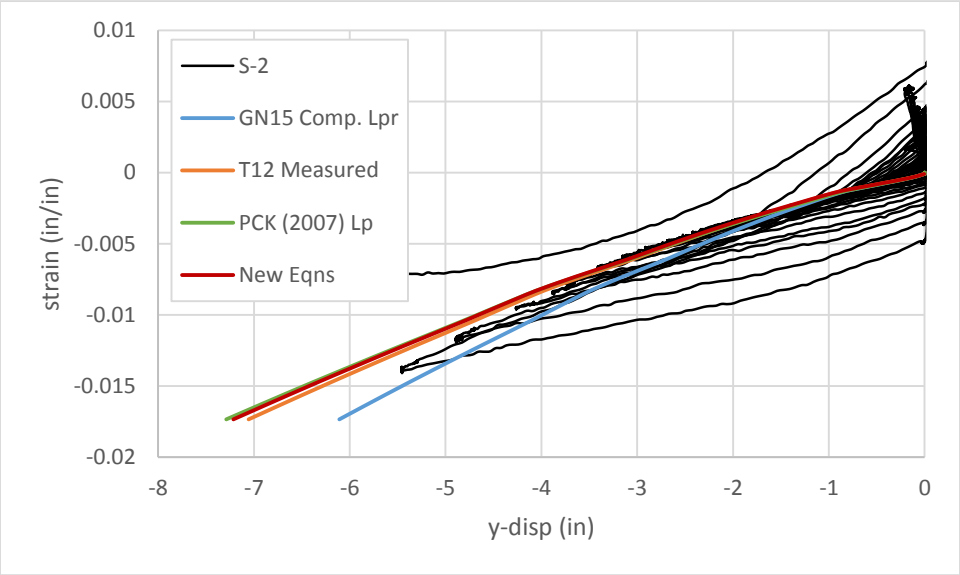

Figure 15-39. Test 12: Compression Strain-Disp. for Bar S (Gauge Length 2 Centered 4.97" above the Footing)

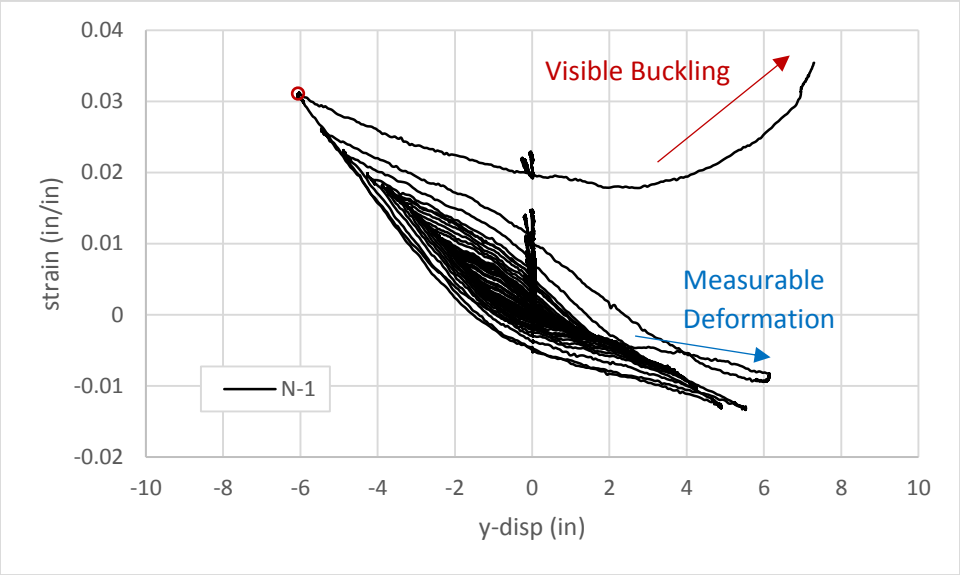

Figure 15-40. Test 12: Strain Hysteresis over the North Buckled Bar (Gauge Length 1 Centered 2.60" above the Footing)

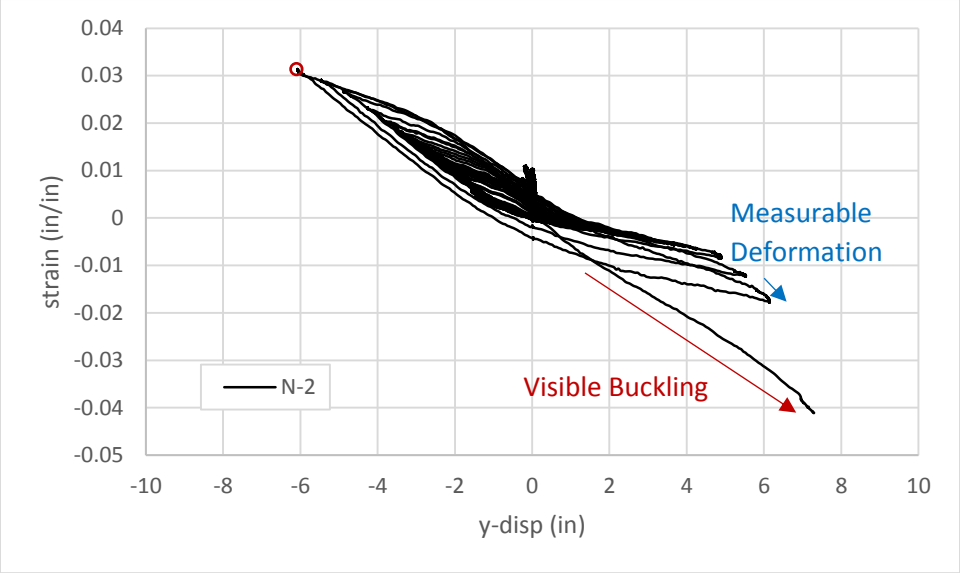

Figure 15-41. Test 12: Strain Hysteresis over the North Buckled Bar (Gauge Length 2 Centered 5.41" above the Footing)

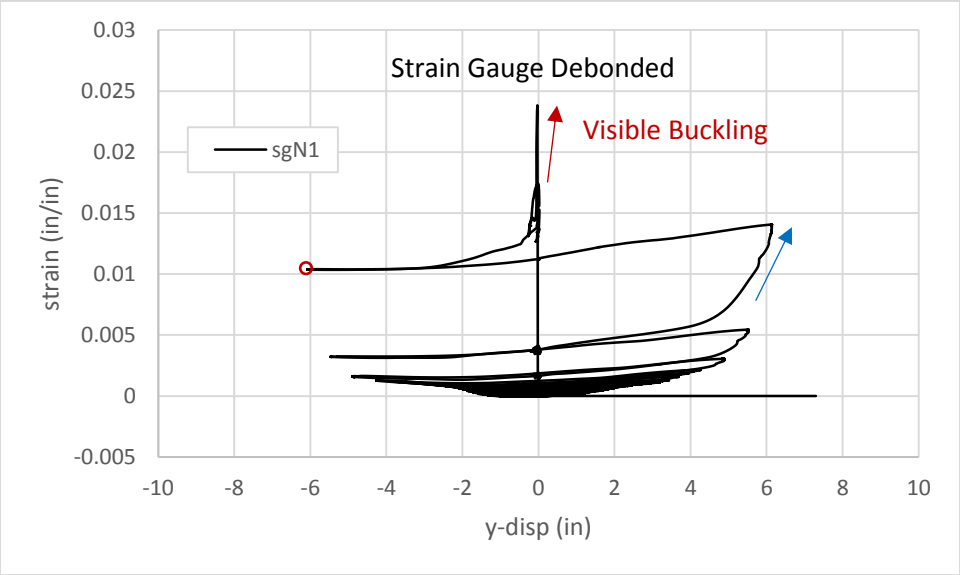

Figure 15-42. Test 12: Spiral Strain Hysteresis for the 1st North Layer above the Footing

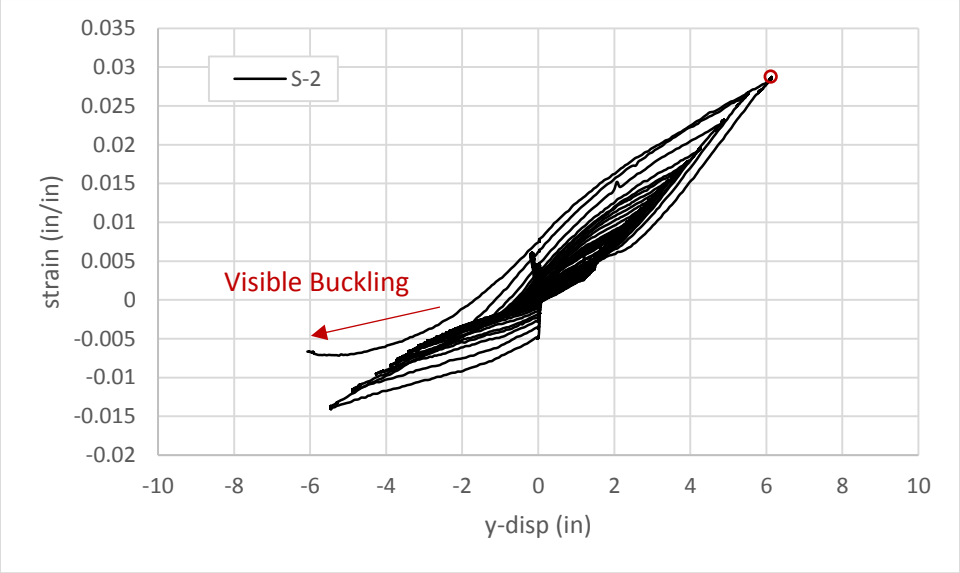

Figure 15-43. Test 12: Strain Hysteresis over the South Buckled Bar (Gauge Length 2 Centered 4.97" above the Footing)

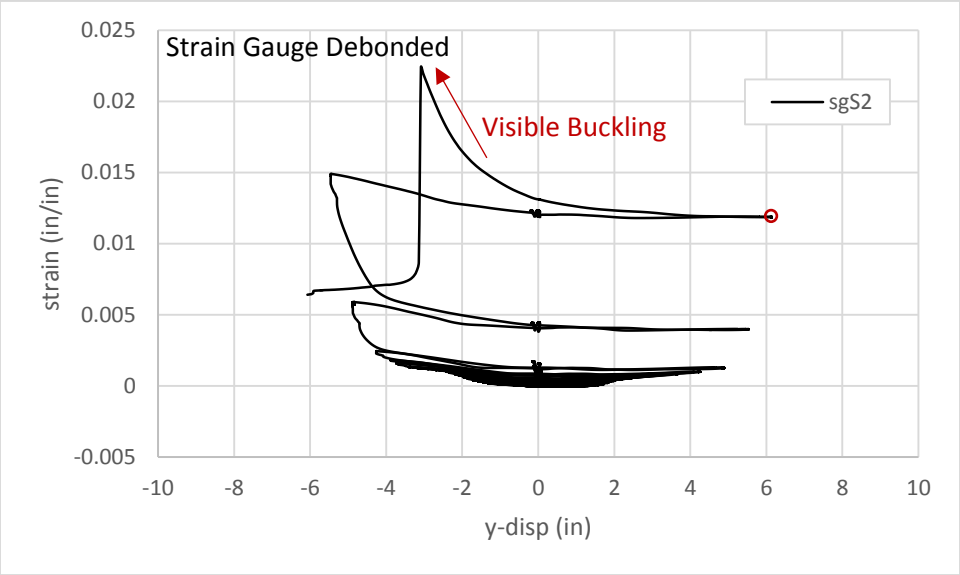

Figure 15-44. Test 12: Spiral Strain Hysteresis for the 2nd South Layer above the Footing

East and West Bar Strains

Vertical strain profiles for East and West reinforcement during x-direction cycles are shown in Figure 15-45 and Figure 15-46. Strains in the lowest four spiral layers during compressive x-direction cycles on the East and West sides of the specimen appear in Figure 15-47 and Figure 15-48. The relationship between strain and displacement for either peak tensile or peak compressive gauge lengths appear in Figure 15-49 through Figure 15-52. These figures contain monotonic moment curvature predictions for respective plastic hinge methods. PCK (2007) Lp refers to the (Priestley, Calvi and Kowalsky 2007) plastic hinge method, GN15 Tension/Compression Lpr refers to the (Goodnight, Kowalsky and Nau 2015a) unidirectional modified plastic hinge method, TX Measured refer to using the measured extent of plasticity and average equivalent strain penetration length from this specific test, and New Equations refers to a new bidirectional plastic hinge method which was created based on this study. Details of the new plastic hinge method appear in a later chapter of this report.

The spiral strain gauge hysteresis for the first layer above the footing on the East side of the specimen is shown in Figure 15-55. Tension strains in this layer increased during $\mu_{\Delta 6}^{-1x} = -7.28$" as three East bars buckled simultaneously, see Figure 15-27. The visual observation of bar buckling was confirmed upon inspection of the East longitudinal bar strain hystereses in Figure 15-53 and Figure 15-54; however, there was measurable outward deformation in the previous compressive cycle.

The spiral strain gauge hystereses for the first and second layers above the footing on the West side of the specimen are shown in Figure 15-58 and Figure 15-59. Tension strains in these layers increased during $\mu_{\Delta 5}^{-1x} = -6.06$" as the West extreme fiber bar buckled, see Figure 15-25. The visual observation of bar buckling was confirmed upon inspection of the West longitudinal bar strain hystereses in Figure 15-56 and Figure 15-57; however, there was measurable outward deformation in the previous compressive cycle. This measurable deformation did not lead to a significant spike in the transverse steel strains.

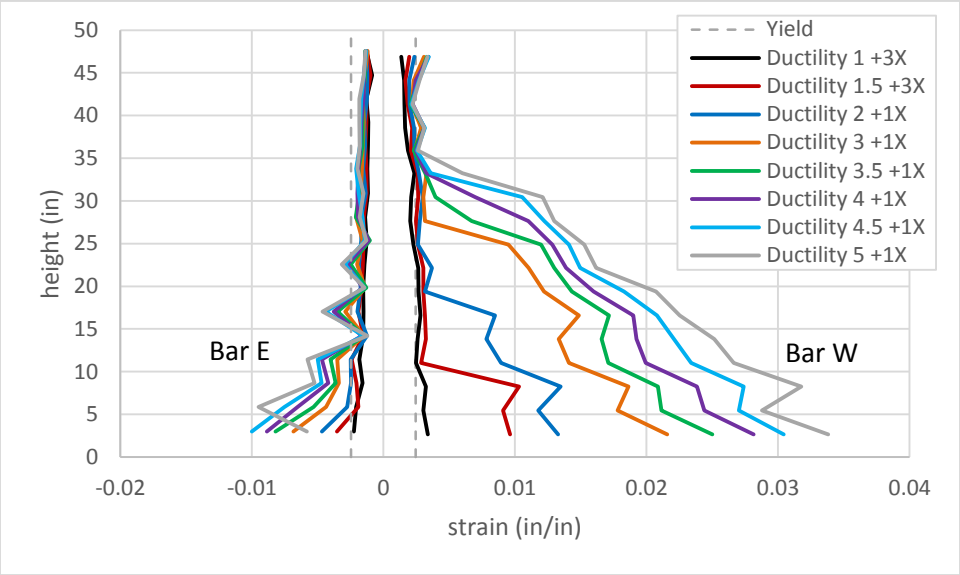

Figure 15-45. Test 12: Vertical Strain Profiles for Loading in the +X-direction

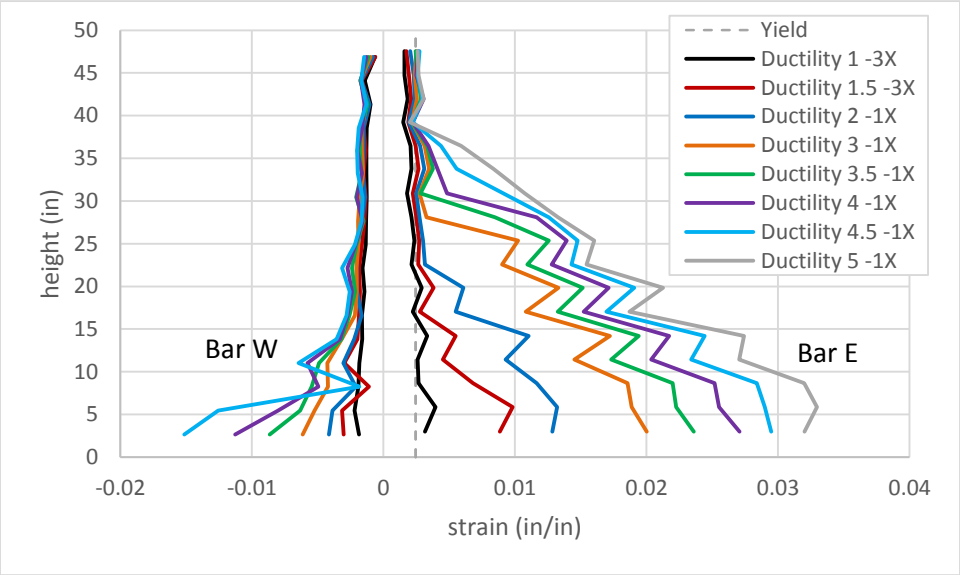

Figure 15-46. Test 12: Vertical Strain Profiles for Loading in the -X-direction

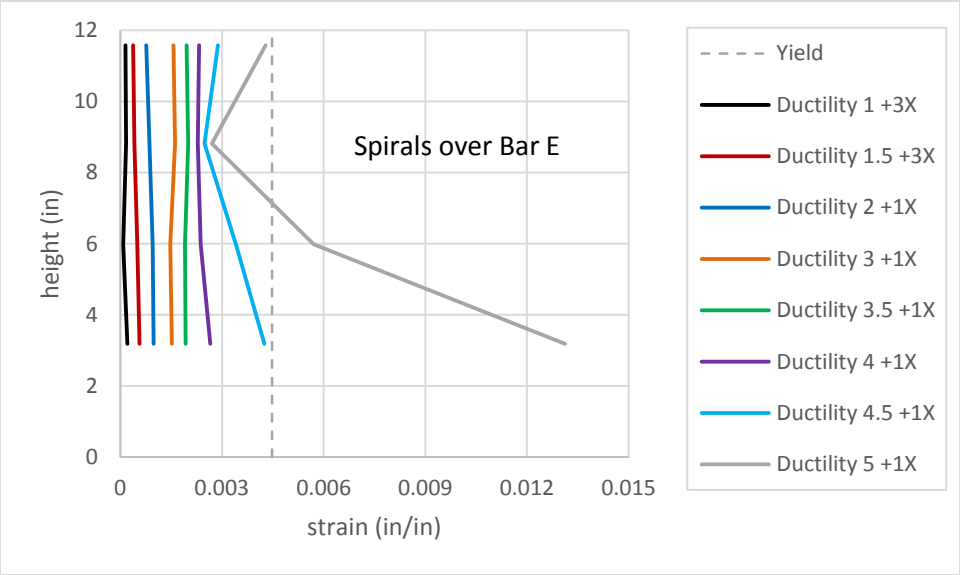

Figure 15-47. Test 12: Spiral Strains Measured Over the East Extreme Fiber Bar during +X Cycles

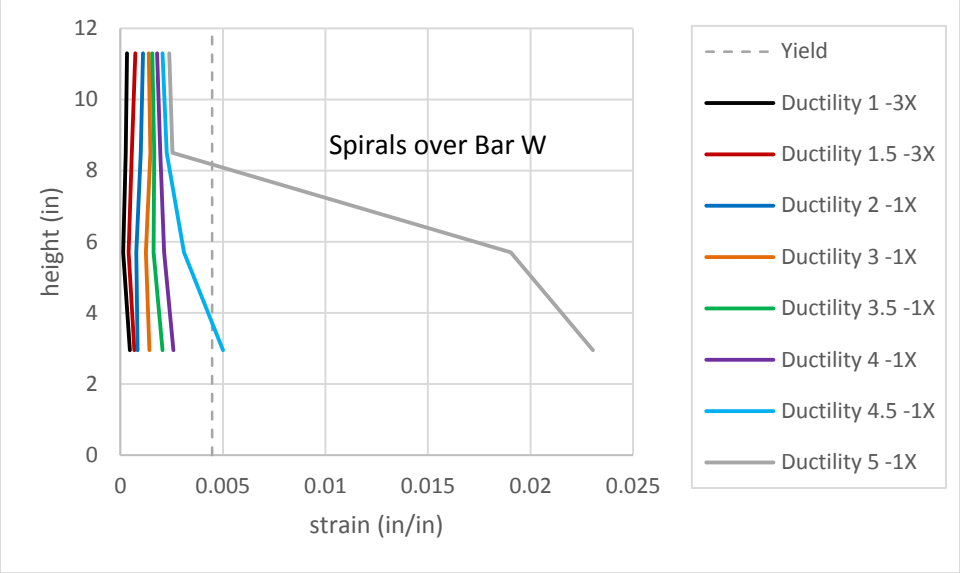

Figure 15-48. Test 12: Spiral Strains Measured Over the West Extreme Fiber Bar during -X Cycles

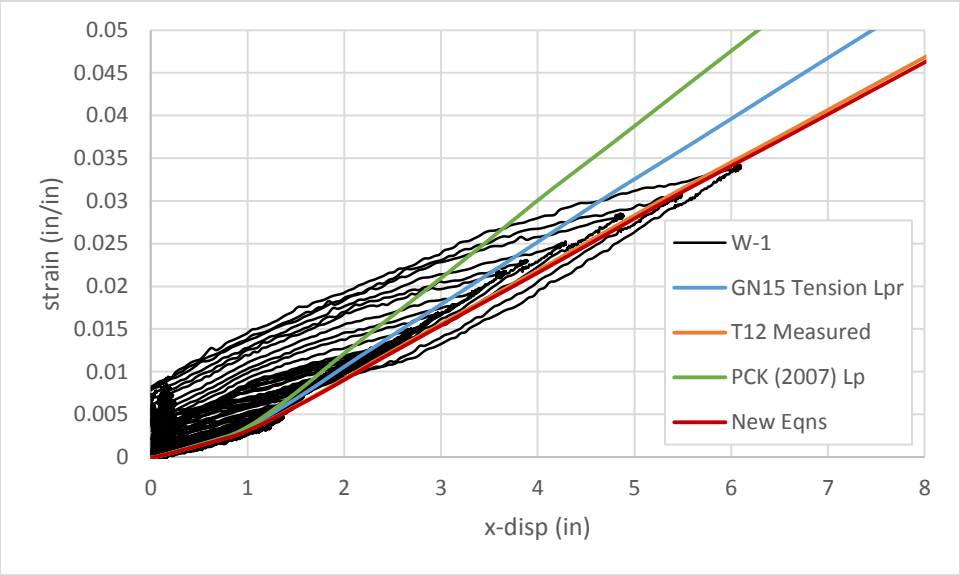

Figure 15-49. Test 12: Tension Strain-Disp. for Bar W (Gauge Length 1 Centered 2.64" above the Footing)

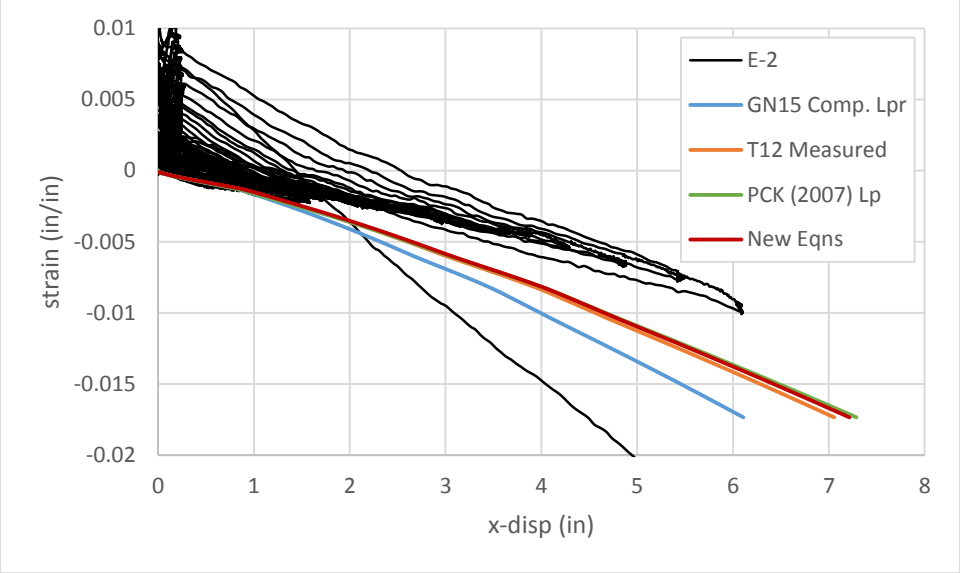

Figure 15-50. Test 12: Compression Strain-Disp. for Bar E (Gauge Length 2 Centered 5.88" above the Footing)

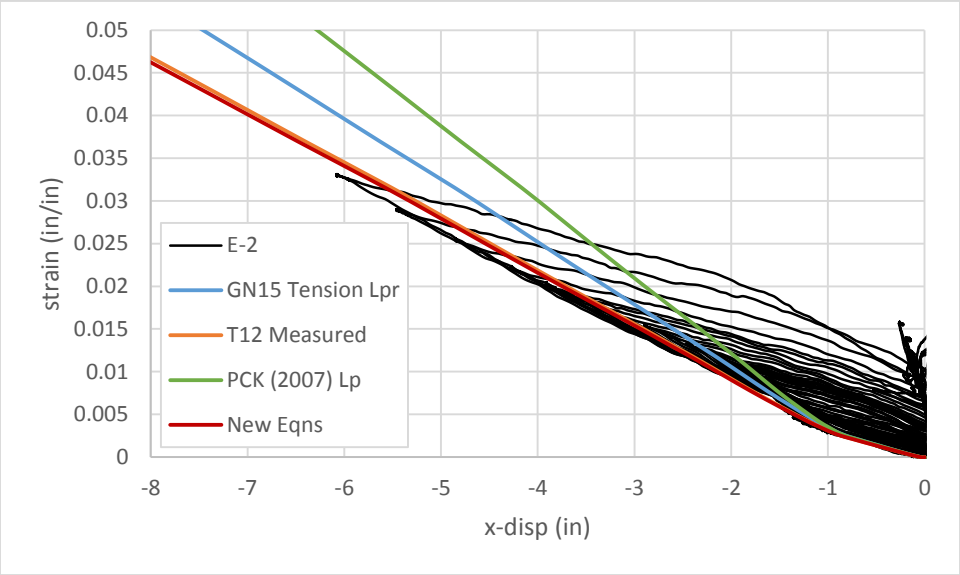

Figure 15-51. Test 12: Tension Strain-Disp. for Bar E (Gauge Length 2 Centered 5.88" above the Footing)

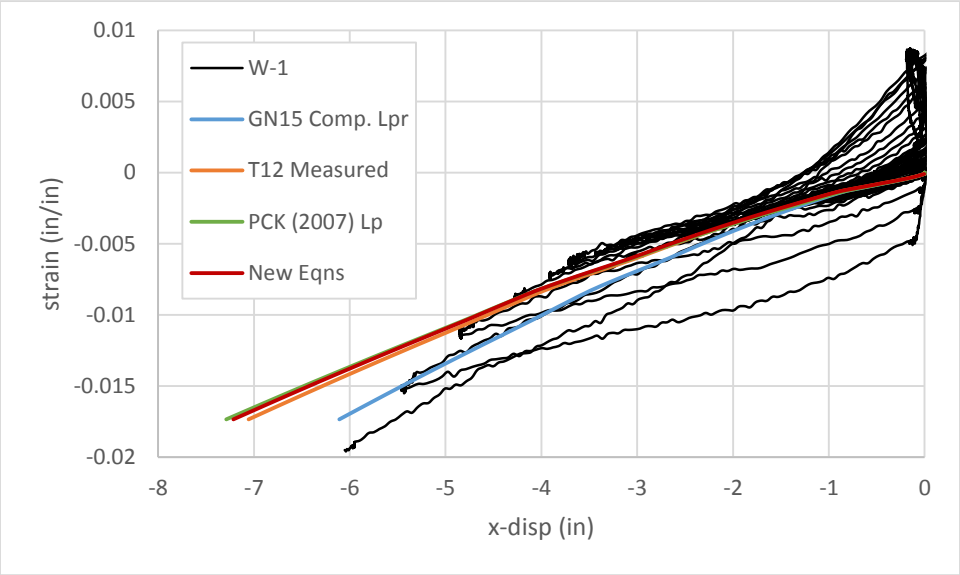

Figure 15-52. Test 12: Compression Strain-Disp. for Bar W (Gauge Length 1 Centered 2.64" above the Footing)

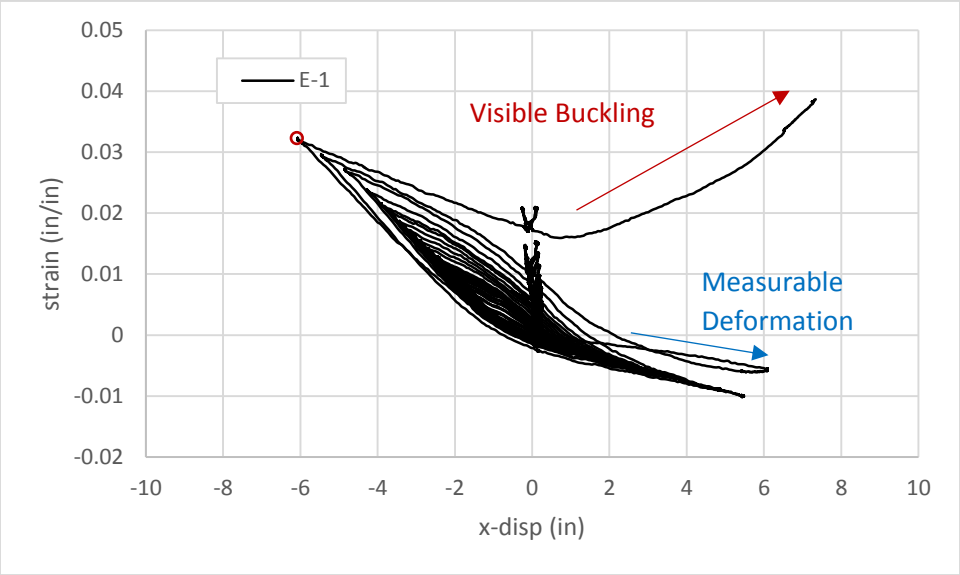

Figure 15-53. Test 12: Strain Hysteresis over the East Buckled Bar (Gauge Length 1 Centered 3.00" above the Footing)

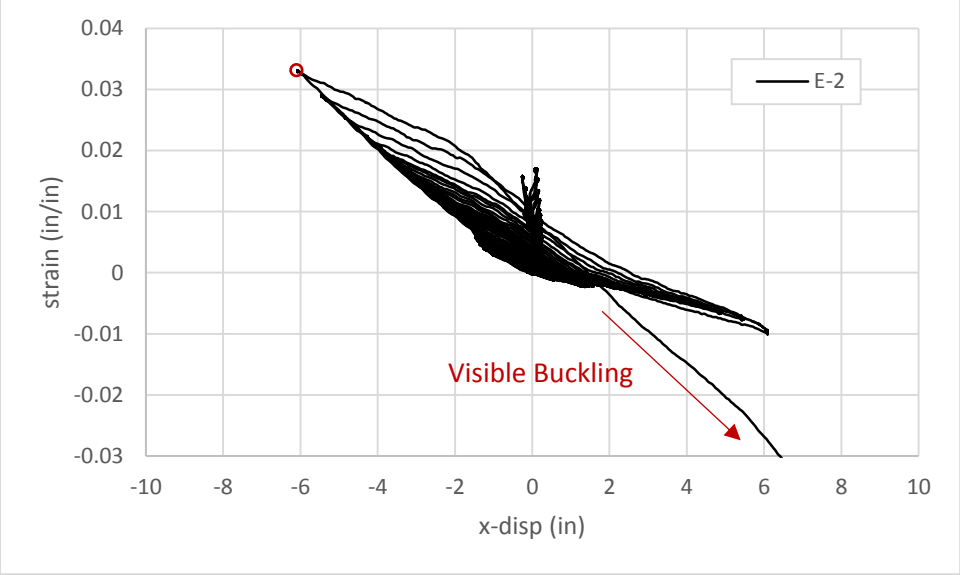

Figure 15-54. Test 12: Strain Hysteresis over the East Buckled Bar (Gauge Length 2 Centered 5.88" above the Footing)

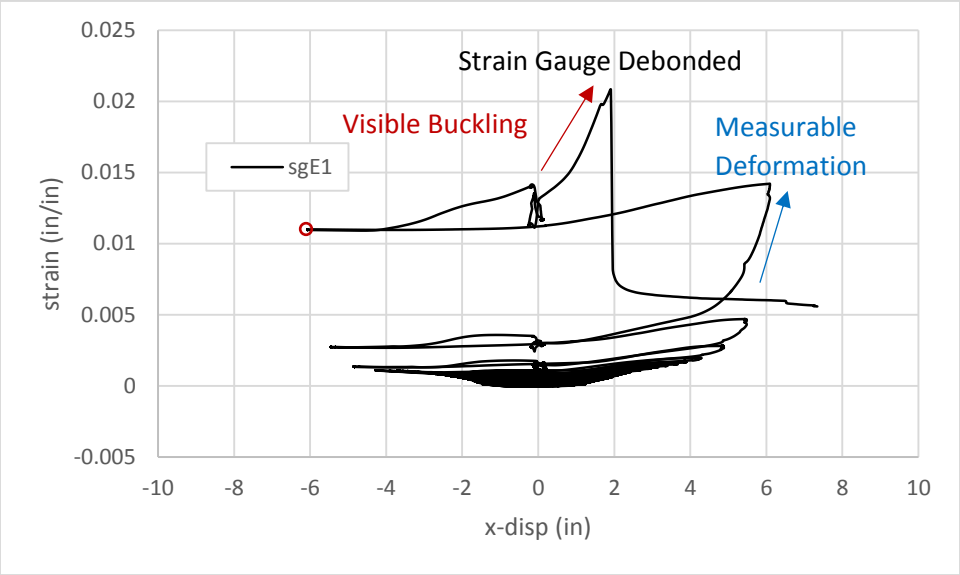

Figure 15-55. Test 12: Spiral Strain Hysteresis for the 1st East Layer above the Footing

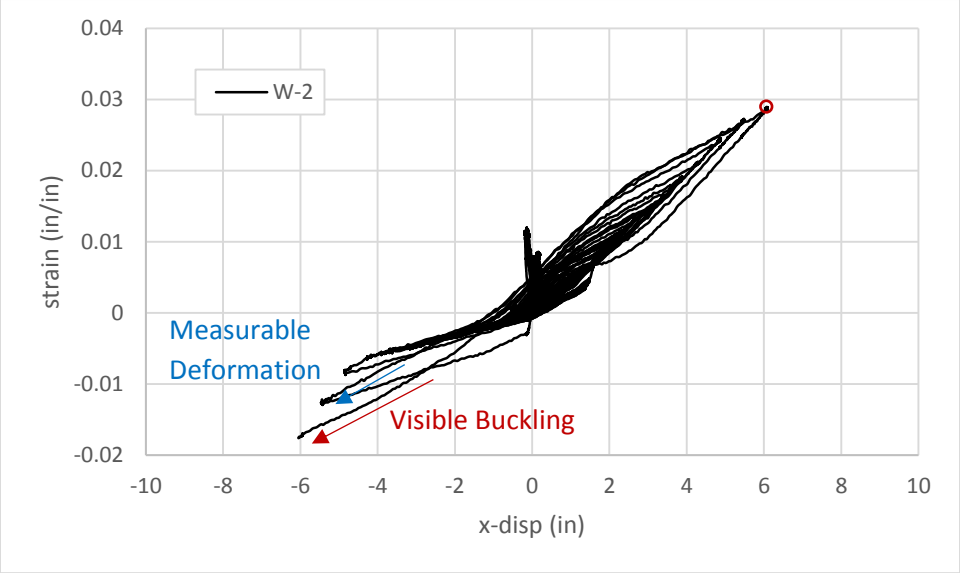

Figure 15-56. Test 12: Strain Hysteresis over the West Buckled Bar (Gauge Length 2 Centered 5.45" above the Footing)

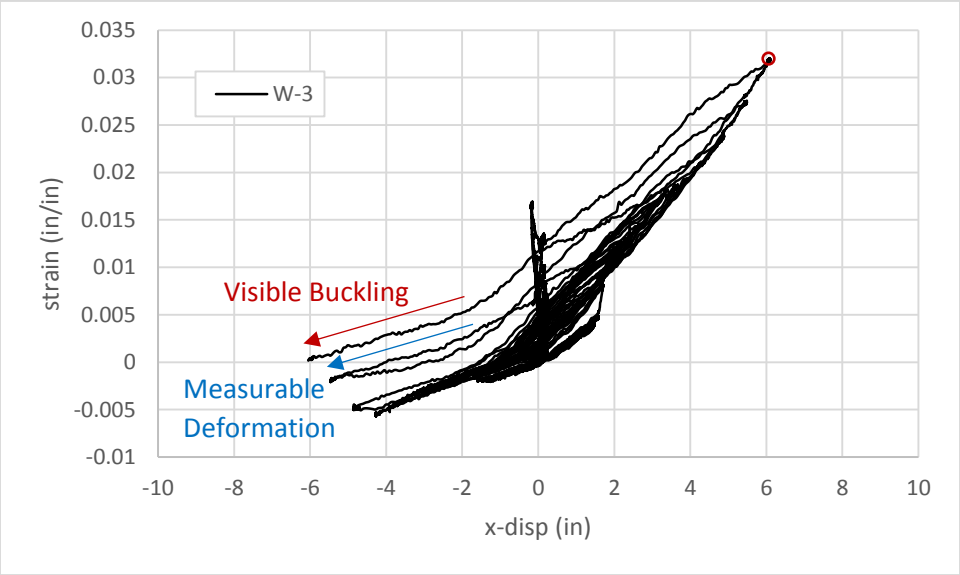

Figure 15-57. Test 12: Strain Hysteresis over the West Buckled Bar (Gauge Length 3 Centered 8.26" above the Footing)

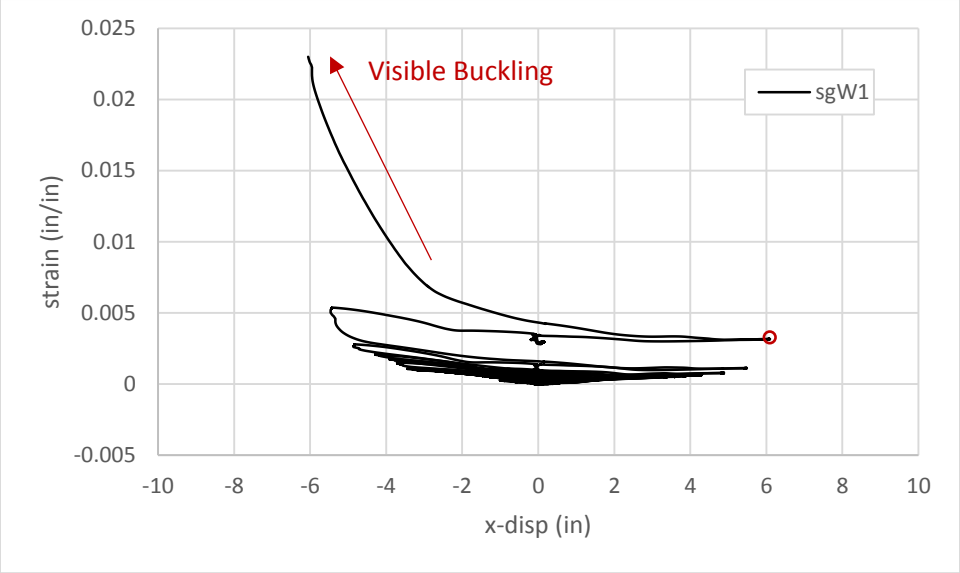

Figure 15-58. Test 12: Spiral Strain Hysteresis for the 1st West Layer above the Footing

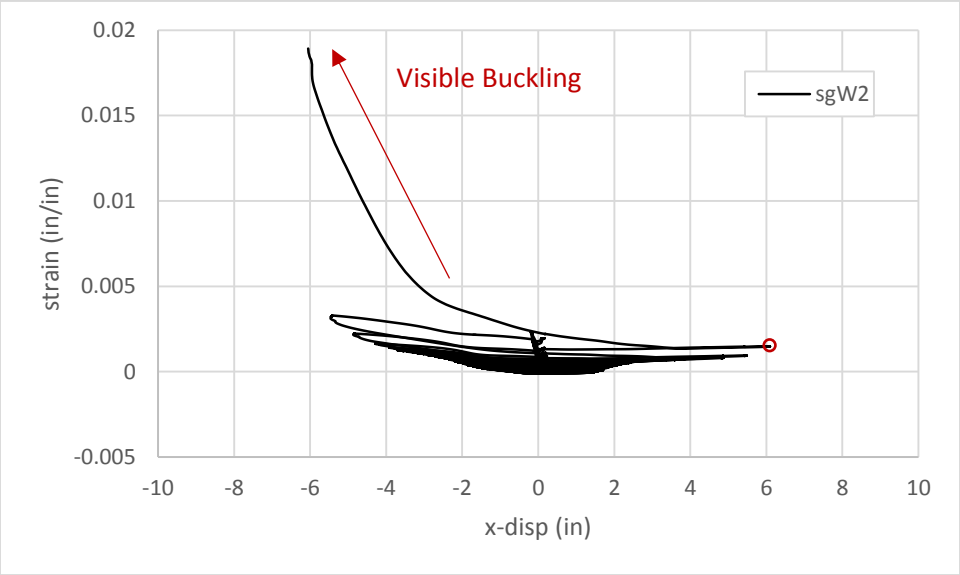

Figure 15-59. Test 12: Spiral Strain Hysteresis for the 2nd West Layer above the Footing

Test 12 - Curvature and Strain Penetration Data

Curvature and stain penetration data for Test 12 is presented in the following section. The methods in which this data was generated are outlined in the summary for Test 1. Sample cross section curvature profiles are shown in Figure 15-60 and Figure 15-61. Vertical curvature profiles for respective loading directions appear in Figure 15-62 through Figure 15-66. Fixed-end rotations attributable to strain penetration of longitudinal reinforcement into the footing are shown in Figure 15-67 through Figure 15-69. Comparison of the measured displacements to those obtained via integration of the measured curvature profiles and extrapolation of the fixed-end rotation to the center of the applied lateral load are shown in Figure 15-70 and Figure 15-71.

The measured extent of plasticity is compared to design recommendations for the tensile triangular plastic hinge length in Figure 15-72. GN15 refers to the (Goodnight, Kowalsky and Nau 2015a) unidirectional tensile hinge length while New Equations refers to a new bidirectional plastic hinge method which was created based on this study. Details of the new plastic hinge method appear in a later chapter of this report. The measured equivalent strain penetration lengths are compared to design recommendations in Figure 15-73. GN15 refers to the (Goodnight, Kowalsky and Nau 2015a) unidirectional Lsp while PCK (2007) refers to the (Priestley, Calvi and Kowalsky 2007) definition of Lsp. Finally, the measured hysteretic response is compared to monotonic predictions in Figure 15-74 and Figure 15-75.

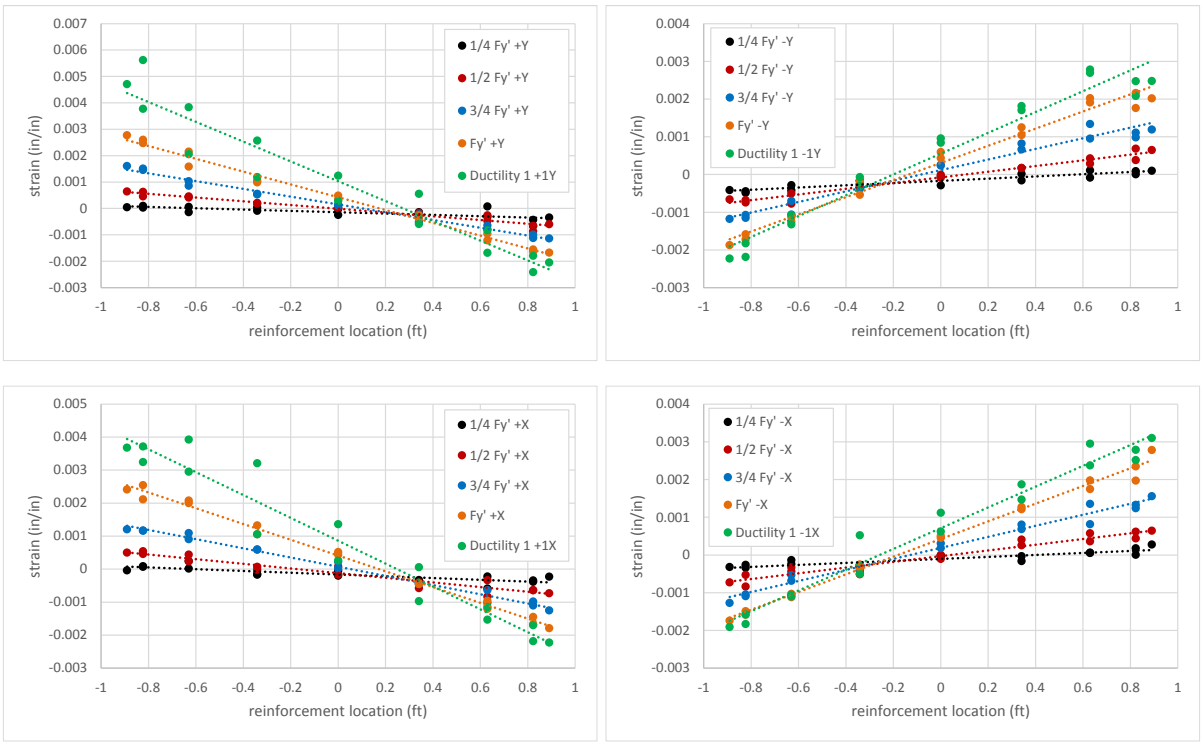

Figure 15-60. Test 12: Elastic Curvature Profiles for the First Instrumented Section above the Footing

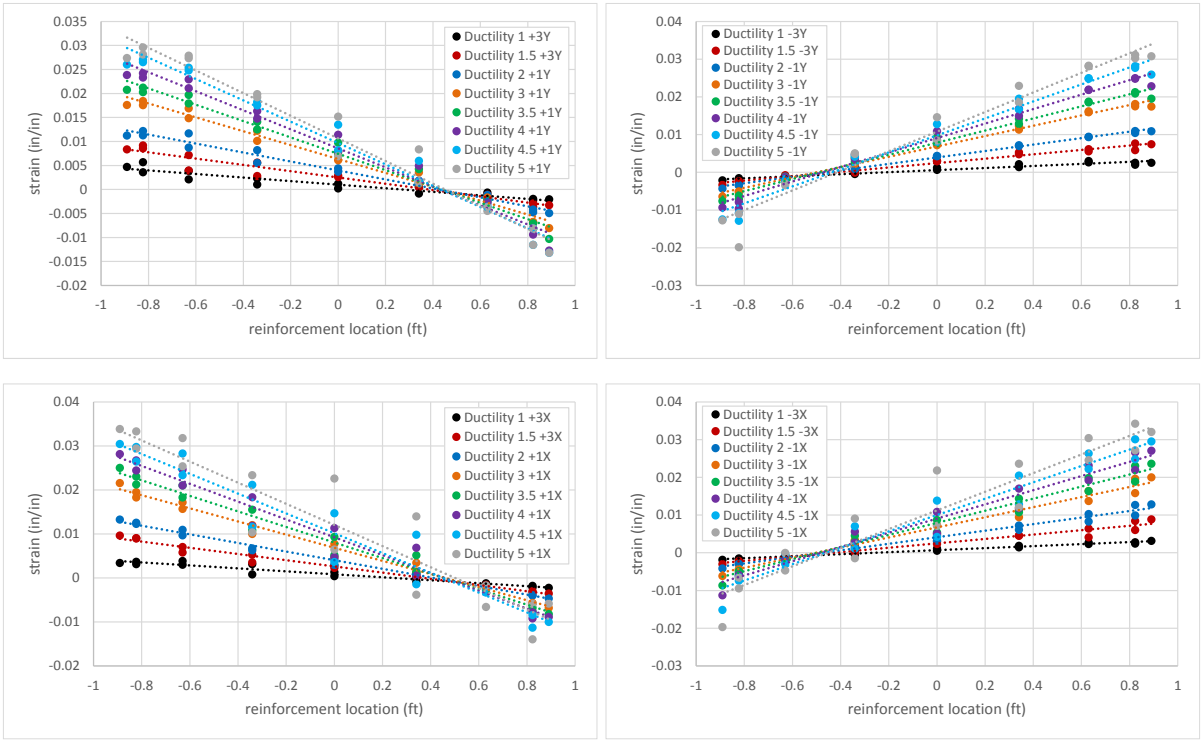

Figure 15-61. Test 12: Curvature Profiles for the First Instrumented Section above the Footing

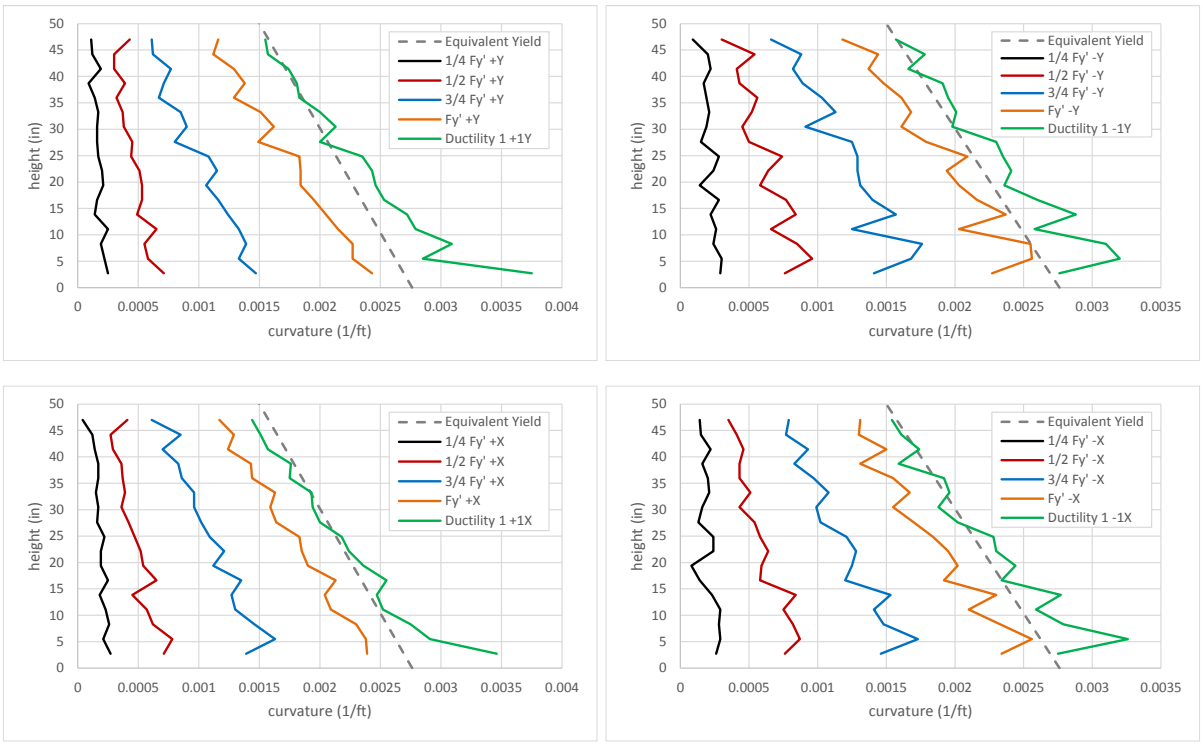

Figure 15-62. Test 12: Elastic Vertical Curvature Profiles

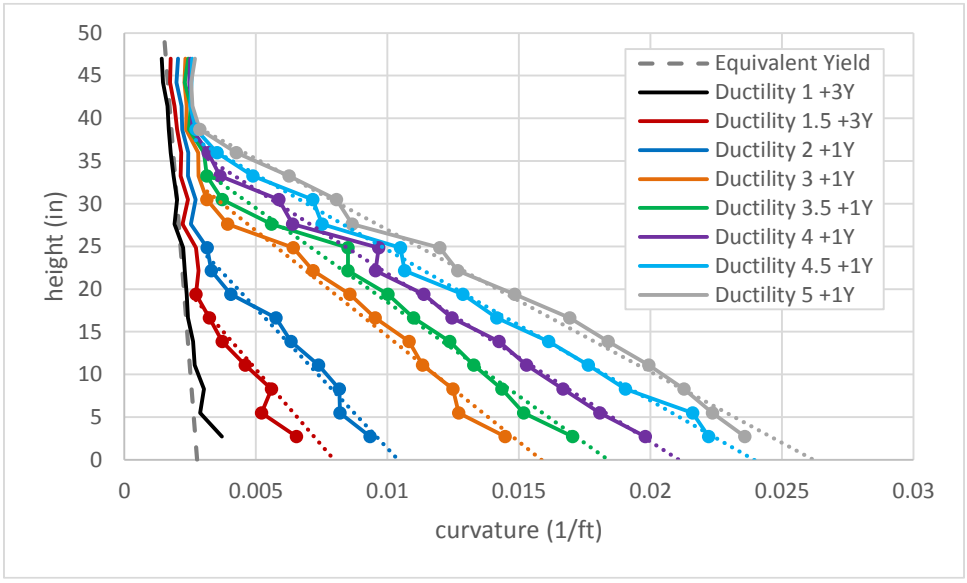

Figure 15-63. Test 12: Vertical Curvature Profiles for Loading in the +Y-direction

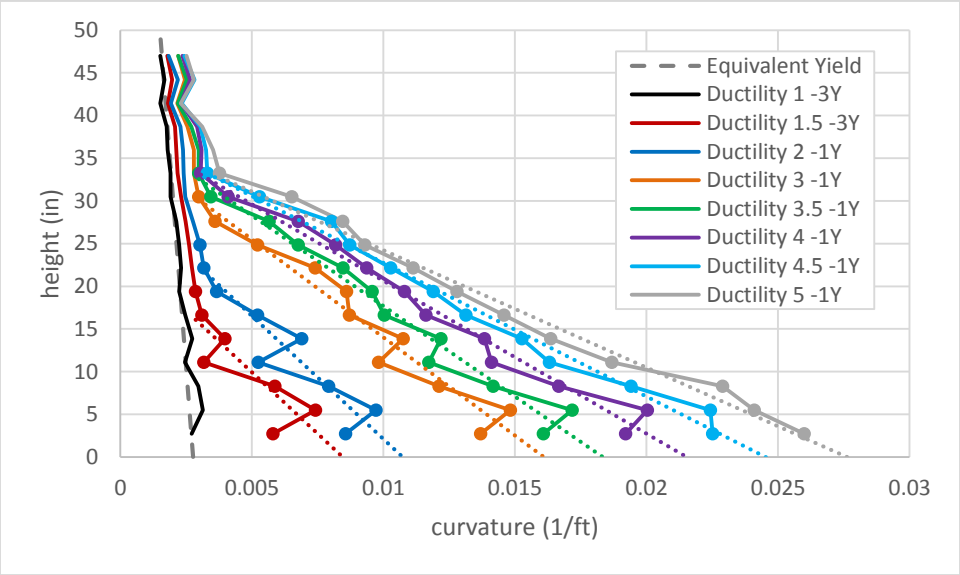

Figure 15-64. Test 12: Vertical Curvature Profiles for Loading in the -Y-direction

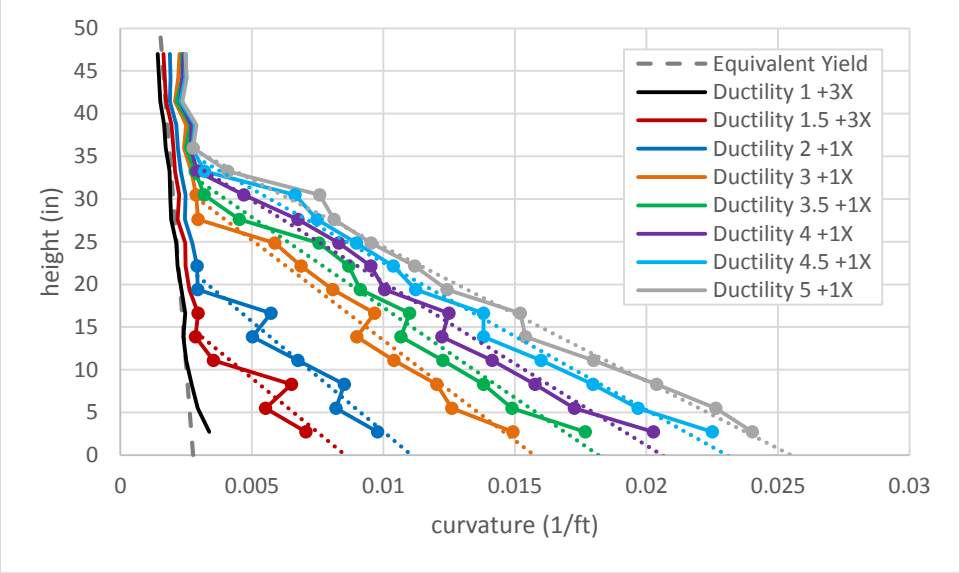

Figure 15-65. Test 12: Vertical Curvature Profiles for Loading in the +X-direction

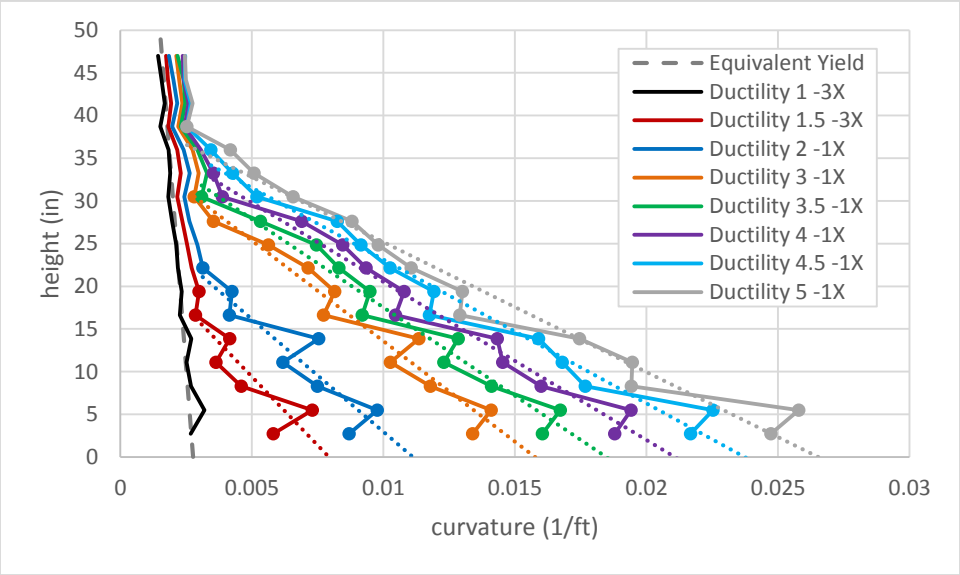

Figure 15-66. Test 12: Vertical Curvature Profiles for Loading in the -X-direction

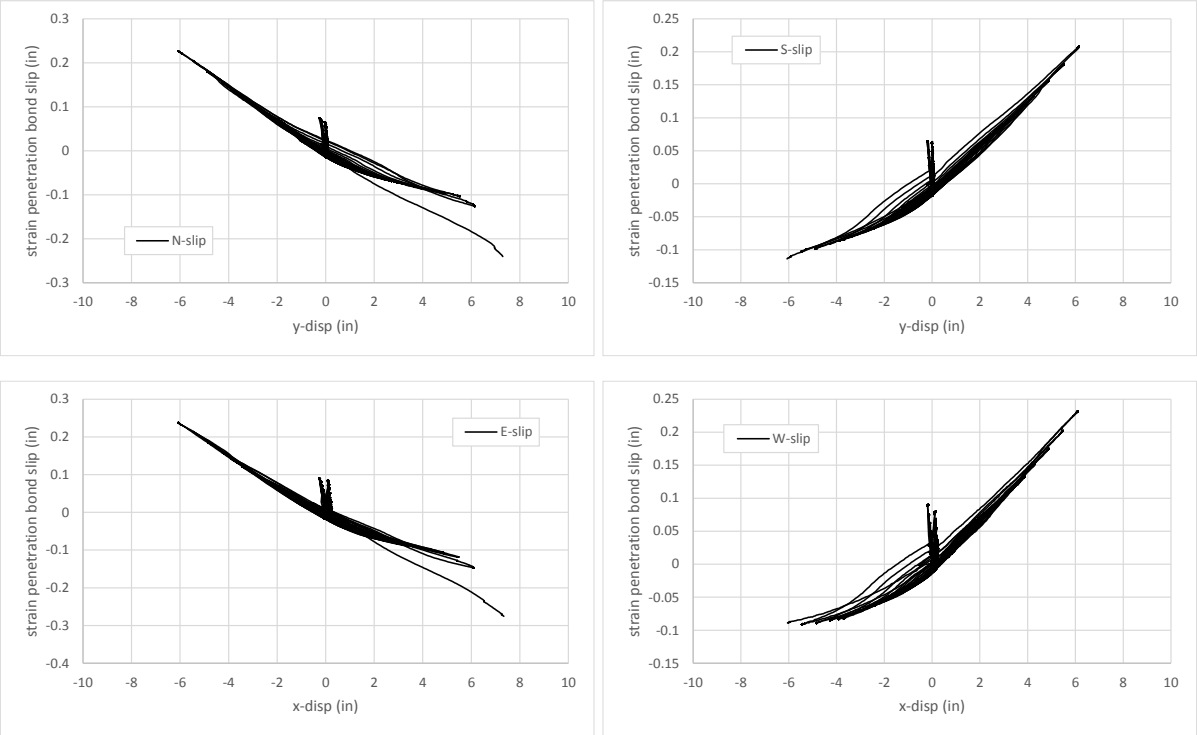

Figure 15-67. Test 12: Extreme Fiber Bar Strain Penetration Bond Slip Hysteresis

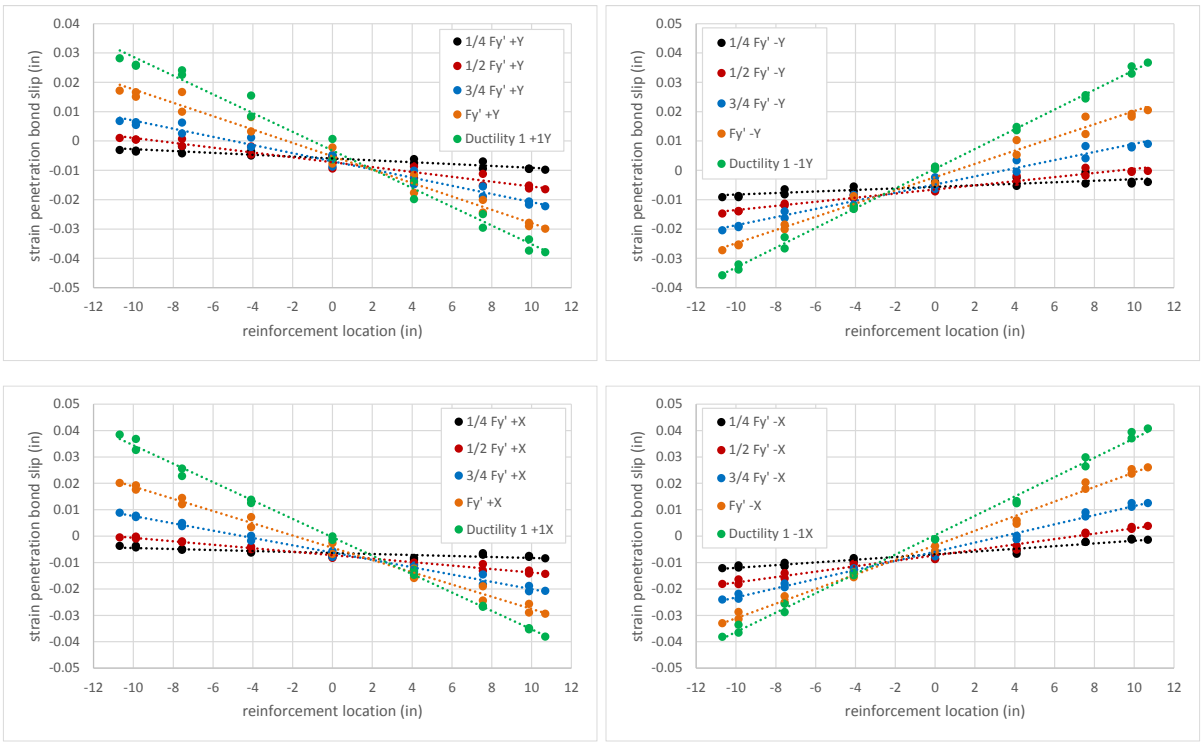

Figure 15-68. Test 12: Fixed End Rotations due to Strain Penetration during the Elastic Cycles

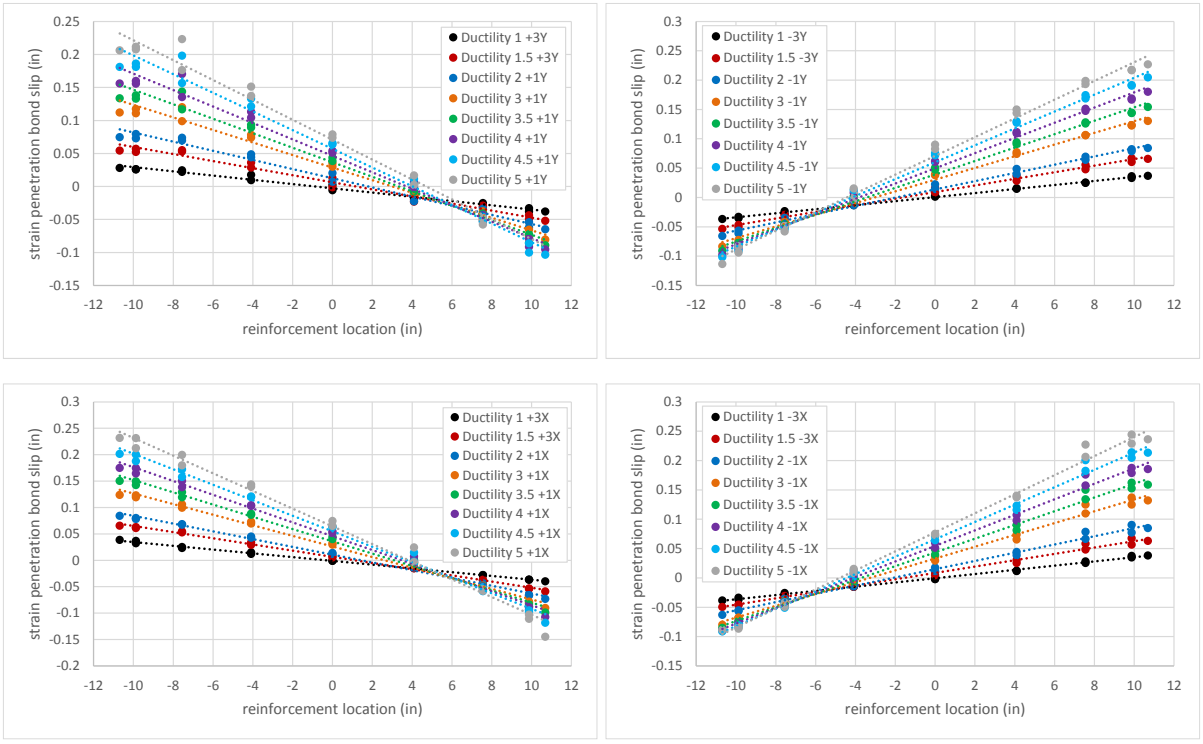

Figure 15-69. Test 12: Fixed End Rotations due to Strain Penetration

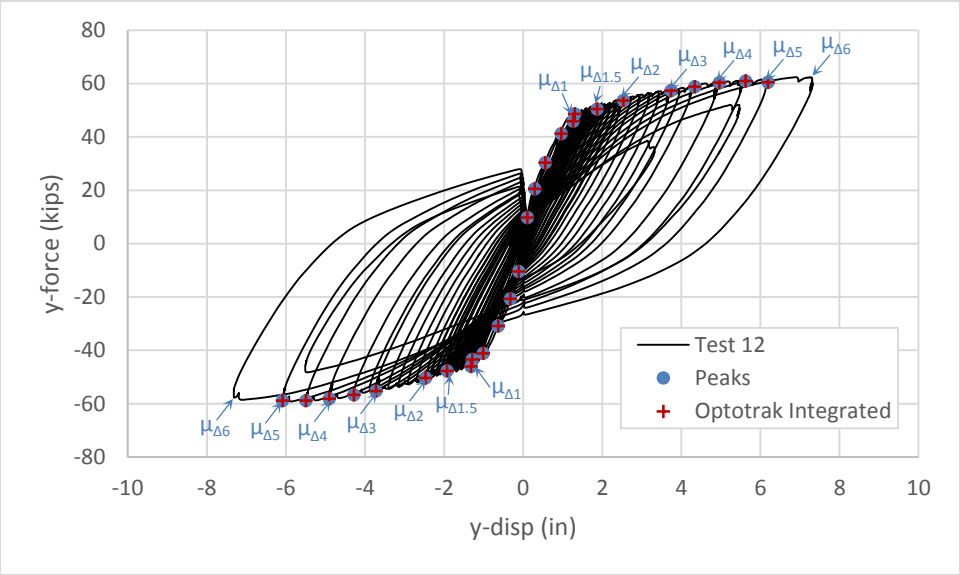

Figure 15-70. Test 11: Optotrak Integrated Flexural Disp. Compared to Measured String Pot. Disp.

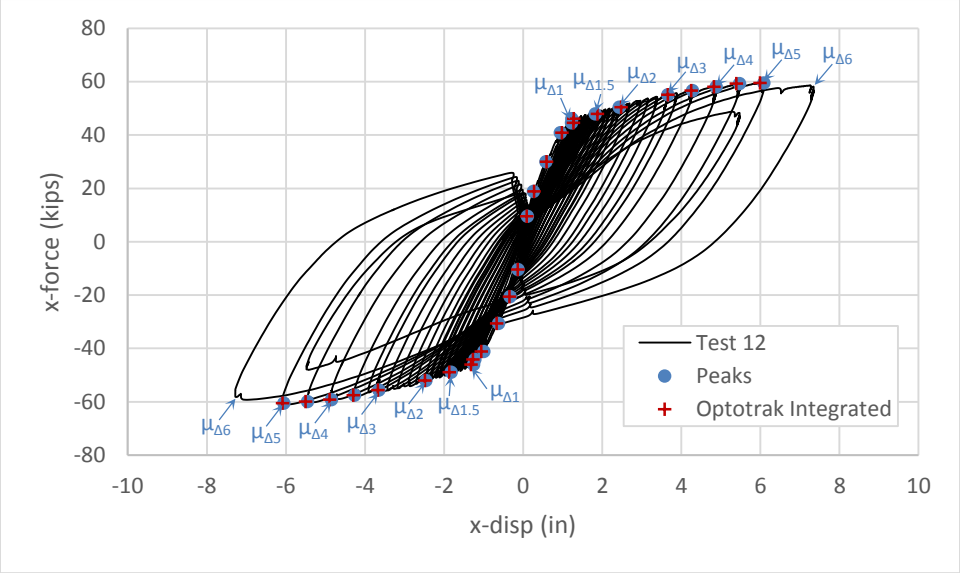

Figure 15-71. Test 11: Optotrak Integrated Flexural Disp. Compared to Measured String Pot. Disp.

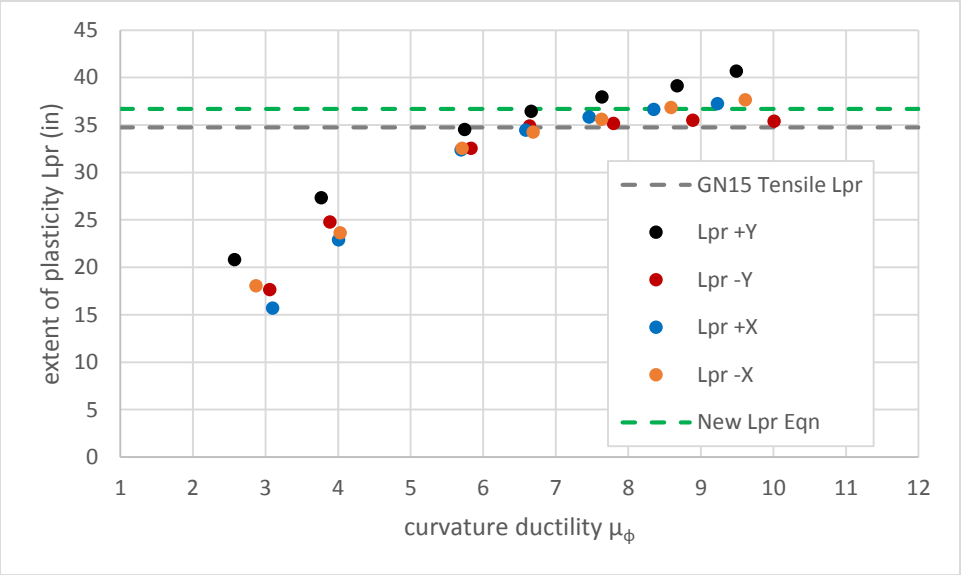

Figure 15-72. Test 12: Measured Extent of Plasticity Compared to Tensile Hinge Lengths

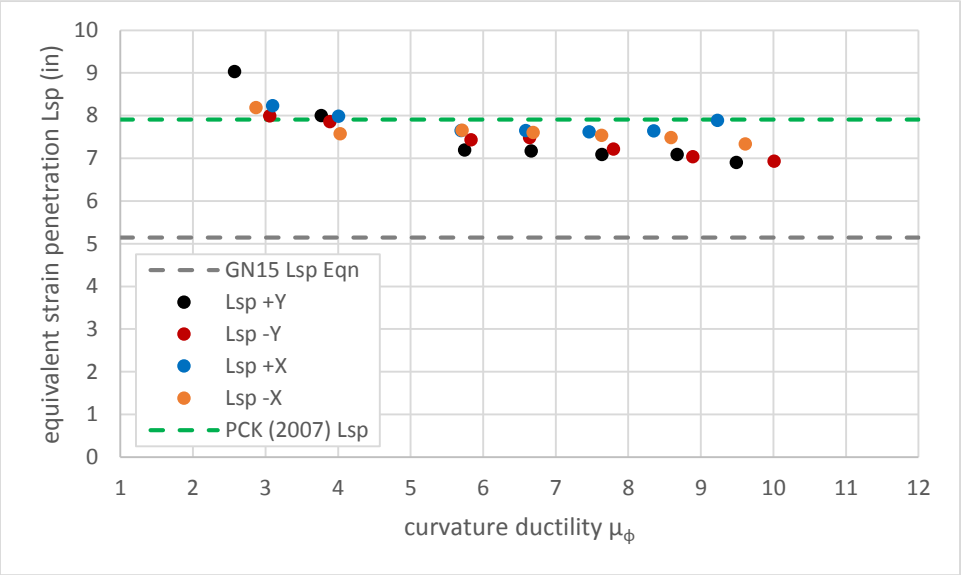

Figure 15-73. Test 12: Measured Equivalent Strain Penetration Lengths Compared to Design Expressions

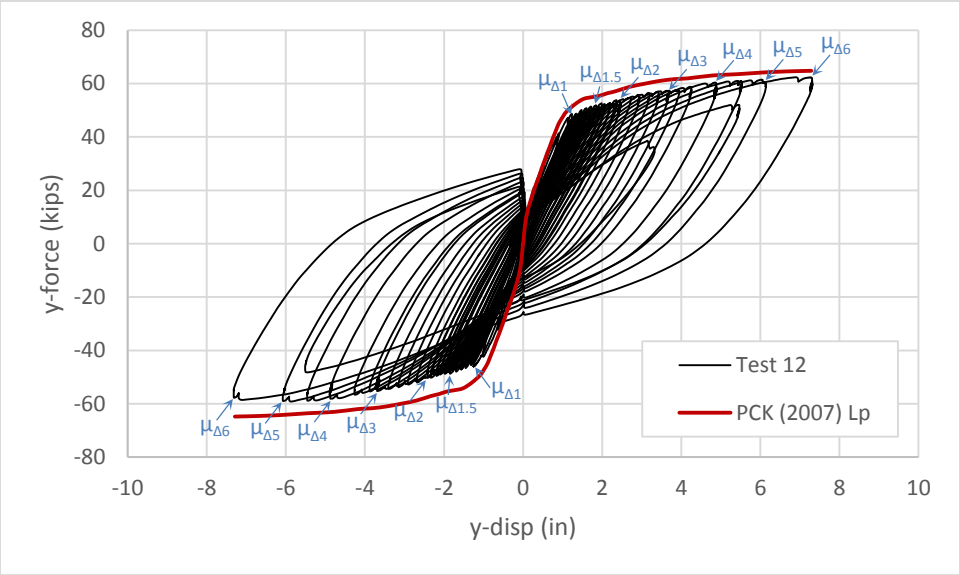

Figure 15-74. Test 12: Y-Direction Hysteretic Response Compared to PCK (2007) Hinge Length Monotonic Prediction

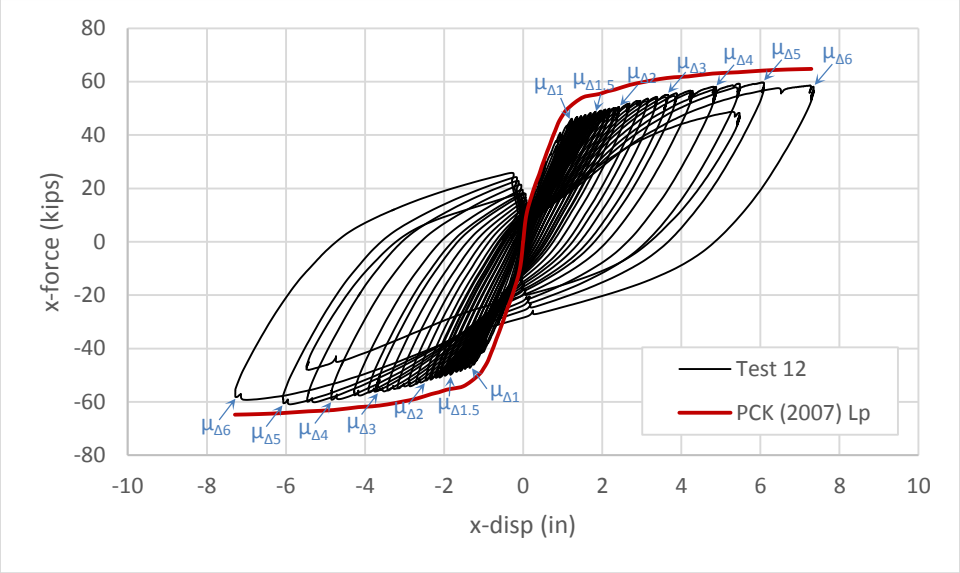

Figure 15-75. Test 12: X-Direction Hysteretic Response Compared to PCK (2007) Hinge Length Monotonic Prediction

Response Comparison to Previous Experiments

Comparison of Megathrust Tests 11 (1%) and 12 (0.7% Transverse Volumetric Steel)

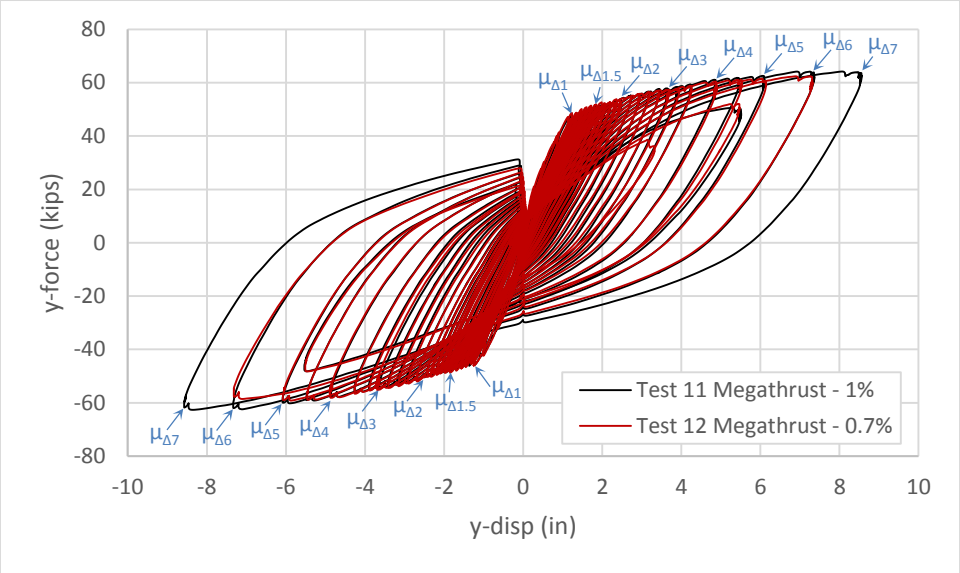

Figure 15-76. Y-Direction Hysteretic Comparison for Megathrust Tests 11 and 12 (% Transverse Steel)

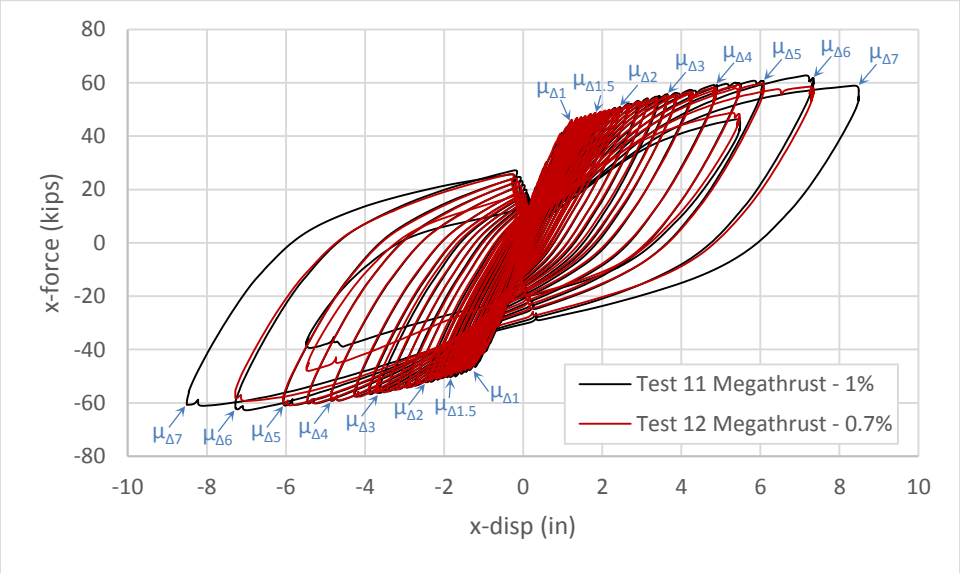

Figure 15-77. X-Direction Hysteretic Comparison for Megathrust Tests 11 and 12 (% Transverse Steel)

Comparison of Megathrust Load History Test 12 and Symmetric Two-Cycle-Set Test 9

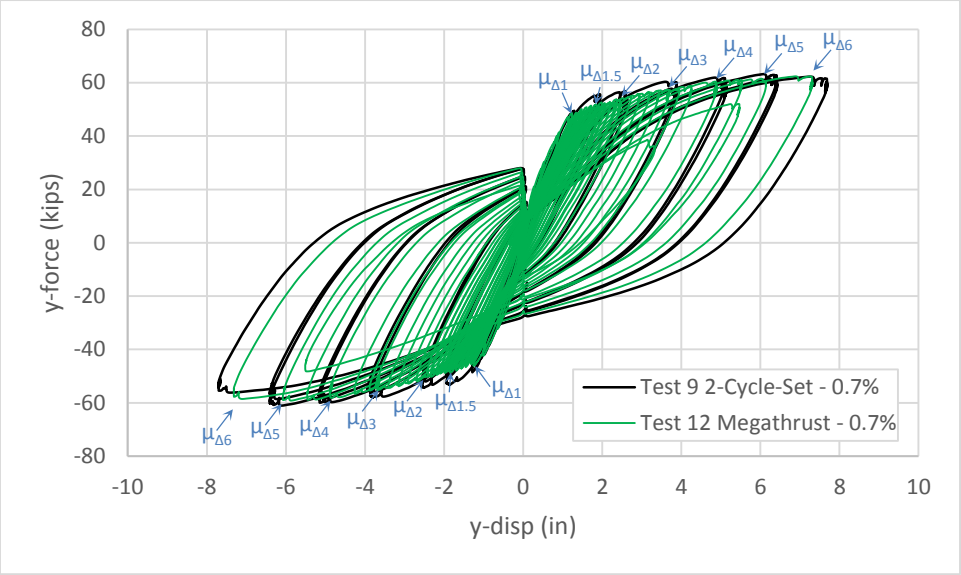

Figure 15-78. Y-Direction Hysteretic Comparison for Sym. Two-Cycle-Set Test 9 and Scaled Megathrust Test 12

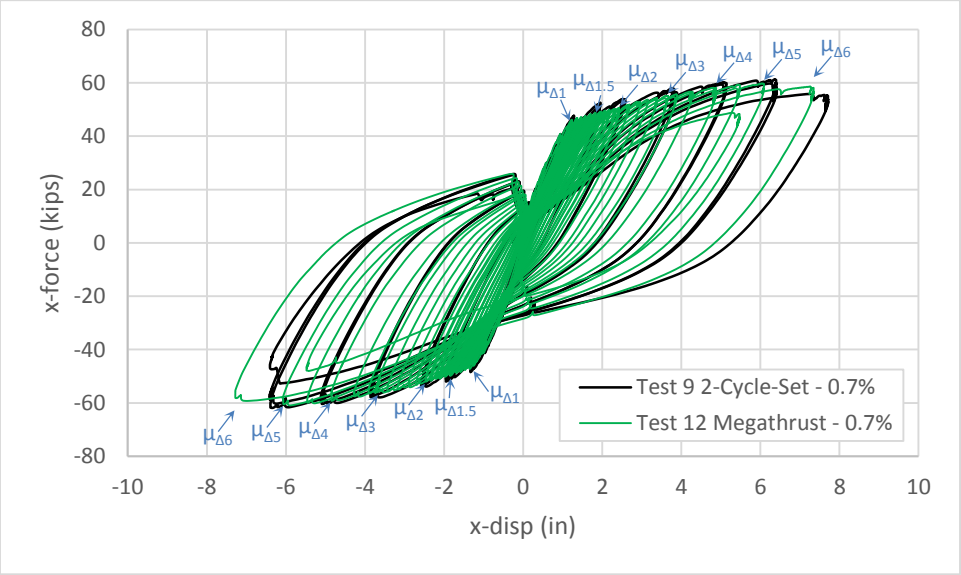

Figure 15-79. X-Direction Hysteretic Comparison for Sym. Two-Cycle-Set Test 9 and Scaled Megathrust Test 12

Chapter 16 – Design Recommendations

Summary of Measured Strain and Curvature Data

In this section, sample data from Megathrust load history Test 11 is presented to illustrate the process in which the measured spread in plasticity was quantified. This data will be referenced in the following two sections which focus on summarizing design recommendations for plastic hinge lengths and performance strain limits. Note that a complete presentation of the measured strain and curvature data is available in each summary report, presented in individual chapters of this report. Test 11 evaluated a 24" diameter column $(L/D = 4.56)$ with $\rho_l = A_{st}/A_g = 1.6\%$ longitudinal steel, a transverse volumetric ratio of $\rho_s = 4A_{sp}/D's = 1.0\%$, and a constant axial load of $191\ kips\ \left(P/f_c'\ A_g = 7.5\%\right)$. Photos of the test setup, orientation of the applied load, and selected bar labeling scheme appear in Figure 16-1 and Figure 16-2.The scaled Megathrust load history for Test 11 recommended in (Bazaez and Dusicka 2016) appears in Figure 16-3 and Figure 16-4. The resulting hysteretic response is shown in Figure 16-5 and Figure 16-6. These figures include data points which mark the occurrence of important damage observations.

Using the Optotrak position monitoring system, strains were computed as the change in three-dimensional distance between adjacent target markers, divided by the original unloaded gauge lengths. The measured strain history in the North extreme fiber bar and the overlaying spiral layer, shown in Figure 16-7 and Figure 16-8, can be used to validate the visible observation of bar buckling and quantify the compressive demand which led to initial yielding of confinement steel.

Cross-section curvatures were computed as the slope of a linear regression through the measured strain profile, see Figure 16-9. Curvature profiles were constructed as shown in Figure 16-10. Procedures developed by (Hines and Seible 2002) were followed to extract important information regarding their shape. Linear least-squared error lines were fit to the plastic portion of the curvature profiles. The base-section curvature is calculated as the intersection of the linear plastic curvature profile with the footing-column interface. The extent of plasticity (L_{pr}) is computed as the intersection of the linear plastic curvature regression and the elastic curvature profile. The elastic profile decreases from the equivalent yield curvature at the footing-column interface to zero at the center of the applied lateral load. The spread of plasticity in the tests is due to the combined effects of moment gradient and tension shift. The moment gradient effect can be described as the influence of larger base-section moments on the distribution of moment and thus curvature along the column length.

Vertical strain profiles in Figure 16-11 depict strains measured in the extreme fiber reinforcing bars. Compressive strains are concentrated near the footing, while tension strains are fanned out to a greater height following the inclined flexural shear crack distribution. This is due in large part to the effects of tension shift, which leads to tension strains above the base section which exceed those that would develop based on the plane sections hypothesis and the moment at that height alone. Tension shift leads to a fanned compression strut pattern which emanates from the compressive toe region of the column, where the local compressive demand may be increased. Since tension strains are spread further above the base section, the magnitude of the peak tensile strain near the footing may be reduced.

Development of fully anchored column longitudinal bars into the footing leads to bond slip along the partially anchored region of the bars near the footing-column interface, as described by (Zhao and Sritharan 2007). (Zhao and Sritharan 2007) note that this bond slip is not a pull-out of the entire bar embedment length resulting from poor bond between the concrete and reinforcing bar. This bond slip is computed as vertical displacement of target markers placed closest to the footing-column interface. Fixed-end rotations attributable to strain penetration of reinforcement into the adjoining member were computed based on the slope of a regression through the measured bond-slips in Figure 16-12.

In the experiments, the lateral displacement is obtained using an array of linear potentiometers placed at the center of the applied lateral load. The measured curvatures in the instrumented region can be integrated using the moment-area method and added to an assumed elastic profile above the instrumented region which linearly decreases from the highest measured horizontal section curvature to zero at the center of the applied lateral load. This integration represents the column flexural deformation, which can be added to the extrapolation of the fixed-end curvature attributable to strain penetration to find the total flexural displacement. This integrated total flexural displacement is compared to the measured string potentiometer displacement in Figure 16-13. The close agreement implies that the relevant deformation quantities have been included and that shear deformation, which were not calculated directly at this stage of the analysis, was negligible in comparison to the flexural displacements.

As previously discussed, the height at which the linear plastic curvature distribution intersects the elastic curvature profile was termed the extent of plasticity (L_{pr}). This height is plotted as a function of base-section curvature ductility in Figure 16-14. The measured spread of plasticity appears to increase linearly, and then level out near maximum response. In (Goodnight, Kowalsky and Nau 2015), the tensile plastic hinge length was calibrated to match the upper bound to the measured spread of plasticity of unidirectional tests. The resulting tensile plastic hinge length, abbreviated as GN15 Tensile Lpr, appears as a grey dashed line. Under bidirectional loading, plasticity was spread further than the expression implies. For a given value of base-section curvature, a larger spread in plasticity would imply lower tensile strains at the base-section. In Figure 16-14, New Equations refers to a new bidirectional plastic hinge method which was created based on this study. Details of the new plastic hinge method appear in the following section of this chapter.

In the Modified Plastic Hinge Method from (Goodnight, Kowalsky and Nau 2015a), an equivalent rectangular curvature block centered at the footing-column interface was used to describe the additional column displacement due to strain penetration of reinforcement into the adjoining member. The width of this block is equal to the base-section curvature while the area of the block represents the fixed-end rotation. The height of this block is termed the equivalent strain penetration length and is equal to the fixed-end rotation divided by the base-section curvature, both of which were measured experimentally. This equivalent strain penetration length is a numerical convenience, which can be used to describe the fixed-end rotation for the equivalent curvature distribution. The measured equivalent strain penetration lengths in each direction of loading appear in Figure 16-15. In (Goodnight, Kowalsky and Nau 2015), an expression was formulated to describe the average equivalent strain penetration length from the unidirectional experiments. This length, abbreviated as GN15 Lsp, is a function of the yield stress of the reinforcement, the longitudinal bar diameter, and the square root of the concrete strength in the adjoining member. The result for the expression,

abbreviated as GN15 Lsp, under predicts the values obtained from this experiment; however, the observation of the equivalent strain penetration length remaining constant over the range of curvature ductility remains valid. In general, the equivalent strain penetration length recommended in (Priestley, Calvi and Kowalsky 2007), abbreviated PCK (2007) Lsp, over predicted the measured behavior, with the exception of the two Megathrust load history experiments which and a significant increase in the amount of inelastic cycles.

The relationship between strain and displacement for either peak tensile or peak compressive gauge lengths appear in Figure 16-16 through Figure 16-19. These figures contain monotonic moment curvature predictions for respective plastic hinge methods. PCK (2007) Lp refers to the (Priestley, Calvi and Kowalsky 2007) plastic hinge method, GN15 Tension/Compression Lpr refers to the (Goodnight, Kowalsky and Nau 2015a) unidirectional modified plastic hinge method, New Equations refers to a new bidirectional plastic hinge method which was created based on this study, and T11 Measured refers to using the measured extent of plasticity and equivalent strain penetration length from Test 11. For Test 11 these values were obtained as $Lpr_t = 35.36"$ and $L_{sp} = 7.60"$ from Figure 16-14 and Figure 16-15, respectively. These values were substituted into the unidirectional modified plastic hinge method from (Goodnight, Kowalsky and Nau 2015a). For compressive strain-displacement, the compressive hinge length of $Lpr_c = 2kL_c$ and the value of $L_{sp} = 7.60"$ were used. For tension strain-displacement $Lpr_t = 35.36"$ and $L_{sp} = 7.60"$ were used. Improvements to tensile strain-displacement prediction were observed when the measured spread of plasticity was used.

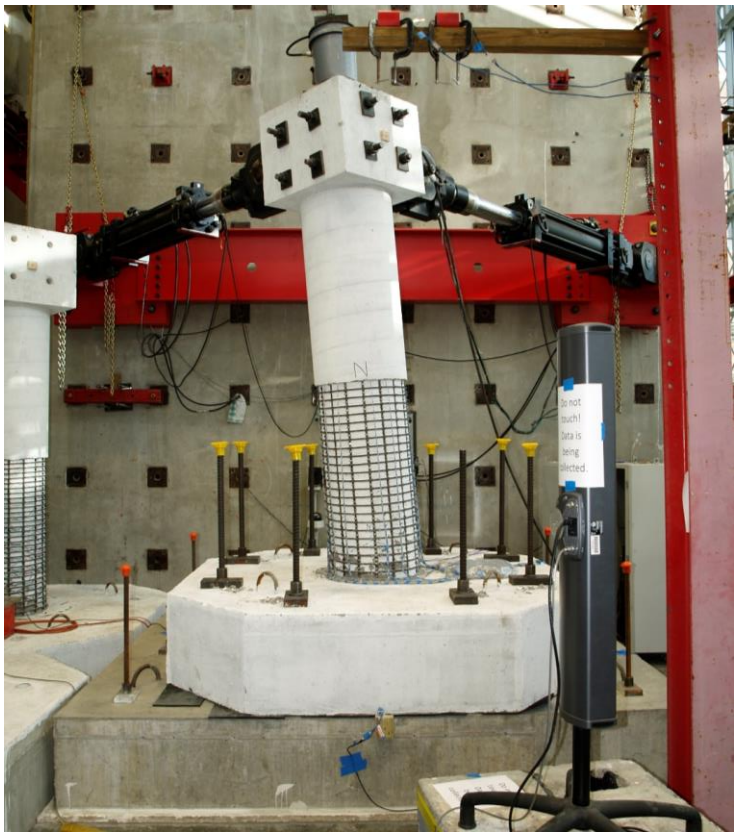

Figure 16-1. Test 11: Deformed Specimen at $\mu_{\Delta 7}^{+1x} = 8.49"$

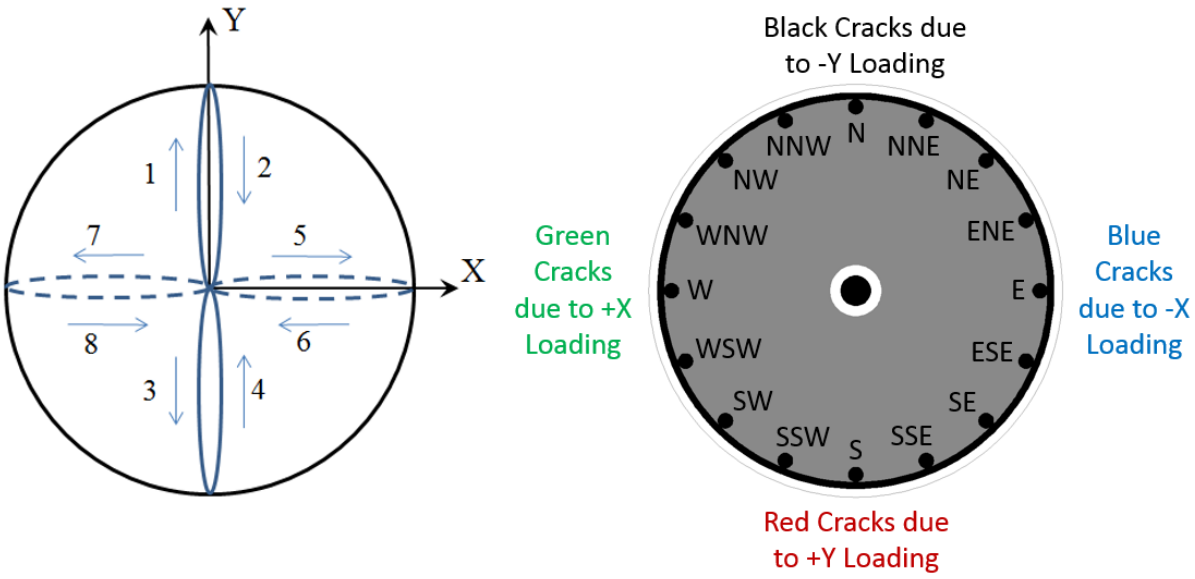

Figure 16-2. Test 11: Bidirectional Load History Orientation and Bar Naming System

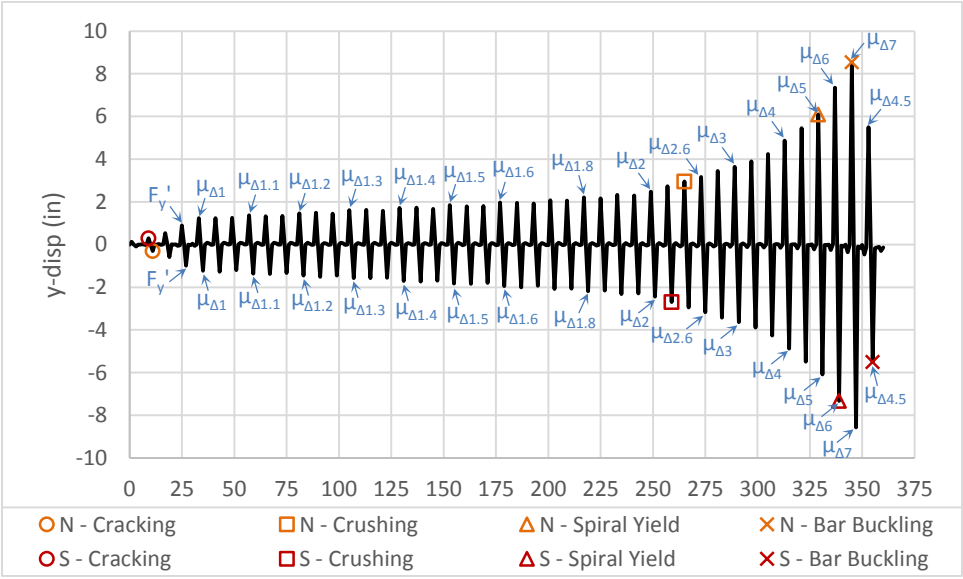

Figure 16-3. Test 11: Y-Displacement History

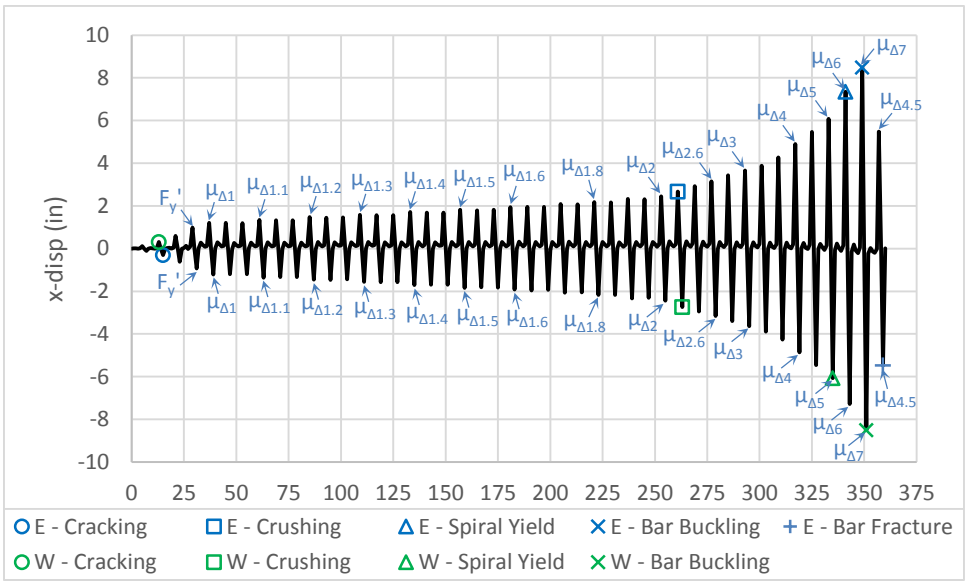

Figure 16-4. Test 11: X-Displacement History

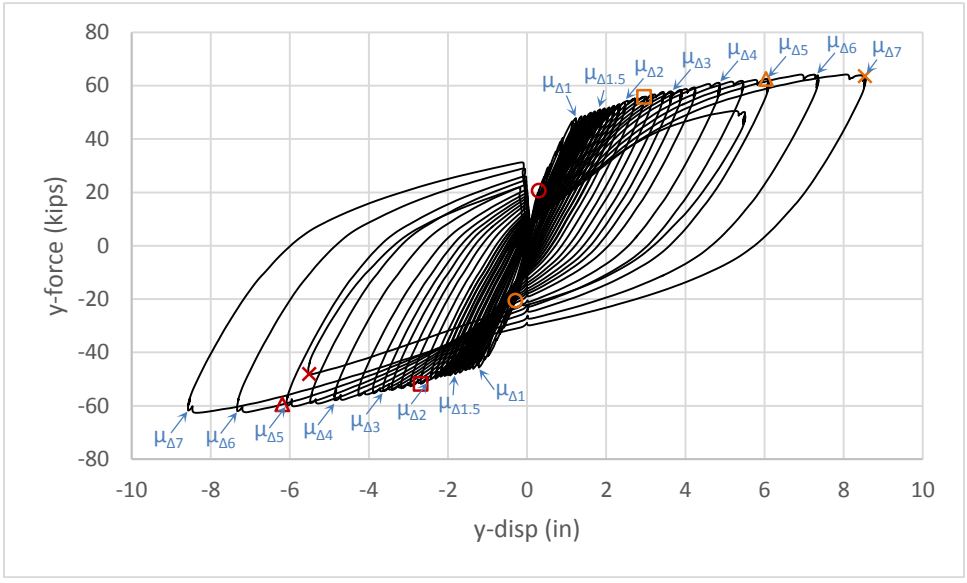

Figure 16-5. Test 11: Y-Direction Hysteretic Response

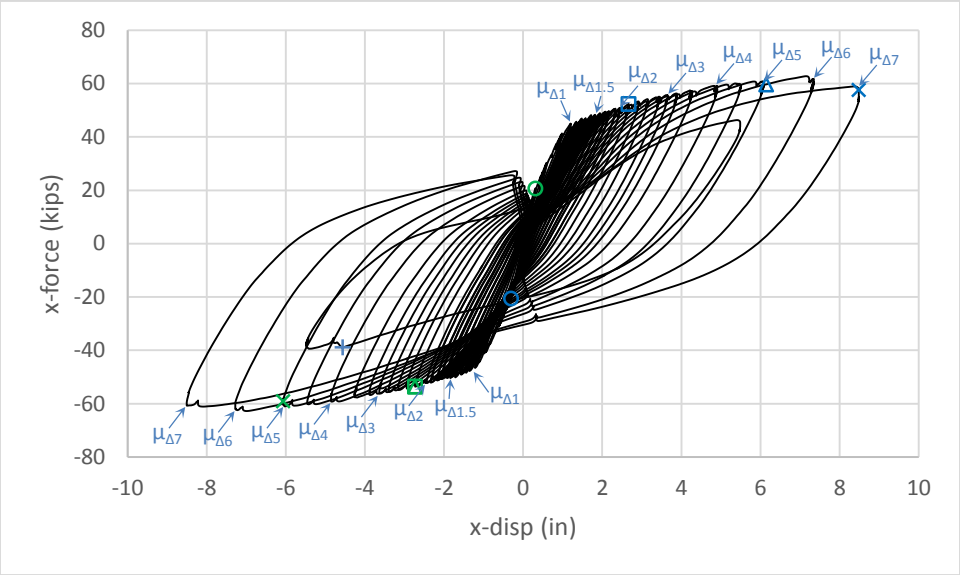

Figure 16-6. Test 11: X-Direction Hysteretic Response

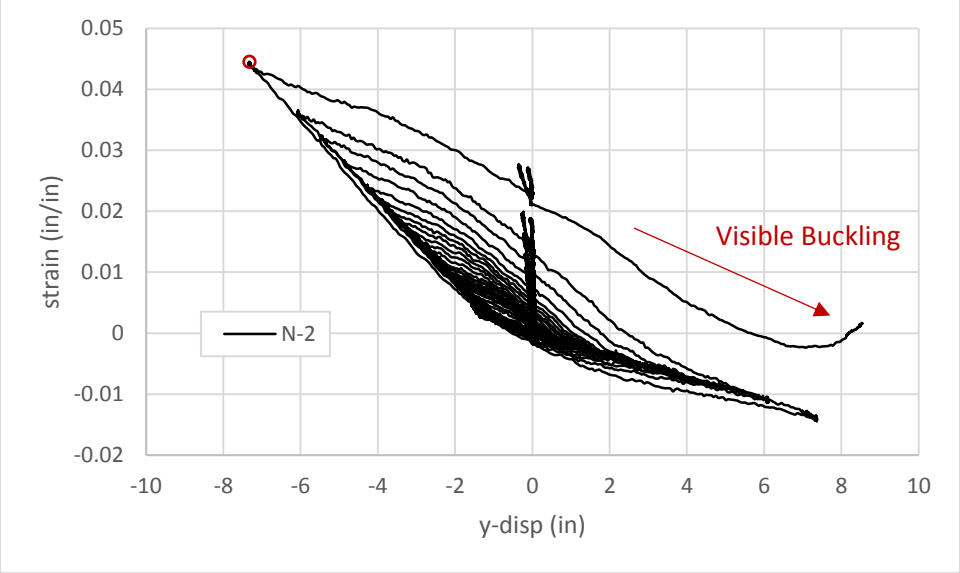

Figure 16-7. Test 11: North Longitudinal Bar Strain Hysteresis to Bar Buckling

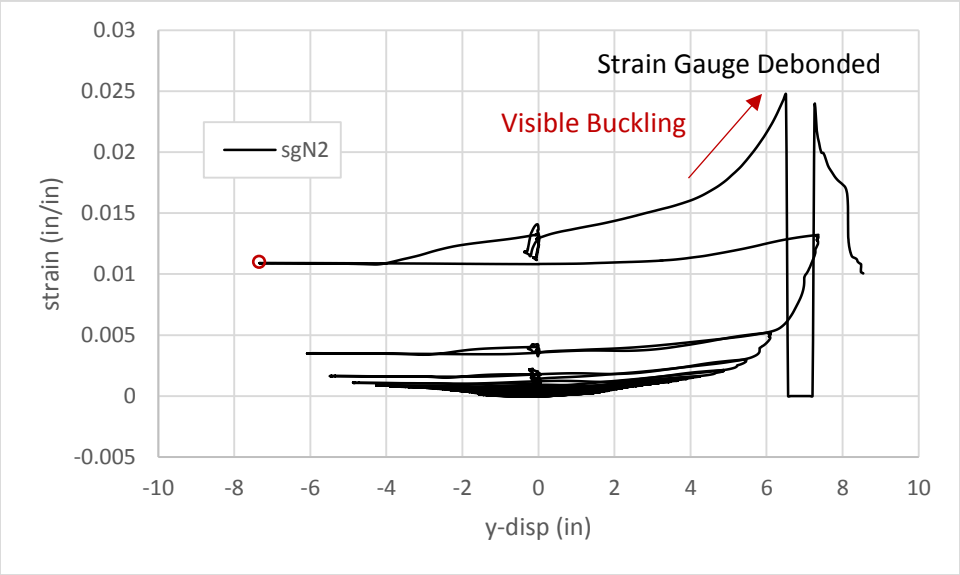

Figure 16-8. Test 11: North Spiral Restraint Strain History to Bar Buckling

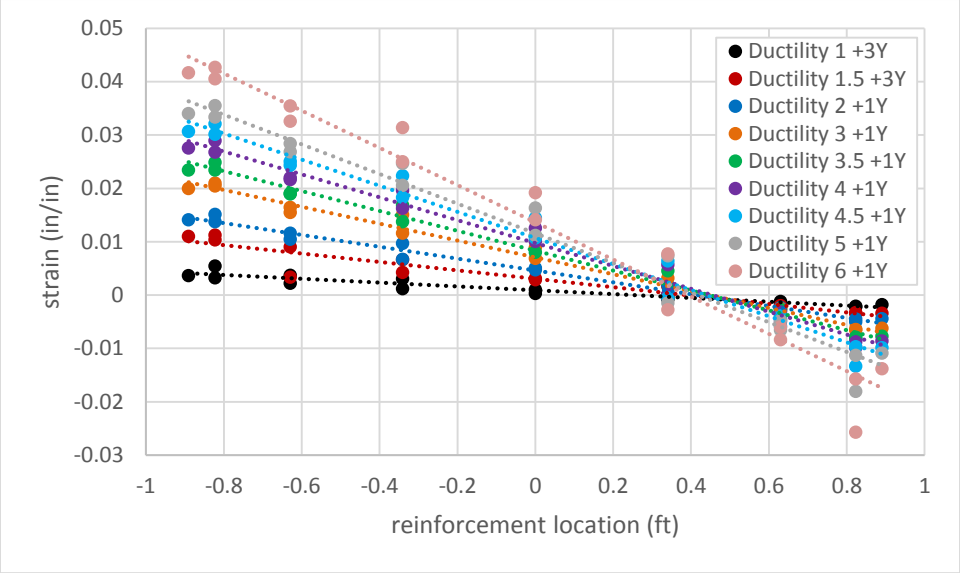

Figure 16-9. Test 11: +Y-Direction Cross Section Curvatures

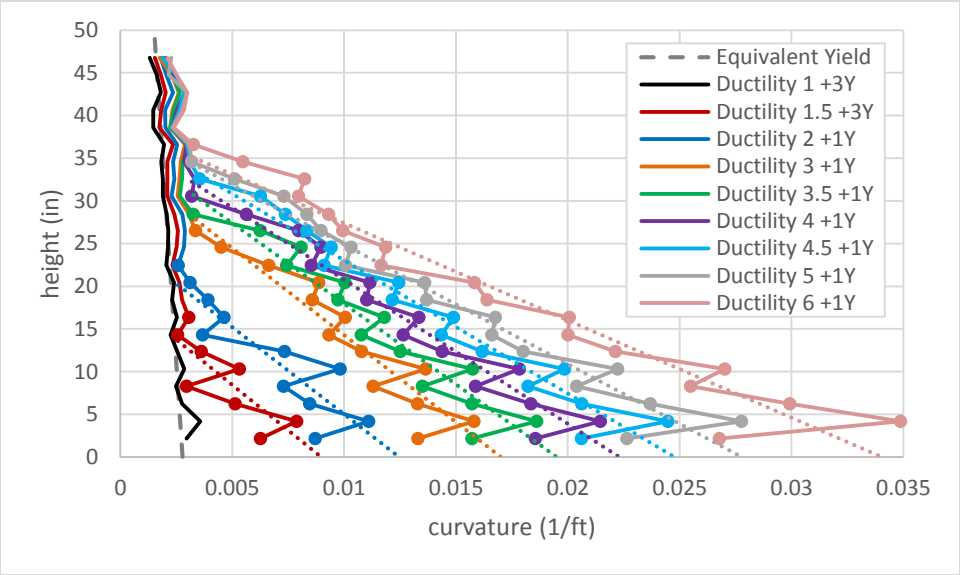

Figure 16-10. Test 11: +Y-Direction Vertical Curvature Profiles

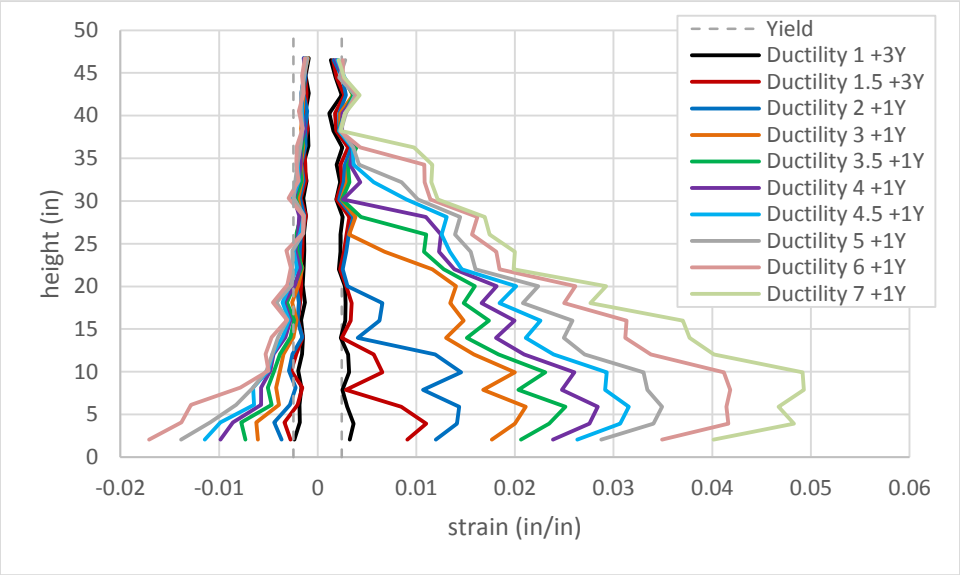

Figure 16-11. Test 11: +Y-Direction Vertical Strain Profile

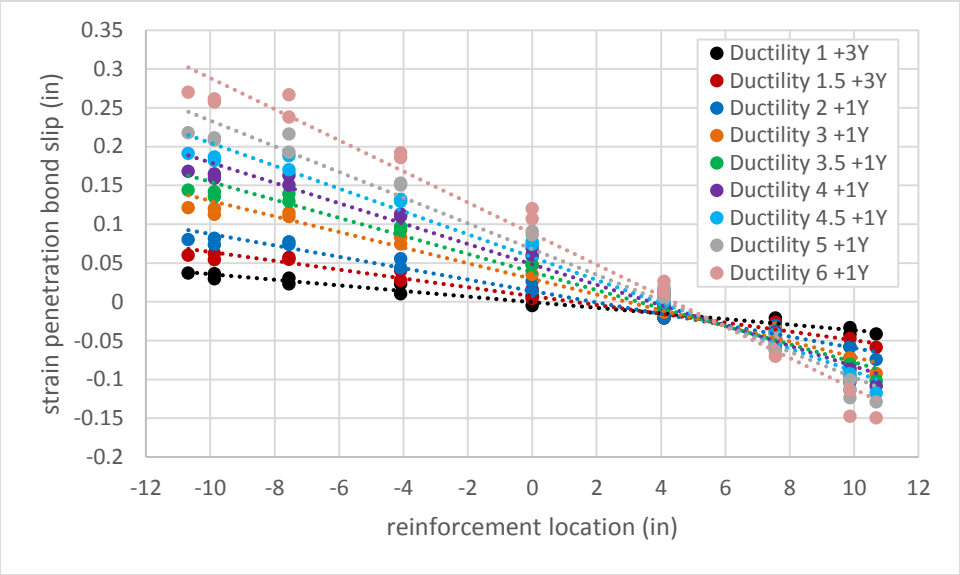

Figure 16-12. Test 11: +Y-Direction Fixed-End Rotations due to Strain Penetration

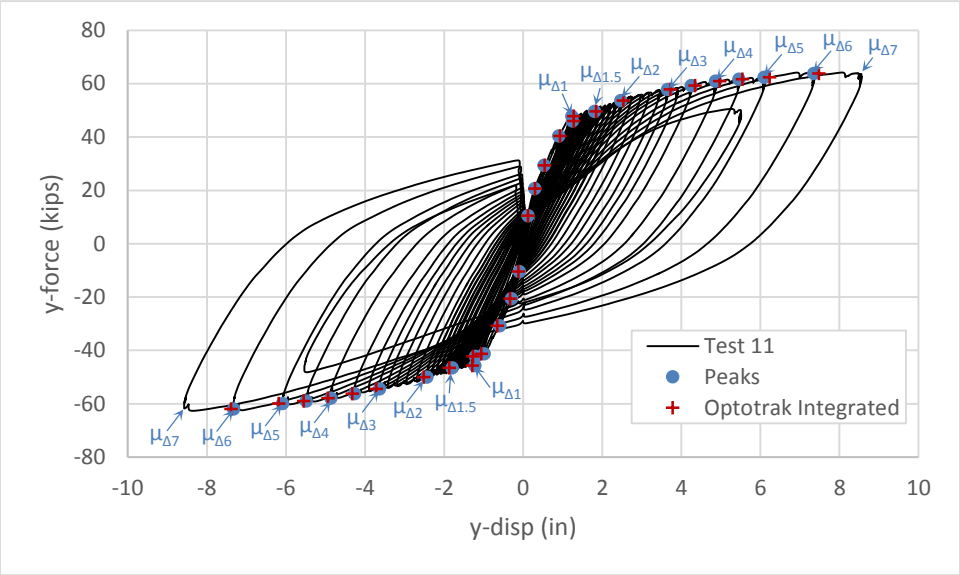

Figure 16-13. Test 11: Optotrak Integrated Flexural Disp. Compared to Measured String Pot. Disp.

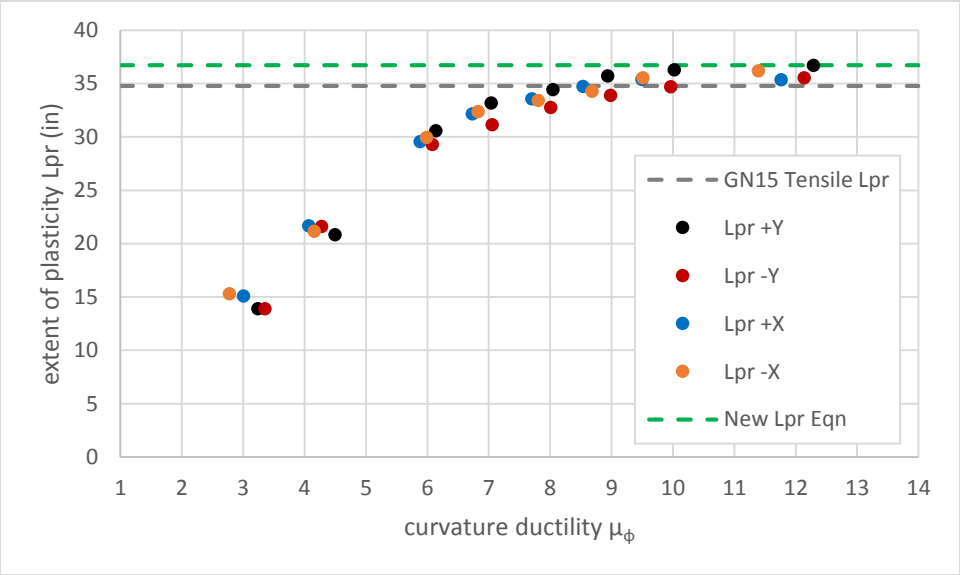

Figure 16-14. Test 11: Measured Extent of Plasticity Compared to Tensile Hinge Lengths

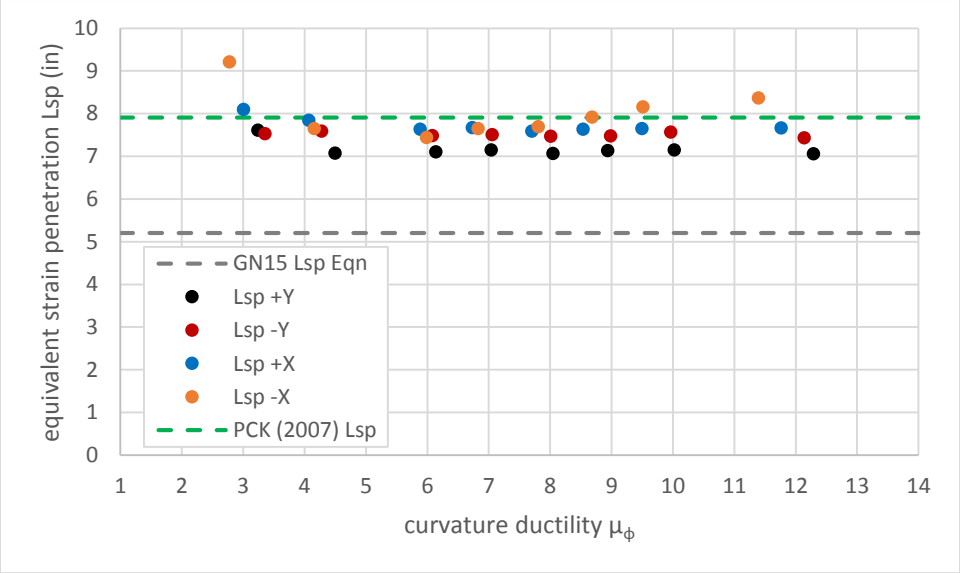

Figure 16-15. Test 11: Measured Equivalent Strain Penetration Lengths Compared to Design Expressions

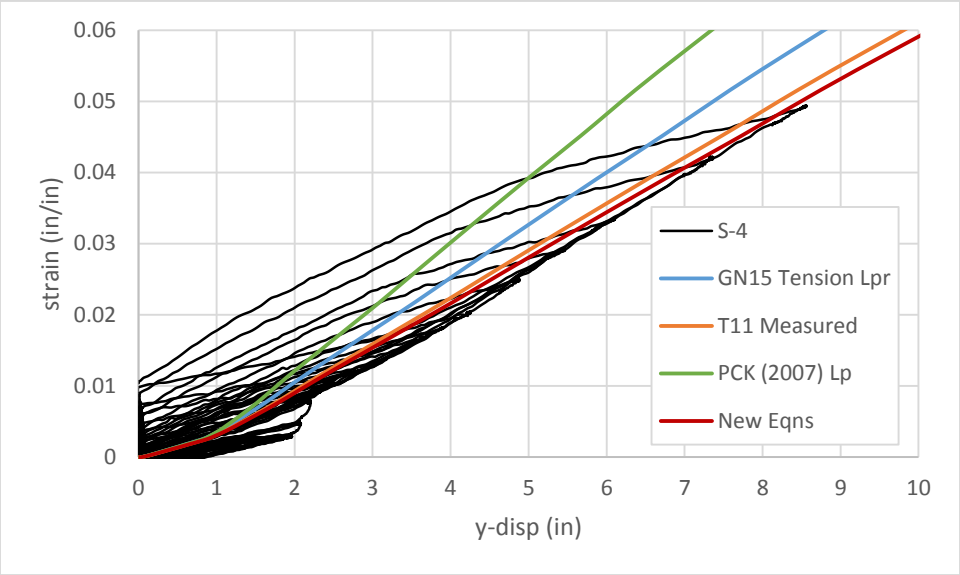

Figure 16-16. Test 11: Tension Strain-Disp. for Bar S (Gauge Length 4 Centered 7.88" above the Footing)

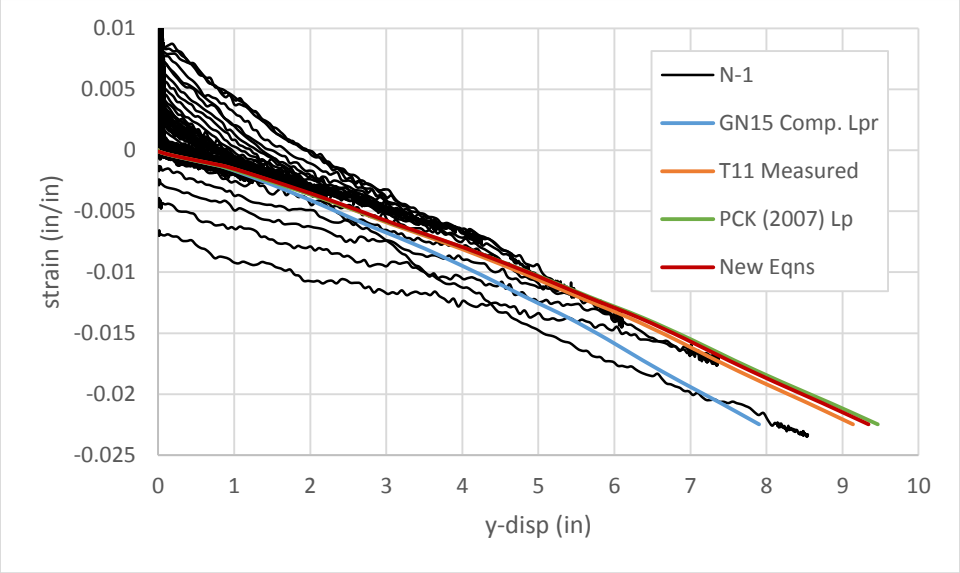

Figure 16-17. Test 11: Compression Strain-Disp. for Bar N (Gauge Length 1 Centered 2.06" above the Footing)

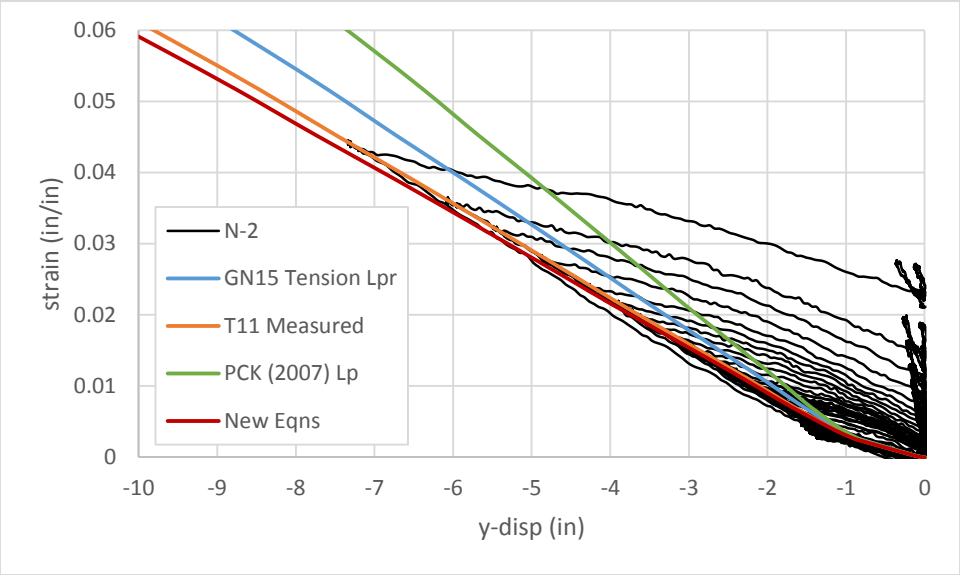

Figure 16-18. Test 11: Tension Strain-Disp. for Bar N (Gauge Length 2 Centered 4.07" above the Footing)

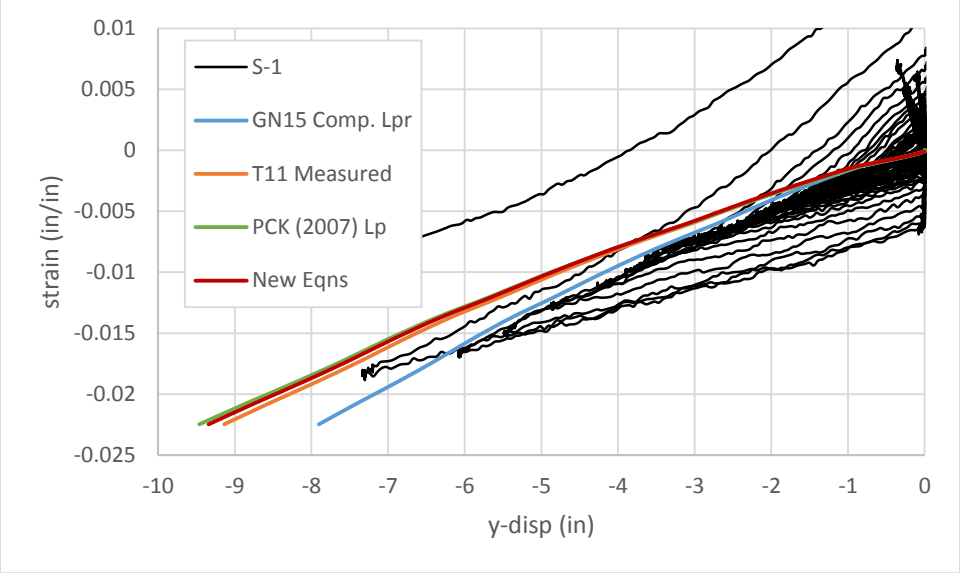

Figure 16-19. Test 11: Compression Strain-Disp. for Bar S (Gauge Length 1 Centered 2.05" above the Footing)

Test Matrix, Material Properties, and Damage Summaries for Column Datasets

The test matrix for the Bidirectional Load Path Dataset of this study appears in Table 16-1. Material properties for the Bidirectional Dataset are shown in Table 16-2, where dbl, fy, εh, fu and εu refer to yield, hardening and ultimate for the longitudinal steel and dbh, fyh, fuh, and εuh refer to yield and ultimate for the transverse steel. Descriptions of the three Type-B load histories appear in Figure 16-20. Details regarding the selection and scaling of the Megathrust load history for Tests 11 and 12 are presented in the first section of Chapter 14. Summaries of the displacements and strains at key damage levels appear in Table 16-3. Δ@Fy' refers to the average measured displacement at the analytical first yield force. The compressive strain at cover concrete crushing and initial yielding of confinement steel are abbreviated as εcc and εsy. The tension strain in the longitudinal steel measured in the peak cycle preceding bar buckling is labeled as εbb. This same data is presented for the Unidirectional Load History Dataset of (Goodnight, Kowalsky and Nau 2015) in Table 16-4 and Table 16-5.

Table 16-1. Test Matrix for the Bidirectional Load Path Dataset of this Study

Test	Load Path	Longitudinal	Ast/Ag	Transverse	4Asp/D's	P/f'cAg
1	2-Cyle-Set	16 #7	0.021	#3@2.75"	0.007	0.074
2	3-Cycle-Set	16 #7	0.021	#3@2.75"	0.007	0.075
3	Asym. 2-Cycle-Set	16 #7	0.021	#3@2.75"	0.007	0.074
4	2-Cycle-Set	16 #7	0.021	#3@2"	0.01	0.06
5	3-Cycle-Set	16 #7	0.021	#3@2"	0.01	0.06
6	Asym. 2-Cycle-Set	16 #7	0.021	#3@2"	0.01	0.059
7	2-Cycle-Set	16 #6	0.016	#3@1.5"	0.013	0.079
8	2-Cycle-Set	16 #6	0.016	#3@2"	0.01	0.074
9	2-Cycle-Set	16 #6	0.016	#3@2.75"	0.007	0.073
10	2-Cycle-Set	16 #7	0.021	#3@1.5"	0.013	0.075
11	Megathrust	16 #6	0.016	#3@2"	0.01	0.075
12	Megathrust	16 #6	0.016	#3@2.75"	0.007	0.074

Table 16-2. Material Properties in the Bidirectional Load Path Dataset of this Study

Test	f'c (ksi)	dbl (in)	fy (ksi)	εh	fu (ksi)	εu	dbh (in)	fyh (ksi)	fuh (ksi)	εuh
1	6.21	0.875	71.2	0.0135	97.9	0.1110	0.375	67.6	105.6	0.0981
2	6.16	0.875	71.2	0.0135	97.9	0.1110	0.375	67.6	105.6	0.0981
3	6.24	0.875	71.2	0.0135	97.9	0.1110	0.375	67.6	105.6	0.0981
4	7.68	0.875	71.2	0.0135	97.9	0.1110	0.375	67.6	105.6	0.0981
5	7.60	0.875	71.2	0.0135	97.9	0.1110	0.375	67.6	105.6	0.0981
6	7.81	0.875	71.2	0.0135	97.9	0.1110	0.375	67.6	105.6	0.0981
7	5.79	0.75	70.3	0.0100	98.7	0.1164	0.375	63.9	93.6	0.1211
8	6.24	0.75	70.3	0.0100	98.7	0.1164	0.375	63.9	93.6	0.1211
9	6.29	0.75	70.3	0.0100	98.7	0.1164	0.375	63.9	93.6	0.1211
10	6.13	0.875	69.6	0.0111	96.7	0.1119	0.375	63.9	93.6	0.1211
11	6.11	0.75	70.3	0.0100	98.7	0.1164	0.375	63.9	93.6	0.1211
12	6.23	0.75	70.3	0.0100	98.7	0.1164	0.375	63.9	93.6	0.1211

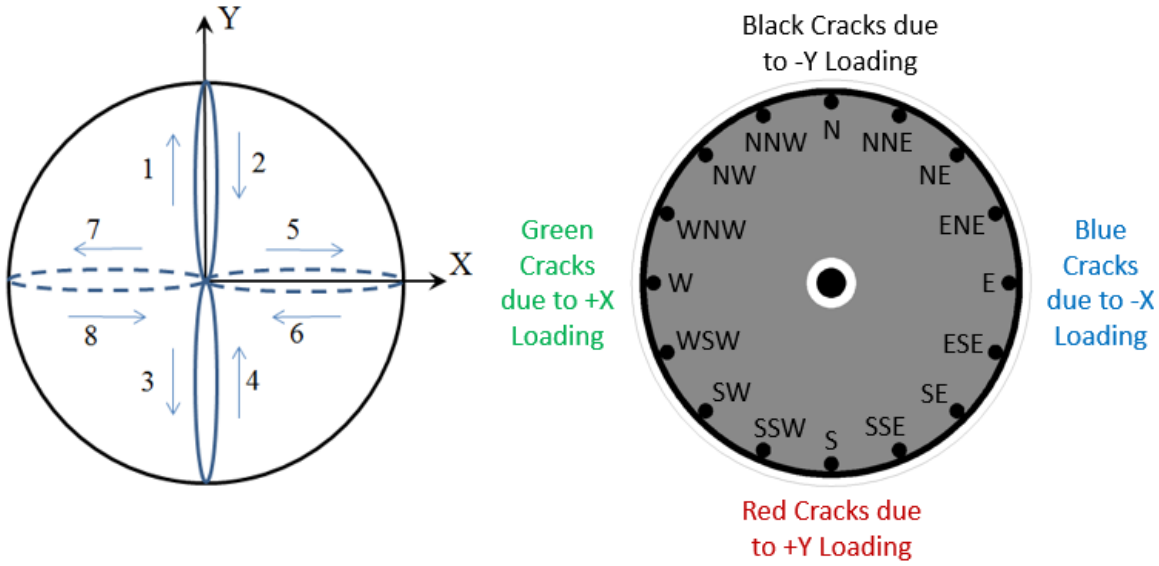

Type-B Symmetric Two-Cycle-Set

- Begins with elastic cycles (1-8) in ¼ yield increments until F_y'
- The equivalent yield displacement is then computed as $\Delta_y = \Delta_y'(M_n/M_y')$
- Two inelastic cycles (1-8) for each displacement ductility level $\mu_{\Delta n} = n \cdot \Delta_y$

Type-B Symmetric Three-Cycle-Set

- Begins with elastic cycles (1-8) in ¼ yield increments until F_y'
- The equivalent yield displacement is then computed as $\Delta_y = \Delta_y'(M_n/M_y')$
- Three inelastic cycles (1-8) for each displacement ductility level $\mu_{\Delta n} = n \cdot \Delta_y$

Type-B Asymmetric Two-Cycle-Set

- Inelastic cycles (1-4) in the Y-direction followed by inelastic cycles (5-8) in the X-direction for each of the following displacement ductility levels $\mu_{\Delta n} = n \cdot \Delta_y$
- $\mu_{\Delta 1}^{\pm Y}$ & $\mu_{\Delta 1}^{\pm X}$, $\mu_{\Delta 1.5}^{\pm Y}$ & $\mu_{\Delta 1}^{\pm X}$, $\mu_{\Delta 2}^{\pm Y}$ & $\mu_{\Delta 1}^{\pm X}$, $\mu_{\Delta 3}^{\pm Y}$ & $\mu_{\Delta 1.5}^{\pm X}$, $\mu_{\Delta 4}^{\pm Y}$ & $\mu_{\Delta 2}^{\pm X}$, etc. where $\mu_{\Delta}^{\pm X}$ lags by two displacement ductility levels until bar buckling is observed, at which time cycling shifts to direct x-direction loading until bar buckling in that direction, followed by symmetric y and x-direction loading until failure

Figure 16-20. Comparison of the Three Type-B Bidirectional Load Histories of this Study

Table 16-3. Limit State Strains and Displacements in the Bidirectional Load Path Dataset of this Study

Test	Region	Δ@Fy' (in)	εcc	Δ@εcc (in)	εsy	Δ@εsy (in)	εbb	Δ@εbb (in)
1	N	1.11	0.00562	3.01	0.00888	4.06	0.0284	6.01
1	S	1.10	0.00652	3.03	0.00823	4.20	0.0389	7.51
1	E	1.13	0.00626	3.02	0.00722	4.10	0.0288	6.04
1	W	1.12	0.00566	3.03	0.00891	4.37	0.0396	7.48
2	N	1.17	0.00420	2.38	0.01086	4.26	0.0315	6.48
2	S	1.12	0.00374	2.38	0.00975	4.82	0.0334	6.44
2	E	1.15	0.00438	2.37	0.01079	4.81	0.0308	6.48
2	W	1.16	0.00480	2.39	0.00867	4.43	0.0311	6.47
3	N	1.13	0.00525	2.26	0.01242	3.86	0.0320	6.01
3	S	1.07	0.00544	2.26	0.01414	4.46	0.0308	6.04
3	E	1.10	0.00422	3.01	0.01016	5.64	0.0301	5.99
3	W	1.08	0.00448	3.01	0.01005	5.64	0.0386	7.53
4	N	0.99	0.00721	2.73	0.01622	3.92	0.0386	6.84
4	S	0.97	0.00753	2.73	0.01294	4.01	0.0474	8.22
4	E	1.04	0.00506	2.73	0.00863	4.77	0.0389	6.85
4	W	1.02	0.00502	2.74	0.01256	5.48	0.0486	8.20
5	N	0.96	0.00758	2.73	0.01904	5.45	0.0404	6.85
5	S	1.00	0.00677	2.73	0.01166	5.16	0.0469	8.20
5	E	1.05	0.00417	2.05	0.00969	5.47	0.0367	6.83
5	W	1.00	0.00565	2.72	0.01131	5.43	0.0425	6.83
6	N	1.05	0.00727	2.73	0.02195	4.08	0.0362	6.85
6	S	1.05	0.00640	2.75	0.01380	4.99	0.0367	6.87
6	E	0.96	0.00267	2.74	0.00509	4.91	0.0380	6.84
6	W	1.06	0.00443	2.76	0.00851	5.34	0.0437	8.21
7	N	0.98	0.00553	2.49	0.02610	7.26	0.0451	7.44
7	S	0.84	0.00510	1.91	0.01669	5.88	-	-
7	E	0.94	0.00364	1.89	0.01129	4.83	0.0436	6.17
7	W	0.89	0.00461	2.48	0.01452	5.48	0.0480	7.48
8	N	0.90	0.00431	1.87	0.01696	5.89	0.0404	7.37
8	S	0.88	0.00403	1.88	0.01395	5.79	0.0424	7.31
8	E	0.95	0.00596	2.46	0.01330	4.71	0.0354	6.11
8	W	0.90	0.00571	2.46	0.01519	4.94	0.0435	7.32
9	N	0.96	0.00610	2.57	0.01170	5.10	0.0344	6.40
9	S	0.92	0.00470	1.90	0.01175	4.82	0.0352	6.41
9	E	0.97	0.00661	2.57	0.01150	4.27	0.0362	6.38
9	W	0.95	0.00598	2.58	0.01786	4.68	0.0379	6.41
10	N	0.96	0.00377	2.03	0.01610	4.64	0.0384	6.82
10	S	0.97	0.00502	2.05	0.01674	5.80	0.0525	8.82
10	E	1.04	0.00682	2.72	0.01786	5.46	0.0370	6.76
10	W	1.00	0.00491	2.74	0.01404	6.42	-	-
11	N	0.99	0.00539	2.96	0.01321	6.04	0.0440	7.32
11	S	0.90	0.00658	2.69	0.01517	6.19	0.0493	8.55
11	E	0.93	0.00479	2.67	0.01817	6.14	0.0435	7.28
11	W	0.98	0.00511	2.73	0.01182	6.06	0.0505	8.49
12	N	0.95	0.00624	2.93	0.01240	5.23	0.0328	6.08
12	S	0.90	0.00483	2.68	0.01101	4.73	0.0315	6.10
12	E	1.00	0.00427	2.19	0.01003	5.42	0.0330	6.06
12	W	0.94	0.00373	2.11	0.01436	5.34	0.0338	6.09

Table 16-4. Specimen Summary for the (Goodnight, Kowalsky and Nau 2015) Unidirectional Dataset

Test	Load History	Dia. (in)	Length (ft)	f_{yh} (ksi)	f_y (ksi)	f_u (ksi)	f_c' (ksi)	d_{bl} (in)	$\frac{A_{st}}{A_g}$	$\frac{4A_{sp}}{D's}$	$\frac{P}{f_c'A_g}$
8	EQ LH2	24	8	74.10	68.08	94.79	6.99	0.75	0.016	0.01	0.054
9	Cyclic LH1	24	8	74.10	68.08	94.79	6.81	0.75	0.016	0.01	0.054
10	EQ LH3	24	8	74.10	68.08	94.79	5.26	0.75	0.016	0.01	0.071
11	EQ LH4	24	8	74.10	68.08	94.79	6.18	0.75	0.016	0.01	0.062
12	EQ LH5	24	8	74.10	68.08	94.79	6.10	0.75	0.016	0.01	0.062
13	Cyclic	24	8	69.89	68.08	92.84	6.10	0.75	0.016	0.013	0.062
14	Cyclic	24	8	64.57	68.08	92.84	6.64	0.75	0.016	0.005	0.057
15	Cyclic	24	8	64.57	68.08	92.84	7.23	0.75	0.016	0.007	0.052
16	Cyclic LH6	24	8	64.57	68.08	92.84	6.71	0.75	0.016	0.013	0.056
17	EQ LH7	24	8	64.57	68.08	92.84	7.59	0.75	0.016	0.013	0.05
18	EQ LH8	24	8	64.57	68.08	82.84	7.81	0.75	0.016	0.013	0.048
19	Cyclic	18	8	65.55	68.14	92.43	6.33	0.75	0.017	0.013	0.1
20	Cyclic	18	8	65.55	68.14	92.43	6.47	0.75	0.017	0.013	0.05
21	Cyclic	18	11	65.55	68.14	92.43	6.39	0.75	0.017	0.013	0.05
22	Cyclic	18	11	65.55	68.14	92.43	6.53	0.75	0.017	0.013	0.1
23	Cyclic	18	13	65.55	68.14	92.43	6.61	0.75	0.017	0.013	0.05
24	Cyclic	18	13	65.55	68.14	92.43	6.47	0.75	0.017	0.013	0.1
25	Cyclic	24	8	63.86	69.70	95.54	6.29	0.875	0.021	0.01	0.05
26	Cyclic	24	8	63.86	69.70	95.54	5.89	0.875	0.021	0.01	0.1
27	Cyclic	24	8	63.86	68.74	93.70	6.15	0.75	0.016	0.01	0.1
28	Cyclic	18	8	63.86	68.74	93.70	6.24	0.75	0.017	0.013	0.15
29	Cyclic	18	8	63.86	68.74	93.70	5.91	0.75	0.017	0.013	0.2
30	Cyclic	18	8	63.86	70.47	97.68	6.05	1	0.031	0.013	0.15

Table 16-5. Limit State Strains and Drifts from the (Goodnight, Kowalsky and Nau 2015) Unidirectional Dataset

Test	Cover Crushing $\varepsilon_{cc}^{Compressive}$		Cover Crushing Δ_{cc}/L		Spiral Yield $\varepsilon_{sy}^{Compressive}$		Spiral Yield Δ_{sy}/L		Bar Buckling $\varepsilon_{bb}^{Tensile}$		Bar Buckling Δ_{bb}/L	
	North	South	North	South	North	South	North	South	North	South	North	South
8	-	0.006	-	0.0252	-	0.0183	-	0.0623	0.051	0.048	0.0755	0.0693
9	0.0041	0.0032	0.0174	0.0176	0.0139	0.0163	0.0526	0.0699	0.053	0.051	0.0700	0.0698
10	0.0026	0.0039	0.0145	0.0177	0.0092	0.0151	0.0519	0.0466	-	0.038	-	0.0522
11	-	-	-	-	-	0.0163	-	0.0413	0.059	0.033	0.0863	0.0529
12	0.0047	0.0044	0.0193	0.0184	0.0165	0.0176	0.0523	0.0594	0.058	0.044	0.0856	0.0680
13	0.0046	0.0036	0.0168	0.0167	0.0166	0.0162	0.0505	0.0673	0.047	0.047	0.0673	0.0677
14	0.0029	0.0030	0.0124	0.0125	-	0.0152	-	0.0500	0.035	0.035	0.0500	0.0500
15	0.0027	0.0041	0.0130	0.0175	0.0199	0.0125	0.0521	0.0347	0.037	0.038	0.0521	0.0521
16	0.0048	0.0038	0.0172	0.0173	0.0120	0.0152	0.0519	0.0519	0.056	0.052	0.0693	0.0696
17	0.0043	0.0043	0.0167	0.0174	0.0148	0.0168	0.0419	0.0470	0.055	0.039	0.0780	0.0523
18	0.0068	-	0.0230	-	0.0147	0.0136	0.0572	0.0384	-	0.047	-	0.0630
19	0.0068	0.0065	0.0239	0.0239	0.0103	0.0119	0.0356	0.0357	0.037	0.032	0.0596	0.0596
20	0.0065	0.0046	0.0246	0.0246	0.0114	0.0109	0.0492	0.0370	0.046	0.037	0.0740	0.0614
21	0.0046	0.0048	0.0299	0.0301	0.0146	0.0102	0.0599	0.0450	0.051	0.036	0.0898	0.0748
22	0.0063	0.0085	0.0316	0.0316	0.0103	0.0124	0.0475	0.0474	0.041	0.053	0.0792	0.0949
23	0.0052	0.0062	0.0356	0.0355	0.0136	0.0151	0.0713	0.0711	0.051	0.048	0.1067	0.1067
24	0.0085	0.0083	0.0367	0.0367	0.0155	0.0131	0.0550	0.0550	0.037	0.048	0.0916	0.0918
25	0.0036	0.0040	0.0158	0.0159	0.0091	0.0125	0.0319	0.0321	0.042	0.035	0.0640	0.0533
26	0.0045	0.0046	0.0155	0.0156	0.0089	0.0121	0.0311	0.0309	0.032	0.024	0.0519	0.0415
27	0.0036	0.0038	0.0144	0.0144	0.0168	0.0124	0.0288	0.0288	0.036	0.024	0.0479	0.0382
28	0.0051	0.0055	0.0208	0.0208	0.0123	0.0143	0.0417	0.0417	0.036	0.030	0.0696	0.0556
29	0.0055	0.0054	0.0210	0.0209	0.0142	0.0103	0.0420	0.0280	0.055	0.036	0.0840	0.0700
30	0.0052	0.0059	0.0230	0.0230	0.0095	0.0094	0.0307	0.0307	0.036	0.033	0.0770	0.0770

Plastic Hinge Method Design Recommendations

Bridge columns are designed as ductile elements which form plastic hinges to dissipate energy in a seismic event. Within the context of performance based design, this results in the need to describe various performance levels using engineering criteria. While several deformation quantities are possible to describe damage, steel and concrete strains are an attractive option as they describe behavior at the material level. In design, curvatures at material strains are translated to lateral displacements using an equivalent curvature distribution.

The Unidirectional Modified Plastic Hinge Method from (Goodnight, Kowalsky and Nau 2015a) was developed to improve the accuracy of strain-displacement predictions. This method was summarized in Chapter 1. Key aspects which differentiate it from the approach recommended in (Priestley, Calvi and Kowalsky 2007) include: (1) a decoupling of column flexure and strain penetration deformation components, (2) a linear plastic curvature distribution which emulates the measured curvature profiles, and (3) separate plastic hinge lengths for tensile and compressive strain-displacement predictions. For the unidirectional experiments, this method proved effective in increasing the accuracy of both tensile and compressive strain-displacement, while maintaining similar levels of accuracy for elastic predictions. Equivalent curvature distributions for this method appear in the left halves of Figure 16-21 and Figure 16-22 for single and double bending, respectively. The right halves of these figures depict the geometry of the plastic hinge method recommended in (Priestley, Calvi and Kowalsky 2007).

The purpose of conducing twelve additional tests was to investigate the impact of bidirectional load path on the definition of performance strain limits and to determine necessary adjustments for the equivalent curvature distributions recommended in design. This section focuses on presenting a simplified plastic hinge method suitable for assessing strain-displacement under either unidirectional or bidirectional loading. The new approach is then compared to the measured strain-displacement relationships in both column datasets.

The test matrix for the Bidirectional Dataset of this study appears in Table 16-1. The twelve columns had 24” diameter cross sections with cantilever lengths of 109.4375” $(L/D = 4.56)$. The main variables in the experiments included longitudinal steel content, transverse steel detailing, and the imposed bidirectional displacement history. A constant axial force of $191\ kips$ was applied, which equated to $\left(P/f_c' A_g \approx 7\%\right)$, depending on the value of f_c' from individual tests. A summary of the material properties for the Gr60 A706 longitudinal and transverse steel appears in Table 16-2. Summary reports for each test appear in receptive chapters of this report. They include details of the applied loading, observed behavior, and analysis of the measured strain and curvature data. The previous section of this chapter was used to illustrate the methods in which the spread of plasticity was quantified through the presentation of sample data from Test 11.

In the experiments, the measured extent of plasticity was found to increase due to the combined effects of moment gradient and tension shift. The proposed tensile hinge length, Lpr_t in Eqn 16-4, was calibrated to match the upper bound of the measured spread of plasticity for columns in the bidirectional and separately the unidirectional datasets, see Figure 16-23 and Figure 16-25. Comparisons of the measured extent of plasticity and design recommendations for bidirectional columns with either #7 or #6 longitudinal reinforcement appear in Figure 16-27 and Figure 16-29, respectively. Statistics comparing the measured upperbound extent of plasticity and those predicted

using either Lpr_t from Eqn 16-4 or recommendations from (Goodnight, Kowalsky and Nau 2015a) for columns in the Unidirectional, Bidirectional, and Combined Datasets appear in Table 16-6. The recommended approach produced a mean measured to predicted extent of plasticity of 1.002 with a coefficient of variation of 0.060 in the Combined Dataset, which is shown graphically in Figure 16-33.

Note that in the Lpr_t expression of Eqn 16-4, the tension shift coefficient was increased for bidirectional loading to account for the larger measured spread in plasticity. This behavior is evident in the measured extent of plasticity for Asymmetric Two-Cycle-Set Tests 3 and 6 presented in Figure 16-31. Displacement amplitudes for loading in the x-direction lagged behind those of the primary y-direction, see Figure 16-20. The upper bound to the measured spread in plasticity in the primary y-direction closely matches the unidirectional recommendations from (Goodnight, Kowalsky and Nau 2015a), while the x-direction is subject to a more rapid spread in plasticity under a previously defined crack pattern and softening due to the prior loading in the orthogonal direction.

Equivalent curvature distributions which reflect the measured shape of the triangular plastic curvature distribution and extent of plasticity L_{pr} appear in the left halves of Figure 16-21 and Figure 16-22 for single and double bending, respectively. The plastic hinge method recommended in (Priestley, Calvi and Kowalsky 2007) is widely accepted in design, due to its simplicity. This method utilizes a rectangular plastic hinge length L_p, which results in the equivalent curvature distributions shown in right halves of Figure 16-21 and Figure 16-22. It can be shown that the equivalent rectangular plastic hinge length L_p is half the height of the triangular plastic hinge length L_{pr}. This equates the effect the plastic curvature geometry on the lateral displacement when using the moment area method. Based on this equivalency, the tensile rectangular hinge length Lp_t in Eqn 16-6 was created.

Compressive strains are more closely related to the moment gradient effect, which can be described using the moment gradient coefficient k in Eqn 16-2 from the (Priestley, Calvi and Kowalsky 2007) hinge method. The same approach was adopted in this study, resulting in the triangular compressive hinge length Lpr_c in Eqn 16-3 and the rectangular compressive hinge length Lp_c in Eqn 16-25. Note that the geometry of the rectangular hinge length in Figure 16-21 and Figure 16-22 includes the equivalent strain penetration length L_{sp}, while flexural displacements and those arising from strain penetration were decoupled in the geometry of the triangular distribution. For columns with low aspect ratios, the lower bound plastic hinge length from (Priestley, Calvi and Kowalsky 2007) was included for both geometries. For a rectangular hinge length, this equates to L_{sp} below and above the footing-column interface. For the triangular geometry, this equates to $2L_{sp}$ above the footing-column interface, since strain penetration at the interface is decoupled into its own geometry.

In this study, the definition of the equivalent strain penetration length L_{sp} in Eqn 16-1 from (Priestley, Calvi and Kowalsky 2007) was adopted. The average measured equivalent strain penetration lengths are compared to design recommendations in Figure 16-24 and Figure 16-26. In both datasets, L_{sp} from Eqn 16-1 overpredicts the measured behavior, resulting in larger fixed-end rotations due to strain penetration. As discussed in the presentation of the Unidirectional Modified Plastic Hinge Method from (Goodnight, Kowalsky and Nau 2015a) in Chapter 1, the measured tensile strain-displacement relationships were slightly conservative when using the measured spread of plasticity and fixed-end rotations, see Table 1-4 and Figure 1-8. One method to counteract this conservatism is to increase the fixed-end rotations while maintaining the definition of the tensile hinge length as a physically measurable quantity. This proved effective, resulting in mean value

tensile-strain displacement predictions. A further benefit of this decision is that the recommended approach collapses down to the accepted (Priestley, Calvi and Kowalsky 2007) plastic hinge method for compressive strain-displacement, with the only difference being that the strain penetration block is centered at the interface in the triangular plastic curvature distribution.

Equivalent Strain Penetration Length and Tension/Compression Plastic Hinge Lengths

Where L_c is the length from the critical section to the point of contraflexure, D is the column diameter, d_{bl} is the longitudinal bar diameter, f_{ye} is the expected yield stress of the longitudinal steel, and f_{ue} is the expected ultimate stress of the longitudinal steel.

$L_{sp} = \alpha f_{ye} d_{bl}$	*Equivalent Strain Penetration Length* *$\alpha = 0.15$ for ksi and $\alpha = 0.022$ for MPa units*	*Eqn 16-1*
$k = 0.2\left(\frac{f_{ue}}{f_{ye}} - 1\right) \leq 0.08$	*Moment Gradient Coefficient*	*Eqn 16-2*
$Lpr_c = 2kL_c \geq 2L_{sp}$	*Triangular Compressive Hinge Length*	*Eqn 16-3*
$Lpr_t = Lpr_c + \beta D$	*Triangular Tensile Hinge Length* *$\beta = 0.8$ for Bidirectional and $\beta = 0.66$ for Unidirectional Loading*	*Eqn 16-4*
$Lp_c = kL_c + L_{sp} \geq 2L_{sp}$	*Rectangular Compressive Hinge Length*	*Eqn 16-5*
$Lp_t = Lp_c + \gamma D$	*Rectangular Tensile Hinge Length* *$\gamma = 0.4$ for Bidirectional and $\gamma = 0.33$ for Unidirectional Loading*	*Eqn 16-6*

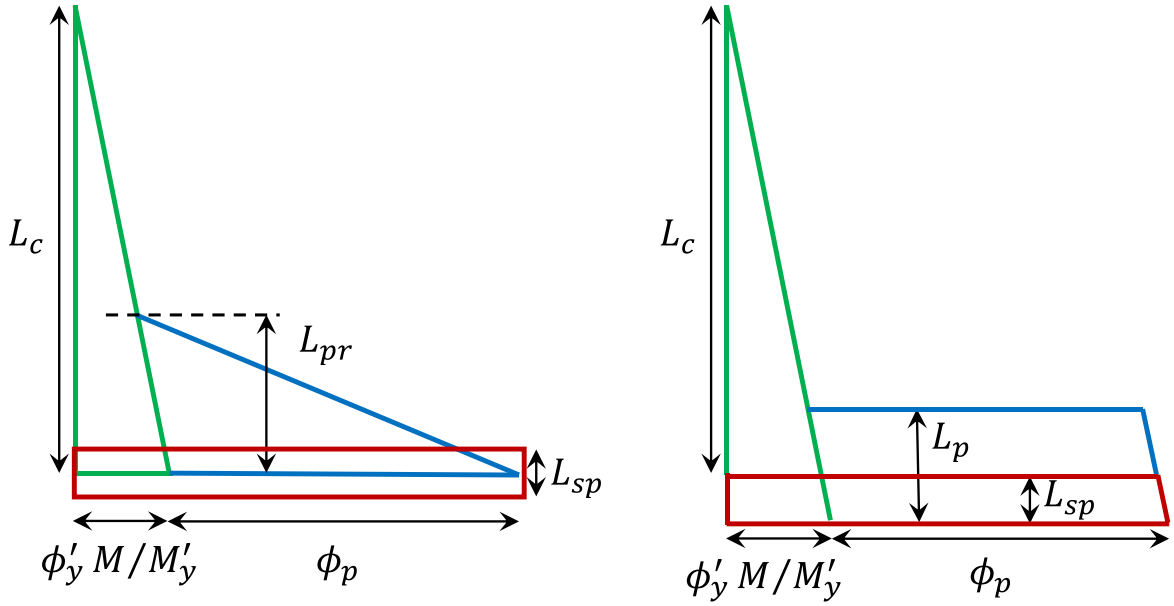

Figure 16-21. Single Bending Equivalent Curvature Profiles, (Left) Triangular and (Right) Rectangular Plastic Hinge Lengths

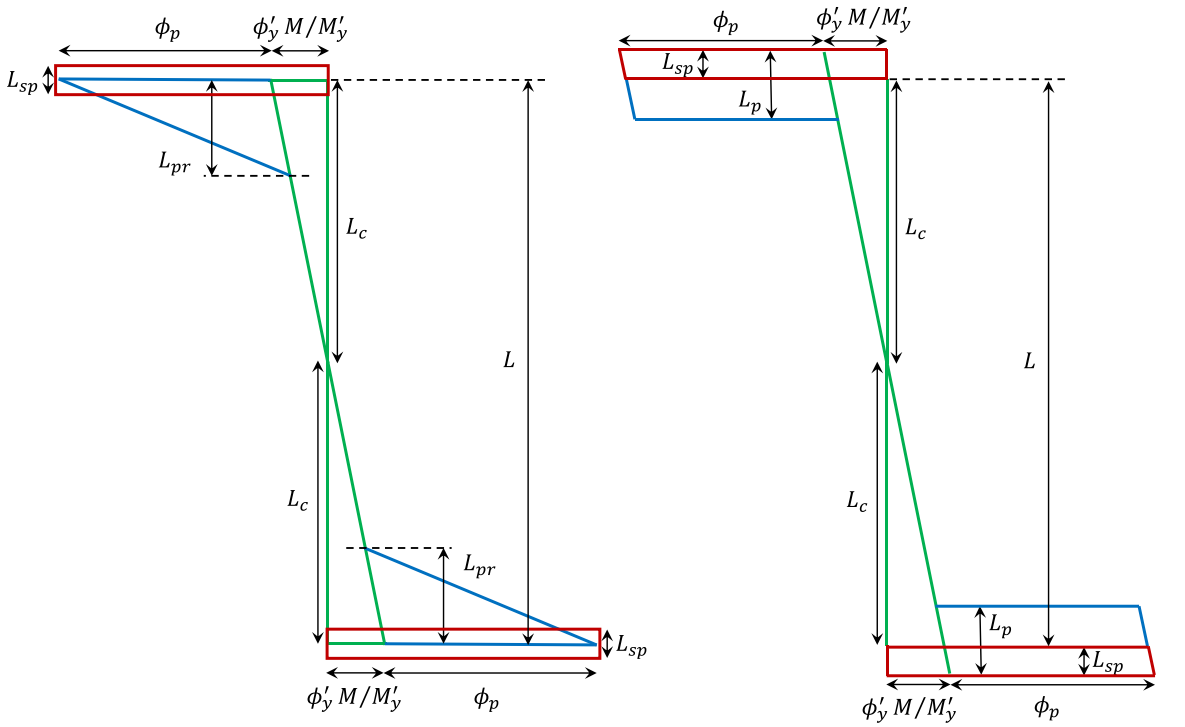

Figure 16-22. Double Bending Equivalent Curvature Profiles, (Left) Triangular and (Right) Rectangular Plastic Hinge Lengths

Equations Needed to Compute Disp. using the Triangular Plastic Curvature Geometry

Note that equations discussed in this section only apply to the triangular plastic curvature geometry presented in the left halves of Figure 16-21 and Figure 16-22 for single and double bending, respectively. Elastic displacements are computed when the base section curvature is either at or below the first yield curvature, ϕ_y'. The elastic displacement of a column in single bending is calculated using Eqn 16-7 and Eqn 16-11. The elastic displacement of a column in double bending is computed using Eqn 16-13 and Eqn 16-17. The elastic displacement is the addition of elastic column flexural, strain penetration, and shear deformations. Shear displacements were negligible for columns in both the unidirectional and bidirectional datasets.

Inelastic displacements are computed when the base section curvature exceeds the first yield curvature, ϕ_y'. The plastic curvature at the base section is obtained by subtracting the elastic curvature from the base section curvature, $\phi_p = \phi_{base} - \phi_y'(M/M_y')$. The ratio M/M_y' accounts for additional post-yield elastic flexibility, which can be simplified to $\phi_p = \phi_{base} - \phi_y$ where $\phi_y = \phi_y'(M_n/M_y')$ for hand calculations. For translation of a tensile strain limit to a lateral displacement, the tensile triangular plastic hinge length should be used, Lpr_t in Eqn 16-4. If instead, a compressive strain limit is translated to a lateral displacement, the compressive triangular plastic hinge length should be employed, Lpr_c in Eqn 16-3. Expressions needed to compute the inelastic displacement of a column in single bending are shown in Eqn 16-8 through Eqn 16-12. Expressions needed to compute the inelastic displacement of a column in double bending appear in Eqn 16-14 through Eqn 16-18. The total displacement is the sum of the elastic column flexural, plastic column flexural, strain penetration, and shear deformation components.

Displacements for a Column in Single Bending ($L_c = L$) with Triangular Hinge Length

$\Delta_e = \phi_{base} L^2/3$	*(Single) Elastic Flexural Displacement before First Yield*	*Eqn 16-7*
$\Delta_e = \phi'_y (M/M'_y) L^2/3$	*(Single) Elastic Flexural Displacement after First Yield*	*Eqn 16-8*
$\phi_p = \phi_{base} - \phi'_y (M/M'_y)$	*Plastic Curvature at the Base Section*	*Eqn 16-9*
$\Delta_p = \phi_p (L_{pr}/2)[L - L_{pr}/3]$	*(Single) Plastic Flexural Displacement*	*Eqn 16-10*
$\Delta_{sp} = L_{sp} \phi_{base} L$	*Displacement due to Strain Penetration*	*Eqn 16-11*
$\Delta_T = (\Delta_e + \Delta_{sp} + \Delta_p + \Delta_{shear})$	*Total Top Column Displacement*	*Eqn 16-12*

Displacements for a Column in Double Bending ($L_c = L/2$) with Triangular Hinge Length

$\Delta_e = \phi_{base} L^2/6$	*(Double) Elastic Flexural Displacement before First Yield*	*Eqn 16-13*
$\Delta_e = \phi'_y (M/M'_y) L^2/6$	*(Double) Elastic Flexural Displacement after First Yield*	*Eqn 16-14*
$\phi_p = \phi_{base} - \phi'_y (M/M'_y)$	*Plastic Curvature at the Base Section*	*Eqn 16-15*
$\Delta_p = \phi_p (L_{pr}/2)[L - 2\,L_{pr}/3]$	*(Double) Plastic Flexural Displacement*	*Eqn 16-16*
$\Delta_{sp} = L_{sp} \phi_{base} L$	*Displacement due to Strain Penetration*	*Eqn 16-17*
$\Delta_T = (\Delta_e + \Delta_{sp} + \Delta_p + \Delta_{shear})$	*Total Top Column Displacement*	*Eqn 16-18*

Equations Needed to Compute Disp. using the Rectangular Plastic Curvature Geometry

Note that equations discussed in this section only apply to the rectangular plastic curvature geometry presented in the right halves of Figure 16-21 and Figure 16-22 for single and double bending, respectively. Elastic displacements are computed when the base section curvature is either at or below the first yield curvature, ϕ'_y. The elastic displacement of a column in single bending is calculated using Eqn 16-20. The elastic displacement of a column in double bending is computed using Eqn 16-26. The elastic displacement is the addition of elastic column flexural, strain penetration, and shear deformations. Shear displacements were negligible for columns in both the unidirectional and bidirectional datasets.

Inelastic displacements are computed when the base section curvature exceeds the first yield curvature, ϕ'_y. The plastic curvature at the base section is obtained by subtracting the elastic curvature from the base section curvature, $\phi_p = \phi_{base} - \phi'_y (M/M'_y)$. The ratio M/M'_y accounts for additional post-yield elastic flexibility, which can be simplified to $\phi_p = \phi_{base} - \phi_y$ where $\phi_y = \phi'_y (M_n/M'_y)$ for hand calculations. For translation of a tensile strain limit to a lateral displacement, the tensile rectangular plastic hinge length should be used, Lp_t in Eqn 16-6. If instead, a compressive strain limit is translated to a lateral displacement, the compressive rectangular plastic hinge length should be employed, Lp_c in Eqn 16-5. Expressions needed to compute the inelastic displacement of a column in single bending are shown in Eqn 16-21 through Eqn 16-24. Expressions needed to compute the inelastic displacement of a column in double bending appear in Eqn 16-27 through Eqn 16-30. The total displacement is the sum of the elastic column flexural, plastic column flexural, strain penetration, and shear deformation components.

Displacements for a Column in Single Bending ($L_c = L$) with Rectangular Hinge Length

$L_{eff} = L + L_{sp}$	*(Single) Effective Length of the Member*	*Eqn 16-19*
$\Delta_e = \phi_{base} {L_{eff}}^2/3$	*(Single) Elastic Flexural Displacement before First Yield*	*Eqn 16-20*
$\Delta_e = \phi'_y(M/M'_y){L_{eff}}^2/3$	*(Single) Elastic Flexural Displacement after First Yield*	*Eqn 16-21*
$\phi_p = \phi_{base} - \phi'_y(M/M'_y)$	*Plastic Curvature at the Base Section*	*Eqn 16-22*
$\Delta_p = \phi_p L_p(L + L_{sp} - 0.5L_p)$	*(Single) Plastic Flexural Displacement*	*Eqn 16-23*
$\Delta_T = (\Delta_e + \Delta_p + \Delta_{shear})$	*Total Top Column Displacement*	*Eqn 16-24*

Displacements for a Column in Double Bending ($L_c = L/2$) with Rectangular Hinge Length

$L_{eff} = L + 2L_{sp}$	*(Double) Effective Length of the Member*	*Eqn 16-25*
$\Delta_e = \phi_{base} {L_{eff}}^2/6$	*(Double) Elastic Flexural Displacement before First Yield*	*Eqn 16-26*
$\Delta_e = \phi'_y(M/M'_y){L_{eff}}^2/6$	*(Double) Elastic Flexural Displacement after First Yield*	*Eqn 16-27*
$\phi_p = \phi_{base} - \phi'_y(M/M'_y)$	*Plastic Curvature at the Base Section*	*Eqn 16-28*
$\Delta_p = \phi_p L_p(L + 2L_{sp} - L_p)$	*(Double) Plastic Flexural Displacement*	*Eqn 16-29*
$\Delta_T = (\Delta_e + \Delta_p + \Delta_{shear})$	*Total Top Column Displacement*	*Eqn 16-30*

Predictive comparison of Plastic Hinge Models

Moment-curvature analysis was performed for each experiment in the Bidirectional Dataset of this study and the Unidirectional Dataset of (Goodnight, Kowalsky and Nau 2015). The plastic hinge model recommended in (Priestley, Calvi and Kowalsky 2007) was used to translate curvatures to displacements, abbreviated as PCK2007. The Modified Plastic Hinge Model recommended in (Goodnight, Kowalsky and Nau 2015a) was used to convert material strains to displacements, abbreviated as GN15. Finally, the same approach was repeated for the proposed method in this study, abbreviated as New.

Datasets were created for the ratio of the measured to predicted displacement at each of the following limit states: (1) analytical column shear force at first yielding of the longitudinal reinforcement, (2) steel tensile strain which preceded bar buckling in the following load reversal, (3) cover concrete compressive strain at initial crushing, and (4) core concrete compressive strain at initial yielding of confinement steel. Statistics comparing the predictive capacity of each plastic hinge method appear in Table 16-7, Table 16-8, and Table 16-9 for the Bidirectional, Unidirectional, and Combined Datasets, respectively.

Alternatively, cumulative probability distributions can be used to visualize the accuracy of the equivalent curvature distributions. The elastic predictive capacity of the models are compared in Figure 16-35, Figure 16-39, and Figure 16-43 for respective datasets. A vertical line at a measured to predicted ratio of one would indicate an accurate result with low variability. The three plastic hinge models produce similar, but slightly conservative results, with the recommended approach providing the most accurate elastic predictions. Note that the recommended approach utilizes the triangular

equivalent curvature distribution, which centers the rotation due to strain penetration at the footing-column interface. If however, the recommended approach uses the rectangular equivalent curvature distribution, the result collapses down to that of the (Priestley, Calvi and Kowalsky 2007) hinge method.

Tensile strain-displacement predictions for the ratio of the measured to predicted peak displacement preceding bar buckling with the measured bar buckling tensile strain as input into the three plastic hinge models appear in Figure 16-34, Figure 16-38, Figure 16-42 for respective datasets. The recommended approach produces a mean measured to predicted bar buckling displacement close to one in both the Unidirectional and Bidirectional Datasets. This enables the use of mean value tensile strain limits. The plastic hinge methods recommended in (Goodnight, Kowalsky and Nau 2015a) and (Priestley, Calvi and Kowalsky 2007) produce conservative tensile strain-displacement predictions, which deter from their use in design.

Compressive strain-displacement predictions for the ratio of the measured to predicted displacement at cover concrete crushing with the measured cover crushing strain as input into the three plastic hinge models appear in Figure 16-36, Figure 16-40, and Figure 16-44 for respective datasets. Compressive strain-displacement predictions for the ratio of the measured to predicted displacement at initial yielding of confinement steel with the measured core concrete compressive strain at spiral yielding as input into the three plastic hinge models appear in Figure 16-37, Figure 16-41, and Figure 16-45 for respective datasets. Compressive-strain displacement predictions for the recommended plastic hinge method in this study collapse down to those made with the (Priestley, Calvi and Kowalsky 2007) approach, with the exception that the strain penetration block is centered at the footing-column interface for the triangular equivalent curvature geometry. The close results show that this change has minimal impact on the compressive strain-displacement predictions, although the results are generally conservative for both datasets, particularly at the higher compressive magnitudes measured at initial confinement steel yielding. As discussed in the next section, compressive strain limits for initial spiral yielding were modified to account for this conservatism in compressive-strain displacement and shift the result towards a mean value prediction.

Examples of the improvement in compressive and tensile strain-displacement predictions for extreme fiber reinforcement in the y-direction loading of Test 11 are shown in Figure 16-16 through Figure 16-19. Strains measured in the peak tensile gauge length of both bars match the tensile strain-displacement relationship predicted using the recommended approach, labeled as New Eqns. Measured strains in the peak compressive gauge lengths match the recommended approach in one direction of loading, while in the opposing direction match the (Goodnight, Kowalsky and Nau 2015) plastic hinge model, abbreviated as GN15 Compressive Lpr. In many instances the measured compressive strains exceeded both models, particularly after significant spiral yielding had occurred and compressive demands were localized over the inelastic spiral layers. Local strain-displacement comparisons and global force-displacement comparisons appear in respective chapters of this report which summarize the test results. It is recommended that global force-displacement response be predicted using the compressive hinge length in the new approach, since it defaults to the (Priestley, Calvi and Kowalsky 2007) hinge method, which is widely accepted in design.

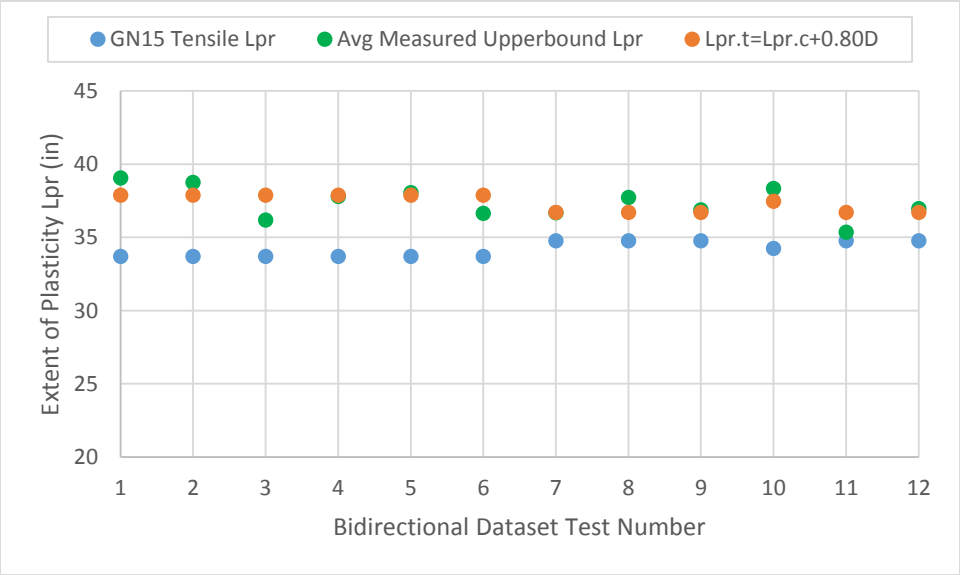

Figure 16-23. Comparison of Average Measured Upperbound Spread of Plasticity to Tensile Hinge Length Expressions

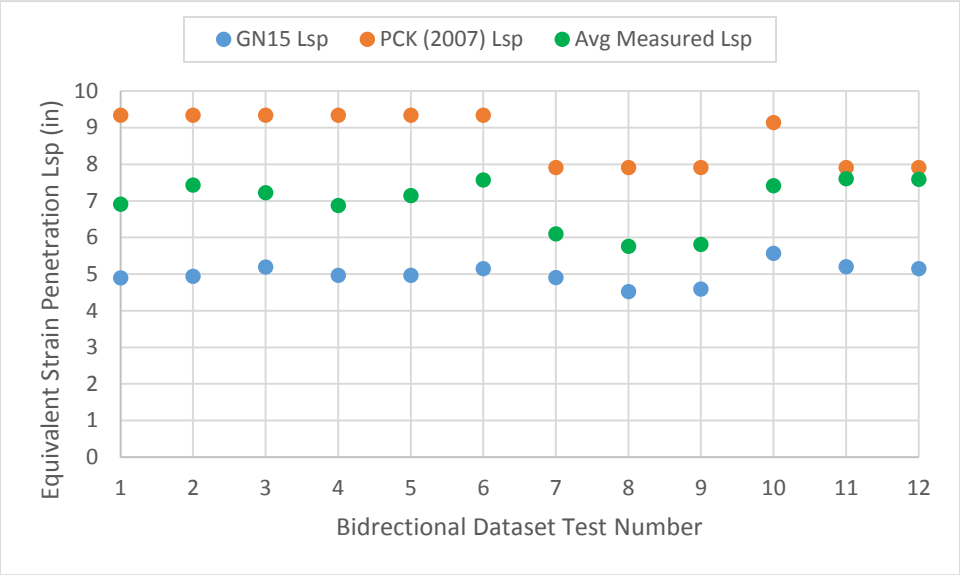

Figure 16-24. Comparison of Average Measured Equivalent Strain Penetration Length to Design Recommendations

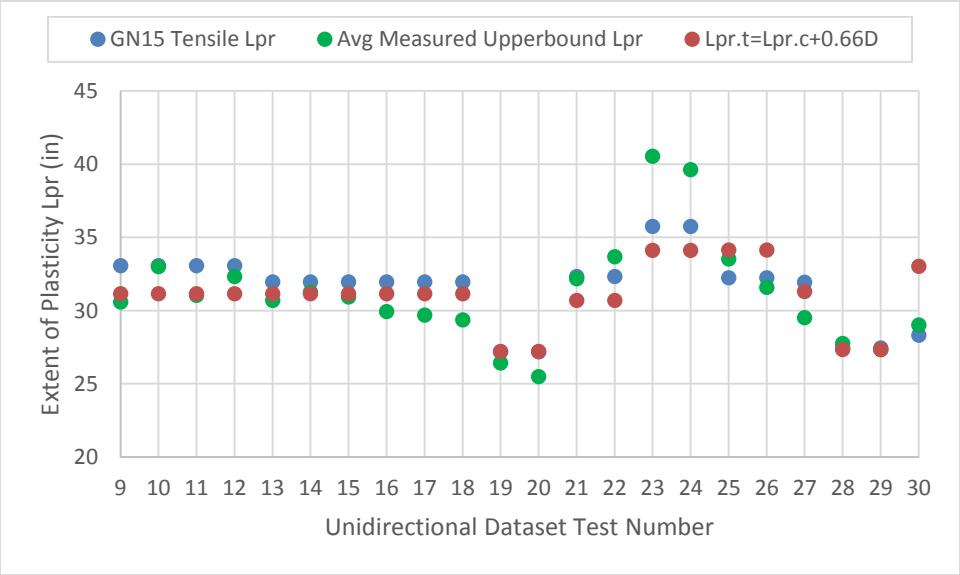

Figure 16-25. Comparison of Average Measured Upperbound Spread of Plasticity to Tensile Hinge Length Expressions

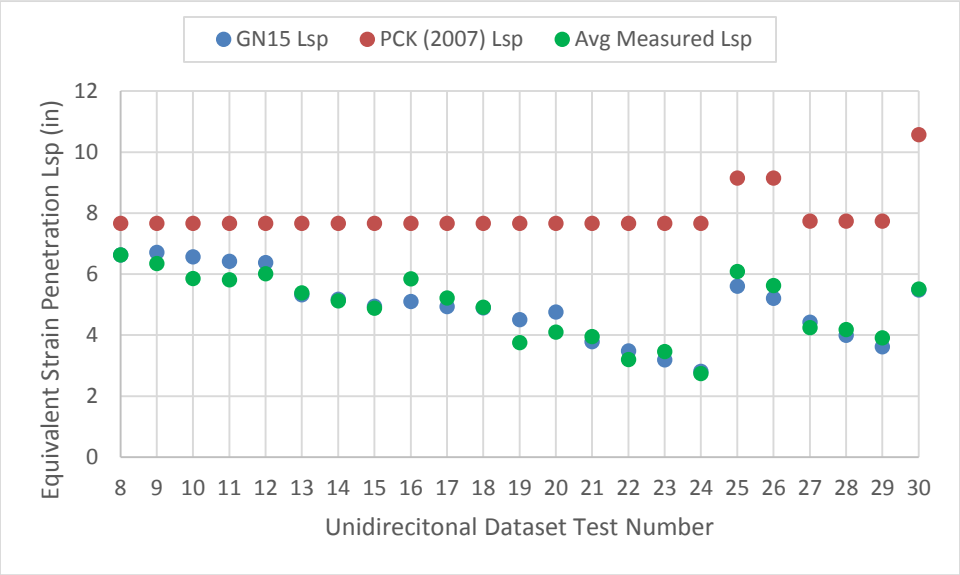

Figure 16-26. Comparison of Average Measured Equivalent Strain Penetration Length to Design Recommendations

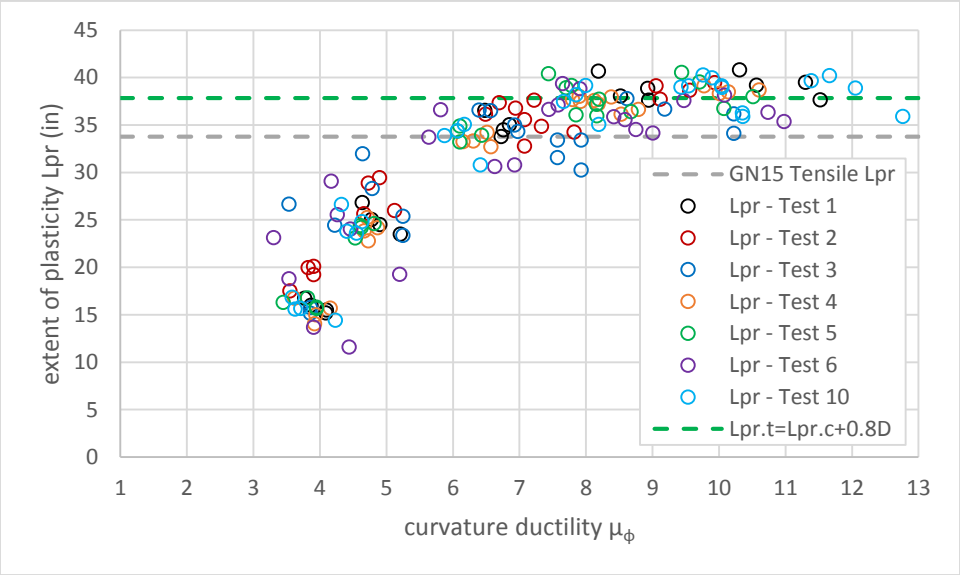

Figure 16-27. Comparison of Measured Lpr and Design Recommendations for Columns with #7 Longitudinal Steel

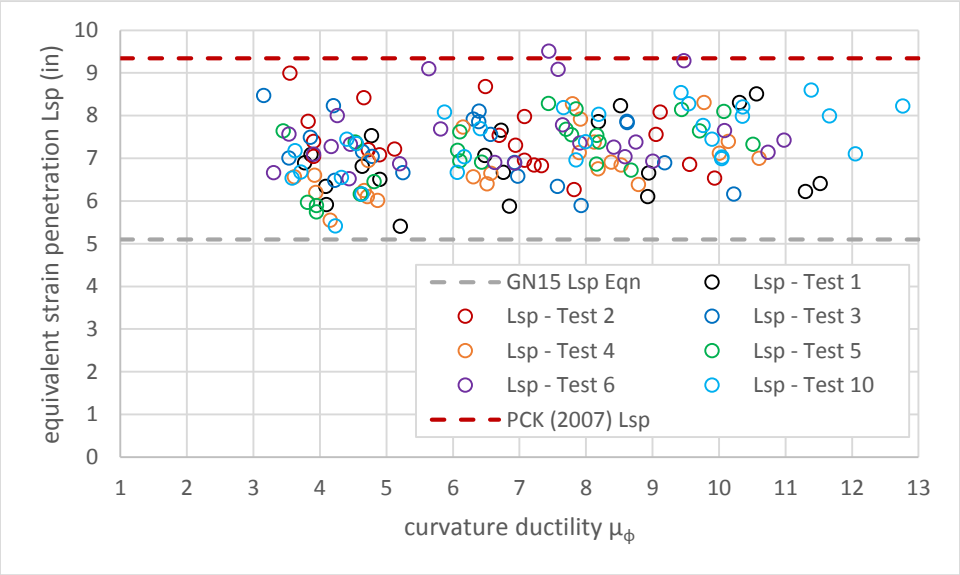

Figure 16-28. Comparison of Measured Lsp and Design Recommendations for Columns with #7 Longitudinal Steel

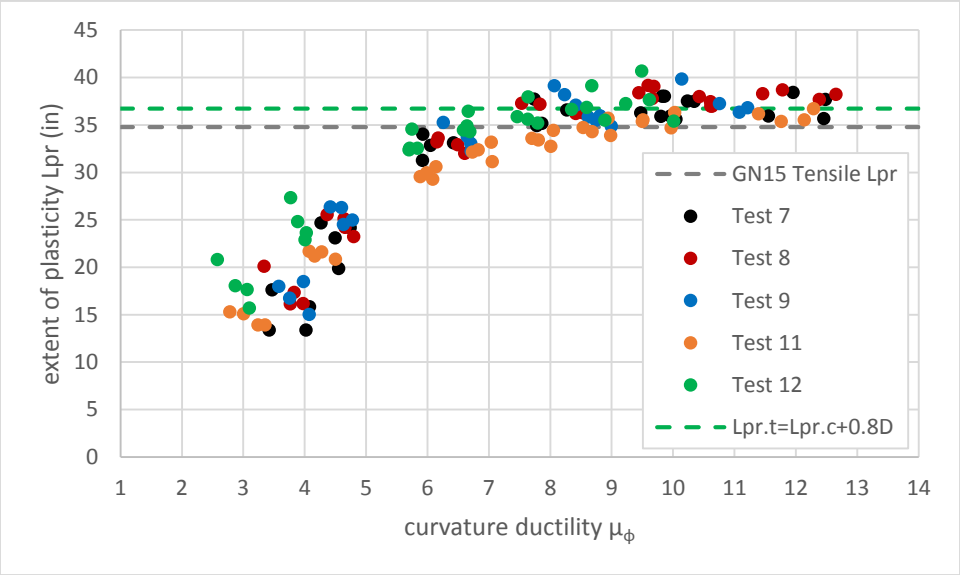

Figure 16-29. Comparison of Measured Lpr and Design Recommendations for Columns with #6 Longitudinal Steel

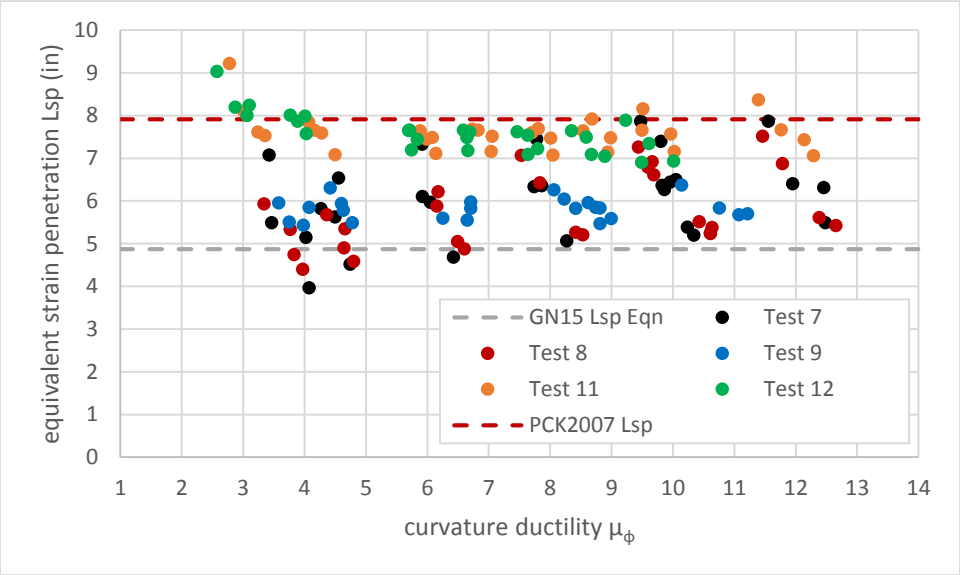

Figure 16-30. Comparison of Measured Lsp and Design Recommendations for Columns with #6 Longitudinal Steel

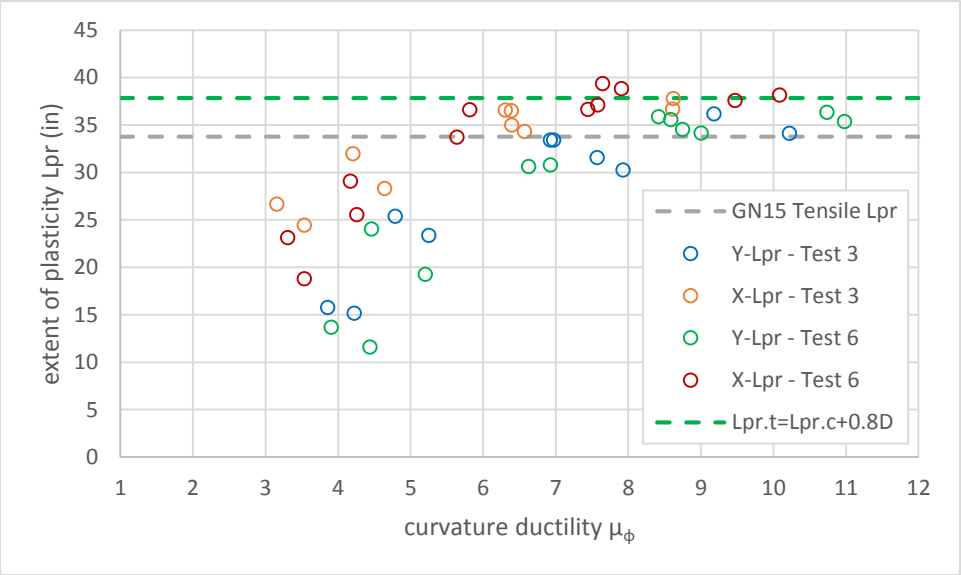

Figure 16-31. Comparison of Measured Lpr and Design Recommendations for Cols. with Asymmetric 2-Cycle-Set Loading

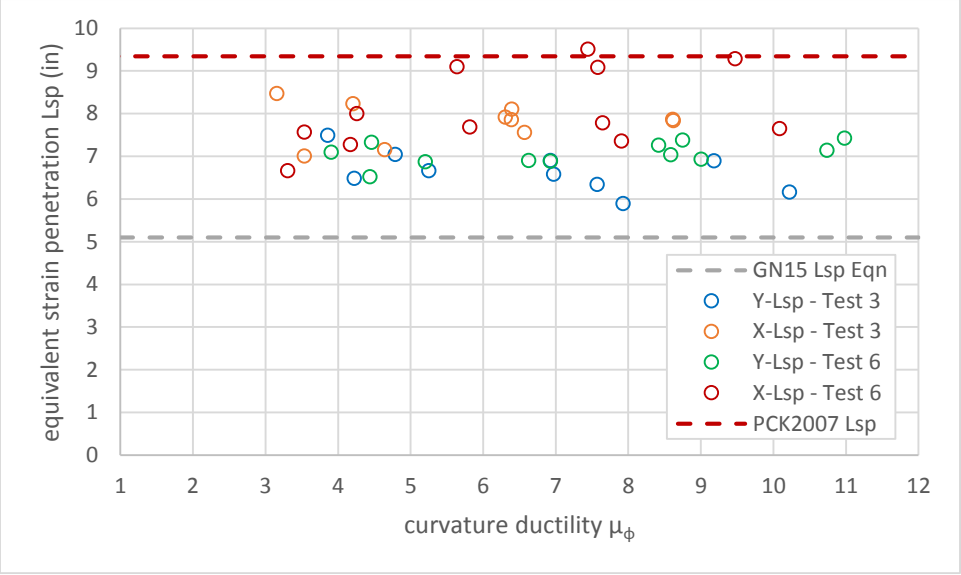

Figure 16-32. Comparison of Measured Lsp and Design Recommendations for Cols. with Asymmetric 2-Cycle-Set Loading

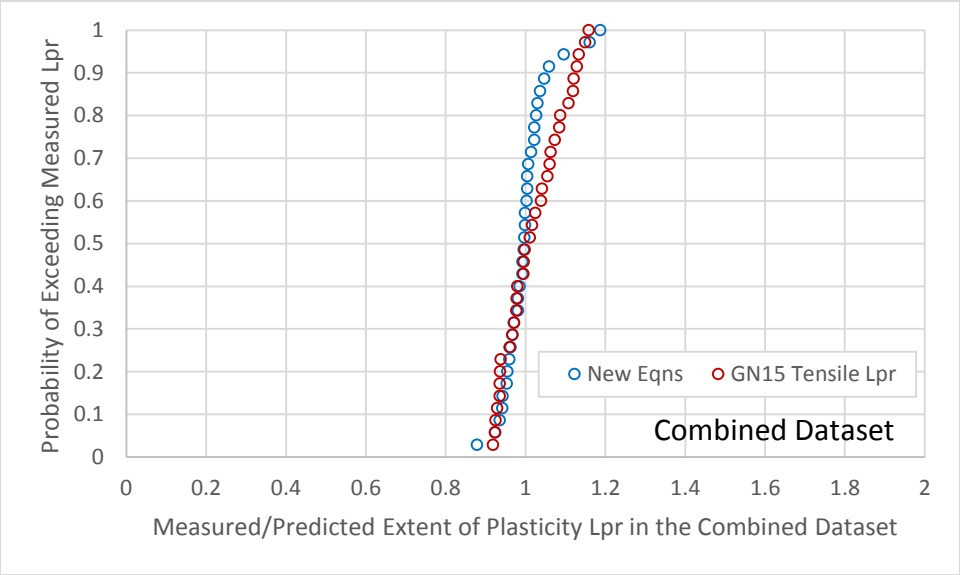

Figure 16-33. Probability of Exceeding the Measured Upperbound Lpr in the Combined Dataset

Table 16-6. Comparison of Measured Upperbound Lpr and Design Recommendations in Respective Datasets

Column Dataset	Tensile Lpr	Mean Measured/Predicted	COV
Unidirectional GN15	GN15	0.984	0.058
	New	1.002	0.072
Bidirectional	GN15	1.094	0.039
	New	1.000	0.026
Combined	GN15	1.022	0.072
	New	1.002	0.060

Table 16-7. Plastic Hinge Model Comparison in Bidirectional Dataset, Statistics for Measured/Predicted Limit State Disp.

Limit State	Model	Mean Measured/Predicted	COV
Analytical First Yield Force Fy' Bidirectional Dataset	PCK2007	1.214	0.062
	GN15	1.247	0.069
	New	1.143	0.060
Cover Concrete Crushing Bidirectional Dataset	PCK2007	0.909	0.200
	GN15	1.090	0.187
	New	0.899	0.194
Initial Confinement Steel Yielding Bidirectional Dataset	PCK2007	0.874	0.244
	GN15	1.111	0.242
	New	0.879	0.240
Longitudinal Bar Buckling Bidirectional Dataset	PCK2007	1.313	0.057
	GN15	1.202	0.062
	New	0.989	0.056

Table 16-8. Plastic Hinge Model Comparison in Unidirectional Dataset, Statistics for Measured/Predicted Limit State Disp.

Limit State	Model	Mean Measured/Predicted	COV
Analytical First Yield Force Fy' Unidirectional GN15 Dataset	PCK2007	1.072	0.059
	GN15	1.087	0.058
	New	1.011	0.056
Cover Concrete Crushing Unidirectional GN15 Dataset	PCK2007	0.799	0.152
	GN15	0.934	0.105
	New	0.784	0.143
Initial Confinement Steel Yielding Unidirectional GN15 Dataset	PCK2007	0.716	0.218
	GN15	0.890	0.190
	New	0.723	0.219
Longitudinal Bar Buckling Unidirectional GN15 Dataset	PCK2007	1.268	0.116
	GN15	1.124	0.061
	New	0.990	0.087

Table 16-9. Plastic Hinge Model Comparison in Combined Dataset, Statistics for Measured/Predicted Limit State Disp.

Limit State	Model	Mean Measured/Predicted	COV
Analytical First Yield Force Fy' Combined Dataset	PCK2007	1.145	0.087
	GN15	1.169	0.094
	New	1.079	0.084
Cover Concrete Crushing Combined Dataset	PCK2007	0.858	0.193
	GN15	1.017	0.177
	New	0.845	0.188
Initial Confinement Steel Yielding Combined Dataset	PCK2007	0.799	0.255
	GN15	1.006	0.250
	New	0.805	0.252
Longitudinal Bar Buckling Combined Dataset	PCK2007	1.291	0.091
	GN15	1.164	0.070
	New	0.989	0.072

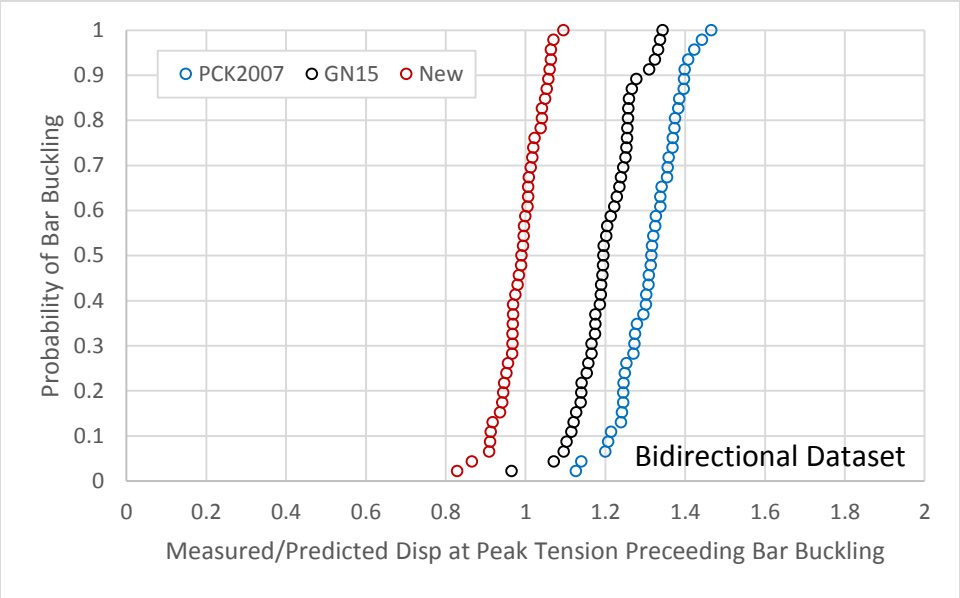

Figure 16-34. Bidirectional Dataset: Cumulative Probability Dist. for Meas/Pred Disp. at Measured Bar Buckling Strain

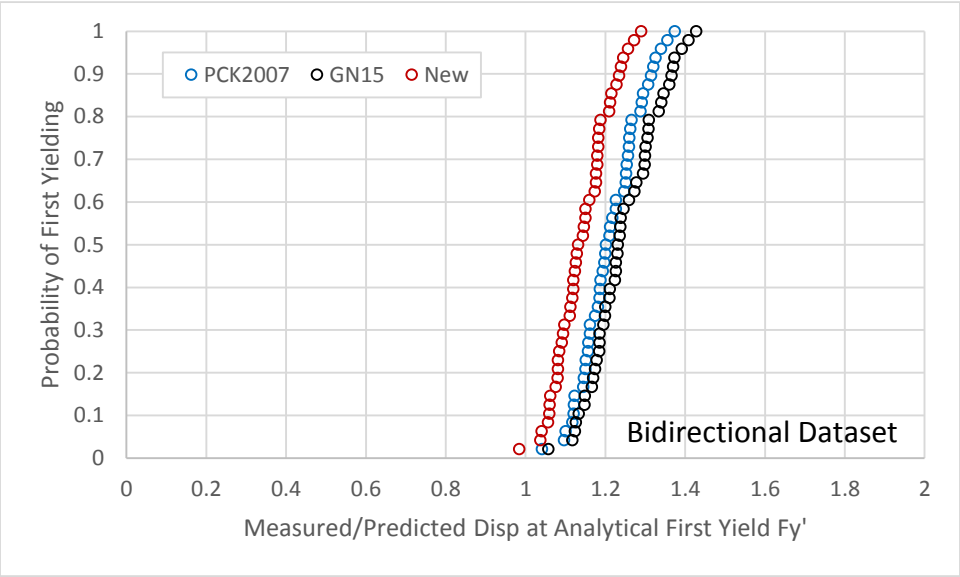

Figure 16-35. Bidirectional Dataset: Cumulative Probability Dist. for Meas/Pred Disp. at the Analytical First Yield Force

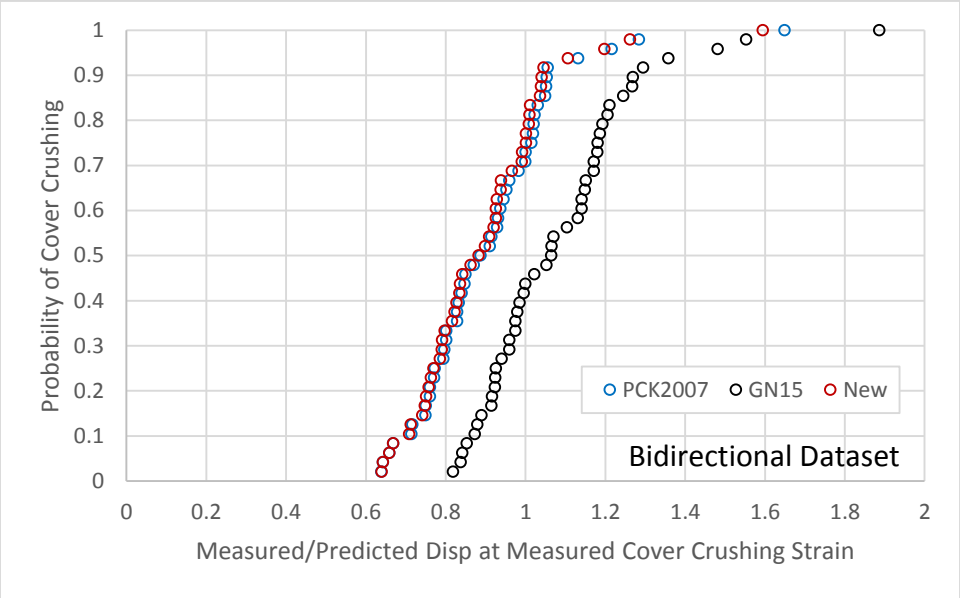

Figure 16-36. Bidirectional Dataset: Cumulative Probability Dist. for Meas/Pred Disp. at Measured Cover Crushing Strain

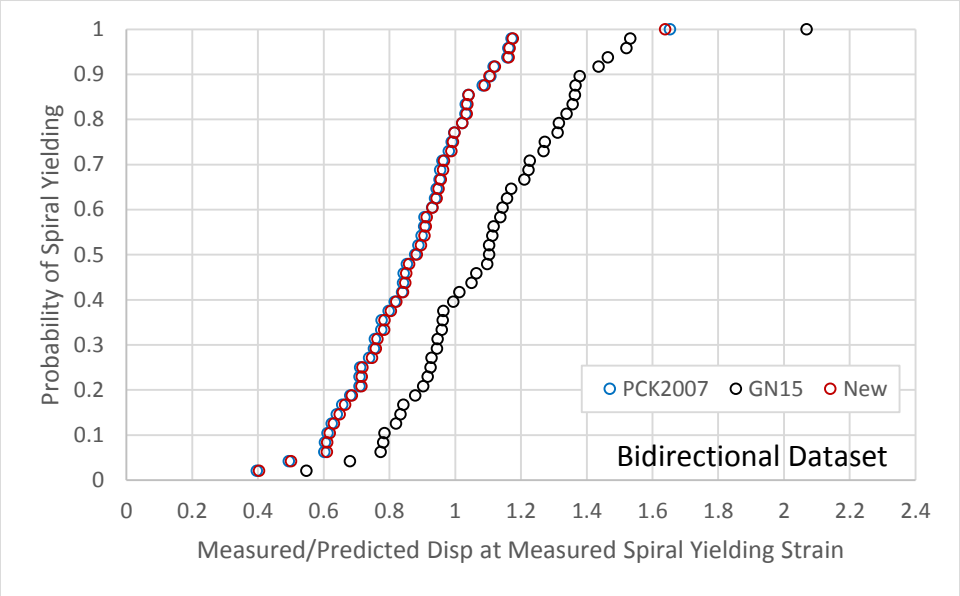

Figure 16-37. Bidirectional Dataset: Cumulative Probability Dist. for Meas/Pred Disp. at Measured Spiral Yielding Strain

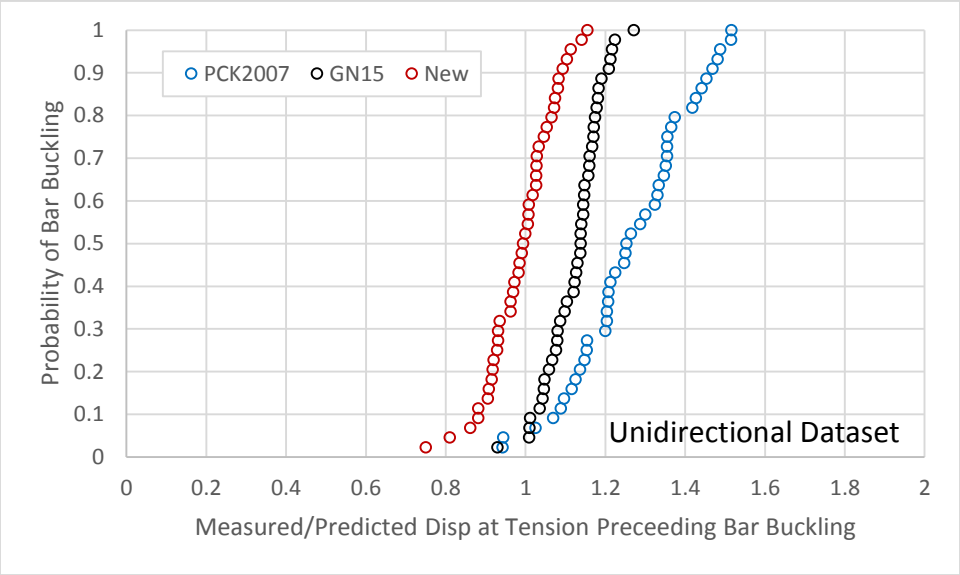

Figure 16-38. Unidirectional Dataset: Cumulative Probability Dist. for Meas/Pred Disp. at Measured Bar Buckling Strain

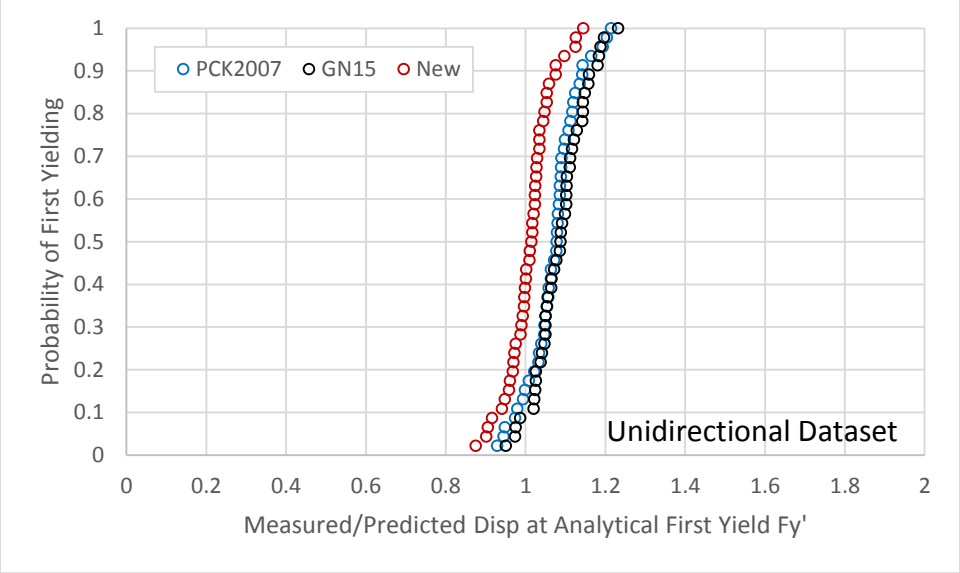

Figure 16-39. Unidirectional Dataset: Cumulative Probability Dist. for Meas/Pred Disp. at the Analytical First Yield Force

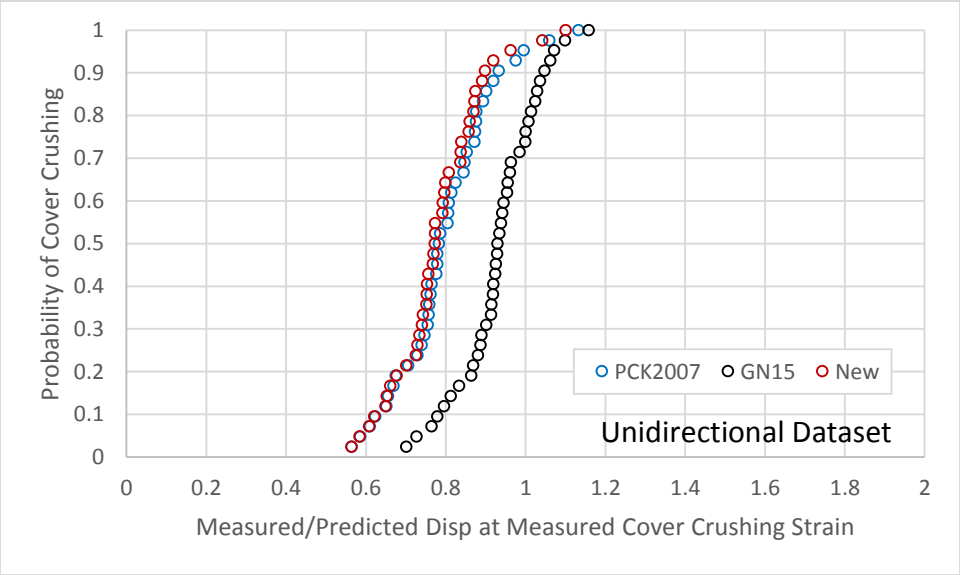

Figure 16-40. Unidirectional Dataset: Cumulative Probability Dist. for Meas/Pred Disp. at Measured Cover Crushing Strain

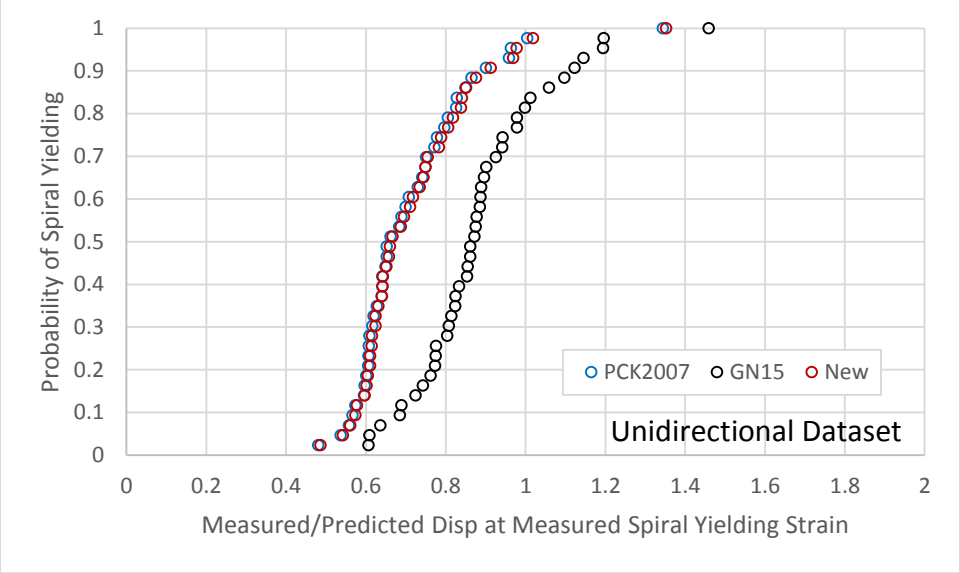

Figure 16-41. Unidirectional Dataset: Cumulative Probability Dist. for Meas/Pred Disp. at Measured Spiral Yielding Strain

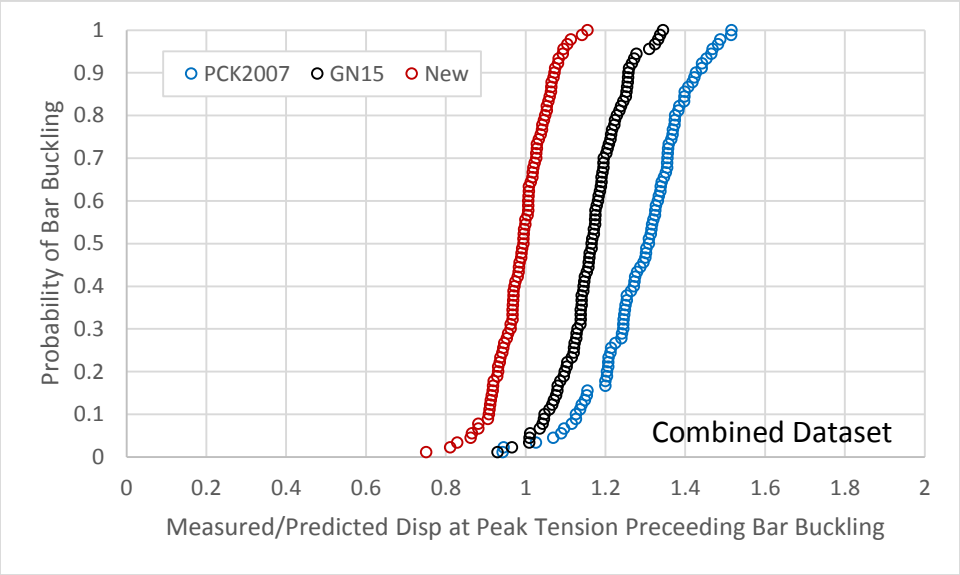

Figure 16-42. Combined Dataset: Cumulative Probability Dist. for Meas/Pred Disp. at Measured Bar Buckling Strain

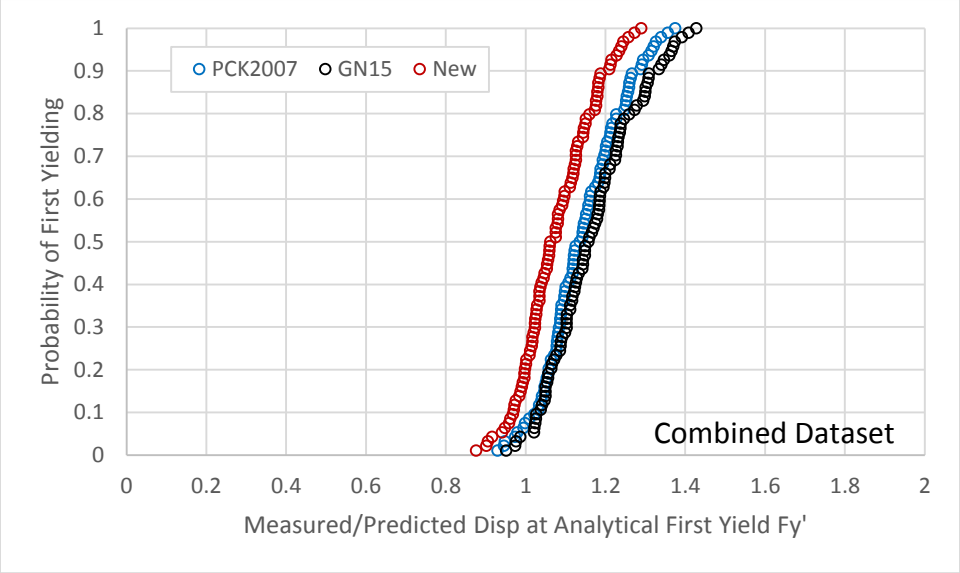

Figure 16-43. Combined Dataset: Cumulative Probability Dist. for Meas/Pred Disp. at the Analytical First Yield Force

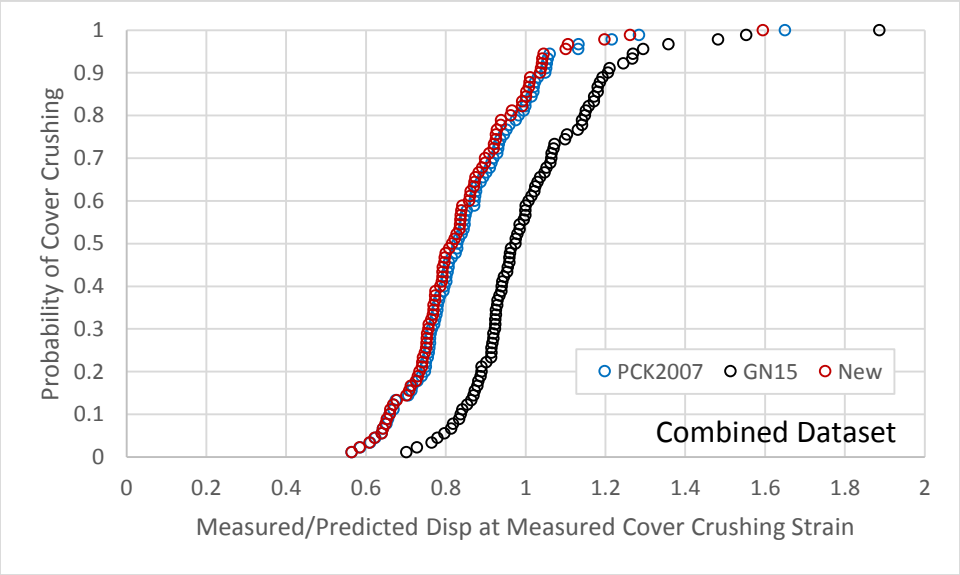

Figure 16-44. Combined Dataset: Cumulative Probability Dist. for Meas/Pred Disp. at Measured Cover Crushing Strain

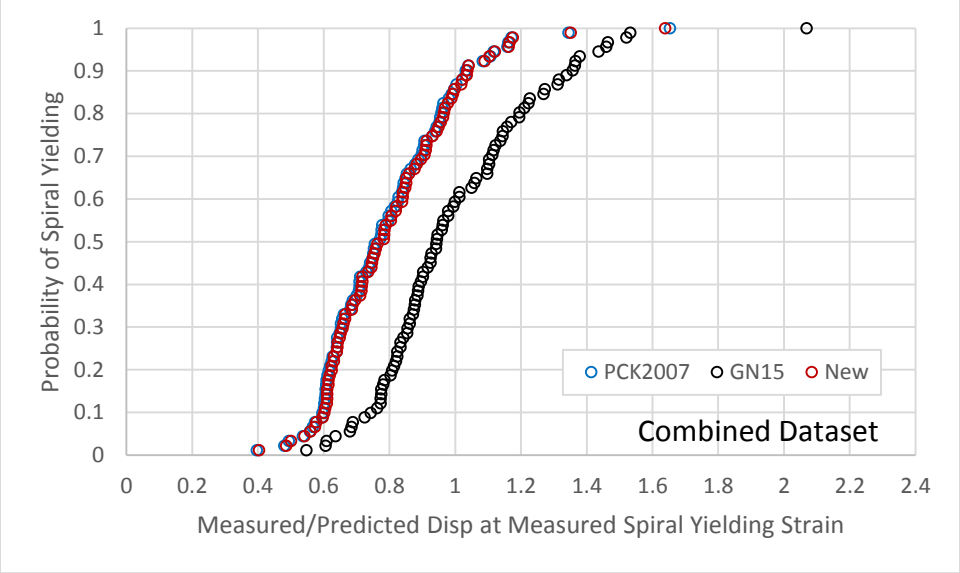

Figure 16-45. Combined Dataset: Cumulative Probability Dist. for Meas/Pred Disp. at Measured Spiral Yielding Strain

Design Recommendations for Performance Strain Limits

The observed damage and measured strain data for columns in the Bidirectional Dataset of this study and the Unidirectional Dataset of (Goodnight, Kowalsky and Nau 2015) were used to develop empirical expressions to predict material strains at key performance limit states. Recommendations from (Kowalsky 2000) and (Goodnight, Kowalsky and Nau 2015b) were evaluated, and when appropriate, new expressions were developed. The ultimate goal of these expressions was to provide mean value displacement predictions for the limit states of cover concrete crushing, initial yielding of confinement steel, and longitudinal bar buckling. Values of interests, material properties, and summaries of the measured limit state strains and displacements appear in Table 16-1 through Table 16-5 for the respective datasets.

Serviceability Limit States

When exceeded, serviceability limit states represent the point at which repair is necessary, interrupting the serviceability of the structure, but not posing a safety concern. The serviceability limit states are characterized by crushing of cover concrete and residual crack widths which exceed 1 mm, which require some degree of intervention to prevent corrosion of internal reinforcing steel. As a result of this study, no changes to the current serviceability strain limits proposed by (Kowalsky 2000) were warranted. The average measured compressive strain at cover concrete crushing was 0.0051, although crushing observations were made at the cycle peaks with larger measured strains.

$$\varepsilon_c = 0.004$$ *Concrete compression strain related to crushing of the cover concrete. Evaluated at the extreme compression fiber.* *Eqn 16-31*

$$\varepsilon_s = 0.015$$ *Steel tensile strain limit related to residual crack widths which exceed 1 mm. Evaluated at the extreme longitudinal reinforcing bar.* *Eqn 16-32*

Table 16-10. Bidirectional Dataset: Cover Concrete Crushing Displacement Predictions with Noted Plastic Hinge Methods

Limit State	Plastic Hinge Method	M/P Displacement in Bidirectional Dataset	
		Mean	COV
$\varepsilon_c = 0.004$ Cover Crushing	PCK (2007)	1.278	0.133
	GN15	1.476	0.141
	New	1.249	0.132

Table 16-11. Cover Concrete Crushing Displacement Predictions using the New Plastic Hinge Method

Limit State	Dataset	Measured/Predicted Displacement	
		Mean	COV
$\varepsilon_c = 0.004$ Cover Crushing	Bidirectional	1.249	0.132
	Unidirectional	0.902	0.143
	Combined	1.087	0.210

Cover concrete crushing displacement predictions in the Bidirectional Dataset of this study and the Unidirectional Dataset of (Goodnight, Kowalsky and Nau 2015) using Eqn 16-31 and the New Plastic Hinge Method appear in Table 16-11, Figure 16-46, and Figure 16-47. The recommended approach produced a mean measured to predicted displacement at cover crushing of 1.087 with a coefficient of variation of 0.210 for columns in the Combined Dataset. Predictions amongst the different column datasets are compared in Figure 16-49. Cover crushing displacement predictions in the Bidirectional Dataset using different plastic hinge methods are summarized in Table 16-10 and Figure 16-48. As discussed in the previous section, compressive strain-displacement predictions for the New Plastic Hinge Method default back to the method recommended in (Priestley, Calvi and Kowalsky 2007), except that the strain penetration block is centered at the footing-column interface in the triangular equivalent curvature geometry.

Intermediate Compressive Limit State Prompting a Change in Repair Strategy

Experimental results suggest that a localization of compressive demand can occur in regions with inelastic transverse steel. This localization can lead to compression strains which exceed predictions made using moment-curvature analysis and an equivalent curvature distribution. Furthermore, inelastic transverse steel restraint resulted in measureable outward deformation of longitudinal reinforcement prior to visible bar buckling observations. As a limit state, yielding of confinement steel prompts a change in repair strategy from epoxy injection of cracks and patching of cover concrete, to the need for additional transverse stiffness via either FRP wraps or steel jackets within the plastic hinge region. An expression which predicts the core concrete compressive strain at initial yielding of confinement steel was created in Eqn 16-33.

The limits of applicability of Eqn 16-33. can be stated as follows: $\left(P/A_g f_c' \leq 0.30\right)$, $\left(\rho_{eff} = \rho_s f_{yh}/f_c' \geq 0.05\right)$, $\left(\rho_l = A_{st}/A_g \leq 0.03\right)$, $(s/d_{bl} \leq 6)$, and $(cover/D \leq 0.1)$. Where $P/A_g f_c'$ is the axial load ratio, ρ_{eff} is the effective confinement ratio, $\rho_s = 4A_{sp}/D's$ is the transverse volumetric steel ratio, ρ_l is the longitudinal steel ratio, s/d_{bl} is the transverse steel spacing to longitudinal bar diameter ratio, $cover/D$ is the concrete cover to column diameter ratio, and L is the length from the critical section to the point of contraflexure. These limits reflect the datasets in which the method was compared to.

In the expression, A_{st}/A_g is the longitudinal reinforcement ratio and λ is a compression strain-displacement modification factor which makes the expression compatible with the New Plastic Method and the approach recommended in (Priestley, Calvi and Kowalsky 2007). The force required to maintain stability of higher levels of longitudinal reinforcement takes away from the remaining strain component utilized for core concrete confinement. Setting $\lambda = 1$ provides strains with match those observed in the physical tests, while selecting $\lambda = 0.8$ compensates for the unconservative compressive strain-displacement predictions in the noted plastic hinge methods, see Figure 16-45.

$$\varepsilon c_{sy} = \lambda\left(0.022 - 0.48\frac{A_{st}}{A_g}\right)$$

Concrete compression strain at initial yielding of confinement steel. Evaluated at the centerline of the transverse steel, i.e. the concrete core. Eqn 16-33

$\lambda = 1$ provides a strain which matches those measured experimentally at initial spiral yielding

$\lambda = 0.8$ provides a strain with is compatible with the New Plastic Hinge Method and PCK (2007)

Table 16-12. Bidirectional Dataset: Displacement at Initial Spiral Yielding Predictions with Noted Plastic Hinge Methods

Limit State	λ Eqn Modifier	Plastic Hinge Method	M/P Disp. in Bidirectional Dataset	
			Mean	COV
εc_{sy} Eqn 16-33 Initial Spiral Yielding	1	PCK (2007)	0.856	0.130
	1	GN15	1.059	0.145
	1	New	0.848	0.129
	0.8	New	1.015	0.133

Table 16-13. Spiral Yielding Strain and Displacement Predictions using the New Plastic Hinge Model

Limit State	Dataset	M/P Strain λ=1		M/P Disp. λ=0.8	
		Mean	COV	Mean	COV
εc_{sy} Eqn 16-33 Initial Spiral Yielding	Bidirectional	1.005	0.295	1.015	0.133
	Unidirectional	1.001	0.182	0.870	0.239
	Combined	1.003	0.247	0.945	0.198

Comparisons of the measured compressive strains at initial spiral yielding and those predicted using Eqn 16-33 with $\lambda = 1$ in the Bidirectional and Unidirectional Datasets appear in Figure 16-50 and Figure 16-52, respectively. Initial spiral yielding displacement comparisons made using Eqn 16-33 with $\lambda = 0.8$ and the New Plastic Hine Method are shown in Figure 16-51 and Figure 16-53. Here the influence of the compressive strain-displacement modification factor λ is apparent, shifting predictions closer to the measured values. A cumulative probability distribution plotting the accuracy of Eqn 16-33 with $\lambda = 1$ in predicting the measured compressive strains at initial spiral yielding in the Combined Dataset is shown in Figure 16-54, alongside predictions made using recommendations in (Goodnight, Kowalsky and Nau 2015b). Predictions for individual datasets appear in Figure 16-55. The new approach produces a mean measured to predicted core concrete compressive strain at initial spiral yielding of 1.003 with a coefficient of variation of 0.247 in the Combined Dataset.

A full comparison of the strain and displacement predictive capacity of the approach is summarized in Table 16-13 for the Bidirectional, Unidirectional, and Combined Datasets. Statistics for initial spiral yielding displacement predictions within the Bidirectional Dataset with the noted plastic hinge methods appear in Table 16-12. This data is presented graphically in Figure 16-56. Comparisons of the impact of the compressive strain-displacement modification factor λ for displacement predictions within the Unidirectional and Combined Datasets are shown in Figure 16-57 and Figure 16-58, respectively. Comparisons of initial spiral yielding displacement predictions in the noted datasets using Eqn 16-33 with $\lambda = 0.8$ and the New Plastic Hine Method are shown in Figure 16-59.

The approach produces mean measured to predicted spiral yielding displacement of 1.015 with a coefficient of variation of 0.133 in the Bidirectional Dataset, but conservatively predicts the behavior measured in the Unidirectional Dataset, as indicated by the mean of 0.870 and coefficient of variation of 0.239. The majority of columns in design will be subjected to bidirectional hazards, which is why the compressive strain-displacement modification factor λ was selected to fit to the Bidirectional Dataset.

Damage Control Limit States

The damage control limit state represents the limit of economical repair, and is defined by longitudinal bar buckling or significant damage to the core concrete. Bar buckling was observed to occur after reversal from a peak tensile strain while the bar was under net elongation, but compressive stress. Although prior compression was important to describing the restraint provided by transverse steel, expression developed based on the peak tensile strain before bar buckling upon reversal of load were found to produce the most accurate results. Furthermore, higher levels of tensile strain reduce the tangent modulus of the reinforcement during the subsequent stress reversal.

Using the measured reinforcement strains in both column datasets, an expression for the peak tensile strain preceding bar buckling, Eqn 16-34, was developed. In the expression, $\rho_s = 4A_{sp}/D's$ is the transverse volumetric steel ratio, f_{yhe}/E_s is the yield strain of the transverse steel, and $P/f'_{ce}A_g$ is the axial load ratio. These parameters are known or may be reasonably approximated at the onset of design, and later confirmed after finalizing the transverse steel detailing. As a prediction, expected material properties should be used. Sufficient confinement steel should be provided such that the (Mander, Priestley and Park 1988) Ultimate Concrete Compressive Strain, in Eqn 16-35, exceeds the core concrete strain at the bar buckling displacement, otherwise it becomes the damage control limit state. As a prediction, expected material properties should also be used in Eqn 16-35, refer to (Mander, Priestley and Park 1988) for additional details.

The limits of applicability of Eqn 16-34 can be stated as follows: $\left(P/A_g f'_c \leq 0.30\right)$, $\left(\rho_{eff} = \rho_s f_{yh}/f'_c \geq 0.05\right)$, $\left(\rho_l = A_{st}/A_g \leq 0.04\right)$, $(s/d_{bl} \leq 6)$, and $(cover/D \leq 0.1)$. Where $P/A_g f'_c$ is the axial load ratio, ρ_{eff} is the effective confinement ratio, $\rho_s = 4A_{sp}/D's$ is the transverse volumetric steel ratio, ρ_l is the longitudinal steel ratio, s/d_{bl} is the transverse steel spacing to longitudinal bar diameter ratio, $cover/D$ is the concrete cover to column diameter ratio, and L is the length from the critical section to the point of contraflexure. These limits reflect the datasets in which the method was compared to.

$$\varepsilon s_{bb} = 0.032 + 790\rho_s \frac{f_{yhe}}{E_s} - 0.14\frac{P}{f'_{ce}A_g}$$

Peak tension strain prior to bar buckling. Evaluated at the location of the extreme longitudinal reinforcing bar. Eqn 16-34

$$\varepsilon c_u = 0.004 + \frac{1.4\rho_s f_{yhe}\varepsilon_{uh}}{f'_{cce}}$$

Mander et al. (1988) Ultimate Concrete Compressive Strain. Evaluated at the centerline of the transverse steel, i.e. the concrete core. See reference for additional details. Eqn 16-35

Table 16-14. Bidirectional Dataset: Bar Buckling Displacement Predictions with Noted Plastic Hinge Methods

Limit State	Plastic Hinge Method	M/P Displacement in Bidirectional Dataset	
		Mean	COV
εs_{bb} Eqn 16-34 Bar Buckling	PCK (2007)	1.320	0.118
	GN15	1.206	0.098
	New	0.993	0.111

Table 16-15. Bar Buckling Strain and Displacement Predictions using the New Plastic Hinge Model

Limit State	Dataset	M/P Strain		M/P Displacement	
		Mean	COV	Mean	COV
εs_{bb} Eqn 16-34 Bar Buckling	Bidirectional	1.006	0.119	0.993	0.111
	Unidirectional	1.006	0.167	1.012	0.187
	Combined	1.006	0.143	1.002	0.153

Table 16-16. Bar Buckling Strain and Displacement Predictions using the New Plastic Hinge Model

Limit State	Dataset	M/P Peak Displacement Preceding Bar Buckling	
		Mean	COV
Mander et al. (1988) ε_{cu} in Eqn 16-35	Bidirectional	0.993	0.140
	Unidirectional	0.936	0.189
	Combined	0.965	0.166

A comparison of the measured peak tensile strains preceding bar buckling and those predicted using Eqn 16-34 in the Bidirectional and Unidirectional Datasets appears in Figure 16-60 and Figure 16-62, respectively. Comparisons of the measured peak tensile displacement preceding bar buckling and those predicted using Eqn 16-34 and the New Plastic Hinge Method are shown in Figure 16-61 and Figure 16-63. Displacements at which the (Mander, Priestley and Park 1988) ε_{cu} from Eqn 16-35 was reached when evaluated using the New Plastic Hinge model also appear in the figures.

A full comparison of the strain and displacement predictive capacity of the peak tensile bar buckling strain approach is summarized in Table 16-15 for the Bidirectional, Unidirectional, and Combined Datasets. Statistics for predictions of the peak tensile displacement preceding bar buckling within the Bidirectional Dataset with the noted plastic hinge methods appear in Table 16-14. Statistics for the measured to predicted peak displacement preceding bar buckling evaluated using the (Mander, Priestley and Park 1988) ε_{cu} in Eqn 16-35 and the New Plastic Hinge Method are summarized in Table 16-16. In design, the smaller of the two displacements represents the damage control level.

A cumulative probability distribution which plots the measured to predicted peak tensile strain preceding bar buckling in the Combined Dataset using either Eqn 16-34 or recommendations from (Goodnight, Kowalsky and Nau 2015b) is shown in Figure 16-64. The new approach produces a mean measured to predicted peak tensile strain preceding bar buckling of 1.006 with a coefficient of variation of 0.143 within the Combined Dataset. Strain predictions with this approach in individual datasets are shown in Figure 16-65.

Predictions for the peak tensile displacement preceding bar buckling in the Bidirectional Dataset using Eqn 16-34 with the noted plastic hinge methods appear in Figure 16-66. Cumulative probability distributions for measured to predicted peak tensile displacement preceding bar buckling using Eqn 16-34 and the New Plastic Hinge Method for the Bidirectional, Unidirectional, and Combined Datasets appear in Figure 16-67. The new approach produces a mean measured to predicted peak tensile displacement preceding bar buckling of 1.002 with a coefficient of variation of 0.153 within the Combined Dataset.

Finally, comparisons of measured to predicted peak displacements preceding bar buckling evaluated using the (Mander, Priestley and Park 1988) ε_{cu} in Eqn 16-35 and the New Plastic Hinge Model appear in Figure 16-68 and Table 16-16.

Bar Buckling Displacement Predictions for the (Berry 2006) PEER Column Dataset

Bar buckling predictions were made within the (Berry 2006) Bridge Column Subset of the PEER Column Database. Details of this dataset including references for individual tests appear in Table 16-18. Columns in the dataset conformed to the following criteria: $\left(P/A_g f_c' \leq 0.30\right)$, $\left(\rho_{eff} = \rho_s f_{yh}/f_c' \geq 0.05\right)$, $\left(\rho_l = A_{st}/A_g \leq 0.04\right)$, $(s/d_{bl} \leq 6)$, and $(cover/D \leq 0.1)$. Where $P/A_g f_c'$ is the axial load ratio, ρ_{eff} is the effective confinement ratio, $\rho_s = 4A_{sp}/D's$ is the transverse volumetric steel ratio, ρ_l is the longitudinal steel ratio, s/d_{bl} is the transverse steel spacing to longitudinal bar diameter ratio, $cover/D$ is the concrete cover to column diameter ratio, and L is the length from the critical section to the point of contraflexure. Bar buckling displacement predictions within the dataset are summarized in Table 16-17 and Figure 16-69. For this dataset, the New Plastic Hinge Method combined with the (Mander, Priestley and Park 1988) ε_{cu} in Eqn 16-35 produced the most accurate bar buckling displacement predictions. Of the two peak tensile strain preceding bar buckling approaches, the new method recommended in this study produced the most accurate results.

Table 16-17. Bar Buckling Displacement Predictions within the (Berry 2006) PEER Column Dataset

Dataset	Approach	Measured/Predicted Bar Buckling Displacement	
		Mean	COV
(Berry 2006) PEER Bridge Columns	New Bar Buckling Eqn and New Plastic Hinge Method	1.191	0.324
	Mander et al. (1988) εcu and New Plastic Hinge Method	0.975	0.252
	GN15 Bar Buckling Eqn and GN15 Plastic Hinge Method	1.250	0.271

Table 16-18. (Berry 2006) PEER Column Dataset

Reference, Specimen Designation	Dia. (mm)	Length (mm)	f_{yh} (MPa)	f_y (MPa)	f_u (MPa)	f'_c (MPa)	d_{bl} (mm)	$\frac{A_{st}}{A_g}$	$\frac{4A_{sp}}{D's}$	$\frac{P}{f'_c A_g}$	Δ_{bb} (mm)	$\frac{\Delta_{bb}}{L}$
Wong et al. 1990, No. 1	400	800	300	423	577	38.0	16	0.032	0.015	0.19	40	0.050
Stone & Cheok 1989, Flexure	1520	9140	493	475	1.4 f_y	35.8	43	0.02	0.006	0.069	538	0.059
Stone & Cheok 1989, Shear	1520	4570	435	475	1.4 f_y	34.3	43	0.02	0.015	0.071	285	0.062
Cheok and Stone 1986, N1	250	750	441	446	1.4 f_y	24.1	7	0.02	0.015	0.101	77.2	0.103
Cheok and Stone 1986, N2	250	750	441	446	1.4 f_y	23.1	7	0.02	0.015	0.211	44.7	0.060
Cheok and Stone 1986, N3	250	1500	441	476	1.4 f_y	25.4	7	0.02	0.007	0.096	102.4	0.068
Cheok and Stone 1986, N4	250	750	441	446	1.4 f_y	24.4	7	0.02	0.015	0.1	53.3	0.071
Cheok and Stone 1986, N5	250	750	441	446	1.4 f_y	24.3	7	0.02	0.015	0.2	48.3	0.064
Cheok and Stone 1986, N6	250	1500	476	446	1.4 f_y	23.3	7	0.02	0.007	0.105	67.2	0.045
Kunnath et al. 1997, A2	305	1372	434	448	690	29	9.5	0.02	0.01	0.094	68.3	0.050
Kunnath et al. 1997, A4	305	1372	434	448	690	35.5	9.5	0.02	0.01	0.086	57	0.042
Kunnath et al. 1997, A5	305	1372	434	448	690	35.5	9.5	0.02	0.01	0.086	75	0.055
Kunnath et al. 1997, A6	305	1372	434	448	690	35.5	9.5	0.02	0.01	0.086	75	0.055
Kunnath et al. 1997, A7	305	1372	434	448	690	32.8	9.5	0.02	0.01	0.093	80	0.058
Kunnath et al. 1997, A8	305	1372	434	448	690	32.8	9.5	0.02	0.01	0.093	80	0.058
Kunnath et al. 1997, A9	305	1372	434	448	690	32.5	9.5	0.02	0.01	0.093	63	0.046
Kunnath et al. 1997, A10	305	1372	434	448	690	27	9.5	0.02	0.01	0.101	82	0.060
Kunnath et al. 1997, A12	305	1372	434	448	690	27	9.5	0.02	0.01	0.101	81	0.059
Hose et al. 1997, SRPH1	610	3660	414	455	746	41.1	22.2	0.026	0.009	0.148	320	0.087
Kowalsky et al. 1997, FL3	457	3656	445	477	620	38.6	15.9	0.036	0.009	0.281	340	0.093
Lehman et al. 1998, 415	610	2438	607	462	630	31	15.9	0.015	0.007	0.072	127	0.052
Lehman et al. 1998, 815	610	4877	607	462	630	31	15.9	0.015	0.007	0.072	445	0.091
Lehman et al. 1998, 1015	610	6096	607	462	630	31	15.9	0.015	0.007	0.072	635	0.104
Lehman et al. 1998, 407	610	2438	607	462	630	31	15.9	0.007	0.007	0.072	127	0.052
Lehman et al. 1998, 430	610	2438	607	462	630	31	15.9	0.03	0.007	0.072	178	0.073
Calderone et al. 2000, 328	610	1829	607	441	602	34.5	19	0.027	0.009	0.091	125	0.068
Calderone et al. 2000, 828	610	4877	607	441	602	34.5	19	0.027	0.009	0.091	465	0.095
Calderone et al. 2000, 1028	610	6096	607	441	602	34.5	19	0.027	0.009	0.091	889	0.146
Henry and Mahin 1999, 415p	610	2438	607	462	1.4 f_y	37.2	15.9	0.015	0.007	0.12	127	0.052
Henry and Mahin 1999, 415s	610	2438	607	462	1.4 f_y	37.2	15.9	0.015	0.004	0.06	127	0.052
Ang et al. 1981, No. 1	400	1600	308	308	465	26	16	0.026	0.008	0.208	60	0.038
Vu et al. 1998, NH3	457	910	430	428	1.4 f_y	39.4	15.9	0.024	0.012	0.15	50	0.055
Moyer & Kowalsky 2003, C1	457	2438	434	565	696	32.7	19.1	0.021	0.009	0.043	149.9	0.061
Moyer & Kowalsky 2003, C2	457	2438	434	565	696	34.2	19.1	0.021	0.009	0.043	261.6	0.107
Moyer & Kowalsky 2003, C3	457	2438	434	565	696	31.7	19.1	0.021	0.009	0.043	261.9	0.107
Moyer & Kowalsky 2003, C4	457	2438	434	565	696	33.9	19.1	0.021	0.009	0.043	335.3	0.138

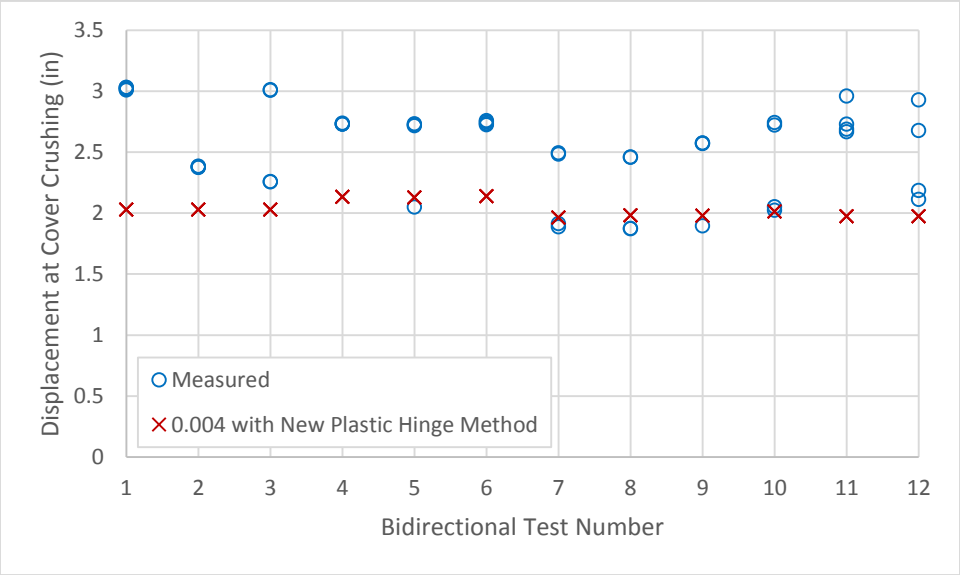

Figure 16-46. Bidirectional Dataset: Predictions for Displacement at Cover Concrete Crushing

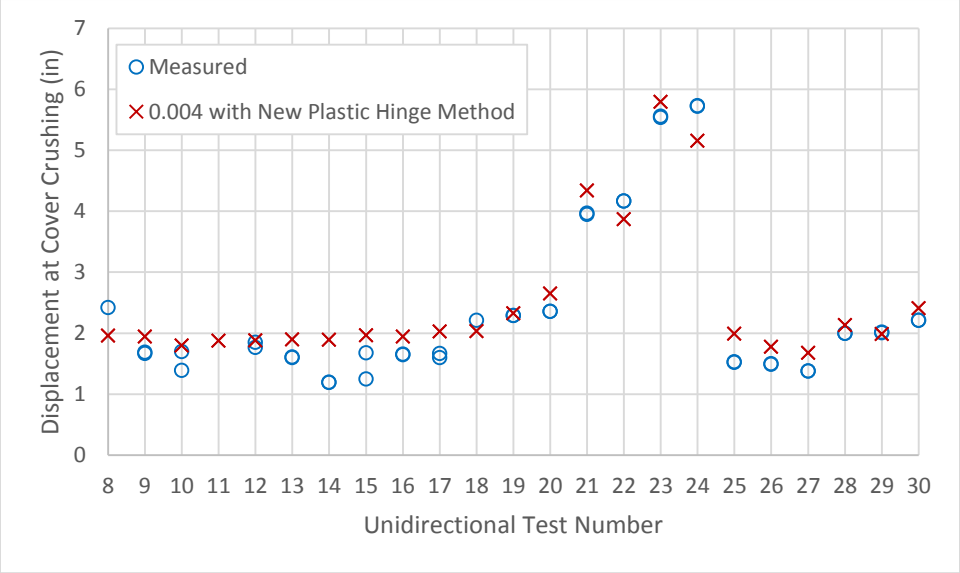

Figure 16-47. Unidirectional Dataset: Predictions for Displacement at Cover Concrete Crushing

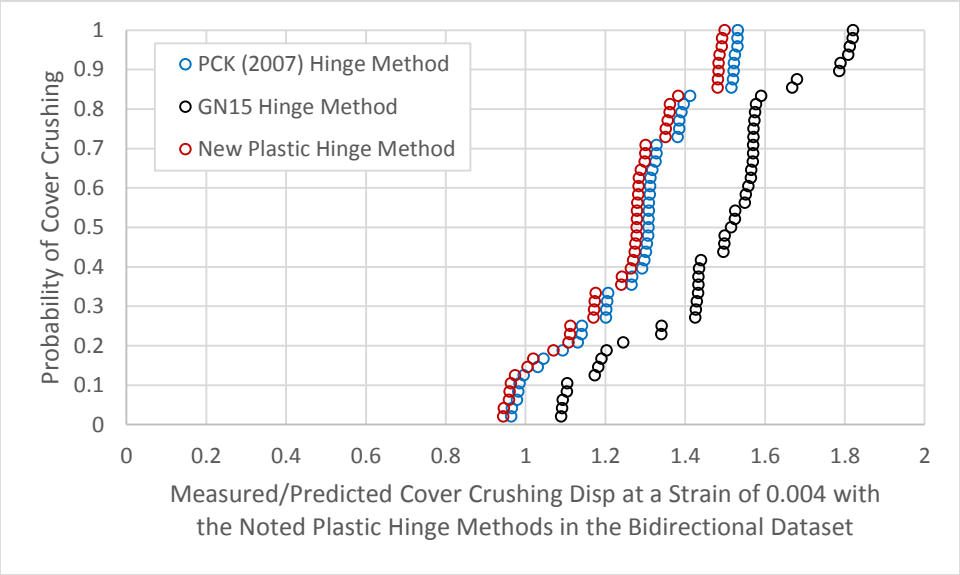

Figure 16-48. Bidirectional Dataset: Predictions for Cover Crushing Disp. with Noted Hinge Methods

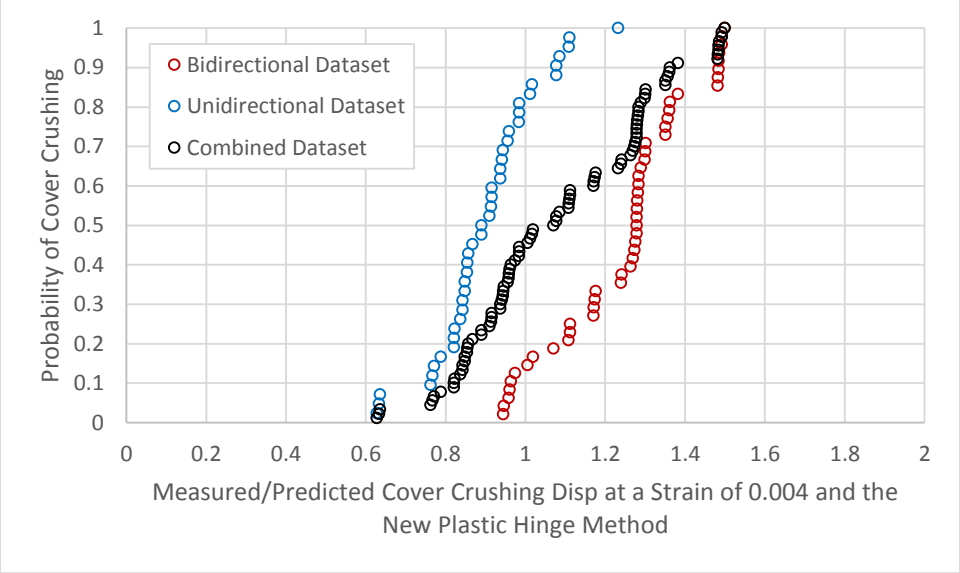

Figure 16-49. Predictions for Cover Crushing Disp. in Noted Datasets with the New Plastic Hinge Method

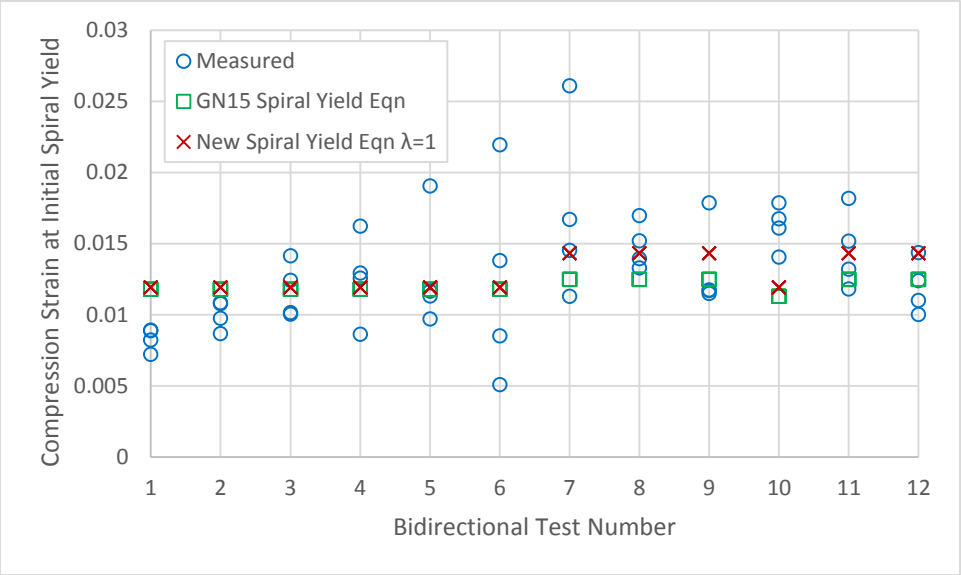

Figure 16-50. Bidirectional Dataset: Predictions for Compression Strain at Initial Confinement Steel Yielding

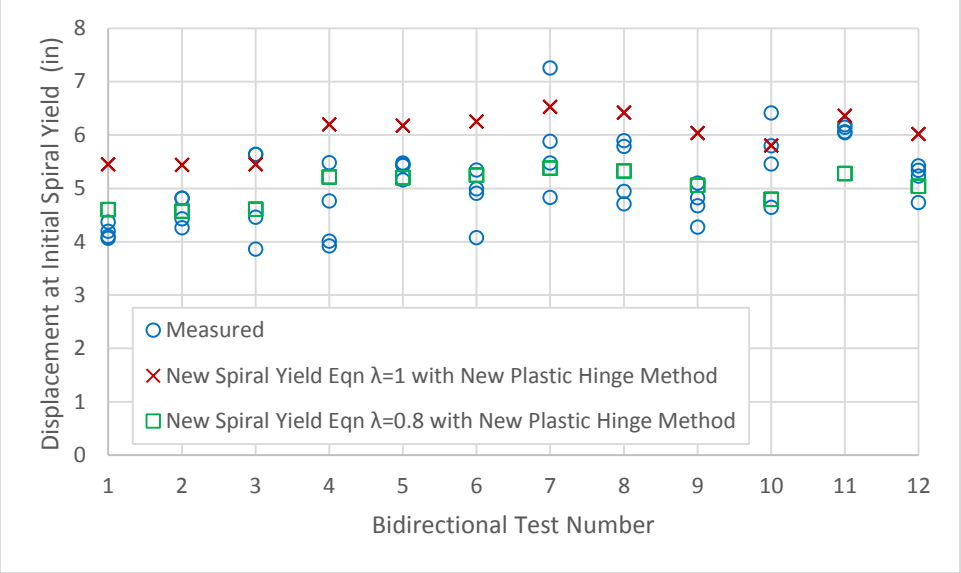

Figure 16-51. Bidirectional Dataset: Predictions for the Displacement at Initial Confinement Steel Yielding

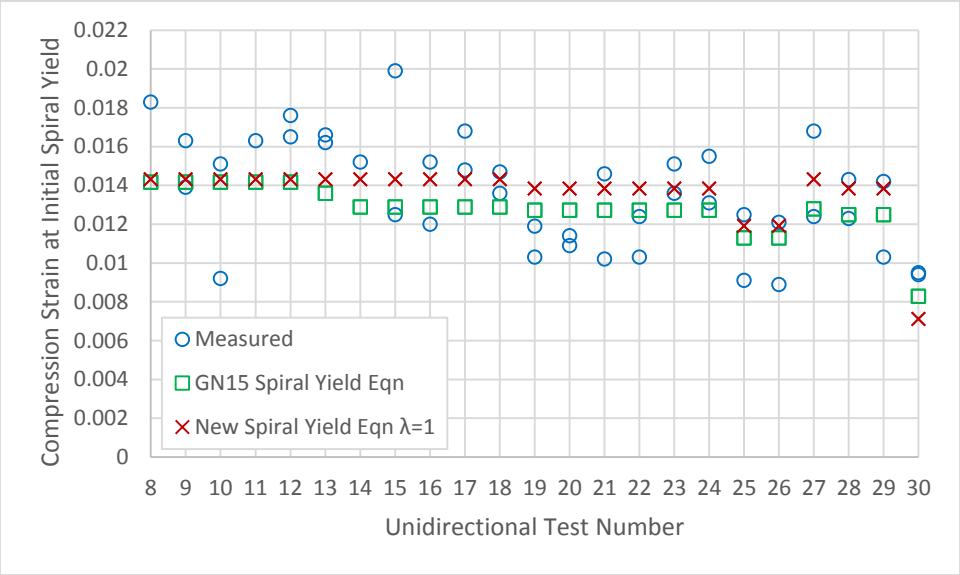

Figure 16-52. Unidirectional Dataset: Predictions for Compression Strain at Initial Confinement Steel Yielding

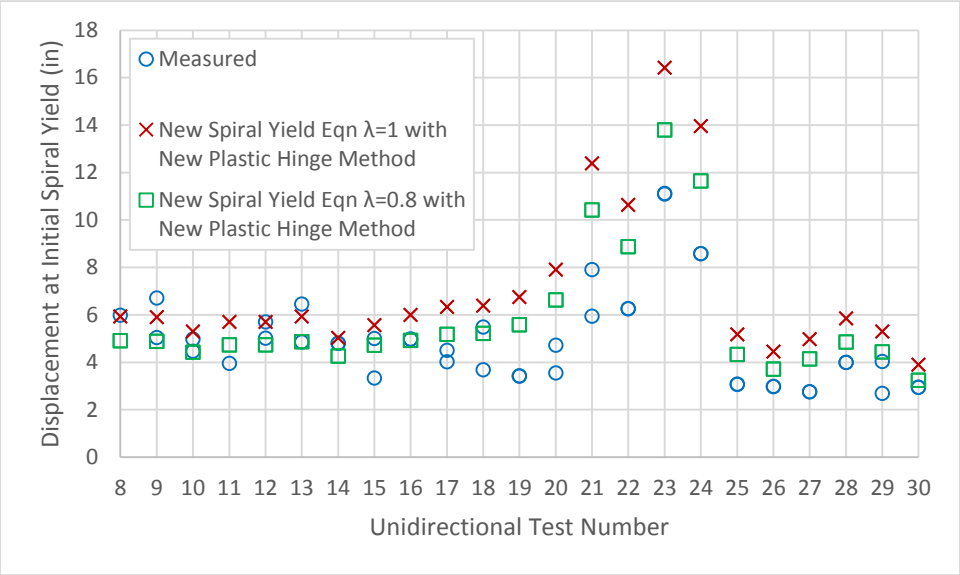

Figure 16-53. Unidirectional Dataset: Predictions for the Displacement at Initial Confinement Steel Yielding

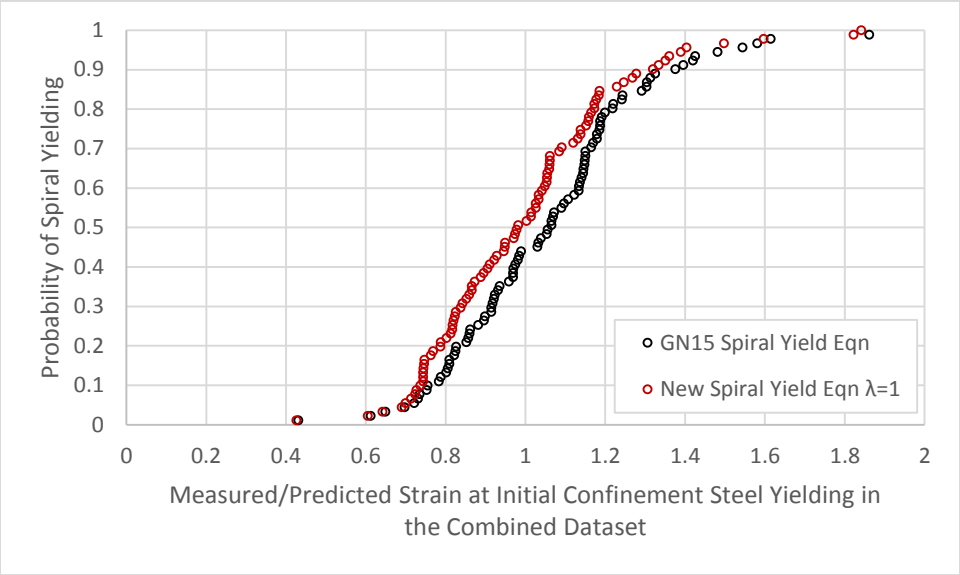

Figure 16-54. Combined Dataset: Predictions for Compression Strain at Initial Confinement Steel Yielding

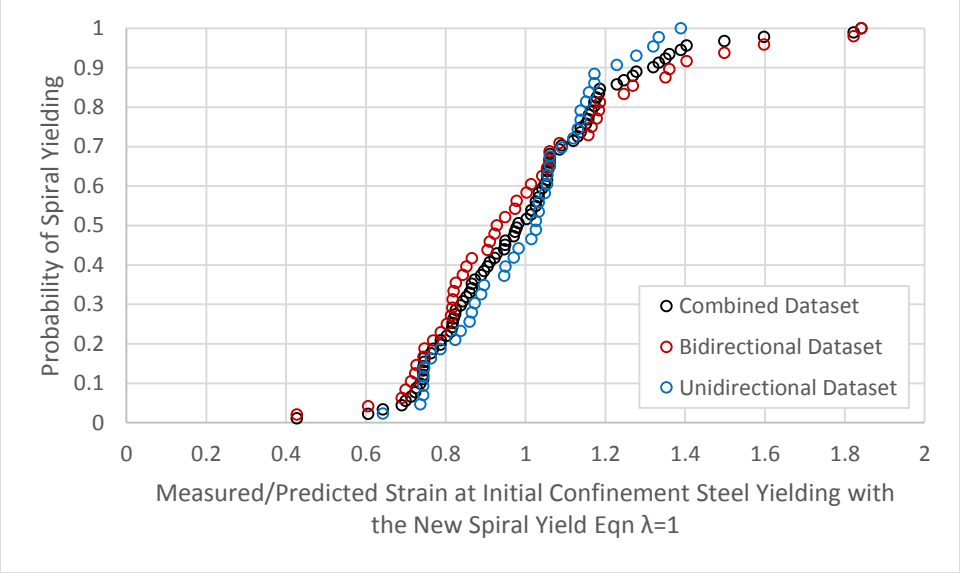

Figure 16-55. Predictions for Compressive Strain at Initial Spiral Yielding in the Noted Datasets

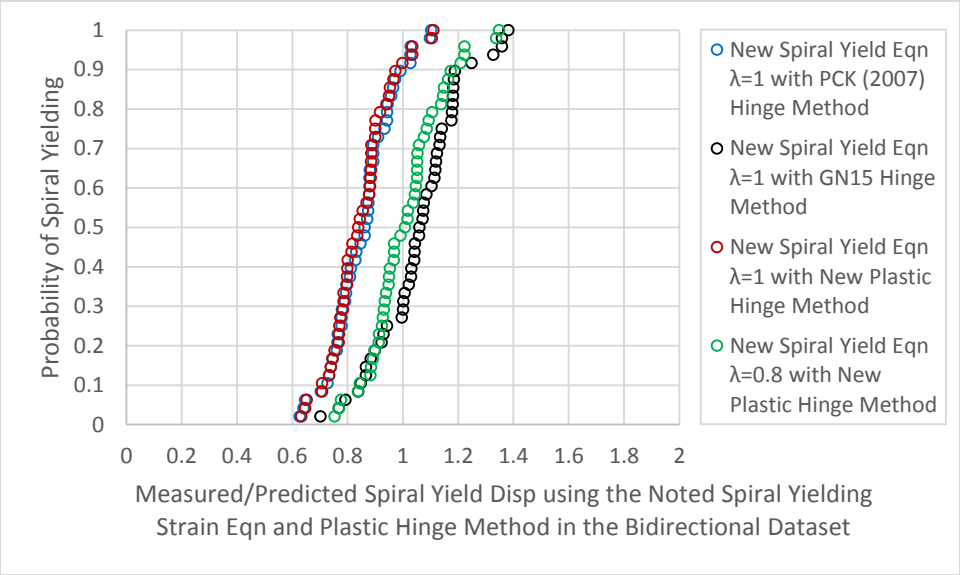

Figure 16-56. Bidirectional Dataset: Predictions for the Displacement at Initial Confinement Steel Yielding

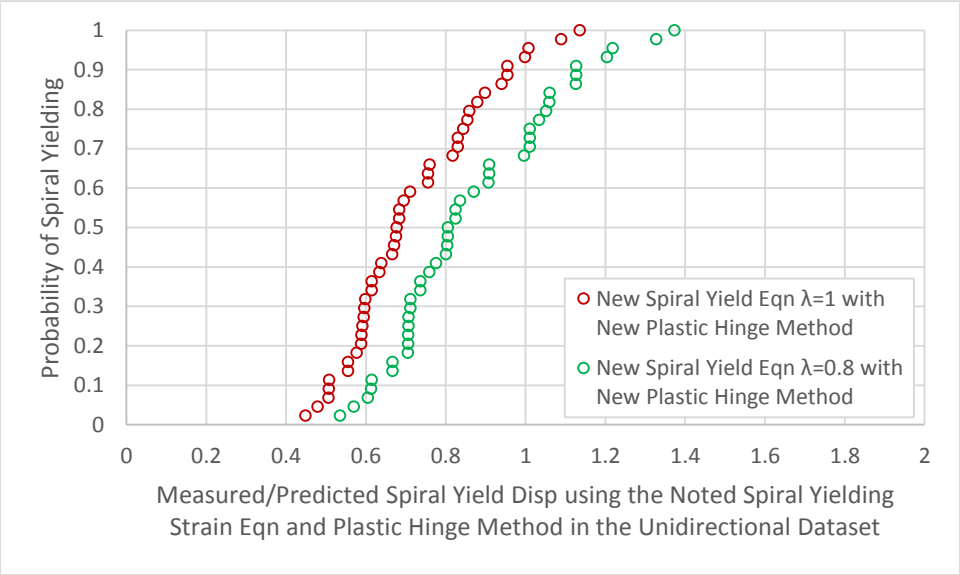

Figure 16-57. Unidirectional Dataset: Predictions for the Displacement at Initial Confinement Steel Yielding

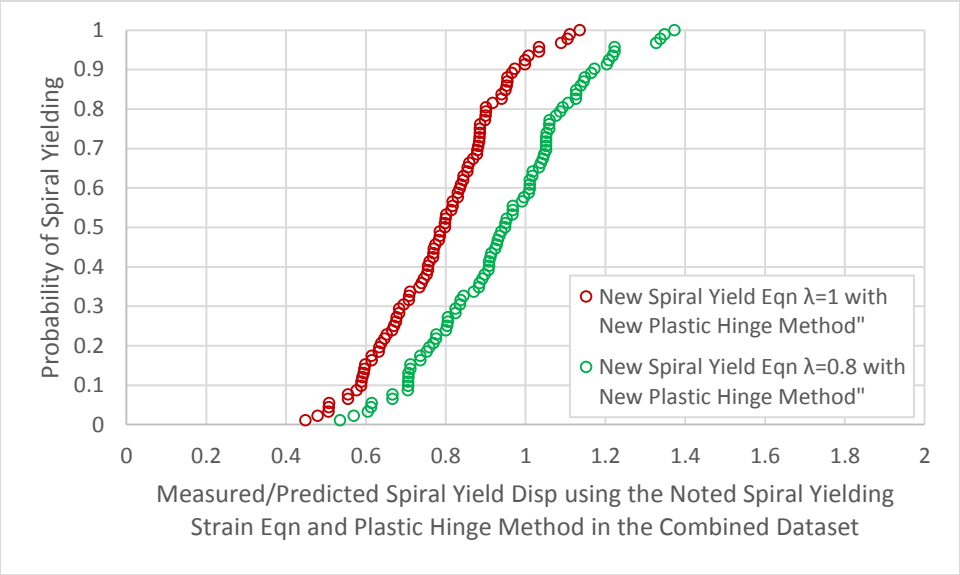

Figure 16-58. Combined Dataset: Predictions for the Displacement at Initial Confinement Steel Yielding

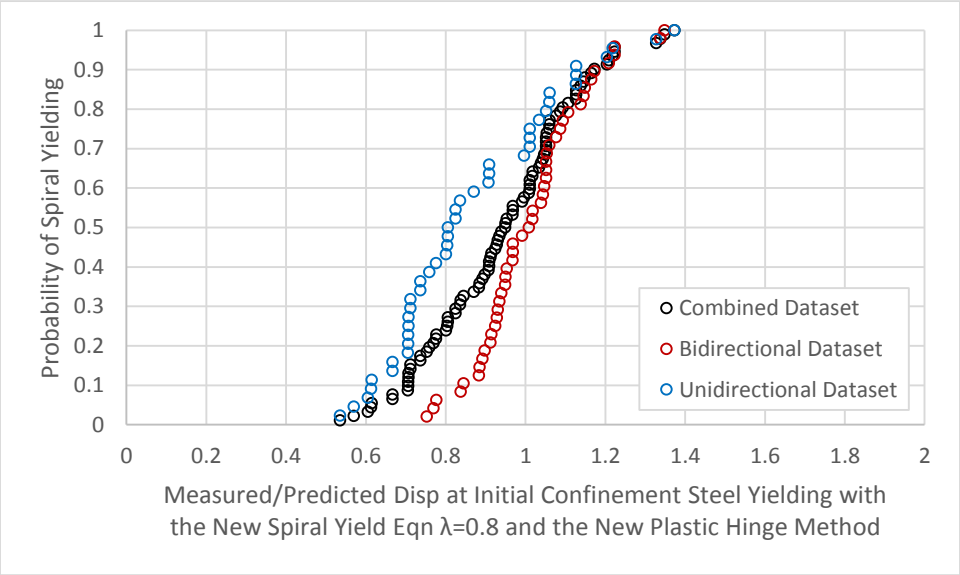

Figure 16-59. Predictions for the Displacement at Initial Confinement Steel Yielding in Noted Datasets

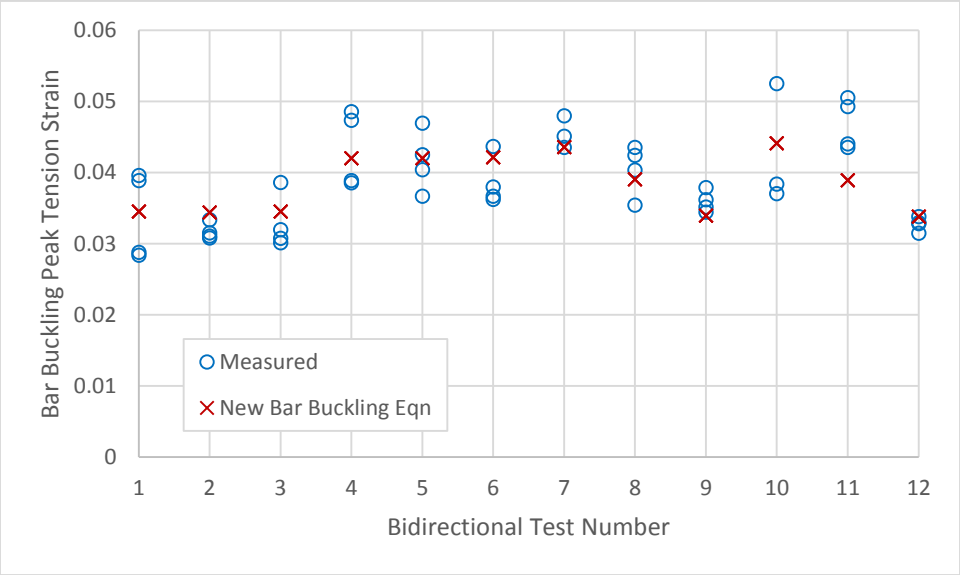

Figure 16-60. Bidirectional Dataset: Predictions for the Bar Buckling Peak Tensile Strain

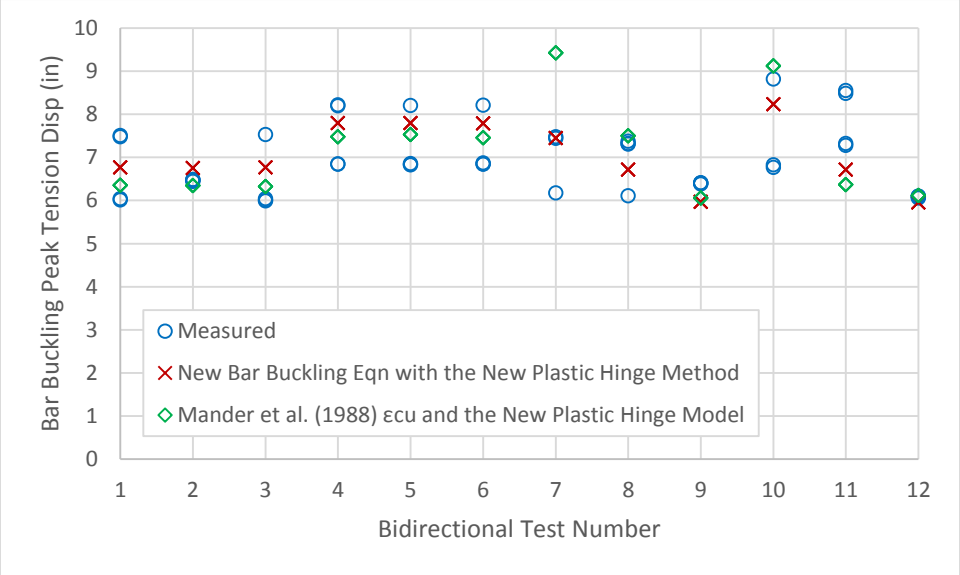

Figure 16-61. Bidirectional Dataset: Predictions for the Bar Buckling Peak Tensile Displacement

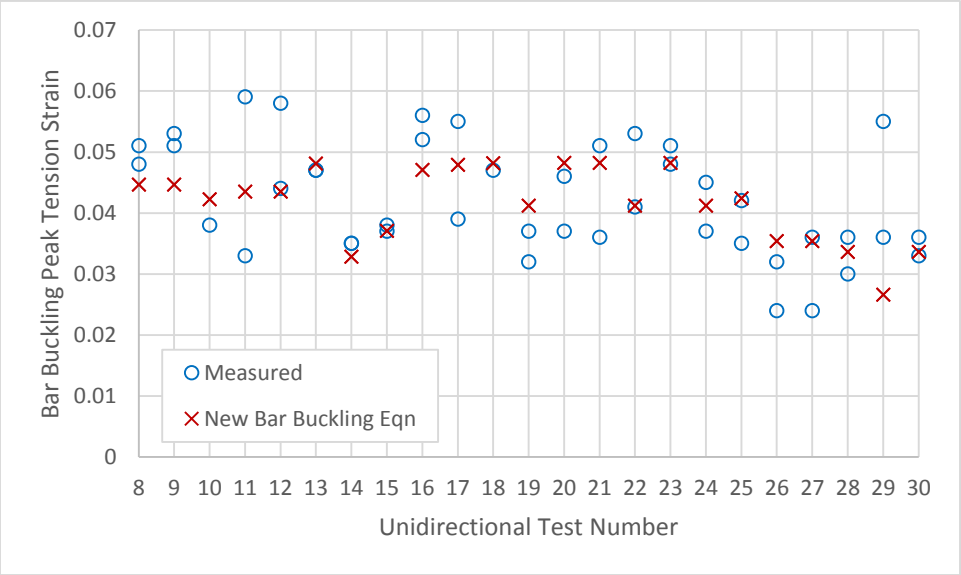

Figure 16-62. Unidirectional Dataset: Predictions for the Bar Buckling Peak Tensile Strain

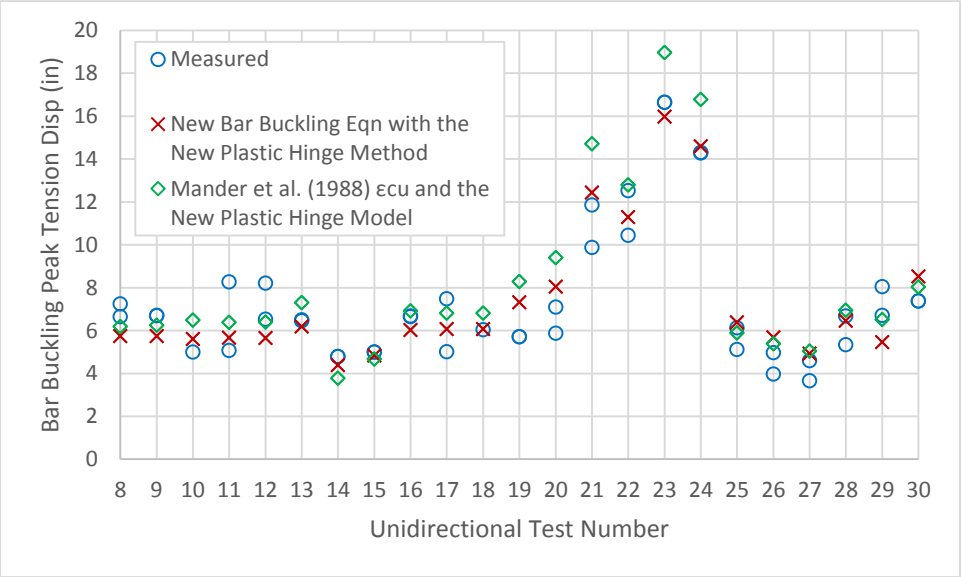

Figure 16-63. Unidirectional Dataset: Predictions for the Bar Buckling Peak Tensile Displacement

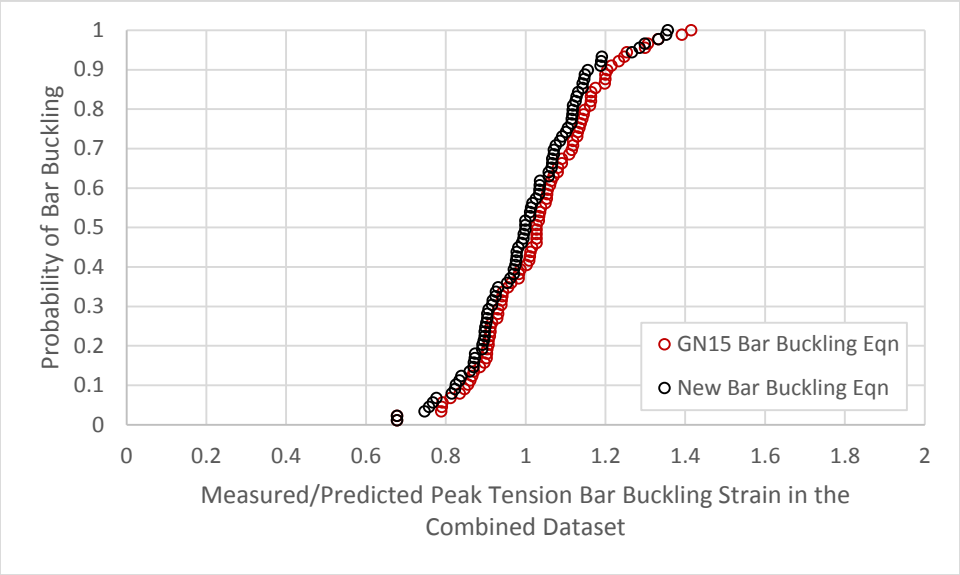

Figure 16-64. Combined Dataset: Predictions for the Bar Buckling Peak Tensile Strain

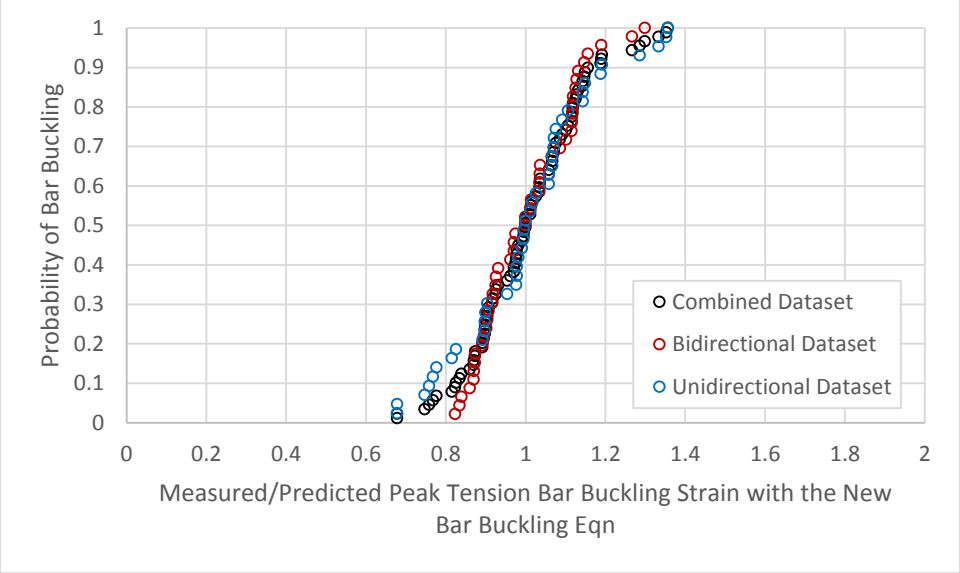

Figure 16-65. Predictions for the Bar Buckling Peak Tensile Strain in the Noted Datasets

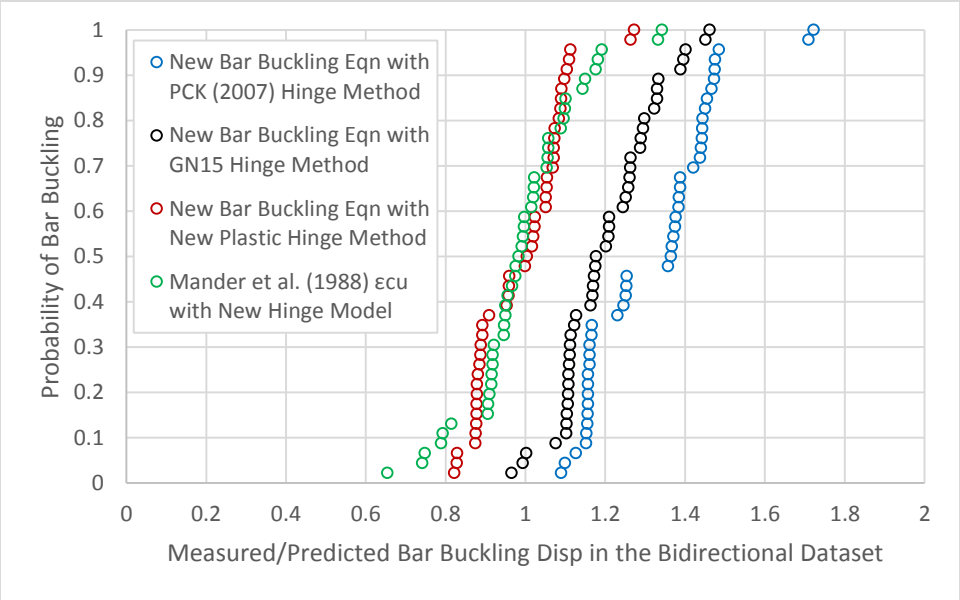

Figure 16-66. Bidirectional Dataset: Predictions for the Bar Buckling Peak Tensile Disp. with the Noted Hinge Methods

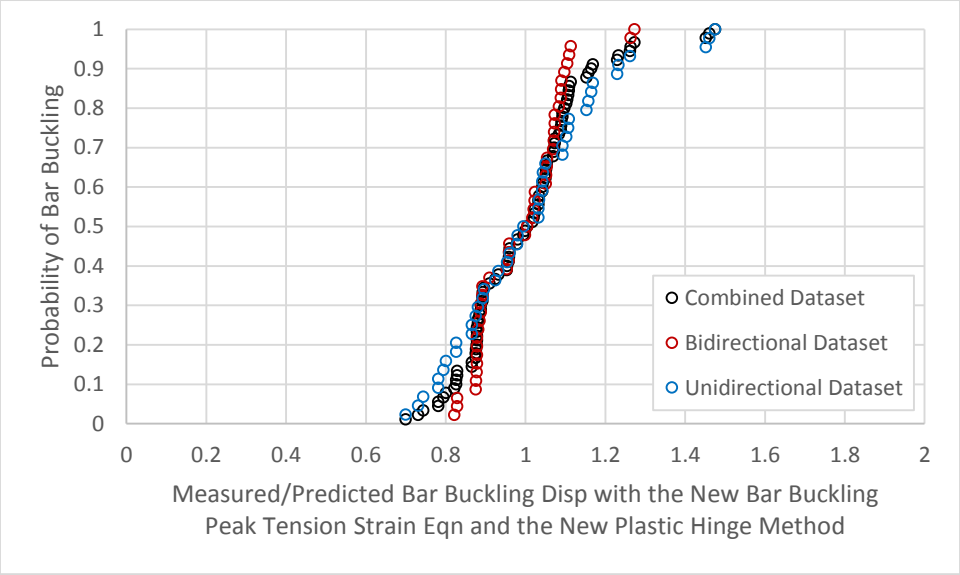

Figure 16-67. Predictions for the Bar Buckling Peak Tensile Displacement in the Noted Datasets

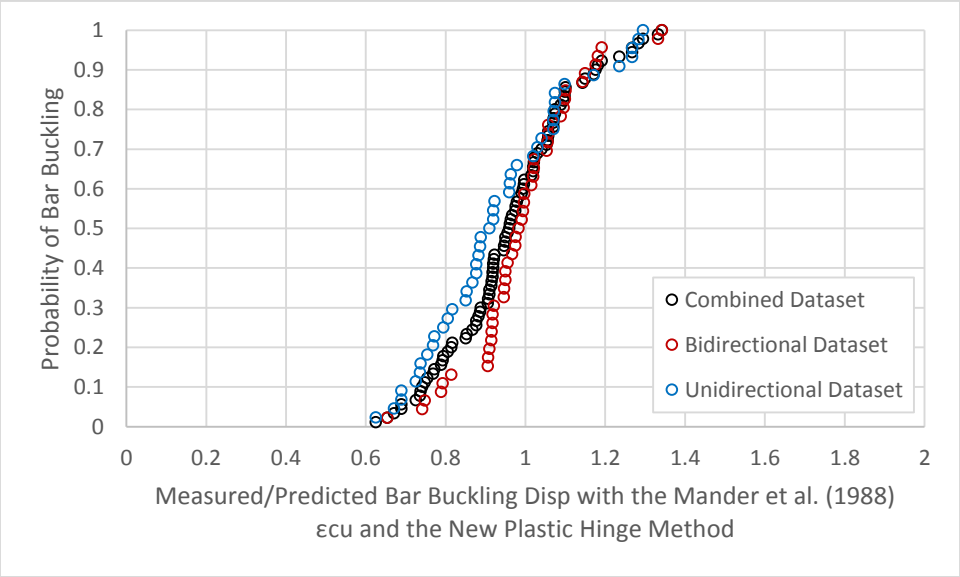

Figure 16-68. Predictions for the Bar Buckling Peak Tensile Displacement in the Noted Datasets

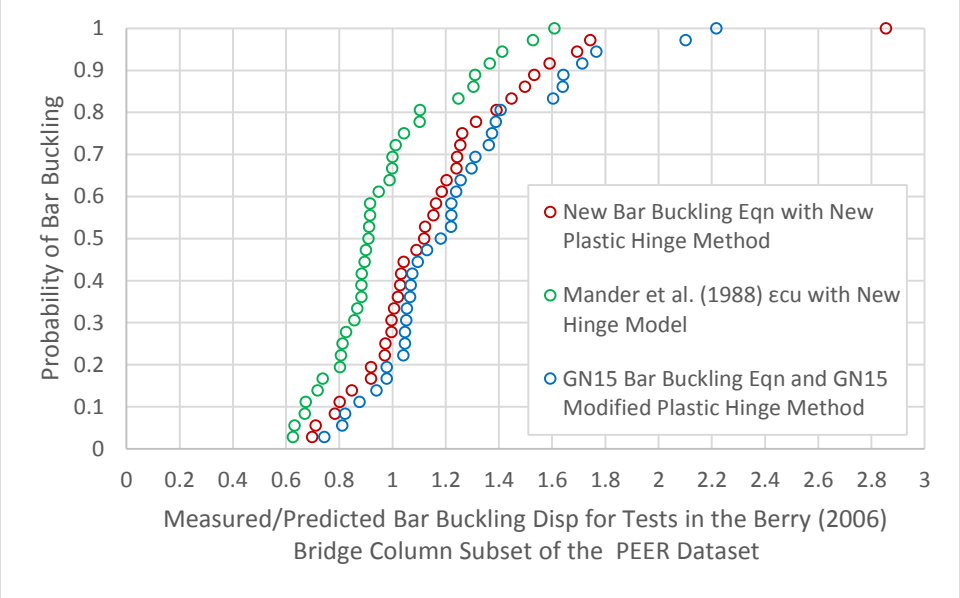

Figure 16-69. Bar Buckling Displacement Predictions within the (Berry 2006) PEER Column Dataset

References

Alemdar, Z. F. 2010. *Plastic Hinging Behavior of Reinforced Concrete Bridge Columns.* PhD Thesis, Lawrence, Kansas: University of Kansas, 308 pp.

Babazadeh, A., R. Burgueño, and P Silva. 2015. "Use of 3D Finite-Element Models for Predicting Intermediate Damage Limit States in RC Bridge Columns." *J. Struct. Eng.* 141 (10): 04015012.

Baker, A. L. L. , and A. M. N. Amarakone. 1964. "Inelastic hyperstatic Frame Analysis." *Proc. of the Int. Symposium on the Flexural Mechanics of Reinforced Concrete.* Miami: ASCE-ACI. 85-142.

Bazaez, Ramiro, and Peter Dusicka. 2016. "Cyclic Loading for RC Bridge Columns Considering Subduction Megathrust Earthquakes." *Journal of Bridge Engineering* 21 (5). doi:10.1061/(ASCE)BE.1343-5592.0000891.

Berry, M. P. 2006. *Performance Modeling Strategies for Modern Reinforced Concrete Bridge Columns.* PhD. Thesis, Seattle, Washington: University of Washington.

Berry, M. P., D. E. Lehman, and L. N. Lowes. 2008. "Lumped-Plasticity Models for Performance Simulation of Bridge Columns." *ACI Struct. J.* 105 (3): 270-279.

Bousias, S. N., G. Verzelettim, M. N. Fardis, and E. Gutierrez. 1995. "Load Path Effects in Column Biaxial Bending with Axial Force." *J. Eng. Mechanics* 121 (5): 596-605.

Corley, W. G. 1966. "Rotational Capacity of Reinforced Concrete Beams." *Journal of the Structural Division, ASCE* 92 (ST5): 121-146.

Dhakal, R. P., and K. Maekawa. 2002. "Modeling for Postyield Buckling of Reinforcement." *J. Struct. Eng.* 128 (9): 1139-1147.

Feng, Y, M. J. Kowalsky, and J. M. Nau. 2015. "Finite-Element Method to Predict Reinforcing Bar Buckling in RC Structures." *J. Struct. Eng.* 141 (5): 04014147.

Feng, Y., M. J. Kowalsky, and J. M. Nau. 2015a. "Effect of Seismic Load History on Deformation Limit States for Longituidnal Bar Buckling in RC Circular Columns." *J. Struct. Eng.* 141 (8): 04014187.

FIB Task Group on Bond Models. 2000. "Bond of Reinforcement in Concrete." Bulletin 10, Lausanne, Switzerland, 427 pp.

Goodnight, J. C., M. J. Kowalsky, and J. M. Nau. 2013. "Effect of Load History on Performance Limit States of Circular Bridge Columns." *J. Bridge. Eng.* 18 (12): 1383-1396.

Goodnight, J. C., M. J. Kowalsky, and J. M. Nau. 2015a. "Modified Plastic Hinge Method for Circular RC Bridge Columns." *J. Struct. Eng.* (Under Review).

Goodnight, J. C., M. J. Kowalsky, and J. M. Nau. 2015b. "Performance Strain Limits for Circular RC Bridge Columns." *EQ Spectra* (Accepted).

Goodnight, J. C., M. J. Kowalsky, and J. M. Nau. 2015. *The Effects of Load History and Design Variables on Performance Limit States of Circular Bridge Columns.* Juneau, AK: Alaska Deptartment of Transportation and Public Facilities, Volumes 1 and 2.

Hines, E. M., and F. Seible. 2002. *Experimental Spread of Plasticity in Reinforced Concrete Bridge Piers.* Structural Systems Research Project 2001/08, San Diego, La Jolla, California: University of California.

Hines, E. M., J. I. Restrepo, and F. Seible. 2004. "Force-Displacement Characterization of Well Confined Bridge Piers." *ACI Struct. J.* 104 (4): 537-548.

Ketchum, M., V. Chang, and T. Shantz. 2004. *Influence of Design Ground Motion Level on Highway Bridge Costs.* Report PEER 6D01, Berkeley, CA: Pacific Earthquake Engineering Research Center, University of California Berkeley.

Kowalsky, M. J. 2000. "Deformation Limit States for Circular Reinforced Concrete Bridge Columns." *J. Struct. Eng.* 126 (8): 869-878.

Kowalsky, M. J., and M. J. N. Priestley. 2000. "Improved Analytical Model for Shear Strength of Circular Reinforced Concrete Columns in Seismic Regions." *ACI Struct. J.* 97 (3): 388-396.

Mander, J. B. 1983. *Seismic Design of Bridge Piers.* PhD Thesis, Christchurch, New Zealand: University of Canterbury.

Mander, J. B., M. J. N. Priestley, and R. Park. 1988. "Theoretical Stress-Strain Model for Confined Concrete." *J. Struct. Eng.* 144 (8): 1804-1826.

Mattock, A. H. 1967. "Discussion of "Rotational Capacity of Reinforced Concrete Beams" by Corley, W. G. (1966)." *Jornal of the Structural Division, ASCE* 93 (ST2): 519-522.

Mazzoni, S., and J. P. Moehle. 2001. "Seismic Response of Beam-Column Joints in Double-Deck Reinforced Concrete Bridge Frames." *ACI Struct. J.* 98 (3): 259-269.

Montejo, L. A., and M. J. Kowalsky. 2007. *CUMBIA - Set of Codes for the Analysis of Reinforced Concrete Members.* Technical Report No. IS-07-01, Raleigh: North Carolina State University.

Osorio, E., J. M. Bairán, and A. R. Marí. 2012. "Effects of Biaxial Shear Loading on the Seismic Response of RC Columns." *Proceedings of the 15th World Conference on Earthquake Engineering.* Lisbon, Portugal.

Park, R., and T. Paulay. 1975. *Reinforced Concrete Structures.* New York: Wiley.

Park, R., M. J. N. Priestley, and W. D. Gill. 1982. "Ductility of Square-Confined Concrete Columns." *Journal of the Structural Division, ASCE* 108 (ST4): 929-950.

Paulay, T., and M. J. N. Priestley. 1992. *Seismic Design of Reinforced Concrete and Masonry Buildings.* New York: Wiley.

Priestley, M. J. N., and R. Park. 1987. "Strength and Ductility of Concrete Bridge Columns under Seismic Loading." *ACI Struct. J.* 84 (1): 61-76.

Priestley, M. J. N., F. Seible, and G. M. Calvi. 1996. *Seismic Design and Retrofit of Bridges.* New York: John Wiley & Sons.

Priestley, M. J. N., G. M. Calvi, and M. J. Kowalsky. 2007. *Displacement-Based Seismic Design of Structures.* Pavia: IUSS Press.

Rutledge, S. T., M. J. Kowalsky, R. Seracino, and J. M. Nau. 2013. "Repair of Reinforced Concrete Bridge Columns Containing Buckled and Fractured Reinforcement by Plastic Hinge Relocation." *J. Bridge Eng.* 19 (8): A4013001.

Sawyer, H. A. 1964. "Design of Reinforced Concrete Frames for Two Failure States." *Proc. of the Int. Symposium on the Flexural Mechanics of Reinforced Concrete.* Miami: ASCE-ACI. 405-431.

Scott, M. H., and G. L. Fenves. 2006. "Plastic Hinge Integration Methods for Force-Based Beam-Column Elements." *J. Struct. Eng.* 132 (2): 244-252.

Terzic, V., and B. Stojadinovic. 2015. "Evaluation of Post-Earthquake Axial Load Capacity of Circular Bridge Columns." *ACI Struct. J.* 112 (1): 23-33.

Tsuno, K., and R. Park. 2004. "Experimental Study of Reinforced Concrete Bridge Piers Subjected to Bi-Directional Quasi-Static Loading." *J. Struct. Eng. / Earthquake Eng. JSCE* 21 (1): 11-26.

Wong, Y. L., T. Paulay, and M. J. N. Priestley. 1993. "Response of Circular Reinforced Concrete Columns to Multi-Directional Seismic Attack." *ACI Struct. J.* 90 (2): 180-191.

Wong, Y-L., T. Paulay, and M. J. N. Priestley. 1993. "Response of Circular Reinforced Concrete Columns to Multi-Directional Seismic Attack." *ACI Struct. J.* 90 (2): 180-191.

Zhao, J., and S. Sritharan. 2007. "Modeling of Strain Penetration Effects in Fiber-Based Analysis of Reinforced Concrete Structures." *ACI Struct. J.* 104 (2): 133-141.